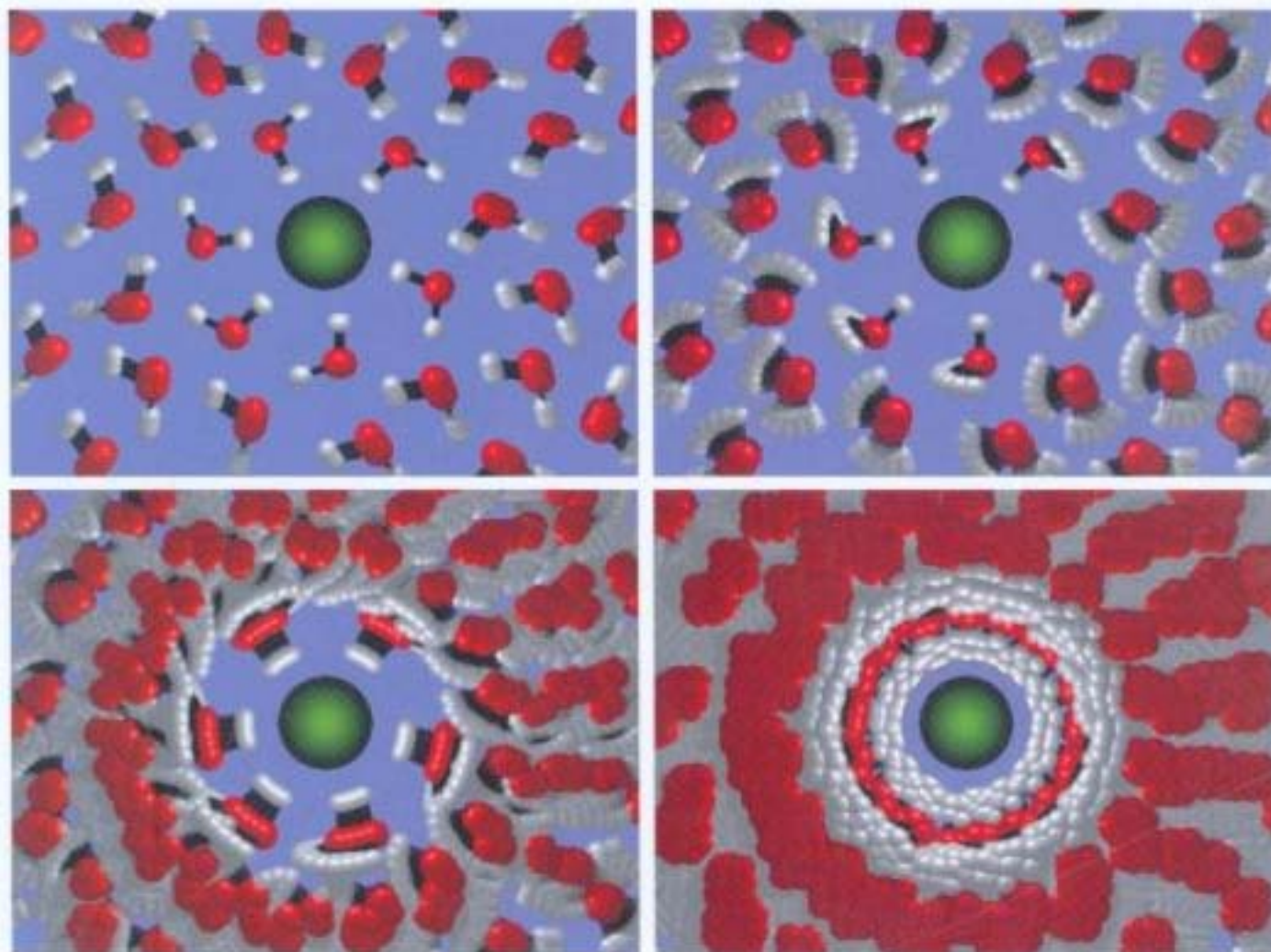




FEMTOCHEMISTRY and FEMTOBIOLOGY

Ultrafast Events in Molecular Science



Editors
Monique M. Martin
James T. Hynes

ELSEVIER B.V. Sara Burgerhartstraat 25 P.O. Box 211, 1000 AE Amsterdam The Netherlands	ELSEVIER Inc. 525 B Street, Suite 1900 San Diego, CA 92101-4495 USA	ELSEVIER Ltd The Boulevard, Langford Lane Kidlington, Oxford OX5 1GB UK	ELSEVIER Ltd 84 Theobalds Road London WC1X 8RR UK
--	---	---	---

© 2004 Elsevier B.V. All rights reserved.

This work is protected under copyright by Elsevier B.V., and the following terms and conditions apply to its use:

Photocopying

Single photocopies of single chapters may be made for personal use as allowed by national copyright laws. Permission of the Publisher and payment of a fee is required for all other photocopying, including multiple or systematic copying, copying for advertising or promotional purposes, resale, and all forms of document delivery. Special rates are available for educational institutions that wish to make photocopies for non-profit educational classroom use.

Permissions may be sought directly from Elsevier's Rights Department in Oxford, UK: phone (+44) 1865 843830, fax (+44) 1865 853333, e-mail: permissions@elsevier.com. Requests may also be completed on-line via the Elsevier homepage (<http://www.elsevier.com/locate/permissions>).

In the USA, users may clear permissions and make payments through the Copyright Clearance Center, Inc., 222 Rosewood Drive, Danvers, MA 01923, USA; phone: (+1) (978) 7508400, fax: (+1) (978) 7504744, and in the UK through the Copyright Licensing Agency Rapid Clearance Service (CLARCS), 90 Tottenham Court Road, London W1P 0LP, UK; phone: (+44) 20 7631 5555; fax: (+44) 20 7631 5500. Other countries may have a local reprographic rights agency for payments.

Derivative Works

Tables of contents may be reproduced for internal circulation, but permission of the Publisher is required for external resale or distribution of such material. Permission of the Publisher is required for all other derivative works, including compilations and translations.

Electronic Storage or Usage

Permission of the Publisher is required to store or use electronically any material contained in this work, including any chapter or part of a chapter.

Except as outlined above, no part of this work may be reproduced, stored in a retrieval system or transmitted in any form or by any means, electronic, mechanical, photocopying, recording or otherwise, without prior written permission of the Publisher.

Address permissions requests to: Elsevier's Rights Department, at the fax and e-mail addresses noted above.

Notice

No responsibility is assumed by the Publisher for any injury and/or damage to persons or property as a matter of products liability, negligence or otherwise, or from any use or operation of any methods, products, instructions or ideas contained in the material herein. Because of rapid advances in the medical sciences, in particular, independent verification of diagnoses and drug dosages should be made.

First edition 2004

Library of Congress Cataloging in Publication Data

A catalog record is available from the Library of Congress.

British Library Cataloguing in Publication Data

A catalogue record is available from the British Library.

ISBN: 0 444 51656 5

© The paper used in this publication meets the requirements of ANSI/NISO Z39.48-1992 (Permanence of Paper).
Printed in The Netherlands.

CONTENTS

1. GAS PHASE AND CLUSTERS

Ultrafast electron diffraction and transient complex structures - From gas phase to crystallography A.-H. Zewail	3
Experimental and theoretical studies of pump-probe electron diffraction: time-dependent and state-specific signatures in small cyclic molecules P.-M. Weber, R.-C. Dudek, S. Ryu and R.-M. Stratt	19
Cluster size effects on bound excited states of SO ₂ T.-E. Dermota, D.-P. Hydustry, N.-J. Bianco and A.-W. Castleman, Jr.	25
Micro solvation dynamics at the passage of conical intersections observed in argon clusters of excited tetrakis(dimethylamino)ethylene S. Sorgues, J.-M. Mestdagh, E. Gloaguen, J.-P. Visticot and B. Soep	29
Femtosecond photon echo measurements of electronic coherence relaxation of I ₂ in the presence of He, Ar, N ₂ , O ₂ , C ₃ H ₈ V.-V. Lozovoy, M. Comstock, I. Pastirk and M. Dantus	33
Probing reaction dynamics with Rydberg states: The ring opening reaction of 1,3-cyclohexadiene N. Kuthirummal and P.-M. Weber	37
Femtosecond photoelectron spectroscopy of trans-Stilbene C. Dietl, E. Papastathopoulos and G. Gerber	41
Azobenzene photoisomerization: Two states and two relaxation pathways explain the violation of Kasha's rule T. Schultz, S. Ullrich, J. Quenneville, T.-J. Martinez, M.-Z. Zgierski, A. Stolow	45
Comparison of ultrafast photoninduced processes in indole (NH ₃) _n and indole (H ₂ O) _n clusters H. Lippert, V. Stert, C.-P. Schulz, I.-V. Hertel and W. Radloff	49
How to disentangle evaporation and picosecond excited-state dynamics in molecular clusters S. Martrenchard, C. Dedonder-Lardeux and C. Jouvet	53

Vibrational relaxation of photoexcited Na ₃ F V. Blanchet, J.-M. L'Hermite, A. Le Padellec, B. Lamory and P. Labastie	57
Femtosecond infrared strong field ionisation of metal clusters produced by kHz laser ablation M. Smits, C.-A. de Lange, A. Pegoraro, D.-M. Rayner and A. Stolow	61
The structure of carboxylic acid dimers: results by time-resolved femtosecond degenerate four-wave mixing spectroscopy V.-V. Matylitsky, M.-F. Gelin, C. Riehn and B. Brutschy	65
Collision induced rotational energy transfer. A new scaling law probed by fs CARS G. Knopp, P. Beaud, P. Radi, M. Tulej and T. Gerber	69
Different schemes and recent results for high-resolution rotational coherence spectroscopy with picosecond and femtosecond laser pulses C. Riehn, V.-V. Matylitsky, A. Weichert, M.-F. Gelin, W. Jarzeba and B. Brutschy	73
 2. QUANTUM CONTROL	
Shaped laser pulses acting as photonic reagents H. Rabitz	79
Energy flow in photosynthetic light harvesting: spectroscopy and control W. Wohlleben, T. Buckup, J.-L. Herek, H. Hashimoto, R.-J. Cogdell and M. Motzkus	91
Control of nonlinear optical excitation with multiphoton intrapulse interference J.-M. Dela Cruz, I. Pastirk, V.-V. Lozovoy, K.-A. Walowicz and M. Dantus	95
Infrared femtochemistry: Vibrationally induced molecular dissociation and its control employing shaped fs MIR laser pulses T. Witte, L. Windhorn, J.-S. Yeston, D. Proch, M. Motzkus and K.-L. Kompa	103
Spectrally resolved femtosecond two-colour three-pulse photon echoes for studies of molecular dynamics: influence of pulse wavelengths and pulse sequence Lap Van Dao, C. Lincoln, M. Lowne and P. Hannaford	107
Closed loop optimization of the ionization process in NaK. Learning from the optimal pulse shape A. Lindinger, C. Lupulescu, M. Plewicky, S.-M. Weber, A. Merli, F. Vetter and L. Wöste	111

Femtosecond dynamics of NaI and CsI aggregated with CH ₃ CN E. Charron, D.-T. Stibbe and A. Suzor-Weiner	115
Control of the production of highly charged ions in femtosecond laser cluster fragmentation S. Zamith, Y. Ni, S.-A. Aseyev, E. Springate, M.-J.J Vrakking	119
Free phase optimization of CpMn(CO) ⁺ ₂ as a fragment of CpMn(CO) ₃ by means of shaped femtosecond laser pulses C. Lupulescu, A. Lindinger, A. Merli, M. Plewicky and L. Wöste	123
Adiabatic control of bond distance in selective non Franck-Condon transitions I.-R. Sola, B.-Y. Chang, V.-S. Malinovsky and J. Santamaria	127
Adiabatic rapid passage in molecules in solution excited by an intense ultrashort chirped pulse B.-D Fainberg and V.-A. Gorbunov	131
Ultrafast non-Franck-Condon transitions: is it possible ? N.-E. Henriksen and K.-B. Møller	135
Quantum control beyond spectral interference and population control: Can resonant intense laser pulses freeze the population ? M. Wollenhaupt, A. Assion, O. Graefe, C. Horn, D. Liese, C. Sarpe-Tudoran, M. Winter and T. Baumert	139
Ultrafast time reversal mirror at 800 nm based on photosensitive naphthalocyanine doped solids J.-P. Galaup, S. Fraigne, J.-L. Le Gouët, J.-P. Likforman and M. Joffre	143
3. HYDROGEN-BOND DYNAMICS, WATER AND PROTON TRANSFER	
Ultrafast motion of water molecules near ions H.-J. Bakker, M.-F. Kropman and A.W. Omta	149
Ultrafast vibrational dynamics of hydrogen-bonded dimers in solution T. Elsaesser, K. Heyne, N. Huse and E.-T.J. Nibbering	157
2D photon-echo spectroscopy of hydrogen-bond dynamics in liquid water M.-S. Pshenichnikov, S. Yeremenko and D.-A. Wiersma	165
Three-dimensional spectroscopy of vibrational energy relaxation in liquids Z. Wang, A. Pakoulev, Y. Pang and D.-D. Klott	169

On ultrafast IR spectroscopy in water K.-B. Møller, R. Rey and J.-T. Hynes	177
Isotope effect on the IVR dynamics after ultrafast IR excitation of the hydrogen bond in salicylaldehyde M. Petkovic and O. Kühn	181
Femtosecond solvation dynamics of hydrogen-bonding complexes E. Pines, D. Pines, Y.-Z. Ma and G.-R. Fleming	185
Bimodal intermolecular proton transfer in water: photoacid-base pairs studied with ultrafast infrared spectroscopy M. Rini, O.-F. Mohammed, B.-Z. Magnes, E. Pines and E.-T.J. Nibbering	189
Symmetry breaking wavepacket motion and absence of deuterium isotope effect in ultrafast excited state proton transfer S. Lochbrunner, K. Stock, C. Schrieffer and E. Riedle	193
Excited-state proton transfer dynamics of 6-hydroxyquinoline in acidic and alkaline aqueous solutions O. Poizat, G. Buntinx, E. Bardez and V. Alain	197
Ultrafast intermolecular proton transfer from 10-hydroxy-camptothecin S. Ashkenazi, P. Leiderman, D. Huppert, K.-M. Solntsev and L.-M. Tolbert	201
Reaction dynamics of aqueous peroxyxynitrite and peroxyxynitrous acid J. Thøgersen, D. Madsen, J. Larsen, S.-J. Knak Jensen and S.-R. Keiding	207

4. SOLVATION PHENOMENA, FLUIDS AND LIQUIDS

Dynamics of water at surface of complex systems: Study of aqueous micelles and proteins S. Pal, S. Bandyopadhyay, S. Balasubramanian and B. Bagchi	213
The solvated electron in methanol. Novel time- and frequency-resolved pump-probe spectroscopy of short-lived precursors A. Thaller, R. Laenen and A. Laubereau	221
Femtosecond dynamics of the solvated electron in water studied by time-resolved Raman Spectroscopy M. Mizuno, S. Yamaguchi and T. Tahara	225
Femtosecond transient spectroscopy of the photoionization of indole in water T. Bizjak, P.-B. Bisht, S. Lochbrunner and E. Riedle	229

Short-time water caging and transient electron-OH couplings in liquid phase B. Brozek-Pluska, A. Hallou, D. Glijer, B. Charles, Y. Gauduel	233
Fluorescence dynamics of coumarin C522 in water and in cyclodextrin cavity P. Bodis, I. Bugár, T. Palszegi, D. Velic and D. Chorvát	237
Solvation dynamics of electron in ethylene glycol at 300 K B. Soroushian, I. Lampre, S. Pommeret and M. Mostafavi	241
Solvation dynamics of coumarin 153 in benzene-acetonitrile and benzene-methanol mixtures: a Molecular Dynamics study M. Kozinski, W. Jarzeba and R. Vuilleumier	245
Femtosecond dynamics of excess electrons in a molten Na-NaBr system H. Brands, N. Chandrasekhar, H. Hippler and A.-N. Unterreiner	249
Electronic solvation dynamics in non-polar supercritical fluids P. Larrégaray, A. Cavina and M. Chergui	253
Femtosecond photolysis of CH ₂ I ₂ in supercritical fluids: Competition between photodissociation and isomerization C. Grimm, J. Zerbs, M.-F. Kling and J. Schroeder	257
Femtosecond degenerate four-wave mixing of cycloalkanes H.-M. Frey, D. Kummlı, M. Keller, R. Leist and S. Leutwyler	261
Femtosecond liquid dynamics studied by two-dimensional Raman spectroscopy K.-J. Kubarych, C.-J. Milne and R.-J.D. Miller	265

5. RELAXATION AND REACTIONS IN SOLUTION

The impact of different molecular environments and chemical substitution on timescales of intramolecular vibrational energy redistribution in aromatic molecules B. Abel	271
Dihydroazulene molecular switches: Via ultrafast spectroscopy to the first bidirectional switch U. Schmidhammer, V. De Waele, G. Buntinx and E. Riedle	279
The ultrafast dynamics of some photochromic naphthopyrans R.-G. Brown, M. Maafi, P. Foggi and L. Bussotti	283
Femtochemistry of organic Peroxides: Ultrafast formation and decarboxylation of carbonyloxy radicals B. Abel, M. Buback, C. Grimm, M. Kling, S. Schmatz and J. Schroeder	287

Femto- and nano-second photoionization of sterically hindered phenols in non-protic solvents – Antithetical product formation R. Hermann, T. Leichtner, S. Naumov, O. Brede	291
Coherent nuclear motion of reacting excited-state molecules in solution observed by ultrafast two color pump-probe spectroscopy S. Takeuchi and T. Tahara	295
Probing of coherent oscillations by multiphoton ionization S.-A. Trushin, W. Fuß, W.-E. Schmid and T. Yatsushashi	299
Coherences in the time-resolved fluorescence of the TCNE-HMB complex: simulation versus experiment A.-V. Pisiakov, M.-F. Gelin and W. Domcke	303
Quantum-dynamical modeling of ultrafast processes in complex molecular systems : multiconfigurational system-bath dynamics using Gaussian wavepackets I. Burghardt and G.-A. Worth	307
A simple approach for the calculation of femtosecond pump-probe spectra for electronically nonadiabatic systems M.-F. Gelin, A.-V. Pisiakov and W. Domcke	311
Ultrafast charge separation and radiationless relaxation processes from S_2 excited electronic states of directly linked Zinc-porphyrin-acceptor dyads S. Taniguchi, N. Mataga, H. Chosrowjan, N. Yoshida and A. Osuka	315
Femtosecond times-resolved studies on bimolecular electron transfer processes S. Pagès, B. Lang and E. Vauthey	319
Ultrafast photoinduced charge transfer in fluorinated derivatives of DMABN S. Murali, P. Changenet-Barret, C. Ley, P. Plaza, W. Rettig, M.-M. Martin and A.-I. Tolmachev	323
Influence of solute-solvent interactions on the quenching dynamics of perylene derivatives in an electron donating solvent A. Morandeira, A. Fürstenberg and E. Vauthey	327
Effect of excitation wavelength on the charge recombination dynamics of excited donor acceptor complexes O. Nicolet, A.-I. Ivanov and E. Vauthey	331

6. TIME-RESOLVED X-RAYS

- Time-resolved x-ray diffraction from small molecules in solution
M. Wulff, M. Lorenc, A. Plech, H. Ihee, S. Bratos, F. Mirloup and R. Vuilleumier 337
- Time-dependent x-ray scattering signal of laser heated liquids
F. Mirloup, R. Vuilleumier, S. Bratos, M. Wulff and A. Plech 349
- Structural dynamics and electronic structure changes probed with lasers and X-rays
W. Gawelda, M. Saes, M. Kaiser, A. Tarnovsky, S.-L. Johnson, D. Grolimund, R. Abela, M. Chergui and C. Bressler 353

7. PROTEIN DYNAMICS

- Multidimensional and dual frequency infrared analogues of NMR: Applications to peptides and isotopomers of secondary structures
I.-V. Rubtsov, J. Wang, C. Fang, M.-L. Cornelio, Y.-S. Kim, A.-K. Chamley, A.-B. Smith III, S. Decatur and R.-M. Hochstrasser 365
- Ultrafast conformational dynamics in light triggered cyclic peptides
W. Zinth, A. Sieg, T. Schrader, S. Spörlein, P. Hamm, J. Bredenbeck, J. Helbing, C. Renner, L. Moroder, H. Carstens, P. Tavan and J. Wachtveitl 373
- Femtosecond visible pump – midinfrared probe setup for the study of protein dynamics. Isomerization in Photoactive Yellow Protein
M.-L. Groot, L.-J.G.W. van Wilderen, D.-S. Larsen, M.-A. van der Horst, I.-H.M. van Stokkum, K.-J. Hellingwerf and R. van Grondelle 381
- Transient two-dimensional infrared spectroscopy – towards measuring ultrafast structural dynamics
J. Bredenbeck, J. Helbing and P. Hamm 387
- Reaction driven modes in carboxymyoglobin: pathway of force transduction for functionally relevant protein motions
M. Armstrong, J.-P. Ogilvie, M.-L. Cowan, A.-M. Nagy and R.-J.D. Miller 391
- Ultrafast studies of ferric complexes of Hemoglobin I from *Lucina pectinata*
E. Ramirez, C. Ramos, M. Rodriguez, R. Pietri, M. Chergui and J. Lopez-Garriga 395

8. PRIMARY PROCESSES IN PHOTOBIOLOGY

- The mechanism of energy transfer and trapping in Photosystem I
H.-M. Vaswani, M. Yang, A. Damjanovic and G.-R. Fleming 401
- Ultrafast photoreaction dynamics in protein nanospaces (PNS) as revealed by fs fluorescence dynamics studies on photoactive yellow protein (PYP) and related systems
N. Mataga, H. Chosrowjan, S. Taniguchi, N. Hamada and F. Tokunaga 409
- Isomerization process in the native and denatured photoactive yellow protein probed by subpicosecond absorption spectroscopy
P. Changenet-Barret, A. Espagne, P. Plaza, M.-M. Martin and K.-J. Hellingwerf 417
- Chemical structure effect on the excited-state relaxation dynamics of the PYP chromophore
A. Espagne, P. Changenet-Barret, S. Charier, J.-B. Baudin, L. Jullien, P. Plaza and M.-M. Martin 421
- Ultrafast excited state dynamics in green fluorescent protein chromophore
A. Toniolo, S. Olsen, L. Manohar and T.-J. Martínez 425
- Ultrafast dynamics in the excited state of wild-type Green Fluorescent Protein
K. Winkler, J. Lindner, M. Seidel and P. Vöhringer 433
- Excited-state dynamics in the Green Fluorescent Proteins : the cases of wild type, UV-Mutant, and isolated synthetic analogues of the GFP chromophore
P. Didier, L. Guidoni, G. Schwalbach, A. Follenius-Wund, C. Pigault, M. Bourotte and J.-Y. Bigot 437
- Fast excited-state reaction in the photoreceptor pigment-protein complex of the ciliate *Blepharisma japonicum*
M. Mahet, P. Plaza, M.-M. Martin, G. Checcucci and F. Lenci 441
- Excited state dynamics of the carotenoid peridinin
T. Polivka, D. Zigmantas, R.-G. Hiller and V. Sundström 445
- Pump-probe and pump-deplete-probe spectroscopy on carotenoids with N=9-15
T. Buckup, J. Savolainen, W. Wohlleben, H. Hashimoto, R.-J. Cogdell, J.-L. Herek and M. Motzkus 453
- Ultrafast photophysics of the protonated Schiff base of retinal in alcohols studied by femtosecond fluorescence up-conversion
G. Zgrablic, K. Voïtchovsky, M. Kindermann, M. Chergui and S. Haacke 457

9. DYNAMICS IN DNA, POLYMERS AND MACROMOLECULES

- Ultrafast excited-state dynamics in DNA and RNA polymers
B. Cohen, C.-E. Crespo-Hernández, P.-M. Hare and B. Kohler 463
- Femtosecond fluorescence studies of DNA constituents
T. Gustavsson, A. Sharonov, S. Marguet, D. Onidas and D. Markovitsi 471
- Ultrafast vibrational spectroscopy on DNA
O.-F.A. Larsen and S. Woutersen 475
- Ultrafast dynamics of normal and damaged DNA
M.-M. Somoza and M.-A. Berg 479
- Sub-5-fs pulse generation from a noncollinear optical parametric amplifier and its application to ultrafast dynamics in polymers
T. Kobayashi 483
- Unveiling electronic phase relaxation in a strongly disordered conjugated polymer
J. Sperling, F. Milota, A. Torschanoff, V. Szöcs, L. Kuna, C. Benesch and H.-F. Kauffmann 491
- Energy transfer in light-harvesting Zn porphyrin dendrimers
J. Larsen, J. Andersson, T. Polívka, J. Sly, M.-J. Crossley, V. Sundström and E. Åkesson 495
- Femtosecond fluorescence upconversion studies of chiral self-assembled supramolecules in solution
P. Toele, H. Wang, H. Zhang, M. Glasbeek, J.-J. van Gorp and E.-W. Meijer 499
- Energy transfer process in dendrimers containing a perylene-terrylene donor-acceptor system investigated by femtosecond multicolor transient absorption spectroscopy
G. Schweitzer, S. Jordens, G. De Belder, M. Lor, E. Fron, K. Müllen and F.-C. De Schryver 503

10. SURFACES, INTERFACES, NANOSTRUCTURES AND SOLIDS

- Femtosecond time-resolved studies on spectral sensitization of AgBr nanocrystals
K. Yoshihara, I.-V. Rubtsov, K. Ebina, F. Satou, Ji-Won Oh, S. Kumazaki, T. Suzumoto and T. Tani 509
- Ultrafast scattering of electrons in TiO₂
M. Bonn, F. Wang, J. Shan, T.-F. Heinz and E. Hendry 517

- Influence of molecular spacers on ultrafast heterogeneous electron transfer
R. Ernstorfer, L. Gundlach, S. Felber, C. Zimmermann, R. Eichberger, Q. Wei,
E. Galoppini and F. Willig 521
- Stepwise electron injection in the dye-sensitized nanocrystalline films of ZnO and
TiO₂ with novel coumarin dye
A. Furube, R. Katoh, T. Yoshihara, K. Hara, S. Murata, H. Arakawa and
M. Tachiya 525
- Heterogeneous electron transfer probed with femtosecond two-photon
photoemission spectroscopy
I. Gundlach, R. Ernstorfer, C. Zimmermann, R. Eichberger, S. Felber, L. Töben,
E. Galoppini, Q. Wei and F. Willig 529
- Time resolved ultrafast energy transfer from electrons photoexcited in Pt(111) to
adsorbed CO during photodesorption
F. Fournier, W. Zheng, S. Carrez, H. Dubost and B. Bourguignon 533
- Femtosecond fluorescence up-conversion microscopy: a new method to study
ultrafast dynamics in microstructures
T. Fujino and T. Tahara 537
- Solvation dynamics at water-ZrO₂ interfaces
A. Tortschanoff, E. Portuondo, F. van Mourik, J.-E. Moser, S. Steinemann
and M. Chergui 541
- Time-resolved absorption spectroscopy of metal nanoparticles in colloidal solution
I. Bugár, I. Capek, J. Ivan, L. Chitu, E. Majková and D. Chorvát 545
- Determination of femtosecond dephasing times of organic dyes confined in a single
spherical microparticle
P. Sandeep and P.-B. Bisht 549
- Femtosecond pump-probe investigation of primary photoinduced processes in
C₆₀/Sn nanostructures
S.-V. Chekalin, V.-O. Kompanets, N.-F. Starodubtsev, V. Sundström
and A.-P. Yartsev 553
- Elementary reaction steps of iodine enclosed into zeolites
A. Materny and G. Flachenecker 557
- Nonlinear spectroscopy study of vibrational self-trapping in hydrogen bonded
crystals
J. Edler and P. Hamm 561

PREFACE

This book reflects the heights of knowledge of ultrafast chemical processes attained in these early years of the XXIst century: the latest research in femtosecond and picosecond molecular processes in Chemistry and Biology, carried out around the world, is described here in more than 110 articles. The results were presented and discussed at the VIth International Conference on Femtochemistry, in Paris, France, from July 6 to July 10, 2003. The articles published here were reviewed by referees selected from specialists in the Femtochemistry community, guaranteeing a collective responsibility for the quality of the research reported in the next 564 pages.

Femtochemistry is an ever-growing field, where new research areas are constantly opening up, and one which both stimulates and accompanies the development of ultrafast technologies. The award of the Nobel Prize to Ahmed H. Zewail in 1999 testifies to the world-wide recognition of this field of Chemistry. Since the first Femtochemistry Conference, held in Berlin in 1993, the studies of primary molecular events have quickly expanded to include a large variety of molecular media ---isolated molecules and clusters in supersonic jets, solutions and liquids, polymers, solids and nanoparticles, nanostructures and surfaces--- and an increasing variety of molecular systems with a clear growth in the number of studies devoted to complex molecular ensembles and biological molecules. Progress in determining molecular routes and mechanisms as well as in femtosecond optical pulse shaping has helped to propel advances in the control of molecular dynamics, including complex molecular systems and biological molecules in condensed phases. The increasing interest in femtobiology and chemistry at the frontier with biology is an obvious indicator of the present impact of life sciences in our society. New materials and reactions at surfaces are also some of the relatively new topics that promise rapid developments. New methodologies and technologies for probing and following in real time molecular dynamical phenomena have appeared within the last ten years or so. These methods, based on multidimensional IR spectroscopies, ultrafast X-ray and electron diffraction techniques, are well represented in this book. Of ever-improving performance, they are now applied to the characterization of structural dynamics of an increasing number of chemical and biological systems.

This book reports the state of research in Femtochemistry and Femtobiology presented at Paris, at the Maison de la Chimie, in July 2003, representing the tenth anniversary of the

conference. The five previous meetings of the series were held in various cities of Europe : Berlin (1993) organized by Jörn Manz, Lausanne (1995) by Majed Chergui, Lund (1997) by Villy Sundström, Leuven (1999) by Frans De Schryver and Toledo (2001) by Abderrazzak Douhal. We wish to thank them all here for their help and support, with a particular acknowledgment to our immediate predecessor Abderrazzak Douhal who was so generous with his advice.

Among the novel research efforts presented at the Paris meeting were the Keynote Lecture given by Ahmed Zewail (USA) and the six Plenary Lectures given by Huib Bakker (The Netherlands), Herschel Rabitz (USA), Robin Hochstrasser (USA), Michael Wulff (France), Graham Fleming (USA) and Gerhard Ertl (Germany). We thank them all for their contributions.

We express our sincere thanks, for their generous contribution to the success of the meeting, to the distinguished senior scientists who chaired a session at the meeting : Savo Bratos (France), Guy Buntinx (France), A. Welford Castleman (USA), David Clary (England), Frans De Schryver (Belgium), Ken Eisenhal (USA), Yann Gauduel (France), Bertrand Girard (France), Joshua Jortner (Israel), Takayoshi Kobayashi (Japan), Karl Kompa (Germany), Jörn Manz (Germany), Claude Rullière (France).

We also express our gratitude to Pierre Potier, member of the French Academy of Sciences, President of the Foundation of Maison de la Chimie for having honored us by his presence at the opening of the Conference and his warm welcome to his "house". We also express our appreciation to Pascale Briand, who was the joint Director of Ecole Normale Supérieure for Sciences during the preparation of the meeting, for her support and her heartening and visionary talk at the opening session. Let both receive our warmest thanks.

The organization of the meeting in Paris gave us the opportunity to gather French experts of the field in a French Advisory Committee : Jean-Yves Bigot (Strasbourg), Savo Bratos (Paris), Guy Buntinx (Lille), Alain Fuchs (Orsay), Geoffrey Gale (Palaiseau), Yann Gauduel (Palaiseau), Bertrand Girard (Toulouse), Jean-Louis Martin (Palaiseau), Claude Rullière (Bordeaux), Benoit Soep (Saclay), Michael Wulff (Grenoble). Let them find here our deep thanks for their advice, contributions and help.

We are very grateful to the members of the Local Organization Committee: Irène Burghardt (Paris), Pascale Changenet-Barret (Paris), Guilhem Gallot (Palaiseau), Thomas Gustavsson (Saclay), Damien Laage (Paris), Isabelle Lampre (Orsay), Jean-Pierre Lemaistre (Paris), Christian Ley (Paris), Séverine Martrenchard (Orsay), Pascal Plaza (Paris) and

Rodolphe Vuillemier (Paris), who all worked hard in a collective effort so that the meeting would run smoothly, and who exhibited exemplary responsibility, solidarity and friendship. We also thank three PhD students and a postdoctoral fellow, Agathe Espagne, Mathilde Mahet, Olivier David and Bruno Nigro, for their active and cheerful help. We also express our gratitude to Dominique Ho Tin Hoe and Sandrine Faure who worked efficiently and enthusiastically, most often behind the scenes. We wish to emphasize Sandrine Faure's dedication in helping for the preparation of the present book and wish to thank her here once more. We are also thankful for the assistance at the Department of Chemistry of ENS-Paris, from Yvon Poncel, Anne Halloppe, Cristelle Berezaie, Daniel Jaouen and Jean-François Sallefranque.

Finally we gratefully acknowledge financial support from the following Agencies, Companies and Institutions : European Science Foundation, Scientific Programme on Femtochemistry and Femtobiology ULTRA, Conseil régional d'Ile-de-France, Fondation de la Maison de la Chimie, Ministère Délégué à la Recherche et aux Nouvelles Technologies, Département des Sciences Chimiques du CNRS, Département de Recherche sur l'Etat Condensé, les Atomes et les Molécules (DRECAM)/CEA/Saclay, Ecole Normale Supérieure, Département des Sciences Physiques et Mathématiques du CNRS, Section Ile-de-France de la Société Française de Chimie, Optoprim, Thalès-Laser, Photon Lines, Hamamatsu France, Laser 2000, Spectra-Physics, Coherent, Melles Griot Industrie, Newport Micro-Contrôle, Excel Technology France, Clark-MXR Europe-jyhoriba GmbH, Gibert-Joseph Book Store, Paris.

Monique M. Martin

UMR CNRS-ENS 8640, PASTEUR, Department of Chemistry, Ecole Normale Supérieure, Paris, France

James T. Hynes

UMR CNRS-ENS 8640, PASTEUR, Department of Chemistry, Ecole Normale Supérieure, Paris, France

and

Department of Chemistry and Biochemistry, University of Colorado, Boulder, Colorado, USA

December 2003

Ultrafast Electron Diffraction and Transient Complex Structures — From Gas Phase to Crystallography

Ahmed H. Zewail

Laboratory for Molecular Sciences, Arthur Amos Noyes Laboratory of Chemical Physics,
California Institute of Technology, Pasadena, California 91125 U.S.A.

ABSTRACT

This article highlights the recent development of ultrafast electron diffraction at Caltech. This development has made it possible to resolve transient structures both spatially (0.01 Å) and temporally (picosecond and now femtosecond) in the gas phase and condensed media, surfaces and crystals, with wide ranging applications. We also present some advances made in the studies of mesoscopic ionic solvation and biological dynamics and function.

1. ULTRAFAST ELECTRON DIFFRACTION (UED)

The dynamics of molecular systems has now been studied with atomic scale resolution, spanning the very small (NaI) to the very large (DNA, proteins and their complexes) [1]. X-ray and electron diffraction, if endowed with ultrafast temporal resolution, can provide the unique ability of revealing all internuclear coordinates of transient structures with very high spatial resolution. In our laboratory, the method of choice has been ultrafast electron diffraction, for the following reasons: First, the cross-section for electron scattering is six orders of magnitude larger compared to x-ray scattering. Second, UED experiments are ‘tabletop’ scale and can be implemented with ultrafast (femtosecond and picosecond) laser sources. Third, electrons are less damaging to specimens per useful elastic scattering event. Fourth, electrons, because of their short penetration depth arising from strong interaction with matter, can reveal transient structures in gases, surfaces and (thin) crystals.

The development of UED has evolved through different phases. The “dreaming phase” was conceptual and was followed by technical and theoretical advances in order to develop the methodology and obtain our first UED images—the “exploration phase”. The two phases culminated in the breakthrough developments (in 2001) of the third-generation apparatus (UED-3) for the gas phase [2] and (in 2003) the fourth-generation apparatus (UED-4) for the condensed phase and biological systems [3, 4]. These two generations launched the “explosion phase”, where we have been able to image complex molecular structures in the four dimensions of space and time with atomic-scale resolutions. The detection sensitivity of structural change is as low as 1% in the gas phase, and less than a monolayer in the

condensed phase. A variety of phenomena have been studied (Fig. 1), and a comprehensive review of the principles and some applications has recently been published [5]—original citations of developments are in [4, 5].

In UED, several disparate fields of study are involved: femtosecond pulse generation, electron beam optics, CCD detection systems, ultrahigh vacuum (UHV) technology and advanced computation. For UED-3 of isolated reactions, output from a femtosecond laser is split into a pump path and an electron-generation path. The pump laser proceeds directly into the vacuum chamber and excites a beam of molecules. The probe laser is directed toward a back-illuminated photocathode where the laser generates electron pulses via the photoelectric effect; the electrons are accelerated, collimated, focused, and then scattered by the isolated molecules. The resulting diffraction patterns are detected with a CCD camera, and the images are stored on a computer for analysis. The UED-3 apparatus is also equipped with a time-of-flight mass spectrometer (MS-TOF) to aid in the identification of species generated during the course of chemical reactions.

In UED-4, the new features include three interconnected UHV chambers—the sample preparation, load-lock and scattering chambers. The crystal is mounted on a computer-controlled goniometer for high-precision (0.005°) angular rotation; it can be cooled to a temperature of 100 K. The preparation chamber has sputtering and cleaning tools, and is also equipped with low-energy electron diffraction (LEED) and Auger spectroscopy (AS) for characterization of the crystal surface. Molecules can be studied on the surface either as physisorbed or chemically functionalized entities.

In UED-4, as in UED-3, we have characterized the electron and light pulses used. For the 30-keV electrons, we used *in situ* streaking techniques and, for light, the now standard autocorrelation method. We have obtained the fastest streaking speed of 140 ± 2 fs/pixel in UED-4, thus approaching the state-of-the-art in streak cameras. For the extraction field of 10 kV/mm, the spreading time is ~ 20 fs. The measured streaking broadening (“pulse width”) is 322 ± 128 fs. Using the same electron gun design, Jianming Cao, a former member of this group and now at Florida State University, has achieved ~ 300 fs pulses, albeit with a streaking speed of 250 fs/pixel. Dwayne Miller’s group in Toronto recently reported ~ 600 fs resolution. The coherence time of electrons is 10 fs or longer giving a coherence length on the order of a micron. The initiation laser pulse duration is typically 120 fs, and the overall temporal resolution is determined by the geometry of the experiment and the relative widths (shapes) and speeds of the two pulses (see Fig. 2).

The temporally and spatially resolved transient structures elucidated by UED include structures in radiationless transitions, structures in non-concerted organic reactions, structures in non-concerted organometallic reactions, structures of carbene intermediates, dynamic pseudorotary structures, non-equilibrium structures and conformational structures on complex energy landscapes, transient structures of surfaces and bulk crystals, and solid-to-

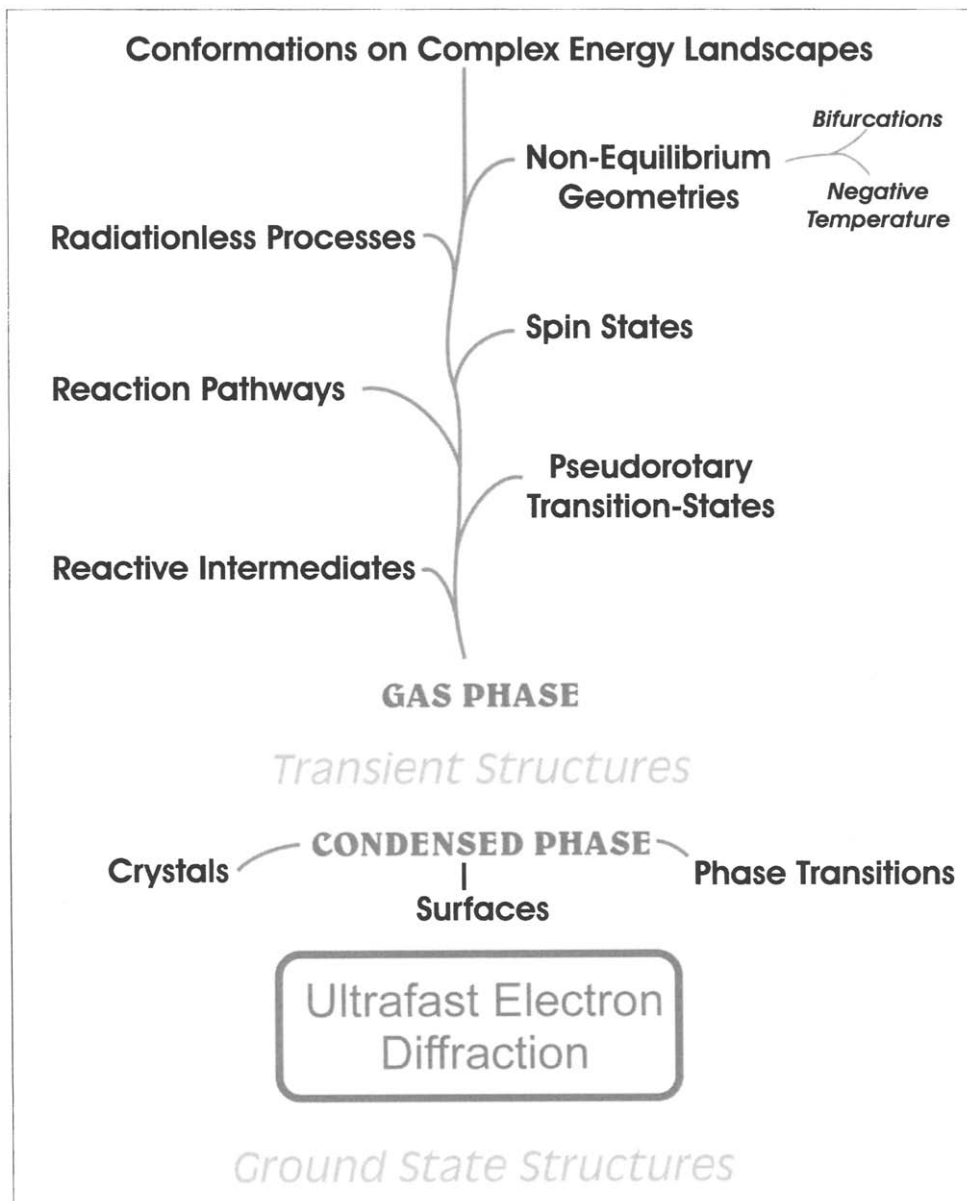


Fig. 1. Scope of UED applications

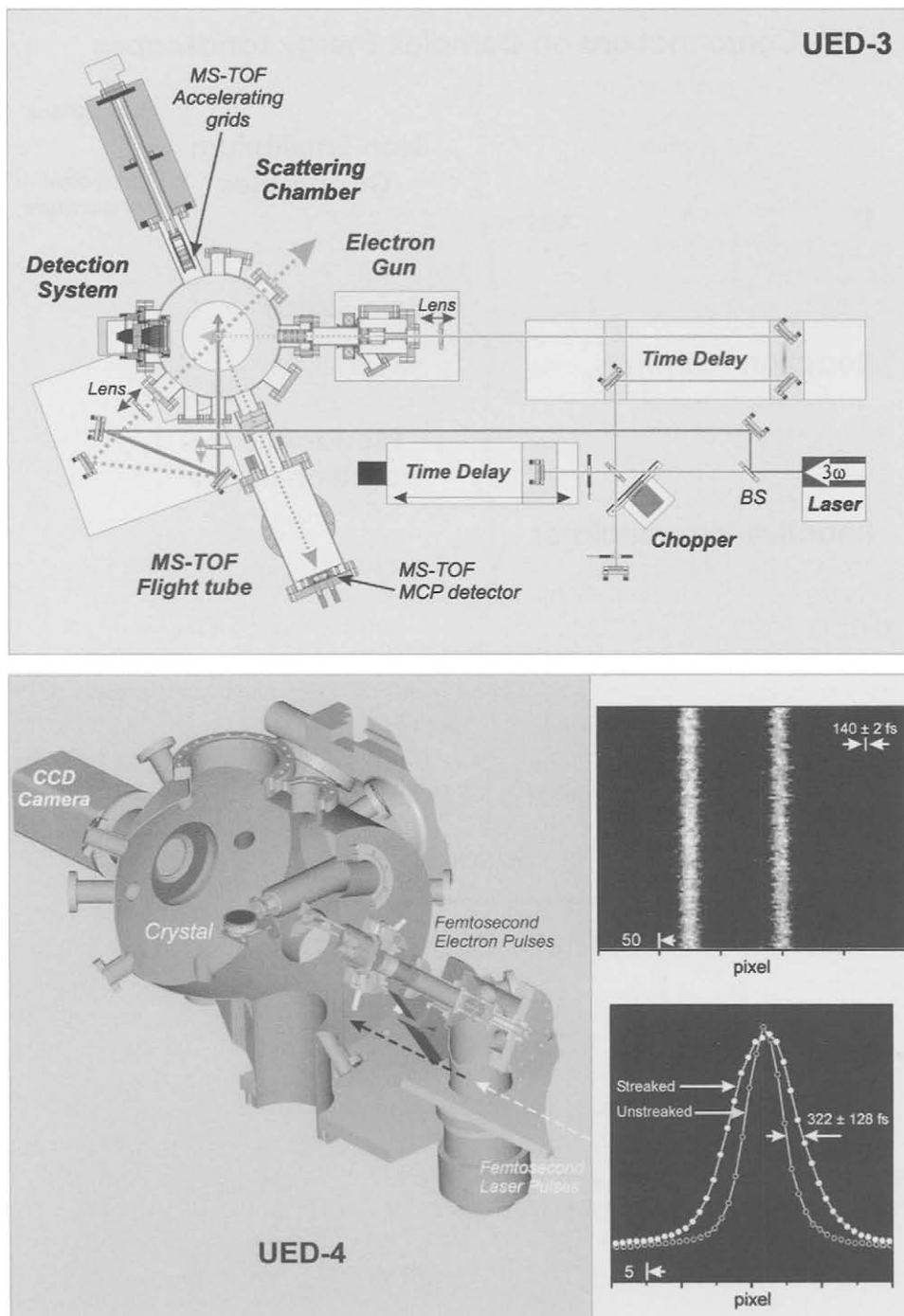


Fig. 2. UED-3 and UED-4 schematics, and the electron pulse streaks measured in UED-4

liquid phase transitions. These studies were reported in the references cited above; for reviews see [4, 5]. Here we give one prototypical example for gas phase reactions and another for crystal surface restructuring and melting.

1.1. Structures in Reactions

We have directly observed the structural dynamics of isolated chemical reactions via changes in diffraction patterns, using what we have termed the diffraction image referencing (diffraction-difference) method. A prototypical case is that of the non-concerted elimination reaction of dihaloethanes. It demonstrates the UED methodology of using different electron pulse sequences to isolate the reactant, intermediates in transition, and product structures. The reaction involves the elimination of two iodine atoms from the reactant to give the product. The structures of all intermediates were unknown, and the challenge lay in determining the structural dynamics of the entire reaction. As detailed elsewhere, this was achieved by referencing the diffraction to different time frames (-95 ps, 0 ps, and +5 ps). The temporal evolution of the two steps of the reaction was also recorded; for the final step as a rise (25 ± 7 ps) and for the intermediate as a decay (26 ± 7 ps).

The molecular structure of the C_2F_4I intermediate was determined from the diffraction-difference curves $\Delta sM(t; 5 \text{ ps}; s)$. Both the bridged and classical C_2F_4I structures were considered in the analysis of the diffraction data. The theoretical curves for the classical structures reproduce the experimental data very well, whereas the fit provided by the theoretical bridged structure is vastly inferior. Thus, we conclude that the structure of the C_2F_4I radical intermediate is, in fact, classical in nature—the iodine atom does not bridge the two carbons. The structural parameters of the C_2F_4I intermediate are given in Fig. 3. The C–I and C–C distances of the C_2F_4I intermediate are, respectively, longer and shorter than those of the reactant, while the C–F' internuclear distance in the radical site ($-CF'_2$) is shorter than that of the $-CF_2I$ site. These results elucidate the increased C–C and decreased C–I bond order resulting from the formation of the transient C_2F_4I structure. Moreover, the $\angle CCF'$ and $\angle F'CF'$ angles become larger than the corresponding angles of the reactant (by $\sim 9^\circ$ and $\sim 12^\circ$ respectively), suggesting that the radical center ($-CF'_2$) of the C_2F_4I intermediate relaxes following loss of the first I atom. The structures and dynamics reported for this reaction are vital in describing the retention of stereochemistry in such class of reactions, and this is the first example of resolving such complex structures during the transition.

1.2. Structures of Surfaces and Crystals

In UED-4, we studied the temporal evolution of bulk and surface structures with atomic scale spatial resolution. The first study was on crystals of silicon, with and without adsorbates. Referencing the diffraction-difference (Fig. 4) to the ground-state structure shows the changes in the structure caused by the initiating pulse, from ground state pattern at negative time to the observed change at positive time. The structural change is evident in the shift with time of the in-phase Bragg peak of the rocking curve, while the increase in vibrational amplitude is reflected in the broadening. The evolution takes place as a rise to a

Structures of Reactant, Intermediate, and Product

∞

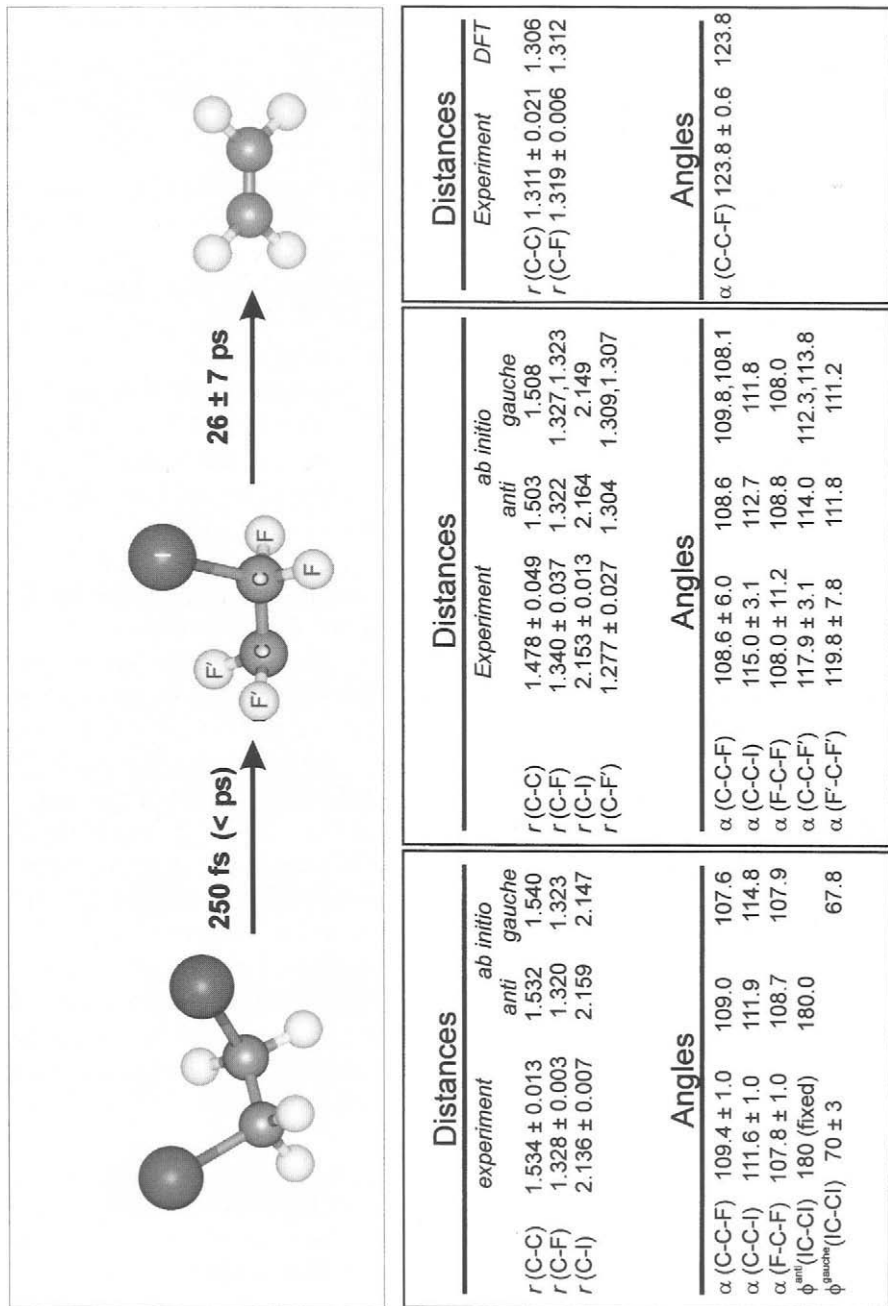


Fig. 3. Structures in halogen elimination reactions

UED: Diffraction Image Referencing

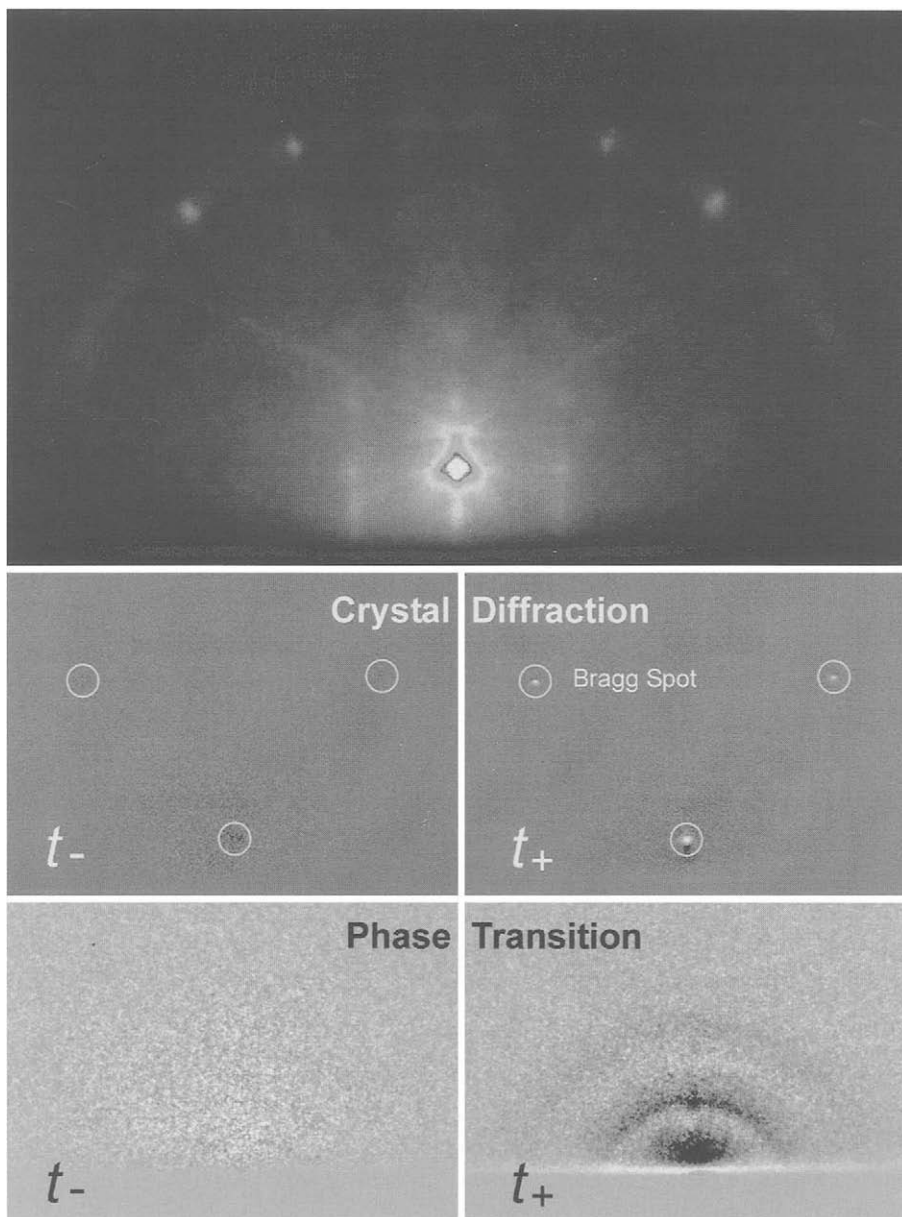


Fig. 4. UED of condensed phases – crystals and solid-to-liquid phase transitions. Shown are the diffraction from the crystal (top); diffraction image referencing of Bragg spots (middle) and of amorphous-to-liquid transition (bottom).

maximum shift and then a decay to the coordinates of the original structure. By gating on a Bragg spot, we can follow the changes with time. These results show the “instantaneous” structural change (2 ps steps of change; total ≤ 10 ps); a homogeneous expansion of the lattice 2.35-Å Si-Si bond by up to 0.04 Å at 50% level of damaging fluence. This is followed by lattice relaxation from a highly non-equilibrium structure to the final ground state structure with Si-Si distances of 2.35 Å. The multiple time constants of restructuring describe the expansion in real space and vibrational temperature as reported elsewhere [3, 4].

For the surface structures (and with hydrogen or chlorine), the results are striking. Gating the streak at the out-of-phase condition, we directly resolve the surface structural interferences and their evolution with time. Remarkably, the two spots change in time, and differently, but maintain the phase coherence [3, 4]. We are therefore able to display the spatial, temporal and phase coherence change of the surface structure, and the spatial patterns are describable within the framework of diffraction theory of condensed matter. The change in the structure is evident in the amplitude change of surface Si atoms. Unlike the result for bulk displacement (0.04 Å), the expansion of surface atoms is larger by an order of magnitude (0.4 Å). The cooling of the surface structure occurs on a time scale different from that of the bulk.

We also studied the structural changes involved in *phase transitions* when the temperature of the lattice is sufficiently high to cause large amplitude disorder. Initiating an ultrashort temperature jump of the amorphous structure with the infrared femtosecond pulse gives new diffraction ring patterns, which we followed as a function of time by referencing to the image of the ground state (Fig. 4). The instantaneous structural change is a phase transition to the liquid state. This is evident in the change of the radial distribution function, as we observe a depletion of the peak of the second coordination shell at ~ 4 Å, and the robustness of the first coordination shell at 2.35 Å. In amorphous silicon, atoms are topologically connected with fourfold coordination, but with the bond angles fluctuating substantially around 109.5° , the tetrahedral angle. In the liquid phase, these fluctuations are further enhanced, and the radial distribution function shows almost no second coordination shell. The temporal evolution of this surface melting is characterized by these regions, each for a different structure.

2. MESOSCOPIC IONIC SOLVATION

Using photoelectron detection in a femtochemistry arrangement, we studied size-selected clusters of ionic systems, covering the transition from gas phase to condensed phase dynamics [6]. We investigated the solvent effect on O_2^- dissociation dynamics, and observed that the addition of one solvent (O_2 , N_2 , Xe or N_2O) gives very different effects on the dynamics of the nuclear motion, whose wave packet bifurcates in two channels. These real time studies of the one-solvent dynamics provide the time scale of the distinctive processes of electron recombination and bond rupture, and vibrational predissociation—with both

channels yielding O_2^- . As with kinetic energy resolution, the photoelectron resolution allows us to examine the dynamics following the bifurcation in these pathways to O_2^- . The manifestation of direct and indirect dissociations are clear in the change of the time scale with solvation, as the direct process is controlled by electron recombination and kinematics of the half-collision, while the indirect process involves energy redistribution. We compared the experimental findings with *ab initio* and statistical rate calculations in these finite-sized ionic clusters. The elementary processes observed in clusters are expected to evolve toward the condensed phase behavior as the number of solvent molecules increases, and this aspect was also studied—the homogeneous solvated and mass-selected $(\text{O}_2)_n^-$.

The evolution is clear in the ultrafast dissociation and recombination dynamics of homogeneous O_2^- clusters, from O_6^- to O_{20}^- . Dissociation and recombination of the mass-selected anionic clusters show solvation effects on two different time scales and dissociation pathways—a bifurcation of the wave packet in two channels of direct dissociation and vibrational predissociation. The emergence of bulk properties from clusters was examined and compared with theory—bulk-type behaviors were deduced from the correlation between vertical detachment energy, or adiabatic electron affinity, and the inverse radius of the cluster. For the rates we found a dependence on the radius, and we related such striking behavior to the dynamics of electron recombination in the direct dissociation process. The solvent evaporation process involves vibrational predissociation, and the experimental rates show reasonable agreement with the calculated values using a statistical theory. The reformation of the bond in solvent cages becomes evident as the cluster size increases. Our fs time resolution provides the time scale for the recombination and subsequent vibration relaxation, which vary with the cluster size. The measured rates reveal the unique feature in the recombination process between molecules, which is absent in the (atom + atom) bond reformation. The time scale for bond breakage is critical to the rate of bond reformation, and molecular orientations and solvent friction plays a significant role, especially at longer times, longer than 1 ps. Recently, we have extended the methodology to study transition-state dynamics of organic reactions on the ground state surface (thermal!) as shown in Fig. 5.

3. BIOLOGICAL DYNAMICS AND FUNCTION

Our efforts at Caltech in this general area of biological studies have been devoted to select features of DNA and protein structure and recognition, including: DNA-mediated electron transfer and DNA-anticancer (daunomycin) drug complex; Human Serum Albumin ligand recognition; dioxygen picket-fence porphyrin recognition; protein-DNA recognition; riboflavin-binding protein and glucose oxidase enzyme; drug (daunomycin)-protein complexes; energy transfer and solvation in protein rubredoxin; proton transfer in model base pairs; nonradiative processes of DNA/RNA nucleotides and nucleosides; and studies of free base tetraphenyl porphyrin and zinc tetraphenyl porphyrin. Here, we shall highlight the more

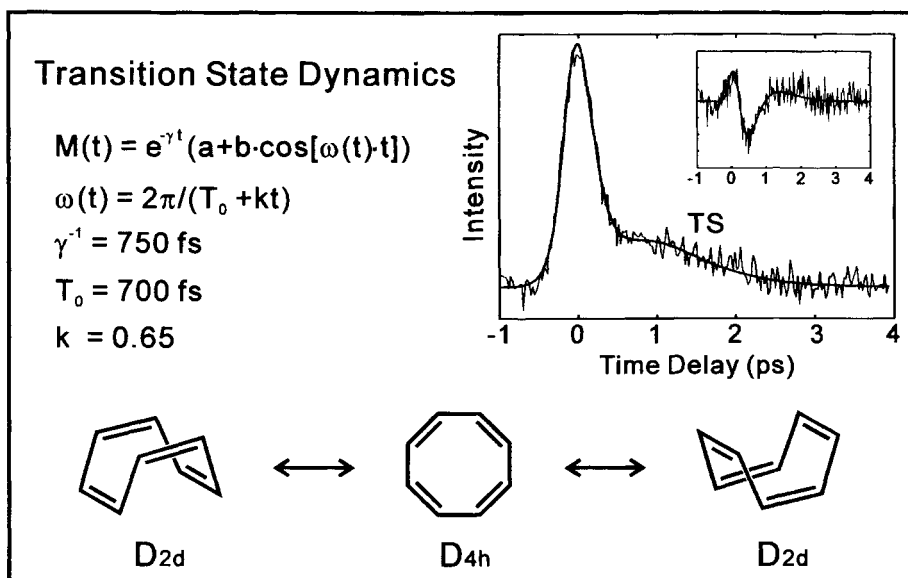
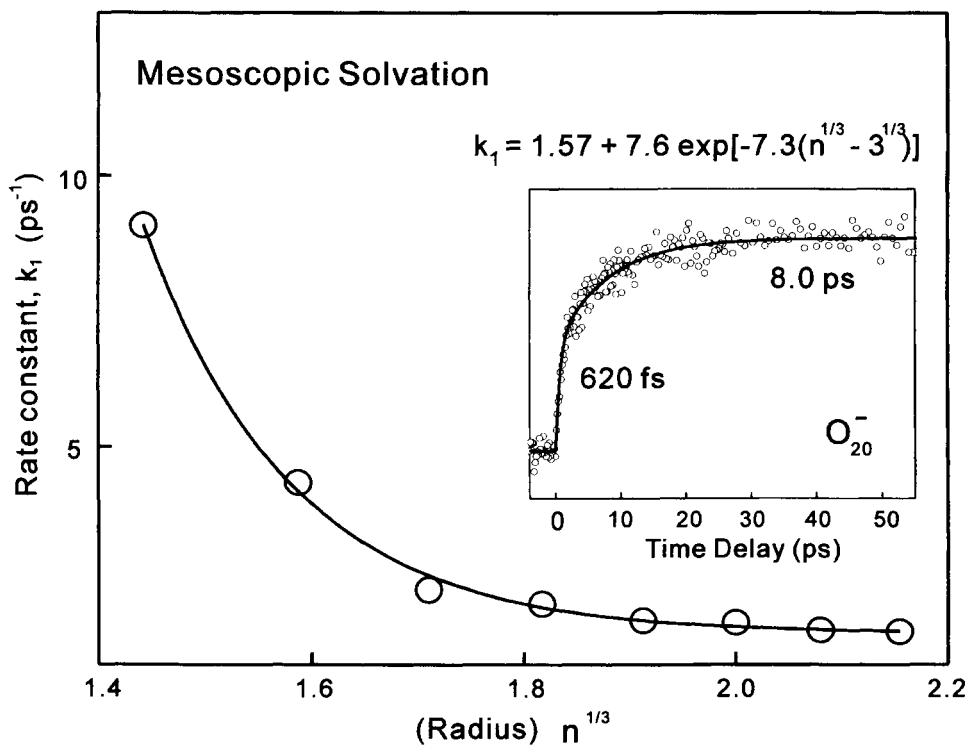


Fig. 5 (Top) Step-wise ionic solvation and dependence of rates on the cluster size, n . (Bottom) Transition-state dynamics on the ground state surface of cyclooctatetraene

recent effort on hydration dynamics which was published in a series of papers and reviewed in [7].

Almost all biological macromolecules—proteins, enzymes, and DNA—are inactive in absence of water. Hydration of a protein/enzyme is particularly important for the stability of the structure and for the function, especially the recognition at a specific site. Progress has been made and numerous experimental and theoretical studies have been published. To elucidate the dynamical nature of interfacial water, however, the time scale of hydration must span the range from bulk-type behavior (femtosecond) and up to buried-water behavior (nanosecond or longer). An understanding of the dynamics of water molecules at the *surface* of proteins and DNA, with spatial (molecular) and temporal (femtosecond) resolution, was the goal of our studies. At the molecular level the questions of interest are many and the following are pertinent to our interest here: (1) How rigid is the structure of water—the time scales?; (2) How homogeneous is the distribution?; and (3) What is the degree of order and how does ordered water influence the function? In general, these questions regarding structures and dynamics are also relevant to interfacial properties such as solvation, molecular orientation at interfaces, hydrophobic bonding, and self-assembly.

The above issues regarding the hydration of proteins are of similar importance to DNA hydration, which plays an important role in its structure, conformation, and function. Of significance to the function is the selective recognition by DNA of small molecules. Studies of x-ray crystallography, thermodynamics, NMR, dielectric relaxation, and molecular dynamics simulation have shown that a significant amount of water molecules are bound to DNA. The molecular picture of hydration in the minor groove of B-DNA is unique. An x-ray crystallographic investigation followed by solution NMR study on a model dodecamer B-DNA duplex showed that the minor groove is hydrated in an extensive and regular manner, with a zigzag “spine” of first and second shell hydration along the floor of the groove. In contrast, hydration within the major groove is principally confined to a monolayer of water molecules. The conformational energy calculation suggested that the presence of the spine of hydration is the prime reason for the further narrowing of minor groove.

At Caltech our studies of surface hydration dynamics on the femtosecond time scale were made on the protein Monellin and enzymes Subtilisin *Carlsberg* and α -Chymotrypsin, and for two types of DNA (dodecamer duplex and Calf Thymus). The spatial resolution in these experiments is determined by the selection of a specific molecular site (tryptophan and ANS in the case of proteins and the drug Hoechst in the case of DNA complexes). The site structure is known from x-ray crystallography and it is the one probed following femtosecond excitation, which defines the zero of time for water translational and rotational motions in the layer. We also made an estimate of the layer thickness by varying the distance (~ 1 nm) of the probe from the surface. From studies of the pH dependence of the enzyme α -Chymotrypsin, we proposed a role of hydration in its function. For DNA, we examined the interfacial water involved in the drug recognition in the minor groove, and whose complex structure has been

determined by x-ray crystallography. We also examined the site- and sequence- selective ultrafast hydration using 2-amino purine as part of the sequence in the strands.

Our experiments probed two types of water, those bound to the surface and those free (bulk); the bound water has residence time two orders of magnitude slower than that of free bulk water (typically, bulk hydration is complete in 1 ps). In the water layer around the surface, the interaction with water involves hydrogen bonding to the polar and charged groups of the surface. When strongly bonded to the surface, the water molecules cannot contribute to solvation dynamics because they can neither rotate nor translate. But the hydrogen bonding is transient and there is a dynamic equilibrium between the free and the bound water molecules, and this is the origin of the apparent “biexponential” behavior observed experimentally (Figs. 6, 7).

In a theoretical model, we considered the dynamics of bound water molecules and when they become free by translational and rotational motions. Two coupled reaction-diffusion equations were solved. The two rate constants, k_{bf} and k_{fb} , were introduced to describe the transition from bound (to the surface) to free (from the surface) and the reverse, respectively. We also took into account the effect of the bulk water re-entry into the layer—a *feedback mechanism*—and the role of orientational order and surface inhomogeneity on the observed decay characteristics. With this in mind, the expressions for the change in density with time were written defining the feedback as follows:



The solutions to the equations give the biphasic behavior with the two rates defined as follows:

$$\tau_{fast} = \frac{1}{(2D_R + Dq^2)}$$

which describes the ultrafast (~ 1 ps) decay at early times. In bulk, the orientational relaxation time (τ_{or}) is 2.6 ps and D_R is $1.9 \times 10^{11} \text{ sec}^{-1}$, with D_R being $(2\tau_{or})^{-1}$.

However, the slow relaxation time now takes the following form:

$$\tau_{slow} = \frac{1}{k_{bf}} \left[1 + (k_{fb} \tau_{fast})^{1/2} \frac{z_l}{\lambda} \right]$$

where $\lambda = (D/k_{fb})^{1/2}$ and z_l is the layer thickness. When z_l and λ become on the order of the molecular dimension and $k_{fb} \tau_{fast} \approx 1$, the maximum value is $\tau_{slow} \approx 2(k_{bf}^{-1})$. The numerical results, the effect of degree of orientation, and the influence of surface heterogeneity are

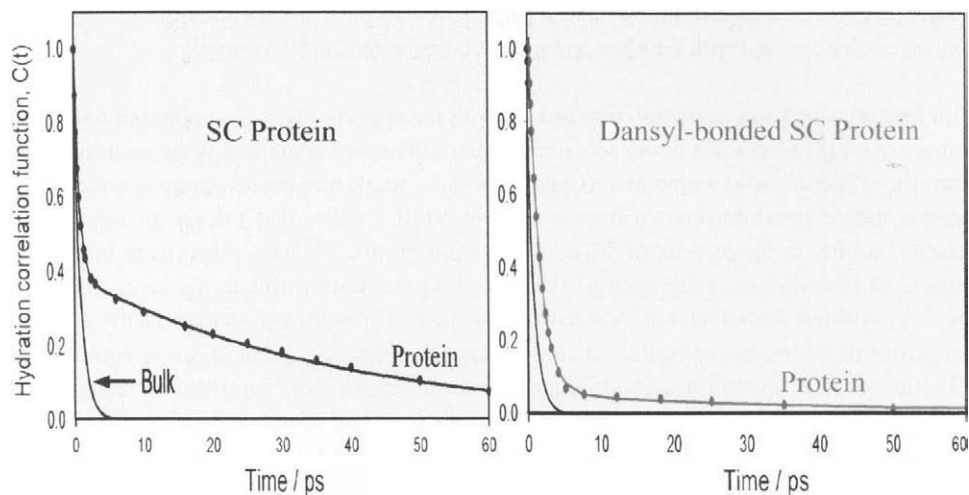


Fig. 6. Hydration surface dynamics of the protein (enzyme) *Subtilisin Carlsberg*, and for comparison that of bulk water, and a probe outside the water layer

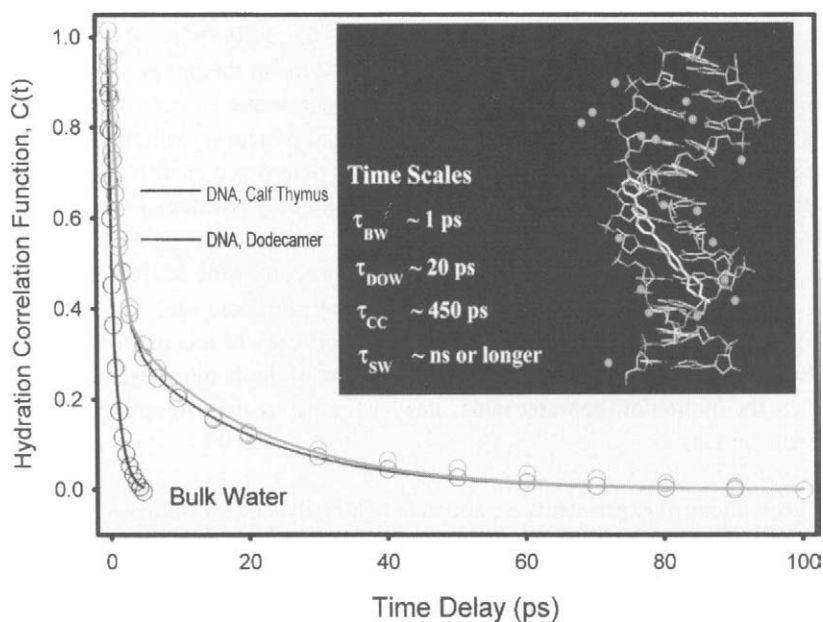


Fig. 7. Hydration of DNA, and with a drug recognized in the minor groove. Time scales are indicated for bulk water, dynamically ordered water, configurational changes and structured water

treated in [8]. The theoretical time scale is consistent with the experimental findings of biphasic behavior, and with the slow component being in the 20-50 ps range.

The femtosecond time resolution provides us with the opportunity of mapping out hydration dynamics on the time scale of the actual molecular motions of water and at the earliest times. The use of the intrinsic amino acid (tryptophan) as a single site probe on the surface of the protein native structure, known from x-ray and NMR studies, and the use of covalently-attached probes to the protein, or drugs in the minor groove of DNA, allow us to follow the change in hydration as a function of time (fs and ps) and to estimate the layer thickness ($\approx 7 \text{ \AA}$) without disturbance of the native structure. Through this change in the spectral properties of the probe molecule—at early times, the spectrum is that of a non-equilibrated structure (“blue spectra”) and at longer times it reaches the equilibrium state (“red spectra”)—we construct the hydration correlation function, which represents the solvent energy fluctuation, and obtain the fundamental time constants for solvation. For comparison, we also studied the same probe in bulk water.

For the structure, the hydrophobic collapse in the interior (of proteins, for example) and the hydrophilic interaction with hydrogen bonded water results in entropic and enthalpic changes that are determinants of the net free energy of stability. For the function, water in the layer has a finite residence time and its dynamics is an integral part of processes of two general categories—molecular recognition and reactions at the active site. Examples include: selective molecular recognition of ligands (substrate) through the unique directionality and adaptability of the hydrogen bond and water motion; enzymatic activity mediated by water located at the molecular distance scale, not diffusive; and protein-protein association through water mediation by entropic water displacement (desolvation) and energetic minimization of charge repulsion. The time scale for the dynamics is uniquely positioned—it must be longer than bulk dynamics and shorter than the time for the unfolding of the active structure. To maintain selectivity and order in the layer, the picosecond time scale seems ideal. For example, for DNA recognition of the drug studied here, the time scale of the twisting and bending of DNA and that of hydration determine the efficacy of recognition for an “intact” double strand structure in bulk water (Fig. 7). Diffusion of the binding ligand is slow, but at the interface the motion of the water molecules is ultrafast in order to optimize entropic and enthalpic interactions.

The new generations of experiments are aimed at linking dynamical studies of these and other processes to the function. We have already begun research in this direction. In a recent publication [9] we reported studies of the femtosecond dynamics of an RNA-protein complex and then compared the results with those obtained for *in vivo* (*E. Coli*) transcription anti-termination activities. In two other studies we measured the activity of the protein Subtilisin *Carlsberg*, discussed above, to a substrate, and the role of hydration in interfacial binding and function of bovine pancreatic phospholipase at a substrate site. The goal in all these studies is to relate structures to the dynamics and hopefully to key features of the (complex!) function.

ACKNOWLEDGEMENTS

We gratefully acknowledge the generous support by the National Science Foundation for building the new generations of UED. Partial support was provided by the Air Force Office of Scientific Research and the Office of Naval Research. I also wish to thank Ramesh Srinivasan for his help with the figures and careful proofreading of the manuscript.

REFERENCES & NOTES

This paper is based on the Keynote Lecture given at the conference; the text for UED is adapted from [2-5], ionic solvation from [6], and for biological studies from [7-9]. The following references are mostly reviews of work in the different areas discussed.

- [1] A.H. Zewail, in: *Les Prix Nobel*, T. Frängsmyr (ed.), Almqvist & Wiksell, Stockholm (2000) 110, and references therein.
- [2] H. Ihee, V.A. Lobastov, U.M. Gomez, B.M. Goodson, R. Srinivasan, C.-Y. Ruan and A.H. Zewail, *Science*, 291 (2001) 458.
- [3] C.-Y. Ruan, F. Vigliotti, V.A. Lobastov, S. Chen, and A.H. Zewail, *Nature*, submitted (2003).
- [4] V.A. Lobastov, R. Srinivasan, F. Vigliotti, C.-Y. Ruan, J.S. Feenstra, S. Chen, S-T. Park, S. Xu, and A.H. Zewail, *Springer Series in Optical Sciences*, F. Krausz, G. Korn, P. Corkum, I. Walmsley (eds.), (2003) 413.
- [5] R. Srinivasan, V.A. Lobastov, C.-Y. Ruan, and A.H. Zewail, *Helv. Chim. Acta*, 86 (2003) 1763, and references therein.
- [6] D.H. Paik, N.J. Kim and A.H. Zewail, *J. Chem Phys*, 118 (2003) 6923; N.J. Kim, D.H. Paik, and A.H. Zewail, *J. Chem Phys*, 118 (2003) 6930; D.H. Paik, D.-S. Yang, I.-R. Lee, and A.H. Zewail, to be submitted.
- [7] S. Pal, and A.H. Zewail, *Chem. Rev.* to be published (2004).
- [8] S.M. Bhattacharyya, Z-G. Wang, and A.H. Zewail, *J. Phys. Chem B*, 107 (2003) 13218; S.K. Pal, J. Peon, B. Bagchi, and A.H. Zewail, *J. Phys. Chem. B*, 106 (2002) 12376.
- [9] T. Xia, H.C. Becker, C. Wan, A. Frankel, R.W. Roberts, and A.H. Zewail, *Proc. Natl. Acad. Sci., U.S.A.*, 100 (2003) 8119.

Experimental and theoretical studies of pump-probe electron diffraction: time-dependent and state-specific signatures in small cyclic molecules

P. M. Weber,^a R. C. Dudek,^b S. Ryu,^a and R. M. Stratt^a

^aDepartment of Chemistry, Brown University, Providence, R.I. 02912, USA

^bFritz-Haber-Institut der Max-Planck-Gesellschaft, Faradayweg 4-6, 14195 Berlin

1. INTRODUCTION

Pump-probe diffraction techniques offer exciting new ways to probe transient structures in molecular, nanoscale, and biological systems. For dilute systems, or very small targets, electron diffraction is the preferred tool, because the cross sections for scattering of electrons from molecules are very large. In our research we show that pump-probe electron diffraction is an excellent technique to probe the dynamics of chemical reactions in the rarified environment of jet expansions, and for probing the diffraction signatures of individually excited vibronic states.

2. CHEMICAL REACTION DYNAMICS

A schematic illustration of our apparatus is displayed in Fig 1. Ultrafast electron pulses are generated by ejecting electrons from a metallic surface using the photoelectric effect.[1] The laser system is comprised of a Titanium-Sapphire oscillator and a 50 kHz regenerative amplifier. The electron beam is generated by the 2nd harmonic of the laser output, consisting of 400 nm pulses with typical pulse energies of 0.1 μ J. It has a time-averaged current of 20 pA, corresponding to 2500 electrons per pulse. Upon rapid acceleration to an energy of 20 keV, the electron beam is focused to a small portion of a gas phase sample within an effusive beam or a free jet expansion. The diffraction pattern is collected on a scintillator, and optically projected onto a liquid-nitrogen cooled CCD. The acquisition of an electron diffraction pattern requires on the order of 5 minutes, depending on the gas phase sample and its vapor pressure. The 3rd harmonic of the laser output, with a pulse energy of 0.3 μ J, intersects the molecular beam and the electron beam at right angles. Both the electron and the laser beams are collimated to a diameter of about 30 μ m.

Pump-probe patterns are obtained by exciting the molecule of interest to an excited state, and subtracting the diffraction pattern with the pump-laser off from a pattern with the pump-laser on. The ultrashort pulsed nature of the laser and the electron pulses allows us to probe structural dynamics by measuring the pump-probe diffraction patterns as a function of the delay time between the laser pulse and the electron pulse.

We have investigated the ring-opening reaction of 1,3-cyclohexadiene upon excitation to the transient ¹B₂ state. Fig. 2 shows the pump-probe difference pattern, for a delay time of 40

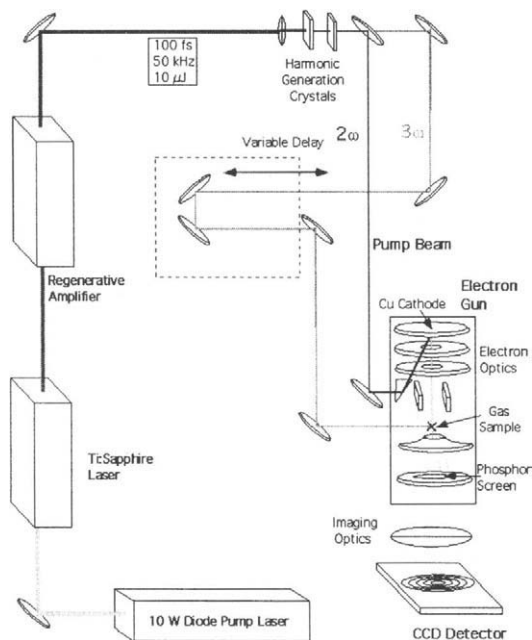


Fig. 1. Experimental layout of the pump-probe electron diffraction experiment. $2\omega = 2^{\text{nd}}$ harmonic, and $3\omega = 3^{\text{rd}}$ harmonic of the Titanium-Sapphire laser operating at 800 nm.

ps. In this difference pattern, all contributions of the atomic scattering, as well as contributions of molecular scattering arising from interferences between bonded and non-bonded atoms that do not change during the reaction, are completely subtracted out. The oscillations that are seen in the difference pattern are therefore due to only those internuclear separations that change during the ring opening reaction.

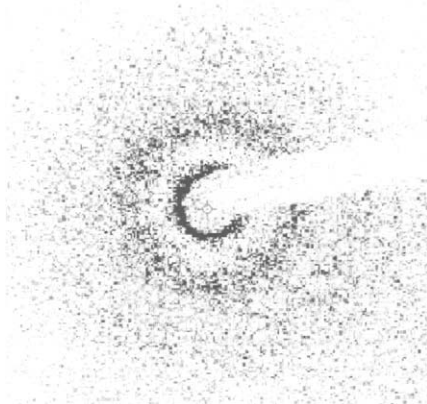


Fig. 2. Pump-probe diffraction pattern of 1,3-cyclohexadiene, upon excitation to the 1B_2 state.

Simulation of the difference signal using known theoretical and experimental structures of the 1,3,5-hexatriene product molecules matches the observed signal to within 10%, without the use of any adjustable parameters. Our fit indicates that the molecule opens up to the completely open tZt form of 1,3,5-hexatriene, within about 20 ps. Within the noise of our instrument, there is no indication for any intermediate existence of the cZt or cZc forms of hexatriene.

The difference diffraction patterns are exceedingly sensitive to slight displacements of the electron beam that might result from pointing instabilities of the laser and electron beams, or from a deflection of the beam by the high intensity laser pulse itself. In our apparatus we found that even a displacement of the electron beam by as little as 3 μm leads to modulations in the difference patterns that can mask the pump-probe signal. We have developed an algorithm to center the diffraction patterns of the modulated molecular part of the signal, rather than the far larger un-modulated atomic part of the signal. The algorithm is based on a cross-correlation of symmetrically equivalent areas of the molecular scattering pattern. By centering the individual diffraction patterns first, and then taking the difference patterns, the systematic deviations that result from pointing instabilities can be accounted for.

Deviations between the experiment and the theoretical fits can arise from multiple sources. On the theoretical side, there might be an inadequacy of the theoretically calculated structures, and inadequate modeling of the thermal motions of the very hot molecules. On the conceptual side, taking the difference patterns implicitly assumes the validity of the independent atom approximation. However, shortcomings of the independent atom approximation are well documented.[2] In the case of the ring-opening reaction of cyclohexadiene this implies that there may be contributions to the difference pattern arising from the different chemical bonding in the reactant and the product molecules.

3. DIFFRACTION SIGNATURES OF SPECIFIC VIBRONIC STATES

We performed a series of theoretical studies on pump-probe diffraction patterns with a two-fold objective: the first aim is to evaluate the effect of electronic and vibrational excitation on electron diffraction patterns, compared to that of structural rearrangements that are the primary goal for observation in structural dynamics measurements. Secondly, we wish to explore to what extent electronic and vibrational probability density distributions are observable using the pump-probe electron diffraction methodology. Previously we have discussed the effect of electronic excitation in atomic systems,[3] and the observability of vibrational excitation in diatomic and triatomic systems.[4,5] We have now extended this work to the 8-atomic molecule s-tetrazine ($\text{C}_2\text{H}_2\text{N}_4$).

In the simulations presented here, we assume that a pump laser excites the molecule to either the vibrationless, or specific vibrational levels of the S_1 electronic state. The diffraction pattern is measured by scattering the electron beam off the excited molecules on a time scale shorter than the rotational motion of the molecules, i.e. on a time scale less than about 10 ps. The diffraction pattern is measured in the plane perpendicular to the electron beam. The diffraction patterns shown here are for an excitation laser polarization parallel to the detector plane, and perpendicular to the electron beam. Since the electronic transition dipole moment of s-tetrazine is perpendicular to the aromatic ring, this pump-pulse polarization selects preferentially those molecules that are aligned with the aromatic plane parallel to the electron beam.

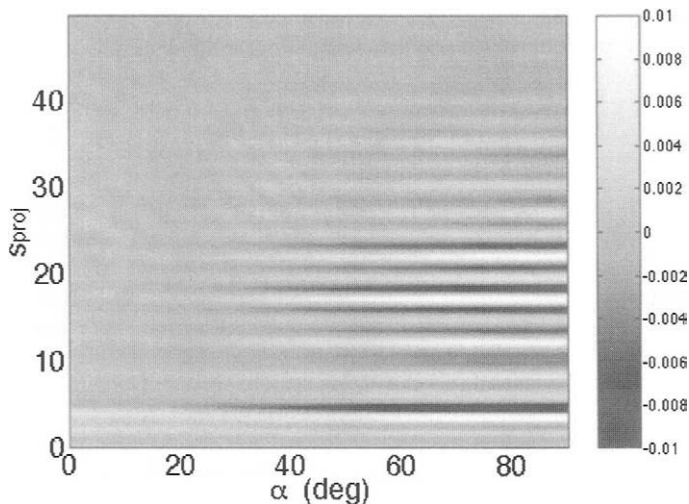


Fig. 3. Difference diffraction pattern of s-tetrazine, between the vibrationless levels of the S_1 and the S_0 electronic states, respectively.

Fig. 3 shows the difference diffraction pattern obtained by subtracting the pattern of the molecules in the S_0 state from that of the molecules in the S_1 electronic state. For this calculation we assume that the wave vector of the incoming electron beam is $k_0 = 100 \text{ \AA}^{-1}$. The ordinate is the projection of the momentum transfer vector, s , onto the plane of the detector, i.e.,

$$s_{proj} = \sqrt{s_x^2 + s_y^2}$$

The abscissa of Fig. 3 gives the rotation angle about the electron beam axis, α , with $\alpha = 0$ the direction of the pump-pulse polarization. The difference signal intensity, divided by the total diffraction signal, is encoded by the gray scale, as given in the intensity bar. To calculate this figure, all vibrational motions were included with their zero point vibrations.

Several important points are concluded from Fig. 3. First, the polarization of the excitation laser causes a dramatic anisotropy in the difference pattern, which reflects the preferential alignment of the excited molecules. Secondly, the most dramatic effect on the diffraction patterns is in the direction of $\alpha = 90^\circ$, i.e. for scattering within the plane of the aromatic ring. This is consistent with a change in the geometry of the molecule upon electronic excitation that preserves the planarity of the molecule. And third, the magnitude of the effect is on the order of $\pm 1.5\%$, putting it into a range that is experimentally relevant and observable.

The effect of vibrational excitation is examined in Fig. 4. Shown here is the difference diffraction pattern of the molecule in the S_1 electronic state with excitation to vibration $16a^8$, vs. the vibrationless level 0^0 of the S_1 electronic state. The gray-scale indicates the difference in the total diffraction signals of the two vibronically excited states, divided by the diffraction signal of the molecule in the ground electronic and vibrational state. Important to note is that this difference pattern has a strong feature at $\alpha = 0^\circ$, i.e. along the direction of the laser

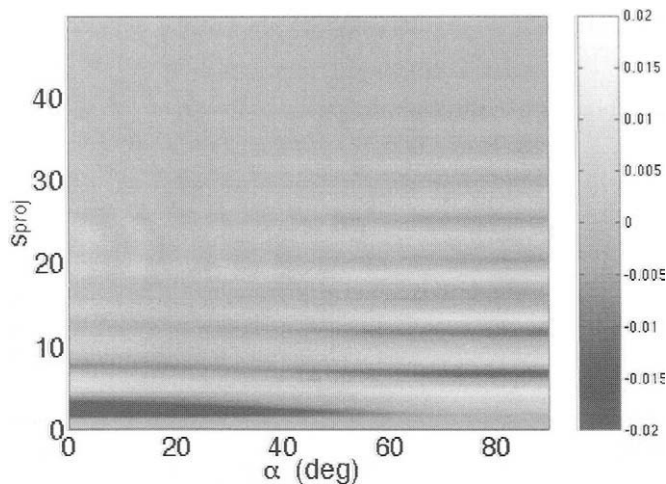


Fig. 4. Difference diffraction pattern of s-tetrazine, for excitation to the $16a^8$ vs. the 0^0 vibration of the S_1 electronic state.

polarization and perpendicular to the orientation of the aromatic ring. Apparently, the out-of-plane motion of vibration 16a is now imaged on the diffraction plane in the direction perpendicular to the direction where the electronic excitation dominates. Clearly, the plane of the detector serves to distinguish electronic excitation, and out-of-plane vibrational excitation in the s-tetrazine molecule. We also note that the change in the diffraction pattern here is on the order of $\pm 2\%$, slightly larger than the effect induced by the electronic excitation. The magnitude of the effect of vibrational excitation is therefore also well within the reach of pump-probe diffraction experiments.

An investigation of the diffraction signatures of specific vibronic states with the vibrations of the same symmetry reveals that even those vibrations have characteristic diffraction signatures. While the overall appearances of these diffraction patterns are similar, they show characteristic spacings and modulation amplitudes. We therefore conclude that different vibrational states have characteristic diffraction signatures, which can be observed using pump-probe electron diffraction.

4. CONCLUSIONS

In summary, we show that pump-probe electron diffraction can be performed with ultrafast time resolution, delivering difference diffraction patterns that reflect modulations arising from only those internuclear separations that change upon laser excitation. While modeling using the independent atom approximation provides reasonable data fits, for more exact work one needs to consider the effects of changes in the chemical bonding, and electronic and vibrational excitation of the molecules. Detailed calculations on the s-tetrazine molecules show that the effect of electronic excitation, in that molecule, leads to changes of the diffraction signals that are on the order of 1.5%. The simulation revealed interesting and observable effects of the anisotropy induced by the polarized pump laser. Furthermore, we

find that excitation of specific vibrations leads to additional distinguishing features in the difference diffraction patterns. These vibronic effects need to be considered for a rigorous analysis of pump-probe diffraction experiments, but can be exploited toward the imaging of vibrational wave functions, on the probability density level. This offers the exciting opportunity to perform tomography experiments where the shapes of vibrational probability density distributions are experimentally observed.

ACKNOWLEDGEMENTS

This research is supported by the Army Research Office under contracts DAAD19-00-0141 and DAAD19-03-1-0140, the Chemical Sciences, Geosciences and Biosciences Division, Office of Basic Energy Sciences, Department of Energy, Grant number DE-FG02-03ER15452, and by the NSF under grants CHE-0131114 and CHE-0212823. We thank Kyoung K. Baek for the results of ab-initio calculations that were used to calculate the difference diffraction patterns.

REFERENCES

- [1] R. C. Dudek and P. M. Weber, *J. Phys. Chem., A*, 105 (2001) 4167.
- [2] L. S. Bartell, "The status of electron scattering theory with respect to accuracy in structure analyses," in I. Hargittai and M. Hargittai (eds), "Stereochemical applications of gas-phase electron diffraction," VCH Publishers, Weinheim, (1988).
- [3] M. Ben-Nun, T. J. Martinez, P. M. Weber, K. R. Wilson, *Chem. Phys. Lett.*, 262 (1996) 405.
- [4] J. D. Geiser and P. M. Weber, *J. Chem. Phys.*, 108 (1998) 8004.
- [5] S. Ryu, P. M. Weber, and R. M. Stratt, *J. Chem. Phys.*, 112 (2000) 1260.

Cluster size effects on bound excited states of SO₂

T.E. Dermota, D.P. Hydutsky, N. J. Bianco and A.W. Castleman, Jr.

Departments of Chemistry and Physics, The Pennsylvania State University, University Park, Pennsylvania 16802, USA

1. INTRODUCTION

Photo-excited SO₂ and SO₂ clusters have been observed to undergo a number of excited state and ion-state processes. Ion-state studies have, for example, identified the energy threshold of the ion-state oxygen loss channel of the SO₂ monomer and dimer [1]. Additionally, studies investigating the metastable decay process of SO₂ clusters and mixed SO₂-water clusters have identified the dissociation pathways and the nature of the charged core of these cationic clusters [2]. The dynamics of oxygen loss of SO₂ and SO₂ clusters following excitation to the C (2 ¹A') state, which couples to a repulsive state, have also been studied to determine the influence of the cluster environment on the dissociation process [3].

In the studies reported here, the excited state dynamics of SO₂ clusters pumped to the coupled ¹A₂, ¹B₁ states and the F band of SO₂ are reported. The behavior of the excited state clusters and the influence of the cluster size on these dynamics have been investigated.

2. EXPERIMENTAL

The experiments were performed on an instrument consisting of an ultrafast laser system coupled to a time-of-flight mass spectrometer equipped with a pulse valve cluster source. The laser system produces pulses with a ~ 100 fs pulse width, a wavelength centered at 800 nm, and a repetition rate of 10 Hz. To perform the experiments reported here, the fundamental output of the laser was tuned to 795 nm. The fundamental output was frequency doubled to 398 nm and tripled to 265 nm for use as the probe and pump pulses, respectively. Clusters were generated by expansion of a 10% mixture of SO₂ in Ar backing gas (total pressure ~ 3 bar) into a high vacuum chamber (10⁻⁶ torr) using a General Valve pulse nozzle.

3. RESULTS AND DISCUSSION

(SO₂)_n clusters were excited by one and two photon absorption of the 265 nm pump pulse. The excited state clusters were then ionized at incremental delay times by the 398 nm probe pulse, allowing detection by mass spectrometry.

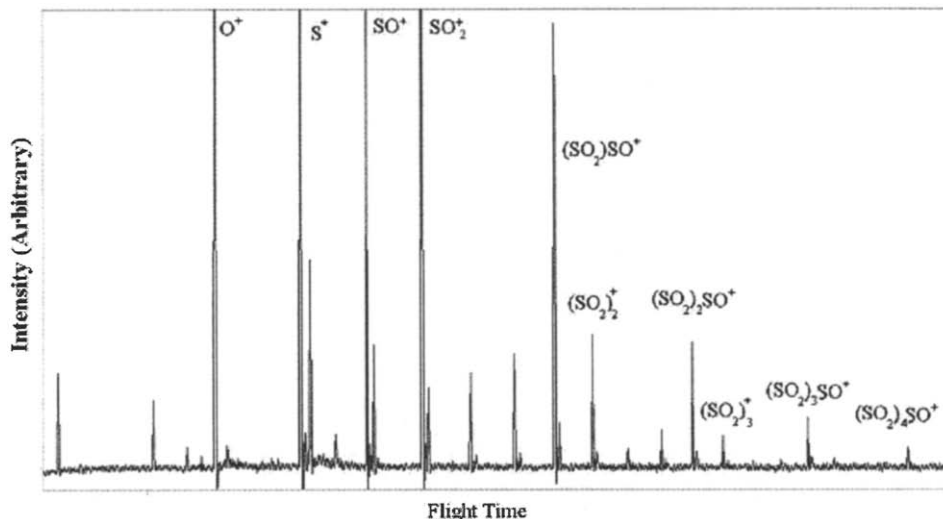


Fig. 1. Typical mass spectrum of SO_2 clusters taken at zero delay time between the pump and probe. Note the dominant intensity of the $(\text{SO}_2)_n\text{SO}^+$ series is due to an ion-state oxygen atom loss channel.

A typical mass spectrum obtained at zero pump-probe delay time (where the ion signal is generally largest) is shown in Fig. 1. The $(\text{SO}_2)_n^+$ cluster series can be seen up to $n = 3$. However, the $(\text{SO}_2)_n\text{SO}^+$ cluster series is present to larger values of n and has greater intensity due to the existence of an oxygen loss channel in the vicinity of the cationic ground state [3]. Therefore, $(\text{SO}_2)_n\text{SO}^+$ is observed as a product of the ion-state oxygen loss by $(\text{SO}_2)_{n+1}^+$. The S^+ and O^+ signals result from the fragmentation of SO_2^+ in excited ion states. Details of the ion-state processes have been discussed in a previous publication [3]. It should be noted that the results of the SO_2 cluster studies were obtained from analysis of the $(\text{SO}_2)_n\text{SO}^+$ clusters but are referred to in the discussion below by the neutral cluster that is believed to be the neutral excited state source of the observed ion signal, namely $(\text{SO}_2)_{n+1}$. In addition to ion state oxygen loss, it is also possible for an SO_2 molecule to evaporate from the cluster due to the addition of some vibrational energy by the ionization event. Molecular evaporation would, however, lead to the loss of the same number of molecules from all cluster sizes and is not expected to exceed one molecule per cluster. Therefore, the cluster size trends discussed below should not be altered by molecular evaporation.

When using a 265 nm pump and a 398 nm probe: a 1+3 pump-probe scheme produces ion signal resulting from excitation of the coupled $^1\text{A}_2$, $^1\text{B}_1$ states [4, 6], a 2+1 pump-probe scheme leads to excitation of an absorption band that has been assigned as the F band [5]. Unfortunately, to the best of our knowledge, assignment of the detailed spectroscopic properties of the F band has not been performed.

Two typical pump-probe transients of the ion signal are shown in Fig. 2. The transient data (points) have been fit using a function consisting of three components: a growth (τ_1) and decay (τ_2) component (dashed line), a fast decay (τ_3) component (dotted line), and a constant intensity plateau component that does not evolve with time (dot-dash line).

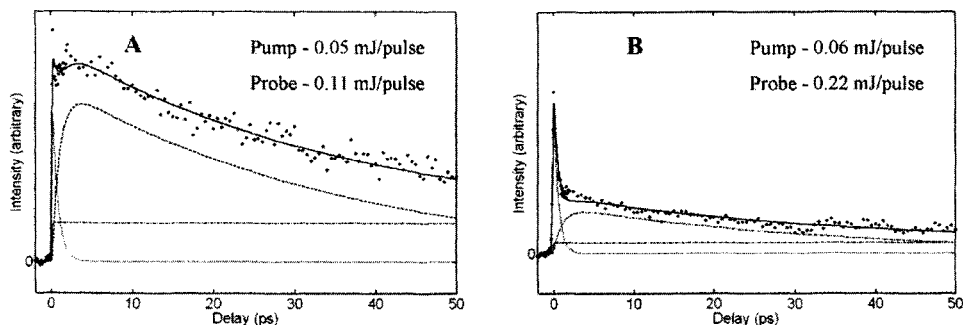


Fig. 2. Pump-probe transients of the $(\text{SO}_2)\text{SO}^+$ ion signal taken at two different probe powers. Note that the lower probe power data (transient A) is dominated by the τ_1 , τ_2 component from the F band whereas the high probe power data (transient B) is dominated by the τ_3 component from the coupled 1A_2 , 1B_1 states.

The fitting function used was constructed from functions derived for use in the analysis of pump-probe dynamics data [7]. The function accounts for the cross correlation of the pump and probe laser pulses and deconvolutes the laser pulse width. A pulse width of 120 fs was used for the analysis of all of the data as this width was found to best represent the cross correlation of the second and third harmonic laser pulses of the laser system.

Due to the difference in the number of probe photons required to ionize the clusters from each state, careful study of the ion signal probe power dependence made it possible to determine the origin of each of the observed components. The τ_1 , τ_2 component is the result of the two photon excitation of the SO_2 F band. The τ_3 decay component is due to the one photon excitation of the coupled 1A_2 , 1B_1 states. The plateau is believed to be due to ion-state fragmentation of larger clusters and does not seem to influence the values of the time constants obtained from the fitting procedure.

The properties of the F band are, unfortunately, not known, making assignment of the time constants to a specific physical process difficult. In general, the growth time τ_1 , about 1 ps, appears to be independent of cluster size since the $(\text{SO}_2)_n$ clusters produce similar values. The F band decay, τ_2 , is altered substantially in the $(\text{SO}_2)_n$ clusters where the decay is slowed with increasing cluster size from about 13 ps to 65 ps for the $n = 1$ to 5 size range. The decay is attributed to a relaxation process that is slowed by interactions between the excited-state species and the surrounding cluster molecules. However, the exact nature of this relaxation process has not yet been determined.

Excitation of the coupled 1A_2 , 1B_1 states results in the decay rate designated τ_3 which appears to be nearly independent of cluster size. A small increase in the value of τ_3 appears to occur for $(\text{SO}_2)_m$ clusters from the monomer (0.6 ps) to the dimer (0.9 ps), but remains constant at about 1 ps for larger cluster sizes. A likely interpretation of the observed decay process can be found in a detailed computational study [6] which reports that following the initial vertical excitation of the 1B_1 state, the excited state wave packet travels from the 1B_1 state into the double wells that result from the crossing of the 1A_2 and 1B_1 states. The transition of the excited state population into the double wells of the 1A_2 and 1B_1 states is believed to lead to the decay observed in the pump-probe experiment because the potential energy well minima of both of these states are outside of Franck-Condon region for the absorption of the probe laser pulse. Therefore, ion signal is not observed once the transition has occurred. The primary discrepancy between the computational results of Ref. [6] and the

experimental findings of this study is that the computational results found the process to occur in fewer than 100 fs [6], significantly faster than the experimental values reported here.

4. CONCLUSIONS

A source of scientific interest for studying the influences of clustering on the electronic excited states of SO₂ is gleaned from the atmospheric implications of SO₂ chemistry. Namely, sulfuric acid resulting from the oxidation of atmospheric SO₂ is a major constituent of acid rain. The oxidation process has been found to be influenced by factors such as clouds and aerosol particles, light intensity, O₃, and peroxides [8]. Thus, the nature of the factors leading to the alteration of atmospheric SO₂ chemistry may be clarified by experimentally studying the excited state dynamics of SO₂ solvated in SO₂ clusters. It appears that the size of a particle containing SO₂ may alter its reactivity since the dynamics of (SO₂)_n clusters show a substantial dependence on n.

The findings of the experiments presented here indicate that the time required for the transition from the initially excited ¹B₁ state to the double wells that result from the crossing of the ¹A₂ and ¹B₁ states is significantly greater than was found from a theoretical treatment of the transition [6]. The increased time in the experimental case is surprising since the transition only requires a small change in the molecular geometry.

The study of the SO₂ F band provides experimental evidence that the SO₂ molecule remains in a bound excited state for a substantial period of time indicating that coupling to dissociative states is not operative in this region of the potential energy surface. Thus, the experiments presented here provide previously unknown information about the properties of the little studied F band of SO₂.

5. ACKNOWLEDGEMENTS

Financial support by the Atmospheric Sciences and Experimental Physical Chemistry Divisions of the U.S. National Science Foundation, Grant No. NSF-0089233, is gratefully acknowledged.

REFERENCES

- [1] J. Erickson, C. Y. Ng, *J. Chem. Phys.*, 75 (1981) 1650.
- [2] Q. Zhong, S. M. Hurley, A. W. Castleman, Jr., *Int. J. Mass Spec.*, 185/186/187 (1999) 905.
- [3] S. M. Hurley, T. E. Dermota, D. P. Hydustry, A. W. Castleman, Jr., *J. Phys. Chem. A*, 107 (2003) 3497.
- [4] K. Kamiya, H. Matsui, *Bull. Chem. Soc. Jap.*, 64 (1991) 2792.
- [5] L. Vusković, S. Trajmar, *J. Chem. Phys.*, 77 (1982) 5436.
- [6] H. Müller, H. Köppel, *Chem. Phys.*, 183 (1994) 107.
- [7] S. Pedersen and A. H. Zewail, *Molecular Physics*, 89 (1996) 1455.
- [8] B. J. Finlayson-Pitts, N. J. Pitts, Jr. *Chemistry of the Upper and Lower Atmosphere* (Academic Press, San Diego, 2000) 296.

Micro solvation dynamics at the passage of conical intersections observed in argon clusters of excited tetrakis(dimethylamino) ethylene

S. Sorgues, J-M. Mestdagh, E. Gloaguen, J-P.Visticot and B.Soep

Laboratoire Francis Perrin (CNRS-URA-2453), DSM/DRECAM/Service des Photons, Atomes et Molécules, C.E.A. Saclay, F-91191 Gif-sur-Yvette Cedex, France

1. INTRODUCTION

Photochemistry in polyatomic molecules is often controlled by initial electronic relaxation, that occurs at very short times. The formation pathway of the reacting electronic state conditions its subsequent photochemical evolution. It has been found in the last ten years that this evolution could proceed within the femtosecond time domain and could not be explained by the existence of a multitude of dissipative channels degenerate with the excited state [1,2,3]. Rather a direct mechanism involving very few coordinates could explain the very rapid evolution from the accessed excited potential energy surface to a lower one of different configuration. Conical intersections (CI) between potential energy surfaces are recognised now as playing this role : the connection between surfaces relating to different electronic configurations. This allows for the very rapid downhill descent of a wavepacket prepared by femtosecond excitation, the mechanism being simply controlled by the dynamics on the connected surfaces. These properties of potential energy surfaces, known for a long time, are now found to be ubiquitous when searched by extensive quantum chemistry calculations, in the ultrafast dynamics of electronically excited organic molecules [4, 5].

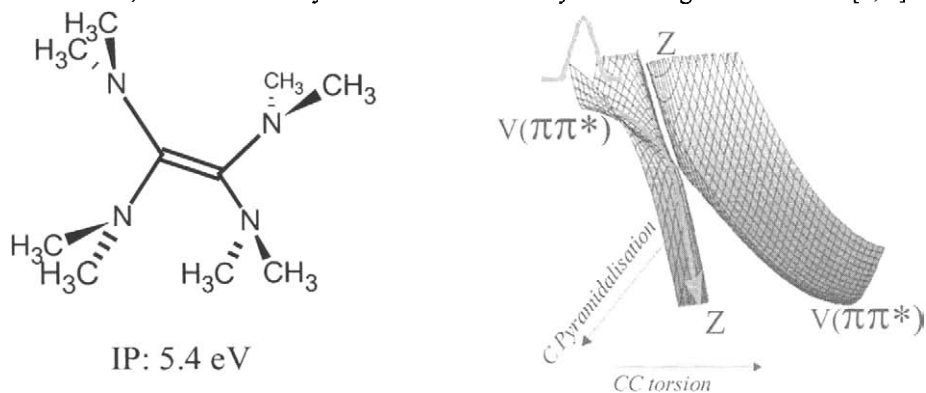


Fig. 1. Left: the TDMAE molecule. Right :schematics of the $V(\pi\pi^*)$ - Z surface crossing in TDMAE.

Importantly, CI's seems to be involved in many classes of physical, chemical and biological processes, from pericyclic reactions to the complex light harvesting and energy conversion functions of chromophores in proteins (See in this volume) and others amply described in this conference. In contrast, direct experimental information on the passage of the vibrational wavepacket through or near CI's is less abundant. It mostly concerns, femtosecond pump-probe experiments on isolated organic molecules in the gas phase.

The relevant ultrafast dynamics in the vicinity of the CI can be reduced to the movement of a vibrational wavepacket along, at least, two deformation coordinates. The movement takes place on potential energy surfaces of dimension n , and the wavepacket switches from one surface to the other in very localised regions surrounding CI's of dimension $n-2$ where two surfaces are exactly degenerate. One class of molecules where conical intersection are built-in by the electronic structure of their excited states is those containing one or more C=C double bonds where a state of mainly valence diradical configuration (V) crosses a charge transfer state, Zwitterionic state (Z). The very nature of these configurations makes the Z state more sensitive to solvation, this is the basis of this work which analyses the effect of model solvent, argon on the downhill wavepacket movement of the excited title molecule in the vicinity of a CI.

2. DOWNHILL V- Z WAVEPACKET MOTION IN TDMAE Ar_n CLUSTERS, EXCITED AT 266 nm AND PROBED AT 800 nm

The decay of the valence state of the bare TDMAE molecule has been analysed in a cold supersonic beam after excitation at 266 nm, in a former work[6]. The ionisation potential of TDMAE is sufficiently low that excitation of the valence state at 266 nm allows probing the V state at 800 nm with an excess energy of 0.8 eV. The monotonic decay of the V state was observed with a 300 fs time constant. This decay is accompanied by the simultaneous rise of the Z state detected with two 800 nm photons. This latter state further decays in 100 ps. This results in a bi-exponential signal for the TDMAE⁺ ions.

Here we have produced in a supersonic expansion of argon at 3 bars large TDMAE Ar_n clusters with $n \approx 60$. The argon atoms presumably form a double solvent shell around TDMAE, the first shell being complete at $n \approx 20$. This size is deduced from geometrical considerations with the first shell argon atoms located at 7 Å of the TDMAE centre. The TDMAE molecule can be supposed to be embedded in argon since the TDMAE-Ar energy is twice that of Ar-Ar,

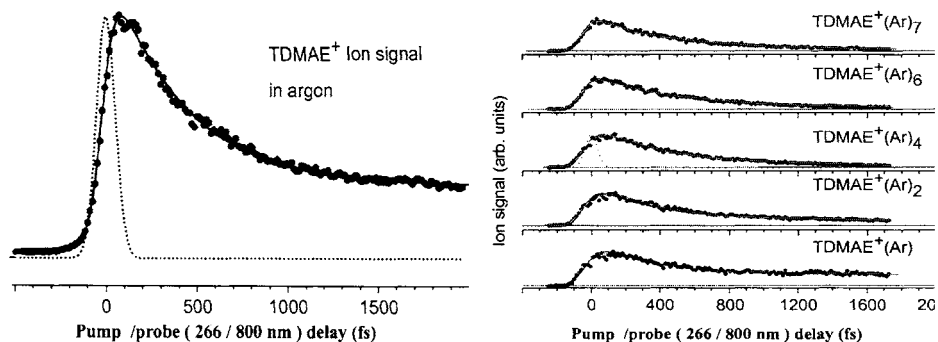


Fig. 2. V-Z decay of argon clusters probed at 800 nm observed at various masses. Left: at the TDMAE⁺ mass. Right: at increasing masses of the clusters, the highest detectable being $n=13$.

using Amar's empirical relationship [7]. These TDMAE⁺ Ar_{n=60} clusters of course evaporate in the same pump/probe conditions (266/800 nm) owing to a total 1.4 eV excess energy (including solvation by the cluster), brought by the excitation of the neutral ground state cluster. Thus, the largest observable argon cluster is n=13, owing to this evaporation in the mass spectrometer. All the decays represented in figure 2 are clearly bi-exponential up to n=7 and have been fitted by a sequential evolution model involving the V-Z evolution followed by the decay of Z as in reference [3]. The second exponential appears as a plateau on figure 2. Two decay constants were used in the fit : 400 fs (V-Z) and 100 ps (Z) and the cross sections for the detection of the V and Z states have been varied for the various clusters; the results are convoluted with the 100 fs cross correlation of the pump and probe lasers. The cross section for Z is maximum at n=0 and falls to 0 at n=7. This can be understood since the detection of Z involves two 800 nm photons and thus can evaporate more argon atoms.

All V-Z decay constants are simulated with the same constant, 400 fs, this shows that the cage of argon around TDMAE has substantially slowed down the downhill wave packet evolution from the 300 fs free molecule decay, as derived in reference [6]. This wavepacket motion is represented in figure 1 (left) and involves two coordinates, the torsion of the central C-C bond towards the 90° equilibrium geometry of the excited V state and the pyramidalisation about the central C atoms as in the molecule pictured at the bottom right of figure 3. These two movements must push away the argon atoms. We expect that the resulting inertial effect is dominant. This effect certainly supersedes an acceleration of the wavepacket movement due to the stabilisation of the Z state (large dipole) in presence of argon. The present effect can be compared also to other situations described in the literature where rapid movements are slowed down by an environment, namely the isomerisation of a molecular chromophore is slowed down when embedded in a cluster or in a solvent. For example, the barrierless *cis* to *trans* isomerisation of stilbene slows from 300 fs in the gas phase, down to ~1.4 ps in solution[8].

This downhill descent of the wavepacket observed at 266/800 nm appears in figure 2 as monotonic, which should lead to the conclusion that the wavepacket is fully spread when landing on the Z surface. This is not the case, as for the bare molecule, and the coherence of the wave packet can be probed with a laser at 400 nm which allows its continuous observation down to the Z surface[9].

3. COHERENT WAVEPACKET OSCILLATIONS OF THE TDMAE-Ar_n CLUSTERS PROBED AT 400 nm

Coherent oscillations are clearly seen in figure 3 (top left) at the TDMAE⁺ mass in TDMAEAr_n clusters. These results are compared with the oscillation of the bare molecule in helium. The oscillations are much slower in argon clusters. The Fourier analysis of the latter oscillations, in figure 3 (top right) suggests the existence of two oscillation periods 410 and 215 fs, instead of the single 250 fs oscillation observed for the cluster free TDMAE molecule. This can be qualitatively interpreted in light of our former work on the free TDMAE molecule[9]. There, we inferred that the deformations of the TDMAE molecule, torsion and pyramidalization, initiated by the V to Z configuration switch near the CI, drive the umbrella oscillation of the dimethylamino groups. Here, the same dimethylamino groups excited, drive the oscillatory motion of the argon environment. This can be imaged in the following way: an oscillator representing the four umbrella deformations is coupled to a deformation oscillation of the Ar_n cage. A simple calculation of the oscillation regime of two coupled oscillators leads to the observed periods T_{osc2}=410 fs and T_{osc1}=215 fs in good agreement with the

observed frequencies as shown by the dashed curves in figure 3 (top right). The initial period (uncoupled movement in TDMAE) is decreased from 250 fs to 215 fs, while the argon motion is slowed to 410 fs. This latter value, which corresponds to a frequency of 81 cm^{-1} can be compared with the expansion of a Rydberg bubble in solid argon, with two comparable regimes: expansion of the cage and damped oscillations including a 75 cm^{-1} frequency[10].

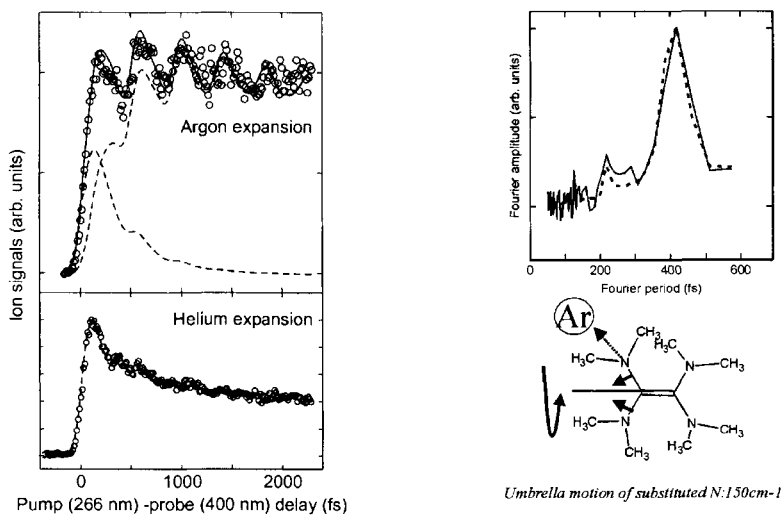


Fig. 3. Top left: detection of the TDMAE⁺ mass in argon expansion with 266/400 nm. This mass peak sums contributions of the free molecule and all evaporated clusters (dominant contribution here). Bottom left: the same in helium expansion. Top right: Fourier analysis of the top left curve, together with the simulation, dashed (see text). Bottom right: scheme of the involved movements of TDMAE.

The present work has allowed the direct observation of the transformation of the movements involved in the passage of a conical intersection connecting the V and Z surfaces of a prototype molecule TDMAE by the presence of a model solvent formed by a cage of argon atoms.

This work was supported by the EEC under contract PICNIC #IHP-RTN-00-2..

REFERENCES

- [1] Z. Dongping, E.W.G. Diau, T.M. Bernhardt, S. De-Feyter, J.D. Roberts, and A.H. Zewail, Chem.Phys. Lett., 298 (1998) 129.
- [2] W. Fuss, S. Lochbrunner, A.M. Muller, T. Schikarski, W.E. Schmid, and S.A. Trushin, Chem. Phys., 232 (1998) 161.
- [3] J.M. Mestdagh, J.P. Visticot, M. Elhanine and B. Soep, J. Chem. Phys., 113 (2000) 237.
- [4] M. Olivucci, F. Bernardi and M.A. Robb, THEOCHEM., 463 (1999) 42.
- [5] D.R. Yarkony, J. Phys. Chem. A. 105 (2001) 6277.
- [6] B. Soep, J.M. Mestdagh, S. Sorgues and J.P. Visticot, Eur. Phys. J. D. 14 (2001) 191.
- [7] F.G. Amar, A structural approach to the analysis of cluster dynamics, in The Chemical Physics of Atomic and Molecular Clusters, G. Scoles, Editor. 1990: Amsterdam. p. 99
- [8] J.Saltiel and Y.P.Sun, in Photochromism-Molecules and Systems, H. Bouas-Laurent and H. Duer, Editors., Elsevier: Amsterdam 1990. p. 64.
- [9] S. Sorgues, J.M. Mestdagh, J.P. Visticot, and B. Soep, Phys.Rev.Lett., 91 (2003) 103001.
- [10] S. Jimenez, M. Chergui, G. Rojas-Lorenzo and J. Rubayo-Soneira, J. Chem.Phys., 114 (2001) 5264.

Femtosecond photon echo measurements of electronic coherence relaxation of I₂ in the presence of He, Ar, N₂, O₂, C₃H₈

V. V. Lozovoy, M. Comstock, I. Pastirk, and M. Dantus

Department of Chemistry and Department of Physics and Astronomy
Michigan State University, East Lansing, MI 48824, USA

Photon Echo (PE) and Reverse Transient Grating (RTG) measurements of the loss of electronic coherence between the X(¹Σ_g⁺) and B(³Π_{0u}⁺) states of molecular iodine are measured by three pulse four wave mixing (FWM). Two cases are considered, relatively low pressure isolated iodine (1-2 Torr), and iodine at high pressure (>10torr) or in the presence of several hundred Torr of buffer gas.

1. LOW PRESSURE NEAT IODINE VAPOR

In the PE signal at low pressure, (Fig. 1(top)) rotational coherence is maintained for hundreds of picoseconds and vibrational and rotational revivals from both ground and excited states are observed. The part of the PE signal around the largest rotational revival (~226 ps) is shown in Fig. 1 (bottom). The fast oscillations (307 fs) are due to a long-lived (~1000 periods) vibronic coherence between the X(¹Σ_g⁺) and B(³Π_{0u}⁺) states of iodine. The RTG data do not show the rotational and vibrational recurrences for time delays longer than 100 ps, and decay with a faster rate than the PE data, indicating that inhomogeneous dephasing is larger than homogeneous dephasing.

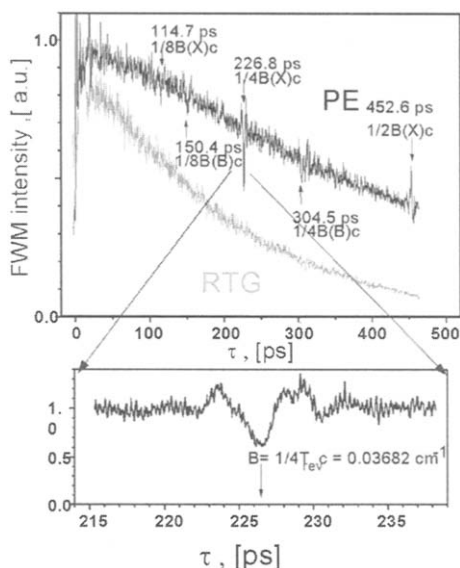


Fig. 1. Here we present the measurements of the RTG (grey) and PE (black) signals on a longer time scale with good temporal resolution, 50fs pulses.

2. HIGH PRESSURE NEAT IODINE VAPOR

A second set of experiments was performed by varying the iodine vapor pressure, using long pulses (1200fs) to blur the vibrational dynamics. In these relatively high-pressure experiments, the PE and RTG decays are identical, and can be fit (see Fig. 2) to the equation:

$$S_{PE}(\tau) = S_{RTG}(\tau) \propto \exp(-2\gamma\tau) \quad (1)$$

Where τ is the delay between the second two pulses, and γ is the homogeneous relaxation rate $\gamma = 1/T_2'$. The signal decay times can then be plotted versus pressure, and a homogeneous dephasing cross section can be extracted.

$$\gamma = \gamma_0 + n\sigma v \quad (2)$$

Where γ_0 is the homogeneous dephasing at zero pressure, n is the number density, v is the average velocity, and s is the homogeneous dephasing cross section. A fit through the experimental data in Fig. 2 allows us to determine a cross-section of $1170 \pm 110 \text{ \AA}^2$ for neat iodine vapor, and a $1/\gamma_0$ of $58 \pm 4 \text{ ns}$. [1] This value is a factor of two larger than that determined two decades ago. [2]

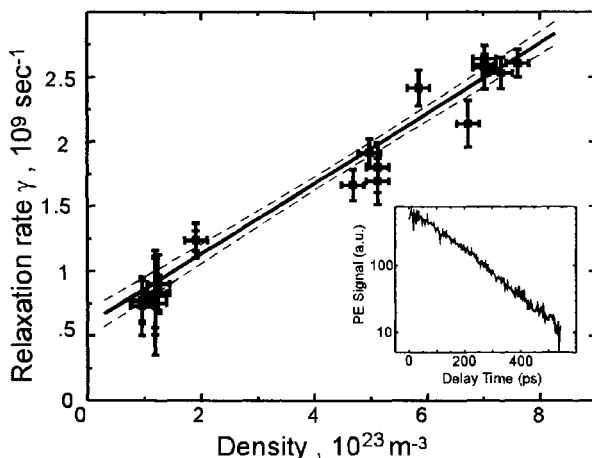


Fig. 2. Plot of homogeneous relaxation rate, γ versus number density for neat iodine vapor. Results for 37 measurements are shown. Horizontal error bars indicate uncertainty in the absorption cross section of iodine, vertical error bars indicate uncertainty in the exponential fitting routine. Dotted lines represent the 90% confidence interval based on a linear least squares fit. Inset is a typical PE data trace plotted on a logarithmic scale. This trace corresponds to a number density of $5 \times 10^{23} \text{ m}^{-3}$.

3. IODINE IN THE PRESENCE OF BUFFER GASES

Measurements of the electronic coherence between the $X(^1\Sigma_g^+)$ and $B(^3\Pi_{0u^+})$ states of iodine were performed in the presence of several types of buffer gas molecules, varying the buffer gas pressure and maintaining a constant iodine pressure of 12 torr. Fig. 3 shows one set of this data for the propane molecule, with example PE and RTG traces, showing the agreement between the experiment, equation (1), and the full theory including inhomogeneous and homogeneous contributions to the dephasing rate. [1]

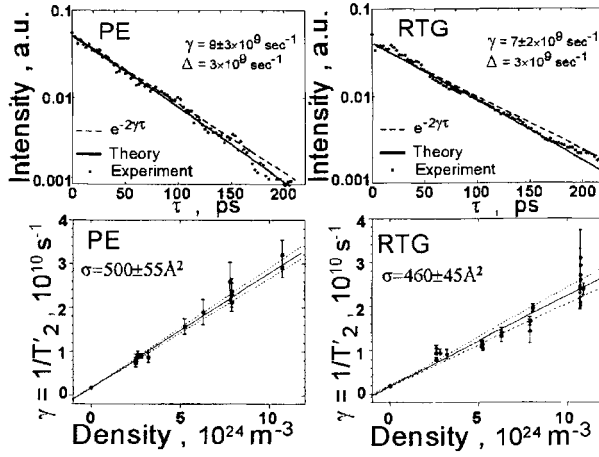


Fig. 3. Above, plots of PE and RTG signals for propane (250torr) showing similar exponential decays. Below, plots of dephasing rate versus number density of the buffer gas propane for both PE and RTG experiments.

Plots of dephasing rate versus buffer gas pressure allow us to extract homogeneous dephasing cross sections according to equation (2). In Fig. 3 (bottom) we show Iodine coherence dephasing data for propane buffer gas. Note the similarity of the extracted cross sections in both the PE and RTG cases. These measurements were repeated for a series of buffer gases and the results are contained in Table 1.[3]

Table.1

Parameters of interaction between coherent state of I_2 and M molecule

Molecule	$\sigma, \text{\AA}^2$	$R = \sigma^{1/2} / \pi^{1/2}$	τ_i, ps^b	$C_{6exp}, \text{J m}^6^c$
He	170 ± 35	7.3 ± 1.5	0.7	8.7×10^{-77}
Ar	370 ± 120	10.8 ± 3.5	3.0	20.5×10^{-77}
N ₂	300 ± 50	9.7 ± 1.6	2.3	14.2×10^{-77}
O ₂	450 ± 40	12.0 ± 1.1	3.0	36.9×10^{-77}
C ₃ H ₈	540 ± 50	13.1 ± 1.2	3.8	50.6×10^{-77}
I ₂ ^a	1170 ± 110	19.3 ± 1.4	10.1	190×10^{-77}

^a previous publications $\sigma = 590 \pm 110$ [2] and $\sigma = 1150 \pm 150$ [3].

^b average time of interaction calculated with $\tau_i = 4R/3v$, where v is average collisional velocity.

^c calculation from experimental data using equation (3)

We find that long-range interactions responsible for decoherence can be modeled by dispersion forces $U(r) = C_6/r^6$ and show no dependence on the number of degrees of freedom in the buffer gas molecules. Dispersion force parameters C_6 were extracted (see Table 1) according to the equation:

$$C_6 = (8/3)\bar{v}\eta(\sigma/\pi)^{2.5} \quad (3)$$

where \bar{v} is the average velocity of the buffer gas molecules. These C_6 parameters have strong correlations with polarizability of buffer gas molecules.

We have used nonlinear optical techniques (photon echo and reverse transient grating spectroscopy) to measure the homogeneous dephasing rate of the electronic coherence between the $X(^1\Sigma_{g+})$ and $B(^3\Pi_{0u+})$ states of molecular iodine in the presence of various buffer gases. We use these measurements to extract homogeneous coherence dephasing cross sections for the buffer gas molecules. We find that homogeneous coherence decay can be modeled by dispersion forces, with the polarizability of the $B(^3\Pi_{0u+})$ state of iodine one order of magnitude larger than the polarizability of the ground $X(^1\Sigma_{g+})$ state. The fragile nature of quantum phase is responsible for the enormous radii (10-20Å) of interaction with the buffer gases.

REFERENCES

- [1] M. Comstock, V.V. Lozovoy, M. Dantus, J. Chem. Phys., 119 (2003) 6546.
- [2] E.T. Sleva, A.H. Zewail, Chem. Phys. Lett., 110 (1984) 582.
- [3] I. Pastirk, V.V. Lozovoy, M. Dantus, Chem. Phys. Lett., 333 (2001) 76.

Probing reaction dynamics with Rydberg states: The ring opening reaction of 1, 3-cyclohexadiene

N. Kuthirummal and P. M. Weber

Department of Chemistry, Brown University, 324 Brook Street,
Providence, Rhode Island 02912, USA.

1. INTRODUCTION

Electrocyclic reactions involving polyenes are important in many natural processes, such as photosynthesis and the natural synthesis of vitamin D [1]. A detailed understanding of the intramolecular energy flow upon excitation is essential to understand the photochemistry of such molecules. For this reason we investigated the energy flow associated with the ring-opening reaction of 1,3-cyclohexadiene (CHD), which often serves as a model system for electrocyclic reactions. We applied a newly developed technique that uses photoionization via Rydberg states as a probe.

A number of investigations have previously been carried out to elucidate the spectroscopy and dynamics of CHD. Experimental investigations [2-7] have been paired with quantum chemical calculations [8-11], to refine the orbital symmetry concepts developed by Woodward and Hoffman, and van der Lugt and Osterhoff [12]. However, a direct and unambiguous experimental study regarding the timescales involved in the curve-crossing from the initially excited state to the ground state, for isolated molecules in the gas phase, is not yet available.

To explore the electronic curve crossing dynamics of CHD, we investigated the time-dependence of a two-color 3-photon photoionization measurement. A schematic representation of the ionization scheme is shown in Fig. 1. In the scheme, the first photon of energy $\hbar\omega_1$ lifts the molecule to the ultrashort-lived 1^1B_2 state, from where the dynamical processes ensue. A second photon, of energy $\hbar\omega_2$, brings the molecules to a high-lying valence state, which relaxes by rapid internal conversion to a set of Rydberg states. A third laser photon, again with energy $\hbar\omega_2$, ionizes the molecules. Since the internal conversion from the high-lying valence to the Rydberg states is very fast, the two-step ionization from the 1^1B_2 and 2^1A_1 states can be considered essentially instantaneous. The binding energy of electrons in the Rydberg levels, E_B , is described by the formula [13]

$$E_B = E_I - E_{Rn} = \frac{Ry}{(n - \delta)^2} .$$

Here E_{Rn} is the energy of the Rydberg states, E_I the ionization energy of the molecule, n the principal quantum number, δ the quantum defect, and Ry the Rydberg constant. A measurement of the photoelectron spectrum immediately provides the Rydberg energies, because

$$\hbar\omega_2 - E_e = E_I - E_{Rn} ,$$

where $\hbar\omega_2$ is the energy of the ionizing photon, and E_e is the kinetic energy of the observed photoelectrons. Although the Rydberg formula is not accurately valid for low n quantum numbers, we could fit the observed transitions into Rydberg series within the experimental uncertainty. In order to follow the decay dynamics of the intermediate states we observe the dependence of the

photoelectron spectrum on the time-delay between the pump pulse with photons of energy $\hbar\omega_3$, and the probe pulses with photon energy $\hbar\omega_2$.

2. EXPERIMENTAL

We used a Spectra Physics 50 kHz Spitfire laser system, in which femtosecond laser pulses from a Ti:Sapphire laser are regeneratively amplified to microJoule energies. The details of laser systems and the experimental apparatus have been published elsewhere [14]. Upon 2nd harmonic generation, the pulses have a duration of less than 150 fs. As the pump pulse we use the 3rd harmonic, with photon energy $\hbar\omega_3 = 4.65$ eV. The time-delayed probe pulse was the second harmonic, with a photon energy of $\hbar\omega_2 = 3.10$ eV. The laser beams are focused by a 200 mm focal length lens, and intersect a molecular beam carrying the CHD molecules seeded in helium. The photoelectron spectrum is observed using a time-of-flight analyzer. The energies of the laser pulses were 80 nJ (third harmonic) and 850 nJ (second harmonic), respectively. The apparatus can deliver energy resolutions below 10 meV for slow electrons (< 1 eV), but for the fast electrons observed here, the spectral resolution was typically 20-30 meV. While the complete photoelectron spectrum shows contributions from other ionization pathways, notably the two-photon ionization with the third harmonic only, the spectra described here are based on the described three-photon ionization process.

3. RESULTS AND DISCUSSION

In the two-color ionization employed here, various ionization pathways can produce highly vibrationally excited ions on account of involvement of Rydberg states. It is particularly difficult to discern between the competing 3-photon ionization pathways involving the combination of photons $\hbar\omega_3 + \hbar\omega_3 + \hbar\omega_2$, and $\hbar\omega_3 + \hbar\omega_2 + \hbar\omega_2$. In our work we were able to unambiguously identify the ionization pathway as the latter, based on the onset of the Rydberg energy spectrum, as well as the power dependence of the intensity of the two-color spectrum. We also note that the intensity of the second harmonic pulse is about 10 times higher than that of the third harmonic pulse.

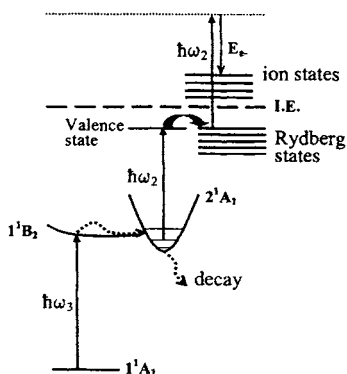


Fig. 1. Two-color 3-photon ionization scheme. CHD is excited by a $\hbar\omega_3$ photon to the 1^1B_2 state, and is then ionized by two $\hbar\omega_2$ photons.

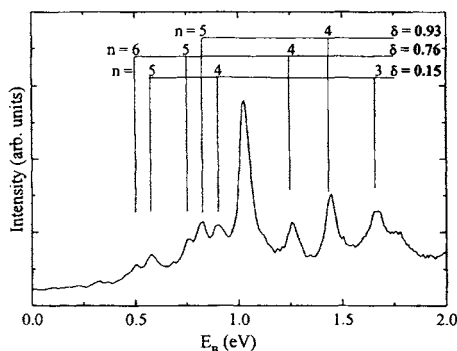


Fig. 2. Three-photon ionization photoelectron spectrum, obtained in the scheme of Fig.1, showing the Rydberg states.

The 3-photon ionization photoelectron spectrum, plotted as the photoelectron signal intensity as a function of the binding energy of the Rydberg states, is shown in Fig. 2. Three series of Rydberg peaks, with quantum defects of 0.93, 0.76, and 0.15 are obtained. From the quantum

defect values, it seems likely that the series correspond to ns , np , and nd states, respectively. Several spectral lines are not labeled. While we can easily calculate their principal quantum numbers and quantum defects, we were not able to identify more than one peak of the respective series in our spectra.

To probe the dynamics of the intermediate states, we measured the dependence of the signal on the delay time between the second and the third harmonic photons. Figure 3 plots the total Rydberg signal as a function of the delay time. Almost identical curves are obtained when the time-dependencies of individual Rydberg peaks are plotted. The instrument function was obtained by observing the 3-photon ionization signal of azulene, and taking the derivative of the signal with respect to time. The Rydberg states of azulene have a very long life time, so that the onset of the Rydberg signal is a fair representation of the cross correlation between the second and the third harmonic pulses.

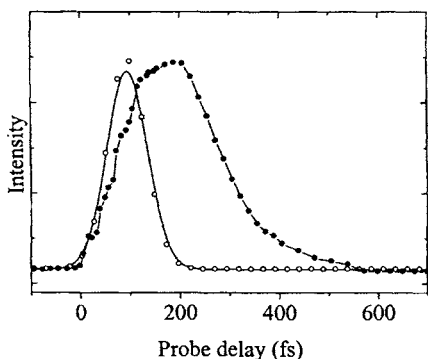


Fig. 3. The decay curve of CHD (●—●) and the instrument function (○—○).

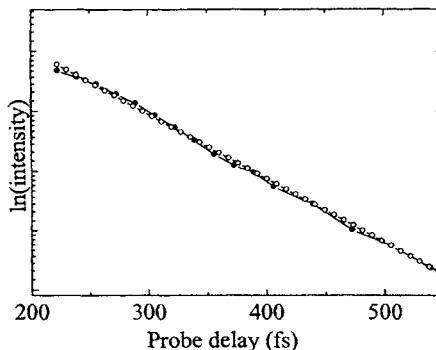


Fig. 4. Logarithmic plot of the decay curve of CHD (●—●) and the exponential fit (○—○).

The observed Rydberg signal of CHD shows an onset that is delayed from the instrument function, leading to a maximum signal about 100 fs after the pump pulse. This suggests that the signal is largely due to the 2^1A_1 state that is populated as a result of rapid curve crossing from the initially populated 1^1B_2 state. We attempted to model the early time dynamics with a model that has a sequential kinetics starting at the 1^1B_2 state, and then populating the 2^1A_1 state, but no satisfactory fit was obtained. Apparently, other processes that occur during the duration of the laser pulses, such as two-photon ionization by two third-harmonic photons, or 3-photon ionization with a $\hbar\omega_3 + \hbar\omega_2 + \hbar\omega_3$ scheme, compete efficiently with the investigated ionization pathway. Nevertheless, at delay times after the overlap between the pump and the probe pulses, we observe a clean single-exponential decay of the Rydberg signal, as illustrated by the logarithmic plot of Fig. 4. Our fit gives a decay time of 93 fs.

We interpret our results as follows. The initially prepared 1^1B_2 state decays rapidly to the 2^1A_1 state, on a time scale that is comparable to the laser pulse duration, i.e. 100 fs. The 2^1A_1 state itself decays on the 93 fs time scale, presumably by crossing to the 1^1A_1 surface via a conical intersection. This result is consistent with the experimental work of Fuß et al. [5], who followed the dynamics in an indirect way by observing fragments such as H^+ , $C_2H_3^+$, $C_3H_3^+$, and $C_6H_6^+$. They concluded that the entire ring opening reaction is complete in about 200 fs. Pullen et al. measured the dynamics in different solvents using transient absorption [3]. They find slightly longer decay times, suggesting that there may be interesting effects of the solvent on the dynamics, even during the early stages of the ring opening reaction.

4. CONCLUSION

In summary, we determined the decay kinetics of the intermediate electronic states involved in the photoinduced electrocyclic ring-opening reaction of 1,3-cyclohexadiene to form 1,3,5-hexatriene. The initially populated 1^1B_2 state decays rapidly to the 2^1A_1 state within the duration of the laser pulse. The 2^1A_1 state crosses to the ground electronic state with a decay time of 93 fs. The experiments show that photoionization via a highly excited valence state, and a set of Rydberg levels, provides a useful probe of the molecular dynamics taking place on electronic surfaces of lower energy. Since all neutral molecules have Rydberg states, it can be presumed that the technique is widely applicable. The internal conversion dynamics to the Rydberg levels is very fast, providing for an accurate representation of the molecular dynamics. Finally, the Rydberg states are long lived, making the Rydberg spectra well defined and straightforward to interpret.

ACKNOWLEDGEMENTS

This research is supported by the Army Research Office under contracts DAAD19-00-0141 and DAAD19-03-1-0140, and the Chemical Sciences, Geosciences and Biosciences Division, Office of Basic Energy Sciences, Department of Energy (DE-FG02-03ER15452).

REFERENCES

- [1] D. Feldman, F.H. Glorieux and J. W. Pike (Eds.), Vitamin D (Academic Press, San Diego, 1997).
- [2] P. J. Reid, S. J. Doig and R.A. Mathies, *Chem. Phys. Lett.*, 156 (1989) 163.
- [3] S. H. Pullen, N. A. Anderson, L. A. Walker II, and R. J. Sension, *J. Chem. Phys.*, 108 (1998) 556.
- [4] S. A. Trushin, W. Fuß, T. Schikarski, W. E. Schmid and K. L. Kompa, *J. Chem. Phys.*, 106 (1997) 9386.
- [5] W. Fuß, W. E. Schmid and S. A. Trushin, *J. Chem. Phys.*, 112 (2000) 8347.
- [6] C.-Y. Ruan, V. A. Lobastov, R. Srinivasan, B. M. Goodson, H. Ihee and A. H. Zewail, *Proc. Nat. Acad. Sci.*, 98, (2001) 7117.
- [7] R. C. Dudek and P. M. Weber, *J. Phys. Chem. A*, 105 (2001) 4167.
- [8] P. Celani, F. Bernardi, M. A. Robb and M. Olivucci, *J. Phys. Chem.*, 100 (1996) 19364.
- [9] S. Lochbrunner, W. Fuss, W. E. Schmid and K. L. Kompa, *J. Phys. Chem. A*, 102 (1998) 9334.
- [10] A. Hofmann and Regina de Vivie-Riedle, *J. Chem. Phys.*, 112 (2000) 5054.
- [11] M. Garavelli, C. S. Page, P. Celani, M. Olivucci, W. E. Schmid, S. A. Trushin and W. Fuß, *J. Phys. Chem. A*, 105 (2001) 4458.
- [12] W. T. A. M. van der Lugt and L. J. Oosterhoff, *J. Am. Chem. Soc.*, 91 (1969) 6042.
- [13] C. P. Schick and P. M. Weber, *J. Phys. Chem. A*, 105 (2001) 3725.
- [14] B. Kim, N. Thantu, P. M. Weber, *J. Chem. Phys.*, 97 (1992) 5384.

Femtosecond photoelectron spectroscopy of trans-Stilbene

C. Dietl, E. Papastathopoulos and G. Gerber

Physikalisches Institut, Universität Würzburg, Am Hubland, 97074 Würzburg, Germany

1. INTRODUCTION

During the last decade there has been a great amount of experimental as well as theoretical work demonstrating the applicability of coherent quantum control in driving quantum mechanical processes towards a desired outcome using specially adapted electric fields [1,2]. Previous studies in our group have shown that optimal electric fields can experimentally be determined by the technique of adaptive femtosecond pulse-shaping to control for instance the outcome of a photo-dissociation reaction using mass spectrometry as an experimental feedback for the optimization procedure [3,4]. Although mass spectrometry is a powerful method for observing photo-dissociation reactions, it is rather limited in studies of intramolecular dynamical processes, like electronic state population transfer or, most interesting here, photoinduced isomerization reactions. In this case the necessary feedback signal for an optimization requires a detection scheme which is selective to the isomeric products. In this work we are particularly interested in the molecule of stilbene, a well known model system for photoinduced isomerization reactions [5-9]. Due to space interaction of the phenyl rings, the vertical ionization potentials of cis- and trans-stilbene isomers are well separated by about 300meV [10]. Therefore the photoelectron spectrum following the excitation of the molecule with an ultrashort probe laser pulse can be used as experimental feedback for a potential feedback controlled optimisation of photoisomerization reaction.

The present work comprises of a first step towards this goal and involves measured photoelectron spectra of trans-Stilbene following the excitation with tuneable femtosecond UV laser pulses. The ionization process occurs in a (1+1) REMPI scheme, using the first excited singlet state (S_1) of trans-Stilbene as an intermediate resonance.

2. EXPERIMENTAL

Tuneable femtosecond UV laser pulses in the wavelength range between 296nm and 316nm were provided by two successive BBO crystals generating the fourth harmonic of the signal pulse from a travelling wave optical parametric amplifier (TOPAS). The TOPAS is pumped by a Chirped Pulse Amplification (CPA) system, delivering laser pulses of central wavelength 800nm, duration of 100fs and 1mJ pulse energy, operating at a repetition rate of 1kHz.

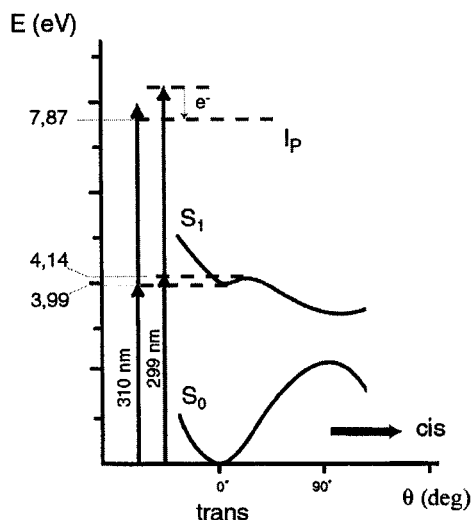


Fig. 1. Energy scheme of the 1+1 REMPI. Approximate potential curves across the isomerization coordinate θ for the ground state S_0 as well as the intermediate S_1 resonance are depicted.

Also laser pulses with central wavelength of 266nm were obtained by frequency tripling the fundamental 800nm laser pulses of the CPA system. Excitation of stilbene with laser pulses of 266nm are of particular interest due to the ease at which tailored pulse shapes can be generated at a central wavelength of 800nm as well as for the second and third harmonics.

Excitation utilizing these laser pulses involves the ionization of the trans-Stilbene molecule to the ground cationic state (D_0) via a two photon vertical transition of the molecule. The transition probability is enhanced due to an intermediate resonance, namely the first excited singlet state (S_1) (s. Fig.1). It should be noted that with the ultrashort pulse duration employed, there is no isomerization dynamics involved in the excitation i.e. only the Frank Condon region is accessible. The pulse energy of all different wavelengths was $0.15\mu\text{J}$ and the pulse duration was kept constant 80-100fs (within 10%). The laser pulses were focused into the interaction region of a magnetic bottle photoelectron spectrometer using a 300mm quartz lens. The intensities reached in this configuration are well below $10^{11}\text{W}/\text{cm}^2$. The resolution of the photoelectron spectrometer is about 30meV for photoelectrons at 1eV of kinetic energy. Trans-Stilbene was evaporated at a temperature of about 70°C and expanded effusively into the interaction region of the spectrometer. Trans-Stilbene was purchased from Aldrich and used without any further treatment.

3. RESULTS AND DISCUSSION

In Fig. 2 photoelectron spectra are shown for different wavelengths of the excitation laser pulses a) 316nm, b) 310nm, c) 301nm and d) 266nm respectively. The laser intensity was

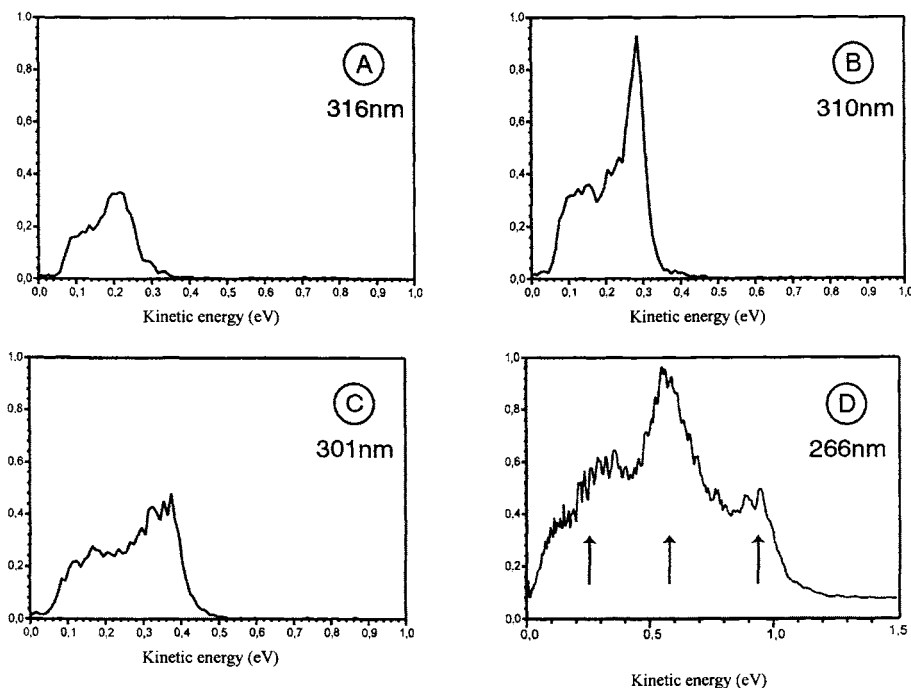


Fig. 2. Photoelectron energy distributions of trans-stilbene following the excitation with different photon energies. a) 316nm, b) 310nm, c) 301nm and d) 266nm.

carefully reduced until no indication of higher order photon absorption, e.g. ATI, was seen. In this intensity regime the integrated photoelectron yield was found to depend quadratically on the laser intensity, as is expected for a two photon absorption far from the saturation regime. At higher laser intensities additional features at higher kinetic energies appear in the spectrum. The photoelectron spectrum shown in Fig.2a has been obtained from two photon ionization employing photon energies below the S_1 band origin (s. Fig.1). With the 316nm photons, non resonant multiphoton ionisation is possible but as seen in the spectrum with a rather small transition probability. When the excitation photon energy is tuned into resonance with the S_1 state at 310nm a strong increase in the ionisation rate is observed. In the case of 310nm excitation the energy position of the main feature observed in the spectrum of Fig 2b corresponds to ionisation into the lowest vibrational states of the cation [11,12]. However, as can be seen from the 301nm spectrum in Fig 2c the excitation probability decreases as the excitation energy exceeds the origin of the intermediate S_1 resonance.

In the case of excitation with 266nm laser pulses, the photoelectron spectrum exhibits some additional features (s. Fig. 2d). The observed peak structure originates from a high vibrational mode at which the parent ion is left after the ionization. For this reason the maximum of the photoelectron distribution is shifted relative to the kinetic energy one would expect for the decay to the origin of the cationic D_0 ground state. The three major peaks (Fig 2d) observed in the spectrum are separated by an energy of approximately 3000cm^{-1} ,

indicating an alternate (C-C) stretching mode. The one photon excitation with 266nm exceeding by almost 0,5eV the origin of the S₁ band of the neutral molecule. The excitation is therefore resonant with highly excited vibrational modes of the S₁ band. Due to the Frank Condon factors, this results in a high probability of leaving the molecule in an excited vibrational state after the ionization.

In order to ensure that the intermediate resonance is in fact the S₁ band despite the large detuning, lifetime measurements were conducted in a pump-probe scheme. The excitation to S₁ is realized with 266nm one photon absorption, and the induced wavepacket motion is monitored by a time delayed probe laser through a two photon 400nm absorption. The isomerization of trans-stilbene exhibits 14psec, which is in agreement to previously reported values [13,14]. The difference in the time constants found for trans-stilbene compared to the value of 320fsec for cis-stilbene, previously measured in our group [15] is due to the known 1200cm⁻¹ barrier along the isomerization coordinate [14].

4. CONCLUSION

In conclusion, we present a spectroscopic study of $\pi\pi^*$ excitation in trans-Stilbene in a molecular beam experiment. The excitation involves a 1+1 REMPI scheme following the interaction of the molecule with femtosecond UV laser pulses. When the excitation is resonant with the origin of the intermediate S₁ state, the measured photoelectron distribution reveals a maximum probability for the 0-0 transition. For higher photon energies (266nm) the photoelectron spectrum exhibits a rather complex distribution, due to the excitation of an alternate (C-C) stretching mode.

REFERENCES

- [1] T. Brixner and G. Gerber, *Chem. Phys. Chem.* 4 (2003) 418
- [2] S.A. Rice and M. Zhao (eds), John Wiley, New York (2000)
- [3] A Assion, T Baumert, M Bergt, B Kiefer, V Seyfried and G. Gerber, *Science* 282 (1998) 919
- [4] N.H. Damrauer *et. al.*, *Eur. Phys. J. D* 20 (2002) 71-76
- [5] J. A. Syage, P. M. Felker and A. H. Zewail, *J. Chem. Phys.* 81 (1984) 4685
- [6] J.S. Baskin, L. Banares, S. Pedersen and A.H. Zewail, *J. Phys. Chem.* 100 (1996) 11920
- [7] J. A. Syage, P. M. Felker and A. H. Zewail, *J. Chem. Phys.* 81 (1984) 4685
- [8] B.I. Greene and R.C. Farrow, *J. Chem. Phys.* 78 (1983) 3336
- [9] D. H. Waldeck, *Chem. Rev.* 91 (1991) 415
- [10] T. Kobayashi, K. Yokota and S. Nagakura, *Bull. Chem. Soc. Jpn.* 48 (1975) 412
- [11] M. Takahashi and K. Kimura, *J. Phys. Chem.* 99 (1995) 1628
- [12] J.M. Smith and J.L. Knee, *Laser Chem.* 14 (1994) 131
- [13] B.I. Greene, R.M. Hochstrasser and R.B. Weisman, *J. Chem. Phys.* 71 (1979) 544
- [14] J. A. Syage, Wm. R. Lambert, P. M. Felker and A. H. Zewail R. M. Hochstrasser, *Chem. Phys. Lett.* 88 (1982) 266
- [15] T. Baumert *et.al.*, *App. Phys. B.* 72 (2001) 105

Azobenzene photoisomerization: Two states and two relaxation pathways explain the violation of Kasha's rule.

T. Schultz^{a,b}, S. Ullrich^a, J. Quenneville^c, T.J. Martinez^c, M.Z. Zgierski^a, A. Stolow^a

^a Steacie Institute for Molecular Sciences, National Research Council, Ottawa, Canada

^b Present address: Max-Born Institute for Non-linear Optics, Berlin, Germany;

^c Department of Chemistry, University of Illinois, Urbana, USA;

1. INTRODUCTION

Azobenzene is a photochromic molecule, which undergoes *trans-cis* isomerization upon irradiation in the near-UV. The photoisomerization reaction is ultrafast, efficient and clean and has attracted much attention for its possible application in molecular electronics, data storage and nonlinear optics [1]. In violation of Kasha's rule, the isomerization yields vary anomalously with the excitation wavelength [2]: the symmetry forbidden and weak transition to $S_1(n\pi^*)$ at 440nm yields up to 25% *cis*-azobenzene, while the strongly allowed $S_2(\pi\pi^*)$ state at 350nm yields only 12% *cis*-azobenzene. Two possible reasons have been proposed to explain the violation of Kasha's rule. Based on the investigation of quantum yields in substituted azobenzenes, Rau suggested a large deformation of the molecular structure along the torsional coordinate in S_2 , which would quench the isomerization reaction proceeding along the inversion coordinate in S_1 [2]. Fujino et al. could not find evidence for torsional motion in time-resolved fluorescence and resonance-Raman spectra but observed ultrafast $S_2 \rightarrow S_1$ internal conversion [3]. To explain the violation of Kasha's rule, Fujino assumed that additional relaxation pathways for high vibrational levels in S_1 could quench the observed quantum yield after excitation of S_2 . We studied the photoisomerization reaction by time-resolved photoelectron spectroscopy (TRPES) and propose a new relaxation pathway, which can reconcile the two conflicting models. First results were recently published in a communication [4]. Here we present an improved data analysis and a detailed discussion of the experimental data.

2. EXPERIMENT AND RESULTS

TRPES has been recently reviewed and details of the experimental method and its interpretation can be found elsewhere [5]. *Trans*-azobenzene was introduced via a helium supersonic molecular beam into the interaction region of a magnetic bottle photoelectron spectrometer. The molecules were photoexcited by a tunable femtosecond laser pulse (pump pulse) with a wavelength of 280-350nm. After a variable time delay, the excited molecules were ionized by a second femtosecond laser pulse (probe pulse) with a wavelength of 200 or 207nm. The emitted photoelectrons were collected as a function of pump-probe time delay and electron kinetic energy.

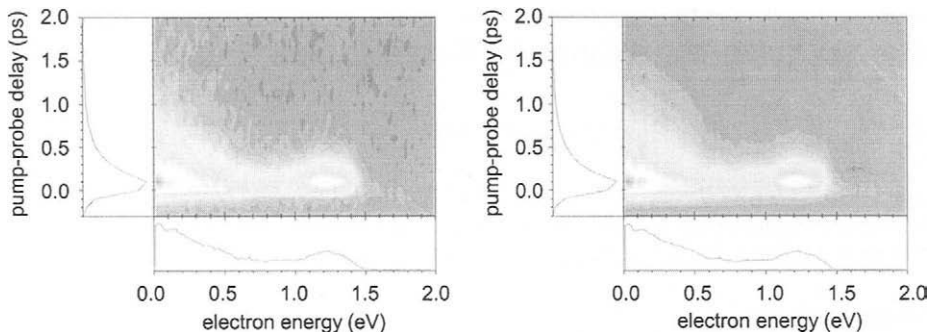


Fig. 1. TRPES of azobenzene with 330nm excitation and 200nm ionisation (left) and global fit (right). The two-dimensional spectrum (contour plot) shows the photoelectron spectra along the x-axis (integrated spectrum shown at bottom) and the evolution with the pump-probe time delay on the y-axis (integrated decay trace shown on the left).

Energy calibration of the photoelectron spectra and determination of the laser cross-correlation were performed by measuring TRPES traces for NO and butadiene. We found Gaussian shaped cross-correlations with a full-width-at-half-max of 120-190fs, depending on the wavelength. In Fig. 1 we show a TRPES trace of azobenzene and a corresponding global fit. The two dimensional data were fit with function (1) to extract the excited state population dynamics $P_i(t)$ and the corresponding photoelectron spectra $I_i(E)$ for each ionization channel i . We assumed exponential rise and decay for the population dynamics and a Gaussian time-profile $g(t)$ for the laser cross-correlation. The simultaneous fit of spectra and dynamics in the two-dimensional data allowed the reliable extraction of dynamics even for overlapping bands.

$$S(E, t) = \sum_i I_i(E) \cdot [P_i(t) \otimes g(t)] \quad (1)$$

A minimum of 3 ionization channels with distinct dynamics were necessary to reproduce the measured data at all excitation wavelengths. The fitted photoelectron bands (Fig. 2a) allowed the determination of ionization potentials as indicated for band ε_1 . For an easy interpretation of the partially resolved bands ε_2 and ε_3 , we defined an effective ionization potential IP_{50} at half the band height. The fitted decay spectra (Fig. 2b) gave lifetimes of 155fs, 0fs and 420fs for band ε_1 , ε_2 and ε_3 respectively, which corresponds to the lifetimes of the intermediate excited states. The lifetimes varied little with excitation wavelength in the investigated range. None of the bands displayed a delayed rise (for all bands we found $\tau_{\text{rise}} \approx 0 \pm 20$ fs) and we assumed direct laser-excitation for all observed excited states.

The measured ionization potentials depended on the excitation energy and are plotted in Fig. 3a. For bands ε_1 and ε_3 , the measured ionization potentials increased linearly with the excitation energy. This is expected from Franck-Condon considerations if vibrational excitation is preserved in the ionisation step. From the observed ionization potentials and using Koopmans' correlations, supported by *ab initio* calculations, we assigned band ε_1 to the ionization channel $S_2(\pi\pi^*) \rightarrow D_0(\pi^1)$ and band ε_3 to the ionization channel $S_{3/4}(\pi\pi^*) \rightarrow D_{2/3}(\pi^1)$. In S_2 and D_0 , the respective π -orbital is delocalized over the molecule and leads to reduced bonding between the nitrogen atoms. This is in contrast with a phenyl-ring localized character of the corresponding π -orbital in $S_{3/4}$ and $D_{2/3}$. Comparing the band shapes with those observed in He^1 -photoelectron spectra [6], we find good correspondence between band

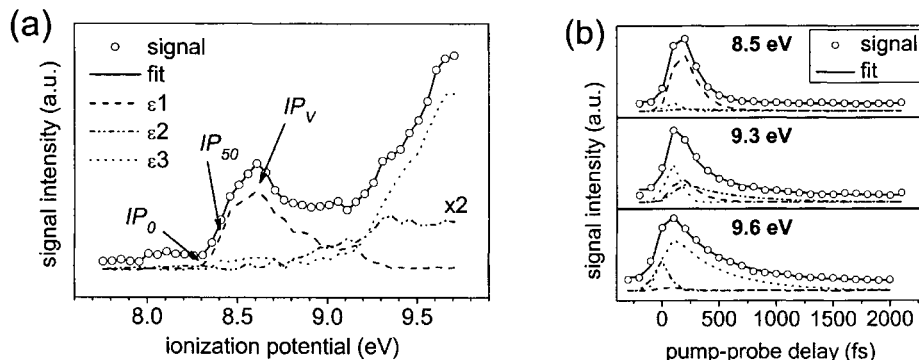


Fig. 2. Integrated photoelectron spectrum (a) and selected decay traces (b) obtained by the global fit shown in Fig. 1. Despite a considerable overlap of the photoelectron bands, the fit was very robust and gave reproducible band shapes and lifetimes of 155, 0 and 420fs for bands ϵ_1 , ϵ_2 and ϵ_3 .

ϵ_1 and D_0 , but band ϵ_3 is both wider and shifted to higher energies than the corresponding signal for $D_{2/3}$. From Franck-Condon arguments, we can thus assume that the structure of S_2 resembles that of the ground state, while that of $S_{3/4}$ may be somewhat deformed. We did not observe a photoelectron band with delayed rise, which might be expected from S_1 after internal conversion from S_2 . We ascribe this to the fact that the corresponding ionization potential for $S_1(n\pi^*) \rightarrow D_1(n^0)$ is shifted out of our detection window due to the large amount of vibrational excitation (>1 eV) in S_1 .

The ionization potential for band ϵ_2 showed no clear correlation with the excitation energy, but varied with the probe wavelength at high excitation energies. This indicated an inverted process with the probe beam exciting a high-lying and short-lived excited state, which is subsequently ionized by the pump beam. The dependence of IP_{50} on the probe wavelength was less pronounced near and below the threshold for $\pi\pi^*$ excitation (~ 3.65 eV) and the shape of band ϵ_2 changed markedly. Here we assume that an additional ‘pre-resonant’ pump-probe ionization process contributed to band ϵ_2 , i.e. the cross-section for non-resonant two-photon ionization was enhanced by near-resonance of the pump beam with the $\pi\pi^*$ states. Similar observations were made in resonance-Raman experiments [7]. The signals from the probe-pump process and non-resonant ionisation have no impact on the analysis and interpretation of the low-lying $\pi\pi^*$ state dynamics. In the excitation spectrum (Fig. 3b), we observed near-degeneracy of S_2 and $S_{3/4}$. This observation was supported by high-level *ab initio* calculations, which predicted three close-lying $\pi\pi^*$ excited states, two of which have considerable oscillator strength [4].

3. DISCUSSION

Our observations clearly show the existence of two near-degenerate photoactive $\pi\pi^*$ states S_2 and $S_{3/4}$ with lifetimes of approx. 150fs and 420fs. The different lifetimes indicate distinct relaxation channels and allow a simple model for the violation of Kasha’s rule: As reported by Fujino et al. [3], S_2 shows ultrafast internal conversion to S_1 without large amplitude motion along the torsional coordinate. This is supported by our observation of a short lifetime and a narrow photoelectron band resembling that observed for ground-state ionization. We expect subsequent relaxation of S_1 similar to that observed for direct S_1 excitation, leading to

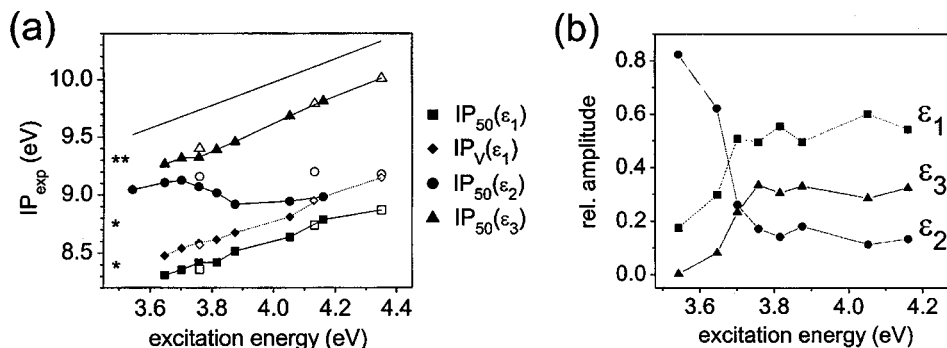


Fig. 3. (a) Ionization potentials for bands ϵ_1 , ϵ_2 and ϵ_3 in dependence of the excitation energy. Full symbols refer to measurements with 207nm ionization pulse, open symbols to 200nm ionization pulse. The sum of the energy from excitation and ionization pulse is shown as black line. Stars denote the four lowest vertical ionization potentials of 8.4, 8.75, 9.3 and 9.3eV [6]. (b) Normalized excitation spectrum showing near degeneracy for the $\pi\pi^*$ states corresponding to bands ϵ_1 and ϵ_3 .

comparable quantum yields. To explain the violation of Kasha's rule, we propose that relaxation of $S_{3/4}$ proceeds with reduced isomerization yield.

Hence the violation of Kasha's rule is neither due to torsional motion in S_2 , nor to additional relaxation channels for hot S_1 but rather to the relaxation of state $S_{3/4}$, which was not identified in previous absorption, fluorescence or resonance-Raman spectra. Compared to ground state ionisation, the photoelectron band for $S_{3/4}$ ionization is broadened and shifted to higher energies, indicating a change in molecular geometry. We can speculate that this may be due to torsional motion preceding electronic relaxation. This would agree with observations reported by Rau [2] and others, who linked the reduction in isomerization yield to the torsional coordinate. The presented model may thus reconcile the apparently contradicting observations in earlier time- and frequency-domain experiments.

REFERENCES

- [1] N. Tamai, H. Miyasaka, *Chem. Rev.*, 100 (2000) 1875.
- [2] H. Rau, *Photochromism: Molecules and Systems*; Dürr, H.; Buas-Laurent, H., Eds.; Elsevier: Amsterdam 1990, p. 165-191.
- [3] T. Fujino, T. Tahara, *J. Phys. Chem. A*, 104 (2000) 4203; T. Fujino, S.Y. Arzhantsev, T. Tahara, *J. Phys. Chem. A*, 105 (2001) 8123.
- [4] T. Schultz, J. Quenneville, B. Levine, A. Toniolo, T. J. Martinez, S. Lochbrunner, M. Schmitt, J. P. Shaffer, M. Z. Zgierski, and A. Stolow, *J. Am. Chem. Soc.*, 125 (2003) 8098.
- [5] S. Lochbrunner, J.J. Larsen, J.P. Shaffer, M. Schmitt, T. Schultz, J.G. Underwood, A. Stolow, *J. Electron Spectrosc. and Relat. Phenom.*, 112 (2000) 183; A. Stolow, *Annual Reviews of Physical Chemistry*, 54 (2003) 89; A. Stolow, *International Reviews in Physical Chemistry*, 22 (2003) 377.
- [6] T. Kobayashi, K. Yokota, S. Nagakura, *J. Electron. Spectrosc. And Relat. Phenom.*, 6 (1975) 167. For a correct band assignment, please refer to: N.E. Petrachenko, V.I. Vovna, G.G. Furin, *J. Fluor. Chem.*, 63 (1993) 85.
- [7] N. Biwas, S. Umopathy, *J. Chem. Phys.*, 107 (1997) 7849.

Comparison of Ultrafast Photoinduced Processes in Indole(NH₃)_n and Indole(H₂O)_n Clusters

H. Lippert^a, V. Stert^a, C.P. Schulz^a, I.V. Hertel^{a,b} and W. Radloff^a

^aMax-Born-Institut für Nichtlineare Optik und Kurzzeitspektroskopie, Max-Born-Str.2A, D-12489 Berlin-Adlershof, Germany

^bFachbereich Physik, Freie Universität Berlin, Arnimallee 14, D-14195 Berlin, Germany

1. INTRODUCTION

To understand the fundamental photochemical processes in biologically relevant molecular systems, prototype molecules like phenol or indole – the chromophores of the amino acids tyrosine respective tryptophan – embedded in clusters of ammonia or water molecules are an important object of research. Numerous studies have been performed concerning the dynamics of photoinduced processes in phenol-ammonia or phenol-water clusters (see e. g. [1,2]). As a main result a hydrogen transfer reaction has been clearly indicated in phenol(NH₃)_n clusters [2], whereas for phenol(H₂O)_n complexes no signature for such a reaction has been found. According to a general theoretical model [3] a similar behavior is expected for the indole molecule surrounded by ammonia or water clusters. As the primary step an internal conversion from the initially excited $\pi\pi^*$ state to a dark $\pi\sigma^*$ state is predicted which may be followed by the H-transfer process on the $\pi\sigma^*$ potential energy surface.

2. RESULTS AND DISCUSSION

Very recently we have analyzed the dissociative H-transfer reaction in indole(NH₃)_n clusters initiated by femtosecond laser pulses in the wavelength region of 250...274 nm [4,5]. In pump-probe experiments we have detected the time-dependent photoion signals as well as the spectra of the coincident photoelectrons. In Figs. 1a, b the ion transients for indole(NH₃)₁ and indole(NH₃)₄ are shown for the pump wavelength of 250 nm. On the short-time scale (Fig. 1a) we found for the heterodimer an ultrafast decay ($\tau_2 \sim 60$ fs) followed by a somewhat slower process ($\tau_3 \sim 600$ fs). The first step is assigned to the internal conversion from the primarily excited $\pi\pi^*$ state (2) to the $\pi\sigma^*$ state (3) whereas the secondary process is related to the H atom transfer from the N-H group of indole to the ammonia surroundings. This is confirmed by the corresponding electron spectra of IndNH(NH₃)₁⁺ (Fig. 2a) measured at the somewhat enlarged pump wavelength of 263nm. The peak at small electron energies (obtained by ionization with one probe photon $h\nu_2$) decreases strongly from $\tau=0$ to $\tau=250$ fs reflecting the internal conversion with the time constant τ_2 . The population of the $\pi\sigma^*$ state is reflected by the somewhat increased signal at larger electron energies (two probe photon ionization) for $\tau=250$ fs. This signal decreases weakly with the time constant τ_3 of 600...800fs (not observable in Fig. 2a) and, afterwards, due to a consecutive slow process with a decay time

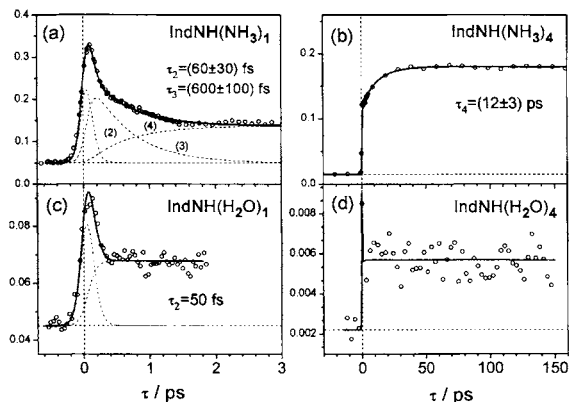


Fig. 1. Ion signals vs. delay time τ between pump (250 nm) and probe (400 nm) pulses. The solid lines are theoretical fit curves.

τ_4 of 15 ps (not shown in Fig. 1a, cf. [5]). For the heterodimer the character of the process with the time constant τ_4 is not yet fully understood. For larger clusters (Fig. 1b) we observe an increase of the photoion signals on a ps time scale which reflects a reorientation of the cluster geometry after the H transfer leading to the equilibrium structure of the parent cluster. This is demonstrated by the time-dependent electron spectra of indole(NH_3) $_4^+$ in Fig. 2b. The nearly vanishing signal at $\tau=0$ grows up on the ps time scale. Within the time of $\tau_4=12$ ps (cf. Fig. 1b) the cluster geometry changes due to reorientation until it resembles the geometry of the ion state and, thus, leading to a large Franck-Condon overlap and efficient ionization by one probe photon absorption. The electron signal on the fs time scale is not observable in this case due to a very weak Franck-Condon factor.

Correlated to the structural reorientation the accompanying IVR processes cause a dissociation of the parent clusters leading to the neutral products $\text{NH}_4(\text{NH}_3)_{n-1}$ which are detected by ionization at different probe wavelengths [6].

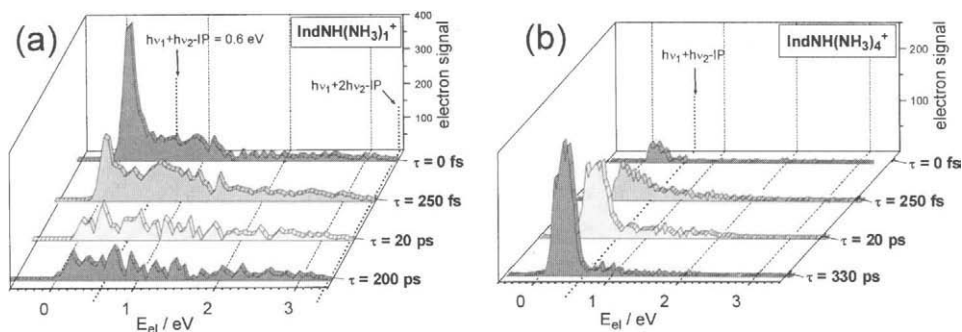


Fig. 2. Photoelectron spectra at different delay times τ between pump (263nm) and probe (400nm) pulses for indole(NH_3) $_1^+$ (a) and indole(NH_3) $_4^+$ (b). The arrows denote the maximum electron energies for one or two probe photon ionization.

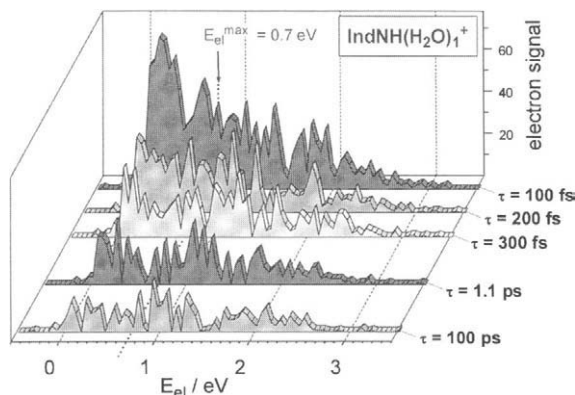


Fig. 3. Photoelectron spectra of indole(H_2O) $_1^+$ at different delay times τ between pump (250nm) and probe (400nm) pulses.

The experiments are repeated for indole(H_2O) $_n$ clusters at nearly identical laser parameters. In Figs. 1c,d the ion transients are represented for indole(H_2O) $_1^+$ and indole(H_2O) $_4^+$ obtained for the pump wavelength of 250 nm and the probe wavelength of 400 nm. As for ammonia we observe a very fast decay (~ 50 fs) of the primarily excited $\pi\pi^*$ state (see Fig. 1c) which is attributed to an internal conversion to the $\pi\sigma^*$ state. The secondary process with the time constant τ_3 , however, is not observed for indole(H_2O) $_n$ clusters, neither for $n=1$ (Fig. 1c) nor for $n=2\dots 6$ (cf. [7]). The corresponding electron spectra for the heterodimer (Fig. 3) demonstrate the ultrafast decay of the low energy signal (up to the one probe photon threshold of 0.7eV) on the fs time scale. For times of a few ps the electron spectra do not change significantly (in agreement with the time-dependent ion signal displayed in Fig. 1c), but afterwards they decrease slowly with the time constant τ_4 of 14ps [7].

Another strong difference between indole(NH_3) $_n$ and indole(H_2O) $_n$ clusters is demonstrated in Figs. 1b,d for $n=4$: in contrast to indole(NH_3) $_4^+$ we observed for indole(H_2O) $_4^+$ an ultrafast peak in the sub-ps range but no signal rise on the ps time scale. The same holds for larger clusters. This means, in indole-water clusters a structural reorientation does not occur (or is not observable). Thus, we assume a missing or – at the most – only a partial H-transfer in indole-water clusters. This result is confirmed by our unsuccessful efforts to detect any dissociation product, although even extremely high probe pulse intensities at 800 nm have been applied [7].

3. CONCLUSIONS

In contrast to indole-ammonia clusters, for which the different steps of the photoinduced H-transfer reaction have been analyzed in detail, we have found no hints for such a reaction in indole(H_2O) $_n$ clusters. Probably, like for phenol(H_2O) $_n$ complexes the endoenergetic character of the reaction $\text{H}+\text{H}_2\text{O}\rightarrow\text{H}_3\text{O}$ is responsible for the missing H-transfer process in the indole(H_2O) $_n$ clusters. Ab initio calculations of the indole-water potential energy surfaces are under way now, to elucidate this process in the heterocluster and to understand the difference with respect to the indole-ammonia complex.

ACKNOWLEDGEMENTS

We thank Dr. F. Noack for his support by providing the laser system in the Femtosecond Application Laboratory of the Max Born Institute. Financial support by the Deutsche Forschungsgemeinschaft through Sonderforschungsbereich 450 is gratefully acknowledged.

- [1] J.A. Syage and J. Steadman, *J. Chem. Phys.*, 95 (1991) 2497-2510.
- [2] G. Gregoire, C. Dedonder-Lardeux, J. Jouvet, S. Martrenchard, A. Peremans and D. Solgadi, *J. Phys. Chem. A*, 104 (2000) 9087-9090.
- [3] A.L. Sobolewski, W. Domcke, C. Dedonder-Lardeux and J. Jouvet, *Phys. Chem. Chem. Phys.*, 4 (2002) 1093-1100.
- [4] V. Stert, L. Hesse, H. Lippert, C.P. Schulz and W. Radloff, *J. Phys. Chem. A*, 106 (2002) 5051-5053.
- [5] H. Lippert, V. Stert, L. Hesse, C.P. Schulz, I.V. Hertel, W. Radloff, *J. Chem. Phys. A*, ASAP 10.1021/jp 0277098, Web Release Date June 10, 2003.
- [6] H. Lippert, V. Stert, L. Hesse, C.P. Schulz, W. Radloff and I.V. Hertel, *Eur. Phys. J. D*, 20 (2002) 445-448.
- [7] H. Lippert, V. Stert, L. Hesse, C.P. Schulz, I.V. Hertel, W. Radloff, *Chem. Phys. Lett.*, 376 (2003) 40-48.

How to disentangle evaporation and picosecond excited state dynamics in molecular clusters

S. Martrenchard, C. Dedonder-Lardeux and C. Jouvét

Laboratoire de Photophysique Moléculaire du CNRS, bât 210, Université Paris-Sud,
91405 Orsay, France

1. INTRODUCTION

During the past few years, our group has performed some experiments that enable to propose new interpretations of previous pump-probe studies on clusters. We want to present here a short summary of these interpretations to enlighten two main ideas:

- evaporation phenomena both in excited and ionic state can not be avoided. Indeed, if a photon triggers an exothermic reaction, excess energy is deposited in the cluster and can be used not only for the reaction process but also for evaporation. The consequence is that critical sizes observed for a dynamical process appearance can be wrong but more dramatic that the dynamical phenomenon probed is not the expected one but evaporation itself.
- short time experiments have to be made in parallel with long times experiments in order to get spectroscopic data related to the size and the structure of the clusters.

This article will deal more with naphthol-ammonia clusters but the case of phenol-ammonia can be quickly summarized here. The dynamical process observed in the excited state of phenol has long been attributed to an excited state proton transfer [1-7]:

$\text{PhOH}^*(\text{NH}_3)_n \rightarrow \text{PhO}^-(\text{NH}_3)_n\text{H}^+$ But we have recently unambiguously proved that the reaction is a neutral hydrogen transfer [8-11]: $\text{PhOH}^*(\text{NH}_3)_n \rightarrow \text{PhO}^\bullet + (\text{NH}_3)_n\text{H}$ by monitoring the ionisation of metastable radicals $(\text{NH}_3)_n\text{H}$ several hundreds ns after clusters excitation when initially excited $\text{PhOH}^*(\text{NH}_3)_n$ have totally decayed.

We don't want to deal here with hydrogen transfer mechanism, which is now better and better understood [12] but with the interpretation of previous experiments. Several groups have recorded pump-probe decays in phenol-ammonia system, attributed to proton transfer, but what was surprising is that the critical size for ESPT appearance was not always the same [4-7], depending on initial clusters size distribution, which is typically the signature of evaporation. Since we are sure that hydrogen transfer is the reactive process in the excited state for the small clusters ($n \leq 5$), we now attribute the pump-probe decays recorded to hydrogen transfer. For the larger ones, the ground state proton transferred structure is the most stable one and is excited by the pump laser: the dynamics probed is then evaporation, like in the case of naphthol, as discussed below.

2. RESULTS AND DISCUSSION

The 1-naphthol- $(\text{NH}_3)_n$ system has also long been considered as a prototype system for the

excited state proton transfer (ESPT) reaction [13-26]. From the observation of red shifted fluorescence (corresponding to naphtholate emission), this reaction was thought to occur when four ammonia molecules are attached to the excited naphthol. Furthermore, a 60ps decay observed in pump-probe experiments for $n=4$ has been assigned to the ESPT rate [24].

On the other hand, red shifted absorption indicates that ground state proton transfer occurs from $n \geq 5$ [13-17,23-25].

However, careful investigations of the evaporative processes in 1-naphthol-(NH₃)_n are crucial for understanding the spectroscopy and the dynamics of this system [27]. These evaporation processes are expected to be particularly important since an exothermic reaction occurs in the ionic clusters, even at vertical ionization threshold : proton transferred structure is much more favorable in the ion than in the neutral.

Ionic evaporation can be evidenced by studying carefully the shape of the mass peaks in time-of-flight mass spectroscopic measurements. The simple method used here to identify evaporation has already been demonstrated [28-31]. It is based on the detection of the translational energy: if an evaporation occurs, some kinetic energy is released and its evaluation allows one to distinguish between non-evaporating clusters and those that have undergone evaporation.

Clusters, produced in a supersonic expansion, are ionized by laser. Delayed pulsed extraction is used to send the ions towards a 1m time-of-flight mass spectrometer perpendicular to the jet axis. During the delay time between ionization and extraction, the ions spot size increases, due to their kinetic energy. The result is a broader mass peak with a width that is related to the kinetic energy released after the ionization and can be deduced after calibration of the experiment.

With this method, we have shown [27] that the two main bands of the excitation spectrum recorded at naphthol-(NH₃)₂⁺ mass peak do not belong to the same species: one band excitation leads to a narrow mass peak and thus corresponds to the direct excitation of 1-2 complex, since the other one leads to a broad peak and corresponds to the excitation of the 1-3 complex, which loses one ammonia molecule in the ionic state.

In the same way, it can be shown that, for $n \geq 3$, all clusters evaporate at least one ammonia molecule in the excitation and/or ionization processes.

This leads to the conclusion that previous results must be shifted from one unit: if there is an excited state proton transfer, it occurs only at $n = 5$ and the ground state proton transfer occurs in clusters with $n \geq 6$.

Not only ionic evaporation has to be considered, but also **excited state evaporation**. Previous pump-probe experiments that conclude to the existence of ESPT show picosecond decays for one cluster size: 1-4 and flat signals for larger ones [24]. For other authors, the decay is observed for the 1-3 complex [20]. Furthermore, the rate of the observed process is also typically the one of evaporation (of one ammonia molecule). In the non reactive Na(NH₃)_n system, evaporation rate has been measured and is also at the tens picoseconds order of magnitude [32]. It is clear that excited state evaporation must also be taken into account.

We have developed a model to take into account these evaporation processes (for more details, in particular kinetic equations, see ref 27) that can be both applied to phenol and naphthol. The main idea is the following: the excited state decays observed correspond to evaporation of ammonia molecules after excitation of ground state proton transferred naphthol-(NH₃)_{n \geq 6} clusters. As in the case of phenolate [31], a strong change in dipole

moment induced by excitation is expected, leading to a strong rearrangement in the system. Thus, excitation with the first photon leads enough excess energy to induce the evaporation of one or two ammonia molecules. Ionization can occur before or after the evaporation. If it occurs before, the produced ion is “hot” and can also evaporate a molecule. If it occurs after, the cold product is ionized and the evaporation in the ion is less important. The same scheme can be applied for the evaporation of the second molecule. With this simple assumption, if evaporation rate and ionization cross section do not vary significantly with the cluster size, for a given complex 1- n , decay in the excited state to give 1-($n-1$) will be approximately compensated by repopulation in the ionic state $1-n^+ \rightarrow 1-(n-1)^+$ and a flat transient will be recorded at the mass 1-($n-1$) in pump-probe experiment. Only a strong change in the evaporation or in the ionization efficiency can modify this flat signal. It is the case for $n=6$ which is the first size for which the ground state structure changes: it is no longer a proton transferred structure: excess energy in S_1 is too small to induce evaporation.

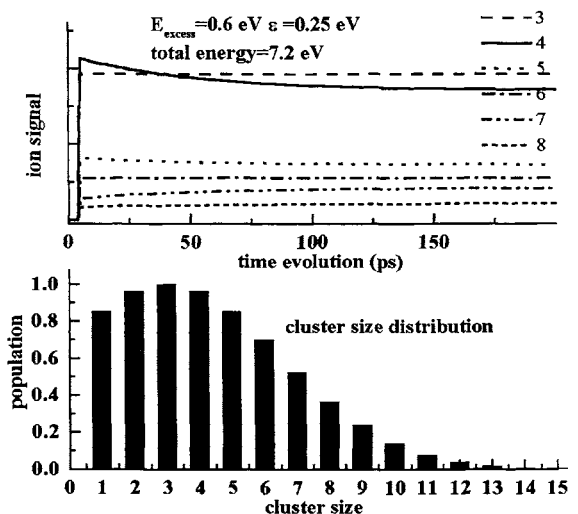


Fig. 1. Top : Simulated picosecond transient for different cluster sizes; E_{excess} is the excess energy in the excited state, ϵ is the binding energy of one ammonia molecule. Bottom : initial cluster size distribution

Fig 1 presents the results obtained for a broad initial size distribution: one can perfectly obtain a decay for the 1-4 mass peak and flat signals for the other channels by taking only the evaporation processes of one and two ammonia molecules into account. Thus, the recorded picosecond decays are not a direct proof of ESPT.

3. CONCLUSION

In these two examples of phenol and naphthol-ammonia clusters, we have evidenced the role played by evaporation phenomena that are expected to be present in a lot of clusters pump-probe studies and can not only hide but replace the reactive processes. Since absorption

selectivity is difficult to obtain when short laser pulses are used, evaporation processes have always to be taken into account in the interpretation of the experiment and if a reaction proceeds slower than evaporation, the excess energy dissipative process is often evaporation itself. It can be a serious hindrance for comparison between reactive processes in clusters and in solution.

REFERENCES

- [1] O. Chesnovsky and S. Leutwyler, *J. Chem. Phys.*, **88** (1988) 4127
- [2] T. Droz, R. Knochenmuss, S. Leutwyler, *J. Chem. Phys.*, **93** (1990) 4520
- [3] C. Jouvét, C. Dedonder-Lardeux, M. Richard-Viard, D. Solgadi and A. Tramer, *J. Phys. Chem.*, **94** (1990), 5041
- [4] S.K. Kim, J.J. Breen, D.M. Willberg, L.W. Peng, A. Heikal, J.A. Syage and A. Zewail, *J. Phys. Chem.*, **99** (1995) 7421
- [5] S.K. Kim, S. Li, E.R. Bernstein, *J. Chem. Phys.*, **95** (1991) 3119
- [6] J.A. Syage and J. Steadman *J. Chem. Phys.*, **95** (1991) 2497
- [7] J.A. Syage, *Faraday Discuss.*, **97** (1994)
- [8] G. Pino, G. Grégoire, C. Dedonder-Lardeux, C. Jouvét, S. Martrenchard and D. Solgadi, *J. Chem. Phys.*, **111** (1999) 10747
- [9] G. Pino, G. Grégoire, C. Dedonder-Lardeux, C. Jouvét, S. Martrenchard and D. Solgadi, *Phys. Chem. Chem. Phys.*, **2** (2000) 893
- [10] G. Grégoire, C. Dedonder-Lardeux, C. Jouvét, S. Martrenchard and D. Solgadi, *J. Phys. Chem. A*, **105** (2001) 5971
- [11] G. Grégoire, C. Dedonder-Lardeux, C. Jouvét, S. Martrenchard, A. Peremans and D. Solgadi, *J. Phys. Chem.*, **104** (2000) 9087
- [12] A. L. Sobolewski, W. Domcke, C. Dedonder-Lardeux, and C. Jouvét, *Physical Chemistry Chemical Physics*, **4** (7) (2002) 1093
- [13] O. Chesnovsky and S. Leutwyler, *Chem. Phys. Lett.*, **121** (1985) 1.
- [14] O. Chesnovsky and S. Leutwyler, *J. Chem. Phys.*, **88** (1988) 4127.
- [15] T. Droz, R. Knochenmuss and S. Leutwyler, *J. Chem. Phys.*, **93** (1990) 4520.
- [16] R. Knochenmuss, I. Fisher and D. C. Lührs, *Isr. J. Chem.*, **39** (1999) 221.
- [17] R. Knochenmuss, *Chem. Phys. Lett.*, **293** (1998) 191.
- [18] J. J. Breen, L. W. Peng, D. M. Willberg, A. Heikal, P. Cong and A. H. Zewail, *J. Chem. Phys.*, **92** (1990) 805.
- [19] S. K. Kim, J. K. Wang and A. H. Zewail, *Chem. Phys. Lett.*, **228** (1994) 369.
- [20] S. K. Kim, J. J. Breen, D. M. Willberg, L. W. Peng, A. Heikal, J. A. Syage and A. H. Zewail, *J. Phys. Chem.*, **99** (1995) 7421.
- [21] S. K. Kim, S. Li and E. R. Bernstein, *J. Chem. Phys.*, **95** (1991) 3119.
- [22] M. F. Hineman, G. A. Brucker, D. F. Kelley and E. R. Bernstein, *J. Chem. Phys.*, **97** (1992) 3341.
- [23] D. F. Kelley and E. R. Bernstein, *Chem. Phys. Lett.*, **305** (1999) 230.
- [24] D. C. Lührs, R. Knochenmuss and I. Fisher, *Phys. Chem. Chem. Phys.*, **2** (2000) 4335.
- [25] R. Knochenmuss, *Chem. Phys. Lett.*, **311** (1999) 439.
- [26] R. Knochenmuss, I. Fischer, *Int. J. of Mass. Spec.*, **220** (2002) 343.
- [27] C. Dedonder-Lardeux, D. Grosswasser, C. Jouvét, S. Martrenchard and A. Teahu, *Phys. Chem. Chem. Phys.* **3** (2001) 4316
- [28] H.J.Hwang and M. El-Sayed, *J. Chem. Phys.*, **94** (1990) 4877
- [29] D.W. Chandler and P.L Houston, *J. Chem. Phys.*, **87** (1987) 1445
- [30] L.M. Yoder, J.R. Parker, K.T. Lorenz and D.W. Chandler, *Chem. Phys. Lett.*, **302** (1999) 602
- [31] E.J. Bieske, M.W. Rainbird and A.E.W. Knight, *J. Chem. Phys.*, **90** (1989) 2068
- [32] G. Grégoire, M. Mons, I. Dimicoli, C. Dedonder-Lardeux, C. Jouvét, S. Martrenchard and D. Solgadi, *J. Chem. Phys.*, **110** (1999) 1521
- [33] G. Granucci, J.T. Hynes, P. Millié and T.-H. Tran-Thi, *J. Am. Chem. Soc.*, **122** (2000) 12243

Vibrational relaxation of photoexcited Na₃F

V. Blanchet, J.M. L'Hermite, A. Le Padellec, B. Lamory, P. Labastie

Lab. Collisions Agrégats Réactivité, CNRS UMR 5589, IRSAMC-UPS, 118 route de Narbonne, 31062 Toulouse, FRANCE

We have investigated the vibrational relaxation of Na₃F by time-resolved photoionization at the threshold. Among the two isomers of Na₃F, we have studied the excited electronic states of the C_{2v} one. The pump-probe signal clearly shows damped oscillations, the period of which is fitted to 390±8 fs, close to twice the previously measured bending mode of Na₂F,[1] while the relaxation time is 1275±50 fs.

1. INTRODUCTION

Small Na_nF_{n-p} clusters can be considered as formed of n Na⁺ ions and $n-p$ F⁻ ions, which tend to form a rock-salt lattice, together with p excess electrons. The electronic arrangement, and hence the ionization potential, is thus very structure dependent, as indeed verified in Refs.[2-9]. In this respect, it may happen that different isomers of the same cluster present a significant difference between their ionization potential, allowing to monitor selectively the passage through one specific isomer in time-resolved experiments. Indeed, the ionization probability may become time-dependent, provided the probe pulse energy is low enough to photoionize only one isomer while the molecule is excited in such a way that it wanders through several structures. Na₃F is such a cluster, with two isomers: the lowest one with a quasi-planar C_{2v} structure and a vertical ionization energy of roughly 4.9 eV, while the second one with a 3D C_{3v} structure and a vertical ionization energy of 4.4 eV.[4,5] These structures are depicted on Fig. 1(a). Such a large difference in vertical ionization energies makes this cluster an ideal system to test the above ideas.

2. PHOTOPHYSIC OF Na₃F

The apparatus has been already described in Ref. [7]. The clusters are produced by laser vaporization of a sodium rod, with helium at about 5 bars as a carrier gas and a small amount of SF₆. The repetition rate is 10 Hz. In this configuration, the vibrational temperature of the formed clusters is roughly 400 K,[10] that gives 85% of C_{2v} geometry and 15% of C_{3v} for a Boltzman distribution. The laser beams are focused onto the cluster beam between the first two plates of an axial Wiley Mac-Laren Time-Of-Flight mass spectrometer with a reflectron. The photoionization efficiency curve as well as the photoabsorption spectrum determined by a photodepletion experiment are displayed on Fig. 1(b) and 1(c) respectively. The ionization threshold is at 4.3 eV, close to the 4.4 eV calculated for the C_{3v} isomer and 4.9 eV for the C_{2v} isomer (see the Fig. 1 (b)). The conclusion arising out of the photodepletion spectrum shown on Fig 1(c) and from *ab initio* calculations of the excited states, [5] is that the observed

spectrum is due to the C_{2v} isomer, and that the photoionization peak at 4.65 eV is a preionization resonance of this isomer (adiabatic ionization potential predicted at 4.26 eV). More information is available in Ref. [11].

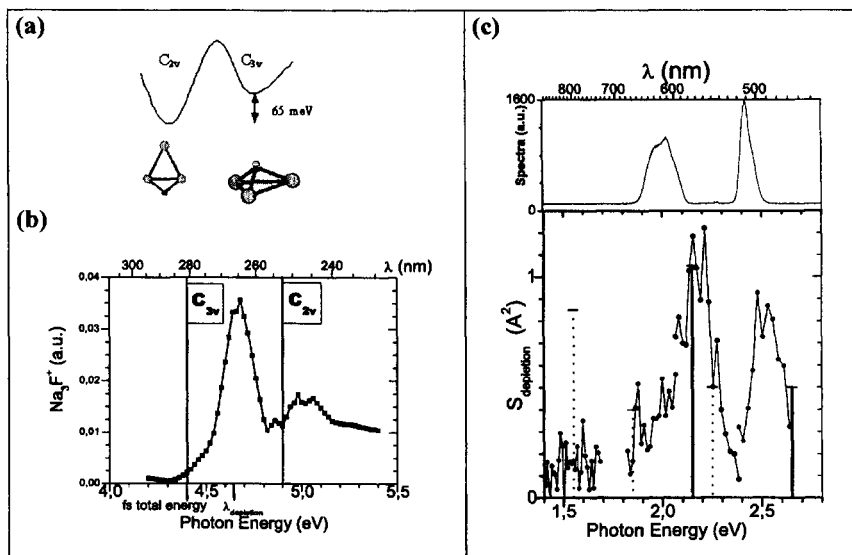


Fig. 1. (a) The two isomers of Na_3F . (b) Photoionization efficiency curve of Na_3F . *Ab initio* vertical ionization energies of the isomers are indicated by vertical lines. The UV probe photon energy used in the photodepletion experiment, as well as the femtosecond pump+probe total energy, is indicated by down arrows. (c) Photoabsorption spectrum of Na_3F determined by photodepletion spectroscopy. The calculated oscillator strengths for vertical excitations are indicated for both the C_{2v} and C_{3v} structures by straight and dotted lines respectively.[5] The spectra of the femtosecond pulses are also indicated.

3. TIME RESOLVED PHOTOIONIZATION

In order to study nuclear and relaxation dynamics in a pump-probe scheme by detecting ion signal, the total pump+probe energy should be just above the C_{3v} vertical ionization potential (4.4 eV), where the signal is likely to be most sensitive to a change of geometry. In order to simplify the dynamics, the vibrational energy in the excited state should be taken as low as possible, which lead us to a pump energy in the rising edge of the first band (~ 2.0 eV, the $1^1B_2+2^1A_1$ electronic state) or either the second band (~ 2.4 eV, the 1^1B_1 one) on the Fig. 1 (c). By selecting these two wavelength ranges, we reach as well the ionization threshold at 4.4 eV.

Each laser pulse is generated by a Non-collinear Optical Parametric Amplifier (NOPA).[12] The input of these devices is taken from the output of a kHz-1mJ chirped pulse amplification. One NOPA generates a 15nm-broadband pulse centered at 510 nm compressed with Brewster-cut fused silica prisms. The second NOPA generates a 40nm-broadband pulse centered at 620 nm compressed with chirped mirrors. On the top of the Fig. 1 (c), the spectrum of the two pulses is shown. The cross-correlation signal, taking into account all the dispersive media on the beam paths, and recorded through a 20 μ m-thick BBO crystal, has a

full-width at half maximum of 180 ± 10 fs (Fig. 2). The linear chirps estimated are both in the range of $\phi''=800$ fs². Several studies have already pointed out the influence of a small linear chirp on the pump or either pulse relative to ultrafast dynamics.[13,14,15,16] Since we detect the ion signal and not a photoelectron spectrum,[17,18,19] the main consequence of a chirp on the pump pulse and probe pulse is to reduce the time-resolution. The poor pulse to pulse stability of the cluster beam is the main source of fluctuations. In order to get rid of spurious temporal variations, we normalize the pump-probe ion yield by the non-zero ion signal obtained with the 2.4 eV pulse alone, considered as proportional to the number of Na₃F clusters in the beam.

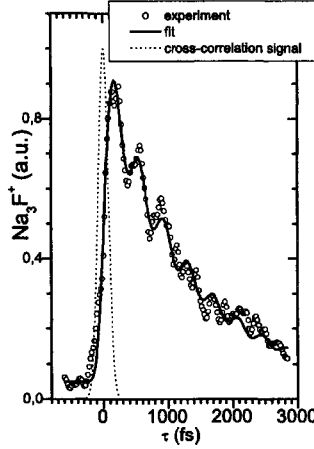


Fig. 2. Fit (solid line) of the pump-probe signal (empty circle symbols) using Eqs. (1–3) with a cross-correlation signal of 180 fs FWHM (dot line).

Every Na_nF_p clusters absorb in the visible range.[11] However among all of them, only Na₃F shows a marked dependence on the time delay. Typical pump-probe signals are shown on Fig. 2. When 2.4 eV excites first Na₃F, the signal shows an oscillatory behavior together with an exponential decay. These oscillations are related to vibrational dynamics and the ability to observe them is fixed mainly by the strong geometry restriction on the ionization probability (only 4.4 eV as total energy). In order to extract the typical time constants of the wavepacket dynamics, the pump-probe signal is modeled by

$$S(\tau) = |g_{cc}(t) \otimes f(t)|^2 \quad (1)$$

where $g_{cc}(t)$ is linked to the cross-correlation signal with a FWHM $\tau_{cc}=180$ fs by $g_{cc}(t) = e^{-2 \ln 2 \times (t/\tau_{cc})^2}$. $f(t)$ models the population in the excited state that might be photoionized. In order to reproduce the main features observed on the Fig. 2, $f(t)$ is a decaying function with an oscillating part :

$$f(t) = e^{-t/2\tau_e} \times \left[(\cos(\Omega t) + \alpha \times \cos(\varphi - \Omega t)) + i(\sin(\Omega t) + \alpha \times \sin(\varphi - \Omega t)) \right] \quad (2)$$

where the pure decay part is homogeneous and characterized by τ_e , the period of the oscillations is 2Ω , α fixes the amplitude of the oscillations, and φ allows to introduce a shift T_s on the first maximum relative to the origin. The best fit parameters are $\tau_e = 1280 \pm 50$ fs ,

$\pi/\Omega = 390 \pm 10$ fs, $\varphi = 3.47 \pm 0.50$ rad, $\alpha = 4.6 \times 10^{-2} \pm 2 \times 10^{-4}$. This results in a time-shift $T_s = 180 \pm 30$ fs, duration necessary to reach the geometry of highest ionization probability. The fit is shown on the Fig. 2.

The oscillations observed may be interpreted as a variation of the ionization potential induced by nuclear motion, or in other words a vibrational excitation in the excited state populated by the pump laser pulse. The C_{2v} isomer of Na_3F is electronically very close to Na_2F+Na . If a bending motion is initiated in the Na_2F part, the F atom may come close to the third Na atom, then back to the initial position, and so on. If the oscillation motion is similar to that of Na_2F , the position of closest distance between F and the third Na will be attained every other oscillation, which means that the period is expected to be roughly twice that of Na_2F measured at 185 fs.[1] The overall time-dependant pump-probe signal vanishes with a decay time of about 1 ps that results from a drop of the Na_3F population open to ionization. Two alternative explanations may be given : either, the population of Na_3F^* decreases due to fragmentation or Na_3F^* evolves toward configurations in which it is no longer ionized. Ideally, the fragmentation hypothesis could be monitored through an increase of the Na_2F signal in the mass spectrum. Unfortunately, the background signal of Na_2F is huge which makes such a tiny variation undistinguishable. Wavepacket dynamics calculations are also performed to get a better insight.[20] Another surprising result from this time-resolved experiment is the absence of a clear time-dependency for negative delay. Indeed as mentioned above (see the Fig. 1 (c)), the 620 nm pulse might also excite the first band, later photoionized by the 510 nm pulse. As a matter of fact, the experimental curve has a small “bump” in this region that may be due to a “probe-pump” scheme with a very small decay time. A main explanation to the absence of visible signature at negative delay, may be easily explained by the strong requirement imposed on the ionization. Indeed a threshold ionization limits the number of geometries that might be probed.

REFERENCES

- [1] S. Vajda, et al. Phys. Rev. Lett. 89 (2002) 213404.
- [2] E.C.Honea, et al. Phys. Rev. Lett. B47 (1993) 7480.
- [3] G. Rajagopal, et al. Phys. Rev. Lett 64 (1990) 2933.
- [4] V. Bonacic-Koutecky, J. Pittner and J Koutecky, Chem. Phys., 210 (1996) 313.
- [5] V. Bonacic-Koutecky and J. Pittner, Chem. Phys., 225 (1997) 173.
- [6] J. Giraud-Girard, D. Maynau, Z. Phys. D23 (1992) 91. J. Giraud-Girard, D. Maynau, Z. Phys. D32 (1994) 249.
- [7] P. Labastie, et al, J. Chem. Phys., 103 (1995) 6362.
- [8] P. Poncharal, J-M. L’Hermite and P. Labastie, Z. Phys. D 40 (1997) 10.
- [9] G. Durand et al, J. Chem. Phys., 110 (1999) 7884.
- [10] P. Labastie et al, Z. Phys. D, 34 (1995) 135.
- [11] J.M. L’Hermite et al., accepted in Eur. Phys. J. D (2003)
- [12] G. Cerullo, M. Nisoli, and S. De Silvestri, App. Phys. Lett. 71 (1997) 3616.
- [13] C. J. Bardeen, Q. Wang, and C. V. Shank, Phys. Rev. Lett. 75 (1995) 3410.
- [14] T. Saito and T. Kobayashi, J. Phys. Chem. 106 (2002) 9436.
- [15] M.-C. Yoon et al., J. Chem. Phys. 118 (2003) 164.
- [16] S. Zamith et al., J. Chem. Phys. 119 (2003) 3763.
- [17] A. Assion et al, Phys. Rev. A 54 (1996) R4605.
- [18] S. Meyer, C. Meier, and V. Engel, J. Chem. Phys. 108 (1998) 7631.
- [19] L. Nugent-Glandorf et al, Phys. Rev. Lett. 87 (2001) 193002.
- [20] M.-C. Heitz et al, J. Chem. Phys 118 (2003) 1282.

Femtosecond infrared strong field ionisation of metal clusters produced by kHz laser ablation

Marc Smits^a, C.A. de Lange^a, Adrian Pegoraro, D. M. Rayner and Albert Stolow

National Research Council, 100 Sussex Drive, Ottawa, Ontario, Canada, K1A 0R6

a) Laboratory for Physical Chemistry, University of Amsterdam, Nieuwe Achtergracht 127-129, 1018 WS Amsterdam, The Netherlands

1. INTRODUCTION

Modern chirped pulse amplification (CPA) femtosecond laser systems permit the study of high order non-linear optical phenomena such as ultra-high harmonic generation, Coulomb explosion, and strong field control of chemical processes. In the quasi-static non-resonant regime, strong field ionisation occurs when the electric part of the laser field suppresses the core potential barrier such that the electron can tunnel out or, at even higher intensities, can escape over the barrier. Tunnelling can only take place when the Keldysh parameter γ is less than unity, i.e. the tunnelling time is less than the laser period [1]. Most characteristics of non-linear ionisation of rare gas atoms are well understood and are successfully described by ADK theory [2]. This theory is based on the single active electron approach and on the adiabatic picture of electron dynamics (the electronic motion is faster than the timescale of the laser field oscillation). Irrespective of the value of the Keldysh parameter, these assumptions are not necessarily valid for molecules or clusters, where many doubly excited states might contribute to the polarisation of the molecule, and where the spatial extent of the molecular orbital might increase the timescale of electronic motion. Although recent studies have proposed a modification of the original Keldysh parameter [3], these studies still neglect the electron dynamics within the potential. In previous publications [4] we show that in the long wavelength limit, ionisation of all studied molecules is harder than expected from any of these theories. We speculated that this was due to a dynamic screening effect due to the polarisation of all bound electron in the laser field, shielding the 'active' electron and thus suppressing ionisation. In this study we demonstrate the existence of these multielectron dynamics by studying non resonant strong field ionisation of small Nickel clusters. Nickel is a typical transition metal with electronic configuration $[\text{Ar}] 3d^8 4s^1$. Nickel clusters as a model system resemble more closely a zero range potential, due to the compact geometry. Furthermore it provides us with a variable parameter: the number of atoms per cluster.

2. EXPERIMENTAL SETUP

For this experiment, a stable kHz rate molecular beam ablation source was developed, matching the kHz repetition rate of most amplified femtosecond lasers [5]. Our vacuum apparatus is presented in Fig 1 and shows the three differentially pumped regions and a Campargue type molecular beam source. The regions are pumped by respectively a Roots Blower ($P < 10^{-1}$ Torr), a diffusion pump ($P < 10^{-4}$ Torr), and a turbo molecular pump ($P < 10^{-6}$ Torr). The first region contains a modified Smalley type cluster source [6] that is employed with a glass growth channel and nozzle. The source is based upon a strong non-resonant interaction of a dithering laser focus with a rotating and translating solid rod, hydrodynamic transport of the ablated material in helium and subsequent supersonic expansion. In the second region residual ions after recondensation of the plasma are removed from the molecular beam by two deflection plates. The final region contains a standard two region linear time of flight Wiley-McLaren mass spectrometer, where the repeller and attracter plates are kept at negative voltage and the final plate and flight tube are kept at ground. Compensation for the potentially high lab-frame molecular beam velocity is provided by two deflection plates, mounted perpendicular to the molecular beam and typically operate at a potential difference of up to 100 V. A narrow slit ($< 500 \mu\text{m}$), kept at ground, is mounted perpendicular to laser propagation, on top of these deflection plates to collect ions only from within a part of the focus where the axial intensity is constant. The ions are detected using microchannel plates, fed directly into a pulse amplifier and discriminator. Mass spectra are individually recorded for each laser shot using a PCI- based multichannel scaler (FastComtec).

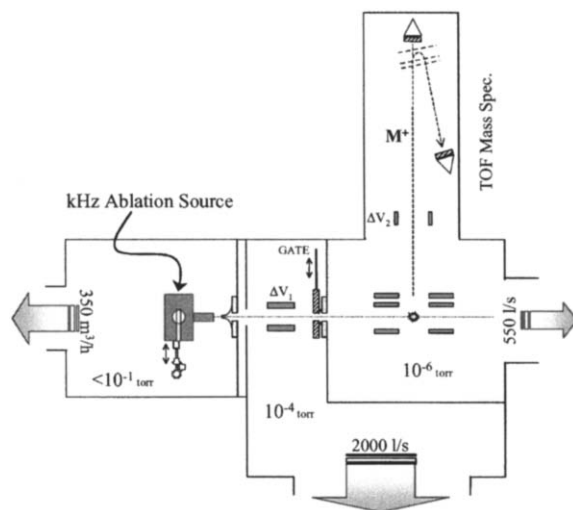


Fig. 1. kHz molecular beam ablation setup with a linear time of flight mass spectrometer.

The energy of the laser pulse is measured using an integrating sphere and a (GeGaAs) photodiode, integrated by a boxcar. To ensure that mass spectra and laser energies are recorded in pairs, a home built amplitude to time converter is used to write the energy as a time delay at the end of each mass spectrum.

Our laser system includes a femtosecond Ti:Sa oscillator (Spectra Physics), and both a regenerative amplifier and a two pass linear amplifier (Positive Light). Part of the amplified femtosecond laser pulses are used to pump an optical parametric amplifier (TOPAS, Quantronix/LightConversion). Either the output of the amplified Ti:Sa (800 nm, 2.5 mJ, 80 fs) or the optical parametric amplifier (1.5 μm , 150 μJ , 90 fs) are used as the source for strong field ionisation. The beam diameter is approximately 1 cm and the light is focused into the mass spectrometer using a 150 mm anti-reflection coated lens (i.e. $f_{\#}=15$). Intensities of over 10^{14} W/cm^2 can be reached for either wavelengths. Absolute laser intensities ($\pm 30\%$) are determined by our calibration method: the so-called saturation intensity of a reference standard (xenon) is measured using an intensity scan and is calibrated to the ADK-value as discussed in detail elsewhere [7].

The light of a Nd:YLF (Positive Light Merlin) ablation laser, synchronised with the femtosecond laser setup (Stanford Research Delay Generator), is focused onto the target rod using a 300 mm lens. The laser energies vary from 5 to 15 mJ per pulse, depending on the ablation characteristics of the metal. Before the first use, the metal rod is quickly sanded and exposure to oxygen is minimised.

3. RESULTS

In Fig. 2 we present one of our preliminary intensity scans of Ni_8 . The saturation intensity is found at the intersection of the extrapolated linear part of the ion signal and the intensity axis, and is an independent measure for the ease of ionisation. Using the measured ionisation potential of Ni clusters, [8] and assuming a Gaussian beam profile ($t=90$ fs, $l=1500$ nm), we calculate the saturation intensity with the ADK theory. So far, most measured saturation intensities for Ni clusters are a factor of approximately 3 times higher than the values predicted by ADK theory. This suppression of ionization clearly shows the anticipated multielectron shielding effect in metal clusters, due to a polarization of the cluster by the remaining electrons. We are currently working on models to include multielectron polarisability into our calculations by describing the clusters as a macroscopic conducting sphere.

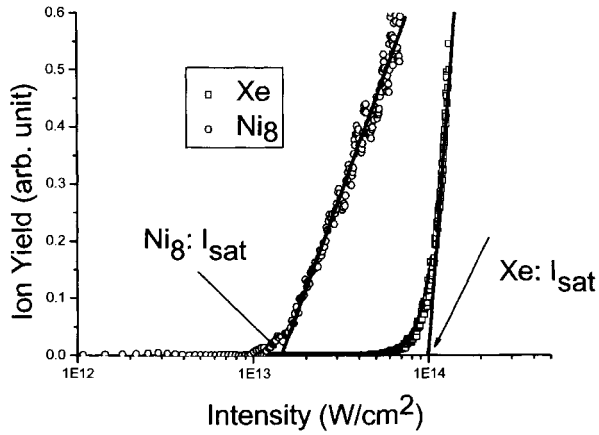


Fig 2. Saturation scan of Ni₈ and calibration scan with Xe.

REFERENCES

- [1] L.V. Keldysh, Sov. Phys. JETP 20, 1307 (1965).
- [2] M.V. Ammosov, N.B. Delone, and V.P. Krainov, Sov. Phys. JETP 64, 1191 (1986).
- [3] M.J. DeWitt, and R.J. Levis, Phys. Rev. Lett. 81, 5101 (1998)
- [4] M. Lezius, V. Blanchet, D.M. Rayner, D.M. Villeneuve, A. Stolow, and M.Y. Ivanov, Phys. Rev. Lett 86, 51 (2001)
- [5] M. Smits, S. Ulrich, T. Schulz, M. Schmitt, J.G. Underwood, J.P. Shaffer, C.A. de Lange, A.J. Alcock, D.M. Rayner, and A. Stolow, Rev. Sci. Instrum (in press, nov. 2003)
- [6] M. E. Geusic, M. D. Morse, S. C. O'Brien, and R. E. Smalley, Rev. Sci. Instrum. 56, 2123 (1985); M. D. Morse, M. E. Geusic, J. R. Heath, and R.E. Smalley, J. Chem. Phys. 83, 2293 (1985)
- [7] S. Hankin, D. Villeneuve, P. Corkum, and D. Rayner, Phys. Rev. A 64 (2001)
- [8] M.B. Knickelbein, S. Yang, and S.J. Riley, J. Chem. Phys **93**, 94 (1990)

The structure of carboxylic acid dimers: results by time-resolved femtosecond degenerate four-wave mixing spectroscopy

V. V. Matylitsky^a, M. F. Gelin^b, C. Riehn^a and B. Brutschy^a.

^aJohann Wolfgang Goethe-Universität Frankfurt / M., Institut für Physikalische und Theoretische Chemie, Marie-Curie-Str. 11, D-60439 Frankfurt / M., Germany

^bInstitute of Molecular and Atomic Physics, Skaryna Avenue 70, Minsk 220072, Belarus.

1. INTRODUCTION

Rotational coherence spectroscopy (RCS) is a powerful time domain method for obtaining structural information on large isolated molecules and clusters. The various strategies and implementations for RCS have been reviewed recently in detail. [Ref. 1 and refs. therein] Particularly, time-resolved femtosecond degenerate four-wave mixing (fs DFWM) allows investigate large species without permanent dipole moment and chromophore and provides high precision data for molecules in the ground state. We report the first rotationally resolved spectra of formic (HCOOH) and acetic (CH₃COOH) acid dimers. They have been investigated by fs DFWM in a gas cell (≈ 10 mbar, 300K) and in a supersonic jet expansion (≈ 60 K).

2. EXPERIMENT AND SPECTRAL SIMULATIONS

The experimental setup and the fs DFWM method have been described in detail elsewhere.[1] Briefly, we used a Ti:Sapphire femtosecond chirped-pulse amplified laser system. Its fundamental output radiation (800 nm, 1 kHz, 0.8 mJ/pulse, 190 fs fwhm autocorrelation) is split into two pump beams and one probe beam of identical energy and polarization. The linearly polarized laser beams are overlapped in the sample (gas cell filled with vapor pressure at room temperature or pulsed supersonic expansion) in the forward box arrangement for four-wave mixing,[2] providing the phase matching condition and allowing for the separation of the coherent signal. The fs-DFWM spectrum is recorded as the four-wave mixing signal intensity vs. the time delay between pump and probe beams.

The spectral simulation procedure is described in more detail elsewhere.[3] Here, we introduce briefly the basic equations. The rotationally-sensitive part of a general fs DFWM signal is expressed through the third order molecular susceptibility $\chi(t)$ as follows [4,5]

$$S(t) = I(t) \otimes |I(t) \otimes \chi(t)|^2 e^{-t/\tau}, \quad \chi(t) \sim \text{Im} \sum_{i,j=A,B,C} \langle [\beta_{ij}, \exp\{-iHt/\hbar\} \beta_{ji} \exp\{iHt/\hbar\}] \rangle$$

where $I(t)$ is the intensity of the laser pulses, τ is a phenomenological decay time, the indices label the axes of the principal moments of inertia, β_{ij} is the imaginary part of the traceless polarizability tensor (PT) of a ground vibronic state. To account for the effect of centrifugal distortions (CDs) on the molecular rotation, the A-reduced Watson parametrization of the nonrigid asymmetric top Hamiltonian H has been adopted.[6] To reproduce

experimental spectra the following parameters were used: the rotational constants (A , B , C), the three CD constants Δ_J , Δ_K , Δ_{JK} (asymmetry-induced CD constants δ_K , δ_J can be set to zero for slightly asymmetric tops), a parametrized polarizability φ ($\beta_{AA} \sim \cos(\varphi)$, $\beta_{BB} \sim \sin(\varphi)$, $\beta_{CC} \sim -(\cos(\varphi) + \sin(\varphi))$), see Ref. [3]), external dephasing time τ , a time shift offset for all transients and a scaling factor for the total intensity of the fs-DFWM signal.

3. RESULTS AND DISCUSSIONS

3.1 Formic acid monomer (HCOOH)

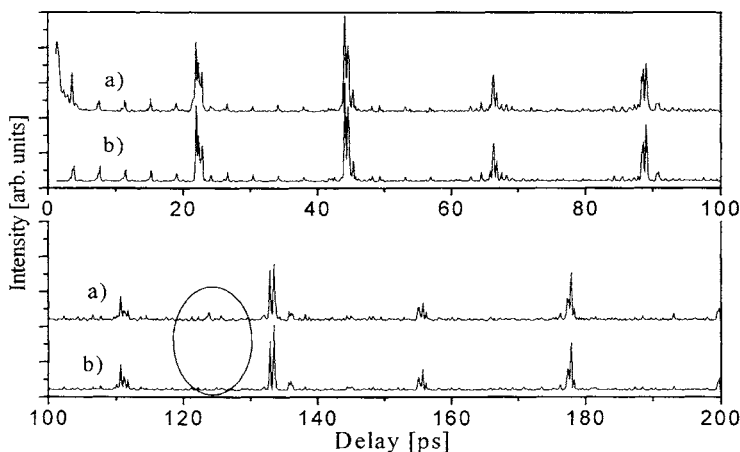


Fig.1. a) Experimental fs DFWM spectrum of formic acid vapor at 10 mbar. b) Fitted simulation of the spectrum based on a nonrigid asymmetric rotor model.

Note, that in the marked region at ≈ 124 ps a J-type recurrence of the formic acid dimer appears in the experimental spectrum.

Fig.1a shows the first 200ps of the fs DFWM spectrum of HCOOH vapor at room temperature. A complete fitting of the spectrum delivers values of rotational and CD constants and information on the diagonal elements of the PT for HCOOH. The rotational and CD constants are in good agreement with reference values from a Fourier-Transform microwave experiment.[7] The experimental spectrum is fitted very well by the simulation (Fig. 2b), except for the region 120-130ps (marked in Fig. 1). The spectral features in this region originate from the formic acid dimer (HCOOH)₂.

3.2 Formic acid dimer (HCOOH)₂

The rotational recurrence located at 124 ps (Fig. 1a) is ascribed to the formic acid dimer, which is known to be present in the formic acid vapor under equilibrium conditions at room temperature. Additional experiments have been performed in order to support this assignment. Fs DFWM spectra in the region 105-145 ps have been measured for pressures from 4mbar up to 20mbar of HCOOH vapor. With increasing pressure, an extra recurrence appeared at ~ 124 ps. (see Ref. [8]) From the equilibrium constant of the dimerization [9] the concentration of the dimer can be calculated to change from 45%(4mbar) to 69%(20 mbar). If one considers the quadratic dependence of the fs DFWM signal on the concentration, we can take the

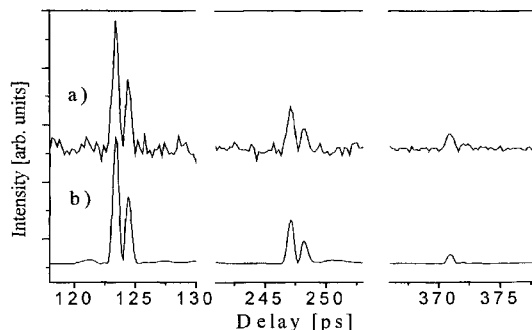


Fig.2. Fs DFWM spectrum of the formic acid dimer (O-H...O/O...H-O type). Magnified regions around J-type recurrences obtained under supersonic jet conditions (≈ 64 K). a) Experimental spectrum. b) Fitted simulation of the spectrum. Extracted constants are given in Table 1.

experimental pressure dependence for the rotational recurrence at 124 ps as evidence for our assignment. Moreover, three successive J-type transients of $(\text{HCOOH})_2$ have been obtained (Fig. 2a) in a seeded supersonic jet expansion, whereas no features of the monomer could be identified under the same conditions. In order to obtain precise rotational and CD constants we performed a fitted simulation of the experimental spectra from the supersonic expansion (Fig. 2b). In Table 1 the fitted parameters for the formic acid OH...O/O...HO dimer structure are listed in comparison with results of *ab initio* calculations.

Table 1

Fitting results for fs DFWM experiments of the formic acid dimer (ground state): rotational constants, CD constants, parametrized polarizability parameter ϕ , Ray's asymmetry parameter κ and temperature T.

	Fs DFWM (jet exper.) [This work]	Calculation B3LYP/6- 311+G(2d,p) ^{a)}	Calculation MP2/ cc-pVTZ [Ref.10]
A [MHz]	6064 ± 1	6056	6034
B [MHz]	2302 ± 3	2306	2327
C [MHz]	1665 ± 3	1670	1679
Δ_J [kHz]	0.1 ± 2		
Δ_{JK} [kHz]	-6.3 ± 0.6		
Δ_K [kHz]	6.9 ± 0.8		
κ	-0.71	-0.71	-0.71
ϕ [rad]	0.38 ± 0.05	0.36	0.43
T [K]	64 ± 5		

a) Calculation performed by D. Kosov (University Frankfurt/M.).

3.3 Acetic acid $(\text{CH}_3\text{COOH})_2$ and per-deuterated acetic acid $(\text{CD}_3\text{COOD})_2$ dimer

Figures 3a and 3a_D show fs DFWM spectra of acetic acid (CH_3COOH) and per-deuterated acetic acid (CD_3COOD) vapor from a gas cell experiment (300K). In contrast to formic acid, acetic acid shows only J-type recurrences from dimeric species in the fs DFWM spectra at room temperature. The difference of 45 ps between the position in time of the recurrences from $(\text{CH}_3\text{COOH})_2$ and $(\text{CD}_3\text{COOD})_2$ is determined by the smaller rotational constants B, C of $(\text{CD}_3\text{COOD})_2$. From the non-linear fitting (Fig 3b, 3b_D) the rotational constants $A=5.7\pm 0.3$ GHz; $B+C=1657.2\pm 1.2$ MHz of the acetic acid dimer $(\text{CH}_3\text{COOH})_2$ and

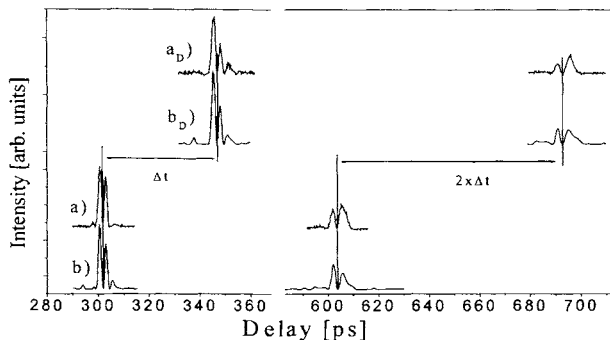


Fig.3. Fs DFWM spectrum of the acetic (a, b) and per-deuterated acetic (a_D , b_D) acid dimer. Magnified regions around J-type recurrences obtained at room temperature (300K). a) and a_D) are the experimental spectra; b) and b_D) are the fitted simulation of the spectra.

$A=5.4\pm 0.4$ GHz; $B+C=1445.2\pm 0.5$ MHz of the per-deuterated acetic acid dimer (CD_3COOD)₂ were extracted. It was not possible to determine the rotational constants B and C independently due to the symmetric prolate top nature of the dimeric structure (Ray's asymmetry parameter $\kappa=-0.965$). More detailed consideration of the fs DFWM spectra taken in the gas cell and in a supersonic expansion for the acetic acid dimer are under way in our laboratory and will be presented in a forthcoming publication.

4. CONCLUSIONS

Fs DFWM spectroscopy was successfully applied for the structural study of molecular clusters in both, a gas cell at room temperature and in a supersonic expansion at reduced temperature.

The rotationally resolved spectra of the doubly hydrogen-bonded complexes ($HCOOH$)₂ and (CH_3COOH)₂ have been measured for the first time by a spectroscopic technique. Rotational constants and the PT evaluated from the fitting of the fs DFWM spectra are in good agreement with results from *ab initio* calculations. The values of the CD constants have been obtained from the analysis based on a new general nonrigid asymmetric rotor approach.

In summary, fs DFWM spectroscopy proves here its strength and importance for the rotationally-resolved spectroscopic investigation of complex molecular systems without dipole moment.

REFERENCES

- [1] C. Riehn, Chem. Phys., 283 (2002) 297
- [2] P. H. Vaccaro in: H. Hirota, R. W. Field, J. P. Maier, S. Tsuchiya (Eds.), *Non-linear Optical Spectroscopy for Molecular Structure and Dynamics*, Blackwell Scientific, IUPAC
- [3] C. Riehn, V. V. Matylitsky, M. F. Gelin, J. Raman Spectrosc., in press.
- [4] M. Morgen, W. Price, P. Ludowise, and Y. Chen. J., Chem. Phys., 102 (22) (1995) 8780.
- [5] M. Cho, M. Du, N. F. Scherer, G. R. Fleming, and S. Mukamel, J. Chem. Phys., 94 (1993) 2410.
- [6] P. R. Bunker, and P. Jensen, *Molecular Symmetry and Spectroscopy*, 2nd ed. National Research Council of Canada, Canada, 1998.
- [7] E. Willemot, D. Dagnois, and J. Bellet, J. Mol. Spectrosc., 73 (1987) 96.
- [8] V. V. Matylitsky, C. Riehn, M. F. Gelin and B. Brutschy, J. Chem. Phys. in press.
- [9] J. Chao, and B. J. Zwolinski, J. Phys. Chem. Ref. Data7 (1978) 363.
- [10] J. Chocholoušová, J. Vacek, P. Hobza, Phys. Chem. Chem. Phys., 4 (2002) 2119.

Collision induced rotational energy transfer. A new scaling law probed by fs CARS

G. Knopp, P. Beaud, P. Radi, M. Tulej and T. Gerber

Paul Scherrer Institut, CH - 5323 Villigen PSI Switzerland

ABSTRACT

Pressure dependent fs-CARS spectra for different colliding species are presented and successfully fitted by using the novel AECS scaling law for rotational energy transfer. The model provides as main fit parameter the relevant interaction time of the colliding molecules τ_c , which is compared to a numerical calculation derived from the interaction potential.

1. INTRODUCTION

The treatment of optical line shapes as relaxation problem of statistical physics was first discussed 1963 by Fano [1]. Since then specifying the average amount of transferred energy during an inelastic molecular collision has been the goal for many theoreticians. Considering the scattering of a particle from a rigid rotator Arthurs and Dalgarno[2] have derived a formalism to calculate the cross section for transitions from the initial state J to the final state J' of the molecule. Based on these early results the infinite order sudden (IOS) theory has been developed [3] and further supplemented to the energy corrected sudden (ECS) approximation [4]. The classical impact theory of Burshtein and Temkin [5] has contributed significantly to the understanding of relation between the band wing shape and the rotational relaxation process. For more than two decades line broadening induced by rotationally inelastic collisions has been approximated by the ECS model. The use of the ECS theory requires base rates Q_L and an expression for an adiabatic correction term Φ_L to construct the matrix $T_{JJ'}$ for rotational energy transfer (RET). The Q_L can either be measured or more often are modelled using semi-empirical energy gap laws leading to the ECS-E (energy corrected) or ECS-P (power corrected) variants of the ECS approximation.

Based on our experimental investigations on the RET upon N_2 - N_2 collisions using femtosecond (fs) CARS spectroscopy, we have developed a novel scaling law for RET in which the collision process is viewed as a quasi bound complex rotating about the center of mass for a short time τ_c . A theory, based on the time-energy uncertainty relation, has been established - the 'Angular momentum and Energy Corrected Sudden approximation' (AECS) - which justifies the use of an angular momentum spacing law and yields a magnitude of an exponentially limiting parameter for the angular momentum transfer $L_c \approx 2 \hbar$ [6] for all investigated collision systems.

The coherent fs time-resolved CARS method is highly sensitive for the investigation of collision induced (or pressure dependent) changes in optical line shapes especially when line mixing occurs and frequency resolved measurements come to their limits [7]. The fs-CARS spectroscopy is applied to various collision systems (N_2 - N_2 , N_2 -rare gas, C_2H_2 - C_2H_2 , CO-CO)

and the detected transient signals are fitted by the using established CARS theory [8] and the AECS scaling law. The defined interaction time τ_c is the crucial free fit parameter describing the energy transfer between the two colliding species.

2. METHOD

The fs-CARS signal is generated by a sequence of three fs-laser pulses having different wave vectors interacting with the medium. Considering the electronically non resonant variant of CARS only, the process might be described by two coinciding initial pulses ('Raman pump') creating a coherent excitation of rotational states in a vibrationally excited (e.g. $\nu=1$) electronic ground state of the molecule. This non-stationary superposition of states evolves in time, until a third pulse ('probe') scatters from the induced polarization and finally results in a coherent emission of light in the phase matched direction $\mathbf{k}_{\text{cars}} = \mathbf{k}_{\text{pu}} - \mathbf{k}_{\text{St}} + \mathbf{k}_{\text{pr}}$, centered around

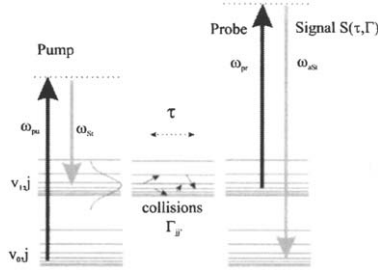


Fig. 1. Schematic of the fs-CARS process.

the anti-Stokes frequency $\omega_{pu} - \omega_{St} + \omega_{pr}$. The CARS signal is measured as a function of the delay time τ between 'Raman-pump' and probe step. The temporal evolution of the molecular ensemble is mainly perturbed by collisions, which is finally reflected by the fs-CARS signal. A schematic of the process is given in Fig.1. In the limit of well separated pulses, the fs-CARS signal is given as [8]

$$S(\tau) = \int_{-\infty}^{\infty} \left| E_{pr}(t) \int_{-\infty}^t E_p(t'-\tau) E_s^*(t'-\tau) \chi^{(3)}(t') dt' \right|^2 dt \quad (1)$$

$$\chi^{(3)}(t') = \left\langle -\frac{i}{\hbar} [\alpha(t'), \alpha(0)] \rho \right\rangle = -\frac{i}{\hbar} \sum_{if} \rho_i \alpha_{if}^2(0) \exp(i\omega_{if} t') C_{if}(t')$$

where ρ_i is the initial population of the i th state. E_{pr} , E_p and E_s are the interacting laser fields, and the term enclosed by the angle brackets is the time correlation of the Raman polarizabilities. The lineshape function C_{if} accounts for the relaxation processes. Dephasing due to inhomogeneous Doppler line broadening is expected to be small compared to the collision induced homogeneous broadening effect. Hence C_{if} might factorize in a homogenous and inhomogeneous part [9], where the homogenous part may be expressed as exponential function of the collision matrix Γ . Considering isolated lines only, the sum of exponentials in the time domain leads to the expected sum of Lorentzian lineshapes in the frequency domain. For mixing lines it is useful to accomplish the G-matrix formalism of Koszykowski *et al* [10] to the time domain. Two features of the fs-CARS are essential for the measurements. First, interference between the vibronically resonant and nonresonant signal contributions occurs

only for the short time window in which all pulses overlap. Second, the sensitivity of the fs-CARS signal to line mixing mechanisms improves with increasing pressure.

3. THE AECS MODEL

The AECS scaling model is based on the results of the ECS approximation. The elements of the relaxation matrix Γ for an isotropic Q branch CARS experiment on N_2 are given as:

$$\Gamma_{JJ'} = (2J'+1) \frac{\rho_{J_>}}{\rho_J} \sum_L (2L+1) \begin{pmatrix} J & L & J' \\ 0 & 0 & 0 \end{pmatrix}^2 \frac{\Phi_L(\omega_{JJ'})^2}{\Phi_L(\omega_{L0})^2} Q_L, \quad J' \neq J \quad (2)$$

$$\Gamma_{JJ} = - \sum_{J' \neq J} \Gamma_{JJ'}$$

This closed expression is basically a result of the angular momentum coupling (where $J_>$ is the larger of J and J') between the states involved in the collision. Nevertheless the functions Φ_L and Q_L have to be modeled and determine the character of the scaling law. In a semiclassical point of view, the quantum number L (for transitions $0 \rightarrow L$) might be identified with the angular momentum $\ell = \mu v b$ of the collision. (v = rel. velocity, b = impact parameter, μ = reduced mass). The AECS scaling proposes the following expressions for insertion into Eq. 2:

$$Q_L = A_0 \exp\left(-\frac{\sqrt{L(L+1)}}{L_c} \frac{\mu}{m_s}\right) \quad \Phi_L(\omega_{JJ'}) = \exp\left(-\frac{2\omega_{JJ'}\tau_c}{\sqrt{L(L+1)}}\right). \quad (3)$$

The possibly transferred rotational energy is considered as restricted according to Heisenbergs uncertainty relation ($\Delta E = \hbar/\tau_c \geq E_{rot} = 1/2\ell^2/\tau_c$) by the lifetime of the collisional intermediate state. From this assumption L_c has been derived to $2\hbar$, and only *two* free fit parameters remain: The interaction time τ_c , which is on the order of several femtoseconds, and A_0 as constant linewidth per Amagat, which comprehends the temperature dependence of the base rates.

4. RESULTS AND DISCUSSION

The model has been tested for different collision systems, e.g. N_2 - N_2 , CO-CO and C_2H_2 - C_2H_2 self-collisions, as well as for various N_2 -rare gas collisions. The experimental results and the AECS model fits are shown in Fig. 2. In the case of the acetylene collisions the AECS model has been modified to account for vibrational energy transfer (VET) and dephasing by introducing a single additional VET-fit parameter. Additionally, the model has been partly extended (without the implementation of new fit parameters) to excellently describe RET of N_2 with heavier mass collision partners (e.g. Ar, Kr) [11]. The table in Figure 3 shows the fitted interaction times for the investigated collision systems. For comparison with a 'classical' interaction time, calculated from the interaction potential (Lennard Jones 12-6) τ_c has been multiplied by 2π . The results from a numerical calculation of τ_c as a function of ℓ for the N_2 - N_2 collision system is also given in Fig. 3. The estimation of $\tau_c \sim b_{av} \bar{v}^{-1}$, and hence being proportional to $(\ell+1/2)$ as derived by De Pristo *et al.*[4] as shown for comparison in the Figure (dotted lines), matches our calculation only in the limit of $L \gg 1$. The AECS model demands a constant interaction time for the relevant L numbers, which approximately matches the calculation considering that due to the form of the Q_L (Eq.3) only low quanta of angular

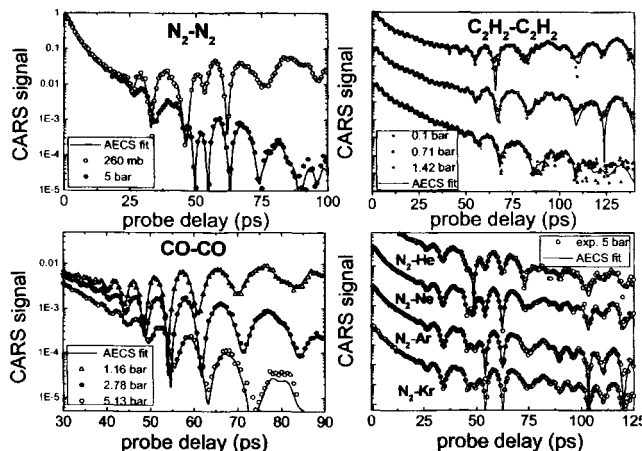


Fig. 2. Fs CARS transients of various collision systems and AECS model fit.

momentum significantly contribute to the energy transfer. The fitted value of $\tau_c \sim 210$ fs for the N_2-N_2 collision at room temperature is in concordance with the averaged calculated value considering hard core collisions only ($L \leq 50$). This, strongly endorse the physical meaning of the model parameters.

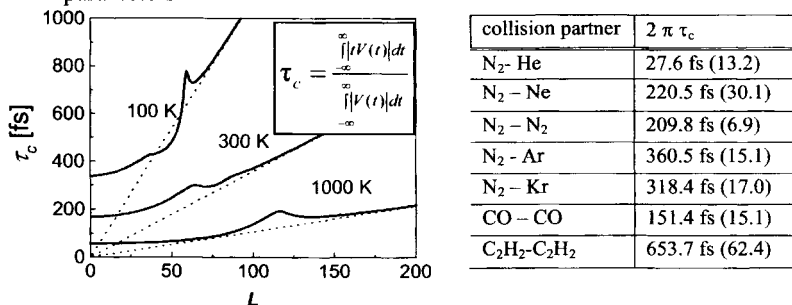


Fig. 3. Numerical calculation of τ_c for the N_2-N_2 collision system from the interaction potential. The table shows fitted values of τ_c for various collision systems from experimental data.

REFERENCES

- [1] U. Fano, Phys. Rev., 131 (1963) 259.
- [2] A. M. Arthurs and A. Dalgarno, Proc. Roy. Soc. (London), A256 (1960) 540.
- [3] R. Goldflam, S. Green, and D.J. Kouri, J. Chem. Phys., 67 (1977) 4149.
- [4] A.E. De Pristo, S.D. Augustin, R. Ramaswamy, H. Rabitz, J. Chem. Phys., 71 (1979) 850.
- [5] S. I. Tempkin and A.I. Burstein, Chem. Phys. Lett., 66 (1979) 52.
- [6] P. Beaud, G. Knopp, Chem. Phys. Lett., 371 (2003) 194.
- [7] G. Knopp, P. Radi, M. Tulej, T. Gerber and P. Beaud, J. Chem. Phys., 118 (2003) 8223.
- [8] S. Mukamel, Principles of Nonl. Optic. Spectrosc., Oxford Univers. Press, New York, 1995.
- [9] D.S. Kuznetsov, V.B. Morozov, A.N. Olenien, V.G. Tunkin, Chem. Phys., 257 (2000) 117.
- [10] M.L. Koszykowski, R. L. Farrow and R.E. Palmer, Opt. Lett., 10 (1985) 478.
- [11] P. Beaud, T. Gerber, P. Radi, M. Tulej, G. Knopp, Chem. Phys. Lett., 373 (2003) 251.

Different schemes and recent results for high-resolution rotational coherence spectroscopy with picosecond and femtosecond laser pulses

C. Riehn^a, V. V. Matylitsky^a, A. Weichert^a, M. F. Gelin^b, W. Jarzęba^c and B. Brutschy^a

^aJohann Wolfgang Goethe-Universität Frankfurt / M., Institut für Physikalische und Theoretische Chemie, Marie-Curie-Str. 11, D-60439 Frankfurt / M., Germany

^bInstitute of Molecular and Atomic Physics, Skaryna Avenue 70, Minsk 220072, Belarus

^cFaculty of Chemistry, Jagiellonian University, Ingardena 3, 30-060 Kraków, Poland

1. INTRODUCTION

Over the last years we have explored several advanced techniques for high-resolution rotational coherence spectroscopy (RCS [1]) in order to study the structures of molecules and clusters in the gas phase [2]. We have provided spectroscopic examples demonstrating: (i) mass-selectivity (Fig.1, [3]), (ii) that the rotational constants of the ground and electronic excited states can be obtained independently with high precision (10^{-6} - 10^{-5} , [4]), (iii) that the transition dipole moment alignment, (iv) centrifugal distortion constants, and (v) information on the polarizability tensor can be obtained (Fig.1, [5]). Here we review results pertaining to points (i), (ii), (iv) and (v) [2,3,5].

For pump-probe photoionization (PPI, Fig.1) the first laser pulse is tuned into resonance with the (vibrationless) electronic transition of the molecule, the second pulse is red-shifted in wavelength, so that the enhanced $(1+1')$ photoion signal can be easily identified. When a time-of-flight mass spectrometer is used for detection the mass-selective photoion signal as a function of time delay can be recorded as the RCS spectrum of the electronically excited state, which is particularly useful for the specific investigation of molecular clusters.

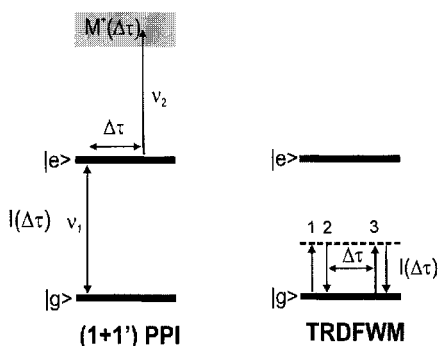


Fig. 1. Pump-probe photoionization (PPI) and time-resolved degenerate four-wave mixing (TRDFWM) schemes for rotational coherence spectroscopy (RCS).

Time-resolved degenerate four-wave mixing (TRDFWM or femtosecond DFWM, Fig.1) can be envisaged as a transient grating spectroscopy. The first two laser pulses generate a grating of coherently Raman excited molecules in the electronic ground state. The time dependence of this grating of aligned molecules is probed by diffraction of a third delayed laser pulse. The process is non-resonant, so that neither chromophore nor dipole moment has to be present in the molecule under study. It provides background free detection so that a high signal/noise ratio (up to 10^4) can be achieved. Examples for these two recently implemented RCS schemes will be discussed in the following.

2. RCS OF THE ELECTRONICALLY EXCITED STATE: PHOTOIONIZATION

The mass-selective RCS scheme of $(1+1')$ pump-probe photoionization is exemplified here for the molecule cyclohexylbenzene (CHB, Fig. 2a, [2]). The extracted rotational constants can be compared to results of *ab initio* geometry optimizations for the electronically excited state carried out at the CIS/6-31G(d) level. Experimentally we have obtained 2388 ± 13 MHz and 953.7 ± 0.9 MHz, the calculations resulted in 2426.4 MHz and 953.8 MHz for A' and $(B+C)'$, respectively. CHB represents, in the ground and electronically excited state, a prolate symmetric top with the symmetric top axis, i.e., *a*-axis, close to the long axis of the phenyl ring. The cyclohexyl group resides in its chair conformation and is oriented perpendicularly to the aromatic plane. These structural features are consistent with our experimental and theoretical results. For the ground electronic state we obtained 2469.9 MHz and 961.4 MHz for A'' and $(B+C)''$ from the calculation at the HF/6-31G(d) level and 960.6 \pm 2.0 MHz for $(B+C)''$ from a time-resolved degenerate four-wave mixing experiment (Fig. 2b). Although electron correlation is not accounted for in the applied level of theory, the change of rotational constants upon electronic excitation is described well [4].

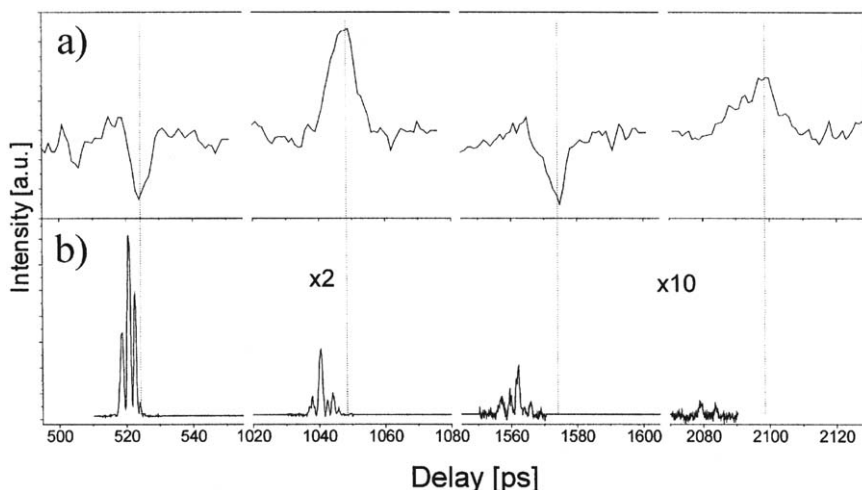


Fig. 2. RCS of cyclohexylbenzene. Experimental data a) from pump-probe photoionization in a molecular beam ($T \approx 10$ K) [2], b) from time-resolved degenerate four-wave mixing in a gas cell ($T \approx 305$ K).

The reduction in the *A* constant compares well with the related system of para-cyclohexylaniline (pCHA, [4]) and can be traced back to the compression of the short axis of the

aromatic ring (quinoidal distortion). However, the rotational constants B and C are decreasing upon electronic excitation contrary to a corresponding increase in pCHA. This difference can be tentatively ascribed to the influence of the amino group in the latter molecule. Whereas the elongation of the long aromatic axis leads to a decrease in B and C for CHB, it is compensated in pCHA by a significant shortening of the C-N bond. Hence, by the example of CHB we have demonstrated the scheme of time-resolved (1+1') photoionization for RCS and the analysis of structural changes for large molecular systems upon photoexcitation.

3. RCS OF THE GROUND STATE: TIME-RESOLVED DEGENERATE FOUR-WAVE MIXING

The method of fs DFWM spectroscopy and our theoretical model for the spectral simulation is discussed in our second contribution in this volume. The experimental setup has been detailed in a former publication [5]. Here, we would like to highlight some special features of this technique with emphasis on the possibility to obtain, besides the rotational constants, centrifugal distortion constants (CDs) and information on the polarizability tensor (PT).

The former feature is demonstrated by a part of the fs DFWM spectrum of benzene as depicted in Fig. 3. The data displayed is an extension to the published spectra in Ref. [5]. The experimental trace in Fig. 3a shows regions around the J-type recurrences at a total time delay of ca. 1.5 ns. In Fig. 3b a simulated spectrum is given, computed on the basis of a symmetric oblate rotor with the rotational constant $B'' = 5689$ MHz and the CDs $D_J = 1.1$ kHz and $D_{JK} = -1.4$ kHz. For comparison in Fig. 3c the same recurrences are calculated with all CDs set to zero. It can be seen that the CDs cause a strong modulation, splitting and time shift in the recurrences. Even recurrences are differently affected than odd ones. One can conclude that high temperatures do not prevent the occurrence of rotational recurrences and thus, the application of RCS. On the contrary, they enable the determination of CDs by analysis of spectral features at long time delay and hence, reflect the non-rigidity of molecules.

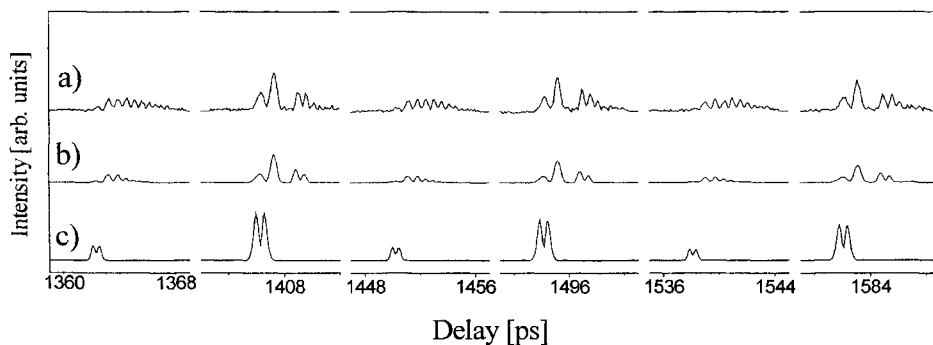


Fig. 3. Fs DFWM of benzene (5 mbar, 298K): a) experiment at long time delay (extension of data from Ref.[5]); b) fitted simulation for oblate rotor with centrifugal distortion (CD); c) simulation with CDs set to zero.

The second important feature of fs DFWM spectroscopy is its dependence on the polarizability tensor. The first 50 ps of the experimental fs DFWM spectrum of formic acid vapor are plotted in Fig. 4a and a fitted simulation is given in Fig. 4b, [6]. From the resulting fitting parameters it is deduced that the the polarizability tensor has 'oblate symmetry'.

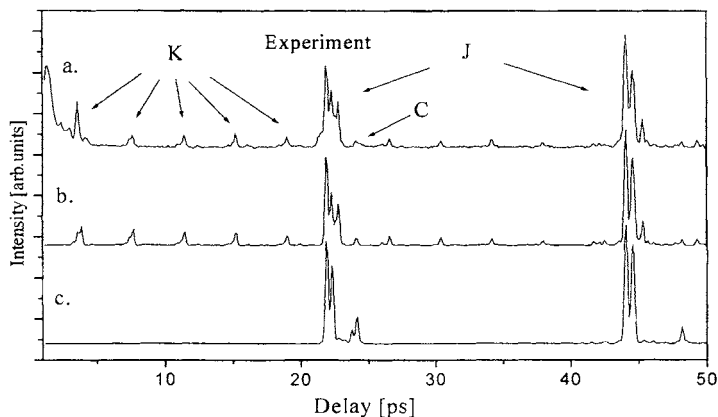


Fig. 4. Fs DFWM of formic acid vapor (10 mbar, 298K [6]): a) experiment; b) fitted simulation with 'oblate' polarizability tensor (PT), c) simulation with 'prolate' PT.

As a cross-check of this result a spectral simulation with a PT of 'prolate symmetry' is given in Fig. 4c. The difference to the other traces is seen in the missing K-type recurrences. The occurrence of K-type transients in fs DFWM spectra can be rationalized by significant components of the polarizability tensor perpendicular to the symmetric top axis. Finally, it was demonstrated that the types and intensities of recurrences in fs DFWM spectra are a sensitive measure for the symmetry of the PT of the corresponding molecule.

4. CONCLUSIONS

Two recent developments of RCS are time-resolved (1+1') pump-probe photoionization (PPI) and time-resolved degenerate four-wave mixing (fs DFWM) which are devoted to the exploration of molecular structure in the electronically excited and ground state, respectively. Whereas the former method is typically applied together with mass-selective detection to samples seeded in a molecular beam, the latter can be used for the investigation of samples in both, a supersonic expansion or a gas cell. From the analysis of the corresponding spectra the rotational constants and transition dipole moment alignment (PPI) or rotational and centrifugal distortion constants and information on the polarizability tensor (fs DFWM) can be obtained with high precision. The methodology of rotational coherence spectroscopy has been considerably extended by new implementations so that more complex molecular structures can be tackled in the future.

REFERENCES

- [1] J. S. Baskin, P. M. Felker, A. H. Zewail, *J. Chem. Phys.*, 84 (1986) 4708.
- [2] C. Riehn, *Chem. Phys.*, 283 (2002) 297.
- [3] C. Riehn, A. Weichert, B. Brutschy, *Phys. Chem. Chem. Phys.*, 2 (2000) 1873.
- [4] C. Riehn, A. Weichert, U. Lommatzsch, M. Zimmermann, B. Brutschy, *J. Chem. Phys.*, 112 (2000) 3650.
- [5] V.V. Matylitsky, W. Jarzęba, C. Riehn, B. Brutschy, *J. Raman Spectrosc.*, 33 (2002) 877.
- [6] V.V. Matylitsky, C. Riehn, M. F. Gelin, B. Brutschy, *J. Chem. Phys.*, 119 (2003) 10553.

Shaped laser pulses acting as photonic reagents

H. Rabitz^a

^aDepartment of Chemistry, Princeton University, Princeton, NJ, USA, 08544

ABSTRACT

In recent years, great strides have been made in controlling quantum phenomena through the use of tailored laser pulses. These shaped pulses interact with molecules in a manner acting effectively as reagents with fleeting existence, yet they may have a lasting dynamical impact on a molecule or material. This paper discusses the basic concepts of quantum control, especially drawing on the ability to perform massive numbers of closed loop control experiments. Particular attention is given to the prospect of deducing control mechanisms and the introduction of special closed loop control techniques to reveal Hamiltonian information. Recent computations and experiments point to an increasing ability to control and understand quantum systems through closed loop laboratory techniques.

1. INTRODUCTION

Since the earliest days of laser development, a longstanding dream has been to use these special light sources as a means to manipulate atomic- and molecular-scale dynamical events. The concepts of quantum control are central to making the dream a reality. Quantum control refers to the redirection or regulation of quantum dynamical events[1]. Controlling quantum phenomena requires more than just applying an ultrafast laser pulse to a quantum system to produce coherent dynamics. The dynamics likely will not be controlled unless the laser pulse is specifically shaped for that objective. Laser-molecule interactions may be thought of as physically analogous to traditional reagent-molecule interactions. Just as reagents may be chosen to influence the selective products, shaped laser pulses may be viewed as photonic reagents serving a similar purpose. A potential advantage of photonic reagents is the ability to go from one candidate shaped pulse to another in much less than a second in the laboratory.

Figure 1 depicts the evolution of a quantum system from the initial state $|\psi_i\rangle$ to a set of possible final states. A particular one, $|\psi_f\rangle$, is the desired target, while all other final states $|\psi'_f\rangle$, $|\psi''_f\rangle$, etc., are to be avoided. The basic principle underlying this process is to create maximum constructive interference in state $|\psi_f\rangle$ while producing destructive interferences in the other accessible states $|\psi'_f\rangle$, $|\psi''_f\rangle$, etc.

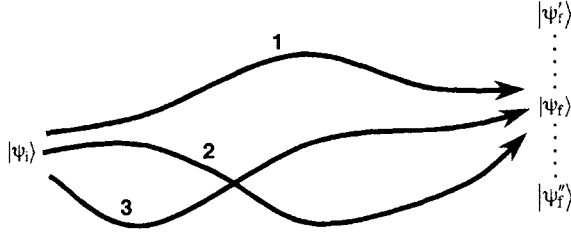


Fig. 1. Quantum control aims to steer a system from the initial state $|\psi_i\rangle$ to a desired final state $|\psi_f\rangle$, while avoiding the other accessible states $|\psi_f'\rangle, |\psi_f''\rangle, \dots$. Each of the labeled quantum pathways 1, 2, 3, ... connecting states $|\psi_i\rangle$ and $|\psi_f\rangle$ would have an associated amplitude $\langle \psi_f | U^\ell | \psi_i \rangle$, $\ell = 1, 2, 3, \dots$.

The quantum dynamics under the control-free Hamiltonian H_0 is assumed to be incapable of producing the desired evolution $|\psi_i\rangle \rightarrow |\psi_f\rangle$. Thus, a suitable control interaction $V_c(t)$ is introduced

$$i\hbar \frac{\partial |\psi\rangle}{\partial t} = (H_0 + V_c)|\psi\rangle, \quad |\psi(0)\rangle = |\psi_i\rangle \quad (1)$$

such that $|\psi\rangle$ follows the evolution $|\psi_i\rangle \rightarrow |\psi_f\rangle$ to an acceptable degree. The control may take on various forms, but a common interaction is $V_c(t) = -\mu \cdot \epsilon(t)$, where μ is the electric dipole moment and $\epsilon(t)$ is the laser electric field. The control goal is to find the laser field that manipulates the dynamics in the desired fashion shown in Fig. 1.

This paper will first summarize the underlying concepts of laboratory closed loop learning control with shaped laser pulses for manipulating quantum systems[2]. This technique is proving to be very successful for directing dynamical events in systems ranging from atoms out to highly complex biological molecules[3-13]. Some particular features of these closed loop experiments will be discussed in Section 2. The growing success of these closed loop experiments have outpaced an understanding of the underlying quantum control mechanisms. An algorithm for revealing such mechanisms will be discussed in Section 3. A closed loop technique also will be presented in Section 4 for deducing high quality Hamiltonian information despite the presence of possibly significant laboratory data noise. Finally, the conclusions in Section 5 will include consideration on what may lie ahead.

2. CLOSED LOOP CONTROL OF QUANTUM SYSTEMS

In principle, a laser control field $\epsilon(t)$ could be designed with the evolution $|\psi_i\rangle \rightarrow |\psi_f\rangle$ reliably producing an acceptable value for $\langle \psi_f | O | \psi_i \rangle$, where O is a chosen observable operator. This design problem may be best treated variationally, seeking an optimal control $\epsilon(t)$ for this purpose[14,15]. The practical implementation of quantum optimal control theory (OCT) poses challenging numerical tasks due to the need to repeatedly solve the Schrödinger equation, Eq.

(1), while searching for the control field. The resultant optimal field design would then be transferred to the laboratory for creation and application to the quantum system for its action. In practice, the serious computational design tasks involved, particularly for the most interesting complex systems, leads to the need for introducing approximations that may influence the delicate balance of constructive and destructive wave interferences called for in Fig. 1. In addition, the Hamiltonian components, H_0 and μ , will typically have significant uncertainties, again, likely compromising the quality of the resultant control designs. Notwithstanding these difficulties, many OCT designs have been performed in recent years, covering applications including the control of rotational, vibrational, electronic, reactive, and solid-state dynamics[16]. Much has been learned about the control of quantum phenomena through these simulations, and further valuable insights are expected from future studies on model systems. Perhaps the main point deduced from these studies is the key operating principle: the control field must adjust itself to take advantage of all dynamical opportunities to best satisfy the objective. Quantum systems with many particles or atoms typically have multi-spectral dynamics, calling for the control field to in turn have broad frequency character in order to manage all of the relevant dynamical motions. The broad frequency structure of the required laser fields naturally leads to considering shaped laser pulses as the controls.

Given the underlying difficulties of practically executing computational control designs and then successfully utilizing the designs in the laboratory on systems of practical interest (i.e., polyatomic molecules), the challenge is to overcome these problems. The ability to perform massive numbers of laser control experiments guided by learning algorithms, has proved to be the means to circumvent these problems[2]. The result is the closed loop model-free control technique, shown in Fig. 2. This procedure operates by drawing on the following characteristics:

1. The quantum system. The quantum system in the laboratory “knows” its own Hamiltonian and “solves” its own Schrödinger equation with full precision and as rapidly as possible when exposed to a laser field $\epsilon(t)$. The quantum system acts as an excellent analog computer, circumventing the field design difficulties of Hamiltonian uncertainty and computational bottlenecks.
2. The control laser. Laser pulse shaping to create trial photonic reagents is an evolving technology with the ability to rapidly go from one pulse shape to another under computer control.

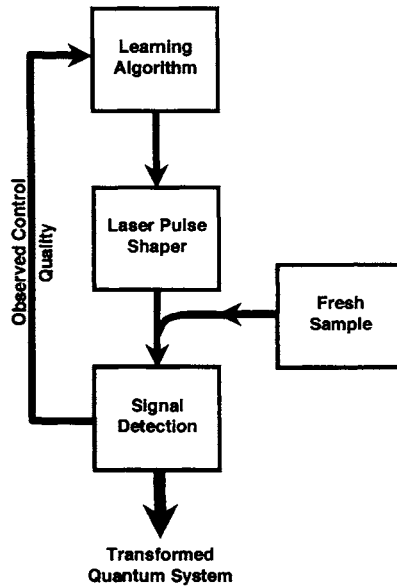


Fig 2. The components forming a closed loop apparatus for control quantum phenomena. Using a new sample upon each cycle of the loop sidesteps the issue of the observation process disturbing the system in an unknown way. The key to success of such control experiments lies in the ability to traverse the loop under very high duty cycle to rapidly home in on the target physical objective.

3. Quantum system objectives. Typical objectives involve steering the quantum system out the desired channel versus that of other accessible channels. The detection of these outcomes is often simple and does not require extensive offline computations to deduce the relative success of an applied control field $\epsilon(t)$.
4. Learning algorithms. Fast pattern recognition algorithms exist which can assess the large sets of rapidly evolving experiments to deduce the attractive features of the laser control fields that are drawing the quantum system closer to meeting its dynamical objectives. Genetic or evolutionary algorithms are especially attractive for this purpose, as they can be quite robust even in the presence of extensive laboratory noise.

The closed loop control concept depicted in Fig. 2 draws together all of these features to produce a high duty cycle “machine” employing photonic reagents for automatically steering the quantum dynamics in a desired fashion. An especially attractive feature of the concept in Fig. 2 is its ability to be self-starting often without any prior control field designs for the photonic reagents.

The closed loop logic for controlling quantum systems has been put to increasing use in recent years, starting with the initial experiments of Wilson[3] in 1997. Many successful

examples exist, ranging from manipulating atoms out through biological systems[4-13]. These initial developments point to a very exciting period lying ahead, with the means now available for systematically identifying the basic rules and guidelines for what types of phenomena may be successfully controlled through shaped laser pulses acting as photonic reagents.

3. REVEALING PHOTONIC REAGENT CONTROL MECHANISMS

Closed loop learning control experiments are showing increasing success in the laboratory, but they often leave mysterious the mechanisms by which controlling photonic reagents achieve the desired dynamical manipulations[17]. The control mechanisms are especially obscure in cases that employ high intensity laser fields. The outcome from an experiment is a quantitative measure of reaching the desired target and knowledge of the control field. In principle, modeling could then be used with the control to deduce the operating mechanism. Examples of such efforts have been reported in the case of control over molecular fragmentation[8], and a similar approach was taken to analyze the control mechanism for manipulating high harmonics[9]. The main difficulty with extracting control mechanisms this way stems from a lack of detailed knowledge about typical system Hamiltonians and the intensive nature of the calculations. It is exactly these daunting difficulties that led to the suggestion[2] of performing the control experiments as closed loop laboratory operations in Fig. 2 to circumvent these theoretical difficulties. The high duty cycle of the control experiments opens up the possibility of using them beyond achieving control itself, to now reveal the underlying mechanisms. This effort is expected to involve special tailored modulation around the already identified optimal control field[18].

A fundamental issue concerns how to define control mechanism in the context of coherent quantum dynamics. Mechanism will likely be understood in a variety of ways, depending on the particular circumstances and control goals. However, an attractive perspective is to consider mechanism defined in terms of the amplitudes connecting the initial and final states, as depicted in Fig. 1. A rank ordering of the magnitude of these amplitudes $\langle \psi_f | U^\ell | \psi_i \rangle$, $\ell = 1, 2, 3, \dots$ and their subsequent physical interpretation in terms of quantum pathways should provide a clear picture of the control mechanism. The notion of quantum pathways connecting the initial and final states is central to this concept, and the nature of the pathways will depend on the choice of physical representation of the evolving quantum system. Two examples are shown in Fig. 3, where case (a) is represented by a small set of discrete eigenstates and the pathways are defined by the linkages from one state to another connecting the initial and final states. In contrast, case (b) shows a complex molecule undergoing selective laser fragmentation. A discrete level representation would likely be far too complex for mechanistic interpretation in the latter case, while a coordinate space representation is reasonable. In this case, the individual

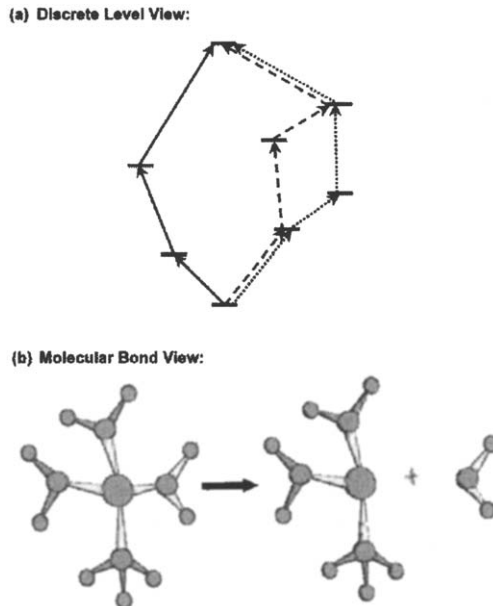


Fig. 3. Mechanistic pathways are depicted connecting the initial and final states of two categories of quantum systems. In case (a), the system has a modest number of levels and hence, a discrete representation is appropriate. The three of many possible pathways shown connecting the initial and final states would each have an associated amplitude. In case (b), a bond or coordinate space picture is a more natural perspective to consider for understanding the pathway to products, in this case, dissociation. The various light-shaded bonds indicate examples of possible locations where tailored radiation might enter to control the dynamics.

bonds may act as antennae to accept different portions of the radiative pulse leading to the fragmentation. The mechanism would be revealed by knowledge of the quantum amplitudes expressed in this coordinate space picture to discover how the bonds and atoms cooperate to produce the final fragmentation.

The full development of these mechanism analysis tools has not been achieved at this time, but some of the basic features have been set forth[18]. The key concept is to introduce further modulation into the optimal control field $\epsilon(t)$ to reveal the dominant quantum pathways. This task calls for special care, as the control field already is temporally modulated in a delicate fashion to manipulate the quantum system. A way around this difficulty is feasible by introducing a new pseudo time-like variable s such that $\epsilon(t) \rightarrow \epsilon(t, s)$. In practice, s is a parameter taking on discrete values s_1, s_2, \dots , where each value characterizes a new modulation experiment. We may view this process as an encoding of the electric field which, in turn, encodes the Hamiltonian $H(t) \rightarrow H(t, s)$ in a fashion such that the amplitudes $\langle \psi_f | U^\ell | \psi_i \rangle$, $\ell = 1, 2, 3, \dots$ associated with the pathways in Fig. 1 may be deduced by decoding the new observed signal $O \rightarrow O(s)$ in the laboratory.

The latter procedure, in a modeling context, has been simulated[18]. In this case, the original Hamiltonian matrix elements $H_{ij}(s) = E_i \delta_{ij} - \mu_{ij} \epsilon(t)$ are replaced with the encoded form

$H_{ij}(s) = E_i \delta_{ij} - \mu_{ij} m_{ij}(s) \epsilon(t)$. Here, $\epsilon(t)$ is the optimal field deduced to meet the posed physical objective, and the reference Hamiltonian H_0 is diagonal with eigenvalues $\{E_i\}$. Each dipole matrix element μ_{ij} is replaced by its modulated form $\mu_{ij} m_{ij}(s)$, where $m_{ij}(s)$ may be freely chosen just so it produces a unique encoding to reveal the role of μ_{ij} in the system output signal. In the simulation, the output was taken as the time evolution matrix $U(s)$, which is now a function of s . Simple Fourier encoding with $m_{ij}(s) = \exp(iv_{ij}s)$ is convenient, with the set of frequencies $\{v_{ij}\}$ chosen for their ability to provide a unique encoding. With Fourier encoding, the resultant decoding reduces to performing an inverse Fourier transform of $O(s)$, or $\langle i|U(s)|j \rangle$ in the present simulations. Figure 4 shows an illustration of the type of mechanism information that may be extracted with this technique. The physical goal in Fig. 4 was an optimal transfer of population $|1\rangle \rightarrow |3\rangle$, which was readily achieved to high fidelity (i.e., the final population in state $|3\rangle$ is ~ 0.99) with an optimal field $\epsilon(t)$. The encoding-decoding analysis identified the dominant mechanistic pathways contributing to this transition in Fig. 4a. Moreover, the true meaning of optimality and constructive/destructive interference was revealed in the process. For the desired transition $|1\rangle \rightarrow |3\rangle$, the contributing amplitudes constructively interfered by lining up in the complex plane in Fig. 4b. In contrast, the amplitudes contributing to the undesired transitions, such as $|1\rangle \rightarrow |4\rangle$ in Fig. 4c, destructively interfered to cancel each other in the complex plane by pointing in opposite directions. It is expected that much may be learned about the mechanisms of controlled quantum dynamics by Hamiltonian encoding-decoding analyses such as these. Ultimately, this process can be set up as a closed loop procedure in the laboratory working in sync with the original closed loop machine in Fig. 2, aiming at attaining quantum control. The dual loops are indicated in Fig. 5. Importantly, operating the machine in Fig. 5 requires no additional hardware beyond that of the control apparatus in Fig. 2. The added components consist of software for directing the encoding process and decoding the signals into mechanism information.

4. TEACHING LASERS TO IDENTIFY QUANTUM HAMILTONIANS

The primary goal of quantum control is the manipulation of dynamics phenomena. To practically meet this goal, the closed loop procedure in Fig. 2 was suggested to circumvent the lack of detailed quantitative information about the Hamiltonians of most realistic systems[2]. This paucity of quantitative Hamiltonian information is an especially serious matter, as it is expected that delicate quantum wave interference will be required to obtain the highest degree of control.

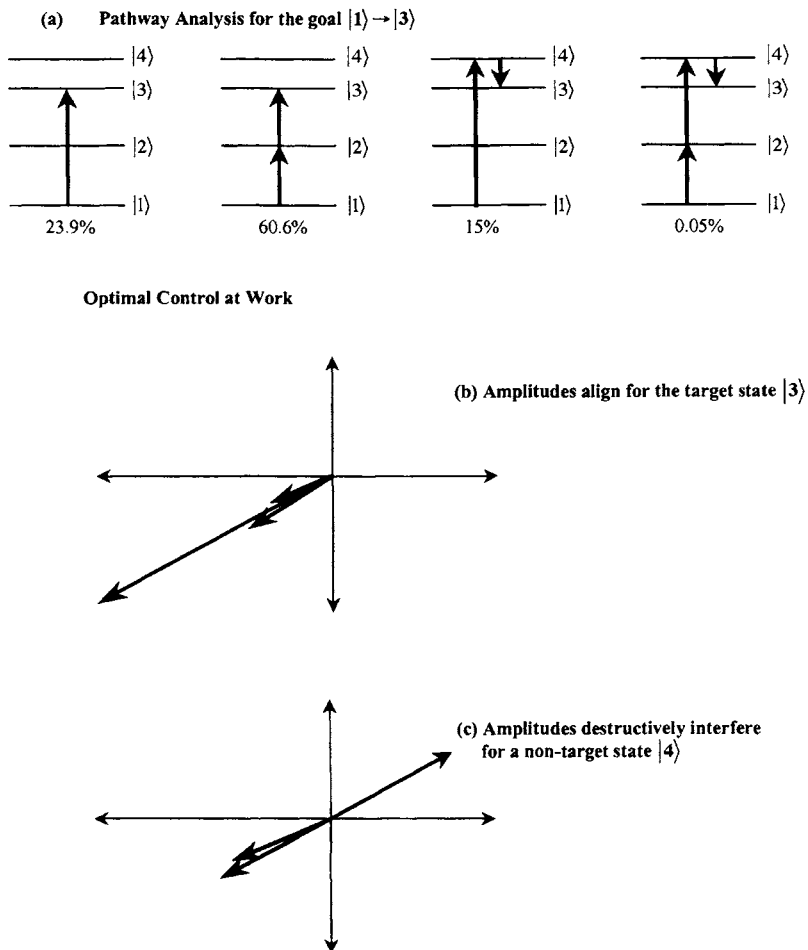


Fig. 4. An illustration of a Hamiltonian encoding-decoding analysis for revealing quantum control mechanisms. The contributions of the main pathways for the desired transition $|1\rangle \rightarrow |3\rangle$ are shown in (a). The three dominant quantum amplitudes $\langle 3|U^\ell|1\rangle$, $\ell = 1, 2$, and 3 are found to optimally cooperate with each other indicated by their lining up in the complex plane for an efficient control process, as shown in (b). In contrast, the amplitudes connecting the undesired transition $|1\rangle \rightarrow |4\rangle$ destructively interfere, as indicated by the three contributing pathways in (c).

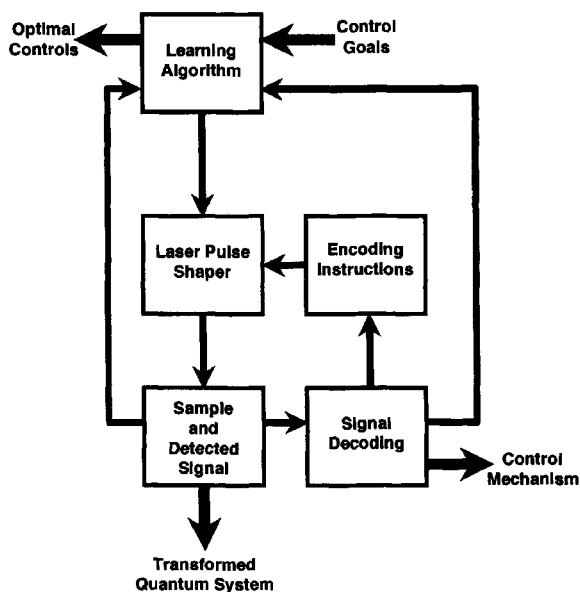
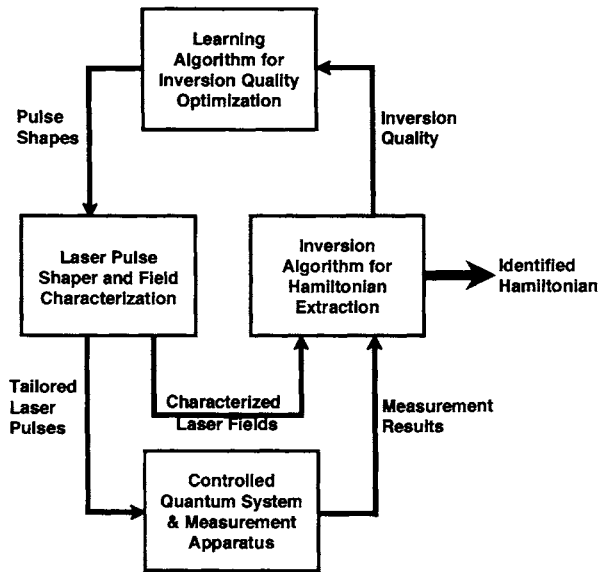


Fig 5. The components forming a closed loop apparatus for achieving quantum control (see Fig. 2) and identifying the control mechanisms. The mechanistic information also may be used to guide the control process, as indicated by the information flow from signal decoding to the learning algorithm.

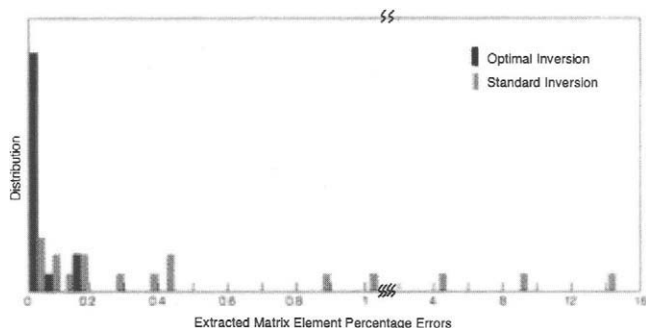
The statements above may be turned around, as they also suggest that controlled quantum dynamics data should be rich sources of sensitive information about system Hamiltonians[19]. Beyond the needs arising in quantum control, there is great interest in determining quantitative information about Hamiltonian structure in H_0 and μ for many applications. At first, it might appear difficult to extract high quality Hamiltonian information from pulsed laser control experiments because of laboratory noise. It may be argued that the data inversion process could act to amplify that noise and seriously contaminate the desired Hamiltonian information. However, the ability to perform massive numbers of control experiments opens up the prospect of seeking out those special experiments that are capable of filtering out the data noise. Figure 6 shows a schematic of such a Hamiltonian identification machine, whose components differ from that of closed loop control alone in Fig. 2 due to the presence of inversion occurring during closed loop operations, along with the need to measure the laser field upon each experiment. A simulation[19] of such closed loop machine operations is shown in Fig. 7. In this case, simulated population data with 1% errors is taken for inversion to extract the 64 Hamiltonian matrix elements from a ten-state system. Operating optimally through closed loop learning, the algorithm revealed an experiment that dramatically improved the quality of the inverted Hamiltonian matrix elements. The optimally inverted matrix elements had an average error that was an order of magnitude smaller than that of the laboratory data. In contrast, when operating in a conventional mode with simply a large number of quasi-random pump-probe experiments, the extracted information was of significantly poorer quality, including errors larger than that of the laboratory data itself.

Making optimal Hamiltonian identification a practical reality will primarily have to deal the significant computational tasks involved in the inversion step of Fig. 6. Fortunately, these operations should be amenable to cluster or grid computing, as well as other accelerating procedures. The paradigm in Fig. 6 suggests the generation of a new class of high throughput laboratory machines under full control for optimally extracting detailed system information.



Reprinted from J.M. Geremia and H. Rabitz, *Phys. Rev. Lett.* **89**, 236902 (2002), copyright 2002 by the American Physical Society.

Fig. 6. A closed loop apparatus for optimally identifying quantum Hamiltonian information. The closed loop operations aim to reveal one or more control experiments that identify the best quality Hamiltonian information. Hamiltonian quality is used as the feedback signal for the learning algorithm guiding the laboratory experiments.



Reprinted from J.M. Geremia and H. Rabitz, *Phys. Rev. Lett.* **89**, 236902 (2002), copyright 2002 by the American Physical Society.

Fig. 7. A simulation of the Hamiltonian identification concept in Fig. 6 for a 10-state quantum system, with the observations being state populations. The data errors were taken as 1%. The closed loop optimal inversion was capable of finding a single experiment, which dramatically filtered out the data noise to produce Hamiltonian matrix elements with an order of magnitude better quality than that of the data noise. In contrast, a standard inversion involving 5000 observations gave significantly poorer results, including amplification of the laboratory noise.

5. CONCLUSION

The field of quantum control goes back some 40 years to the earliest days of lasers, but in a practical sense, we may consider the field as only a few years young, considering the exact emerging laboratory successes especially using closed loop learning control techniques. The diversity of applications already examined speaks well for the future breadth and scope of control over quantum phenomena. These applications may range from delicate manipulation of molecular structures out to the management of quantum information systems. Furthermore, the unique ability to perform massive numbers of precisely controlled experiments opens up the prospect of learning about mechanism, deducing Hamiltonian structure, and possibly creating specialized closed loop analytical instrumentation. There is a significant need to perform systematic studies over large sets of physical systems, and this prospect is now feasible given the ease of performing automated closed loop control experiments. At the core of all of these developments is the ability to create shaped laser pulses, where a particular pulse can be thought of as a photonic reagent. Perhaps ultimately, we will be able to mix and match ordinary and photonic reagents in a flexible way to best control matter as well as analyze its dynamics.

ACKNOWLEDGMENT

The author acknowledges support from the National Science Foundation.

REFERENCES

- [1] H. Rabitz, H., R. de Vivie-Riedle, M. Motzkus, and K. Kompa, K., *Science*, 288 (2000) 824.
- [2] R.S. Judson and H. Rabitz, *Phys. Rev. Lett.*, 68, (1992) 1500.
- [3] C.J. Bardeen, V.V. Yakolev, K.R. Wilson, S.D. Carpenter, P.M. Weber, and W.S. Warren, *Chem. Phys. Lett.*, 280 (1997) 151.
- [4] A. Assion, T. Baumert, M. Bergt, T. Brixner, B. Keifer, V. Seyfried, M. Strehle, and G. Gerber, *Science*, 282 (1998) 919.
- [5] D. Meshulach and Y. Silberberg, *Nature*, 396 (1998) 239; T. Hornung, R. Meier, D. Zeidler, K.L. Kompa, D. Proch, and M. Motzkus, *Appl. Phys. B*, 71 (2000) 277.
- [6] A. Glab, T. Rozgonyi, T. Feurer, R. Sauerbrey, and G. Szabó, *Appl. Phys. B*, 71 (2000) 267.
- [7] R.J. Levis, G. Menkir, and H. Rabitz, *Science*, 292 (2001) 709.
- [8] C. Daniel, J. Full, L. González, C. Lupulescu, J. Manz, A. Merli, S. Vajda, and L. Wöste, *Science*, 299 (2003) 536.
- [9] R. Bartels, S. Backus, I. Christov, H. Kapteyn, and M. Murnane, *Chem. Phys.*, 267 (2001) 277.
- [10] J.L. Herek, W. Wohlleben, R.J. Cogdell, D. Zeidler, and M. Motzkus, *Nature*, 417 (2002) 533.
- [11] M. Bergt, T. Brixner, C. Dietl, B. Kiefer, and G. Gerber, *J. Organometallic Chem.*, 661 (2002) 199.
- [12] J. Kunda, B. Baumann, S. Arlt, F. Morier-Genoud, U. Siegner, and U. Keller, *Appl. Phys. Lett.*, 77 (2000) 924.
- [13] T.C. Weinacht, J.L. White, and P.H. Buckbaum, *J. Phys. Chem. A*, 103 (1999) 10166.
- [14] A.P. Pierce, M.A. Dahleh, and H. Rabitz, *Phys. Rev. A*, 37 (1988) 4950; S. Shi, A. Woody, and H. Rabitz, *J. Chem. Phys.*, 88 (1988) 6870.
- [15] R. Kosloff, S.A. Rice, P. Gaspard, S. Tersigni, and D.J. Tannor, *Chem. Phys.*, 139 (1989) 201.
- [16] S. Rice and M. Zhao, *Optical Control of Molecular Dynamics*, John Wiley & Sons, New York, 2000.
- [17] H. Rabitz, *Science*, 299 (2003) 525.
- [18] A. Mitra, I. Solá, and H. Rabitz, *Phys. Rev. A*, 67 (2003) 043409; A. Mitra and H. Rabitz, *Phys. Rev. A*, 67, (2003) 033407.
- [19] J.M. Geremia and H. Rabitz, *Phys. Rev. Lett.*, 89 (2002) 263902.

Energy flow in photosynthetic light harvesting: spectroscopy and control

W. Wohlleben^a, T. Buckup^a, J.L. Herek^b, H. Hashimoto^{c,d}, R.J. Cogdell^c and M. Motzkus^a

^aMax-Planck-Institut für Quantenoptik, 85748 Garching, Germany

^bFOM-Institute for Atomic and Molecular Physics, 1098 SJ Amsterdam, The Netherlands

^cIBLS, University of Glasgow, Glasgow G12 8QQ, United Kingdom

^dPermanent address: Osaka City University, Osaka 558-8585, Japan

1. INTRODUCTION

The function of a light-harvesting antenna complex is to harvest sunlight and, through a series of energy transfer steps both within and between complexes, to make the energy available to the reaction centre, where it is used to fuel the primary dark reactions of photosynthesis. Harvested excitation energy from the absorption of blue-green light in carotenoids undergoes ultrafast partitioning between excitation energy transfer (EET) to bacteriochlorophyll (BChl) and losses by internal conversion (IC) within the carotenoid (Car) [1]. The classical scheme of the energy flow (Fig. 1) describes the carotenoid IC as a sequential process from the absorbing Car S_2 state, $1B_u^+$ in the idealised C_{2h} symmetry, to the lower-lying Car S_1 ($2A_g^-$) state and further on to the ground state Car S_0 ($1A_g^-$). The EET channel takes roughly half of the excitation energy directly from Car S_2 to the BChls, which ultimately resides in the lowest-lying singlet state of the complex, BChl B850 Q_y . Recently we reported feedback-optimised coherent control of the energy flow pathways in the antenna complex LH2 of *Rps. acidophila* [2]. By excitation of Car S_0 - S_2 with shaped femtosecond pulses, the ratio IC/EET was changed by $\sim 35\%$ as compared to excitation with transform-limited pulses.

Here we present additional data in order to extract a characteristic 'control' frequency and establish a detailed picture of the laser-chromophore interaction and the ensuing dynamics. This work demonstrates the use of coherent control as a valuable tool for the spectroscopy of complex molecules.

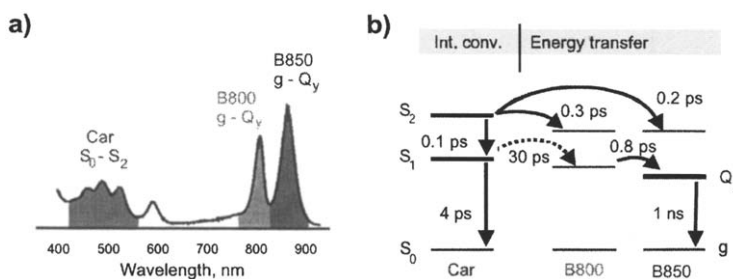


Fig. 1. Light harvesting complex LH2 from *Rps. acidophila*. a) Absorption spectrum. b) Standard model of the energy flow rates upon excitation of Car S_2 [3].

2. SPECTROSCOPY BY COHERENT CONTROL

As described previously [2], we excite selectively the Car S_0 - S_2 absorption (Fig. 1a) with pulses at 525nm that have passed through a 4-f-shaper. We detect the transient absorption simultaneously at 580nm (Car S_1 - S_n) for the IC channel and at 880nm (BChl B850 g- Q_y) for the EET channel (Figs. 1b and 2a). The excitation pulses have 30fs transform limited duration as long as the shaper is inactive and the signals in the IC and EET channels are measured at an excitation intensity of 8×10^{14} photons/cm². The signal of IC is quantified by integrating the transient at 580nm across 5-20ps probe delay. The signal of EET is quantified by averaging the asymptotic absorption at 880nm at 20ps delay. An optimisation of the pulse shape for maximal ratio IC/EET naturally converges to a solution of multipulse excitations [2].

The multipulse excitation is generated by a modulation of the spectral phases,

$$\Phi(\omega) = a \sin(b(\omega - \omega_0) + c), \quad (1)$$

with period $2\pi/b$, modulation depth a , and phase c relative to the center of the spectrum ω_0 . Fourier transformation of Eq. (1) shows that the higher the value of a , where $0 < a < \pi$, the more intensity is found in replica pulses of an equispaced multipulse sequence with $\Delta\tau = b$ (Fig. 2a). Parameter c controls the relative carrier phases between successive pulses of the sequence.

The optimal parameters for maximal IC/EET converge reproducibly in successive optimisation runs. Most importantly, we find that the optimal value of the periodic modulation is $2\pi/v_{\text{light}}b = 160 \pm 25 \text{ cm}^{-1}$ (Fig. 2b). The control of IC/EET is best if the modulation is as deep as possible, with $a = \pi$, generating ~ 8 subpulses. Previously we have shown that also parameter c , and thus the relative carrier phase, has a decisive influence on the control effect [2].

The mechanism of control with multipulse excitation is likely due to dynamics of the carotenoid donor. The presumably incoherent EET process [1] would not support the observed dependence on the carrier phase via the parameter c . Furthermore, the control effect does not suffer from annihilation at higher excitation intensities [2], as would be characteristic for the delocalised excitons in the B850 ring [1]. However, it is well known that femtosecond pulses populate higher ground state vibrational levels by impulsive Raman scattering (IRS) [4], and that the periodic phase modulation (Eq. 1) makes IRS selective for specific vibrations

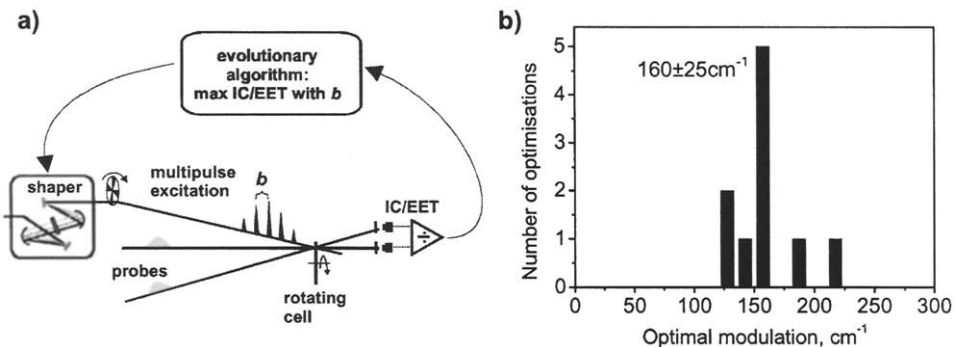


Fig. 2. Optimisation of internal conversion with multipulse excitation. a) Experimental setup: Coherent multipulse sequences are generated by periodic modulation of the spectral phases. The multipulse spacing b is optimised for maximal ratio IC/EET by an evolutionary algorithm. b) Histogram of optimal modulation $2\pi/v_{\text{light}}b$ (i.e. multipulse separation) by successive optimisations.

[5, 6]. The selectivity of Raman excitation can be derived in three simple equations: The Raman excitation P of a mode of energy Ω_R is given by

$$P(\Omega_R) \propto \left| \int d\omega E(\omega) E^*(\omega - \Omega_R) \right|^2, \quad (2)$$

with the electric field $E(\omega) = A(\omega) \exp\{i\Phi(\omega)\}$. Each Raman frequency pair contributes the phase term $\Phi(\omega) - \Phi(\omega - \Omega_R)$. Interference is constructive, if for the entire spectrum holds:

$$\Phi(\omega) = \Phi(\omega - \Omega_R). \quad (3)$$

The periodic modulation Eq. (1) selects a Raman level Ω_R^{res} , (m an integer number):

$$\Omega_R^{\text{res}} = m \frac{2\pi}{b}. \quad (4)$$

The multipulse laser field generated by Eq. (1) is thus synchronised to the vibrational wave packet in a specific coordinate. Here the experiments on LH2 finds $2\pi/v_{\text{light}}b = 160 \pm 25 \text{cm}^{-1}$ (Fig. 2b) as effective mode for maximal IC/EET. In the carotenoid, this low frequency mode can be identified with a b_u mode that induces an angle alternation or bending of the CCC backbone [7]. Excursion along such an asymmetric coordinate is necessary to couple Car S_2 and S_1 or, more specifically, to reach a point where the C_{2h} symmetry is broken such that the electronic surfaces of S_2 and S_1 can cross via a conical intersection [7]. Selective IRS of the coupling b_u mode facilitates IC and is thus responsible for the control of the energy flow ratio IC/EET. If IC is faster, EET is less efficient, as we have demonstrated in the transients after optimally shaped multipulse excitation [2]. The influence of the carrier phase parameter c [2] is attributed to vibrational wavepacket interference [8], but not yet fully understood.

We have thus identified a mechanistic picture of the IC dynamics and their control that allows attribution of the measured optimal modulation to a specific mode. However, the mechanism is based on the assumption that IRS is relevant in carotenoids. In the following experiment we strive to directly detect that assumed hot ground state by the corresponding redshifted ground-state Car S_0 - S_2 absorption.

3. DETECTION OF THE HOT GROUND STATE

We studied lycopene in solution, which has a conjugation system identical to that of rhodopin glucoside (the native carotenoid of *Rps. acidophila*) yet is less susceptible to degradation. The experimental approach is different from above, since now unshaped, i.e. transform-limited pulses (30fs duration) excite the Car S_0 - S_2 ($v=0$ - $v'=0$) transition at 505nm. As measured by its fluorescence, the S_2 state lives 100-200 fs in carotenoids with conjugation length $N=11$ in solution [1]. At a delay of $T=50$ fs, another transform-limited pulse, now at 795nm (110fs duration), depletes the population in the Car S_2 state by pumping its near-infrared absorption band (Fig. 3a). Every state that is populated by IC from the initially absorbing Car S_2 state should now show less population, but not the hypothetical hot ground state populated by IRS. Indeed, the absorption signal on the low-frequency side of cold ground state absorption (~ 530 nm) is exempt from depletion (Fig. 3b) and can thus be identified with the anticipated

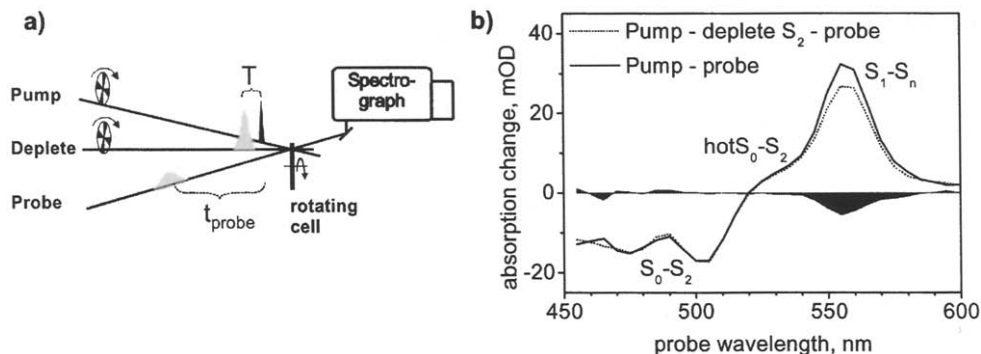


Fig. 3. Pump-deplete-probe spectroscopy on lycopene in hexane. a) Experimental setup: After excitation and depletion of Car S_2 with a delay of $T=50$ fs, a white-light probe pulse at delay $t_{\text{probe}}=2$ ps measures the transient absorption spectrum. b) Spectra without (solid curve) and with depletion pulse (dotted) and their difference (shaded area). Only the Car S_1 state is depleted; the ground state bleach (S_0 - S_2) and positive absorption feature on its low energy side (hot S_0 - S_2) are unaffected.

hot ground state [10]. This result strongly supports the proposed mechanism of coherent control via selective IRS. Further support comes from similar studies in a series of carotenoids with $N=11-19$, in which the positive transient absorption signal to the red side of the ground state bleach shows a constant lifetime of 6.2 ± 0.4 ps [9]. We attribute this time constant to ground state vibrational relaxation.

4. CONCLUSION

Excitation of Car S_2 in LH2 with optimally shaped multipulse sequences allowed extraction of a characteristic molecular vibration of $160 \pm 25 \text{cm}^{-1}$, attributed to an asymmetric b_u coordinate that facilitates the internal conversion pathway [7]. The mechanism of preparation is explained by the well established concept of coherently controlled impulsive Raman scattering [5, 6]. To corroborate this model, we identified the transient absorption signal of the hot ground state [10] that is created by impulsive Raman scattering [4]. To that aim we have again gone beyond pump-probe spectroscopy by introducing pump-deplete-probe spectroscopy [9]. Coherent control is thus employed as a spectroscopic tool to measure the frequency of the promoting mode of IC in a biological molecule.

REFERENCES

- [1] V. Sundström, T. Pullerits, R. van Grondelle, *J. Phys. Chem. B*, 103 (1999) 2327.
- [2] J.L. Herek, W. Wohlleben, R.J. Cogdell et al., *Nature*, 417 (2002) 533.
- [3] A. Macpherson, J.B. Arellano, N.J. Fraser et al., *Biophys. J.*, 80 (2001) 923.
- [4] Y.-X. Yan, E.B. Gamble, K.A. Nelson, *J. Chem. Phys.*, 83 (1985) 5391.
- [5] A.M. Weiner, D.E. Leaird, G.P. Wiederrecht et al., *Science*, 247 (1990) 1317.
- [6] N. Dudovich, D. Oron, Y. Silberberg, *J. Chem. Phys.*, 118 (2003) 9208.
- [7] W. Fuß, Y. Haas, S. Zilberg, *Chem. Phys.*, 259 (2000) 273.
- [8] N.F. Scherer, R.J. Carlson, A. Matro et al., *J. Chem. Phys.*, 95 (1991) 1487.
- [9] W. Wohlleben, T. Buckup, J.L. Herek et al., *J. Phys. Chem B*, submitted, (2003)
- [10] P.O. Andersson, T. Gillbro, *J. Chem. Phys.*, 103 (1995) 2509.

Control of nonlinear optical excitation with multiphoton intrapulse interference

J.M. Dela Cruz, I. Pastirk, V.V. Lozovoy, K.A. Walowicz and M. Dantus

Department of Chemistry, Michigan State University East Lansing MI 48824,
E-mail: dantus@msu.edu

1. INTRODUCTION

Here we present the latest results from our group focused on the design of tailored femtosecond pulses to achieve control of nonlinear optical excitation in large molecules based on the concept of multiphoton intrapulse interference (MII) [1-4]. Our goal is to elucidate well-defined and reproducible pulse shapes that can be used to enhance or suppress particular nonlinear optical transitions in large molecules such as laser dyes and proteins in solution. We demonstrate the use of MII to probe the local and microscopic environment of molecules by selective two-photon laser induced fluorescence (LIF).

The probability for two-photon excitation, $S^{(2)}$, using phase-modulated pulses at frequency $\omega = \Delta + \omega_0$, where ω_0 is the carrier frequency, can be calculated from [2]

$$S^{(2)} \propto \int g^{(2)}(2\omega) \left| \int E(\omega + \Omega) E(\omega - \Omega) d\Omega \right|^2 d\omega \quad (1)$$

where $E(\omega) = |E(\omega)|e^{i\phi(\omega)}$ is the electric field of the laser. In this expression, we assume a broad nonlinear two-photon absorption spectrum, $g^{(2)}(2\omega)$ and ignore intramolecular dynamics to simulate our experimental results.

We demonstrate the MII method, which couples the sensitivity of multiphoton excitation on the spectral phase of the laser pulses to probe microscopic chemical environment-induced changes in the multiphoton excitation spectrum of sensitive reporter molecules. We carry out the optimization of the required phase functions in solution and provide theoretical simulations. We show experimental images whereby pH-selective two-photon microscopy is achieved and demonstrate how selective excitation can be used to enhance contrast and, consequently, to achieve functional imaging, using fluorescent probes sensitive to changes in their local environment.

2. EXPERIMENTAL SECTION

Experiments were performed using a titanium sapphire laser oscillator capable of producing pulses with bandwidths up to 80 nm FWHM. The output of the oscillator was evaluated to make sure there were no changes in the spectrum across the beam and was compressed with a double prism pair arrangement. The pulse shaper uses prisms as the dispersive elements, two cylindrical concave mirrors, and a spatial light modulator (CRI Inc. SLM-256), composed of two 128-pixel liquid crystal masks in series. The SLM was placed at the Fourier plane [5]. After compression and pulse shaping, ~ 200 pJ pulses were used to interrogate the samples.

We use a single beam method, called multiphoton intrapulse interference phase scan (MIIPS) [4, 6], to measure both the sign and magnitude of phase distortions in the pulse. In MIIPS, a well-known reference function is scanned across the spectrum of the pulse to reveal the unknown phase across the pulse. We defined Gaussian spectra of the desired width and center wavelength by amplitude shaping. We then measured the quadratic and cubic phase distortions in the pulse by scanning a phase function defined by

$$f(\Delta) = \alpha \cos(\gamma\Delta - \delta), \quad (2)$$

where the amplitude α was set to 1.5π rad, γ was set to 20 fs (approximately the pulse duration), Δ is the frequency detuning from the center of the pulse, and δ is a parameter that determines the position of the maximum retardance (or the relative position of superimposed phase function). The MIIPS data is a two dimensional collection of SHG spectra as a function of δ , as shown in Fig. 1. For each phase in the scan, the second harmonic spectrum obtained from a thin 0.015 mm β BBO crystal is recorded. Changes in the SHG spectrum are then used to obtain the spectral phase of the laser pulses. The MIIPS measurement takes place at the location of the sample; therefore, the exact phase at the sample is obtained. For transform-limited pulses, the MIIPS data shows equally spaced parallel linear features given by

$$\delta_{TLmax}(\lambda) = (\lambda - \lambda_0) \gamma \alpha \omega^2 / 2\pi c \pm \pi/2; \quad (3)$$

deviations from these parallel lines indicate distortions in the spectral phase. The expression required to retrieve arbitrary spectral phases, is given elsewhere [6].

The MIIPS of compensated pulses is shown in Fig. 1b. To corroborate phase information retrieved from MIIPS, phase characterization was also done using second harmonic generation frequency resolved optical gating (SHG-FROG) [7]. SHG-FROG traces of the pulses before and after compensation are shown in Fig. 1c and 1d. The final pulse-shaping step involved the controlled phase modulation of transform-limited pulses.

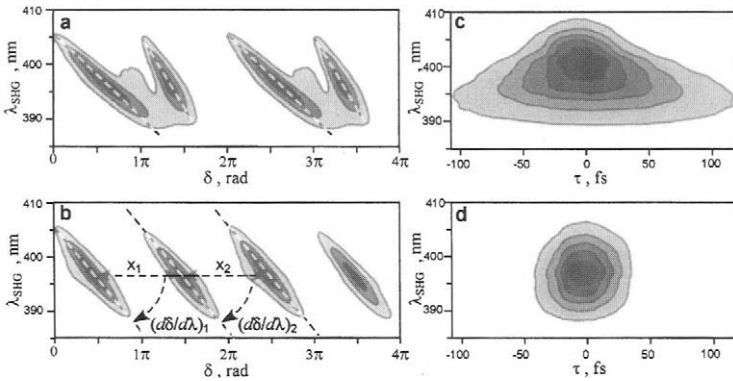


Fig. 1. Spectral phase modulation in the femtosecond pulses is characterized (a) and compensated (b) using the MIIPS method. SHG-FROG traces for the pulses in panels (a) and (b) are shown in panels (c) and (d).

The laser was focused by a 50 mm focal length lens onto a 10 mm path length quartz cell containing the dye solution. Fluorescence perpendicular to the excitation beam was collected near the front face of the cell to minimize dispersion in the sample. We took advantage of the narrow acceptance angle of the optical fiber for spatial filtering and imaged the signal onto an Ocean Optics spectrometer. The experiment involved scanning the parameter δ and detection of the fluorescence of the sample (spectrally integrated). Signal integration time was typically 500 msec per spectrum for each value of δ , and the data scan, with 256 different phase positions was averaged over 3 cycles of δ from 0 to 4π rad.

The samples used were 10^{-5} M aqueous solutions of 8-hydroxypyrene-1,3,6-trisulfonic acid trisodium salt (HPTS or 3sPyOH) (Sigma-Aldrich) in buffers of pH 6 and pH 10. UV-Vis absorption spectra of the dye solutions at different pH environments were obtained with a Hitachi U-4001 uv-vis spectrophotometer.

For the imaging experiment, shaped laser pulses, with an energy of 0.2-1 nJ per pulse and 87 MHz repetition rate, were mildly focused to a spot size of ~ 200 microns in diameter on the sample. Two-photon induced fluorescence was collected by an infinity corrected apochromatic microscope objective and imaged into a liquid nitrogen cooled CCD detector. The sample was prepared by mixing 1 mL of acrylonitrile-vinylidene chloride polymer with 100 μ L of 10^{-2} M aqueous HPTS. To achieve the desired pH of 6 and 10, HCl and NaOH, respectively, were added to the mixture. Both mixtures were then smeared to an approximate thickness of 0.07 ± 0.03 mm on contiguous regions of a microscope glass slide, and then allowed to cure for 20 minutes. Some mixing of the solvent water may have occurred at the interface between the two regions. Local changes in the fluorescence intensity observed for transform-limited pulses may reflect changes in the local sample thickness. The images were captured without optical filters in the collection optics or post image manipulation; they are shown in false color (both regions fluoresce at 515 nm). The background counts, obtained when the laser is off, were subtracted.

3. RESULTS

In Fig. 2 we show the dependence of two-photon LIF on phase modulation [4]. These measurements were obtained using 23 fs transform-limited pulses that were shaped to have a Gaussian spectrum centered at 842.6 nm with a bandwidth of 48 nm FWHM and spectral phase defined by Equation 2. Fig. 2a shows the experimental two-photon LIF intensity from HPTS in a pH 10 solution (dots) as a function of δ . The signal shows a sinusoidal modulation. Fig. 2b shows the experimental two-photon LIF intensity from HPTS in a pH 6 solution (dots) as a function of δ . The signal is modulated, however, there is a clear phase shift compared to pH 10. The shift comes about from pH-induced changes in the two-photon absorption spectrum. The laser spectrum and intensity remain unchanged throughout the experiments. The emission spectrum from the dye is independent of pH so detection is always at the same wavelength (515 nm).

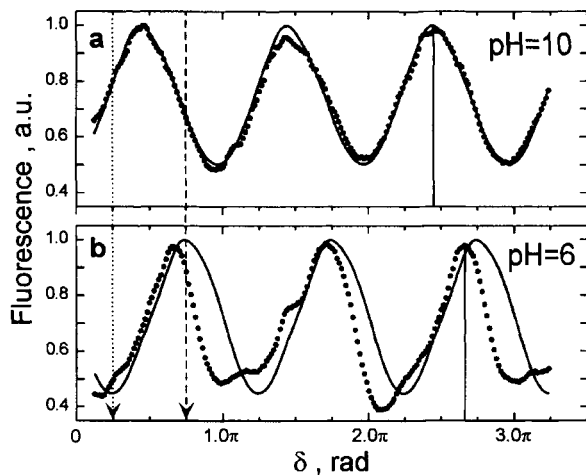


Fig. 2. Intensity of the two-photon induced fluorescence of HPTS solution at pH 10 (a) and pH 6 (b) are plotted as a function of δ . Simulations (continuous lines) based on Eq. 1 are in good agreement with the experimental data (dots).

Simulations of the experimental signal were performed using Equation 1 without adjustable parameters. The spectrum of the pulse and the absorption spectrum of HPTS were measured experimentally. An examination of the molecular structure of HPTS shows that it has no center of symmetry. Since parity restrictions may be relaxed in this case, the similarity between one-photon and two-photon absorption spectra is expected. The spectral phase $\phi(\Omega)$ imprinted by the phase mask was the same used for the simulations. Both experimental and theoretical data were normalized such that the signal intensity is unity and the background observed is zero. The experimental data (dots) generally agree with the calculated response (continuous line) of the dyes in all pH environments (see Fig. 2).

4. DISCUSSION

The MII method is used in this experiment to control two-photon excitation. More specifically, the interference process, which is controlled by the phase introduced in the pulse, suppresses two-photon transitions at specific frequencies within the two-photon bandwidth [2]. In other words, the interference can be used to tune multiphoton transition probability at specific frequencies. This effect can be envisioned using a thin second harmonic crystal, as shown in the MIIPS traces in Fig. 1. Notice that as δ is scanned the maximum intensity in the second harmonic signal scans as well from longer to shorter wavelengths [1, 2]. By considering this effect together with the two-photon absorption spectrum, we are able to calculate the expected signal using Equation 1 with very good agreement.

HPTS is a highly water-soluble, pH-sensitive dye with a pK_a of ~ 7.5 in aqueous solution [8]. When in alkaline medium, $pH > 7.5$, acid-base equilibrium is totally displaced toward the anion form ($3sPyO^-$) of the dye. The electronic character of $3sPyO^-$ remains unchanged after photo-excitation, and corresponds to a singlet-excited state [9]. Fluorescence from this state undergoes a fast 0.4 ps Stokes shift and has a maximum at 515 nm and a lifetime of 5.3 ± 0.1 ns [10].

In acidic medium, $\text{pH} < 7.5$, the conjugate acid form (3sPyOH) dominates in the ground state. Two-photon excitation yields the excited state (3sPyOH^*). Fluorescence from this state undergoes a fast 0.3 ps Stokes shift and has a maximum near 450 nm. HPTS has a very high fluorescence quantum yield (almost 100% in both alkaline and acidic solution, when excited with light of wavelengths shorter than 400 nm) [11]. Proton transfer in the excited state takes place in 87.5 ps [9, 10], to yield the conjugate base (3sPyO^*), with a fluorescence maximum at 515 nm and a lifetime of 4.8 ± 0.5 ns. Therefore, in both acidic and basic environments, the emission spectrum is unchanged. The nature of the excited state dynamics involves a three-step mechanism of the proton transfer reaction, whereby an intermediate state (unionized acid form) with significant charge transfer character converts to the fluorescent excited anionic state [10].

Recently, two-photon microscopy has gained acceptance for biological imaging applications, given the method's higher resolution, background-free signal, lower background scattering, greatly improved depth of focus, and reduced photon induced damage [12-15]. Two-photon microscopy has also been valuable in multiple-probe staining, where two-photon transitions excite different probe molecules that emit at different wavelengths [15, 16], and in functional imaging of living cells [17-20]. The only drawback to multiphoton microscopy is that selective excitation cannot be realized. Experiments based on dual channel fluorescence detection [21, 22] bring about selective detection, provided very different wavelengths are used, typically green and red. This selectivity cannot be achieved when the reporter molecules have a similar fluorescence spectrum. For example, in the case of HPTS, the fluorescence spectrum is independent of pH.

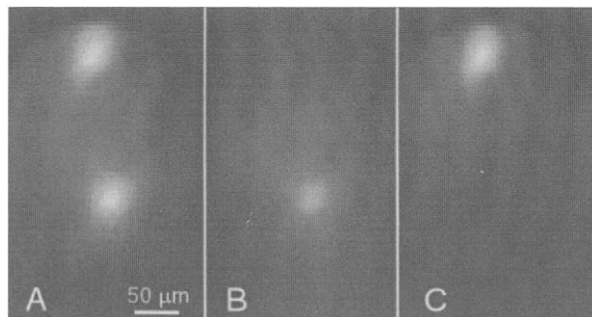


Fig. 3. Experimental demonstration of two-photon selective microscopy. The HPTS-labeled sample being imaged has acidic (bottom side) and a basic (top side) regions. Images were obtained with (A) 23-fs transform-limited pulses centered at 842 nm, and (B and C) phase shaped pulses optimized for selective excitation.

The results in Fig. 3, demonstrate selective two-photon microscopy images using shaped femtosecond laser pulses. In this experiment, we selectively excite regions that differ in pH using HPTS as the fluorescent probe. Here selective imaging is achieved with a fluorescent probe that emits at 515 nm in both acid and basic pH, making it incompatible with dual fluorescence detection. Fig. 3A shows an image obtained with transform-limited pulses (time duration is 23 fs at 842.6 nm), where fluorescence from HPTS under both acidic and basic conditions occurs without selectivity. However, when laser pulses are optimally shaped for selective excitation, fluorescence switches on and off depending on whether the chemical environment of the molecule is acidic or basic. The pulses were shaped with $\alpha=1.5\pi$ rad and $\gamma=20$ fs. For the acidic probe, γ was optimized to 0.75π rad; for the basic probe, γ was

0.25π rad. Figs. 3B and 3C show images obtained under these conditions. Very high contrast is observed between the two different pH regions.

Pulse shaping and, in particular, the use of MII provide a number of advantages for multiphoton microscopy. (a) A very short pulse laser is set up once and optimized once (no subsequent tweaking). (b) The short pulse duration has the advantages of higher multiphoton excitation efficiency and broader bandwidth. (c) As the phase is optimized for selective excitation, maximum efficiency is maintained; there is no need for tuning, realigning, tweaking, compensating for chirp, and renormalizing. (d) The system is computer-controlled and can take advantage of phase compensation at the sample using MIIPS as described here. (e) MII can be used to control two- or three-photon excitation. (f) During the selective excitation experiments the intensity and spectrum of the laser remain constant; therefore, one-photon processes like absorption, reflection, and scattering remain constant as well. (g) Selective photochemistry can be realized through shaped pulse excitation and this can be used for selective multiphoton microlithography.

5. CONCLUSION

Selective excitation of large fluorescent probes is achieved by optimizing the overlap between the power spectrum of the pulse and the two-photon absorption spectrum of a molecule. Phase modulation of ultrashort pulses through multiphoton intrapulse interference can be used to probe chemical changes that take place within cells as they respond to external changes in their environment. The effect can be further enhanced using even shorter (larger bandwidth) fs pulses. The principles of MII can be similarly applied to other biologically relevant local environment parameters, like sodium or calcium ion concentration.

ACKNOWLEDGEMENTS

This research was funded by the Chemical Sciences, Geosciences and Biosciences Division, Office of Basic Energy Sciences, Office of Science, U.S. Department of Energy. MD is a Camille Dreyfus Teacher-Scholar. We thank Prof. Gary Blanchard for allowing us to use his microscope for the imaging experiment.

REFERENCES

- [1] K. A. Walowicz, I. Pastirk, V. V. Lozovoy and M. Dantus, *J. Phys. Chem. A*, 106 (2002) 9369.
- [2] V. V. Lozovoy, I. Pastirk, K. A. Walowicz and M. Dantus, *J. Chem. Phys.*, 118 (2003) 3187.
- [3] I. Pastirk, J. M. Dela Cruz, K. A. Walowicz, V. V. Lozovoy and M. Dantus, *Optics Express*, 11 (2003) 1695.
- [4] J. M. Dela Cruz, I. Pastirk, V. V. Lozovoy, K. A. Walowicz and M. Dantus, *J. Phys. Chem. A*, (2003, in press).
- [5] A. M. Weiner, *Rev. Sci. Instr.*, 71 (2000) 1929.
- [6] V. V. Lozovoy, I. Pastirk and M. Dantus, *Opt. Lett.*, (2003, submitted).
- [7] R. Trebino, K. W. DeLong, D. N. Fittinghoff, J. N. Sweetser, M. A. Krumbugel, B. A. Richman and D. J. Kane, *Rev. Sci. Instr.*, 68 (1997) 3277.
- [8] O. S. Wolfbeis, E. Furlinger, H. Kroneis and H. Marsoner, *Fresenius Z. Anal. Chem.*, 314 (1983) 119.
- [9] T. H. Tran-Thi, T. Gustavsson, C. Prayer, S. Pommeret and J. T. Hynes, *Chem. Phys. Lett.*, 329 (2000) 421.
- [10] T. H. Tran-Thi, C. Prayer, P. H. Millie, P. Uznanski and J. T. Hynes, *J. Phys. Chem. A*, 106 (2002) 2244.
- [11] S. G. Schulman, W. R. Vincent and W. J. M. Underberg, *J. Phys. Chem.*, 85 (1981) 4068.

- [12] W. Denk and J. H. Strickler, *Science*, 248 (1990) 73.
- [13] W. Denk, *J. Biomed. Opt.*, 1 (1996) 296.
- [14] K. Konig, *J. Microsc. -Oxf.*, 200 (2000) 83.
- [15] P. T. C. So, C. Y. Dong, B. R. Masters and K. M. Berland, *Annu. Rev. Biomed. Eng.*, 2 (2000) 399.
- [16] K. W. Dunn, R. M. Sandoval, K. J. Kelly, P. C. Dagher, G. A. Tanner, S. J. Atkinson, R. L. Bacallao and B. A. Molitoris, *Am. J. Physiol. - Cell Physiol.*, 283 (2002) C905.
- [17] J. W. Wang, A. M. Wong, J. Flores, L. B. Vosshall and R. Axel, *Cell*, 112 (2003) 271.
- [18] T. G. Oertner, *Exp. Physiol.*, 87 (2002) 733.
- [19] K. A. Kasichke, H. Vishwasrao, A. A. Heikal and W. W. Webb, *Biophys. J.*, 82 (2002) 2420.
- [20] C. R. Rose, Y. Kovalchuk, J. Eilers and A. Konnerth, *Pflugers Arch.*, 439 (1999) 201.
- [21] T. Winkler, U. Kettling, A. Koltermann and M. Eigen, *Proc. Natl. Acad. Sci. USA*, 96 (1999) 1375.
- [22] M. Rarbach, U. Kettling, A. Koltermann and M. Eigen, *Methods*, 24 (2001) 104.

Infrared femtochemistry: Vibrationally induced molecular dissociation and its control employing shaped fs MIR laser pulses

T. Witte, L. Windhorn, J. S. Yeston, D. Proch, M. Motzkus, and K.L. Kompa

Max-Planck-Institut für Quantenoptik
Hans-Kopfermann-Str. 1, 85748 Garching, Germany

1. INTRODUCTION

Vibrations drive chemical reactions. This often-heard statement sounds trivial if understood as a description of chemical changes occurring via vibrational excitation of chemical bonds. A more difficult question to answer is, which and how many vibrations are reaction-relevant and which amount of energy (number of vibrational quanta) is needed in which mode. The barriers of chemical reactions are typically between 1 and 3 eV in comparison with the energy regime of infrared quanta ranging from .03 to .3 eV. This relation shows that one generally has to assume multiphoton excitation in the relevant infrared modes.

An additional obstacle for successful infrared laser chemistry is given by the very rapid (typically ps) intramolecular vibrational energy relaxation (IVR). Only if it is possible to keep the vibrational energy localized where it is beneficial for the reaction to occur, and if direct coupling between the initial and final state is possible, does infrared laser chemistry have a chance. This picture of directly driving chemical reactions by selective vibrational excitation is an old dream of IR laser-based chemistry. It is obviously contradicting the traditional view of chemical reaction activation which assumes that vibrational, rotational and translational modes of the molecule are equilibrated prior to reaction. Nevertheless, it remains yet to be explored whether with recently available femtosecond infrared sources and corresponding pulse shaping techniques such questions could potentially be addressed.

Different types of chemical reactions involve different types of vibrational modes, e.g. dissociation reactions may be controlled by stretching vibrations, isomerizations by skeletal modes, and so on. The argument that infrared quanta are relatively energy-poor and infrared transitions generally have low absorption cross sections, especially if multiphoton excitation is required, limits the choice of suitable molecular transitions. With respect to these constraints the type of reaction chosen and described below was dissociation, involving molecules with maximal transition dipole moments, comparatively weak bonds to be broken, and vibrational excitation in the mid-infrared spectral range.

2. RESULTS AND DISCUSSION

In this contribution we demonstrate vibrationally induced molecular dissociation in two polyatomic molecules, namely chromium hexacarbonyl and diazomethane (Fig. 1), employing fs mid-infrared laser sources [1,2]. As will be shown below, in both cases the initially excited mode does not lead directly to reaction but provides the doorway to access the right combination of modes. Thus both reactions have three steps: (1) Stepwise multiphoton excitation of the doorway mode, (2) sharing of energy with other modes, and (3) formation of

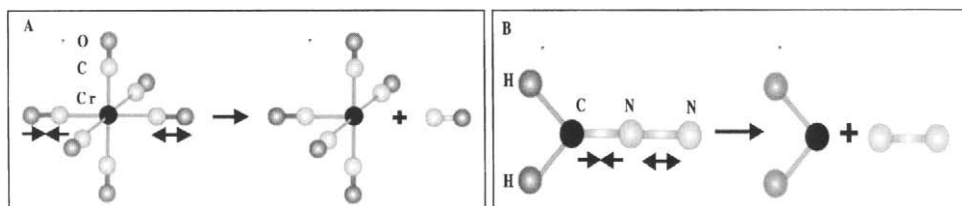


Fig. 1. MIR induced dissociation of (A) chromium hexacarbonyl ($\text{Cr}(\text{CO})_6$) upon excitation of its T_{1u} asymmetric CO-stretch at 2000 cm^{-1} , and of (B) diazomethane (CH_2N_2) following excitation of its asymmetric CNN stretch at 2100 cm^{-1} .

the products. Localized vibrational energy deposition has been achieved by vibrational ladder climbing employing broadband femtosecond laser pulses in the MIR, that is, stepwise multiphoton excitation within the anharmonic potential. This resulted in selective bond excitation to levels as high as $\nu = 7$, corresponding to an accumulated energy of approximately 13000 cm^{-1} , which was most probably limited only by the pulse spectrum running out of resonance with the anharmonic ladder. For both molecules, the deposited energy exceeded the dissociation barrier for the molecules' weakest bonds, and dissociation was observed. Here we highlight selected issues regarding these dissociation reactions and their implication for future concepts for control in infrared femtochemistry.

2.1 Coherent control of molecular vibrational excitation and subsequent dissociation [1]:

As a first test system, we chose the cleavage of CO from chromium hexacarbonyl upon resonantly, and selectively, exciting its asymmetric CO-stretch with unmodulated 90 fs laser pulses at 2000 cm^{-1} (Fig. 1A). This reaction requires vibrational excitation to $\nu=7$ within the fs pulse. Since the vibrational potential is characterized by an anharmonic energy shift of $\sim 15\text{ cm}^{-1}$ per excitation step, this lies within the spectral FWHM of 150 cm^{-1} . Following excitation, a subsequent mode-coupling process channels the energy into the metal-CO bond with currently unknown time constant, upon which dissociation of CO occurs. The cumulative dissociation was deduced from a change in the sample cell's absorbance after MIR irradiation. The coherent energy deposition via vibrational ladder climbing was controlled and optimized by applying negatively chirped laser pulses, which in fact means an ordering of the laser pulses' frequencies such that the central frequency decreases during the excitation. Thus, the excitation pulse could be adapted to the decreasing level spacing within the anharmonic potential. Control of vibrational excitation afforded control of the ground-state unimolecular dissociation. Note that in this case, the excitation mode is almost completely separated from the eventual reaction coordinate. The proof of control is shown in Fig.2 (left). We find that negatively chirped MIR laser pulses optimize the population transfer to levels $\nu=7$ and above, whereas ordering the pulses' frequencies to mismatch the subsequent resonances significantly (positive chirp) decreases the ladder climbing efficiency. If we investigate the dependence of the dissociation yield on the amount of the negative chirp ("blue-to-red" frequency sweep) we observe the smallest conversion for the least negative chirp (smallest temporal half width FWHM, see Fig. 2 (right)). Gradual enhancement of the negative chirp while keeping the spectrum constant leads to a maximal increase in conversion by a factor of ~ 10 for a negative chirp of $\sim 180\text{ cm}^{-1}\text{ps}^{-1}$, for which the pulse's half width is $\sim 800\text{ fs}$. Note that with increasing chirp and constant energy density, the pulse's intensity actually decreases. Thus, intensity dependent effects such as multiphoton absorption do not play a role. We have also modelled

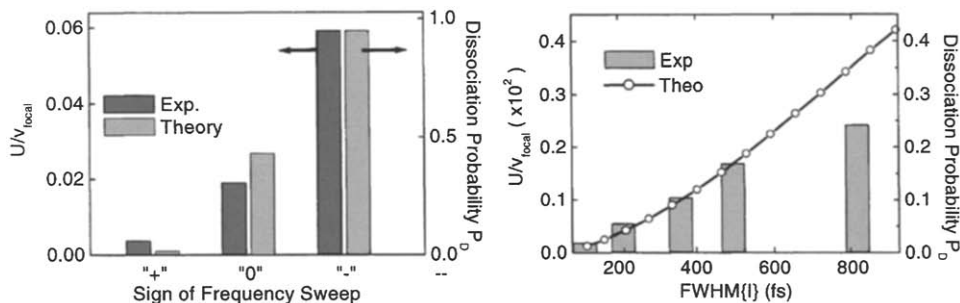


Fig. 2. Left: Dissociation yield U for a positive chirp ("+"), no chirp ("0"), and negative chirp ("-"); experiment (gray, left scale) and theory (light gray, right scale). Right: The dissociation yield U is a steep function of negative chirp; experiment (bars, left scale) and theory (open circles, right scale).

the multilevel excitation process in a one-dimensional potential (i.e. no coupling was included) and find excellent agreement in the behavior of the dissociation yield as a function of the chirp parameters. This experiment represents the first chirp controlled dissociation of a molecule in the ground electronic state. The reactivity of the molecule was effectively enhanced or hindered by an adapted or a mismatched chirp of the excitation pulse. A time window of at least 1 ps was identified during which ladder climbing can be coherently controlled.

2.2 MIR induced dissociation on a sub-statistical time scale [2]:

Encouraged by these results, we investigated the excitation of the CNN asymmetric stretch (2100 cm^{-1}) in diazomethane and achieved ultrafast C-N bond scission, which requires to surmount a barrier of $\sim 12000 \text{ cm}^{-1}$ (see Fig. 1B). The choice of diazomethane was suggested primarily by the possibility of a time resolved investigation, and more importantly, by the fact that excitation of the asymmetric CNN stretching mode has a large projection on the reaction coordinate for C-N bond scission, which is essential for a directed dissociation. We added a fs probe beam in the visible in order to detect nascent methylene by laser induced fluorescence in real time. The results of the pump-probe study, for which the MIR excitation pulses were unchirped, are shown in Fig. 3 (left). The main graph shows a transient over 100 ps, which exhibits a very rapid rise in fluorescence signal followed by a slower rise. The insert documents the exponential rise of the fast component. A biexponential fit yielded time constants of 480 fs and 36 ps. A time constant of 36 ps is consistent with the thermalization of 6 quanta, as intuitively expected given the dissociation threshold of 12000 cm^{-1} . The fast time constant of half a picosecond, however, is significantly faster than could be expected for a statistical process. Thus it must be postulated that after excitation a fraction of the molecules directly proceeds to dissociation on a sub-ps timescale. A detailed investigation reveals that as a second mode the CH_2 out-of-plane bend plays an integral role in the dissociation pathway. Multiphoton excitation of diazomethane first drives the molecule along the CN stretch. But the barrier for C-N bond scission in the *planar* molecular geometry exceeds the lowest energy pathway by $10,000 \text{ cm}^{-1}$, as also depicted in the potential energy surface shown in Fig. 3 (right). Substantial CH_2 out-of-plane *bending* is therefore required prior to dissociation. Because for the expected six quanta in the CNN stretch, the out-of-plane bending angle must be greater than 75° to circumvent the dissociation barrier. The planar configuration corresponds to a maximum rather than a minimum in the CH_2 bending coordinate. The wave-

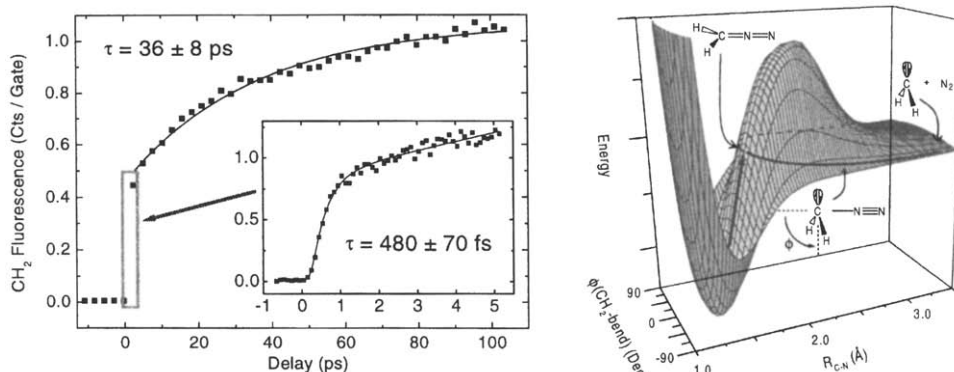


Fig. 3. Left: Transient fluorescence signal of nascent CH_2 after dissociation of CH_2N_2 with unchirped MIR laser pulses. A biexponential fit yields time constants of 480 fs (insert) and 36 ps. Right: Proposed pathway of sub-statistical dissociation on the potential energy surface with respect to the reaction coordinates $R_{\text{C-N}}$ and CH_2 out-of-plane bend. See text for details.

packet motion is unstable and fluctuations in the out-of-plane bend give access to the lowest-energy dissociation channel. In this sense the energy is directly channeled into the bending coordinate to induce bond scission. Thus it was shown for the first time that in favorable cases strong coupling of a molecular system to the laser field can outmaneuver intramolecular vibrational coupling. A unimolecular dissociation was driven faster than the statistical limit using vibrational excitation confined to the ground electronic state.

3. SUMMARY

Together, these results illustrate the potential of quantum control in infrared femtochemistry. The second experiment demonstrates the possibility of vibrational pre-dissociation originating from high-lying vibrational levels with a large projection onto the reaction coordinate. It also suggests that in favorable cases the number of vibrational modes required in total is limited. The coherently controlled energy deposition by ladder climbing to above 1.5 eV with suitable IR fs laser pulses, as shown in the first experiment, might be further optimized by properly shaped fs laser pulses, for which techniques are currently developed [3,4]. As localized deposition will be crucial, this represents a most powerful tool to attain this goal. Exciting scenarios for future experiments are abundant. They may include the simultaneous and ultimately coherent excitation of several vibrational modes, which in conjunction channel a molecular wavepacket into a desired direction. They may also incorporate feedback control technology, involving complex infrared transients that steer the molecular dynamics. Thus in the present case both concept-driven and tool-driven arguments converge to point to new possibilities of experimental quantum chemistry that may even find practical applications.

REFERENCES

- [1] T. Witte, T. Hornung, L. Windhorn, D. Proch, R. de Vivie-Riedle, M. Motzkus, K.L. Kompa, *J. Chem. Phys.* 118 (2003) 2021
- [2] L. Windhorn, J.S. Yeston, T. Witte, W. Fuss, M. Motzkus, D. Proch, K.L. Kompa, C.B. Moore, *J. Chem. Phys.* 119 (2003) 641
- [3] T. Witte, D. Zeidler, D. Proch, K.L. Kompa, M. Motzkus, *Opt. Lett.* 27 (2002) 131
- [4] T. Witte, K.L. Kompa, M. Motzkus, *Appl. Phys. B* 76 (2003) 467

Spectrally resolved femtosecond two-colour three-pulse photon echoes for studies of molecular dynamics: influence of pulse wavelengths and pulse sequence

Lap Van Dao, C. Lincoln, M. Lowe and P. Hannaford

Centre for Atom Optics and Ultrafast Spectroscopy, School of Biophysical Sciences and Electrical Engineering, Swinburne University of Technology, Melbourne, Australia 3122

1. INTRODUCTION

Recently, there has been much interest in the development and application of multidimensional coherent nonlinear femtosecond techniques for the study of electronic and vibrational dynamics of molecules [1]. In such experiments more than two laser pulses have been used [2-4] and the combination of laser pulses in the sample creates a nonlinear polarization, which in turn radiates an electric field. The multiple laser pulses create wave packets of molecular states and establish a definite phase relationship (or coherence) between the different states. The laser pulses can create, manipulate and probe this coherence, which is strongly dependent on the molecular structure, coupling mechanisms and the molecular environment, making the technique a potentially powerful method for studies of large molecules.

In this paper we report the use of spectrally resolved two-colour three-pulse photon echoes to expand the information that can be obtained from time-resolved vibrational spectroscopy. The experiments allow the study of intramolecular dynamics and vibrational structure in both the ground and excited electronic states and demonstrate the potential of the technique for studying structural dynamics.

2. EXPERIMENTS AND DISCUSSION

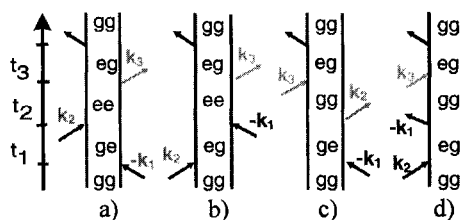


Fig. 1. Feynman diagrams for the interaction of a three-pulse sequence with a two-level system.

In a two-colour three-pulse photon echo experiment we illuminate the sample with two pump pulses delayed by time t_{12} and having wave vectors k_1 and k_2 at the same wavelength followed by a probe pulse of wave vector k_3 delayed with respect to the second pump pulse

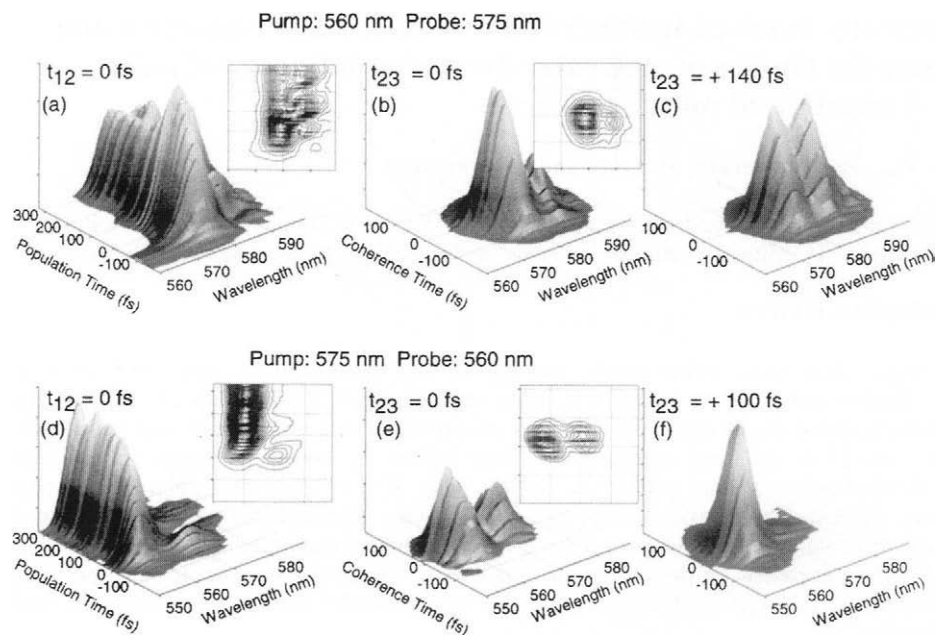


Fig. 2. Photon echo spectra vs. population time (a, d) and coherence time (b, c, e, f) at fixed other delay time for pump or probe pulse wavelength at the maximum (575 nm) and on the blue side (560 nm) of the absorption maximum. The inset shows the contour plot of corresponding figure

by time t_{23} . The probe pulse can be varied in wavelength to be shorter or longer than the wavelength of the pump pulses. The three laser pulses create a third-order polarization $P^{(3)}(t, t_{12}, t_{23})$ that is dependent on the time ordering and carrier frequencies of the applied pulses. The temporal evolution of $P^{(3)}$ can in principle be derived from the spectrally resolved measurement of the photon echo signal. The Feynman diagrams for the interaction of a sequence of three pulses with a two-level system (e.g., two electronic states each consisting of several vibrational levels) are shown in fig.1. For $t_{23} > 0$ the four diagrams show that signals can be generated by either free-induction decay (b, d) or stimulated photon echo (a, c) processes, depending on the timing sequence of the pulses. Variation of t_{12} and t_{23} reveals the dynamics of the coherence and population ensembles, respectively, created by the two pump pulses. In principle, both ground and excited electronic molecular vibration may contribute to the photon echo signal. Suitable selection of the wavelengths of the pump and probe pulses together with spectral resolution of the echo signals allows one to separate the dynamical processes. Depending on the selected wavelengths (i.e., the selected transitions) only one of the four diagrams will describe the main contribution to the observed echo signal.

The femtosecond (fs) laser system consists of a Ti:Sapphire laser and a regenerative amplifier pumping two independent optical parametric amplifiers that provide laser pulses of around 100 fs duration over a very broad range of wavelengths (250-2000 nm). The signal is detected in the transmitted phase-matching direction $\mathbf{k}_4 = \mathbf{k}_3 + \mathbf{k}_2 - \mathbf{k}_1$ and recorded by a spectrometer with spectral resolution ≈ 2 nm. The spectra are measured by scanning over the

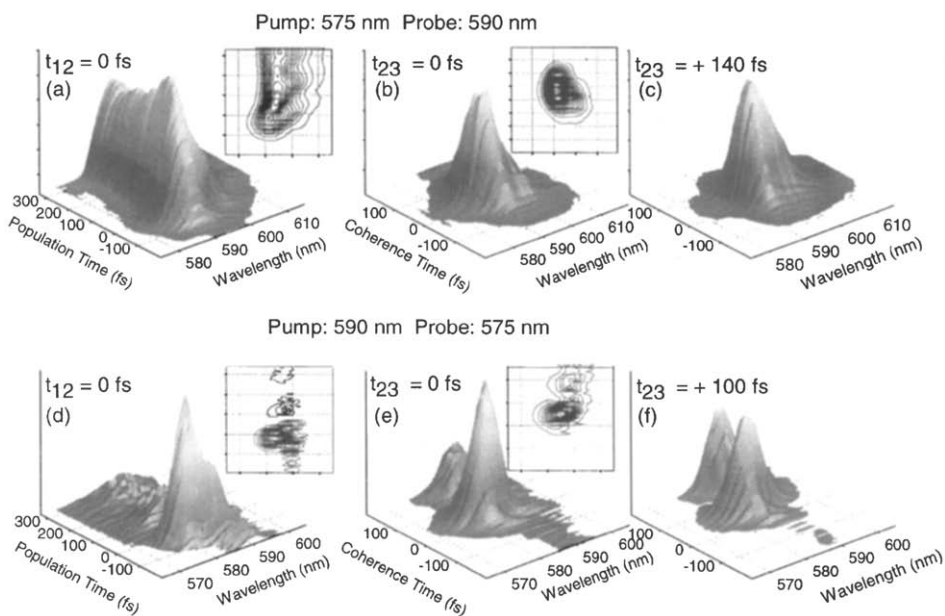


Fig. 3. Photon echo spectra vs. population time (a, d) and coherence time (b, c, e, f) at fixed values of other delay time for pump or probe pulse at the maximum (575 nm) and on the red side (590 nm) of the absorption maximum. The inset shows the contour plot of corresponding figure.

coherence time t_{12} or population times t_{23} at a fixed other delay time. The sample is the laser dye Rhodamine Rh101, 10^{-4} M in Methanol, in a flow cell to avoid thermal effects by strong excitation. The maximum of the linear absorption occurs at 575 nm.

For a difference of probe and pump wavelengths of ± 15 nm (i.e., larger than the pulse width of ~ 8 nm) four combinations have been studied for pump and probe wavelengths of 560, 575 and 590 nm. Figure 2 shows photon echo spectra for two combinations of pump and probe wavelength, 560 nm and 575 nm, versus the population time at fixed coherence time $t_{12} = 0$ fs (fig. 2a, 2d) and versus coherence time at fixed population times $t_{23} = 0$ fs (fig. 2b, 2e), $t_{23} = 140$ fs (fig. 2c) and $t_{23} = 100$ fs (fig. 2f).

Similar spectra are shown in fig. 3 for two other combinations of pump and probe wavelength, 575 and 590 nm. When the pump wavelength is longer than 575 nm the first interaction can involve transitions from high vibrational levels of the ground state.

The spectra measured at each of a range of different coherence times t_{12} and population times t_{23} can be different because the wavelengths of \mathbf{k}_2 and \mathbf{k}_3 are not the same. When the pump wavelength is shorter than the probe, we observe:

- (i) An increase of the signal on the red side of the echo spectrum at longer population times when scanning the coherence time t_{12} (fig. 2b, 2c and fig. 3b, 3c), and
- (ii) A delayed increase on the red side when scanning the population time t_{23} (fig. 2a and fig. 3a).

In this case the pulse sequence favours the generation of population and coherence ensembles in the *excited state* of the molecule according to the Feynman diagrams (a) and (b). The time evolution of the spectrum reflects the relaxation of those ensembles and can be used to determine the dynamics of molecules in the excited state. Some oscillations in the intensity of the echo spectrum versus population time are observed with several beat periods corresponding to the splitting of vibrational levels

By contrast, when the pump wavelength is longer than the probe, enhancement of the echo signal occurs on the blue side when scanning either the coherence time (fig. 2e, 2f and fig. 3e, 3f) or the population time (fig. 2d and fig. 3d). These results are interpreted as reflecting the dynamics of vibration in the electronic *ground state* (Feynman diagrams (c), (d)).

Scanning of the population time in these experiments yields detailed information about the vibrational relaxation and scanning of the coherence time allows a study of the splitting of the vibrational levels.

3. CONCLUSION

In summary, spectrally resolved 3-pulse 2-colour photon echoes provide a potential tool to study the molecular structure dynamics on a femtosecond time scale and will be used to study chemical and physical processes involving nonequilibrium relaxation in both ground and excited states of molecules.

REFERENCES

- [1] S. Mukamel, *Ann. Rev. Phys. Chem.* 51 (2000) 691, and references therein.
- [2] R. Agarwal, B.S. Prall, A.H. Rizvi, M. Yang, G.R. Fleming, *J. Chem. Phys.* 116 (2002) 6243, and references therein.
- [3] J.D. Hybl, A.W. Albrecht, S.M.G. Feader, D.M. Jonas, *Chem. Phys. Lett.* 297 (1998) 307.
- [4] L.D. Book, A.E. Ostafin, N. Ponomarenko, J.R. Norris, N.F. Scherer, *J. Phys. Chem.* 104 (2000) 8295.

Closed loop optimization of the ionization process in NaK. Learning from the optimal pulse shape.

**A. Lindinger, C. Lupulescu, M. Plewicki*, S. M. Weber, A. Merli, F. Vetter, and
L. Wöste**

Institut für Experimentalphysik, Freie Universität Berlin, Arnimallee 14, D-14195 Berlin,
Germany

*Email address: plewicki@physik.fu.berlin.de

ABSTRACT

The ionisation process of the NaK dimer is investigated by applying evolution strategies to optimize the spectral phase of fs pulses interacting with the molecules. The obtained optimal pulse structure with three intensity maxima is presented. As an explanation of the ionization process a simple model of wave packet propagation on given potential energy surfaces is proposed.

1. INTRODUCTION

Optimization experiments, combining pulse-shaping techniques with evolution strategy algorithms in a closed loop, are a well known scheme in the fs-spectroscopy toolbox. This routine allows solving of multidimensional problems in relatively short times. It has been successfully adapted to inspect processes like population transfer, fragmentation, ionization and high harmonic generation [1,2,3,4]. An iterative procedure guides the system as near as possible to the desired state by finding an optimal pulse form.

Generally our intention is to enhance the efficiency of a photochemical reaction and afterwards to translate the obtained optimal pulse texture into processes induced in the molecule. Therefore it is adequate to begin with well-known systems with simple potential energy surfaces, which will allow interpreting the results intuitively. NaK fulfills this condition as a model system very well. Additionally it can be ionized with three photons originating from fs oscillators.

2. EXPERIMENTAL SETUP

The laboratory layout consists of a molecular beam apparatus and a laser system. NaK clusters are created in an adiabatic coexpansion of mixed alkali vapour and argon carrier gas through a nozzle of 70 μm diameter into the vacuum. Directly after the nozzle the cluster beam passes a skimmer. Next, the laser beam coming from perpendicular direction irradiates the dimers and eventually excites and ionizes them. The emerging ions are extracted by ion optics, mass selected by QMS and recorded by a computer.

The laser pulses are generated by a Ti:sapphire oscillator (Tsunami; Spectra Physics) whereby the central wavelength was set to 775 nm with a bandwidth of about 8 nm (FWHM)

and an energy of 10 nJ. Since pulses from an oscillator are used, high repetition rate of the laser gives the opportunity of averaging over the noise of molecular beam and laser instabilities by integrating signal in time over many laser-molecule interactions. The resulting outcome offers low noise to signal ratio.

The pulse shaper is a device made of a pair of gratings and lenses, arranged in a zero dispersion compressor, and a liquid crystal modulator placed in the Fourier plane. Liquid crystal arrays allow one to influence independently spectral phase and amplitude with discretization of 128 pixels each.

The closed loop experiment contains a self-learning algorithm combined with pulse shaper and ion detection hardware. The intensity of photoions is taken as a feedback for the algorithm that creates laser field patterns in an iterative way. When the ion intensity(s) approaches desired limits, the optimization is ended. In case of ionization, this means that the intensity of ions can no longer be enlarged, hence the best possible solution is found. More detailed description of the algorithm could be found in [5]. The generated optimal pulse form is measured by intensity cross-correlation and XFROG technique.

3. RESULTS

In the performed experiment an almost monotonic rise of the ion yield during the optimization process was observed (Fig 1). After approximately 120 iterations (generations) the signal could not be increased which means, that the optimal pulse was found. In the presented run only the phase has been modified in order to keep the pulse energy constant. According to our experience, when a single ion signal is optimized, the rise of the ion yield is smoother with phase only optimization, due to modest intensity changes in the laser pulse and also smaller searching space for the algorithm.

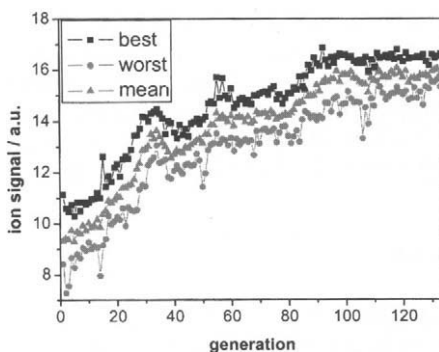


Fig.1. Progression of the NaK⁺ signal during optimization. In an early stage of the optimization, spectral phases are randomly chosen which results in small ion signal. After nearly 120 generation the algorithm converges.

The mass spectrum was recorded for molecules interacting with unshaped and optimized pulses. The comparison (Fig.2.) shows improvement of the NaK⁺ intensity by a factor of $I_{optimal}/I_{unshaped}=1.6$. Another important feature of the molecular beam, visible in Fig.2. is the lack of any larger molecules, which means that NaK ions originate only from NaK dimers and not from fragmented trimers, tetramers, etc.

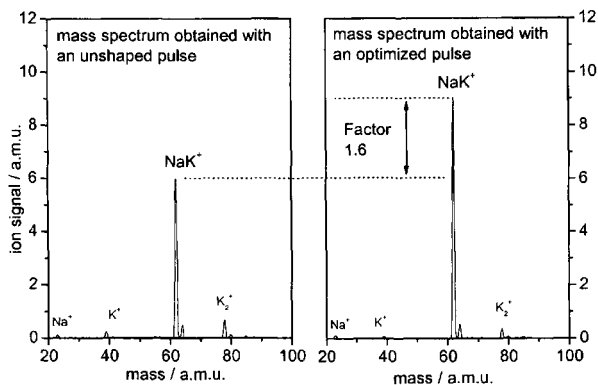


Fig.2. Mass spectra measured with an unshaped pulse (left) and with an optimized one (right).

The intensity cross-correlation and XFROG trace of the optimal pulse contains three sub-pulses (Fig.3). The time separation between the sub-pulses almost matches 1.5 times the oscillation period of the first excited state ($T_{osc} = 440\text{fs}$) [6].

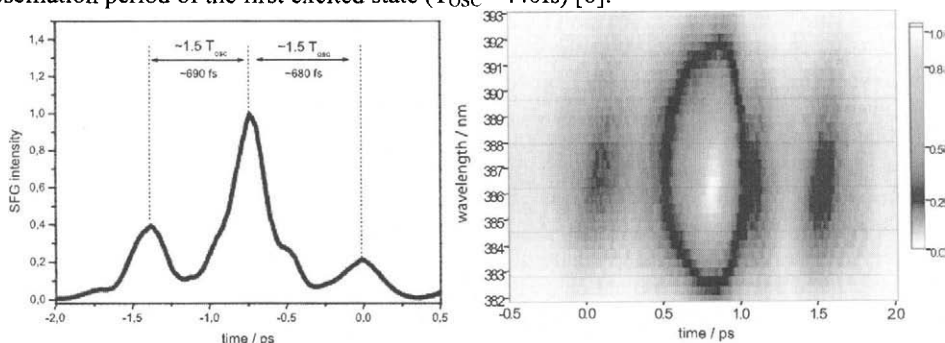


Fig.3. Intensity cross-correlation and XFROG trace of the optimal pulse.

The relative intensities of sub pulses and their position in time suggest a simple scheme of ionization (Fig.4). The first peak transfers some population from the ground state to the first excited $A(2)^1\Sigma^+$ state. Due to the Franck-Condon principle and resonance conditions, the wavepacket is created at the inner turning point. After 1.5 oscillation periods in the $A(2)^1\Sigma^+$ state, it is located at the outer turning point wherefrom it can be effectively transferred to the ionic state. The second sub-pulse ionizes the molecule in a two photon process and additionally generates a secondary wavepacket on the first excited state. Again, after the second wavepacket is located at the outer turning point, it is being transformed into the ionic state by the third sub-pulse.

There are some questions to be answered. Is the role of the third sub-pulse properly interpreted? What is the relevance of position and intensity? As well one could ask what is the purpose of the distortion on the trailing edge of the second sub-pulse in optimal pulse structure.

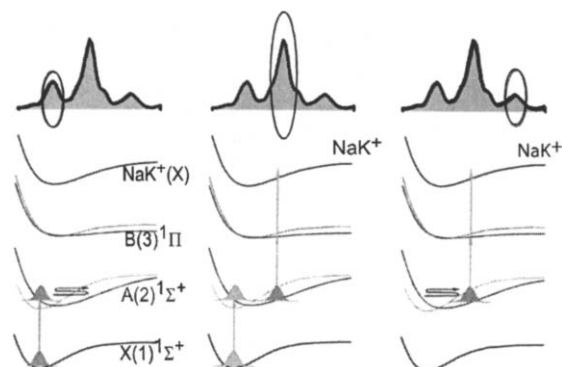


Fig.4. Optimal photo-induced transition from the neutral ground state of NaK to the ionic ground state.

These questions may be answered by applying a few parameter algorithm. By introducing a few parameter optimization the search space can be narrowed, for example to permit only simple pulse trains. Suggested parameters in the time- and frequency domain are: time distances between pulses, intensities, spectral FWHM, zero order spectral phase and chirp up to 3rd order. The number of sub-pulses, maximal and minimal pulse distances can be set. One could also gain additional information by comparing results obtained from free optimization to those that emerged from few parameter optimization. The relevance of certain structural features of optimal pulses can be investigated in this manner.

4. SUMMARY

A closed loop optimization experiment was presented in order to investigate the ability to control the ionization of NaK clusters in a molecular beam. The analysis of the optimized pulse shows that the maximum intensity of the ion signal was obtained with a pulse structure containing intensity maxima separated by a multiple of half vibrational periods. The proposed simple model in order to explain the pulse structure is based on previously performed pump-probe experiments [6].

ACKNOWLEDGMENTS

The authors would like to thank V. Bonačić-Koutecký and B. Schäfer-Bung for stimulating discussions. The presented work is supported by the Deutsche Forschungsgemeinschaft (SFB 450).

REFERENCES

- [1] C.J. Bardeen, V.V. Yakovlev, K.R. Wilson, S.D. Carpenter, P.M. Weber, and W.S. Warren *Chem. Phys. Lett.* 280 (1997) 151.
- [2] A. Assion, T. Baumert, M. Bergt, T. Brixner, B. Kiefer, V. Seyfried, M. Strehle, and G. Gerber. *Science*, 282 (1998) 919.
- [3] T. Hornung, R. Meier, and M. Motzkus. *Chem. Phys. Lett.* 326 (2000) 445.
- [4] S. Vajda A. Bartelt, C. Kaposta, T. Leisner, C. Lupulescu, S. Minemoto, P. Rosendo-Francisco and L. Wöste, *Chem. Phys.* 267 (2001) 231.
- [5] A. Bartelt, dissertation thesis (2002).
- [6] A. Bartelt, S. Minemoto C. Lupulescu, S. Vajda, and L. Wöste, *Eur. Phys. J. D* 16 (2001) 127.

Femtosecond dynamics of NaI and CsI aggregated with CH₃CN

E. Charron, D. T. Stibbe and A. Suzor-Weiner

Laboratoire de Photophysique Moléculaire du CNRS, Université Paris XI, 91405 Orsay cedex, France.

1. INTRODUCTION

Major advances in laser technology over the last fifteen years have resulted in lasers which can operate on the femtosecond scale. By bringing the pulse time down to significantly less than the time taken for many chemical reactions, these ultrafast lasers have allowed an unprecedented ability to probe inside a chemical reaction as it is taking place. These new techniques have resulted in a greatly increased understanding of the dynamics and mechanisms of elementary chemical reactions. One such technique, that of pump-probe experiments [1], first put into practice by Zewail and colleagues, has allowed the observation of the formation and evolution of several transition states [2]. This ability has naturally led to the quest to control the reaction with laser pulses [3]. To this end, different control schemes have been proposed. The coherent control scheme of Brumer and Shapiro [4] takes advantage of different pathways to the same end products. By varying the probability amplitudes and phases of each pathway through modulating the laser parameters, it is possible to influence the outcome of a reaction using constructive or destructive interferences. Another method, the variation of the delay between pump and probe laser pulses was first proposed by Tannor *et al* [5]. Further exploits have attempted to produce perfectly crafted laser pulses which allow the greatest possibility of control, the so-called optimal control theory [6]. This last scheme has been implemented recently [7] following an original idea of Judson and Rabitz [8].

Following another experimental approach, Grégoire *et al* [9] have tried to understand the influence of an increasing number of solvent molecules on the femtosecond dynamics of diatomic molecules, including the dimers NaI and CsI. Due to its relative simplicity, the isolated NaI molecule has been studied extensively with pump-probe techniques both experimentally [10], and theoretically [11,12]. In this report, we investigate theoretically the femtosecond pump-probe ionization of NaI and CsI when aggregated with a molecule of acetonitrile CH₃CN.

2. FEMTOSECOND VIBRATIONAL DYNAMICS

The pump-probe scheme that we use is as follows : the molecule is initially excited by a pump laser photon ($\hbar\omega_1$) to the first excited neutral state. The dynamics is then followed with a probe laser by one-photon ionization ($\hbar\omega_2$). Compared to a free diatomic, solvation by CH₃CN brings two new factors come into play. Firstly, the potential energy curves of the diatomic are modified by the presence of the neighboring molecule. Secondly, the fragmentation dynamics of the diatomic is changed as there may be collisions with, and a transfer of energy to, the acetonitrile.

In order to treat this complex system, we have reduced the number of dimensions involved in the calculation to the minimum necessary for a reasonable description of the

pump-probe dynamics. In the experiments performed by Grégoire *et al* [9], no breakup of the acetonitrile molecule was observed, and we thus assume a rigid acetonitrile. In addition, recent calculations [13] have revealed the linear structure of the electronic ground state of the complex, and we assume that this structure is conserved during the pump-probe process. Within these approximations, two independent dimensions remain, the distance R between the center of mass of the acetonitrile molecule and the alkaline atom, and the distance r between the center of mass of $\text{CH}_3\text{CN-X}$, where $X = \text{Cs}$ or Na , and the iodine atom. The two-dimensional potential surfaces of the ground and first excited states of the complex, later denoted as $V_g(r, R)$ and $V_e(r, R)$, as well as the ground state surface of the ion, $V_+(r, R)$, have been calculated as sums of two-body interactions, using various ab-initio techniques [14].

3. THEORETICAL TREATMENT

The treatment presented here extends a previous calculation by Charron and Suzor-Weiner [12], and the reader is referred to [12] and [14] for full details. Here we only present a brief summary. The vibrational dynamics of the molecule is followed by solving the time-dependent Schrödinger equation for the nuclear wavefunctions associated with the ground and first excited electronic states. To calculate the total ionization probability, we use a simple extension of the first-order perturbative approximation developed by Braun *et al* [15] which neglects the kinetic energy in the evolution operator during the probe pulse. In the case of a Gaussian probe pulse, this yields the following integral expression for the total ionization probability as a function of the pump-probe delay τ :

$$S(\tau) \propto \iint \tilde{w}(r, R) |\Psi_e(r, R, \tau)|^2 dr dR, \quad (1)$$

where

$$\tilde{w}(r, R) = \text{Erf} \left(\frac{(V_+(r, R) - V_e(r, R) - \hbar\omega_2) \Delta t_2}{2\hbar\sqrt{2 \ln(2)}} \right) - 1. \quad (2)$$

In this expression, Erf denotes the error function, while Δt_2 is the full width at half maximum (FWHM) of the Gaussian probe pulse. The calculation of the total ionization probability $S(\tau)$ therefore only requires the knowledge of the excited state wavepacket $\Psi_e(r, R, \tau)$ at time $t = \tau$. Note that the origin of time ($t = 0$) is chosen here as the peak intensity of the pump pulse, and consequently the quantity τ in Eq. (1) corresponds to the pump-probe delay.

4. RESULTS

In the case of NaI, the ground state potential surface of $\text{CH}_3\text{CN}\cdots\text{NaI}$ has a minimum around ($r_e = 9.49$ au, $R_e = 6.91$ au), about which the initial wavefunction is centered. The excited state surface, however, is dissociative in the $(\text{CH}_3\text{CNNa})\cdots\text{I}$ direction and weakly bound in the $\text{CH}_3\text{CN}\cdots\text{Na}$ direction. Similarly, the ground state potential surface of $\text{CH}_3\text{CN}\cdots\text{CsI}$ has a minimum around ($r_e = 8.49$ au, $R_e = 8.47$ au), while the excited state surface is dissociative in the $(\text{CH}_3\text{CNCs})\cdots\text{I}$ direction and weakly bound in the $\text{CH}_3\text{CN}\cdots\text{Cs}$ direction. An excited state wavepacket $\Psi_e(r, R, t)$ is created in both cases with a pump pulse of duration 50 fs (FWHM) and wavelength 242 nm. Figure (1) shows its trajectory (for NaI on the left and for CsI on the right), defined by the averaged positions $\langle r \rangle$ and $\langle R \rangle$.

In the case of NaI, this trajectory shows the sodium and iodine atoms being forced apart on the excited potential : the iodine atom moves off quickly from the other particles, while the sodium moves initially towards the acetonitrile molecule, colliding with it at time $t \approx 10$ fs. The sodium then bounces off the acetonitrile, and a three-body fragmentation takes place. Note that since the mass of Na (23) is much less than that of I (127), the Na atom gains most of the fragmentation energy when the Na...I bond is broken. This kinetic energy is larger than the binding energy of the $\text{CH}_3\text{CN}\cdots\text{Na}$ complex, thus leading to dissociation. With CsI, a dramatic change is observed : with its much greater mass (133), the Cs atom takes only about half the available energy. This energy is low enough to allow for the formation of a loose bond with the acetonitrile, while the I continues to dissociate away, leaving a vibrationally excited new molecule : $\text{CH}_3\text{CN}\cdots\text{Cs}$ (see panel (b) of Figure (1)).

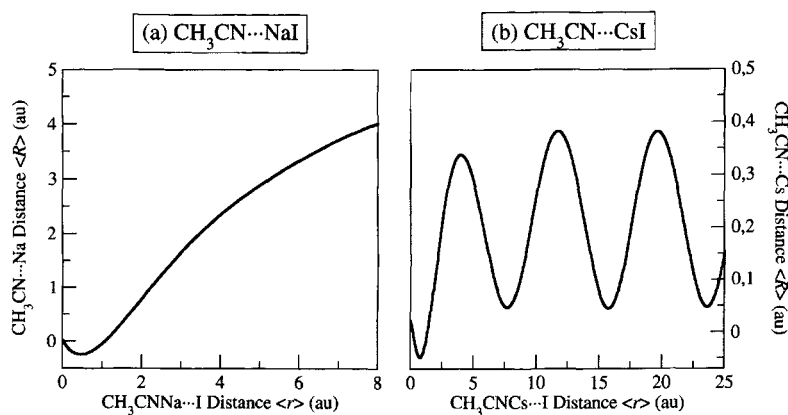


Fig. 1. Average trajectory ($\langle r \rangle, \langle R \rangle$) of the excited state wavepacket $\Psi_e(r, R, t)$ with time. $\text{CH}_3\text{CN}\cdots\text{NaI}$ is shown on the left panel (a) and $\text{CH}_3\text{CN}\cdots\text{CsI}$ on the right panel (b). Note that the origin of the graph, $r = 0$ and $R = 0$, is chosen as the point of minimum energy of the ground state.

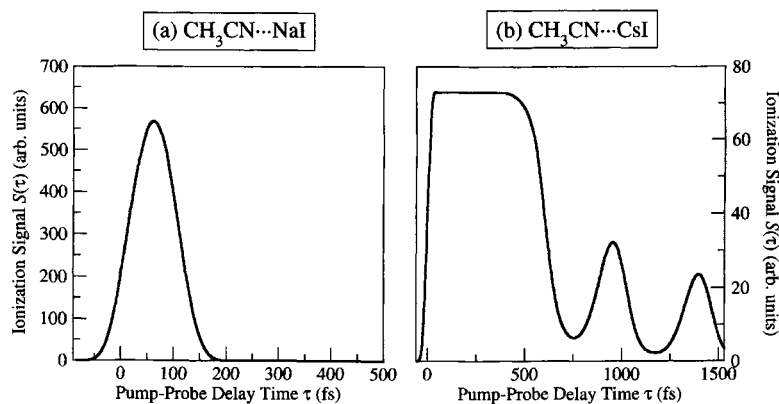


Fig. 2. Ionization signals $S(\tau)$ as functions of the pump-probe delay τ . $\text{CH}_3\text{CN}\cdots\text{NaI}$ is shown on the left panel (a) and $\text{CH}_3\text{CN}\cdots\text{CsI}$ on the right panel (b). The probe duration and wavelength are 50 fs (FWHM) and 315 nm for NaI and 378 nm for CsI.

The ionization signal $S(\tau)$ (see Eqs. (1) and (2)) is strongly dependent on the potential difference ($V_+ - V_e$) between the excited and ion surfaces at the average position of the excited state wavepacket. Therefore, the dramatic change observed between the trajectories of $\text{CH}_3\text{CN}\cdots\text{NaI}$ and of $\text{CH}_3\text{CN}\cdots\text{CsI}$ (see Figure (1)) can also be seen in the ionization signal $S(\tau)$ shown Figure (2). The ion signal only shows a single maximum for $\text{CH}_3\text{CN}\cdots\text{NaI}$ while a series of peaks is observed for $\text{CH}_3\text{CN}\cdots\text{CsI}$. This is in good qualitative agreement with the signals observed by Grégoire *et al* in their experiment [9]. The ionization signal therefore gives a clear signature of the three body breakup of the $\text{CH}_3\text{CN}\cdots\text{NaI}$ complex and of the formation of the vibrationally excited $\text{CH}_3\text{CN}\cdots\text{Cs}$ complex.

5. CONCLUSION

We have completed a simulation of the pump/probe excitation and ionization of CsI and NaI each aggregated with a single molecule of acetonitrile. The ionization signal for $\text{CH}_3\text{CN}\cdots\text{NaI}$ shows a maximum followed by a drop to zero as the excited system proceeds with a three-body fragmentation. In the case of $\text{CH}_3\text{CN}\cdots\text{CsI}$, however, an oscillating ionization signal is obtained which maps the vibrations of a weak bond formed between CH_3CN and Cs , after dissociation of the I atom. It is interesting to note that the addition of a single molecule of acetonitrile can suppress the oscillations seen in the isolated NaI molecule [12] while inducing an oscillating ionization signal in the case of Cs , an effect which was not achievable with the gas phase CsI molecule [9]. Our results corroborate the experimental findings of Grégoire *et al* [9], and can be explained by the mass difference between Na and Cs . We now plan to explore the possibilities of control of these reactions.

REFERENCES

- [1] W. R. Lambert, P. M. Felker and A. H. Zewail, *J. Chem. Phys.* 75 (1981) 5958.
- [2] J. Manz and L. Wöste, *Femtosecond Chemistry*, VCH 1996. A. Zewail, *Femtochemistry*, World Scientific, Singapore, 1994. M. Chergui, *Femtochemistry*, World Scientific, Singapore, 1995.
- [3] R. Gordon and S. Rice, *Annu. Rev. Phys. Chem.* 48 (1997) 601. S. Rice, *Nature* 403 (2000) 496. E. Charron and B. Sheehy, *Molecules and clusters in intense laser fields*, Cambridge University Press (2000).
- [4] M. Shapiro, J. W. Hepburn and P. Brumer, *Chem. Phys. Lett.* 149 (1988) 451.
- [5] D. J. Tannor, R. Kosloff and S. A. Rice, *J. Chem. Phys.* 85 (1986) 5805.
- [6] S. Shi, A. Woody and H. Rabitz, *J. Chem. Phys.* 88 (1988) 6870.
- [7] A. Assion *et al*, *Science* 282 (1998) 919.
- [8] R. S. Judson and H. Rabitz, *Phys. Rev. Lett.* 68 (1992) 1500.
- [9] G. Gregoire, M. Mons, I. Dimicoli, C. Dedonder-Lardeux, C. Juvet, S. Martrenchard and D. Solgadi, *Eur. Phys. J. D* 11 (2000) 227. G. Gregoire, PhD. Thesis, Université Paris XI, (1999).
- [10] T. Rose, M. Rosker and A. Zewail, *J. Chem. Phys.* 88 (1988) 6672. M. Rosker, T. Rose and A. Zewail, *Chem. Phys. Lett.* 146 (1988) 175. A. Mohkatari, P. Cong, J. Herek and A. Zewail, *Nature* 348 (1990) 225. P. Cong, A. Mokhtari and A. Zewail, *Chem. Phys. Lett.* 172 (1990) 109. P. Cong, G. Roberts, J. Herek, A. Mohkatari and A. Zewail, *J. Chem. Phys.* 100 (1996) 7832. A. Assion, M. Geisler, J. Helbing, V. Seyfried and T. Baumert, *Phys. Rev. A* 54 (1996) R4605. C. Juvet *et al*, *J. Phys. Chem. A* 101 (1997) 2555 (1997).
- [11] V. Engel, H. Metiu, R. Almeida, R. Marcus and A. Zewail *Chem. Phys. Lett.* 152 (1988) 1. V. Engel and H. Metiu, *Chem. Phys. Lett.* 155 (1989) 77. H. Metiu and V. Engel, *J. Chem. Phys.* 93 (1990) 5693.
- [12] E. Charron and A. Suzor-Weiner, *J. Chem. Phys.* 108 (1998) 3922.
- [13] G. Grégoire, V. Brenner and P. Millié, *J. Phys. Chem. A* 104 (2000) 5204.
- [14] D. Stibbe, E. Charron and A. Suzor-Weiner, *J. Chem. Phys.* 116 (2002) 10753.
- [15] M. Braun, C. Meier and V. Engel, *J. Chem. Phys.* 103 (1995) 7907.

Control of the production of highly charged ions in femtosecond laser cluster fragmentation

S. Zamith, Y. Ni, S.A. Aseyev, E. Springate, M.J.J. Vrakking

FOM Institute for Atomic and Molecular Physics (AMOLF)
Kruislaan 407, 1098 SJ Amsterdam, The Netherlands

1. INTRODUCTION

The interaction of high intensity laser with clusters has been the subject of many theoretical and experimental studies. Remarkable phenomena in this interaction are the very efficient coupling of the laser energy in the cluster [1], the emission of electrons [2] and ions with high kinetic energies [3], X-ray emission [4] and nuclear fusion in deuterium clusters [5]. In this contribution we discuss the implication of recent experiments in our laboratory for the nanoplasma model [6]. In this model, ionisation starts at the beginning of the laser pulse and forms an overdense plasma. Due to the hydrodynamic pressure (or Coulomb explosion in case of small clusters) the plasma expands and the electron density n_e drops, until it reaches 3 times the critical density n_{crit} , when the field *inside* the cluster reaches a maximum. In other words: the plasma frequency decreases until it becomes resonant with the laser frequency. Heating of the plasma then leads to the formation of very energetic electrons and ions.

One of the main validations of the nanoplasma model was a measurement of electron kinetic energy distributions by Shao *et al* [7]. They observed a bimodal distribution, with 'warm' electrons emitted along the polarisation axis, and 'hot' electrons with an isotropic distribution. The nanoplasma model predicted a bimodal distribution, with 'hot' electrons being produced at the resonance, and 'warm' ones created at the beginning of the interaction.

More support for the nanoplasma model has been provided by measurements of ion kinetic energies up to 1 MeV [2], as a function of cluster size [8], cluster ion species, laser pulse length and intensity. This supports the idea that the interaction is dominated by the resonant heating point. To maximise the heating, the point where the electron density equals $3n_{\text{crit}}$ should fall close to the peak of the laser pulse. For example, large clusters expand more slowly so there is an optimum cluster size for a given pulse length. However, the earlier interpretation of the electron energy spectrum [7] was recently challenged by Kumarappan *et al* [9] who found a correlation between the strength of the warm electron peak and the ion energies as a function of pulse-length, suggesting a common mechanism for the generation of both. These authors observed a warm electron peak extending to 5 keV and an additional signal implying either a significant photon component in the signal or electrons with energies greater than 5 keV.

2. RESULTS AND DISCUSSION

In our laboratory we have recently performed two experiments, looking at the production of energetic electrons and highly charged ions as a function of the laser and cluster parameters. In the first series of experiments we studied the production of high kinetic energy electrons as

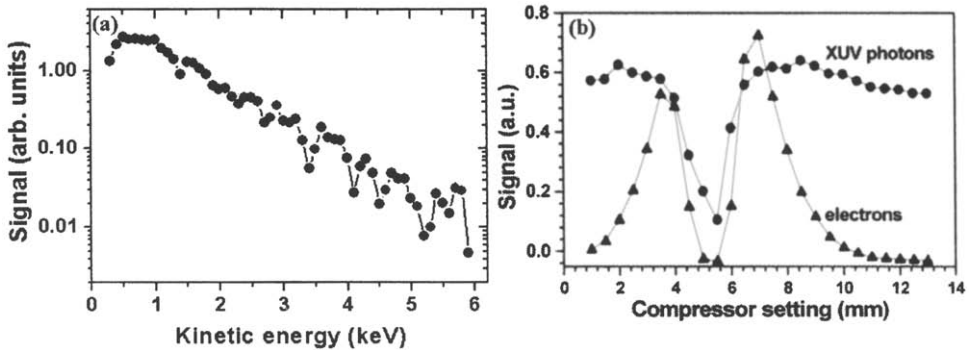


Fig. 1. (a) Measured electron kinetic energy distribution for the interaction of an intense femtosecond laser ($\sim 10^{16}$ W/cm², 100 fs) with large Xe clusters ($\langle N \rangle \cong 10^6$ atoms/cluster) [10]. (b) Integrated signal in the XUV photon peak and the hot part of the electron peak (recorded using a stopping voltage of 2 kV), as a function of the displacement of one of the two gratings in the compressor of the laser system with respect to the position where the shortest pulses are generated. The largest hot electron yield is observed for a grating displacement of about 2 mm, corresponding to a pulse duration of 500 fs.

a function of the laser pulse duration, while in the second series of experiments we used an optimal control technique to maximize the formation of highly charged ions.

In the first experiment we used a reflectron type spectrometer to measure the kinetic energy distribution of electrons emitted by the interaction of an intense femtosecond laser with large Xe clusters [10].

Fig. 1a displays the kinetic energy distribution obtained from the irradiation of Xe clusters consisting of $\sim 10^6$ atoms/cluster by a 100 fs, 10^{16} Wcm⁻², 800 nm laser pulse. In this measurement, which was taken along the polarization direction of the laser, the electrons are emitted with a monotonically decreasing kinetic energy distribution, with energies up to 6 keV. Despite extensive systematic variations in all experimental parameters (laser energy and pulse duration, cluster size and species), we could never observe the bi-modal kinetic energy distribution of Shao *et al* [7] in our experiment. We did see a double-peaked structure in our time-of-flight measurements, but the arrival time of the first peak would correlate either with photons or with electrons with >100 keV kinetic energy, and therefore we attributed this peak to the former [10]. We found that the electrons were emitted along the polarisation axis, whereas the photons were emitted isotropically. Confronting these observations with the prediction from the nanoplasma model, we believe that possible resonance effects in the model may well be averaged out in the experiment, since – after all – the experiment involves the use of clusters with a wide size distribution and furthermore an integration over the focal volume of the laser. Though we did not see evidence for the plasma resonance in the electron kinetic energy distributions, these first experiments did provide clues that the resonance occurs. As Fig. 1b shows, measurements of the electron and photon signals as a function of the pulse duration clearly show that the maximum electron and photon signals are obtained for pulses of about 500 fs (and *not* for the shortest possible pulse durations). In terms of the nanoplasma model, the plasma frequency decreases as the cluster expands, and at some point will be equal to the laser frequency. Having a long pulse allows the plasma to expand so that the resonance is reached at the maximum amplitude of the laser pulse.

In the second experiment, we carried out an optimal control experiment on the production of highly charged ions [11]. The optimal control technique [12] consists of varying a large number of parameters that characterize the laser pulse shape in an automated way in order to

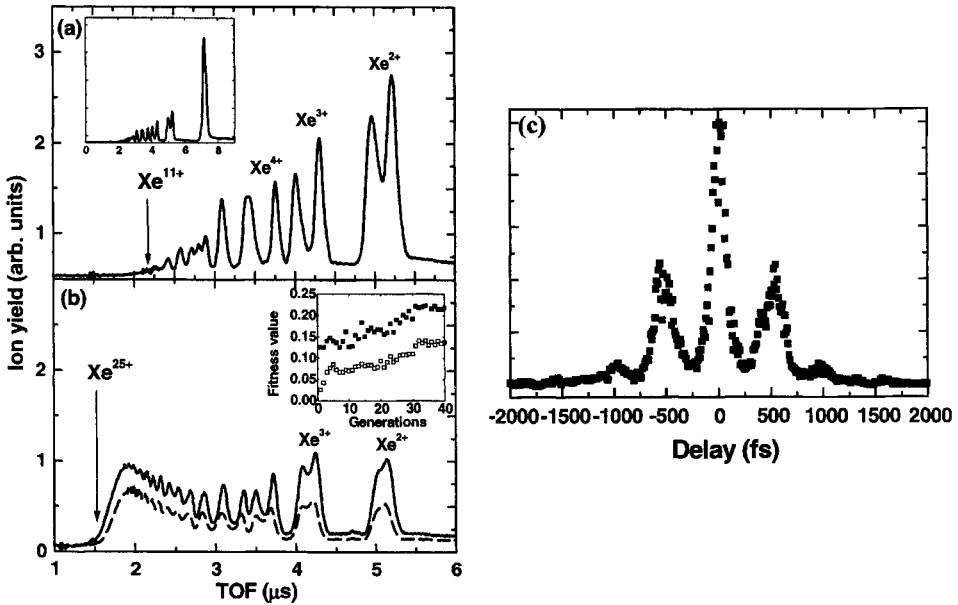


Fig. 2. Time-of-flight (TOF) traces for the interaction of Xenon clusters ($\langle N \rangle \approx 1.6 \cdot 10^4$) with (a) a Fourier Transform-limited 100 fs, 800 nm, 10^{15} W cm^{-2} laser pulse; and (b) the optimum result obtained by means of an 80-parameter unrestricted optimisation (dashed line) and a restricted 3-parameter optimisation (full line). The inset in (b) shows the evolution of the fitness value for the 80 parameter optimisation (full squares: maximum fitness, open squares: average fitness). (c) Autocorrelation trace of the optimal pulse corresponding to the 80 parameters optimisation. The pulse shapes consists of two pulses of 120 fs of equal amplitude separated by ~ 500 fs.

optimise an experimental quantity. In our case we varied the phases applied across the laser spectrum using a pulse-shaper set-up. By varying the phases different pulses shapes were generated that were experimentally tested for their ability to produce highly charged ions. The optimisation was performed with the help of a simple genetic algorithm [13].

Fig. 2a displays the ion time-of-flight (TOF) distribution obtained when $\langle N \rangle \approx 1.6 \cdot 10^4$ Xe clusters interacted with a Fourier Transform-limited 100 fs 800 nm, 10^{15} W cm^{-2} laser pulse. The TOF displays a number of peaks corresponding to ions up to Xe^{11+} . The peaks in the TOF are quite broad, and even display a double peak structure due to the fact that ions are emitted in forward-backward directions with respect to the detector. Both the charge state reached and the kinetic energy of the ions are signatures of collective effects in the cluster ionisation. For example, when only atoms were present in the atomic beam, the maximum charged state reached was 4+.

The results of two different optimisations of the production of charged states $>11+$ are presented in Fig. 2b. The dashed curve is the TOF distribution obtained when optimising 80 independent phases across the spectrum. By contrast with the Fourier Transform-limited pulse, ions up to 25+ are present in the TOF distribution! The corresponding pulse shape (as determined from the autocorrelation in Fig. 2c) is a sequence of two pulses of equal amplitude and separated by 500 fs. To test the importance of the time delay between the two pulses, we performed restricted optimisations where a periodic phase was applied across the spectrum along with a quadratic term. In this case the period and amplitude of the oscillatory part

controlled the delay and the peak heights of the individual pulses, while the amplitude of the quadratic term controlled their duration. The optimisation led to the full line TOF distribution in Fig. 2b. A slightly better optimisation was achieved than in the unrestricted case. This is due to the more rapid convergence of the genetic algorithm in a 3-parameter search space. The optimal pulse shape consisted of two pulses of equal amplitudes, again separated by 500 fs, and with an individual pulse duration of 180 fs.

The pulse shapes from the optimal control experiment provide strong support to the nanoplasma model. The optimal result can easily be interpreted in terms of a first pulse that creates an overdense plasma which subsequently undergoes expansion and a second pulse, which interacts with the plasma when the plasma frequency equals the laser frequency.

3. CONCLUSION

In conclusion we have shown how optimal control experiments on the formation of highly charged ions in femtosecond laser-cluster interactions provide strong evidence for the validity of the nanoplasma model. By contrast, our results on the formation of high kinetic energy electrons in these interactions disagree with the experiments of Shao et.al[7], which thus far had arguable been the most convincing evidence for the nanoplasma model.

This work is part of the research program of the "Stichting voor Fundamenteel Onderzoek der Materie (FOM)", which is financially supported by the "Nederlandse organisatie voor Wetenschappelijk Onderzoek (NWO)". We acknowledge the technical assistance from A. Buijserd and N. Dijkhuizen. S. Zamith and E. Springate acknowledge the European Community for receiving a Marie-Curie Individual Fellowship Grant.

REFERENCES

- [1] T. Ditmire, R. A. Smith, J. W.G. Tisch, and M. H.R. Hutchinson, *Phys. Rev. Lett.* **78** (1997) 3121
- [2] T. Ditmire, J.W.G. Tisch, E. Springate, M.B. Mason, N. Hay, R.A. Smith, J.P. Marangos and M.H.R. Hutchinson, *Nature*, **386** (1997) 54
- [3] T. Ditmire, E. Springate, J. W. G. Tisch, Y. L. Shao, M. B. Mason, N. Hay, J.P. Marangos, and M.H.R. Hutchinson, *Phys. Rev. A*, **57** (1998) 369
- [4] A. McPherson, B.D. Thompson, B.-D, A.B. Borisov, K. Boyer and C.K. Rhodes, *Nature* **370** (1994) 631
- [5] T. Ditmire, J. Zweiback, V. P. Yanovsky, T. E. Cowan, G. Hays, and K. B. Wharton, *Nature* (London) **398** (1999) 489
- [6] T. Ditmire, T. Donnelly, A.M. Rubenchik, R.W. Falcone, and M.D. Perry, *Phys. Rev. A* **53** (1996) 3379
- [7] Y.L. Shao, T. Ditmire, J.W.G. Tisch, E. Springate, J.P. Marangos and M.H.R. Hutchinson, *Phys. Rev. Lett.*, **77** (1996) 3343
- [8] E. Springate, N. Hay, J. W. G. Tisch, M. B. Mason, T. Ditmire, M. H. R. Hutchinson, and J. P. Marangos, *Phys. Rev. A* **61** (2000) 063201
- [9] V. Kumarappan, M. Krishnamurthy and D. Mather, *Phys. Rev. A* **66** (2002) 033203
- [10] E. Springate, S.A. Aseyev, S. Zamith, and M. J.J. Vrakking, *Phys. Rev. A*, in press
- [11] S. Zamith, Y. Ni, S.A. Aseyev and M. J.J. Vrakking, submitted.
- [12] R. S. Judson and H. Rabitz, *Phys. Rev. Lett.* **68** (1992) 1500
- [13] D.E. Goldberg, *Genetic Algorithms in Search, Optimization and Machine Learning* (Addison-Wesley Longman, Inc., 20th printing, 1999)

Free phase optimization of $\text{CpMn}(\text{CO})_2^+$ as a fragment of $\text{CpMn}(\text{CO})_3$ by means of shaped femtosecond laser pulses

C. Lupulescu, A. Lindinger, A. Merli, M. Plewicky, and L. Wöste

Institut für Experimentalphysik, Freie Universität Berlin, Arnimallee 14, D-14195 Berlin, Germany

1. ABSTRACT

This contribution deals with optimal control experiments of fragmentation/ionization ratio in the photo-excited $\text{CpMn}(\text{CO})_2$, as a fragment arising from cyclopentadienyl manganese tricarbonyl ($\text{CpMn}(\text{CO})_3$) by using shaped femtosecond laser pulses. The resulting optimized pulse form reflects the capability of the optimization method to find tailored pulses, rather than an unshaped pulse. The optimal laser field should correlate with the ultrafast molecular dynamics during the photo-fragmentation process.

2. INTRODUCTION

The dissociative tendencies of organometallic compounds with transition metals and CO ligands make these species apt model systems for influencing the dynamics of photo-dissociation processes. Based on a suggestion of Rabitz et al. [1], we have carried out active control experiments on the photo-excited $\text{CpMn}(\text{CO})_3$ [2] by using the computer controlled feedback optimization loop. By employing an evolutionary algorithm for optimizing the phase and/or the amplitude of the applied laser field, the yield of the resulting parent and/or fragment ions can be influenced. This was first demonstrated by Gerber et al. [3]. Moreover, interesting features about the investigated system and the irradiated photo-chemical process can be extracted from the obtained pulse shapes. In many cases free optimizations lead to optimal pulse shapes, which are very complicated and difficult to interpret. It was shown that by joining experimental and theoretical efforts one could decode an optimal pulse generated from adaptive feedback experiments in the case of $\text{CpMn}(\text{CO})_3$ [4]. Here the optimal pulse was designed to maximize the ion yield of $\text{CpMn}(\text{CO})_3$ and to avoid other competing fragmentation channels (e.g. into $\text{CpMn}(\text{CO})_2^+$, $\text{CpMn}(\text{CO})^+$, or CpMn^+). The optimized laser field consisted of two dominant subpulses with optimal frequencies and time separations, which excited and ionized the target ion $\text{CpMn}(\text{CO})_3^+$, respectively [4]. The ratio first fragment/parent ion produced by an unshaped pulse was $\text{CpMn}(\text{CO})_2^+ : \text{CpMn}(\text{CO})_3^+ = 1.52 : 100$. After the optimization, the ion yield of $\text{CpMn}(\text{CO})_3^+$ increased by a factor of 1.6 (see Fig. 9a in [4]), whereas the relative ratio $\text{CpMn}(\text{CO})_2^+ : \text{CpMn}(\text{CO})_3^+$ was modified to 0.73:100, i.e. by a factor of 0.48 with respect to the ratio produced by a short pulse. The optimization of the $\text{CpMn}(\text{CO})_2^+$ ion yield should give additional information into the dynamics involved during the control process. One would expect an optimal laser field consisting of two main subpulses [5]. These subpulses would sequentially excite the mother molecule and ionize the fragment species: an almost unchirped pulse (or with a small chirp) for the excitation of the parent molecule and a strong downchirped pulse which would ionize

the fragments after an optimal time delay (see Fig. 3a in [4]). The optimal laser pulse expected in the experiment should offer additional information about the optimized process.

2. EXPERIMENTAL APPARATUS

The experimental setup is divided in two parts: a supersonic molecular beam and a femtosecond laser system (Fig. 1).

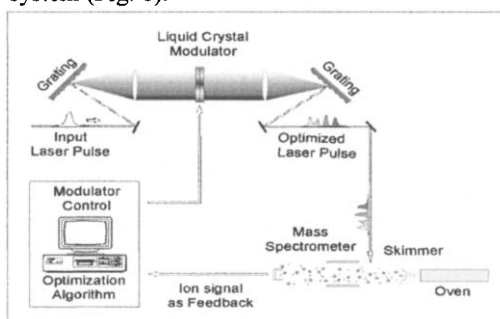


Fig.1. The experimental setup containing the pulse shaper, the molecular beam and the computer controlled feedback loop.

The supersonic jet of cold molecules was generated by co-expanding the $\text{CpMn}(\text{CO})_3$ sample vapor with argon carrier gas through a $90\ \mu\text{m}$ nozzle into the vacuum. After passing through a skimmer, the jet was irradiated by the laser pulses between the electrical lenses of a quadrupole mass analyzer. Details about our experimental setup can be found in [2]. The laser system consists of a home-built tunable Ti:sapphire oscillator (Kapteyn-Murnane), which seeds a commercial multipass amplifier (Quantronix, Odin) with an output of 1 mJ at 805 nm and 1 kHz repetition rate. The amplified pulses have a duration of 180 fs, i.e. 2.8 times longer than a transform-limited pulse assuming a gaussian shape. The pulse shaper system allows a simultaneous and independent modulation of the phase and/or the amplitude of the laser pulses by applying voltages to a double mask liquid crystal spatial light modulator (SLM-256, CRI) consisting of 2×128 pixels. The SLM is placed in the Fourier plane of a zero-dispersion compressor, which is a folded setup of two gratings (600 l/mm) and two cylindrical-concave mirrors ($f = 130\ \text{mm}$) in a 4f-arrangement. In order to avoid the damage of the SLM, in the optimization experiment only $230\ \mu\text{J}$ were allowed to pass through the liquid crystals. The shaped pulses are then focused onto the cold molecules and the current of the desired mass-selected ion is taken as feedback signal. The laser pulses were analyzed by means of SHG-FROG technique. The amplitude and phase were calculated from the FROG trace by an iterative phase-retrieval procedure [6]. In the optimization experiment, an algorithm based on evolutionary strategies [7] is applied in order to find the pulse shape in the 128-dimensional searching space, which yields to the highest feedback signal. A detailed description of the algorithm can be found in [2].

3. RESULTS AND DISCUSSION

We present the results obtained for the free phase optimization of the photo-ionization yield of $\text{CpMn}(\text{CO})_2$. It is indeed possible that the optimized pulse shapes can slightly differ, while the optimized ion yield is almost the same for repeated optimization experiments. This may

be due to high complexity of the parameter manifold (searching for solutions in a 128-dimensional space), on which the evolutionary algorithm tries to find the best solution.

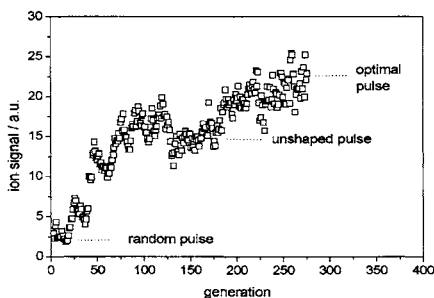


Fig.2. Progression of the ion signal during the free phase optimization of the $\text{CpMn}(\text{CO})_2^+$.

This solution could be reached under our experimental conditions by somewhat different pulse structures, since their deviations in fitness are too small to be distinguished. Here, we show the pulse form that we have frequently obtained in the optimization runs under the given experimental conditions. We have performed exclusively phase optimization in order to keep the pulse energy constant. In Fig. 2 the learning curve of the optimization algorithm obtained by recording the ion yield for each generation is shown. Although instabilities were present in the molecular beam, the evolutionary algorithm was able to converge after approx. 250 generations. The best individual in one generation might produce a lower ion signal in the next generation if additionally all other individuals generate less ion yield than the previous best one, during molecular beam instabilities. This could lead to a decrease of the ion signal in the evolution of the best individual. The $\text{CpMn}(\text{CO})_2^+/\text{CpMn}(\text{CO})_3^+$ mass peak ratio before the optimization was 1: 65. After the $\text{CpMn}(\text{CO})_2^+$ yield optimization, the ratio of fragment/mother ion yield was improved by a factor of 1.5 (to 1:43) with respect to the ion signal produced by an unshaped pulse. This indicates that the control experiment lead to a substantial increase of the desired product. The time-wavelength profile and the pulse form of optimal laser pulse acquired for $\text{CpMn}(\text{CO})_2^+$ are shown in Fig. 3. The FROG trace (Fig. 3a) exhibits mainly three intensity maxima (subpulses). After the phase-retrieval procedure (FROGGUI, [6]), which gives the amplitude and the phase of the electric field of the optimal pulse, the corresponding retrieved amplitude consists of three subpulses with the ratios of approx. 1:2:15 (Fig. 3b).

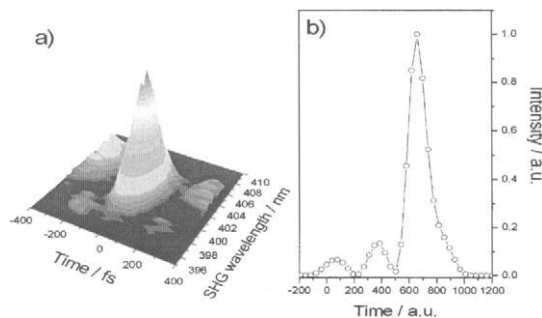


Fig. 3 The SHG FROG trace (a) and the amplitude profile (b) of the optimal laser field obtained after maximizing the $\text{CpMn}(\text{CO})_2^+$ yield.

The time separation between the first two subpulses is approx. 300 ± 15 fs and between the second and the third subpulse is about 280 ± 15 fs. The time duration of the subpulses measured at FWHM is 140 fs, 125 fs and approx. 125 fs, respectively. Intuitively the time-profile of the optimized pulse might suggest a two-photon excitation process performed by the first subpulse. The second subpulse is created approx. 300 fs later. It might ionize the $\text{CpMn}(\text{CO})_2^+$ fragment. Since its intensity is twice as high as the first subpulse, it could again excite the $\text{CpMn}(\text{CO})_3$ molecule from the electronic ground state in one or more of the electronic excited states. After 280 fs, when the third and most intense subpulse arrives, the excited fragment species could be subsequently ionized in a multiphoton step. Simultaneously, the last subpulse could again excite the parent molecule and subsequently ionize its $\text{CpMn}(\text{CO})_2^+$ fragments. The time separation between the three intensity maxima subpulses is not half of the oscillation period of any of the b^1A'' or c^1A' states [4]. The long time delay between the two subpulses (300 fs and 280 fs, respectively) might be due to repeated oscillations on the involved electronic states and delayed fragmentation into the a^1A'' state, followed by a multi-photon ionization. This assumptions should certainly be verified in future by theoretical calculations combined with one-color pump-probe experiments. Further work on the first fragment ion, $\text{CpMn}(\text{CO})_2^+$, employing optimization experiments of both phase and amplitude is currently under progress.

4. SUMMARY AND OUTLOOK

We have performed adaptive control on $\text{CpMn}(\text{CO})_2^+$ (the first fragment emerging from $\text{CpMn}(\text{CO})_3^+$) by exclusively optimizing the phase of the laser pulse. The experiment increased the relative ion yield of the chosen reaction path. It is known that after performing a free optimization experiment in a 128-dimensional space, some components of the pulse might not contribute to the effect and are therefore not considered by the optimization [8]. Hence, an important step towards understanding the acquired pulses is to reduce the unimportant components of the light field, by adding "genetic pressure" to the cost functional [8].

ACKNOWLEDGMENTS

The authors thank Prof. J. Manz and Dr. L. González for the fruitful discussions. C. Lupulescu kindly acknowledges Gottlieb Daimler- und Karl Benz-Stiftung. This project was financed by Deutsche Forschungsgemeinschaft in the frame of Sonderforschungsbereich 450.

REFERENCES

- [1] R. S. Judson, H. Rabitz, *Phys. Rev. Lett.* 68 (1992) 1500.
- [2] C. Daniel, J. Full, L. González, C. Kaposta, M. Krenz, C. Lupulescu, J. Manz, S. Minemoto, M. Oppel, Š. Vajda, L. Woeste, *Chem Phys.* 267 (2001) 247.
- [3] A. Assion, T. Baumert, M. Bergt, T. Brixner, B. Kiefer, V. Seyfried, M. Strehle, G. Gerber, *Science* 282 (1998) 919.
- [4] C. Daniel, J. Full, L. González, C. Lupulescu, J. Manz, A. Merli, Š. Vajda, L. Woeste, *Science* 299 (2003), 536.
- [5] J. Manz, L. González, *priv. commun.*
- [6] J. W. Nicholson, J. Jasapara, W. Rudolph, F. G. Omenetto, A. J. Taylor, *Opt. Lett.* 24, (1999) 1774.
- [7] I. Rechenberg, *Evolutionstrategie*, Frommann-Hozboog, Stuttgart, 1994.
- [8] J. M. Geremia, W. Zhu, H. J. Rabitz, *J. Chem. Phys.* 113 (2000) 10841.

Adiabatic control of bond distance in selective non Franck-Condon transitions

I. R. Sola^a, B. Y. Chang^b, V. S. Malinovsky^c and J. Santamaria^a

^aDpt. de Química Física I, Universidad Complutense, 28040 Madrid, Spain

^bSchool of Environmental Science and Applied Chemistry, Kyunghee University, Gyeonggi-do 449-701, Korea

^cMCTP & FOCUS Center, Dpt. of Physics, University of Michigan, Ann Arbor, MI 48109

One of the most interesting applications of Femtochemistry is the stroboscopic measuring of observables related to molecular motion, for instance the vibrational periods or the breaking of a bond [1]. Because femtosecond laser fields are broadband, a wave packet is created by the coherent excitation of many vibrational states, which subsequently evolves in the electronic potential following mostly a classical trajectory. This behavior is to be contrasted to narrow band selective excitation, where perhaps only two (the initial and the final) states participate in the superposition, following typically a very non-classical evolution. In this case one usually is not interested in the evolution of other observables than the populations.

The use of strong fields to drive the dynamics leads to somehow similar effects than those of ultrafast pulses. If the Rabi frequency or energy of the interaction is much larger than the energy spacing between adjacent vibrational states, a wave packet is formed during the laser action. The same laser can prepare and control the dynamics of the wave packet [2]. Both short time widths and large amplitudes can concur in the experiment. However, the precise manipulation of dynamic observables usually becomes more difficult as the duration of the pulses decreases.

Adiabatic passage schemes are particularly suited to control population transfer between states, since the adiabatic following condition assesses the stability of the dynamics to fluctuations in the pulse duration and intensity [3]. The time evolution of the wave function does not depend on the dynamical phase, and is therefore slow in comparison with the vibrational time scale. This fact guarantees that the time variation of the observables during the controlled dynamics will be slow. Adiabatic methods can therefore be of great utility to control dynamic observables that do not commute with the Hamiltonian. We are interested in the control of the bond length of a diatomic molecule [4].

Consider, to be specific, a molecule like Na₂. In Fig. 1(a) we show some singlet electronic potential curves. A selective transition between the initial state $\phi_0^X(x)$ and the ground state of the excited potential $V_{1g}(x)$, $\phi_0^B(x)$, is highly non Franck-Condon and thus involves a large displacement of the molecular bond. If the transition between these states can be adiabatically controlled, then it will be in principle possible to follow or control the bond length as the transition proceeds. The first problem involves the smallness of

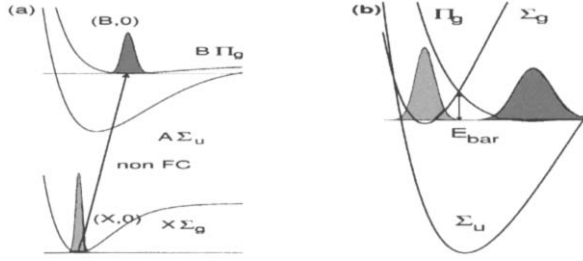


Figure 1: (a) Singlet electronic states of Na₂ between which the chosen non Franck-Condon transition takes place. (b) Potential curves displaced by the photon energies.

the Franck-Condon factors. It is sometimes possible to overcome this problem by two-photon absorption, for instance using two pulses that drive the excitation via the electronic potential $V_{\Sigma_u}(x)$ in Na₂.

We study two adiabatic schemes that use a sequence of time-delayed transform limited pulses. The first one, known as STIRAP (Stimulated Raman adiabatic passage) controls the population transfer between three vibrational states. The frequency of the first pulse $[\mathcal{E}_1(t)]$ is tuned in resonance with the transition from $\phi_0^X(x)$ to the intermediate state $\phi_{10}^A(x)$, and the frequency of the second pulse $[\mathcal{E}_2(t)]$ is resonant with the transition from $\phi_{10}^A(x)$ to $\phi_0^B(x)$; $\phi_{10}^A(x)$ is the intermediate state that maximizes the Franck-Condon factors for both transitions at the same time, working as an efficient wave function bridge between the initial and target wave functions [5]. Using counterintuitive pulses, such that $\mathcal{E}_2(t)$ precedes $\mathcal{E}_1(t)$, the wave function of the system has the interesting form [3]

$$\Psi_S(x, t) = \frac{1}{\Omega_0(t)} \left(\Omega_2(t) \phi_0^X(x) - \Omega_1(t) \phi_0^B(x) \right) \quad (1)$$

where the Rabi frequencies are defined as $\Omega_1(t) = \mathcal{E}_1(t) \mu_{ib} / \hbar$, $\Omega_2(t) = \mathcal{E}_2(t) \mu_{bf} / \hbar$ and $\Omega_0(t) = \sqrt{\Omega_1(t)^2 + \Omega_2(t)^2}$ (μ_{ib} and μ_{bf} are the dipole moments). The population is transferred from the initial to the target state independently of the pulse parameters, as long as the dynamics is adiabatic ($\Omega_0 \cdot \sigma \gg 1$, where σ is the width of the pulse [3]) and the Rabi frequency of the pulses are smaller than the vibrational energy spacing to avoid the excitation of other states [5]. The intermediate state is never excited since $\Psi_S(x, t)$ is orthogonal to $\phi_{10}^A(x)$.

The second scheme that we study is known as APLIP [6] (Adiabatic passage by light-induced potentials). It uses strong fields so that a wave packet is formed during the excitation. In APLIP, the transition to the intermediate potential is off resonant. When the frequency of the first pulse is tuned to the blue of the resonance, $\Delta = V_{\Sigma_u}(x) - \hbar\omega_1 < 0$, so that the shifted intermediate potential is below $V_{\Sigma_g}(x)$ and $V_{\Pi_g}(x)$ [see Fig.1(b)]. In the red detuning case $\Delta > 0$ and $V_{\Sigma_u}(x)$ is above both the initial and final potentials. In the numerical calculations we use $|\Delta| = 0.02$ a.u. The large Stark shifts modify the potentials. Assuming adiabatic evolution, in the adiabatic representation the dynamics of the system is governed by a single electronic adiabatic potential or LIP [6-8]:

$$\dot{\Psi}_A(x, t) = -i\hbar [\mathbb{T} + U_{LIP}(x, t)] \Psi_A(x, t) \quad (2)$$

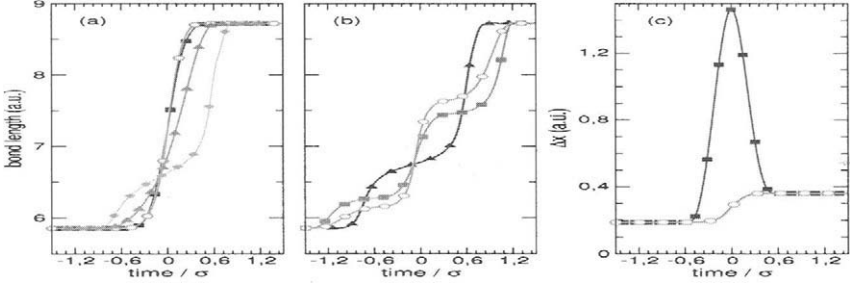


Figure 2: (a) Time variation of the bond length using counterintuitive pulse sequences in STIRAP with time delay $\tau = 4$ ps (squares) and in APLIP for different time delays $\tau = 4$ ps (circles), $\tau = 2$ ps (triangles) and $\tau = 0.5$ ps (diamonds). $\mathcal{E}_0 = 5 \cdot 10^{-4}$ a.u. for STIRAP and $8 \cdot 10^{-2}$ a.u. in APLIP. (b) Time variation of the bond length in APLIP using intuitive sequences and red detuning with $\tau = 4$ ps, $\mathcal{E}_0 = 0.5 \cdot 10^{-2}$ a.u. (squares), $\tau = 4$ ps, $\mathcal{E}_0 = 1.2 \cdot 10^{-2}$ a.u. (circles), and with $\tau = 0.5$ ps, $\mathcal{E}_0 = 0.8 \cdot 10^{-2}$ a.u. (triangles). (c) Time variation of the wave packet width or bond spread in counterintuitive sequence using STIRAP (squares) and APLIP (circles) corresponding to the results shown in (a).

where T is the kinetic energy operator. Moreover, when the dynamics is fully adiabatic [8], the wave function is always the vibrational eigenstate of lowest energy in the LIP. This fact implies that the wave function is clearly bounded by $U_{LIP}(x, t)$ and its width can be controlled by the width of the potential well. The evolution of the observables differs in the intuitive and counterintuitive sequences [7,8].

The main differences in the mechanism of adiabatic transfer in STIRAP and APLIP can be sketched from Fig. 1(b). In STIRAP the Stark shifts are minimal. The initial and final states are in resonance, and the population is transferred in a tunneling like fashion. The pulse sequence opens and closes the coupling so that the tunneling occurs only from left to right in the figure. From this perspective we expect the time evolution of the observables to exhibit some typical quantum properties. On the other hand, in APLIP the Stark shifts must be larger than the energy barrier (E_{bar}) that separates the equilibrium conformations of both potentials, so that the minimum energy of the initial potential or left well is pushed above the energy barrier and the wave packet slides down to the right well. The dynamic Stark shifts provide the electronic lever mechanism that moves the wave packet. This simplified description of APLIP anticipates a more classical like evolution of the observables.

From Eq.(1) the average bond distance in STIRAP is

$$\bar{x}_S(t) \equiv \langle \Psi_S(x, t) | x | \Psi_S(x, t) \rangle = \cos^2 \theta(t) \bar{x}_0^X + \sin^2 \theta(t) \bar{x}_0^B \quad (3)$$

where $\theta(t) = \arctan(\Omega_2(t)/\Omega_1(t))$, $\bar{x}_0^X = \langle \psi_0^X(x) | x | \psi_0^X(x) \rangle$ and $\bar{x}_0^B = \langle \psi_0^B(x) | x | \psi_0^B(x) \rangle$. In APLIP, the bond length is calculated as $\bar{x}_A(t) = \langle \Psi_A(x, t) | x | \Psi_A(x, t) \rangle$.

In Fig.2 we show the evolution of the bond length of the molecule as the non Franck-Condon transition proceeds, both in STIRAP and in APLIP for intuitive and counterintuitive sequences. The calculations were obtained by solving the Schrödinger equation using sine square pulses with FWHM $\sigma = 5$ ps. The results show that the dynamics

of the bond length as measured by the average internuclear distance is very similar in STIRAP and APLIP using the counterintuitive sequence: $\bar{x}(t)$ is practically insensitive to the maximum Rabi frequency, but is relatively sensitive to the ratio between Rabi frequencies. The rate of change of $\bar{x}(t)$ can be slowed down by decreasing the time delay τ of the pulses in both cases.

The dynamics of $\bar{x}(t)$ using intuitive sequences in APLIP is considerably different. It involves two intermediate steps at $\bar{x}(t) \geq \bar{x}_0^X$ and $\bar{x}(t) \leq \bar{x}_0^B$ at initial and late times respectively, where the bond length is almost constant. The exact value of $\bar{x}(t)$ in these plateau regions is quite robust to the ratio of Rabi frequencies, but it can be controlled by the peak amplitude of the pulses. Therefore, the intuitive sequence provides a more robust scenario than the counterintuitive one for preparing the system at certain bond lengths. Additional control can be achieved by changing the time delays.

There is a fundamental difference between the properties of the molecular bond length in the STIRAP and APLIP processes that is overlooked by the average bond distance. In APLIP the wave function is always localized around the average internuclear distance, since it is constrained by the electronic forces exerted by $U_{LIP}(x, t)$; $\bar{x}(t)$ is also stable since it corresponds to the minimum of a potential, and it is quasi-static, since the rate of change of $U_{LIP}(x, t)$ can be arbitrarily controlled. Therefore, it truly corresponds to the classical notion of a bond length.

In STIRAP, however, the average distance does not correspond to a bond length; it is a dynamical property related to a superposition state that has no classical analog. Indeed, since the wave function transfer proceeds in a tunneling like fashion, the probability of finding the state at the average value (the bond length), which is in the middle of the barrier E_{bar} , is practically zero during the transfer, $\langle \bar{x}(t) | \Psi_S(t) \rangle \approx 0$. In Fig.2(c) we show the bond spread or standard deviation of the internuclear distance, $\Delta x(t) = \sqrt{\langle \Psi(t) | x^2 | \Psi(t) \rangle - \bar{x}(t)^2}$. In STIRAP, $\Delta x(t)$ is much larger than in APLIP, due to the high degree of delocalization of the wave function.

We expect that the different properties of the wave function and thus the different meanings of the bond length in one or the other scheme will have clear distinct signatures in experimental measurements of *e.g.* cross sections. We also expect that preparing the wave function at intermediate bond lengths via one or other method will have interesting consequences in different molecular events, like chemical reactions. Finally, these or similar adiabatic schemes may be used to control other dynamical properties by mixing vibronic states of different electronic configurations [4].

This work was partially funded by the Dirección General de Investigación Científica y Técnica under Project No. BQU2002-00173.

- [1] A. Zewail, *Angew. Chem. Int. Ed. Engl.* 39 (2000) 2586.
- [2] S. Rice and M. Zhao, *Optical Control of Molecular Dynamics*, Wiley, New York, 2000.
- [3] K. Bergmann, H. Theuer, and B. W. Shore, *Rev. Mod. Phys.* 70 (1998) 1003.
- [4] B. Y. Chang, H. Rabitz and I. R. Sola, *Phys. Rev. A* 68 (2003) 031402.
- [5] I. R. Sola, B. Y. Chang, V. Malinovsky, and J. Santamaria, in *Femtochemistry and Femtobiology*, edited by A. Douhal and J. Santamaria, World Scientific, Singapore, 2002.
- [6] B. M. Garraway and K.-A. Suominen, *Phys. Rev. Lett.* 80 (1998) 932.
- [7] I. R. Sola et al., *Phys. Rev. Lett.* 85 (2000) 4341.
- [8] B. Y. Chang et al., *J. Chem. Phys.* 114 (2001) 20.

Adiabatic rapid passage in molecules in solution excited by an intense ultrashort chirped pulse

B.D. Fainberg^{a,b} and V.A. Gorbunov^a

^aHolon Academic Institute of Technology, Department of Sciences, 52 Golomb St., Holon 58102, Israel

^bRaymond and Beverly Sackler Faculty of Exact Sciences, School of Chemistry, Tel-Aviv University, Tel-Aviv 69978, Israel

1. INTRODUCTION

Chirped pulses are very efficient for achieving population transfer in atomic and molecular systems. Total electronic population inversion of molecules can be achieved using coherent light-matter interactions like adiabatic rapid passage (ARP) [1]. Although the overwhelming majority of chemical reactions are carried out in liquid solution, there are very few theoretical studies of nonperturbative active control of the quantum dynamics related to population transfer and product selection for a reactant molecule embedded in a solvent. These are the picture of "moving" potentials of one of us for incoherent description of the chirped pulse interaction with molecules in solution [2,3], and theoretical studies of optical control of molecular dynamics in a liquid by ARP [4,5] and stimulated Raman adiabatic passage (STIRAP) [6].

In Ref. [4] we have studied an intense chirped pulse excitation of a molecule coupled with a dissipative environment taking into account electronic coherence effects. We considered a two state electronic system with relaxation treated as diffusion on electronic potential energy surfaces with respect to the generalized coordinate α . We solved numerically equations for the density matrix of a molecular system under the action of chirped pulses of carrier frequency ω with temporal variation of phase $\varphi(t)$:

$$\frac{1}{2} E(t) \exp[-i\omega t + i\varphi(t)] + c.c. \quad (1)$$

when the interaction with a dissipative environment could be described as the Gaussian-Markovian modulation of transition frequency with the correlation function $k(t) = \langle \alpha(0)\alpha(t) \rangle = \sigma_{2s} \exp(-|t|/\tau_s)$, $\sqrt{\sigma_{2s}}$ is the amplitude of modulation, and τ_s is the correlation time (the total model). An inhomogeneously-broadened system with frozen nuclear motion ($\tau_s \rightarrow \infty$) was invoked to model the corresponding population transfer without relaxation. Comparison of these two models enables us to separate the effects of relaxation and inhomogeneous broadening. We have shown that the type of population transfer (coherent, by ARP, or incoherent) strongly depends on the pulse chirp, its sign and the detuning of the exciting pulse carrier frequency with respect to the frequency of Franck-Condon transition.

For the positively chirped (PC) pulses and small detuning, relaxation does not hinder a coherent population transfer. Moreover, under these conditions the relaxation favors more efficient population transfer with respect to the system with frozen nuclear motion.

In the present work we offer a simple and physically clear explanation of all the numerical results of Ref. [4] with careful examination of all the conditions needed for ARP by using time-dependent adiabatic potentials. One of these requirements, the adiabatic criterion

$$\left| \frac{d\omega(t)}{dt} \right| \ll |\Omega(t)|^2, \quad (2)$$

was fulfilled for the excitation under consideration [4]. Here $\omega(t) = \omega - d\phi/dt$ is the instantaneous pulse frequency, $\Omega(t) = DE(t)/\hbar$ - the Rabi frequency, D - the dipole moment operator.

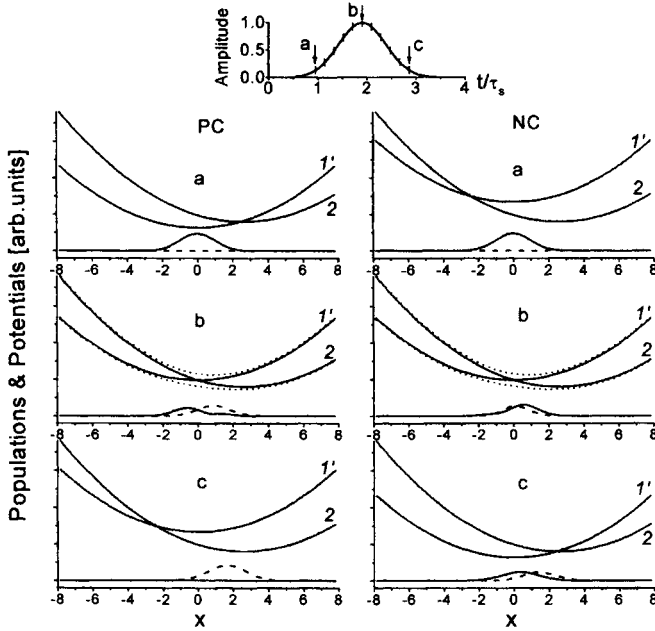


Fig.1. Population wave packets of the ground (solid line) and excited (dashed line) states in the beginning (a), in the middle (b) and at the end (c) of exciting pulse for positive (left column, $\Phi'(v)=10^4$ fs²) and negative (right column, $\Phi'(v)=-10^4$ fs²) chirp. $\Phi'(v)$ is the chirp rate in the frequency domain [2-4], $x = \alpha/\sigma_{2s}^{1/2}$, $\sigma_{2s}^{1/2} = 546$ cm⁻¹, $\tau_s = 70$ fs, $Q'=5$ (the saturation parameter [4]). Solid lines 2 and 1' are effective *diabatic* potentials related to excited state 2 and "photonic replication" 1' of the ground state. The corresponding time-dependent *adiabatic* potentials are shown by dotted lines. Inset: Electric field amplitude $E(t)$, the arrows show the instants of time corresponding to figures a, b and c.

2. TIME EVOLUTION OF POPULATION WAVE PACKETS

To realize the ARP, one needs to add one more condition to the adiabatic criterion Eq. (2): *a transition must start and come to the end far from resonance*. We have studied the time behavior of population wave packets for the model with relaxation by solving coupled differential equations of Sec. III of Ref.[4] (see Fig.1). The study shows that the last condition is realized only for PC excitation and small detuning of the exciting pulse carrier frequency with respect to the frequency of Franck-Condon transition (Fig.1, the left column). Therefore, the Landau-Zener (LZ) model can describe such a situation. When the pulse chirp is negative (Fig.1, the right column) and/or the detuning is not small, the process either comes to the end or starts near the resonance where an adiabatic state is a mixture of the ground and excited diabatic states. By this means the motion of population wave packets in the time-dependent adiabatic potentials explains all the dependences of the excited state population on the chirp sign and detuning of the pulse carrier frequency with respect to the frequency of Franck-Condon transition observed in Ref. [4]. In addition, such a simple picture explains why the relaxation favors more efficient population transfer with respect to the system with frozen nuclear motion (without relaxation).

3. ADIABATIC RAPID PASSAGE BETWEEN RANDOMLY FLUCTUATING LEVELS

To evaluate the range of parameters where relaxation favors population transfer, we have generalized the LZ model to the crossing of "moving" potentials for constant-intensity radiation with a linear PC ($d^2\phi/dt^2 = \mu = \text{const} < 0$). Using Zener's approach [7], we obtained the following expression for probability W_{12} of transition $1 \rightarrow 2$ during a single crossing of "moving" potentials

$$W_{12} = 1 - \exp\left[-2\pi(\Omega/2)^2 / |\dot{\alpha} - \mu|\right] \quad (3)$$

where $\dot{\alpha} \equiv d\alpha/dt$. Similar to Refs. [2-4], we consider α as a stochastic Gaussian variable. Consequently, we must average Eq. (3) over random crossing of levels described by Gaussian random noise induced by intra- and intermolecular fluctuations. Such a procedure includes averaging with respect to α and its time derivative (see Eq.(3)). It can be easily done for a *differentiable* (non-Markovian) Gaussian process (see Refs.[8,9]), bearing in mind an independence of α and $\dot{\alpha}$ from each other for such processes [10]. Therefore, we will consider here a *non-Markovian* Gaussian noise, as opposed to Refs. [2-4], that enables us to make a simple estimate without numerical simulations. In addition, we consider a slow modulation limit when $\sigma_{2s}\tau_s^2 \gg 1$. Averaging Eq.(3) and evaluating the corresponding integral by the method of steepest descent, we obtain the following expression for the population of excited electronic state 2

$$n_2 = 1 - \frac{2}{\sqrt{3}} \exp\left\{-\frac{3}{2} \left[\pi\Omega^2 / \left(2\sqrt{-\dot{k}(0)} \right) \right]^{2/3} \right\} \quad (4)$$

Here $\ddot{k}(0)$ is the second derivative of the correlation function $k(t)$ of the energetic fluctuations evaluated at zero. This result is valid for $\mu^2 / [-\ddot{k}(0)] \leq 1$ and adiabatic condition Eq.(2).

One can see that n_2 is close to 1 for strong interaction when $\Omega^{4/3} \gg [-\ddot{k}(0)]^{1/3}$. Using results of Ref. [11], one can show that in order of magnitude, $[-\ddot{k}(0)]^{1/4}$ is equal to $1/T'$ - reciprocal irreversible dephasing time. By this means relaxation does not destroy ARP for strong interaction when the Rabi frequency exceeds the reciprocal irreversible dephasing time:

$$|\Omega| > 1/T' \quad (5)$$

The last condition was fulfilled in simulations of Ref. [4], though in the last case T' is determined independently of $\ddot{k}(0)$ [11], which does not exist for the Gaussian-Markovian process. If $|\Omega| \leq 1/T'$, ARP is destroyed by relaxation (see Fig.7a of Ref. [4]).

4. CONCLUSION

We have developed a simple and physically clear picture of ARP in molecules in solution by careful examination of all the conditions needed for ARP. The relaxation effects were considered in the framework of the LZ model for random crossing of levels. The model enables us to include into consideration non-Markovian Gaussian-correlated noise. It explains all the numerical results obtained in Ref. [4].

ACKNOWLEDGMENTS

This work was supported by the Israel Science Foundation (Grant No. 41/00-1) and the Ministry of Absorption of Israel.

REFERENCES

- [1] K. Bergmann, H. Theuer and B.W. Shore, *Rev. Mod. Phys.*, 70 (1998) 1003.
- [2] B.D. Fainberg, *J. Chem. Phys.*, 109 (1998) 4523.
- [3] B.D. Fainberg and V. Narbaev, *J. Chem. Phys.*, 113 (2000) 8113.
- [4] B.D. Fainberg and V.A. Gorbunov, *J. Chem. Phys.*, 117 (2002) 7222.
- [5] Y. Nagata and K. Yamashita, *Chem. Phys. Lett.*, 364 (2002) 144.
- [6] M. Demirplak and S. A. Rice, *J. Chem. Phys.*, 116 (2002) 8028.
- [7] C. Zener, *Proc. R. Soc. London, Ser. A*, 137 (1932) 696.
- [8] L.D. Zusman, *Sov. Phys.- JETP*, 42 (1975) 794.
- [9] D.E. Makarov, M. Topaler, *Chem. Phys. Lett.*, 245 (1995) 343.
- [10] A.A. Sveshnikov, *Applied Methods of the Theory of Random Functions*, Pergamon Press, New York, 1966.
- [11] B.D. Fainberg, *Opt. Spectr.*, 68 (1990) 305.

Ultrafast non-Franck-Condon transitions: is it possible?

N. E. Henriksen and K. B. Møller

Department of Chemistry, Technical University of Denmark, 2800 Kgs. Lyngby, Denmark

1. INTRODUCTION

Ultrashort (femtosecond) laser pulses can be used to steer molecular dynamics including chemical reactions [1-3]. Given some initial state, the aim of laser control is to guide a system into a desired final state ("product"). In the work reported here, we wish to provide some additional insight into the dynamics induced by ultrashort laser pulses and discuss what objectives can be obtained. Thus, this work is an exploratory study, to determine the type of dynamics which might be induced by laser light. We are concerned not only with creating a predetermined product but with the possibility of creating this product within a given time.

In a Born-Oppenheimer (BO) description the different electronic states of a molecule provide the potential energy surfaces (PESs), which govern the nuclear dynamics. An infinitely short ("delta") laser pulse induces a perfect vertical or Franck-Condon transition – meaning that the nuclear part of the wave function remains unchanged by the interaction with the electric field (when transition dipole moment is considered constant over the extension of the nuclear part) [4,5]. Consider, for instance, a vibrational degree of freedom in a molecule having the PESs V_1 and V_2 and assume that the molecule initially is in its vibrational ground state on V_1 . Then – pictorially speaking – a delta pulse creates a copy of the initial nuclear wave packet (a Franck-Condon wave packet) at rest on a down-hill slope on V_2 , see Fig. 1(a). This wave packet will start to oscillate in the vibrational coordinate in question with its initial location defining one of the turning points. This one-dimensional picture is valid for a multidimensional system with sufficient mode decoupling.

Here we report our exploration of the possibility of inducing an ultrafast non-Franck-Condon transition, which we defined to be the creation of a wave packet at "the other" turning point of the above-mentioned oscillation, see Fig. 1(b), faster than the time it takes the Franck-Condon packet to reach that turning point due to the natural (field-free) dynamics. We have explored two possible routes for inducing non-Franck-Condon transitions, namely phase-tailoring of a weak-field ultraviolet (UV) pulse [6] and a two-pulse scheme combining a transform limited weak-field UV pulse with a strong infrared (IR) field [7].

2. ELECTRONIC TRANSITIONS BY A WEAK ULTRAVIOLET PULSE

We denote the vibrational wave packet associated with electronic state i by $\chi_i(q,t)$ and μ_{21} is the transition dipole moment. Initially the system is in the vibrational ground state on V_1 and treating the interaction with the field $E_{UV}(t)$ within first-order perturbation theory gives the following expression for the nuclear wave packet on V_2 :

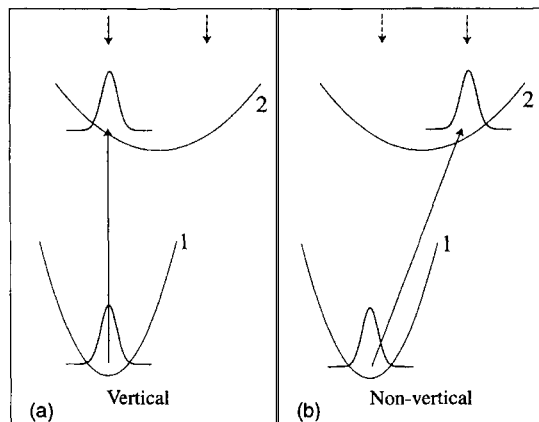


Fig. 1. Schematic of vertical (a) and non-vertical (b) electronic transitions with the electronic energies represented by displaced harmonic potentials. The initial state is the vibrational ground state on V_1 . The wave packet on V_2 in (a) is the Franck-Condon wave packet and the dashed arrows mark the positions of the turning points for the oscillation this wave packet will undergo under field-free conditions.

$$\begin{aligned} \chi_2(q, t) &= \frac{i}{\hbar} \int_{\tau}^{\tau+\Delta} dt' E_{UV}(t') \int_{-\infty}^{\infty} dq' K_2(q, t; q', t') \mu_{21} \chi_1'(q', t') \\ \chi_1'(q', t') &= \int_{-\infty}^{\infty} dq_0 K_1(q', t'; q_0, t_0) \chi_1(q_0, t_0) \end{aligned} \quad (1)$$

Here K_i is the nuclear time propagator associated with electronic state i in the absence of the UV field, τ is the onset and Δ is the duration of the UV field. Often the wave packet $\chi_1'(q', t')$ is sufficiently localized such that μ_{21} can be considered a constant.

3. ULTRAFAST NON-FRANCK-CONDON TRANSITIONS

The principles of ultrafast Franck-Condon and non-Franck-Condon transitions described in the Introduction are sketched in Fig. 1. The excited-state wave packet in panel (a) is the Franck-Condon wave packet (defining an inner turning point), and panel (b) illustrates the location of this wave packet after half a period on V_2 (defining an outer turning point). Our goal is to create a wave packet at the outer turning point faster than half the vibrational period on V_2 , with the initial state being the vibrational ground state on V_1 .

3.1 Phase-tailored UV pulse

First, we tried to obtain the desired goal by using a single ultrashort phase-tailored UV pulse [6]. In this case the propagator K_i in Eq. (1) simply describe the nuclear dynamics under the influence of the BO potential V_i . The idea that this might be possible has its origin in the facts that (i) when decomposing the wave packet created on V_2 into the eigenstates of V_2 the

phase of each expansion coefficient is determined by the phase of the corresponding spectral component in the field, (ii) the Franck-Condon wave packet is created by an ultrashort bandwidth-limited UV pulse, and (iii) the expansion coefficients for the two excited-state wave packets in Fig. 1 differ *only* by a phase.

Hence, exactly as in the experimental approach (see, e.g., Ref.[8]) to laser-pulse shaping by phase tailoring, we started with an ultrashort bandwidth-limited pulse and then modulated the phases of the spectral components of the pulse. Hence, the phases were set to appropriate values at the discrete frequencies corresponding to the energy levels of V_2 . However, we did not succeed; the duration of the “experiment” (from the onset of the pulse) always came out to be, at least, half a vibrational period on V_2 .

In hindsight that may not be so surprising. From the time-domain expression Eq. (1) we see that $\chi_2(q, t)$ is a (continuous) superposition of wave packets evolving on V_1 until time t' at which time they are lifted vertically to V_2 where they then evolve until time t ; weighted by the strength of the UV field at time t' . Each of the packets will just pick up a phase factor until time t' and subsequently undergo vibrational motion on V_2 . Hence, if the vibrational ground state on V_1 is narrow relative to the displacement and curvature of the two oscillators, no amplitude will build up at the desired location on V_2 (above-mentioned outer turning point) in less than approximately half a vibrational period on V_2 from the onset of the UV pulse.

3.2 Combined IR and UV excitation

Given the lack of success with the phase-tailored UV pulse we tried a different approach: a two-pulse scheme, where a weak-field ultrashort UV pulse is combined with a strong infrared (IR) field [7]. The strong IR field affects the nuclear dynamics such that the propagator K_i in Eq. (1) in this case describes the nuclear dynamics under the influence of $V_i + \mu_i E_{\text{IR}}(t)$, where μ_i is the dipole moment in the electronic state i . The idea that this approach may work is based on the fact that the nuclear dynamics no longer takes place on the pure Born-Oppenheimer potentials and this may speed up the process. Various applications of IR+UV two-pulse schemes have been discussed recently [9-12].

We chose a setup with a monochromatic IR field at resonance with the vibrational transition frequency in oscillator V_1 , ω_1 , which is different from the transition frequency in oscillator V_2 , ω_2 , and assumed that non-resonant effects can be neglected. The ultrashort UV pulse was approximated by a delta pulse ($\Delta = 0$).

With this setup, the IR field affects the nuclear dynamics in the lower electronic state (injects energy) in the time interval from t_0 to τ , i.e., prior to excitation to the upper electronic state. In the limit where this time interval is small, the IR field simply boosts the momentum of the wave packet. This implies that the UV delta pulse instead of creating a Franck-Condon wave packet at rest on a down-hill slope on V_2 creates a Franck-Condon wave packet with a positive (mean) velocity.

If the duration of the “experiment” is measured not from the onset of the UV pulse but from t_0 , the time spent in boosting the momentum in the lower electronic state should be less than the time saved evolving on V_2 . For the two harmonic oscillators displaced the distance D , this requirement gives in the limit of τ small (a more general case is analyzed in [7]) the following condition for the strength E_0 of the IR field (m is the mass and q_{e_i} is the equilibrium distance of oscillator V_i):

$$E_0 > \frac{m\omega_2^2 D}{[d\mu_1/dq]_{q=q_{cl}} \omega_1 (\tau - t_0)}, \quad (2)$$

For a simplified model of NaI [7] a minimum IR-field intensity of about 10^{12} W/cm² is required. This is a high intensity, but not so high that ionization is to be expected.

4. Concluding Remarks

The above analysis shows that the IR+UV scheme could be a possible way to create ultrafast non-Franck-Condon transitions. In fact, we illustrated the case where the nuclear dynamics was sped up by the IR field only prior to UV excitation. A more efficient scheme would involve an IR-field induced acceleration of the nuclear motion in both electronic states.

The ideas presented here use a weak UV pulse. One could also imagine using strong UV pulses, e.g. in one of the schemes presented by Solá *et al.* in this book, which alter the BO potentials by mixing them. These schemes usually involve three electronic states. This alters the discussion somewhat since even in the weak-field limit a trivial solution may be found in a pump-dump setup: the wave packet is first excited to a repulsive state, where the (now fast) dynamics takes place and when the wave packet has reached the desired location it is dumped to the excited bound state. Exploring various three-state setups is a topic for future research.

Finally, we remark that the argument presented against the idea of Sec. 3.1 is somewhat crude since it associates amplitude on V_2 only with the centers of moving Franck-Condon wave packets. If considering also the width of the Franck-Condon wave packet and this wave packet already has some amplitude close to the desired location, a scheme for inducing ultrafast non-Franck-Condon transitions using weak UV pulses may possibly be devised using two-pulse wave-packet interferometry: the first pulse creates amplitude in the Franck-Condon region and after only a short time a second (tailored) pulse removes amplitude still remaining in the Franck-Condon region. This idea is also a topic for future research.

This work was supported by the Danish Natural Science Research Council. We have enjoyed illuminating discussions with Volker Engel and Jeff Krause, and during the Femto VI conference also with Jörn Manz, who then kindly sent us Ref. [12] prior to publication.

REFERENCES

- [1] S.A. Rice and M. Zhao, *Optical Control of Molecular Dynamics*, Wiley, New York, 2000.
- [2] P. Brumer and M. Shapiro, *Annu. Rev. Phys. Chem.* 43 (1992) 257.
- [3] N.E. Henriksen, *Chem. Soc. Rev.* 31 (2002) 37.
- [4] E.J. Heller, *Acc. Chem. Res.* 14 (1981) 368.
- [5] N.E. Henriksen, *Adv. Chem. Phys.* 91 (1995), 433.
- [6] N.E. Henriksen and K.B. Møller, *J. Chem. Phys.* 119 (2003) 2569.
- [7] K.B. Møller and N.E. Henriksen, to appear in *Chem. Phys. Lett.* (2004).
- [8] A. Assion, T. Baumert, M. Bergt, T. Brixner, B. Kiefer, V. Seyfried, M. Strehle, and G. Gerber, *Science*, 282 (1998) 919.
- [9] B. Amstrup and N.E. Henriksen, *J. Chem. Phys.* 97 (1992) 8285; 105 (1996) 9115.
- [10] M. Machholm and N.E. Henriksen, *J. Chem. Phys.* 111 (1999) 3051.
- [11] J. Manz, M. Oppel, and G.K. Paramonov, *J. Phys. Chem.* 102 (1998) 4271.
- [12] N. Elghobashi, P. Krause, J. Manz, and M. Oppel, *Phys. Chem. Chem. Phys.* 5 (2003) 4806.

Quantum control beyond spectral interference and population control: Can resonant intense laser pulses freeze the population?

M. Wollenhaupt, A. Assion, O. Graefe, Ch. Horn, D. Liese, C. Sarpe-Tudoran, M. Winter and T. Baumert

Universität Kassel, Fachbereich Physik, Heinrich-Plett-Str. 40, D-34132 Kassel, Germany

1. INTRODUCTION

Many different schemes for quantum control have been demonstrated [1]. Prominent examples of which are the Brumer-Shapiro scheme [2], the Tannor-Kosloff-Rice scheme [3] and techniques based on (higher order-) spectral interference. The striking experiments of Silberberg nicely demonstrated the principle of second order spectral interference [4] and recently applications of higher order spectral interference to large organic molecules in solution were reported [5]. However, Rabitz et al. [6] pointed out that "the operating principle for quantum control of any type is the manipulation of constructive and destructive quantum mechanical interferences". Therefore, the ability to measure and to control the quantum mechanical phase is the key step towards a deeper understanding of quantum control. Since the energy resolved photoelectron spectra from simultaneous excitation and ionization are directly related to the temporal evolution of the excited state (population and phase), this technique is most suited to elucidate details of the quantum control dynamics [7]. In particular, the use of pulse sequences has proven a strong tool to study interference effects in atomic and molecular systems in detail [8]. This scheme was extended to the continuum in order to demonstrate the coherence transfer from femtosecond laser pulses to ultrashort free electron wave packets [9]. A variety of important control mechanisms are only accessible when strong laser fields are employed [10]. Examples of coherent control by intense sequential laser pulses are coherent transients such as the photon echo and Ramsey fringes [11] as well as the STIRAP [12].

In this contribution recent results [13] on the control of the quantum mechanical phase of an atomic state in strong laser fields studied using the Autler-Townes (AT) effect [14] in the photoionization of the K ($4p$) state are discussed. We demonstrate quantum control beyond (i) population control and (ii) spectral interference. (i) We show, that for suitable combinations of the laser intensity of the first pulse and the time delay the second resonant intense laser pulse leaves the excited state population unchanged. However, the knowledge of the

temporal evolution of the population is not sufficient since the second laser directly manipulates the quantum mechanical phase which significantly changes the outcome of the experiment. (ii) Control beyond spectral interference is achieved by controlling the quantum mechanical phase without changing the spectrum of the pulse sequence, i.e., since no phase modulation is applied and only the laser intensity is varied, the N -th order spectra are unchanged. Moreover, an uncommon symmetry of the control parameters delay time and laser intensity is observed: with respect to the interferences in the photoelectron spectra the role of time delay and laser intensity is interchangeable for suitable excitation conditions. This new control mechanism combines phase control and high intensity effects through the use of phase locked pulses and intensities that are large enough to cause Rabi cycling. We believe, that this mechanism is at play in many other circumstances as well and that it opens the door to a deeper understanding of quantum control in intense laser fields.

In our experiment a sequence of two intense laser pulses is used to excite K atoms in an atomic beam from the $4s$ to the $4p$ state. Simultaneously, the pulses ionize the excited atoms from the $4p$ state to the continuum via two-photon ionization (Fig. 1). Photoelectron spectra were taken at various delay times between the two laser pulses and at different laser intensities at a fixed delay time.

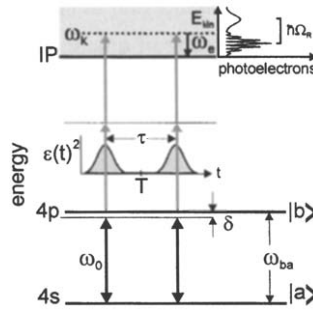


Fig. 1. Energy level diagram for excitation of K atoms.

2. EXPERIMENT

The experiments were carried out in a high vacuum chamber where a beam of atomic potassium K ($4s$) intersects perpendicularly with the femtosecond laser pulses leading to photoionization. The released photoelectrons are detected employing a magnetic bottle time-of-flight electron spectrometer. The 785 nm, 30 fs FWHM laser pulses provided by an amplified 1 kHz Ti:sapphire laser system are split into two beams using a Mach-Zehnder interferometer. In the first experiment the time delay τ is varied in a range of 80 to 100 fs with 0.2 fs resolution at a

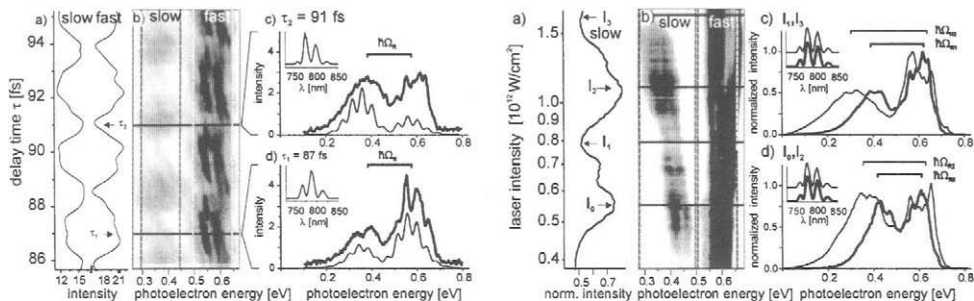


Fig. 2. Left: experimental photoelectron spectra as a function of the delay time τ . Right: Measured photoelectron spectra as a function of the laser intensity at a fixed delay time.

fixed laser intensity of I_0 (0.54×10^{12} W/cm 2). In the second experiment the time delay is kept fixed at 98.6 fs, whereas the energy of both beams is varied from $0.7 I_0$ to $3 I_0$.

3. RESULTS

At first, we discuss the results of the experiment using a variable time delay at a fixed laser intensity of I_0 . Fig. 2(b, left) shows the measured photoelectron spectra as a function of the delay time. Oscillations in the photoelectron signal at the period of the photon frequency of 2.6 fs are observed. The oscillations of slow and fast photoelectrons are out-of-phase. Sections through the photoelectron distribution were taken along the time delay axis for the fast and the slow photoelectrons. In the second experiment the laser intensity was varied but the time delay was fixed Fig. 2(b, right) in order to demonstrate that the control of the interferences is determined by the quantum mechanical phase. The optical spectrum of the pulse sequence remains unchanged for all intensities. A monotonic increase of the splitting of both AT components with increasing laser intensity is observed. The slow electron signal exhibits pronounced oscillations as the intensity is increased.

4. DISCUSSION

The intensity of the first laser is high enough to cause Rabi cycling and, therefore, AT splitting in the photoelectron spectrum. The observed control of interference in the AT doublet arises if the intensity of the first pulse is chosen to yield a population of $|c_b(T)|^2 = 0.5$, i.e. a pulse area of $\Theta = (n+0.5)\pi$. The subsequent time evolution ($t > T$) of c_b depends on the phase $\omega_0 \tau$ of the second laser pulse. If the phase $\omega_0 \tau$ takes half integer multiples of π , $|c_b(t)|^2$ is unchanged during the second laser pulse and the quantum mechanical phase is altered. With

regard to photo ionization the observations are interpreted in terms of the population of the dressed states. For suitable excitation only one of the dressed states is selectively populated and hence, interference is only seen in one AT component.

5. CONCLUSION

We demonstrate coherent control in strong fields beyond (i) population control and (ii) spectral interference, since (i) control is achieved without altering the population during the second intense laser pulse, i.e., the population during the second laser pulse is frozen, and (ii) the quantum mechanical phase is controlled without changing the spectrum of the pulse sequence. The control mechanism relies on the interplay of the quantum mechanical phase set by the intensity of the first pulse and the phase of the second pulse determined by the time delay.

ACKNOWLEDGEMENT

The support of the Deutsche Forschungsgemeinschaft, the Fonds der Chemischen Industrie and the NRC-Helmholtz program is gratefully acknowledged.

REFERENCES

- [1] A. Assion et al., *Science*, **282** (1998) 919; T.C. Weinacht et al., *Phys. Rev. Lett.*, **80** (1998) 5508; A.H. Zewail, *J. Phys. Chem. A*, **104** (2000) 5660; S.A. Rice and M. Zhao, *Optical Control of Molecular Dynamics*, Wiley-Interscience, New York, 2000; M. Shapiro and P. Brumer, *Trans. Far. Soc.*, **93** (1997) 1263.
- [2] P. Brumer and M. Shapiro, *Chem. Phys. Lett.*, **126** (1986) 541.
- [3] D.J. Tannor et al., *J. Chem. Phys.*, **85** (1986) 5805.
- [4] D. Meshulach and Y. Silberberg, *Phys. Rev. A*, **60** (1999) 1287.
- [5] V.V. Lozovoy et al., *J. Chem. Phys.*, **118** (2003) 3187.
- [6] H. Rabitz et al., *Science*, **288** (2000) 824.
- [7] see, for example, work on the Na₂ prototype: A. Assion et al., *Phys. Rev. A*, **54** (1996) R4605; T. Frohnmeyer et al., *Chem. Phys. Lett.*, **312** (1999) 447.
- [8] N.F. Scherer et al., *J. Chem. Phys.*, **93** (1990) 856; M.A. Bouchene et al., *Eur. Phys. J. D*, **2** (1998) 131.
- [9] M. Wollenhaupt et al., *Phys. Rev. Lett.*, **89** (2002) 173001.
- [10] R.J. Levis and H.A. Rabitz, *J. Phys. Chem.*, **106** (2002) 6427.
- [11] P. Meystre and M. Sargent III, *Elements of Quantum Optics*, 3rd ed., Springer, 1999, Berlin; B. W. Shore, *The Theory of Coherent Atomic Excitation 1*, Wiley-Interscience, New York, 1990.
- [12] N.V. Vitanov et al., *Adv. Atom. Molec. Opt. Phys.*, **46** (2001) 55.
- [13] M. Wollenhaupt et al., *Phys. Rev. A*, **68** (2003) 015401.
- [14] S.H. Autler and C.H. Townes, *Phys. Rev.*, **100** (1955) 703.

Ultrafast time reversal mirror at 800 nm based on photosensitive naphthalocyanine doped solids

J.-P. Galaup^{a*}, S. Fraigne^a, J.-L. Le Gouët^a, J.-P. Likforman^{b+} and M. Joffre^b

^aLaboratoire Aimé Cotton, CNRS, Bât 505, Université Paris-Sud, 91405 Orsay cedex, France

^bLaboratoire d'Optique et Biosciences, Ecole Polytechnique, 91128 Palaiseau cedex, France

1. INTRODUCTION

Since the development of titanium-sapphire (Ti:Sa) femtosecond laser source, the domain of research fields or development covered by the use of ultrafast lasers is in continuous expansion. In femtochemistry, it was realized that, when in a photochemical reaction different pathways lead to a given final state, the presence of a well-controlled frequency pulse chirp might greatly enhance the probability with which this final state is reached [1,2]. Chirp control is needed and mastering the phase of the laser pulse is the key point.

Usual techniques for producing high-energy ultrashort pulses use the chirped pulse amplification (CPA) scheme [3], in which a combination of gratings and reflective optics to realize the stretching, amplification and compression stages are employed. The amplification of femtosecond pulses is realized through a three stages combination. First, the Fourier transform femtosecond pulse is stretched up to several picoseconds, and then it is amplified up to thousand times and finally re-compressed to femtoseconds. In such a chain, the stretcher and the compressor are completely symmetrical dispersive devices used in opposite directions. For a perfect recompression, the compressor must fully correct the phase changes introduced by the stretcher and the amplifier. Indeed, they are not aberration free systems and the aberrations they introduced, as well as the aberrations introduced by the amplifier itself are not compensated. At the output, the amplified pulses need then to be cleaned in accordance with their future use. Generally, these spectral phase corrections are achieved with the help of a two grating zero dispersion line in the Fourier plane of which a liquid crystal array is inserted [4,5]. The spectral resolution and the pixelization in the Fourier plane are the most crucial limitations of this shaping technique.

In this note, we present a different approach based on the use of persistent spectral hole burning (PSHB) materials, which can be programmed to combine the roles usually played by the dispersive components and the modulator arrays [6]. A PSHB material is non-pixelated and potentially offers a larger number of addressable points. The shaping process includes two steps: first, engraving a coherent spectral filter with an accumulated storage interferometric procedure, followed with the use of this filter to shape a probe pulse. If the latter pulse is the same as the (short) reference pulse of the engraving process, the "diffracted" or echo pulse reproduces the object pulse or its time-inverted image, depending on the pulse

* Corresponding author: jean-pierre.galaup@lac.u-psud.fr

⁺ Present address: Institut de Physique et Chimie des Matériaux, GONLO, 23, rue du Loess, 67037 Strasbourg, France.

time ordering. Similarly to spatial phase conjugation that leads to self-compensation of spatial phase distortions, the stimulated photon echo technique may lead to spectral phase conjugation i.e. time reversal provided that, because of causality, the reference pulse follows (rather than precedes) the object pulse. Up to now, only few spectral holography experiments have been done in the frequency domain of Ti:Sa lasers around 800 nm [7,8], and, to our knowledge, none demonstrated the control of the phase of femtosecond pulses shaped by use of spectral holography in a PSHB material.

Modifying the phase of an ultra-short laser pulse or correcting a phase change implies that one is able to measure this phase. The spectral interferometry (SI) technique [9] that perfectly suits ultra-short pulses is expected to be the ideal tool: A reference pulse is sent through the device, and the output pulse and a portion of the incident reference pulse are made to frequency beat on the entrance slit of a spectrometer. The resulting spectrogram provides the required information [10,11]. In this work, we adapted the SI technique for measuring the amplitude and phase of photon echo signals produced by diffraction of femtosecond pulses on a spectral hologram, therefore demonstrating the pulse-shaping and time reversal potentialities of our naphthalocyanine based photosensitive material.

2. EXPERIMENTAL DETAILS

Our laser source was a 15-fs, 100MHz, Ti:Sa oscillator. Spectral holograms through persistent spectral hole burning were generated using a phase-locked sequence [12] of two writing pulses separated by a time delay τ , in a collinear geometry. The time delay τ between the two writing pulses was interferometrically controlled by a closed loop and feedback control on piezoelectric transducer acting on a mirror. The cw laser beam used for the active stabilization was delivered by a 690 nm laser diode. The energy density per pulse used to write the holograms was about $2\mu\text{J}/\text{cm}^2$ and the exposure time was 30 s. The sample was a commercially available (Aldrich) free-base naphthalocyanine embedded in polyvinylbutyral ($\text{H}_2\text{Npc/PVB}$) [13]. The 400 μm -thick sample, of dye concentration 10^{-4} mol/l, was cooled down to ~ 4.7 K in a CRYOMECH pulse tube cryostat. The absorption peaked at 783 nm and was 20 nm broad (FWHM). The intensity spectrum of the two-pulse sequence presented spectral fringes of period $1/\tau$, which were recorded with a spectrometer provided the time delay was not too long in comparison with the spectral resolution of the spectrometer used. At the reading stage, one of the writing beams was blocked while the other one was attenuated by more than three orders of magnitude and diffracted on the spectral structure formed by the writing pulses.

The diffracted pulse (the echo) was collinear with the incident pulse but delayed by τ . The spectral interference fringes between the incident and diffracted pulses were recorded using a standard spectrometer and a CCD detector. In our case of a collinear geometry, the third pulse and the echo could interfere onto the detector where spectral interference fringes were observed. Amplitude and phase of the photon echo could then be recovered using Fourier transform spectral interferometry (FTSI) [10,14]. This technique is similar to the phase-locked pump-probe to measure the amplitude and phase of photon echo signals [12]. The reading pulse also acts as a reference pulse in FTSI. The reference pulse used to measure the echo pulse was transmitted through the sample. Therefore, common changes of the echo due to its transmission through the sample did not need to be taken into account. The measurement determined the phase difference between the reference and diffracted pulses, resulting in a measurement of the complex transfer function of the programmable linear filter engraved in the PSHB material.

3. RESULTS AND DISCUSSION

The transmission spectrum of the sample after exposure to the two writing pulses clearly exhibited spectral hole burning reflecting the incident spectral fringes restricted to the absorption region of the sample [15]. The relative absorption change was about 20%. The diffraction efficiency of the spectral grating was about 1% at the peak of the diffracted pulse (800nm).

In order to demonstrate the potential of H_2NPC/PVB for applications such as pulse shaping and time reversal, we introduced a chirp on one of the two writing pulses, hereafter called the object pulse. The chirp resulted from the propagation of the laser pulse through a SF58 glass plate of thickness 1.7 cm. The time delay of 2 ps introduced between the two pulses was chosen large enough so as to enable the separation [10], during the reading procedure, of the incident reading pulse from the photon echo, i.e. the emitted pulse we want to analyze through FTSI. The figure 1 shows the spectral amplitude and phase of the emitted pulse, evidencing a quadratic dependence of the spectral phase.

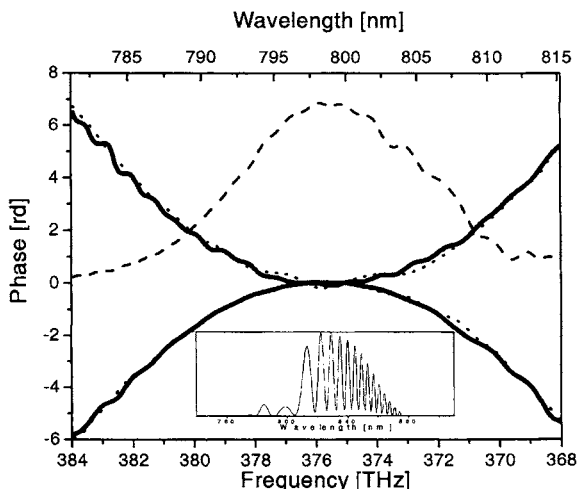


Fig. 1. Demonstration of the phase control of femtosecond chirped pulses. Solid lines: spectral phase of the diffracted pulse for two delays τ and $-\tau$ between the writing pulses. Thin dotted lines: spectral phase difference between the 2 writing pulses for the two cases τ and $-\tau$. The thin dashed line represents the spectral amplitude of the diffracted pulse. Insert: spectral interference fringes between the unchirped and chirped writing pulses at time delay equal 0 at 800nm. The chirp is formed by propagation through a SF58 glass plate of thickness 1.7 cm.

Time reversal was easily achieved by changing the time ordering between the two writing pulses, that is we varied the time delay from $+\tau$ to $-\tau$ and sent the object pulse before the other writing pulse. The recovered spectral phase is now observed to be the opposite of that obtained in the previous case. The dotted curves in figure 1 are the independently measured spectral phase differences between the incident writing pulses for the two cases $+\tau$ and $-\tau$ and they perfectly match the measured phases of the diffracted pulses (solid lines). The

addition of the spectral phase changes for the two cases $+\tau$ and $-\tau$ results in a horizontal flat line, demonstrating the quality of the achieved time reversal. Finally, the insert in figure 1 shows the emitted electric field in time domain, clearly exhibiting the time reversal of the chirped pulse.

The use of optimally shaped pulses to control the temporal evolution of a system is a challenging research field. The flexibility offered by the manipulation of the interacting light in the coherent control of quantum systems has been realized since the middle of the 1980's years and demonstrated for both simple and complex systems such as atoms, molecules, and semiconductors (For a recent review, see [16]). Coherent control of quantum systems may require a more complex phase and amplitude shaping, and for this purpose PSHB materials have the required qualities. The programming of the material can be performed with properly tailored pulse sequences [17]. In principle, it is also possible at the engraving stage, to substitute the preparation pulses, pulse 1 and 2 of the three pulses of the echo sequence, by writing a frequency dependent modulation into the inhomogeneously broadened absorption line of a PSHB burning material with a cw laser controlled both in intensity and frequency. By directly programming the hole burning material, any echo temporal shape should be generated. Persistent hole burning materials could be suitably programmed for coherent control of a process in an open-loop scheme, while transient hole burning could possibly be used in closed-loop scheme. The use of broadband spectrally selective SHB materials for coherent control appears as a challenging prospect, however, besides the material issue, the most important problem to solve should be the realization of highly reliable fast tuned over a few nm wavelength range cw laser sources.

REFERENCES

- [1] D.J. Tannor, R. Kosloff and S.A. Rice, *J. Chem. Phys.* 85 (1986) 5805.
- [2] B. Kohler, V.V. Yakovlev, J. Che, J.L. Krause, M. Messina, K.R. Wilson, N. Schwentner, R.M. Whitnell and Y. Yan, *Phys. Rev. Lett.* 74 (1995) 3360.
- [3] D. Strickland and G. Mourou, *Opt. Commun.* 56 (1985) 219.
- [4] C. Froehly, B. Colombeau and M. Vampouille, in *Progress in Optics*, E. Wolf (Ed.), North-Holland, Amsterdam, 1983, Vol. 20, pp. 65-153.
- [5] A.M. Weiner, *Rev. Sci. Instrum.* 71 (2000) 1929.
- [6] H. Schwöerer, D. Erni, A. Rebane and U.P. Wild, *Opt. Commun.* 107 (1994) 123.
- [7] A. Rebane, M. Drobizhev and C. Sigel, *Opt. Lett.* 25 (2000) 1633.
- [8] O. Ollikainen, C. Nilsson, J. Gallus, D. Erni and A. Rebane, *Opt. Commun.* 147 (1998) 429.
- [9] C. Froehly, A. Lacourt and J.-C. Vienot, *Nouv. Rev. Opt.* 4 (1973) 183 (*in French*).
- [10] L. Lepetit, G. Chériaux and M. Joffre, *J. Opt. Soc. Am. B* 12 (1995) 2467.
- [11] M.F. Emde, W.P. de Boeij, M.S. Pshenichnikov and D.W. Wiersma, *Opt. Lett.* 22 (1997) 1338.
- [12] S. Matsuo and T. Tahara, *Chem. Phys. Lett.* 264 (1997) 636.
- [13] A.V. Turukhin, A.A. Gorokhovskiy, C. Moser, I.V. Solomatina and D. Psaltis, *J. Lumin.* 86 (2000) 399.
- [14] J.-P. Likforman, M. Joffre and V. Thierry-Mieg, *Opt. Lett.* 22 (1997) 1104.
- [15] S. Fraigne, J.-P. Galaup, J.-L. Le Gouët, L. Canioni, B. Bousquet, M. Joffre and J.-P. Likforman, *J. Opt. Soc. Am. B* 20 (2003) 1555.
- [16] T. Brixner and G. Gerber, *Chem. Phys. Chem.* 4 (2003) 419.
- [17] A. Débarre, J.-C. Keller, J.-L. Le Gouët, P. Tchénio and J.-P. Galaup, *J. Opt. Soc. Am. B* 8 (1991) 2529.

Ultrafast motion of water molecules near ions

H. J. Bakker, M. F. Kropman, and A. W. Omta ^a

^aFOM Institute AMOLF, Kruislaan 407, 1098 SJ Amsterdam, The Netherlands

1. INTRODUCTION

Aqueous solvation forms one of the most important but less understood topics of chemical physics. The main problem in the experimental study of aqueous solvation interactions is the distinction of the response of the solvating water molecules from that of the other (bulk) water molecules. With conventional techniques like infrared absorption, NMR, X-Ray and neutron scattering, a lot of knowledge on the *structure* of aqueous solvation shells has been obtained, but very little information on their *dynamics*, because the time scales involved in these techniques are longer than the typical lifetimes of the solvation structures. Hence, our present knowledge of these dynamics mainly originates from molecular dynamics simulations [1,2]. However, recently it was shown that experimental information on the dynamics of solvating water molecules can be obtained by studying the dynamics of the O-H stretch vibrations of these molecules with femtosecond mid-infrared spectroscopy [3]. This information is presented and discussed in this paper.

2. EXPERIMENT

We performed two-color femtosecond mid-infrared pump-probe experiments on dilute (0.1 M) solutions of HDO dissolved in D₂O that contain a high concentration (0.5 - 6 M) of KF, NaCl, NaBr, or NaI. The pulses are tunable between 2.7 and 4 μm , have an energy of ~ 10 μJ , and a duration of approximately 200 fs. The pump and probe pulses are independently tunable and have a bandwidth of 80 and 60 cm^{-1} , respectively.

The pump pulse excites the O-H stretch vibration of approximately 5% of the HDO molecules to the first excited state ($v = 1$). This excitation leads to a bleaching of the linear absorption spectrum ($\ln(T/T_0) > 0$, with T the transmission of the probe and T_0 the transmission of the probe in absence of the pump) due to the depletion of $v = 0$ and stimulated emission out of $v = 1$. In addition, the excitation leads to an induced $1 \rightarrow 2$ absorption ($\ln(T/T_0) < 0$). The latter absorption is redshifted by approximately 270 cm^{-1} with respect to the $0 \rightarrow 1$ transition [4].

3. SPECTRAL DYNAMICS OF HYDRATION SHELLS

In Fig. 1 pump-probe transients of solutions of 6 M NaBr and 1 M NaCl in HDO:D₂O are presented. The probe was polarized at the magic angle (54.7°) with respect to the pump polarization to avoid the measurements being affected by the orientational dynamics of the water molecules. For solutions of NaCl, the largest amplitude is observed for pump and probe frequencies of approximately 3450 cm^{-1} , whereas for solutions of NaBr and

NaI, the largest amplitude is observed for pump and probe frequencies of approximately 3500 cm^{-1} . All transients can be described as a sum of two exponentials, one with a time constant of 800 femtoseconds and one with a much longer time constant. The amplitude of the slow component depends linearly on the concentration of dissolved salt. The time constant of the slow component depends on the nature of the anion, and increases within the halogenic series F^- , Cl^- , Br^- , and I^- . Interestingly, the cation has a much smaller effect on the decay time.

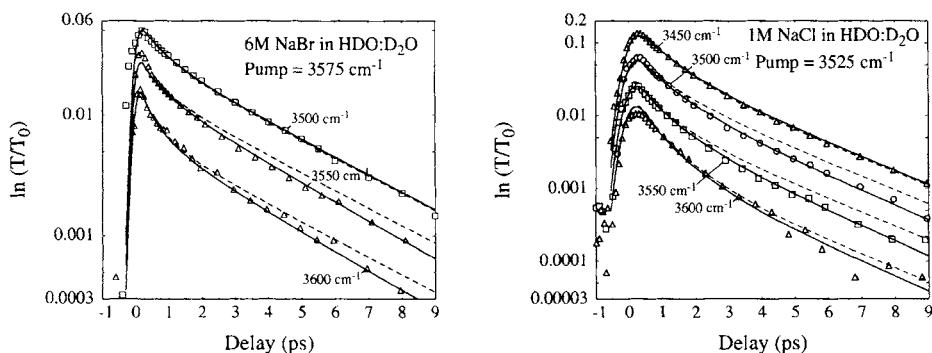


Fig. 1. Pump-probe transients for solutions of 6 M NaBr and 1 M NaCl in HDO:D₂O. The solid curves are calculated with a Brownian oscillator model using a time constant τ_c of 25 ps for the O-H \cdots Br⁻ hydrogen bond and of 12 ps for the O-H \cdots Cl⁻ hydrogen bond. The dashed curves are calculated with the same model using $\tau_c = \infty$.

From the dependence of the time constant and amplitude of the slow component on the nature and concentration of dissolved anions, we conclude that the slow component results from HDO molecules that solvate the anion. The slow component thus mainly represents the vibrational relaxation of an HDO molecule in the first solvation shell of the halogenic anion. The decay time constant of the second component shows a small but significant dependence on the pump and probe frequencies because of the presence of a slow spectral diffusion process with a time constant of approximately 10 picoseconds. Due to this process, excited molecules spectrally diffuse away from the excitation frequency, which leads to a faster decay at probe frequencies close to the pump frequency and to a slower decay at probe frequencies that differ from the pump frequency. In infrared[5] and cw (continuous wave) Raman spectroscopic studies [6] it was found that water molecules form directional O-H \cdots Y⁻ hydrogen bonds with halogenic anions Y⁻. In aqueous systems, the O-H stretch frequency strongly depends on the length of the hydrogen bond that involves the hydrogen atom of the O-H group. Hence, the spectral diffusion likely follows from the (stochastic) modulation of the O-H \cdots Y⁻ (Y⁻ = Cl⁻, Br⁻, I⁻) hydrogen-bond length [7,8]. In order to determine the correlation time constant τ_c of the spectral diffusion, we modeled the data of Fig. 1 with a Brownian oscillator model. All transients can be well fitted with two Brownian oscillators that represent the O-H \cdots O and O-H \cdots Y⁻ components (see Table 1). The results of Table 1 show that the central frequency ω_0 of the absorption band of the O-H \cdots Y⁻ component increases in

the halogenic series Cl^- , Br^- , and I^- , while the width of the absorption band decreases. Both trends reflect a decrease of the strength of the hydrogen-bond interaction between the solvating HDO molecule and the anion.

Table 1. The central frequency ω_0 , width $\Delta\omega$, vibrational lifetime T_1 and spectral diffusion time τ_c of the O-H stretch vibration of different hydrogen-bonded O-H groups.

	ω_0 (cm^{-1})	$\Delta\omega$ (cm^{-1})	T_1 (ps)	τ_c (ps)
O-H \cdots O	3420 ± 10	280 ± 20	0.8 ± 0.1	0.5 ± 0.2
O-H $\cdots\text{Cl}^-$	3440 ± 15	160 ± 15	2.6 ± 0.3	12 ± 3
O-H $\cdots\text{Br}^-$	3470 ± 15	130 ± 15	3.0 ± 0.3	25 ± 5
O-H $\cdots\text{I}^-$	3490 ± 15	105 ± 15	3.7 ± 0.3	18 ± 5

For many hydrogen-bond acceptors the relation between the O-H stretch vibrational frequency and the length of the hydrogen bond has been measured [8,9]. Hence, the width of the O-H $\cdots\text{Y}^-$ absorption component can be used to determine the width of the distribution of O-H $\cdots\text{Y}^-$ hydrogen-bond lengths. For the O-H $\cdots\text{Cl}^-$, O-H $\cdots\text{Br}^-$, and O-H $\cdots\text{I}^-$ hydrogen-bonds, we obtain widths of this distribution of $0.20(0.05)\times 10^{-10}$ m, $0.21(0.05)\times 10^{-10}$ m, and $0.12(0.04)\times 10^{-10}$ m, respectively. These widths are relatively small compared to the width of the O-H \cdots O absorption band of HDO:D₂O of $0.36(0.02)\times 10^{-10}$ m.

The values of τ_c of the solvation shells are surprisingly long in comparison to the value of τ_c of 500 ± 100 fs of the O-H \cdots O hydrogen bond in bulk liquid water, but are quite comparable to the recently calculated residence time of 18 ps of water in the solvation shell of Br^- [10]. However, one should be very careful with this comparison since the characteristic time of the fluctuations of the hydrogen bond is not the same as the residence time in the solvation shell because the breaking of the hydrogen bond does not automatically mean that the water molecule really leaves the shell. The narrow width and long τ_c of the O-H $\cdots\text{Y}^-$ absorption component imply that the first solvation shell forms a stable and well-defined structure. The solvation shells of F^- and of the cations likely show similar dynamics, but unfortunately these dynamics could not be measured because the O-H stretch vibrational lifetime of the water molecules in these solvation shells is comparable to that of bulk HDO:D₂O.

We found that τ_c of the O-H $\cdots\text{Cl}^-$ hydrogen-bond length increases from 14 ± 2 ps at 25 °C, to 24 ± 5 ps at 65 °C, to 30 ± 6 ps at 85 °C. This increase of τ_c can be explained within the framework of the Brownian oscillator model. The time constant τ_c is related to the frequency ω_{HB} of the hydrogen-bond stretch vibration via $\tau_c = \gamma/\omega_{\text{HB}}^2$ [11], with γ the damping of the hydrogen-bond stretch vibration. An increase in temperature leads to a decrease of ω_{HB} , and thus to an increase of τ_c .

4. ORIENTATIONAL DYNAMICS OF HYDRATION SHELLS

To study the orientational relaxation of the excited HDO molecules, we rotated the polarization of the probe pulse by 45 degrees with respect to the pump polarization using a zero-order $\lambda/2$ plate. After the sample the probe is split in two beams, and using two polarizers and two detectors, the transmission changes of the probe parallel to the pump ($\ln(T/T_0)_{\parallel}$) and perpendicular to the pump ($\ln(T/T_0)_{\perp}$) are measured simultaneously.

These signals are then used to calculate the anisotropy parameter R that represents the orientational relaxation of the HDO molecules:

$$R(\tau) = \frac{\ln(T(\tau)/T_0)_{\parallel} - \ln(T(\tau)/T_0)_{\perp}}{\ln(T(\tau)/T_0)_{\parallel} + 2 \ln(T(\tau)/T_0)_{\perp}}. \quad (1)$$

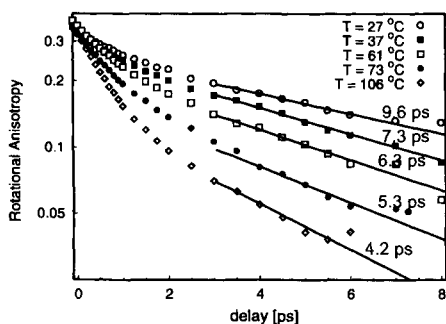


Fig. 2. Anisotropy parameter R as a function of delay τ for a solution of 3 M NaCl in HDO:D₂O at five different temperatures. The pump frequency is 3450 cm⁻¹ and the probe frequency is 3200 cm⁻¹.

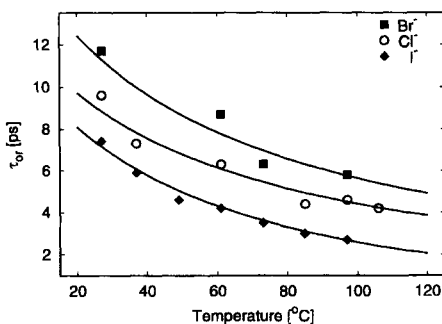


Fig. 3. Measured orientational diffusion time constants τ_{or} of the solvation shells of Cl⁻, Br⁻, and I⁻ as a function of temperature. The solid curves represent fits of the data using Eq. (1).

In Fig. 2, R is presented for a solution of 3 M NaCl in HDO:D₂O at different temperatures. All signals show an overall non-exponential decay, but are close to a single exponential for delays >3 ps. After this delay time, the signals only represent the orientational dynamics of the HDO molecules in the first solvation shell of the Cl⁻ ion, thanks to the difference in lifetimes of the O-H···O and the O-H···Cl⁻ vibrations. At 27 °C, the orientational relaxation time constant τ_{or} of these HDO molecules is 9.6±0.6 ps, which is quite long in comparison with the value of τ_{or} of 2.6 ps of HDO molecules in a solution of HDO in D₂O [12].

In Fig. 3, the orientational diffusion time constants τ_{or} of the first solvation shell of the halogenic anions Cl⁻, Br⁻, and I⁻ are presented as a function of temperature. From the observation that τ_{or} is shorter than τ_c , it follows that the orientational dynamics of the HDO molecules in the first solvation shell of the Cl⁻ ion must result from motions that do not contribute to the spectral diffusion, i.e. that do not affect the length of the O-H···Cl⁻ hydrogen bond. Hence, the observed reorientation represents the orientational diffusion of the complete solvation structure. Also shown in Fig. 3 are fits to the data using the relation between τ_{or} and the temperature T that follows from the Stokes-Einstein relation for orientational diffusion:

$$\tau_{or}(T) = \frac{4\pi\eta(T)r_{h,solv}^3}{3kT}. \quad (2)$$

with $\eta(T)$ the temperature-dependent viscosity, $r_{h,solv}$ the hydrodynamic radius of the solvation structure, and k Boltzmann's constant. The only parameter in this fit is the

radius $r_{h,solv}$. The temperature-dependent viscosities were obtained from the literature [13,14]. For the hydrodynamic radii we find $r_{h,solv}(Cl^-) = 213$ pm, $r_{h,solv}(Br^-) = 237$ pm, and $r_{h,solv}(I^-) = 205$ pm. These radii can be compared to the hydrodynamic radii r_h obtained from the Stokes-Einstein relation for translational diffusion. From the ionic mobility [15], that is directly connected to the translational diffusion, we find $r_h(Cl^-) = 120$ pm, $r_h(Br^-) = 118$ pm, and $r_h(I^-) = 120$ pm. For all halogenic ions, r_h is significantly smaller than $r_{h,solv}$. If $r_{h,solv}$ would equal r_h , the reorientation would be about 8 times as fast, τ_{or} being on the order of 1 ps. This suggests that the (translational) diffusion steps take place for a significant part without the solvation shell, thus reducing the effective size of the ion.

Both r_h and $r_{h,solv}$ are much smaller than expected. The value of r_h is expected to be at least the ionic radius: $r_{ion}(Cl^-) = 181$ pm, $r_{ion}(Br^-) = 196$ pm, and $r_{ion}(I^-) = 220$ pm [15]. Similarly, the value of $r_{h,solv}$ is expected to be comparable to the anion-water hydrogen-bond length: $r_{HB}(Cl^-) = 323$ pm, $r_{HB}(Br^-) = 340$ pm, and $r_{HB}(I^-) = 360$ pm [8]. This deviation illustrates that the Stokes-Einstein relation, in particular the viscosity, is only applicable to macroscopic objects. In the present case the moving objects are of about equal size as the molecules of the viscous liquid. In this regime, the concept of viscosity loses its meaning, and the orientational mobility is governed by the specific interactions between the solvation shell and its surroundings, mainly electrostatic interactions with other ions and hydrogen bonding. If these molecular interactions would have led to the same friction as the macroscopic viscosity, the reorientation would have been 5-10 times slower than observed. Although there is a clear difference in magnitude between friction on a molecular scale and the macroscopic viscosity, their temperature dependence still appears to be quite similar.

5. DYNAMICS BEYOND THE FIRST HYDRATION SHELL

In the previous sections the hydrogen-bond and orientational dynamics of the water molecules in the first solvation shell of halogenic anions were studied. The dynamics of the water molecules *beyond this shell* will give information on the influence of ions on the strength of the hydrogen-bond structure of bulk liquid water. The dynamics of these water molecules can best be studied for solutions of the perchlorate ion (ClO_4^-), because the $OH \cdots ClO_4^-$ absorption band of water molecules in the solvation shell of this anion is quite well spectrally separated from the $OH \cdots O$ absorption band of bulk water molecules. The $OH \cdots ClO_4^-$ absorption band has its maximum at 3575 cm^{-1} , while the absorption band of O-H groups hydrogen-bonded to D_2O molecules peaks at 3400 cm^{-1} .

In Fig. 4 the anisotropy decay is shown for a solution of 6 M $NaClO_4$ in $HDO:D_2O$ using two different combinations of pump and probe frequencies. With a pump frequency of 3575 cm^{-1} and a probe frequency of 3325 cm^{-1} , the decay represents predominantly the orientational relaxation of the $O-H \cdots ClO_4^-$ groups with a time constant τ_{or} of 7.6 ± 0.3 ps. With a pump frequency of 3400 cm^{-1} and a probe frequency of 3150 cm^{-1} , the observed anisotropy decay is mono-exponential and only represents the orientational relaxation of HDO molecules hydrogen bonded to D_2O molecules.

To measure the effect of the presence of ions on the hydrogen-bond structure of bulk water, we studied the concentration dependence of the orientational relaxation of bulk water in aqueous solutions of $Mg(ClO_4)_2$. We chose $Mg(ClO_4)_2$ because Mg^{2+} is considered to be a strong structure-making ion: the viscosity of 1 M $Mg(ClO_4)_2$ is about 30 %

higher than the viscosity of pure water. If the higher viscosity of a $\text{Mg}(\text{ClO}_4)_2$ solution is caused by a homogeneous change in the stiffness of the hydrogen-bond network, the reorientation time of water molecules bonded to other water molecules should increase.

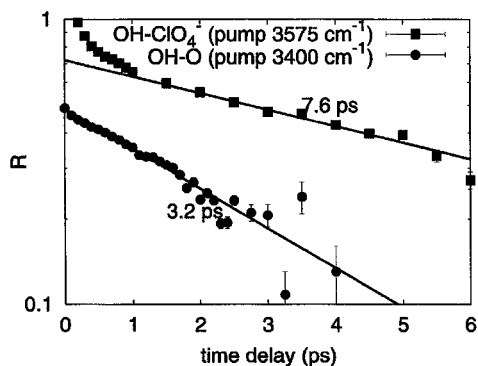


Fig. 4. Anisotropy parameter R as a function of delay τ for a solution of 6 M NaClO_4 in $\text{HDO}:\text{D}_2\text{O}$.

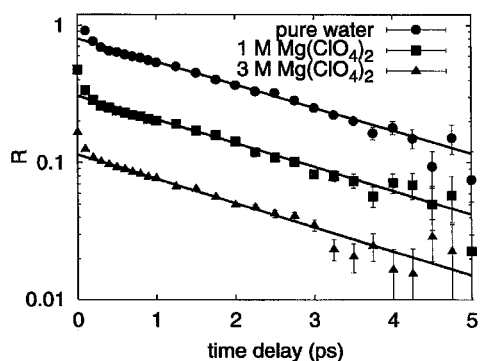


Fig. 5. Delay dependence of R for solutions of 0 M, 1 M, and 3 M $\text{Mg}(\text{ClO}_4)_2$ in $\text{HDO}:\text{H}_2\text{O}$.

In Fig. 5, the measured decay of R for solutions of 0 M, 1 M, and 3 M $\text{Mg}(\text{ClO}_4)_2$ in $\text{HDO}:\text{H}_2\text{O}$ is shown. In these measurements, the $\text{OD}\cdots\text{O}$ band was pumped and probed at the $0\rightarrow 1$ transition using pump and probe pulses at 2500 cm^{-1} . We used the $\text{O}-\text{D}$ vibration to probe the bulk water orientational dynamics, because, due to its long vibrational lifetime of 2 ps, this vibration allows us to measure the anisotropy decay over a much longer delay time interval than when the $\text{O}-\text{H}$ vibration is probed.

Surprisingly, Fig. 5 shows that the decay of R is independent of the salt concentration, which means that the orientational mobility of water-bonded $\text{O}-\text{D}$ groups is not affected by the presence of Mg^{2+} and ClO_4^- ions. These water-bonded $\text{O}-\text{D}$ groups represent both bulk HDO molecules and HDO molecules in the solvation shell of the cation. From fits of the data to a single exponential, we found the same value for τ_{or} of 2.5 ± 0.1 ps at all concentrations. This value agrees well with the orientational correlation time of pure liquid water that was measured with NMR [17] and terahertz spectroscopy [18]. These results show that there is no measurable effect of a high concentration of Mg^{2+} and ClO_4^- ions on the reorientation of water-bonded OD -groups, implying that the ions have a negligible effect on the strength of the hydrogen-bond interactions outside the first solvation shell.

6. CONCLUDING REMARKS

The findings shown in Figs. 2, 3 and 4 show that the orientational mobility of water in ionic solutions is extremely inhomogeneous. In the first solvation shell, the orientational dynamics are observed to be at least a factor of 5 slower than in bulk liquid water, whereas beyond this shell, there is no measurable difference with the bulk.

This means that an aqueous salt solution should not be viewed as a homogeneous liquid with a modified inter-molecular interaction, but rather as a colloidal suspension of inert particles in pure liquid water, with the particles formed by the ions and their first solvation shells. Following this view of an aqueous salt solution, the viscosity at low concentration can be described by the Einstein equation [19]:

$$\frac{\eta - \eta_0}{\eta_0} \approx 2.5\phi$$

with ϕ the volume fraction of the ions and their first solvation shell.

A 30 % increase of the viscosity, as observed for a 1 M $\text{Mg}(\text{ClO}_4)_2$ solution, can be obtained with a solution of 1 M suspended spheres that have a radius of about 3.6 Å. This radius is quite similar to the radius of an ion and its first solvation shell of water molecules. Hence, the increase in viscosity upon adding small spherical ions to liquid water can be fully explained from the rigid nature of the first solvation shell of the ion.

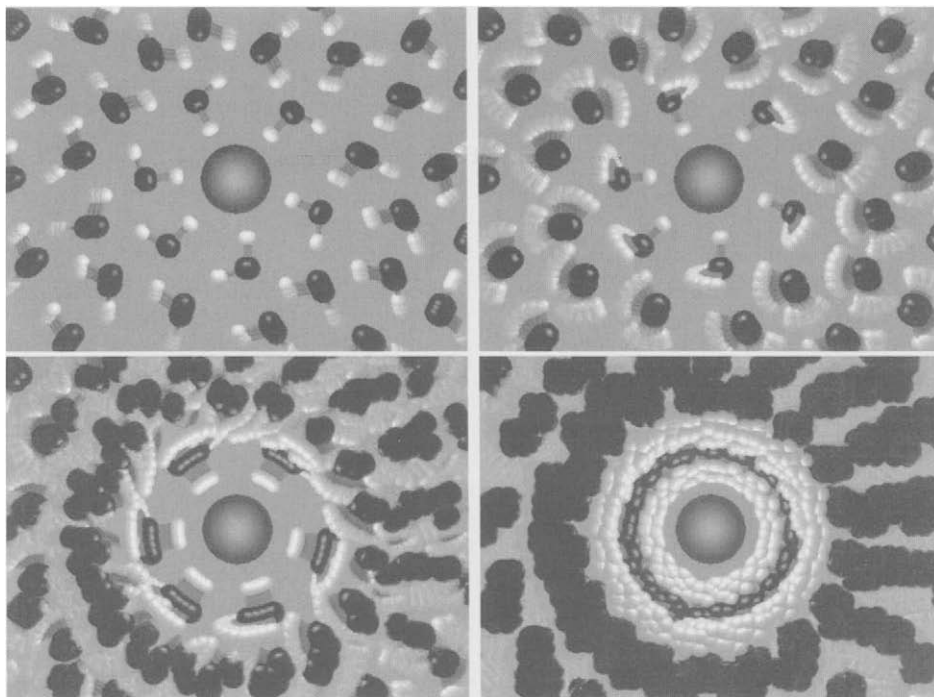


Fig. 6. Schematic pictures of an I^- ion surrounded by water molecules using shutter times of 1 ps (top left) 4 ps (top right), 10 ps (lower left), and 30 ps (lower right).

We now arrive at a rather complete picture of the structure and dynamics of the water molecules near an ion. In Fig. 6 an I^- ion surrounded by water molecules is shown. The

time scales of the different dynamics that take place are illustrated with pictures of the liquid using different shutter times. The top left picture is taken with a shutter time of 1 ps. This time is longer than the hydrogen-bond dynamics ($\tau_c \sim 500$ fs). Hence, the positions of these water molecules are blurred. In the top right picture, the shutter time is 4 ps, which is longer than orientational relaxation time of water molecules outside the first solvation shell of the I^- ion ($\tau_{\text{or}} \sim 2.6$ ps). Hence, both the positions and orientations of these water molecules are blurred. The shutter time of 4 ps is still shorter than the orientational diffusion time constant $\tau_{\text{or}} \sim 8$ ps of the solvation shell, and the characteristic time scale $\tau_c \sim 20$ of the stochastic fluctuations of the O-H... I^- hydrogen-bond length. Hence, the image of the first solvation shell is quite sharp. In the lower left picture, the shutter time is 10 ps, which is longer than the time scale of the orientational diffusion of the first solvation shell. Hence, the orientation of this shell gets blurred, but the distance between the water molecules in the first solvation shell and the I^- ion is still sharp. In the lower right picture, the shutter time is 30 ps, which is longer than all characteristic time scales, so the positions and orientations of all water molecules are no longer well defined. In this picture we can still recognize the radial distribution of the oxygen atoms from the centre of the I^- ion ($g(R)$). This distribution function peaks at the positions corresponding to the first and the second solvation shell.

REFERENCES

- [1] D. E. Smith and L. X. Dang, *J. Chem. Phys.* 100 (1994) 3757.
- [2] K. Hermansson and M. Wójcik, *J. Phys. Chem.* 102 (1998) 6089.
- [3] M. Kropman and H. J. Bakker, *Science* 291 (2001) 2118.
- [4] H. Graener, G. Seifert, and A. Laubereau, *Phys. Rev. Lett.* 66 (1991) 2092.
- [5] P.-Å. Bergström and J. Lindgren, *J. Phys. Chem.* 95 (1991) 8575.
- [6] G. E. Walrafen, *J. Chem. Phys.* 36 (1962) 1035; *ibid* 52 (1970) 4176.
- [7] A. Novak, *Struct. Bonding* 18 (1974) 177.
- [8] W. Mikenda, *J. Mol. Struct.* 147 (1986) 1
- [9] W. Mikenda, S. Steinböck, *J. Mol. Struct.* 384 (1996) 159.
- [10] S. Raugi and M.L. Klein, *J. Am. Chem. Soc.* 123 (2001) 9484.
- [11] G. N. Robertson and J. Yarwood, *Chem. Phys.* 32 (1978) 267.
- [12] H.-K. Nienhuys, R. A. van Santen, and H. J. Bakker, *J. Chem. Phys.* 112 (2000) 8487.
- [13] A. Sacco, A. de Giglio and A. Dell'atti, *J. Chem. Soc., Faraday Trans. I* 77 (1981) 2693.
- [14] D. J. P. Out and J. M. Los, *J. Chem. Sol.* 9 (1980) 19.
- [15] P. W. Atkins, *Physical Chemistry*, Oxford University Press, Oxford, 1990.
- [16] *Water: a comprehensive treatise*, edited by F. Franks (Plenum Press, London, 1973), Vol. 3.
- [17] J.C. Hindman, A. Svirnickas, and M. Wood, *J. Chem. Phys.* 59 (1974) 1517.
- [18] C. Rønne, L. Thrane, P.-O. Åstrand, A. Wallqvist, and S.R. Keiding, *J. Chem. Phys.* 107 (1997) 5319.
- [19] A. Einstein, R. Furth, and A. D. Cowper, *Investigations on the theory of Brownian movement*, Dover, New York, 1926.

Ultrafast vibrational dynamics of hydrogen-bonded dimers in solution

Thomas Elsaesser, Karsten Heyne, Nils Huse, and Erik T.J. Nibbering

Max-Born-Institut für Nichtlineare Optik und Kurzzeitspektroskopie, Max-Born-Str. 2 A,
D-12489 Berlin, Germany

1. INTRODUCTION

Intermolecular hydrogen bonds represent a key structural feature of many molecular systems, including liquid water, alcohols, and biomolecules. For instance, the sequence of hydrogen bonded nucleic base pairs determine the structure and function of DNA. There has been impressive progress in elucidating hydrogen-bonded molecular structure over the last decades. In contrast, the dynamics of hydrogen bonds which occur on a multitude of time scales, and the underlying microscopic interaction mechanisms are much less understood.

Ultrafast vibrational spectroscopy offers a variety of techniques for unraveling the microscopic dynamics of hydrogen bonds occurring in the femto- to picosecond time domain. In particular, different vibrational couplings can be separated in nonlinear experiments by measuring vibrational dynamics in real-time. Both coherent vibrational polarizations and processes of population and energy relaxation have been studied for a number of hydrogen bonded systems in liquids [1].

In this article, we concentrate on hydrogen-bonded cyclic dimers of acetic acid in solution (Fig. 1), a model system with properties characteristic for hydrogen-bonded dimers in general [2-4]: The high-frequency O-H/O-D stretching mode should couple anharmonically to low-frequency modes affecting the geometry of the hydrogen bonds, and to modes in the fingerprint region, among them the O-H/O-D bending and C-O stretching vibrations. In addition, Fermi resonances of the $\nu_{\text{OH/OD}}=1$ state of the O-H/O-D stretching mode with overtone and combination tones of fingerprint vibrations should be relevant for the line shape of the stretching band [4] and might play an important role for population relaxation of the O-H/O-D stretching mode. In dimers with two identical O-H...O or O-D...O hydrogen bonds, excitonic coupling is expected between the two O-H stretching oscillators and - in addition - for the O-H bending, the C=O stretching, and the C-O stretching oscillators. Though such couplings have been invoked to explain the spectral envelope of the O-H/O-D stretching band, their relative strength and role for vibrational dynamics are unresolved. Ultrafast vibrational dynamics of acetic acid dimers have been explored to a very limited extent only. Coupling of the two C=O stretching oscillators has been studied in a series of femtosecond experiments [5] and population relaxation of O-H stretching excitations in picosecond measurements [6].

In the following, we review our recent work on cyclic acetic acid dimers in (nonpolar) solution [7-10]. We address anharmonic couplings of the O-H/O-D stretching oscillators to low-frequency and fingerprint vibrations in two-color pump-probe experiments and explore a potential role of excitonic couplings for ultrafast dynamics by comparing dimers with two identical O-H...O hydrogen bonds with those containing an O-H...O and an O-D...O bond.

2. EXPERIMENTAL TECHNIQUES

Cyclic dimers of CD_3COOH (OH/OH dimers) were prepared by dissolving acetic acid in CCl_4 (concentration 0.2 M), mixed $\text{CD}_3\text{COOH}/\text{CD}_3\text{COOD}$ (OH/OD) dimers by dissolving acetic acid (0.2M) and deuterated acetic acid (1.2M) in CCl_4 [11]. Fig. 1 (a) shows the broad O-H stretching absorption bands of the OH/OH dimers (solid line) and the OH/OD dimers (dashed line).

Ultrafast vibrational dynamics was studied in pump-probe experiments with independently tunable pump and probe pulses. In a first series of measurements, a 100 fs pump pulse excited dimers in the range of the O-H stretching band and the weak delayed probe pulses monitored changes of the O-H stretching absorption. In a second study, the O-H stretching band was excited and absorption changes on the O-H bending and C-O stretching bands were measured. Pump and probe pulses were generated in two separate parametric sources driven by amplified 800 nm pulses from a regenerative Ti:sapphire amplifier (repetition rate 1 kHz, pulse duration 100 fs). The cross correlation between pump and probe

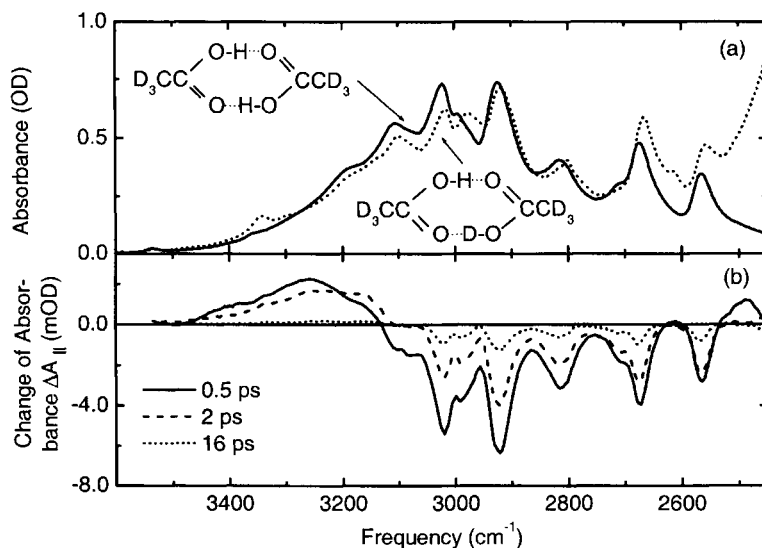


Fig. 1. (a) OH stretching band of OH/OH (solid line) and OH/OD (dotted line) cyclic acetic acid dimers (inset) dissolved in CCl_4 . (b) Change of absorbance $\Delta A_{||}$ of OH/OH dimers measured with parallel polarization of pump and probe for different delay times between pump and probe pulse.

has a temporal width of 130 fs (FWHM), independent of the particular pump and probe frequencies. Experiments were performed both with a spectrally integrated and spectrally dispersed detection (resolution 5 cm^{-1}) of the probe pulses and with parallel and perpendicular linear polarization of pump and probe. The absorbance change corrected for rotational relaxation $\Delta A(t_D)=[\Delta A_{\parallel}(t_D) + 2\Delta A_{\perp}(t_D)]/3$ was derived from measurements with parallel [$\Delta A_{\parallel}(t_D) = -\log(T_{\parallel}(t_D)/T_{\parallel 0})$; $T_{\parallel}(t_D)$, $T_{\parallel 0}$: sample transmission with and without excitation, t_D : delay time) and perpendicular [$\Delta A_{\perp}(t_D)$] polarization. In all experiments, approximately 1 % of the dimers in the sample volume were excited by pump pulses of $1\ \mu\text{J}$ energy.

3. RESULTS AND DISCUSSION

3.1. Nonlinear O-H stretching absorption

Nonlinear O-H stretching absorption spectra of OH/OH dimers are presented in Fig. 1 (b) for 3 different pump-probe delays. The enhanced absorption at frequencies below 2530 cm^{-1} is due to the $\nu_{\text{OH}}=1\rightarrow 2$ transition. The strong bleaching in the center of the steady-state band [cf. Fig. 1 (a)] is caused by the depletion of the $\nu_{\text{OH}}=0$ state and by stimulated emission from the $\nu_{\text{OH}}=1$ state. The spectrum of the absorption decrease displays a series of spectral dips with a spectral position and width that remain unchanged for tens of picoseconds. This finding demonstrates a negligible spectral diffusion within the O-H stretching band on femto- to picosecond time scales. At high probe frequencies between 3150 and 3500 cm^{-1} , one finds a transient increase of absorption due to the vibrationally 'hot' $\nu_{\text{OH}}=0$ ground state which is formed by population relaxation of the $\nu_{\text{OH}}=1$ state. In the hot ground state, the excess energy

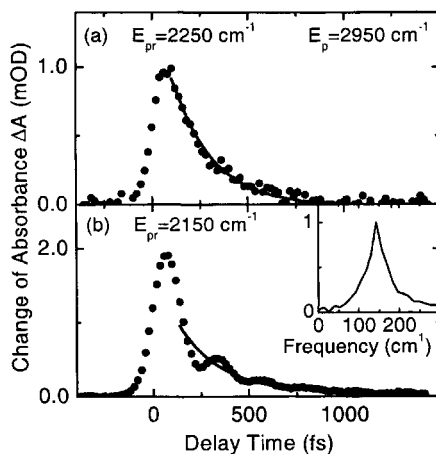


Fig. 2. (a,b) Transient absorption on the $\nu_{\text{OH}}=1\rightarrow 2$ transition of OH/OH dimers (symbols). The spectrally integrated, anisotropy free absorption change ΔA is plotted as a function of the delay time between the pump centered at $E_p=2950\text{ cm}^{-1}$ and the probe centered at E_{pr} . Solid lines: exponential decay with a time constant of 200 fs. Inset of Fig. (b): Fourier transform of the oscillatory component of the transient in Fig. (b) displaying an oscillation frequency of 145 cm^{-1} .

supplied by the absorbed pump photon is contained in a number of modes at lower frequencies whereas the O-H stretching oscillator is deactivated.

The lifetime of the $\nu_{\text{OH}}=1$ state was determined by measuring the time dependent $\nu_{\text{OH}}=1 \rightarrow 2$ absorption. In Fig. 2, we show transients taken with a spectrally integrated detection of the probe centered at $E_{\text{pr}}=2250 \text{ cm}^{-1}$ [Fig. 2 (a), symbols] and at $E_{\text{pr}}=2150 \text{ cm}^{-1}$ [Fig. 2 (b)]. In both transients, the absorption increase decays with a time constant of 200 fs, the $\nu_{\text{OH}}=1$ lifetime. The decay in Fig. 2 (b) is superimposed by oscillations. The Fourier transform of such oscillations gives a frequency of 145 cm^{-1} [inset of Fig. 2 (b)].

Transient absorption changes measured with spectrally integrated probe pulses at higher frequencies exhibit a more complex time evolution. In Fig. 3, we present data taken in the range of the $\nu_{\text{OH}}=0 \rightarrow 1$ transition [Figs. 3 (a,b)] and on the absorption of the hot $\nu'_{\text{OH}}=0$ state [Fig. 3 (c)]. The rise at 2650 and 3250 cm^{-1} displays the 200 fs component, leading to a maximum of the rate-like signal (solid lines) at 600 - 700 fs. The subsequent decay with time constants of 1 ps and 15 ps is related to the transfer of vibrational excess energy from the hot $\nu'_{\text{OH}}=0$ ground state into the surrounding solvent involving collisional interactions between solute and solvent [12]. This vibrational cooling extends over a period of approximately 60 ps [inset of Fig. 3 (c)] after which the dimers are back in their $\nu_{\text{OH}}=0$ ground state.

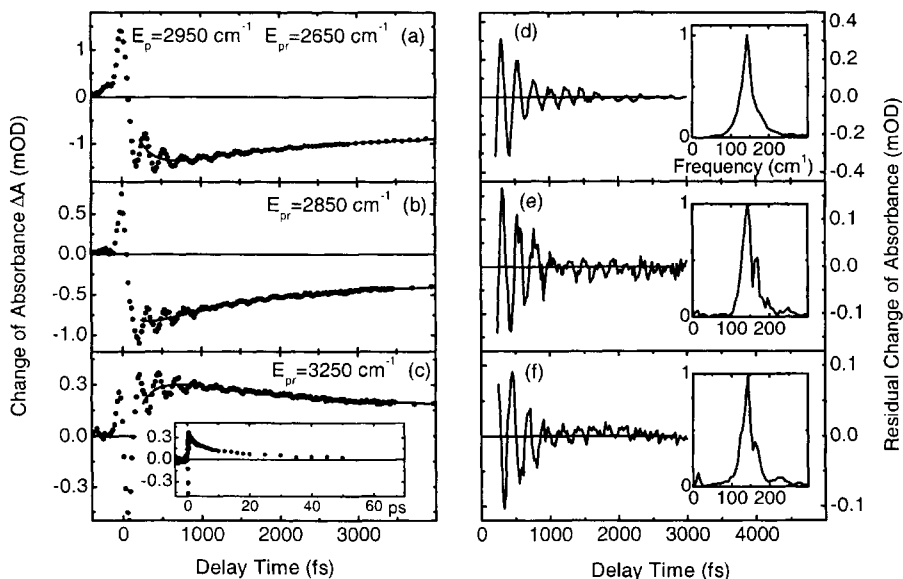


Fig. 3. (a-c) Time resolved changes of the O-H stretching absorption of OH/OH dimers as measured with spectrally integrated probe pulses centered at E_{pr} and corrected for rotational diffusion (symbols, pump pulses centered at $E_{\text{p}}=2950 \text{ cm}^{-1}$). The solid lines represent numerical fits based on exponential kinetic components with time constants of 200 fs, 1 ps and 15 ps. Inset of Fig. (c): Time evolution up to a 70 ps delay time. (d-f) Oscillatory component of the signals in Figs. (a-c) and Fourier transforms (insets).

The transients in Fig. 3 are superimposed by pronounced oscillations. In Figs. 3 (d-f), we plot the oscillatory signal components which were derived from the data in Figs. 3 (a-c) by subtracting the incoherent (rate-like) population kinetics. The oscillations show a common frequency of 145 cm^{-1} and - in addition - contain weak low-frequency components [Fourier transforms in the insets of Figs. 3 (d-f)]. Comparative measurements with OH/OH and OH/OD (mixed) dimers were performed to clarify the microscopic origin of the oscillatory response. In the mixed dimers, one excites a single O-H stretching oscillator, i.e., there is no excitonic coupling of O-H stretching excitations. In Fig. 4, we compare data for OH/OH and OH/OD dimers measured with spectrally resolved probe pulses. The behavior of both systems is identical with the same frequency spectrum of the oscillatory signal components.

We now discuss the origin of the oscillatory absorption changes found in the time-resolved measurements. The frequency of the predominant oscillation of 145 cm^{-1} is identical in the OH/OH and OH/OD dimers. The oscillations cannot be caused by an excitonic coupling of O-H stretching oscillators, as such a coupling is absent in the OH/OD dimers. Instead, they reflect the anharmonic coupling between the O-H stretching excitation at high frequency and low-frequency modes of the dimers [7,8]. As the frequencies of the coupled modes differ by about a factor of 30, an adiabatic separation of time scales is appropriate leading to the schematic picture shown in Fig. 5: The $\nu_{\text{OH}}=0$ and $\nu_{\text{OH}}=1$ states define potential energy surfaces for the quantized low-frequency modes. In the OH/OD dimers with a single O-H stretching oscillator, the coupling results in a progression of vibrational absorption lines for each low-frequency coordinate (Fig. 5 left, arrows). In the presence of two O-H stretching oscillators, excitonic coupling leads to a splitting of the $\nu_{\text{OH}}=1$ potential energy surface which has been described on the basis of cyclic vibrational coordinates $q_{g,u}=q_{\text{OH}1}\pm q_{\text{OH}2}$ and $Q_{i,g,u}=Q_{i1}\pm Q_{i2}$ with $C_2q_{g,u}=\pm q_{g,u}$ and $C_2Q_{i,g,u}=\pm Q_{i,g,u}$ for the O-H stretching and the low-frequency modes i (hydrogen bonds 1 and 2, $i=1,2,\dots$, C_2 : operator for an in-plane rotation of the planar

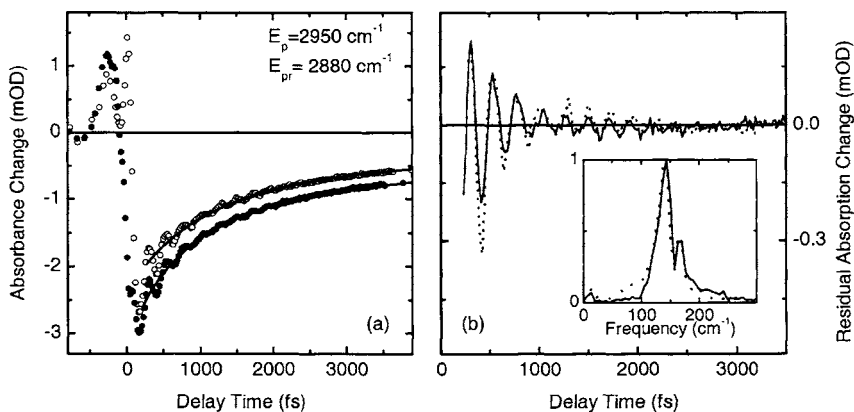


Fig. 4. (a) Time resolved changes of O-H stretching absorption in OH/OH (solid symbols) and OH/OD dimers (open circles) measured with parallel polarization of pump and probe and spectrally resolved detection of the probe at 2880 cm^{-1} . Solid lines: Calculated decay with time constants of 1 and 15 ps. (b) Oscillatory signal components from OH/OH (solid line) and OH/OD dimers (dotted line). The Fourier transforms shown in the inset display a major frequency component at 145 cm^{-1} in both cases.

dimer by π) [2]. Infrared transitions occur between q_u states and two different progressions exist in $Q_{i,u}$ coordinates between the $v_Q=0$ and v_Q levels and from the $v_Q=1$ to v_{Q+} levels (Fig. 5 right). In thermal equilibrium, a single dimer contributes to only one of such progressions as it populates either the $v_Q=0$ or $v_Q=1$ state.

In the femtosecond experiments, the broadband pump pulse generates a coherent superposition of vibrational polarizations on all progression lines overlapping with the pulse spectrum. A quantum coherent excitation, i.e., a low-frequency wavepacket, is generated both in the $v_{OH}=1$ states and - through an impulsive Raman process in the $Q_{i,g}$ coordinates - in the $v_{OH}=0$ state. The wavepacket motion modulates - via anharmonic coupling - the O-H stretching absorption, giving rise to the oscillations found in the pump-probe transients. In each OH/OH dimer, quantum coherence is generated in only one of the progressions, depending on which v_Q level is populated initially. Thus, quantum beats with a frequency determined by the excitonic coupling are absent, i.e., excitonic coupling is suppressed in the nonlinear response. The oscillation frequency of 145 cm^{-1} is close to that of the dimer stretching mode which has been observed in the steady state Raman spectra and affects the length of the intermolecular hydrogen bonds. Our data clearly demonstrate that this motion is underdamped, leading to a periodic change of the hydrogen bond length for picoseconds.

The multi-level character of the coherent O-H stretching polarization has been observed in recent 2- and 3-pulse photon echo studies [9]. The 2-pulse photon echo signal displays a fast initial decay followed by recurrences that are caused by the long-lived coherence on the anharmonically coupled low-frequency modes. One finds a dephasing time of the O-H stretching polarization of 200 fs, in good agreement with the 50 cm^{-1} width of the spectral dips in Fig. 1 (b). Such results demonstrate a predominant homogeneous broadening of the O-H stretching band.

3.2. Anharmonic coupling of the O-H stretching to fingerprint vibrations

Fermi resonances of the $v_{OH}=1$ state with over- and combination tones of modes in the fingerprint region are considered a key element determining the spectral envelope of the O-H stretching bands of cyclic carboxylic acid dimers. In principle, such Fermi resonances open up channels for population relaxation of the O-H stretching modes through the O-H bending

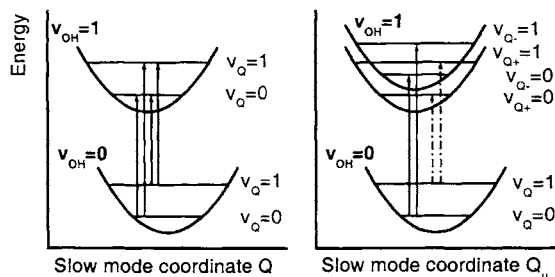


Fig. 5. Schematic potential energy diagram of a low-frequency mode anharmonically coupled to the O-H stretching oscillator in the OH/OD dimer (left) and the OH/OH dimer (right).

and other fingerprint vibrations, a scenario that has been analyzed theoretically [13,14]. For carboxylic acid dimers, the relevance of such relaxation pathways and the more general problem of the underlying anharmonic couplings has remained mainly unexplored. In the following, we present direct evidence for pronounced anharmonic couplings between the O-H stretching oscillators and fingerprint vibrations.

The vibrational bands of the O-H bending and C-O stretching modes are shown in Fig. 6 (a). After excitation of the O-H stretching band, one observes a transient bleaching at the position of the steady-state bands and an enhanced absorption on the red side [Fig. 6 (b)]. The kinetics of bleaching and enhanced absorption is very similar, displaying a perturbed free induction decay at negative delay times and a slow decay with a 15 ps time constant for positive delay times [Fig. 6 (c)]. Different kinetics are observed after direct excitation of the bending mode [Fig. 6 (d)]. Here, the perturbed free induction decay at negative delay times is followed by a fast decay at early positive delay times and the slower 15 ps component. The fast decay with a time constant of 250 fs reflects the depopulation of the $v=1$ state of the O-H bending mode, i.e., the O-H bending lifetime.

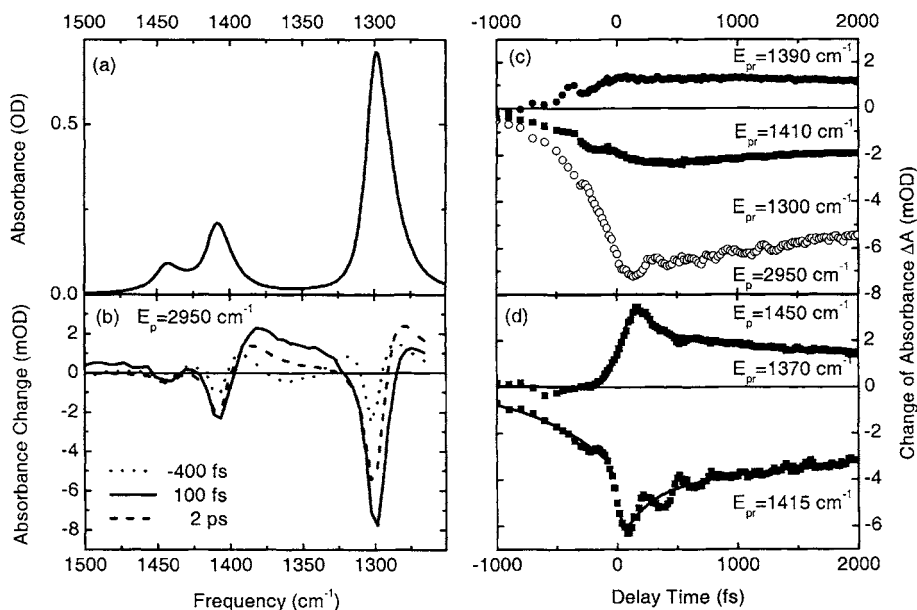


Fig. 6. (a) Linear O-H bending absorption around 1415 cm⁻¹ and C-O stretching band at 1300 cm⁻¹. (b) Transient absorption spectra measured for delay times of -400 fs, 100 fs, and 2 ps after excitation of the O-H stretching band by pulses centered at 2950 cm⁻¹ (parallel polarization of pump and probe). (c) Time resolved, anisotropy free absorption changes at different probe energies E_{pr} after excitation at $E_p=2950$ cm⁻¹. The signals display a perturbed free induction decay at negative delay times. (d) Time resolved, anisotropy free absorption changes measured with excitation of the O-H bending mode by pulses centered at $E_p=1450$ cm⁻¹ (symbols). Solid line: Exponential decay with time constants of 250 fs and 15 ps.

The transients in Fig. 6 (c) display perturbed free induction decays of the O-H bending and C-O stretching modes after excitation of the O-H stretching mode, i.e., such polarizations generated by the probe pulse are perturbed by the pump. This fact gives evidence of the coupling of the O-H stretching mode to the fingerprint modes. In Fig. 6 (c), the bleaching signal at 1410 cm^{-1} and the enhanced absorption at 1390 cm^{-1} exhibit a simultaneous rise without any fast kinetics at early positive delay times. Such absorption changes are dominated by a transient redshift of the O-H bending absorption [spectra in Fig. 6 (b)] which is due to the anharmonic coupling to the O-H stretching oscillator excited by the pump pulse [10]. After the decay of the O-H stretching population (Fig. 2), a similar redshift is caused by other modes which are populated through relaxation of the O-H stretching mode and also couple to the O-H bending mode. Eventually, the redshift decays by vibrational cooling to the solvent with a 15 ps time constant. Compared to such absorption changes caused by anharmonic couplings, effects due to a transient population of the O-H bending mode via relaxation of the O-H stretching mode are of minor relevance. A contribution due to population relaxation should show fast relaxation kinetics, e.g., determined by the $v=1$ lifetime of the O-H bending mode [Fig. 6 (d)]. Such contributions are absent in the measured signals.

In conclusion, we have studied different types of vibrational couplings in cyclic acetic acid dimers in solution. Femtosecond two-color pump-probe experiments reveal underdamped low-frequency motions along intermolecular hydrogen bond coordinates which are induced by excitation of the anharmonically coupled O-H stretching mode. Effects of excitonic coupling of two O-H stretching oscillators are absent in the ultrafast nonlinear response. The O-H stretching mode displays strong couplings to the O-H bending and C-O stretching modes, resulting in a transient redshift of such vibrational lines after O-H stretching excitation. A similar behavior is expected for a larger class of hydrogen bonded dimers, including those in biomolecules.

This work has been supported by the Deutsche Forschungsgemeinschaft (Sonderforschungsbereich 450).

REFERENCES

- [1] H.J. Bakker, in: Ultrafast hydrogen bonding dynamics and proton transfer processes in the condensed phase, T. Elsaesser, H.J. Bakker (Eds.), Kluwer, Dordrecht 2002, p. 31.
- [2] Y. Marechal, and A. Witkowski, *J. Chem. Phys.* 48 (1968) 3697.
- [3] Y. Maréchal, *J. Chem. Phys.* 87 (1987) 6344.
- [4] G.M. Florio, T.S. Zwier, E.M. Myshakin, K.D. Jordan, and E.L. Sibert, *J. Chem. Phys.* 118 (2003) 1735.
- [5] M. Lim, and R.M. Hochstrasser, *J. Chem. Phys.* 115 (2001) 7629.
- [6] G. Seifert, T. Patzlaff, and H. Graener, *Chem. Phys. Lett.* 333 (2001) 248.
- [7] K. Heyne, N. Huse, E.T.J. Nibbering, and T. Elsaesser, *Chem. Phys. Lett.* 369 (2003) 591.
- [8] K. Heyne, N. Huse, E.T.J. Nibbering, and T. Elsaesser, *J. Phys. Condens. Matter* 15 (2003) S129.
- [9] N. Huse, K. Heyne, J. Dreyer, E.T.J. Nibbering, and T. Elsaesser, *Phys. Rev. Lett.*, in press.
- [10] K. Heyne, N. Huse, E.T.J. Nibbering, and T. Elsaesser, *Chem. Phys. Lett.*, in press.
- [11] Y. Fujii, H. Yamada, and M. Mitzuta, *J. Phys. Chem.* 92 (1988) 6768.
- [12] T. Elsaesser, and W. Kaiser, *Annu. Rev. Phys. Chem.* 42 (1991) 83.
- [13] R. Rey, and J.T. Hynes, *J. Chem. Phys.* 104 (1996) 2356.
- [14] C.P. Lawrence, and J.L. Skinner, *J. Chem. Phys.* 119 (2003) 1623.

2D photon-echo spectroscopy of hydrogen-bond dynamics in liquid water

M.S. Pshenichnikov, S. Yeremenko, and D.A. Wiersma

Ultrafast Laser and Spectroscopy Laboratory, Materials Science Centre
University of Groningen, Nijenborgh 4, 9747 AG Groningen, The Netherlands

1. INTRODUCTION

The complexity of the physical properties of liquid water is largely determined by the presence of a three-dimensional hydrogen bond (HB) network [1]. The HB's undergo continuous transformations that occur on ultrafast timescales. The molecular vibrations are especially sensitive to the presence of the HB network. For example, the spectrum of the OH-stretch vibrational mode is substantially broadened and shifted towards lower frequencies if the OH-group is involved in the HB. Therefore, the microscopic structure and the dynamics of water are expected to manifest themselves in the IR vibrational spectrum, and, therefore, can be studied by methods of ultrafast infrared spectroscopy. It has been shown in a number of ultrafast spectroscopic experiments and computer simulations that dephasing dynamics of the OH-stretch vibrations of water molecules in the liquid phase occurs on sub-picosecond timescales [2-14].

The technique of photon echo peak shift (EPS) allows obtaining the most direct information about the frequency fluctuation correlation function [15,16]. Recent EPS experiments on OH-stretch vibration of HDO molecules in liquid D₂O revealed rather unexpected results [17]. The EPS could not be straightforwardly explained in the framework of the already existing theories of molecular dynamics in water. The transient grating (TG) signal exhibited an atypical behavior as well. It decayed mono-exponentially up to about 2 ps and after that leveled-off to a constant offset for the whole experimentally achievable region (~100 ps). It has been suggested [17] that the EPS and TG signals at long delays were largely determined by the blue shift of the absorption spectrum of the probe molecule (HDO) as a result of the temperature increase due to absorption of the pump pulses. The most important outcome of this model was the supposition that the frequency fluctuation correlation function had an unexpectedly long component with a characteristic time of the order 5-15 ps. Furthermore, the thermal blue shift of the chromophore spectrum of ~20 cm⁻¹ was assumed to describe the experimental data adequately. This value can be readily recalculated into an ~30 K temperature raise of the sample [18]. However, a simple estimate on the basis of the excitation pulse energy (~5 μJ), absorption (OD~0.6), focal volume (300-μm thickness and ~80-μm focal diameter), and the water heat capacity (4.16 kJ/mol), yields a temperature raise of <1 K, that is substantially lower than the required value.

In this contribution we present a study of ultrafast dynamics in liquid water employing *heterodyne-detected* TG and EPS techniques. Heterodyne detection allows us to separate the genuine photon echo signal that contains information on water dynamics, from thermal effects. The analysis of the experimental EPS data that includes thermal effects yields a 700-fs

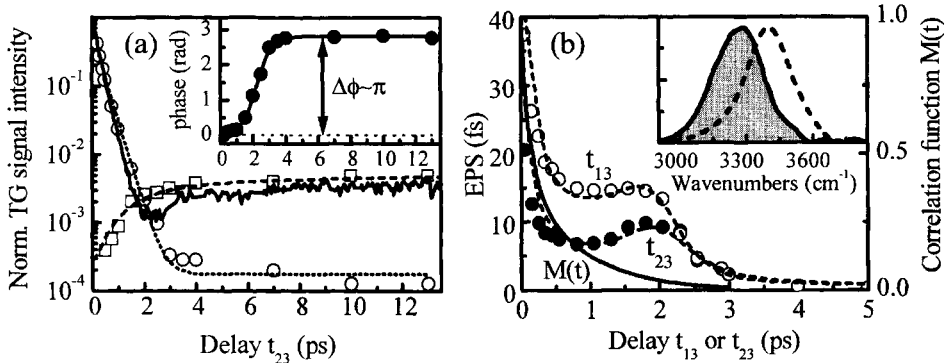


Fig.1. (a): Experimental TG signal (solid line) and amplitudes of its additive components: chromophore response (open circles) and solvent response (open squares) as found from the analysis of heterodyne-detected TG data. Inset: the phase of the TG signal. (b): Experimental EPS data for the fixed delays t_{13} (empty circles) and t_{23} (solid circles), and the theoretical simulations (lines). Inset: the excitation pulse spectra (shaded contour) and the absorption spectrum of the OH-stretch vibration of HDO molecules in D_2O (dashed line).

time constant for the slowest component. This value is in perfect agreement with our previous findings from heterodyne-detected photon echo experiments [19].

2. EXPERIMENTAL

The EPS experiments were carried out according to the procedure described in Ref. [20]. The sample, used in experiments, was a 0.6 M solution of HDO molecules in heavy water at room temperature (maximal OD \sim 0.6). The solution was pumped through a sapphire nozzle to form 100- μ m thick, free-standing jet, that was positioned at the intersection of the laser beams. Use of the free-standing jet instead of a sample cell allowed us to avoid unwanted complications such as temporal broadening of the ultrashort pulses, their adverse scattering, and cross-phase modulation. The excitation pulses were \sim 70 fs in duration and centered around \sim 3 μ m [19]. The excitation pulse spectra and the absorption spectrum of the OH-stretch vibration of HDO molecules in D_2O are shown in the inset to Fig.1b.

3. RESULTS AND DISCUSSION

The TG signal of the OH-stretch vibrational mode of HDO molecules dissolved in D_2O is shown in Fig.1a by a solid line. The initial part of the signal decays with a time constant of \sim 700 fs that is consistent with the population lifetime [4]. However, after reaching a minimum around 2 ps the TG signal begins to *grow* and finally levels-off at \sim 10 ps.

Combining TG experiment with heterodyne detection enabled us to obtain amplitudes and phases of the transient nonlinear polarizations. At short delays the response is mainly determined by the HDO molecules (Fig.1a, open circles). However, at long delays the characteristics of the response change drastically: it narrows in time, its phase is shifted by $\sim\pi$ (Fig.1a, inset), and its spectrum becomes identical to the spectrum of the probe pulse.

Therefore, the TG signal should originate from instantaneous nonlinearity, and for this reason, can *not* be related to HDO. This makes us conclude that the TG signal at long delays results from the grating written in the solvent, i.e. D₂O. The analysis of heterodyne detected TG signal at different delay times yields the dynamics of the amplitudes of the on-resonant (HDO) and off-resonant (D₂O) contributions to the total signal (Fig. 1a).

The mechanism of the solvent response appears in the following way. The population (absorption) spatial grating originally imprinted in HDO by the excitation pulses, relaxes with a lifetime of ~ 700 fs (Fig. 1b, open circles). The energy, stored in the grating, is released by the chromophore to the surrounding solvent molecules (D₂O) giving rise to an increase in local temperature. The temperature raise leads to modifications of the shape and amplitude of the D₂O stretching mode absorption band at $4.5 \mu\text{m}$ and, hence, both absorption and refractive index spatial gratings are being formed. The former is of a little importance for the TG signal at $3 \mu\text{m}$ because its amplitude scales with the inverse squared of the detuning ($\sim 1000 \text{ cm}^{-1}$). However, the spatial modulations of the D₂O refractive index decrease much slower - as the inverse detuning. Therefore, the probe pulse is scattered of the off-resonance grating imprinted in the solvent refractive index (Fig. 1a, open squares). This is reflected in the phase of the heterodyned signal that is almost π -shifted compared to the signal phase at short delays (Fig. 1a, inset). Destructive interference between the chromophore and solvent signals leads to the pronounced gap in the TG signal around 2 ps where the amplitudes of both contributions become equal. The temporal build-up of the refractive index grating is well described by the macroscopic heat diffusion equation (Fig. 1a, dashed line) with a time constant of ~ 1.5 ps.

On the basis of the experimental data we have developed a self-consistent model for the description of the IR photon echo experiments on liquid water. The model comprises the nonlinear and thermal effects and therefore readily allows simulation of the experimental data at delays where the thermal contribution is significant (i.e., longer than 1 ps). In addition to the mechanism described above, the refractive index grating in D₂O originates partly from direct absorption of the excitation pulses by the solvent ($\sim 10\%$ of the total TG signal at long delays). Also, the absorption and refracted index gratings imprinted in HDO, give rise to the plateau in the chromophore response at long delays (Fig. 1a, open circles). The heterodyne-detected TG experiment clearly shows that its relative amplitude does not exceed 10% of the final TG signal which is fully consistent with the estimated local temperature raise of ~ 1 K. Note that only this thermal contribution was included in the previous model [17].

The developed model was applied to the EPS experiment (Fig. 1b) to extract information on the water dynamics. Similar to the previous report [17], the EPS function decreases rapidly at a time scale of ~ 0.5 ps, then raises again at ~ 2 ps, and finally falls off to zero. The EPS functions acquired while keeping the delays t_{13} (empty circles) and t_{23} (solid circles) fixed [20], are shifted along the vertical axis which is a consequence of the relatively short excited-state lifetime (700 fs). The peak in the EPS function around ~ 2 ps is explained in the framework of our model as arising from interference between the chromophore and solvent responses. The delicate balance between phases of genuinely nonlinear and thermal contributions as the delay t_{12} between the two excitation pulses is increased, leads to the enhancement of the integrated signal that is measured in the EPS experiment.

To model the experimental data we used a global-fit procedure to simulate EPS, integrated TG, heterodyne-detected TG, and the linear absorption spectrum simultaneously. The pulse shape and phase were explicitly taken into account, which is of paramount importance for the adequate description of the experimental data. We applied a stochastic modulation model with a bi-exponential frequency fluctuation correlation function of the following form:

$$M(t) = \langle \delta\omega(t)\delta\omega(0) \rangle = \Delta_{fast}^2 \exp(-\Lambda_{fast} t) + \Delta_{slow}^2 \exp(-\Lambda_{slow} t) \quad (1)$$

The quality of the fit is excellent as can be judged from Fig.1(b). The following parameters of the frequency correlation function (Fig.1b, solid line) were obtained in the simulations: $1/\Lambda_{fast} \cong 130$ fs, $\Delta_{fast} \cong 90$ cm⁻¹, $1/\Lambda_{slow} \cong 700 \pm 100$ fs, $\Delta_{slow} \cong 65$ cm⁻¹. These results are in very good agreement with our previous findings from heterodyne-detected two-pulse photon echo experiments [19].

4. CONCLUSION

Our experiments and numerical simulations have proven that interference between chromophore and solvent responses greatly obscures the experimental observables in IR spectroscopy on water at waiting times >0.5 ps. However, the water dynamics can still be obtained if the thermal effects are carefully characterized and self-consistently included in the model. This results in the longest time scale for the frequency correlation function of 700 fs.

REFERENCES

- [1] F. Franks, in F. Franks (Eds.), *Water: A Comprehensive Treatise*, Plenum Press, New York, 1972.
- [2] G. M. Gale, G. Gallot, F. Hache, N. Lascoux, S. Bratos, J-C. Leicknam, *Phys. Rev. Lett.*, **82** (1999) 1068.
- [3] H.J. Bakker, H-K Nienhuys, G. Gallot, N. Lascoux, G. M. Gale, J-C. Leicknam, S. Bratos, *J. Chem. Phys.*, **116** (2002) 2592.
- [4] S. Woutersen, H. J. Bakker, *Phys. Rev. Lett.*, **83** (1999) 2077.
- [5] R. Jimenez, G. R. Fleming, P. V. Kumar, M. Maroncelly, *Nature*, **369** (1994) 471.
- [6] P. Hamm, M. Lim, R. M. Hochstrasser, *Phys. Rev. Lett.*, **81** (1998) 5326.
- [7] F. W. Starr, J. K. Nielsen, H. E. Stanley, *Phys. Rev. Lett.*, **82** (1999) 2294.
- [8] F. Sciortino, P. H. Poole, H. E. Stanley, S. Havlin, *Phys. Rev. Lett.*, **64** (1990) 1686.
- [9] A. Luzar, D. Chandler, *Phys. Rev. Lett.*, **76** (1996) 928.
- [10] A. Luzar, *J. Chem. Phys.*, **113** (2000) 10663.
- [11] C. P. Lawrence, J. L. Skinner, *Chem. Phys. Lett.*, **369** (2003) 472.
- [12] R. Rey, K. B. Moller, J. T. Hynes, *J. Phys. Chem.*, **A106** (2002) 11993.
- [13] M. Diraison, Y. Guissani, J-C. Leicknam, S. Bratos, *Chem. Phys. Lett.*, **258** (1996) 348.
- [14] A. Piryatinski, C. P. Lawrence, J. L. Skinner, *J. Chem. Phys.*, **118** (2003) 9672.
- [15] W. P. de Boeij, M. S. Pshenichnikov, D. A. Wiersma, *Chem. Phys. Lett.*, **253** (1996) 53.
- [16] T. Joo, Y. Jia, J-Y. Yu, M. J. Lang, G. R. Fleming, *J. Chem. Phys.*, **104** (1996) 6089.
- [17] J. Stenger, D. Madsen, P. Hamm, E. T. J. Nibbering, T. Elsaesser, *J. Phys. Chem.*, **A106** (2002) 2341.
- [18] T. Iwata, J. Koshoubu, C. Jin, Y. Okubo, *Applied Spectroscopy*, **51** (1997) 1269.
- [19] S. Yeremenko, M. S. Pshenichnikov, D. A. Wiersma, *Chem. Phys. Lett.*, **369** (2003) 107.
- [20] W. P. de Boeij, M. S. Pshenichnikov, D. A. Wiersma, *J. Phys. Chem.*, **100** (1996) 11806.

Three-dimensional spectroscopy of vibrational energy relaxation in liquids.

Z. Wang, A. Pakoulev, Y. Pang and D. D. Klott*

School of Chemical Sciences, University of Illinois at Urbana-Champaign, 600 S. Mathews Ave., Urbana, IL 61801

ABSTRACT

A three-dimensional vibrational spectroscopy technique with mid-IR pumping and incoherent anti-Stokes Raman probing is used to study vibrational energy relaxation (VR) in hydrogen-bonded liquids. New results on spectral diffusion and vibrational relaxation of OH stretching ν_{OH} of water are presented. Vibrational energy transfer down a molecular chain is probed with angstrom spatial resolution in a series of alcohols where ν_{OH} is pumped and energy transfer through methylene $-\text{CH}_2-$ to terminal methyl $-\text{CH}_3$ groups is probed.

1. INTRODUCTION

Vibrational energy relaxation (VR) in liquids is a fundamental process in chemical physics that remains poorly understood. When a parent vibration is excited, it typically decays on the picosecond time scale. In polyatomic molecules with many vibrational states, excitation of a higher frequency parent vibration leads to a complicated chain of events termed vibrational cooling (VC). In VC, parent decay could excite one or more daughter vibrations. The leftover energy is transferred to collective excitations of the liquid [1]. Ultimately all the daughter and higher energy collective excitations will decay in secondary processes resulting in a bulk increase in the thermodynamic temperature by an amount ΔT [2-4]. In the past several years, a number of multidimensional vibrational spectroscopy techniques have been used to study liquids. Most of these techniques involve vibrational coherences, so they are of limited use in probing VR. Although coherence decays can sometimes be related to population relaxation, successive generation of daughter vibrations is essentially impossible to observe with a coherent probe. In the 1970's, Laubereau and Kaiser combined picosecond mid-IR excitation with an incoherent anti-Stokes Raman probe [5]. With the lasers available at that time, they could study the decay of parent CH and OH stretching transitions ν_{OH} and ν_{CH} of several liquids and in certain cases observe a few of the daughter vibrations [6]. In our laboratory we have developed a powerful spectrometer based on a 1 ps amplified Ti:sapphire laser system with dual optical parametric amplifiers. This spectrometer produces a powerful mid-IR pump pulse tunable in the $3700\text{-}2200\text{ cm}^{-1}$ range, plus a fixed 532 nm probe pulse. The combination of a tunable pump pulse and multichannel detection of the incoherent anti-Stokes spectrum leads to an important type of 3D vibrational spectroscopy [7]. The three dimensions are the pump wavenumber, the probe wavenumber and time. In this paper, we discuss two problems studied with 3D vibrational spectroscopy: (1) VR and spectral

* Author to whom correspondence should be addressed. Electronic mail dlott@scs.uiuc.edu

diffusion in water, and (2) vibrational energy transfer within molecules probed with angstrom spatial resolution.

2. WATER STUDIES

Water is an interesting and important liquid. As the combination of multidimensional vibrational spectroscopy and molecular dynamics helps us understand water better, more and more complex dynamics have been revealed [8,9]. We can briefly explain why a liquid of triatomic molecules turns out to be so immensely complicated: *Water's three atoms bestow all the complexity of multiple intramolecular vibrations, and in addition in water there are more hydrogen bonds (~3.57) than atoms!*

Multidimensional spectroscopy of ν_{OH} provides new information about spectral diffusion and VR. With a few exceptions [3,4], most experiments have concentrated on dilute solutions of the HOD molecule in D_2O (reviewed in ref. [10]). Our recent work has focused on water itself. Although one might expect ν_{OH} hydrogen bond dynamics to be similar in HOD/ D_2O and water, VR is entirely different. Figure 1 is a schematic of the energy levels for ν_{OH} VR in HOD/ D_2O and in water. There are seven VR pathways for ν_{OH} of HOD/ D_2O [10], but only two in water [11]. The two water ν_{OH} VR pathways are $\nu_{\text{OH}} \rightarrow \delta_{\text{H}_2\text{O}}$ (~1700 cm^{-1}) and $\nu_{\text{OH}} \rightarrow$ ground state (~3350 cm^{-1}), where $\delta_{\text{H}_2\text{O}}$ is the water bending vibration near 1640 cm^{-1} , and the values in parentheses indicate the amount of energy deposited into the collective vibrations of the liquid. Back in 2000, our group studied VR of HOD/ D_2O with ν_{OH} pumping [12]. To illustrate the complexities of VR in this system, Fig. 1 also shows some IR-Raman data. We have directly observed the decay of the parent and the appearance and decay of three daughter vibrations, $\nu_{\text{OD}}(\text{D}_2\text{O})$, δ_{HDO} and $\delta_{\text{D}_2\text{O}}$.

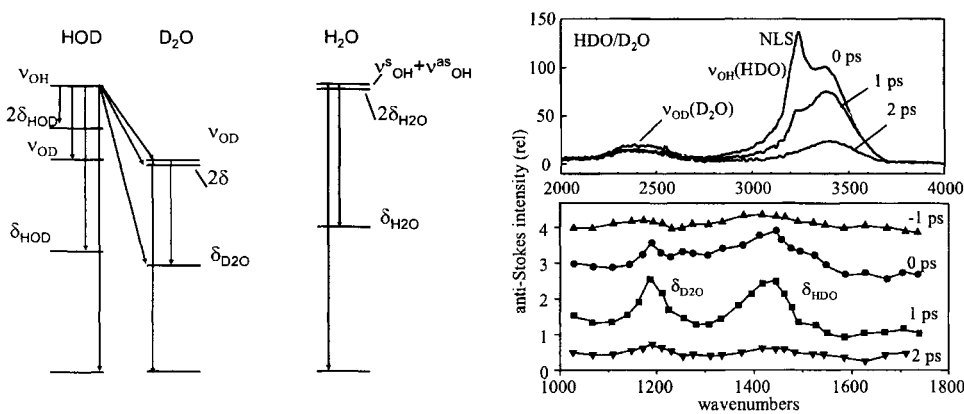


Fig. 1. (left) Vibrational relaxation (VR) pathways of ν_{OH} of HOD in D_2O and of ν_{OH} of water. For HOD there are four intramolecular pathways and three intermolecular pathways to the D_2O solvent. For water, there are only two pathways, although the daughter $\delta_{\text{H}_2\text{O}}$ might be located on the same or on an adjacent molecule. In each pathway the leftover energy appears as excitations of lower frequency collective modes of the liquid. (right) Anti-Stokes Raman transients for HOD in D_2O . (Reproduced from ref. [12]). NLS is an artifact produced by nonlinear light scattering. The spectra in the bending region are offset for clarity. The data show the parent $\nu_{\text{OH}}(\text{HOD})$ as well as three of the six possible daughter vibrations.

It is now generally accepted that spectral diffusion in ν_{OH} on the >100 fs time scale is caused largely by the making and breaking of hydrogen bonds [8,9]. One important question about hydrogen bond dynamics involves the multicomponent vs. continuous environment question. In theoretical simulations of water hydrogen bonding, there are broad distributions of the O-H \cdots O bond angles and lengths, suggesting continuously varying environments. Theorists often define hydrogen bonds as “made” or “broken” based on certain sharp cut-off criteria for the O-H \cdots O bond angles and lengths, making it possible to count the number of hydrogen bonds at each simulated water molecules (the average number is 3.57), so that well-defined hydrogen bonding environments with 4, 3, 2 or even fewer bonds can be identified. Recent work by the groups of Casey Hynes and Jim Skinner [8,9] show that the ν_{OH} spectrum of different hydrogen-bonded configurations are distinguishable, but they overlap a great deal. Due to this overlap, it is not possible to resolve individual environments with ordinary vibrational spectroscopy. Laenen and Laubereau [13,14] studied HOD/D₂O with two-color pump-probe techniques and concluded there were at least three well-defined subbands in the ν_{OH} spectra. On the basis of comparisons to simulations, these bands were assigned to (I) “ice-like”, (II) “bridged” and (III) “bifurcated” hydrogen bonded sites. Laenen argued that the subband method of analysis made more sense than looking at transients at individual probe wavelengths because single-wavelength transients always contain a mixture of spectral diffusion and VR. In subsequent work in other laboratories on HOD/D₂O, the discrete environment picture was ignored in favor of a continuous distribution picture, where ν_{OH} dynamics were explained in terms of spectral diffusion plus a wavenumber-dependent VR lifetime [15].

Some IR-Raman data on water with ν_{OH} pumping at 3115 cm^{-1} are shown in Fig. 2. The decay of ν_{OH} and the appearance of $\delta_{\text{H}_2\text{O}}$ are clearly seen. Figure 2 also compares the equilibrium Stokes Raman spectrum of ν_{OH} to transient anti-Stokes spectra at $t = 1$ ps with pumping on the red edge, the band center and the blue edge. The transient spectra can be accurately fit at all times and all pump wavenumbers with two overlapping Gaussian vibrational subbands [16], a broader (FWHM $\approx 500\text{ cm}^{-1}$) red-shifted subband and a narrower (FWHM $\approx 200\text{ cm}^{-1}$) blue-shifted subband. The amplitudes, peak locations and widths of

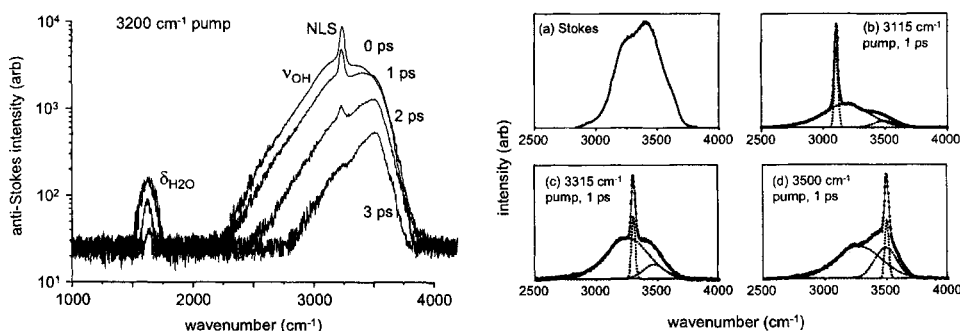


Fig. 2. (left) Anti-Stokes transient spectra of water with ν_{OH} pumping at 3200 cm^{-1} . The sharp feature at 3200 cm^{-1} is due to nonlinear light scattering (NLS). The blueshift with increasing time is due to spectral diffusion and a longer lifetime in the blue. Reproduced from ref. [11]. (right) (a) Stokes Raman spectrum of water. (b)-(d) Anti-Stokes transients after pumping on the red edge, band center and blue edge. The data are fit by the sum of two overlapping Gaussian subbands plus one Gaussian for the NLS artifact. Reproduced from ref. [16].

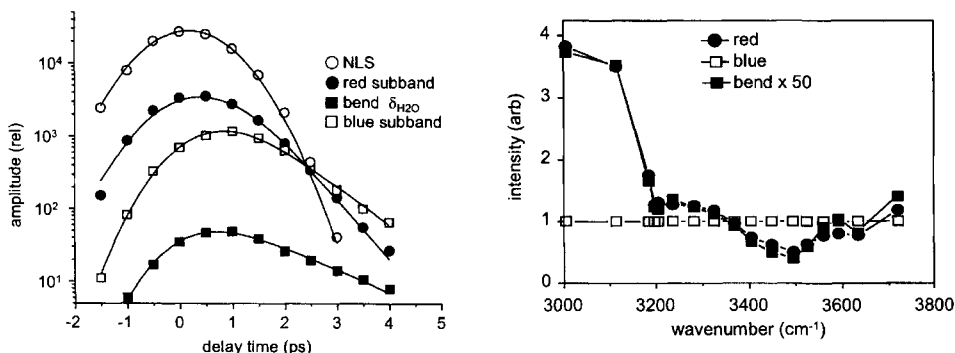
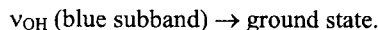
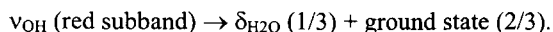


Fig. 3. (*left*) Time dependence of the red and blue subbands and $\delta_{\text{H}_2\text{O}}$ with 3115 cm^{-1} pumping. The NLS artifact gives the apparatus time response. (*right*) Relative intensities of red and blue subbands and $\delta_{\text{H}_2\text{O}}$ as a function of pump wavenumber, normalized to the blue subband intensity. The $\delta_{\text{H}_2\text{O}}$ intensities are multiplied by 50. Reproduced from ref. [11].

these two subbands vary with time, but each subband has a well-defined lifetime T_1 . The time dependences of the ν_{OH} subband intensities and the daughter $\delta_{\text{H}_2\text{O}}$ bending vibration are shown in Fig. 3. The red subband, which is directly excited by the 3115 cm^{-1} pump pulse, rises instantaneously. The red subband data were fit with the convolution of the apparatus response measured via nonlinear light scattering (NLS) plus an exponential decay, giving $T_1 = 0.55 \pm 0.05 \text{ ps}$. The blue subband, not directly pumped by 3115 cm^{-1} pulses, has a delayed rise. Those data were fit by the convolution of the apparatus response with a 0.55 ps exponential build up and an exponential decay giving $T_1 = 0.75 \pm 0.05 \text{ ps}$. The bend vibration $\delta_{\text{H}_2\text{O}}$ showed a delayed build up, so the signals were fit with a 0.55 ps build up and an exponential decay. The best fit for the $\delta_{\text{H}_2\text{O}}$ lifetime was $T_1 = 1.4 (\pm 0.2) \text{ ps}$.

With anti-Stokes probing it is possible to determine the absolute quantum yield for generation of daughter $\delta_{\text{H}_2\text{O}}$ by parent ν_{OH} decay [11]. The quantum yield is found from the ratio of anti-Stokes intensities and the ratio of Raman cross-sections obtained from the Stokes spectrum. In water this is complicated by having two parent subbands. Figure 3 shows how the $\delta_{\text{H}_2\text{O}}$ intensity changes as the pump wavenumber is tuned through the ν_{OH} absorption. In Fig. 3, we normalized the signal at each pump wavenumber to the blue subband intensity to account for variations in laser parameters and sample absorption. In this format the blue subband intensity remains constant while the red subband and bend intensities change by a factor of ~ 8 as the pump wavenumber is tuned. Figure 3 shows that the bend intensity is highly correlated with the red subband and apparently uncorrelated with the blue subband. Thus $\delta_{\text{H}_2\text{O}}$ is primarily generated by red subband decay, and blue subband decay creates little or no δ_{OH} . The quantum yield for stretch-to-bend is $\phi = 0.33 (\pm 0.05)$ for the red subband and $\phi \approx 0$ for the blue subband. Thus,



In conclusion, the water ν_{OH} Raman spectrum can be explained with two overlapping subbands. Even though these subbands overlap, they are easily distinguished with 3D

vibrational spectroscopy, since they have different spectral diffusion, different lifetimes and different VR pathways. However 3D spectroscopy does not unambiguously identify the nature of the subbands. The properties of the smaller blue subband, namely a narrower width, a longer lifetime, weaker coupling to the bending vibration and higher temperature sensitivity suggest that it represents water molecules with a broken hydrogen bond to one H atom, although this tentative structural interpretation needs to be confirmed by simulations.

3. WATCHING VIBRATIONAL ENERGY WITH ANGSTROM RESOLUTION

We have for the first time directly observed vibrational energy transfer (VET) across molecules of different lengths using vibrational reporter groups (atomic groups with nearly local-mode vibrational excitations) [17]. The distances between vibrational donors and acceptors were varied in units of one carbon-carbon bond length (~ 1.5 Å), so that the distance-dependence of VET could be investigated. We studied a series of different alcohols at ambient temperature, that have the general structure $\text{CH}_3\text{-R-OH}$, where R is a hydrocarbon. Using the IR-Raman technique, ν_{OH} was pumped and ν_{CH} transitions were probed. Although IR-Raman and related IR-IR techniques [18-22] have been used to study ethanol and other alcohols in the past, prior studies have not had the time resolution and sensitivity needed to observe the distance dependence of VET across molecular dimensions.

We stress that VET from ν_{OH} to ν_{CH} of alcohol molecules is not an efficient process. Both types of excitations have short VR lifetimes of about 1 ps, which result from decay to daughters including OH and CH bending and CO stretching in the 1000-1500 cm^{-1} range [23]. Owing to these short lifetimes, VR competes effectively with VET, so that at most a few percent of the initial OH stretch excitation makes its way down a molecular chain.

Although VET from a vibrational donor to an acceptor on another part of a molecule seems reminiscent of electronic energy transfer between dye molecules, it is fundamentally quite different. Electronic energy transfer typically results from through-space interactions, such as a dipole-dipole interaction in the case of Förster transfer, between electronic states of molecules with overlapping emission and absorption spectra. Through-space VET is not expected to be significant between ν_{OH} and ν_{CH} located a few angstroms apart, because typical dipole moments and spectral overlap factors for vibrational transitions do not provide energy transfer rates that are remotely competitive with the VR lifetimes. Instead VET is fundamentally mechanical, and occurs via a through-bond interaction involving solvent-assisted anharmonic coupling [1].

Broadly speaking, we can envision two different paradigms for excitation energy to be transferred from OH or a terminal CH_3 , as shown in Fig. 4. In a *vibrational cascade*, vibrational excitation percolates down the energy levels. If this mode were dominant, Fig. 4 shows that ν_{OH} decay would first excite the higher energy “a” states $\nu_{\text{a}}(\text{CH}_3)$ and $\nu_{\text{a}}(\text{CH}_2)$, followed by the lower energy “s” states $\nu_{\text{s}}(\text{CH}_2)$ and $\nu_{\text{s}}(\text{CH}_3)$. ($\nu_{\text{a}}(\text{CH}_2)$ is not shown explicitly in Fig. 4 because this transition is not seen in the Raman or IR spectra of these alcohols). In *through-bond transfer*, vibrational excitation would run from OH across the intervening C-H groups, first to CH_2 and then to CH_3 . Figure 4 shows that energetically this involves a *first step down in energy* from ν_{OH} to $\nu_{\text{s}}(\text{CH}_2)$, followed by *steps up in energy* to $\nu_{\text{s}}(\text{CH}_3)$ and $\nu_{\text{a}}(\text{CH}_3)$. Keep in mind that in our studies of ambient liquids, $k_{\text{B}}T \approx 200$ cm^{-1} , so steps up or down in energy of this magnitude are facile.

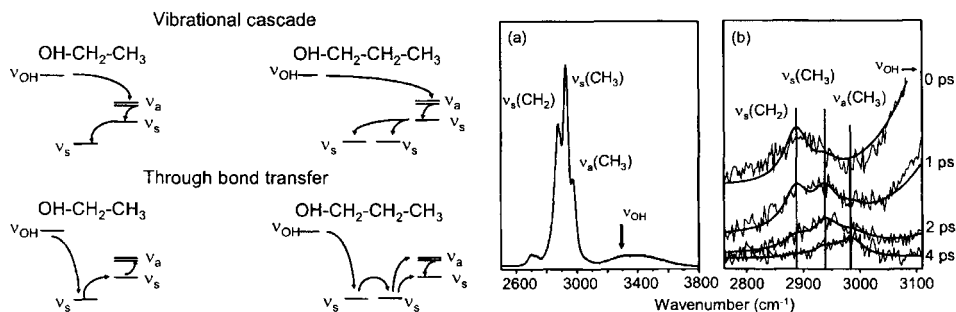


Fig. 4. (left) Energy level diagrams for possible vibrational energy transfer (VET) processes from OH to CH stretching of ethanol and 1-propanol. (top) Vibrational cascade moves down in energy in each step (bottom) Through-bond VET moves first down then up in energy. (right) (a) Stokes spectrum of ethanol. (b) Anti-Stokes transient spectra. The OH excitations pumped by the laser are cut off to the right. Vibrational energy first flows downhill from OH to CH₂, then later moves uphill in energy to CH₃, indicating through-bond vibrational energy transfer. Reproduced from ref. [17].

The Stokes Raman spectrum of ethanol at right in Fig. 4 shows that we can clearly resolve the OH stretch and the CH stretch of methylene and methyl. Note the Raman cross-section for ν_{OH} is about ten times smaller than for ν_{CH} . The anti-Stokes transient spectra in Fig. 4 at far right were obtained with ν_{OH} pumping at 3300 cm^{-1} . At shorter delay times, the ν_{OH} intensity (cut off at the right hand side) is about ten times larger than the ν_{CH} intensity. Given the relative cross-sections, we see that only a few percent of ν_{OH} is transferred to ν_{CH} . The rest disappear into lower energy states [23]. In the first 1 ps, the predominant daughter of ν_{OH} decay in the ν_{CH} region is the methylene stretch $\nu_{\text{s}}(\text{CH}_2)$. Subsequently the energy in the methylene group does something apparently startling. It moves *uphill in energy* from $\nu(\text{CH}_2)$ to $\nu(\text{CH}_3)$. Thus the data in Fig. 4 clearly distinguish between the two possibilities illustrated at left in Fig. 4. Energy transfer from ν_{OH} to $\nu(\text{CH}_3)$ in ethanol *occurs by through-bond transfer*, moving from OH first to CH₂ before arriving at CH₃, as opposed to a vibrational cascade down the energy levels from OH to CH₃ to CH₂.

Figure 5 shows the time dependence of the OH and CH stretches of methylene and terminal methyl groups in ethanol, 1-propanol, 1-butanol and 2-propanol. The vertical markers in each panel indicate the peak of the OH population and the 95% point of the CH₃(a) population. The time interval between the markers for ethanol is 1.0 ps, for 1-propanol it is 1.4 ps and for 1-butanol it is 1.7 ps. Thus to a rough approximation, adding an additional methylene group increases the time for vibrational flow from one end of an alcohol molecule to the other by ~ 0.4 ps. In 2-propanol, energy flowing from OH to a terminal methyl passes through only a single intervening CH atomic group. The markers in Fig. 5d show the time for energy flow from OH to CH₃ in 2-propanol is almost exactly the same as in ethanol, 1.0 ps. The efficiency of energy transfer through CH in 2-propanol, where the intervening group has only one CH stretch excitation, is about one-third the efficiency of energy transfer through CH₂ in ethanol, where the intervening group has two CH stretch excitations.

Carbon-carbon bond lengths in unsaturated molecules are typically 0.15 nm, so a 0.4 ps time constant for VET across a methylene group roughly corresponds to a velocity of 375

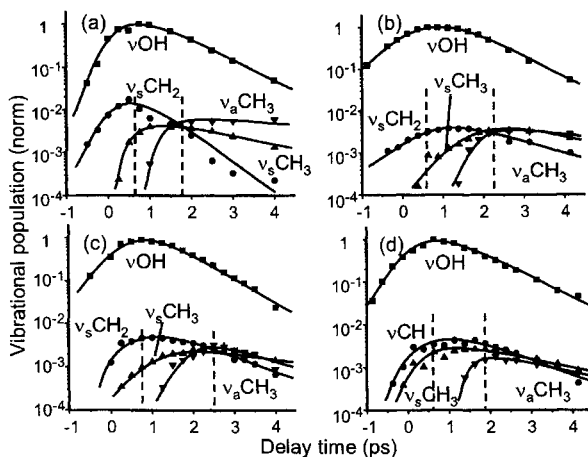


Fig. 5. Time-dependent populations of OH and CH stretching of (a) ethanol, (b) 1-propanol, (c) 1-butanol and (d) 2-propanol. The dashed vertical lines indicate the peak of the ν_{OH} population and the 95% point of the $\nu_{\text{a}}\text{CH}_3$ population. Reproduced from ref. [17].

m/s. That is a relatively high velocity, about ten percent greater than Mach 1. However it is only about one-third the speed of sound in ethanol. The overall efficiency for VET from OH to $\nu_{\text{a}}(\text{CH}_3)$ states is quite poor, so it will be interesting if we can find other useful vibrational reporter groups with longer lifetimes, and intervening groups that are better conductors of vibrational energy, so our studies could be extended to larger molecules and longer distances.

4. CONCLUSION

The 3D IR-Raman technique provides a wealth of new information about incoherent VR processes of molecules in liquids. In particular, the ability to simultaneously probe both parent and daughter vibrations proved immensely useful. The main drawback of this technique is the difficulty in observing the weak incoherent signal against a variety of possible optical backgrounds generated by the intense pump and probe pulses. Besides continuing our explorations of water and VET with high spatial resolution, future work in our lab will involve developing methods to study the temperature dependence in liquids and to study solids at low temperature.

5. ACKNOWLEDGEMENT

This material is based on work supported by the National Science Foundation under award number DMR-0096466, by Air Force Office of Scientific Research contract F49620-03-1-0032, and by Army Research Office contract DAAD19-00-1-0036.

REFERENCES

- [1] V. M. Kenkre, A. Tokmakoff, and M. D. Fayer, *J. Chem. Phys.*, 101 (1994) 10618.
- [2] L. K. Iwaki, J. C. Deak, S. T. Rhea, and D. D. Dlott, in: *Ultrafast Infrared and Raman Spectroscopy*, eds. M. D. Fayer (Marcel Dekker, New York, 2000).
- [3] A. J. Lock, S. Woutersen, and H. J. Bakker, *J. Phys. Chem., A* 105 (2001) 1238.

- [4] A. J. Lock and H. J. Bakker, *J. Chem. Phys.*, 117 (2002) 1708.
- [5] A. Laubereau and W. Kaiser, *Rev. Mod. Phys.*, 50 (1978) 607.
- [6] A. Seilmeier and W. Kaiser, in: *Ultrashort Laser Pulses and Applications*, Vol. 60, eds. W. Kaiser (Springer Verlag, Berlin, 1988), p. 279.
- [7] D. D. Dlott, *Chem. Phys.*, 266 (2001) 149.
- [8] C. P. Lawrence and J. L. Skinner, *Chem. Phys. Lett.*, 369 (2003) 472.
- [9] R. Rey, K. B. Møller, and J. T. Hynes, *J. Phys. Chem. A*, 106 (2002) 11993.
- [10] C. P. Lawrence and J. L. Skinner, *J. Chem. Phys.*, 119 (2003) 1623.
- [11] A. Pakoulev, Z. Wang, Y. Pang, and D. D. Dlott, *Chem. Phys. Lett.*, 380 (2003) 404.
- [12] J. C. Deák, L. K. Iwaki, and D. D. Dlott, *J. Phys. Chem.*, 104 (2000) 4866.
- [13] R. Laenen, C. Rauscher, and A. Laubereau, *Phys. Rev. Lett.*, 80 (1998) 2622.
- [14] R. Laenen, C. Rauscher, and A. Laubereau, *J. Phys. Chem. B*, 102 (1998) 9304.
- [15] G. M. Gale, G. Gallot, and N. Lascoux, *Chem. Phys. Lett.*, 311 (1999) 123.
- [16] Z. Wang, A. Pakoulev, Y. Pang, and D. D. Dlott, *Chem. Phys. Lett.*, 378 (2003) 281.
- [17] Z. Wang, A. Pakoulev, and D. D. Dlott, *Science*, 296 (2002) 2201.
- [18] E. J. Heilweil, M. P. Casassa, R. R. Cavanagh, and J. C. Stephenson, *J. Chem. Phys.*, 85 (1986) 5004.
- [19] R. Laenen and C. Rauscher, *Chem. Phys. Lett.*, 274 (1997) 63.
- [20] S. Woutersen, U. Emmerichs, and H. J. Bakker, *J. Chem. Phys.*, 107 (1997) 1483.
- [21] R. Laenen and K. Simconidis, *Chem. Phys. Lett.*, 299 (1999) 589.
- [22] R. Laenen, C. Rauscher, and A. Laubereau, *J. Phys. Chem.*, A 101 (1997) 3201.
- [23] L. K. Iwaki and D. D. Dlott, *J. Phys. Chem. A*, 104 (2000) 9101.

On ultrafast IR spectroscopy in water

K. B. Møller,^a R. Rey,^b and J. T. Hynes^c

^aDepartment of Chemistry, Technical University of Denmark, 2800 Kgs. Lyngby, Denmark

^bDepartament de Física i Enginyeria Nuclear, Universitat Politècnica de Catalunya, Campus Nord B4-B5, Barcelona 08034, Spain

^cDépartement de Chimie, Ecole Normale Supérieure, 24 Rue Lhomond, 75231 Paris Cedex 5, France and Department of Chemistry and Biochemistry, University of Colorado, Boulder, CO 80309, USA

1. INTRODUCTION

Recently, modern ultrafast spectroscopic methods have opened a new experimental window on the molecular dynamics of water, examining the OH-stretch dynamics for the experimentally convenient aqueous system of HOD diluted in D₂O using ultrafast infrared (IR) [1-6], IR-Raman [7], or photon echo [8] spectroscopy.

One major focus of these experiments has been the excited OH vibration population lifetime. This is currently interpreted as being dominated by either vibrational predissociation [2], i.e. the breaking of the hydrogen bond of an excited OH stretch [9], or by vibrational relaxation of the excited OH without such IR-induced bond breaking [7,10,11] (see Ref. 12 for a recent review).

Recently [13,14] we have focused on the theoretical interpretation of spectral diffusion, i.e., the OH frequency's dynamical modulation. Experimental interpretations have considered that the vibrational frequency of an OH involved in a hydrogen bond is a measure of the length (OO distance) of that bond, and often involve the image of overdamped OO motion. We performed Molecular Dynamics (MD) simulations to test this picture, and to study the spectral diffusion in the OH stretch associated with a hole burned in the ground state. Some major results of those studies are recounted here.

2. COMPUTATIONAL MODELS AND METHODS

Our MD simulations were performed applying standard techniques to a system comprising 108 rigid water (1 HOD and 107 D₂O) molecules, using the SPC/E interaction potential. The time step was 1 fs; the mean temperature was 298 K with a 0.5 ps coupling constant.

The instantaneous OH frequency was calculated at each time step in an adiabatic approximation (fast quantal vibration in a slow classical 'bath'). We applied second-order perturbation theory, in which the instantaneous solvent-induced frequency shift from the gas-phase value is obtained from the solute-solvent forces and their derivatives acting on a rigid OH bond. This method is both numerically advantageous and allows exploration of sources of various solvent contributions to the frequency shift.

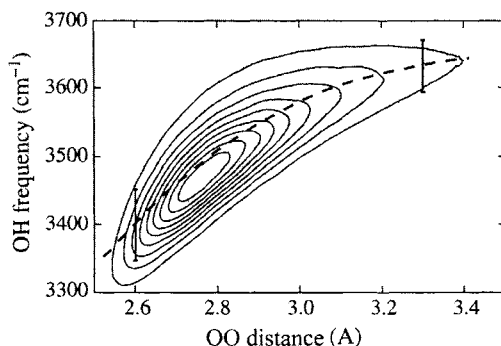


Fig. 1. Density-of-states histogram of simultaneous OO distances and OH frequencies. The dashed line gives the average OH frequency for each OO distance (widths are indicated by the vertical solid lines).

3. OH FREQUENCY AND ITS RELATION TO THE HYDROGEN BOND LENGTH

Analysis of the solvent-induced frequency shift's origin indicated that the major contributions come from solute-solvent forces (and not their derivatives) and that the Coulomb interactions are overwhelmingly dominant [13-15]. Further, since approximately 70 % of the frequency shift is induced by the D₂O closest to the H in HOD, we analyzed the relationship between the OH frequency and the HOD -closest D₂O OO distance.

Figure 1 [13,14] displays a density-of-states histogram of simultaneous OO distances and instantaneous OH frequencies. While there is indeed a general trend of higher frequency (smaller shift) with increasing OO distance (weaker hydrogen bond), we make two important remarks. First, the distribution is quite disperse, and the OHO angle in the hydrogen bond and orientation of the deuterium atoms on the closest D₂O molecule play significant roles in this dispersion. Second, individual system trajectories (on the plane defined by Fig. 1) reveal that these may take major departures from the general trend; the instantaneous OH frequency may increase substantially while the OO distance is decreasing and *vice versa*. This raises the question: what is actually 'seen' of the hydrogen-bond dynamics by observing the spectral evolution (diffusion) of the OH stretch?

4. HYDROGEN-BOND DYNAMICS AND SPECTRAL DIFFUSION

The actual nature of the OO dynamics was easily obtained via MD simulations, which showed that the OO motion is clearly *underdamped* with an amplitude of about 0.4 Å and a period of about 160 fs, a result consistent with older experimental results (e.g Raman, neutron scattering) indicating a 200 cm⁻¹ vibration.

Turning to the experimental IR pump-probe signals reported in Refs. 3 and 4 where the pump pulse transfers population from the OH stretch ground state to OH stretch first excited state ($\nu = 0 \rightarrow 1$) and the dynamics of the thereby induced transmission is followed by the probe pulse. The interpretation of the obtained signals is complicated by the fact that, apart from the bleaching due to the $\nu = 0 \rightarrow 1$ transition, excited state emission ($\nu = 0 \leftarrow 1$) and absorption ($\nu = 1 \rightarrow 2$) also contribute to the induced transmission. Woutersen and Bakker [4] successfully fit their IR signal to a simple sum of these three contributions, dynamics in the ground and excited state being described as a Markovian Gaussian Random Process, with the same decay time constant, $\tau = 500$ fs, for both states. A somewhat different treatment by

Gale *et al.* [3] gave a 700 fs decay time constant. In the spirit of the Woutersen and Bakker approach, we simulated the ground-state contribution to the IR signal by following the evolution of the subensemble obtained by excluding configurations corresponding to those where the OH stretch would have been excited by the pump laser. We examined cases where a hole was created on either side of the average equilibrium OH frequency. We observed that initially Gaussian-shaped holes do not retain this shape during the evolution, a behavior in contrast with the pervasive Gaussian assumption in spectral diffusion studies.

Figure 2 [13,14] (top) displays the evolution of average OH frequency of the remaining (non-excluded) configurations for excitation to the blue and to the red side of the average equilibrium OH frequency. Both results are mildly bimodal in time and biexponential fits give a short time scale of 30-60 fs and a long one of 500-800 fs. The latter correspond well to the experimental time scales reported in Refs. 3 and 4, where a time scale <100 fs would be difficult to resolve with the pulse duration used. However, a sub-100 fs time scale has been extracted from photon echo studies [8] and from very recent IR experiments [6] as well. However, the biexponential analysis is very crude since the results in Fig. 4 clearly show an oscillatory feature at approximately 160 fs, which equals the period of the OO motion. (This feature has now been observed in a very recent experiments by Fecko *et al.* [6]). A much better fit is obtained using the form [14]

$$A \cos(\omega_{00}t) e^{-t/\tau_1} + B e^{-t/\tau_2} + (1 - A - B) e^{-t/\tau_3}, \quad (1)$$

from which we obtained [14] the time scales of about 70 fs, 100 fs, and 1 ps. The 1 ps time scale is reasonably related to the time scale extracted from the experiments in Refs. 3 and 4, and we now turn to its interpretation .

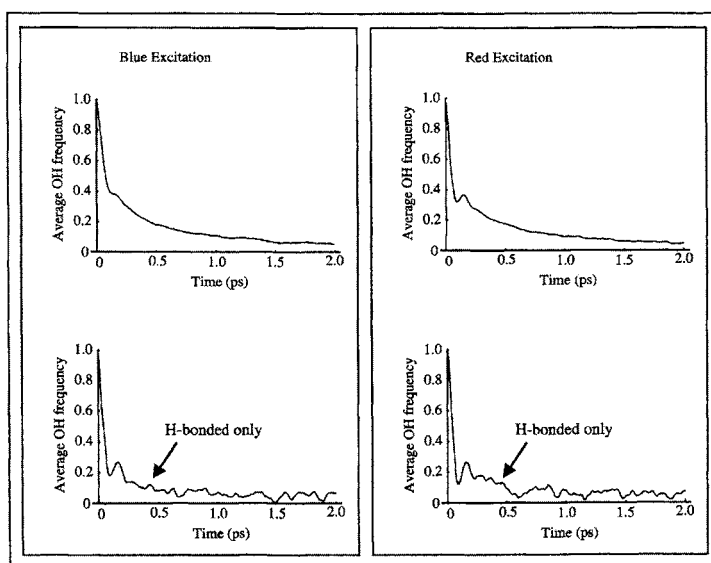


Fig. 2. Time evolution of the average OH frequency (normalized to its initial value) of the molecules remaining in the ground state as a result of laser excitation.

Figure 2 (bottom) displays the evolution of average OH frequency of the remaining (non-excluded) configurations when we only included trajectories for which HOD remained hydrogen bonded for at least 2 ps. Fitting these results using Eq. (1) again gave the time scales of about 70 fs and 100 fs [14] and, more important, only a very small component with a time scale of about 2 ps or more. Hence, the 1 ps component was missing for the hydrogen-bonded systems, which suggests that this component is related to breaking and making of hydrogen bonds, a conclusion consistent with the fact that the lifetime of a hydrogen bond is about 1 ps.

5. CONCLUDING REMARKS

In our MD simulations [13,14] of HOD in D₂O we found that the dynamics of an intact hydrogen bond is underdamped, that the relationship between the OH stretch frequency and the length of the hydrogen bond in which the OH is involved is characterized by considerable dispersion, and that the time scale for spectral diffusion on the order of a picosecond is related to hydrogen bond breaking and making. Related conclusions have been reached by Lawrence and Skinner [16], and more recently by Fecko *et al.* [6].

This work was supported by EC TMR network HPRN-CT-2000-19, the SNF, MCYT project BFM2001-2077, the CNRS, and NSF grant CHE-0108314.

REFERENCES

- [1] R. Laenen, C. Rauscher, A. Laubereau, *Phys. Rev. Lett.* 80 (1998) 2622; *J. Phys. Chem. B* 102 (1998) 9304.
- [2] S. Woutersen, U. Emmerichs, H.-K. Nienhuys, H.J. Bakker, *Phys. Rev. Lett.* 81 (1998) 106. H.-K. Nienhuys, S. Woutersen, R.A. van Santen, H.J. Bakker, *J. Chem. Phys.* 111 (1999) 1494.
- [3] G.M. Gale, G. Gallot, F. Hache, N. Lascoux, S. Bratos, J.-C. Leicknam, *Phys. Rev. Lett.* 82 (1999) 1068. S. Bratos, G.M. Gale, G. Gallot, F. Hache, N. Lascoux, J.-C. Leicknam, *Phys. Rev. E* 61 (2000) 5211.
- [4] S. Woutersen, H.J. Bakker, *Phys. Rev. Lett.* 83 (1999) 2077.
- [5] H.J. Bakker, S. Woutersen, H.-K. Nienhuys, *Chem. Phys.* 258 (2000) 233. G. Gallot, N. Lascoux, G.M. Gale, J.-C. Leicknam, S. Bratos, S. Pommeret, *Chem. Phys. Lett.* 341 (2001) 535. H.J. Bakker, H.-K. Nienhuys, G. Gallot, N. Lascoux, G.M. Gale, J.-C. Leicknam, S. Bratos, *J. Chem. Phys.* 116 (2002) 2592.
- [6] C.J. Fecko, J.D. Eaves, J.J. Loparo, A. Tokmakoff, P.L. Geissler, *Science* 301 (2003) 1698.
- [7] J.C. Deak, S.T. Rhea, L.K. Iwaki, D.D. Dlott, *J. Phys. Chem. A* 104 (2000) 4866.
- [8] J. Stenger, D. Madsen, P. Hamm, E.T.J. Nibbering, T. Elsaesser, *Phys. Rev. Lett.* 87 (2001) 027401; *J. Phys. Chem. A* 106 (2002) 2341.
- [9] A. Staib, J.T. Hynes, *Chem. Phys. Lett.* 104 (1993) 197.
- [10] R. Rey, J.T. Hynes, *J. Chem. Phys.* 104 (1996) 2356.
- [11] C.P. Lawrence, J.L. Skinner, *J. Chem. Phys.* 117 (2002) 5827; *ibid.* 119 (2003) 1623.
- [12] R. Rey, K.B. Møller, J.T. Hynes, *Ultrafast Vibrational Population Dynamics of Water and Related Systems: A Theoretical Perspective*, to appear in *Chem. Rev.* (2004).
- [13] R. Rey, K.B. Møller, J.T. Hynes, *J. Phys. Chem. A* 106 (2002) 11993.
- [14] K.B. Møller, R. Rey, J.T. Hynes, *On Hydrogen Bond Dynamics in Water and Ultrafast Infrared Spectroscopy: A Theoretical Study*, to appear in *J. Phys. Chem. A* (2004).
- [15] J.T. Hynes, R. Rey in M.D. Fayer, (Ed.), *Ultrafast Infrared and Raman Spectroscopy*, Marcel Dekker, New York, 2001.
- [16] C.P. Lawrence, J.L. Skinner, *J. Chem. Phys.* 117 (2002) 8847; *ibid.* 118 (2003) 264; *Chem. Phys. Lett.* 369 (2003) 472.

Isotope effect on the IVR dynamics after ultrafast IR excitation of the hydrogen bond in salicylaldimine

M. Petković and O. Kühn

Institut für Chemie, Physikalische und Theoretische Chemie
Freie Universität Berlin, Takustrasse 3, D-14195 Berlin, Germany

1. INTRODUCTION

The presence of intramolecular hydrogen bonds (HBs) leads to a pronounced anharmonicity of the potential energy surface (PES) for vibrational dynamics. As a consequence HBs can be identified and characterized by the shift and shape of the infrared (IR) absorption of A–H stretching vibrational transitions [1]. Depending on the HB's strength, the coupling to low-frequency vibrations modulating the HB geometry, or the resonance interaction with, e.g., the A–H bending overtone transition might be responsible for the broad and often structured IR absorption [2,3]. A detailed interpretation is difficult to achieve, a point which is illustrated by the attempts made for malonaldehyde [4]. The situation is even more complicated in the condensed phase where the effect of intramolecular anharmonicity has to be disentangled from the dephasing induced line-broadening due to the interaction with the environment. Here, ultrafast time-resolved IR spectroscopy can provide crucial information, e.g., on the vibrational transitions hidden under a broad absorption band [5].

The simulation of time-resolved experiments requires the knowledge of the multidimensional PES as well as the solution of the appropriate dynamical equations [6]. Recently, we have shown that an all-Cartesian reaction surface (CRS) Hamiltonian approach [7], combined with a high-dimensional nuclear wave packet propagation using the multi-configuration time-dependent Hartree (MCTDH) method [8], provides an ideal setup for studying the intramolecular vibrational energy redistribution (IVR) dynamics of HB systems [9,10]. Although this emphasizes the intramolecular aspect of the overall dynamics, it may lead to the identification of effective models for the condensed phase case [11].

In this contribution we extend our previous studies on the HB spectroscopy and dynamics of salicylaldimine (SA, see Fig. 1) focussing on the influence of isotopic H/D substitution on the IVR dynamics. In the following Section 2 the CRS Hamiltonian is briefly introduced. In Section 3 numerical results of a seven-dimensional (7D) wave packet propagation are discussed.

2. THEORETICAL MODEL

We will use the 7D CRS Hamiltonian which has been determined and analyzed in Ref. [10] (DFT/B3LYP, 6-31+G(d,p)). In short, the large-amplitude motion of the H/D atom is restricted to the (x, y) plane of the molecule (cf. Fig. 1). The origin of the molecule-fixed coordinate system is at the center of mass, with the axes pointing along the principal axes of inertia for the enol configuration. The H/D motion couples strongly to 5 in-plane skeleton modes, $\mathbf{Q} = (Q_4, Q_6, Q_{14}, Q_{26}, Q_{30})$, which are described in harmonic approximation

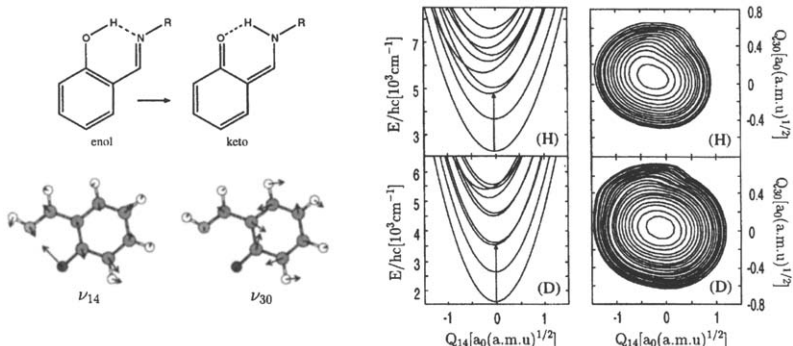


Figure 1: Left: Enol–keto tautomerism in salicylaldimine (SA) and normal mode displacements for skeleton modes ν_{14} and ν_{30} . Middle: H/D diabatic potential energy curves $U_\alpha(Q_{14})$ for mode ν_{14} (lowest states: ground state, bending and stretching fundamental, first bending overtone; arrows indicate laser excitation). Right: two–dimensional (Q_{14}, Q_{30}) cuts through the *adiabatic* PES (obtained upon diagonalizing the field–free part of Eq. (1)) which has dominantly H/D stretching character but includes state and mode couplings (contours from 0 to 7400 cm^{-1}).

(frequencies at enol configuration (336, 451, 861, 1333, 1513) cm^{-1}). Diabatic H/D–atom states $|\alpha\rangle$ (energies E_α) are introduced for the skeleton modes fixed at the enol configuration $\mathbf{Q} = 0$. The total vibrational state vector $|\Psi\rangle$ can be expanded in terms of the diabatic states as $|\Psi(t)\rangle = \sum_{\alpha=1}^v \psi_\alpha(t)|\alpha\rangle$, where $v = 10$ in the numerical simulations. The time–dependent functions $\psi_\alpha(t)$ were obtained from a numerically exact solution of the time–dependent Schrödinger equation using the MCTDH method [8,12]. The respective CRS Hamiltonian in diabatic representation is (\mathbf{P} is the momentum for the mass–weighted skeleton modes):

$$H = \frac{1}{2}\mathbf{P}^2 + \sum_{\alpha,\beta} [U_\alpha(\mathbf{Q})\delta_{\alpha\beta} + V_{\alpha\beta}(\mathbf{Q})(1 - \delta_{\alpha\beta}) - d_{\alpha\beta}\mathcal{E}(t)] |\alpha\rangle\langle\beta|. \quad (1)$$

Here, the diabatic PES for the motion of the skeleton modes are $U_\alpha(\mathbf{Q}) = E_\alpha - \mathbf{f}_{\alpha\alpha}\mathbf{Q} + 1/2\mathbf{Q}\mathbf{K}_{\alpha\alpha}\mathbf{Q}$ and the coupling between the diabatic states is given by $V_{\alpha\beta}(\mathbf{Q}) = -\mathbf{f}_{\alpha\beta}\mathbf{Q} + 1/2\mathbf{Q}\mathbf{K}_{\alpha\beta}\mathbf{Q}$. The $\mathbf{f}_{\alpha\beta}$ and $\mathbf{K}_{\alpha\beta}$ are the diabatic state matrix elements of the forces and the Hessian for the skeleton modes, respectively. Exemplary PES are shown in Fig. 1. Note that Eq. (1) is exact within the reaction surface approximation, i.e., no assumption concerning an adiabatic separation of H–atom and skeleton motions has been made.

The last term in Eq. (1) describes the coupling to the laser field which has the form $\mathcal{E}(t) = \mathcal{E}_0\Theta(t)\Theta(\tau - t)\sin^2(\pi t/\tau)\cos(\Omega t)$, where \mathcal{E}_0 is the amplitude, τ the duration, and Ω the center frequency of the pulse. The dipole moment vector is oriented in the plane of the molecule; $d_{\alpha\beta}$ are the respective matrix elements. Here, we will focus on the excitation of the stretching vibration which in our coordinate system is mostly polarized along the x axis. Thus, we will take into account only the x component of the dipole moment, assuming that the laser field is polarized accordingly [10].

3. DISCUSSION OF NUMERICAL RESULTS

In Fig. 2 we show the IR spectrum in the O–H/D stretching region of our 7D model. The data have been obtained by a Fourier–transform of the dipole–dipole correlation function, where the

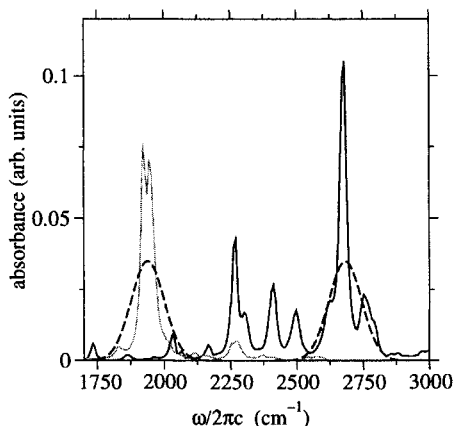


Figure 2: IR absorption in the O–H/D stretching region for the 7D model of SA (H: black, D: grey). The small broadening results from an artificial damping of the correlation function with a time constant of 0.5 ps. The spectra of the laser pulses used in Fig. 3 are shown as dashed lines.

propagation was performed with the field-free part of Eq. (1) [6,10]. For the normal (H) species we observe a broad band extending from 2200–2800 cm^{-1} and showing considerable substructure. Experimental spectra have been recorded - but not fully assigned - for SA-Ph in CCl_4 solution in [13]. Here, one finds two broad bands around 2600 and 2750 cm^{-1} . Given some solvent-induced broadening this correlates well with the present OH-stretching type transitions. Upon deuteration the calculated main absorption band due to the O–D stretching transition shifts to the red and narrows considerably to the range 1800–2050 cm^{-1} . Additionally, any substructure is only marginally discernible, except that the main transition shows a double peak structure.

Next, we focus on the dynamics after ultrafast IR excitation of the main absorption peaks (cf. Fig. 1). The laser pulse spectra are shown in Fig. 2. Clearly, they are broad enough to excite a coherent superposition, i.e., a vibrational wave packet, in both cases. The dynamics is analyzed using the expectation values of the energy of the H/D reaction coordinates, $E_{xy}(t) = \sum_{\alpha} E_{\alpha} \langle \Psi(t) | \alpha \rangle \langle \alpha | \Psi(t) \rangle$, and of the energies of the *uncoupled* skeleton modes, $E_{Q_i}(t) = 1/2 \sum_{\alpha} \langle \Psi(t) | \alpha \rangle [P_i^2 + [K_{\alpha\alpha}]_{ii} Q_i^2] \langle \alpha | \Psi(t) \rangle$.

The IVR dynamics for the normal species shown in Fig. 3 (left) is characterized by a rapid energy flow, out of the reaction coordinates on a time scale of ~ 700 fs, a value which correlates well with preliminary experimental data for SA-Ph in CCl_4 [13]. The decay comes along with an excitation of *all* skeleton modes, i.e., the energy is quickly randomized and the initial wave packet dephases. The situation changes considerably upon deuteration, see Fig. 3 (right). Here, we find after an initial decay of $E_{xy}(t)$ a revival at about 1250 fs indicating an only marginally randomization on this time scale. Indeed, initially most of the excitation goes into modes ν_{26} and ν_{14} . The other modes become appreciably excited only for times longer than 1250 fs. This observation is in accord with the IR spectrum which is less structured for the deuterated species, indicating the modification of the density of states of the skeleton modes as well as of the anharmonic couplings for lower excitation energy.

In summary, using a combination of a 7D reaction surface and a numerically exact wave packet propagation, we have shown that the IVR dynamics in SA after ultrafast IR laser excitation changes qualitatively upon deuteration of the hydrogen bond.

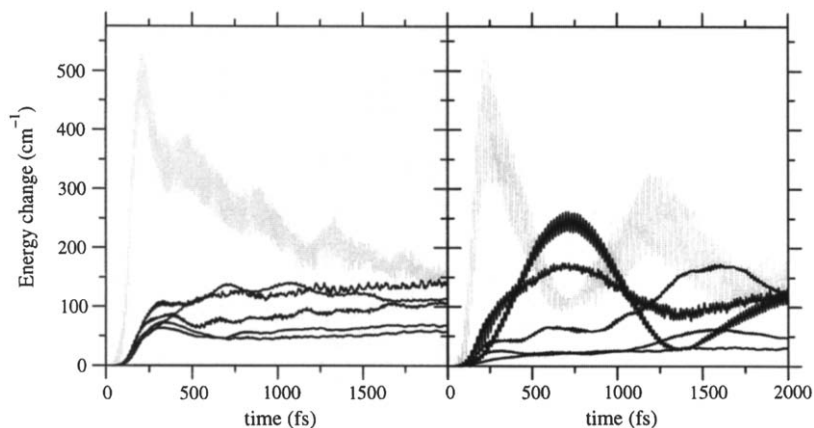


Figure 3: Energy change with respect to time zero after ultrafast excitation ($\mathcal{E}_0 = 0.004 E_h/ea_0$, $\tau = 260$ fs, $\Omega/2\pi c = 2680/1935$ cm $^{-1}$ (H/D)). The data correspond to (from top at $t = 750$ fs): E_{xy} (grey), $E_{Q_{26}}$, $E_{Q_{14}}$, $E_{Q_{30}}$, E_{Q_6} , and E_{Q_4} (left, OH), and $E_{Q_{26}}$, $E_{Q_{14}}$, E_{xy} (grey), $E_{Q_{30}}$, E_{Q_4} , and E_{Q_6} (right, OD).

ACKNOWLEDGMENTS

This work has been financially supported by the DFG–Sfb 450 and the Fonds der Chemischen Industrie (O.K.). The authors gratefully acknowledge stimulating discussions with J. Manz (FU Berlin) and J. Dreyer, K. Heyne, E.T.J. Nibbering, and T. Elsaesser (MBI Berlin).

REFERENCES

- [1] S. Bratos, J.–C. Leicknam, G. Gallot, and H. Ratajczak, *Ultrafast Hydrogen Bond Dynamics and Proton Transfer Processes in the Condensed Phase*, T. Elsaesser and H.J. Bakker (eds.), Kluwer Academic, Dordrecht, 2002, p. 5.
- [2] O. Henri–Rousseau and P. Blaise, *Adv. Chem. Phys.*, 103 (1998) 1.
- [3] O. Henri–Rousseau, P. Blaise, and D. Chamma, *Adv. Chem. Phys.* 121 (2002) 241.
- [4] N. Došlić and O. Kühn, *Z. Phys. Chem.*, (2003) in press.
- [5] J. Stenger, D. Madsen, J. Dreyer, E.T.J. Nibbering, P. Hamm, and T. Elsaesser, *J. Phys. Chem. A*, 105 (2001) 2929.
- [6] V. May and O. Kühn, *Charge and Energy Transfer Dynamics in Molecular Systems*, 2nd Edition, Wiley–VCH, Berlin, 2004.
- [7] B. A. Ruf and W.H. Miller, *J. Chem. Soc. Faraday Trans. 2*, 81 (1988) 1523.
- [8] M. H. Beck, A. Jäckle, G.A. Worth, and H.–D. Meyer, *Phys. Rep.*, 324 (2000) 1.
- [9] H. Naundorf, G. A. Worth, H.–D. Meyer, and O. Kühn, *J. Phys. Chem. A*, 106 (2002) 719.
- [10] M. Petković and O. Kühn, *J. Phys. Chem. A*, 107 (2003) 8458.
- [11] O. Kühn, *J. Phys. Chem. A*, 106 (2002) 7671.
- [12] G.A. Worth, M. Beck, A. Jäckle, and H.–D. Meyer, *The MCTDH Package*, Version 8.3, University of Heidelberg, Heidelberg, 2002.
- [13] K. Heyne, J. Stenger, J. Dreyer, E.T.J. Nibbering, and T. Elsaesser, unpublished work.

Femtosecond solvation dynamics of hydrogen-bonding complexes

E. Pines^a, D. Pines^a, Y.-Z. Ma^b and G. R. Fleming^b

^aChemistry Department, Ben-Gurion University of the Negev, P.O.B. 653, Beer-Sheva 84105 Israel

^bDepartment of Chemistry, University of California Berkeley, and Physical Biosciences Division, Lawrence Berkeley National Laboratory, Berkeley, CA 94720-1460 USA

1. INTERMOLECULAR HYDROGEN-BONDING INTERACTIONS

Hydrogen-bonds are among the most common chemical interactions in condensed phases [1-3]. Some notable examples for the importance of the hydrogen-bonding interactions are the physical properties of liquid water and ice which are largely determined by the extensive hydrogen-bond network existing in bulk water, bimolecular proton-transfer reactions which usually proceed along one or several hydrogen-bonds connecting between the proton donor (acid) and the proton acceptor (base) and the 3-D structure of large biomolecules such as the DNA molecule, which are stabilized by specifically "engineered" hydrogen-bonding interactions.

Hydrogen-bonds also consist an important part of solute-solvent interactions in solution [4, 5]. These interactions are usually referred to as "specific" solute-solvent interactions. The terminology is used to distinguish between hydrogen-bonding interactions which are short-range and solute-solvent interactions originating with the dielectric properties of the solvent which are long-range compared to the molecular graining of the solvent.

In this study we focus on the dynamic aspects of the hydrogen-bonding interaction of some hydroxy-photoacids (ROH) [6]. By optically exciting the photoacid, we have induced a sudden increase in the acidity of the OH group. The enhanced acidity has caused a sudden increase in the hydrogen-bonding interactions of the photoacid usually of the type O-H...O. The hydrogen-bonding complex (ground-state) of the photoacid was prepared in solutions of the photoacid in non-polar solvents and in presence of suitable complexing oxygen bases such as DMSO.

There have been several experimental observations indicating that the response of an existing hydrogen-bond interaction to a sudden change in its interaction potential is ultrafast [7, 8]. In particular, a recent observation by Rini et al. [9] has demonstrated that bimolecular proton transfer along an existing hydrogen-bond may be faster than 150fs when the proton transfer is between a strong photoacid directly hydrogen-bonded to a strong base. The question rises, then, does such an ultrafast proton transfer reaction proceeds before the hydrogen-bond connecting the acid and base relaxes to its new equilibrium 'bond' length following the optical excitation of the photoacid? In such a case, the relevant time-scale for bimolecular proton-transfer along a pre-existing hydrogen-bond may be as fast as the stretching period of the O-H bond (ca. 10fs). However, if the heavy atom distance (O...O) needs to relax prior to the proton transfer reaction, than the proton transfer rate may be limited by the relatively slow hydrogen-bond dynamics (about 100-200fs).

2. THE TIME-RESOLVED STUDIES OF HPTA-DMSO COMPLEXES IN DCM SOLUTIONS

A direct estimation of the O...O time-response following the optical excitation of a strong photoacid, 8-hydroxypyrene 1,3,6 tris-dimethylsulfonamide (HPTA), is reported below. Fig. 1a

shows the large effect on the optical spectra of HPTA of adding small amounts of a weak oxygen-base, DMSO, to solutions of HPTA in dichloromethane (DCM).

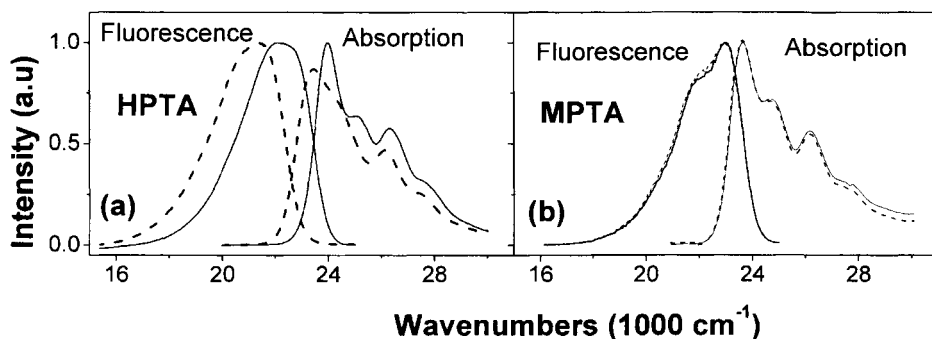


Fig. 1. Fluorescence and absorption spectra of HPTA (1a) and MPTA (1b) in pure DCM – solid lines and in DCM in the presence of 10^{-2} M DMSO – dashed lines.

In contrast, practically no effect was observed when DMSO was added to solutions of MPTA, the methoxy analogue of the photoacid, where the acidic hydrogen atom of the photoacid was replaced by a methyl group (Fig. 1b).

Fig. 2 shows the effect of creating hydrogen-bonding complexes between HPTA and oxygen-bases on the solvation correlation function of HPTA, $C(t)$ [10]. Utilizing a pump-probe set-up described elsewhere [11], with 400 nm excitation, the dynamic Stokes shift of HPTA was analyzed with about 50fs time-resolution. The hydrogen-bonded HPTA exhibited much faster dynamics than the solvation dynamics of the uncomplexed HPTA in pure DCM.

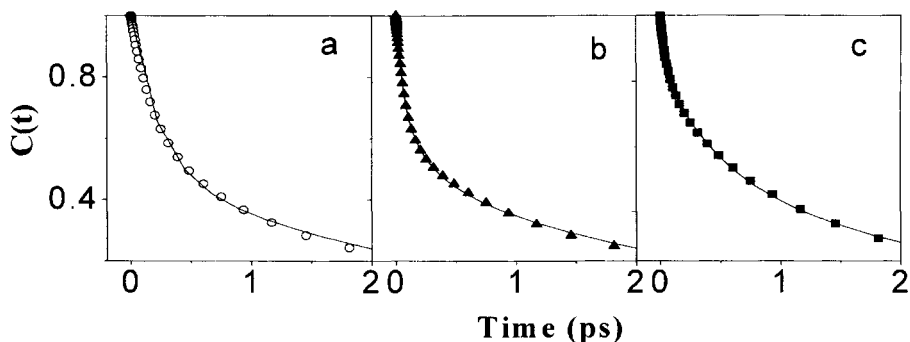


Fig. 2. Plots of calculated $C(t)$ (a) of 5×10^{-4} M HPTA in pure DCM (circles), (b) in presence of 9×10^{-3} M DMSO (triangles) and (c) in presence of 0.1M dioxane (squares). Parameters of the fits, (solid lines) are shown in Table 1.

The detailed comparison between the $C(t)$ of uncomplexed HPTA and the $C(t)$ of complexed HPTA (Table 1) shows that the dynamics of the hydrogen-bonded HPTA contain an additional sub-100fs component over the solvation dynamics found in the pure solvent.

Table 1.

Parameters for the multiexponential fit of $C(t)$, $C(t) = A_1 \exp(-t/\tau_1) + A_2 \exp(-t/\tau_2) + A_3 \exp(-t/\tau_3)$, of HPTA in various solutions.

	DCM	DCM + 9×10^{-3} M DMSO	DCM + 0.1 M dioxane
A_1 (%)	-	28	15
τ_1 (fs)	-	56	60
A_2 (%)	40	29	33
τ_2 (ps)	0.26	0.26	0.26
A_3 (%)	60	43	52
τ_3 (ps)	2.3	2.3	2.3

A reconstruction of the measured time-dependent absorption spectra of the hydrogen-bonding complexes of HPTA with DMSO in DCM is shown in Fig. 3 as the superposition of the absorption and the gain bands of the photoacid.

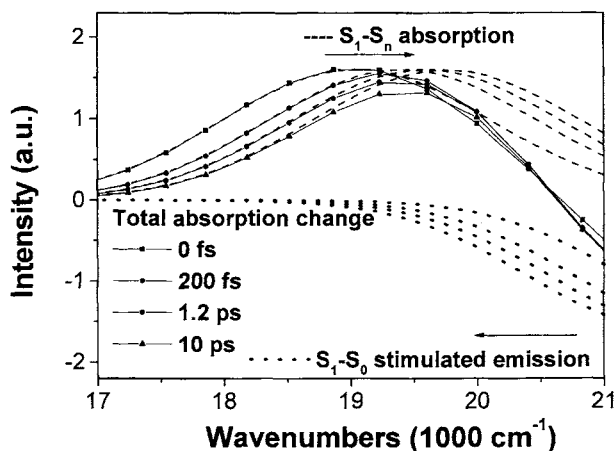


Fig. 3. Reconstruction of the transient absorption spectra of HPTA in DCM in the presence of 9×10^{-3} M DMSO at different pump-probe delays. The time-zero absorption and gain bands of the photoacids are moving toward each other following the relaxation of the solute-solvent interactions to their steady-state values. Full lines are the superposition of the individual absorption and gain bands of HPTA.

We suggest that the additional (over the solvation dynamics in the pure solvent) sub-100fs transient observed in the $C(t)$ of the hydrogen-bonding complexes of HPTA is due to transient changes in the hydrogen-bonding complexes of the type portrayed in Fig. 4 [1, 12]. The time scale is that of the heavy-atom movement within the O-H...O (hydrogen) bond in the electronic excited state of ROH. It resembles, yet it is faster than, the inertial response of the solvent [12-23].

It appears that hydrogen-bonds are potentially fast enough so to allow for bimolecular proton-transfer to occur along relaxed hydrogen-bond links, thus making the preparation of such links, which may involve relatively slow solvent fluctuations, the primary event that establishes the proton transfer coordinate.

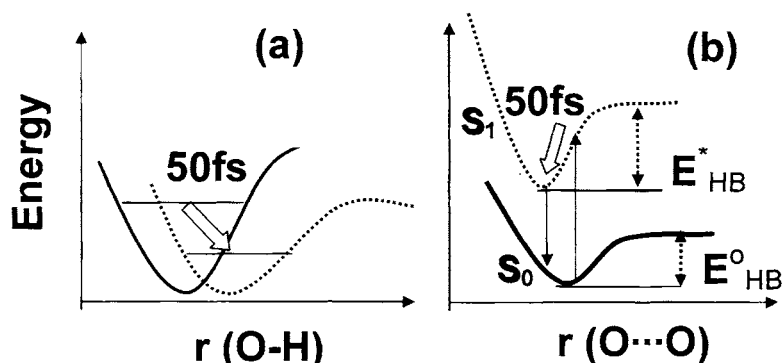


Fig. 4. (a) Schematic response of the covalent O–H bond to the optical excitation of the hydrogen-bonded photoacid. The relaxed state of the hydrogen-bonded photoacid has a (slightly) longer O–H bond-length and a smaller zero-energy value than the locally excited state [24]. (b) Schematic response of the OH \cdots O bond to the optical excitation of the hydrogen-bonded photoacid. E^0_{HB} and E^*_{HB} are the hydrogen-bond interaction energy in the ground-state and the excited-state of the photoacid, respectively, the excited-state interaction being larger. The arrows symbolize the optical transitions.

Acknowledgment

GRF acknowledges financial support of the National Science Foundation.

REFERENCES

- [1] G. C. Pimentel, A. L. McClellan, *The Hydrogen Bond*, Freeman, USA, San-Francisco, 1960, Ch. 3, p. 67-141.
- [2] M. D. Joesten, L. J. Schaad, *Hydrogen Bonding*, Marcel Dekker, USA, New York, 1974, Ch. 1, p. 2-27.
- [3] G. A. Jeffrey, W. Saenger, *Hydrogen Bonding in Biological Structures*, Springer-Verlag, Germany, Berlin, 1991.
- [4] R. W. Taft, J.-L. Abboud, M. J. Kamlet, *J. Am. Chem. Soc.*, 103 (1981) 1080.
- [5] C. Reichardt, *Solvents and Solvent Effects in Organic Chemistry*, VCH, Weinheim, 1990.
- [6] E. Pines, D. Pines, in *Ultrafast hydrogen bonding dynamics and proton transfer processes in the condensed phase*, H. Bakker, and T. Elsaesser (eds.), Netherlands, Dordrecht, Kluwer, 2003, p.155-184.
- [7] C. Chudoba, E. T. J. Nibbering, T. Elsaesser, *Phys. Rev. Lett.*, 81 (1998) 3010.
- [8] C. Chudoba, E. T. J. Nibbering, T. Elsaesser, *J. Phys. Chem. A*, 103 (1999) 5625.
- [9] M. Rini, B.-Z. Magnes, E. Pines, E. T. J. Nibbering, *Science*, 301 (2003) 349.
- [10] M. Maroncelli and G. R. Fleming, *J. Chem. Phys.*, 86 (1987) 6221.
- [11] Q.-H. Xu, Y.-Z. Ma, G. R. Fleming, *Chem. Phys. Lett.*, 338 (2001) 254.
- [12] G. van der Zwan, J. T. Hynes, *J. Chem. Phys.*, 78 (1983) 4174.
- [13] E. W. Castner Jr, M. Maroncelli, G. R. Fleming, *J. Chem. Phys.*, 86 (1987) 1090.
- [14] P. F. Barbara, W. Jarzaba, *Adv. Photochem.*, 15 (1990) 1.
- [15] P. J. Rossky, J. D. Simon, *Nature*, 370 (1990) 263.
- [16] S. J. Rosenthal, X. Xie, M. Du, G. R. Fleming, *Chem. Phys.*, 95 (1991) 4715.
- [17] R. Jimenez, G. R. Fleming, P. V. Kumar, M. Maroncelli, *Nature*, 369 (1994) 471.
- [18] C. F. Chapman, R. S. Fee, M. Maroncelli, *J. Phys. Chem.*, 99 (1995) 4811.
- [19] M. L. Horng, J. A. Gardecki, A. Papazyan, M. Maroncelli, *J. Phys. Chem.*, 99 (1995) 17311.
- [20] B. M. Ladanyi, R. M. Stratt, *J. Phys. Chem.*, 100 (1996) 1266.
- [21] D. S. Larsen, K. Ohta, G. R. Fleming, *J. Chem. Phys.*, 111 (1999) 8970.
- [22] X. J. Jordanides, M. J. Lang, X. Song, G. R. Fleming, *J. Phys. Chem. B*, 103 (1999) 7995.
- [23] R. Rey, K. B. Møller, J. T. Hynes, *J. Phys. Chem. A*, 103 (2002) 11993.
- [24] B.-Z. Magnes, D. Pines, N. Strashnikova, E. Pines, *Solid State Ionics*, 2003 (in press).

Bimodal intermolecular proton transfer in water: photoacid-base pairs studied with ultrafast infrared spectroscopy

M. Rini^a, O. F. Mohammed^a, B.-Z. Magnes^b, E. Pines^b, and E. T. J. Nibbering^a

^aMax Born Institut fuer Nichtlineare Optik und Kurzzeitspektroskopie, Max Born Strasse 2A, D-12489 Berlin, Germany

^bDepartment of Chemistry, Ben-Gurion University of the Negev, P.O.B. 653, Beer-Sheva 84105, Israel

1. INTERMOLECULAR PROTON TRANSFER IN THE LIQUID PHASE

Exploring the mechanism of proton transfer between acid and bases is of fundamental importance for the understanding of e.g. the autoionization of water and the associated von Grotthuss mechanism, acid-base neutralizations, enzyme catalysis, and proton pumps through membranes. In the pioneering work of Weller and Eigen [1,2] intermolecular proton transfer between acid and bases is understood to be controlled by mutual diffusion forming an encounter pair, with an apparent reaction radius (contact separation) of typically 6 to 8 Å. Within the Eigen-Weller model of acid-base reactions, the lower limit for on-contact proton exchange rate is typically $(10 \text{ ps})^{-1} \text{ M}^{-1}$ for the overall reaction rate to be diffusion limited. Direct access to the actual proton transfer remains problematic due to the slower diffusion process dominating the overall dynamics.

2. PHOTOACIDS AS MODEL SYSTEMS FOR PROTON TRANSFER

Photoacids have been the subject of intense investigations since the landmark discovery of Förster [3] that the extreme fluorescence Stokes shift observed for several classes of aromatic dyes can be explained to be due to excited state proton transfer. Photoacids can be used as a means of light triggered proton transfer, thus enabling time-resolved studies [4]. The photoacidity, with typically a decrease in $\text{p}K_a$ of 5-10 units upon excitation, is a research subject on its own, where traditionally a charge transfer from the oxygen atom of the OH-group to the aromatic ring is thought to be responsible for the increased acidity of the photoacid. A more detailed, yet to be verified, explanation invokes the fact that for aromatic systems electronic states excited along the short and long axes are often energetically close, with a possible occurrence of state inversion due to polar interactions with the solvent. In the case of pyranine (8-hydroxy-1,3,6-trisulfonate-pyrene), a widely used dye stain, it has been argued that the initially excited state cannot be the one responsible for the fluorescence emission, and thus a state inversion should occur [5]. We have studied pyranine with femtosecond mid-infrared spectroscopy in the fingerprint region in H_2O (between $850\text{-}1350 \text{ cm}^{-1}$), where vibrational bands of the sulfonate-groups are located, and D_2O ($1250\text{-}1800 \text{ cm}^{-1}$) where aromatic ring and C-O modes have their resonances. When exciting around 400 nm in the electronic origin transition, the photoacid vibrational bands in the S_1 -state appear within

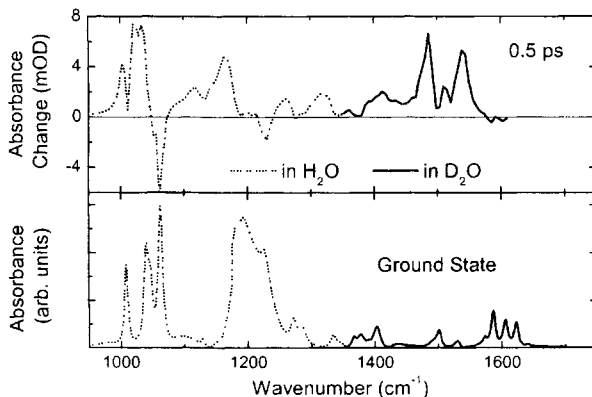


Fig.1. IR spectrum of pyranine in H₂O (dotted lines) and D₂O (solid lines) in the ground state (bottom panel) and absorbance changes after photoexcitation (top panel).

time resolution (150 fs), after which no changes in intensity have been observed in the time range up to 10 ps (see Fig. 1). At longer delay times, after correction for rotational diffusion effects, the decay of these bands, (and the rise of bands associated with the conjugated photobase) is explained by the proton (deuteron) transfer to the solvent with a time constant of 90 (250) ps (Fig. 2). An identical band structure is observed when exciting with excess energy at 349 nm. In the latter case the photoacid bands appear slightly red-shifted, due to anharmonic coupling with highly excited Raman-active modes. Subsequent blue-shifting is then the consequence of intramolecular vibrational redistribution and cooling, taking place on a time scale up to 20 ps, similar to observations in excited state intramolecular hydrogen transfer [6,7]. From these results we conclude that a) the absorption band of pyranine between 330 and 420 nm is due to a transition to a single excited state, and b) state inversion – if it occurs at all – can only proceed at a rate much faster than 150 fs.

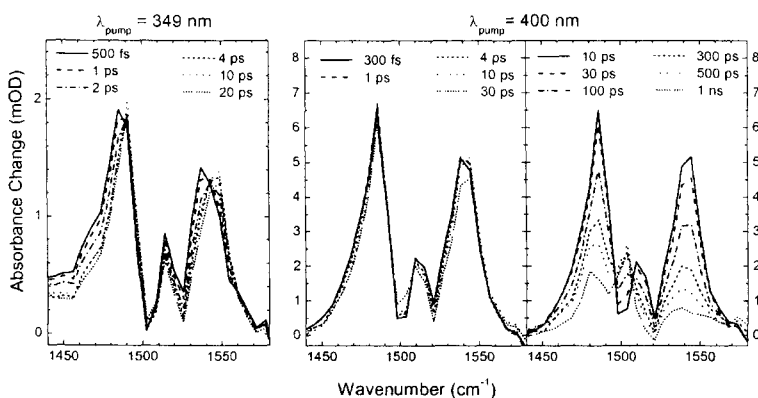


Fig. 2. Transient spectra of pyranine in D₂O excited at 349 nm (left panel) and at 400 nm (centre and right panel).

3. PHOTOACID-BASE NEUTRALIZATION REACTIONS

The neutralization reaction between pyranine and acetate has been studied with time-resolved fluorescence single-photon counting [8] and UV-pump/VIS-probe [9] spectroscopy, from which it was concluded that the Eigen-Weller model of proton transfer is valid. Application of ultrafast mid-infrared spectroscopy of this neutralization reaction has led to new insight in the proton transfer mechanism [10]. When exciting pyranine dissolved at a fixed concentration of 20 mM in D₂O, with varying amounts of the base acetate added (ranging from 0.25 M – 4 M), the deuteron transfer reaction can be followed in real time by inspection of the decay of the 1486 cm⁻¹ marker mode of the photoacid, the rise of signal at the 1503 cm⁻¹ transition of the anion, and the rise of the C=O band of acetic acid at 1720 cm⁻¹ (Fig. 3). The potential of the method lies in the intrinsic option where one can grasp both the dynamics at the deuteron donating side (i.e. the photoacid → photobase transition) and the deuteron accepting side (the acetic acid generated by deuteron transfer). At low base concentrations (0.25-0.5 M) deuteron transfer to the solvent, followed by deuteron pick-up by acetate, dominates the dynamics, as can be learnt from a faster rise of the photobase signal than of the acetic acid band. This feature cannot be observed in time-resolved fluorescence or UV-pump/VIS-probe measurements where it was indirectly studied by monitoring the proton-scavenging effect on the geminate recombination reaction of the photoacid [11, 12]. At high base concentrations (> 1 M) identical rise times for photobase and acetic acid are observed indicating a dominant direct deuteron scavenging mechanism from the photoacid by the base.

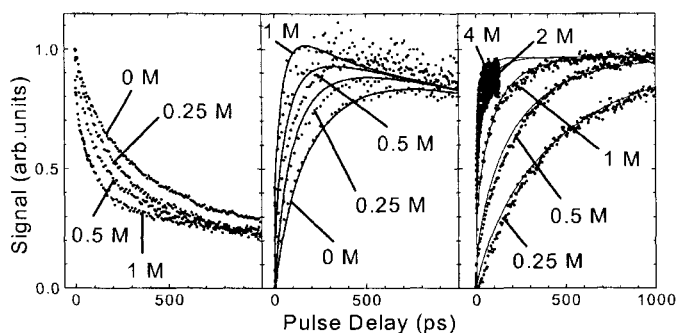


Fig. 3. Decay of the photoacid band at 1486 cm⁻¹ (left panel), the rise of the conjugated photobase band at 1503 cm⁻¹ (centre panel) and acetic acid band at 1720 cm⁻¹ (right panel) as function of acetate concentration. The photoacid and photobase signals are in addition affected by rotational diffusion.

At these high concentrations the observed reaction dynamics are bimodal. The two contributions to the signals can be ascribed to pyranine-acetate complexes with a pre-formed hydrogen bond along the reaction coordinate, and initially uncomplexed pyranine, that first has to form an encounter pair with acetate before a reaction can proceed. The pre-formed complex shows deuteron transfer faster than 150 fs. In contrast, for the fraction of initially uncomplexed pyranine, where the reaction coordinate is established by the diffusion of the reactants and by solvent fluctuations, a much slower bimolecular reaction rate on contact ($a = 6.3 \text{ \AA}$) of $(30 \text{ ps})^{-1} \text{ M}^{-1}$ is found from our data analysis using theory of diffusion-controlled bimolecular reaction dynamics [13] assuming fully screened potential at the high base concentrations used. The fact that the deuteron transfer reaction in the pre-formed “tight”

pyranine-acetate complex is at least 2 orders of magnitude faster than the “loose” pyranine-acetate encounter complex, leads to the important finding that the deuteron transfer mechanism as initially suggested by Eigen and Weller has to be refined (Fig. 4). One explanation follows the line of argument that the acid and base in the encounter complex can only react after substantial rearrangement of water molecules in the solvation shells before acid and base reach direct contact, and the slower reaction rate of the encounter complex is due to this bottleneck solvent rearrangement dynamics. An alternative explanation lies in the possibility of a von Grothuss-type hopping of the proton from the acid to the base via solvation shell water molecules, in which case acid and base never reach direct contact and the overall concerted proton transfer reaction is considerably slower than the hopping time of the proton along a single hydrogen-bond. The latter suggestion can be related to recent numerical studies of the von Grothuss mechanism of proton conductivity [14] and HF ionization and ion pair formation in water [15].

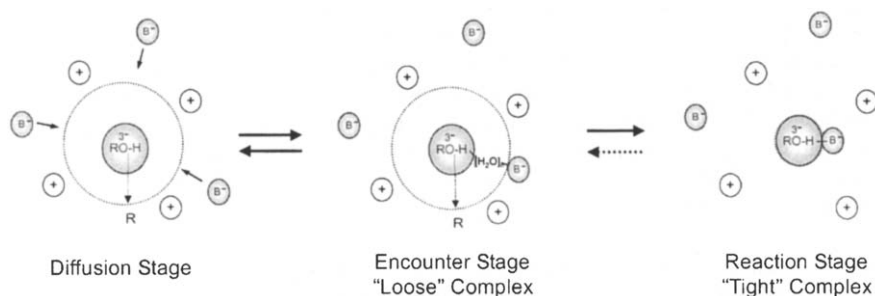


Fig. 4. Schematic representation of the observed dynamics. Initially uncomplexed photoacid first forms an encounter complex through diffusion. This “loose” complex either rearranges to a “tight” complex, or reacts via the hydrogen bonded network between photoacid and base. A pre-formed photoacid-base complex can directly react with extremely fast rates.

REFERENCES

- [1] A. Weller, *Prog. React. Kin.* 1 (1961) 187.
- [2] M. Eigen, *Angew. Chem. Int. Ed.* 3 (1964) 1.
- [3] Th. Förster, *Die Naturwissenschaften* 36 (1949) 186.
- [4] E. Pines and D. Pines, in *Ultrafast Hydrogen Bonding Dynamics and Proton Transfer Processes in the Condensed Phase*, T. Elsaesser and H.J. Bakker (eds.), Kluwer, Dordrecht, the Netherlands, 2002.
- [5] T.-H. Tran-Thi, C. Prayer, Ph. Millié, P. Uznanski and J.T. Hynes, *J. Phys. Chem. A* 106 (2002) 2244.
- [6] M. Rini, A. Kummrow, J. Dreyer, E. T. J. Nibbering and T. Elsaesser, *Faraday Discuss.* 122 (2003) 27.
- [7] M. Rini, J. Dreyer, E. T. J. Nibbering and T. Elsaesser, *Chem. Phys. Lett.* 374 (2003) 13.
- [8] E. Pines, B.-Z. Magnes, M.J. Lang and G.R. Fleming, *Chem. Phys. Lett.* 281 (1997) 413.
- [9] L. Genosar, B. Cohen and D. Huppert, *J. Phys. Chem. A* 104 (2000) 6689.
- [10] M. Rini, B.-Z. Magnes, E. Pines and E.T.J. Nibbering, *Science* 301 (2003) 349.
- [11] S.Y. Goldberg, E. Pines and D. Huppert, *Chem. Phys. Lett.* 192 (1992) 77.
- [12] E. Pines and G.R. Fleming, *Chem. Phys.* 183 (1994) 393.
- [13] A. Szabo, *J. Phys. Chem.* 93 (1989) 6929.
- [14] D. Marx, M.E. Tuckerman, J. Hutter and M. Parrinello, *Nature* 397 (1999) 601.
- [15] K. Ando and J.T. Hynes, *J. Phys. Chem. A* 103 (1999) 10398.

Symmetry breaking wavepacket motion and absence of deuterium isotope effect in ultrafast excited state proton transfer

S. Lochbrunner, K. Stock, C. Schrieffer, and E. Riedle

LS für BioMolekulare Optik, LMU München, Oettingenstr. 67, 80538 München, Germany

ABSTRACT

The double proton transfer of [2,2'-Bipyridyl]-3,3'-diol is investigated by UV-visible pump-probe spectroscopy with 30 fs time resolution. We find characteristic wavepacket motions for both the concerted double proton transfer and the sequential proton transfer that occur in parallel. The coherent excitation of an optically inactive, antisymmetric bending vibration is observed demonstrating that the reactive process itself and not only the optical excitation drives the vibrational motions. We show by the absence of a deuterium isotope effect that the ESIPT dynamics is entirely determined by the skeletal modes and that it should not be described by tunneling of the proton.

1. INTRODUCTION

Recently we performed UV-visible pump-probe measurements with 30 fs time resolution on various molecules exhibiting excited state intramolecular proton transfer (ESIPT) [1-4]. The results led to a very precise picture of the process. The ESIPT proceeds as a ballistic wavepacket motion along skeletal coordinates from the Franck-Condon region to the product well. The initial deformation of the molecule that corresponds to this wavepacket motion reduces the proton donor/acceptor distance. This leads to a change of the electronic configuration and the bonds alter and subsequently the nuclei move towards their new equilibrium positions. A few participating normal modes are coherently excited by the process leading to a characteristic ringing of the molecule and to oscillations in the pump-probe signal.

Two consequences arise from this model: First, the coherent excitation of normal modes can result from the reactive process and must not be caused by the optical excitation. Optically inactive modes can be excited if they contribute to the reaction path. Second, the proton is passively shifted by the skeletal movements and stays all the time in its local potential well. A substitution of the proton by a deuteron should therefore not influence the dynamics. In contrast strong variations are expected, if tunneling of the proton is the central step.

We test these predictions on the double proton transfer system [2,2'-Bipyridyl]-3,3'-diol (BP(OH)₂) dissolved in cyclohexane. The molecule contains two H-chelate rings and exhibits inversion symmetry in the electronic ground state. Glasbeek and coworkers found that after optical excitation the molecule can undergo concerted double proton transfer leading to the diketo form or single proton transfer leading to a monoketo intermediate which does not show inversion symmetry [5]. The monoketo yield increases with shorter excitation wavelengths [6]. The monoketo intermediate transforms in a second step to the final diketo within 10 ps. The initial steps of the proton transfer have not been observed in real time up to now.

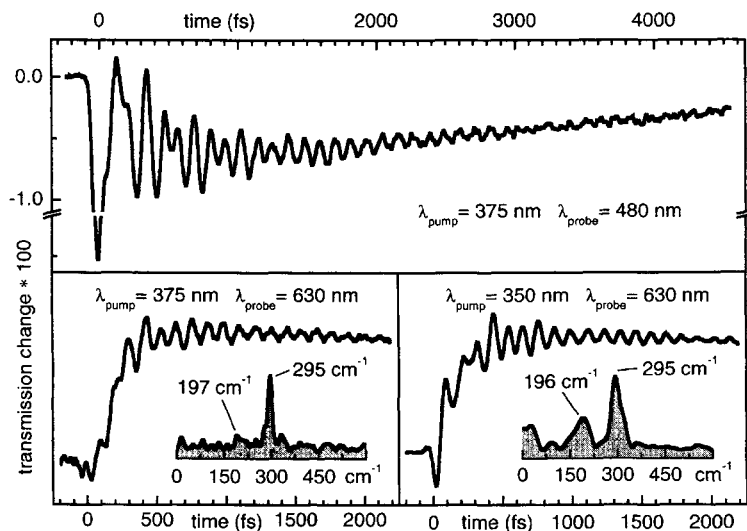


Fig. 1. Transient transmission at different excitation and probe wavelengths. Insets show the Fourier transformations of the oscillatory contributions at 630 nm for different excitation wavelengths.

2. SYMMETRY BREAKING WAVEPACKET DYNAMICS

We performed transient absorption measurements on $\text{BP}(\text{OH})_2$ with a spectrometer based on two noncollinearly phase matched optical parametric amplifiers (NOPAs) pumped by an homebuilt regenerative Ti:Sapphire laser system or a CPA 2001 (Clark-MXR) [1,7]. The tunable UV pump pulses are generated by frequency doubling the output of one of the NOPAs. The other NOPA provides the visible probe pulses. The cross correlation between pump and probe pulses has a typical width (FWHM) of 40 fs. The sample is a cyclohexane solution of $\text{BP}(\text{OH})_2$ pumped through a flow cell with a 120 μm thick channel.

Fig. 1 shows measurements with excitation at 375 nm and 350 nm and probe wavelengths of 480 nm and 670 nm. The change of the sample transmission is depicted in dependence on the delay time. Strong oscillations are observed in all traces. In the spectral region of the product fluorescence at $\lambda_{\text{probe}} = 630$ nm we find an emission rise with a significant delay with respect to the pump pulse. We interpret the delay as the time the optically prepared wavepacket needs to travel from the Franck-Condon region to the product minimum [2,4]. The initial motion is driven by the electronic configuration change due to the optical excitation. A further configuration change occurs shortly before the product minimum, namely the change from the enol to the keto form. The oscillating signal components originate from coherently excited vibrational modes in the product form of the proton transfer. They are dominated by two contributions, one at 196 cm^{-1} and the other at 295 cm^{-1} . This is demonstrated by the Fourier transformations of the oscillatory contributions shown in Fig. 1.

We performed DFT calculations of $\text{BP}(\text{OH})_2$ in the electronic ground state and found two vibrational normal modes fitting nicely to the observed frequencies (see Fig. 2). The low frequency mode at 196 cm^{-1} is attributed to an antisymmetric in-plane bending vibration. This motion alternately reduces the distance between the proton donors and acceptors in the two H-chelate rings. Therefore we believe that it promotes the single proton transfer by enabling the electronic configuration change in that chelate ring where the first contraction occurs (Fig. 3).

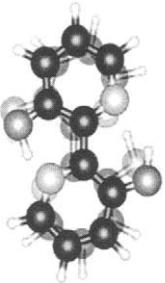
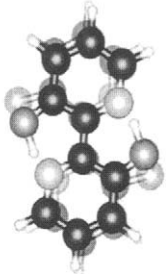
Calc.	206 cm^{-1}		318 cm^{-1}	
Exp.	196 cm^{-1}		295 cm^{-1}	

Fig. 2. Normal modes from DFT calculations. Comparison of calculated and measured frequencies.

After the ESIPT the molecule exhibits a pronounced ringing in this mode. The 295 cm^{-1} mode is a symmetric in-plane stretching vibration (see Fig. 3). The corresponding contraction of the molecule reduces the donor acceptor distances in both chelate rings simultaneously and initiates the electronic configuration change of the concerted ESIPT. The concerted double proton transfer leads therefore to a ringing of the molecule in this second mode.

This assignment is further proven by comparing measurements at different excitation wavelengths (see Fig. 1). Changing the excitation from 375 nm to 350 nm increases the yield for the monoketo intermediate by a factor of 3 from 10 % to 30 % [6]. Correspondingly, the amplitude of the signal oscillations at 196 cm^{-1} is much smaller for pumping at 375 nm than at 350 nm. Obviously, the 196 cm^{-1} mode is excited more strongly if more monoketo is generated, demonstrating that this mode contributes indeed to the single proton transfer. The oscillatory contribution at 295 cm^{-1} is of comparable strength for both excitation wavelengths. Since the yield for the concerted transfer varies only by a factor of 1.3 the strength of the 295 cm^{-1} mode is much less affected by the excitation wavelength.

The 196 cm^{-1} mode is antisymmetric and thereby optically inactive and does not appear in the Raman spectrum. Since a direct optical excitation of the mode is excluded by symmetry selection rules we conclude that it is solely excited by the single proton transfer which breaks the symmetry. This demonstrates for the first time that the coherent excitation of a vibrational mode results exclusively from an ultrafast reactive process.

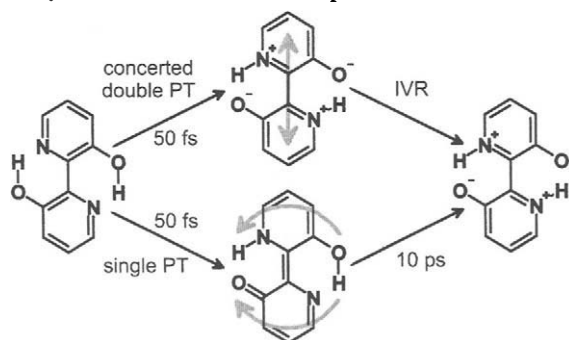


Fig. 3. Excitation of vibrational modes due to different reaction channels. Concerted double proton transfer leads to a symmetric stretching vibration and symmetry breaking single proton transfer to an antisymmetric bending motion. Damping of the vibrational motion by internal vibrational redistribution is indicated by “IVR”.

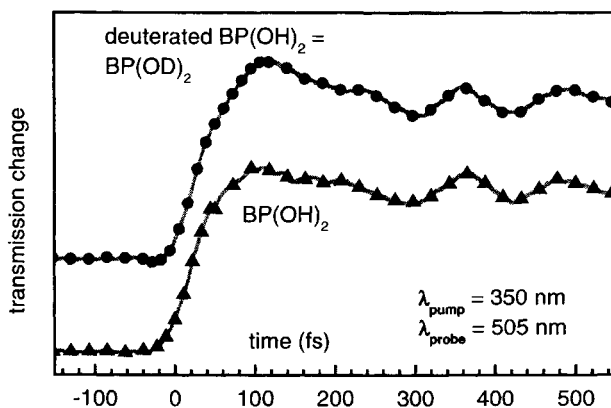


Fig. 4. Comparison of the transient transmission of $\text{BP}(\text{OH})_2$ (triangles) and $\text{BP}(\text{OD})_2$ (circles) excited at 350 nm and probed at 505 nm. No differences in the delay of the emission rise and the oscillation pattern are observed.

3. ABSENCE OF DEUTERIUM ISOTOPE EFFECT

The protons of the hydroxy groups were deuterated by dissolving $\text{BP}(\text{OH})_2$ in cyclohexane and shaking the solution with deuterated water for several hours. After precipitation pump-probe measurements of $\text{BP}(\text{OD})_2$ in cyclohexane were recorded and are compared to $\text{BP}(\text{OH})_2$ in Fig. 4. Both samples were excited at 350 nm and probed at 505 nm. The delay of the emission rise of about 50 fs is equal in both cases and the coherent excitation of the vibrations is identical with respect to frequencies, phases and amplitudes. The ESIPT dynamics is obviously not altered by the deuteration and the mass of the proton has no influence on the transfer speed. This excludes that tunneling of the proton determines the speed of the transfer and the measurements provide the first proof for the passive behavior of the proton in the ESIPT.

4. CONCLUSIONS

We observe the coherent excitation of an optically inactive mode proving that the reactive process itself and not only the optical excitation drives the observed vibrational motions. Further we demonstrate that during the ESIPT the proton is adiabatically shifted from one site to the other and tunneling of the proton is not rate determining. The dynamics is entirely controlled by the skeletal modes. Interestingly, this is quite similar to ground state proton transfer of HCl, where the fluctuations of the water environment enable the adiabatic process [8].

REFERENCES

- [1] A.J. Wurzer, S. Lochbrunner, E. Riedle, *Appl. Phys. B*, 71 (2000) 405.
- [2] S. Lochbrunner, A.J. Wurzer, and E. Riedle, *J. Chem. Phys.*, 112 (2000) 10699.
- [3] K. Stock, T. Bizjak, and S. Lochbrunner, *Chem. Phys. Lett.*, 354 (2002) 409.
- [4] S. Lochbrunner, A.J. Wurzer, and E. Riedle, *J. Phys. Chem. A*, DOI: 10.1021/jp035203z.
- [5] H. Zhang, P. van der Meulen and M. Glasbeek, *Chem. Phys. Lett.*, 253 (1996) 97.
- [6] D. Marks, P. Proposito, H. Zhang, and M. Glasbeek, *Chem. Phys. Lett.*, 289 (1998) 535.
- [7] E. Riedle, M. Beutter, S. Lochbrunner, J. Piel, S. Schenkl, S. Spörlein, W. Zinth, *Appl. Phys. B*, 71 (2000) 457.
- [8] K. Ando and J.T. Hynes, *J. Phys. Chem. B*, 101 (1997) 10464.

Excited-state proton transfer dynamics of 6-hydroxyquinoline in acidic and alkaline aqueous solutions

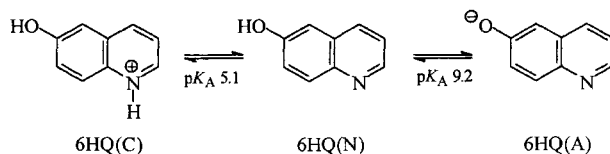
O. Poizat^a, Guy Buntinx^a, E. Bardez^b and V. Alain^b

^aLaboratoire de Spectrochimie Infrarouge et Raman (UMR 8516 de l'Université et du CNRS), Centre d'Etudes et de Recherches Lasers et Applications (FR 2416 du CNRS), Bât. C5, Université des Sciences et Technologies de Lille, 59655 Villeneuve d'Ascq, France

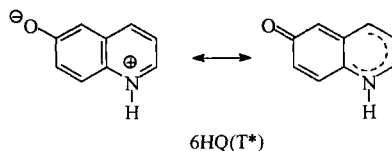
^bLaboratoire de Chimie Générale, Conservatoire National des Arts et Métiers, 292 rue Saint-Martin, 75003 Paris, and Laboratoire de Photophysique et Photochimie Supramoléculaires et Macromoléculaires (CNRS UMR 8531), Ecole Normale Supérieure de Cachan, 61 Avenue du Président Wilson, 94235 Cachan Cedex, France

1. INTRODUCTION

The amphoteric 6-hydroxyquinoline (6HQ) molecule has a weak acidic hydroxyl function ($pK_A = 9.2$) and a weak basic imine function ($pK_A = 5.1$) in the ground-state [1]. A cationic (quinolinium) form 6HQ(C), an anionic (quinolinate) form 6HQ(A), and a neutral form 6HQ(N) are thus predominantly present in acidic, alkaline, and neutral aqueous solutions, respectively, according to the following acid-base equilibria:



Steady-state fluorescence measurements as a function of the pH revealed [1] that, in the lowest excited state, both the acidity of the hydroxyl group and the basicity of the nitrogen atom are considerably enhanced: phenol deprotonation upon excitation of 6HQ(C) occurs in 10 M HClO₄ whereas imine protonation upon excitation of 6HQ(A) arises in 12 M NaOH. In neutral aqueous solution, simultaneous proton release and proton capture was suggested to arise on both sites of the excited 6HQ(N) molecule. The essential stable form in a large range of pH is thus the excited tautomer, 6HQ(T*) [1]. These proton transfer processes are coupled to an intramolecular electron redistribution yielding a neutral ketonic configuration, which strongly lowers the probability of the back proton transfers in the excited state [1]:



6HQ(N), 6HQ(C), 6HQ(A), and 6HQ(T) absorb at 326, 344, 358, and 408 nm, and fluoresce at 380, 450, 490, and 585 nm, respectively [1, 2]. The excited state proton transfer dynamics

is almost unexplored. Recent investigations by picosecond time-resolved fluorescence [3, 4] led to opposed conclusions concerning the chronology of the double proton transfer process in neutral water. We present a sub-picosecond transient absorption investigation of the photoinduced tautomerization of 6HQ in acidic and alkaline aqueous solutions.

2. EXPERIMENTAL

10^{-3} M solutions of 6HQ (Kodak) in distilled, deionized water containing distilled perchloric acid (Aldrich 99.999%) or potassium hydroxide pellets (Aldrich 99.99%) were circulating in a flow cell (2.5 mm optical path length). The subpicosecond transient absorption experiment has been already described [5]. The polarizations of the laser pump (266 nm) and continuum probe pulses were set at the magic angle (overall time resolution 300 fs).

3. PHOTOPHYSICS OF 6HQ IN ALKALINE AQUEOUS SOLUTION

Fig. 1 (left) shows transient spectra recorded after excitation of the quinolate form 6HQ(A) in 1 M KOH. These spectra result from the superimposition of absorption (positive ΔOD) and of bleaching or stimulated emission (negative ΔOD) signals. The deep and narrow gorge seen at all times at 360 nm corresponds to the position of the ground state 6HQ(A) absorption [1, 2]. It is likely due to bleaching. The 1-ps spectrum (part A) displays a sharp band peaking below 350 nm and a weaker one at 394 nm. It undergoes a fast evolution until 5 ps, with a broadening of the 394 nm band that shifts to 398 nm and the appearance of a hole at 530 nm. Then, up to 100 ps, a new absorption band grows at 485 nm whereas the 398 nm band shifts to 408 nm. In addition, the negative band at 530 nm is replaced by a new one around 610 nm. An isosbestic point is present at 560 nm. The exponential fits of the 610-nm decay and 485-nm rise kinetics lead to the same characteristic time of 30 ± 5 ps. Finally, from 100 to 1500 ps, one observes the concomitant disappearance of all signals (610 nm hole and 350, 408, and 484 nm absorptions) with an approximate decay time of 900 ps. An isosbestic point is again noticed at 535 nm between the negative and positive signals during the decay kinetics. These observations attest that the 100-ps spectrum corresponds to a single transient species, the precursor of which is characterized by the 5-10 ps spectrum.

We ascribe the 100-ps spectrum to the excited-state tautomer, 6HQ(T*), as the negative band at 610 nm corresponds without ambiguity to its stimulated emission ($S_1 \rightarrow S_0$). The bathochromic shift of this band relative to the position of the 6HQ(T*) fluorescence (580 nm) is due to the superimposition of the tautomer $S_1 \rightarrow S_n$ absorption in the high energy side of the emission band. We ascribe then the 5-10 ps spectrum to the precursor excited state 6HQ(A*) produced initially by the excitation of the ground state anion 6HQ(A). This assignment is confirmed by the negative signal around 530 nm, likely due to the stimulated emission of 6HQ(A*). Its shift relative to the 6HQ(A*) fluorescence ($\lambda_{\max} = 490$ nm) is again explained by the presence of overlapping $S_1 \rightarrow S_n$ absorption and $S_1 \rightarrow S_0$ emission signals in the 400-500 nm region. We suggest that the spectral evolution observed in the 0-5 ps range is due to some kind of relaxation dynamics of the excited state 6HQ(A*) such as solvation or

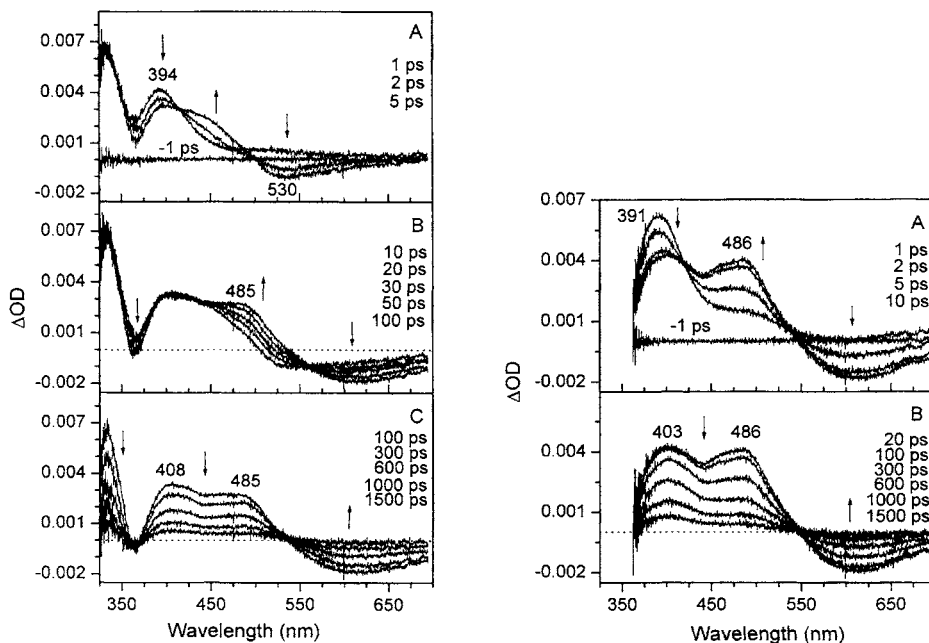


Fig. 1. Transient absorption spectra of 6HQ in $\text{H}_2\text{O} + 1 \text{ M KOH}$ (left) and in $\text{H}_2\text{O}/\text{HCl}$ at pH 1.5 (right) at different time delays after excitation at 266 nm. Vertical arrows indicate the signal evolution.

vibrational/conformational relaxation. The absence of transient signal after decay of $6\text{HQ}(\text{T}^*)$ indicates that the molecules recover directly the initial ground-state anionic form $6\text{HQ}(\text{A})$. The radiationless relaxation of $6\text{HQ}(\text{T}^*)$ is immediately followed by ground-state quinolinium deprotonation, $6\text{HQ}(\text{T}) + \text{OH}^- \rightarrow 6\text{HQ}(\text{A}) + \text{H}_2\text{O}$, as expected in highly basic medium (a $1.4 \times 10^{10} \text{ s}^{-1}$ pseudo-first order rate is deduced [6] from the diffusion coefficient and activity coefficient of OH^- (1 M) in water). The reaction scheme is summarized in Figure 2 (left). According to the value of $\text{p}K_{\text{A}}^* \geq 14$ estimated for the excited state of $6\text{HQ}(\text{T})$ [6], the excited-state back proton transfer must be very slow compared to the forward transfer process $6\text{HQ}(\text{A}^*) \rightarrow 6\text{HQ}(\text{T}^*)$ even in 1 M KOH. This is consistent with the assumption [1] that the stable configuration of $6\text{HQ}(\text{T}^*)$ is dominantly ketonic, with a reduced charge separation and an attenuated quinolinium acidity compared to the zwitterionic form. Interestingly, the excited-state imine protonation is much faster in $6\text{HQ}(\text{A})$ (30 ps) than in the 6-methoxyquinoline molecule (1.9 ns [7]). This large difference confirms the previous statement that the negative charge of the oxy group in $6\text{HQ}(\text{A}^*)$ enhances considerably the basicity of the nitrogen atom [1]. The 30-ps characteristic time found for this forward transfer is slightly shorter than the 46-ps decay time reported for the $6\text{HQ}(\text{A}^*)$ fluorescence in alkaline aqueous solution [3].

4. PHOTOPHYSICS OF 6HQ IN ACID AQUEOUS SOLUTIONS

Fig. 1 (right) shows the transient spectra obtained after excitation of $6\text{HQ}(\text{C})$ in a $3 \times 10^{-2} \text{ M HClO}_4$ aqueous solution (pH 1.5). The shortest time spectrum presents a strong absorption at 391 nm and a shoulder around 500 nm. It decays with a characteristic time of 2.2 ps to yield a new spectrum with 2 absorption bands at 403 and 486 nm and a negative one

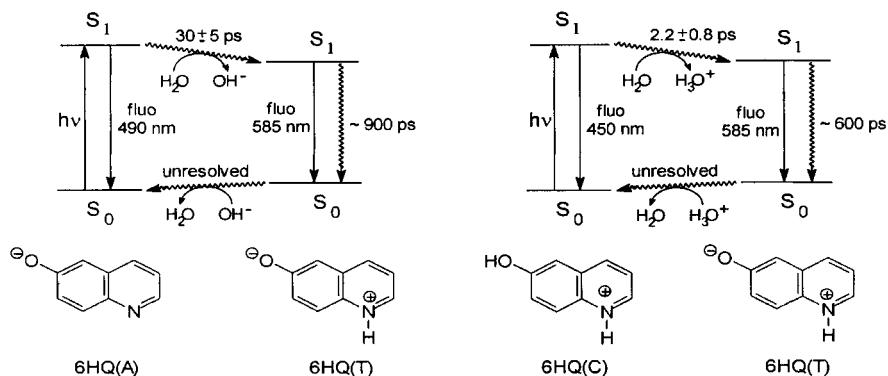


Fig. 2. Excited-state proton transfer reaction schemes in alkaline (left) and acid (right) solutions.

at 610 nm (isosbestic points at 420 and 540 nm). Then, all signals disappear simultaneously (isosbestic point at 550 nm) with a rate constant of $\sim(600 \text{ ps})^{-1}$. The absence of signal below 360 nm is due to the extinction of the probe light by the residual, strongly absorbing 6HQ(C). At 12 M HClO_4 , a single spectrum was observed, constant in shape and intensity from 0 to 1500 ps, similar to the 1-ps spectrum obtained in 3×10^{-2} M HClO_4 , and a fluorescence ($\lambda_{\text{max}} = 446 \text{ nm}$) lifetime of 24 ns was measured.

The final transient spectrum (10-1500 ps) is similar to that in alkaline solution (100-1500 ps). It corresponds thus to the excited-state tautomer 6HQ(T*). The precursor spectrum (1-ps spectrum in Fig. 2) is ascribed to the parent excited state 6HQ(C*) produced initially by excitation of 6HQ(C). This assignment is confirmed by the fact that only this parent excited-state spectrum is present in 12 M HClO_4 where the hydroxyl group cannot deprotonate [1]. The high rate of excited-state hydroxyl deprotonation measured at pH 1.5 ($\tau = 2.2 \text{ ps}$) cannot be suspected of being significantly affected by the reprotonation kinetics since the maximum pseudo first-order rate of back proton transfer, estimated from the proton diffusion coefficient in water, is much slower ($1.5 \times 10^9 \text{ s}^{-1}$, $\tau = 670 \text{ ps}$). As in alkaline solution, no transient signal is detected after decay of 6HQ(T*): proton capture by 6HQ(T) to yield back 6HQ(C) follows immediately the 6HQ(T*) deactivation. The reaction scheme is shown in Figure 2 (right).

The excited-state deprotonation of the hydroxyl group of 6HQ(C) in acid aqueous solution is notably faster (2.2 ps) than the excited-state protonation of the nitrogen atom of 6HQ(A) in alkaline solution. It suggests that, in neutral solution, the excited state of the neutral form 6HQ(N) should undergo hydroxyl deprotonation prior to imine protonation. Preliminary results at pH 7 confirm indeed [6] that the excited tautomer is produced from 6HQ(N*) via two consecutive proton transfers in the order $6\text{HQ}(\text{N}^*) \rightarrow 6\text{HQ}(\text{A}^*) \rightarrow 6\text{HQ}(\text{T}^*)$.

REFERENCES

- [1] E. Bardez, A. Chatelain, B. Larrey and B. Valeur, *J. Phys. Chem.*, 98 (1994) 2357.
- [2] S. F. Mason, J. Philip and B. E. Smith, *J. Chem. Soc. A*, (1968) 3051.
- [3] T. G. Kim, Y. Kim and D.-J. Jang, *J. Phys. Chem. A*, 105 (2001) 4328.
- [4] H. Yu, H.-J. Kwon and D.-J. Jang, *Bull. Korean Chem. Soc.*, 18 (1997) 156.
- [5] G. Buntinx, R. Naskrecki and O. Poizat, *J. Phys. Chem.*, 100 (1996) 19380.
- [6] O. Poizat, E. Bardez, G. Buntinx and V. Alain, in preparation.
- [7] E. Pines, D. Huppert, M. Gutman, N. Nachliel and M. Fishman, *J. Phys. Chem.*, 90 (1986) 6366.

Ultrafast intermolecular proton transfer from 10-hydroxycamptothecin

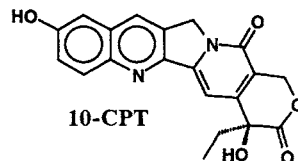
S. Ashkenazi,^a P. Leiderman,^a D. Huppert,^a K. M. Solntsev^b and L. M. Tolbert^b

^aRaymond and Beverly Sackler Faculty of Exact Sciences, School of Chemistry, Tel Aviv University, Tel Aviv 69978, Israel

^bSchool of Chemistry and Biochemistry, Georgia Institute of Technology, Atlanta, GA 30332-0400, USA

1. INTRODUCTION

Fluorescence probes are widely used for the investigation of biologically important systems. In most cases the steady-state spectral data is used for the characterization of properties of their microenvironment. Surprisingly, few synthetic probes are known to utilize their excited-state reactivity, such as excited-state proton transfer, as an additional tool for the investigation of complex systems. Proton transfer, in both the ground and excited states, is a fundamental process in chemistry and biology. For 50 years it has been known that the acidity of various hydroxyaromatic compounds (ROH) increases significantly upon excitation, and, therefore, protolytic photodissociation (excited-state proton transfer to solvent or PTTS) has been studied intensively. Camptothecin (CPT) is a pentacyclic alkaloid, first isolated from extracts of the Chinese tree *Camptotheca acuminata*. This brightly fluorescent compound was found to be a potent inhibitor of the growth of leukemia cells by exhibiting a unique mechanism of action: inhibition of DNA topoisomerase II [1]. A more potent water-soluble analog of CPT, 10-hydroxycamptothecin (10-CPT), has a subunit identical to 6-hydroxyquinoline (6HQ). Hydroxyquinoline derivatives are known to be both strong photoacids and strong photobases and, therefore, undergo efficient tautomerization in the very wide range of pH resulting in weak tautomer (zwitterion) emission [2]. In the only known report on 10-CPT spectral properties, Mi and Burke [3] considered 10-CPT dual fluorescence in methanol-water mixtures as solvent polarity-dependent without taking into account any possible PTTS. We report here the study of the ultrafast excited state intermolecular proton transfer processes of 10-CPT to a water-methanol mixture.



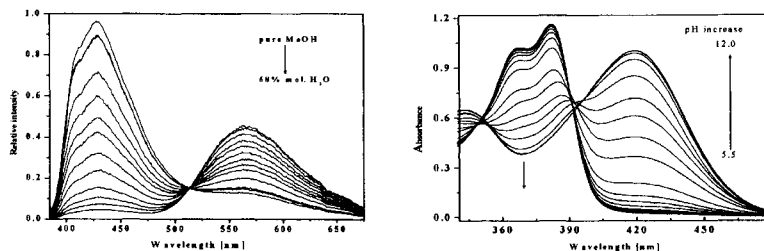


Fig. 1. Left: the emission spectra of 10-CPT in methanol-water mixtures. Right: the absorption spectra of 10-CPT in 68% mol water mixture as function of pH.

2. RESULTS AND DISCUSSION

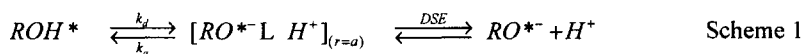
2.1. Absorption and emission spectra

The absorption and emission spectra of 10-CPT in water-methanol mixtures at room temperature (ca. 22 °C) in the pH range from neutral to basic in general exhibit a well-known naphthol-type behavior [4]. The absorption spectra in neutral water and methanol are nearly identical, the latter having a 3 nm bathochromic shift. The equilibrium between neutral (ROH, 380 nm) and *O*-deprotonated (RO⁻, 420 nm) forms of 10-CPT is characterized by a p*K*_a of 8.9 in a 68% mole H₂O mixture (Fig. 1 right). The protonation of quinolinium nitrogen has a p*K*_a of around 1.0, more than 3 p*K*_a units lower than the parent 6HQ.

The emission spectra of 10-CPT in water-methanol mixtures exhibits dual fluorescence (Fig. 1 left). The appearance of the low energy emission band at 570 nm for 10-CPT in a neat methanol solution indicates an efficient PTTS process. The large fluorescence quantum yield and similarity of the emission at neutral and basic solutions is evidence of the excited anion (RO^{-*}) formation, in contrast to 6HQ, for which double PTTS leads to the tautomer [2]. With the increase of water content in the mixtures, we observed a substantial decrease in the fluorescence intensity of the nondissociated form of 10-CPT at 430 nm and a concomitant increase of RO^{-*} intensity at 570 nm. This is a well-known effect in hydroxyaromatic compounds [4] and is attributed to the increase of the protolytic photodissociation rate with increasing water concentration.

2.2. Time-resolved measurements

The relatively simple spectral and kinetic behavior of 10-CPT in methanol-water mixtures can be described by a well-developed reversible diffusion influenced two-step model (Scheme 1). We successfully applied this scheme in the experimental and theoretical studies of reversible ESPT processes in solution.



The first step is described by back-reaction boundary conditions with intrinsic rate constants k_d and k_a . This is followed by a diffusion second step in which the hydrated proton is removed from the parent molecule. This latter step is described by the Debye-Smoluchowski equation (DSE).

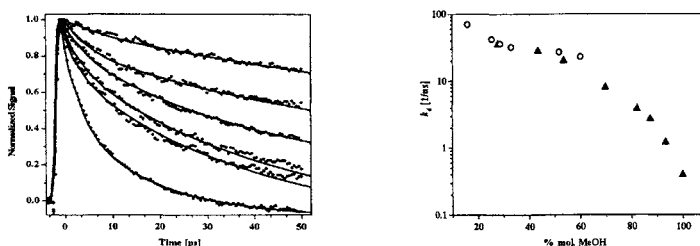


Fig. 2. Left: Pump probe signal of 10 CPT in methanol-water mixtures. The pump was at 390 nm and the probe at 550 nm. Water mole fraction top to bottom: 0, 0.18, 0.28, 0.40, 0.48, 0.84.

Right: Dependence of the dissociation rate constant k_d on solvent composition. (\blacktriangle) data measured using the TCSPC technique, (\circ) data measured by the pump probe technique.

Time-resolved data from the solutions at room temperature (ca. 22 °C) were obtained using a femtosecond pump-probe technique with a time resolution of about ~ 150 fs, as well as time correlated single photon counting (TCSPC) with a limited time resolution of about 20 ps [5]. Fig. 2 left shows the pump-probe signal of 10-CPT in water/methanol mixtures measured at 550 nm after excitation of the sample by a ~ 100 fs pulse at 390 nm. As seen, the larger the water mole fraction, the faster the decay rate. At the highest water mole fraction, the probe pulse transmission, ΔT , changes signs from $\Delta T < 0$ to $\Delta T > 0$ at about 20 ps. The signal consists of two distinct time regimes, a short-time component with an amplitude of about 0.2 and a 3 ps lifetime, and a long-time component of about 14 ps at $x_{\text{H}_2\text{O}} \sim 0.8$. In our previous study [5], we measured the direct proton-transfer rate between a photoacid, 8-hydroxypyrene-1,3,6-trisulfonate (HPTS), and a base, acetate anion in water and D_2O , using a pump-probe technique with ~ 150 fs time resolution. We attribute the positive part of the signal to absorption due to the optical transition $\text{ROH}(S_1) \rightarrow \text{ROH}(S_2)$. The negative component arises from the RO^* stimulated emission due to transition to the ground state. The total signal at 550 nm was analyzed by:

$$-\Delta T \propto \sigma_{\text{ROH}^*} S(t) - \sigma_{\text{RO}^*} (1 - S(t)) + A \exp(-t/\tau_{\text{short}}) \quad (1)$$

where σ_{ROH^*} denotes the absorption cross section of the S_1 to a higher excited-state $S_1 \rightarrow S_n$ transition of ROH and σ_{RO^*} denotes the emission cross section of RO^* . $S(t)$ and $(1 - S(t))$ are the excited-state survival probabilities of ROH^* and RO^* respectively as calculated by the SSDP program [6]. The short component, τ_{short} , arises from changes in both σ_{ROH^*} and σ_{RO^*} , and its origin is probably related to ultrafast hydrogen-bonded complex formation. The

computer fits to the signals with the abovementioned time components are shown in Fig. 2 left as solid lines. A similar analysis was performed with the data obtained from the TCSPC method.

2.3. Composition dependence of proton transfer rate and nature of the proton acceptor

The dissociation rate coefficient, k_d , depends nonlinearly on the mole fraction of water (Fig. 2 right), showing a strong variation in the methanol-rich region and changing very little in the water rich region (0-60% methanol). A similar effect was observed for 5CN2OH [4] and 5CN1OH [7]. It was explained by (a) preferential solvation of the hydroxyl moiety by water and (b) a gradual change in the solvation energy of the CIP.

Table 1. Parameters Used in Fitting the Signal Decay of 10-CPT in methanol-water using the pump-probe technique [4].

$X(\text{H}_2\text{O})$	k_d [ns ⁻¹]	k_a [Å ns ⁻¹]	ϵ	D_{H^+} [10 ⁻⁵ cm ² s ⁻¹]	R_D [Å]	pK_a^*
0	5	3	32.6	3.6	17.1	0.49
0.18	13	6	41.0	2.5	13.6	0.096
0.40	23	23	50.9	2.3	11.0	0.22
0.67	32	28	63.3	3.9	8.8	0.00
0.75	42	36	66.8	4.7	8.3	-0.04
0.87	83	84	72.6	6.7	7.6	-0.03

Previously we suggested analyzing the water dependence of k_d using the assumption that PTTS to water and methanol can be considered as two parallel processes. In this case, the nature of the proton-accepting water cluster can be determined by an analysis of the dissociation constant dependence on water concentration using

$$k_d = k_m + k_w[\text{H}_2\text{O}]^n \quad (2)$$

where k_m is the dissociation rate in pure methanol, k_w is its water dependent component and n is roughly associated with the number of water molecules involved in the proton transfer step. We found a correlation between the photoacid strength and the size of water cluster acting as primary proton acceptor [4]. The apparent size of the water cluster n decreased from 2.0 for HPTS with $pK_a^* = 1.4$ down to 0.8 for 5,8-dicyano-2-naphthol with $pK_a^* \sim 4.5$. Our results show that, for, 10-CPT, n is about 1.4 and $pK_a^* \sim 0$. Therefore, we confirm the abovementioned hypothesis that n probably reflects the structure of the contact ion pair that may vary for the photoacids with different pK_a^* 's.

3. CONCLUSIONS

We have demonstrated that the novel antitumor agent 10-hydroxycamptothecin has remarkable excited-state acidity. In contrast to simple 6-hydroxyquinoline, no tautomerization is observed. The implications for the use of proton transfer dynamics in studying the microenvironment of cells remains to be demonstrated.

ACKNOWLEDGMENT

Support of this research by the U. S. National Science Foundation and the U.S.-Israel Binational Science Foundation is gratefully acknowledged.

REFERENCES

- [1] M. Potmesil and H. Pinedo (eds.), *Camptothecins: New Anticancer Agents*, CRC Press, Boca Raton, FL, 1995.
- [2] E. Bardez, A. Châtelain, B. Larrey and B. Valeur, *J. Phys. Chem.* 98 (1994) 2357.
- [3] Z. Mi and T. G. Burke, *Biochem.* 33 (1994) 10325.
- [4] K. M. Solntsev, D. Huppert, N. Agmon and L. M. Tolbert, *J. Phys. Chem. A* 104 (2000) 4658.
- [5] L. Genosar, B. Cohen and D. Huppert, *J. Phys. Chem. A* 104 (2000) 6689.
- [6] E. B. Krissinel and N. Agmon, *J. Comput. Chem.* 17 (1996) 1085.
- [7] E. Pines, D. Pines, T. Barak, B.-Z. Magnes, L. M. Tolbert and J. E. Haubrich, *Ber. Bunsen. Phys. Chem.* 102 (1998) 511.

Reaction dynamics of aqueous peroxynitrite and peroxynitrous acid

J. Thøgersen, D. Madsen^a, J. Larsen^b, S. J. Knak Jensen and S. R. Keiding

Dept. of Chemistry, University of Aarhus, Langelandsgade 140, DK 8000 Århus C, Denmark

^aFOM-Institute, AMOLF, Kruislaan 407, 1098 SJ, Amsterdam, The Netherlands

^bDepartment of Chemical Physics, Chemical Centre. P. O. Box 124, Se-22100 Lund, Sweden.

1. INTRODUCTION

The reaction dynamics of peroxynitrite, ONOO^- , and peroxynitrous acid, HONOO , are currently subject to intense investigation especially in biomedical sciences. Studies suggest that peroxynitrite is formed *in vivo* through reactions between nitric oxide and superoxide [1]. Under physiological conditions the peroxynitrite anion becomes partly protonated ($pK_a=6.8$) to form peroxynitrous acid and the two species have been implicated in the onset of numerous degenerative diseases [2]. The need for additional information about these detrimental processes warrants detailed investigations of reactions involving these species. The present investigation is thus motivated by the possible formation of peroxynitrite from far-UV photolysis of nitrate.

The results presented below do indeed show that peroxynitrite is produced in high yields in 1 ps. The prompt formation and subsequent protonation of peroxynitrite offers a unique opportunity for studying bimolecular reactions under conditions where secondary reaction can safely be ruled out. In this work we measure the bimolecular reaction kinetics of $\text{ONOO}^- + \text{H}^+ \rightarrow \text{HONOO}$ as a function of $[\text{H}^+]$ and find it to be in excellent agreement with seminal theoretical work by Smoluchowsky.

2. EXPERIMENT

The double-beam transient absorption spectrometer utilized in this work is described in detail elsewhere [3]. Briefly, the output from a 1 kHz Ti:Sapphire laser is frequency quadrupled to generate the 200 nm photolysis pulses. The probe pulses are generated by frequency doubling the output of an optical parametric amplifier (OPA) pumped at 400 nm or by sum-frequency mixing of the OPA output with 400 nm and 800 nm pulses. The sample consisted of a 0.1 mm jet of aqueous KNO_3 solution. The acidity of the solutions was adjusted by addition of $\text{HNO}_3(\text{aq})$.

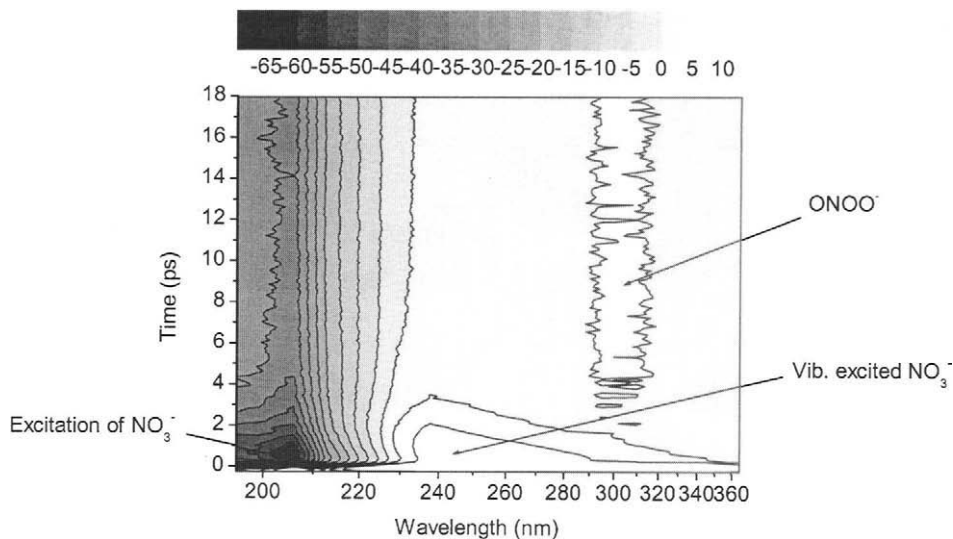


Fig. 1. The transient absorption dynamics of nitrate in neutral aqueous solution

3. RESULTS AND DISCUSSION

Fig. 1 shows the transient absorption of aqueous nitrate induced by the 200 nm photolysis pulses and measured in the spectral range from 194 – 368 nm. The removal of ground state nitrate is seen as the strong bleaching centered at 206 nm. This absorption partially recovers indicating that $44 \pm 8\%$ of the excited molecules return to the electronic ground state of nitrate and relax to the vibrational ground state in 2 ps. The vibrationally relaxing nitrate molecules are seen as the blue-shifting absorption transient extending out to 360 nm. A slightly larger fraction, $48 \pm 8\%$, of the excited molecules isomerize to form peroxyxynitrite as indicated by the wide absorption centered at 305 nm, while a small residual absorption around 240 nm indicates that the formation of peroxyxynitrite is accompanied by minor amounts of $\text{NO} + \text{O}_2^-$ or $\text{NO}^- + \text{O}_2$ (not visible in Fig. 2). Correcting the transients for the absorption pertaining to vibrationally excited nitrate shows that peroxyxynitrite is formed in 1 ps. In order to further elucidate the dynamics of the ONOO^- , we measured the transient absorption at 310 nm out to 500 ps (not shown). The measurement revealed that the ONOO^- concentration increases by only $3 \pm 1\%$ from its value after 1 ps indicating that contributions to the peroxyxynitrate formation from secondary geminate recombination, like the biologically important radical reaction $\text{NO} + \text{O}_2^-$, are only of minor importance.

The nearly constant peroxyntirite concentration observed in neutral solution changes dramatically when $[H^+]$ of the solution is increased. Fig. 2 compares the transient absorption of aqueous nitrate at $[H^+] = 10^{-7}$ M and $[H^+] = 0.140$ M. The peroxyntirite concentration drops rapidly as protonation leads to the formation of peronitrous acid (peroxyntirous acids absorbs relatively weakly around 240 nm and is not observable in Fig. 2.). In Fig. 3 the peroxyntirite concentration is represented by the transient absorption at 310 nm as a function of $[H^+]$. As expected the formation of peroxyntirous acid increases with the concentration of protons. The protonation of peroxyntirite can be viewed as a prototypical diffusion limited bimolecular reaction and thus constitutes an excellent test bed for diffusion models.

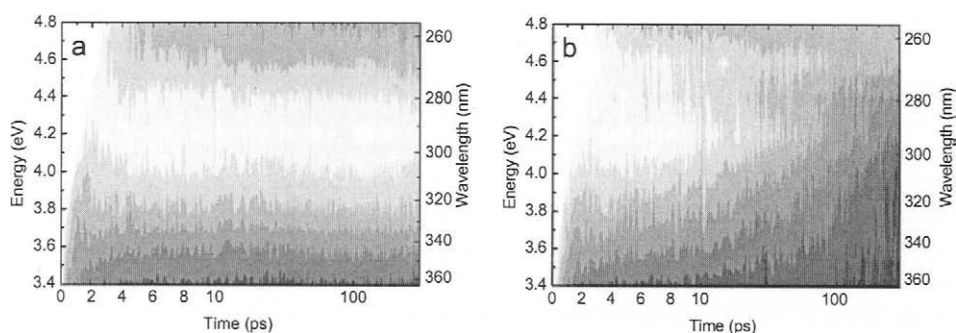


Fig. 2. The transient absorption dynamics of aqueous nitrate at a. $[H^+] = 10^{-7}$ M and b. $[H^+] = 0.140$ M. Notice that the time scale is linear from 0-10 ps, while it is logarithmic from 10-100 ps.

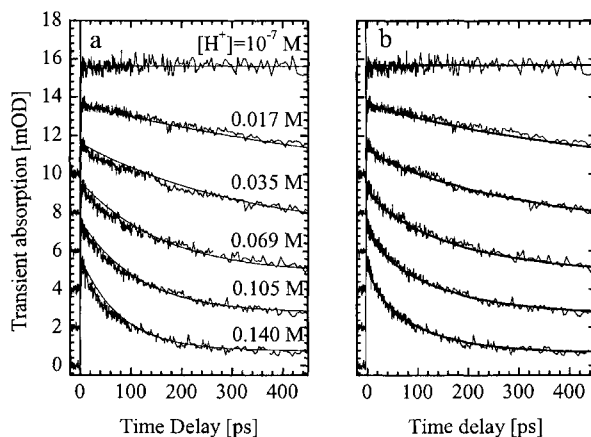


Fig. 3. The transient absorption pertaining to peroxyntirite measured as a function of $[H^+]$. The reaction kinetics are compared to those predicted by diffusion models assuming a. steady-state and b. time-dependent proton distribution.

Experimentally it has proven very difficult to investigate bimolecular reaction kinetics. Although optical techniques have been developed with femtosecond time resolution, the bimolecular nature of the reactions precludes standard femtosecond pump-probe experiments, as a common starting time for the reaction is not readily established. Here we initiate the fast bimolecular acid-base reaction by converting a very weak base, NO_3^- to a weak base ONOO^- and follow the reaction $\text{ONOO}^- + \text{H}^+$ as a function of $[\text{H}^+]$.

Classical reaction dynamics assumes a uniform distribution of reacting molecules. Consider two molecules A and B in a liquid environment. Assume that the two molecules will react to form the molecule AB if they are separated by less than the reaction radius, R . If the distribution of (diffusing) B molecules around the (stationary) A molecules is constant then the concentration of B molecules will decay exponentially corresponding to a time-independent rate constant k_{AB} . For a diffusion limited reaction, with diffusion constant D , the rate constant is given by $k_{AB} = 4\pi N_A R D$. Most chemical reactions are analyzed under these assumptions. However, at short times, approximately of the order of $\tau < R^2/D$, the distribution of B molecules around the A molecules will be non-uniform leading to a reaction rate different from the time independent rate k_{AB} . For small molecules in aqueous solution τ is of the order 0.1-1 ns. Smoluchowski and Noyes were the first to discuss this deviation from classical chemical kinetics [4,5], and they introduced a time dependent reaction rate $k_{AB}(t)$ to account for the non-uniform distribution at short times. A time dependent reaction rate typically leads to a non-exponential decay in the concentration of the reactants. Diffusion models assuming a steady-state and time-dependent distribution of protons result in the well-fitting curves displayed in Fig. 3a and 3b, respectively. A closer inspection of figure 3a reveals a small but significant deviation between experiment and theory. In contrast the agreement with diffusion models assuming a time dependent proton distribution is immaculate. The perfect agreement observed in Fig. 3b clearly shows the non-exponential nature of the early diffusion phase predicted by Smoluchowsky [4].

REFERENCES

- [1] W.A. Pryor and G.L. Squadrito, American Journal of Physiology (Lung Cell. Moll. Physiol.) 268, (1995), L699.
- [2] J.S. Beckman, T.W. Beckman, J. Chen, P. A. Marshall and B. A. Freeman, Proc. Natl. Acad. Sc. U. S. A. 87 (1990), 1620.
- [3] D. Madsen, J. Larsen, S.J. Knak Jensen, S.R. Keiding and J. Thøgersen, To appear in JACS, 2003.
- [4] M.V. Smoluchowski. Z. Phys. Chem. Stoechiom. Verwandtschaftsl. 92, (1917), 129
- [5] R.M. Noyes. Journ. Chem. Phys. 22, (1954), 1349.

Dynamics of water at surface of complex systems: Study of aqueous micelles and proteins

S. Pal^a, S. Bandyopadhyay,^b S. Balasubramanian,^{c*} and B. Bagchi^{a*}

^aS.S.C.U., Indian Institute of Science, Bangalore-560012, India.

^bDepartment of Chemistry, Indian Institute of Technology, Kharagpur-721302, India.

^cC.P.M.U., Jawaharlal Nehru Centre for Advanced Scientific Research, Jakkur, Bangalore-560064, India.

ABSTRACT

The structure, energetics, and dynamics of interfacial water molecules in an aqueous micelle of cesium perfluorooctanoate and in a small protein (enterotoxin) have been investigated using large scale *atomistic molecular dynamics simulations*. The interfacial water molecules are found to be more structured than those in the bulk and exhibit markedly slower dynamics. The lifetime of the hydrogen bond between water and the polar head group is substantially longer than that among the water molecules in the bulk. A significant *blue shift* in the librational band of the interfacial water molecules is observed. Around 90% of the interfacial water molecules form one or two hydrogen bonds with the polar head groups of the surfactants. The hydrogen bond lengths of the latter species differ by as much as 10%. The study of the protein, enterotoxin reveals that while water dynamics generally slow down in the hydration layer, the molecules in the vicinity of the second β turn of this protein exhibit faster dynamics than those near other regions of the protein. Since this β turn is believed to play a critical role in the receptor binding of this protein, the faster dynamics of water near it may have biological significance.

1. INTRODUCTION

The nature of the hydration layer around proteins, DNAs, and self-assemblies has been a subject of great scientific and technological importance for many years [1-5]. A typical picture of the hydration layer is shown in Fig. 1. Many earlier studies considered the hydration layer as almost rigid to give rise to an increased effective radius of the biomolecules/self-assemblies. For example, the rotational correlation time of myoglobin in aqueous solution is found to be 45 ns, in contrast to the Debye-Stokes-Einstein (DSE) estimate of 14 ns from its crystallographic radius [5]. This has often been taken as evidence of a rigid hydration layer, although the hydration layer here needs to be rather thick (equal in thickness to 50% of the radius of myoglobin!) to fully account for the decreased diffusion. Early nuclear magnetic resonance (NMR) studies found long residence time of water molecules close to proteins [6]. However, recent experimental studies have observed that although noticeable slowing down of water dynamics indeed occurs near complex chemical and biological surfaces [7, 5], the hydration layer is *not* really rigid and exhibits ultrafast, ps or even sub-ps, dynamics in the short time.

*For Correspondence: bala@jncasr.ac.in, bbagchi@sscu.iisc.ernet.in

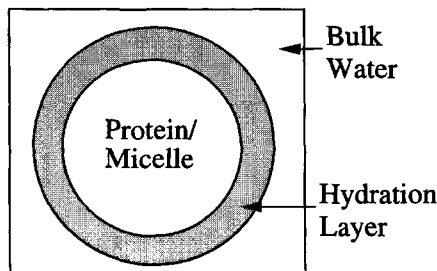


Fig. 1: Schematic representation of the hydration shell.

This bimodal dynamics of hydration water is intriguing. A model based on dynamic equilibrium between quasi-bound and free water molecules on the surface of biomolecules (or self-assembly) predicts that the orientational relaxation at a macromolecular surface should indeed be bi-exponential, with a fast time component (few ps) nearly equal to that of the free water while the long time component is equal to the inverse of the rate of bound to free transition [4]. In order to gain an in depth understanding of hydration dynamics, we have carried out detailed atomistic molecular dynamics (MD) simulation studies of water dynamics at the surface of an anionic micelle of cesium perfluorooctanoate (CsPFO), a cationic micelle of cetyl trimethylammonium bromide (CTAB), and also at the surface of a small protein (enterotoxin) using classical, non-polarizable force fields. In particular we have studied the hydrogen bond lifetime dynamics, rotational and dielectric relaxation, translational diffusion and vibrational dynamics of the surface water molecules. In this article we discuss the water dynamics at the surface of CsPFO and of enterotoxin.

2. WATER DYNAMICS AT THE SURFACE OF AN ANIONIC MICELLE (CsPFO)

The surfactant is cesium perfluorooctanoate, with cesium being the counterion. The CsPFO-H₂O system has been well studied experimentally and is regarded as a typical binary system to exhibit micellization. As the details of the simulation have been discussed elsewhere [8], we directly proceed to the discussion of the significant results.

2.1 Identity and Structure

We define an interfacial water molecules as ones that are present within the first coordination shell of the carbonyl carbon atom of the polar head group (PHG) of the surfactant, *i.e.*, those within a distance of 4.35\AA [9]. This distance can be rationalized from the limit of the O-O distance of 3.5\AA , and the C-O distance in the PHG of 1.26\AA . In our system, on the average, 363 water molecules constitute the hydration shell. We then explore the possibility of whether interfacial water molecules are hydrogen bonded to a PHG or not. The water molecules that form hydrogen bond(s) with the PHG can be termed as "bound", denoted by IBW (interfacial bound water) while the rest are free, denoted by IFW (interfacial free water). IBW can be further distinguished on the basis of the number of hydrogen bonds that they make with the PHGs of the surfactants. This can be either one or two and they are denoted by IBW1 and IBW2, respectively. The IBW2 water molecule forms two hydrogen bonds with two *different* PHGs of the micelle. Thus, all the interfacial water molecules can be classified into three types, namely, IFW, IBW1, and IBW2. The three species, in dynamical equilibrium with each other and with bulk water, are present in the ratio of 1:8:1, with a *predominance of water molecules that are singly hydrogen bonded to polar headgroups*. We have calculated the monomer energy

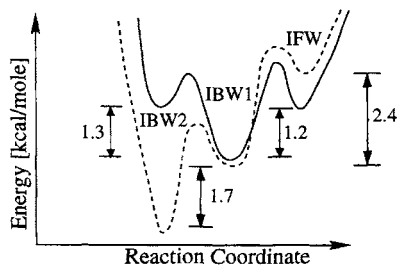


Fig. 2: Schematic description of the free energy (solid line) and internal energy (dashed line) profiles of the interfacial water species. The energy differences are obtained from simulations.

distribution of the different species and it is seen that the interfacial water molecules have peaks at lower energies – the doubly bonded species (IBW2) have the lowest potential energy. A schematic representation of both the internal and free energy of the three species, the latter calculated from their average concentration, are shown in Fig. 2. Despite the reduced monomer energy arising out of two water-headgroup hydrogen bonds, *the IBW2 state is much less prevalent than the IBW1 state due to entropic considerations* (less number of suitable configurations). Another notable result is that the length of the two hydrogen bonds of IBW2 species differs, on the average, by more than 10% [8].

2.2 Hydrogen Bond Life Time Dynamics

The lifetime of the hydrogen bonds that the bound water molecules form with the polar headgroups of the surfactant are characterized in terms of two time correlation functions, $S_{HB}(t)$ and $C_{HB}(t)$, defined as [10],

$$S_{HB}(t) = \frac{\langle h(0)H(t) \rangle}{\langle h \rangle}$$

$$C_{HB}(t) = \frac{\langle h(0)h(t) \rangle}{\langle h \rangle} \quad (1)$$

where $h(t)$ is the hydrogen bond life time function which is unity if the hydrogen bond between the pair is intact at time t and zero if it is broken, and $H(t)$, on the other hand, is unity only if the tagged bond remains *continuously* hydrogen bonded from time $t=0$ to the present time t .

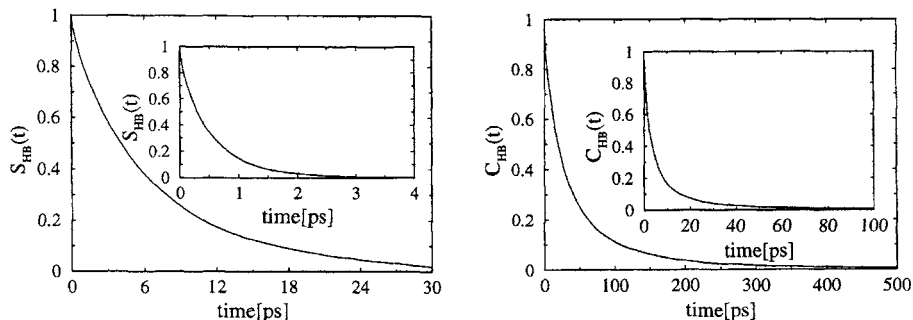


Fig. 3: Hydrogen bond lifetime correlation function for bound water molecules in the CsPFO micellar solution. Inset: The same for bulk water. Note the much slower decay of the bound water species.

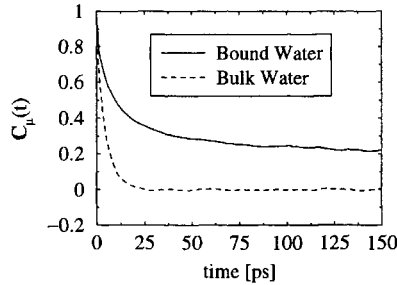


Fig. 4: Dipolar reorientational time correlation function, $C_\mu(t)$ for bound water molecules in the micellar solution, and for bulk water molecules.

Thus, $S_{HB}(t)$ decays as soon as the bond breaks for the first time while $C_{HB}(t)$ allows bond breaking at intermediate times. In Fig. 3, we show the water-surfactant hydrogen bond lifetime correlation functions, $S_{HB}(t)$ and $C_{HB}(t)$. The decay of $S_{HB}(t)$ for the bound species is *much slower than the corresponding decay for the water-water hydrogen bond in pure water* [8].

2.3 Orientational Relaxation

An important signature of the dynamics of water molecules is the reorientation of its dipole vector that can be probed by dielectric and NMR measurements. We have calculated the single molecule dipole-dipole time correlation function (TCF), defined as,

$$C_\mu(t) = \frac{\langle \vec{\mu}_i(t) \cdot \vec{\mu}_i(0) \rangle}{\langle \vec{\mu}_i(0) \cdot \vec{\mu}_i(0) \rangle} \quad (2)$$

where $\vec{\mu}_i(t)$ is the dipole moment vector of i -th water molecule at time t , and the angular brackets denote averaging over water molecules.

In Fig. 4, we show the single particle dipolar orientational relaxation ($C_\mu(t)$) of bound water molecules (within 4.35\AA from any surfactant headgroup), comparing it to its relaxation in bulk. *Note the pronounced slower decay of the former* [9].

2.4 Vibrational Dynamics

The power spectra, obtained by a Fourier cosine transform of the velocity auto time correlation function of oxygen atoms of the interfacial water molecules are displayed in Fig. 5a. Relative to water in the bulk, we observe a clear *blue* shift in the frequency corresponding to the O..O..O bending mode by about 40 cm^{-1} for these interfacial water molecules while the stretching mode seems not to be affected by the interface, consistent with earlier observations on aqueous protein solutions. The most significant change in the vibrational spectrum occurs for the librational mode of the different kinds of water molecules which are shown in Fig. 5b. The librational mode of IBW2 is most affected, and is shifted considerably, by about 150 cm^{-1} , whereas that of the IBW1 species is blue shifted by about 100 cm^{-1} relative to bulk water and is observed at 600 cm^{-1} . These data agree well with recent incoherent, inelastic neutron scattering(IINS) experiments on aqueous DNA and membrane solutions, where the vibrational signature of interfacial water molecules was found to be predominant in the $400\text{--}600\text{ cm}^{-1}$ range [11]. The hydrogen atoms also contribute to the O..O..O bending mode at around 60 cm^{-1} , whose shift to higher frequencies is also observed from the oxygen spectrum. These frequency shifts in the bending and librational modes must arise from the strong, and longer lived water-PHG hydrogen bond. Evidence for the strength, and the lifetime of these bonds have been provided elsewhere [8].

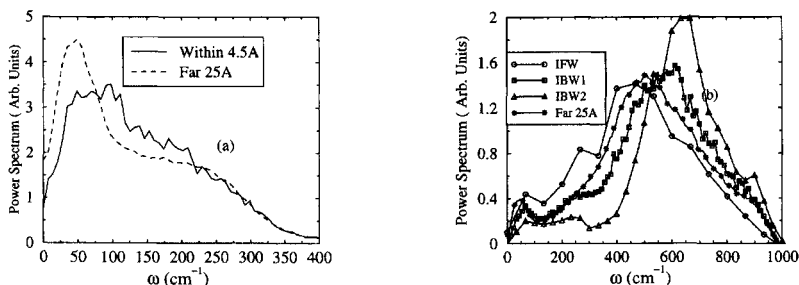


Fig. 5: (a) Power spectrum of oxygen atoms of bound and free water molecules. (b) Power spectrum of hydrogen atoms of different kinds of water molecules.

Therefore, one may conclude that *water structure on the surface is more rigid*. While this is of course expected on simple arguments, the strong effect on bending and librations, while the negligible effect on stretching were not anticipated, but is in agreement with IINS results [11].

2.5 Dielectric Relaxation

Dielectric relaxation (DR) measures the complex dielectric function, $\epsilon(\omega)$, that can be decomposed into real and imaginary parts as,

$$\epsilon(\omega) = \epsilon'(\omega) - i\epsilon''(\omega) \quad (3)$$

where $\epsilon'(\omega)$ and $\epsilon''(\omega)$ are the real part (permittivity factor) and imaginary (dielectric loss) parts respectively. $\epsilon(\omega)$ is related to TCF of the total dipole moment of the system by the fluctuation-dissipation theorem. In Fig. 6, we show the Cole-Cole plot of the contribution from water to the dielectric function. *Note that the collective relaxation of the water molecules becomes markedly non-Debye in the presence of the micelle* [8]. This is due to the bimodal dynamics of the hydration layer.

3. WATER DYNAMICS AT THE SURFACE OF A SMALL PROTEIN, ENTEROTOXIN

The protein that we study here is the toxic domain of heat stable Enterotoxin (PDB ID: 1ETN). Heat stable Enterotoxins (ST) are produced by *E. Coli* bacteria in the intestine and are responsible for acute diarrhea in humans and animals. They display a remarkable ability

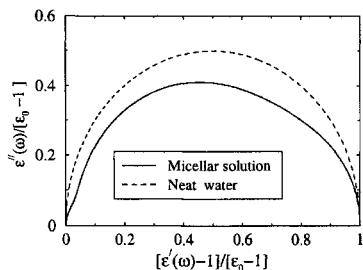


Fig. 6: The Cole-Cole plot of the contribution from water to the frequency dependent dielectric function. The reduced real part $[\epsilon'(\omega)]$ is plotted against the reduced imaginary part $[\epsilon''(\omega)]$. Note the non-Debye character in the micellar solution.

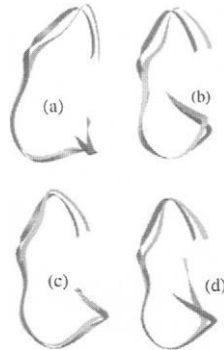


Fig. 7: Secondary structure of representative configurations of the protein in solution obtained during the molecular dynamics trajectory(dark), compared with the structure in the crystal(gray).

to retain their activity even at 100°C, hence the moniker, “heat-stable”. Similar enterotoxins are also secreted by other pathogenic bacteria. These class of peptides typically contain 18 or 19 amino acid residues, and share a common 13 amino acid sequence, which is [12]:

Cys⁵-Cys-Glu-Leu-Cys-Cys¹⁰-Asn-Pro-Ala-Cys-Ala¹⁵- Gly-Cys (Full peptide position)

Cys¹-Cys-Glu-Leu-Cys⁵-Cys-Asn-Pro-Ala-Cys¹⁰-Ala-Gly-Cys (Toxic domain position)

Since this domain is conserved in several enterotoxins, one expects this 13 residue domain to be the primary reason for the toxicity of the 19-residue long protein. 1ETN has a simple secondary structure : it has got 3 beta (β) turns. The β_1 spans from Cys⁶ to Cys⁹, β_2 from Asn¹¹ to Cys¹⁴, and β_3 from Cys¹⁴ to Cys¹⁷. In addition, the crystal structure contains 5 intramolecular (i.e., within the protein) hydrogen bonds that also add to the stability of the conformation. The 1ETN structure is reasonably rigid (because of 3 disulfide bridges, and 5 intramolecular hydrogen bonds), making it an ideal candidate for studies by computer simulations using empirical intermolecular potentials.

Atomistic molecular dynamics simulations of one molecule of 1ETN soaked in water were performed under constant volume and temperature conditions (NVT). Details of the simulation can be found elsewhere [13].

3.1 Protein Structure and Local Dynamics

In Figs. 7, we show the secondary structure of the simulated protein in solution and compare it against that obtained from the crystalline sample. We observed that the *secondary structure of the simulated sample is essentially identical to the crystal structure, except for a marginal difference in the β_3 segment of the protein.*

3.2 Reorientational Dynamics of Water in Hydration Layer

Shimonishi and coworkers observed that the residues in the second β turn are proximal to the receptor in the binding of enterotoxin [12]. This ties in with the observation that the toxicity of the protein too is unaffected by changing specific residues in the first and the third β turns, while the activity was considerably affected when similar mutations were effected in the residues of the second β turn. In order to relate to these biochemical studies, we have classified the hydration layer of 1ETN into three regions, based on their proximity to each of the three β turns.

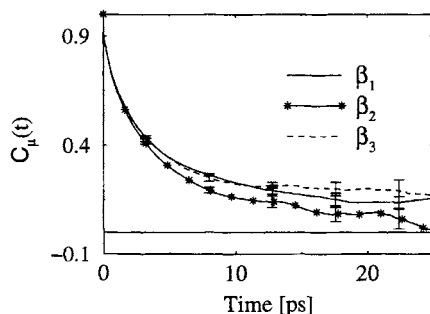


Fig. 8: Reorientational time correlation function of the water dipole, $C_\mu(t)$, for water molecules in the three segments of the protein.

The active site of various proteins are, in general, hydrophobic in nature. In Fig. 8, we present the dipole-dipole TCF, $C_\mu(t)$, for the water molecules near (within 5\AA) the three segments, namely, β_1 , β_2 , and β_3 , of the protein. *Water molecules near the β_2 segment exhibit a marginally faster ability to reorient than those near the first and the third segments of the protein.*

4. DEVELOPMENT OF MICROSCOPIC THEORIES

In sharp contrast to the large number of experimental and computer simulation studies reported in literature, there have been relatively few analytical or model dependent studies on the dynamics of protein hydration layer. A simple phenomenological model, proposed earlier by Nandi and Bagchi [4] explains the observed slow relaxation in the hydration layer in terms of a dynamic equilibrium between the bound and the free states of water molecules within the layer. The slow time scale is the inverse of the rate of bound to free transition. In this model, the transition between the free and bound states occurs by rotation. Recently Mukherjee and Bagchi [14] have numerically solved the space dependent reaction-diffusion model to obtain the probability distribution and the time dependent mean-square displacement (MSD). The model predicts a transition from sub-diffusive to super-diffusive translational behaviour, before it attains a diffusive nature in the long time. However, a microscopic theory of hydration layer dynamics is yet to be fully developed.

5. CONCLUSIONS

We have carried out an in depth analysis of the structure and dynamics of water molecules in the hydration layer. We find the existence of three kinds of waters at the interface, based on the number of hydrogen bonds they make with PHG. Despite possessing two hydrogen bonds, the concentration of the IBW2 species is low due to entropic effects. We observed a blue shift in the O..O bending mode of about 40 cm^{-1} . The librational mode of the water molecule, at around 500 cm^{-1} in the bulk, undergoes a blue shift of about 100 cm^{-1} . The study of a biologically relevant small protein, Enterotoxin, reveals that although the overall structure of the protein in solution is similar to that in its crystalline state, there are also differences. The intramolecular vibrational degrees of freedom show a low frequency dynamics with a time constant of around 250 fs, that can be probed through spectroscopy. We find the reorientation of water dipole is significantly faster for molecules near the second β segment than for those near the first and the third segments of the protein. The collective dynamics of water that

influences its ability to solvate other molecules, exhibits slow dynamics with a characteristic slow component of 27 ps. This is likely to come from water molecules in the hydration layer that are strongly bound to the biomolecule.

ACKNOWLEDGMENTS: The research reported here was supported in part by grants from the Department of Science and Technology (DST), Department of Biotechnology (DBT), Council of Scientific and Industrial Research (CSIR), Government of India.

REFERENCES

- [1] R. Pethig, *Annu. Rev. Phys. Chem.*, 43 (1992) 177.
- [2] T.H. Ghaddar, E.W. Castner, Jr., and S.S. Isied, *J. Am. Chem. Soc.*, 122 (2000) 1233.
- [3] A. Douhal, J. Santamaria (eds), *Femtochemistry and Femtobiology: Ultrafast Dynamics in Molecular Science*, World Scientific, Singapore, 2002; R. Jimenez, G. R. Fleming, P. V. Kumar, and M. Maroncelli, *Nature*, 369 (1994) 471.
- [4] N. Nandi and B. Bagchi, *J. Phys. Chem. B*, 101 (1997) 10954; N. Nandi, K. Bhattacharyya, and B. Bagchi, *Chem. Rev.*, 100 (2000) 2013.
- [5] B. Bagchi, *Annu. Rep. Prog. Chem., Sect. C*, 99 (2003) 127.
- [6] G. Otting, E. Liepinsh, and K. Wüthrich, *Science*, 254 (1991) 974.
- [7] X.J. Jordanides, M.J. Lang, X. Song, and G.R. Fleming, *J. Phys. Chem. B*, 103 (1999) 7995; K. Bhattacharyya, *Acc. Chem. Res.*, 36 (2003) 95.
- [8] S. Pal, S. Balasubramanian, and B. Bagchi, *Phys. Rev. E*, 67 (2003) 061502; *Phys. Rev. Lett.*, 89 (2002) 115505; *J. Phys. Chem. B*, 107 (2003) 5194, *Curr. Sci.*, 84 (2003) 428.
- [9] S. Balasubramanian, and B. Bagchi, *J. Phys. Chem. B*, 105 (2001) 12529; *J. Phys. Chem. B*, 106 (2002) 3668; S. Balasubramanian, S. Pal, and B. Bagchi, *Curr. Sci.*, 82 (2002) 845.
- [10] F. H. Stillinger, *Adv. Chem. Phys.*, 31 (1975) 1; D. C. Rapaport, *Mol. Phys.*, 50 (1983) 1151; A. Luzar and D. Chandler, *Nature*, 379 (1996) 53, A. Chandra, *Phys. Rev. Lett.*, 85 (2000) 768.
- [11] S. Ruffle, I. Michalarias, J.C. Li, and R.C. Ford, *J. Am. Chem. Soc.*, 124 (2002) 565.
- [12] T. Sato, H. Ozaki, Y. Hata, Y. Kitagawa, Y. Katsube, and Y. Shimonishi, *Biochem.*, 33 (1994) 8641.
- [13] S. Balasubramanian, S. Bandyopadhyay, S. Pal, and B. Bagchi, *Curr. Sci.*, 85 (2003) 000.
- [14] A. Mukherjee, and B. Bagchi, *Phys. Chem. Comm.*, 28 (2003) 6.

The solvated electron in methanol. Novel time- and frequency-resolved pump-probe spectroscopy of short-lived precursors.

A. Thaller, R. Laenen and A. Laubereau

Technische Universität München, Physik-Department E11,
James-Franck-Strasse, 85748 Garching, Germany

1. INTRODUCTION

Almost 150 years after the first report on electron detachment in liquids [1], the solvated electron is still of high interest. This is partly due to the important role played by electric charges in a liquid environment in chemical and biological processes. In spectroscopic studies, the solvated electron is often used as a microscopic probe for the structural dynamics, since the solvent molecules strongly influence the electron properties [2]. These interactions manifest in a change of the optical absorption which is governed by the transition from an s-like groundstate to a p-like excited state of the electron in its interaction potential with the solvation shell [3]. Using ultrashort laser pulses, the generation process of the solvated electrons could be studied in various liquids, e.g. water and alcohols [4]. With typical lifetimes of the solvated electron in the order of 10^{-9} s, the trapped charges were furtherly studied by pump-probe-spectroscopy monitoring the relaxation process following (re-)excitation of the already formed species. In spite of experiments of this kind that were conducted on the electron in its equilibrated ground state in the liquid environment, various questions were left open, especially regarding the nature of the intermediate states following the detachment process.

The present study shows a combined investigation of both the generation process of solvated electrons and of pump-probe-spectroscopy of intermediate states including the final equilibrated ground state. As shown previously [5], the formation of the solvated electron in methanol takes place within ~ 10 ps. About an order of magnitude slower than in water, the timescale of this process allows to investigate the precursor states in much more detail using a state-of-the-art laser system.

2. EXPERIMENT AND DISCUSSION

For our experiments, we use an amplified Ti:Sapphire laser system described elsewhere [6]. The 100 fs-laser pulses are centered at 820 nm and partly converted to the third harmonic at 273 nm (4.55 eV) for ionization via two-photon absorption in a sample jet of neat methanol at room temperature. Probing pulses in the visible range are obtained generating a white light continuum while parametric conversion processes yield infrared pulses in the range of 1.1 to 5.5 μ m. The detection of the probe transmission is carried out both in parallel and perpendicular polarization planes. To (re-)excite the photo-detached electrons, part of the original laser pulse can be applied with variable delay time (termed preparation time) after the UV ionization pulse. The intermediate states of the electron can be selectively excited by choosing an appropriate preparation time. In this way, both the generation process and the pump-probe dynamics of the precursor states including the final ground state can be investigated [8].

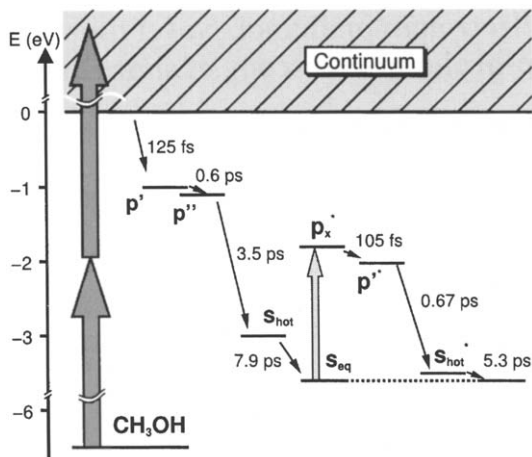


Fig. 1. Energy level scheme representing the rate equation system for modeling the generation process (left) and the relaxation following the excitation of s_{eq} (right). Similar relaxation channels describe the processes following excitation of s_{hot} and p'/p'' , respectively. The 272 nm generation pulse is represented by the thick upward arrows and the 820 nm excitation pulse by the thin upward arrow. Exponential decay is depicted by the downward arrows with corresponding decay time constants. The energy scale merely serves as a coarse reference. The assignments of the various intermediate states as p- or s-like represents a result of the study. Probing transitions are omitted.

All measured probe absorption data are treated in a global, self-consistent analysis: Transients computed from a single rate equation system with discrete initial, intermediate and final states are fitted to the measured dynamics. Each of those states can contribute to the overall probe signal via a wavelength-dependent absorption coefficient that represents important spectral information to identify the nature of the individual level. Figure 1 exemplarily shows an energy level scheme illustrating a part of the rate equation system. The indicated ordinate positions of the various levels already refer to the results of the data analysis. The isotropic (rotation-free) probe-absorption bands of the intermediate states passed by in the solvation process are shown in Fig. 2, as obtained from the data analysis. The generation of solvated electrons starts with two-photon absorption of the UV preparation pulse and subsequent ionization of a methanol molecule. This leads to a detached (possibly quasifree) electron e_{free}^- , with broad absorption centered around $2 \mu\text{m}$. Since there is no indication of geminate recombination in the transient signal traces (data not shown) and because of the initial electron excess energy of approximately 2.6 eV it is quite plausible that the initial separation of the electron from the methanol molecule is rather large and electron-radical interactions can be neglected on the timescale of the experiment. Within ~ 125 fs after excitation, the electron seems to get trapped in a suitable configuration of methanol molecules. The accompanying spectrum of a first detectable intermediate state (p' in Fig. 2) is composed of a broad absorption band ranging over the whole probing interval with a distinct dip at $\sim 1.2 \mu\text{m}$. It is important to note that this spectral dip is accompanied by a pronounced anisotropy in the measured probe transmission change (data not shown). Therefore we propose that the dip originates from stimulated emission out of the intermediate state p' to a corresponding, unoccupied lower state (not shown in Fig. 1). The electron appears to be initially trapped in an excited, p-like state. The finding nicely corresponds to the pronounced asymmetry of pretraps found in numerical simulations [7]. Within ~ 0.6 ps, the spectrum shifts towards shorter wavelengths (see p'' in Fig. 2) attributed to a cooling of the electron's local

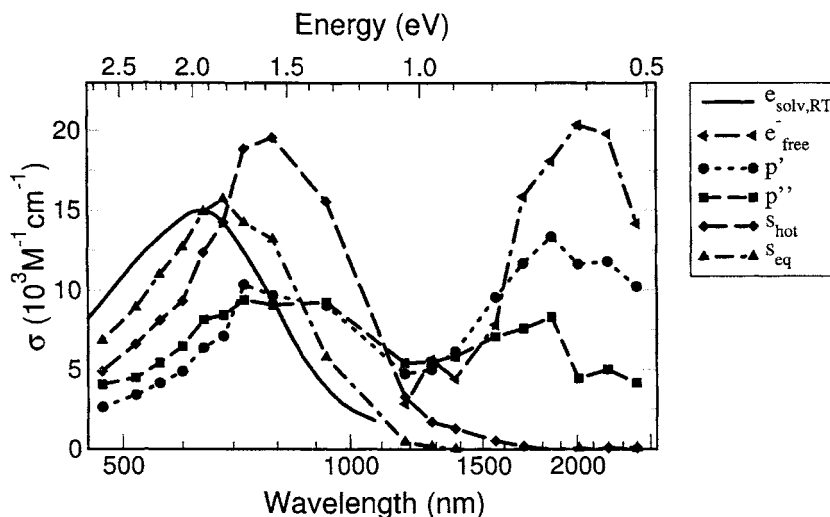


Fig. 2. Spectra of the transient states during electron solvation as obtained by fitting the rate equation system to all measured data.

environment. Still, the electron appears to be trapped in a p-like state. The absorption of the subsequent species, however, evolving with a time constant of ~ 3.5 ps, shows a completely different signature. Its position and shape are consistent with the ground state absorption of the solvated electron in a hot local environment (S_{hot}) [9]. The following relaxation on a time scale of ~ 7.9 ps leading to the spectral absorption labeled S_{eq} (Fig. 2) is correspondingly interpreted as ground state cooling. We assign this semifinal state to the quasi-equilibrated solvated electron although it has not yet arrived at room temperature (compare solid curve in Fig. 2). These results are in excellent agreement with previous experiments conducted with notably smaller UV preparation pulse intensities [5].

To investigate the intermediate states furtherly, we apply an 820 nm pump pulse to the sample with preparation times of respectively 0.5 ps, 5 ps and 60 ps, in order to selectively excite the precursors p'/p'' , S_{hot} and S_{eq} (called reexcitation in the following). On the right hand side of Fig. 1 an example is shown for the considered relaxation channel after reexcitation of S_{eq} . It is important to note that the complete rate equation system models all four experiments, with and without reexcitation pulse, selfconsistently. The spectra derived from the analysis are interpreted in analogy to the generation process described above. The results suggest that shortly after the reexcitation of S_{hot} and S_{eq} the electron is in an excited state p'' with a lifetime of 1.14 ps and 0.6 ps, respectively. After relaxation to a hot ground state S_{hot} ground state cooling seems to occur with a time constant of 6.2 ps and 5.3 ps, respectively. A completely different case is the reexcitation of the early p'/p'' states 0.5 ps after the generation pulse. Here, the data support the picture that the electron escapes (energetically but not necessarily locally) its potential well. Within ~ 140 fs it is re-trapped in a p-like state. The subsequent dynamics shows conversion to a hot ground state followed by ground state cooling.

3. CONCLUSIONS

Comparing the time constants for the three relaxation situations following re-excitation of the respective intermediate states, a significant slowing-down of the relaxation steps for shorter

preparation time delay is found. The shorter time delay for re-excitation should be equivalent to a higher temperature of the local environment of the electron. To understand the observed correlation it is interesting to recall that with increasing temperature the H-bonding between methanol molecules is weakened. This corresponds to an increase in molecular mobility (translational and rotational motion) obviously allowing the solvation shell to adapt faster to the pump-induced p-like electronic charge distribution. The faster this adaptation takes place the better the p-like state may be supported by the solvation shell leading to an extended excited state lifetime of the electron. The measured increased cooling times for re-excitation after shorter delay time may be also attributed to a temperature-induced H-bond weakening: With the H-bonds acting as the main coupling channel for energy transport to the environment, cooling is suggested to take longer for a correspondingly decreased efficiency of this channel.

REFERENCES

- [1] W. Weyl, *Ann. Phys. Chem.* 123 (1864) 350.
- [2] E.J. Hart and M. Anbar, *The hydrated electron*, Wiley, New York, 1970.
- [3] S. Bratos, J.-Cl. Leicknam, D. Borgis und A. Staib, *Phys. Rev. E*, 55 (1997) 7217.
- [4] B. Bagchi, *Annu. Rev. Phys. Chem.* 40 (1989), 115, and references therein.
- [5] T. Scheidt and R. Laenen, *Chem. Phys. Lett.* 371 (2003) 445.
- [6] R. Laenen, T. Roth and A. Laubereau, *Phys. Rev. Lett.* 85 (2000) 50.
- [7] M. Hilczer and M. Tachiya, *J. Phys. Chem.* 100 (1996) 7691.
- [8] A. Thaller, R. Laenen and A. Laubereau, to be published.
- [9] V. Herrmann and P. Krebs, *J. Phys. Chem.*, 99 (1995) 6794.

Femtosecond dynamics of the solvated electron in water studied by time-resolved Raman spectroscopy

Misao Mizuno, Shoichi Yamaguchi and Tahei Tahara

Molecular Spectroscopy Laboratory,
The Institute of Physical and Chemical Research (RIKEN), Hirosawa, Wako 351-0198, Japan

1. INTRODUCTION

When an electron is injected into a polar solvent such as water or alcohols, the electron is solvated and forms so-called the solvated electron. This solvated electron is considered the most basic anionic species in solutions and it has been extensively studied by variety of experimental and theoretical methods. Especially, the solvated electron in water (the hydrated electron) has been attracting much interest in wide fields because of its fundamental importance. It is well-known that the solvated electron in water exhibits a very broad absorption band peaked around 720 nm. This broad absorption is mainly attributed to the $s \rightarrow p$ transition of the electron in a solvent cavity. Recently, we measured picosecond time-resolved Raman scattering from water under the resonance condition with the $s \rightarrow p$ transition of the solvated electron, and found that strong transient Raman bands appeared in accordance with the generation of the solvated electron [1]. It was concluded that the observed transient Raman scattering was due to the water molecules that directly interact with the electron in the first solvation shell. Similar results were also obtained by a nanosecond Raman study [2]. This finding implies that we are now able to study the solvated electron by using vibrational spectroscopy. In this paper, we describe new information about the ultrafast dynamics of the solvated electron in water, which are obtained by time-resolved resonance Raman spectroscopy.

2. EXPERIMENTAL

The experimental setup for time-resolved Raman spectroscopy was based on a 1 kHz Ti:sapphire regenerative amplifier system. We used the third harmonic of the output as the pump pulse to generate solvated electrons. The fundamental pulse or the output of a H_2 Raman shifter was used to probe Raman scattering. The Raman scattering was analyzed by

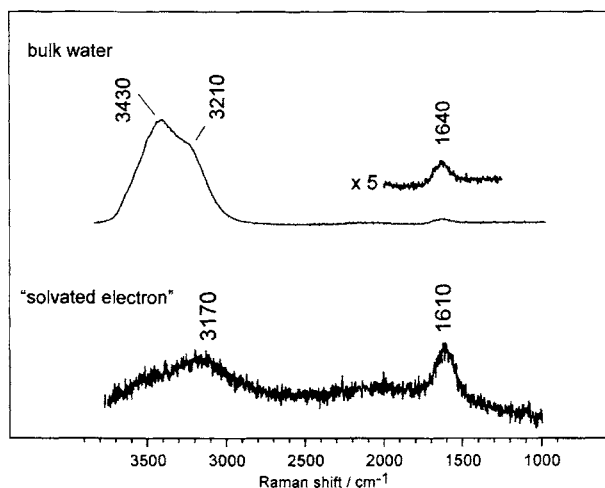


Fig.1 The resonance Raman spectrum of solvated electrons in water (bottom; 620 nm excitation) and the non-resonance Raman spectrum of bulk water (top; 600 nm).

a spectrometer and detected by a liquid-nitrogen cooled CCD camera. We used a picosecond Ti:sapphire laser system for picosecond experiments and a femtosecond laser system for femtosecond experiments.

3. RESULT AND DISCUSSION

3.1. Resonance Raman scattering from solvated electrons in water

In Figure 1, a resonance Raman spectrum of the solvated electron is compared with the spectrum of bulk water. The similarity between the two spectra manifests that the transient Raman spectrum of the solvated electron is basically the spectrum of water. In other words, we selectively observe Raman scattering of the water molecules that solvate the electron in the first solvation shell, taking advantage of the resonance effect. Two transient Raman bands are observed around ~ 3170 cm^{-1} and ~ 1610 cm^{-1} , which are assigned to the OH stretching and OH bending vibrations of the solvating water molecules, respectively. Both of the vibrational frequencies show downshifts compared to those of bulk water, indicating strong interaction between the solvating water and the electron. The magnitude of the resonance enhancement was evaluated to be as high as $\sim 10^5$ (the OH bend) and $\sim 10^3$ (the OH stretch). These very high enhancement factors imply that the electronic state of the electron and the vibrational state of solvating water molecules are strongly coupled, and hence we should treat the local solvation structure as a “quasi-molecule” or a “water cluster anion”.

3.2. Raman depolarization ratio: Time-scale of relaxation among three sublevels in p-state

The excited p-state of the solvated electron in water has three sublevels, p_x , p_y and p_z . If the local structure around the electron is isotropic, these three sublevels of the p-state are degenerated and equivalently contribute to the resonance Raman process. Then, the three diagonal components of the Raman tensor (α_{xx} , α_{yy} , and α_{zz}) should have the same value, and the Raman depolarization ratio becomes zero ($\rho = 0$). Therefore, the polarized resonance Raman spectra provide unique information about the degeneracy of the sublevels in the excited p-state in resonance. We performed polarization measurements of the transient Raman band in the OH bend region, and observed a non-zero Raman depolarization ratio for the OH bending vibration. This result clarifies that the three sublevels of the p-state do not equally contribute to the resonance Raman process, and that non-degeneracy of the p_x , p_y and p_z states is observable within a time scale of the resonance Raman process ($2 \sim 3$ fs). A theoretical calculation indicated that the three sublevels are non-degenerated because of the non-spherical nature of the solvent cavity [4]. However, this non-degeneracy of the sublevels had few experimental supports, and a previous femtosecond absorption experiment concluded that the relaxation among the three sublevels occurs very rapidly within 80 fs [5]. If we adopt this value as the upper limit, the redistribution time of the three sublevels of the excited p-state is considered to be in the range of $2\sim 3$ fs $< \tau < 80$ fs.

3.3. Femtosecond time-resolved measurements: formation and relaxation dynamics of the solvated electron in water

In order to obtain direct new information about ultrafast formation/relaxation dynamics of the solvated electron in water, we also performed femtosecond time-resolved Raman measurements. We used 800-nm pulses for probing, which are resonant with not only the absorption of the equilibrated solvated electron but also that of the precursor [4]. The observed femtosecond time-resolved Raman spectra are shown in Figure 2. The reabsorption effect on the observed Raman signal has been already corrected by using a correction curve that was made on the basis of femtosecond time-resolved absorption spectra of the aqueous solvated electron and the evaluation of the optical path length in the present experimental configuration. The temporal intensity change of the transient OH bend band is compared with that of the transient absorption at 800 nm in Figure 3. As clearly seen, the transient Raman band appeared within a few hundreds of femtosecond. This rise-up of the transient Raman band is much faster than the equilibration time of the solvated electron, which means that the precursor state, the “wet electron”, also provides strong resonance Raman scattering. The strong resonance enhancement is directly related to the nature of the electronic transition in resonance, so that, in this case, it is attributed to the $s \rightarrow p$ nature of the transient absorption. Therefore, the present femtosecond time-resolved Raman data

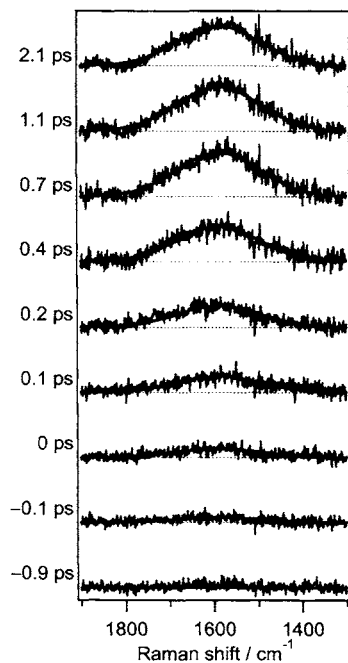


Fig 2. Femtosecond time-resolved Raman spectra of solvated electrons in water (pump 267 nm; probe 800 nm).

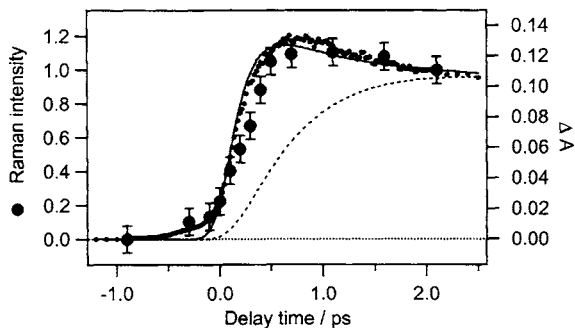


Fig 3. Comparison of the rise-up of the transient signals (black circles, transient Raman; dots with a fitted curve, transient absorption at 800 nm). The broken curve represents the appearance of the equilibrated solvated electron which is calculated according to ref 6.

indicate that the precursor state is also the *s*-state of the solvated electron, and support the assignment that the precursor state is “hot” state of the solvated electron in the electronically ground state. We also found that the rise-up time of the Raman band is slightly delayed, compared to the appearance of the transient absorption at 800 nm. This seems to mean that there exists time when a transient species that gives rise to only absorption appears in very early stage after the injection of the electron.

REFERENCES

- [1] M. Mizuno and T. Tahara, *J. Phys. Chem. A*, 105 (2001) 8823.
- [2] M. J. Tauber and R. A. Mathies, *J. Phys. Chem. A*, 105 (2001) 10952.
- [3] M. Mizuno and T. Tahara, *J. Phys. Chem. A*, 107 (2003) 2411.
- [4] J. Schinitker, K. Motakabbir, P.J. Rossky, R. Friesner, *Phys. Rev. Lett.*, 60 (1988) 456.
- [5] M. Assel, R. Laenen, A. Laubereau, *Chem. Phys. Lett.*, 317, 13 (2000).
- [6] V. H. Vilchiz, J. A. Kloepfer, A. C. Germaine, V. A. Lenchenkov, S. E. Bradforth, *J. Phys. Chem. A*, 105 (2001) 1171.

Femtosecond transient spectroscopy of the photoionization of indole in water

T. Bizjak^a, P. B. Bisht^b, S. Lochbrunner^a and E. Riedle^a

^aLehrstuhl für BioMolekulare Optik, Sektion Physik, Ludwig-Maximilians-Universität, Oettingenstr. 67, 80538 München, Germany

^bPhysics Department, Indian Institute of Technology Madras, Chennai, TN, 600 036, India

ABSTRACT

The photodynamics of electronically excited indole in water is investigated by UV-visible pump-probe spectroscopy with 80 fs time resolution and compared to the behavior in other solvents. In cyclohexane population transfer from the optically excited L_a to the L_b state happens within 7 ps. In ethanol ultrafast state reversal is observed, followed by population transfer from the L_b to the L_a state within 6 ps. In water ultrafast branching occurs between the fluorescing state and the charge-transfer-to-solvent state. Presolvated electrons, formed together with indole radicals within our time resolution, solvate on a timescale of 350 fs.

1. INTRODUCTION

The femtosecond UV-visible broadband absorption study of the photoionization of indole in different solvents is reported, and for the first time considered together with steady state measurements. Indole is a chromophore of many nitrogen heterocyclic biomolecules such as the essential amino acid tryptophan or the highly effective anticancer agent indole-3-carbinol. It is a model compound to study the response of these molecules to photoexcitation. Photoionization of organic compounds in solution is of large interest since it contributes to the damage of biological substances by UV radiation. The geminate recombination after ionization of indole has been studied successfully by time resolved methods [1] whereas the exact mechanism of the ionization is not yet clarified. Indole in water shows the unusual behavior of strong fluorescence and simultaneously ultrafast photoionization. To understand the underlying mechanisms the electronic dynamics of indole solvated in cyclohexane and ethanol is compared to water, where photoionization occurs as additional channel.

Transient spectra of solvated indole are measured in a 120 μm liquid jet with a crosscorrelation of 80 fs by means of a white light continuum (450 - 740 nm) generated in a sapphire disc. The molecules are excited at 270 nm with pump pulses generated by frequency doubling the output of a noncollinearly phase matched optical parametric amplifier [2]. Due to the short pump pulses there is a small yet finite probability for two-photon ionization in pure solvents. This allows us to study the spectral properties of the generated solvated electrons by measurements in pure solvents. The transient spectra of the indole solution are corrected for these solvent contributions.

2. DYNAMICS OF INDOLE IN NONPOLAR AND POLAR SOLVENTS

Indole in cyclohexane and ethanol is excited at 270 nm populating a mixture of the L_a and L_b states. The L_a and L_b states differ in their spectral structure (Fig. 1a) and Stokes shifts [3]. The unstructured spectrum of the L_a state shows a large Stokes shift due to the large change of the dipole moment upon electronic excitation. The dipole moment of the L_b state is similar to the ground state value. In nonpolar solvents like cyclohexane, the L_b state is energetically below the L_a state and its emission spectrum exhibits vibronic structure. In the polar solvent ethanol state reversal occurs after the electronic excitation and the L_a state becomes responsible for the more red shifted fluorescence [4].

Transient spectra are measured to characterize the evolution of the electronically excited indole. Broad spectra due to excited state absorption appear within our time resolution (80 fs) and give rise to a step like decrease of the transmission. They span the probed region with a broad maximum at 640 nm. The time dependence of the absorption is characterized by a monotonic increase or decrease (see Fig. 1b) for $\lambda_{\text{probe}} = 740 \text{ nm}$). From the lack of gradual spectral shift we conclude a population transfer between the L_a and L_b state and that the transient absorption in the detection window is stronger for the L_a state than that for the L_b state. The signal from indole in cyclohexane relaxes with a time constant of 7 ps. This decrease of the signal is due to the population transfer from the L_a state to the lower lying L_b state. In ethanol the polar solvent shell rearranges after the optical excitation of the indole. This leads to a very rapid state reversal and the L_a state slides energetically below the L_b state. The further increase of the transient absorption shows the subsequent population transfer from the L_b to the L_a state with a time constant of 6 ps. Solvation dynamics of ethanol is known to occur partly on the 5 ps time scale and might support the population transfer.

On the timescale shown in Fig. 1 b) the signal of indole in both solvents does not return to zero. After the relaxation from the initially excited state the indole molecules are still electronically excited and they decay on a nanosecond timescale to the electronic ground state.

In cyclohexane no photoionization occurs after excitation of the L_a state and in ethanol the ionization threshold is at 256 nm [5] which is not reached even with the blue wing of our 270 nm excitation pulse with a width of 3.3 nm. To investigate the ultrafast photoionization we also investigate the ultrafast dynamics of indole dissolved in water.

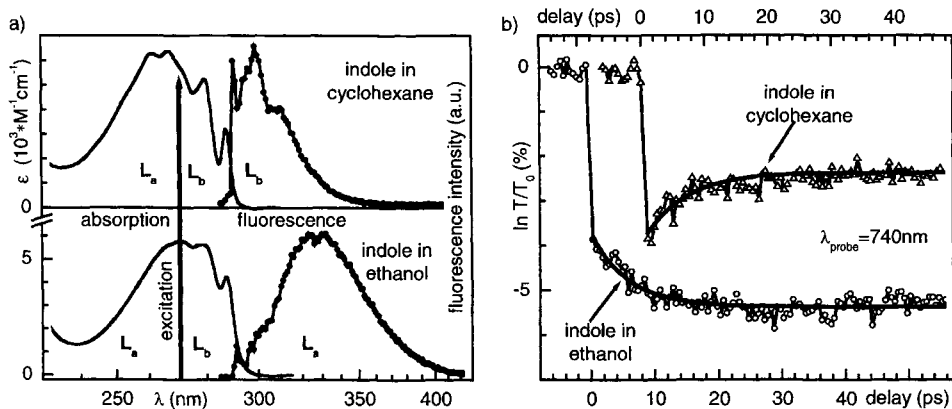


Fig. 1. a) Absorption and fluorescence spectra of indole solvated in cyclohexane and ethanol. b) Time resolved transmission change of indole probed at 740 nm.

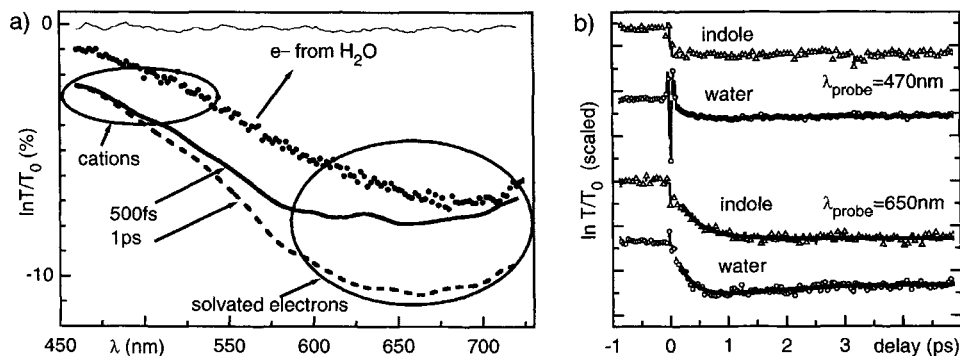


Fig. 2. a) Transient spectra of indole solvated in water 500 fs (solid thick line) and 1 ps (broken line) after the excitation. The dotted trace shows the spectrum of the solvated electron. b) Time resolved transmission change of the indole solution (triangles) and pure water (circles) at 470 nm and 650 nm.

3. DYNAMICS OF INDOLE IN WATER

The steady state spectra of indole solvated in water show similar behavior as those from indole solvated in ethanol (see Fig. 1a)). Due to the larger dipole moment of the water molecules a somewhat larger Stokes shift of the fluorescence spectrum is observed.

The transient spectra of indole dissolved in water at a delay of 500 fs and 1 ps after excitation are shown in Fig. 2a) and the time dependent transmission changes probed at 470 and 650 nm in Fig. 2b). Within our time resolution an instantaneous transmission decrease is found at all probe wavelengths due to the appearance of indole cations that absorb at shorter wavelengths and presolvated electrons that absorb at longer wavelengths [1]. In the blue (470 nm) no significant changes are observed thereafter indicating that the cation is generated in less than 80 fs and does not exhibit any significant dynamics on the ps timescale. In the red (650 nm) the transmission subsequently shows a further decrease, which is fitted by an exponential decay time of about 350 fs. We interpret the 350 fs dynamics as due to relaxation processes associated with the solvated electrons generated by the photoionization of the indole molecule. The spectral dependence of this contribution is similar to the spectrum of the solvated electron in pure water supporting this assignment (see Fig. 2a)).

Comparison of the evolution of the transient absorption in pure water with the indole solution demonstrates that the dynamics of the generated electrons depends on the donor molecule. The initial evolution in pure water is similar to that in indole (350 ± 50 fs), but shows an additional contribution on a timescale of 1 - 2 ps (Fig. 2b)). The formation of electrons stemming from indole is similar to the ionization and solvation process in pure water, but the time constant corresponding to the dielectric relaxation is missing. It indicates that the electron is not completely separated from the indole cation and the interaction with the parent molecule disables the dielectric relaxation that occurs in pure water on the timescale of 1 - 2 ps.

4. MODEL OF EXCITED STATE DYNAMICS

From the transient spectrum recorded a few picoseconds after the excitation a quantum yield for the photoionization of 45 ± 15 % is determined. The given error takes into account the un-

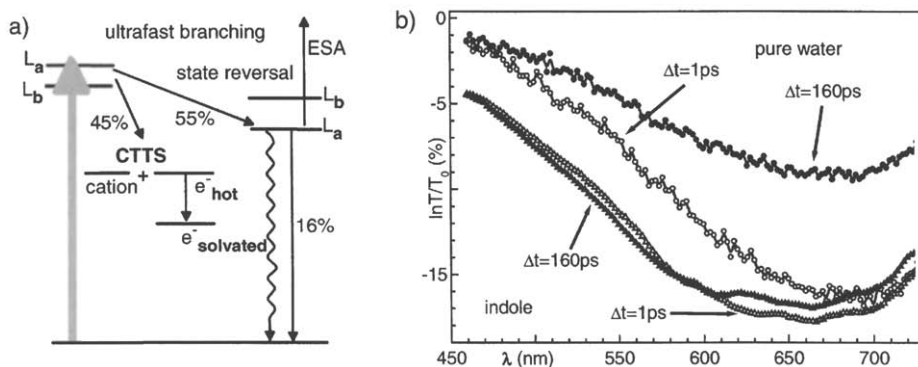


Fig. 3 a) Model of excited state dynamics. b) Transient spectra of indole in water 1 ps (open triangles) and 160 ps (solid triangles) after excitation compared to pure water (open and solid circles).

certainty arising from the excited state absorption which contributes to the transient spectra. This value is larger than previously reported ones [6]. Most probably recombination processes on the sub-ns timescale reduce the amount of solvated electrons detected by the earlier measurements. This demonstrates that for the accurate determination of quantum yields and branching ratios a sufficient time resolution is necessary to avoid product losses.

From the steady state fluorescence spectrum of indole in water a fluorescence quantum yield of about 0.09 is determined. Since the cation appears in less than 80 fs a branching of the excited state population has to occur immediately after photo excitation. We propose the model shown in Fig. 3a). A fraction of 45 % experiences photoionization, whereas the rest of the population relaxes to a fluorescing state, which can not ionize any more. A charge transfer to solvent state (CTTS), that was also introduced by other authors [4,7], is created within 80 fs. The presolvated electrons, also known as wet or hot electrons, form solvated electrons with a time constant of 350 fs. Afterwards the solvated electrons show no recombination within the next 160 ps contrary to solvated electrons in pure water as is shown in Fig. 3b).

5. CONCLUSIONS

The population transfer between the excited L_a and L_b states of 6.5 ± 2 ps is determined from indole dissolved in ethanol and cyclohexane. In water the appearance of presolvated electrons within the time resolution of our experiment and the fluorescence quantum yield of 0.09 indicate an ultrafast branching between the fluorescing state and the CTTS state immediately after photoexcitation. The solvation of the generated electrons shows the same initial dynamics of 350 fs for solvated indole and for pure water but differs on longer timescales.

REFERENCES

- [1] J. Peon, G.C. Hess, J-M.L. Pecourt, T. Yuzawa, B. Kohler, *J. Phys. Chem. A* 103 (1999) 2460.
- [2] T. Wilhelm, J. Piel, and E. Riedle, *Opt. Lett.*, 22 (1997) 1494.
- [3] P.R. Callis, *Methods in Enzymology*, 278 (1997) 113.
- [4] D. Creed, *Photochem. Photobiol.*, 39 (1984) 537.
- [5] A. Bernas, D. Grand, and E. Amouyal, *J. Phys. Chem.* 84 (1980) 1259.
- [6] R. Klein, I. Tatischeff, M. Bazin, and R. Santus, *J. Phys. Chem.* 85 (1981) 670.
- [7] H.B. Steen, M.K. Bowman, and L. Kevan, *J. Phys. Chem* 80 (1976) 482.

Short-time water caging and transient electron-OH couplings in liquid phase

B. Brozek-Pluska^b, A. Hallou^a, D. Glijer^a, B. Charles^c, Y. Gauduel^a.

^aLaboratoire d'Optique Appliquée, CNRS UMR 7639, Ecole Polytechnique - ENS Techniques Avancées, 91761 Palaiseau Cedex, France Tel : +33 (0)1 69 31 97 26

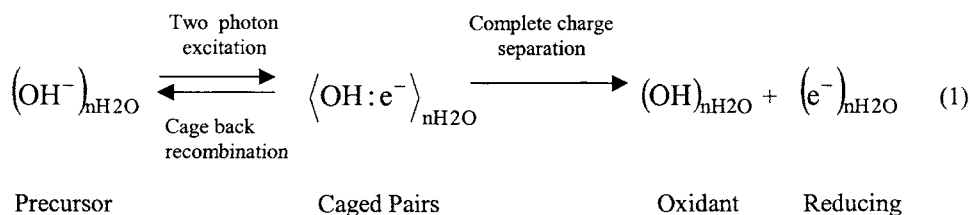
^bInstitute of Applied Radiation Chemistry, Technical University of Lodz, Wroblewskiego 15 street, 93-590 Lodz, Poland

^cEcole Nationale Supérieure de l'Electronique et de ses Applications, Cergy Pontoise, France

1. INTRODUCTION

The detailed description of time dependent reactant-solvent couplings that assist or impede elementary oxidoreduction processes are attracting growing experimental and theoretical interest for physical and biological chemistry. Ultrafast spectroscopic techniques allow the real time investigation of state distribution and dispersive elementary processes. The short-time dynamics of charge transfer processes can be influenced by the interactions between newly created electronic configurations of reactants (solutes) and surrounding solvent molecules (solvent caging). When solute-solvent caging effects are strong, early cage back geminate recombination and ultrafast presolvation charge transfer processes may occur [1-3].

Here, we focus our attention on the interplay that exists between solvation processes and ultrafast redox reaction in the vicinity of the strong oxidant hydroxyl radical (OH). This diatomic radical represents one of the most efficient oxidant of cellular components (proteins, lipids, DNA), contributes to Haber-Weiss reaction and plays some important role in fundamental radiation or stratospheric chemistry. Presently, we have investigated short-time water caging effect on transient electron delocalization-relocalization in the vicinity of nascent aqueous OH radicals. This specific electronic channel is represented by Eq.(1).



This simple oxidoreduction reaction involves complex OH⁻ - water molecules interactions whose the spectral signatures are assigned to Charge-Transfer-To-Solvent states (CTTS states). Indeed, the anionic precursor of the hydrated OH radical represents an interesting system for the direct investigation of elementary redox events in a protic molecular solution.

2. EXPERIMENTAL RESULTS AND DISCUSSION

Following a two photon excitation of hydrated hydroxyl ions ($\text{H}_2\text{O}/\text{NaOH} = 55$) with femtosecond UV pulses ($\lambda_{\text{pump}} = 310 \text{ nm}$, $E_{\text{excitation}} = 2 \times 4 \text{ eV}$), short-time electron transfer trajectories have been investigated by near-IR and UV absorption spectroscopies at room temperature. The energy of the pump beam is $\sim 10^{11} \text{ W cm}^{-2}$.

In a pump-probe configuration, using photodiodes for the detection, significant absorption spectroscopic data are reported in Fig.1. Following the interaction of UV photons with aqueous OH^- ion, two well defined electronic trajectories are observed in the first 4 ps.

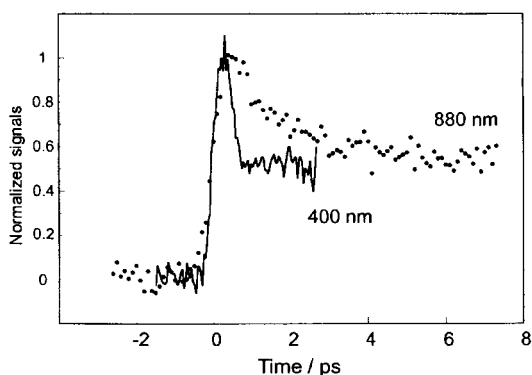


Fig.1. Normalized ultraviolet and near-infrared spectroscopic signals assigned to elementary electron transfer processes following the femtosecond UV excitation of aqueous hydroxyl ion (OH^-). The molecular ratio of the electrolyte solution NaOH is 55 at 294K.

Computed fits of experimental signals probed at different wavelengths allow for the careful investigation of ultrafast electronic pathways (Fig.2). The transient signal at 400 nm is assigned to a very short-lived CTTS* state of aqueous hydroxyl ions (OH^-)_{aq}. This excited state is instantaneously populated, typically in less than 50 fs and follows a pseudo first order dynamics with a frequency rate of $\sim 5 \times 10^{12} \text{ s}^{-1}$. Semi-quantum MD simulations emphasize that transient excited CTTS states play a crucial role in photoinduced electron transfers [4-6].

For a molecular ratio of 55, the time-dependent near-IR signal probed at 1.41 eV (880 nm) is assigned to an early prehydration electron transfer step (PHET) within a transient three body complex $(\text{HO}^-\cdot\text{Na}^+)_{\text{H}_2\text{O}}$. This 3s-like electronic configuration is understood as transient electron repartitioning between the center of mass of the OH^- vibrator and water molecules. The incomplete electron delocalization in the hydration shells of OH^- radicals favors an efficient cage-back recombination. This PHET is characterized by a frequency of $1/0.380 \text{ ps} = 2.6 \pm 0.05 \times 10^{12} \text{ s}^{-1}$ (Fig.2). This dynamics is faster than the local lifetime of a OH^- radical, typically less than 2 ps in light water [7]. The incomplete recovery of UV and near-IR signals is due to a significant contribution of fully relaxed electrons. After a complete photodetachment process from OH^- donor, the electrons become deeply trapped in water bulk. The 1s-like ground states of fully hydrated electrons exhibits a long-lived behavior, typically in the sub-nanosecond temporal regime. The complex aspect of early quantum branching ratio between ultrafast electronic trajectories will be discussed in a forthcoming paper.

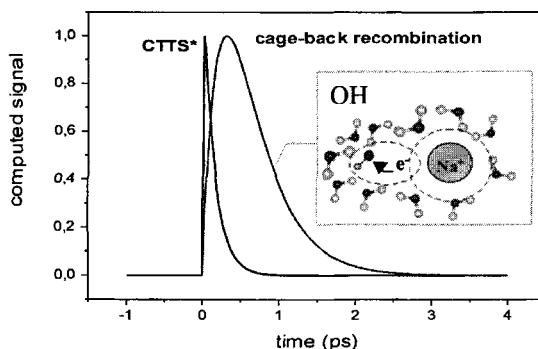


Fig.2. Comparative dynamics of two nonequilibrium electronic configurations triggered by femtosecond UV excitation of aqueous hydroxyl ion (OH^-). The computed dynamics are extracted from UV and n-IR spectroscopic data performed at 400 and 880 nm respectively.

An interesting and fundamental point that emerges from UV and near-IR spectroscopic studies is that short-time water caging effects can influence the quantum branching between different electronic repartitioning processes. Indeed, UV excited CTTS states can be understood as predissociative electronic configurations and near-IR $(\text{HO}:\text{e}^-)_{\text{H}_2\text{O}}$ pairs as nonequilibrium electrons oscillating between nascent OH radicals and water traps. Femtosecond results reported in Fig.3 raise that branching between prehydration redox reaction and predissociative electronic configurations are dependent on the electron donor.

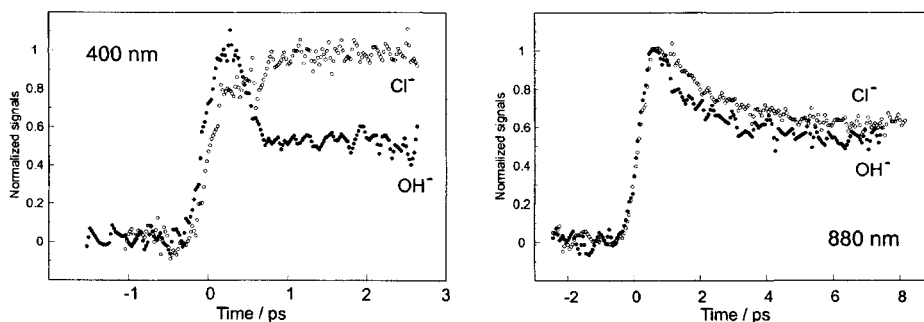


Fig.3. Comparative effects of Y^- ($\text{Y} = \text{Cl}^-$ vs OH^-) on the short-time dependence of electronic configurations following a femtosecond UV excitation with 4 eV photon. The molecular ratio of aqueous ionic solutions equals 55 ($R = \text{H}_2\text{O}/\text{NaY}$).

For a same molecular ratio of aqueous NaY solutions ($\text{Y} = \text{OH}^-$, Cl^-), experimental data underlines specific effects of nascent OH radicals on transient UV and near-IR electronic configurations. Complex investigations of PHET reactions in the polarization CTTS well of aqueous Cl^- and OH^- ions are in progress. We should wonder whether a change in the size of ionic radius ($\text{OH}^- \sim 1.76 \text{ \AA}$ vs $\text{Cl}^- \sim 2.35 \text{ \AA}$) or in the separation of the energy levels influence early branchings of ultrafast electronic trajectories. A key point of these studies is that the spectroscopic predictions of computed model-dependent analysis are compared to a direct identification of transient spectral bands, using a cooled Optical Multichannel Analyzer

(OMA 4) equipped with CCD detector. A 3D spectral data is reported in Fig.4. The transient near-IR band is the signature of electron-Cl atom pairs whose the complete disappearance occurs in less than 2 ps. On this figure, the long lived contribution of 1s-like ground states of fully hydrated electrons is clearly observed in the red spectral region.

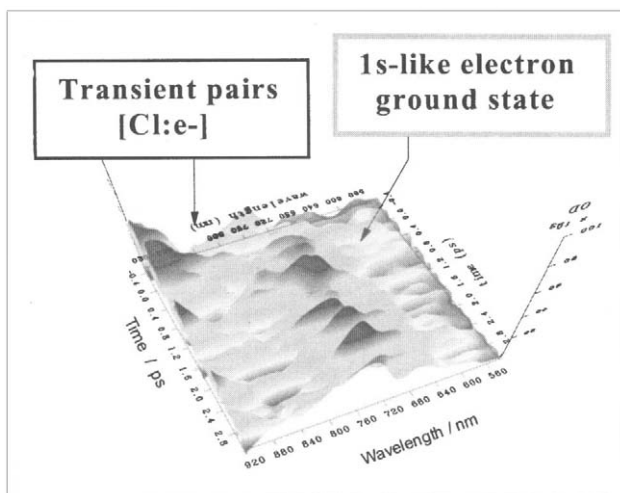


Fig.4. 3D absorption signatures of transient electronic configurations triggered by the femtosecond UV excitation of aqueous sodium chloride solution ($\text{H}_2\text{O}/\text{NaCl} = 55$).

Because the kinetic energy dissipation of an excess electron by surrounding water molecules plays an essential role during the formation of electron-radical pairs, the influence of the quantum polarization of water molecules and OH radical must be investigated in detail. Further experimental studies on the short-time dependence of vibronic couplings in aqueous environment would permit to understand the contribution of Jahn-Teller effects on the crossing of an elementary redox reaction with OH radical.

3. CONCLUSIONS

Femtosecond spectroscopic investigations in the spectral range 400-880 nm have permitted to discriminate specific OH effects on the dynamics of short lived UV excited CTTS states and transient near-IR $(\text{HO}\cdot\text{e}^-)_{\text{H}_2\text{O}}$ pairs. The complex nature of ultrafast prehydration elementary redox reactions with nascent OH radical (strong acid) must be contemplated in the framework of ion-pairs dynamics, ion-solvent correlation function, short-range ordering water molecules, solvent screening or anisotropic electric field effects and short-time vibronic couplings.

REFERENCES

- [1] Y. Gauduel, H. Gelabert, F. Guilloud, *J. Am. Chem. Soc.*, 122 (2000) 5082.
- [2] Y. Gauduel, A. Hallou, B. Charles, *J. Phys. Chem. A*, 107 (2003) 2011.
- [3] B. Brozek-Pluska, A. Hallou, D. Glijer, Y. Gauduel, in preparation
- [4] W.S. Sheu, P.J. Rossky, *J. Am. Chem. Soc.*, 115 (1993) 7729.
- [5] A. Staib, D. Borgis, *J. Chem. Phys.*, 103 (1995) 2642.
- [6] S. Bradforth, P. Jungwirth, *J. Phys. Chem. 2*, 106 (2002) 1286.
- [7] B. Halle, G. Karlstrom, *J. Chem. Soc. Faraday Trans. 70* (1983) 1047.

Fluorescence dynamics of coumarin C522 in water and in cyclodextrin cavity

P. Bodis^a, I. Bugar^b, T. Palszegi^c, D. Velic^{a, b *} and D. Chorvat^b

^aKomensky University, Department of Physical and Theoretical Chemistry, Mlynska dolina CH-1, 842 15 Bratislava, Slovakia

^bInternational Laser Center, Ilkovicova 3, 812 19 Bratislava, Slovakia

^cSlovak Technical University, Department of Chemical Physics, Radlinskeho 9, 812 37 Bratislava, Slovakia

1. INTRODUCTION

Solvation and influence of environment are some of the most fundamental processes in chemistry. Only advancement of laser technology has allowed to study these processes on femtosecond time scale and in this way to describe them in greater details. One of the methods, how to characterize solvent-solute interaction, is time-resolved fluorescence spectroscopy. We present fluorescence dynamics of the supramolecular host-guest complex consisting of cyclodextrin as β -cyclodextrin and coumarin as C522. The molecule of C522 as a guest is shown in Fig. 1 along with β -cyclodextrin ring forming a "bucket" structure as a host.

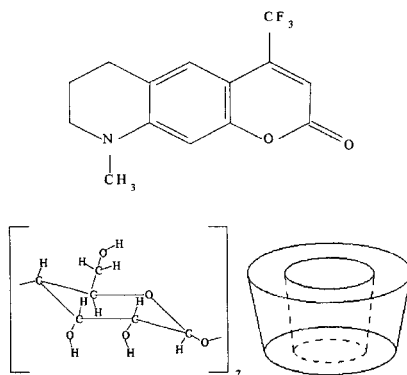


Fig. 1. Upper part shows coumarin C522 and lower part β -cyclodextrin and its schematic structure

The inclusions and dynamics of various molecules into cyclodextrins, cyclic oligosaccharides generally serving as a hydrophilic cover for the hydrophobic guest, and formations of

*corresponding author, velic@ilc.sk

supramolecular structures have been demonstrated [1-3]. A similar host-guest inclusion complex was also tested with an attempt to form a surface functional supramolecular self-assembled layer [4]. In this study, our focus is on a comparison of the C522 fluorescence dynamics in aqueous solution representing free environment and in aqueous β -cyclodextrin solution forming together host-guest complex representing restricted environment. The fluorescence dynamics of the host-guest cyclodextrin-coumarin complexes have been modeled by using molecular dynamics [1], multishell continuum model, and molecular hydrodynamic theory [3]. In this study, the collective molecular coordinates, based on Brownian oscillator model for the fast molecular relaxation processes, serve as a basis for the time-resolved fluorescence signal simulation procedure [5].

2. METHODS

2.1. Time-resolved fluorescence spectroscopy

Femtosecond Ti-Sapphire oscillator (CDP, TiF50, 100 fs, 80 MHz, 0.3 W, 800 nm) pumped with diode pumped solid state laser (Coherent, Verdi) was used to excite the system. The time- and spectral-resolved fluorescence spectra of C522 were measured by using up-conversion set-up (CDP, FOG100). The β -cyclodextrin, $C_{42}H_{70}O_{35}$, and coumarin C522, $C_{14}H_{12}F_3NO_2$, used in these experiments were produced by Cyclolab and Radiant Dyes Chemie, respectively. All experiments were performed at room temperature and used water was twice deionised.

2.2. Brownian oscillator model

The frequency ω and gate pulse time-delay t_d dependent fluorescence up-conversion signal $F(\omega, t_d)$ have been theoretically modeled by using an overdamped multi-mode Brownian oscillator model [5]. The deconvoluted fluorescence spectrum is given by

$$\tilde{F}(\omega, T') = \int_{-\infty}^{\infty} dt \int_{-\infty}^{\infty} dt' e^{i\omega t} e^{i\Omega_{exc} t'} I_{gate}(t/2) I_{exc}(t'/2) \exp(-F_{Re}(g; t, t', T')) \cos(F_{Im}(g; t, t', T')) \quad (1)$$

where T' is the average time interval during which excited state dynamics occurs, Ω_{exc} is the excitation frequency, $I_{gt}(t/2)$ and $I_{exc}(t'/2)$ represent the Gaussian pulse intensities and t , and t' are time variables. Further, F is the line broadening which determines dephasing and the spectral diffusion functions and causes the dynamic Stokes shift of the fluorescence peak intensity and both real and imaginary parts were found explicitly. The dependence on line-shape functions is $g(t)$, specified for a combination of T' , t , and t' , and it is determined by the auto-correlation function of the dynamically fluctuating part of the excited versus ground state electronic energy gap.

3. RESULTS AND DISCUSSION

The host-guest β -cyclodextrin-C522 complex formation was determined based on fluorescence blue shift as a function of the increasing β -cyclodextrin concentration from 10^{-6} to 10^{-2} M. Similar result was observed for coumarin C6 [4] and this blue shift was considered along with anisotropy results as a proof of the host-guest formation. Time-resolved fluorescence spectroscopy was utilized to differentiate between fluorescence dynamics of

C522 in free aqueous environment and in β -cyclodextrin cavity restricted environment. The experimental fluorescence decay curves were fitted by single exponential function to extract time constants t_1 . The time constants for C522 in water, and in aqueous solution of β -cyclodextrin were determined at fluorescence wavelengths of 500 nm and 520 nm to be 1.37 ps and 2.02 ps, and 2.97 ps and 7.14 ps, respectively. At the wavelength of 540 nm, water resulted in 3.25 ps and β -cyclodextrin resulted in a flat response in the measured 30 ps interval. The wavelength dependence of these relaxations is in agreement with a contribution of higher excited states to lower excited states resulting in the slower relaxation at then longer wavelengths. The time-resolved results showed that the fluorescence dynamics of C522 in β -cyclodextrin host-guest complex is slower than in water. The slower relaxation dynamics in the solvation response is due to restrictive geometry imposed by the β -cyclodextrin cavity. The possible relaxation components may be caused by motion of the coumarin molecule in and out of the cavity, fluctuations of the β -cyclodextrin "bucket" or reorientation of highly constrained water molecules in the cavity [1]. However, the most probable model is based on the highly constrained water molecules in the β -cyclodextrin cavity which are likely to lose their translational degrees of freedom and can relax only by orientational motions [3].

In the Brownian oscillator overdamped model as an attempt to simulate the solvation dynamics, the explicit forms of the line-shape functions $g_i(t)$ are

$$g_i(t) = (\Delta_i^2 / \Lambda_i^2) (\Lambda_i t - 1 + e^{-\Lambda_i t}) + i (\lambda_i / \Lambda_i) (1 - e^{-\Lambda_i t}) \quad (2)$$

where λ_i is the i^{th} additive component of the stationary Stokes shift, Δ_i is the amplitude of electronic excitation energy gap fluctuation with correlation time Λ_i^{-1} . The Stokes shifts corresponding to free and β -cyclodextrin cavity restricted water are λ_{water} as

$$\lambda_{\text{water}} = [p_{\text{fast}} \lambda_{\text{water,fast}} + (1 - p_{\text{fast}}) \lambda_{\text{water,slow}}] \quad (3)$$

where $\lambda_{\text{water,fast}}$ and $\lambda_{\text{water,slow}}$ are shifts caused by the fast and slow relaxations of the water around C522 having portion p_{fast} . The β -cyclodextrin cavity Stokes shift contribution is λ_{CD} and the fluorescence signal $\tilde{F}(\omega, T')$ of C522 in free water and in aqueous β -cyclodextrin solution as portion c_{CD} is given as

$$\tilde{F}(\omega, T') = c_{\text{CD}} \tilde{F}_{\text{CD}}(\omega, T') + (1 - c_{\text{CD}}) \tilde{F}_{\text{water}}(\omega, T') \quad (4).$$

Experimental data and simulated results are shown in Fig. 2. In a case of water, good qualitative and quantitative agreements were observed for 500 nm and only fair for 520 nm. At the wavelength of 540 nm, a qualitative estimate is not in agreement, where further optimization of parameters is needed. In a case of β -cyclodextrin, good qualitative and quantitative agreements were observed for all wavelengths. The following parameters of the multi-mode Brownian oscillator model for water were used as $p_{\text{fast}} = 0.64$, $\Lambda_{\text{w,fast}} = 0.0091$, $\lambda_{\text{w,fast}} = 3550$, $\Lambda_{\text{w,slow}} = 0.0046$, $\lambda_{\text{w,slow}} = 1850$, and $I_{\text{max}} = 22$. The following parameters were

used for β -cyclodextrin as $p_{\text{fast}} = 0.69$, $\Lambda_{w,\text{fast}} = 0.0084$, $\lambda_{w,\text{fast}} = 3740$, $\Lambda_{w,\text{slow}} = 0.005$, $\lambda_{w,\text{slow}} = 1660$, $\Lambda_{\text{CD}} = 0.0048$, $\lambda_{\text{CD}} = 4220$, $c_{\text{CD}} = 0.54$, and $I_{\text{max}} = 63$.

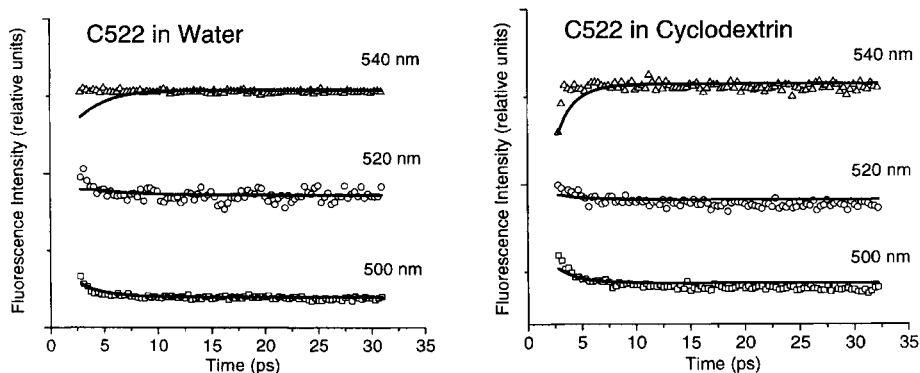


Fig. 2. Left and right parts show the fluorescence dynamics of C522 in water and in β -cyclodextrin aqueous solution for the fluorescence wavelengths of 500 (squares), 520 (circles), and 540 (triangles) nm, respectively. The experimental and simulation data are scatter and line, respectively.

4. CONCLUSIONS

Time-resolved fluorescence of coumarin C522 was determined in water and in host-guest complex with β -cyclodextrin, representing free aqueous and cavity restricted environments, respectively. Experimental fluorescence clearly showed faster dynamics in a case of water. The time parameters of monoexponential fit for water and β -cyclodextrin at 500 nm and 520 nm were determined to be 1.37 ps and 2.02 ps, and 2.97 ps and 7.14 ps, respectively. Multi-mode Brownian oscillator model, as an attempt to simulate the solvation dynamics, supported these fluorescence dynamics results.

ACKNOWLEDGEMENT

Support of Slovak agency VEGA (1/0216/03) is acknowledged.

REFERENCES

- [1] S. Vajda, R. Jimenez, S. J. Rosenthal, V. Fidler, G. R. Fleming, E. W. Castner, *J. Chem. Soc., Faraday Trans.* 91(1995)867.
- [2] A. Douhal, T. Fiebig, M. Chachisvilis, A. H. Zewail, *J. Phys. Chem. A* 102(1998)1657.
- [3] N. Nandi, K. Bhattacharyya, B. Bagchi, *Chem. Rev.* 100(2000)2013.
- [4] D. Velic, G. Koehler, *Chem. Phys. Lett.* 371(2003)483.
- [5] A. Douhal and J. Santamarie (eds.), *Femtochemistry and Femtobiology*, I. Bugar, D. Chorvat jr., T. Palszegi, P. Mach, J. Urban' V. Szocs, World Scientific Publishing, (2002)298.

Solvation dynamics of electron in ethylene glycol at 300 K

B. Soroushian,^a I. Lampre,^a S. Pommeret ^b and M. Mostafavi ^a

^a Laboratoire de Chimie Physique/ELYSE, UMR 8000, CNRS / Université Paris-Sud, Centre d'Orsay, Bât. 349, 91405 Orsay Cedex, France.

^b CEA/Saclay, DSM/DRECAM/SCM URA 331 CNRS, 91191 Gif-sur-Yvette, Cedex, France

1. INTRODUCTION

The solvated electron was observed for the first time almost 40 years ago in water by pulse radiolysis measurements through its strong visible absorption band [1]. Afterwards, it was found that the absorption spectrum of the solvated electron is solvent dependent [2]. For instance, for the series of alcohols the wavelength of the absorption band maximum ranges from 575 nm in ethylene glycol (EG) to 820 nm in 2-propanol [3]. More recently, considerable experimental works have been devoted to the electron solvation dynamics, mainly in water [4] but also in polar solvents [5]. It was reported that, in alcohols, the solvation dynamics occurs in several steps followed by a slow process attributed to the cooling of the solvated electron as it relaxes vibrationally in its ground state [6]. Lately, a study concerning the solvation dynamics of photoejected electrons from I⁻ in EG was published [7]. Only the kinetics signals at two different wavelengths were observed and two thermalization times of 8 and 27 ps were given for 800 and 500 nm, respectively.

Ethylene glycol is a very viscous liquid and the molecule presents two close OH groups. It has to be noticed that, among all the different solvents studied by pulse radiolysis, the transition energy of the solvated electron absorption band is maximum in liquid ethylene glycol. For these reasons, the electron in EG seems to have a "special" behaviour and it is of great interest to study the dynamics of the formation of equilibrated solvated electron. Within this context, the present communication deals with the dynamics of solvation in EG of electrons produced by photoionisation of the solvent at 263 nm. The formation of solvated electrons is followed by pump-probe transient absorption spectroscopy in the visible spectral range from 425 to 725 nm and also in near IR. For the first time, the absorption spectrum of the precursor of the equilibrated electron is observed in EG. Our results are shortly compared by those obtained in water and methanol.

2. EXPERIMENTAL

Experiments were performed using a commercial kilohertz femtosecond Ti:Sapphire laser system (Spectra Physics) delivering laser pulses at 790 nm with a duration of 110 fs and an energy of 750 μ J. The pump beam at 263 nm (third harmonic) was produced by frequency doubling and sum-frequency mixing in two BBO crystals. Then, the pump beam was focused on a 300 μ m thick ethylene glycol jet in order to produce electrons by photoionisation of the

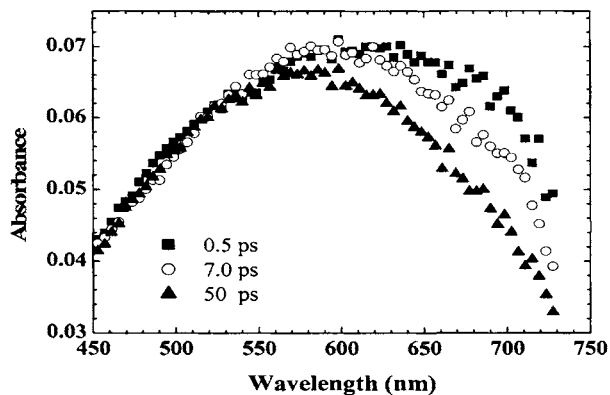


Fig. 1. Transient absorption spectra recorded in ethylene glycol after photoionisation of the solvent by a 263 nm laser pulse.

solvent. The pump pulse duration and energy was about 110 fs fwhm and 20 μ J, respectively. As a probe beam, we used a white light continuum generated by the fundamental pulses at 790 nm in a 1 mm plate of fused silica. After scanning the sample the probe beam was dispersed on a polychromator and detected on a CCD camera. So, time resolved absorption spectra ranging from 425 to 725 nm and also in the near IR were measured.

Ethylene Glycol from Aldrich (spectrophotometry grade) was used without further purification. The experiments were performed at 300 K.

3. RESULTS

Fig. 1 depicts the time evolution of the electronic absorption spectrum recorded in ethylene glycol upon photoionisation of the solvent at 263 nm. We point out that only the red part of the spectrum evolves in the first tens of picoseconds while the blue side remains unchanged. The decreasing of the absorbance for the wavelengths higher than 600 nm induces shrinkage of the spectrum and leads to a blue shift of the absorption maximum from 630 to 575 nm. The absorption spectrum obtained at 50 ps corresponds to the well-known spectrum of the solvated electron in ethylene glycol characterised by a broad absorption band peaking at 575 nm as obtained in nanosecond pulse radiolysis measurements. At longer time delay the shape of the spectrum does not evolve any more but its intensity drops as the electron concentration decreases due to its geminate recombination with the parent radical cation. It is worth noticing that, in contrast to what have been reported for the electron solvation dynamics in water and in alcohols at room temperature, we do not observe a hypsochromic translation of the electron absorption spectrum.

The disappearance of an absorption band in the near IR domain is corroborated by the transient absorption signals recorded at three different wavelengths after photoionisation of

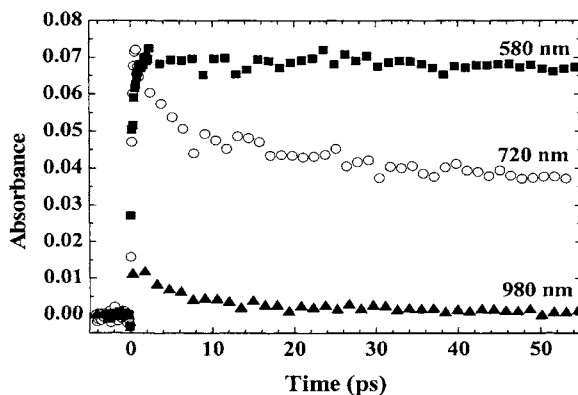


Fig. 2. Transient absorption signals recorded at three different wavelengths after photoionisation of ethylene glycol by a 263 nm laser pulse.

ethylene glycol at 263 nm (Fig. 2). Indeed, the observed kinetics differ significantly. After a fast rise within less than 2 ps, the signal at 580 nm remains quasi-constant for the next 50 ps. In contrast, the absorbances in the red spectral domain decrease. The absorbance at 980 nm in the near IR vanishes within 20 ps while the signal at 720 nm follows a two-components decay and is divided by 2 after 50 ps.

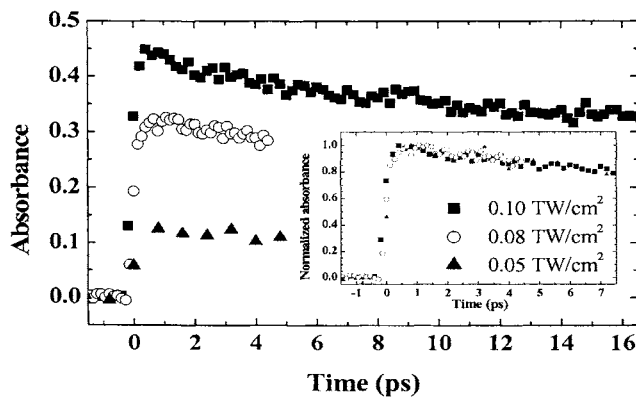


Fig. 3. Transient absorption signals recorded at 715 nm after photoionisation of ethylene glycol at 263 nm with three laser power densities. Inset : the same signals after normalisation.

In order to study the influence of electron concentration on the observed dynamics, we performed experiments with different laser power densities. As an illustration, the transient absorption signals recorded at 715 nm in ethylene glycol upon photoionisation of the solvent at 263 nm with three different laser power densities are presented in Fig.3. As expected for a two-photon ionization process, the signal intensity increases roughly with the square of the power density. However, the recorded decay kinetics does not depend on the 263 nm laser power density since the normalised transient signals are identical (Cf. Fig.3 inset). That result indicates that the same phenomena occur whatever the power density and consequently that the solvation dynamics are independent of the electron concentration in our experimental conditions i.e. we are still within the independent pair approximation as opposed to our previous work on hydrated electron [8].

4. CONCLUSION

Using pump-probe transient absorption spectroscopy in the visible spectral range from 425 to 725 nm and also in near IR, we followed the formation of equilibrated solvated electron in ethylene glycol. Our study shows that the excess electron in EG presents an important and wide absorption band in the visible and the near IR at very short delay time after the pump pulse. The red part of that absorption band exhibits strong changes within the first few picoseconds while the blue part of it does not exhibit any structural changes. The time-resolved results present an "uncommon" behaviour of the electron in EG compared to what have been reported in water and in methanol at room temperature. That behaviour reveals that a hot state of the ground state of solvated electron which absorbs in the blue part is quickly formed after a few hundred of femtoseconds and that state relaxes to the equilibrated one in the picosecond time range. That relaxation is accompanied by the decrease in absorbance only in the red part of the absorption spectra. More details concerning that peculiar solvation dynamics will be given in a forthcoming paper.

REFERENCES

- [1] E. J. Hart and J. W. Boag, *J. Am. Chem. Soc.*, 84, (1962),4090 ; E. J. Hart and M. Anbar (eds), *The Hydrated Electron*; Wiley Interscience: New York, 1970 and the references therein.
- [2] F.Y. Jou and G.R. Freeman, *J. Phys. Chem.* 83, (1979) 2383.
- [3] K. Okazaki, K. M. Idrissali and G. R. Freeman, *Can. J. Chem.* 62, (1984) 2223.
- [4] some of the references are the following: Y. Gauduel, S. Pommeret, A. Migus and A. Antonetti, *J. Phys. Chem.*, 93 (1993) 3880; A. Migus, Y. Gauduel, J. L. Martin and A. Antonetti, *Phys. Rev.Lett.* 58 (1987) 1559; Y.Gauduel, S. Pommeret, A. Migus and A. Antonetti, *J. Phys. Chem.* 93 1(993) 3880; M. Assel, R. Laenen, and A. Laubereau, *J. Phys. Chem.*, A 102 (1998) 2256; M. Assel, R. Laenen, and A. Laubereau, *J. Chem. Phys.*, 111 (1999) 6869.
- [5] M. Sander, U. Brummund, K. Luther and J. Troe, *J. Phys. Chem.* 97 (1993) 8378; C. Pepin, T. Goulet, D. Houde and J.-P. Jay-Gerin, *J. Phys. Chem.* 98 (1994) 7009; X. Shi, F.H. Long, H. Lu and K.B. Eisenthal, *J. Phys. Chem.* 99 (1995) 6917; C. Silva, P.K. Walhout, P.J. Reid and P.F. Barbara, *J. Phys.Chem. A* 102 (1998) 5701.
- [6] T. Scheidt and R. Laenen. *Chem. Phys. Lett.* 371 (2003) 445.
- [7] J. A. Kloepfer, V. H. Vilchiz, V. A. Lenchenkov, A. C. Germaine, and S. E. Bradforth, *J. Chem. Phys.* 113 (2000) 6288.
- [8] S. Pommeret, F. Gobert, M. Mostafavi, I. Lampre and J-C. Mialocq. *J. Phys. Chem.* 105 (2001) 11400.

Solvation dynamics of coumarin 153 in benzene-acetonitrile and benzene-methanol mixtures: a Molecular Dynamics study

M. Koziński^{a,b}, W. Jarzęba^a and R. Vuilleumier^{b,*}

^aFemtochemistry Group, Faculty of Chemistry, Jagiellonian University
ul. Ingardena 3, 30-060 Kraków, Poland

^bLaboratoire de Physique Théorique des Liquides, Université Pierre et Marie Curie
4 place Jussieu, F-75005 Paris, France

1. INTRODUCTION

Time-resolved fluorescence from sub-picosecond to the nanosecond time-scale of dye molecules like coumarins has been widely used to study solvation dynamics in liquids [1]. As the dye is photoexcited, its dipole moment abruptly changes. Then by monitoring the time-dependent fluorescence energy one can have access to the solvent dynamical response to the charge reorganization in the dye. The microscopic interpretation of these experiments has greatly benefited from Molecular Dynamics (MD) studies [2]. Recently, few experimental [3–5] and theoretical [6, 7] works have been performed on solvation dynamics in liquid mixtures. A number of new phenomena can arise in mixtures which are not present in pure solvents, like association, mutual diffusion and preferential solvation [6]. We present here a

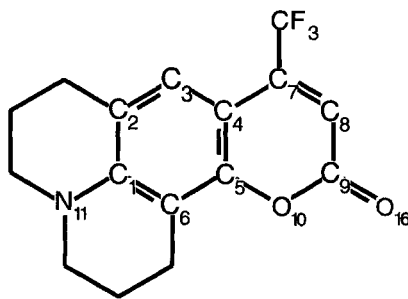


Fig. 1. Structure of the amino-coumarin C153. The atom labeling will be used throughout the paper.

Molecular Dynamics study of the time-dependent fluorescence of coumarin 153 (C153 – see Fig. 1) in benzene-acetonitrile and benzene-methanol mixtures. The solvation dynamics in benzene-acetonitrile mixtures will be analyzed by inspection of the time-dependent local populations of the two constituents around the coumarin dye.

*Corresponding author (email: vuilleum@lptl.jussieu.fr)

2. METHODS

All molecules in the different systems were represented by rigid, non-polarizable models. The intermolecular interactions consisted of Lennard-Jones potentials (with the Lorentz-Berthelot combination rule) between heavy atoms and coulombic potentials with atomic partial charges. The parameters for acetonitrile and benzene were taken from the literature [8, 9]. However, for the methanol parameters we have changed the atomic charges of a previously published model [10] in order to give better account of the dielectric constant of methanol [11]. The coumarin model was taken from Kumar and Maroncelli [2]. The models for the ground electronic state, S_0 , and the first excited singlet state, S_1 , differ only in the charge repartition. A better description of the ground state charges was added to the original coumarin model from the result of a Hartree-Fock calculation using 6-31g** basis-set. The resulting ground and excited states dipole moments of the C153 are 6.8 D and 14.4 D, respectively.

Apart from pure benzene and pure polar solvents, either acetonitrile or methanol, we have considered $x_p = 0.2$ and $x_p = 0.7$ molar fractions of the polar solvent. Systems ranging from 256 (pure benzene) to 512 (pure polar solvents) molecules were used. From well equilibrated (1 ns) simulations with the coumarin in the ground state S_0 , one to two hundred equally distant configurations were selected. In these configurations the coumarin state was switched to the S_1 state and the solvent was let to relax in a series of 10 ps long *NVE* simulations. The solvent response was monitored using the normalized time-dependent stokes-shift function:

$$S(t) = \frac{\overline{\Delta E}(t) - \overline{\Delta E}(\infty)}{\overline{\Delta E}(0) - \overline{\Delta E}(\infty)} \quad (1)$$

where $\Delta E = E(S_1) - E(S_0)$ is the energy difference between the ground and excited state of the coumarin and the overbar means averaging over the initial configurations.

3. RESULTS

The variations of the simulated steady state solvatochromism, as a function of the polar solvent molarity, were found to be in good agreement with the experimental work of Królicki *et al.* [4], both for absorption and fluorescence. The difference of Stokes-shifts between benzene and acetonitrile is 981 cm^{-1} , compared to 1230 cm^{-1} obtained experimentally. These numbers are 870 cm^{-1} and 1910 cm^{-1} , respectively, for methanol.

In Fig. 2, the simulated solvent response functions, $S(t)$, are displayed for benzene-acetonitrile and benzene-methanol mixtures. To quantitatively compare this dynamics to the experimental work of Luther *et al.* on benzene-acetonitrile mixtures three exponential fits of the solvent response function were performed. The resulting weights, a_i , $i = 1 \dots 3$, and times τ_i , $i = 1 \dots 3$ are reported in Table 1 and can be compared with the corresponding experimental values (Table 2). Good agreement between the two is achieved, except for the longer time at $x_p = 0.2$ which may be due to statistical inaccuracy.

It can be seen from the tables and from Fig. 2.a. that the addition of small amount of acetonitrile in benzene speeds up the initial decay of the solvent response, usually assigned to inertial motions [6]. On the other hand, the solvent response at times longer than 1 ps is at first only slightly modified by the presence of acetonitrile. Only large amount of acetonitrile lead to a faster decay of the solvent response function in this non-inertial regime.

In order to gain some microscopic insight into the mechanisms giving rise to the observed time-dependent Stokes-shift, we have calculated the benzene center-of-mass and acetonitrile

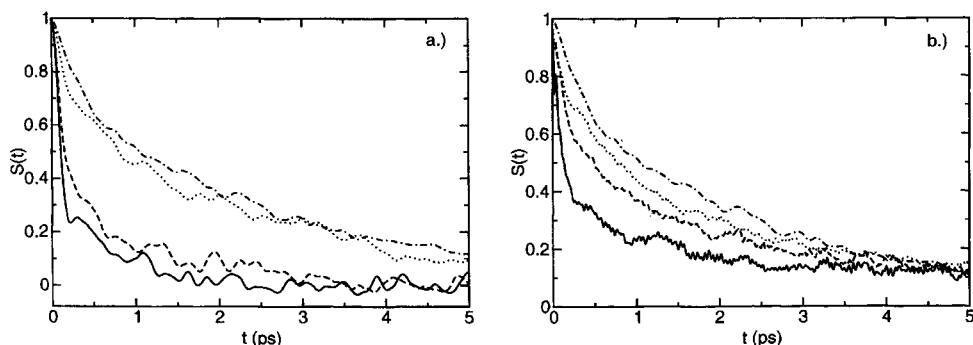


Fig. 2. Solvent response functions $S(t)$ for benzene-acetonitrile (a) and benzene-methanol (b) mixtures. Solid lines: pure polar solvents, $x_p = 1.0$; dashed lines: $x_p = 0.7$; dotted line: $x_p = 0.2$; dotted-dashed line: pure benzene, $x_p = 0$.

Table 1

Three exponential fits parameters of the MD solvent response functions in benzene-acetonitrile mixtures.

x_a	a_1	τ_1	a_2	τ_2	a_3	τ_3
0.0	0.22	0.28	0.58	1.78	0.20	7.40
0.2	0.28	0.19	0.48	1.75	0.24	4.50
0.7	0.66	0.15	0.34	1.26		
1.0	0.67	0.097	0.33	0.72		

sites populations around distinct coumarin sites (within a radius of 5 Å). At low concentration of acetonitrile (see Fig. 3.a), the dynamics of benzene population around the sites C_4 and C_9 is well correlated with the non-inertial solvent response function. The observed increase of benzene population around C_4 and decrease around C_9 with time sum up to an apparent displacement of benzene molecules away from the carbonyl group of C153, towards the piperidine rings, while going from the ground state to the excited state. As the benzene molecules are bulky, these motions are slow and could explain the observed slow decay of $S(t)$ at $x_p=0.2$. We did not find strong evidence of the same phenomenon at high acetonitrile concentration. However it appeared in this latter case that rotation of acetonitrile occurs to accommodate to the dipole moment change. For example (see Fig. 3.b), around the N_{11} site of coumarin an

Table 2

Three exponential fits parameters of the experimental solvent response functions in benzene-acetonitrile mixtures [3].

x_a	a_1	τ_1	a_2	τ_2	a_3	τ_3
0.0	0.32	0.22	0.61	1.68	0.07	6.29
0.2	0.50	0.09*	0.40	1.54	0.10	8.73
1.0	0.69	0.089	0.31	0.63		

* This time was fixed.

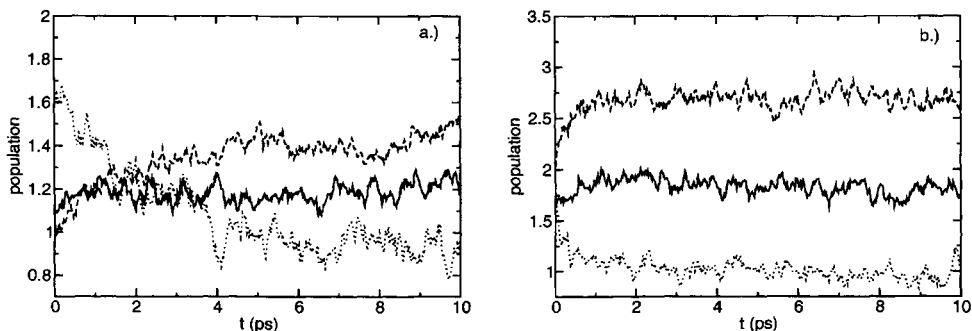


Fig. 3. Dynamics of solvent populations around coumarin sites (a) benzene population around coumarin C_4 (solid line), C_1 (dashed line) and C_9 (dotted line) for $x_p=0.2$. (b) populations of acetonitrile C (solid line), N (dashed line) and CH_3 group (dotted line) around coumarin N_{11} for $x_p=0.7$.

increase of acetonitrile's N population is observed, concomitant with the decrease of the acetonitrile's CH_3 group population.

In the benzene-methanol case, the first inertial component exhibits similar dependence on x_p as in acetonitrile mixtures (see Fig. 2.b). The same is still true at intermediate times around 1-2 ps and a similar picture as in Fig. 3.a. can be observed at $x_p=0.2$. However, the addition of methanol to benzene gives rise to a very long decay time (see Fig. 2.b), which may be associated with the slow hydrogen bond network relaxation of methanol. It should be noted that no significant change of the hydrogen bond from methanol to the coumarin carbonyl group is observed between the S_0 and S_1 states.

4. CONCLUSIONS

In this work we presented the results of Molecular Dynamics simulations performed to study the solvatochromism and the dynamic Stokes-shift of coumarin 153 in mixtures of solvents. We showed the ability of MD to reproduce available data of the time-dependent Stokes-shifts. Moreover, MD allowed us to interpret these dynamics in benzene-acetonitrile mixtures in terms of motions of benzene around the coumarin or rotation of acetonitrile. The role of benzene in the solvation process of C153 seems to be more important than usually assumed.

REFERENCES

- [1] L. Reynolds, J. A. Gardecki, S. J. V. Frankland, M. L. Horng, M. Maroncelli, *J. Phys. Chem.*, 100 (1996) 10337.
- [2] P. V. Kumar, M. Maroncelli, *J. Chem. Phys.*, 103 (1995) 3038.
- [3] B. M. Luther, J. R. Kimmel, N. E. Levinger, *J. Chem. Phys.*, 116 (2002) 3370.
- [4] R. Królicki, W. Jarzęba, M. Mostafavi, I. Lampre, *Bull. Pol. Acad. Sci. Chem.*, 50 (2002) 435.
- [5] T. Molotsky, D. Huppert, *J. Phys. Chem. A*, 107 (2003) 2769.
- [6] B. M. Ladanyi, B. C. Perng, *J. Phys. Chem. A*, 106 (2002) 6922.
- [7] L. R. Martins, A. Tamashiro, D. Laria, M. S. Skaf, *J. Chem. Phys.*, 118 (2003) 5955.
- [8] D. M. F. Edwards, P. A. Madden, I. R. McDonald, *Mol. Phys.*, 51 (1984) 1141.
- [9] Y. Danten, B. Guillot, Y. Guissani, *J. Chem. Phys.*, 96 (1992) 3782.
- [10] M. Haughney, M. Ferrario, I. R. McDonald, *J. Phys. Chem.*, 91 (1987) 4934.
- [11] M. Koziński, R. Vuilleumier, article in preparation.

Femtosecond dynamics of excess electrons in a molten Na-NaBr system

H. Brands, N. Chandrasekhar, H. Hippler, and A.-N. Unterreiner

Universität Karlsruhe, Institut für Physikalische Chemie, D-76128 Karlsruhe, Germany

ABSTRACT

We investigated the ultrafast dynamics in a Na-NaBr melt at 1073 K by fs pump probe absorption spectroscopy. A simple model was used to simulate the dynamics of polaron-, bipolaron- and Drude-type electrons. The relaxation times for polarons and bipolarons are 210 fs and 3 ps, respectively. The existence of an isosbestic point at ~ 1.35 eV indicates an inter-conversion between bipolarons and Drude-type electrons.

1. INTRODUCTION

Metal-metal halide (M-MX) liquid solutions provide a relatively simple example of electron localization in disordered systems and have been extensively investigated in recent years, both experimentally [1-3] and theoretically [4-6]. From these studies the following physical picture emerges: In extremely dilute solutions the excess electron localizes in states that are liquid-state counter parts of the F-centres in solids (polaron-type species), i.e. electrons are trapped in an anion 'vacancy'. Part of these excess electrons occupies states in salt rich solutions with mobilities of the order of $10^{-1} \text{ cm}^2 \text{ V}^{-1} \text{ s}^{-1}$. Such electrons are neither strongly localized nor completely free. They are characterized as Drude electrons [2]. At higher metal concentrations various F-centres can interact with each other forming spin-paired dimeric species, e.g. bipolarons. Theoretical calculations predict bipolarons to be more stable by ~ 0.5 eV relative to polarons [4]. At high metal concentrations ($x_{\text{Na}} > 0.1$) metal-molten salt solutions at elevated temperatures exhibit a continuous metal-nonmetal (M-NM) transition. At low and intermediate concentrations the absorption band in the Na-NaBr system can be quantitatively described by a single Gaussian and a 'Drude' part whereas two Gaussians plus the contribution from the Drude-type electrons are needed in the K-KCl system [7]. The intensity of the band in Na-NaBr scales linearly with the metal concentration which is not the case in K-KCl mixtures. It was concluded that the nature of electronic defects cannot be decided from the optical absorption spectra alone and more detailed studies are necessary to understand the behaviour of the Na-NaBr system [7]. Ultrafast investigations of excess electrons in molten alkali halide systems with fs time resolution may help unravel the nature of the species and their dynamical behaviour. Only recently we have reported the first study of the K-KCl dynamics at elevated temperatures with fs time resolution [8]. Here, we report the relaxation dynamics of localized electrons in a Na-NaBr melt at intermediate metal concentrations ($x_{\text{Na}} = 0.012$) on an ultrafast timescale.

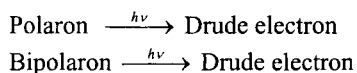
2. EXPERIMENTAL

The laser system consisted of a home-built Ti:sapphire fs laser oscillator and regenerative amplifier (RGA). The pulse duration was 50 fs at 800 nm and 1 kHz repetition rate. The output of the RGA was split into two parts. One part was used as pump pulse. The other part served as a source for the generation of probe pulses with the help of a non-collinear optical parametric amplifier (NOPA, Clark). The sample preparation was explained elsewhere [7]. Briefly, sodium (Alfa Aesar) was used as received and sodium bromide (Alfa Aesar) was dried and re-crystallized under vacuum. The preparation of the samples was carried out in a glovebox under argon atmosphere. Localized electrons were generated by heating the metal-salt mixture to 800 °C, i.e. well above the melting point of the salt.

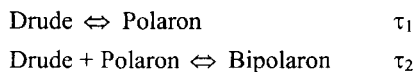
3. RESULTS AND DISCUSSION

The absorption spectrum of Na-NaBr peaks at 785 nm. Around this wavelength, the formation of localized electrons is indicated by a strong transient bleach after excitation. An additional contribution at zero-time (see inset in Fig. 1) was attributed to the signal from the sapphire windows of the sample cell as confirmed in our earlier study in the K-KCl system [8]. Transients were recorded at probe wavelengths between 555 and 1527 nm. A more detailed data set will be given elsewhere [10]. As can be seen in Fig. 1, the transient bleach at 600 nm is fast followed by a slow recovery which extends on a ps timescale. A similar trend is observed at all probe wavelengths from 555 nm to 846 nm whereas at 1036 nm a transient bleach is followed by a transient absorption. At 910 nm, however, the transient bleach recovers within 1 ps. When probe wavelengths are increased farther into the NIR region the transient bleach gradually diminishes while the transient absorption increases being the dominant component above 1300 nm. The following mechanism has been used to simulate the relaxation dynamics of excess electrons in Na- NaBr:

Photolysis:



Relaxation:



Within the pulse duration, polarons and bipolarons dissociate into Drude-type electrons and the subsequent bleach recovery at various probe wavelengths indicates the reformation of those species. On the other hand, the equilibrated absorption spectrum of Drude-type electrons is substantially red-shifted [7] compared to the F-centre absorption band. According to our mechanism polarons and bipolarons form Drude-type electrons after ultrafast excitation which leads to an increase of the transient absorption in the NIR region.

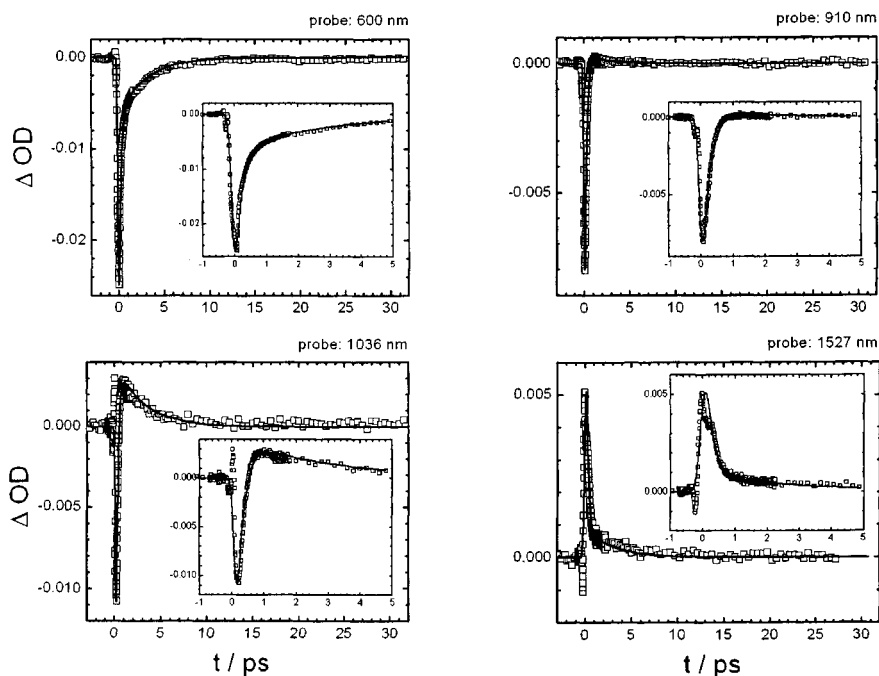


Fig. 1. Ultrafast response of localized electrons in a Na-NaBr melt: \square are experimental points while solid lines represent fitting results. Pump wavelength: 800 nm, probe wavelengths as indicated. Insets highlight the first 5 ps.

The relaxation time τ_1 is found to be (210 ± 40) fs in fairly good agreement with theoretical calculations [4] where polarons undergo hopping processes from one localized state to the other at a hopping rate of $3 \times 10^{12} \text{ s}^{-1}$ (corresponding to an effective residence time of ~ 300 fs). Furthermore, τ_1 is equivalent to the relaxation time found for the relaxation process in K-KCl [8]. This supports the idea that diffusional motion controls the ultrafast dynamics in molten alkali halides as proposed by theoretical calculations [4]. The second time constant τ_2 has been determined to be (3 ± 0.6) ps and will be tentatively assigned to the formation process of bipolarons. Earlier studies [6] have suggested that spin-paired species such as bipolarons are formed more favourably in Na-NaBr system. Calculations [5] on the dynamical properties of the bipolarons have predicted a lifetime for the dissociation process of about 7 ps. This result is based on slower diffusion constants for bipolarons compared to F-centre-type species. As a consequence, one would expect a consistently longer time for the formation process of bipolarons compared to polarons. Following our simple model, τ_2 represents the time required for Drude electrons to recombine with polarons to form bipolarons. The transient absorption between 950 nm and 1527 nm is attributed to Drude-type electrons in agreement with our earlier findings for the K-KCl system [8]. In the present investigation, however, the transient absorption is more pronounced indicating an increased concentration of “free” (Drude-type) electrons in Na-NaBr as in the K-KCl system [7,9].

Finally, we address the transient response at 910 nm. At this wavelength, the transient could be fitted by a mono-exponential function with a time constant of roughly 200 fs and one might be tempted to assign this to polaron dynamics only. However, a thorough analysis including the reconstruction of transient absorption spectra [10] has proven the existence of an isosbestic point at ~ 1.35 eV for delay times exceeding 700 fs. Freyland and co-workers, on the other hand, have analyzed equilibrated absorption spectra of Na-NaBr in terms of the contribution of polarons/bipolarons and Drude-type electrons [7]. This analysis resulted in a Gaussian function to describe the polarons and bipolarons and a simple Drude model for weakly localized electrons. The intersection of these two curves is located at ~ 1.4 eV. Combining our results with these findings we conclude that the isosbestic point in the transient spectra is due to an inter-conversion between Drude-type electrons and bipolarons. This inter-conversion was theoretically predicted in Na-NaBr melts [6] where bipolarons undergo hopping processes similar to those observed in the F-centre-type system. Such jumps lead to a dissociation of bipolarons and subsequently to a recombination either in the same spatial position or in an adjacent site. We note that an isosbestic point could not be found in our previous study in K-KCl. Taking into account the analysis by Freyland and co-workers, the intersection of the contribution of Drude-type electrons and bipolarons is located at ~ 0.5 eV for K-KCl which is beyond our detection window (≥ 0.8 eV). Further studies in the Na-NaI system (intersection at ~ 1 eV) should shed more light on this issue.

We thank the DFG (SFB 195, "Lokalisierung von Elektronen in makroskopischen und mikroskopischen Systemen") for financial support of this work.

REFERENCES

- [1] P. P. Edwards and C. N. R. Rao, (eds.), *The Metallic and Non-metallic States of Matter. An Important Facet of the Chemistry and Physics of the Condensed State*, Taylor and Francis: London, 1985, p. 139; P. P. Edwards, and C. N. R. Rao C. N. R. (eds.), *Metal-Insulator Transitions Revisited*, Taylor and Francis, London, 1995, p. 167.
- [2] W. W. Warren, Jr., B. F. Campbell, and G. F. Brennert, *Phys. Rev. Lett.*, 58 (1987) 941.
- [3] W. Freyland, *Z. Phys. Chem.*, 184 (1994) 139.
- [4] A. Selloni, P. Carnevali and M. Parrinello, *Phys. Rev. Lett.*, 59 (1987) 823.
- [5] E. S. Fois, A. Selloni, M. Parrinello and R. Car, *J. Phys. Chem.*, 92 (1988) 3268.
- [6] L. F. Xu, A. Selloni and M. Parrinello, *Chem. Phys. Lett.*, 162 (1989) 27.
- [7] D. Nattland, Th. Rauch and W. Freyland, *J. Chem. Phys.*, 98 (1993) 4429.
- [8] S. Dogel, W. Freyland, H. Hippler, D. Nattland, C. Nese and A. N. Unterreiner, *Phys. Chem. Chem. Phys.*, 5 (2003) 2934.
- [9] M. Sørliie, T. Øsvold and R. Hugeln, *Proceedings of the International Symposium in Honor of H. A. Øye*, Trondheim, Norway, 1995.
- [10] H. Brands, N. Chandrasekhar, H. Hippler and A.-N. Unterreiner (to be submitted to *Phys. Chem. Chem. Phys.*).

Electronic solvation dynamics in non-polar supercritical fluids

P. Larrégaray, A. Cavina and M. Chergui

Laboratoire de Spectroscopie Ultrarapide de la Phase Condensée, ICMB,
Faculté des Sciences de Base, BSP, Ecole Polytechnique Fédérale de Lausanne,
CH-1015 Lausanne-Dorigny, Switzerland

1. INTRODUCTION

Solvation dynamics is usually investigated by following in “real time” the response of the medium to an impulsive redistribution of charge of a solute. Experimentally, short pulse excitation of a chromophore creates instantaneously a “new” molecule, to which the surrounding solvent molecules respond. In the past, much attention has been devoted to polar solvation in the liquid phase, due to its importance in biology and preparative chemistry.[1] Non polar liquid media have less been investigated and some have questioned whether there is a real fundamental distinction between polar and non-polar solvation mechanisms.[2,3] Contrary to liquids, studies of non-polar solvation dynamics in supercritical fluids (SCFs) are very rare [4] and a molecular level description of the solvation process is still needed. In particular, the strong local density fluctuations appearing near the critical point [5], which are responsible for most of the unusual solvation properties of SCFs, may influence significantly the solute-solvent structural and dynamical properties. Here, we investigate SC Argon as a model non-polar solvent.

In this work, based on the fact that they are extremely sensitive probes of the medium structure and dynamics because of their extended orbitals [6], Rydberg states are used to get an insight into the non-polar solvation dynamics. We first investigated experimentally steady-state (absorption and fluorescence) spectroscopy of the NO X $^2\Pi$ -A $^2\Sigma^+(3s\sigma)$ Rydberg transition over a wide range of thermodynamical conditions in the Ar supercritical (SC) domain. Then, molecular dynamics (MD) simulations, whose validity was checked by reproducing the steady-state spectroscopic observables, were used to explore the details of structural rearrangements and solvation dynamics upon excitation of a Rydberg state. In particular, the influence of the near-critical local density fluctuations on solvation dynamics was analyzed.

2. EXPERIMENT AND MD SIMULATIONS

Our experimental set-up (described in ref. 7), allows us to record steady state absorption and emission spectra over a wide range of densities (10^5 to 20 at/nm³) in the Ar supercritical domain ($T_c = 150.8$ K, $P_c = 49$ bar). Representative absorption and emission spectra are shown in figure 1. These spectra could be reproduced with a good accuracy by means of equilibrium MD simulations performed with a standard procedure [8]. In these simulations, the NO X-Ar and Ar-Ar interaction potentials were taken from the literature [9]. We extracted an analytical NO A-Ar pair potential by an iterative fit of the experimental spectra, valid for the whole supercritical domain.

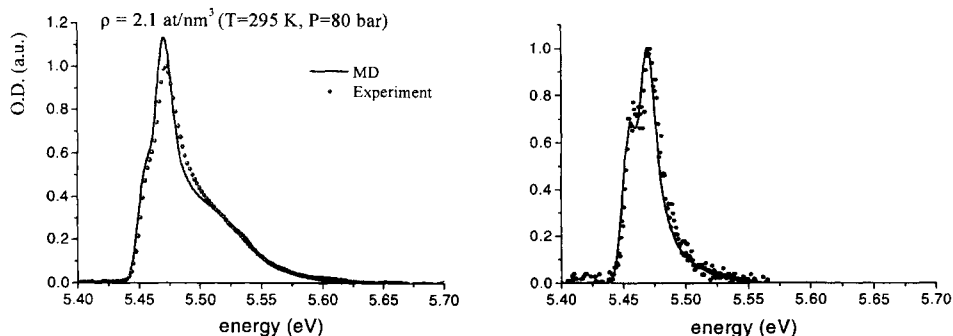


Figure 1: NO X($v=0$)-A($v'=0$) representative steady-state absorption (left) and emission (right) spectra. The solid lines correspond to MD simulations and the dots to experimental results.

The technical details of these simulations will be presented in a future publication [7]. Fig.1 shows the kind of agreement we could achieve between experiment and simulations. The quality of this agreement, which was found identical over the whole range of densities, made us confident in the validity of MD simulations to investigate further solute-solvent structural properties and solvation dynamics in the supercritical domain.

3. DISCUSSION: INFLUENCE OF LOCAL DENSITY FLUCTUATIONS ON SOLVATION PROPERTIES

In order to investigate the effects of local density fluctuations on solvation properties, we decided to study two supercritical thermodynamic state points of the same density (5.7 at/nm^3) but at different temperatures (295 and 153 K). The low temperature state point, close to the Ar critical point ($T_c = 150.8 \text{ K}$, $\rho_c = 8.1 \text{ at/nm}^3$), is expected to involve significant local density enhancements [5].

Fig. 2 shows the simulated equilibrium absorption and fluorescence spectra for the two state points (left column). The low temperature absorption spectrum is slightly broader and blue shifted with respect to the room temperature one. For fluorescence, this trend is reversed and the low temperature spectrum is slightly narrower and red shifted. To understand this feature, we analyzed the solvent structure around NO in the ground and excited electronic states. Fig. 2 displays the room and low temperatures NO-Ar radial distribution functions, $g(r)$ (RDF), predicted by equilibrium MD simulations for the NO X ground-state and NO A excited-state (right column). For the NO ground state, the height of the first maximum, related to the average number of Ar solvent atoms in the close vicinity of NO, as well as the existence of a second maximum for the low temperature RDF is indicative of a much higher local Ar density around the NO chromophore. For the excited state, no peak appears in the RDF and the low temperature NO-Ar RDF is lower than its ambient counterpart at short distances. This indicates a much more important depletion of the Ar atoms around the excited NO A chromophore close to the critical point. This transition, from a local density enhancement in the ground state to a depletion in the excited state, is a direct consequence of the high compressibility of a near critical solvent added to the attractive or repulsive character of the NO-Ar interaction potential [5]. Furthermore, as the solvent molecules in the close vicinity of NO (within a distance of 6 \AA) contribute to a blue shift of the X-A transition, the

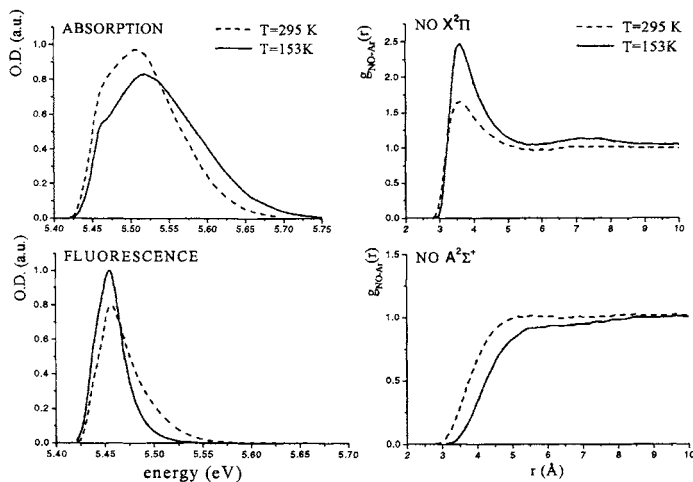


Figure 2: *Left column*- NO Absorption (upper panel) and emission (lower panel) spectra at near critical conditions and room temperature for a density of 5.7 at/nm^3 . *Right column*: NO-Ar radial distribution functions $g(r)$ for the NO ground (upper panel) and excited (lower panel) states for the same state points

features observed in the steady-state spectra reflect directly the local solvent density.

In addition, we note that the absorption and emission spectra have very different widths and shapes, which suggests that the medium response upon the NO A excitation must be in a highly non-linear regime [10]. Such non-linear effects in solvation dynamics, already observed but generally overlooked for polar media [1], have not been reported in non-polar media [4]. Within the linear approximation, the solvation response function, which is usually taken as the normalized time dependent Stokes shift (TDSS), is equal to the equilibrium transition energy correlation function (ECF), $\langle \Delta V(0)\Delta V(t) \rangle$, evaluated for either the ground or excited state [10]. These ECF were simulated for both the ground and excited NO electronic states for the room temperature and near critical conditions. In addition, for both thermodynamical conditions, the TDSS were evaluated thanks to non-equilibrium MD simulations [10]. In Fig. 3, we observe that the ECF evaluated for the ground and excited states differ significantly for the near critical state point (left panel). This difference is less pronounced for the room temperature state point (right panel). In particular, the long time decay appearing for the NO ground state ECF at near critical conditions can be related to the long fluctuation time of clusters existing around NO in these conditions [7].

The differences between the TDSS and the equilibrium ECF are further evidence that the medium response to the NO ($X \rightarrow A$) transition is in a non-linear regime. This non-linear character, related to the short range of the NO-Ar non-polar interactions, shows that the medium reorganization differs significantly from the relaxation processes occurring upon thermal fluctuations in the ground or excited electronic state. As the NO X-Ar interaction potential is attractive and the NO A-Ar potential essentially repulsive, this non-linearity may appear intuitively straightforward. However, at a given density, the validity of the linear regime approximation depends significantly on temperature (Fig. 3). This shows that the structure and dynamics of solvent molecules also play an important role.

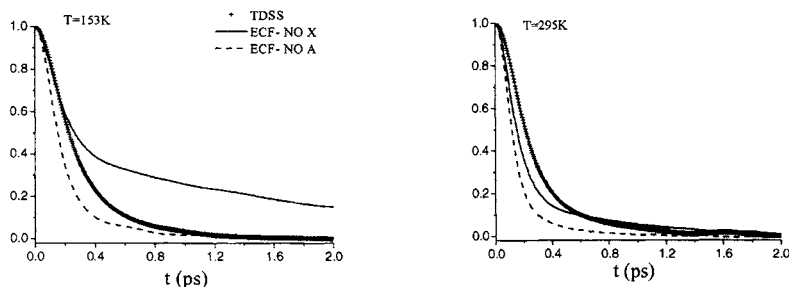


Figure 3 : Normalized time dependent Stokes shift (TDSS) and NO ground and excited states transition energy correlation functions (ECF) for the low and room temperature state points.

Another striking point is the near equivalence between the TDSS evaluated for the near critical and room temperature state point. As a consequence, it appears that the different time scales involved in the medium reorganization upon the NO ($X \rightarrow A$) transition are almost independent of the local density. This hypothesis was further checked by simulating the TDSS corresponding to a much higher density (17 at/nm^3) in the supercritical domain. This TDSS was again found nearly identical to the ones presented in Fig. 3. In view of the high non-linearity of the relaxation process and the near independence of this response with density, it seems that the NO ($X \rightarrow A$) transition dramatically perturbs the medium local structure. This contrasts with the studies in matrices where, because of ordered medium and its cohesion, recurrences of the first shells of solvation could be observed both experimentally [6] and in MD simulations [9].

As a conclusion, our experimental/simulation study of the supercritical Ar solvent response, upon a Rydberg transition, reveals a highly non-linear character of the medium reorganisation. Simple model systems, such as the one used here, may provide a working basis for the development of a formal description of the non-linear response in condensed phase media.

REFERENCES

- [1] R.M. Stratt and M. Maroncelli, *J. Phys. Chem.*, 100 (1996) 12981.
- [2] B. M. Ladanyi and R.M. Stratt, *J. Phys. Chem.*, 100 (1996) 1266.
- [3] P. V. Kumar and M. Maroncelli, *J. Chem. Phys.*, 112 (1998) 5370.
- [4] S.A. Egorov, *J. Chem. Phys.*, 118 (2003) 10643.
- [5] S. C. Tucker, *Chem. Rev.*, 99 (1999) 391.
- [6] C. Jeanin, M. T. Portella-Oberli, S. Jimenez, F. Vigliotti, B. Lang and M. Chergui, *Chem.Phys.Lett.*, 316 (2000) 51.
- [7] A. Cavina, P. Larrégaray and M. Chergui, to be published.
- [8] M.P. Allen and D. J. Tildesley, *Computer Simulation of Liquids* (Oxford University, New York, 1987).
- [9] S. Jimenez, M.Chergui, G. Rojas-Lorenzo and J. Rubayo-Soneira, *J. Chem. Phys.*, 114 (2001) 5264.
- [10] E. Carter and J. T. Hynes, *J. Chem. Phys.*, 94 (1991) 5961.

Femtosecond photolysis of CH_2I_2 in supercritical fluids: Competition between photodissociation and isomerization

C. Grimm, J. Zerbs, M.F. Kling, and J. Schroeder

Institut für Physikalische Chemie, Universität Göttingen, Tammannstr. 6,
D-37077 Göttingen, Germany, e-mail: jschroe2@gwdg.de

1. INTRODUCTION

Among the effects that a dense fluid environment may have on the dynamics of elementary chemical reactions, competition between reactant escape from a solvent cage and in-cage reaction certainly is one of the phenomena most easily understood on an intuitive basis. A prominent example is the “photolytic cage effect” proposed by Franck and Rabinowitsch in the mid 1930s [1] who predicted a solvent-cage induced reduction of the photodissociation quantum yield of iodine atoms from unity in the low pressure gas phase to a lower value in liquid as was later observed by Noyes et al. [2,3]. Luther and Troe [4] found a reduction of the quantum yield in supercritical solution already at fairly low densities. Systematic quantum yield studies [5] led to a refinement of Noyes’ original diffusion model and revealed basic characteristics of the cage effect such as a negligible contribution of “inertial” direct cage escape and the central role of competition between diffusive escape and vibrational energy relaxation of recombined iodine molecules. A more complex view of cage dynamics resulted from time-resolved experiments [6-8] which revealed the role of trapping in weakly bound electronically excited states followed by radiative or non-radiative return to the ground state. These findings were corroborated by classical [9-11] and mixed quantum-classical [12-14] MD simulations which suggest that branching between escape and recombination occurs early within the first few picoseconds after excitation. In recent experimental reinvestigations of the density dependence of the quantum yield accompanied by classical MD simulations [15,16], it was found that for solvents as diverse as xenon and n-heptane quantum yields strongly correlate with reduced solvent density, supporting the idea of a purely kinematic effect.

As the halogen photolytic cage effect seems to be well understood, it is of fundamental interest to carry out similar investigations on small polyatomic molecules to assess effects of internal energy, intramolecular multidimensional dynamics, or branching between different in-cage reactions and cage escape. Until now, systematic studies in supercritical solution are not available, partially because suitable systems have not been identified. Recently, however, diiodomethane (CH_2I_2) emerged as a promising candidate. Its photodissociation is sufficiently rapid not to be quenched in liquid solution [17,18], and a fast in-cage reaction product was observed and identified as iso-diiodomethane ($\text{CH}_2\text{I-I}$) by femtosecond transient absorption spectroscopy [19] and time-resolved resonance Raman spectroscopy [20,21]. The interpretation and assignment of transient absorbance signals obtained from femtosecond pump-probe spectroscopy has led to controversial interpretations, although the data presented by three different groups are in good agreement [17-19]. So far, little is known about the

competing processes that determine isomer quantum yield. To what extent do hot radicals geminately recombine with iodine atoms to parent molecules in the solvent cage? Can direct or diffusive cage escape compete with both reaction channels, i.e. recombination reactions to parent and isomer? What is the branching ratio between these three different routes and how does it change with solvent environment? How does the direct dissociation in the gas phase turn into isomerization as the solvent cage gradually builds up? Is there possibly a direct route on a solvent-modified potential energy surface from electronically excited CH_2I_2 to ground state isomer which avoids the radical intermediate? The answers to questions like these are, of course, strongly interrelated and depend very much on the ability to identify experimentally observed transients with species and processes. As a first step in this direction we report on femtosecond photolysis experiments with diiodomethane in supercritical CO_2 [22] and CHF_3 .

2. RESULTS AND DISCUSSION

Measurements in supercritical CO_2 and CHF_3 at $T=308$ K were carried out at a pump wavelength of 304 nm, which is close to the maximum of the first absorption band of diiodomethane. In general, transient absorbance traces show a temporal shape qualitatively identical to that found in liquid solution [17-19]. They consist of a sharp sub-picosecond peak followed by an exponential picosecond rise to a plateau value which remains constant for 100-300 ps. We are aware that solvent artefacts tend to obscure the signal in the sub-picosecond regime. Fortunately, they were found to be much less intense in supercritical solution than in common liquid solvents. This allowed us to apply careful normalization procedures to peak amplitudes in order to correct for pump pulse fluctuations. In general, two prominent effects are observed as the pressure is raised from about 10 to 100 MPa: (i) a threefold increase of the plateau absorbance and (ii) a decrease of the picosecond absorbance rise time by a factor of 2-3 depending on the probe wavelength.

Reconstructed transient absorption spectra normalized to band area (Fig.1) at all pressures in supercritical solvents CO_2 , CHF_3 , and C_2H_6 show a region of nearly constant absorbance around 405-410 nm, accompanied by a decay of the red wing and a red-shift and rise of the maximum. Assuming that at delay times from about 5 ps the transient absorbance is dominated by a single species, this spectral evolution is characteristic of collisional vibrational cooling of a polyatomic molecule [23] and is attributed to the initially hot isomer formed by in-cage recombination of iodine atoms and CH_2I radicals [19]. It appears that vibrational cooling occurs on a time scale [24] close to the one we found for isomer formation which causes a decrease of the effective single exponential time constant across the absorption band from longer to shorter probe wavelength. At around 410 nm one may observe isomer kinetics practically free of contributions from vibrational relaxation. As we checked experimentally, the formation rates shown in Fig.2b are equivalent to those obtained from the time dependence of the band integral.

As the transient absorption band centred at 380 nm is assigned to *iso*-diiodomethane, the plateau absorbance A_p is a direct measure of the isomerization quantum yield. As shown in Fig.2a, it increases almost linearly within the density range studied, whereas the rise time decreases linearly over the same range. The closing of the isomerization channel towards lower densities, however, is not yet reached in the pressure range investigated here. The acceleration of isomer formation with increasing reduced density may indicate a crucial role of product stabilization by vibrational energy transfer to the fluid. Further studies toward lower densities are needed to clarify the details of the isomerization mechanism.

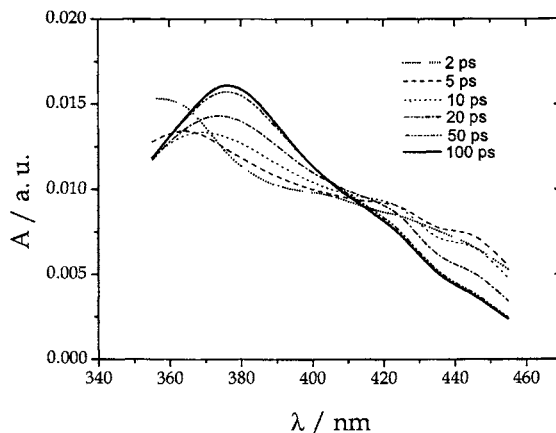


Fig. 1. Transient absorption spectra following excitation of CH_2I_2 at 304 nm in sc CHF_3 at of 51 MPa normalized to band area.

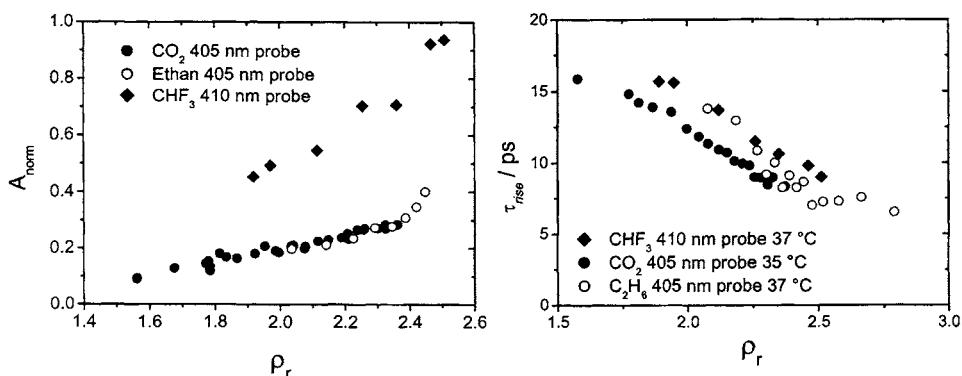


Fig. 2. a) *left*: Plateau absorbance normalized to initial peak maximum. b) *right*: Picosecond rise time. Both plotted versus reduced density of the fluid solvent.

The transient absorbance in the first 5 ps may contain a significant contribution from the internally hot ground state radical that is produced by ultrafast photodissociation of the parent diiodomethane. [25,26] While its initial excess rotational energy is expected to relax to thermal equilibrium in just a few collisions [27], vibrational relaxation will be at most an order of magnitude faster than that of the parent molecule [25] which in sc CO_2 takes around 50 ps. [24] On the basis of existing hot radical spectra [28] and the initial excess energy we estimated that the contribution of the hot radical to the initial transient absorbance at 410 nm could be about 40 percent [22]. This view is corroborated by the viscosity dependence of the initial transient absorption anisotropy shown in Fig.3 which seems to be dominated by orientation relaxation of the vibrationally hot CH_2I radical. At present, we are trying to verify this conclusion by measuring spectra of the hot radical with higher time resolution than previously possible [28].

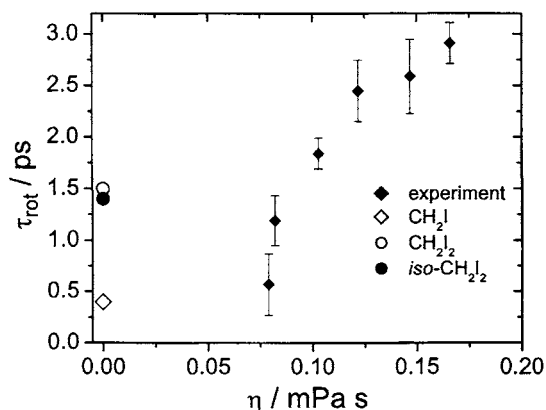


Fig. 3. Orientation relaxation times in sc CO₂ obtained from anisotropy decay at 370 nm. Extrapolation to zero viscosity comes closest to the calculated free rotor time of the CH₂I-radical.

REFERENCES

- [1] J. Franck, E. Rabinowitsch, *Trans.Faraday.Soc.* 30 (1934) 120.
- [2] J. Zimmerman, R. M. Noyes, *J.Chem.Phys.* 18 (1950) 658.
- [3] L. Meadows, R. M. Noyes, *J.Am.Chem.Soc.* 82 (1960) 1872.
- [4] K. Luther, J. Troe, *Chem.Phys.Lett.* 24 (1974) 85.
- [5] B. Otto, J. Schroeder, J. Troe, *J.Chem.Phys.* 81 (1984) 202.
- [6] A. L. Harris, J. K. Brown, C. B. Harris, *Ann.Rev.Phys.Chem.* 39 (1988) 341.
- [7] R. Zadoyan, Z. Li, C. C. Martens, V. A. Apkarian, *Chem.Phys.Lett.* 218 (1994) 504.
- [8] J.-K. Wang, Q. Liu, A. H. Zewail, *J.Phys.Chem.* 99 (1995) 11309.
- [9] D. L. Bunker, B. S. Jacobson, *J.Am.Chem.Soc.* 94 (1972) 1843.
- [10] J. N. Murrell, A. J. Stace, R. Dammel, *JCS Faraday Trans.2* 74 (1978) 1532.
- [11] M. Ben-Nun, R. D. Levine, *J.Phys.Chem.* 97 (1993) 2334.
- [12] M. Ben-Nun, R. D. Levine, D. M. Jonas, G. R. Fleming, *Chem.Phys.Lett.* 245 (1995) 629.
- [13] W. Wang, K. A. Nelson, L. Xiao, D. F. Coker, *J.Chem.Phys.* 101 (1994) 9663.
- [14] V. S. Batista, D. F. Coker, *J.Chem.Phys.* 105 (1996) 4033.
- [15] H. Ooe, Y. Kimura, M. Kerazima, N. Hirota, *J.Phys.Chem.A* 103 (1999) 7730.
- [16] D. Schwarzer, J. Schroeder, C. Schröder, *Z.Phys.Chem.* 215 (2001) 183.
- [17] B. J. Schwartz, J. C. King, J. Z. Zhang, C. B. Harris, *Chem.Phys.Lett.* 203 (1993) 503.
- [18] K.-I. Saitow, Y. Naitoh, K. Tominaga, K. Yoshihara, *Chem.Phys.Lett.* 262 (1996) 621.
- [19] A. N. Tarnovsky, J. L. Alvarez, A. P. Yartsev, V. Sundström, E. Åkesson, *Chem.Phys.Lett.* 312 (1999) 121.
- [20] X. M. Zheng, D. L. Phillips, *J.Phys.Chem.A* 104 (2000) 6880.
- [21] W. M. Kwok, C. S. Ma, A. W. Parker, D. Phillips, M. Towrie, P. Matousek, D. L. Phillips, *J.Chem.Phys.* 113 (2000) 7471.
- [22] Ch. Grimm, M. Kling, J. Schroeder, J. Troe, J. Zerbs, *Isr.J.Chem.* (2003)
- [23] D. Schwarzer, J. Troe, M. Votsmeier, M. Zerezke, *Journal of Chemical Physics* 105 (1996) 3121.
- [24] K. Sekiguchi, A. Shimojima, O. Kajimoto, *Chem.Phys.Lett.* 356 (2002) 84.
- [25] S. L. Baughcum, S. R. Leone, *J.Chem.Phys.* 72 (1980) 6531.
- [26] H. F. Xu, Y. Guo, S. L. Liu, X. X. Ma, D. X. Dai, G. H. Sha, *J.Chem.Phys.* 117 (2002) 5722.
- [27] G. Käb, V. S. Vikhrenko, *Phys.Chem.Chem.Phys.* 3 (2001) 2223.
- [28] J. Sehested, T. Ellermann, O. J. Nielsen, *Int.J.Chem.Kin.* 26 (1994) 259.

Femtosecond degenerate four-wave mixing of cycloalkanes

H. M. Frey, D. Kummli, M. Keller, R. Leist, and S. Leutwyler

Departement für Chemie und Biochemie
University of Bern, Freiestr. 3
3000, Bern 9, Switzerland

1. INTRODUCTION

Rotational Raman spectroscopy is a powerful tool to determine the structures of molecules. In particular, besides electron diffraction, it is the only method that can probe molecules that exhibit no electric dipole moment for which microwave or infrared data do not exist. Although rotational constants can be extracted from vibrational spectra via combination differences or by known correction factors of deuterated species the method is the only one that yields directly the rotational constant B_0 . However for cyclopropane, the rotational microwave spectrum, recording the weak $\Delta K=3$ transitions could be measured by Brupacher [20].

After the introduction of frequency resolved CARS by Maker and Terhune [1], time resolved experiments became possible with the invention of high power lasers with femtosecond resolution. Leonhardt [2] and for example Hayden [3] performed femtosecond CARS experiments in liquids. A first femtosecond time resolved CARS experiment in gas phase was performed by Motzkus et. al. [4] where the wave packet dynamics of the dissociation of NaI was monitored. The first observation of wave packet dynamics in gaseous iodine was reported by Schmitt et al. [5]. They were able to observe dynamics in both, the ground and excited state with the same experiment. A summary of high resolution spectroscopy in gas phase by nonlinear methods is given by Lang et al. [6].

The rotational dynamics of nitrogen and carbon dioxide were recorded by Akhmanov and Koroteev [7]. The transients look similar to the transients by Morgen et al. [8], recorded with time resolved Raman induced polarization spectroscopy [9]. A fs-DFWM experiment was performed by Frey et al. [10] on diatomics and linear polyatomics. To prevent collisional dephasing, they transferred the method into the expansion zone of a molecular beam. In succession, experiments on linear molecules and symmetric tops were performed on molecules like CHCl_3 [11] and C_6H_6 [12]. Transients of asymmetric tops like the near oblate pyrimidine, pyrazine and pyridine [13] and SO_2 [11] were reported in the following years.

2. EXPERIMENTAL AND THEORETICAL BACKGROUND

The theoretical background has been treated by Mukamel [14] in detail. An approach to describe the experiments according to the density matrix formalism has been given by Dantus and Mukamel [15].

Time resolved femtosecond degenerate four-wave mixing is based on the response of the third order polarisability. With a femtosecond pulse rotational levels are coherently prepared by a

χ^3 process. The sample loses its alignment due to rotation but due to quantization of energy the molecules will be aligned after a characteristic time over and over again. The time dependence of the third order polarisability has been described by Mukamel and is given below:

$$I_{CARS}(t) \approx \left| \sum_J \sum_{\Delta J=0,\pm 1,\pm 2} I(J) e^{(iE_J^{\Delta J} / \hbar - \Gamma)t} \right|^2 \quad (1)$$

The signal intensity for a rotational transition depending on the rotational quantum number is [16]:

$$I_{CARS}(J) \propto (\omega_0 \pm \omega)^4 (2J+1) g_J b_{J,K}^{J,K} e^{-F(J,K)hc/kT} \quad (2)$$

where ω_0 is the frequency of the exciting line, ω is the transition frequency, g_J are the statistical weights of the initial state, $b_{J,K}^{J,K}$ are the Plazcek Teller [17] coefficients and the exponential term is the Boltzman distribution at the given temperature with $F(J,K)$ being the energy of the initial level. The intensity is summed up for possible transitions e.g. the O-, P-, R- and S-branches and the signal evolving in time can be simulated.

The experimental setup has been described in detail elsewhere [10]. The current setup includes a peltier cooled GaAs photomultiplier to record weak signals. The intensity of the three beams was kept below 10 μ J for each beam in order to prevent distortion of the transients. At higher intensities a time independent signal can be observed and negative values of the exponent on Eq. 1 deplete the transient. The transients were recorded with a time resolution of 33 fs which is below the temporal width of the pump, dump and probe pulses (80fs from Grenouille measurement).

3. RESULTS

In the following chapter we will present the transients obtained. The transients are analyzed according to the preceding chapter. In Table 1 the molecular constants obtained from fitting are summarized. Note, that the second rotational constant C can not be determined directly. When using high intensity laser beams additional transients appear that can be related to C-type transients. From their position, an approximate value (+/- 0.1GHz) can be obtained that is used in the simulation. It was set to 12 GHz in the simulation for cyclopropane and to 6.5 GHz for the cyclobutane simulations. This has only an effect on the thermal population of the sample as the term $(C-A)K^2$ of the well known term equation for symmetric top cancels when calculating the Raman transitions.

Despite the low pressure, both, the cyclopropane and the cyclobutane signals fade due to collisional dephasing. The effect is stronger for the larger molecule cyclobutane. As a consequence, fewer recurrences could be recorded for C_4H_8 and the values obtained are less accurate. Investigations in molecular beams could circumvent this, but with the drawback that the temperature of the sample is not known. The accuracy of the constants in the limit of the approximation is obtained from extrapolating microwave data of deuterated species. In combination with molecular beam experiments the method will yield new and more accurate constants.

Table 1
Rotational constants obtained by femtosecond four-wave mixing (values in cm^{-1})

	Cyclopropane		Cyclobutane	
	This work	Brupacher et al.[20]	This work	Li et al. [18]
B_0	0.67028(12)	0.6702469(9)	0.3553(1)	0.3558(3)
D_j	8.22(38)E-7	9.66686E-7	8.708(8)E-8	1.09E-6
D_{jk}	-3.91(34)E-7	-1.24924E-7	-1.16(2)E-7	-1.29E-6

Cyclopropane is an equilateral triangle. The angle of 60° is far from the relaxed value for a saturated alkane. The results are the so called banana bonds that have a C-C distance of 1.51 Å. This bond length is shorter than a C-C bond in ethane but longer than the single bond in butadiene. In Fig. 1 (left) we show the transient recorded at 6.5E-3 bar in a cell.

Cyclobutane is not planar. To relief H-H repulsion the molecules has an envelope form. The barrier from one to the other puckering state is 510 cm^{-1} measured by infrared spectroscopy [18]. The molecule can tunnel between the two isomers. This has direct implications on the rotational spectrum obtained. With no tunneling the molecule has a D_{2d} symmetry, with tunnelling the symmetry is D_{4h} . The vibration along the puckering coordinate is the lowest vibration at $\sim 200 \text{ cm}^{-1}$. The bandwidth of the laser is too small to excite this vibration. A vibrational Raman transition would result in a continuous but varying signal in Fig 1. The intensity ratio recurrence/half recurrence confirms the D_{2d} symmetry. In addition the tunnel splitting has been determined to be 3 cm^{-1} , which translates into a tunnelling time of $0.8 \mu\text{s}$. This is considerably longer than the duration of the experiment.

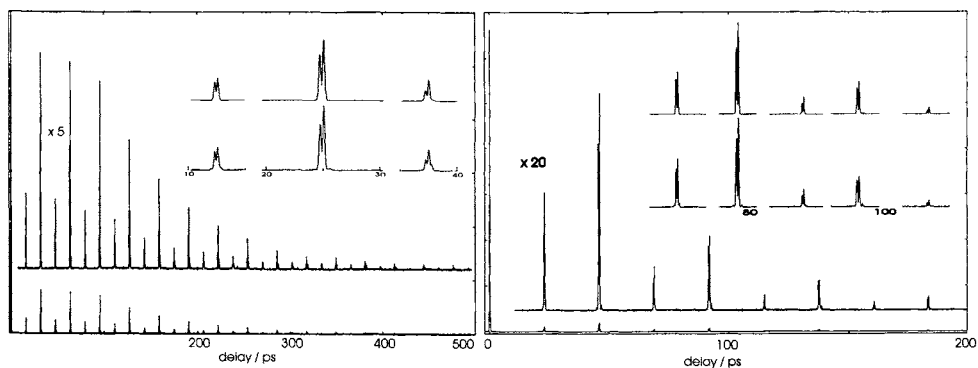


Fig. 1. Degenerate four-wave mixing transient of cyclopropane (left) and cyclobutane (right). The upper traces in the insets are simulations. The recurrences in cyclobutane are very weak compared to the coherence peak at time zero.

With the selection rules $\Delta J=0,1,2$ an alternation of the recurrences is expected as the signal due to $\Delta J=2$ transitions overlaps with the $\Delta J=1$ recurrences. Neglecting the shape of the transient, which is comparable for neighbouring peaks the intensity alternation would be 1:2. In addition the spin statistics give rise to weak "subrecurrences" which will be treated in a later publication.

4. CONCLUSIONS

We have presented time resolved high resolution rotational Raman spectroscopy of cyclopropane and cyclobutane. Cycloalkanes exhibit no electric dipole moment and conventional microwave and infrared spectroscopies are not possible. From time resolved femtosecond Raman spectroscopy, a backgroundfree method, with a signal/noise ratio of 10^3 or better, we are capable to extract the rotational constants and their higher order centrifugal distortion constants with high accuracy. Moreover the experiment is sensitive enough to probe the intensity distribution of Raman lines of molecules that show alternation of intensity due to spin statistics. The width of the recurrences is very sensitive to the population of the initial state; therefore the temperature has to be known. To determine the rotational constants however it is sufficient to know an approximate or even to fit the temperature. Molecular beam experiments exclude collisional dephasing which is equivalent with a higher accuracy of the molecular constants. According experiments are planned in near future in our laboratories.

REFERENCES

- [1] P.D. Marker and R.W. Terhune, *Phys. Rev. A*, 137 (1965) 801.
- [2] R. Leonhardt, W. Holzzapfel, W. Zinth and W. Kaiser, *Chem. Phys. Lett.*, 133 (1987) 373.
- [3] C.C. Hayden, D.W. Chandler, *J. Chem. Phys.* 103, (1995) 10465.
- [4] M. Motzkus, S. Pedersen and A.H. Zewail, *J. Phys. Chem.*, 100 (1996) 5620.
- [5] M. Schmitt, G. Knopp, A. Materny and W. Kiefer, *Chem. Phys. Lett.*, 280 (1997) 339.
- [6] T. Lang, M. Motzkus, H.M. Frey, P. Beaud, *J. Chem. Phys.*, 115 (2001) 5418.
- [7] S.A. Akhmanov, N.I. Koroteev, S.A. Magnitskii, V.B. Morozov, A.P. Tarasevich and V.G. Tunkin, *J. Opt. Soc. Am. B*, 2 (1996) 640.
- [8] M. Morgen, W. Price, L. Hunziker, P. Ludowise, M. Blackwell and Y. Chen, *Chem. Phys. Lett.*, 209 (1993) 1.
- [9] P.W. Joireman, L. Connell, S. M. Ohline and P. Felker, *J. Chem. Phys.*, 96 (1992) 4118.
- [10] H. M. Frey, P. Beaud, T. Gerber, B. Mischler, P.P. Radi, and A.P. Tzannis, *Appl. Phys. B*, 68 (1999) 735.
- [11] H.M. Frey, P. Beaud, T. Gerber, B. Mischler, P.P. Radi, and A.P. Tzannis, *J. Raman Spec.*, 31 (2000) 71.
- [12] V. V. Matyilitsky, W. Jarzaba, C. Riehn, B. Brutschy, *J. Raman Spec.*, 33 (2002) 877
- [13] H.M. Frey, A. Müller, and S. Leutwyler, *J. Raman Spec.*, 33 (2002) 855.
- [14] S. Mukamel, *Principles of nonlinear optical spectroscopy*, Oxford University Press: New York, (1995).
- [15] B. I. Grimberg, V. LKozovoy, M. Dantus and S. Mukamel, *J. Phys. Chem. A*, 106 (2002) 697
- [16] A. Weber, *High resolution Raman studies in gases*, in "The Raman effect" (A. Anderson, Ed.), Vol. 2, Chap. 9, pp.543-757, Marcel Decker, New York, 1973.
- [17] G. Placzek and E. Teller, *Z. Phys.*, 81 (1933) 209.
- [18] H. Li, C. Miller and L. Philips, *J. Chem. Phys.*, 100 (1994) 8590.
- [19] S. Yamamoto, M. Nakata, T. Fukuyama and K. Kuchitsu, *J. Phys. Chem.*, 89 (1985) 3298.
- [20] Th. Brupacher, Ch. Styger, B. Vogelsanger, I. Ozier and A. Bauder, *J. Mol., Spectrosc.* 138 (1989) 197.

Femtosecond liquid dynamics studied by two-dimensional Raman spectroscopy

K. J. Kubarych, C. J. Milne and R. J. D. Miller

Departments of Chemistry and Physics, University of Toronto, 80 St George St., Toronto, ON Canada M5S 3H6

1. INTRODUCTION

The role the solvent plays in chemical reactions cannot be ignored, but often it cannot be observed. Lacking the symmetric order of solids or the isolation of gases, liquids are intrinsically more complicated than the other states of matter due to the inherent randomness and the subtle interplay of various many-body interactions. In understanding the dynamics of liquids in chemical processes, it is sensible to look first at dynamics of pure liquids. The timescales on which interesting phenomena occur span many orders of magnitude, but the basic interactions are fundamentally determined by vibrational periods, and these are generally sub-picosecond. Liquids motions are characterized by frequencies that are smaller than typical intramolecular bond vibrations, and are generally in the range from $10\text{-}500\text{ cm}^{-1}$. Though tremendous recent progress has been made in the study of intramolecular vibrations[1], their couplings[2] and even hydrogen bonded systems[3], these approaches yield only a local picture of the liquid. In order to build a picture of a solvent, we need to focus on the larger scale dynamics involving many solvent molecules, and direct our attention toward collective dynamics. This is, however, a conceptually challenging prospect that places significant demands on the state of the art of both theoretical descriptions and experimental techniques.

1.1 Background

Low frequency spectra of liquids are notably deficient of any structure, and it has long been hoped that a technique would be discovered that provides the same type of line narrowing enjoyed in echo-based electronic and NMR spectroscopy. Tanimura and Mukamel observed that such a technique was possible, and proposed a two-time interval, fifth-order Raman pulse sequence capable of distinguishing, for example, inhomogeneous and homogeneous contributions to the lineshape.[4] The pulse sequence, shown in Fig. 1, is simply an extension of conventional time-domain third-order Raman-based methods. At the

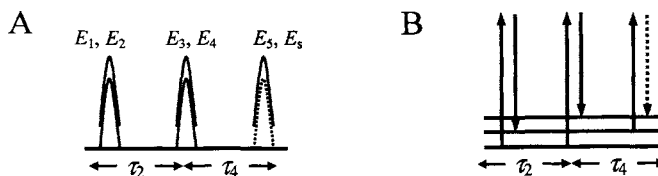


Fig. 1. Two showing the fifth-order Raman pulse sequence. (A) Definition of fields, (B) Energy level diagram showing one possible Liouville space pathway.

time origin, a pair of pulses, E_1 and E_2 , prepare a vibrational coherence via a stimulated Raman interaction. Following a time delay, τ_2 , a second pair of pulses, E_3 and E_4 , transfer the initial coherence via another Raman interaction. After a second time delay, τ_4 , a probe pulse, E_5 , diffracts off of the net induced polarization into the signal direction, E_s . By applying the formalism developed, for example, by Mukamel, it can be shown that the signal in the impulsive limit is proportional to the three-point time correlation function of the polarizability. From the point of view offered by this correlation function, the only difference between the fifth-order Raman experiment and conventional resonant echoes, is that rather than measuring correlations of the dipole operator, fifth-order Raman measures the correlations of the polarizability.

Although inhomogeneity in the low frequency spectrum of liquids differs from the conventional picture of a distribution of "sites", based on our understanding of hydrogen bonded systems, it is altogether reasonable to expect the persistence of long ranged order, albeit only for short times. Slow interconversion of distinct liquid environments would reveal itself as an "echo" feature in the two-dimensional response with a ridge-like feature where the two time delays are equal (i.e. $\tau_2 = \tau_4$).[4]

By identifying a frequency one is naturally led to consider some periodic motion, and while the motions in liquids are not "bound" in any usual sense, they nevertheless may persist long enough to permit a harmonic picture of the dynamics. Indeed, such an instantaneous normal mode (INM) view has been very useful in developing a microscopic theory of certain liquid dynamics. Harmonic theories succeed in reproducing third-order Raman responses of liquids, yet it is precisely this success which hints where these theories might fail. Third-order Raman spectroscopy is essentially a "harmonic" spectroscopy, and it is thus largely insensitive to anharmonicities in the dynamics. Fifth-order Raman, on the other hand, is highly sensitive to the subtle details of the intermolecular potential and to anharmonicity.

2. EXPERIMENTAL CONCERNS

Along with the rich information about broadening mechanisms and anharmonicity that is inherently inaccessible by lower-order experimental approaches, comes a significant experimental challenge. Fifth-order Raman signal generation requires a nonlinearity either in the coupling to the electric fields (nonlinear polarizability), or in the dynamics (anharmonicity). Furthermore, the efficiency of three successive stimulated Raman interactions is rather low. Finally, due to the high-order of the interaction, there exist cascaded third-order signals that exit the sample in the same direction as the signal field, may be larger than the desired signal, and contain no information beyond what is readily measured by third-order techniques.[5] Using a passively-phase-locked, two-color diffractive-optic based approach with heterodyne detection, we have made significant progress in answering many of the experimental challenges that are inherent to two-dimensional Raman spectroscopy.

2.1 Diffractive Optics and Phase Matching

Due to the high nonlinear order of 2D Raman, there is considerable freedom in choosing the interacting beam configuration such that the signal is still phase-matched and emitted in a background-free direction. This freedom allows one to design a geometry where the overall phase matching for the unwanted third-order cascaded contribution is greatly reduced. Our crossed-beam geometry is almost perfectly phase-matched for the fifth-order Raman signal and increases the third-order phase-mismatch by orders of magnitude over the perfectly phase-matched case.[6] A single, custom-designed diffractive optic generates the

required phase-matching geometry. This greatly simplifies alignment while providing a beam in the signal direction, allowing the use of heterodyne detection where the observable is proportional to the electric field rather than its intensity. Since the signal is generated at the probe wavelength (800 nm), any scattered pump light (400 nm) is readily removed with spectral filtering.

2.2 Polarization selectivity

With complete control over the polarization of all 6 beams we have investigated the full fifth-order Raman tensor.[7] More recently we have used this control to investigate the “Dutch Cross” polarization configuration. This geometry was initially proposed[8] as a simple way to reduce the nuclear signal of the third-order cascades by nearly four orders of magnitude. The realization of Jansen et. al. was that by using a symmetric polarization configuration the nuclear signal of the cascaded third-order contaminants would be suppressed. The $R_{-L-L11LL}^{(5)}$ fifth-order response is as follows: the first pump pair has a polarization angle of -60° with respect to the middle pump pair and the probe/signal have a polarization angle of 60° with respect to the middle pump pair.

3. RESULTS

Figure 2 shows the fifth-order Raman results of liquid CS_2 for two different arrangements of field polarizations. Fig. 2A shows a depolarized tensor element, R_{121211} , where “1” and “2” represent orthogonal polarizations, and the indices are in reverse order. This result is typical of the fifth-order response of liquid CS_2 , where we observe an initially rapid and subsequently very slow decay of the signal along the τ_4 axis ($\tau_2 = 0$), while the signal along τ_2 and the diagonal ($\tau_2 = \tau_4$) decays very rapidly. The general form of the R_{121211} response is very similar to the fully-polarized response, R_{111111} (not shown), though the former lacks the large hyperpolarizability contribution near $\tau_2 = \tau_4 = 0$.

The “Dutch Cross” configuration is shown in Figs. 2B and C. While the response has a similar slow decay along τ_4 , and very rapid decay along τ_2 (not shown), there are two noteworthy differences. A node is observed in the response along τ_4 ($\tau_2 = 0$), and the location in time of this node (~ 100 fs) appears to be related to the duration of the ~ 70 fs pulses used in the experiment, and likely results from a difference in sign between the electronic and nuclear contributions to the response. Attempts to further reduce the pulse duration are underway and will allow a more definitive assignment. The other distinguishing feature of this polarization configuration is the pronounced diagonal feature at ~ 100 fs with a subsequent rapid decay by

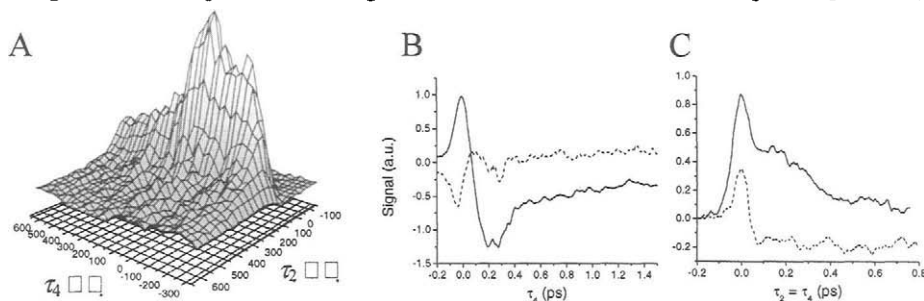


Fig. 2. Heterodyne detected fifth-order Raman response of liquid CS_2 for two different polarization conditions: (A) R_{121211} and (B, C) the ‘Dutch Cross’, $R_{-L-L11LL}$ configuration. The solid curves are the in-phase signals, and the dashed lines are the $\pi/2$ shifted signals (not discussed). Panels B, and C show slices along τ_4 and the diagonal. $L = 60^\circ$

500 fs. Due to the near cancellation of cascaded signals in the Dutch Cross configuration, these results indicate that our experimental conditions are successful in isolating the direct fifth-order signal, regardless of its microscopic explanation.

4. RECENT THEORETICAL WORK

In order to provide such an explanation, there has been a recent surge of interest in the theoretical community in calculating the fifth-order Raman response of simple liquids. Jansen *et al.* used finite-field molecular dynamics to simulate liquid CS₂, taking into account all possible interaction-induced effects as well using a variety of polarizability models.[9] Their results are consistent with our experimental work, a long-lived ridge along the probe delay, negligible signal along the pump delay and a peak along the diagonal around 100 fs. Saito and Ohmine performed a complete MD simulation on liquid CS₂ using 32 molecules and flexible molecular potentials.[10] These results are intriguing in that they predict a peak at ~100 fs and short dephasing times along the diagonal (<500 fs), similar to our results, but they also predict a node in the fifth-order response along the probe delay. Under certain polarization conditions, we observe a similar node but it is within the width of our laser pulses (<100 fs) and we attribute this to the sign change between the electronic hyperpolarizability, which is not included in the MD simulation, and the nuclear signal along τ_4 . The work of Jansen *et al.* predicts no such node. Ma and Stratt have produced both MD[11] and INM[12] results for liquid xenon and find as a signature of the fifth-order response a long-lived ridge along τ_4 and negligible re-phasing along the time-diagonal, while identifying the importance of anharmonicity due to failures of conventional INM to reproduce the correct response. More recent work by Ma and Stratt has begun to shed some light on the role of polarization selectivity in fifth-order Raman in a model system of a single CS₂ molecule embedded in an Xe solvent. It would be particularly interesting to have an estimate of the relative importance of dynamical anharmonicity versus the nonlinear coupling to the laser fields (nonlinear polarizability), and there is a suggestion that field polarizations can emphasize one or the other. On the other hand, it will be most enlightening to see the fifth-order Raman response of another liquid—presumably one with microscopic dynamics different from those of CS₂—now that the majority of experimental problems have been solved. Indeed, yet another theoretical approach has recently been applied to the fifth-order Raman response of CS₂ by DeVane *et al.*[13] showing remarkable agreement with our data.

REFERENCES

- [1] I. V. Rubtsov, J. Wang, R. M. Hochstrasser, Proc. Nat. Acad. Sci. USA 100 (2003) 5601.
- [2] M. Khalil, N. Demirdöven, A. Tokmakoff, Phys. Rev. Lett. 90 (2003) 47401.
- [3] A. W. Omta, M. F. Kropman, S. Woutersen, H. J. Bakker, Science 301 (2003) 347.
- [4] Y. Tanimura, S. Mukamel, J. Chem. Phys. 99 (1993) 9496.
- [5] D. A. Blank, L. J. Kaufman, G. R. Fleming, J. Chem. Phys. 111 (1999) 3105.
- [6] V. Astinov, K.J. Kubarych, C.J. Milne, R.J.D. Miller, Opt. Lett., 25 (2000) 853.
- [7] K.J. Kubarych, C.J. Milne, S. Lin, R.J.D. Miller, J. Chem. Phys., 116 (2002) 2016.
- [8] T.I.C. Jansen, J.G. Snijders, K. Duppen, J. Chem. Phys. 114 (2001) 10910.
- [9] T.I.C. Jansen, K. Duppen, J.G. Snijders, Phys. Rev. B 67 (2003) 134206.
- [10] S. Saito, I. Ohmine, Phys. Rev. Lett. 88 (2002) 207401.
- [11] A. Ma, R.M. Stratt, J. Chem. Phys. 116 (2002) 4962.
- [12] A. Ma, R.M. Stratt, J. Chem. Phys. 116 (2002) 4972.
- [13] R. DeVane, C. Ridley, B. Space, T. Keyes, J. Chem. Phys. 119 (2003) 6073.

The impact of different molecular environments and chemical substitution on timescales of intramolecular vibrational energy redistribution in aromatic molecules

B. Abel

Institut für Physikalische Chemie der Universität Göttingen, Tammannstrasse 6,
37077 Göttingen, Germany.

1. INTRODUCTION

Vibrational energy flow within and between polyatomic molecules drives chemistry and governs their reactivity [1]. In the past decade intramolecular vibrational energy redistribution (IVR) in isolated molecules has been investigated with good success [2,3]. Much less, however, is known about IVR in solution where the intramolecular energy redistribution process is influenced by the surrounding solvent [4]. Unfortunately, generalizable mechanisms and principles, such as known for isolated molecules, have not been clearly identified yet. Moreover, it has not even been identified how and to what extent the solvent influences the intramolecular process that we call IVR for isolated molecules. The reason for this lack of knowledge is that IVR for a particular molecule could not yet be measured in the gas phase *and* in solution with the same technique. As a consequence, it was nearly impossible to correlate timescales of isolated and solvated molecules and to obtain a quantitative understanding of IVR and its underlying mechanisms in solution. Also the impact of chemical substitution on IVR remained largely unclear in solution. It is not by chance that benzene and toluene in the gas phase have become the benchmark systems for experimental [5] and theoretical IVR studies [6,7] during the past two decades.

Details of our experimental approach that is similar to the technique recently introduced by Crim *et al.* [8,9] have been published elsewhere [10-12]. The main feature of the approach is that the initially excited non-stationary "states" in the two quanta region of the C-H stretch vibration are Franck-Condon (FC) inactive, but as energy redistributes in the molecule, the population of isoenergetic (zeroth order) combination vibrations having quanta in the FC-active modes causes an increase in the absorption on the long wavelength wing of the electronic absorption spectrum. The limited number of FC-active modes of the molecules can be identified by resonance Raman and dispersed fluorescence experiments [11,13,14]. Subsequent intermolecular vibrational energy transfer (VET) to the surrounding solvent decreases the absorption again.

2. THE IMPACT OF A SOLVENT ON IVR OF BENZENE AND TOLUENE [15]

In the experiments described here we excited both molecules, i.e., benzene and toluene, in the two quanta region of the CH-stretch vibration with a short femtosecond (fs) laser pulse

centered at 1.7 μm . The recorded transient absorption profiles in general show a characteristic rise that we interpret as IVR and a subsequent slower decay which we attribute to intermolecular vibrational energy transfer (VET). In previous reports from our lab we have explained how transient absorption profiles can be converted into energy profiles [11]. Therefore, the measured absorption of a near UV-laser pulse following the excitation pulse is an observable for the time dependent energy content in the Franck-Condon (FC) active modes and for the redistributed energy in the molecule. An experimental trace for benzene in the gas phase ($p = 4$ bar, $T = 408$ K) is displayed in Fig. 1a. Interestingly, a fast rise approximately within the time resolution of the experiment ($\tau_{IVR}^{(1)}$) and a slower rise on a 100 picosecond (ps) timescale ($\tau_{IVR}^{(2)}$) followed by a very slow decay (τ_{VET}) on a nanosecond (ns) timescale was observed. For many experiments in solution a simple model with two sequential first order steps described by single exponential expressions for the rise and the decay was sufficient for the description of the time profiles [10]. However, if several FC-active modes in differently fast populated tiers are probed such as displayed in Fig. 2 the traces cannot be described by the simple model described in Ref. [11].

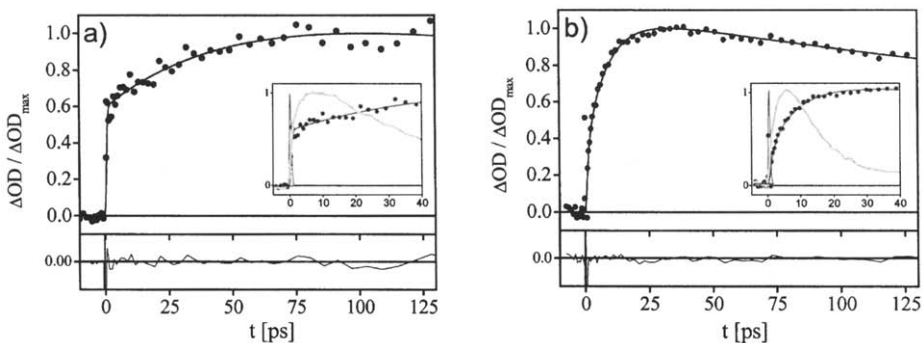


Fig. 1. a) Normalized transient absorption time profiles for benzene (\bullet) in the gas phase (4 bar, $T = 408$ K) for $\lambda_{pump} = 1670$ nm and $\lambda_{probe} = 275$ nm. Also shown is a fit using the model described in the text ($-$). b) Normalized transient absorption time profiles for toluene (\bullet) in the gas phase (4 bar, $T = 421$ K) for $\lambda_{pump} = 1678$ nm and $\lambda_{probe} = 280$ nm. The solid line is a fit using the model described in the text. Residuals show the quality of the fits. The insets display the traces on a shorter timescale, the cross correlation of the experiment, and the comparison with the solution experiment in Fig. 3 (grey line).

Such a situation is obviously encountered for benzene in Fig. 1a. In order to analyze the observed time profiles and to determine the time constants for the different IVR and VET processes the functional form of Eq. 1 was used (within the simple model mentioned above).

$$S(t) \propto \exp\left(-\frac{t}{\tau_{VET}}\right) - \left[A_{inst} \cdot \exp\left(-\frac{t}{\tau_{IVR}^{(1)}}\right) + (1 - A_{inst}) \cdot \exp\left(-\frac{t}{\tau_{IVR}^{(2)}}\right) \right] \quad (1)$$

It implies two different IVR processes superimposed on each other (see Fig. 2) and a subsequent VET process. For a realistic comparison of experimental and modeled traces the simulation was convoluted with the cross correlation function of pump and probe pulses. It is

displayed in the inset of Fig. 1a. Good agreement between experiment and theory was obtained when $\tau_{IVR}^{(1)} < 0.5$ ps. The remaining parameters in this refined model are $\tau_{IVR}^{(2)}$, τ_{VET} , and the relative amplitudes, A_{inst} and $(1-A_{inst})$, being correlated with the relative contributions of the IVR rate coefficients. The time constant for VET in the gas phase ($\tau_{VET} = 555 \pm 90$ ps) was *calculated* from the known energy transfer data for benzene-benzene collisions (as well as for toluene-toluene collisions) in the gas phase derived by Barker and co-workers [16]. This procedure enabled us to obtain $\tau_{IVR}^{(2)} = 55 \pm 7$ ps and $A_{inst} = 0.5 \pm 0.05$ with good precision.

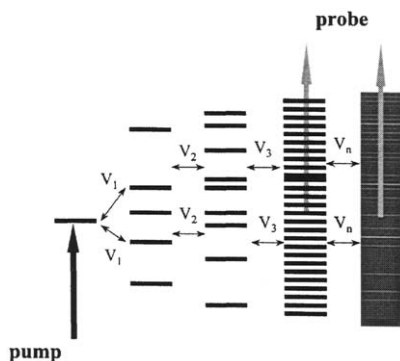


Fig. 2. Pump and probe scheme within a tiers picture (schematic). The zeroth order bright state which is not Franck-Condon (FC) active in the electronic transition is excited via the near IR- laser pulse. FC-active modes in later tiers having no population at $t=0$ are probed and their time dependent population is a measure for IVR (V_i being matrix elements connecting zeroth order states) in the molecule giving rise to an enhancement of the electronic absorption.

In Fig. 3a benzene has been measured in $CF_2Cl-CFCl_2$ solution. This experiment is compared with the gas phase result in the inset of Fig. 1a. For the determination of the kinetic parameters (including τ_{VET}) the same model has been used as described above with the parameters A_{inst} and $\tau_{IVR}^{(1)}$ kept fixed ($\tau_{IVR}^{(2)} = 3.8 \pm 0.8$ ps, $\tau_{VET} = 55 \pm 5$ ps), which implies that the ultrafast timescale is not influenced by the solvent. These data clearly suggest that in the case of benzene in the gas phase IVR dynamics proceeds on at least two distinct timescales, i.e., one on a sub-picosecond and one on a much longer timescale.

From an analysis of the eigenstate resolved frequency domain spectra of benzene in the first C-H stretch overtone region it is expected that the IVR process in the isolated benzene molecule consists of at least two steps [5]. In the first step (≈ 100 -200 fs), the initial excitation is rapidly redistributed among a first tier of states (see Fig. 2) which is observable in the spectrum observed by Page and co-workers [17]. Then, in a second, slower step (≥ 10 -20 ps), further redistribution occurs into a larger bath of available states being responsible for the linewidths and the timescales observed by Nicholson and Lawrence [18] and others [5]. In fact, in our direct time domain experiments we observe an ultrafast timescale and a slower one with an overall effective time constant of $\tau_{IVR}^{(2)} = 55 \pm 7$ ps which is somewhat larger than reported from studies in the frequency domain [5]. It should be noted, however, that $\tau_{IVR}^{(2)}$ in the present case may be an average of more than one time constant, and that the data in Ref. [5] and [18] are likely only sensitive to the intermediate timescales or provide lower bounds

for $\tau_{IVR}^{(2)}$. Wyatt *et al.* [19,20] have recently calculated IVR in 30-mode benzene and projected the energy flow in time on the normal modes. Their analysis is actually in good agreement with our picture, assumptions, and the observed timescales. Since we assume [11,13,14] that we definitely observe the E_{2g} FC-active mode at 608 cm^{-1} and likely also the A_{1g} mode of benzene at 994 cm^{-1} (possibly as a superposition) the agreement between theory and experiment can be regarded to be quite satisfactory.

A comparison of gas phase (Fig. 1) and solution experiments (Fig. 3) in the case of benzene unambiguously reveals the existence, the effect, and the magnitude of solvent assisted IVR. While the ultrafast IVR component appears to be not influenced by the solvent the picosecond timescale of IVR is contracted in solution. That appears to be the reason why the traces for experiments in solution could be modelled with one effective (average) exponential for the IVR in earlier studies [11] and why the visible impact of chemical substitution on the rates of IVR in solution is only moderate. It may simply be hidden in solution even if the effect is pronounced for isolated molecules.

For the case of toluene experiments in the gas phase and in $\text{CF}_2\text{Cl-CFCl}_2$ are displayed in Figs. 1b and 3b. In the inset of Fig. 1b the signal is shown on a shorter timescale together with the solution experiment and the cross correlation function of pump and probe pulses. The time resolved traces have been modelled as in the case of benzene. In the case of toluene the initial fast rise is less pronounced ($A_{inst} = 0.25 \pm 0.05$) than for benzene. This is likely a consequence of the different FC-factors of the different FC-active modes involved which also may depend somewhat upon the probe wavelength. For toluene in the gas phase $\tau_{IVR}^{(2)} = 8.7 \pm 0.9\text{ ps}$ and $\tau_{VET} = 500 \pm 80\text{ ps}$ have been determined. As in the case of benzene the parameters $A_{inst} = 0.25 \pm 0.05$ and $\tau_{IVR}^{(1)} < 0.8\text{ ps}$ were kept constant for the gas phase and the solution experiment in the analysis. For toluene in solution we found $\tau_{IVR}^{(2)} = 4.7 \pm 0.8\text{ ps}$ and $\tau_{VET} = 12 \pm 2\text{ ps}$, respectively.

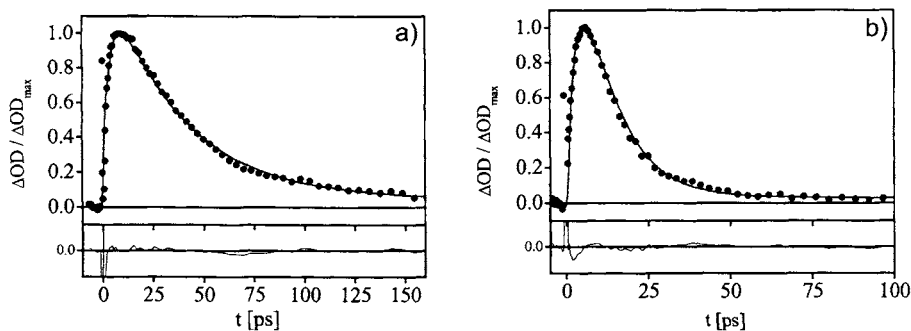


Fig. 3. a) Normalized transient absorption time profiles for benzene (●) in $\text{CF}_2\text{Cl-CFCl}_2$ solution for $\lambda_{\text{pump}} = 1670\text{ nm}$ and $\lambda_{\text{probe}} = 275\text{ nm}$. b) Normalized transient absorption time profiles for toluene (●) in $\text{CF}_2\text{Cl-CFCl}_2$ solution for $\lambda_{\text{pump}} = 1678\text{ nm}$ and $\lambda_{\text{probe}} = 280\text{ nm}$. The solid lines (—) are fits using the model described in the text. Residuals show the quality of the fits.

We also assume for toluene that the ultrafast IVR timescale is not (or hardly) affected by the solvent, however, the secondary timescale is again significantly contracted which is the

reason why the rise of the signal attributable to IVR in solution can approximately be described by a single exponential.

Most surprising here is the change of the timescale for secondary IVR in the case of toluene as opposed to benzene when comparing the gas phase signals in Fig. 1 which is not seen or largely covered in solution (Fig. 3). For the slower IVR component in the gas phase we observe a significant acceleration by a factor of 5-6 (see Tab. 1) which appears to be a direct consequence of the additional internal rotor at the aromatic ring. As was first pointed out by Parmenter and co-workers [21] the interaction of this degree of freedom with the vibrational motions of the ring can induce rapid IVR.

3. VIBRATIONAL RELAXATION OF C₆H₆ IN A SUPERCRITICAL FLUID [22]

The filled circles in Fig. 4 display a transient absorption signal of benzene in supercritical (sc) CO₂ ($\lambda_{\text{pump}}=1670$ nm, $\lambda_{\text{probe}}=278$ nm) at a temperature of 328 K and a pressure of 100 bar, corresponding to a reduced density of $\rho_{\text{red}}=0.7$. Again, the transient is characterized by a fast initial rise with $\tau_{\text{IVR}}^{(1)} < 0.5$ ps, but clearly, the following slower IVR and VET processes are accelerated with respect to the gas phase. Fitting of Eq. (1) to the signal by using the same amplitude ratio for slow and fast IVR component as in the diluted gas phase yields $\tau_{\text{IVR}}^{(2)} = 11 \pm 1$ ps and $\tau_{\text{VET}} = 78 \pm 7$ ps.

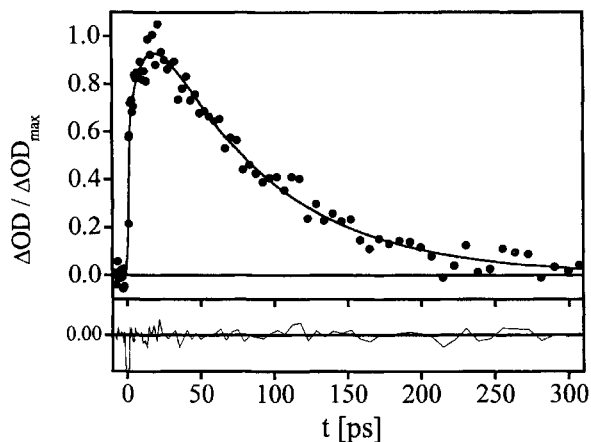


Fig. 4. Experimental trace (●) for benzene in supercritical CO₂ (100 bar, 328K, 0.2 M). The solid line is a fit to the model (see text).

These findings provide direct evidence for our conclusion, that interactions with the *weakly interacting* molecular environment not only reduce the VET relaxation time, but also can significantly enhance certain slow components of IVR while the fast intramolecular timescales are probably not affected significantly.

The VET rate constants $k_{\text{VET}} = 1/\tau_{\text{VET}}$ of benzene in scCO₂ as presented in Fig. 5 for various reduced densities $\rho_{\text{red}} = \rho/\rho_{\text{crit}}$ show the same *S-shaped* density dependence as previously observed for the vibrational energy relaxation of azulene in supercritical fluids

[23]. This behavior can be attributed to the local CO_2 -density around the solute and can be rationalized within the framework of the isolated binary collision model. The deactivation rate of the excited molecule in this case is proportional to the collision frequency $Z(\rho, T)$ which is correlated with the local density [23].

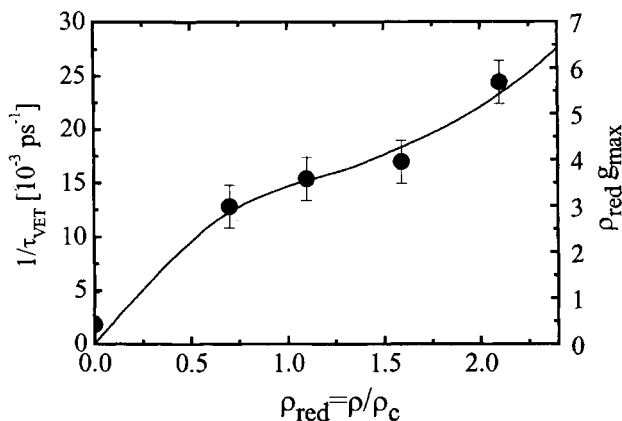


Fig. 5. VET rate constants of benzene in scCO_2 as a function of reduced density (filled circles). The solid line represents calculations of the local density at the position of the first maximum of the radial distribution function around an attractive solute in a Lennard-Jones fluid (see Fig. 7 and text for details). Experimental conditions: $\rho_{red} = 2.1$ (500bar, 318K), $\rho_{red} = 1.6$ (150 bar, 318K), $\rho_{red} = 1.2$ (100bar, 318K), $\rho_{red} = 0.7$ (100bar, 328K).

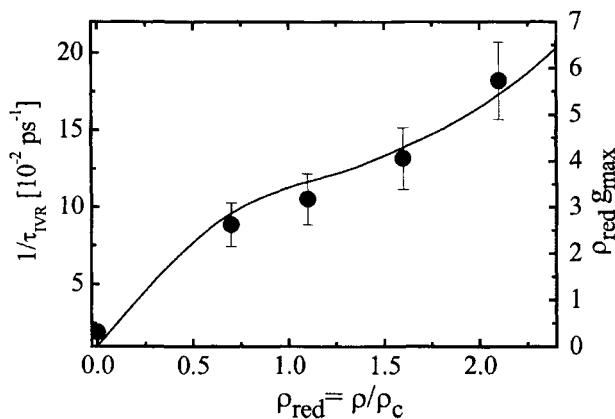


Fig. 6. Rate constants for the slow IVR component of benzene in the gas phase ($\rho \rightarrow 0$) and in scCO_2 (filled circles). Experimental conditions and solid line as in Fig. 5.

Inspection of the slower IVR rate constants $k_{IVR}^{(2)} = 1/\tau_{IVR}^{(2)}$ of benzene in scCO_2 displayed in Fig. 6 shows a very similar density dependence as found for $k_{VET}(\rho)$. Under nearly collision

free conditions $k_{IVR}^{(2)}$ is governed by anharmonic couplings intrinsically present in the benzene molecule (Fig. 1a). At higher fluid densities interactions with the bath enhance the effect of these couplings and accelerate $k_{IVR}^{(2)}$. At the highest CO₂ density we find an IVR time constant of (6 ± 1) ps which is already very close to 4 ps observed in a weakly interacting solvent like 1,1,2-trichlorotrifluoroethane.

In order to understand $k_{VET}(\rho)$ and $k_{IVR}^{(2)}(\rho)$ of benzene in more detail we calculated local densities from a simple model assuming benzene and CO₂ to be Lennard-Jones particles and employing the (constant NVT) Monte Carlo method. The solvent parameter σ_s and ϵ_s were chosen such that the critical data of the Lennard-Jones fluid match those of CO₂ [24], i.e. $\sigma_s = 0.365$ nm and $\epsilon_s/k_B = 232.2$ K. For benzene we assumed an effective diameter of $\sigma_b = 0.546$ nm which leads to $\sigma_{sb} = (\sigma_s + \sigma_b)/2 = 0.456$ nm using standard combination rules. The well depth for the solute-solvent interactions is a parameter in these calculations and was adjusted to $\epsilon_{sb}/k_B = 500$ K. The temperature was $T = 318$ K and calculations were performed with 500 particles. Fig. 7 shows radial density distributions $\rho_{red} \cdot g(r)$ around benzene for various CO₂-bath densities derived from these simulations. The curves were obtained by constantly increasing the reduced density from $\rho_{red} = 0.1613$ to 2.581. While at large distances ($r/\sigma_v > 4$) all the distributions are separated by a constant value, this is not the case in the immediate surrounding of the solute represented by the first maximum $\rho_{red} \cdot g_{max}$. Around the critical density the local density increases significantly less than at lower or higher densities giving rise to a characteristic S-shaped density dependence of $\rho_{red} \cdot g_{max}$. It is important to remember at this point that $\rho_{red} \cdot g_{max}$ is also proportional to the collision number Z . In Figs. 5 and 6 the density dependence of $\rho_{red} \cdot g_{max}$ is scaled in such a way, that it matches the experimental data.

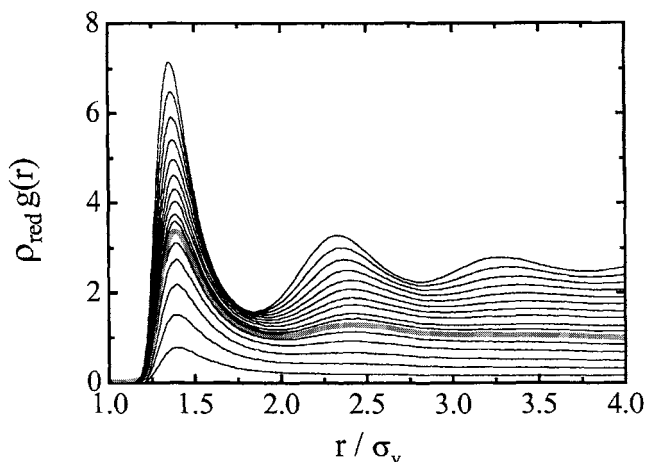


Fig. 7. Radial density distributions around benzene in CO₂ at reduced densities between $\rho_{red} = 0.1613$ (lowest curve) and 2.581 (upper curve) in steps of 0.1613 (grey line: closest to the critical density).

For both plots the agreement between model and experiment is very good given the simplicity of the model. The present results suggest that the IVR-acceleration linearly scales with the average number of solvent molecules present in the first solvation shell. Since the

collision number scales with the local density the observed IVR acceleration may simply be governed by the "collision number" of benzene in different molecular environments. At present we favor this dynamic picture over an alternative one in which the effect may be due to the presence and (the more static) interaction of the surrounding molecules ("cluster picture"). In conclusion, the present work unambiguously demonstrates the power of fs-transient absorption spectroscopy for the investigation of IVR and VET of molecules in the gas, liquid, and supercritical phase [15,22]. This and few other recent approaches [25,26] enable for the first time a correlation of timescales in different molecular environments and to elucidate mechanistic details of solvent induced/enhanced IVR.

4. ACKNOWLEDGEMENTS

Interesting discussions and fruitful collaborations with Dr. J. Assmann, R. von Bente, Dr. A. Charvat, O. Link, and Prof. D. Schwarzer over the years and financial support from the Deutsche Forschungsgemeinschaft within the Sonderforschungsbereich 357 and the Graduiertenkolleg 782 are gratefully acknowledged.

REFERENCES

- [1] J. Assmann, M. Kling, B. Abel, *Angew. Chem. Int. Ed.* 42 (2003) 2226.
- [2] A. H. Zewail, *Angew. Chem. Int. Ed.* 39 (2000) 2586; A. H. Zewail, *J. Phys. Chem. A* 104 (2000) 5660.
- [3] D. J. Nesbitt, R. F. Field, *J. Phys. Chem.* 100 (1996) 12735.
- [4] Z. Wang, A. Pakoulev, D. D. Klott, *Science* 296 (2002) 220.
- [5] A. Callegari, U. Merker, P. Engels, H. K. Srivastava, K. K. Lehmann, *J. Chem. Phys.* 113 (2000) 10583.
- [6] E. L. Siebert, W. P. Reinhardt, J. T. Hynes, *Chem. Phys. Lett.* 92 (1982) 455.
- [7] E. L. Siebert, W. P. Reinhardt, J. T. Hynes, *J. Chem. Phys.* 81 (1984) 1115.
- [8] D. Bingemann, A. King, F. F. Crim, *J. Chem. Phys.* 113 (2000) 5018.
- [9] C. M. Cheatum, M. M. Heckscher, D. Bingemann, F. F. Crim, *J. Chem. Phys.* 115 (2001) 7086.
- [10] J. Assmann, A. Charvat, D. Schwarzer, C. Kappel, K. Luther, B. Abel, *J. Phys. Chem. A* 106 (2002) 5197.
- [11] J. Assmann, R. von Bente, A. Charvat, B. Abel, *J. Phys. Chem. A* 107 (2003) 1904.
- [12] A. Charvat, J. Aßmann, B. Abel, D. Schwarzer, K. Henning, K. Luther, J. Troe, *Phys. Chem. Chem. Phys.* 3 (2001) 2230.
- [13] G. H. Atkinson, C. S. Parmenter, *J. Mol. Spec.* 73 (1978) 51.
- [14] J. H. Callomon, T. M. Dunn, I. M. Mills, *Phil. Trans. Roy. Soc. (London)* A259 (1966) 499.
- [15] R. v. Bente, O. Link, A. Charvat, B. Abel, D. Schwarzer, *J. Phys. Chem. A* (2004) in press.
- [16] B. M. Toselli, J. R. Barker, *J. Chem. Phys.* 97 (1992) 1809.
- [17] R. H. Page, Y. R. Shen, Y. T. Lee, *J. Chem. Phys.* 88 (1987) 4621.
- [18] J. A. Nicholson, W. D. Lawrance, *Chem. Phys. Lett.* 236 (1995) 336.
- [19] T. J. Minehardt, J. D. Adcock, R. E. Wyatt, *Chem. Phys. Lett.* 303 (1999) 537.
- [20] T. J. Minehardt, J. D. Adcock, R. E. Wyatt, *J. Chem. Phys.* 110 (1999) 3326.
- [21] C. S. Parmenter, B. M. Stone, *J. Chem. Phys.* 84 (1986) 4710.
- [22] R. v. Bente, A. Charvat, O. Link, B. Abel, D. Schwarzer, *Chem. Phys. Lett.* (2004) in press.
- [23] D. Schwarzer, J. Troe, M. Zerezke, *J. Chem. Phys.* 107 (1997) 8380.
- [24] J. J. Potoff, A. Z. Panagiotopoulos, *J. Chem. Phys.* 109 (1998) 10914.
- [25] C. G. Elles, M. J. Cox, F. F. Crim, *J. Chem. Phys.* (2004), submitted.
- [26] H. S. Yoo, M. J. DeWitt, B. H. Pate, *J. Phys. Chem. A* (2004), submitted.

Dihydroazulene Molecular Switches: Via Ultrafast Spectroscopy To The First Bidirectional Switch

U. Schmidhammer^(a), V. De Waele^(a, *), G. Buntinx^(b) and E. Riedle^(a)

^(a) Lehrstuhl für BioMolekulare Optik, Sektion Physik, Ludwig-Maximilians-Universität, Oettingenstr. 67, 80538 München, Germany

^(b) LASIR (UMR 8516), CERLA (FR 2416), USTL, Bât C5, 59655 Villeneuve d'Ascq Cedex, France

ABSTRACT

We demonstrate by using ultrafast time resolved spectroscopy that the photoconversion from dihydroazulene (DHA) to vinylheptafulvene (VHF) is governed by two mechanisms: The ring opening proceeds on the excited energy surface on the picosecond time scale. It is followed by an internal conversion to the VHF ground state that is accelerated by the presence of a conical intersection in the case of cyclopenta-DHA. This conical intersection hinders the photoinduced back reaction from the final VHF products. However, we successfully photoconverted the cyanophenyl-VHF-cis back to the DHA in an experiment with two delayed pulses. This opens the route to the development of bistable dihydroazulene switches.

1. INTRODUCTION

The realization of the common logic or even mechanic functions at the molecular level is an exciting and active area of research [1]. Toward this end, the photochromic compounds constitute an important link to convert light into chemical energy or information. The dihydroazulenes (DHA) are very established compounds for molecular switching [2]. They fulfill important requirements like efficiency of the photoconversion and good fatigue resistance. On the other hand, the switching of DHA can only be photoinduced in one direction: Under irradiation in the near UV the molecule undergoes an efficient ring opening reaction based on a 10π electrocyclization and is converted to the vinylheptafulvene isomer (VHF). The back-reaction proceeds by thermal activation. This behavior can in specific cases restrain the application of DHA and it is important to elucidate the parameters that govern the photochromism and are responsible for the absence of optical bistability.

To this aim we study the DHA/VHF photoconversion in an approach that combines broadband transient absorption with 100 fs pulses and two color experiments with sub-30 fs pulses. The former provides a clear identification of the transient states involved in the process, while the later allows us to determine precisely the kinetics of the process. Through the analysis of the coherent signal observed in addition we are able to identify the structural evolution of DHA directly after the application of the ultrashort pump pulse.

* present address: Laboratoire de Chimie Physique d'Orsay, UMR 8000 CNRS - Université Paris Sud 11, 91405 Orsay, France

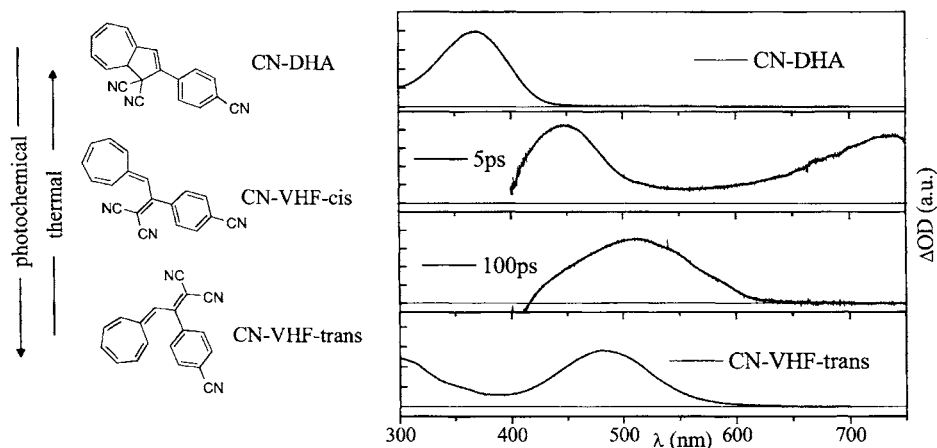


Fig. 1. Species involved in the photochromism of CN-DHA and the corresponding cw respectively transient spectra of the photochemical reaction path to CN-VHF-trans. The latter was triggered with laser pulses at 375 nm.

2. INVESTIGATIONS ON THE PHOTOCHROMIC REACTION PATHS

We compare the ultrafast dynamics of the 1,1(8aH)-azulendicarbonitrile,2-(4-cyanophenyl) derivative (hereafter CN-DHA/CN-VHF) with the related but distinctly different DHA derivative 1,2,3,8a,9-pentahydrocyclop[*a*]azulene-9,9-dicarbonitril (CP-DHA). The final product formed by irradiation of CN-DHA at its S_1 - S_0 absorption band around 370 nm is the CN-VHF-trans isomer. Therefore, the complete process involves a cis-trans isomerization besides the ring opening (Fig. 1). The broadband transient absorption spectra [3] reveal that an absorption band around 510 nm is formed via an excited state within the first 15 ps. This ground state absorption band is red shifted by 30 nm compared to CN-VHF-trans and can therefore be attributed to the S_0 state of CN-VHF-cis. The rearrangement to the final trans

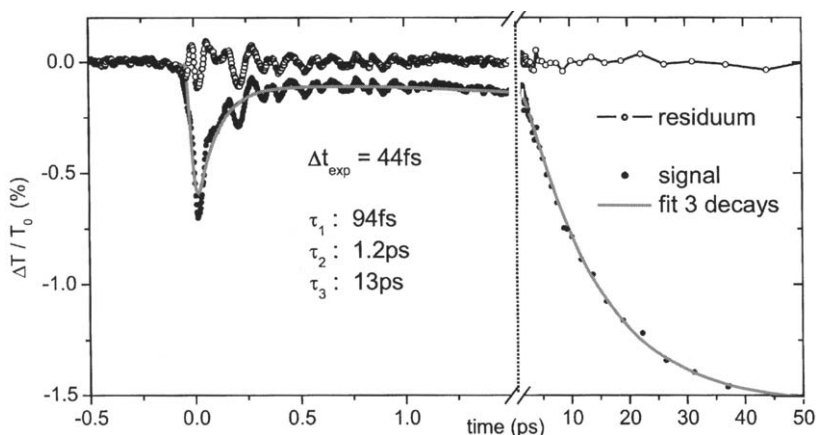


Fig. 2. Transmission change of CN-DHA induced at 350 nm and probed at 545 nm: exponential dynamics and oscillatory behavior of the coherently excited vibronic wavepacket. Ring opening (1.2 ps) and internal conversion (13 ps) to CN-VHF-cis take place on different time scales.

conformer takes place within 10 μs as shown by a flash photolysis experiment [3].

Thus, the ring opening itself is an ultrafast process on the S_1 excited state clearly separated from the cis-trans isomerization. Its kinetics are elucidated by two color experiments [4]. The exponential behavior is the same for all the probed wavelengths between 485 nm and 690 nm (Fig. 2): There is a very fast structural relaxation within 100 fs followed by the 1.2 ps ring opening. After subtraction of these exponential contributions strong oscillations remain which appear immediately after the pulse excitation and thus do not result from a fast reactive process. Moreover, by analyzing the residuum via Fourier transformation a phase jump of π is observed for probe wavelengths longer than 530 nm compared to those of the blue spectral region. We therefore assign the observed modulation to the coherent vibronic wavepacket oscillating around the DHA S_1 state minimum. Four normal modes at 150, 190, 330 and 500 cm^{-1} were identified which contribute towards the planarisation of the azulene and support thus the ring opening. By the damping time of their oscillations we can estimate the intramolecular vibrational relaxation (IVR) to occur on the order of a few hundred femtoseconds.

The photoconversion of CP-DHA to its VHF isomer is described by theoretical studies [5] with the same two reactive coordinates as found by our experimental investigations of CN-DHA: the ring opening coordinate and the internal conversion coordinate. Nevertheless, the behavior of CP-DHA is found to be distinctly different (Fig. 3, [6]). The complete process proceeds via a single exponential decay of 600 fs. Despite rigorously identical experimental conditions as for CN-DHA, the ring-opening dynamics can not be distinguished from the internal conversion and moreover no oscillations of the excited wavepacket are observed. This reveals the direct formation the CP-VHF S_1 state within the pump pulse duration. Thus the wavepacket initially coherently excited at the CP-DHA Franck-Condon geometry, which is strongly different from the CP-VHF one, immediately dephases by vibrational redistribution over a high density of VHF normal modes. Concerning the very fast internal conversion to the CP-VHF ground state, it is governed by a conical intersection as predicted by [5].

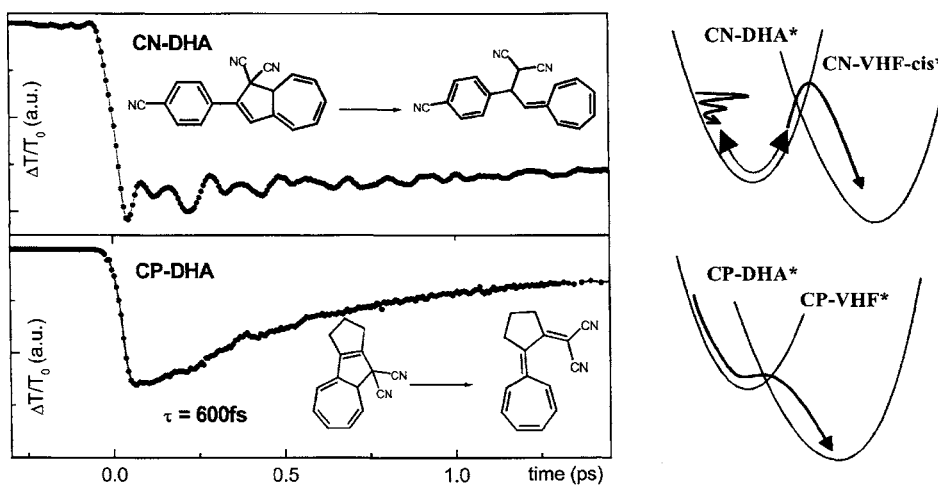


Fig. 3. Primary dynamics of CN-DHA and CP-DHA excited at 350 nm and probed at 630 nm and the deduced model of the S_1 energy surfaces. For both systems the ring opening to the VHF proceeds on the excited state but the energy surfaces must be distinctly different due to the strongly pronounced wavepacket oscillations of CN-DHA and its lower efficiency.

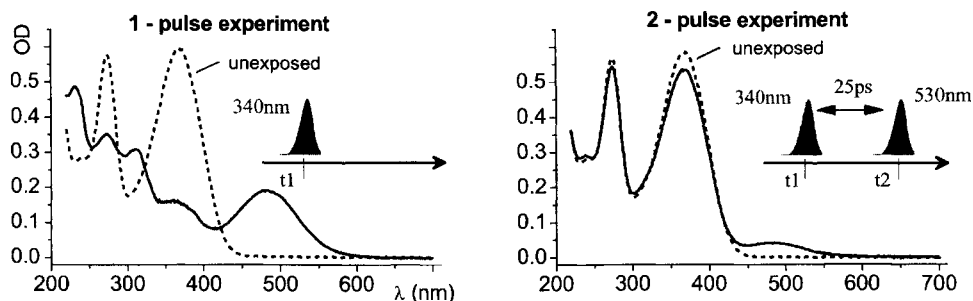


Fig. 4. Cw absorption spectra recorded before and after the one pulse experiment (left hand side) respectively the two pulses experiment (right hand side).

3. PHOTOINDUCED RING CLOSURE FROM THE TRANSIENT CN-VHF-CIS S_0

It is the strong interaction between the excited state and the ground state via the conical intersection that hinders the optical bistability of the CP-DHA compound. In contrast CN-DHA shows a much smaller efficiency of the internal conversion which indicates that no conical intersection is involved. We can therefore raise the question whether a photoinduced backreaction from the transient CN-VHF-cis ground state is possible.

This idea was probed by irradiating two samples of CN-DHA with the same concentration and volume in a one pump pulse and a two pump pulses experiment [7]: In the one pulse experiment the photoconversion to CN-VHF-trans was triggered at 340 nm under similar conditions as in the two color time resolved measurements. The irradiation time t was chosen such that a significant amount of CN-VHF-trans was converted. In the two pulses experiment an additional pulse at 530 nm which was delayed by 25 ps from the first pulse excited the transient CN-VHF-cis for the same time t . After the irradiation much less CN-VHF-trans is found in the two pulse experiment than in the one pulse experiment (Fig. 4). We conclude that a significant amount of CN-DHA was regenerated from the transient species by the second pulse. Photodegradation and thermal activation by the 530 nm pulses were eliminated as possible reasons for the observed effect.

This experiment demonstrates that when manipulated by femtosecond pulses, the CN-DHA derivative possesses the remarkable property of multimode switching: a thermal switch between the VHF-cis and DHA via the VHF-trans conformation and an ultrafast photo-reversible switch between the DHA and VHF-cis conformers.

REFERENCES

- [1] Molecular Switches, B. L. Feringa, Weinheim, 2001.
- [2] T. Mrozek, H. Gömer and J. Daub, Chem. Eur. J., 7 (2001) 1028.
- [3] V. De Waele, G. Buntinx, U. Schmidhammer and E. Riedle, in preparation.
- [4] V. De Waele, M. Beutter, U. Schmidhammer, E. Riedle and J. Daub, submitted to CPL.
- [5] M. Baggio-Pasqua, M.J. Bearpark, P.A. Hunt and M. A. Robb, J. Am. Chem. Soc., 124 (2002) 1456.
- [6] J. Ern, M. Petermann, T. Mrozek, J. Daub, K. Kuldová and C. Kryschi, Chem. Phys., 259 (2000) 331.
- [7] V. De Waele, U. Schmidhammer, T. Mrozek, J. Daub and E. Riedle, J. Am. Chem. Soc., 124 (2002) 2438.

The ultrafast dynamics of some photochromic naphthopyrans

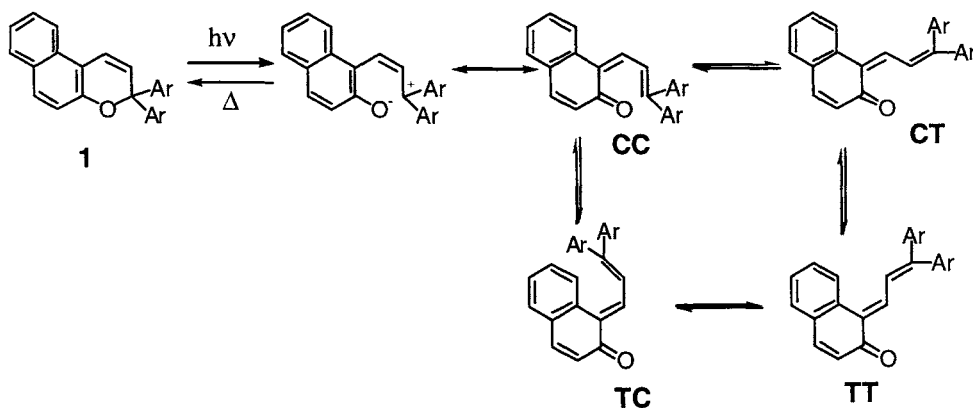
R.G. Brown^a, M. Maafi^a, P. Foggi^b and L. Bussotti^b

^aSchool of Applied Sciences, University of Glamorgan, Pontypridd. S. Wales. UK.

^bLENS, via Nello Carrara,1, Sesto F.no 50019 Italy.

1. INTRODUCTION

Photochromic materials find wide use in the ophthalmic industry and it is becoming clear that future ophthalmic products will increasingly incorporate naphthopyrans (especially naphtho[2,1-*b*]pyrans - structure **1**) as their photochromic element. The attraction of the naphthopyrans as photochromic materials stems from their broad range of intense vibrant colours combined with control over the rate of fade and resistance to fatigue [1]. The mechanism of photochromism is shown in Scheme 1 for 3,3-diaryl-3*H*-naphtho[2,1-*b*]pyrans. It is conventionally accepted that the trans open isomers are preferred, with the CT form preferred to the TT form [1, 2]. The excited state responsible for the ring scission process was proposed as the excited singlet state [3] on the basis of nanosecond flash photolysis measurements and this is borne out by the ultrafast work of Aubard *et al* [4] who report a lifetime for ring scission of 450 fs from the first excited singlet state for **1** in acetonitrile. Here we report similar measurements on three naphtho[2,1-*b*]pyran derivatives.



Scheme 1. Species involved in the photochromic behaviour of 3,3-diaryl-3*H*-naphtho[2,1-*b*]pyrans.

2. EXPERIMENTAL

3,3-diphenyl-3*H*-naphtho[2,1-*b*]pyran was a gift from James Robinson Ltd. and was used as received. All solvents were spectrophotometric grade from Aldrich Ltd. and were used as received. Absorption spectra were recorded on a Hewlett-Packard 8452A diode array spectrometer. The experimental set-up for measuring transient absorption spectra at LENS has been described elsewhere [5-7].

3. RESULTS AND DISCUSSION

3,3-diphenyl-3*H*-naphtho[2,1-*b*]pyran and its two derivatives with methoxy (**2**) and *N,N*-dimethylamino (**3**) groups substituted at the *para* positions of both phenyl rings all form essentially colourless solutions in organic solvents at room temperature. On continuous irradiation with UV light, the ring opening reactions depicted in Scheme 1 take place and visible colour develops in the solution. If the irradiation is then switched off, the visible absorbance decreases, the colour of the solution fades and the original spectrum of the closed species is regenerated. Both the photocoloring and fading curves are best reproduced by biexponential functions, the parameters from which can provide information about the quantum yields for the photochemical reaction(s) and the rate constants for the thermal reactions which are taking place as well as the absorption properties of the ring-opened species [1, 8].

Transient spectra over the wavelength range 350 – 630 nm were recorded for **1** – **3** in organic solution at time delays between 100 fs and 850 ps following excitation. The transient spectra for all three compounds exhibit significant absorption in the visible part of the spectrum, with substantial growth in intensity in the first ten ps (Figures 1a and 2a). After this time, the overall absorbance only changes a relatively small amount but the spectral shape and / or position varies. In the case of compound **1**, the visible absorption transient appears to be comprised of two spectral components with absorption maxima at approximately 410 and 440 / 450 nm (Figure 1b). For compound **2** a single absorption band is evident which undergoes a consistent red shift from a maximum at approximately 480 nm at 10 ps delay to 510 nm at 850 ps delay (Figure 2b). Compound **3** exhibits behaviour which is an amalgam of the other two in that there are two spectral bands at 440 and 525 nm at 10 ps delay, the latter of which is the dominant one and which red-shifts (but only by 5 - 10 nm) at longer delay times.

In the light of the complex behaviour at longer delay times (> 10 ps), we have not tried to analyse the kinetic behaviour of the three compounds over this time period. Further experimental work needs to be carried out to validate and supplement our existing data. However, at the earliest delay times, the behaviour of the three compounds appears to be consistent and the variation of transient absorbance with time around the transient absorption maxima are successfully fitted by bi-exponential functions for all three compounds. The time constants for these fits are given in Table 1.

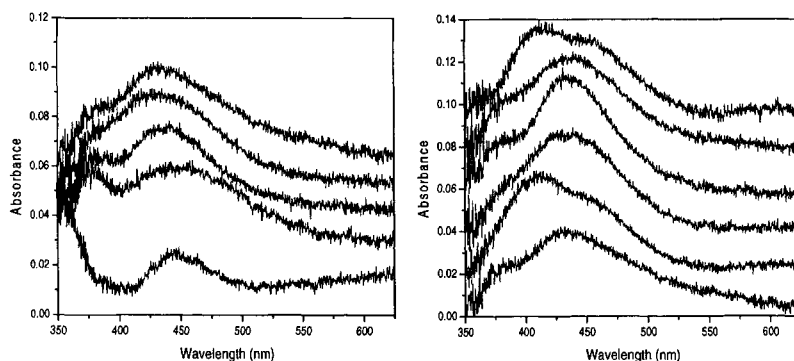


Fig. 1. Transient spectra obtained from compound **1** in ethyl acetate: (a) Delay times 200fs, 1 ps, 3.4 ps, 5.8 ps and 9.8 ps in ascending order; (b) 9.8 ps, 20 ps, 50 ps, 150 ps, 450 ps and 850 ps in ascending order. Successive spectra are offset for clarity.

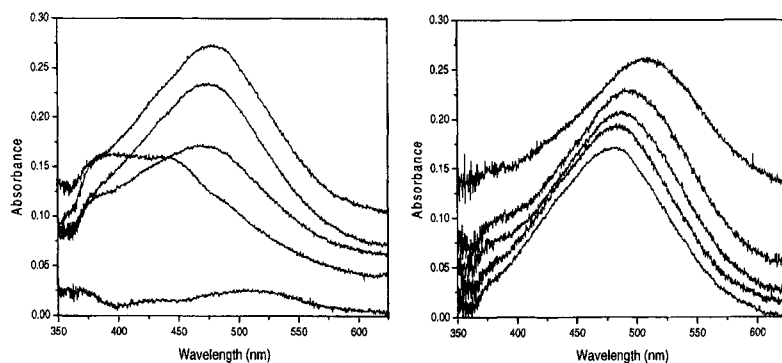


Fig. 2. Transient spectra obtained from compound **2** in ethanol: (a) Delay times 200fs, 1 ps, 3.0 ps, 6.2 ps and 9.6 ps in ascending order; (b) 10 ps, 20 ps, 50 ps, 150 ps and 450 ps in ascending order. Successive spectra are offset for clarity.

Table 1. Time constants for fits to the absorbance vs time profiles for studied compounds.

Compound	Solvent	τ_1 / fs	τ_2 / ps
1	Ethyl acetate	700	6.0
2	Ethanol	200	3.9
3	Ethanol	1200	8.0

The behaviour of compound **1** that we observe is in reasonable agreement with that previously reported by Aubard *et al* [4] in that the transients observed at delay times < 10 ps reproduce much of the previously reported behaviour and the time constants extracted from the kinetic analysis (700 fs and 6.0 ps) are of a similar magnitude to those reported before of 450 fs and 1.8 ps. We see no reason to disagree with the assignment of these two time constants to the initial pyran ring cleavage ($\tau < 1$ ps) and the transformation of the product of the ring cleavage (a *cis* ring-opened isomer) to a *trans* ring-opened isomer ($\tau = 1.8$ or 6.0 ps). It is, however, interesting to note the marked red shift in the transient spectra of **2** (and, to a lesser extent of **3**) at the longer delay times. This is very similar to the behaviour of a spirooxazine noted by Tamai and Masuhara [9] which was attributed to the relaxation of the non-planar primary photoproduct to a metastable merocyanine. A similar interpretation may be appropriate here.

Acknowledgements

We thank the University of Glamorgan and the European Community (under the contract HPRI-CT1999-00111) for financial support for this work.

REFERENCES

- [1] B. Van Gemert in "Organic Photochromic and Thermochromic Compounds Volume 1: Main Photochromic Families", J. C. Crano and R. J. Guglielmetti (eds.), Plenum Press, New York and London, (1999) 111.
- [2] S. Delbaere, B. Luccioni-Houze, C. Bochu, Y. Teral, M. Campredon and G. Vermeersch, *J. Chem. Soc. Perkin Trans. 2*, (1998) 1153.
- [3] J. Lenoble and R. S. Becker, *J. Photochem.*, 33 (1986) 187.
- [4] J. Aubard, F. Maurel, G. Buntinx, O. Poizat, G. Levi, R. Guglielmetti and A. Samat, *Mol. Cryst. Liq. Cryst.*, 345 (2000) 215.
- [5] S. Ameer-Beg, R. G. Brown, P. Matousek, M. Towrie, E. Nibbering, F. V. R. Neuwahl and P. Fogg, *J. Phys. Chem.*, 105 (2001) 3709.
- [6] F.V.R. Neuwahl, L. Bussotti and P. Fogg, in "Research Advances in Photochemistry and Photobiology", Vol. 1, Global Research Network, Trivandrum, Kerala, India (2000) 77.
- [7] P. Fogg, L. Bussotti and F.V.R. Neuwahl, *Int. J. Photoenergy*, 3 (2001) 103.
- [8] M. Maafi and R. G. Brown, "Photophysics and Kinetics of Naphthopyran Derivatives I. General Analytical Solutions for the Kinetics of AB(k, ϕ) and ABC(k, ϕ) Systems", submitted for publication in *Int. J. Chem. Kinet.*
- [9] N. Tamai and H. Masuhara, *Chem. Phys. Lett.*, 191 (1992) 189.

Femtochemistry of Organic Peroxides: Ultrafast Formation and Decarboxylation of Carbonyloxy Radicals

B. Abel, M. Buback, Ch. Grimm, M. Kling,[‡] S. Schmatz and J. Schroeder

Institut für Physikalische Chemie, Universität Göttingen, Tammannstraße 6,
D-37077 Göttingen, Germany, E-mail: mkling@uclink.berkeley.edu

1. INTRODUCTION

Detailed studies on the decomposition of organic peroxides are of fundamental interest and of high importance in polymerization reactions. The time-scales of intermediate radical formation and of their subsequent decomposition determine process parameters such as the initiator efficiency in radical polymerizations. An improved understanding of the mechanism and dynamics of photo-induced fragmentation is achieved by systematic investigations in which quantum-chemical calculations are carried out in conjunction with highly time-resolved experiments.

We have investigated the UV-induced decomposition of several organic peroxides, $R_1-C(O)-O-OR_2$ with R_1 being phenyl, benzyl or an aryloxy species and R_2 being *tert*-butyl or an arylcarbonyl group. The decomposition is assumed to proceed via two sequential bond scissions. After formation of two primary free radicals, $R_1-C(O)O$ and OR_2 , upon photo-excitation, the carbonyloxy radicals $R_1-C(O)O$ may decarboxylate in a subsequent step to yield the radical species R_1 and CO_2 . Although previous studies provided insight into the principal reaction channels and into some structural aspects of peroxide decomposition,^[1] they could not reveal mechanistic details of the photodissociation dynamics due to insufficient spectral and/or time resolution. After exploring the ultrafast formation of CO_2 in our first studies,^[2] we have recently measured the time-evolution of intermediate and product radicals by femtosecond pump-probe spectroscopy. We carried out density functional (DFT) calculations on structure and energetics of reactant and transition states of intermediate carbonyloxy radicals to provide the input parameters for quantitative modeling of the experimental data via statistical rate theories. Our approach^[3] will be illustrated for the decomposition of two peroxides, di(1-naphthoyl) peroxide (D1NPO, with R_1 = naphthyl and R_2 = naphthylcarbonyl) and *tert*-butyl 2-peroxy-naphthylcarbonate (TBNC, with R_1 = naphthyl and R_2 = *tert*-butyl). Naphthylcarbonyloxy radicals (Nph- CO_2) being the intermediates in D1NPO decomposition are known to be relatively stable exhibiting μ s-lifetimes in solution at ambient temperature.^[4]

[‡] Current address: Department of Chemistry, UC Berkeley, D90 Hildebrand Hall, Berkeley, CA 94720, USA

As will be shown, insertion of a bridging oxygen atom between the naphthyl and the CO₂ moiety, as in the naphthyloxycarbonyloxy radical (Nph-O-CO₂) intermediate from TBNC decomposition causes the lifetime of this radical to be several orders of magnitude lower than that of Nph-CO₂.

2. RESULTS AND DISCUSSION

As is shown for the decomposition of DINPO in Fig.1, the lifetimes of transient intermediates and products can be probed directly via ultrafast absorption spectroscopy in different spectral regions: 1-naphthylcarbonyloxy radicals may conveniently be observed in the visible range,^[4] whereas CO₂ is detected via the IR absorption of the ν_3 fundamental at around 4.3 μm .^[2] Competing processes, such as vibrational cooling of hot intermediates or solvation may produce overlapping spectral absorptions, which requires probe wavelengths to be scanned over broad spectral ranges (UV to IR) to identify suitable observation windows.

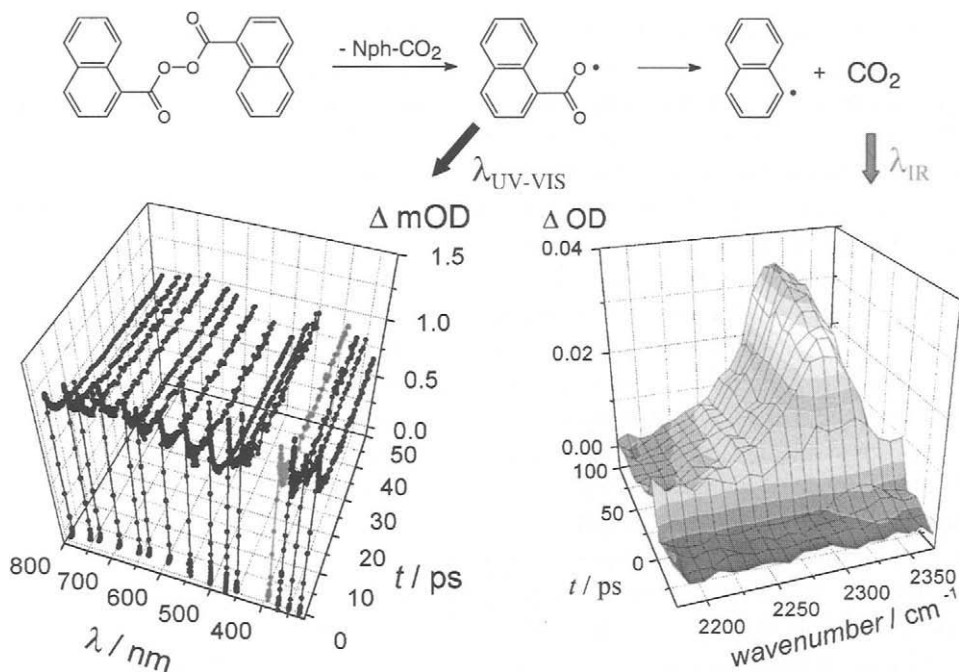


Fig. 1 Decomposition of di(1-naphthyl) peroxide.^[3] Left: transient decays at probe wavelengths in the visible region; right: complementary transient spectra of nascent "hot" CO₂ near 4.3 μm .

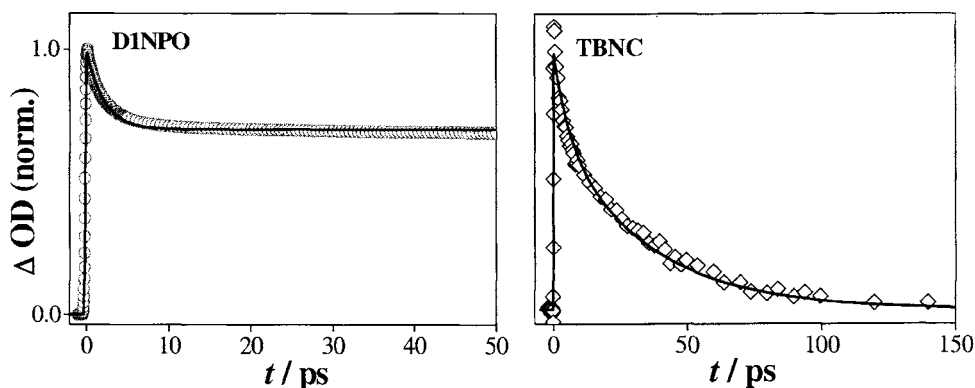
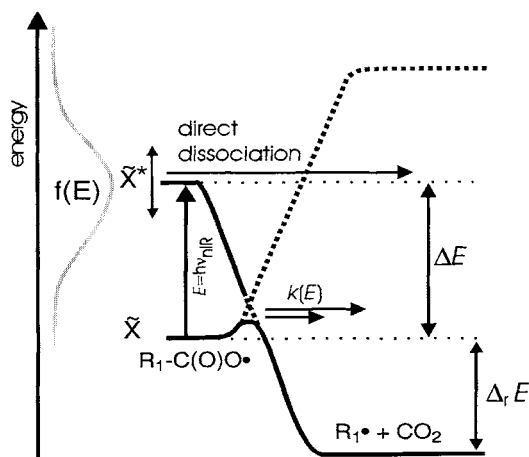


Fig. 2 Normalized transient absorption of 1-naphthylcarboxyloxy (left) and of 2-naphthylcarboxyloxy radicals (right) during photo-induced decomposition of DINPO (\circ , 266 nm pump / 390 nm probe in propylene carbonate) and TBNC (\diamond , 282 nm pump / 600 nm probe in *n*-heptane); — simulation as described in the text; note the different time scales.

Shown in Fig. 2 are examples of two kinetic traces of transient absorbance difference which reflect formation and decarboxylation of carboxyloxy radicals after photo-induced decomposition of DINPO and TBNC. A detailed understanding of the kinetics is obtained from modeling the data. Within the experimental time resolution (150 fs), peroxide primary dissociation produces carboxyloxy radical intermediates, which decay either directly from an electronically excited state within about 500 fs or in a statistical unimolecular reaction on a ps to μ s time-scale in the electronic ground state (see Fig. 3). In the case of DINPO photodissociation at 266 nm, the excited state of the 1-naphthylcarboxyloxy radical is too high energetically to be populated to any relevant extent.^[3] The reaction on the ground state PES can be treated by statistical unimolecular rate theory.

Fig. 3 Schematic potential energy diagram illustrating alternative decarboxylation pathways of carboxyloxy radicals $R_1\text{-CO}_2$. $f(E)$ denotes the initial internal energy distribution of the carboxyloxy radical, $k(E)$ is the specific rate constant for decarboxylation of the intermediate radical, ΔE denotes the energy separation of electronic ground and excited state of the carboxyloxy radical, and $\Delta_r E$ is its dissociation energy into CO_2 and product radical R_1 . For further details see Ref. [3].



The simulations, shown as solid lines in Fig. 2, are based on energies and frequencies obtained from DFT calculations. The observed carbonyloxy decay kinetics (Fig. 2) is dominated by vibrational relaxation of initially “hot” carbonyloxy radicals, which is well described by a single time constant of 7.5 ps with the applied solvents,^[3] and by thermal decarboxylation at ambient temperature after relaxation (that is at delay times above 20 ps) of ca. 1 μ s and 34 ps for 1-naphthylcarbonyloxy and 2-naphthyloxy carbonyloxy radicals, respectively. The initial average excess energy available for ground state decarboxylation depends on the branching ratio between the ground and excited state channels. While the decarboxylation reaction occurs entirely on the ground-state potential energy surface with 1-naphthylcarbonyloxy radicals, the excited-state channel significantly depletes the high-energy tail of the distribution in case of the 2-naphthyloxy carbonyloxy radical from TBNC photo-dissociation. These findings are consistent with excess energies observed for the product CO₂ in transient ps IR-experiments.^[2]

The barriers for decarboxylation of 1-naphthylcarbonyloxy and 2-naphthyloxy carbonyloxy radicals are deduced from calculations and experimental data to be 9.3 kcal mol⁻¹ and 2.9 kcal mol⁻¹, respectively, including corrections for zero-point energy.^[3] Our investigations have shown that decarboxylation of carbonyloxy radicals with bridging groups between the aromatic and the CO₂ moieties generally involves a lower barrier for the ground-state reaction which is associated with a considerably faster (ps-ns range) rate than that of the corresponding arylcarbonyloxy radical (ns- μ s lifetimes).^[3] The large contribution of direct decarboxylation via an electronically excited state channel for carbonyloxy radicals with a bridging group suggests that the energy gap between the ground state and the relevant excited state is smaller than for resonance-stabilized arylcarbonyloxy radicals. It cannot be ruled out that decarboxylation of aryloxy carbonyloxy radicals may also take place via a low-lying electronically excited state from which the reaction is symmetry-forbidden in the case of the arylcarbonyloxy radicals.

REFERENCES

- [1] Najiwara, T.; Hashimoto, J.; Katsunori, S.; Sakuragi, H. *Bull. Chem. Soc. Jpn.*, 76 (2003) 575 and references cited therein.
- [2] Aschenbrücker, J.; Buback, M.; Ernsting, N. P.; Schroeder, J.; Steegmüller, U. *Ber. Bunsenges. Phys. Chem.*, 102 (1998) 965; Aschenbrücker, J.; Buback, M.; Ernsting, N. P.; Schroeder, J.; Steegmüller, U. *J. Phys. Chem. B.*, 102 (1998) 5552; Buback, M.; Kling, M.; Seidel, M. T.; Schott, F.-D.; Schroeder, J.; Steegmüller, U. *Z. Phys. Chem.*, 215, (2001) 717.
- [3] Abel, B.; Abmann, J.; Buback, M.; Kling, M.; Schmatz, S.; Schroeder, J. *Angew. Chem. Int. Ed.*, 42 (2003) 299; Abel, B.; Assmann, J.; Botschwina, P.; Buback, M.; Kling, M.; Oswald, R.; Schmatz, S.; Schroeder, J.; Witte, T. *J. Phys. Chem. A*, 107 (2003) 5157; Abel, B.; Assmann, J.; Buback, M.; Grimm, Ch.; Kling, M.; Schmatz, S.; Schroeder, J.; Witte, T. *J. Phys. Chem. A* 2003, in press.
- [4] Tateno, T.; Sakuragi, H.; Tokumaru, K. *Chem. Lett.* 20 (1992) 1883.

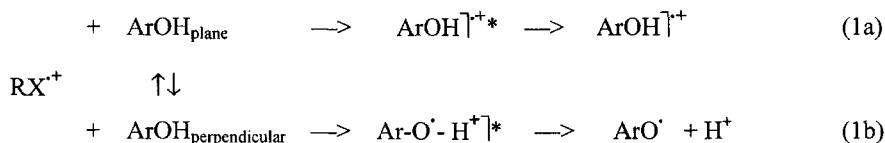
Femto- and nanosecond photoionization of sterically hindered phenols in non-protic solvents - antithetical product formation

R. Hermann, T. Leichtner, S. Naumov, O. Brede

University of Leipzig, Interdisciplinary Group Time-Resolved Spectroscopy, Permoserstrasse 15, D-04303 Leipzig, Germany; e-mail: hermann@mpgag.uni-leipzig.de

1. INTRODUCTION

Phenol radical cations exist only in strong acidic solutions ($pK_a \ll -1$) [1, 2]. However, in non-polar media phenol radical cations with lifetimes up to some hundred nanoseconds were obtained by pulse radiolysis [3]. The free electron transfer from phenols ($ArOH$) to primary parent solvent radical cations (RX^+) (1) resulted in the parallel and synchronous generation of phenol radical cations as well as phenoxy radicals in equal amounts, caused by an extremely rapid electron jump in the time scale of molecule oscillations since the rotation of the hydroxyl groups around the C – OH is strongly connected with pulsations in the electron distribution of the highest molecular orbitals [4 - 6].



The question whether or not similar effects play a role in the photoionization of phenols, could be studied only in aprotic surroundings (ionization energy around 8 eV). By using photon energies of about 5eV biphotonic ionization but also monophotonic fragmentation of the phenol molecule leading to phenoxy radicals [6] takes place. To overcome this complication we used sterically hindered phenols where the first excited singlet relaxes by internal conversion only [7]. Results of biphotonic ionization with UV lasers of different pulse durations are reported and interpreted in this paper.

2. EXPERIMENTAL

The solutions were photolyzed by 266 nm quanta of a Nd:YAG laser (FWHM < 3ns, energies up to 15 mJ) equipped with an optical absorption detection setup and by 253 nm quanta of a 10 Hz Ti:Sapphire laser system generating 250 fs pulses up to 2 mJ at 253 nm. Absorption measurements were performed by the pump-probe technique.

3. RESULTS AND DISCUSSION

3.1 Femtosecond photolysis

N_2 -purged solutions of $5 \times 10^{-4} \text{ mol dm}^{-3}$ of the sterically hindered phenols in acetonitrile were photolyzed with fs-pulses. After tens of picoseconds a band between 400 and 450 nm

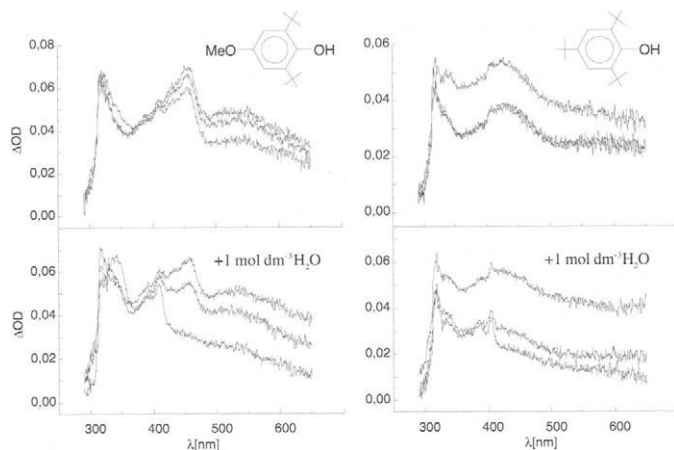
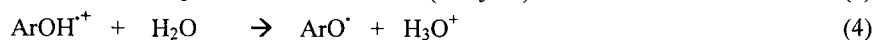
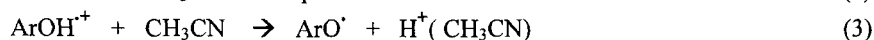


Fig. 1: Spectra measured 50, 250 and 1000 ps (downwards from the top) upon fs-laser photolysis of $5 \times 10^{-3} \text{ mol dm}^{-3}$ 2,6-di-tert.-butylphenol (left) or 4-methyl-2,6-di tert.-butyl phenol (right) in pure acetonitrile and in samples containing 1 mol dm^{-3} water (below).

appeared (Figure 1). Except of the para-methoxy-substituted derivative, in acetonitrile, this band decayed with an average lifetime of 500 ps. According to the very high density of the uv photons and in analogy to absorption spectra known from pulse radiolysis [3-5] the broad absorption bands were assigned to phenol radical cations. Two characteristic peaks appeared, obviously driven by the water influence, in acetonitrile samples and in samples containing 1 mol dm^{-3} water. In most cases the double peak signal is generated from the phenol radical cation in the presence of water and stands for the phenoxyl radical [8]. It can thus be stated that *exclusively* phenol radical cations are the direct product of the fs-photolysis. The decay of these species can be described by three reactions: neutralization by reaction with the counter charge (2), self-deprotonation in acetonitrile [9] (3) and deprotonation by water (4).



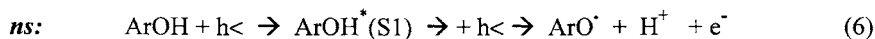
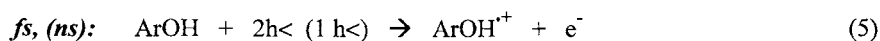
In the observed time range the neutralization (2) is mainly governed by non-homogeneous kinetics. Looking on the influence of the substitution pattern at the aromatic ring, the decay of the cation of 4-methyl-2,6-di-tert.-butylphenol was the fastest, whereas the 4-methoxy-substituted phenol was slower concerning reaction (2) according to known electronic effects. The deprotonation by water (4) appeared for all examples diffusion-controlled with $k_4 \approx 5 \times 10^9 \text{ dm}^3 \text{ mol}^{-1} \text{ s}^{-1}$ in accordance with data by pulse radiolysis [9].

3.2. Nanosecond photolysis in n-butyl chloride

From pulse radiolysis lifetimes of phenol radical cations between 300 and 500 ns are known [4, 9]. Laser photolysis (3 ns, 266nm up to 15 mJ) of N_2 -purged solutions of up to $10^{-3} \text{ mol dm}^{-3}$ phenols yields phenoxyl radicals as dominating products (Figure 2). In the spectrum only a little hint for the phenol radical cations exists. The inset shows that the phenoxyl radical formation does not depend linearly from the energy but appears by biphotonic absorption contradictory to the fs-experiments described above.

3.3. Interpretation of the results

Only little information exists on photoionization and radical cations of phenols. Gadosi et al. [10] photolyzed phenols substituted with two- or more methoxyl groups and observed methoxyl substituted phenol radical cations due to the extreme laser power used and because of their extreme low ionization potentials more than 1 eV lower than that of other phenols. Therefore, monophotonic ionization of such phenols could happen. In our experiments we are sure that either for the fs- or ns-photolysis experiments biphotonic ionization took place. The observed results should be considered on hand of a *Jablonski* scheme, cf. Figure 3. For the fs-photolysis we assume non-resonant conditions where the two photons are absorbed instantaneously without any interposed relaxation to electronically excited levels, cf. reaction (5), which leads directly into the continuum. This process starts from the HOMO level of the ground state, certainly from both the plane as well as the perpendicular molecule states with electron distribution over the whole system [5]. This differs from the introducing mentioned pulse radiolytically induced electron transfer ionization (1a, b) where other (HOMO-2) levels are involved too. In so far the biphotonic fs-ionization leads to the same products as a monophotonic process with photons of sufficiently high energy, cf. Figure 3 and reaction (5).



In the nanosecond biphotonic photolysis the vibronically excited level reached by absorption of the first photon relaxes by IC to the first excited state (Figure 3), which is stronger acid than the ground state by up to six orders in magnitude [11]. Quantum chemical calculations showed that the O – H bond becomes a bit longer and the C – OH bond becomes shorter and more rigid. The lifetimes of the first excited singlet state of the sterically hindered phenols

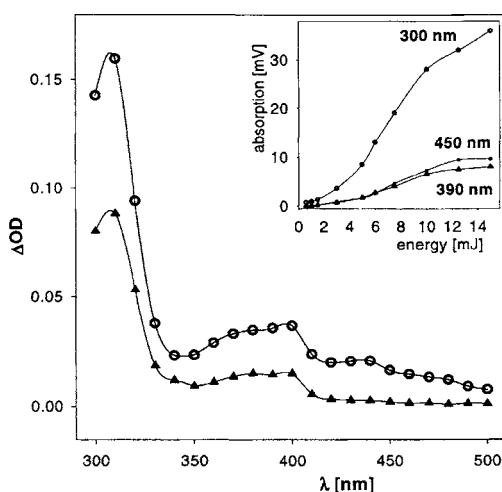


Fig. 2: Transient spectrum taken in the ns-laser photolysis (15 mJ) of a O_2 purged solution of $10^{-3} \text{ mol dm}^{-3}$ 4-methyl-2,6-di-tert-butylphenol in n-butyl chloride taken (\circ) 10 ns and (\triangleright) 8 ns after the pulse. The inset shows the photonicity in the transient maxima where the 450 nm curve was threefold amplified (absorption given for $I_0 = 300 \text{ mV}$).

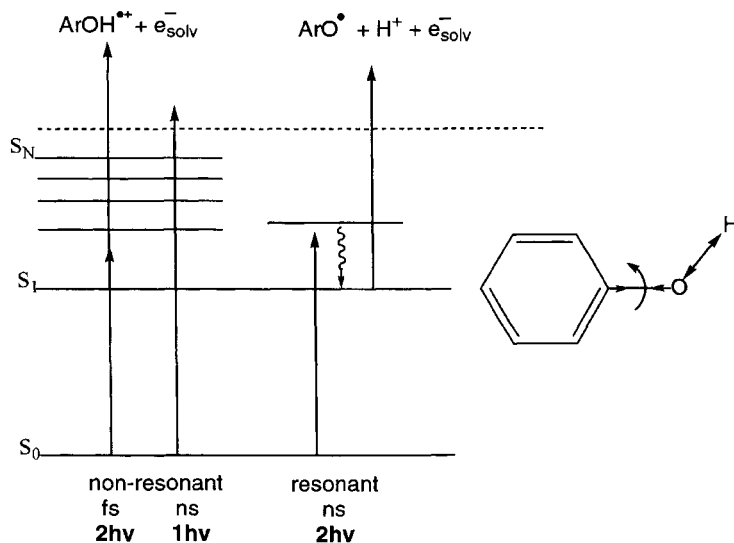


Fig. 3: Energy level scheme of phenol indicating the mechanistic differences for fs- and ns-biphotonic ionization as well as the assumed path for the monophotonic process according to [10].

are 100 to 300 ps. They are rather short compared to other phenols [6] but long enough for warranting a sufficiently high concentration for the subsequent process. The second photon is absorbed by the more acidic first excited singlet state, and ionization of it leads to a concomitant deprotonation under phenoxyl radical generation (6). There is practical no chance for radical cation formation, except by a very inefficient monophotonic contribution which could explain the very minor radical cation yield under these conditions. Although the phenol radical cations represent a much more acidic species than the first excited singlet state, its metastability could be explained by the resonance stabilization of the molecule in the very preferred plane configuration (particularly activation energy of C – OH group rotation).

REFERENCES

- [1] W.T. Dixon, D. Murphy, J. Chem. Soc., Faraday Trans. 2, 74 (1978) 432.
- [2] W.T. Dixon, D. Murphy, J. Chem. Soc., Faraday Trans. 2, 72 (1976) 1221.
- [3] O. Brede, H. Orthner, V. Zubarev, R. Hermann, J. Phys. Chem. 100 (1996) 7097.
- [4] G.R. Mahalaxmi, R. Hermann, S. Naumov, O. Brede, PCCP 2 (2000) 4947.
- [5] O. Brede, R. Hermann, W. Naumann, S. Naumov, J. Phys. Chem. A 106 (2002) 1398.
- [6] R. Hermann, G.R. Mahalaxmi, T. Jochum, O. Brede, J. Phys. Chem. A 106 (2002) 2379.
- [7] O. Brede, S. Naumov, R. Hermann, Chem. Phys. Lett 355 (2002) 1.
- [8] E.J. Land, M. Ebert, Trans. Faraday Soc. 63 (1967) 1181.
- [9] G.R. Mahalaxmi, S. Naumov, R. Hermann, O. Brede, Chem. Phys. Lett. 337 (2001) 335.
- [10] T.A. Gadosi, D. Shukla, L.J. Johnston, J. Phys. Chem. A 103 (1999) 8834.
- [11] E. Van der Donckt, Prog. React. Kinet. 5 (1970) 273.
- [12] J. Feitelsson, E. Hayon, A. Treinin, J. Amer. Chem. Soc. 95 (1973) 1025.

Coherent nuclear motion of reacting excited-state molecules in solution observed by ultrafast two color pump-probe spectroscopy

Satoshi Takeuchi and Tahei Tahara

Molecular Spectroscopy Laboratory, The Institute of Physical and Chemical Research (RIKEN), 2-1 Hirosawa, Wako 351-0198, Japan.

1. INTRODUCTION

Probing of the nuclear wavepacket motion generated by sufficiently short optical pulses enables us to observe the motion of nuclei in real time. This time-domain measurement of the nuclear motion has been receiving a great deal of attention in femtosecond spectroscopy [1, 2]. Especially, such measurements for ultrafast reactive systems give us an opportunity to observe the coherent nuclear dynamics in the early stage of the reaction [3]. It is very interesting to know the initial motion of nuclei and its relevance to the reaction coordinate, when the reactions are accompanied with a large structural change.

Unlike the case of simple diatomic molecules, the reaction coordinate in polyatomic molecules does not simply correspond to the change of a particular chemical bond. Therefore, it is not yet clear for polyatomic molecules how the observed wavepacket motion is related to the reaction coordinate. Study of such a coherent vibration in ultrafast reacting system is expected to give us a clue to reveal its significance in chemical reactions. In this study, we employed two-color pump-probe spectroscopy with ultrashort pulses in the 10-fs regime, and investigated the coherent nuclear motion of solution-phase molecules that undergo photodissociation and intramolecular proton transfer in the excited state.

2. EXPERIMENTAL

Time-resolved pump-probe absorption measurements were carried out by using 10-fs pulses generated from noncollinear optical parametric amplifiers (NOPAs). For independent tuning of the pump and probe wavelengths, we employed two NOPAs that were synchronously driven by regeneratively amplified Ti:sapphire laser pulses (800 nm, 1 mJ, 100 fs, 1 kHz). In each NOPA, a white-light continuum pulse was noncollinearly amplified in a BBO crystal that was pumped by the second harmonic at 400 nm, and the amplified pulse was compressed in time by a pair of prisms. The output of the first NOPA was frequency-doubled to generate a pump pulse in the ultraviolet region. The pump pulse was about 60 fs at 295 nm and 17 fs at 360 nm in duration after dispersion compensation. The output of the second NOPA in the visible region was used as a probe and a reference pulse. Both the pump (0.3 μ J) and probe

(0.3 nJ) pulses were focused into a spot size of 100 μm on a 50- μm thick jet stream of the sample solution. The intensities of the probe and reference pulses were detected by photodiodes and the signals were processed on a shot-to-shot basis for the evaluation of pump-induced absorbance change.

3. RESULTS AND DISCUSSION

3.1. Photodissociation of diphenylcyclopropanone

With $S_2 \leftarrow S_0 (\pi\pi^*)$ excitation, diphenylcyclopropanone (DPCP) dissociates and forms the excited state of diphenylacetylene [4] (Fig 1a). Our sub-picosecond transient absorption measurements showed a new short-lived band around 480 nm that is assignable to the initially populated S_2 state, and revealed that the dissociation takes place from this precursor excited state with a 0.2-ps time constant [5]. It is interesting to observe the coherent nuclear motion of this reactive excited state, since the dissociation involves a large structural change associated with the opening of the highly strained three-membered ring. In order to observe the wavepacket motion, we measured time-resolved absorption with probe at 525 nm that is resonant with the $S_n \leftarrow S_2$ DPCP absorption. As shown in Fig. 1b, this precursor absorption showed a weak but significant oscillatory modulation (~ 0.1 -ps period) on the 0.2-ps decay due to the ultrafast photodissociation. This means that DPCP exhibits a $\sim 330\text{-cm}^{-1}$ coherent

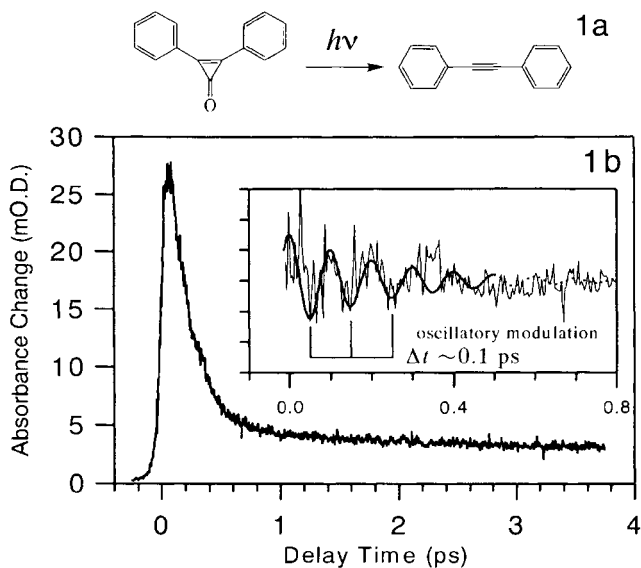


Fig. 1. (a) Photodissociation of diphenylcyclopropanone. (b) Time-resolved absorption signal of diphenylcyclopropanone in cyclohexane (2.5 mM) measured with a 70-fs time resolution. The pump and probe wavelengths were 295 nm and 525 nm, respectively. Extracted oscillatory component is also shown in the inset.

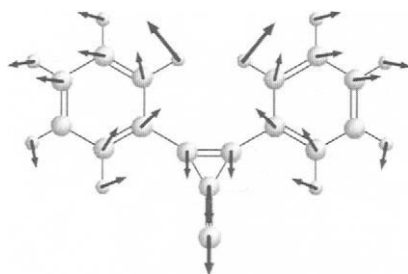


Fig. 2. Nuclear motion of the ground-state vibration at 386 cm^{-1} that corresponds to the excited-state wavepacket motion observed in the dissociative S_2 state.

vibration in the dissociative excited state. On the basis of the results of a density functional calculation, we assigned the observed excited-state vibration to a motion corresponding to the totally symmetric ground-state vibration at 386 cm^{-1} (Fig. 2). This result suggests that the dissociative excited state of DPCP shows a coherent, skeletal deformation that changes the Ph-C=C-Ph structure, along with the displacement of the carbonyl group.

3.2. Excited-state intramolecular proton transfer of 10-hydroxybenzoquinoline

In nonpolar solvents, 10-hydroxybenzoquinoline (10-HBQ) is converted from the enol to the keto form in a time as short as 100 fs after photoexcitation [6]. In order to examine the coherent nuclear dynamics in this ultrafast reaction, we excited this molecule by ultrashort uv pulses at 360 nm and measured time-resolved stimulated emission around 620 nm from the reacting excited state with a 27-fs resolution. As shown in Fig. 3, the observed

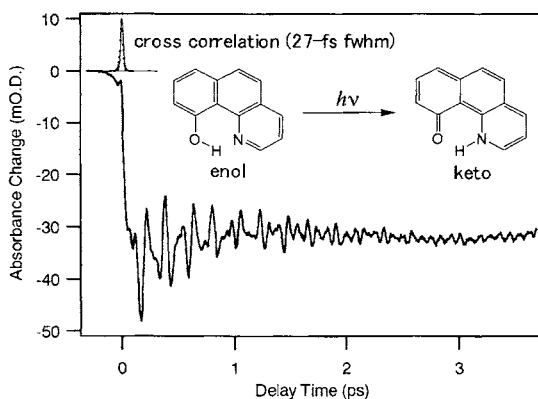


Fig. 3. Time-resolved stimulated emission signal of 10-hydroxybenzoquinoline (10-HBQ) in cyclohexane (30 mM) with excitation at 360 nm and probe at 620 nm. Photoinduced intramolecular proton transfer reaction of 10-HBQ is also shown in the inset.

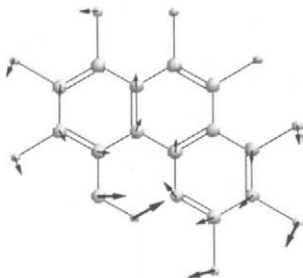


Fig. 4. Nuclear motion of the ground-state vibration at 243 cm^{-1} that corresponds to the observed wavepacket motion in the reacting excited state.

signal showed a complicated oscillatory feature until a delay time of 4 ps that is well longer than the reaction time. This manifests that the molecule exhibits a coherent nuclear motion during, and even after, the reaction. A Fourier transform analysis indicated that four vibrational modes in the $200 - 700\text{ cm}^{-1}$ region contribute to the observed oscillation. Especially, a theoretical calculation indicated that the lowest frequency mode at 242 cm^{-1} involves an in-plane skeletal deformation motion that substantially modulates the -O-H N-hydrogen-bond length (Fig. 4). This is reminiscent of the nuclear motion that we expect for the reaction coordinate of the proton transfer reaction of 10-HBQ.

REFERENCES

- [1] L. Dhar, J. A. Rogers, K. A. Nelson, *Chem. Rev.*, 94 (1994), 157.
- [2] S. Takeuchi and T. Tahara, *Chem. Phys. Lett.*, 326 (2000), 430.
- [3] S. Lochbrunner, A. J. Wurzer, and E. Riedle, *J. Chem. Phys.*, 112 (2000), 10699.
- [4] Y. Hirata and N. Mataga, *Chem. Phys. Lett.*, 193 (1992), 287.
- [5] S. Takeuchi and T. Tahara, submitted.
- [6] P. T. Chou, Y. C. Chen, W. S. Yu, Y. H. Chou, C. Y. Wei, and Y. M. Cheng, *J. Phys. Chem. A*, 105 (2001), 1731.

Probing of coherent oscillations by multiphoton ionization

S.A. Trushin^a, W. Fuß^a, W.E. Schmid^a and T. Yatsushiri^{a,b}

^aMax-Planck-Institut für Quantenoptik, D-85741 Garching, Germany

^bDep. of Chemistry, Osaka City University, 558-8585 Osaka, Japan

1. INTRODUCTION

Pumping a molecule by a femtosecond pulse to an electronically excited state S_n creates a vibrational wave packet in this state. Ultrafast internal conversion through a conical intersection may give rise to a periodic motion in a lower potential well, which can be observed as a coherent oscillation in pump-probe spectroscopy. If the vibration is excited by the slope on entering the well, its assignment gives information on the relaxation or reaction path direction. We have previously shown such cases in the photodissociation of metal hexacarbonyls $M(CO)_6$, where the vibrations found in the ground-state products $M(CO)_5$ were found to be orthogonal to all Franck-Condon active modes of the reactant [1]. This observation excludes that the observed oscillations just result from coherent superposition of Franck-Condon active vibrations by the pump laser, which would be the alternative mechanism how a vibration in the product could be stimulated. For probing and detection of such oscillations we used ionization with high laser intensities at 800 nm in the gas phase, recording the ion yields mass-selectively as a function of the pump-probe delay time.

Recently we found coherent oscillations also in molecules such as 4-dimethylamino-benzonitrile [2] or 4-(1-piperidino)-benzonitrile (PIPBN) [3], and their assignment indeed gave information on components of the reaction coordinate. The reaction in question is an intramolecular charge transfer (CT) between two nearly degenerate excited states: the L_b state (S_1 in the gas phase, symmetry species 1B in C_2) that is practically localized on the benzene ring, and the CT state that involves charge transfer from the amino nitrogen to the benzonitrile moiety. In the experiment in this work and in [2,3] we excited the molecules to the S_2 (L_a , symmetry 2A) state by a 70 fs pulse at 270 nm. The L_a and CT states are just two locations on one potential energy surface (PES), and this surface is crossed by the L_b PES in the form of a conical intersection (CI), as shown in Fig. 1. The wave packet passes through the CI and branches there. The one entering first into the S_1 well oscillates there coherently, whereas the other arriving later from the CT state seems to have lost its coherence [2,3]. The vibration was assigned in PIPBN to amino-group wagging (planarization/pyramidalization) in S_1 [3].

The oscillatory modulation of the signals are especially pronounced (up to 20 %) in the molecule PIPBN, both in the parent (M^+) and fragment ($M^+ - 1$) ion signals. In this work, we study it further, aiming at the mechanism of the signal modulation. For this purpose we varied the probe wavelength over the wide range from $\lambda_{pr} = 0.4$ to 2.1 μm , corresponding to 2–7 as a minimum number of photons required to ionize S_1 ($IE = 3.9$ eV). Not only a funda-

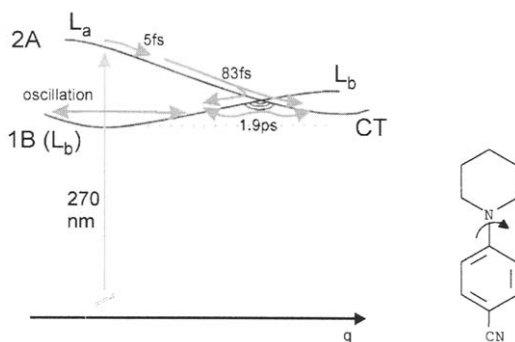


Fig. 1. Potentials and reaction path for PIPBN. In its formula, a component (amino group twist) of the reaction coordinate q is given by the arrow [3].

mental with period 1.06 ps was found, but also an overtone (0.53 ps). The fundamental disappears at some λ_{pr} . An interpretation is attempted of the λ_{pr} dependence of the amplitudes and phases of both oscillations.

2. RESULTS

The oscillations show up between ≈ 0.5 and >7 ps as a modulation of a plateau, that is normalized to 1 and displaced for every probe wavelength in Fig. 2. The signal in this time range is from S_1 , the only long-lived excited state [3]. Noticing for instance the peaks at 2.1 ps, it is easy to recognize that at $\lambda_{pr} > \text{ca. } 700$ nm the fundamental oscillations are in phase, but are out of phase for $\lambda_{pr} < \text{ca. } 660$ nm. At 679 and 405 nm, the fundamental practically disappears and the overtone is clearly brought out. But it can also be recognized as a component in some

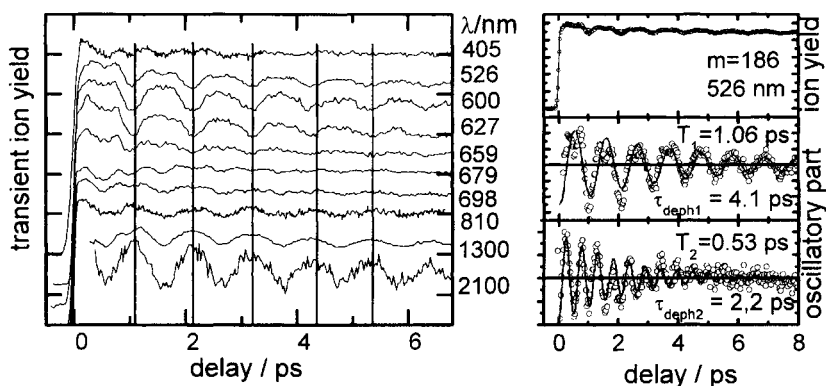


Fig. 2. Transient PIPBN parent-ion signal at different probe wavelengths normalized to the plateau value around 6 ps (left). On the right, the signal at 526 nm is decomposed into the nonperiodic part, the fundamental and overtone oscillations (fit lines shown).

other signals. It has a damping time of 2.2 ps, whereas the corresponding time for the fundamental is 4.2 ps. By Fourier transformation, we extracted the amplitudes and phases of both oscillations. They are shown in Fig. 3 versus the probe wavelengths. The phase jump of the fundamental near 679 nm is evident. By contrast, the overtone has a constant phase over λ_{pr} . The relative phases imply that in every minimum of the fundamental, there is also a minimum of the overtone (right panel of Fig. 2).

While the amplitudes are hard to compare at different wavelengths (and the amplitudes in Fig. 3a are therefore only rough), these quantities are better defined at a given wavelength. We found that for long λ_{pr} their relative values (amplitude/average signal) did not depend on the probe laser intensity, which was varied over a factor of 3.

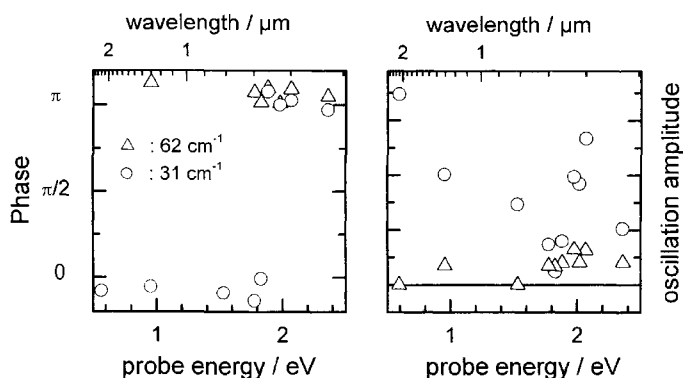


Fig. 3. Amplitude and phase of the fundamental (circles) and overtone (triangles) oscillations at different λ_{pr} .

3. DISCUSSION

Most coherent oscillations observed in the literature are connected with a resonance, the quality of which is modulated by a vibration. This can be just the transition observed in transient absorption. It can also be an intermediate resonance in a multiphoton observation such as ionization. The energy of the transition depends on a vibrational coordinate, along which the two potentials involved are not parallel. Hence the position of the absorption maximum will oscillate due to the vibration. A λ_{pr} in the long-wavelength wing will lead to an oscillation that is out of phase to the case with λ_{pr} in the short-wavelength wing, and with λ_{pr} in the maximum, one will observe only an overtone (see, e.g., [4]). This interpretation seems appropriate for our results near 680 nm (1.8 eV), and an intermediate resonance at this wavelength is conceivable. With this λ_{pr} , two photons are just enough to ionize the molecule from the S_1 state.

However, this resonance can hardly play any role over all the large wavelength range extending up to 2.1 μm . Furthermore, a resonant transition should be easy to saturate, so that the modulation should disappear at higher intensities. This is in contrast to observation at the longer wavelengths. Therefore we assume that the ionization probability P_{ion} depends on the vibrational coordinate x not (only) due to an intermediate resonance, but because the ionization energy IE depends on it. A Taylor series and expansion of the derivatives gives

$$P_{\text{ion}}(x) = P_{\text{ion}}(0) + x \cdot \frac{dP_{\text{ion}}}{dx} + \frac{1}{2} x^2 \cdot \frac{d^2 P_{\text{ion}}}{dx^2} \quad (1)$$

$$\frac{dP_{\text{ion}}}{dx} = \frac{dP_{\text{ion}}}{dIE} \cdot \frac{dIE}{dx} \quad \frac{d^2 P_{\text{ion}}}{dx^2} = \frac{dP_{\text{ion}}}{dIE} \cdot \frac{d^2 IE}{dx^2} + \frac{d^2 P_{\text{ion}}}{dIE^2} \cdot \left(\frac{dIE}{dx} \right)^2 \quad (2)$$

$$x = a_1 \sin(\omega t) + a_2 \sin^2(\omega t) \quad (3)$$

The third line describes oscillation of a wave packet in an anharmonic potential (phase term omitted). Eq. (1) would be valid also in the presence of an intermediate resonance. In Eq. (2), the λ_{pr} dependence is only in the P_{ion} terms. The fundamental arises from the sin terms (hence from dP_{ion}/dx) and the overtone from the \sin^2 terms. A phase jump of the fundamental is expected at a λ_{pr} where dP_{ion}/dx and hence dP_{ion}/dIE change sign. From these derivatives (proportional to the fundamental amplitude in Fig. 3) we can infer that P_{ion} has a maximum at 680 nm and a minimum near 405 nm. The maximum could reflect either an intermediate resonance or a two-photon resonance with an autoionizing state. The minimum is likely to announce a further rise of P_{ion} at shorter λ_{pr} due to the lower order of ionization.

The observation that the minima of the fundamental coincide with minima of the overtone requires that the coefficient of the \sin^2 terms is negative at all wavelengths. Collecting terms this means

$$\frac{dP_{\text{ion}}}{dIE} \left(\frac{d^2 IE}{dx^2} + 2 \frac{a_2}{a_1} \frac{dIE}{dx} \right) + \frac{d^2 P_{\text{ion}}}{dIE^2} \left(\frac{dIE}{dx} \right)^2 < 0 ? \quad (\text{at all } \lambda_{\text{pr}}) \quad (4)$$

However, depending on λ_{pr} , different combinations of signs of the P_{ion} derivatives are inferred from the data. Since the parentheses do not depend on λ_{pr} , this means that it is not possible to find an $IE(x)$ that would obey (4). We conclude that P_{ion} depends on x in a more intricate way than only via $IE(x)$. A dependence of P_{ion} mainly on IE is, however, expected in the field-ionization model, probably applicable at the long wavelengths, where intensities as high as $10^{13} \text{ W cm}^{-2}$ were used.

REFERENCES

- [1] S.A. Trushin, W. Fuß, W.E. Schmid, Chem. Phys. 259 (2000) 313.
- [2] S.A. Trushin, T. Yatsuhashi, W. Fuß, W.E. Schmid, Chem. Phys. Lett. 376 (2003) 282.
- [3] T. Yatsuhashi, S.A. Trushin, W. Fuß, W. Rettig, W.E. Schmid, S. Zilberg, Chem. Phys. (2003) in press.
- [4] A.T.N. Kumar, F. Rosca, A. Widom, P.M. Champion, J. Chem. Phys. 114 (2001) 701.

Coherences in the time-resolved fluorescence of the TCNE-HMB complex: simulation versus experiment

A. V. Pislakov^a, M. F. Gelin^b, and W. Domcke^a

^a Institute of Physical and Theoretical Chemistry, Technical University of Munich, Germany

^b Institute of Molecular and Atomic Physics, National Academy of Sciences of Belarus

1. INTRODUCTION

There are many systems of different complexity ranging from diatomics to biomolecules (the sodium dimer, oxazine dye molecules, the reaction center of purple bacteria, the photoactive yellow protein, etc.) for which coherent oscillatory responses have been observed in the time and frequency gated (TFG) spontaneous emission (SE) spectra (see, e.g., [1] and references therein). In most cases, these oscillations are characterized by a single well-defined vibrational frequency. It is therefore logical to anticipate that a single optically active mode is responsible for these features, so that the description in terms of few-electronic-states-single-vibrational-mode system Hamiltonian may be appropriate.

The TCNE-HMB complex, exhibiting an ultrafast electron-transfer (ET) reaction, is well suited for testing this assumption. Although it is formed by relatively large organic molecules with many inter- and intramolecular vibrational modes, underdamped oscillatory responses with only one dominant frequency have recently been clearly observed at an ultrafast time scale via time-resolved fluorescence [1,2] and pump-probe [3] spectroscopy. To understand and explain the origin of these oscillations, Lin and co-workers have performed *ab initio* molecular orbital calculations, identified all vibrational modes of the electronic ground state and proposed a new theoretical model of the ET process in TCNE-HMB [4]. In a subsequent work [5], they simulated the time-resolved responses. There remain, however, several problems which deserve further investigation. The approach developed in [5] does not take into account a finite duration of the gate pulse and is limited therefore to ideal (snapshot) spectra. What is more important, the consideration in [5] is confined to the interpretation of a single cut of the TFG SE spectrum at a fixed wavelength, but other available observables are not discussed. Within the approach developed in [6,7], in the present contribution we perform an improved analysis of various time-resolved responses reported in [1,2], i.e., (i) the time- and frequency-resolved (3D) fluorescence spectrum; (ii) cuts of the TFG SE spectrum at different wavelengths; (iii) the frequency-integrated fluorescence signal. In addition, we systematically study the effect of different system parameters on the signals. The details are given elsewhere [8]. In the present contribution, we describe briefly the model and present some of our simulations.

2. MODEL

As in paper [5], we start from a system Hamiltonian consisting of three (one ground $|g\rangle$ and two nonadiabatically coupled excited $|\phi_1\rangle$ and $|\phi_2\rangle$) electronic states strongly coupled to a reaction mode, which in turn is weakly coupled to a dissipative environment (see Fig. 1). The bath degrees of freedom are integrated out in the framework of Redfield theory, and the signals are calculated according to the explicit formulas derived in [6,7].

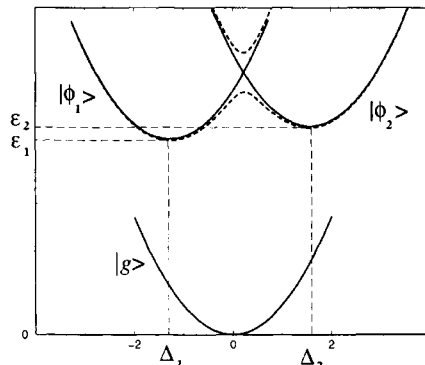


Fig. 1: Diabatic (solid) and adiabatic (dashed) potential-energy surfaces.

The majority of the system parameters has been taken from ab initio calculations [4,5]. Namely, the oscillator frequency $\Omega = 160 \text{ cm}^{-1}$, vertical excitation energies $\varepsilon_1 = 13910 \text{ cm}^{-1}$, $\varepsilon_2 = 14310 \text{ cm}^{-1}$, horizontal displacements $\Delta_1 = -1.28$, $\Delta_2 = 1.57$. We have checked, furthermore, that small changes of these parameters had a little effect on the signals. From the fit of absorption spectrum, Lin and co-workers [4] give the value of $1/3$ for the ratio of electronic transition dipole moments of the $|\phi_1\rangle$ and $|\phi_2\rangle$ states. We have shown that the introduction of the second partially bright state ($\mu_{10} = \mu_{20}/3$) changes the signal only slightly. So, we further assume that $|\phi_1\rangle$ is dark ($\mu_{10} = 0$), since in this case the integral signal is directly related to the diabatic population [7]. The remaining system parameter, the nonadiabatic electronic coupling V_{12} , is the most important quantity which is responsible for the ultrafast dynamics. We have obtained the best fits with $V_{12} = 0.3\Omega = 48 \text{ cm}^{-1}$. The experimental parameters are as follows: the temperature is 300 K, the pump-pulse central frequency is 15748 cm^{-1} , and the pump and gate pulse durations are $1/(5\Omega)$. According to [7], this is within the good resolution limit, so that the experimental TFG spectrum is close to an ideal (snapshot) one, as was assumed in [5]. The best-fit parameters of the spectral function of the bath [7] were found to be the following: cutoff frequency $\omega_c = \Omega$ and the dimensionless system-bath coupling strength $\eta = 0.45$. In order to achieve an agreement between the experimental and calculated signals, we have additionally introduced the optical dephasing $\Gamma_{deph} = \Omega$ into the doorway and window functions [6,7], which controls the lifetime of the optical coherence.

3. RESULTS AND INTERPRETATIONS

The general TFG SE spectrum as a function of detection frequency and delay time, calculated for the TCNE-HMB complex, is shown in Fig. 2a. The time evolution of the signal monitors the ET dynamics: qualitatively it reflects the combined effect of ET and damped vibrational wave packet (WP) dynamics in the donor state, which give rise to a characteristic step structure. Due to the presence of electronic coupling, a fraction of the WP is transferred to the (dark) acceptor state each time the moving WP hits the crossing region, i.e., when the system tunnels to a (dark) acceptor state, producing a sudden loss (jump) of the amplitude in the cut at a given frequency. In addition, the signal maps directly the periodic coherent WP motion in the excited state between classical turning points, where the local maxima of the peak-shift occur.

For explicit comparison with the experimental signals, one has to focus on a detailed analysis of particular cuts of the TFG SE spectrum. As an illustration, Fig. 2b demonstrates the calculated time-resolved signal at $\lambda = 774 \text{ nm}$, as well as the experimental signal reported

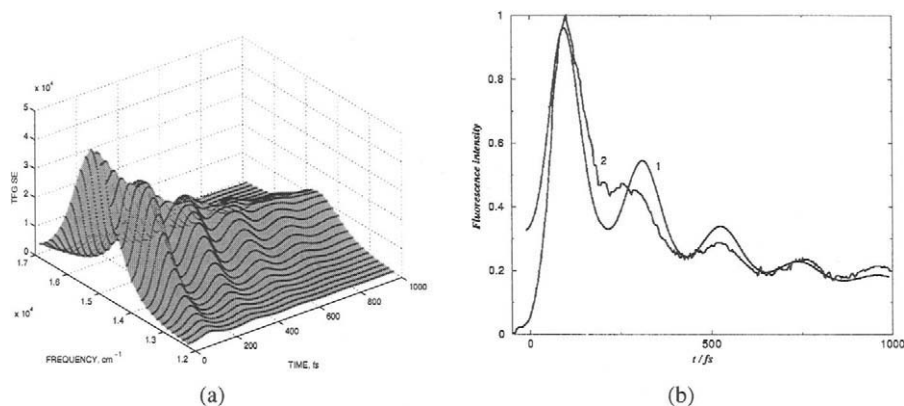


Fig. 2: **(a)** TFG SE spectrum of TCNE-HMB. **(b)** Cut at 774 nm: 1- calculated, 2- experimental [2]. by Rubtsov and Yoshihara [2]. The main features in the experimental signal are semiquantitatively reproduced: the oscillatory behavior and the overall decay (see also [5]). Moreover, since the experimental time resolution is quite good, agreement is achieved even at short times. The theoretical and experimental cuts differ in the vicinity of $t = 200$ fs where the calculated signal exaggerates oscillatory features. The discrepancy perhaps originates from various dephasing effects arising due to the multimode nature of the system under study. To arrive at a more quantitative agreement, one has to add to the single optically active mode one (or several) other system modes.

Within the present model, we can predict cuts of the fluorescence signal at any frequency. It is shown in [8] that the signal amplitude is larger for those detection wavelengths which are closer to the vertical transition. Our simulation nearly reproduces the ratio of the amplitudes of the different experimental cuts. On the other hand, our model cannot describe another effect observable in the experimental transients: at the red tail of the spectrum, the long-time limit of the experimental signal is higher, which indicates that the overall decay is slower. In our model, the decay is approximately the same for all frequencies.

The temporal evolution of the simulated peak position of the fluorescence spectrum is shown in Fig. 3a. The corresponding experimental peak-shift (figure 2 in [5]) consists of an oscillatory and an exponential part. Our model reproduces the weakly damped oscillatory part of the peak shift, but does not describe the large Stokes shift of 1400 cm^{-1} . The reason is that our single-mode model does not take into account other system modes and, what is more important, solvent modes, which contribute to the overall shift of the SE spectrum. The model may be improved by including an additional overdamped solvent mode.

Both the experimental and simulated integral signals $I(t)$ (Fig. 3b) show characteristic step-like behavior, which is typical for ET systems with vibrational coherence [7]. There are several factors which determine the dynamics of the ET process, among which the most important are the nonadiabatic electronic coupling and the dissipation strength. Our explanation and those of others [1,2,5] agree in that the steps (oscillations) in the signal are due to WP motion and that their period is determined by the oscillator frequency. However, Rubtsov and Yoshihara [1] suggested that the observed features in the signal may be attributed to non-Condon effects, while in our model the short-time dynamics is mostly determined by the nonadiabatic electronic coupling. We do not need to additionally invoke non-Condon effects. (Actually, a WP moving between the dark and bright states is, in a sense, a non-Condon effect.)

Fig. 3b shows significant deviations of the calculated integral signal from the experimental

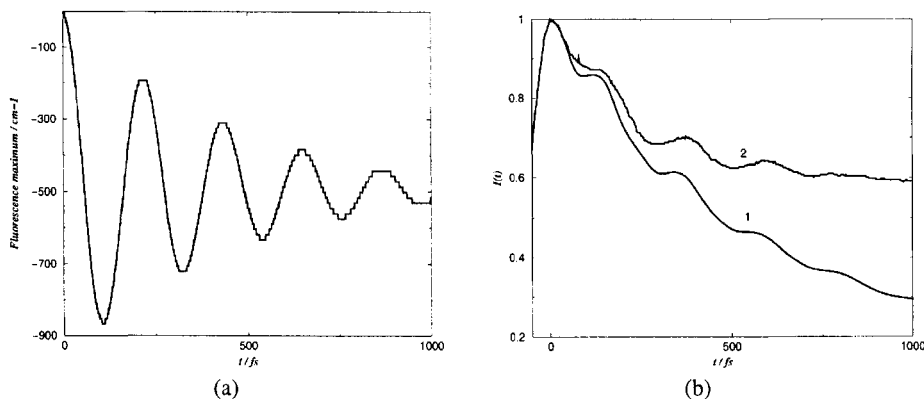


Fig. 3: (a) Peak shift of the fluorescence spectrum. (Note that the y-axis origin is chosen as $\nu_{max}(0)$.) (b) Frequency-integrated fluorescence signal: 1- calculated, 2 - experimental [2].

one: the former decays much faster. It turns out that the cuts and the integral signals cannot simultaneously be fitted within our model. Roughly speaking, the experimental cuts decay to 0.2 in 1000 fs and the integral signal decays to 0.6 during the same time. In contrast, the two types of signals calculated within our model exhibit nearly the same long-time decay. Different decay rates for the integral signal and cuts could be, in principle, due to the effect of nonadiabatic coupling or brightness of the $|\phi_1\rangle$ state. Indeed, for the limiting situations $V_{12} = 0$ or $\mu_{10} = \mu_{20}$, the integral signal is a constant, irrespective of the system-bath coupling. But a variation of V_{12} and μ_{10} (within the limits which give a reasonable fit of the cuts) is shown to result in no substantial improvements of the quality of the fit of the integral signal. This may indicate that our model need be improved and extended (see several suggestions in [8]). However, we must mention another possible reason for the different decay rates for the cuts and $I(t)$. The experimental integral signal is less reliable than cuts, since it has been constructed on the basis of only a few points in the spectrum, while the cuts at fixed wavelengths are very accurate [9].

Summarizing, it is demonstrated that the developed model correctly reproduces the general trends in various experimentally measured responses, which include cuts of time- and frequency-gated spectra at particular frequencies, peak-shifts of the fluorescence spectra, and integral signals. Moreover, the relative shapes and intensities of the spectral cuts at different frequencies are correctly reproduced. For a more complete and quantitative description of the experimental data, the theoretical model has to be augmented by including additional system and/or solvation modes.

REFERENCES

- [1] I. V. Rubtsov and K. Yoshihara, in *Femtochemistry*, Ed. De Schryver et al, Wiley 2001.
- [2] I. V. Rubtsov and K. Yoshihara, *J. Phys. Chem. A* 103 (1999) 10202.
- [3] K. Wynne, C. Galli, and R. M. Hochstrasser, *J. Chem. Phys.* 100 (1994) 4797.
- [4] M. Hayashi, T. S. Yang, J. Yu, A. Mebel, and S. H. Lin, *J. Phys. Chem. A* 101 (1997) 4156.
- [5] M. Hayashi, T. S. Yang, J. Yu, A. Mebel, S. H. Lin, I. V. Rubtsov, and K. Yoshihara, *J. Phys. Chem. A* 102 (1998) 4256.
- [6] M. F. Gelin, A. V. Pislakov, and W. Domcke, *Phys. Rev. A* 65 (2002) 062507.
- [7] A. V. Pislakov, M. F. Gelin, and W. Domcke, *J. Phys. Chem. A* 107 (2003) 2657.
- [8] A. V. Pislakov, Ph. D. thesis, Technical University of Munich, 2003.
- [9] Prof. K. Yoshihara, personal communication.

Quantum-dynamical modeling of ultrafast processes in complex molecular systems: multiconfigurational system-bath dynamics using Gaussian wavepackets

I. Burghardt^a and G. A. Worth^b

^aDépartement de Chimie, Ecole Normale Supérieure,
24 rue Lhomond, F-75231 Paris cedex 05, France

^bDepartment of Chemistry, King's College London,
Strand, London WC2R 2LS, U.K.

1. INTRODUCTION

Quantum dynamical processes in complex molecular systems often evolve around a “reactive core” composed of relatively few degrees of freedom which carry the dominant part of the dynamics. The latter are generally coupled to a much larger set of degrees of freedom which effectively act as an environment inducing dissipation and dephasing – but which in itself can be highly structured and may exhibit specific features guiding the dynamical process. The understanding of ultrafast dynamical processes in such systems therefore necessitates taking into account the environment, or at least part of the environment, explicitly. To this end, we have recently developed a new hybrid technique specifically adapted to a generalized system-bath perspective [1–3]. This new method is a variant of the multiconfiguration time-dependent Hartree (MCTDH) method for wavepacket propagation [4,5] which is itself a very powerful quantum-dynamical technique suitable for multimode dynamics. Our method extends MCTDH to even higher-dimensional systems while allowing for an explicit but approximate treatment of a chosen subset of “environmental” modes. The avenue we have chosen to this end is to combine MCTDH with time-dependent Gaussian basis functions [1].

First applications of the new method, denoted G-MCTDH [1–3], include the energy relaxation and decoherence of an anharmonic oscillator coupled to a bath of up to 60 harmonic oscillators [3] and the strongly anharmonic dynamics in the Hénon-Heiles system [2]. A further development focuses on an “on-the-fly” scheme which couples the Gaussian quantum dynamics with electronic structure calculations [6]. In the present contribution, the G-MCTDH method is used to model the decay dynamics at the S_2 – S_1 conical intersection (CI) in pyrazine [7,8]. We refer to the model Hamiltonian introduced in Ref. [8] which distinguishes a four-mode “core” and a less strongly coupled intramolecular “bath” of up to 20 modes. This partitioning carries over to the dynamical system-bath description by the hybrid method. In the following, we briefly recapitulate the key elements of the method, and proceed to illustrate its accuracy and efficiency in obtaining the wavepacket autocorrelation function which reflects the decay dynamics induced by the conical intersection.

2. MCTDH INCLUDING GAUSSIAN FUNCTIONS

Similarly to the parent MCTDH method [4,5], the G-MCTDH variant [1–3] uses a wavefunction ansatz corresponding to a multiconfigurational form. For coupled electronic states, the wavefunction takes the form $|\Psi\rangle = \sum_{s=1}^r \Psi^{(s)} |s\rangle$, with component wavefunctions

$$\Psi^{(s)}(\mathbf{r}_1, \dots, \mathbf{r}_P, t) = \sum_J A_J^{(s)}(t) \Phi_{J,\text{hybrid}}^{(s)}(\mathbf{r}_1, \dots, \mathbf{r}_P, t) \quad (1)$$

where the hybrid configurations $\Phi_{J,\text{hybrid}}^{(s)}$ are Hartree products composed of a class of “primary” modes ($\kappa = 1, \dots, M$) and a class of “secondary” modes ($\kappa = M + 1, \dots, P$) [1–3],

$$\Phi_{J,\text{hybrid}}^{(s)}(\mathbf{r}_1, \dots, \mathbf{r}_P, t) = \prod_{\kappa=1}^M \varphi_{j_{\kappa,s}}^{(\kappa,s)}(\mathbf{r}_{\kappa}, t) \prod_{\kappa=M+1}^P g_{j_{\kappa,s}}^{(\kappa,s)}(\mathbf{r}_{\kappa}, t) \quad (2)$$

Here, the $\varphi_{j_{\kappa,s}}^{(\kappa,s)}$'s represent the general time-dependent basis functions of the standard MCTDH method [4,5] while the $g_{j_{\kappa,s}}^{(\kappa,s)}$'s represent time-dependent Gaussian functions,

$$g_j^{(\kappa,s)}(\mathbf{r}_{\kappa}, t) = \exp[\mathbf{r}_{\kappa} \cdot \mathbf{a}_j^{(\kappa,s)}(t) \cdot \mathbf{r}_{\kappa} + \boldsymbol{\xi}_j^{(\kappa,s)}(t) \cdot \mathbf{r}_{\kappa} + \eta_j^{(\kappa,s)}(t)] \quad (3)$$

Note that each of the modes, or “particles” κ can be multidimensional. Indeed a key aspect of the G-MCTDH method is the combination of (potentially many) degrees of freedom in such multidimensional Gaussian particles.

Equations of motion for the time-dependent coefficients $A_J^{(s)}$, time-dependent single particle functions $\varphi_{j_{\kappa,s}}^{(\kappa,s)}$, and time-dependent Gaussian parameters $\Lambda_j^{(\kappa,s)} = \{\mathbf{a}_j^{(\kappa,s)}, \boldsymbol{\xi}_j^{(\kappa,s)}, \eta_j^{(\kappa,s)}\}$ can be derived *via* the Dirac-Frenkel variational principle [1], leading to

(i) the dynamical equation for the coefficient vector

$$i\dot{\mathbf{A}}^{(s)} = \left(\mathbf{S}^{(s)}\right)^{-1} \left[\sum_{s'} H^{(ss')} - i\boldsymbol{\tau}^{(s)} \delta(s - s') \right] \mathbf{A}^{(s')} \quad (4)$$

involving time dependent overlap (\mathbf{S}) and differential overlap ($\boldsymbol{\tau}$) matrices [1–3];

(ii) the dynamical equations in the “primary” subspace, which keep the same form as in conventional MCTDH,

$$i\dot{\boldsymbol{\varphi}}^{(\kappa,s)} = \left(1 - \hat{P}^{(\kappa,s)}\right) \left[\boldsymbol{\rho}^{(\kappa,s)}\right]^{-1} \sum_{s'} \hat{H}^{(\kappa,ss')} \boldsymbol{\varphi}^{(\kappa,s')} \quad (5)$$

(iii) the Gaussian parameter dynamics in the “secondary” subspace,

$$i\dot{\boldsymbol{\Lambda}}^{(\kappa,s)} = \left[\mathbf{C}^{(\kappa,s)}\right]^{-1} \mathbf{Y}^{(\kappa,s)} \quad (6)$$

$$\text{where } C_{j_{\alpha,l}\beta}^{(\kappa,s)} = \rho_{jl}^{(\kappa,s)} \left(S_{jl,\kappa}^{(s,\alpha\beta)} - \left[\mathbf{S}^{(s,\alpha 0)} \left(\mathbf{S}^{(s)} \right)^{-1} \mathbf{S}^{(s,0\beta)} \right]_{jl} \right)^{(\kappa,s)} \quad (7)$$

$$Y_{j_{\alpha}}^{(\kappa,s)} = \sum_{s'} \sum_l \left(\langle H_{jl,\kappa}^{(\alpha 0,ss')} \rangle_{jl} - \left[\mathbf{S}^{(s,\alpha 0)} \left(\mathbf{S}^{(s)} \right)^{-1} \langle \mathbf{H}_{jl}^{(ss')} \rangle \right]_{jl} \right)^{(\kappa,ss')} \quad (8)$$

For a single, multidimensional Gaussian in a given electronic state s and moving in a mean field generated by the primary modes, the classical-like equations of motion by Heller [10] are recovered. The multiconfigurational form leads to a coupling between the Gaussian functions, and is key for the exact description of the quantum dynamics [1–3].

3. S_2 – S_1 CONICAL INTERSECTION MODEL FOR PYRAZINE

To illustrate the potential of the hybrid method in describing the role of an intramolecular “bath” in the decay dynamics induced by a conical intersection, we consider the model of Ref. [7,8] for the S_2 – S_1 CI in pyrazine. Fig. 1 shows the wavepacket autocorrelation function $C(t) = \langle \Psi(0) | \Psi(t) \rangle$ for an increasing number of bath modes. G-MCTDH hybrid calculations for 4 core (primary) modes plus n_b bath (secondary) modes are compared with reference calculations by the standard MCTDH method.

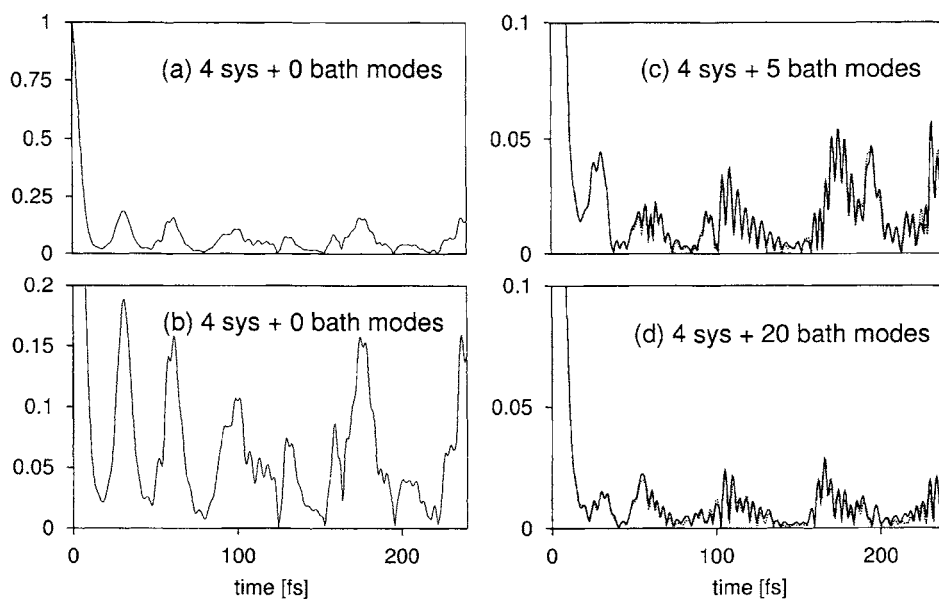


Fig. 1. The autocorrelation function $C(t) = \langle \Psi(0) | \Psi(t) \rangle$ is shown for a wavepacket initially prepared on the upper diabatic surface [7]. Panels (a) and (b): $C(t)$ for the four “core” modes calculated by the standard MCTDH method for the model Hamiltonian H_S of Eq. (9), shown on different scales in the two panels. Panel (c): G-MCTDH calculation (bold line) as compared with standard MCTDH calculation (dotted line) for the composite system with four core modes (combined into two 2-dimensional particles $\varphi_j^{(\kappa)}$) plus five bath modes (combined into two particles of dimensions 2 and 3, respectively). In the G-MCTDH calculation, the bath particles correspond to the multidimensional Gaussians $g_j^{(\kappa)}$ of Eq. (3); more specifically, the $g_j^{(\kappa)}$ s are of frozen Gaussian type [1–3], with the width matrix fixed. The number of functions n_κ per particle κ in the multiconfigurational form Eqs. (1)–(2) was $([19, 13]_{\text{core}}, [10, 10]_{\text{bath}})$ for S_1 , and $([11, 8]_{\text{core}}, [10, 10]_{\text{bath}})$ for S_2 , for both the G-MCTDH and MCTDH calculations. Panel (d): analogously to (c), results for the composite system with four core modes and 20 bath modes. The latter were combined into 5 multidimensional particles; the number of functions n_κ per particle were $([19, 13]_{\text{core}}, [5, 5, 5, 5, 5]_{\text{bath}})$ for S_1 and $([11, 8]_{\text{core}}, [5, 5, 5, 5, 5]_{\text{bath}})$ for S_2 .

The Hamiltonian underlying the calculations of Fig. 1 is based on a diabatic model potential [7–9] of system-bath type, $H = H_S + H_B$, where the “system” and “bath” parts are coupled *via* the conical intersection. Here, H_S refers to a four-mode core composed of three “tuning” type modes $\{Q_1, Q_2, Q_3\}$ and a coupling mode Q_4 ,

$$H_S = \sum_{i=1,3} \frac{\omega_i}{2} \left(-\frac{\partial^2}{\partial Q_i^2} + Q_i^2 \right) + \begin{pmatrix} -\Delta & 0 \\ 0 & \Delta \end{pmatrix} + \begin{pmatrix} 0 & \lambda \\ \lambda & 0 \end{pmatrix} Q_4 + \sum_{j=1,3} \begin{pmatrix} \kappa_j^{(1)} & 0 \\ 0 & \kappa_j^{(2)} \end{pmatrix} Q_j \quad (9)$$

while the bath part H_B includes tuning type (diagonal) contributions from the n_b oscillators constituting the intramolecular “bath”,

$$H_B = \sum_{b=1}^{n_b} \frac{\omega_b}{2} \left(-\frac{\partial^2}{\partial Q_b^2} + Q_b^2 \right) + \sum_{b=1}^{n_b} \begin{pmatrix} \kappa_b^{(1)} & 0 \\ 0 & \kappa_b^{(2)} \end{pmatrix} Q_b \quad (10)$$

Fig. 1 illustrates the very good agreement between the hybrid calculations and MCTDH reference calculations for the same number of configurations, for $n_b = 5$ vs. $n_b = 20$ bath oscillators. Despite the overall anharmonicity of the system, the calculations in general required no more Gaussian functions than conventional basis functions as used in the reference calculations.

4. CONCLUSIONS AND OUTLOOK

The G-MCTDH hybrid method provides a very general approach to system-bath type situations where the time scales of system vs. environment dynamics are similar, the system-bath coupling is not necessarily weak, and interaction potentials give rise to specific effects in the dynamics. The results of Fig. 1 illustrate that while the bath modes have an important effect in accelerating the decay of the autocorrelation function, they do not simply induce an exponential decay: Fine structure details appear in the autocorrelation function which are indicative of high-frequency components associated with long-lived resonance states [7]. This highlights the necessity of an explicit dynamical modeling of the bath. Beyond the intramolecular situation considered here, work is currently in progress to extend the method to solute-solvent type situations involving finite temperatures and dissipation.

REFERENCES

- [1] I. Burghardt, H.-D. Meyer, and L. S. Cederbaum, *J. Chem. Phys.*, 111 (1999) 2927.
- [2] G. A. Worth and I. Burghardt, *Chem. Phys. Lett.*, 368 (2003) 502.
- [3] I. Burghardt, M. Nest, and G. A. Worth, *J. Chem. Phys.*, 119 (2003) 5364.
- [4] U. Manthe, H.-D. Meyer, and L. S. Cederbaum, *Chem. Phys. Lett.*, 165 (1990) 73.
- [5] M. H. Beck, A. Jäckle, G. A. Worth, and H.-D. Meyer, *Phys. Rep.*, 324 (2000) 1.
- [6] G. A. Worth, M. A. Robb, and I. Burghardt, A novel algorithm for non-adiabatic direct dynamics using variational Gaussian wavepackets, *Faraday Discuss. Chem. Soc.*, submitted.
- [7] G. A. Worth, H.-D. Meyer, and L. S. Cederbaum, *J. Chem. Phys.*, 109 (1998) 3518.
- [8] S. Krempel, M. Winterstetter, H. Plöhn, and W. Domcke, *J. Chem. Phys.*, 100 (1994) 926.
- [9] H. Köppel, W. Domcke, and L. S. Cederbaum, *Adv. Chem. Phys.*, 57 (1984) 59.
- [10] S.-Y. Lee and E. J. Heller, *J. Chem. Phys.*, 76 (1982) 3035.

A simple approach for the calculation of femtosecond pump-probe spectra for electronically nonadiabatic systems

M.F. Gelin^a, A.V. Pisliakov^b, and W. Domcke^b

^aInstitute of Molecular and Atomic Physics, National Academy of Sciences of Belarus, 220072 Minsk, Belarus

^bInstitute of Physical and Theoretical Chemistry, Technical University of Munich, 85747 Garching, Germany

1. INTRODUCTION. A standard and universal description of various nonlinear spectroscopic techniques can be given in terms of the optical response functions (RFs) [1]. These functions allow one to perturbatively calculate the nonlinear response of a material system to external time-dependent fields. Normally, one assumes that the Born-Oppenheimer approximation is adequate and it is sufficient to consider the ground and a certain excited electronic state of the system, which are coupled via the laser fields. One then can model the ground and excited state Hamiltonians via a collection of vibrational modes, which are usually assumed to be harmonic. The conventional damped oscillator is thus the standard model in this case [1].

If the system under consideration possesses non-adiabatic electronic couplings within the excited-state vibronic manifold, the latter approach no longer is applicable. Recently, we have developed a simple model which allows for the explicit calculation of RFs for electronically nonadiabatic systems coupled to a heat bath [2]. The model is based on a phenomenological dissipation ansatz which describes the major bath-induced relaxation processes: excited-state population decay, optical dephasing, and vibrational relaxation. The model has been applied for the calculation of the time and frequency gated spontaneous emission spectra for model nonadiabatic electron-transfer systems. The predictions of the model have been tested against more accurate calculations performed within the Redfield formalism [2]. It is natural, therefore, to extend this

description to time and frequency resolved pump-probe (PP) signals. The details will be given elsewhere [3]. In the present contribution, we describe briefly the model and give explicit analytical expressions for the integral PP signal [1]. It is hoped that these simple formulas may be useful for a (at least) qualitative interpretation of observed PP spectra. The present work may be considered as an extension of the formulation of paper [4] towards nonadiabatic systems.

2. THE MODEL. We write the system Hamiltonian H as a sum of the Hamiltonians in the ground ($|g\rangle$) and excited ($|e\rangle$) electronic states, $H = |g\rangle h_g \langle g| + |e\rangle h_e \langle e|$. Furthermore, we assume that $|e\rangle$ consists of several coupled electronic substates $|\psi_q\rangle$, i.e. $|e\rangle = |\psi_1\rangle \otimes |\psi_2\rangle \dots \otimes |\psi_N\rangle$, $h_e = \sum_{p,q} |\psi_p\rangle h_e^{pq} \langle \psi_q|$. We further postulate the following kinetic equation for the density matrix $\rho(t) = \sum_{a,b=g,e} |a\rangle \rho_{ab}(t) \langle b|$

$$\partial_t \rho(t) = -\frac{i}{\hbar} [H(t), \rho(t)] - \frac{i}{\hbar} [H_{int}(t), \rho(t)] - (\Gamma_{el} + \Gamma_{vib}) \rho(t). \quad (1)$$

The first term in Eq. (1) describes the density matrix evolution under dissipation and field free conditions. The system-field interaction in the dipole approximation is given by

$$H_{int}(t) = -E(t) \sum_q \xi_q |g\rangle \langle \psi_q| + H.c.$$

Here $E(t)$ is a sum of the pump and probe pulses, and ξ_q^2 is the oscillator strength for the transition between the ground ($|g\rangle$) and excited ($|\psi_q\rangle$) electronic states. The damping operators are defined as follows [2]:

$$\Gamma_{el} \rho(t) = \xi_e |e\rangle \langle \rho_{ee}(t) \langle e| + \xi_{eg} (|g\rangle \langle \rho_{ge}(t) \langle e| + H.c.); \quad (2)$$

$$\Gamma_{vib} \rho(t) = \sum_{a=e,g} \nu_a (1 - \rho_a^B Tr) |a\rangle \langle \rho_{aa}(t) \langle a|. \quad (3)$$

Here Tr means the trace over vibrational (not electronic) coordinates, $\rho_a^B \equiv Z_a^{-1} \exp(-h_a/kT)$, and Z_a are the corresponding partition functions. The proposed damping operator consists of the two contributions, Γ_{el} and Γ_{vib} , which are responsible for the electronic and vibrational relaxation, respectively. The first term in the operator (2) reflects the excited-state population decay, so that $T_1 \equiv 1/\xi_e$ is simply the excited

state lifetime. The second term in (2) is responsible for the relaxation of electronic coherences, and $T_2 \equiv 1/\xi_{eg}$ is the corresponding optical dephasing time. Explicitly, $1/T_2 \equiv 1/(2T_1) + 1/\bar{T}$, where \bar{T} is the pure dephasing time. Γ_{vib} has been introduced to ensure vibrational relaxation of the density matrix in each electronic state to its equilibrium form, so that $\tau_a \equiv 1/\nu_a$ can be regarded as vibrational relaxation times ($a = e, g$).

3. PP SIGNALS. The model outlined in Sec. 2 allows one to express the non-linear RFs of a dissipative material system through those of the corresponding bath-free system [2]. These RFs can be directly applied for the calculation of various spectroscopic signals, in particular, PP signals. We have further made the following three explicit assumptions, which are discussed in detail in [2]: (i) the pump and probe laser pulses are well separated in time, so that the doorway-window (DW) formalism is applicable [1,2]; (ii) the pump and probe pulses of the frequency Ω_1 and Ω_2 are adequately described by exponential envelopes $E_i(t) = \exp(-\Gamma_i|t|)$ ($i = 1, 2$); (iii) the eigenvalue representation for the ground and excited state Hamiltonians is feasible:

$$h_g|n\rangle = E_n|n\rangle, \quad h_e|\alpha\rangle = E_\alpha|\alpha\rangle;$$

$$\rho_g^B(n) = Z_g^{-1} \exp\{-E_n/kT\}, \quad \rho_e^B(\alpha) = Z_e^{-1} \exp\{-E_\alpha/kT\}$$

(hereafter, the eigenvalues and eigenfunctions of h_g and h_e are denoted by Latin and Greek letters, respectively). The corresponding frequencies are defined as follows:

$$\omega_{\alpha n} = (E_\alpha - E_n)/\hbar, \quad \omega_{\alpha\beta} = (E_\alpha - E_\beta)/\hbar, \quad \omega_{nm} = (E_n - E_m)/\hbar.$$

These assumptions are sufficient to derive analytical formulas for the PP signals. Let us introduce the functions ($i = D, W$)

$$X_{\alpha\beta}^i(\Omega, \Gamma, \bar{\Gamma}) = \sum_{n,p} V_{np}^\alpha V_{np}^\beta Q_n^i \left\{ \frac{1}{\bar{\Gamma} - i\omega_{\alpha n}} \frac{1}{\bar{\Gamma} - i\omega_{\beta n}} + \frac{1}{2\Gamma - i\omega_{\alpha\beta}} \frac{1}{\bar{\Gamma} - i\omega_{\beta n}} + \frac{1}{2\Gamma + i\omega_{\alpha\beta}} \frac{1}{\bar{\Gamma} - i\omega_{\alpha n}} \right\} + c.c.,$$

$$X_{nm}^{i;pq}(\Omega, \Gamma, \bar{\Gamma}) = \sum_\alpha V_{np}^\alpha V_{mq}^\alpha Q_m^i \left\{ \frac{1}{\bar{\Gamma} - i\omega_{\alpha m}} \frac{1}{\bar{\Gamma} - i\omega_{\alpha n}} + \frac{1}{2\Gamma - i\omega_{nm}} \frac{1}{\bar{\Gamma} - i\omega_{\alpha n}} + \frac{1}{2\Gamma + i\omega_{nm}} \frac{1}{\bar{\Gamma} - i\omega_{\alpha m}} \right\} + c.c.,$$

$$X_g(\Omega, \Gamma, \bar{\Gamma}) = \sum_{n,p;\alpha} \frac{(V_{np}^\alpha)^2 \rho_g^B(n)}{\bar{\Gamma} - i\omega_{\alpha n}} \left\{ \frac{1}{\bar{\Gamma} - i\omega_{\alpha n}} + \frac{1}{\Gamma} \right\} + c.c.,$$

$$X_e(\Omega, \Gamma, \bar{\Gamma}) = \sum_{n,p;\alpha} \frac{(V_{np}^\alpha)^2 \rho_e^B(\alpha)}{\bar{\Gamma} - i\bar{\omega}_{\alpha n}} \left\{ \frac{1}{\bar{\Gamma} - i\bar{\omega}_{\alpha n}} + \frac{1}{\bar{\Gamma}} \right\} + c.c.$$

Here $V_{nq}^\alpha \equiv C_{nq}^\alpha \xi_{\alpha q}$, where C_{nq}^α are the expansion coefficients of the excited state eigenvectors in terms of the ground state vibrational eigenvectors ($|\alpha \rangle \equiv \sum_{n,q} C_{nq}^\alpha |n \rangle |\psi_q \rangle$) and

$$Q_n^i = \begin{cases} \rho_g^B(n), & i = D \\ 1, & i = W \end{cases}, \quad \bar{\omega}_{\alpha n} \equiv \Omega - \omega_{\alpha n}, \quad \bar{\Gamma}_k \equiv \Gamma_k + \xi_{eg} \quad (k = 1, 2).$$

Then the integral PP signal [1], which consists of a sum of the ground and excited state contributions $S(t, \Omega_1, \Omega_2) = S_g(t, \Omega_1, \Omega_2) + S_e(t, \Omega_1, \Omega_2)$, is described by the following expressions

$$S_e(t, \Omega_1, \Omega_2) = \sum_{\alpha,\beta} \left\{ X_{\alpha\beta}^W(\Omega_2, \Gamma_2, \bar{\Gamma}_2) e^{-(i\omega_{\alpha\beta} + \nu_e + \xi_e)t} X_{\beta\alpha}^D(\Omega_1, \Gamma_1, \bar{\Gamma}_1) \right\} + (1 - e^{-\nu_e t}) e^{-\xi_e t} X_e(\Omega_2, \Gamma_2, \bar{\Gamma}_2) X_g(\Omega_1, \Gamma_1, \bar{\Gamma}_1); \quad (4)$$

$$S_g(t, \Omega_1, \Omega_2) = \sum_{n,m;p,q} \left\{ X_{nm}^{W:ipq}(\Omega_2, \Gamma_2, \bar{\Gamma}_2) e^{-(i\omega_{nm} + \nu_g)t} X_{mn}^{D:iqp}(\Omega_1, \Gamma_1, \bar{\Gamma}_1) \right\} + (1 - e^{-\nu_g t}) X_g(\Omega_2, \Gamma_2, \bar{\Gamma}_2) X_g(\Omega_1, \Gamma_1, \bar{\Gamma}_1). \quad (5)$$

When there is a single bright excited electronic state $|\psi_p \rangle$, the summation over p and q disappears. The expressions for the dispersed PP signal are obtained similarly.

4. ACKNOWLEDGMENT. This work has been supported by the Deutsche Forschungsgemeinschaft through SFB 377. M.F.G. thankfully acknowledges support from the Alexander von Humboldt Stiftung.

REFERENCES

- [1] S. Mukamel, *Principles of Nonlinear Optical Spectroscopy* (Oxford University Press, New York, 1995).
- [2] M.F. Gelin, A.V. Pislakov and W. Domcke, *J. Chem. Phys.*, 118 (2003) 5287 .
- [3] M.F. Gelin, A.V. Pislakov and W. Domcke, to be published.
- [4] Yi. Yan and S. Mukamel, *Phys. Rev. A* 41 (1990) 6485.

Ultrafast charge separation and radiationless relaxation processes from S_2 excited electronic states of directly linked Zinc-porphyrin-acceptor dyads

Seiji Taniguchi^a, Noboru Mataga^a, Haik Chosrowjan^a,
Naoya Yoshida^b and Atsuhiko Osuka^b

^aInstitute for Laser Technology, Utsubo-Hommachi 1-8-4, Nishi-ku, Osaka, 550-0004, Japan

^bDepartment of Chemistry, Graduate School of Science, Kyoto University, Kyoto 606-8502, Japan

1. INTRODUCTION

Photoinduced electron transfer (ET) is one of the important fundamental processes underlying most photochemical and photobiological reactions. Among various factors regulating the photoinduced ET reactions, the energy gap law dependence is a diagnostic tool in testing ET theories. Recently we have attempted to utilize a large energy gap for charge separation (CS) from S_2 state of Zinc-porphyrin (Zn-5,15-bis (3,5-di-tert-butylphenyl)-porphyrin: ZP) to directly linked electron acceptor (a series of imide compounds abbreviated as I) to confirm unambiguously the existence of the inverted region. By means of the detailed femtosecond fluorescence studies on the series of ZP-I compounds in polar solvents such as tetrahydrofuran (THF), triacetin (GTA) and acetonitrile (ACN), we have succeeded in demonstrating unequivocally as the first example for the photoinduced CS reaction the bell-shaped energy gap law (EGL) with a distinct inverted region [1,2]. In addition, these results for EGL observed in polar solvents THF, GTA and ACN were reproduced satisfactorily by means of the Ulstrup-Jortner equation [3] assuming the nonadiabatic mechanism and the averaged single frequency $h\nu_m$ (intramolecular high frequency mode) coupled with CS reaction [1,2,4].

However, whether the k_{CS} (rate constant for CS) $\sim -\Delta G_{CS}$ relation could be reproduced satisfactorily by this equation in nonpolar or less polar solvents was not clear. On the other hand, it is important for the photochemistry of the higher excited state to elucidate the underlying mechanisms of their competing or associated processes ($S_2 \rightarrow S_1$ internal conversion (IC), charge recombination (CR), etc.) leading to the lower energy states.

In the present study, we have confirmed the modification of the EGL for the CS from S_2 induced by the change of solvent polarity by comparing the EGL in toluene (Tol) and methylcyclohexane (MCH) solution with that in THF. Moreover, we have compared the rate constants (λ_p) of the S_1 state formation by S_2 excitation with the decay rate constants (λ_r) of S_2 state in ZP-I series and examined also solvent polarity effects on these rate constants comparing THF with Tol or MCH solutions.

2. EXPERIMENTAL

Structural formulas of the ZP and ZP-I dyads are shown in Fig. 1. The absorption spectra of ZP-I dyads indicate that the excitation energies of the ZP S_2 and S_1 states are practically the same throughout the ZP-I series. The peak position of the Soret absorption band of the ZP-I dyads are only slightly red shifted from that of free ZP, and are practically the same as that of $ZnAr_3P$. These results indicate a rather weak D-A electronic interaction in the ground state of ZP-I systems despite of their directly linked structure, which can be ascribed to the nearly perpendicular conformation between ZP and I molecular planes [2].

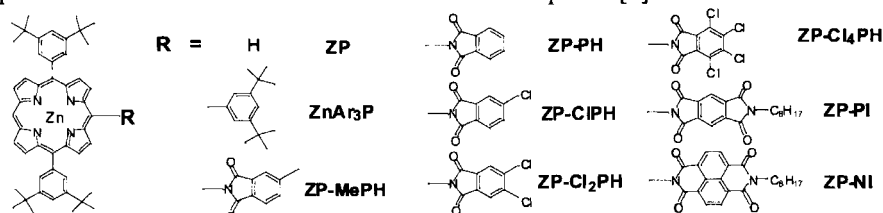


Fig. 1. Structural formulas of the ZP and I dyads

The measurements of the fluorescence dynamics were made by a femtosecond fluorescence up-conversion apparatus similar to that described elsewhere [2]. The *fwhm* of the instrumental response was ~ 110 fs. The polarization axis of the pump pulse was set at 54.7° with respect to the probe to suppress the anisotropy effects.

The calculation methods of the free energy gaps for CS from S_2 state ($-\Delta G_{CS}$) are given elsewhere [2]. For example, the $-\Delta G_{CS}/eV$ values in THF are: 0.56 for ZP-MePH, 0.57 for ZP-PH, 0.63 for ZP-ClPH, 0.68 for ZP-Cl₂PH, 0.88 for ZP-Cl₄PH, 1.15 for ZP-PI and 1.42 for ZP-NI.

3. RESULTS AND DISCUSSION

3.1. Comparison of the λ_f estimated from the S_2 fluorescence decay with the rate constants of the S_1 state production (λ_p) by S_2 excitation for the ZP-I series

The S_2 fluorescence dynamics of these systems (excitation at 405nm and monitoring at 435nm) undergoing ultrafast CS reactions in 100fs regime could be accurately reproduced by single exponential functions in all solvents examined here. Using the obtained decays τ , the rate constants k_{CS} have been determined by the equation $k_{CS} = \tau^{-1} - \tau_0^{-1}$, where τ_0 (~ 2.3 ps) is the lifetime of the S_2 state of ZP (or $ZnAr_3P$) monomer itself.

The S_1 fluorescence dynamics were measured under the condition of excitation at 423nm and monitoring at 640nm. In ZP (or $ZnAr_3P$), the slow rise components caused by $S_2 \rightarrow S_1$ Internal conversion (IC) were observed and the rise time (~ 2 ps) showed good agreement with the S_2 fluorescence decay time. In ZP-I systems except for ZP-NI, fast rise components with several 100fs lifetime were observed due to the S_1 state formation. The lifetimes of S_1 formation are nearly the same or slower (~ 200 fs) than those decay times of corresponding S_2 fluorescence. The S_1 fluorescence decay with the lifetime 1.3ps in THF and 2.4ps in Tol was observed for ZP-PI, which is caused by CS process in the S_1 state after the production of the S_1 state. In the case of ZP-NI, the observed rise of the S_1 fluorescence (~ 300 fs) was obviously faster than the decay time of S_2 fluorescence (~ 800 fs). On the contrary, the S_1 fluorescence decay time was nearly the same with the decay time of S_2 fluorescence. This result may be

interpreted as follows: The CS reaction from the S_2 state of ZP-NI is rather deeply in the inverted region, while the CS reaction from the S_1 state may be in the normal region near to the top region. Therefore, CS reaction from the S_1 state becomes considerably faster than that from the S_2 state. In this case, CS from the S_1 state will be observed as the S_1 fluorescence rise and the S_1 state formation will be observed as the S_1 fluorescence decay [4].

In Fig. 2, the rate constants of S_2 fluorescence decay ($\lambda_f=1/\tau$) and the inverses of S_1 fluorescence rise by S_1 state formation (λ_p) of ZP-I systems in Tol and THF are plotted against $-\Delta G_{CS}$. In Tol solutions, λ_p at the top regions are little bit delayed relative to λ_f , which shows that the charge recombination (CR) to the S_1 state after charge separation from the S_2 state is the main process for the S_1 formation in these systems. The results in MCH basically showed the same features with those in Tol (data not shown). On the other hand, λ_f and λ_p values are rather close in THF which seems to suggest the ultrafast S_1 state formation by CR from the vibrationally unrelaxed CS state in the course of the vibrational redistribution relaxation.

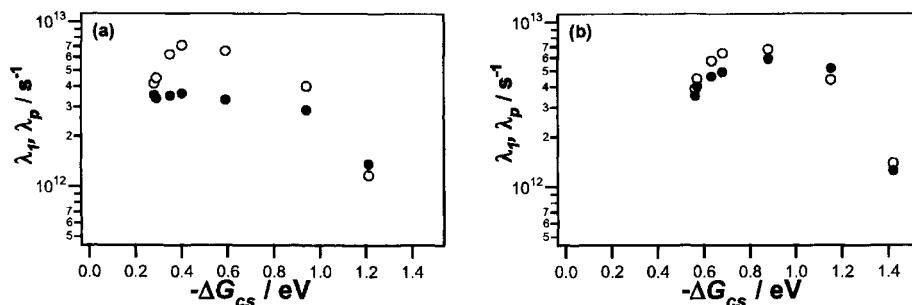


Fig. 2. The values of S_2 decay rate constant λ_f (●) estimated from the S_2 fluorescence decay times and the rate constant of the S_1 state formation λ_p (○) by S_2 excitation obtained from the S_1 fluorescence dynamics for ZP-I series in (a) Tol and (b) THF solutions plotted against $-\Delta G_{CS}$ values.

3.2. The k_{CS} vs. $-\Delta G_{CS}$ EGL for the CS reaction from the S_2 state of ZP-I series and its solvent dependencies: Comparative studies on MCH, Tol and THF solutions

In Fig. 3, observed k_{CS} values of ZP-I systems for the reaction from the S_2 state are plotted against $-\Delta G_{CS}$ in the case of the MCH, Tol and THF solutions. We have examined these results by means of the well-known Ulstrup - Jortner equation [3] assuming the nonadiabatic mechanism and the averaged single frequency $h\nu$ coupled with CS (eq.(1)).

$$k_{CS} = \sqrt{\frac{\pi}{\hbar^2 \lambda_s k_B T}} |V|^2 \sum_n (e^{-S} S^n / n!) \exp \left\{ -\frac{(\lambda_s + \Delta G + n\hbar \langle \omega \rangle)^2}{4\lambda_s k_B T} \right\} \quad (1)$$

where V is the D-A electronic tunneling matrix element, $S = \lambda_s / \hbar \langle \omega \rangle$ is the electron-vibration coupling constant, λ_s is the reorganization energy associated with the averaged angular frequency $\langle \omega \rangle$ of $h\nu$ and λ_s is the solvents reorganization energy.

The observed results in polar solvents THF can be well reproduced by this equation with reasonable parameter values. However, such satisfactory reproduction of the observed results including those in nonpolar or less polar solutions seems to be difficult. In Fig. 3, simulations by means of eq.(1) are shown for the observed results in MCH, Tol and THF solutions with

best fit parameters : $V = 0.022\text{eV}$, $\lambda_v = 0.31\text{eV}$, $\hbar\langle\omega\rangle = 0.15\text{eV}$, for all three solutions, $\lambda_v(\text{MCH}) = 0.078\text{eV}$, $\lambda_v(\text{Tol}) = 0.28\text{eV}$ and $\lambda_v(\text{THF}) = 0.56\text{eV}$. The solid line calculated with these parameters for THF solution agrees satisfactorily with the observed results. However, the calculated results for the MCH and Tol solutions seem to show an essential deviation from the observed one. Namely, the observed results in MCH and Tol solutions indicate that the EGL seems to extend over wider range of $-\Delta G_{CS}$ values than the calculated ones in the inverted region as shown by the broken lines in Fig. 3. This result in less polar solvents may be ascribed to a little change of the EGL for the CS reaction from S_2 state caused by the change of the solvent reorganization energy and EGL in MCH and Tol solutions may not be described by eq.(1) with single averaged hfm approximation but multi-mode approximation seems to be necessary. This means also that the EGL for the ultrafast photoinduced CS from S_2 state of the present ZP-I systems becomes somewhat resembled to that of the intramolecular radiationless transition (IC) in the weak coupling limit where the excited state potential energy surface is embedded in that of the lower state. Nevertheless, the extent of the crossing between the S_2 state and the CS state surfaces seems to be still considerable leading to the existence of the normal region in EGL, although it becomes less prominent compared with that in more polar solutions and the contribution of the inverted region extending over wider range of $-\Delta G_{CS}$ values becomes more prominent in less polar solvents. Such tendency in the EGL actually seems to be more enhanced in the nonpolar solvent MCH.

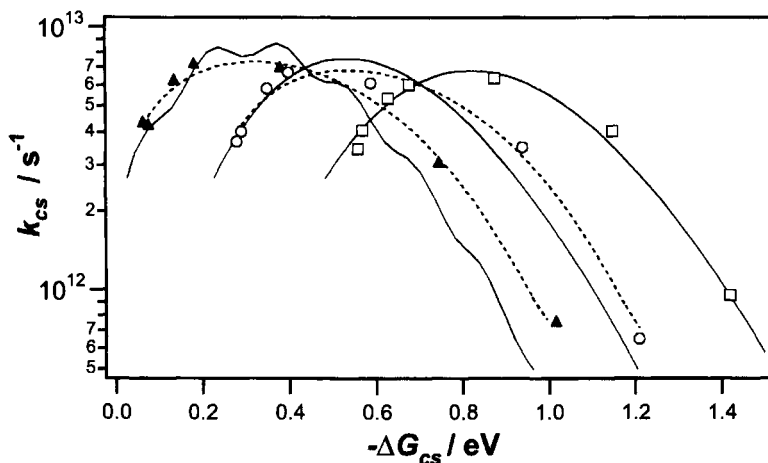


Fig. 3. k_{CS} vs. $-\Delta G_{CS}$ relations in MCH (\blacktriangle), Tol (\circ), THF(\square) and simulations (solid lines) with Ulstrup - Jortner equation (eq.(1)). The dashed lines are extrapolations just for eye guidance.

REFERENCES

- [1] N. Mataga, H. Chosrowjan, Y. Shibata, N.Yoshida, A. Osuka, T. Kikuzawa and T. Okada, *J. Am. Chem. Soc.*, 123 (2001) 12422.
- [2] N. Mataga, H. Chosrowjan, S. Taniguchi, Y. Shibata, N. Yoshida, A. Osuka, T. Kikuzawa and T. Okada, *J. Phys. Chem. A*, 106 (2002) 12191.
- [3] Ulstrup and J. Jortner, *J. Chem. Phys.*, 63 (1975) 4358.
- [4] N. Mataga, S. Taniguchi, H. Chosrowjan, A. Osuka and N. Yoshida, *Photochem. Photobiol. Sci.* 2 (2003) 493.

Femtosecond time-resolved studies on bimolecular electron transfer processes

S. Pagès, B. Lang and E. Vauthey

Department of Physical Chemistry, University of Geneva, 30 Quai Ernest Ansermet, CH 1211 Geneva, Switzerland

1. INTRODUCTION

Bimolecular photoinduced electron transfer between an electron donor and an electron acceptor in a polar solvent may result in the formation of free ions (FI). Weller and co-workers [1] have invoked several types of intermediates for describing this process (Fig. 1a): exciplex or contact ion pair (CIP), loose ion pair (LIP), also called solvent separated ion pair. The knowledge of the structures of these intermediates is fundamental for understanding the details of bimolecular reactions in solution. However, up to now, no spectroscopic technique has been able to differentiate them. The UV-Vis absorption spectra of the ion pairs and the free ions are very similar [2]. Furthermore, previous time resolved resonant Raman investigations [3] have shown that these species exhibit essentially the same high frequency vibrational spectrum.

Therefore, we have developed a pump/pump-probe experiment to obtain more informations on the structures of these geminate ion pairs. It allows the investigation of the excited states dynamics of the transient species at different time delays after photo-triggering the charge transfer, by monitoring the ground state recovery (GSR) of those transient species (Fig. 1b). In the present study, we have used perylene (Pe) as fluorescer (electron donor) and either trans-1,2-dicyanoethylene (DCE) or 1,4-dicyanobenzene (DCB) as quencher (electron acceptor) in acetonitrile (ACN).

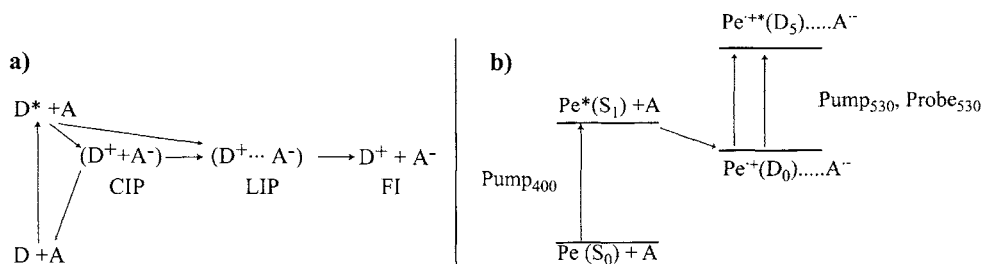


Fig. 1. a) Formation of the geminate ion pair upon electron transfer b) Energy diagram for ground state recovery measurements on the electron transfer product.

2. EXPERIMENT

The principle of the experiment is as follows: a first pump pulse at 400 nm (Pump_{400}) excites the electron donor (Pe) into its S_1 electronic state. After a variable time delay Δt_1 (up to 1 ns) a conventional pump-probe measurement is performed at 530 nm (Pump_{530} and Probe_{530}) on the ensuing transient species (Fig. 1b). It allows us to determine the GSR dynamics of the Pe^+ cation upon excitation in its $D_0 - D_5$ absorption band as a function of time delay after photo-triggering the charge transfer reaction, i.e. as a function of the ‘‘age’’ of the transient.

Pump_{400} is obtained from the frequency doubled output of a commercial amplified Ti:Sapphire system (Spectra-Physics). Its duration is about 100 fs. Pump_{530} and Probe_{530} are provided by a home-built non collinear optical parametric amplifier (NOPA) and have a duration of about 20 fs after compression. A classical detection scheme, synchronously chopping the pump beam and using reference photodiodes, improves the sensitivity of the set-up. This results in a resolution of relative transmission change of less than 10^{-4} . In all experiments, detection is achieved at the magic angle. With this set-up, a conventional two-color pump-probe experiment can be easily carried out as well.

3. RESULTS AND DISCUSSION

3.1. Pump_{400} - Probe_{530} measurements

Figure 2 shows the build-up of the ion pair population upon the electron transfer reaction. With DCE as quencher, the driving force of the electron transfer is $\Delta G_{\text{et}} = -0.54$ eV, whereas with DCB it is $\Delta G_{\text{et}} = -0.26$ eV. As shown in Fig. 2, the formation of the ion pair is faster when the reaction is more exergonic. This is in agreement with prediction of Marcus theory for the normal region ($-\Delta G_{\text{et}} < \lambda$) [4]. With DCB, the signal reaches a plateau within the first 200 ps and remains constant up to 1 ns. With DCE, we observe a rise of the signal within the first 20 ps corresponding to the formation of the cation followed by a decrease due to charge recombination of the geminate ion pairs. For this system, the free ion yield has been estimated to be of the order of 2 % while for the Pe-DCB system it amounts to 27 %. The faster charge recombination observed with DCE is due to the smaller driving force for the charge recombination ($\Delta G_{\text{CR}} = -2.31$ eV), compared with DCB ($\Delta G_{\text{CR}} = -2.59$ eV). This is in agreement with prediction of Marcus theory for the inverted region ($-\Delta G_{\text{CR}} > \lambda$).

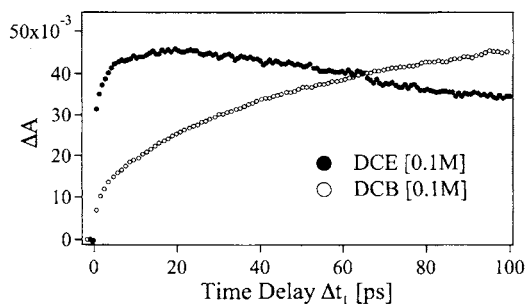


Fig. 2. Formation of the ion pair upon electron transfer quenching of Pe^* by DCB and DCE in ACN.

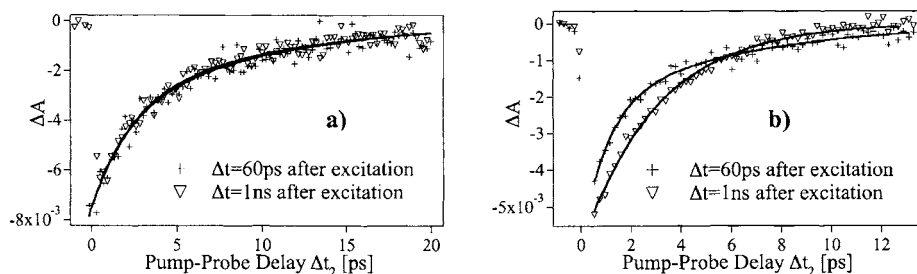


Fig.3. GSR of Pe^+ formed upon electron transfer quenching of Pe^* by a) DCE and b) DCB in ACN (see experimental section for details).

3.2. Pump₄₀₀ / Pump₅₃₀ - Probe₅₃₀ measurements

Figure 3 shows the GSR dynamics measured using the pump/pump-probe set-up. With DCE as quencher, the GSR dynamics can be well reproduced using a biexponential function ($A_1=0.5$, $\tau_1=2.2$ ps and $A_2=0.5$, $\tau_2=10$ ps). The time constants are independent of the “age” of the transient. In contrast, with DCB as quencher, the GSR kinetics fits better with a biexponential function ($A_1=0.62$, $\tau_1=1.1$ ps and $A_2=0.38$, $\tau_2=6.2$ ps) at short time delay between the 400-nm and 530-nm pump pulses, $\Delta t_1 < 100$ ps, whereas at long time delay $\Delta t_1=1$ ns it fits better with a monoexponential function ($\tau=3.0$ ps). The biexponential nature of the GSR dynamics implies the existence of two competing deactivation channels of the Pe^{+*} excited state (pathways 1 and 2+3 in Fig. 4): the first one is the relaxation from D_5 to D_0 by internal conversion (pathway 1). However, as long as the ions are in close contact, a charge recombination back to the initial, neutral excited state $\text{Pe}^*(S_1)$ is also possible (pathway 2). Charge recombination of ion pairs to an electronically excited product has recently been shown to be highly efficient [5,6]. Afterwards, a second electron transfer may occur and repopulate the D_0 state of the transient ion pair (pathway 3). This second pathway (2+3) could be responsible for the second observed relaxation time constant.

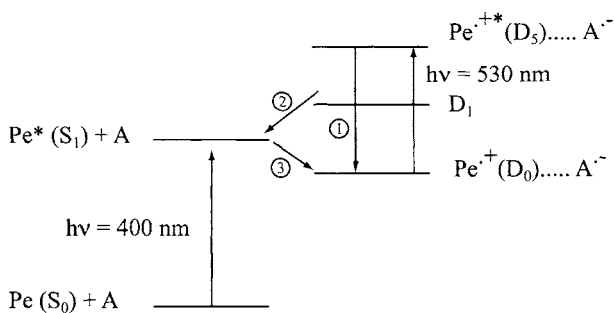


Fig.4. Possible mechanism for the GSR of Pe^+ in the complex.

The single exponential GSR dynamics measured with DCB at $\Delta t_1 = 1$ ns indicates the predominance of a single deactivation pathway for the excited cation. This might be due to the fact that most of the absorbance at 530 nm is due to “quasi-free ions”, i.e. pairs with a too large interionic distance for pathway 2+3 to be efficient. This is in agreement with the relatively large free ion yield found with this system. Thus the evolution of the GSR dynamics from biexponential to monoexponential should be due to an increase of the interionic distance.

When using DCE as quencher (Fig.3a), the second deactivation channel remains open until $\Delta t_1=1$ ns. The small free ion yield for this system indicates that charge recombination is much more efficient and therefore much more rapid than charge separation. Furthermore, we know from time resolved fluorescence decay measurements that electron transfer quenching is still not finished at $\Delta t_1=1$ ns. Consequently the absorbance should be dominated by “fresh” geminate ion pairs, over the whole timescale investigated. Thus, the GSR dynamics of Pe^+ in presence of DCE^- should be independent of Δt_1 , which is confirmed by our experimental observations.

4. CONCLUSION

This investigation shows that the GSR dynamics of Pe^+ can be used as a probe to monitor the time evolution of the ion pair formed upon electron transfer quenching. Indeed, at short interionic distance, an additional deactivation pathway of the excited cation, probably a back electron transfer to the excited reactant, is operative. Further experiments will be carried out to confirm this hypothesis. First, a three-color pump/pump-probe measurement will allow to probe the $\text{Pe}^*(\text{S}_1)$ population in order to see if the deactivation pathway 2+3 is really operative. Second, higher quencher concentrations have to be used in order to ensure faster formation of ET product and to make the interpretation of the data easier.

Although it is not yet possible to assign a spectroscopic fingerprint to a particular GIP structure, above results demonstrate the ability of our experiment to afford new informations about the ion pair dynamics.

- [1] A. Z. Weller, *Pure & Appl. Chem.*, 54 (1982) 1885.
- [2] N. Mataga, Y. Kanda and T. Okada, *J. Phys. Chem.*, 90 (1986) 3880.
- [3] E. Vauthey, A. W. Parker, B. Nohova and D. Phillips, *J. Am. Chem. Soc.*, 116 (1994) 9182.
- [4] R. A. Marcus, N. Sutin, *N. Biochim. Biophys. Acta*, 811 (1985) 265.
- [5] A. Morandeira, L. Engeli, E. Vauthey, *J. Phys. Chem. A*, 106 (2002) 4833.
- [6] P.-A. Muller, E. Vauthey, *J. Phys. Chem. A*, 105 (2001) 5994.

Ultrafast photoinduced charge transfer in fluorinated derivatives of DMABN

S. Murali^{a)}, P. Changenet-Barret^{b)}, C. Ley^{b)}, P. Plaza^{b)}, W. Rettig^{a)}, M.M. Martin^{b)} and A.I. Tolmachev^{c)}

^{a)} Institut für Chemie, Humboldt-Universität zu Berlin, Brook-Taylor-str. 2, D-12489 Berlin, Germany

^{b)} Département de Chimie, UMR CNRS-ENS 8640, Ecole Normale Supérieure, 24 rue Lhomond, 75231 Paris Cedex 05, France

^{c)} Institute for Organic Chemistry of the National Academy of Sciences of Ukraine, Murmanskaja 5, Kiev-94, 253660, Ukraine

1. INTRODUCTION

Dimethylaminobenzonitrile (DMABN) is the prototype system of molecules which form a Twisted Intramolecular Charge Transfer (TICT) state after optical excitation [1,2]. TICT states are revealed by their often considerably, solvent-polarity-induced, red-shifted emission with mostly forbidden character due to the twisted conformation of the emitting species. The energetics of TICT states are governed by the donor and acceptor strengths of the moieties on both sides of the twisted bond. In principle, with sufficiently strong donors and acceptors, the TICT state energy can be lowered very far below that of the spectroscopically relevant state in absorption, i.e. the locally excited (LE) state. Fluorine is a strong acceptor which exerts relatively little sterical hindrance. Its introduction into DMABN is expected to lower the TICT state energy considerably and thus to increase its formation rate. In order to check the charge transfer nature of the emitting state and tentatively measure its formation rate, time-resolved absorption spectroscopy has been employed in this investigation.

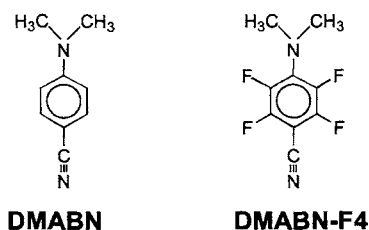


Fig. 1. Chemical structure of DMABN and DMABN-F4

2. EXPERIMENTAL

2.1. Materials

The structures of the investigated compounds and their abbreviations are shown in Fig. 1. The absence of impurity traces was confirmed by thin layer chromatography. All the solvents used were of Merck Uvasol quality.

2.2. Apparatus and methods

Absorption spectra were measured on an ATI UNICAM UV Series Spectrometer UV4-021113. An Aminco-Bowman Series 2 luminescence spectrometer was used for the fluorescence measurements.

Time-resolved transient absorption and gain experiments were performed by the pump-probe technique using a home-made dye laser described in details elsewhere [3]. Subpicosecond pulses were generated at 610 nm and frequency doubled in order to obtain excitation pulses at 305 nm. The probe was a white-light continuum produced by focusing the residual 610-nm beam in a 1-cm water cell. The differential absorbance spectra were recorded in the 340-700 nm range through a polychromator by a CCD camera. The spectra were averaged over 500 laser shots and corrected from the group velocity dispersion in the probe beam. The experimental time resolution was estimated to be about 1.5 ps.

3. RESULTS AND DISCUSSION

The absorption and fluorescence spectra of DMABN-F4 in solvents of low and high polarity are depicted in Fig. 2. The corresponding spectra of DMABN are also presented for comparison. Both absorption and fluorescence spectra of DMABN-F4 are red-shifted with respect to those of DMABN (300 nm instead of 282 nm and 456 nm instead of 341 nm, in hexane). The bathochromic shifts of fluorescence upon fluorine substitution are consistent with a strong charge-transfer (CT) character of the emitting state.

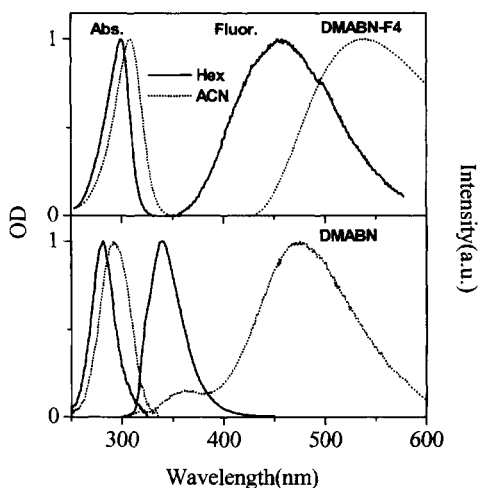


Fig. 2. Normalized absorption and fluorescence spectra of DMABN-F4 (up) and DMABN (down) in n-hexane and acetonitrile at room temperature.

The solvatochromism slope obtained for DMABN-F4, by applying the Mataga equation [4], is smaller than that of DMABN. This would be in line with the slightly smaller dipole moment expected for the TICT state of DMABN-F4 due to the effect of the fluorine atoms which attract the negative charge and change the charge distribution within the benzonitrile radical anion. Preliminary quantum yield and lifetime measurements indicate that the emission is forbidden and supports the formation of a TICT state in DMABN-F4 even in non-polar solvents. In acetonitrile, DMABN exhibits two fluorescence bands whereas DMABN-F4 exhibits only one single and red-shifted emission band (see Fig. 2). The excited-state equilibrium seems, thus, to be completely shifted to the CT state side even in alkanes. On this basis, a transient absorption spectrum corresponding to the radical anion of the acceptor part is expected at very short times [1,5].

The transient absorption spectrum of DMABN-F4 in acetonitrile, recorded at 1-ps delay shows an absorption band near 360 nm (Fig. 3a). This band can be attributed to the CT state by comparison with that reported for DMABN in acetonitrile at 100 ps (Fig. 3b). For the latter, both the LE state decay and CT state risetime were found to be 6 ps in time-resolved fluorescence measurements with a 4-ps time-resolution streak-camera [6]. From various studies, the CT formation time is now well known to be 4-6 ps [1] so that, at 100 ps, only the CT state is present. Fig. 3a shows that, for DMABN-F4, the CT state is populated in less than 1 ps in acetonitrile. We can thus conclude from the present observation that the access to the CT state for DMABN-F4 is significantly faster than for DMABN in acetonitrile.

In *n*-hexane, a similar band with a maximum at around 384 nm was observed with a comparably fast risetime, so that one can conclude that the photoinduced charge-transfer process in this fluorinated derivative is a quasi-barrierless process in both polar and non-polar solvents. Preliminary DFT calculations indicate that in vacuum DMABN-F4 is nonplanar in the ground state in contrast to DMABN [7]. The fact that the observed CT state absorption spectrum is blue-shifted compared to that of DMABN and of the benzonitrile anion radical (Fig. 3) might be an indication that the equilibrium geometry of the CT state of DMABN-F4 is different from that of the TICT state of DMABN or might be due to the influence of the four fluorine atoms.

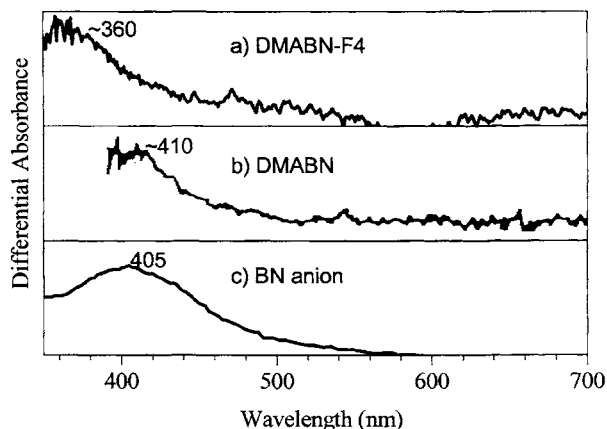


Fig. 3. (a) Transient absorption spectra of DMABN-F4 in acetonitrile at 1 ps (this work) compared to that of (b) DMABN in acetonitrile at 100 ps (reproduced with the permission of T. Okada [5]) and of (c) the stationary absorption spectra of the benzonitrile anion in tetrahydrofuran [8]

4. CONCLUSION

The present results indicate that DMABN-F4 emits a strongly red shifted fluorescence with a mostly forbidden character. In contrast to DMABN, the red-shifted fluorescence is also observed in non-polar solvents. Transient absorption measurements give evidence that the CT state is formed in less than 1 ps, in both acetonitrile and hexane. In acetonitrile, this is significantly faster (> 6 times) than for DMABN.

REFERENCES

- [1] Z.R. Grabowski, K. Rotkiewicz, W. Rettig, *Chem. Rev.*, 103 (2003) 3899.
- [2] W. Rettig, J. Mattay (ed.), *Topics in Current Chemistry*, Vol. 169 "Electron Transfer I", Springer Verlag, Berlin, 1994, 253.
- [3] N. Dai Hung, P. Plaza, M. M. Martin and Y. H. Meyer, *Appl. Opt.*, 31 (1992) 7046.
- [4] N. Mataga, N. Kubota, *Molecular interactions and electronic spectra*, Marcel Dekker Inc., New York, 1970.
- [5] T. Okada, N. Mataga and W. Baumann, *J. Phys. Chem.*, 91 (1987) 760.
- [6] P. Chagnenet, M. M. Martin, P. Plaza, Y. H. Meyer, *J. Phys Chem. A*, 101 (1997) 8186.
- [7] S. Murali, V. Kharlanov, A. I. Tolmachev, P. Chagnenet-Barret, C. Ley, P. Plaza; M. M. Martin, W. Rettig, in preparation.
- [8] T. Shida, *Electronic absorption spectra of radical ions*, Elsevier, Amsterdam, 1988, 239.

Influence of solute-solvent interactions on the quenching dynamics of perylene derivatives in an electron donating solvent

A. Morandeira, A. Fürstenberg and E. Vauthey

Department of Physical Chemistry, University of Geneva, 30 Quai Ernest-Ansermet, CH-1211 Geneva 4, Switzerland

1. INTRODUCTION

Electron transfer (ET) reactions play a key role in both natural (photosynthesis, metabolism) and industrial processes (photography, polymerisation, solar cells). The study of intermolecular photoinduced ET reactions in solution is complicated by diffusion. In fact, as soon as the latter is slower than the ET process, it is not anymore possible to measure k_{ET} , the intrinsic ET rate constant, directly [1]. One way to circumvent this problem, it is to work in a reacting solvent [2]. However, in this case, the relationship between the observed quenching rate constant and k_{ET} is not clear. Indeed, it has been suggested that several solvent molecules could act as efficient donors [3]. In this situation, the measured rate constant is the sum of the individual k_{ET} .

We present here our investigation of the influence of solute-solvent interactions on the quenching dynamics of perylene (Pe) and derivatives in an electron donating solvent, N,N-dimethylaniline (DMA) [4]. The electron acceptors and the donor solvent are shown in Fig. 1.

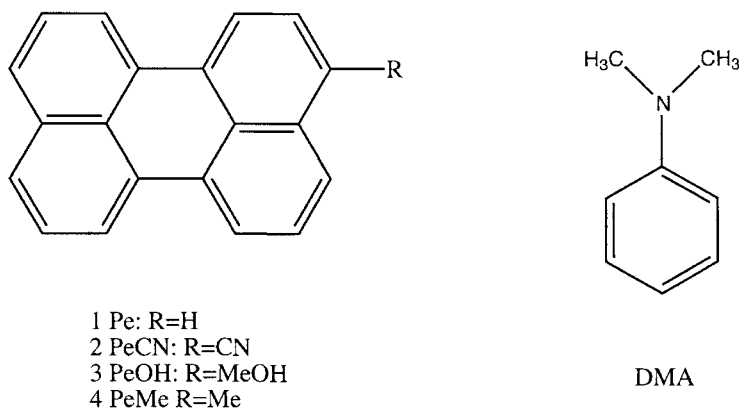


Fig. 1. Structures of the electron acceptors and the donor solvent

2. EXPERIMENTAL AND RESULTS

The fluorescence quenching of Pe and derivatives has been investigated by fluorescence upconversion. Excitation was performed with the frequency-doubled output of a Ti:Sapphire amplifier. The instrument response time was around 240 fs with 0.4 mm thick samples. The data were analysed by iterative reconvolution of the instrument response function with trial functions. For most samples, measurements were carried out at three different wavelengths (438, 475, and 490 nm). Global fits were done with all the available data.

In each case, the fluorescence of the acceptor was strongly quenched due to ET ($\tau_{fl} \approx 4$ ns in chlorobenzene in absence of quencher). Typical fluorescence decays and best multiexponential fits are shown in Fig. 2 and Table 1. The two major observations are [4]: the fluorescence decay is about 10 times faster with PeCN than with the other electron acceptors and the decays are highly non-exponential.

3. DISCUSSION: A THREE-DONOR TYPES MODEL

To interpret our data, we have developed a simple model which takes into account the orientation of the n donor molecules in the first solvent shell with respect to the acceptor. The donor molecules can be sorted into three types. Donors that are in an optimal position to quench the acceptor molecules (D_a), donors that have first to rotate (D_b) and those which need translational motion (D_c). Hence, the rate constant, k_q , for the fluorescence decay of an acceptor with a given solvent configuration is the sum of the individual ET rate constants with the donors of the first solvent shell

$$k_q = n_a k_{ET} + n_b k_R + n_c k_T + k_{fl} \quad (1)$$

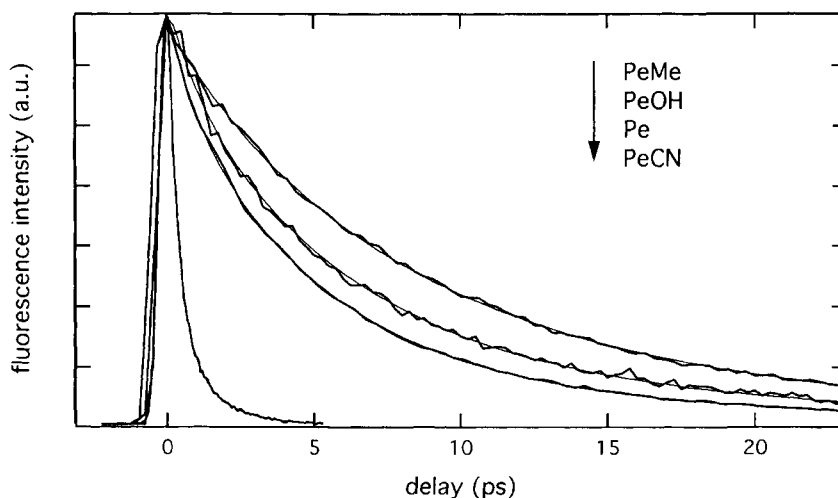


Fig. 2. Time-profiles of the fluorescence at 475 nm upon excitation at 400 nm of Pe, PeCN, PeOH and PeMe in DMA monitored by fluorescence upconversion and best triexponential fits.

where n_a , n_b and n_c are the number of donor molecules in an optimal position to quench the acceptor, the number of donor molecules which first need to reorientate and the number of donor molecules which need translational motion, respectively. k_R is the rotational rate constant of the solvent molecules. k_T is the translational rate constant of the solvent molecules. k_{fl} is the natural lifetime of the acceptor.

There are many possible arrangements of the donor molecules around the acceptors in solution. Consequently, the monitored fluorescence decay is non-exponential. The observed signal, $I(t)$, is the sum of the fluorescence decay of each possible arrangement weighted according to its probability to occur

$$I(t) = \sum_{i=1}^n P_i \exp(-k_{qi}t). \quad (2)$$

To test this simple model, we fitted the experimental data by means of Eq. 2 (for convenience, instead of the raw data, we used the best multiexponential fits). n , the number of donor molecules in the first solvent shell, k_R , and k_T , could be estimated. The other parameters, P_a, P_b, P_c (the probability of a donor molecule of being D_a, D_b or D_c respectively) and k_{ET} , the intrinsic ET rate constant, were obtained from the fit.

The model could reproduce well the fluorescence decays of Pe, PeCN and PeOH in DMA (see Fig. 3A and Table 2), giving a physical explanation to the much faster decay of PeCN. The k_{ET} is essentially the same for the three perylene derivatives, but n_a , that is, the number of molecules in an optimal position to quench the acceptor, is significantly larger for PeCN. This is in good agreement with the fact that the driving force of the ET reaction is almost the same for the four donor-acceptor pairs ($\Delta G_{ET} \approx -0.15$ eV).

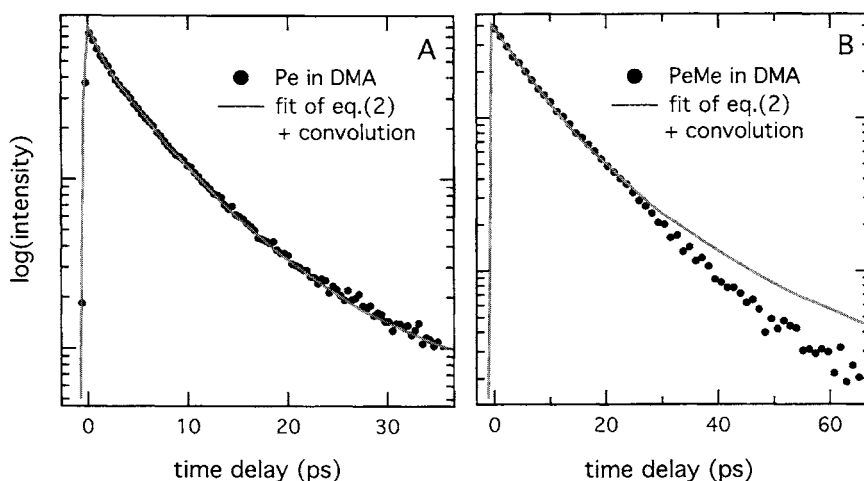


Fig 3. Comparison of the best fit of Eq. 2 with the triexponential function reproducing the decay of Pe (A) and PeMe (B) fluorescence in DMA.

Table 1

Amplitudes, A_i , and time constants, τ_i , obtained from a triexponential fit to the fluorescence decay of the acceptors in DMA and average lifetime, τ_{av} .

	A_1	τ_1	A_2	τ_2	A_3	τ_3	τ_{av}
		(ps)		(ps)		(ps)	(ps)
Pe	0.11	13.3	0.66	4.9	0.23	0.87	4.9
PeCN	0.01	2.5	0.13	0.97	0.86	0.30	0.42
PeOH	0.24	12.0	0.56	5.4	0.20	1.0	6.1
PeMe	0.68	11.4	0.32	4.7	-	-	9.3

Table 2

Parameters obtained from the fit of Eq. 2 to the fluorescence decay of the acceptors in DMA. In the calculations: $n=16$, $\tau_R=27$ ps and $\tau_T=800$ ps.

	τ_{ET} (ps)	P_a	P_b	n_a
Pe	1.1	0.016	0.303	<1
PeCN	1.3	0.232	0.476	3-4
PeOH	1.0	0.011	0.260	<1
PeMe	-	-	0.200	-

The failure of the model to reproduce satisfactorily the dynamics of PeMe (Figure 3B) can be attributed to its slower dynamics. Diffusional processes then become more relevant and our rough estimation of k_T , by means of the Stokes-Einstein expression, is probably not good enough. Much better agreement can be obtained when the translational diffusion coefficient is calculated with the semiempirical expression of Spemol and Wirtz [5].

The fact that PeCN is surrounded by a much larger number of optimal donors than the other acceptors must be due to its particular interactions with the solvent. PeCN has a higher permanent dipole moment than the other acceptors. Further, its dipole moment points from the aromatic plane towards the cyano group, while for DMA, the dipole moment points from the amino group to the aromatic ring. Consequently, a sandwich-type geometry between donor and acceptor is favoured. This configuration is known to be propitious to ET. For the other acceptors, dipole-dipole interaction is either negligible (Pe, PeMe) or it does not lead to a geometry favouring ET (PeOH). Hence, the probability of finding a donor in an optimal position is much lower.

5. CONCLUDING REMARKS

Dipole-dipole interactions between the reactants can strongly influence the dynamics of bimolecular ET reactions. Until now, this effect has been largely neglected.

According to our investigation, one should be very careful when identifying the quenching rate constant measured in pure donating solvents with the rate constant of bimolecular ET. This assumption was found to be valid with Pe and PeOH, but not with PeCN.

REFERENCES

- [1] S. Nishikawa, T. Asahi, T. Okada and N. Mataga, Chem. Phys. Lett., 185 (1991) 237.
- [2] K. Yoshihara, Adv. Chem. Phys., 107 (1999) 371 and references therein.
- [3] E. W. Castner, D. Kennedy and R. J. Cave, J. Phys. Chem. A, 104 (2000) 2869.
- [4] A. Morandeira, A. Fürstenberg, J.-C. Gumy and E. Vauthey, J. Phys. Chem. A, 28 (2003) 5375.
- [5] A. Spemol and K. Z. Wirtz, Naturforschung, 8a (1953) 522.

Effect of excitation wavelength on the charge recombination dynamics of excited donor acceptor complexes

O. Nicolet^a, A. I. Ivanov^b and E. Vauthey^a

^a Department of Physical Chemistry, University of Geneva, 30 Quai Ernest Ansermet, CH-1211 Geneva 4, Switzerland

^b Department of Physics, Volgograd State University, 2-nd Prodolnaya Str. 30, Volgograd, 400062, Russia

1. INTRODUCTION

An important rule of organic photochemistry is that the quantum yield of a photochemical reaction does not depend on the excitation wavelength. This rule, which is valid in most cases, is based on the very different timescales for relaxation (solvent and vibrational) and chemical reaction. However, when the chemical process is ultrafast and takes place in the sub-ps time domain, this separation is no longer valid and non-equilibrium reaction dynamics predominates. We have recently shown that the effects of driving force, solvent and temperature on the dynamics of charge recombination (CR) of a series of excited donor-acceptor complexes (DACs) can be well accounted for by a model where CR occurs while the excited state, a charge transfer (CT) state, relaxes to the equilibrium [1]. Non-equilibrium dynamics could also offer an alternative explanation to the absence of the normal region predicted by Marcus theory for weakly exergonic electron transfer (ET) reactions [2]. A prediction of this simple model, that was not tested in this previous study, is a dependence of the CR dynamics on the excitation wavelength. Indeed, the CR dynamics should depend on how far from equilibrium the excited state of the DAC, the CT state, is populated.

To test this idea, both theoretical and experimental investigations have been carried out.

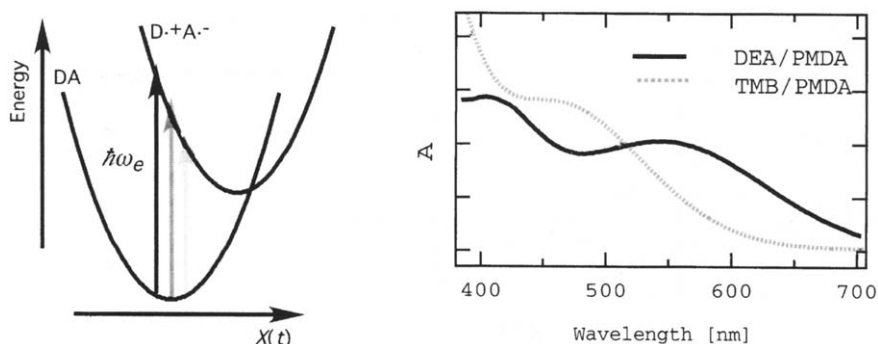


Fig. 1. (Left) Schematic representation of reactant and the product potentials for CR of a DAC; (right) Absorption spectra of DEA/PMDA and TMB/PMDA complexes in ACN.

2. THEORY

The CT excitation and the ensuing CR are described within the framework of the time-dependent perturbation theory in the electronic coupling V . The time dependent CR rate constant is [3]:

$$k_{CR}(t) = V^2 \frac{\sqrt{2\pi}}{\sigma(t)} \exp\left(-\frac{|Q^* - Q(t)|^2}{2\sigma^2(t)}\right) \quad (1)$$

where $Q^* = \Delta G + \lambda$, $Q(t) = 2\lambda(1 + kT\delta\omega_e / \sigma_0^2)X(t)$, $\sigma_0^2 = 2\lambda kT + \tau_e^{-2}$, $\delta\omega_e = \Delta G + \hbar\omega_e - \lambda$, $\sigma^2(t) = 2\lambda kT(1 - 2\lambda kTX^2(t) / \sigma_0^2)$, $X(t) = (\pi\lambda)^{-1} \int_0^\infty J(\omega)\omega^{-1} \cos\omega t d\omega$, ΔG is the driving force for CR, λ is the reorganisation energy, ω_e is the excitation pulse carrier frequency and $J(\omega)$ is the spectral density of the classical vibrational modes.

Because of the time dependence of the k_{CR} and of the non-exponential decay of the excited DAC population, the following time independent rate constant is used :

$$k_{eff}^{-1} = \int_0^{t_0} \exp\left[-\int_0^{t_1} k_{CR}(t_2) dt_2\right] dt_1 \quad (2)$$

where t_0 is the time after which the excited state population has decreased by a factor 100. Finally the magnitude of the spectral effect is defined as :

$$\phi = \left(k_{eff}(\omega_e^+) - k_{eff}(\omega_e^-)\right) / k_{eff}(\omega_e^-) \quad (3)$$

where ω_e^+ and ω_e^- are the frequencies at half maximum of the CT band. A positive spectral effect corresponds to an increase of k_{CR} with increasing ω_e .

In the simplest model investigated, including a single Debye mode ($X(t) = \exp(-t / \tau_L)$, τ_L being the longitudinal dielectric relaxation time), the spectral effect was found to be small and negative $-0.2 < \phi < 0$, with $V < kT$ and $\tau_L = 1$ ps. The stronger effect occurs at $-\Delta G = \lambda$.

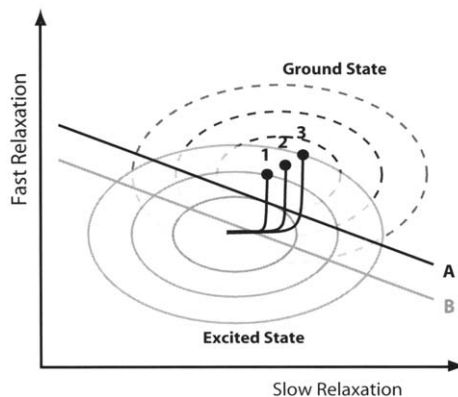


Fig. 2. Wavepacket trajectories on the excited free energy surface for a two Debye modes model. The term crossing line A and B are for weakly and moderately exergonic CR, respectively.

With two Debye modes with different relaxation times ($\tau_{L1} = 500$ fs and $\tau_{L2} = 10$ ps), the spectral effect can be positive or negative. A positive effect is predicted for weakly exergonic CR (see Fig. 2 A). Upon low frequency excitation, the wavepacket intersects the term crossing line while moving along the fast coordinate (trajectory 1). On the other hand, the slow coordinate is more involved upon high excitation frequency (trajectory 3). In the latter case, the wavepacket spends more time in the vicinity of the term crossing line and the system has a larger CR probability. The maximum positive effect should be expected in the vicinity of $-\Delta G = \lambda_2 - \lambda_1$, where λ_1 and λ_2 are the reorganisation energies associated with the fast and slow mode, respectively.

Qualitatively similar results are obtained from numerical calculations with a semi-classical model (hybrid model) including high frequency quantum modes and taking into account the contribution of inertial motion to solvent relaxation. The positive spectral effect is predicted in the normal regime, and this region becomes narrower and is shifted to lower exergonicity upon increasing V . On the other hand, the negative spectral effect is predicted in the inverted region.

A marked spectral effect requires a significant electronic coupling, i.e. a situation where the formalism used is no longer applicable. In order to extend the area of applicability a many mode generalisation of the stochastic approach [4] was applied. Both approaches give qualitatively the same results, although there are considerably quantitative differences.

3. EXPERIMENT

The DACs were composed of 1,2,4-trimethoxybenzene (TMB) or N,N-diethylaniline (DEA) as donors with pyromellitic dianhydride (PMDA) as acceptor. Two polar solvents with different relaxation dynamics were used: acetonitrile (ACN) with a solvation time of the order of 500 fs and valeronitrile (VaCN) with a solvation time of 4.7 ps. The absorption spectra of these two complexes are shown in Figure 1. The CR dynamics of the excited DACs were investigated using the multiplex transient grating technique [5]. Excitation was performed either at 400 nm with 100 fs pulses or between 485 nm and 585 nm using 45 fs pulses. White light pulses generated by self-phase modulation were used for probing.

Just after CT excitation of the DACs, the TG spectrum consists of a band centred at 670 nm (see Figure 3) and due to the radical anion of PMDA. Its decay, which can be reasonably well reproduced with a monoexponential function, is due to CR to the neutral ground state.

For the TMB/PMDA DAC in VaCN, a continuous and weak increase of the CR time constant with decreasing excitation wavelength (negative spectral effect) is observed (see Table 1). For this complex, excitation occurs predominantly via the low energy CT transition. For DEA/PMDA, a smaller but similar wavelength dependence, close to the limit of error, can be detected upon excitation in the low energy CT band. CR is unambiguously slower upon 400 nm excitation. At this wavelength, however, absorption is essentially due to the high energy CT band.

The presence of two CT bands is typical for complexes with mono-substituted benzenes. Upon substitution, the degeneracy of the HOMOs of benzene is lifted. Therefore, the two CT bands can be associated to two complexes with a distinct geometry. For the DEA/PMDA DAC, the substantially slower CR dynamics observed upon 400 nm excitation should be therefore due to the different geometry of the DAC rather than to the spectral effect. Such a slower CR dynamics might be related to a smaller V and/or to a larger driving force.

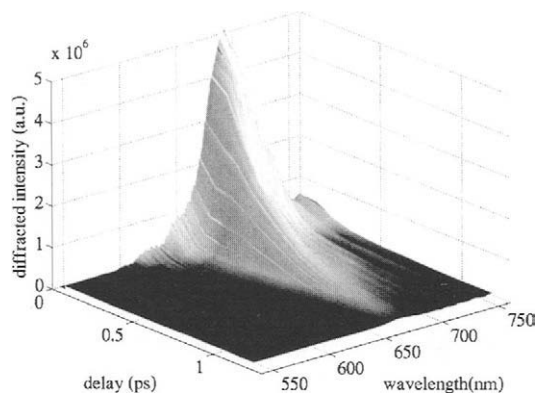


Fig. 3. Multiplex transient grating spectrum measured with the complex PMDA/DEA in ACN.

Table 1: Measured, k_{CR} , and calculated, k_{calc} , CR rate constants

DAC	Solvent	Excitation (nm)	k_{CR} (ps^{-1})	k_{calc} (ps^{-1})
TMB/PMDA	VaCN	400	1	--
		515	1.14	0.57
		530	1.31	--
DEA/PMDA	VaCN	550	1.47	0.64
		490	0.77	0.34
	ACN	540	0.83	0.38
		400	1.31	--
		485	2.38	1.09
	585	2.63	1.21	

Table 1 shows that the spectral effect measured in the low energy CT band is weak and negative. The k_{calc} values in the last column are the rate constants obtained from numerical calculations with the hybrid model. For these calculations, V was 0.025 eV, λ_{hf} and λ_{lf} , the reorganisation energies associated to the high and low frequency modes, were taken as 0.3 and 0.7 eV, respectively. These two values were estimated from the analysis of the CT absorption bands, using Hush theory. Finally, the driving force for CR amounts to -1.67 and -1.25 eV for TMB/PMDA and DEA/PMDA, respectively. Although the calculated values are about twice as large as those measured, the observed spectral effect is very well reproduced for DEA/PMDA. For TMB/PMDA, the agreement is not as good, the measured effect being larger by a factor of about 2 than that calculated. However, more measurements with other donor-acceptor complexes and solvents have still to be carried out to confirm these first results.

- [1] N. Mataga, H. Miyasaka, Adv. Chem. Phys., 107 (1999) 431 and references therein
- [2] O. Nicolet and E. Vauthey, J. Phys. Chem. A, 106 (2002) 5553
- [3] A.I. Ivanov, F. N. Belikeev, R. G. Fedunov, E. Vauthey, Chem. Phys. Lett., 372 (2003) 73
- [4] L. D. Zusman, Chem. Phys., 49 (1980) 295
- [5] C. Högeman, M. Pauchard, E. Vauthey, Rev. Sci. Instrum., 67 (1996) 3449

Time-resolved x-ray diffraction from small molecules in solution

M. Wulff^a, M. Lorenc^a, A. Plech^b, H. Ihee^c, S. Bratos^d, F. Mirloup^d and R. Vuilleumier^d

^aEuropean Synchrotron Radiation Facility, Grenoble Cedex 38043, BP 220, France

^bFachbereich Physik der Universitaet Konstanz, Universitaetsstrasse 10, D-78457 Konstanz, Germany

^cDepartment of Chemistry (School of Molecular Science - BK21), Korea Advanced Institute of Science and Technology, Daejeon, 305-701, Republic of Korea

^dLaboratoire de Physique Théorique des Liquides, Université Pierre et Marie Curie, Case courrier 121, 4, Place Jussieu, Paris Cedex 75252, France

We describe beamline ID09B at the European Synchrotron Radiation Facility (ESRF), a laboratory for optical pump and x-ray probe experiments to 100-picosecond resolution. The x-ray source is a narrow-band undulator, which can produce up to 1×10^{10} photons in one pulse. The 3% bandwidth of the undulator is sufficiently monochromatic for most diffraction experiments in liquids. A Ti: sapphire femtosecond laser is used for reaction initiation. The laser runs at 896 Hz and the wavelength is tunable between 290-1160 nm. The doubled (400 nm) and tripled wavelength (267 nm) are also available. The x-ray repetition frequency from the synchrotron is reduced to 896 Hz by a chopper. The time delay can be varied from 0 ps to 1 ms, which makes it possible to follow structural processes occurring in a wide range of time scales in one experiment.

We present a preliminary study on the structural dynamics of photo-excited iodine in methanol. At early time delays after dissociation, 1 – 10 ns, the change in the diffracted intensity $\Delta S(q, \tau)$ is oscillatory and the high- q part $4 - 8 \text{ \AA}^{-1}$ is assigned to free iodine atoms. At later times, 10-100 ns, expansive motion is seen in the bulk liquid. The expansion is driven by energy released from the recombination of iodine atoms. The $\Delta S(q, \tau)$ curves between 0.1 and 5 μs coincide with the temperature differential dS/dT for static methanol with a temperature rise of 2.5 K. However, this temperature is five times greater than the temperature deduced from the energy of dissociated atoms at 1 ns. The discrepancy is ascribed to a short-lived state that recombines on the sub-nanosecond time scale.

1. INTRODUCTION

The high intensity of x-ray beams from modern synchrotrons has made it possible to conduct optical pump and x-ray probe experiments to a time resolution of 100 ps, i.e. the limit given by the x-ray pulse length of a synchrotron. In these machines, the brightest

beams are produced by undulators. An undulator is an array of magnets that produce an oscillating magnetic field in a straight section of the synchrotron. The magnetic field forces the electrons into a “slalom”-like motion. Polychromatic flashes of x-rays are produced at the turning points, and the emission from successive turning points interferes. The interference frequency, or x-ray frequency, is determined by the time it takes for an electron to run through one period in the orbit [1]. The interference boosts the intensity at the given frequency and the spectral bandwidth becomes narrower [2]. Note that the interference is a *single-electron* effect, i.e. the emission from several electrons in a bunch adds incoherently. The spectrum of the U17 undulator in beamline ID09B at the ESRF is shown in Fig. 1. The figure gives the spectral flux produced by one bunch of 2×10^{11} electrons.

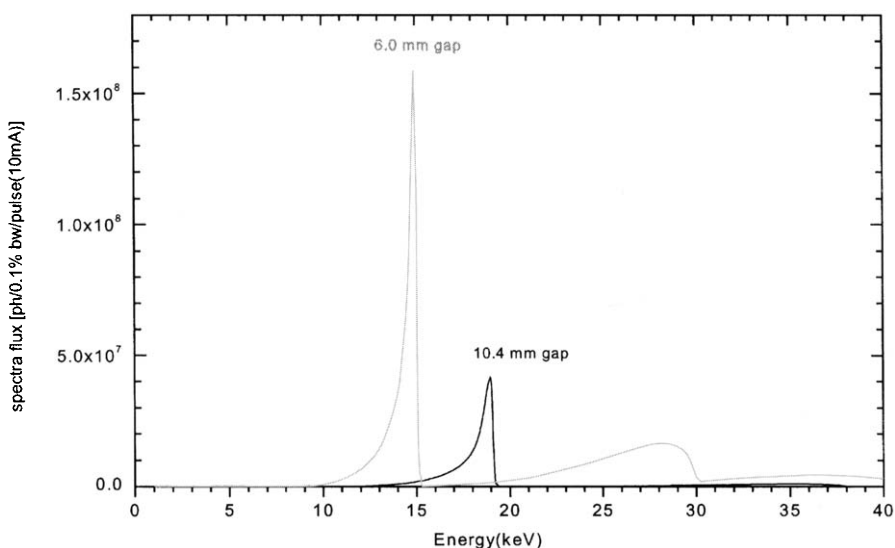


Fig. 1. Spectra from the U17 undulator. The red curve is the 6.0 mm gap spectrum used for Laue diffraction from proteins and the black curve, the 10.4 mm gap spectrum used for liquid experiments.

The weakest point in synchrotron work is the relatively poor time resolution of 100 ps. This time scale is 10^3 – 10^4 longer than the chemical time scale set by the formation and breakage of bonds. Laser-driven plasma sources can generate sub-picosecond x-ray pulses, but their 4π emission makes it difficult to focus more than 5×10^4 photons per pulse on a small sample. That restricts its application to strongly scattering samples, for example, Bragg diffraction from laser-excited surfaces of semiconductors. Non-thermal melting was recently studied using a plasma source [3]. The X-ray Free Electron Laser (XFEL) will eventually produce 100 fs x-ray pulses of tremendous intensity and spectral purity, but we

will have to wait until 2008 for the first prototype, which is being designed at SLAC in Stanford (the LCLS project).

An alternative structural probe is electron diffraction, which can be used to measure the structural change of gas molecules. The time resolution of this technique may be as low as a few picoseconds. In Table 1, we compare electron diffraction to x-ray diffraction. The relative scattering cross-section of electrons is about million times higher than that of x-rays [4]. This makes electron diffraction the method of choice for gas-phase studies [5]. Fortunately, one can make up for the deficiency by increasing the x-ray flux. Thus, a state-of-the-art DC electron gun can generate $\sim 10^4$ electrons in a bunch with a pulse length of a few picoseconds [5], while the ID09B beamline can produce $\sim 10^9$ - 10^{10} x-ray photons per pulse. Therefore, with the same repetition rate, the overall scattering power of electrons is 10 to 100 times higher than that of x-rays. However, the number of solute molecules in time-resolved x-ray diffraction in solution is 10 to 1000 times higher than that in ultrafast electron diffraction in the gas phase, thus resulting in the same overall signals from solute molecules. One big difference is that the gas-phase sample in electron diffraction is free from the background from the solvent, which constitutes the major part of the total signal in a liquid. This huge background complicates the data processing and analysis, but in the end, it gives us valuable information about the solvent change, which is absent in gas-phase electron diffraction. The consequence of the high scattering cross section of electrons is its low penetration depth, which makes difficult the application of electron diffraction to typical liquid samples. By comparison, prospective parameters for the future XFEL (TESLA) is also listed and one can see that XFEL will provide at least 10 times more signal with femtosecond time resolution.

Table 1

Comparison between ultrafast electron diffraction (UED), x-ray diffraction (UXD), and the prospective X-ray Free Electron Laser (XFEL)

	UED	UXD	XFEL
Relative scattering power	10^6	1	1
Number of scattering particles	4×10^4 / pulse	10^9 / pulse	10^{12} / pulse
Repetition rate	1 kHz	900 Hz	10 Hz
Overall scattering power	10 ~ 100	1	10
Number of solute molecules	$\sim 10^{11}$	$10^{12} \sim 10^{14}$	$10^{12} \sim 10^{14}$
Overall relative signal from solute	1	1 ~ 10	10 ~ 100
Background from solvent	none	huge	huge
Pulse width	1-5 ps	60-120 ps	100 fs
q-range	1.5 – 18.5 \AA^{-1}	0.2 – 15 \AA^{-1}	0.2 – 15 \AA^{-1}

We have used x-ray diffraction in our laboratory to probe transient structures of laser-excited liquids, small-molecule crystals and protein crystals. The diffraction patterns are recorded on a CCD detector that makes efficient use of most of the diffracted x-rays. Several experimental protocols have been developed: Laue diffraction from proteins [6-8], small-molecule diffraction [9,10] and diffraction from liquids [2,11,12]. In proteins, the

narrow-bandwidth Laue method has greatly improved the data quality and outclassed the traditional wiggler approach [13]. As a new application, Laue diffraction was recently used in a study of laser excited iodine in CCl_4 where the 3% bandwidth provides a good compromise between q -resolution and flux. This is due to the natural positional and orientational dispersion in a liquid [14]. The exposure time in a liquid experiment is typically 10 seconds, 500-1000 times shorter than an equivalent monochromatic exposure. As a result, we can now collect complete structural data of a chemical reaction in solution in 2 – 3 hours per sample. We will briefly describe the x-ray source and its optics.

2. THE X-RAY SOURCE

The straight sections in the ESRF storage ring can accommodate three 1.6-m long in-air undulators, or two 2.0-m long in-vacuum undulators. The in-air undulators operate at 11.0-mm gap, the in-vacuum undulators at 6.0 mm. In the in-vacuum undulator, the magnets are brought much closer to the electron beam. That increases the magnetic field and hence the acceleration of the electrons. With an in-vacuum undulator in a high-energy synchrotron as the ESRF, it is possible to raise the fundamental energy to 15-20 keV with fairly weak higher harmonics, see Fig. 1. This mono-harmonic feature comes at the expense of tunability (low K). The fundamental of the U17 device is 15.0 keV (0.83 Å) at 6 mm gap and 20.3 keV at 20 mm gap. The undulator parameters are shown in table 2. The U46 in-air undulator will be replaced in January 2005 by a U20 in-vacuum undulator, with a fundamental energy of 9.0 keV.

Table 2

Undulator parameters as of October 2003. E_f is the undulator fundamental, E_c the critical energy of the bending magnet radiation in the "slalom" motion.

period (mm)	poles	minimum gap (mm)	B_{\max} (T)	E_f (keV)	E_c (keV)	K	P (W/200 mA)
17	236	6.0	0.544	15.03	13.2	0.86	450
46	71	16.0	0.643	0.64	15.6	2.76	289

3. THE X-RAY OPTICS

The first optical element in the raw polychromatic beam is the channel-cut monochromator. It is a two-bounce monochromator cut from a monolithic piece of silicon. The diffracting surface is (111) which gives a band pass $\delta E/E = 1.4 \times 10^{-4}$. The energy can be varied between 4 – 50 keV. The next element is the cylindrical focusing mirror. Gravity bends the mirror into a toroid with a meridional curvature of 9.9 km, which is needed to focus on the sample, 22 m downstream. The incidence angle is 2.722 mrad. The mirror surface is coated with platinum that reflects in the range 0 – 27 keV. The meridional curvature is fine tuned by a stepper motor acting from below the mirror. The slope-error of the optical surface is as low as 0.67 μrad (rms) in the 450-mm central zone. That gives a focal spot as small as 0.10 x 0.06 mm^2 in the horizontal and vertical direction respectively.

Finally we are installing second monochromator based on multilayer optics (ML). The aim is to make better use of the polychromatic spectrum from the undulator. By varying the Bragg angle of the second ML, the bandwidth can be tuned between 0.2 – 2.0%. It will be installed side by side with the channel-cut monochromator. The multilayers are deposited on flat blocks of silicon with a slope error of 0.4 μ rad (rms). The system will be cryogenically cooled. There will be two ML stripes with the compositions Ru/Al₂O₃ (d = 40 Å, 10-20keV) and Ir/Al₂O₃ (d = 25.5 Å, 20-32 keV). The ML optics will also suppress the second harmonic. Note that ML optics together with the U20 undulator will give access to the polychromatic beam from higher harmonics of the undulators, which otherwise can not be used in polychromatic experiments. The q range will increase from 9 to 15 Å⁻¹. The flux numbers are shown in Table 3.

Table 3

Flux numbers for pump and probe experiments at 15 keV (U17).

Beamline configuration	Single-pulse flux ph/pulse (10mA)	Flux at 896.6 Hz ph/s (10mA)
Mirror (white beam)	1.1×10^{10}	9.6×10^{12}
Multilayers + mirror	1.7×10^9	1.5×10^{12}
Monochromator + mirror	2.4×10^7	2.2×10^{10}

4. THE RECOMBINATION OF IODINE IN SOLUTION

As an example of a time resolved diffraction experiment, we will describe the dissociation and recombination of molecular iodine in solution using the standard model developed by Harris [15] and others. The interaction energy of two iodine atoms in the gas phase is shown in Fig 2. If the solvent is chemically inert, as in the case of CCl₄, this potential is a good starting point. The I₂ molecule is first excited to a mixture of the B and ¹π_u state by a pulse of green light (530 nm, 2.340 eV, 150 fs). Calculations of the transition matrix elements show that the B and ¹π_u states are populated as 5.2 : 1 [16]. Both curves are initially repulsive and the molecule moves apart. After a few collisions in the cage, the majority of atoms recombine (geminate recombination); others escape as atoms. The separated atoms recombine diffusively in 10-100 ns (non-geminate recombination). The collisions with the cage cool the excited molecules and the molecules relax towards the minima on either the X or the A/A' curve. The molecules that relax along the X potential are cooled in a process called vibrational cooling, which takes 50 – 200 ps depending on the solvent. The A/A' molecules relax to a meta-stable state with a bond length of 3.0 Å. The lifetime of the A/A' state depends on the polarity of the solvent; it varies from 60 ps in alkane solvents to 2.7 ns in CCl₄. We expect that the A/A' state decays to the ground state via collisions with the solvent that expand the molecule to the cage boundary. Here the energy-gap to the ground state is smaller which facilitates curve crossing to the ground state [17,18].

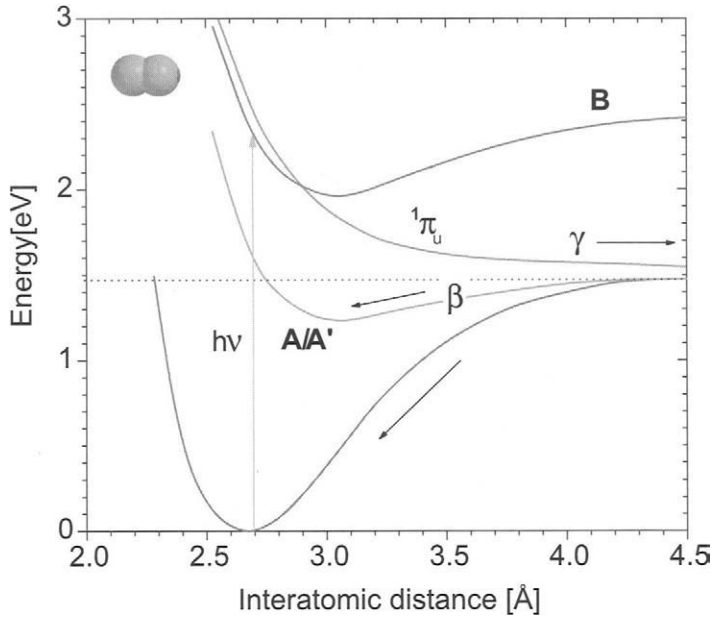


Fig. 2. The energy of two iodine atoms as a function of their distance.

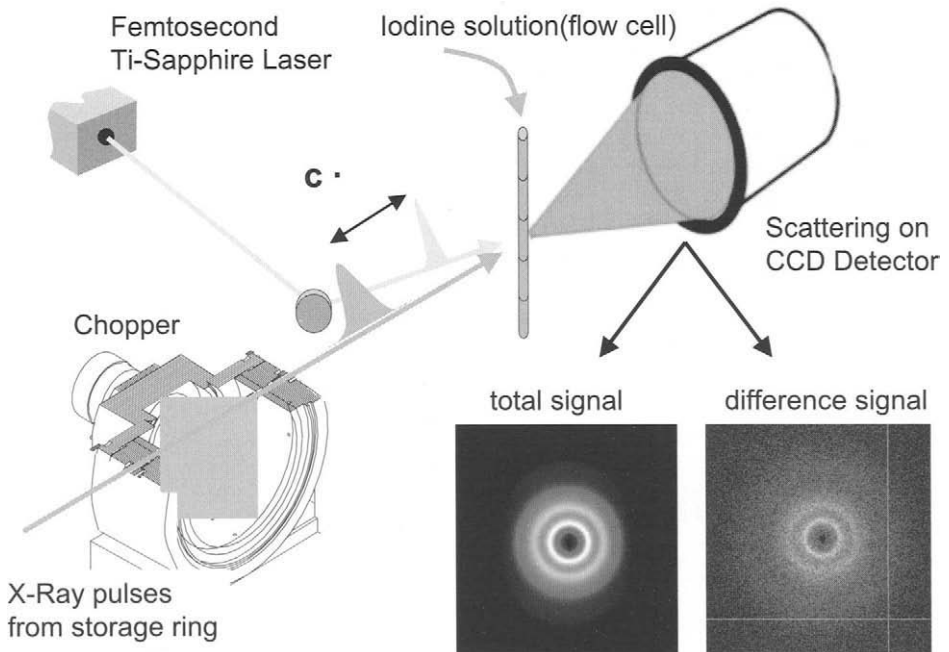


Fig.3. The laser pump and x-ray pump set-up on beamline ID09B.

The diffracted intensity from the solute and the solvent is recorded on a CCD detector in an angular dispersive way, see Fig. 3. The detector is a 16-bit MARCCD with a diameter of 132 mm. The intensity $S_{\text{tot}}(q, \tau)$ is measured as a function of the scattering vector q and the time delay τ . Note that $q = 4\pi \sin(\theta)/\lambda$, where 2θ is the scattering angle and λ the x-ray wavelength. The intensity has two contributions: elastic scattering (diffraction) $S_{\text{elas}}(q, \tau)$ and inelastic Compton scattering $S_{\text{inelas}}(q, \tau)$. The Compton scattering is an atomic property, and thus independent of changes in molecular structure [19,20]. Consequently the Compton contribution cancels out in the difference, i.e. $\Delta S_{\text{tot}}(q, \tau) = \Delta S_{\text{elas}}(q, \tau)$ for patterns with and without laser excitation.

The diffracted intensity from a molecule in the gas phase is expressed by the Debye Equation [21]:

$$S(q) = I_0 r_0^2 P \sum_{n,m} f_n(q) f_m(q) \frac{\sin(q r_{nm})}{q r_{nm}}.$$

Here I_0 is the intensity of the x-ray beam, $r_0 = e^2/mc^2$ is the classical electron radius (2.82×10^{-15} m). $P(\theta, \phi)$ is the polarization of the x-rays; it depends on the angle between the polarization and the scattering vector. For horizontally polarized x-rays, it takes the form $P(\theta, \phi) = 1 - \sin^2 2\theta \sin^2 \phi$, where 2θ is the scattering angle and ϕ the azimuthal angle with respect to the vertical direction. The formfactor $f(q)$ is the Fourier transform of the atomic electron density:

$$f(q) = \int_0^\infty 4\pi r^2 \rho(r) \frac{\sin(qr)}{qr} dr.$$

We note that the sum above is over all pairs of atoms in the molecule and that the intensity decreases as r_{ij}^{-1} ; the interference length is relatively long-range. The scattered intensity in the forward direction $q = 0$ reduces to:

$$S(q = 0) = I_0 r_0^2 \left(\sum Z_n \right)^2,$$

where Z_n is the number of electrons in atom n . The forward scattering is the coherent scattering from all the electrons in the molecule. If we consider the reaction $I_2 \rightarrow 2 I$, the difference intensity between dissociated and non-dissociated states is proportional to $2Z^2 - 4Z^2 = -2Z^2$. The negative intensity change in the forward scattering is normally the signature of dissociation.

The intensity from a diatomic molecule is:

$$S(q) = 2I_0 r_0^2 P(\theta, \varphi) f_I^2(q) \left(1 + \frac{\sin(qr(I-I))}{qr(I-I)} \right),$$

where $r(I-I)$ is the bondlength 2.666 \AA of gas-phase iodine. The first stage in the data analysis is usually to fit the high- q difference data to a gas-phase expression for the molecular change (see later).

The concentration of iodine should be optimized, if possible, to give the highest possible signal to noise in the difference pattern. If we neglect x-ray absorption (thin sample & high x-ray energy) and if the laser absorption follows Beer-Lambert's law (no saturation), one can show that the optimal signal to noise is obtained for an optical density

OD of ~ 0.55 for a parallel geometry of the laser and x-ray beams. By definition, $OD = \epsilon \cdot c \cdot t$, where ϵ is the molar-extinction-coefficient at the excitation wavelength, c the concentration and t the sample thickness. If iodine is excited at the peak of the absorption band at 530 nm, $\epsilon = 81 \times 10^3$ liter/mole/m, $t = 3 \times 10^{-4}$ m, the optimal concentration is $c = 0.022$ mole/liter. The concentration of liquid CCl_4 is 10.4 mole/liter. That gives a ratio of I_2 to CCl_4 of 1: 471. This highlights the prime difficulty in liquids: the signal to background is always small and that requires an intense x-ray beam. In a recent study of I_2 in CCl_4 , the difference signals were 10^{-2} - 10^{-4} of the solvent background.

We will now examine the difference spectra from iodine in methanol (CH_3OH) at 75 mM concentration. Iodine makes a charge transfer with oxygen [22], and the excited-state structure is not known. The charge transfer shifts the absorption peak from 530 nm to 445 nm. In practice we can excite the complex with 400 nm light from the second harmonic of the Ti: sapphire laser. Note that the solvent background is fairly weak due to its low effective Z value. The U17 undulator was operated at 9.0 mm gap at a fundamental energy of 18.2 keV. The spectrum was measured and the effective energy of the experiment calculated as the centre of mass (COM) of the photon-energy distribution. The COM calculation includes all known absorptions (windows, air, capillary, sample and detector). That gives an E_{COM} of 17.55 keV (0.706Å). The x-rays were focused to 0.10×0.06 mm² and the slits before the sample set to 0.10×0.07 mm². The flux on the sample was 2×10^{11} ph/s and the exposure time ~ 5 s per frame. The liquid sample was pumped through the focal point in a capillary and the flow speed adjusted to have a fresh sample for every new x-ray pulse. The ground state of the sample was recorded as a negative time delay (reference) at -3ns. The CCD images were collected in pairs of negative (reference) and positive time delays in order to check for drifts. The exposure time was scaled to the synchrotron current; the detector was always exposed to the same level. The detector was placed 42.5 mm from the sample and the scattering angle recorded between $2 < 2\theta < 56^\circ$.

The CCD image from the ground state of I_2 in methanol is shown in Fig. 4. Note the beamstop in the center (black area) and the yellow cone of scattering from methanol. The x-ray polarization is evident from the elongated diffraction pattern. The picture to the right is the difference image for a time delay of 100 ps. Note the black ring surrounding the beamstop and the whiter ring at higher angles. The dark ring is the negative signal from free I atoms. The radial intensity is shown in Fig. 5 for 100 ps and 1 μs . Note that the scattering changes sign after 1 μs at small q . The 1 μs curve is the unambiguous signature of expansion in the solvent host. The expansion is driven by the energy released by recombining iodine. The expansion is not an artifact of laser heating; it is an intrinsic feature from the recombination of iodine atoms in a liquid, and therefore cannot escape diffraction measurement.

The difference amplitude $\Delta S_{\text{elas}}(q, \tau)$ can be expressed in absolute units by scaling to the methanol background. The difference curves can thus be written in units of the classical electron radius r_0^2 per CH_3OH molecule. The high- q part of the difference curves between 1 - 10 ns is readily fitted to the difference in Debye scattering between I_2 and 2I. We thus believe that atomic scattering is the dominant contribution to the signal between 1 - 10 ns. The analysis shows that 4% of the I_2 molecules are excited at 1 ns. Now, given that each excited molecule receives $h\nu$ of energy from the laser, we can calculate the temperature rise

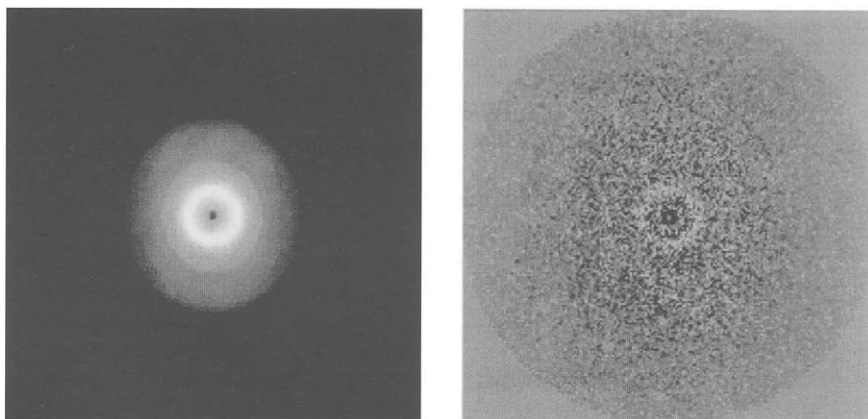


Fig. 4. The diffraction pattern from the ground state of iodine in methanol is shown on the left. The beamstop is seen as a dark circular area in the centre and the bright ring is the correlation peak from the liquid. The picture on the right is the subtraction of the ground state from the 100 ps frame. Note the black ring around the beamstop. That is the signature of dissociation.

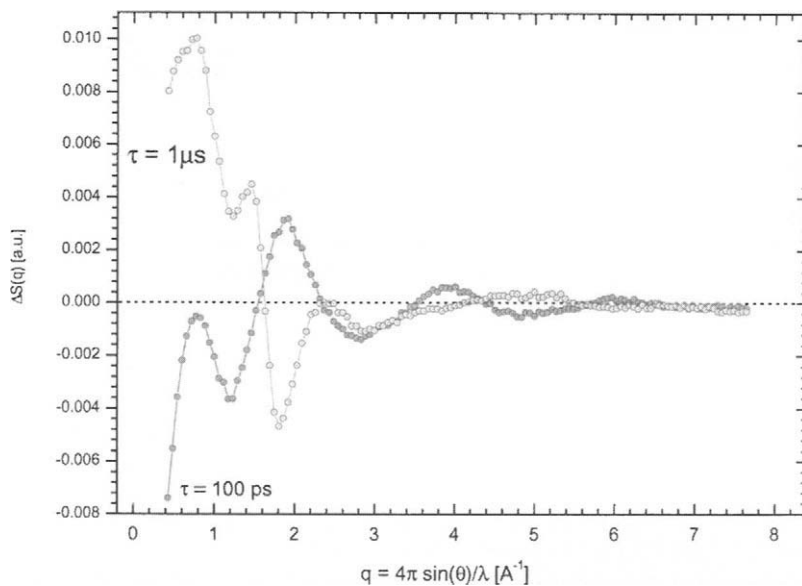


Fig. 5. The laser induced change in the radially averaged scattering intensity. The curves have been scaled to the intensity of the liquid background at $Q = 5.76 \text{ \AA}$.

from the known density of excited iodine and the heat capacity. We infer a temperature rise of 0.57 K. However, from the amplitude of the 1 μ s time point, i.e. the magnitude of the expansion, we deduce a temperature rise of 2.8 K. This indicates that 80% of the laser energy is absorbed into processes that are “invisible” in the 1-10 ns data. This result is in line with the study of I_2 in CCl_4 , which showed that 87% of the excited iodine recombines geminately [12]. We have seen similar effects for HgI_2 in methanol.

We have investigated this discrepancy more closely by scanning the laser pulse in steps of 25 ps though time-zero to look for additional oscillation features at the earliest times. Fig. 6 shows the average photosignal of iodine in methanol from a fine slicing experiment. This shows the definition of time zero, which can be derived from the data. The black line is a fit of the instant onset smeared out by the temporal response function of the beamline. The derivative of this function is a gaussian with a 110 ps pulse length (fwhm), which is consistent with the bunch length measurement from the machine. This explains the time resolution and the accuracy of the experiment. It turns out that the total intensity is greatest at 50 ps which may indicate that we are seeing the tail of the exponential decay of the A/A' state (Fig. 6). However the q -dependence of the 100 ps curve does not fit that of a simple inflated I_2 molecule if we constrain the bond lengths to 3.0-3.5 Å. This may be the signature of a A/A' -state complex with methanol, or a A/A' state caged by methanol and we plan to investigate this problem in more details by incorporating Molecular Dynamics simulations, which may account for the solute/solvent interaction in a qualitative way.

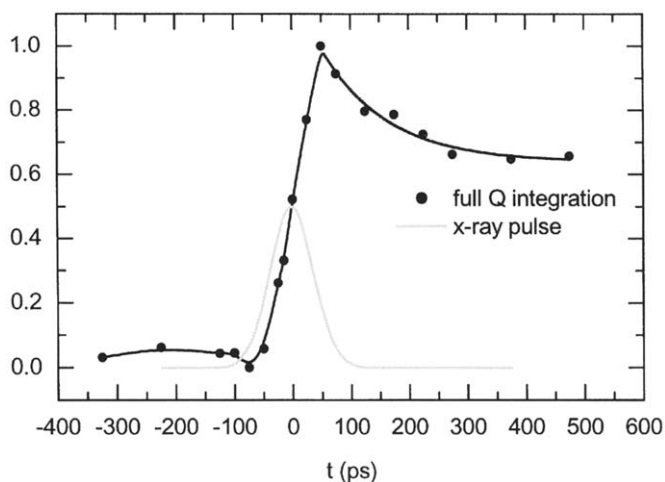


Fig. 6. The q -integrated photosignal of iodine in methanol from a time-slicing experiment. The red curve is the temporal profile of the x-ray pulse.

ACKNOWLEDGEMENT

The authors wish to thank Laurent Eybert, Laurent Claustre, Wolfgang Reichenbach, Richard Neutze, Armin Geis, Dominique Block and Peter Trommsdorff for help and discussions. Finally we would like to acknowledge financial support from the EU-grant HPRI-CT-0415.

References

- [1] J. Als-Nielsen and D. Mc Morrow. Elements of modern x-ray physics, J. Wiley & Sons, New York, 2001.
- [2] F. Schotte, S. Techert S, P. A. Anfinrud, V. Srajer, K. Moffat and M. Wulff. Recent Advances in the Generation of Pulsed Synchrotron Radiation Suitable for Picosecond Time-resolved X-ray Studies. Third-Generation Hard X-ray Synchrotron Radiation Sources. Edited by Dennis Mills, (ISBN 0-471-31433-1). 345-401, 2002
- [3] A. Rousse, C. Rischel, S. Fourmaux, I. Uschmann, S. Sebban, G. Grillon, Ph Balcou, E. Forster, J.P. Geindre, P. Audebert, J.C. Gauthier and D. Hulin, *Nature*, 410 (2001) 65.
- [4] M. H. Pirenne, *The Diffraction of X-rays and Electrons by Free Molecules*, The University Press, Cambridge, 1946.
- [5] H. Ihee, V. A. Lobastov, U. M. Gomez, B. M. Goodson, R. Srinivasan, C. Y. Ruan, A. H. Zewail, *Science*, 291 (2001) 458
- [6] V. Srajer, T. Teng, T. Ursby, C. Pradervand, Z. Ren, S. Adachi, W. Schildkamp, D. Bourgeois, M. Wulff and K. Moffat, *Science*, 274 (1996) 1726.
- [7] B. Perman, V. Srajer, Z. Ren, T-Y. Teng, C. Pradervand, T. Ursby, F. Schotte, M. Wulff, R. Kort, K. Hellingwerf and K. Moffat, *Science*, 279 (1998) 1946.
- [8] F. Schotte, M. Lim, T. A. Jackson, A. V. Smirnov, S. Jayashree, J.S. Olson, G. N. Phillips, M. Wulff, P. A. Anfinrud, *Science*, 300 (2003) 1944.
- [9] S. Techert, F. Schotte and M. Wulff, *Phys. Rev. Lett.*, 86 (2001) 2030.
- [10] E. Collet, M. H. Lemée-Cailleau, M. Buron-Le Cointe, H. Cailleau, M. Wulff, T. Luty, S. Y. Koshihara, M. Meyer, L. Toupet, P. Rabiller, S. Techert, *Science*, 300 (2003) 612.
- [11] R. Neutze, R. Wouts, S. Techert, J. Davidson, M. Kocsis, A. Kirrander, F. Schotte, M. Wulff *Phys. Rev. Lett.*, 87 (2001) 195508.
- [12] A. Plech, R. Randler, A. Geis and M. Wulff. *J. Synchrotron Rad.*, 9 (2002) 287.
- [13] D. Bourgeois, U. Wagner, M. Wulff, *Acta Cryst. D*, 56 (2000) 973.
- [14] Plech, M. Wulff, S. Bratos, F. Mirloup, R. Vuilleumier, F. Schotte and P.A. Anfinrud. submitted.
- [15] A.L. Harris, J.K. Brown, and C.B. Harris, *Ann. Rev. Phys. Chem.*, 39 (1988) 341.
- [16] J. Tellinghuisen, *J. Chem. Phys.*, 58 (1973) 2821.
- [17] D.F. Kelley, A.N. Abul-Haj and D.-J. Jang, *J. Chem. Phys.*, 80 (1984) 4105.
- [18] J.T. Hynes, R. Kapral, and G.M. Torrie, *J. Chem. Phys.*, 72 (1980) 177.
- [19] F. Hajdu, *Acta Cryst. A*, 28 (1972) 250.
- [20] G. Palinkas, *Acta Cryst. A*, 29 (1973) 10.
- [21] B.E. Warren, *X-ray diffraction*, chapter 10, Dover, New York, 1969.
- [22] A. Khan, *J. Chem. Phys.*, 96 (1992) 1194.

Time-dependent x-ray scattering signal of laser heated liquids

F. Mirloup^a, R. Vuilleumier^{a*}, S. Bratos^a, M. Wulff^b and A. Plech^c

^aLaboratoire de Physique Théorique des Liquides, Tour 16-15, 5^{ème} étage, c.c. 121
Université Pierre et Marie Curie
4 place Jussieu, F-75005 Paris, France

^bEuropean Synchrotron Radiation Facility
F-38043 Grenoble Cedex, BP 220, France

^cFachbereich Physik der Universitaet Konstanz
Universitaetsstrasse 10, D-78457 Konstanz, Germany

1. INTRODUCTION

Pump-probe x-ray diffraction [1–3] is bound to play an important role in the future for studies of ultrafast chemical events, particularly in the liquid state. The diffuse scattering from liquids, by contrast to crystals, demands high x-ray flux but a few applications have already been performed with time-scale as short as 100 ps [4, 5]. In these experiments, as in all pump-probe set-ups, the incoming laser pump pulse deposits energy in a localized region of the liquid, for example to a solvated chromophore to initiate a photo-chemical reaction. Sooner or later, this energy is dissipated as heat into the liquid, driving temperature and pressure changes in the laser illuminated volume. From its nature the x-ray probe is sensitive to the ensuing structural changes of the liquid, which will always at some point in time contribute to the pump-probe signal. In an other context, these effects have been the subject of numerous photo-thermal gratings or photo-lensing studies [6–8]. In this paper we present the calculation of the induced temperature and pressure changes in the liquid and its application to the determination of a pump-probe x-ray diffraction signal. We will limit ourselves to cases where the heat deposited is small, leading to temperature rises of only a few percents, and to delays large enough for local equilibrium to be satisfied (well defined local pressure and temperature). The first of these assumptions is believed not to be restrictive for many applications and the second should be verified for times larger than typically 100 ps. This will allow us to study the response of the solvent at first order and to use hydrodynamics. We will then illustrate these effects for the case of liquid tetrachloromethane subject to an impulsive heat deposition. Tetrachloromethane (CCl₄) is a common organic solvent and it has a large number of electrons giving rise to a large scattering signal.

* Author to whom correspondence should be send (email: vuilleum@lptl.jussieu.fr)

2. THEORY

Considering local equilibrium, the liquid structure in a small portion of space around a point \mathbf{r} is determined at time t by the local thermodynamical variables $T(\mathbf{r}, t)$ and $P(\mathbf{r}, t)$. If further the variation of temperature $\delta T(\mathbf{r}, t)$ and pressure $\delta P(\mathbf{r}, t)$ with respect to the reservoir temperature T_0 and pressure P_0 is small, the x-ray scattering signal of a small volume $d^3\mathbf{r}$ at \mathbf{r} , which contains $dn(\mathbf{r})$ molecules, can be written to first order:

$$dS(q, t|\mathbf{r}) = S(q|T_0, P_0) dn(\mathbf{r}) + \left. \frac{\partial S(q)}{\partial T} \right|_P \delta T(\mathbf{r}, t) dn(\mathbf{r}) + \left. \frac{\partial S(q)}{\partial P} \right|_T \delta P(\mathbf{r}, t) dn(\mathbf{r}), \quad (1)$$

where q is the norm of the scattering vector. $S(q|T_0, P_0)$ is the equilibrium liquid x-ray form-factor per molecule and $\left. \frac{\partial S}{\partial T} \right|_P$ and $\left. \frac{\partial S}{\partial P} \right|_T$ are its partial derivatives with respect to T and P respectively. At large q , $S(q|T_0, P_0)$ behaves like the gas phase form-factor of the solvent molecules, while the other terms in the rhs of eq. (1) go quickly to zero; so that term can be fully subtracted from $dS(q, t|\mathbf{r})$ in the experiment. Then by integrating along the x-ray beam path in the liquid, the resulting total difference signal at time t per molecule is:

$$\Delta S(q, t) = \delta \bar{T}(t) \left. \frac{\partial S}{\partial T} \right|_P + \delta \bar{P}(t) \left. \frac{\partial S}{\partial P} \right|_T = \left(\delta \bar{T}(t) - \frac{\chi_T}{\alpha_P} \delta \bar{P}(t) \right) \left. \frac{\partial S}{\partial T} \right|_P + \frac{\chi_T}{\alpha_P} \delta \bar{P}(t) \left. \frac{\partial S}{\partial T} \right|_V \quad (2)$$

where $\delta \bar{T}(t)$ and $\delta \bar{P}(t)$ are the average temperature and pressure variations at time t in the region illuminated by the x-ray beam², χ_T is the isothermal compressibility of the liquid and α_P its thermal expansion coefficient. In this last expression, $\left. \frac{\partial S}{\partial T} \right|_P$ and $\left. \frac{\partial S}{\partial T} \right|_V$ can be either determined theoretically by Molecular Dynamics simulations, as will be presented below for liquid CCl_4 , or they can be experimentally measured from static structure factors of the liquid under different thermodynamical conditions. We will now determine $\delta \bar{T}(t)$ and $\delta \bar{P}(t)$ for a laser heated liquid.

If the viscosity and the thermal diffusion are neglected, it can be shown that, calling $Q(\mathbf{r}, t)$ the total heat per unit volume deposited in \mathbf{r} at time t , the pressure variation $\delta P(\mathbf{r}, t)$ is determined by [8]: $\frac{1}{c^2} \frac{\partial^2 \delta P}{\partial t^2} - \Delta \delta P = \frac{\alpha_P \rho_0}{C_p} \dot{Q}$, in which c is the speed of sound and C_p is the heat capacity at constant pressure of the liquid. By analogy with the retarded potentials in electrodynamics the solution of this equation can be written as $\delta P(\mathbf{r}, t) = \frac{\alpha_P \rho_0}{C_p} \int d^3\mathbf{r}' \frac{\dot{Q}(\mathbf{r}', t - \frac{|\mathbf{r}-\mathbf{r}'|}{c})}{|\mathbf{r}-\mathbf{r}'|}$, and will in general depend on the geometry of the set-up. For a spatially gaussian laser profile of width $2a$, this solution takes the following form on the axis of the pump laser [6, 7]:

$$\delta \bar{P}(t) = \frac{\alpha_P}{\chi_T} \int_{-\infty}^t dt' \frac{\dot{Q}(t')}{C_v} e^{-\left(\frac{c(t-t')}{a}\right)^2}. \quad (3)$$

Together with eq. (3), the temperature variation is obtained from the thermodynamical relation:

$$\delta \bar{T} = \frac{\bar{Q}}{C_p} - \frac{h \delta \bar{P}}{C_p} \quad (4)$$

with $h = (C_v - C_p)\chi_T/\alpha_P$. Equations (2), (3) and (4) are the main theoretical results of this paper. Finally, the average density variation, $\delta \bar{\rho}(t)$, from the equilibrium density ρ_0 is then given by $\delta \bar{\rho}(t) = \rho_0 \chi_T \delta \bar{P}(t) - \rho_0 \alpha_P \delta \bar{T}(t)$.

²Since we have kept only first order terms, we have $dn(\mathbf{r}) = d^3\mathbf{r}/\rho_0$, with ρ_0 the equilibrium density of the fluid, and $\delta \bar{T}(t)$ and $\delta \bar{P}(t)$ are true volume averages.

When the total heat Q is deposited faster than the time scale $\tau = a/c$, the temperature first follows closely the heat deposited in the sample, $\delta T_{initial}(t) = Q(t)/C_v$, while the pressure is $\delta P_{initial}(t) = (\alpha_P Q(t))/(\chi_T C_v)$, which correspond to a constant density. Then after a time τ the pressure relaxes adiabatically to the external pressure while the density is lowered and the temperature decreases by a factor $1/\gamma = C_v/C_p$. The derivatives $\left. \frac{\partial S}{\partial T} \right|_V$ and $\left. \frac{\partial S}{\partial T} \right|_P$ appearing in Eq. (2) then correspond to the early time and long time parts of the difference signal.

3. LIQUID TETRACHLOROMETHANE

For illustrative purposes, we now consider the case of a tetrachloromethane sample initially at ambient conditions ($P_0 = 1$ Bar and $T_0 = 300$ K) and heated instantaneously. We call Q the heat deposited at time $t = 0$, thus $Q(t) = H(t) \cdot Q$ and $\dot{Q}(t) = \delta(t) \cdot Q$ ($H(t)$ is the Heaviside function). In the following we will assume a mild heating, $Q = 1/C_p$. It corresponds to a final temperature rise of 1 K, which for example would be produced by the relaxation of about 5 mM of photoexcited I_2 molecules in the sample. Finally, we take $a = 0.05$ mm, typical of lasers focal point sizes, leading to $\tau = 53.7$ ns ($c = 930$ m/s in CCl_4). At these length and time scales, heat conduction and viscosity can be shown to be negligible in CCl_4 . Taking these characteristic values, $\delta \bar{P}(t)$ and $\delta \bar{T}(t)$ can be obtained from eqs. (3) and (4).

The liquid structure factor of CCl_4 and its derivatives with respect to temperature at fixed pressure or fixed volume, needed by eq. (2), were evaluated by Molecular Dynamics (MD) simulations. We have used the OPLS model for tetrachloromethane [9] In this model, the CCl_4 molecules are described as rigid tetrahedra ($d_{C-Cl} = 1.769$ Å) and the intermolecular potentials are atom centered 6-12 Lennard-Jones potentials plus the coulombic interaction with partial charges on C and Cl. We performed NVT simulations with 512 molecules for about 1 ns each. The different x-ray structure factors were obtained from the accumulated partial radial distribution functions [10], using the atomic form-factors from the DABAX database [11]. In order to estimate the partial derivatives of the structure factor, we have used finite differences: we considered two different temperatures, $T_1 = 300$ K and $T_2 = 328$ K, and two molar volumes, $V_1 = 97.3$ cm³ · mol⁻¹ and $V_2 = 100.65$ cm³ · mol⁻¹ which are the molar volumes along the liquid-vapor coexistence line for the two temperatures T_1 and T_2 respectively [12]. Three simulations were then run for the temperature and molar volume conditions (T_1, V_1) , (T_2, V_1) and (T_2, V_2) , from which the partial derivatives, $\left. \frac{\partial S}{\partial T} \right|_V$, $\left. \frac{\partial S}{\partial T} \right|_P$, were obtained. Also, an experimental $\left. \frac{\partial S}{\partial T} \right|_P$ curve was obtained using synchrotron radiation from thermostated CCl_4 at two slightly different temperatures. The agreement with simulation is satisfactory (see Fig. 1.a).

Figure 1.b shows the predicted time-dependent x-ray scattering of CCl_4 heated by an impulsive source. The scattering signal appears nearly unchanged from $t = 100$ ps after the heating stopped to up to 10 ns: during this period, the pressure inside the illuminated region is $17 \cdot 10^5$ Pa ($\alpha_P = 1.22 \cdot 10^{-3}$ K⁻¹ and $\chi_T = 1.03 \cdot 10^{-9}$ Pa) and the temperature is 301.45 K ($1/\gamma = 0.69$). The x-ray scattering difference signal is then rather small: only slight structural rearrangements occur due to the temperature rise at constant volume. This makes this signal difficult to resolve numerically and the spurious oscillations below 1.5 Å⁻¹ are due to numerical uncertainties. The signal then suddenly becomes larger around 50 ns, with a prominent peak at 1.15 Å⁻¹, and exhibits clear isobestic points. The pressure relaxes adiabatically down to the external pressure while the temperature is lowered to 301 K. As the density is lowered, the average intermolecular distance increases leading to the predicted strong signal after 100 ns.

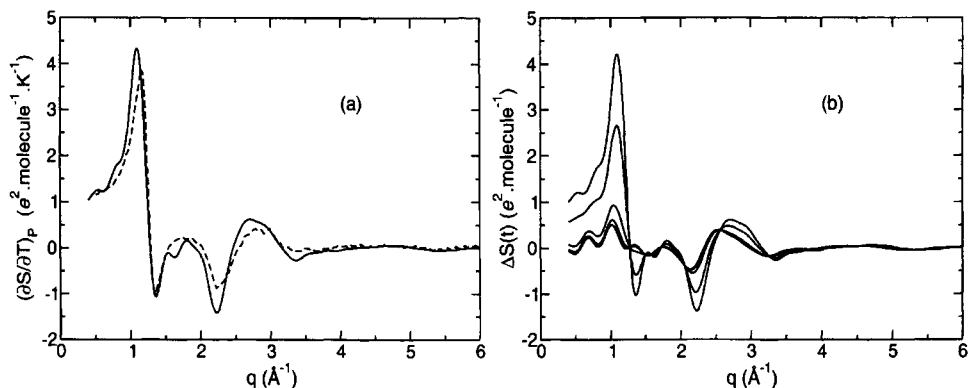


Fig. 1. (a) Derivative of the liquid form-factor of CCl_4 at constant pressure at 300 K. Solid line: MD simulation, dashed line: experimental. (b) Time-dependent x-ray scattering of heated CCl_4 from our linear response model. From bottom to top at 1.2 \AA^{-1} : 100 ps, 10 ns, 20 ns, 50 ns and 100 ns.

4. DISCUSSION

In this paper we have presented a linear response model for the time-dependent x-ray scattering signal of a laser heated liquid. The phenomena described here will appear in practically all pump-probe x-ray diffraction experiments in liquids, although the precise signal depends on the liquid itself. To this respect, an interesting case would be water around 4°C , for which the density does not depend on temperature at first order: second order response should be included in that case but one can foresee that the resulting signal will be smaller than for other organic liquids. Finally, it should be noted that the time dependence of the pressure relaxation can be controlled by external parameters like the width of the focal point. At earlier times however, the signal follows adiabatically the heat deposited in the sample.

REFERENCES

- [1] J. R. Helliwell, P. M. Rentzepis, *Time-resolved Diffraction*, Oxford science publications, 1997.
- [2] S. Techert, F. Schotte, M. Wulff, *Phys. Rev. Lett.*, 86 (2001) 2030–2033.
- [3] M. Wulff, A. Plech, L. Eybert, R. Randler, F. Schotte, P., *Faraday Discuss.*, 122 (2003) 13–26.
- [4] R. Neutze, R. Wouts, S. Techert, J. Davidsson, M. Kocsis, A. Kirrander, F. Schotte, M. Wulff, *Phys. Rev. Lett.*, 87 (2001) 195508.
- [5] A. Geis, D. Block, M. Bouriau, F. Schotte, S. Techert, A. Plech, M. Wulff, H. Trommsdorff, *J. of Lumin.*, 94-95 (2001) 493.
- [6] P. R. Longaker, M. M. Litvak, *J. Appl. Phys.*, 40 (1969) 4033.
- [7] F. R. Grabiner, D. R. Siebert, G. W. Flynn, *Chem. Phys. Lett.*, 17 (1972) 189.
- [8] L. M. Lyamshev, K. A. Naugol'nykh, *Soviet Physics Acoustics*, 27 (1981) 357.
- [9] E. M. Duffy, D. L. Severance, W. L. Jorgensen, *J. Am. Chem. Soc.*, 114 (1992) 7535.
- [10] B. E. Warren, *x-ray Diffraction*, Dover, New-York, 1969.
- [11] <http://www.esrf.fr/computing/scientific/dabax>.
- [12] D. R. Lide, H. V. Kehiaian, *CRC Handbook of Thermophysical and Thermochemical Data*, CRD Press, 1994, p. 81.

Structural dynamics and electronic structure changes probed with lasers and X-rays

W. Gawelda^{a,b}, M. Saes^a, M. Kaiser^a, A. Tarnovsky^a, S. L. Johnson^b, D. Grolimund^b, R. Abela^b, M. Chergui^a and Ch. Bressler^a

^aInstitut de Physique de la Matière Condensée, Université de Lausanne, CH-1015 Lausanne, Switzerland*

*New address: LSUCP, ICMB, Faculté des Sciences, BSP, EPFL, CH-1015 Lausanne-Dorigny, Switzerland

^bSwiss Light Source and Paul Scherrer Institut, CH-5232 Villigen PSI, Switzerland

1. INTRODUCTION

Over the past years, much effort has been invested to combine the ultrashort time resolution of lasers with the high atomic-scale resolution of structural techniques, such as electron diffraction, x-ray diffraction, and x-ray absorption spectroscopy (XAS). The latter is a mature technique to probe the electronic and structural properties of a large class of systems, ranging from solid-state materials to proteins [1]. A variety of fine structure near the characteristic edge of a selected element delivers this information, the so-called XANES or X-ray Absorption Near Edge Structure, while at higher energies the so-called EXAFS or Extended X-ray Absorption Fine Structure, is observed. In many-body systems, these features are caused by the presence of adjacent atoms and their proper analysis delivers information about the local geometric structure to high accuracy [1].

Research based on time-resolved XAS in an optical pump-x-ray probe scheme has first been implemented at synchrotron radiation sources. Mills *et al.* [2] used a 20 Hz repetition rate Nd:YAG laser to photolyse carbonmonoxymoglobin (MbCO) and monitor the photolysis product with time-resolved XAS around the K-edge of the iron atom. Other studies were carried out on different types of photolyzed systems in liquids, by Thiel *et al.* [3], Clozza *et al.* [4], Chance *et al.* [5,6] and Chen *et al.* [7,8,9]. All these studies were limited to the nanosecond or longer time domain. We recently reported on time-resolved XANES studies of a Ruthenium complex in water solution reaching the picosecond time scale [10]. This work allows us to evaluate the feasibility of future time-resolved XAS experiments, which we present below together with our new results.

2. EXPERIMENTAL CONSIDERATIONS

When extending the pump-probe scheme into the x-ray domain, we deal with two very different pump and probe light sources with respect to their pulse intensities. This poses stringent boundary conditions on the sample design in order to guarantee a feasible experiment [11]. To start with, we estimate the signal-to-noise ratio that one can anticipate with current technology. Hereby, we restrict the calculations to pump-probe experiments in

transmission mode. While most ultrafast XAS studies nowadays exploit 30-100 ps long x-ray pulses from a synchrotron, they already provide us with much insight into the details of a desired set-up exploiting future femtosecond hard x-ray sources. Since the goal here is to lay the grounds towards femtosecond temporal resolution, we will consider only femtosecond laser systems as the excitation source. Commercial femtosecond lasers are nowadays limited to 1-5 W of average output power, which is roughly constant for all pulse repetition rates. E.g., for a 1 kHz repetition rate the pulse energy at 800 nm lies between 0.5 and 3 mJ, which translates to about $10^{15} - 10^{16}$ laser photons per pulse available for sample excitation. The weakest link is therefore given by the rather low x-ray pulse intensity, which typically contains $10^3 - 10^6$ photons per pulse (and 0.1 % bandwidth) at different 3rd generation synchrotron radiation beamlines. As a consequence, the experiment should be designed to require the least amount of incident x-ray probe photons for the largest possible signal-to-noise ratio.

In the pump-probe experiments, we can describe the transmitted x-ray intensity as a function of the amount of excited species, thus modifying the stationary Lambert-Beer law with respect to the time dependent photoexcitation yield $f(t)$. As a result, we can define the signal as the natural logarithm of the ratio of transmitted intensities between the laser-pumped (I_1^{pump}) and unpumped (I_1^{unp}) sample, which yields [12]

$$S = \ln \left(\frac{I_1^{unp}}{I_1^{pump}} \right) = f n_{sam} \Delta \sigma_{ex} d \quad (1)$$

with n_{sam} being the sample concentration, $\Delta \sigma_{ex}$ being the difference in absorption cross section between the ground and excited state species, and d is the sample thickness. (Using the logarithm to the base 10 instead of the natural logarithm yields the definition for the change in optical density (ΔOD) due to photoexcitation, which is commonly employed in optical pump-probe measurements).

In the experiment, the transmission intensities for the excited and the dark sample are determined by the number of x-ray photons (I_1) recorded on the detector behind the sample, and we typically accumulate for several pump-probe shots. In the absence of external noise sources the accuracy of such a measurement is governed by the shot noise distribution, which is given by Poisson statistics of the transmitted pulse intensity. Indeed, we have demonstrated that we can suppress the majority of electronic noise in experiment, which validates this rather idealistic treatment [13,14]. Applying the error propagation formula to eq. (1) then delivers the experimental noise of the measurement, and we can thus calculate the signal-to-noise ratio S/N as a function of the input parameters. Most important is hereby the sample concentration n_{sam} at the chosen sample thickness d . Via the occasionally very different absorption cross sections in the optical (pump) and the x-ray (probe) domains it will determine the fraction of excited state species as a function of laser fluence.

Regardless of the choice of the sample thickness, the *total* amount of sample particles in the x-ray probe beam under optimized conditions is directly proportional to the x-ray spot size and inversely proportional to the x-ray absorption cross section, whose photoinduced (small) changes we want to measure [12]. Typical x-ray foci at synchrotrons are in the 0.1 – 0.3 mm range. For the examples treated below, this means that we have between 10^{14} and 10^{16} molecules in the probed volume. In order to achieve a reasonable photoinduced signal we should excite as many solute molecules as possible. Neglecting the optical absorption cross sections for photoexcitation for the moment, this requires on the order of 10^{15} laser photons per pulse, or ca. 0.25 mJ of pulse energy (e.g., at 800 nm). In other words, one should aim to

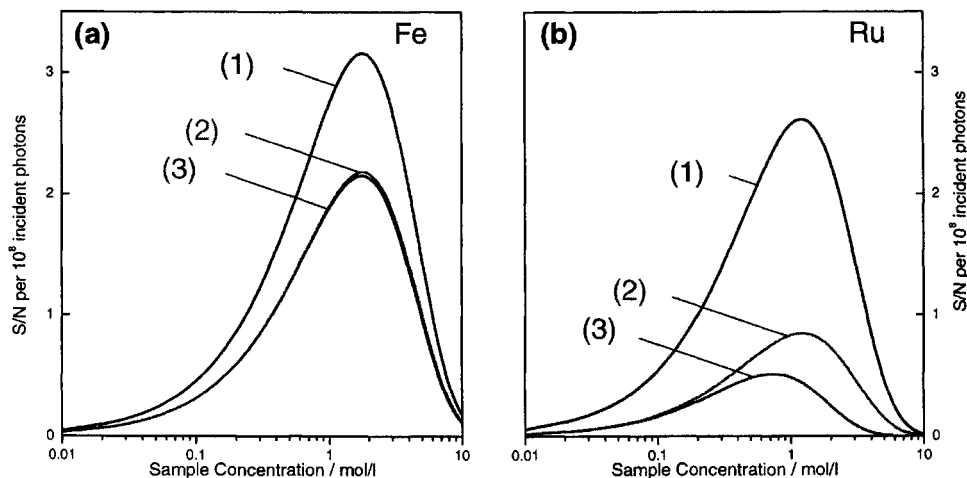


Fig. 1. S/N as a function of sample concentration for aqueous solutions of $[\text{Fe}^{\text{II}}(\text{bpy})_3]^{2+}$ (a) and $[\text{Ru}^{\text{II}}(\text{bpy})_3]^{2+}$ (b). Curve (1) shows the result for the metal atom without ligands and solvent, (2) in an aqueous solution without ligands and, (3) in an aqueous solution including ligand and counterion (here: 2Cl^-) contribution (see text for details).

increase the laser pulse intensity, until full excitation is achieved, while remaining below pump intensities, which begin to stimulate effects (e.g. nonlinear absorption) that do not belong to the investigated process. As long as we are in the linear regime of the pump process, it is always preferable to increase the laser pulse intensity and sacrifice the repetition rate of the laser system. For the aforementioned laser systems, this argument motivates the use of a 1 kHz femtosecond laser rather than a multi-MHz system, which has orders of magnitude less energy per pulse.

2. NUMERICAL EXAMPLES: THE CASE OF TRANSITION METAL COMPOUNDS

To illustrate the above discussion, we will consider the case of transition metal complexes, which are interesting in photochemistry and in biology. Static EXAFS oscillations represent typically 1 to 20 % modulations of the edge height. In the following we seek to measure the EXAFS with a noise level of $\chi = 1\%$ (relative to the absorption edge jump) of the selected transition metal. We further assume a reasonable value of $f = 10\%$ for the amount of excited state species, and we will calculate the required number of incident x-ray photons to measure the EXAFS with a signal-to-noise ratio of $S/N = 1$ (for 1 % changes relative to the edge jump). The results will then deliver a reasonable estimate for the feasibility of such an experiment. Note that the number of required x-ray photons for such an experiment scales with

$$I_0 \propto \left[\frac{S/N}{f \cdot \chi} \right]^2 \quad (2)$$

which means that we can adjust our results for experimentally derived f -values, as well as demand a larger S/N or be able to measure a smaller EXAFS χ .

Without *a priori* knowledge of the actual sample (and its response to photoexcitation) and its solvent (including guest-host interactions) it may appear impossible to calculate pump-probe signals. However, under certain conditions we can obtain quite useful results. First, we will consider H₂O as a prototype solvent. Changing the solvent to other first-row solvents (e.g., acetonitrile, hexane, etc.) will not seriously affect the results due to their rather similar absorptions in the hard x-ray domain. Heavier solvents however, e.g., CCl₄, could seriously alter the results, and are not applicable to the results shown below. Without knowing the actual sample we can nevertheless obtain quite accurate results, if the sample absorption remains comparable to the solvent absorption of the displaced volume. For hydrocarbons containing samples this is usually the case, and we demonstrate this for two example species, ruthenium-tris-bipyridine and iron-tris-bipyridine.

Fig. 1 shows the signal-to-noise ratio S/N as a function of sample concentration for both species. For each sample we have calculated 3 cases: (1) displays the dependence for a hypothetical sample containing only the central atom neglecting solvent contributions and the residual sample atoms, (2) shows the case of the central atom only in a water environment, and (3) shows the full calculation including the water solvent and the 3 bipyridine ligands. The calculations were performed around the Fe K edge (ca. 7.1 keV), and the Ru L_{III} -edge (ca. 2.84 keV). For iron we see that introducing the water solvent (with $d = 0.5$ mm) decreases S/N by less than a factor of two, since the solvent transmission is quite high at this x-ray energy. Introducing the entire [Fe(bpy)₃]²⁺ molecule including two Cl⁻ counterions delivers nearly the same result as without the ligand, since the difference in absorption between H₂O and the sample ligands and counterions is very small. This is a little different when calculating [Ru(bpy)₃]²⁺Cl₂⁻ dissolved in water (Fig. 1b). Since water already absorbs 90 % of the incoming x-radiation at the Ru L_{III} edge, curves (1) (without solvent) and (2) (with solvent) differ by a factor of 3. If we introduce the entire sample we obtain a modified curve (3), which has a reduced S/N value and a smaller optimized concentration. This results mainly from the rather strong Cl-absorption (cross section) around 2.84 keV. It clearly reduces the signal-to-noise ratio and also optimizes at a somewhat lower concentration in order to obtain the ideal sample-only transmission around 10.85 % [12].

Both cases, however, illustrate that we can obtain very reliable results for K -edge elements with absorption edges above ca. 5 keV, while for L edges around 2.5 keV we might overestimate the maximum S/N value by less than a factor of 2, which is therefore not too much different from the simple case calculated with the metal atom only in the H₂O solvent. Fig. 2a shows the results for a selection of transition metals with absorption edges in the 2 – 22 keV range. For the L edges the sample thickness was kept constant at $d = 0.1$ mm, while for the K edges the thickness was changed from 0.3 mm (Sc), over 0.5 mm (Ti – Co) and 1 mm (Ni – Mo), to 2 mm (Ru and Rh).

The results in Fig. 2a are displayed in the shaded region in Fig. 2b, where the required number of x-ray photons to achieve $S/N = 1$ are plotted as a function of photoexcitation yield f . Each experiment (element) will exhibit an f -dependence on a curve parallel to, e.g., curve (1) in the figure, according to eq. (2). Thus the shaded region includes the range of curves obtained for the transmission metals, as shown in Fig. 2a, whose data points would be found at $f = 10\%$ in Fig. 2b. The shaded region thus displays the feasibility range for time-resolved EXAFS, and the vertical arrow indicates the expected range in general. Time-resolved XANES usually exhibits larger signals, thus their feasibility range should lie at somewhat smaller x-ray doses. Curves (1) to (3) were generated from experimental data on the transient

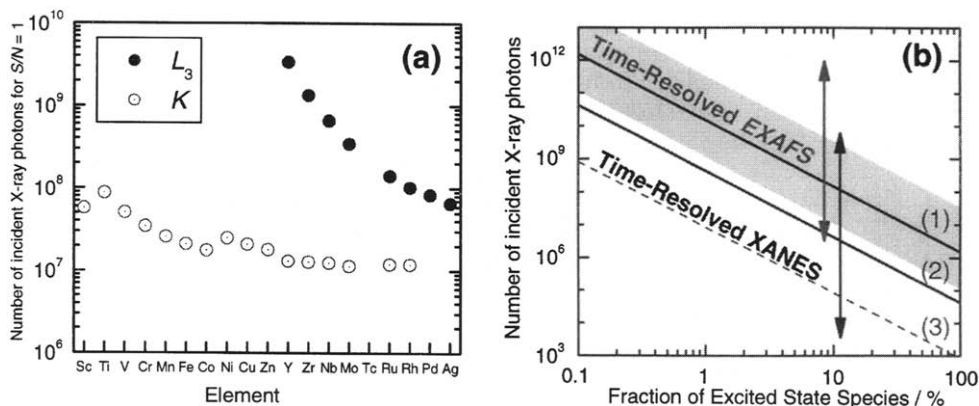


Fig. 2. a) Required number of incoming x-ray photons to observe time-resolved EXAFS of transition metal compounds in H₂O solution with a signal-to-noise ratio $S/N=1$. No ligand or counterion contributions were included (see Fig. 1). Input parameters are: $f=10\%$, $\chi=1\%$ (relative to the absorption edge jump of the selected element). The maxima of curves 2) in Fig. 1 for Fe and Ru correspond to the data points for these elements. b) Feasibility range for time-resolved x-ray absorption spectroscopy. The shaded region indicates the required x-ray dose per data point as a function of the fraction of activated species for the calculated EXAFS experiments on transition metal compounds shown in a). Curves (1) to (3) are extrapolated from experimental results (see section 3. for details) of time-resolved XANES.

XANES of a solvated organometallic complex (aqueous $[\text{Ru}(\text{bpy})_3]^{2+}$, see below for details). Curve (1) displays the result for $S/N=85$, while (2) corresponds to a single scan with $S/N=7$. Indeed, they are shifted as expected due to eq. (2), and curve (3) displays the feasibility limit for this system with $S/N=1$. From this figure we can see that ultrafast XAS studies can be envisioned with as little as $10^6 - 10^8$ x-ray photons per data point.

3. PHOTOEXCITED AQUEOUS TRIS-(2,2'-BIPYRIDINE)-RUTHENIUM(II)

Aqueous $[\text{Ru}^{\text{II}}(\text{bpy})_3]^{2+}$ is a model system for Metal-to-Ligand Charge Transfer (MLCT) reactions. Its excited state properties have been readily studied with optical spectroscopies [15,16]. However, little is known about its excited state structure, which we investigated via time-resolved x-ray absorption spectroscopy. The reaction cycle is described by Fig. 3 (where the superscripts on the left hand side of the ground and excited state compounds denote the

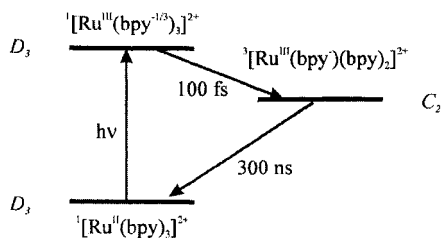


Fig. 3. Photochemical reaction cycle of $[\text{Ru}^{\text{II}}(\text{bpy})_3]^{2+}$ initiated by excitation of the MLCT transition.

spin multiplicity). Light absorption by $[\text{Ru}^{\text{II}}(\text{bpy})_3]^{2+}$ results in the formation of a Franck-Condon MLCT singlet excited state, $^1(\text{MLCT})$, which undergoes sub-picosecond intersystem crossing to a long-lived triplet excited state, $^3(\text{MLCT})$, with near-unity quantum yield [15,16]. A time-resolved XAS experiment should identify the change of oxidation state upon charge transfer via XANES, and the geometric structure in the $^3\text{MLCT}$ by XANES and EXAFS.

We carried out a pump-probe experiment combining laser pump and x-ray probe pulses at the *Advanced Light Source* (ALS) in Berkeley. Herefore we exploit a special electron bunch filling pattern of the ALS [10,14]. The storage ring is filled with several 2 ns-spaced bunches generating a ca. 550 ns long "superbunch", followed by a ca. 100 ns empty section, in which one single electron bunch (the "camshaft" pulse) is placed. This filling pattern allows us to record the intensity of this single X-ray pulse with a suitably fast (and sensitive) avalanche photodiode (APD) detector. The amplified femtosecond laser is synchronized to this camshaft pulse so that the latter follows every laser pulse at 1 kHz repetition rate and at a fixed time delay. Details of the experimental setup can be found in Refs. 10, 14, and 17. The single X-ray pulses are recorded at twice the laser repetition rate (i.e., at 2 kHz), and we monitor - after pair wise subtraction of adjacent X-ray pulse intensities - the transient XAS in transmission mode. This scheme allows us to improve our detection sensitivity to nearly the shot-noise limit of the X-ray source [14,17].

The oxidation states of (ground state) Ru^{II} and (photoexcited) Ru^{III} complexes exhibit pronounced differences in their *L*-edge XANES [18,19]. This is shown in Fig. 4a around the Ru $L_{\text{II,III}}$ edges. A pre-edge absorption feature in the L_{III} edge at 2841.0 eV (denoted *B* in Fig. 4) characterizes the bivalent compounds due to the $2p_{3/2} \rightarrow 4d_{3/2} (e_g)$ transition [20], next to a weaker transition around 2851 eV (feature *C*). Removal of the weakest bound electron from the fully occupied $4d_{5/2}(t_{2g})$ ground state level generates a trivalent ruthenium compound, opening up an additional absorption due to the allowed $2p_{3/2} \rightarrow 4d_{5/2} (t_{2g})$ (feature *A'*) in addition to an oxidation state induced shift. Thus we observe the appearance of the *A'/B'* doublet structure in the trivalent L_{III} XANES, together with the energetic $B \rightarrow B'$ and $C \rightarrow C'$ shift (Fig. 4), resulting from the change of oxidation state of the Ru central atom and formation of $^3(\text{MLCT})$ (Fig. 3). Below the Ru L_{III} edge we also observe the chlorine *K* edge absorption due to the Cl^- counterions of the dissolved $[\text{Ru}^{\text{II}}(\text{bpy})_3]\text{Cl}_2$ sample.

Figure 4b shows the measured transient difference absorption spectrum as a function of the x-ray probe energy *E*, recorded 50 ps after laser excitation (data points with error bars) for a sample containing 80 mmol/l solution of $[\text{Ru}^{\text{II}}(\text{bpy})_3]^{2+}$ in H_2O . This transient contains all the electronic changes from the reactant state absorption spectrum, $R(E)$, to the product state absorption spectrum, $P(E,t)$, at the time *t* after photoexcitation. With $f(t)$ being the fraction of excited state species at time *t*, the transient absorption spectrum $T(E,t)$ is given by

$$T(E,t) = f(t) \cdot [P(E,t) - R(E)] \quad (3)$$

Thus we can directly deduce the XANES spectrum of the product state from the measured transient signal and the reactant state XAS, if we know $f(t)$. Alternatively, we can derive $f(t)$, if we know the exact shape of the product state XAS, $P(E,t)$. The details are given in ref. 14. The resulting spectrum for the $[\text{Ru}^{\text{III}}(\text{bpy})(\text{bpy})_2]^{2+}$ species is shown in Fig. 4a (trace P). It contains an energetic shift of all features by 1.2 eV, together with the photoinduced appearance of the *A'* feature, as expected. The *A'-B'* splitting (4 eV) and the *B'/A'* intensity ratio (ca. 2.3) is indeed close to the values observed for $[\text{Ru}^{\text{III}}(\text{NH}_3)_6]^{3+}$ complex [18,20], which has the same valency and a similar coordination symmetry (O_h versus D_3) as the bipyridine complex.

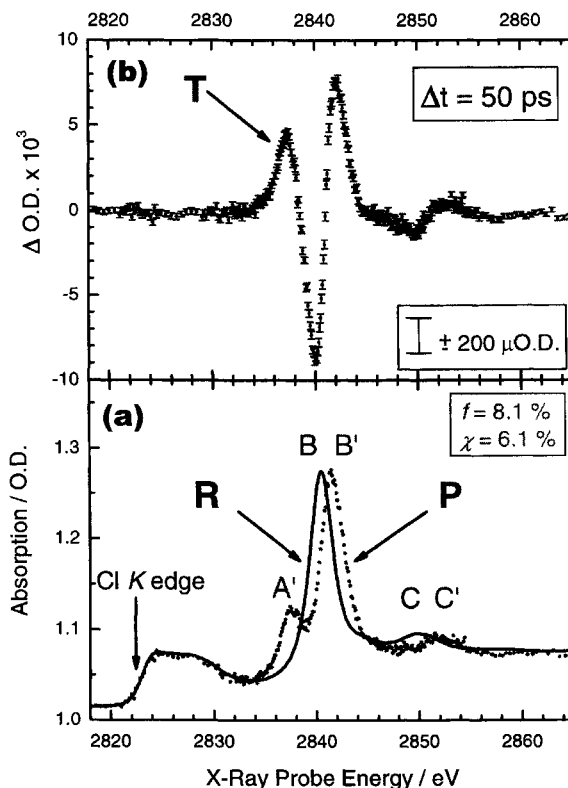


Fig. 4. a) Static L_{III} -edge x-ray absorption spectrum of ground state $[\text{Ru}^{\text{II}}(\text{bpy})_3]^{2+}$ (trace R), and excited state absorption spectrum (trace P) generated from the transient data curve T in (b) via eq. 2. b) Transient x-ray absorption spectrum (T) of photoexcited aqueous $[\text{Ru}^{\text{II}}(\text{bpy})_3]^{2+}$ measured 50 ps after laser excitation.

A crucial aspect of ultrafast pump-probe spectroscopies is the ability to scan the time between pump and probe pulses. This was successfully done for the first time between an optical pump pulse and an x-ray probe pulse in our experiment [10,13,14,17]. Figure 5 shows an example of such a scan in the nsec (a) and the psec (b) time domain with the x-ray energy set near the minimum of the signal in Fig. 4b, thus allowing us to observe the appearance of the photoinduced bleach signal. Once the electron has been excited to the $^1(\text{MLCT})$ state we can observe the induced oxidation state change of the Ru central atom, and therefore the time sequence of this pump-probe signal is entirely governed by the cross correlation time of the exciting laser and the probing x-ray pulses. While this is convenient to both set and confirm the actual timing, we can also exploit this for measuring kinetic traces out to several hundred nanoseconds (Fig. 5a), allowing thus a direct comparison with optical-only experiments [14].

These experiments provide us with quantitative values concerning the required x-ray dose and the achievable signal-to-noise ratio. We will therefore compare these results with the numerical results given before. Fig. 4 contains the average of 25 spectra, corresponding to ca. 2.3×10^8 photons per data point, as derived via a statistical analysis of the recorded individual

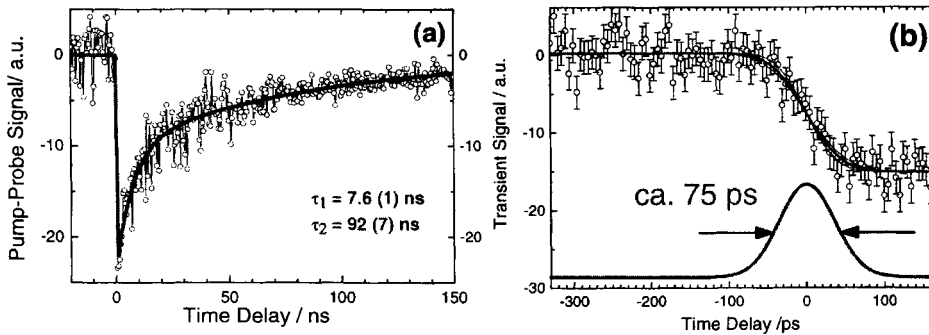


Fig. 5. Scans of the pump-probe time delay between the laser pump pulse and the x-ray probe of the transient X-ray absorption signal of $[\text{Ru}^{\text{II}}(\text{bpy})_3]^{2+}$ (the x-ray energy is set at the minimum of the signal in fig. 20.b) over several tens of nsec (a) and in the psec time domain (b). The latter represents the cross-correlation signal between the 200 fs laser pulse and the 70-80 ps long x-ray pulse (indicated by the Gaussian-shaped derivative of the fit curve to the data).

x-ray pulses [12,13,14,17]. Using the beamline specifications [17] we calculate 2.5×10^8 incident x-ray photons per pulse in close agreement to our measurement. The achieved sensitivity level is remarkable: In Fig. 4b the error bars are $< 200 \mu\text{O.D.}$, which is not easy to achieve in optical-only experiments using amplified femtosecond lasers with many orders of magnitude larger pulse intensities. One important reason for this lies in the extremely stable operation conditions of modern synchrotrons. The flux variation at a beamline end station is dominated by the theoretically calculated shot noise.

The high sensitivity of the transient data is related to the data quality of the product state absorption spectrum shown in Fig. 4a calculated via eq. (2), and we yield a sensitivity of $\chi = 6.2 \%$ (relative to the Ru L_{III} absorption edge jump) for $f = 8.1 \%$ (thus for achieving $S/N = 1$). Under these experimental conditions (sample thickness 0.1 mm, and a concentration of 80 mmol/l) we utilized the above-derived value of 2.3×10^8 x-ray photons per data point. This we can scale and compare to our numerical results. Trace (3) in Fig. 1b describes the full calculation for aqueous $[\text{Ru}^{\text{II}}(\text{bpy})_3]^{2+}$ as a function of concentration. For 80 mmol/l we calculate $S/N = 0.136$ for 10^8 incoming x-ray photons, which corresponds to 5.37×10^7 required photons for $S/N = 1$, $f = 10 \%$ and $\chi = 1 \%$. With eq. 2 we now scale these results towards the experimentally determined values in Fig. 4a, and yield $I_0 = 2.1 \times 10^8$ calculated photons, as compared to 2.3×10^8 incoming photons per data point used in the experiment. The agreement between these values and those of the beamline source specifications is tantalizing and supports the extrapolations drawn for the other transition metal compounds, as shown in Fig. 2b. Curve (1) in Fig. 2b has been extrapolated from the measurement shown in Fig. 4b. E.g., for the dominant XANES transient around 2840 eV we achieve a signal-to-noise ratio of 85 (peak to peak), while curve (2) corresponds to the single time delay scan shown in Fig. 5b, which has a $S/N = 7$. Consequently, photoinduced changes with $S/N = 1$ would be found somewhere along trace (3) in Fig. 2b. This not only supports the validity of the numerical results shown in Fig. 2a, but also demonstrates that time-resolved XAS can be employed with only $10^6 - 10^8$ incident X-ray photons per data point, and this amount of collected photons lies within the capabilities of sub-picosecond x-ray sources to become available in the near term future.

4. CONCLUSIONS

This work demonstrated a number of new results and opportunities for ultrafast XAS: 1) it is possible to work with highly dilute solutions in transmission mode without dramatic loss of signal-to-noise ratio. This is very promising as one can envision the study of samples, for which large concentrations are impossible to reach. Biologically relevant samples are usually investigated in solutions with up to 1 mmol/l concentration, and we therefore can envision such studies on the ultrafast time scales in the near future. 2) It is possible to scan the time delay between the laser pump pulse and the x-ray probe pulse, and therefore follow the evolution of the system from the start. 3) It also demonstrated the operation of an optical-x-ray cross-correlator (Fig. 6.b). The time resolution is not a limiting factor and the experiments are feasible with sources of shorter x-ray pulses, provided the flux is not too low.

REFERENCES

- [1] D. C. Koeningsberger and R. Prins (eds.), *X-ray Absorption Spectroscopy*, John Wiley and Sons, New York, 1988.
- [2] D.M.Mills, A. Lewis, A. Harootian, B. Smith, *Science* 223 (1984) 811.
- [3] D.J. Thiel, P. Livins E. A. Stern and A. Lewis, *Nature* 362 (1993) 40.
- [4] A. Clozza, A.C. Castellano, S. D. Longa, A. Giovannelli, A. Bianconi, *Rev. Sci. Instrum.* 60 (1989) 2519.
- [5] M.R.Chance, M. D. Wirt, E. M. Scheuring, L. M. Miller, A. Xie and D. Sidelinger, *Rev. Sci. Instrum.* 64 (1993) 2035.
- [6] H. Wang, G. Peng, L.M.Miller, E. M. Scheuring, S. J. George, M. R. Chance and S. P. Cramer, *JACS* 119 (1997) 4921.
- [7] L. X. Chen, P.L. Lee, D. Gosztola, W. A. Svec, P.A. Montano and M. R. Wasielewski, *J. Phys. Chem.* B103 (1999) 3270.
- [8] L. X. Chen, W.J.H. Jäger, G. Jennings, D.J. Gosztola, A. Munkholm and J.P. Hessler, *Science* 292 (2001) 262.
- [9] L. X. Chen, G. Jennings, T. Liu, O.J. Gosztola, J.P.Hessler, D.V. Sealtrito and G.J. Meyer, *JACS* 124 (2002) 10861.
- [10] M. Saes, C. Bressler, R. Abela, D. Grolimund, S. L. Johnson, P. A. Heimann, M. Chergui, *Phys. Rev. Lett.* 90 (2003) 047403.
- [11] C. Bressler, M. Saes, M. Chergui, D. Grolimund, R. Abela, P. Pattison, *J. Chem. Phys.* 116 (2002) 2954.
- [12] Ch. Bressler and M. Chergui, submitted to: *Chem. Rev.* (2003)
- [13] C. Bressler, M. Saes, M. Chergui, D. Grolimund, R. Abela, in: *Femtochemistry and Femtobiology*, A. Douhal, J. Santamaria (eds.), World Scientific, New Jersey (2003), 449
- [14] M. Saes, W. Gawelda, M. Kaiser, A. Tarnovsky, C. Bressler, M. Chergui, S. L. Johnson, D. Grolimund, R. Abela, accepted for publication in: *Synchr. Rad. News* (2003)
- [15] N. H. Damrauer, G. Cerullo, A. Yeh, T. R. Boussie, C. V. Shank, J. McCusker, *Science* 275 (1997) 54
- [16] A. T. Yeh, C. V. Shank, J. K. McCusker, *Science* 289 (2000) 935
- [17] M. Saes, F. van Mourik, W. Gawelda, M. Kaiser, M. Chergui, C. Bressler, D. Grolimund, R. Abela, T. E. Glover, P. A. Heimann, R. W. Schoenlein, S. L. Johnson, A. M. Lindenberg, R. W. Falcome, accepted for publication in: *Rev. Sci. Instrum.* (2003)
- [18] T. K. Sham, *J. Chem. Phys.* 83 (1997) 3222
- [19] C. Sugiura, M. Kitamura, S. Muramatsu, *J. Chem. Phys.* 84 (1986) 4824
- [20] F. M. F. deGroot, Z. W. Hu, M. F. Lopez, G. Kaundl, F. Guillot, M. Tronc, *J. Chem. Phys.* 101 (1994) 6570

Multidimensional and dual frequency infrared analogues of NMR: Applications to peptides and isotopomers of secondary structures

I. V. Rubtsov^a, J. Wang^a, C. Fang^a, M. L. Cornelio^a, Y. S. Kim^a, A. K. Charnley^a, A. B. Smith III^a, S. Decatur^b and Robin M. Hochstrasser^a

^aDepartment of Chemistry, University of Pennsylvania, Philadelphia, PA 19104, USA
Hochstra@sas.upenn.edu.

^bDepartment of Chemistry, Mount Holyoke College, Massachusetts 01075, USA

1. INTRODUCTION

An important challenge is the development of methods to time resolve structural changes in complex systems. Because of its time resolution, multidimensional infrared spectroscopies 2D-IR and 3D-IR, can contribute to this challenge complementing the knowledge on average structures obtained by the established methods of structural biology and their time dependent variants. The multidimensional infrared experiment arose from many years of theoretical and experimental research on laser technology, nonlinear optics and infrared spectroscopy. The manipulation of multidimensional data sets in time or frequency domains are also basic material in NMR even though the practical aspects of the two experiments are quite different and they arose quite independently.

In my talk I surveyed recent advances in the methodology and selected 2D-IR spectra of secondary structures. The results promise to provide structurally based kinetic probes for conformational dynamics, sharp tests of anharmonic potential surfaces and novel information regarding the transient and equilibrium vibrational dynamics of peptides. The heterodyned 2D-IR approach has proven useful in determining structures of peptides in solution and the anharmonic nature of the potential surfaces of peptides and secondary structures [1-10], as have polarized photon echo [2,6,10-12] or pump-probe techniques [4,13-16].

The nonlinear response can also be created by sequences of IR pulses having different center frequencies exciting more than one type of molecular vibration in each molecule. Such dual frequency experiments can provide intermode couplings and intermode angular relations, yielding additional structural information [15-17]. In the present work we have obtained a full 2D-IR spectrum in which the two frequency axes correspond to the quite different spectral regions at 3300 cm⁻¹ and 1650 cm⁻¹: the amide-A and amide-I modes influence each other in N-H···O=C hydrogen bonding configurations.

Isotopic replacements have been essential in the interpretation of vibrational spectra and their relationship to structure. Of particular interest in applications of 2D-IR: they shift frequencies into regions where their couplings can be measured, free from interference with other modes. For the amide-I mode the shift by ¹³C=¹⁸O displaces the amide group frequency beyond the range of the distribution of frequencies found in most secondary structures. Our strategy is to insert both ¹³C=¹⁶O and ¹³C=¹⁸O labels into an α -helix and create a pair of isotopic peaks separated by approximately 20 cm⁻¹. The couplings between the labels and the band states will show also up in the off diagonal regions of the 2D-IR spectrum.

2. 2D-IR SPECTROSCOPY WITH SINGLE AND DUAL FREQUENCY PULSES

2.1 Methods

We use either spectral or time domain interferometry [2,6,18] to acquire these signals. In both approaches, three IR pulses with wavevectors k_1 , k_2 , and k_3 are incident on the sample at intervals τ and T (see Figure 1). The complex polarization $P(t;\tau,T)$ created for times t after the third pulse generates an electric field $E(t;\tau,T)$ that is then heterodyned with a local oscillator pulse in the spectral or time domain to obtain $\text{Re}[E(t;\tau,T)]$. When the time delay between the first two pulses, τ , is scanned, the complex 2D-IR spectrum $S(\omega_t, \omega_\tau)$ is obtained from the Fourier transform of $\text{Re}[E(t;\tau,T)]$, along t and τ , yielding frequency axes ω_t and ω_τ . In other experiments the delay between the local oscillator and the signal is fixed and $S(\omega_t, \tau)$ is measured directly by sending the echo and local oscillator to a monochromator at each value of τ .

2.2 Obtaining pulses with different center frequencies

The two pulses with different center frequencies used in the dual frequency experiments were obtained by a variety of methods illustrated in Figure 2. One was a pump/probe configuration with different frequencies in each arm (A), the other involved one OPA output being sent to two difference frequency generators (B) and in C we used two OPA's that were coupled by amplifying the same continuum pulse in each one. When the pulses overlap there is significant phase noise in the nonlinear signals when their pulse-to-pulse phases are not stabilized. The stability of our pulses is illustrated in Figure 3. A and B are heterodyned signals with pulses at two different frequencies as indicated in A. A heterodyned photon echo from the acetic acid dimer in CCl_4 with two pulses having nearly the same frequency but from different but coupled OPA's is shown in D.

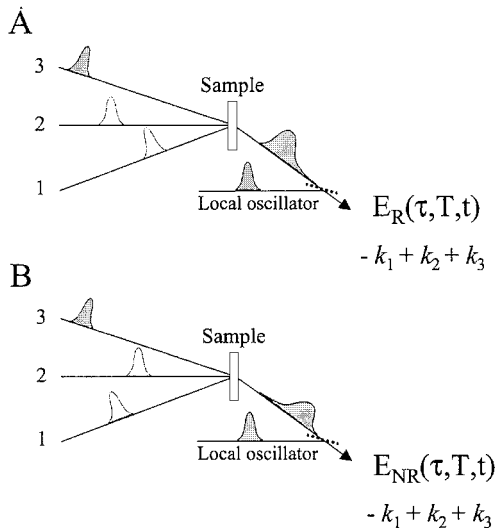


Fig. 1. Time sequence of the three-pulse single- or dual-frequency (shaded and unshaded) heterodyned 2D-IR experiments. (A) Rephasing; (B) Nonrephasing sequences. The signal is observed in the $k_2 + k_3$ - k_1 direction.

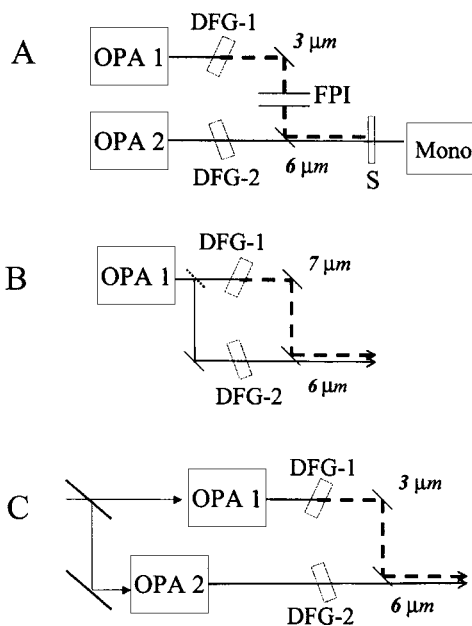


Fig. 2. Illustrations of three dual frequency 2D-IR experiments using one or two sets of OPAs and DFGs. (A) 3- and 6- μm with Febry-Perot interferometer filter; (B) 6- and 7- μm ; (C) 3- and 6- μm .

2.3 Dual frequency 2D-IR

The use of two frequencies is a useful alternative to ultrashort pulse shaping and impulsive limit experiments. It can permit avoidance of pulse distortion that arises in regions of strong solvent or solute absorption and it provides a broad selection of anharmonic couplings and an increased number of structural constraints. The 2D-IR spectrum is simplified considerably by the use of two frequencies as shown in Figure 4, which depicts the locations of some of the rephasing and nonrephasing spectral components for the Liouville paths in the response of two oscillators. The radii of the circles in Figure 4 depict the strength of the field generated from that particular Liouville path. Each path corresponds to a particular coherence transfer: for example the (I, II) peak arises from pulse k_1 inducing a coherence 0-I which is transferred to a coherence II-0 by the pair of pulse k_2 and k_3 . In practice the signals are not circles but rather ellipses elongated along the diagonal, manifesting the presence of a distribution of diagonal contributions. The projections onto the ω_r axis are equal for the rephasing and nonrephasing spectra as can be seen by inspecting the addition of peaks along the ω_r axis at a particular value of ω_i in Figure 4. The dual frequency 2D-IR spectra were acquired with three IR pulses as follows: two at 3 and one at 6 μm ; or two at 6 μm and one at 7 μm . Joint nonlinear responses were stimulated from both the amide-A (N-H) and either the amide or ester carbonyl transitions or from amide-I and amide II transitions.

2.4 Correlations in the frequency distributions of modes

The correlation of the vibrational frequency distributions of two modes can be determined from 2D-IR experiments and such effects are particularly evident in dual frequency experiments. For example, positive correlations between the amide-A and amide-I frequencies apparent from the spectra of acylalaninemethoxide (AcAlaOMe) in Figure 5, imply that when

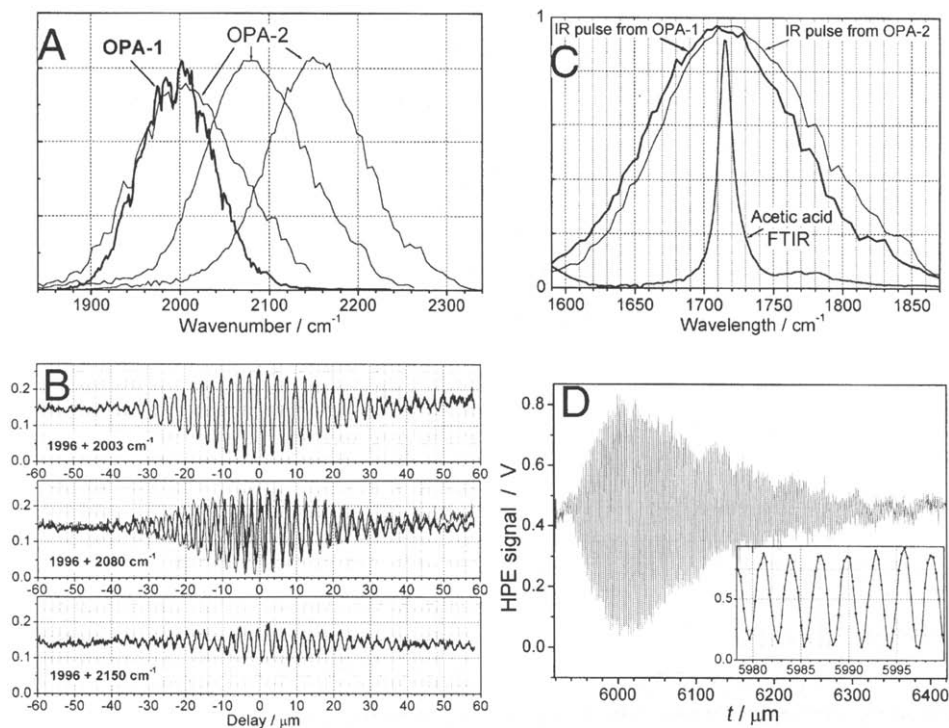


Fig. 3. Phase Locked IR Pulses Time domain interferometry. (A) Output IR pulses from two tunable OPA-DFGs in the 4- μm frequency regime. (B) Three examples of interferograms generated by these IR pulses. (C) Linear IR absorption spectrum of acetic acid overlapped with the output of two OPAs. (D) Photon echo signal from acetic acid upon t -scan. The x -axis is the delay of the translation stage and the insert is a blow-up of a small region.

a solvent fluctuation slightly weakens the C=O bond a contribution of the structure having C=N increases and both the C=O and N-H frequencies decrease. Because the NH mode

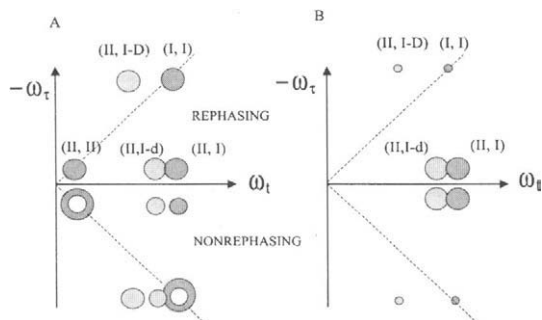


Fig. 4. Locations of the diagonal and off-diagonal peaks in the 2D-IR spectra in the rephasing (upper) and nonrephasing (lower) quadrant of (ω_τ, ω_t) . (A) single-frequency; (B) two pulses one centered at ω_I and the other at ω_{II} . D and d are the diagonal and off-diagonal anharmonicities, respectively. The cross peaks near (I, II) and the (II, II-D) peaks are omitted for clarity.

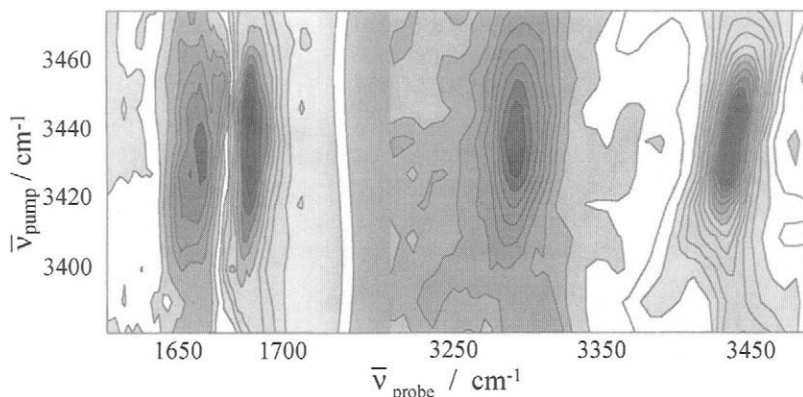


Fig. 5. Dual-frequency (3-, 6- μm) 2D-IR pump/probe of AcAlaOMe in chloroform acquired with magic angle polarization

becomes more localized as its frequency increases the amide-I mode, which includes NH bending, is also increased in frequency. A negative correlation between the amide-I frequency and the anharmonicity of the combination of N-H and amide-I modes is observed implying that a smaller anharmonicity results in a higher amide-I frequency. The off-diagonal anharmonicities are just a few cm^{-1} but are readily measured because the nonlinear signals derive from the differences between two large signals that cancel when there is no direct or indirect coupling between the modes. In the diagonal amide-A peaks correlations are found between the diagonal anharmonicities and the fundamentals, readily seen from Figure 5. The use of dual frequencies significantly enlarges the scope of 2D-IR vibrational spectroscopy. Interesting qualitative models of the anharmonic potential surfaces of peptides emerge from dual color results [17] shown in Figure 6 from which we find the amide I and amide II frequency distributions to be largely anticorrelated. We think of this in terms of solvent induced mixing of valence bond structures where an increase in the zwitterionic form of

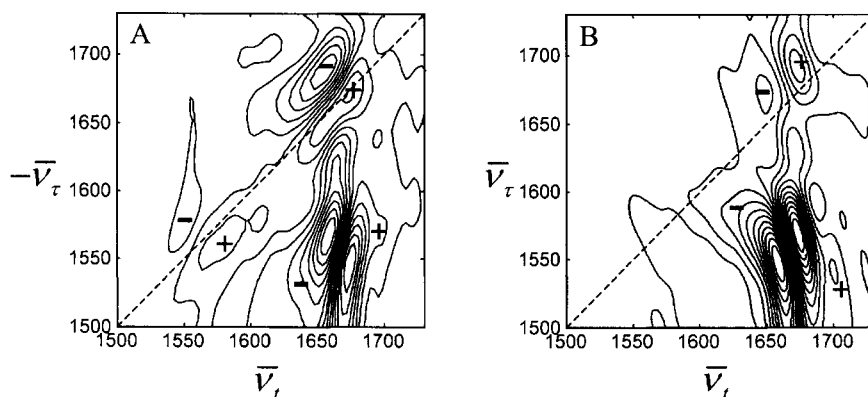


Fig. 6. Real parts of dual-frequency 2D-IR spectra of NMA. (A) rephasing; (B) nonrephasing.

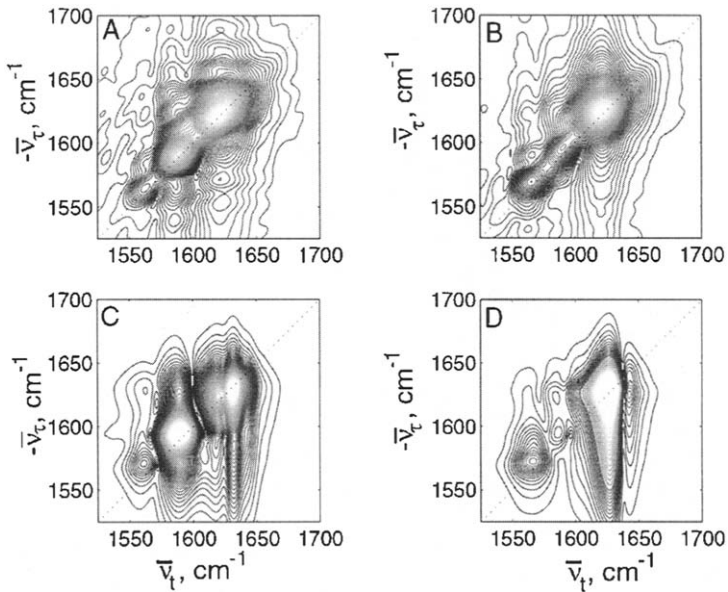


Fig. 7. Measured and simulated absolute magnitude 2D-IR rephasing spectra of a 25mer α -helix with double isotope substitutions denoted as [$^{13}\text{C}=\text{}^{16}\text{O}$, $^{13}\text{C}=\text{}^{18}\text{O}$]. (A) [12,13], (B) [11,13]. Experimental condition: D_2O -phosphoric acid buffer at 0°C . (C) and (D) are corresponding simulations.

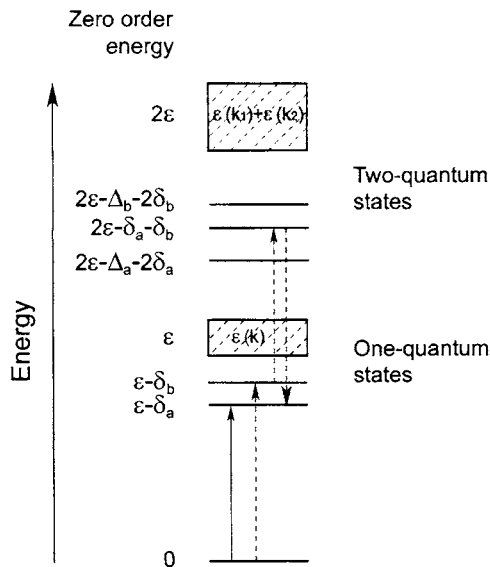


Fig. 8. An overview of the zero order energy levels of the doubly isotopically tagged helix. The isotope shifts are δ_a ($^{13}\text{C}=\text{}^{18}\text{O}$) and δ_b ($^{13}\text{C}=\text{}^{18}\text{O}$) while Δ_a and Δ_b are diagonal anharmonicities. The shaded areas represent the helix one- and two-exciton bands that become perturbed by the isotopes. The solid (bra evolution) and dashed (ket evolution) arrows represent one of the Liouville paths contributing to the echo.

NMA, as might occur in for NMA molecules associated with particular solvent configurations, causes a reduction in the C=O frequency and an increase of the C-N frequency.

2.5 2D-IR of isotopically substituted helices

We have measured the coupling between nearby amide units on an α -helix and other structures and compared them with theoretical models. We succeeded in obtaining the 2D-IR spectra of doubly isotopically substituted 25 residue α -helical structures. The presence of $^{13}\text{C}=\text{}^{16}\text{O}$ and $^{13}\text{C}=\text{}^{18}\text{O}$ labels at two known residues on the helix labeled as [m,n] enabled the coupling between different amide-I modes to be measured. I also presented the 2D-IR spectrum of the β -hairpin from the GB1 protein with two isotopically replaced residues. Typical spectra of are shown in Figure 7 for some of the α -helix examples. The 2D-IR in this case arises from the one-exciton and two-exciton states of a helix as illustrated in Figure 8. The couplings between the isotopomers and between them and the helix band states were identified as cross peaks leaving no doubt that the states of the helix and isotopomers are delocalized. The cross peaks between the isotopic transitions result from the vibrational frequency of an amide mode at one position being influenced by whether or not there is an excitation at some other position. The results were compared with simulations, also illustrated in Figure 7. The off-diagonal anharmonicities from the experiment agree reasonably with those obtained from transition charge interactions for all but the nearest neighbors for which there is through bond interaction between the adjacent amide groups.

3. CONCLUSIONS

Following a review of progress in 2D-IR of biological systems, I reported on dual frequency 2D-IR echoes covering the amide-A, amide-I and amide II band regions of peptide groups in small molecules, α -helices and a β -hairpin. Experiments with isotopomers and engineered structures permitted the otherwise complicated response functions for molecules to be considerably simplified. From these we have determined the correlations of the instantaneous frequencies of these modes and obtained new knowledge of the spatial properties of equilibrium vibrational dynamics of small peptides and the anharmonic coupling of amide units in a variety of structures. The 2D-IR method has significant potential for applications in structural biology.

ACKNOWLEDGEMENT

This research was supported by NIH(GM12592 and RR01348) and NSF.

REFERENCES

- [1] P. Hamm, M. Lim, and R. M. Hochstrasser, *J. Phys. Chem. B* 102 (1998) 6123.
- [2] M. C. Asplund, M. T. Zanni, and R. M. Hochstrasser, *Proc. Natl. Acad. Sci. USA* 97 (2000) 8219.
- [3] A. Piryatinski, S. Tretiak, V. Chernyak, and S. Mukamel, *J. Raman Spec.* 31 (2000) 125.
- [4] S. Woutersen and P. Hamm, *J. Phys. Chem. B* 104 (2000) 11316.
- [5] C. Scheurer, A. Piryatinski, and S. Mukamel, *J. Am. Chem. Soc.* 123 (2001) 3114.
- [6] M. T. Zanni, M. C. Asplund, and R. M. Hochstrasser, *J. Chem. Phys.* 114 (2001) 4579.
- [7] M. T. Zanni and R. M. Hochstrasser, *Curr. Opin. Struct. Biol.* 11 (2001) 516.
- [8] P. Hamm and R. M. Hochstrasser, in *Ultrafast Infrared and Raman Spectroscopy*, edited by M. D. Fayer (Marcel Dekker Inc., New York, 2001), pp. 273.
- [9] N.-H. Ge and R. M. Hochstrasser, *Phys. chem. Comm.* 3 (2002) 1.
- [10] N.-H. Ge, M. T. Zanni, and R. M. Hochstrasser, *J. Phys. Chem. B* 106 (2002) 962.
- [11] S. Gnanakaran and R. M. Hochstrasser, *J. Am. Chem. Soc.* 123 (2001) 12886.
- [12] M. T. Zanni, S. Gnanakaran, J. Stenger, and R. M. Hochstrasser, *J. Phys. Chem. B* 105 (2001) 6520.
- [13] P. Hamm, M. Lim, W. F. DeGrado, and R. M. Hochstrasser, *Proc. Natl. Acad. Sci. USA* 96 (1999) 2036.
- [14] P. Hamm, M. Lim, W. F. DeGrado, and R. M. Hochstrasser, *J. Chem. Phys.* 112 (2000) 1907.
- [15] I. V. Rubtsov and R. M. Hochstrasser, *J. Phys. Chem. B* 106 (2002) 9165.
- [16] I. V. Rubtsov, J.-P. Wang, and R. M. Hochstrasser, *J. Phys. Chem. A* 106 (2003) 9165.
- [17] I. V. Rubtsov, J.-P. Wang, and R. M. Hochstrasser, *Proc. Natl. Acad. Sci. USA* 100 (2003) 5601.
- [18] O. Golonzka, M. Khalil, N. Demirdöven, and A. Tokmakoff, *Phys. Rev. Lett.* 86 (2001) 2154.

Ultrafast conformational dynamics in light triggered cyclic peptides

W. Zinth^a, A. Sieg^a, T. Schrader^a, S. Spörlein^a, P. Hamm^b, J. Bredenbeck^b, J. Helbing^b, C. Renner^c, L. Moroder^c, H. Carstens^a, P. Tavan^a and J. Wachtveitl^d

^aLehrstuhl für BioMolekulare Optik, Ludwig-Maximilians-Universität München, Oettingenstr. 67, 80538 München, Germany

^bUniversität Zürich, Physikalisch Chemisches Institut, Winterthurer Str. 190, 8057 Zürich, Switzerland

^cMax-Planck-Institut für Biochemie, Am Klopferspitz 18A, 82152 Martinsried, Germany

^dInstitut für Physikalische und Theoretische Chemie, Johann Wolfgang Goethe Universität, Marie-Curie-Str. 11, 60439 Frankfurt, Germany

1. INTRODUCTION

In living organisms proteins perform various functions such as transmission of information, transport of molecules, muscular motion, chemical synthesis, structure building, gene expression [1]. In spite of this variety of functions, proteins are built according to an extremely simple principle: They are basically linear polymers of amino acids where the amino acid chain is arranged in a three-dimensional structure. Nature uses a set of 20 amino acids differing in their specific side groups. The sequence of amino acids determines the three-dimensional structure and the function of the protein. After synthesis of a protein in the ribosomes, the amino acid chain is in a non-specific, the "random coil" conformation. Only after the subsequent folding of the amino acid chain into a well-defined three-dimensional structure – the "native form" – the protein is enabled to fulfil its biological functions. In many proteins this folding process occurs spontaneously covering several orders of magnitudes in time. Folding of a typical protein is finished on the time scale of seconds. A detailed understanding of the protein folding process, i.e. the way from an amino acid sequence to the three-dimensional structure with its well defined function, would be extremely helpful in medicine (diagnosis and treatment of diseases related to the misfolding or aggregation of proteins). For biotechnology this understanding would pave the way to the *de novo* synthesis of proteins with unprecedented functions.

At present we are far from an understanding of the protein folding process. Even numerical methods as e.g. molecular dynamics simulations do not lead to realistic predictions. Experiments on the folding process have been performed initially on the millisecond time-scale. It was only recently that new techniques – temperature jump or triplet-triplet quenching experiments – allowed a first access to the nanosecond time domain [2-4]. However, the elementary reactions in protein folding occur on the femto- to picosecond time-scale (femtobiology). In order to allow experiments in this temporal range we developed a new

experimental approach [5-7]. We employ a specific molecule, where the structural change can be induced by light and where one can follow the molecular reactions as a function of time by ultrafast spectroscopy. We use the combination of a photochemically active molecule (azobenzene, which changes its structure by photoisomerization) linked to a peptide chain. The azobenzene peptide allows to trigger structural changes of the peptide by an ultrashort light pulse. These structural changes may be detected in two ways: (i) by visible – ultraviolet spectroscopy of the trigger molecule one observes the isomerizational motion of the trigger. In addition, as we will show below, the peptide acts back on the trigger molecule. Its absorption is modulated by the structural change of the peptide chain. (ii) Transient infrared spectroscopy yields direct information on the structural changes of the peptide moiety.

In this paper we will present recent experiments on different types of azobenzene molecules with transient visible and IR-spectroscopy which show that ultrafast structural changes of peptide molecules occur on the time-scale of 10 ps.

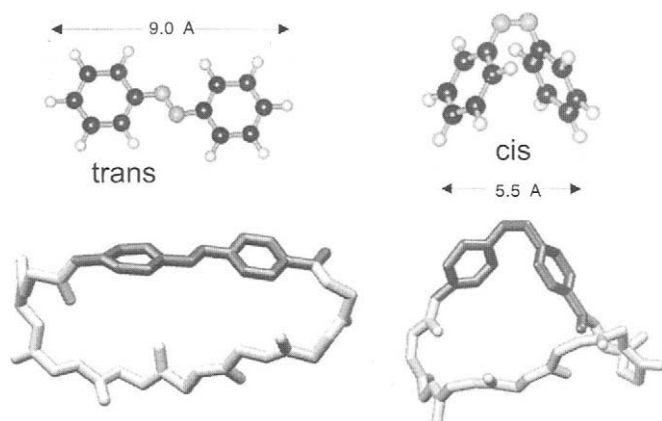


Fig. 1. Azobenzene and the azobenzene peptide c-APB in the *trans* and *cis* form.

2. THE MOLECULAR SYSTEM

The newly developed chromopeptides contain azobenzene as the optical trigger. For azobenzene both isomers can be prepared to high concentrations by illumination with light at specific wavelengths. The *trans* isomer is stable while the *cis* isomer thermally reconverts to the *trans* form at room temperature on the time-scale of one day. It is well known that photoisomerization of azobenzene is ultrafast. The *cis* to *trans* reaction is basically finished within 100 fs. The large change of the edge to edge distance (see Fig. 1) of the azobenzene molecule upon isomerization makes it an ideal trigger for fast structural changes of an attached peptide. The connection to a peptide chain is accomplished by appropriate substitution. Two different types of azobenzene derivatives are used in the present study: (i) 4-aminophenyl-azobenzoic acid (APB) which forms a trigger molecule where the structural changes induced by photoisomerization are directly transferred to the peptide chain and (ii) 4-aminomethylphenyl-azobenzoic-acid (AMPB) where the additional methylene group adds some degrees of flexibility. As peptide of choice we used (H-Ala-Cys-Ala-Thr-Cys-Asp-Gly-Phe-OH), the active site fragment of thioredoxin reductase, a thiol protein oxido-reductase. The trigger

molecules are connected to the peptide chain forming cyclic compounds. NMR analysis showed distinct structural differences of the peptide part upon isomerization of the trigger molecule [8,9]. Apparently the *cis* to *trans* isomerization leads to conformational transitions of the peptide part from a more variable *cis* peptide to a more constrained *trans* peptide. Additional rigidity may be introduced by the formation of a disulfide bridge between the two cysteines resulting in a bicyclic molecule (bc-AMPB). This paper is focussed on fast conformational changes in cyclic c-APB. For comparison we used a linear peptide where the peptide chain is opened between Gly and Phe.

3. MATERIAL AND METHODS

The APB and AMPB peptides were prepared as described elsewhere [5,6,8,9]. All samples are dissolved in DMSO at concentrations in the 1-mM-range (visible spectroscopy) and in the 4-mM-range (IR-spectroscopy). The solutions were pumped through flow cells (fused silica and CaF₂ for the visible and IR experiments, respectively) to ensure exchange of the illuminated sample volume between the laser pulses. The initial *cis* isomeric state was prepared by cw-illumination at appropriate wavelengths. The experimental set-ups are described in detail in [7,10,11]. In all experiments the pump and probe technique was used with pulses from a regenerative chirped pulse amplifier, operated at 1kHz. Optical parametric processes, second harmonic generation, difference frequency mixing, or fs-continuum generation are used to produce excitation (480 nm for the visible experiment, 420 nm for the IR-experiment) and probing pulses ($\approx 6 \mu\text{m}$ IR probing and 350 – 650 nm visible probing). Temporal resolution was set to 80 fs and 700 fs for the visible and IR experiments, respectively.

4. RESULTS

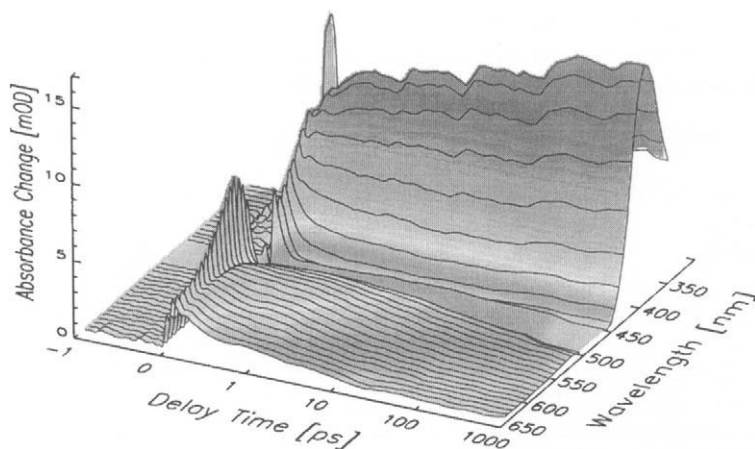


Fig. 2. Transient absorbance change of c-APB measured as a function of time delay and probing wavelength.

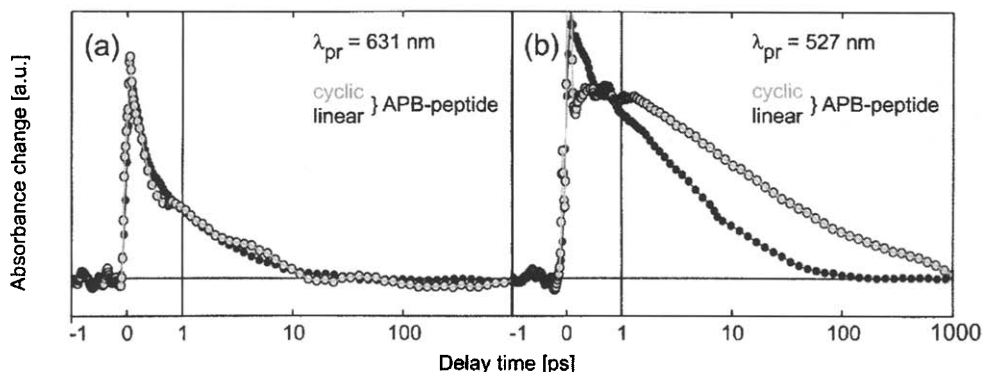


Fig. 3. Transient absorbance change for the two APB-peptides c-APB and l-APB. The decay of the excited state absorption (a) is similar for the two molecules. However, the groundstate absorption (b) in c-APB shows slower absorption transients not seen in the linear molecule. These slower processes are related to the peptide motion on the 10-100 ps time domain.

Transient absorption dynamics for probing wavelengths between 350 nm and 650 nm are shown in Fig. 2 for the *cis* to *trans* photoreaction of the cyclic c-APB-peptide. The data exhibit a number of interesting features: shortly after time zero one observes an absorption increase throughout the whole investigated spectral range. At longer wavelengths where the signal is dominated by excited state absorption, the absorption increase relaxes within 10 ps. A more detailed analysis indicates that the related processes have time constants of ~ 230 fs and 2.7 ps. In this wavelength range the cyclic and the linear APB peptides show a very similar time dependence (Fig. 3a). Towards shorter wavelengths, where absorption from the electronic ground state of azobenzene is found, the dynamics of the c-APB contain considerable contributions with slower time-dependence. Here (in addition to the picosecond components) slower processes with ~ 60 ps and 1.4 ns are observed. Since these slow components are absent in the linear peptide (see Fig. 3b) we can relate them to structural changes in the peptide moiety. At short wavelengths < 400 nm we see the absorption increase caused by the π - π^* band of the newly formed *trans* isomer.

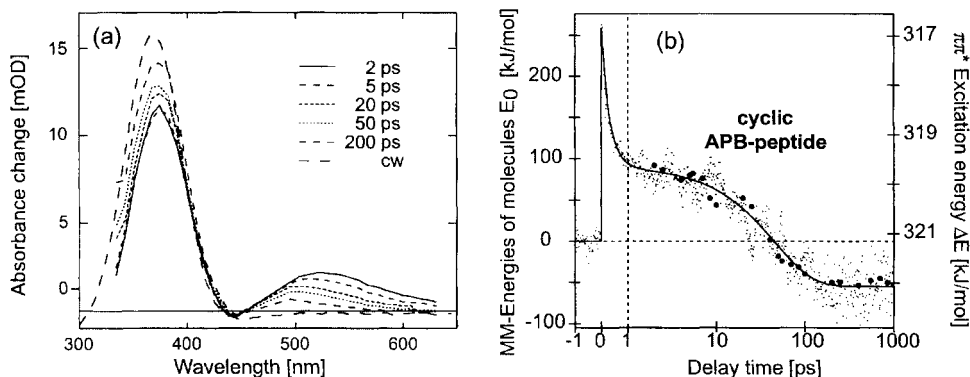


Fig. 4. (a) Absorbance change recorded for c-APB at certain delay times t_D . These spectra show the spectral shift of the newly formed *trans* bands on the 10 - 100 ps time scale. (b): excitation energy corresponding to the peak absorption of the ≈ 350 nm band plotted as a function of time (filled circles) and time dependence of the energy within the peptide determined by MD-simulations (points).

Here the long lasting absorption transients are also well seen. Even a first inspection of the absorption transient in Fig. 2 reveals spectral shifts of the absorption bands throughout the whole time range. They are well resolved in the absorption spectra plotted for specific delay times (Fig. 4a). Here a blue shift with time both of the $n-\pi^*$ (~ 500 nm) and the $\pi-\pi^*$ (~ 350 nm) absorption band is evident. The position of the newly formed $\pi-\pi^*$ band of the *trans*-molecules (350 nm) is of special interest. It is plotted in Fig. 4b as a function of time delay (filled circles). At later delay times this spectral shift is dominated by a ~ 50 ps kinetic compound.

Transient IR spectroscopy in the range of the amide I band is a direct tool to follow the structural dynamics of the peptide moiety. IR difference spectra on the bicyclic molecule bc-AMPB are plotted in Fig. 5. Shortly after excitation the absorption is dominated by a red shift. Such a red shift is expected for a strong vibrational excitation of the molecule. On the time-scale of a few picosecond this red shift decays to a large extent and is replaced by a dispersive feature of opposite sign at $t_D = 20$ ps. At later delay times this feature changes details of its shape, it sharpens up and some substructure appears around 1680 cm^{-1} . After 1.7 ns the shape is similar, but not completely identical to the difference spectrum recorded with stationary FTIR spectroscopy. This time dependence shows that the dominant structural change responsible for the IR difference spectrum occurs on the 20 ps time-scale and that minor structural changes continue until nanoseconds and even later times.

5. DISCUSSION

The experimental results on the various samples may be summarized as follows: (i) The excited electronic state absorption decays rapidly on the time-scale of pico- or subpicoseconds. (ii) Longer lasting absorption changes are observed in spectral ranges with chromophore absorption for the cyclic and bicyclic peptides. (iii) Infrared experiments have clearly shown that absorption transients in the pico- to nanosecond range occur. They monitor directly structural change of the peptide backbone.

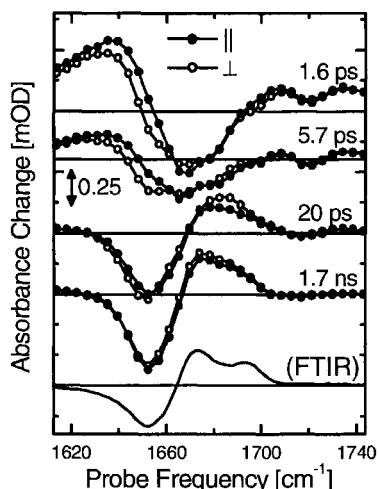


Fig. 5. Transient IR-absorption change in the bc-AMPB peptide. Within 20 ps pronounced absorption changes happen, which are related with changes in the peptide backbone.

5.1. Decay of the S₁-state:

Free *cis*-azobenzene, excited at 480 nm displays a biexponential decay of the excited state S₁ with time constants of ~0.1 ps and 0.9 ps. Here the ultrafast kinetic component dominates the absorption change (it contains ~ 90 % of the whole amplitude). A direct interpretation would relate the fast component to a free isomerizational motion, where the most direct reaction path on the S₁ and S₀ potential energy surface is used without disturbance. The slower process may be assigned to a less direct motion due to hindrance by the surrounding solvent molecules. This interpretation is supported by the observation of the absorption changes in the APB and AMPB peptides. Here both reaction parts are slowed down by a factor of 2 - 3 and both show similar amplitudes: The peptide molecules hinder the motion of the azobenzene switch and slow down considerably the initial kinetics. However, in all samples the transition to the ground state is finished within a few picoseconds.

5.2 Motions of the peptide moiety

The most direct way to observe structural changes of the peptide backbone is via transient IR spectroscopy of the amide I band around 1700 cm⁻¹ [10]. These experiments exhibit absorption changes occurring on the picosecond to nanosecond time domain. However, the dominant spectral changes occur during the first 20 ps. This allows to separate the reaction of the peptide into a strongly driven phase, where the direct action of the isomerized chromophore leads to strong and ultrafast structural changes and into a weakly driven diffusive part on the longer time scale. It is interesting to note that the peptide motion can also be monitored via the visible/ultraviolet spectroscopy [7]. In the time-scale of picoseconds we see pronounced spectral changes which can be assigned to a decay of a red shift of the *trans* azobenzene bands (see Fig. 4a). The reason for this absorption change can be explained via the scheme in Fig. 6, left: While the ground state potential energy surface of the azobenzene chromophore in the vicinity of the *trans* configuration depends strongly on the nuclear coordinates, the potential energy surfaces of the excited electronic state have a much shallower shape. As a consequence, one would expect a red shift of the absorption spectra as long as the chromophore has not acquired its planar shape. By that way the strain between the peptide and the chromophore causes a red shift. The experimental observation then shows, that for cyclic c-APB a strain exists between the chromophore and the peptide, which relaxes mostly on the 50 ps time-scale. This observation indicates that prominent structural changes occur on this time domain in full agreement with the IR experiments.

5.3 Molecular dynamics simulations of the light induced structural dynamics

High quality Molecular Dynamics (MD) simulations have been performed considering electrostatic interactions and the DMSO solvent [7,12]. 10 trajectories over 1 ns were calculated and analysed. In Fig. 4b the calculated energy contents of the azopeptide c-APB is plotted as a function of time (points and solid fit curve). During the initial part of the isomerization of the azobenzene a large fraction of the excitation energy is dumped into the surrounding solvent. When the ground state is reached, the energy contents of the azopeptide stays constant before it decays on the 50 ps timescale. It is interesting to compare the change in energy with the spectral shift of the *trans* absorption band determined in the experiment (open circles in Fig. 4b). After a few picoseconds the spectral shift goes in parallel with the change in energy of the azopeptide. Apparently the visible absorption spectrum monitors the energy contents of the molecule and with that the stress between chromophore and peptide chain. Thus the visible/UV absorption can be used to monitor the structural changes of the peptide moiety.

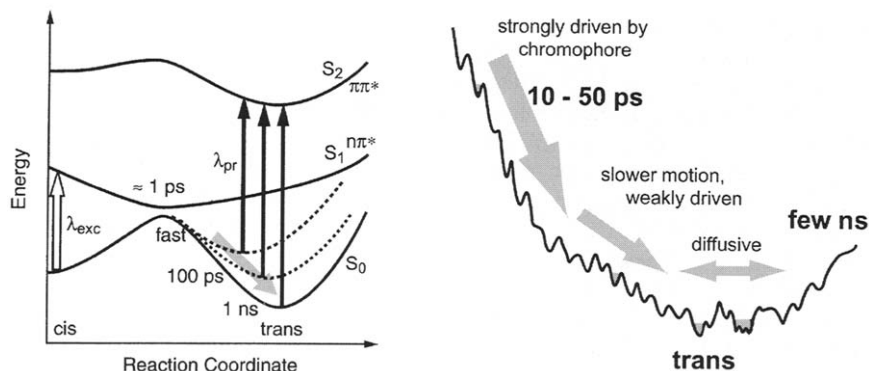


Fig. 6. Left: schematic potential energy curves explaining the absorption transients seen in the newly formed *trans*-absorption bands. The strain between the peptide part and the azobenzene chromophore delays the transition to the relaxed ground state and causes the blue-shift observed as a function of time. Right: View of the two phases of peptide motion occurring after the initial isomerization of the azobenzene chromophore.

In conclusion: visible and IR experiments on the timescale of femtoseconds and picoseconds in combination with molecular dynamics simulations have given a detailed picture of the fast structural dynamics in light triggered azobenzene peptides. This reaction exhibits three phases:

1. The initial motion of the light triggered switch, the isomerization of azobenzene, is ultrafast and occurs on the timescale of 200 fs and 2 ps.
2. In a strongly driven phase the peptide responds within 10 to 100 ps to the new structure of the chromophore.
3. Finally biased diffusive processes lead to slower structural changes, spanning a wider range of time constants.

REFERENCES

- [1] L. Stryer: Biochemistry, 4th ed. W.H. Freeman and Company, New York, 1995.
- [2] S. Williams, T.P. Causgrove, R. Gilmanshin, K.S. Fang, R.H. Callender, W.H. Woodruff and R.B. Dyer, Biochemistry, 35 (1996) 691.
- [3] P.A. Thompson, V. Munoz, G.S. Jas, E.R. Henry, W.A. Eaton and J. Hofrichter, J. Phys. Chem. B, 104 (2000) 378.
- [4] O. Bieri, J. Wirz, B. Hellrung, M. Schutkowski, M. Drewello and T. Kiefhaber, Proc. Natl. Acad. Sci. U. S. A., 96 (1999) 9597.
- [5] R. Behrendt, C. Renner, M. Schenk, F.Q. Wang, J. Wachtveitl, D. Oesterhelt and L. Moroder, Angew. Chem.-Intern. Ed., 38 (1999) 2771.
- [6] R. Behrendt, M. Schenk, H.-J. Musiol and L. Moroder, J. Pept. Sci., 5 (1999) 519.
- [7] S. Spörlein, H. Carstens, H. Satzger, C. Renner, R. Behrendt, L. Moroder, P. Tavan, W. Zinth and J. Wachtveitl, Proc. Natl. Acad. Sci. U. S. A., 99 (2002) 7998.
- [8] C. Renner, R. Behrendt, S. Spörlein, J. Wachtveitl and L. Moroder, Biopolymers, 54 (2000) 489.
- [9] C. Renner, J. Cramer, R. Behrendt and L. Moroder, Biopolymers, 54 (2000) 501.
- [10] J. Bredenbeck, J. Helbing, A. Sieg, T. Schrader, W. Zinth, C. Renner, R. Behrendt, L. Moroder, J. Wachtveitl and P. Hamm, Proc. Natl. Acad. Sci. U. S. A., 100 (2003) 6452.
- [11] M. Seel, E. Wildermuth and W. Zinth, Meas. Sci. Tech., 8 (1997) 449.
- [12] G. Mathias, W. Egwolf, M. Nonella and P. Tavan, J. Chem. Phys., 118 (2003) 10847.

Femtosecond visible pump – midinfrared probe setup for the study of protein dynamics. Isomerization in Photoactive Yellow Protein

**M.L. Groot^a, L. J.G.W. van Wilderen^a, D. S. Larsen^a, M. A. van der Horst^b,
I. H.M. van Stokkum^a, K. J. Hellingwerf^b and R. van Grondelle^a**

^aFaculty of Sciences, Vrije Universiteit, 1081 HV Amsterdam, The Netherlands

^bLaboratory for Microbiology, Swammerdam Institute for Life Sciences, University of Amsterdam, Nieuwe Achtergracht 166, 1010 WV Amsterdam, The Netherlands

1. INTRODUCTION

To catch proteins at work is necessary for our understanding of how biological cells function. In general a protein may catalyze a certain event by modulating the transition state from which the desired product is formed. Following the formation of such a transition state the next few steps will occur on an ultrafast timescale and these steps may be decisive for the success of the biological process. Enzymes such as protochlorophyll-oxidoreductase, or photoreceptor proteins, heme proteins, or the photosynthetic reaction center, which can be put into the transition state by the absorption of a photon from a femtosecond light pulse, in principle allow the study of these very first events. Visible pump – midinfrared probe spectroscopy is a method that allows to follow the physical movements and conformational changes of cofactor-protein complexes in real time, as has been showed by the work of for example the groups of Zinth, Hamm, Hochstrasser, Anfinrud and Diller. Here we describe our experimental setup in detail and give a description of the results obtained on the initial photocycle steps of Photoactive Yellow Protein.

2. VISIBLE PUMP – MIDINFRARED PROBE SETUP

All proteins and their cofactors show complex spectra in the midIR region 1000-1800 cm^{-1} . Typical midIR absorbers are C=O, C=C, C-C, N-H stretches, and their change in precise spectral position allows us to follow the structural rearrangement of the protein and cofactor in time. Good examples are the transfer of charge, the rearrangement of H-bonds and cis-trans isomerization of a chromophore (like in PYP). Moreover, polarized measurements allow determination of the dynamic reorientation of these chromophores.

We have developed a setup for time-resolved vibrational spectroscopy that is especially suited for the study of proteins and enzymes. The setup consists of an integrated Ti:sapphire oscillator-regenerative amplifier laser system (Hurricane, SpectraPhysics) operating at 1 kHz, 800 nm, producing 85 fs pulses of 0.8 mJ. A portion of this 800-nm light is used to pump a noncollinear optical parametric amplifier to produce the excitation pulses with center wavelength tunable between 470 and 700 nm. The excitation pulses are not compressed, since the midinfrared pulse length and inherent vibrational line widths of the samples are limiting,

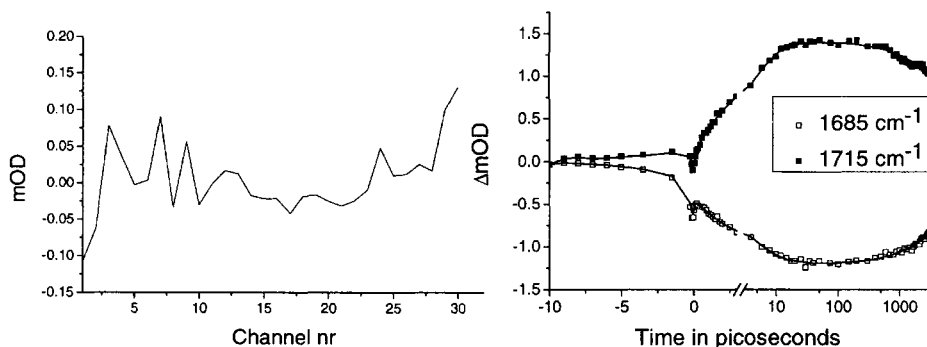


Fig. 1. A. Noise level expressed in milli optical density, obtained after 1 minute of data acquisition. B. Time dependent absorption change of the keto group of the primary donor of the bacterial reaction center, at 1685 cm^{-1} and 1715 cm^{-1} upon excitation at 600 nm, noise level $30\text{ }\mu\text{OD}$, measured in the Lissajous scanner. The solid line through the data points is a fit with $t_1 = 3.8\text{ ps}$, $t_2 = 16\text{ ps}$, $t_3 = 4\text{ ns}$ and $t_5 = \infty$. The time scale is linear up to 3 ps and logarithmic thereafter.

and have a duration of about 60 fs. They are focused with a 20 cm lens into the sample. A second portion of the 800-nm light is used to pump an optical parametric generator and amplifier with difference frequency generator (TOPAS, Light Conversion) to produce the midIR probe pulses. The probe pulses are attenuated to an intensity of about 1 nJ, focused with a 5 cm lens and spatially overlapped with the excitation beam in the sample. After overlap in the sample, the mid-IR probe pulses are dispersed in a spectrograph (Chromex) and imaged onto a 32-element MCT detector (Infrared Associates). The signals of the detector array are amplified (Infrared Associates) and fed into 32 home-built integrate-and-holds that are read out every shot with a National Instruments acquisition card (PCI6031E). A phase-locked chopper operating at 500 Hz is used to insure that every other shot the sample was excited and the change in transmission and hence optical density between two consecutive shots can be measured.

A spectral selection on sets of 500 spectra is applied, typically only the ones that deviate less than 2% from the average are selected, with acceptance percentages of 80-100%. Thus in 1 minute of data collection a noise level of 10^{-5} can be obtained for one single spectrum (see fig 1A), or a noise level of $30\text{ }\mu\text{OD}$ in a full data set consisting of 80 time points in a few hours (see fig. 1B). In a single experiment a spectral probe window of about 200 cm^{-1} is covered, so partly overlapping regions have to be measured to obtain a wider window. The cross correlation of the visible and IR pulses is measured in GaAs and is typically about 180 fs. The polarization of the excitation pulse with respect to the IR probe pulses is set with a Berek polarizer.

Most of the proteins and enzymes that we want to study have a photocycle time longer than 1 ms. Therefore, to ensure a fresh sample spot for each laser shot, we designed a Lissajous sample scanner. In short, the sample is moved perpendicular to the beam on three eccentrics that lead to a scan pattern filling a $20\times 20\text{ mm}$ surface. The velocity in the corners and at the sides is too low to refresh the sample after each laser shot, therefore these shots are discarded (~16-18%). The laser comes back at the same sample position after about a minute.

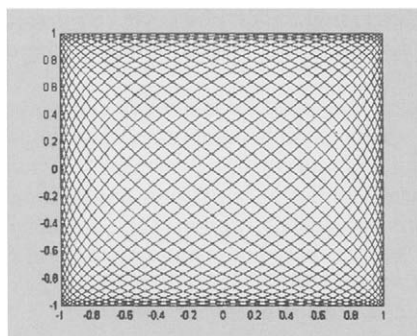


Fig. 2. Scan pattern of the Lissajous sample scanner, filling a 20x20 mm CaF₂ surface in about 1 minute.

The samples are contained in a demountable cell consisting of 2 CaF₂ plates separated by a spacer of 10 or 20 micron. The sample cell is filled through two metal tubes drilled through and glued to the first CaF₂ plate. The sample cell is held to the Lissajous scanner by three magnetic supports.

The excitation laser gives rise to a thermal lens effect in the sample, leading (due to its relatively long life time) to an offset in some of the channels. This effect is small and varies depending on the alignment between 0.1 and 1 mOD. However, compared to the small transient pump-probe signals this is still relatively large. Experiments with different alignments and thus varying thermal baseline effects showed us that this could be corrected for by subtracting the signal before $t < -10$ ps. From ~ -2 ps to 0 signals arise from perturbed free induction decay, as described by [[1],[2]].

All data sets are analysed using global analysis [[3],[4]]. Since part of the noise is correlated, i.e. baseline noise or amplitude noise of the whole spectrum, this kind of analysis is excellently suited to extract more reliable information from the data than a single-trace analysis. If the data contains sufficient information, or extra information is available, a target analysis is applied (i.e. a specific model is fitted to the data) from which spectra of physical states result.

3. PHOTOACTIVE YELLOW PROTEIN

Activation of PYP by blue light induces a negative phototactic response that enables the bacterium *Halorhodospira halophila* to swim away from harmful exposure to intense blue light (see for a review ref. [[5]]). Due to its rich and complex photocycle and its excellent (photo)chemical stability, PYP has become a model system for the study of biological signal generation in photoreceptor proteins. Light-induced signal generation in biology involves the amplification of an initially small configurational change generated in an active site, into a conformational change of a larger scale that converts the protein into its signalling state. The initial configurational change in the photocycle of PYP [[6]], i.e. *trans/cis* isomerization of its intrinsic chromophore (*p*-coumaric acid [[7],[8]]), is similar to that in other photosensors, like (bacterio)rhodopsin and (bacterio)phytochromes. A key characteristic of the PYP photocycle is a partial unfolding of the protein [[8]] on a sub-millisecond time scale, triggered by the absorption of a photon.

We have studied the initial steps in the PYP photocycle by detecting the absorption changes in the structure sensitive 1800-1100 cm^{-1} region, initiating the reaction with 60-fs 475-nm excitation.

In figure 4 we show the spectra that result from a target analysis on the data, using a model in agreement with that used to analyse visible pump-probe data. Four lifetimes are present in our data: 2 ps, 9 ps, 0.9-1 ns, and a non-decaying component (>10 ns). Note that in these spectra negative bands are due to the disappearance of *trans*-absorption, and positive (going) bands originate from excited- or product-state absorption. The assignment of the dynamic bandshifts for each of the ES, I_0 and I_1 states is based on literature reports [[9]-[19]] and on experiments performed on a mutant in which the residue Glu46 (glutamate) has been replaced by a glutamine (data not shown), and is given in table 1.

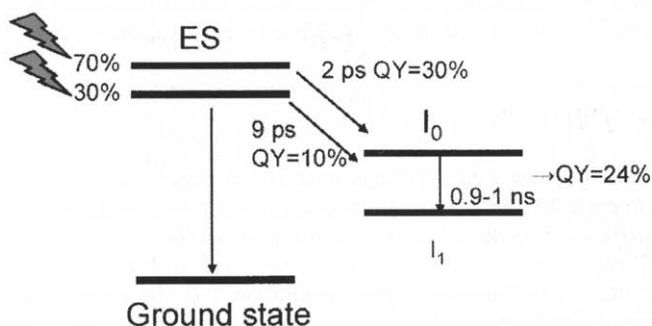
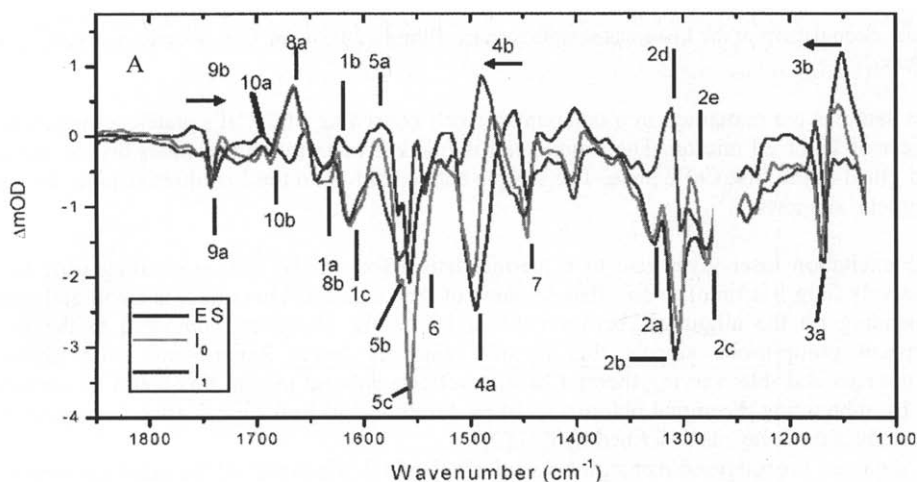


Fig. 3. (top) Species-associated difference spectra of WT PYP upon 475-nm excitation, fitted to the model depicted in the lower figure. The ES decay was fitted with a biexponential rate of $(2 \text{ and } 9 \text{ ps})^{-1}$, the I_0 to I_1 transition rate was $(0.9 - 1 \text{ ns})^{-1}$. Since the quantum yield of I_0 and I_1 states was only 24%, their presence in the raw data was ~ 4 times smaller relative to the ES spectrum.

We observe that upon photoexcitation the *trans* bands of the chromophore are bleached and shifts of the phenol-ring bands occur. The latter are ascribed to charge translocation, which probably plays an essential role in driving the *trans* to *cis* isomerization process. We conclude that breaking of the hydrogen bond of the chromophore's C=O group with amino acid Cys69 and formation of a stable *cis* ground state occur in ~ 2 ps. Dynamic changes also include rearrangements of the hydrogen bonding network of the amino acids around the chromophore. Relaxation of the coumaryl tail of the chromophore occurs in 0.9-1 ns, which event we identify with the I_0 to I_1 transition observed in visible spectroscopy. A more extensive discussion of these data is given in ref [[20]].

Table 1. Assignment of features observed in the midIR difference spectra for the states ES, I_0 and I_1 . Frequencies are in cm^{-1} , in the left column +/- denotes a positive and negative band respectively, and in the right three columns +/- indicates the presence/absence of these bands in the different states. This assignment is based on refs [9]-[19] and is discussed in more detail in ([20]).

Frequency/Assignment		ES	I_0	I_1
-1633/+1621/-1607 C=C pCA <i>trans</i> → <i>cis</i> markers	1a-c	~	+	+
-1326/-1302/-1274/+1308/+1289 C-C(-S-)=O pCA <i>trans</i> → <i>cis</i>	2a-e	+	+	+
-1168 Phenol ring Y9a pCA <i>trans</i> → <i>cis</i> and ionic markers	3a,b	+ 1149b	+ 1155b	+ 1173b
-1495 Phenol ring Y19a, ring-O ⁻ symmetric stretch ionic marker	4a-b	+ 1457b	+ 1476b	+ 1486b
+(1580-1585)/-1565/-1555 Phenol ring Y8b ionic	5a-c	+	+	-
-1540 Phenol ring Y8a	6	+	+	+
-1444 Phenol ring Y19b	7	+	+	+
+1665/-(1635-1640) C=O of pCA	8a-b	-	+	+
-1740 COOH stretch of Glu46	9a-b	+ 1755	+ 1732	+ 1732
+1693/-1685 Arg52 C=N	10a,b	~+	+	+

4. CONCLUSIONS

We conclude that visible pump – midinfrared probe spectroscopy on the femto- to nanosecond-time scale yields very valuable information on the structural dynamics of proteins, which is difficult to obtain otherwise. We have shown that the sensitivity of detection in our setup is such that changes of single amino acids can be resolved, and that it is possible to work with proteins having a very long photocycle, such as PYP, which has a photocycle time of about 1 second.

REFERENCES

- [1] Joffre, M., Hulin, D., Migus, A., Antonetti, A., Benoit a la Guillaume, C., Peyghambarian, N., Lindberg, M., Koch, S. W. *Optics Letters*, 13 (1988) 276
- [2] Hamm, P., *Chemical Physics*, 200 (1995) 415
- [3] Holzwarth, A.R. "Data analysis of time-resolved measurements," in *Biophysical Techniques in Photosynthesis* (Eds. Amesz, J. and Hoff, A. J.), Kluwer, Dordrecht, 1996, pp. 75-92,
- [4] Hoff, W.D., van Stokkum, I.H.M., van Ramesdonk, H.J., van Brederode, M.E., Brouwer, A.M., Fitch, J.C., Meyer, T.E., van Grondelle, R., Hellingwerf, K.J. *Biophys. J.*, 67 (1994) 1691
- [5] Hellingwerf, K.J., Hendriks, J., Gensch, T. *J. Phys. Chem. A.*, 107 (2003) 1082
- [6] Meyer, T.E., Yakali, E., Cusanovich, M.A., Tollin, G. *Biochemistry*, 26 (1987) 418
- [7] Hoff, W.D., Dux, P., Hard, K., Devreese, B., Nugteren-Roodzant, I.M., Crielaard, W., Boelens, R., Kaptein, R., Van Beeumen, J., Hellingwerf, K.J. *Biochemistry*, 33 (1994) 13959
- [8] Baca, M., Borgstahl, G.E.O., Boissinot, M., Burke, P.M., Williams, D.R., Slater, K.A., Getzoff, E.D. *Biochemistry*, 33 (1994) 14369
- [9] Brudler, R., Rammelsberg, R., Woo, T.T., Getzoff, E.D., Gerwert, K. *Nat. Struct. Biol.*, 8 (2001) 265
- [10] Imamoto, Y., Shirahige, Y., Tokunaga, F., Kinoshita, T., Yoshihara, K., Kataoka, M. *Biochemistry*, 40 (2001) 8997
- [11] Xie, A., Hoff, W.D., Kroon, A.R., Hellingwerf, K.J. *Biochemistry*, 35 (1996) 14671
- [12] Imamoto, Y., Kataoka, M., Liu, R.S.H. *Photochem. Photobiol.*, 76 (2002) 584
- [13] Unno, M., Kumauchi, M., Sasaki, J., Tokunaga, F., Yamauchi, S. *Biochemistry*, 41 (2002) 5668
- [14] Xie, A., Kelemen, L., Hendriks, J., White, B.J., Hellingwerf, K.J., Hoff, W.D. *Biochemistry*, 40 (2001) 1510
- [15] Van Thor, J.J., Pierik, A.J., Nugteren-Roodzant, I., Xie, A., Hellingwerf, K.J. *Biochemistry*, 37 (1998) 16915
- [16] Zhou, Y., Ujj, L., Meyer, T.E., Cusanovich, M.A., Atkinson, G.H. *J. Phys. Chem. A.*, 105 (2001) 5719
- [17] Kim, M., Mathies, R.A., Hoff, W.D., Hellingwerf, K.J. *Biochemistry*, 34 (1995) 12669
- [18] Brudler, R., Meyer, T.E., Genick, U.K., Devanathan, S., Woo, T.T., Millar, D.P., Gerwert, K., Cusanovich, M.A., Tollin, G., Getzoff, E.D. *Biochemistry*, 39 (2000) 13478
- [19] Tamm, L.K., Tatulian, S.A. *Quarterly Reviews of Biophysics*, 30 (1997) 365
- [20] Groot, M.L., Van Wilderen, L.J.G.W., Larsen, D.S., Van der Horst, M.A., Van Stokkum, I.H.M., Hellingwerf, K.J., Van Grondelle, R. *Biochemistry*, 42 (2003) 10054

Transient two-dimensional infrared spectroscopy – towards measuring ultrafast structural dynamics

Jens Bredenbeck, Jan Helbing, and Peter Hamm

Physikalisch-Chemisches Institut, Universität Zürich, Winterthurerstrasse 190, CH-8057 Zürich, Switzerland

1. INTRODUCTION

Ultrafast two-dimensional infrared spectroscopy (2D-IR) is a promising tool for the investigation of molecular structures [1-3] and their equilibrium fluctuations [2, 4]. Similar to 2D-NMR spectroscopy [5], cross-peaks between coupled states emerge in 2D-IR spectra, and contain structural information [2, 6]. The outstanding feature of 2D-IR spectroscopy is the combination of its structure resolution power with an intrinsic sub-picosecond time resolution, freezing in all but the fastest molecular motions. This makes it particularly suited for application to fast dynamical processes, offering means to resolve equilibrium distributions of fast interconverting structures [7]. Most promising is the extension of the 2D-IR technique to the non-equilibrium regime, where its high time resolution can be put to full use [8]. This is the topic of this contribution. In principle, changes of molecular structures can thereby be followed from the sub-ps timescale up to milliseconds. We have recently reported first steps in this direction, employing transient 2D-IR spectroscopy (T2D-IR) to study the picosecond conformational transition of a photo-switchable cyclic peptide [9,10]. Here we demonstrate the application of T2D-IR to an electronically excited state, the metal-to-ligand charge-transfer (MLCT) state in rhenium(I) carbonyl complex [Re(CO)₃Cl(dmbpy)] (dmbpy=4,4'-dimethyl-2,2'-bipyridine). MLCT in rhenium(I) polypyridyl carbonyls and other metal carbonyls has been studied in considerable detail by time resolved IR spectroscopy (see [11-13] and references therein). Upon excitation at 390 nm MLCT occurs and a large frequency shift of the CO vibrations is observed (see the FTIR and UV-IR pump-probe spectra in Fig. 1 a and d). This change in vibrational frequency can be attributed to an ultrafast change in the electronic structure and the subsequent vibrational Stokes shift due to solvation, which takes place on a picosecond timescale [11, 12]. We present two dimensional infrared spectra of the transient species in the course of the solvation process, with characteristic cross peaks that depend on the relative orientations and couplings between the three carboxyl groups of the complex.

2. METHOD AND RESULTS

Fig. 1 b shows the 2D-IR spectrum of the rhenium complex (4 mM in DMSO) in the electronic ground state. The 2D-IR spectrum is measured according to our double-resonance scheme [2, 14], employing a spectrally narrow IR pump pulse and a broadband IR probe pulse

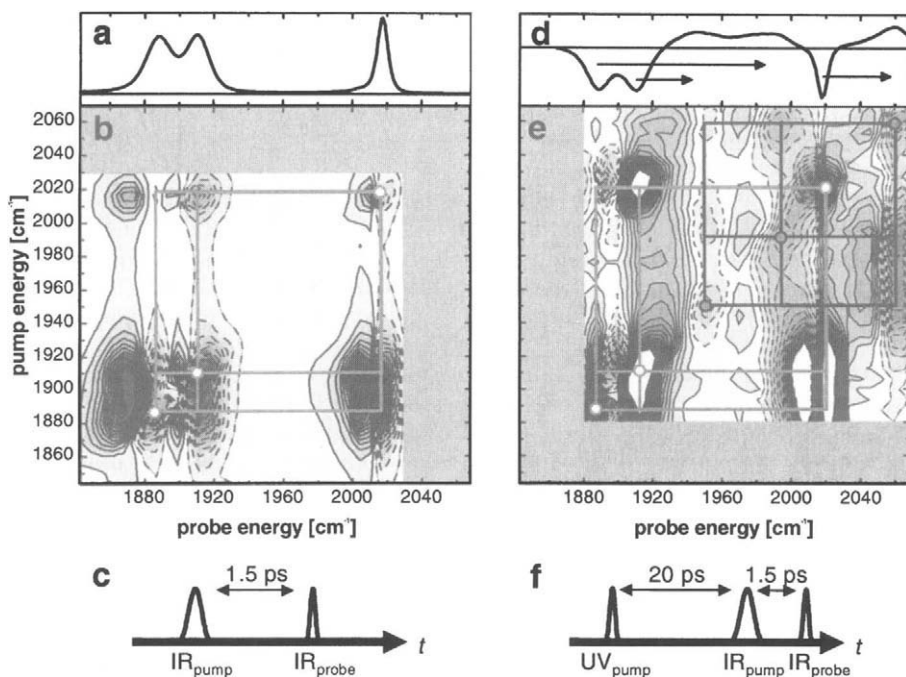


Fig. 1: left: FTIR spectrum (a) and 2D-IR spectrum (b) of the ground state for perpendicular polarization of pump and probe pulse. A broadband IR probe pulse measures the spectral change as a function of delay and frequency of a narrowband IR pump pulse (c). right: time resolved absorption spectrum (d, magic angle polarization) and transient 2D-IR spectrum (e) recorded 20 ps after UV excitation. The T2D-IR spectrum was recorded with magic angle between UV-pump (500 fs, 5 μ J) and IR-pump polarizations and perpendicularly polarised IR-pump and probe beams, pulse sequence (f).

as depicted in the pulse sequence in Fig. 1 c. To construct 2D-IR spectra as a function of pump and probe frequencies, the center frequency of the narrowband IR pulse (700 fs, 12 cm^{-1} FWHM, 50-100 nJ) is scanned across the spectral range of interest (vertical axis) and the absorption changes are recorded by dispersing the broad band probe pulse (100 fs, 250 cm^{-1}) and imaging it onto an array detector (horizontal axis). Like in a 2D-NMR spectrum the 2D-IR spectrum features diagonal peaks and cross-peaks that report couplings, in this case not coupling between spins but between vibrations [2]. In Fig. 1 b the diagonal peaks are marked by open dots and the respective cross-peaks are connected by grey lines. In contrast to 2D-NMR, each 2D-IR peak is a double-peak consisting of a negative and positive contribution indicated by the dashed and solid contours. The negative signal at the position of the $\nu=0$ to $\nu=1$ transition is due to bleaching and stimulated emission while the positive absorption signal stems from the $\nu=1$ to $\nu=2$ transition, and is shifted to the red by the anharmonicity of the CO vibration. Structural information is encoded in the cross-peaks of the 2D-IR spectrum in essentially two ways [2]. Their *polarization dependence* can be deduced from 2D measurements employing parallel as well as perpendicular polarization of the pump and probe pulse. This yields the relative orientation of the vibrational transition dipole moments, which is essentially a model-free information. It can be translated into structural information if the orientation of the transition dipole moments in the molecular structure is known, for example

from symmetry considerations or quantum chemistry calculations. This works particularly well for localized modes. Another source of structure information is the *cross-peak intensity*. It is related to the constants of coupling between vibrations. The coupling constants can be translated into structural information based on structure dependent coupling models. This has been successfully demonstrated for the amide-I mode of peptides and proteins [1, 2, 15-17]. A prerequisite for the extension of this structure determination approach to the non-equilibrium regime is the ability to resolve transient cross-peaks in T2D-IR spectra as demonstrated here. The T2D-IR experiment is essentially a UV-pump IR-narrowband-pump IR-broadband-probe scheme as displayed in the pulse sequence of Fig. 1 f. It can be regarded as the combination of time resolved UV-IR and 2D-IR pump-probe spectroscopy. Instead of just measuring transient changes in IR absorption after UV excitation, a more sophisticated probe is applied in form of a 2D experiment [10]. As one can typically not convert 100 % of the initial species into the product species, the 2D-IR spectrum recorded after the UV pulse always contains contributions from both excited and not excited molecules. In order to obtain a signal that is only due to molecules that have absorbed a UV photon, we therefore collect two sets of 2D-IR spectra simultaneously - one with the UV pulse on and one with the UV pulse off - and subtract them from each other. Hence, as it is common practice in conventional pump-probe spectroscopy, the T2D-IR spectra are difference spectra. Fig. 1 d shows the UV-pump IR-probe spectrum after 20 ps, where negative signals originate from the depleted ground state and positive signals from the excited state. Similarly the T2D-IR spectrum, shown underneath, features signals originating from the depleted ground state, as well as the signals of the excited state. The ground state diagonal peaks are again marked by open dots and the respective cross-peaks are connected by grey lines. The excited state signals are shifted along the diagonal and are marked in black. However, in the transient spectrum the signs of the ground state signals are interchanged with respect to the excited state signal, which is coded like the conventional 2D-IR spectrum. The most intriguing features in the T2D-IR spectrum of the rhenium complex are the well resolved cross peaks in the excited state. The same information as contained in the regular 2D-IR spectra can now be inferred for transient species from T2D-IR spectra, by exploiting the polarization dependence and relative intensity of the *transient* cross-peaks [19]. In addition, the dynamics of homogeneous and inhomogeneous contributions to the excited state lineshapes can be resolved from the shape of the transient diagonal peaks [10], which can also help to resolve distributions of structures [2, 16,18] as well as the anharmonicity of the vibrations [14] - in this case for the excited state.

3. ALTERNATIVE PULSE SEQUENCES

The above experiment, which corresponds to the pulse sequence in Fig. 2a, is the straightforward extension of the 2D-IR concept to the non-equilibrium regime i. e. recording a 2D-IR spectrum after a variable delay with respect to the UV pulse. However, we have also carried out other types of T2D-IR experiments. For example, T2D-IR measurements can be performed in a hole-burning mode (pulse sequence Fig. 2b): At a distinct time after the UV-pulse, the narrowband IR pulse burns a hole into the transient spectrum. The subsequent evolution of this 2D hole in time is then monitored by varying the delay of the broadband IR probe pulse. In this way ultrafast 2D-IR hole burning experiments on a non-equilibrium ensemble, generated by the trigger pulse, are possible. Interesting effects like the spectral narrowing in time can be observed [19]. Another useful set of T2D-IR spectra is generated by

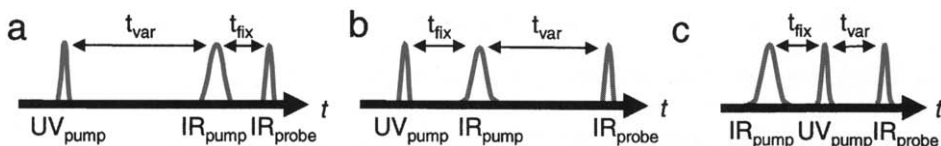


Fig. 2: Pulse sequences for a - regular T2D-IR spectroscopy. b - transient 2D hole burning spectroscopy. c - T2D-IR in the band labeling mode.

exchanging the order of the pulses and applying the narrowband IR pump pulse before the UV pulse arrives on the sample (pulse sequence in Fig. 2c). In this way it is possible to "label" selectively certain vibrations of the initial state by transferring population from the $v=0$ to the $v=1$ state of this vibration. After triggering the photo-process with the UV pulse, the subsequent evolution of this label can be monitored, correlating vibrations of the initial and the transient state [20]. By applying this method to the rhenium carbonyl complex we were recently able to show that the order of the vibrational modes is interchanged upon MLCT as indicated by the arrows in the top right hand spectrum of Fig. 1 [20].

The use of T2D-IR spectroscopy in its various modes is not limited to MLCT. It is applicable to all kinds of photo-triggered processes. Besides the investigation of electronically excited states, photo-chemical reactions like isomerizations and dissociations can be explored. Application to a photo-switchable peptide has already been demonstrated [10]. Conformational dynamics of biomolecules that are triggered by laser-induced T-jump or the control of pH by photo-acids, can also be investigated.

REFERENCES

- [1] P. Hamm, M. Lim, W.F. DeGrado, R.M. Hochstrasser, *Proc. Natl. Acad. Sci.*, 96 (1999) 2036.
- [2] Sander Woutersen and Peter Hamm, *J. Phys. Condens. Matter*, 14 (2002) R1035.
- [3] O. Golonzka, M. Khalil, N. Demirdöven, and A. Tokmakov, *J. Chem. Phys.*, 115 (2001) 10814.
- [4] S. Woutersen, Y. Mu, G. Stock, and P. Hamm, *Proc. Natl. Acad. Sci.*, 98 (2001) 11254.
- [5] R.R. Ernst, G. Bodenhausen, and A. Wokaun, *Principles of Nuclear Magnetic Resonance in One and Two Dimensions*; Oxford University Press, 1987.
- [6] M.T. Zanni and R.M. Hochstrasser, *Curr. Opin. Struc. Biol.*, 11 (2001) 516.
- [7] S. Woutersen, R. Pfister, P. Hamm, Y. Mu, D.S. Kosov, and G. Stock. *J. Chem. Phys.*, 117 (2003) 6833.
- [8] C. Scheurer, A. Piryatinski, and S. Mukamel, *J. Am. Chem. Soc.*, 123 (2001) 3114.
- [9] J. Bredenbeck, J. Helbing, A. Sieg, T. Schrader, W. Zinth, C. Renner, R. Behrendt, L. Moroder, J. Wachtveitl, and P. Hamm, *Proc. Natl. Acad. Sci.*, 100 (2003) 6452.
- [10] J. Bredenbeck, J. Helbing, R. Behrendt, C. Renner, L. Moroder, J. Wachtveitl and P. Hamm, *J. Phys. Chem. B*, 107 (2003) 8654.
- [11] J.B. Asbury, Y. Wang, and T. Lian, *Bull. Chem. Soc. Jpn.*, 75 (2002) 973.
- [12] D.M. Dattelbaum, K.M. Omberg, J.R. Schoonover, R.L. Martin, and T.J. Meyer, *Inorg. Chem.*, 41 (2002) 6071.
- [13] J.R. Schoonover and G.F. Strouse, *Chem. Rev.*, 98 (1998) 1335.
- [14] P. Hamm, M. Lim, and R.M. Hochstrasser, *J. Phys. Chem.*, 102 (1998) 6123.
- [15] S. Krimm and J. Bandekar, *Adv. Protein Chem.*, 38 (1986) 181.
- [16] J. Bredenbeck and P. Hamm, *J. Chem. Phys.*, 119 (2003) 1569.
- [17] H. Torii and M. Tasumi, *J. Raman Spectrosc.*, 29 (1998) 81.
- [18] S. Mukamel, *Principles of nonlinear optical spectroscopy*; Oxford University Press, 1995.
- [19] J. Bredenbeck, J. Helbing, and P. Hamm, in preparation.
- [20] J. Bredenbeck, J. Helbing, and P. Hamm, *J. Am. Chem. Soc.*, submitted.

Reaction driven modes in carboxymyoglobin: pathway of force transduction for functionally relevant protein motions

M. Armstrong¹, J. P. Ogilvie², M. L. Cowan², A. M. Nagy², and R. J. D. Miller²

¹ Department of Physics and Astronomy, University of Rochester, Rochester, NY, USA

² Departments of Physics and Chemistry, University of Toronto, Toronto ON, Canada

1. INTRODUCTION

Heme proteins form the cornerstone for our understanding of the general phenomena of molecular cooperativity; where the binding affinity of diatomic ligands in hemoglobin and associated changes in quaternary structure with ligation state is the best characterized example. At the heart of this problem is understanding how the initially localized reaction forces couple to the global protein coordinate to execute these functionally relevant motions. The energetics for this process are derived from one or a few chemical bonds and at the instant the bond is formed or broken, the motions are necessarily localized over atomic length scales at the active site and subject to quantum effects. How the reaction forces propagate out to the mesoscale (classical limit of mechanics) appropriate to drive protein motions is an open question. Following the initial motions subsequent to a bond breaking event is ideally suited to femtosecond approaches in which the fastest motions can be resolved and the dynamic range extended out to time scales commensurate with the strongly correlated motions of global protein fluctuations/motions. From a practical standpoint, the heme proteins provide ideal model systems for studying the relationship between protein structure and function since they are well-characterized and their ligands can be photodissociated with unit quantum efficiency on the truly femtosecond timescale. In this study, we report the results of ultrafast pump-probe spectroscopy of carboxymyoglobin (MbCO) to determine the initial structure changes of the ligand dissociation process using pulses of less than 10 fs in the 500-600 nm spectral region.

2. METHODS

The ultrafast pulses used in the experiment were generated in a noncollinear optical parametric amplifier pumped by a standard 1 kHz Ti:Sapphire regenerative amplifier system. The broadband (>70 nm) output was compressed using a combination of chirped mirrors and a deformable mirror as described previously [1], to provide pump (0.5 μ J) and probe (0.1 μ J) pulses of <10 fs centered at 525 nm. In myoglobin, this wavelength excites the Q-band, which contains vibrational information that is distinct from the Soret-band.[2] The pump-probe signal was dispersed in a monochromator (2 nm bandwidth), and a wavelength

dependence for all samples was conducted between 520-540 nm. The frequency content of the pump-probe signals was determined with linear predictive singular value decomposition (LPSVD) and Fourier transform techniques.[3] The heme protein samples were purchased from Sigma-Aldrich, dissolved in 0.2 M Tris buffer and prepared as previously described to give an OD of 1 at 530 nm.[4][5]

3. RESULTS

Typical pump-probe data are shown in Figure 1, showing an initial spike at $t=0$ due to electronic polarizability effects. Subsequent to this, pronounced oscillations are evident in the MbCO data, with the best signal-to-noise data obtained at 538 nm.[6] Several distinct frequencies were consistently present in the MbCO time domain signals, at frequencies that were identified with the vibrational modes of the heme porphyrin.[7] The largest contribution was found to be the ν_7 mode ($667 \pm 4 \text{ cm}^{-1}$), at a frequency shifted from the equilibrium MbCO Raman peak at 678 cm^{-1} . [7] This shift is in the direction corresponding to the deoxy species, in accordance with other studies.[8] A second dominant frequency (1363 cm^{-1}) was identified as the ν_4 mode, and is also shifted in frequency towards the equilibrium deoxyMb peak. The fact that the observed frequencies in the MbCO samples are shifted towards the deoxyMb values indicates that they correspond to oscillations in the photodissociated species. The pump probe data for deoxyMb did not show significant amplitude in either the ν_4 or ν_7 modes, further suggesting that the oscillations in MbCO are related to the dissociation process.

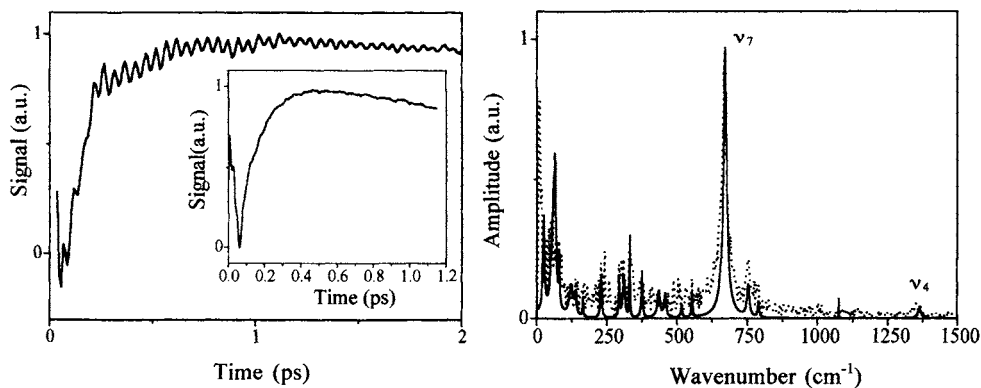


Figure 1 – Left: Raw pump-probe signal for MbCO at 538 nm. Full data scans were recorded for 7 ps; here only the first 2 ps are shown since the oscillations have decayed appreciably within this time. The inset shows typical data for cytochrome c (detection wavelength 523 nm) showing no apparent oscillations. Right: FFT (dashed) and LPSVD (solid) fits to the MbCO data showing the dominant ν_7 mode at 667 cm^{-1} .

Additional control studies were conducted on cytochrome c: a heme protein with a methionine ligand that can be dissociated with high quantum efficiency,[5] and nearly identical optical and vibrational properties to MbCO. Over the same wavelength range, no oscillatory

signals were observed in cytochrome c, as depicted in the inset of Figure 1 which shows representative data. The lack of oscillatory signals in this heme protein further supports the idea that the modes observed in MbCO are driven by the CO dissociation: the excited state dynamics associated with the dissociation of this larger ligand are too slow to impulsively drive the high frequency ν_7 and ν_4 modes.

To investigate the relationship between the reaction driven ν_7 mode and the subsequent protein motions along the dissociative pathway, further modulations of the frequency of the ν_7 mode by the surrounding intramolecular and protein bath fluctuations were found using an instantaneous frequency (IF) analysis. The IF was derived from the data by applying a Gaussian filter around the ν_7 mode in the Fourier spectrum. An inverse Fourier transform produced the time trace $TT(t)$ given by:

$$TT(t) = A(t)e^{i\phi(t)} \quad (1)$$

The IF was calculated as: [9]

$$IF(t) = \frac{1}{2\pi} \frac{d\phi(t)}{dt} \quad (2)$$

Figure 2 shows the results of the IF analysis, revealing strong modulation at 50 cm^{-1} and other low frequency modes, similar to observations by Champion *et al.* [10][11] For comparison, the IF was also calculated using a sliding window FFT method, yielding similar results as shown in Figure 2. The observation of these low frequency modes is perhaps the most important result of the study. The 50 cm^{-1} mode in particular has been identified with the doming motion of the heme [12] and the lower frequencies can be correlated to the globin

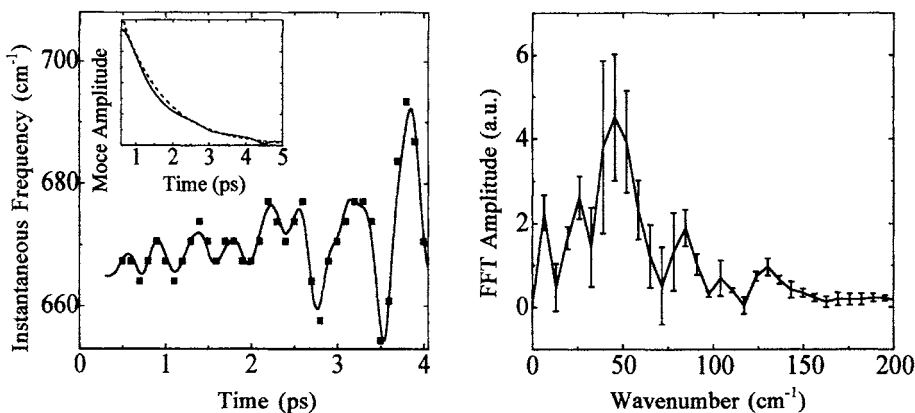


Figure 2 – Left: IF analysis, using a 100 cm^{-1} Gaussian filter (solid) (other filter widths gave similar results). The sliding window FFT results are shown for comparison (squares). The inset illustrates the exponential decay of the ν_7 mode. Right: FFT of the IF showing a large peak near 50 cm^{-1} . The resolution of this plot is fundamentally limited by the decay of the ν_7 mode.

motions.[13][14] This observed coupling suggests a pathway by which the reaction driven displacements of the ν_7 and ν_4 modes ultimately lead to lower frequency, spatially extended motions. In this way, local events at the binding site propagate outwards to produce mesoscale motions necessary for protein function.

REFERENCES

- [1] M. Armstrong, P. Plachta, E. A. Ponamarev, R. J. D. Miller, *Opt. Lett.*, 26 (2001) 1152.
- [2] T. G. Spiro *Biological Applications of Raman Spectroscopy: Resonance Raman Spectra of Heme and Metalloproteins*, (1988) Wiley, New York.
- [3] W. H Press, S. A. Teukolsky, W. T. Vetterling, B. P. Flannery, *Numerical Recipes in C*, 1994, Cambridge University Press, Cambridge.
- [4] G. Dadusc, G. D. Goodno, H. L. Chiu, J. P. Ogilvie, R. J. D. Miller, *Isr. J. Chem.* 38, (1998) 191.
- [5] W. Wang, Y. Xiong, A. Demidov, F. Rosca, T. Sjodin, W. Cao, M. Sheeran, P. M. Champion, *J. Phys. Chem B* 104, (2000) 10789.
- [6] M. R. Armstrong, J. P. Ogilvie, M. L. Cowan, A. M. Nagy, R. J. D. Miller, *Proc. Natl. Acad. Sci.*, 100 (2003) 4990.
- [7] S. Hu, K. M. Smith, T. G. Spiro *J. Am. Chem. Soc.* 118 (1996) 12638.
- [8] Y. Mizutani and T. Kitagawa, *Science* 278 (1997) 443.
- [9] B. Boashash *Proc. IEEE* 80 (1992) 520.
- [10] L. Zhu, P.L.M. Huang, J. T. Sage, P.M. Champion, *Phys. Rev. Lett.* 72 (1994) 301.
- [11] F. Rosca, A. T. N. Kumar, D. Ionascu, X. Ye, A. Demidov, P.M. Champion, *Bull. Chem. Soc. Jpn.*, 75 (2002) 1093.
- [12] X.-Y. Li, M. Z. Zgierski, *Chem. Phys. Lett.* 188 (1992) 16.
- [13] Y. Seno, N. Go, *J. Mol. Biol.*, 216, (1990) 95.
- [14] Y. Seno, N. Go, *J. Mol. Biol.*, 216, (1990) 111.

Ultrafast studies of ferric complexes of Hemoglobin I from *Lucina pectinata*

E. Ramirez¹, C. Ramos¹, M. Rodríguez¹, R. Pietri¹, M. Chergui² and J. Lopez-Garriga¹

1. University of Puerto Rico, Mayagüez Campus, Chemistry Department

2. Université de Lausanne, Switzerland, Physics Department

1. INTRODUCTION

Invertebrate hemeprotein has been increasingly studied because they provide insight into how the heme pocket microenvironment electronically affects the ligand interaction within vertebrate and invertebrate hemeproteins [1]. Currently, a mixture of different degrees of steric constraint, hydrogen bonding, local polarity and proximal effect are being proposed to control the selection and stability of these metal-ligand interactions [2]. The elucidation of the factors controlling carbon monoxide (CO), nitrogen monoxide (NO) and dioxygen (O₂) discrimination in hemoglobin and myoglobin is an area of increasing active research. Ultrafast time scale experiments on vertebrate hemoglobin have determined the formation of two short-lived species upon absorption of a visible photon by the heme. These spectrophotometrically detected species were called HbI* (490 nm) and HbII* (450 nm) and were previously assigned to electronic excited states of the unligated heme. It has been suggested that after NO photoexcitation from the heme three principal processes were taking place: two steps electronic relaxation ($\tau_1 \rightarrow 100$ fs and $\tau_2 \rightarrow 400$ -1000 fs), vibrational cooling ($\tau_3 \rightarrow 3$ -tens ps) and ligand recombination (τ_4 and τ_5) [4]. The NO and CO molecules showed very similar dynamics at short timescales with certain hemeproteins, which could be a product of photophysical processes and/or conformational effects [5]. Several models have been proposed which explain the difference of the non-exponential contribution observed with different bimolecular ligands. The heme pocket non-equilibrium relaxation or distal relaxation is proposed to explain the non-exponential CO recombination, while the inhomogeneous model [6] and multiple site model [4] are used to discuss the non-exponential recombination observed with NO. The energy barrier generated after photoexcitation controls the time scale at which the ligand is able to return to the active site and rebound to the iron atom.

Although, relevant information about ferrous hemeproteins kinetics, dynamics and ligand photodissociation pathways has been obtained, less is known about ferric hemeproteins photophysical processes. Recent studies performed with HbI-CN and Mb-CN at ultrafast time scale, have suggested that some of the transients intermediaries observed after ferrous complexes ligand photodissociation are observed in ferric Mb and HbI [7]. However, time-resolved infrared data shows that the complex remained six coordinated after photoexcitation. In this work we present ultrafast data on ferric HbI-NO, HbI-N₃, HbI-H₂S and metHbI complexes that suggest a mechanism for the photoinduced reduction of HbI species.

2. EXPERIMENTAL PROCEDURE

Sample separation and ligand complex preparation of Hemoglobin I from *Lucina p.* was performed according to the methods described in the literature [8]. The laser experimental

arrangement included a diode laser (532 nm) used to pump a mode-locked Ti:Sapphire laser, which generated ~ 80 fs pulses at 800 nm. The laser pulse power was enhanced using a regenerative amplifier cavity which is pumped by doubled Q-switch ND:YLF laser. The system yielded pulses of ~ 100 fs of 700 μJ at 800 nm and a 1kHz of repetition rate. A second beam was obtained by focusing part of the fundamental light into a 500 μm BBO crystal which doubles the frequency. This beam was used as a pump and routed through an optical delay line and a chopper before reaching the sample. The other portion of the fundamental light was focused onto a 1-cm water-filled cuvette to generate a white light continuum that was used as the probe beam. Pump and probe beams were focused and overlapped into a 1.0 mm thick motorized spinning cell containing the sample. Changes in the sample were detected after pump excitation the transmission of probe beam was focused onto a fiber bundle and passed into a monochromator. The intensity of the white light probe was measured with a photomultiplier tube connected to a lock-in amplifier system to extract the signal.

3. RESULTS

3.1 Transient absorption signal formation HbI-NO, HbI-N₃, HbI-H₂S and metHbI

Figure 1 shows that after photoexcitation the ferric complexes HbI-H₂S, HbI-N₃, HbI-NO and metHbI exhibit an absorption transient formation near ~ 435 nm, which were formed in ~ 300 fs. Time decays varies from 4.5 ps to 6 ps. More than 95 % of signal recovery was observed within 20 ps after photoexcitation. These transients appear to be similar to those observed and assigned to a reduced species of ferrous heme protein complexes [6]. An absorption transient formation at 455 nm was also observed and corresponds to formation of the excited states Hb_{II}* [3]. As with the ferrous HbI complexes, the species formed was observed immediately

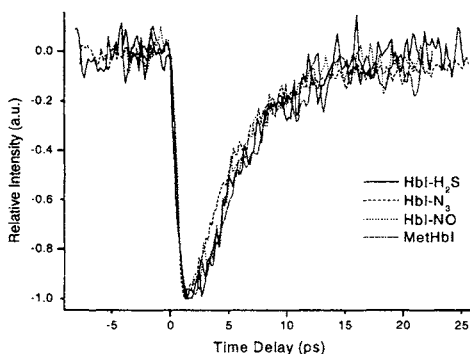


Fig. 1. Transient absorption spectra for HbI-H₂S (straight), HbI-N₃ (dash), HbI-NO (dot) and metHbI (dash/dot) at 445 nm, 440 nm, 435 nm and 430 nm, respectively

after photoexcitation. The Hb_{II}* fitted well with the decay time constants of approximately 3-4 ps. UV-Vis spectrum of HbI complexes was obtained before and after ultrafast laser experiments. The HbI-NO sample maintain its characteristic absorption bands, but show some heme degradation noticeable by the decrease in band intensity. However, the metaquo HbI complex showed a Soret band displacement after laser exposure from 407 nm to 412 nm. Shifts for the Q-bands from 502 nm and 634 nm to 542 nm and 570 nm were also observed.

3.2 Bleaching transients of HbI-NO, HbI-N₃, HbI-H₂S and metHbI

The bleaching signal for HbI-NO, HbI-H₂S, HbI-N₃ and metaquo HbI were observed at 410 nm, 410 nm, 415 nm and 407 nm, respectively, and similar to the ferrous complexes, the sharp rise in the probe transmission signal suggests that the ligand photodissociation occurs within the time resolution of our experiment. The transient spectra were well fitted with time constants of 600 fs and ~3 ps. Similar time constants have been previously observed [9]. More than 90 % of the signals were recovered after 10 ps of photoexcitation.

3.3 MetHbI, HbI-H₂S and HbI-N₃ with carbon monoxide atmosphere

Figure 2 shows that an immediate change in the sample is observed after photoexcitation when the sample is placed in a CO atmosphere. Each spectrum changes from its original azide signal to one similar to the HbI-CO signal, until the sample behaves exactly as a HbI-CO derivative. Azide and HbI-CO photodissociation are in competition.

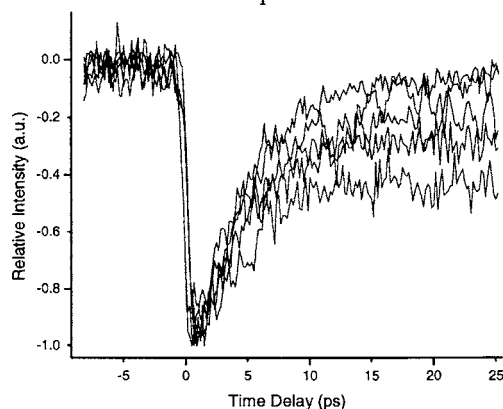


Fig. 2. Spectral evolution of HbI-N₃ at 440 nm; a. HbI-N₃, b-e represent HbI-N₃ in a CO atmosphere with a difference between them of 5 minutes.

4. DISCUSSION

Formation of a transient specie in the 430 nm region of the ferric derivatives, plus the fact that subsequent to the ultrafast measurements a ferrous oxy HbI species was observed, led to the suggestion that probably a reduction of a ferric to a ferrous derivative was taking place. In order to determine if a ferrous specie was formed, a series of spectra was taken with met-HbI with a carbon monoxide atmosphere (HbI:CO). The ferric complexes studied present a band formation at 430 nm. This specie is formed in 300 fs. It has been reported that photoreduction in Mb heme occurs when it is photoexcited with a 400 nm pulsed laser [10]. Although, little photoreduction is induced with exposure at this wavelength, the nature of the ultrafast pulsed laser generates an extremely high photon flux. Hemoglobin I photoreduction take place when the sample is exposed to a femtosecond laser source with power ranging from 0.3 μ J to 10 μ J, showing a population dependency with power intensities. The spectral band displacement observed in UV-Vis spectrum obtained after ultrafast experiments confirmed that a reduced species was formed. However, all species show similar dynamics which ends in 15 ps. When ferric samples are photoexcited in a CO atmosphere the reduced species formed is stable enough for CO to interact with the heme at longer time scales. The formation of the

HbI-CO complex suggests that the photoinduced ferrous derivative has similar structural and chemical properties to deoxy HbI. This is because no difference was observed between the fully reduced by photoinduction and the chemically reduced HbI-CO complex spectra [10].

Diagram 1 shows the proposed process that is taking place after photoexcitation. Ferric ligated HbI (A) produces the excited species (B) instantaneously. Complexes which remain six coordinated returned fast to its ground states, can be suggest that upon laser exposure the excited states (B) relaxed to a state similar to a ground state, by accept an electron which turns it to a ligated HbI species (C). The reduced HbI species (C) decay by two different pathways; the first one led to the formation of a ligated ferric HbI derivative (A), while the second one produced and unligated ferrous derivative (D). The ferrous specie formed is stable enough to let the CO molecule to interact with the active site and formed HbI-CO (E). The photoinduced

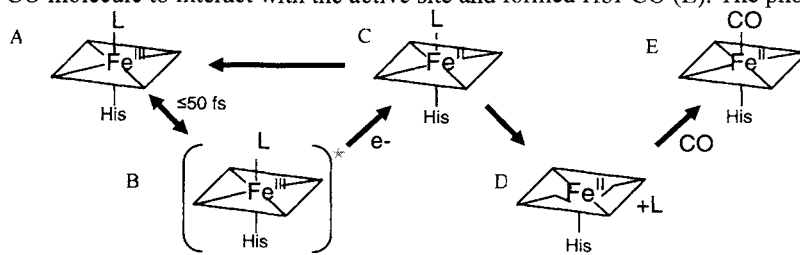


Diagram 1. Proposed mechanism ferric HbI after laser exposure.

reduction process could occur by an electron transfer from the orbital a_{2u}, b_{2u} to the $eg(\pi^*)$ [11]. A π radical cation is formed in the porphyrin after an electron pass from $eg(\pi^*)$ to the metal "d" orbitals. It cannot be excluded the possibility of that some amino acid might take place in the process. Sample photoinduced reduction is a step involved in ferric HbI processes after photoexcitation, which could or could not led to heme-ligand bond breakage.

5. ACKNOWLEDGEMENTS

This work was supported in part by grants from NIH-COBRE II 1P20RR016493 (JL), NIH-SCORE S06GM08224 (JL), and NSF (MCB-9974961).

REFERENCES

- [1] S. N. Vinogradov, and R. E. Weber. *Phys. Rev.*, 81 (2001) 569.
- [2] G. N. La Mar, B. D. Nguyen, Z. Xuefeng, and V. Krishnamurthi. *J of Biol. Chem.*, 273 (1998) 9517.
- [3] S. Franzen, L. Kiger, C. Poyart, and J-L Martin. *Biophys. J.*, 80 (2001) 2372
- [4] Y. Koholodenko, E. A. Gooding, Y. Dou, M. Ikeda, and R. Hochstrasser. *Biochem.*, 38 (1999) 5918.
- [5] M. H. Vos, G. Lipowski, J-C Lambry, J-L Martin, and U. Liebl. *Biochem.*, 40 (2001) 7806.
- [6] J. W. Petrich, J-C Lambry, K. Kuczera, M. Karplus, C. Poyart, and J-L Martin. *J. Mol. Biol.*, 238 (1994) 437.
- [7] J. Helbing, J. Brendenbeck, P. Hamm, L. Bonacina, F. van Mourik, A. González, F. Chausserd, M. Chergui, R. Pietri, C. Ramos, and J. López. *Biophys. J.*, (2003) Submitted.
- [8] D. W. Kraus and J. B. Wittenberg. *J. Biol. Chem.*, 265 (1990) 16043.
- [9] W. Cao, J. I. Christian, P. Champion, F. Rosla, and J T Sage. *Biochem.* 40 (2001) 5728.
- [10] Y. Gu, P. Li, J. T. Sage, and P. Champion. *J. Am. Chem. Soc.*, 115 (1993) 4993.
- [11] H. Sakai, H. Onuma, M. Umeyama, S. Takeoka and, E. Tsuchida. *Biochem.* 39 (2000) 14595.

The mechanism of energy transfer and trapping in Photosystem I

H. M. Vaswani^a, M. Yang^b, A. Damjanović^c, G. R. Fleming^a

^aDepartment of Chemistry, University of California, Berkeley and Physical Biosciences Division, Lawrence Berkeley National Laboratory, Berkeley, California

^bDepartment of Chemistry, Chungbuk National University, Cheongju 361-763, South Korea

^cJohns Hopkins University, Department of Biophysics, 012 Jenkins Hall, Baltimore, MD

1. INTRODUCTION

The collection and transfer of excitation energy to the reaction centers of the photosynthetic unit of bacteria, cyanobacteria, and higher plants, known as light harvesting, is one of the most exquisitely effective processes in nature, with efficiencies approaching 100%. Discovering the design principles at work in these photosynthetic antenna and reaction center complexes has been a preoccupation of ultrafast spectroscopy for many years. Indeed George Porter, writing in 1986, stated that 'The study of photosynthesis is, and probably always will be, the greatest odyssey of the photochemist' [1]. A full molecular-level understanding of the principles underlying plant and bacterial light harvesting has required the availability of atomic resolution structures for the (bacterio)chlorophyll-protein complexes that comprise the antenna system [2-14]. In parallel, the need to characterize the systems experimentally at a much deeper level than that of a single ensemble averaged rate constant has stimulated the development of new spectroscopic techniques, such as the one- and two-color photon echo peak shift methods [15-18].

The first system to be studied and characterized at a truly microscopic level was the purple bacterial light harvesting complex LH2 [2,13,19-35]. The beautifully 9- or 8-fold symmetric complexes revealed a mixture of weak and moderately strong electronic coupling, and showed that in many cases the principle of maximum overlap of donor emission and acceptor absorption spectra was ignored by the natural system. Indeed the conclusion from this system and from the purple bacterial reaction center is that optical spectroscopy is intrinsically incapable of revealing the way in which the individual molecules 'see' each other. This means that, at the present time, the general design principles of light harvesting structures can only be revealed by a combination of experiment and theory.

One striking aspect of LH2 and the structurally similar LH1 complex is the high symmetry and structural regularity of their quasi-one dimensional ring structures [2,9,13]. This regular structure leads, amongst other things, to a clear energy funnel in the purple bacterial photosynthetic unit with LH2 containing 800 and 850 nm absorbers and the reaction center-encircling LH1 complex containing 870 or 875 nm absorbers. These energy shifts are achieved through a combination of bacteriochlorophyll (BChl)-protein interaction and BChl-BChl excitonic interactions.

The structure of the core antenna of Photosystem I (PSI) stands in striking contrast to the bacterial system. The 96 non-equivalent chlorophyll (Chl) molecules are very densely

packed in a three dimensional arrangement with little apparent symmetry or regularity [5]. This immediately raises the question of whether there are new design principles at work in PSI as compared to the bacterial system. In particular, no obvious energy funnel is apparent; indeed there are antenna Chls which absorb to the red of the primary electron donor, P700 [36,37]. In this article we summarize the experimental timescales for energy transfer in PSI [38-41] and compare them with results from a detailed quantum dynamical calculation [42,43]. The remarkable success of the calculations in reproducing the experimental timescales encourages exploration of the design principles at work in PSI and enables us to present snapshots of the way in which energy flows through this spatially and energetically disordered system.

2. PHOTOSYSTEM I

Figure 1 shows three views of the structure of Photosystem I of the *cyanobacterium Synnechococcus elongatus*. The left hand column shows the space filling representation (van der Waals radius) for the chlorophyll molecules only, the central column shows the space filling representation of the entire complex (Chls, carotenoids, protein), while the right hand column shows the licorice representation. The primary electron donor, P700 is shown (in the center of the structure) in black. Looking down from above the membrane plane (top row) one sees the central reaction center (RC) region of 6 Chls, plus the two 'linker' Chls [5], spatially segregated from the bulk of the antenna. This spatial segregation is similar to that achieved by the reaction center/LH1 combination of purple bacteria [44,45], and is presumably necessary to ensure the correct flow of electrons in the RC. All RC/antenna systems appear to exploit the stronger distance dependence of electron transfer vs. energy transfer to isolate the electron transfer components from the bulk of the antenna system.

The 88 antenna Chls are roughly segregated to the upper and lower membrane planes (Fig. 1, third row), but aside from this little spatial order is evident. What is particularly striking in the space filling views is that, aside from the region immediately surrounding the RC, the Chls fill almost the entire volume of the protein.

Given the density of Chl in PSI, it is immediately obvious that any detailed description of energy transfer in this system will need to handle both weakly coupled (Forster-type) and strongly coupled (excitonic) systems self consistently. It is also evident that discerning rate limiting steps and optimizing principles may not be straightforward.

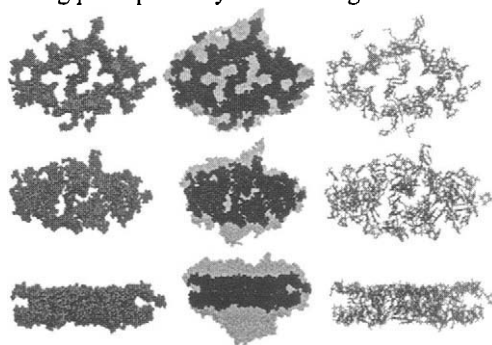


Fig. 1. Space filling in Photosystem I illustrated from three points of view: above the membrane plane (top), side view (bottom) and in between (middle). The left hand column shows the Chls in PSI with the special pair highlighted in black. The middle column contains all of the atoms in the structure with the Chls in black. The right hand column depicts the Chls in the licorice representation.

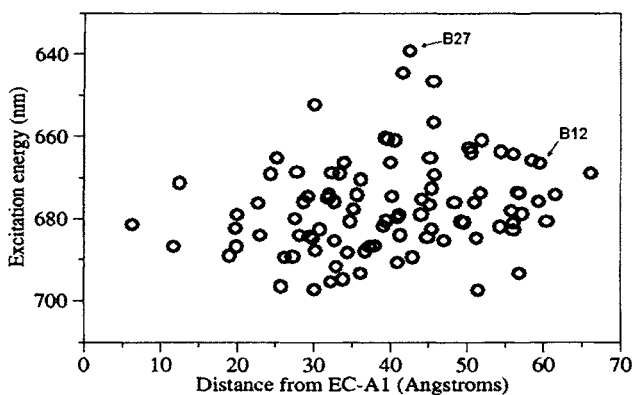


Fig. 2. Calculated Q_y excitation energies of Chls in PSI and its relation to the distance of the Chl from Chl EC-A1, one of the two Chls in the special pair, P700.

3. THE ENERGY LANDSCAPE OF PHOTOSYSTEM I

Photosystem I represents a classic example of a system where high quality structural information, though essential, is inadequate to understand the dynamical behavior of a biological system. The absorption spectrum of PSI is very broad compared to the spectrum of Chl in solution. The dense packing revealed in Figure 1 can be expected to produce a broad range of spectral shifts through intermolecular interactions. In addition, the Chls are bound in 96 non-equivalent sites each with their own unique set of polar, hydrogen bonding, and macrocycle distortion interactions. Our solution to this problem was to calculate the electronic excitation energies of all 96 Chls, including their neighboring protein residues and use these results to construct a 96×96 Hamiltonian for the complex. This is then used to calculate the low temperature spectrum of the entire complex, and then coupled with a spectral density taken from experiment [46-48], to calculate the ambient temperature spectrum [49-51]. The calculated excitation energies are summarized in Figure 2 in which excitation energies are plotted as a function of distance from Chl EC-A1, one of the two Chls that constitute the primary electron donor, P700. A very broad distribution of energies is evident, but there is clearly no evidence for a downhill (funnel) energy landscape in the bulk antenna.

4. ENERGY FLOW IN PHOTOSYSTEM I

A recent combined fluorescence up-conversion and streak camera study of PSI by the van Grondelle and Fleming groups resulted in a global fit to the wavelength resolved fluorescence decay that involved four exponential components [38]. These were: 38 ps, assigned to the overall trapping time for excitation; 3.6 ps, assigned to energy equilibration between the bulk Chls and the red shifted Chls; 360 fs, assigned to energy equilibration among the bulk Chls of the antenna; and a 9.8 ps component, suggested to be related to energy flow between individual monomeric PSI units in the overall trimeric assembly of PSI found in cyanobacteria. Of course, in making such a global fit to the fluorescence data, one has no idea whether these timescales can be ascribed simple physical meanings of the type suggested above, or result from complex averages of microscopic timescales. In order to gain microscopic insight into the mechanism of energy transfer and trapping in PSI, we carried out a detailed quantum dynamical calculation of the entire process.

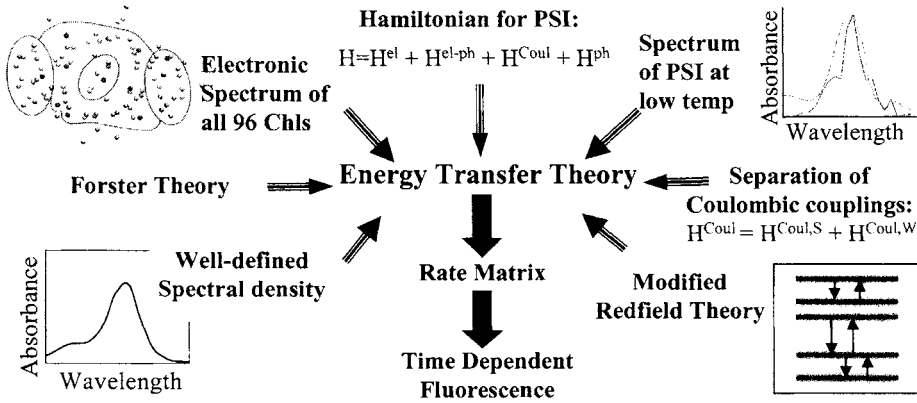


Fig. 3. The elements required to obtain dynamical information on PSI.

5. CALCULATION OF ENERGY TRANSFER IN PHOTOSYSTEM I

The ingredients of our calculation of energy transfer and trapping in PSI are shown schematically in Figure 3. These calculations are challenging because of the presence of groups of moderately or strongly interacting pigments, along with pigments spaced at distances that make a weak coupling picture inappropriate. Our calculation is based on a modified version of Redfield theory developed by Mukamel and coworkers [52] and extended by Yang and Fleming [53], and is described in detail in ref [43]. This formulation reduces to Forster theory when the excitation is localized on individual molecules, and is practically applied by using a cutoff value of $J_{cutoff} = 120 \text{ cm}^{-1}$ for the Coulombic coupling to partition H^{Coul} into $H^{Coul,S} + H^{Coul,W}$. Couplings for which $H_{nm}^{Coul} > J_{cutoff}$ (n and m label individual Chls) enter into $H^{Coul,S}$, couplings weaker than J_{cutoff} enter into $H^{Coul,W}$. We express the total Hamiltonian in the exciton basis set $|\mu\rangle, |\mu'\rangle$, which is obtained by diagonalization of $H^{el} + H^{Coul,S}$. The rate of energy transfer is controlled by the off-diagonal Hamiltonian for the two states $|\mu\rangle$ and $|\mu'\rangle$:

$$H_{\mu\mu'} = \langle \mu | H^{el-ph} + H^{Coul,W} | \mu' \rangle$$

If $H_{nm}^{Coul} > J_{cutoff}$, the Coulomb interaction $H^{Coul,S}$ is included in the Hamiltonian of the exciton basis states and $H^{Coul,W} = 0$. In this case energy transfer is brought about by electron-phonon coupling. If $H_{nm}^{Coul} < J_{cutoff}$, the Coulomb contribution to the exciton states is negligible ($H^{Coul,S} = 0, H^{Coul,W} = J_{nm}$) and is, in fact, the perturbation responsible for energy transfer.

The magnitude of the off-diagonal Hamiltonian (i.e. the energy transfer rate) thus depends on the strengths of the electron-phonon and Coulombic couplings and also the overlap of the two exciton wavefunctions[53]. Energy transfer rates from state μ' to state μ , are calculated via the golden rule [54] and used as inputs to a master equation calculation of the excitation transfer kinetics in PSI, in which the dynamical information is included in the matrix \mathbf{K} .

Finally time dependent fluorescence spectra and kinetics can be obtained from the rate matrix and the spectrum of each eigenstate, μ . The time dependent fluorescence, $F(t)$, can be written in terms of the eigenvalues and eigenvectors of the rate matrix \mathbf{K} :

$$F(t) = \sum_{m=1}^N a_m \exp(-t/\tau_m)$$

where $-\tau_m^{-1}$ is the m^{th} eigenvalue of \mathbf{K} , and the amplitudes, a_m , are determined by the weighting factor for each eigenstate at the excitation and emission wavelengths as well as by the rate matrix. Thus the 96 time constants present in the rate matrix can be investigated for any desired combination of excitation and detection wavelength. When plots of a_m vs. τ_m are examined, the time constants with substantial amplitudes can be clustered into four groups: sub 100 fs, 0.3 ps, 2-3 ps and 35-40 ps [43]. Global fitting of up-conversion data leads to time constants of 360 fs, 3.6 ps, 9.6 ps and 38 ps [38,39]. The experiments did not have sufficient time resolution to determine sub 100 fs time constants. Aside from this, our calculated times are in remarkable agreement with the experimental values, with the exception of the 9.6 ps component, which does not appear with significant amplitude in the calculations. Holzwarth et al. have suggested that this component arises at the interface of two monomeric PSI complexes[55], and since our calculation relates to a single PSI complex, it should not be expected to be present. Given the remarkable similarity of the remaining time constants between experiment and calculation, it seems reasonable to explore some of the details of the energy flow revealed by the calculation.

One interesting set of questions relates to the energy landscape. Is the energy landscape optimized to minimize the trapping time, or would some other arrangement be superior? How sensitive is the pathway for energy flow to the location/energy of the initially excited chlorophyll? In Figure 4a, snapshots of the excitation distribution for Chls B12 and B27 are shown (Chl labeling as in ref. [5]). Both molecules are in the peripheral PsaB antenna: Chl B12 is on the luminal side, 60 Å from Chl EC-A1, whereas Chl B27 is on the stromal side 43 Å from Chl EC-A1. Both examples illustrate the high connectivity of the PSI network and are rather similar after 5 ps with excitation visiting much of the antenna before final trapping. However, the two initial conditions evolve quite differently on short timescales and the snapshots show that the initial pathway away from Chl B12 involves only a small number of neighbors (~3). By contrast, for Chl B27, even at 100 fs substantial amplitude exists on at least ten sites. After a few picoseconds, once amplitude has leaked out of the initial position, the high connectivity of PSI results in very similar distributions.

Significant amplitude builds up on similar Chls in both series. One way to address whether this arises from spatial or energetic (or both) considerations is to examine snapshots where the antenna energy landscape is artificially set flat (Figure 4b). The initial trapping on Chl B12 is clearly a result of spatial isolation, however by 500 fs, energetics is clearly playing a role—compare the views at 500 fs—the homogeneous system has visited significantly more sites than in the calculated energy landscape model. The influence of the energy landscape is particularly striking for initial excitation of Chl B27, though again by 5 ps the distributions for Chl B27 and Chl B12 are very similar. Overall, the excitation is distributed considerably more evenly in the flat-landscape model, as would be expected, and the significance of specific sites to the energy flow to P700 is diminished.

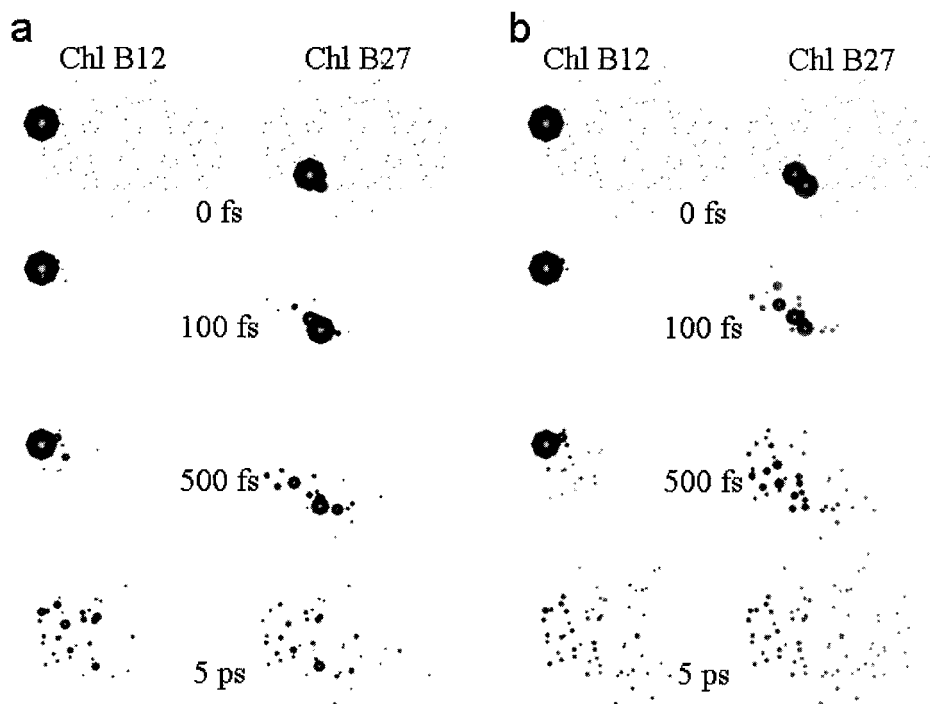


Fig. 4. (a) Snapshots of the energy distribution after initial excitation of Chls B12 (left) and B27 (right). All Chls are illustrated by dots at 0 fs for clarity, after 0 fs, only Chls with substantial excitation are illustrated. (b) Same as (a) except in an artificially flat energy landscape.

The total trapping time (ensemble averaged) is 38 ps for the rough landscape model (in agreement with experiment) and 25 ps for the flat landscape model. It is evident from all the snapshots in Figure 4 that energy flow through the antenna is a major contributor to the overall trapping time. Detailed analysis shows that there are three major contributions to the overall trapping timescale [43,56] and that energy transfer around the reaction center is dominated by entropic rather than enthalpic (i.e., energy funnel) considerations. Diffusion to the region surrounding the reaction is very rapid and appears to be complete in around 5 ps as Fig. 4 clearly shows. Less evident from the snapshots is that back transfer, including transfer back from the reaction center Chls, makes a very substantial contribution to the overall trapping time. A kinetic domain model was developed to analyze the energy flow in spatially and energetically disordered energy transfer systems and can be used to systematically expose the major contributions to the trapping time [56].

6. CONCLUDING COMMENTS

An accurate microscopic model for energy transfer and trapping in Photosystem I has been developed. The model reveals two rate determining processes—energy diffusion through the antenna, and processes leading to excitation of P700, once excitation has reached the RC Chls. Note that in Figure 4 the amplitude on the RC Chls (aside from P700) is small at all times. Given the short trapping time for the flat energy landscape, one might wonder if the

rough energy landscape is advantageous. It would not be possible to pack Chls at the density of PSI without significant coupling and consequent energy shifting of the origin site energies. However, because of the high spatial connectivity of the antenna, it is very difficult for energy to become trapped for times longer than a few ps, obviating the need for an energy funnel. Thus the gain in cross-section and spectral coverage more than compensates for the very small decrease in charge separation quantum yield. Elsewhere, we have shown that the energy landscape of the bulk antenna does not strongly influence the overall trapping time, but that the energy configuration of the six reaction center Chls and the two linker Chls does appear to be highly optimized.

7. ACKNOWLEDGEMENTS

This work was supported by the Director, Office of Science, Office of Basic Energy Sciences, Chemical Sciences Division of the U.S. Department of Energy under Contract No. DE-AC03-76SF00098 and used resources provided by the National Energy Research Scientific Computing Center (contract number DE-AC03-76SF0098). Figures 1, 4 and 5 were produced in VMD [57].

REFERENCES

- [1] G. Porter, *Journal of the Chemical Society, Faraday Transactions 2: Molecular and Chemical Physics*, 82 (1986) 2445.
- [2] G. McDermott, S. M. Prince, A. A. Freer, A. M. Hawthornthwaite-Lawless, M. Z. Papiz, R. J. Cogdell and N. W. Isaacs, *Nature*, 374 (1995) 517.
- [3] E. Hofmann, P. M. Wrench, F. P. Sharples, R. G. Hiller, W. Welte and K. Diederichs, *Science*, 272 (1996) 1788.
- [4] P. Fromme and H. T. Witt, *Biochim. Biophys. Acta*, 1365 (1998) 175.
- [5] P. Jordan, P. Fromme, H. T. Witt, O. Klukas, W. Saenger and N. Krauss, *Nature*, 411 (2001) 909.
- [6] W. Kuehlbrandt, *J. Mol. Biol.*, 202 (1988) 849.
- [7] A. Camara-Artigas, R. E. Blankenship and J. P. Allen, *Photosynth. Res.*, 75 (2003) 49.
- [8] K. McLuskey, S. M. Prince, R. J. Cogdell and N. W. Isaacs, *Acta Crystallogr., Sect. D: Biol. Crystallogr.*, D55 (1999) 885.
- [9] S. Karrasch, P. A. Bullough and R. Ghosh, *EMBO Journal*, 14 (1995) 631.
- [10] K.-H. Rhee, E. P. Morris, D. Zheleva, B. Hankamer, W. Kuhlbrandt and J. Barber, *Nature*, 389 (1997) 522.
- [11] C. Frazao, F. J. Enguita, R. Coelho, G. M. Sheldrick, J. A. Navarro, M. Hervas, M. A. De la Rosa and M. A. Carrondo, *J. Biol. Inorg. Chem.*, 6 (2001) 324.
- [12] A. Zouni, H.-T. Witt, J. Kern, P. Fromme, N. Krauss, W. Saenger and P. Orth, *Nature*, 409 (2001) 739.
- [13] J. Koepke, X. Hu, C. Muenke, K. Schulten and H. Michel, *Structure*, 4 (1996) 581.
- [14] M. Z. Papiz, S. M. Prince, A. M. Hawthornthwaite-Lawless, G. McDermott, A. A. Freer, N. W. Isaacs and R. J. Cogdell, *Trends Plant Sci.*, 1 (1996) 198.
- [15] T. Joo, Y. Jia, J.-Y. Yu, M. J. Lang and G. R. Fleming, *J. Chem. Phys.*, 104 (1996) 6089.
- [16] R. Agarwal, B. S. Prall, A. H. Rizvi, M. Yang and G. R. Fleming, *J. Chem. Phys.*, 116 (2002) 6243.
- [17] M. Yang and G. R. Fleming, *J. Chem. Phys.*, 110 (1999) 2983.
- [18] J.-Y. Yu, Y. Nagasawa, R. van Grondelle and G. R. Fleming, *Chem. Phys. Lett.*, 280 (1997) 404.
- [19] R. van Grondelle, J. Dekker, T. Gillbro and V. Sundstrom, *Biochim. Biophys. Acta*, 1187 (1994) 1.
- [20] G. R. Fleming and R. V. Grondelle, *Curr. Opin. Struc. Biol.*, 7 (1997) 738.
- [21] R. J. Cogdell, P. K. Fyfe, S. J. Barrett, S. M. Prince, A. A. Freer, N. W. Isaacs, P. McGlynn and C. N. Hunter, *Photosynth. Res.*, 48 (1996) 55.

- [22] R. J. Cogdell, N. W. Isaacs, A. A. Freer, J. Arrelano, T. D. Howard, M. Z. Papiz, A. M. Hawthornthwaite-Lawless and S. Prince, *Prog. Biophys. Molec. Biol.*, 68 (1997) 1.
- [23] G. D. Scholes, I. R. Gould, R. J. Cogdell and G. R. Fleming, *J. Phys. Chem. B*, 103 (1999) 2543.
- [24] V. Sundstrom, T. Pullerits and R. van Grondelle, *J. Phys. Chem. B*, 103 (1999) 2327.
- [25] G. D. Scholes and G. R. Fleming, *J. Phys. Chem. B*, 104 (2000) 1854.
- [26] N. J. Fraser, H. Hashimoto and R. J. Cogdell, *Photosynth. Res.*, 70 (2001) 249.
- [27] T. Renger, V. May and O. Kuhn, *Phys. Rep.*, 343 (2001) 138.
- [28] R. van Grondelle and V. Novoderezhkin, *Biochemistry*, 40 (2001) 15057.
- [29] A. Y. Borisov, *Biochemistry (Moscow, Russ. Fed.)*, 68 (2003) 152.
- [30] R. Jimenez, S. N. Dikshit, S. E. Bradforth and G. R. Fleming, *J. Phys. Chem.*, 100 (1996) 6825.
- [31] R. Jimenez, F. van Mourik, J. Y. Yu and G. R. Fleming, *J. Phys. Chem.*, B, 101 (1997) 7350.
- [32] B. P. Krueger, G. D. Scholes and G. R. Fleming, *J. Phys. Chem. B*, 102 (1998) 5378.
- [33] B. P. Krueger, G. D. Scholes, R. Jimenez and G. R. Fleming, *J. Phys. Chem. B*, 102 (1998) 2284.
- [34] B. P. Krueger, J. Yom, P. J. Walla and G. R. Fleming, *Chem. Phys. Lett.*, 310 (1999) 57.
- [35] R. Agarwal, A. H. Rizvi, B. S. Prall, J. D. Olsen, C. N. Hunter and G. R. Fleming, *J. Phys. Chem. A.*, 106 (2002) 7573.
- [36] L.-O. Palsson, C. Flemming, B. Gobets, R. van Grondelle, J. P. Dekker and E. Schlodder, *Biophys. J.*, 74 (1998) 2611.
- [37] B. Gobets and R. van Grondelle, *Biochim. Biophys. Acta*, 1507 (2001) 80.
- [38] J. T. M. Kennis, B. Gobets, I. H. M. V. Stokkum, J. Dekker, R. V. Grondelle and G. R. Fleming, *J. Phys. Chem. B*, 105 (2001) 4485.
- [39] B. Gobets, I. H. M. v. Stokkum, M. Rogner, J. Kruip, E. Schlodder, N. V. Karapetyan, J. P. Dekker and R. v. Grondelle, *Biophys. J.*, 81 (2001) 407.
- [40] A. N. Melkozernov, S. Lin and R. E. Blankenship, *Biochemistry*, 39 (2000) 1489.
- [41] A. N. Melkozernov, S. Lin, R. E. Blankenship and L. Valkunas, *Biophys. J.*, 81 (2001) 1144.
- [42] A. Damjanovic, H. M. Vaswani, P. Fromme and G. R. Fleming, *J. Phys. Chem. B.*, 106 (2002) 10251.
- [43] M. Yang, A. Damjanovic, H. M. Vaswani and G. R. Fleming, *Biophys. J.*, 85 (2003) 140.
- [44] X. Hu and K. Schulten, *Biophys. J.*, 75 (1998) 683.
- [45] X. Hu, A. Damjanovic, T. Ritz and K. Schulten, *Proc. Natl. Acad. Sci. USA*, 95 (1998) 5935.
- [46] J. K. Gillie, P. A. Lyle, G. J. Small and J. H. Golbeck, *Photosynth. Res.*, 22 (1989) 233.
- [47] J. K. Gillie, G. J. Small and J. H. Golbeck, *J. Phys. Chem.*, 93 (1989) 1620.
- [48] V. Zazubovich, S. Matsuzaki, T. W. Johnson, J. M. Hayes, P. R. Chitnis and G. J. Small, *Chem. Phys.*, 275 (2002) 47.
- [49] Y. Jia, J. M. Jean, M. M. Werst, C.-K. Chan and G. R. Fleming, *Biophys. J.*, 63 (1992) 259.
- [50] S. Mukamel, *Principles of Nonlinear Optical Spectroscopy*, Oxford University Press: New York, 1995.
- [51] Y. Nagasawa, S. A. Passino, T. Joo and G. R. Fleming, *J. Chem. Phys.*, 106 (1997) 4840.
- [52] W. M. Zhang, T. Meier, V. Chernyak and S. Mukamel, *J. Chem. Phys.*, 108 (1998) 7763.
- [53] M. Yang and G. R. Fleming, *Chem. Phys.*, 282 (2002) 163.
- [54] P. A. M. Dirac, *Proc. Roy. Soc. (London)*, A114 (1927) 243.
- [55] A. R. Holzwarth, G. Schatz, H. Brock and E. Bittersmann, *Biophys. J.*, 64 (1993) 1813.
- [56] M. Yang and G. R. Fleming, *J. Chem. Phys.*, 119 (2003) 5614.
- [57] W. Humphrey, A. Dalke and K. Schulten, *J. Molec. Graphics*, 14 (1996) 33.

Ultrafast photoreaction dynamics in protein nanopaces (PNS) as revealed by fs fluorescence dynamics studies on photoactive yellow protein (PYP) and related systems

N. Mataga,^a H. Chosrowjan,^a S. Taniguchi,^a N. Hamada^b and F. Tokunaga^b

^aInstitute for Laser Technology, Utsubo-Hommachi 1-8-4, Nishi-ku, Osaka 550-0004, Japan

^bDepartment of Earth and Space Science, Osaka University, Toyonaka, Osaka 550-0043, Japan

Abstract: Ultrafast photoreactions in PNS of PYP have been studied by means of fs fluorescence up conversion method. Conclusions obtained are: (a) Photoreaction in PNS (chromophore twisting) occurs from vibrationally unrelaxed fluorescence state and coherent oscillations in the fluorescence decay curves have been observed for the first time. (b) Comparative studies on fluorescence dynamics of mutants and w.-t. PYP have proved that the w.-t. PYP is best engineered for the ultrafast reaction. (c) The coherent oscillations in the fluorescence decay completely disappeared and the reaction was much slower in the denatured state, demonstrating the supremely important role of PNS for the photoreaction.

1. INTRODUCTION

When chromophores in photoresponsive or photosensory proteins absorbing in the visible region, such as photoactive yellow protein (PYP), rhodopsin (Rh) for vision, biological photosynthetic reaction center (RC), bacteriorhodopsin (bR) and other photoactive proteins of various photoresponsive bacteria and even several other enzymes such as flavoproteins (FP) which are not necessarily involved in the photobiological reactions, the light absorption can lead to ultrafast and highly efficient reactions. Such photoinduced ultrafast reactions taking place in protein nanopace (PNS, space of a few nanometer scale involving the chromophore and surrounding protein environment interacting with it and probably facilitating its ultrafast and highly efficient photoreactions) are characteristic to those photoactive proteins. Elucidation of the roles played by PNS in those photoreactions is the most important urgent problem that confronts us in our investigations.

From such a viewpoint, we are examining primary processes of photoreactions of PYP [1] which functions as a blue light photoreceptor for a negative phototaxis of the purple sulfur bacterium *Ectothiorhodospira halophila*, some FP's [2] and Rh [3] by means of the fs fluorescence up-conversion measurements. In this article, we will discuss our latest results of fs fluorescence dynamics studies on PYP, because PYP is very stable for repeated irradiation which induces photocycles so that the very accurate experimental results can be obtained rather easily and also the preparation of the site-directed mutants as well as the PYP analogues with modified chromophores are rather easy. However, before that, we will summarize briefly results of our previous investigations.

1.1. On the ultrafast conversions from excited FC (Franck-Condon) state to FI (Fluorescence) state of chromophores in PNS of photoactive proteins PYP, Rh and FP

The ultrafast photoreactions in PNS of these proteins take place immediately after conversion from the FC state to vibrationally unrelaxed or only partially relaxed FI state [1-3]. For PYP [1] and Rh [3], the primary process is twisting of the chromophore, which causes the ultrafast fluorescence quenching, in the course of the isomerization, while the primary process for FP [2] is the ultrafast electron transfer leading to the fluorescence quenching reaction in PNS. Thus, in spite of the different molecular structures of PYP, Rh and FP chromophores and different kind of photoinduced reactions, these photoresponsive proteins show ultrafast and highly efficient photoreactions from FI state of similar nature (vibrationally unrelaxed or only partially relaxed), suggesting the supremely important role of the PNS controlling the reactions.

1.2. Comparative studies on fs fluorescence dynamics of w.-t. (wild type) PYP and site-directed mutants

We examined the effect of the modification of PNS by site-directed mutagenesis on the primary process [1]. In Fig. 1 a schematic image of the w.-t. PYP chromophore in PNS is indicated.

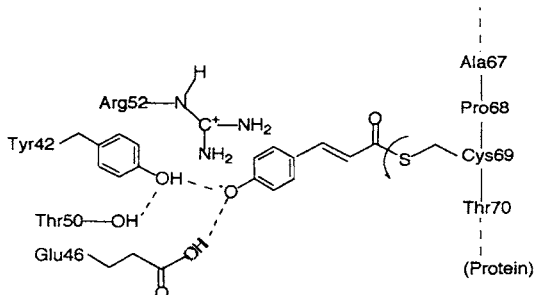


Fig. 1. A schematic image of w.-t. PYP chromophore linked to protein by thioester linkage and hydrogen bonded with surrounding amino acid residues in PNS.

We have also examined the fs-ps fluorescence dynamics of various mutants, the preparation of which were described elsewhere [4]. In these mutants, the hydrogen bonding networks surrounding the chromophore are weakened or partially broken or the structure of the protein where the chromophore is linked by thioester bond becomes looser, leading to the more disordered PNS structure.

When the PYP chromophore is excited in the PNS, intramolecular charge transfer (CT) from the phenolate anion part to the thioester bond takes place instantaneously, which induces twisting of the chromophore, leading to the ultrafast fluorescence quenching. In relation to this mechanism of photoinduced twisting, X-ray crystallography on w.-t. PYP crystal in which twisted state was cryotrapped below $-100\text{ }^{\circ}\text{C}$ indicated that the twisted state was formed by flipping its thioester bond avoiding collisions resulting from the large-scale movement of its aromatic ring and also avoiding the large rearrangements of the hydrogen bonding network at the phenolate anion part [5].

We have confirmed that, without exception, the fluorescence decay dynamics of mutants are slowed compared with w.-t. PYP, i.e., the photoinduced chromophore twisting in PNS is slowed by mutations.

Thus, the PNS structure becomes looser and more disordered by mutation, causing the twisting motion of the chromophore more random and the twisted state formation considerably slower, demonstrating the supreme importance of the well-ordered PNS for the ultrafast and highly efficient twisting reaction of the chromophore in PNS.

1.3. Fluorescence decay dynamics of PYP at blue and red edges as well as the maximum of the steady state spectrum

The FI state of PYP formed by ultrafast conversion from the FC state may not be vibrationally relaxed (1.1). Therefore, the fluorescence decay dynamics of the chromophore probably exhibits coherent oscillations coupled with the twisting. In relation to this problem, we have observed faster initial decay of FI intensity on both blue and red edges of the FI spectrum of w.-t. PYP and several mutants but no detectable dynamics Stokes shift. This result of the spectral sharpening in the initial stage of the fluorescence decay might originate from a little damping of the coherent vibrations coupled with the twisting of the chromophore along the reaction coordinate [1]. We have recently observed similar wavelength dependence of the fluorescence decay dynamics in the case of Rh for the first time [3], and very similar result was reported also for the fluorescence dynamics of bR [6]. Therefore, the similar mechanism of the fluorescence decay dynamics due to the chromophore twisting coupled with the coherent oscillations may be applicable also for these systems.

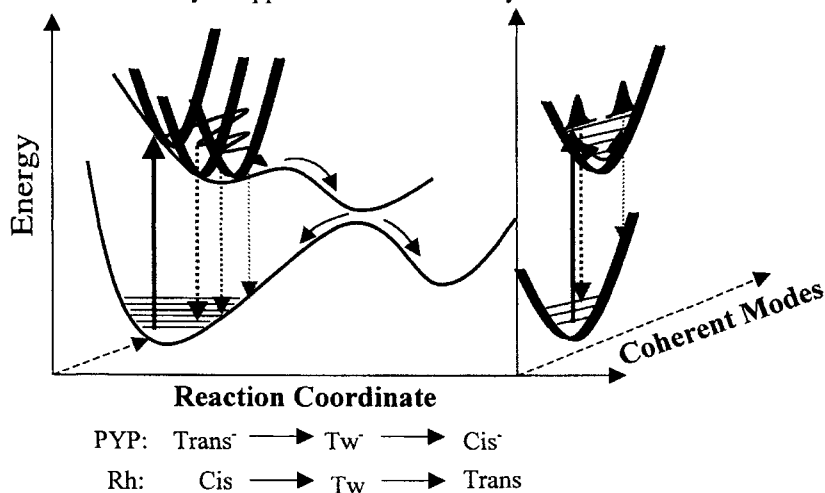


Fig. 2. Simplified schematic image of the reaction coordinate diagram for excited chromophores of PYP and Rh undergoing the twisting and the coherent vibrations.

In Fig. 2, a schematic image of the reaction coordinate diagram for the photoinduced twisting of the chromophore in PNS is indicated, showing that a slight narrowing of the fluorescence bandshape at the early stage of the decay may be due to a little damping of the coherent vibrations coupled with twisting. Accordingly, with improved time resolution of the apparatus, it may be possible to observe such coherent oscillations in the fluorescence decay dynamics of these proteins, PYP, Rh and bR. Among these proteins, PYP is an ideal candidate for elucidation of the details of the dynamics and mechanisms of the primary photoreaction process. Actually, with improved time resolution of the apparatus, we have

recently observed such coherent oscillations in the fluorescence decay dynamics of w.-t. PYP and various site-directed mutants for the first time [1(b), (c)].

2. EXPERIMENTAL

The fluorescence dynamics measurements were carried out with fluorescence up-conversion apparatus [1(b)] based on Ti:Sapphire laser (820 nm, 800 mW, 76 MHz, ~65 fs). The fwhm of the instrumental response was ~110 fs.

3. RESULTS AND DISCUSSION

3.1. Ultrafast fluorescence decay dynamics of w.-t. PYP and its mutants in PNS coupled with coherent vibrations

In Fig. 3, the oscillating parts extracted from the fluorescence decay curves of the w.-t. PYP at blue and red edges of the spectrum are shown, which is in accordance with the simplified schematic image of the Fl dynamics of Fig. 2.

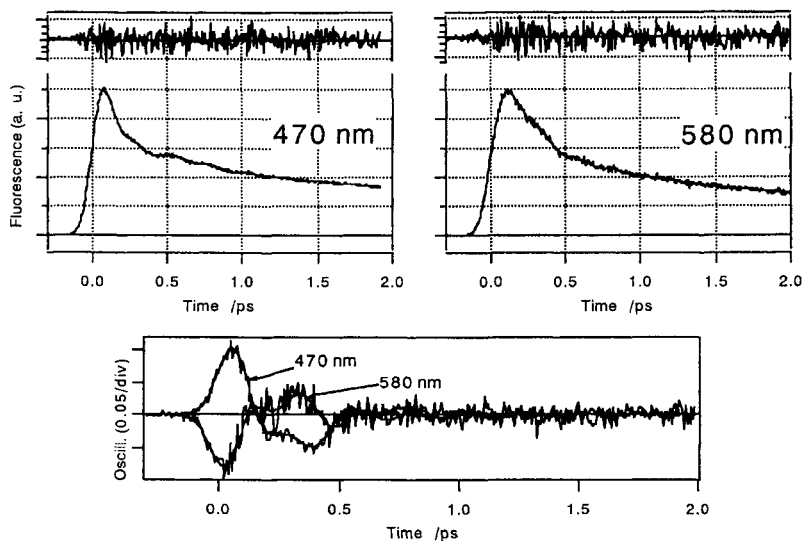


Fig. 3. Oscillating parts extracted from the Fl decay curves of the w.-t. PYP at blue and red edges of the spectrum.

Thus, we have measured fluorescence decay dynamics of w.-t. PYP and also various site-directed mutants and those fluorescence curves can be well reproduced by the following equation with two coupled oscillating modes.

$$F(t) = Const + \sum_i a_i \exp(-t/\tau_i) + \sum_j b_j \exp(-t/\tau_j^d) \sin(\varphi_j + \omega_j t) \quad (1)$$

where, $\omega_j = 2\pi\nu_j$, $i, j = 1, 2$, $\nu_1 \sim 130 - 150 \text{ cm}^{-1}$, $\tau_1^d \sim 500 \text{ fs}$,

τ_j^d : damping time, $\nu_2 \sim 40 - 70 \text{ cm}^{-1}$, $\tau_2^d \sim 250 \text{ fs}$

ν_1 ($\sim 140 \text{ cm}^{-1}$) value is nearly constant throughout w.-t. PYP and various mutants but the ν_2 ($\sim 50 \text{ cm}^{-1}$) value shows considerable variations depending upon the disorders in PNS caused by the mutations. In the denatured PYP, the large dynamic Stokes shift of the fluorescence due to solvation is clearly observed ($\Delta\nu \sim 4850 \text{ cm}^{-1}$ compared with $\Delta\nu \sim 2200 \text{ cm}^{-1}$ of w.-t. PYP, Table 1), and the twisting of the chromophore becomes much slower compared with that in PNS and both coherent oscillations are over-damped in the completely disordered environment of the unfolded protein.

In the mutants for which the spectroscopic data are exhibited in Table 1, the hydrogen bonding network between the phenolate anion part of the chromophore and surrounding

Table 1
Spectroscopic data of w.-t. PYP, denatured PYP, several mutants and analogues

	$\lambda_{\text{abs}}/\text{nm}$	$\lambda_{\text{fl}}/\text{nm}$	$\Delta\nu/\text{cm}^{-1}$
w.-t. PYP	446	494	2200
Denatured PYP	400	496	4850
T50V (Thr50 \rightarrow Val)	457	496	1760
E46Q (Glu46 \rightarrow Gln)	460	501	1780
Locked chromophore	444	467	1100
Ferulic acid	459	533	3030

amino acid residues is weakened or partly destroyed, leading to the red shifts of the spectra and smaller reorganization energies ($\Delta\nu$) due to the chromophore-PNS interactions compared with that of the w.-t. PYP. Nevertheless, the coherent oscillation ν_1 is not practically affected by the mutations.

An important problem here is the elucidation of the roles of the oscillations ν_1 and ν_2 coupled with the ultrafast twisting of the chromophore in PNS. For that purpose, we are examining assignment of those low frequency vibrations by means of the resonance Raman spectroscopy in $100 - 300 \text{ cm}^{-1}$ spectral region. Recent results of this study and some MO theoretical calculations of the normal modes both in the ground and S_1 state of the chromophore indicate that the $\sim 140 \text{ cm}^{-1}$ mode can be assigned to out-of-plane γ_{16} intrachromophore vibration probably coupled with the twisting of the chromophore, to start the flipping around thioester bond triggering the isomerization [7].

3.2. Effects of the PNS environment on the fluorescence dynamics of PYP analogues

In order to examine further the effect of the PNS and PNS-chromophore interactions upon the ultrafast twisting reactions of the PYP chromophore, we are examining also the effect of the PNS environment on the fluorescence dynamics of the PYP analogues where the PYP chromophore is replaced with similar but a little different chromophores. Among those PYP analogues, we show here results of the fluorescence dynamics studies of those with (a) locked chromophore and (b) ferulic acid chromophore.

The wavelengths of the steady state absorption (λ_{abs}) and fluorescence (λ_{fl}) spectral peaks and magnitudes of the fluorescence Stokes shift ($\Delta\nu$) of these PYP analogues in comparison with those of w.-t. PYP, denatured PYP and several site-directed mutants are given in Table 1. The observed fluorescence decay curves at various wavelengths of these PYP analogues are

shown in Fig. 4. For the locked chromophore, the twisting at $-\text{CH}=\text{CH}-$ bond as well as the flipping at the thioester bond are difficult due to its rigid structure. Therefore, the fluorescence lifetime of this analogue is very long (≥ 60 ps) without the fast component in 100 fs – 1 ps regime. This result agrees with the previous report [8], although we have recognized a slight oscillation in the fluorescence decay curves, due to the higher time resolution of our measurement than the previous one [8].

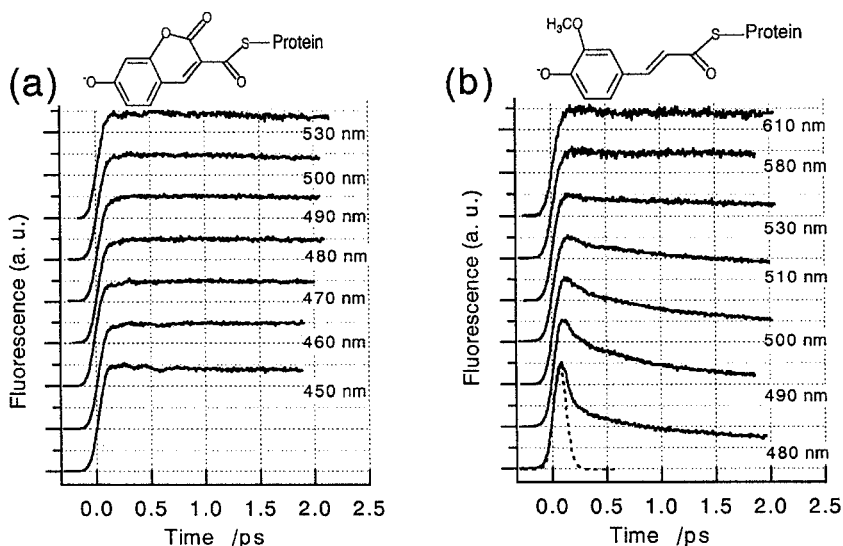


Fig. 4. Fluorescence dynamics studies on PYP analogues: effects of the PNS - chromophore interactions.

However, the ferulic acid analogue in Fig. 4 (b) shows a wavelength dependence of the fs fluorescence dynamics very different not only from that of the locked chromophore analogue but also quite different from those of the w.-t. PYP and various site-directed mutants [1]. Namely, extremely fast decay of fluorescence can be observed at the blue edge of the spectrum, the decay becomes slower with increase of the observation wavelength and at the red edge of the spectrum very rapid rise corresponding to the extremely fast decay at the blue edge can be observed.

On the other hand, the coherent oscillations observed in the fluorescence decay curves of the w.-t. PYP and mutants becomes almost absent in the ferulic acid analogue. This result may be caused by the looser and disordered PNS environment for the analogue chromophores leading to the rapid damping of its coherent oscillations. Presumably, the hydrogen bonding networks surrounding phenolate anion part of the chromophore in the ground state of the analogues may not be as stable as in the w.-t. PYP and some mutants because of the different substitutions and different substitution positions in the phenyl ring.

Because of such disordered PNS and rapid damping of coherent vibrations which induce the flipping of the thioester linkage, the twisting of the chromophore in the excited state may become much slowed in the ferulic acid analogue. When such analogue chromophore is excited, a large change of its electronic structure due to the intramolecular CT from the electron donating substituents to the phenyl ring and further to the cinnamic acid thioester part will take place instantaneously. This electronic structure change of the excited chromophore

will induce a large reorganization in the interactions between the surrounding amino acid residues and excited chromophore leading to the ultrafast relaxation caused by the disordered short range amino acid residue – chromophore interactions, which will induce an extremely fast and large dynamic Stokes shift of the fluorescence (probably much faster than that of the chromophore of the denatured PYP in water).

3.3. Analysis of the ultrafast dynamic Stokes shift of the fluorescence of ferulic acid analogue in comparison with that of the denatured PYP.

In order to confirm above possibilities, we have obtained time-dependent spectra by spectral reconstruction procedure [9] (Fig. 5). From the time dependent spectra, spectral shift

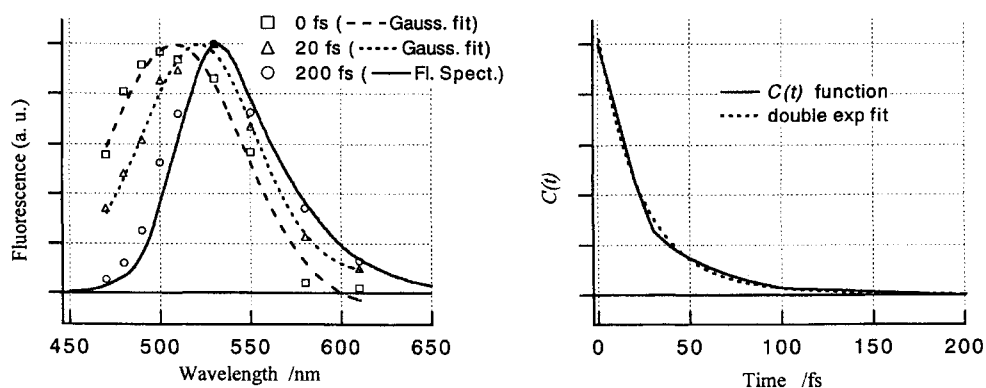


Fig. 5. Time dependent fluorescence spectra and spectral shift correlation function for ferulic acid analogue.

correlation function, $C(t) = [\nu(t) - \nu(\infty)] / [\nu(0) - \nu(\infty)]$, has been obtained. $C(t)$ can be reproduced satisfactorily by double exponential fit with ~ 25 fs (98 %) and ≥ 150 fs (2 %) components for ferulic acid analogue.

We have examined also dynamic Stokes shift of the fluorescence of denatured PYP to compare with the results in Fig. 5 by obtaining the correlation function $C(t)$ with the same procedure. $C(t)$ can be reproduced exactly by a double exponential fit with 670 fs (85 %) and 60 fs (15 %) components.

Therefore, the much faster reorganization of the excited chromophore – surrounding PNS environment interactions leading to the much faster dynamic Stokes shift of fluorescence than that observed for the PYP chromophore in bulk water environment takes place in this PYP analogue.

In relation to the fluorescence dynamics of the PYP analogues quite different from those of the w.-t. PYP and its various site-directed mutants as described above, we try here comparative discussions on the natures of the excited chromophore – PNS environment interactions on the basis of the spectroscopic data given in Table I, where the most important informations concerning the natures of the excited chromophore – PNS environment interactions are contained in $\Delta\nu$, the reorganization energy due to such interactions. Compared with that of w.-t. PYP, the $\Delta\nu$ values of the mutants T50V and E46Q are considerably smaller. In these mutants, the hydrogen bonding interactions between amino

acid residues and phenolate anion part of the chromophore in PNS are weakened or partly destroyed, which leads to the decrease of the contributions from the chromophore – PNS environment hydrogen bonding interactions to the reorganization energy $\Delta\nu$, resulting in the considerably smaller $\Delta\nu$ values.

Contrary to these mutants, $\Delta\nu$ values of PYP analogues are considerably larger than that of the w.-t. PYP except the value of the locked chromophore, where the extent of the intramolecular CT by photoexcitation producing a large dipole moment which interacts strongly with the PNS environment seems to be considerably smaller compared with the ferulic acid analogue chromophore and also w.-t. PYP and mutants in Table 1. For the ferulic acid analogue, ultrafast relaxations due to the strong interactions between the large dipole moment produced by photoinduced intrachromophore CT and nearby amino acid residues in the considerably disordered PNS probably take place, showing ultrafast and large dynamic Stokes shift of fluorescence, as discussed also in the previous sections.

In the case of the denatured PYP, the chromophore is surrounded by completely disordered environment of the water. The relaxations due to the interactions between the excited chromophore with a large dipole moment and surrounding disordered water environment produce a large extent dynamic Stokes shift of the fluorescence. Nevertheless, it is much slower compared with that taking place in the disordered PNS of the ferulic acid analogue as demonstrated in the analysis of the previous section (3.3).

4. CONCLUDING REMARKS

Based on our fs fluorescence dynamics studies on w.-t. PYP, various site-directed mutants, several PYP analogues and denatured PYP, we have demonstrated the supreme importance of the well-regulated PNS structure for the ultrafast and highly efficient photoinduced twisting of the chromophore leading to the isomerization.

REFERENCES

- [1] (a) N. Mataga, H. Chosrowjan, Y. Shibata, Y. Imamoto and F. Tokunaga, *J. Phys. Chem. B*, 104 (2000) 5191. (b) N. Mataga, H. Chosrowjan, Y. Shibata, Y. Imamoto, M. Kataoka and F. Tokunaga, *Chem. Phys. Lett.*, 352 (2002) 220. (c) N. Mataga, H. Chosrowjan, S. Taniguchi, N. Hamada, F. Tokunaga, Y. Imamoto and M. Kataoka, *Phys. Chem. Chem. Phys.*, 5 (2003) 2454.
- [2] N. Mataga, H. Chosrowjan, Y. Shibata, F. Tanaka, Y. Nishina and K. Shiga, *J. Phys. Chem. B*, 104 (2000) 10667.
- [3] H. Kandori, Y. Furutani, S. Nishimura, Y. Shichida, H. Chosrowjan, Y. Shibata and N. Mataga, *Chem. Phys. Lett.*, 334 (2001) 271.
- [4] (a) Y. Imamoto, T. Ito, M. Kataoka and F. Tokunaga, *FEBS Lett.* 374 (1995) 157. (b) K. Mihara, O. Hisatomi, Y. Imamoto, M. Kataoka and F. Tokunaga, *J. Biochem.* 121 (1997) 876.
- [5] U. K. Genick, S. Soltis, P. Kuhn, I. L. Canestrelli and E. D. Getzoff, *Nature* 392 (1998) 206.
- [6] M. Du and G. R. Flemming, *Biophys. Chem.*, 48 (1993) 101.
- [7] H. Chosrowjan, S. Taniguchi, N. Mataga, M. Unno, S. Yamauchi, N. Hamada and F. Tokunaga, *J. Phys. Chem. B*, to be published.
- [8] P. Changenet, H. Zhang, M. J. van der Meer, K. J. Hellingwerf and M. Glasbeek, *Chem. Phys. Lett.*, 282 (1998) 276.
- [9] W. Jarzeba, G. C. Walker, A. E. Johnson and P. F. Barbara, *Chem. Phys.* 152 (1991) 57.

Isomerization process in the native and denatured photoactive yellow protein probed by subpicosecond absorption spectroscopy

P. Changenet-Barret^a, A. Espagne^a, P. Plaza^a, M. M. Martin^a and K. J. Hellingwerf^b

^aDépartement de Chimie, UMR 8640 ENS-CNRS PASTEUR, Ecole Normale Supérieure, 24 rue Lhomond, 75231 Paris Cedex 05, France

^bLaboratory for Microbiology, Swammerdam Institute for Life Science, Nieuwe Achtergracht 166, 1018 WV Amsterdam, The Netherlands

1. INTRODUCTION

The Photoactive Yellow Protein (PYP) is the blue-light photoreceptor that presumably mediates negative phototaxis of the purple bacterium *Halorhodospira halophila* [1]. Its chromophore is the deprotonated *trans*-p-coumaric acid covalently linked, via a thioester bond, to the unique cystein residue of the protein. Like for rhodopsins, the *trans* to *cis* isomerization of the chromophore was shown to be the first overall step of the PYP photocycle, but the reaction path that leads to the formation of the *cis* isomer is not clear yet (for review see [2]). From time-resolved spectroscopy measurements on native PYP in solution, it came out that the excited-state deactivation involves a series of fast events on the subpicosecond and picosecond timescales correlated to the chromophore reconfiguration [3-7]. On the other hand, chromophore H-bonding to the nearest amino acids was shown to play a key role in the *trans* excited state decay kinetics [3,8]. In an attempt to evaluate further the role of the mesoscopic environment in the photophysics of PYP, we made a comparative study of the native and denatured PYP. The excited-state relaxation path and kinetics were monitored by subpicosecond time-resolved absorption and gain spectroscopy.

2. EXPERIMENTAL

Time-resolved transient absorption and gain experiments were performed by the pump-probe technique using a home-made dye laser described in details elsewhere [9]. For the present experiment, subpicosecond pulses were generated simultaneously at 430 nm and 570 nm. The pulses at 430 nm were used as the pump, and a white-light continuum probe was produced by focusing the 570-nm pulses in a 1-cm water cell. The differential absorbance spectra were recorded in the 340-700 nm spectral range through a polychromator by a CCD camera. The spectra were averaged over 500 laser shots and corrected for group velocity dispersion in the probe beam. The time resolution of the apparatus was estimated to be around 1.5 ps.

Wild-type PYP was prepared as described in [10]. Samples of PYP in native conformation were prepared in 10 mM phosphate buffer (pH = 7.5), using HPLC grade water. Denaturation of PYP was achieved by adding solid guanidinium chloride to 7 M final concentration. After denaturation, the pH was set to 9.6 with KOH, in order to deprotonate the chromophore. The absorbance of each sample was adjusted to 1 per mm at the absorption maximum.

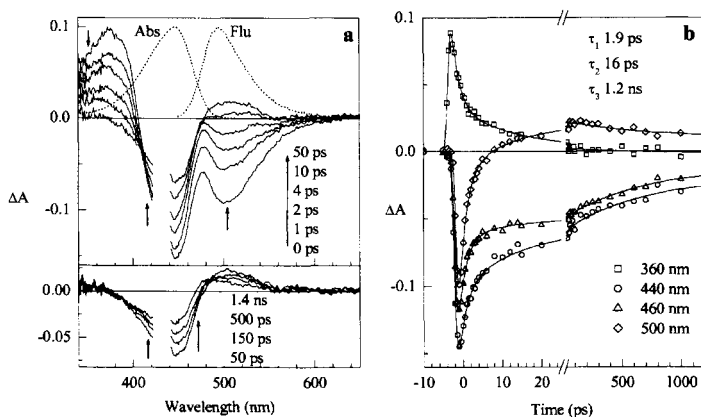


Fig. 1. (a) Differential absorbance spectra of native PYP, after excitation at 430 nm, at different pump-probe delays. The scattered pump light around 430 nm has been masked. Steady-state absorption and fluorescence spectra are represented with dotted lines. (b) Kinetics extracted from the transient spectra at selected wavelengths

3. RESULTS AND DISCUSSION

3.1. Time-resolved transient absorption spectra of native PYP

Fig. 1. displays the differential absorbance spectra (a) of native PYP and the associated kinetics at selected wavelengths (b). Compared to the previously reported transient spectra [4,6,7,11], the probed region has been extended to the ultraviolet down to 340 nm. Upon excitation, three bands are formed, an excited-state absorption band peaking at 370 nm, the ground state bleaching and the stimulated emission bands both located in the region of the steady-state spectra. For pump-probe delays up to 50 ps, the three bands decrease. At 50 ps, the 370-nm transient absorption band is no longer observed and the stimulated emission band has been replaced by a broad transient absorption band. At longer delays, the band turns into a blue-shifted transient absorption band while the bleaching band is still decaying. At 1.4 ns, the observed transient absorption band corresponds quite well to the absorption spectrum previously reported and attributed to the formation of the PYP *cis* isomer (I_1) [12,13].

A global kinetics analysis of the transient spectra has been performed, requiring in general the sum of triexponentials. Below 400 nm, kinetics are biexponential with 1.9 ps (wt. 70 %) and 16 ps (wt. 30 %) lifetimes. In the other spectral regions, the kinetics exhibit triexponential decays with an additional 1.2-ns lifetime corresponding to the formation of the I_1 absorption band. The apparent decay of the stimulated emission is found to be biexponential with time components of 1.9 ps (wt. 80 %) and 16 ps (wt. 20%). It is worth noting that time-resolved fluorescence measurements showed multiexponential decays with comparable lifetimes [3,5]. Biexponential decays of the PYP stimulated emission has also been reported and attributed to the existence of two excited states simultaneously populated upon excitation [4,7,13]. It is clear from the steady-state spectroscopy of wild-type PYP (see Fig. 1a, upper part) that the fluorescence is not the mirror image of the absorption spectrum, the latter being about $1,000\text{ cm}^{-1}$ broader. This is a common feature of the steady-state spectroscopy of several PYP chromophore analogues that is likely due to the presence of two electronic bands lying under the absorption spectra [14].

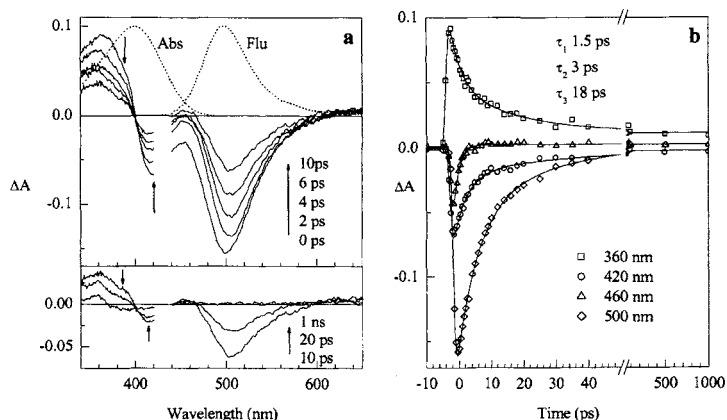


Fig. 2. (a) Differential absorbance spectra of denatured PYP, after excitation at 430 nm, at different pump-probe delays. The scattered pump light around 430 nm has been masked. Steady-state absorption and fluorescence spectra are represented in dotted lines. (b) Kinetics extracted from the transient spectra at selected wavelengths

The excited-state deactivation of PYP was previously reported to be associated to the formation of distinct precursors of I_1 absorbing in the 480-500-nm spectral region [4,6,7]. The kinetics observed in different spectral regions (Fig. 1b) are indeed complex, likely due to the overlap of several bands at the selected wavelengths.

3.2. Time-resolved transient absorption spectra of the denatured PYP

Differential absorbance spectra of the denatured PYP at different pump-probe delays and the associated kinetics at selected wavelengths are presented in Fig. 2. At short times, the transient spectra of the denatured PYP look like those of the native protein. Upon excitation, the excited-state absorption, the ground-state bleaching and the stimulated emission bands are formed. After 10 ps, the three bands have decreased and the, initially negative, local maximum located between the bleaching and the stimulated emission bands has become slightly positive. In the meantime, the stimulated emission band exhibits a positive dynamical Stokes shift. Such an effect, that is also observed in the time-resolved fluorescence experiments on the denatured PYP, is attributed to a charge redistribution in the chromophore upon excitation, followed by solvation dynamics [3,15]. After 1 ns, a bleaching signal remains indicating that part of the excited-state population did not return to the ground state. At the same time, a long-lived photoproduct, absorbing at 360 nm and which we have not yet fully characterized, is also detected. This photoproduct has been attributed to the "instantaneous" production of the chromophore radical cation - and solvated electron - by biphotonic laser ionization [16]. This is a reasonable assumption since we previously observed formation of solvated electrons due to a biphotonic ionization of *p*-trans-coumaric acid in basic aqueous solution [17]. It has nevertheless to be stressed that such a nonlinear reaction pathway bears no relationship with the standard, sun-driven, one-photon photocycle of PYP.

Kinetics extracted from the transient spectra were fitted to a biexponential function with 3 ps and 18 ps lifetimes, except in the spectral region located between the bleaching and the stimulated emission bands where the decays were fitted to one exponential function with a 1.5 ps lifetime. Decays in the stimulated emission band are biexponential with an average lifetime of about 10 ps, which is comparable to the fluorescence lifetime reported in [3].

Interestingly, the transient spectroscopy of the denatured PYP is quite similar to that of a phenyl thioester analogue of the chromophore [14]. It is however worth noting that the amplitude of the 450 nm absorption band is smaller and the stimulated emission lifetime is longer than those of the analogue. These differences may be due to some solvent effect since a high concentration of guanidinium chloride has been used for PYP denaturation. Finally, the striking feature in the transient spectroscopy of the denatured PYP is the similarity with that of the native PYP, both showing complex decay kinetics with a rising transient absorption band in the red edge of the bleaching band. This similarity leads us to think that the early events in native PYP could be controlled, in part, by the intrinsic properties of the chromophore. This seems to be in contradiction with the idea that the mesoscopic environment forces the protein to deactivate quickly along a photochemical path different from that in the free chromophore in solution.

4. CONCLUSION

The transient absorption spectroscopy of the denatured PYP is found to be similar to that of the native protein in the early stages of the excited-state deactivation. This behavior seems to indicate that the intrinsic properties of the chromophore play a determining role in the complex primary photoprocesses of the native PYP.

REFERENCES

- [1] W. W. Sprenger, W. D. Hoff, J. P. Armitage and K. J. Hellingwerf, *J. Bacteriol.*, 175 (1993) 3096.
- [2] K. J. Hellingwerf, J. Hendriks and T. Gensch, *J. Phys. Chem. A*, 107 (2003) 1082.
- [3] N. Mataga, H. Chosrowjan, Y. Shibata, Y. Imamoto and F. Tokunaga, *J. Phys. Chem. B*, 104 (2000) 5191.
- [4] T. Gensch, C. C. Gradinaru, I. H. M. van Stokkum, J. Hendricks, K. J. Hellingwerf and R. van Grondelle, *Chem. Phys. Lett.*, 356 (2002) 347.
- [5] P. Changenet, H. Zhang, M. J. van der Meer, K. J. Hellingwerf and M. Glasbeek, *Chem. Phys. Lett.*, 282 (1998) 276.
- [6] S. Devanathan, A. Pacheco, L. Ujj, M. Cusanovich, G. Tollin, S. Lin and N. Woodbury, *Biophys. J.*, 77 (1999) 1017.
- [7] Y. Imamoto, M. Kataoka, F. Tokunaga, T. Asahi and H. Masuhara, *Biochem.*, 40 (2001) 6047.
- [8] Y. Zhou, L. Ujj, T. E. Meyer, M. A. Cusanovich and G. H. Atkinson, *J. Phys. Chem. A*, 105 (2001) 5719.
- [9] N. Dai Hung, P. Plaza, M. M. Martin and Y. H. Meyer, *Appl. Opt.*, 31 (1992) 7046.
- [10] J. Hendriks, T. Gensch, L. Hviid, M. A. van der Horst, K. J. Hellingwerf and J. J. van Thor, *Biophys. J.*, 82 (2002) 1632.
- [11] M.-L. Groot, L. J. G. W. van Wilderen, D. S. Larsen, M. A. van der Horst, I. H. M. van Stokkum, K. J. Hellingwerf and R. van Grondelle, *Biochem.*, 42 (2003) 10054.
- [12] W. D. Hoff, I. H. M. van Stokkum, H. J. van Ramesdonk, M. E. van Brederode, A. M. Brouwer, J. C. Fitch, T. E. Meyer, R. van Grondelle and K. J. Hellingwerf, *Biophys. J.*, 67 (1994) 1691.
- [13] L. Ujj, S. Devanathan, T. E. Meyer, M. A. Cusanovich, G. Tollin and G. H. Atkinson, *Biophys. J.*, 75 (1998) 406.
- [14] P. Changenet-Barret, A. Espagne, N. Katsonis, S. Charier, J.-B. Baudin, L. Jullien, P. Plaza and M. M. Martin, *Chem. Phys. Lett.*, 365 (2002) 285, see also this book.
- [15] N. Mataga, H. Chosrowjan, S. Taniguchi, N. Hamada, F. Tokunaga, Y. Imamoto and M. Kataoka, *Phys. Chem. Chem. Phys.*, 5 (2003) 2454.
- [16] D. S. Larsen, Private communication, Poster 58, Femtochemistry VI, Paris, 6-10 July 2003.
- [17] P. Changenet-Barret, P. Plaza and M. M. Martin, *Chem. Phys. Lett.*, 336 (2001) 439.

Chemical structure effect on the excited-state relaxation dynamics of the PYP chromophore

A. Espagne, P. Changenet-Barret, S. Charier, J.-B. Baudin, L. Jullien, P. Plaza and M.M. Martin

Département de Chimie, UMR 8640 ENS-CNRS PASTEUR, Ecole Normale Supérieure, 24 rue Lhomond, 75231 Paris Cedex 05, France

1. INTRODUCTION

The Photoactive Yellow Protein (PYP) is thought to be the photoreceptor responsible for the negative phototaxis of the bacterium *Halorhodospira halophila* [1]. Its chromophore, the deprotonated 4-hydroxycinnamic (or *p*-coumaric) acid, is covalently linked to the side chain of the Cys69 residue by a thioester bond. *Trans-cis* photoisomerization of the chromophore was proved to occur during the early steps of the PYP photocycle. Nevertheless, the reaction pathway leading to the *cis* isomer is still discussed (for a review, see ref. [2]). Time-resolved spectroscopy showed that it involves subpicosecond and picosecond components [3-7], some of which could correspond to a flipping motion of the chromophore carbonyl group [8,9].

In order to better understand the early photophysics of PYP, we have carried out a comparative study of three model chromophores, the deprotonated *trans-p*-coumaric acid (pCA^{2-}) and its amide (pCM^-) and phenyl thioester (pCT^-) analogues, in aqueous solution (see structures in Fig. 1). The excited-state relaxation dynamics was followed by subpicosecond transient absorption and gain spectroscopy.

2. EXPERIMENTAL

*Trans-p*CA was purchased from Sigma. *Trans-p*CM and *trans-p*CT have been synthesized for this study [10]. Deprotonation of *p*CA and *p*CM was achieved by adding 0.05 M of KOH in HPLC grade water. Samples of deprotonated *p*CT were prepared in a borate Britton-Robinson buffer at pH 10.2 [10]. The absorbance was adjusted to 1 per mm at the absorption maximum.

Transient absorption and gain spectroscopy was performed by the pump-probe technique using a subpicosecond set-up described in detail elsewhere [10-12]. For the present experiments, the pump was set at 355 nm (pCA^{2-} and pCM^-) or 430 nm (pCT^-) and the probe was a white-light continuum produced by focusing 570 nm pulses in a 1-cm water cell. The

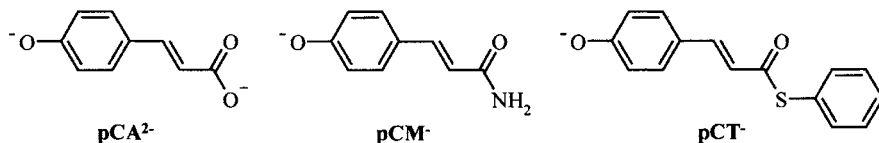


Fig. 1. Chemical structure of deprotonated *p*-coumaric acid (pCA^{2-}) and its two analogues

differential absorbance (ΔA) spectra were averaged over 500 shots and corrected from the group velocity dispersion in the probe beam. The time-resolution was about 1 ps.

3. RESULTS AND DISCUSSION

3.1. Transient absorption spectroscopy of pCA^{2-} and pCM^-

Fig. 2 depicts the differential absorbance (ΔA) spectra of pCM^- in aqueous solution. The spectra are similar to those of pCA^{2-} [11]. Three bands are formed during the excitation pulse. The positive band below 420 nm and the negative band peaking at 465 nm are respectively assigned to the excited-state absorption (ESA) and the stimulated emission (SE). Both bands decay simultaneously in about 10 ps and 4 ps respectively for pCA^{2-} and pCM^- . At long wavelengths, the broad positive band which remains unchanged for all pump-probe delays is attributed to the absorption of solvated electrons formed by a biphotonic ionization of the phenolate group [11].

The rapid and concomitant decay of the SE and ESA bands indicates that an efficient non-radiative process occurs from the excited state of pCA^{2-} and pCM^- . Previous experiments on pCA^{2-} gave evidence that this non-radiative process is correlated to the *trans-cis* isomerization reaction. The *trans* excited-state decay leads to the ground-state *cis* isomer without any detectable intermediate, following a mechanism comparable to that of *trans*-stilbene [11]. A similar process can be invoked for pCM^- because steady-state photolysis of pCM^- led to a stable photoproduct that we identified as the *cis* isomer by 1H NMR. In water, photoisomerization of pCM^- is thus found to be faster than that of pCA^{2-} . The transient spectroscopy of pCM^- in alcohols showed a positive dynamical Stokes shift of the SE band indicating substantial photoinduced charge redistribution. Such a charge redistribution, which was not observed for pCA^{2-} [11], might be the cause for a lower isomerization barrier.

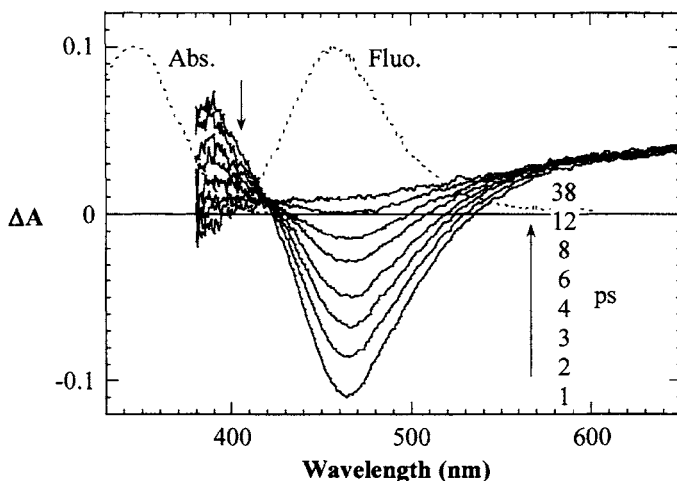


Fig. 2. Differential absorbance (ΔA) spectra of pCM^- in water (KOH 0.05 M) after excitation at 355 nm. Steady-state absorption and fluorescence spectra are represented in dotted lines

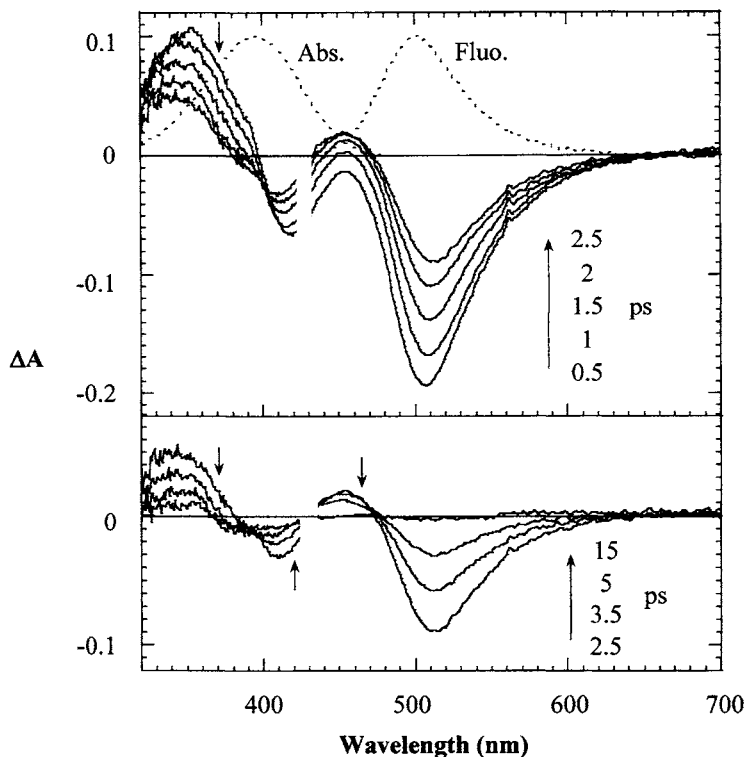


Fig. 3. Differential absorbance (ΔA) spectra of pCT in water (pH 10.2) after excitation at 430 nm. The spectral region corresponding to the scattered pump light is masked. Steady-state absorption and spontaneous emission spectra are also represented in dotted lines

3.2. Transient absorption spectroscopy of pCT

Fig. 3 shows the ΔA spectra of pCT in aqueous solution at pH 10.2. Compared to the spectra we previously reported [10], the signal-to-noise ratio has been improved and the probed region has been extended beyond 380 nm. Three bands are formed instantaneously after excitation: a positive UV absorption band at 350 nm attributed to ESA, a small negative band at 420 nm due to the ground-state bleaching and a strong negative SE band at 510 nm. The shape of the bleaching band is different from that of the steady-state absorption spectrum because of the overlap with the 350-nm ESA band. For delays between 0 and 2.5 ps, the three initial bands decay while an absorption band develops at 450 nm. The formation of the latter in 1.1 ps is concomitant to the decay of the red side of the 350-nm ESA band but not to that of its blue side, a spectral region that was not probed in our previous work [10]. The blue side exhibits a slower decay of about 2 ps which is close to the SE decay (2.4 ps). The 450-nm absorption band decays in 3.3 ps. For a 15 ps delay, a weak bleaching signal and a small absorption band peaking at 355 nm are left, indicating an incomplete ground-state repopulation after the decay of the excited-state, due to the formation of a photoproduct absorbing at 355 nm. The lifetime of the latter was found to be larger than 1 ns. A similar behavior was recently reported for a methyl thioester derivative of *p*-coumaric acid [13]. The nature of the photoproduct is still unclear to us. As the expected *cis* isomer could not be

observed in steady-state photolysis, its spectrum is not known. Further experiments are in progress to characterize the nature of this photoproduct.

We previously proposed a mechanism involving a rapid equilibrium between the initial emissive state and the 450-nm absorbing species owing to their close decay rates [10]. In the present measurements the wavelength-dependence of the UV ESA band decay time is likely due to the presence of several absorbing species. We previously discussed the existence of two electronic transitions underlying the ground-state absorption band of pCT⁻ [10]. One might infer that the complexity of the kinetics probed across the 320-600 nm spectral range results from the simultaneous excitation of these two quasi-degenerate excited states by the pump. We have undertaken studies in different solvents in order to identify competing or cascading steps. Although the excited-state relaxation mechanism of pCT⁻ is not clear yet, the present study demonstrates that it is quite different from those of pCA²⁻ and pCM⁻ in water. The excited-state deactivation of pCT⁻ is much faster and proceeds through a more complex pathway, involving the formation, on the picosecond time-scale, of a red-shifted intermediate absorbing between the bleaching and the SE. It is worth mentioning the similarity of this intermediate with the earliest intermediate of the PYP photocycle that was found to appear in the same spectral region, on the same time-scale [4,5,7].

4. CONCLUSION

The excited-state deactivation pathway of PYP model chromophores is found to depend strongly on the substituent adjacent to the carbonyl group. The photoisomerization reaction of the deprotonated *p*-coumaric acid (pCA²⁻) and of its amide analogue (pCM⁻) in solution does not show any spectroscopically detectable intermediate, which is quite different from PYP. On the contrary, the phenyl thioester derivative pCT⁻ exhibits a photophysical behavior in solution surprisingly close to that of the protein during its initial deactivation step. This study highlights the determining role of the thioester bond in the primary molecular events in PYP.

REFERENCES

- [1] W.W. Sprenger, W.D. Hoff, J.P. Armitage and K.J. Hellingwerf, *J. Bacteriol.*, 175 (1993) 3096.
- [2] K.J. Hellingwerf, J. Hendriks and T. Gensch, *J. Phys. Chem. A*, 107 (2003) 1082.
- [3] H. Chosrowjan, N. Mataga, N. Nakashima, Y. Imamoto and F. Tokunaga, *Chem. Phys. Lett.*, 270 (1997) 267.
- [4] A. Baltuška, I.H.M. van Stokkum, A. Kroon, R. Monshouwer, K.J. Hellingwerf and R. van Grondelle, *Chem. Phys. Lett.*, 270 (1997) 263.
- [5] L. Ujj, S. Devanathan, T.E. Meyer, M.A. Cusanovich, G. Tollin and G.H. Atkinson, *Biophys. J.*, 75 (1998) 406.
- [6] P. Changenet, H. Zhang, M.J. van der Meer, K.J. Hellingwerf and M. Glasbeek, *Chem. Phys. Lett.*, 282 (1998) 276.
- [7] Y. Imamoto, M. Kataoka, F. Tokunaga, T. Asahi and H. Masuhara, *Biochem.*, 40 (2001) 6047.
- [8] U.K. Genick, S.M. Soltis, P. Kuhn, I.L. Canestrelli and E.D. Getzoff, *Nature*, 392 (1998) 206.
- [9] Z. Ren, B. Perman, V. Srajer, T.-Y. Teng, C. Pradervand, D. Bourgeois, F. Schotte, T. Ursby, R. Kort, M. Wulff and K. Moffat, *Biochem.*, 40 (2001) 13788.
- [10] P. Changenet-Barret, A. Espagne, N. Katsonis, S. Charier, J.-B. Baudin, L. Jullien, P. Plaza and M.M. Martin, *Chem. Phys. Lett.*, 365 (2002) 285.
- [11] P. Changenet-Barret, P. Plaza and M.M. Martin, *Chem. Phys. Lett.*, 336 (2001) 439.
- [12] N. Dai Hung, P. Plaza, M.M. Martin and Y.H. Meyer, *Appl. Opt.*, 31 (1992) 7046.
- [13] D.S. Larsen, M. Vengris, I.H.M. van Stokkum, M.A. van der Horst, R.A. Cordfunke, K.J. Hellingwerf and R. van Grondelle, *Chem. Phys. Lett.*, 369 (2003) 563.

Ultrafast excited state dynamics in the green fluorescent protein chromophore

A. Toniolo,^a S. Olsen,^b L. Manohar,^a and T. J. Martínez^{a,b}

^aDepartment of Chemistry and The Beckman Institute, University of Illinois, 600 S. Mathews, Urbana, IL 61801

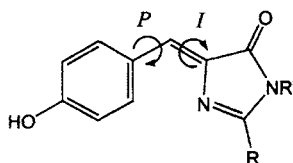
^bCenter for Biophysics & Computational Biology, University of Illinois, Urbana, IL 61801

1. INTRODUCTION

The textbook picture of photoinduced *cis-trans* isomerization in unsaturated hydrocarbons is one-dimensional, focusing on simple torsion about a C=C bond.[1] The resulting large amplitude motion seems inconsistent with the steric constraints imposed by protein environments. This observation led to many proposals for minimal-volume photoisomerization pathways in protein environments.[2-6] Recent work has shown that the mechanism for photoisomerization is considerably more complicated than simple torsion, implying that the inconsistency mentioned above may be only apparent. In fact, photoisomerization often involves both torsion and pyramidalization,[7-11] leading to excited state dynamics much more akin to a “slicing” motion[12,13] as opposed to the “sweeping” motion most naturally envisioned for a simple torsion. Thus, the question which must be raised anew is to what extent the protein environment modifies the photochemical reaction pathway associated with photoisomerization. In this note, we report on our theoretical studies of photoisomerization in the chromophore of green fluorescent protein (GFP).

1.1. Green Fluorescent Protein

GFP is an autofluorescent protein which has become a powerful tool in molecular and cell biology.[14,15] The GFP chromophore is formed autocatalytically from cyclization and oxidation of a Ser-Tyr-Gly tripeptide (in wild type *A. Victoria*) resulting in the *p*-hydroxybenzylidene-imidazolinone (HBI) molecule shown in Sketch 1. The R and R' groups represent the covalent



Sketch 1.

connection to the protein and there are two isomerizable bonds denoted P (phenol) and I (imidazolinone). Ultrafast experiments with isotopic substitution have established that the photoreaction in the protein environment involves excited state proton transfer. Although there has been some debate about the nature of the protonation states involved,[16] most studies support a neutral chromophore as depicted in Sketch 1 and a phenolate anionic form.[15] In spite of the fact that the chromophore is buried deep within the protein and is surrounded by ionizable residues, the protein does not appear to significantly tune its absorbance, even relative to the gas phase. Model compounds in solution or gas phase as well as chromophore-containing protein digests possess absorbance maxima very close to those seen in the protein.[14,17-25] However, the subsequent photochemistry is quite different in the protein and for models in solution. GFP fluoresces, as can be inferred from its name, and does so with high quantum yield ($\Phi_f=0.8$) and with a respectable fluorescence lifetime ($\tau\approx 3\text{ns}$).[14] However, early attempts to observe the fluorescence of chromophore models in solution met with failure,[22,23,26,27] with complete ground state recovery observed within 5ps of excitation.[27-29] This recovery has been reported to be only weakly dependent on viscosity.[27-29] Chromophore models in frozen solution do fluoresce, and do so with emission energies consistent with those observed in the protein.[22] It is generally believed[30] that the nonradiative decay observed in solution is a consequence of photoisomerization about one of the isomerizable bonds depicted in Sketch 1, probably mediated by a conical intersection.[31-33]

1.2. Photoisomerization Pathways

Simple torsion about a double bond has been referred to as the “one-bond-flip” or OBF mechanism. At least two “minimal volume” isomerization pathways have been proposed, along with several variants (see Figure 1). The “bicycle pedal” mechanism involves simultaneous torsion about two double bonds, and is now generally believed to be unfavourable on the excited state. However, there is evidence that it may play a role in the thermal isomerization of chromophores such as retinal-protonated Schiff base (RPSB) in protein environments.[34] The “hula twist” mechanism involves simultaneous torsion about a double bond and an adjacent single bond. Weber, et al. have investigated the energetic feasibility of such motion in the GFP chromophore using a semiempirical method and found it to be possible, but less favourable than simple torsion about one double bond.[30] The present work does not assume any reaction pathway, but rather follows the excited state dynamics directly. Furthermore, we can study the isomerization of the chromophore in vacuum and solution, allowing some quantification of the

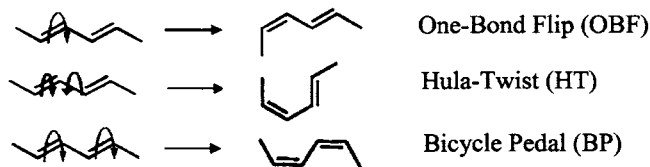


Fig. 1. Idealized photoisomerization mechanisms. These can lead to different final products as shown. However, one should realize that hot ground state reactions could also occur, obscuring a simple relationship between products and excited state dynamics.

role of the solvent environment in the observed pathway. Studies in the protein environment will also be interesting, and these are underway. However, we leave these for future publication.

2. THEORY

2.1 *Ab Initio* Multiple Spawning Dynamics

Traditional treatments of molecular dynamics proceed from analytic potential energy surfaces which must be fit to experimental or theoretical data beforehand.[35] This fitting process is time-consuming and error-prone, and thus recent developments have turned to “direct dynamics” approaches which recomputed the potential energy surfaces as needed, simultaneously with the molecular dynamics. Approaches using *ab initio* electronic structure theory to compute the potential energy surface date back to the late 70’s,[36] but were generally considered computationally intractable until recently.[37-39] These *ab initio* molecular dynamics (AIMD) methods have usually been confined to dynamics occurring on a single electronic state, generally the ground state. We have developed the full multiple spawning (FMS) dynamics method as a foundation for AIMD methods including quantum mechanical effects in real-time dynamics, particularly the nonadiabatic effects associated with the breakdown of the Born-Oppenheimer approximation near true and avoided crossings of multiple electronic states.[40,41] In brief, the FMS method uses a set of time-dependent nonorthogonal frozen Gaussian basis functions[42] as a basis set for the nuclear wavefunction and then solves the resulting Schrodinger equation for the time-dependence of the complex coefficients.[40,41] An important point is that the basis set is adaptive, and is expanded in a deterministic way in order to capture quantum mechanical effects such as population transfer between different electronic states. The local nature of the Gaussian basis functions allows us to use simplifying approximations in order to calculate the required integrals, providing the needed locality in order to interface with electronic structure theory. We have shown that it is possible to carry out *ab initio* multiple spawning (AIMS) calculations of photodynamics which solve the electronic and nuclear Schrodinger equations simultaneously. Applications ranging from diatomic molecules up to medium sized organic molecules like azobenzene and the chromophore of photoactive yellow protein (PYP) have been presented.[7-10,40,43-50]

2.2. Large Molecules and Condensed Phases

Rapid development of the AIMS method has led to an increase in the accessible molecular size from one degree of freedom to almost 100 degrees of freedom in the last seven years, in spite of the fact that *ab initio* methods applicable to excited electronic states formally exhibit exponential scaling of computational effort with molecular size. Nevertheless, AIMS calculations are computationally challenging and there seems to be no way at present to model condensed phase photochemistry with this approach. Recent attempts to use density functional theory (DFT) based methods for excited state dynamics hold some promise in this respect,[51,52] although there remain fundamental questions concerning the treatment of excited states in DFT. We have recently[53] investigated the possibility of an alternative approach—using modified semiempirical methods in conjunction with hybrid quantum mechanical/molecular mechanical (QM/MM) treatments[54-56] in order to describe the potential energy surfaces and their nonadiabatic couplings. We have shown that multireference semiempirical methods with standard parameter sets can predict the nuclear configurations which give rise to conical intersections with surprising

accuracy.[53,57] However, the energetics is often qualitatively incorrect—for example, the conical intersection which has been shown to dominate the dynamics in ethylene is predicted to lie above the Franck-Condon point. Thus, any excited state dynamics based on standard parameter sets should be considered quite suspect. Reoptimization of the semiempirical parameters for specific ground state molecular processes has been advocated by other workers.[58] A natural approach is then to consider reoptimization for the ground and excited states of a chromophore in order to reproduce key *ab initio* and/or experimental results. If the reparameterization reproduces not only geometries and energetics but also *ab initio* electronic properties of the electronically excited solute, it could be quite accurate in the framework of a QM/MM treatment.

3. RESULTS

We used HBI as a model of the GFP chromophore, which amounts to replacing the R and R' moieties depicted in Sketch 1 with H atoms. We detail first the procedure for reoptimization of the semiempirical parameters, along with an assessment of the quality of the resulting PESs. Next, we describe the results of direct FMS dynamics for the neutral form of the GFP chromophore in isolation and also in aqueous solution. All *ab initio* calculations are done using the MolPro electronic structure theory package[59] using the 6-31G basis set.[60] Semiempirical calculations are done with a highly modified version of the MOPAC2000 program,[61] including FMS dynamics, QM/MM methods, analytic nonadiabatic coupling evaluation, and conical intersection search algorithms.[53,57,62] The SPC representation[63] is used for the MM force field of water in the QM/MM FMS dynamics calculations. Technical details concerning implementation may be found in previous papers.[40,41,53,57,62]

3.1 Reparameterization of GFP Chromophore Potential Energy Surfaces

Since it is known that the GFP photocycle involves various protonation states of the chromophore, we have chosen to include four ionic forms in the reparameterization. These are the neutral depicted in Sketch 1, the phenolate anion, the zwitterion which deprotonates phenol and protonates the N atom which is not connected to the protein, and the enol. For each of the protonation states listed, the ground state geometry is optimized with the state-averaged[64,65] complete active space self-consistent field method,[66] averaging over the lowest two electronic states with equal weights and including two electrons in two active orbitals, i.e. SA-2-CAS(2/2). Geometry optimizations using SA-2-CAS(2/2) wavefunctions are also performed on S_1 to find local minima twisted about either of the isomerizable bonds and to find S_0/S_1 minimal energy conical intersections (MECIs). We could not find a local minimum on S_1 corresponding to twisting about the P bond for the neutral, and we instead used a geometry obtained by minimizing on S_0 for P-bond torsion fixed at 90° . The anionic form has local minima and MECIs corresponding to twisted geometries about either of the I or P bonds. However, the neutral has neither a local minimum nor an MECI corresponding to torsion about the P-bond. Vertical excitation energies at the S_0 minima and relative energies for each of the optimized geometries are then computed using equation-of-motion coupled cluster[67] with single and double excitations (EOM-CCSD). The 25 lowest energy canonical orbitals are left uncorrelated in the EOM-CCSD calculations.

Table 1
Data Points Used in Reparameterization (tw=twisted, energies in eV)

	EOM-CCSD		R-AM1		AM1		w_i	
	S_0	S_1	S_0	S_1	S_0	S_1	S_0	S_1
Neutral								
S_0 Min	0.00	4.21	0.00	4.42	0.00	3.61	---	5.0
S_0 P-tw Min	0.23	4.62	0.12	4.85	0.10	4.19	2.0	1.0
S_1 I-tw Min	2.57	3.20	2.35	2.90	1.71	2.61	0.5	5.0
S_0/S_1 I-tw MECI	3.40	3.40	3.21	3.21	3.81	3.81	---	5.0
Zwitterion								
S_0 Min	1.10	3.38	1.20	1.98	1.09	2.21	0.5	2.0
S_0/S_1 MECI	1.77	1.77	1.66	1.66	2.27	2.27	---	1.0
Enol								
S_0 Min	1.16	3.33	1.54	3.07	1.03	3.11	0.5	1.0
Anion								
S_0 Min	0.00	3.12	0.00	3.35	0.00	2.65	---	5.0
S_1 I-tw Min	1.38	2.68	1.52	2.46	1.22	1.87	0.5	2.0
S_1 P-tw Min	1.28	2.81	0.87	2.72	0.99	1.90	0.5	2.0

The resulting *ab initio* data provide the input for the reparameterization. Specifically, we define a target function

$$f(\mathbf{X}) = \frac{\sum_i \left(\frac{y_{0,i} - y_{s,i}}{y_{0,i}} \right)^2 w_i}{\sum_i w_i} \quad (1)$$

where i indexes the data points, \mathbf{X} is a vector containing all the semiempirical parameters which are to be reoptimized, $y_{0,i}$ and $y_{s,i}$ are *ab initio* and semiempirical values, respectively, and w_i is a positive weight. This function is then minimized using a simplex optimization procedure.[68] The data points used in the optimization are described in Table 1. Energies of the neutral, zwitterion, and enol forms are all referenced to the neutral S_0 minimum and energies of the anion are referenced to the anion S_0 minimum. It is important to recognize that we define the geometries associated with the data in terms of an optimization condition. For example, the S_0 minima for each protonation state, as well as the S_1 minima and the S_0/S_1 MECIs are all reoptimized for every candidate parameter set. This means that Eq. (1) cannot be analytically differentiated and that its evaluation requires many geometry optimizations. We do not explicitly include any information about the difference between the *ab initio* and semiempirical geometries in the target function, instead using this as a check after the optimization is complete. The optimized parameters are available from the authors on request. We have carried out numerous checks of the resulting ground and excited state PESs along one-dimensional cuts. There is insufficient space to show these here, but we simply state that the R-AM1 PESs are smooth, compare favourably to those obtained from EOM-CCSD, and appear to be improvements over AM1 (judged by agreement with EOM-CCSD) for practically all 1D cuts examined.

3.2 Excited State Dynamics of GFP Chromophore

The R-AM1 parameters have been used to carry out FMS dynamics of the isolated and solvated GFP chromophore. We model the solvated chromophore using QM/MM with an MM treatment of 150 surrounding water molecules. There is a major difference between the isolated and solvated chromophore which affects the excited state lifetime—in the solvated chromophore, the S_1 minimum coincides with the MECI. Thus, internal conversion is much faster in solution than in the gas phase. Traces of the P- and I-bond torsion angles are shown in Figure 2. The left panel provides the results in the gas phase and the right panel corresponds to a QM/MM calculation with 150 surrounding MM water molecules. The dihedral angles are defined in such a way that idealized HT motion corresponds to both values moving towards negative values with the same slope. First, note that the time scales are quite different for the two panels. Almost all population has been transferred to S_0 after 100fs in solution, while more than 60% remains on S_1 after 400fs in the gas phase. This is a simple consequence of the fact that the MECI is the absolute minimum in solution, as mentioned above. Another interesting point is that the torsional dynamics is very similar for the first 100fs in both solution and gas phase cases. Finally, the observed torsional dynamics initially follows the behaviour expected for HT motion, but then the P-bond turns around and rotates in the opposite direction. In other words, what is seen is an “aborted” HT mechanism. Closer investigation (not shown here) reveals that the torsion angles are dominated by motion of the central H atom, driven by a pyramidalization of the bridge C atom. Thus, this is partially a kinematic effect, due to the light mass of the H atom.

4. CONCLUSIONS

We have presented the first published results of a QM/MM wavepacket dynamics study of a photochemical reaction. The photoisomerization mechanism for the GFP chromophore that we observe has the signatures of HT motion, *even in the complete absence of an environment*. The HT mechanism is “aborted” in both the gas phase and solution, but the

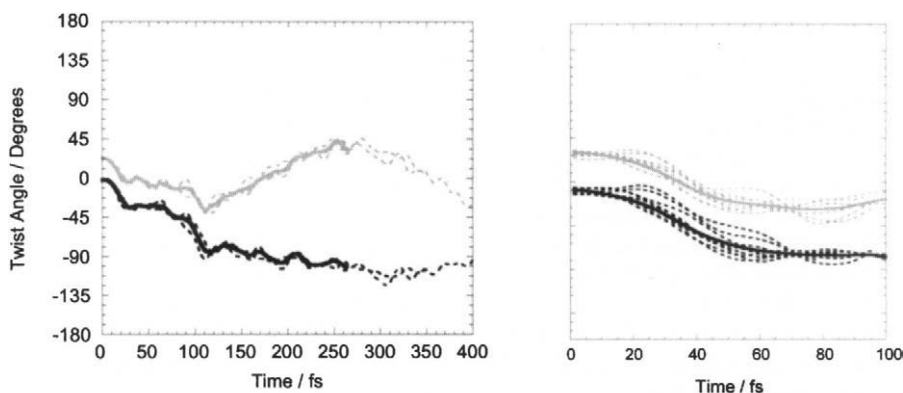


Fig. 2. Evolution of twist angle around the P-bond (grey) and I-bond (black) after photoexcitation of the neutral form of GFP chromophore in the gas phase (left panel) and solvated by 150 water molecules (right panel). Solid lines are population-weighted averages over the trajectory basis functions. Dashed lines represent the twist angles for the individual trajectory basis functions. The sense of rotation for the two torsions is defined such that HT motion corresponds to both angles moving towards more negative values.

initial motion along the HT coordinate is significant and found to be a consequence of the combined torsion and pyramidalization motions which dominate the excited state dynamics in this and many other photoisomerization reactions.

REFERENCES

- [1] A. Gilbert and J. Baggot, *Essentials of Molecular Photochemistry* (CRC Press, Boca Raton, 1991).
- [2] R. S. H. Liu, D. Mead, and A. E. Asato, *J. Am. Chem. Soc.* 107 (1985) 6609.
- [3] R. S. H. Liu and A. E. Asato, *Proc. Natl. Acad. Sci.* 82 (1985) 259.
- [4] R. S. H. Liu and D. T. Browne, *Acc. Chem. Res.* 19 (1986) 42.
- [5] R. S. H. Liu, *Acc. Chem. Res.* 34 (2001) 555.
- [6] A. Warshel, *Nature* 260 (1976) 679.
- [7] M. Ben-Nun and T. J. Martínez, *Chem. Phys. Lett.* 298 (1998) 57.
- [8] M. Ben-Nun and T. J. Martínez, *Chem. Phys.* 259 (2000) 237.
- [9] M. Ben-Nun, J. Quenneville, and T. J. Martínez, *J. Phys. Chem.* 104A (2000) 5161.
- [10] J. Quenneville, M. Ben-Nun, and T. J. Martínez, *J. Photochem. Photobiol. A* 144 (2001) 229.
- [11] J. Quenneville and T. J. Martínez, *J. Phys. Chem.* 107A (2003) 829.
- [12] D. C. Todd, G. R. Fleming, and J. M. Jean, *J. Chem. Phys.* 97 (1992) 8915.
- [13] A. B. Myers and R. A. Mathies, *J. Chem. Phys.* 81 (1984) 1552.
- [14] R. Y. Tsien, *Annu. Rev. Biochem.* 67 (1998) 509.
- [15] M. Zimmer, *Chem. Rev.* 102 (2002) 759.
- [16] A. A. Voityuk, M. Michel-Beyerle, and N. Rösch, *Chem. Phys. Lett.* 272 (1997) 162.
- [17] L. H. Andersen, A. Lapiere, S. B. Nielsen, I. B. Nielsen, S. U. Pedersen, U. V. Pedersen, and S. Tomita, *Eur. Phys. J. D* 20 (2002) 597.
- [18] S. B. Nielsen, A. Lapiere, J. U. Andersen, U. V. Pedersen, S. Tomita, and L. H. Anderson, *Phys. Rev. Lett.* 87 (2001) 228102/1.
- [19] V. Helms, C. Winstead, and P. W. Langhoff, *J. Mol. Struct. THEOCHEM* 506 (2000) 179.
- [20] A. F. Bell, X. He, R. M. Wachter, and P. J. Tonge, *Biochem.* 39 (2000) 4423.
- [21] C. W. Cody, D. C. Prasher, W. M. Westler, F. G. Prendergast, and W. W. Ward, *Biochem.* 32 (1993) 1212.
- [22] M. Chatteraj, B. A. King, G. U. Bublitz, and S. G. Boxer, *Proc. Natl. Acad. Sci.* 93 (1996) 8362.
- [23] H. Niwa, S. Inouye, T. Hirano, T. Matsuno, S. Kojima, M. Kubota, M. Ohashi, and F. I. Tsuji, *Proc. Natl. Acad. Sci.* 93 (1996) 13617.
- [24] W. W. Ward and S. H. Bokman, *Biochem.* 21 (1982) 4535.
- [25] W. Ward, H. J. Prentice, A. F. Roth, C. W. Cody, and S. C. Reeves, *Photochem. Photobiol.* 35 (1982) 803.
- [26] S. Kojima, H. Ohkawa, T. Hirano, S. Maki, H. Niwa, M. Ohashi, S. Inouye, and F. I. Tsuji, *Tetrahedron Lett.* 39 (1998) 5239.
- [27] D. Mandal, T. Tahara, N. M. Webber, and S. R. Meech, *Chem. Phys. Lett.* 358 (2002) 495.
- [28] N. M. Webber, L. Konstantin, L. Litvinenko, and S. R. Meech, *J. Phys. Chem.* 105B (2001) 8036.
- [29] K. L. Litvinenko, N. M. Webber, and S. R. Meech, *Chem. Phys. Lett.* 346 (2001) 47.
- [30] W. Weber, V. Helms, J. A. McCammon, and P. W. Langhoff, *Proc. Natl. Acad. Sci.* 96 (1999) 6177.
- [31] D. R. Yarkony, *Rev. Mod. Phys.* 68 (1996) 985.
- [32] M. Garavelli, F. Bernardi, M. Olivucci, T. Vreven, S. Klein, P. Celani, and M. A. Robb, *Faraday Disc.* 110 (1998).
- [33] M. Klessinger and J. Michl, *Excited States and Photochemistry of Organic Molecules* (VCH Publishers, New York, 1995).

- [34] G. S. Harbison, S. O. Smith, J. A. Pardo, C. Winkel, J. Lugtenburg, J. Herzfeld, R. Mathies, and R. G. Griffin, *Proc. Natl. Acad. Sci.* 81 (1984) 1706.
- [35] G. C. Schatz, *Rev. Mod. Phys.* 61 (1989) 669.
- [36] C. Leforestier, *J. Chem. Phys.* 68 (1978) 4406.
- [37] M. Parrinello, *Solid State Comm.* 102 (1997) 107.
- [38] M. E. Tuckerman, P. J. Ungar, T. Vonrosenvinge, and M. L. Klein, *J. Phys. Chem.* 100 (1996) 12878.
- [39] B. Hartke and E. A. Carter, *Chem. Phys. Lett.* 189 (1992) 358.
- [40] M. Ben-Nun and T. J. Martínez, *Adv. Chem. Phys.* 121 (2002) 439.
- [41] M. Ben-Nun and T. J. Martínez, *J. Chem. Phys.* 108 (1998) 7244.
- [42] E. J. Heller, *J. Chem. Phys.* 75 (1981) 2923.
- [43] C. Ko, B. Levine, A. Toniolo, L. Manohar, S. Olsen, H.-J. Werner, and T. J. Martínez, *J. Am. Chem. Soc.* 125 (2003) 12710.
- [44] T. J. Martínez, *Chem. Phys. Lett.* 272 (1997) 139.
- [45] K. Thompson and T. J. Martínez, *J. Chem. Phys.* 110 (1999) 1376.
- [46] T. Schultz, J. Quenneville, B. Levine, A. Toniolo, T. J. Martínez, S. Lochbrunner, M. Schmitt, J. P. Shaffer, M. Z. Zgierski, and A. Stolow, *J. Am. Chem. Soc.* 125 (2003) 8098.
- [47] M. Ben-Nun and T. J. Martínez, *J. Phys. Chem.* 103A (1999) 10517.
- [48] M. Ben-Nun and T. J. Martínez, *J. Am. Chem. Soc.* 122 (2000) 6299.
- [49] T. J. Martínez and R. D. Levine, *J. Chem. Phys.* 105 (1996) 6334.
- [50] T. J. Martínez and R. D. Levine, *Chem. Phys. Lett.* 259 (1996) 252.
- [51] I. Frank, J. Hutter, D. Marx, and M. Parrinello, *J. Chem. Phys.* 108 (1998) 4060.
- [52] D. Marx and N. L. Doltsinis, *Phys. Rev. Lett.* 88 (2002) 166402.
- [53] A. Toniolo, G. Granucci, and T. J. Martínez, *J. Phys. Chem.* 107A (2003) 3822.
- [54] A. Warshel and M. Levitt, *J. Mol. Bio.* 103 (1976) 227.
- [55] J. Gao, *Acc. Chem. Res.* 29 (1996) 298.
- [56] M. J. Field, P. A. Bash, and M. Karplus, *J. Comp. Chem.* 11 (1990) 700.
- [57] A. Toniolo, M. Ben-Nun, and T. J. Martínez, *J. Phys. Chem.* 106A (2002) 4679.
- [58] I. Rossi and D. G. Truhlar, *Chem. Phys. Lett.* 233 (1995) 231.
- [59] H.-J. Werner, P. J. Knowles, R. D. Amos, A. Bernhardsson, A. Berning, P. Celani, D. L. Cooper, M. J. O. Deegan, A. J. Dobbyn, F. Eckert, C. Hampel, G. Hetzer, T. Korona, R. Lindh, A. W. Lloyd, S. J. McNicholas, F. R. Manby, W. Meyer, M. E. Mura, A. Nicklass, P. Palmieri, R. Pitzer, G. Rauhut, M. Schütz, H. Stoll, A. J. Stone, R. Tarroni, and T. Thorsteinsson, (2000).
- [60] W. J. Hehre, R. Ditchfield, and J. A. Pople, *J. Chem. Phys.* 56 (1972) 2257.
- [61] J. J. P. Stewart, (Fujitsu Limited, Tokyo, Japan, 1999).
- [62] G. Granucci and A. Toniolo, *Chem. Phys. Lett.* 325 (2000) 79.
- [63] L. X. Dang and B. M. Pettitt, *J. Phys. Chem.* 91 (1987) 3349.
- [64] K. K. Docken and J. Hinze, *J. Chem. Phys.* 57 (1972) 4928.
- [65] P. J. Knowles and H. J. Werner, *Chem. Phys. Lett.* 115 (1985) 259.
- [66] B. O. Roos, in *Advances in Chemical Physics: Ab Initio Methods in Quantum Chemistry II*, edited by K. P. Lawley (John Wiley and Sons Ltd., 1987), pp. 399.
- [67] J. F. Stanton and R. J. Bartlett, *J. Chem. Phys.* 98 (1993) 7029.
- [68] W. H. Press, S. A. Teukolsky, W. T. Vetterling, and B. P. Flannery, *Numerical Recipes in FORTRAN* (Cambridge Press, Cambridge, 1992).

Ultrafast dynamics in the excited state of wild-type Green Fluorescent Protein

K. Winkler^a, J. Lindner^a, M. Seidel^a, and P. Vöhringer^{a,b}

^aMax-Planck-Institut für biophysikalische Chemie, AG Biomolekulare und Chemische Dynamik, Am Fassberg 11, 37077 Göttingen, Germany

^bUniversité Louis Pasteur, Faculté de Chimie, 6 rue Blaise Pascal, 67000 Strasbourg, France

1. INTRODUCTION

The primary events which give rise to luminescence from protein environments have recently raised considerable attention [1, 2]. An elucidation of the underlying photophysical and photochemical elementary processes including their time scales will help establish fundamental principles involved in photon emission from protein structures. Such information is highly valuable in tailoring optical bio-fluorophores with spectrochemical properties that are optimally adapted for applications such as protein/membrane/DNA interactions, gene expression, or non-invasive protein localization. The photoactive protein, green fluorescent protein (GFP), from the pacific jellyfish *Aequoria Victoria* is prototypical for bioluminescence from β -barrel tertiary structures. This structural motif serves to effectively protect the chromophore (p-hydroxybenzylidene-imidazolidinone) from the aqueous surroundings and hence, to prevent solvent-assisted quenching after photo-excitation. Furthermore, the β -barrel interior provides an extended network of hydrogen-bonds in which the chromophore is embedded and which proves to be essential for a primary excited state proton transfer (ESPT) followed by the characteristic green emission. Temperature-dependent dynamic fluorescence spectroscopy have led to a Förster-type kinetic model in which both the ground and excited electronic states of the GFP chromophore are characterized by two distinct conformations, A and B corresponding to absorptive resonances centered around 400 nm and 477 nm, which can interconvert by means of proton transfer [1-3]. In the excited state, proton transfer from A^* occurs on a time scale of several picoseconds via barrier crossing to an intermediate, I^* , which is responsible for the characteristic green emission. Presumably, I^* constitutes an environmentally unrelaxed configuration of the proton-transferred form, B^* , of the excited state. Here, we present complementary femtosecond time- and frequency-resolved pump-probe, fluorescence upconversion (FIUp) and time correlated single photon counting (TCSPC) experiments to quantify the elementary dynamics accompanying ESPT in wt-GFP.

2. EXPERIMENTAL

Wt-GFP was expressed in *E. coli* and purified as described in Ref. [4]. Time- and frequency resolved pump-probe transients were recorded with 40-fs, 400-nm excitation pulses and probe pulses with durations of approximately 40 fs throughout the visible spectral range. Since photo-conversion strongly alters the GFP response, rapid scan data acquisition was performed

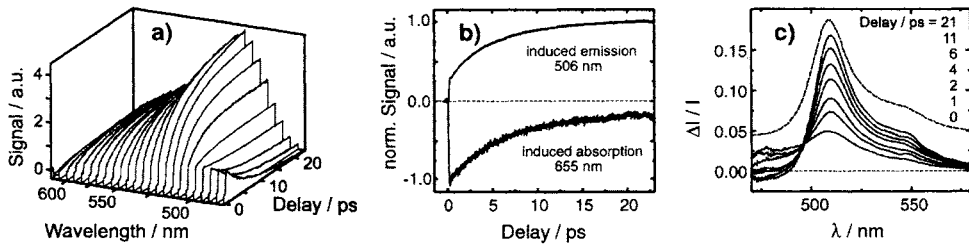


Fig. 1. a) Probe wavelength-dependent transients for GFP. b) Pump-probe transients emphasizing the matching behavior of induced emission and near-infrared induced absorption. (c). Comparison of DTS (solid) and stationary emission (dashed).

with pulse energies of less than 1 nJ while spinning the sample at 5000 rpm. FIUp experiments were carried out with 170-fs, 388-nm excitation pulses using a 1 mm type-I BBO crystal for mixing the spontaneous fluorescence with 775-nm gate pulses. The time resolution of this setup was roughly 300 fs. TCSPC was performed with a frequency-doubled mode-locked Ti-Sapphire oscillator as an excitation source at 400 nm. Its repetition rate was reduced by a pulse picker to 2 MHz. The TCSPC electronics allowed for a time resolution of 220 ps.

3. RESULTS

3.1. Time and frequency-resolved pump-probe

Femtosecond pump-probe transients are shown in Fig. 1a using detection wavelengths covering the stationary fluorescence spectrum of GFP. In this spectral range, a strong stimulated emission rises in a highly non-exponential fashion on time scales of about 20 ps. Furthermore, a fraction of the emission appears within the time resolution of our experiment, hence, this emission is termed “prompt”. For wavelengths longer than 630 nm, a pronounced transient absorption decays on similar time scales of roughly 20 ps (see Fig. 1b).

Transient differential transmission spectra (DTS) at various time delays are depicted in Fig. 1c together with the stationary fluorescence spectrum of GFP. The following features are worth highlighting: (i) at the shortest delays, the stimulated fluorescence is spectrally much broader than the stationary emission however, a shoulder reminiscent of the vibrational substructure of GFP is already discernible. (ii) After about 7 ps, the DTS and the stationary spectrum are indistinguishable for wavelengths longer than the emission maximum. (iii) For delays larger than 1 ps, an isosbestic point clearly exists at a wavelength of 496 nm. (iv) A residual long-time transient absorption is observed for wavelengths shorter than 480 nm.

3.1. Fluorescence upconversion and time correlated single photon counting

The pure emission dynamics uncontaminated by transient absorptions was measured by FIUp. Representative signals are shown in Fig. 2a with detection at 450 nm and 530 nm. It can be seen that the fluorescence decay in the ultraviolet is a mirror image of the fluorescence rise observed in the green spectral region. Both rise and decay occur multi-exponentially on a time scale consistent with the pump-probe results. Again, some “prompt” emission is visible even when spontaneous fluorescence is detected. The transient anisotropy (Fig. 2b) that was derived from fluorescence signals recorded parallel and perpendicular with respect to the polarization of the excitation pulse is essentially constant below 100 ps indicating that the spatial orientation of the optical chromophore does not change at all during this time period.

TCSPC data emphasizing the fluorescence decay on nanosecond time scales are shown in

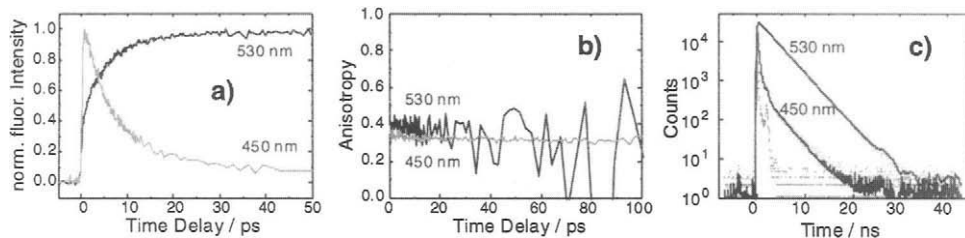


Fig. 2. a) FIUp transients for GFP detected at 530 and 450 nm. b) Transient anisotropy of the GFP fluorescence traces shown in a). (c) TCSPC signal for GFP detected at 530 and 450 nm.

Fig. 2c. It can be seen that at 530 nm, the fluorescence decays mono-exponentially with the fluorescence lifetime of 3.24 ns. The rise of the emission seen below 50 ps in the corresponding FIUp data is obviously not resolved here. In contrast, the TCSPC data at 450 nm is described by a triple-exponential decay whose dominant component has a correlation time well below the time resolution. This component is obviously equivalent to the fluorescence decay observed in the FIUp experiment. A minor contribution has a correlation time of about 3.2 ns and reflects again the fluorescence lifetime that was also detected at 530 nm. The most characteristic component at 450 nm however has a time constant of about 300 ps. It is important to emphasize that this 300 ps decay does not have a rising counterpart when emission near the maximum of the stationary fluorescence spectrum is recorded. In other words, the above mentioned mirror image correspondence of the fluorescence dynamics between 450 nm and 530 nm holds only on time scales shorter than 20 ps. Finally, in contrast to picosecond time scales, the anisotropy deduced from the TCSPC data displays a pronounced decay. This decay is reminiscent of the rotational diffusion of the entire protein indicating that the optical chromophore is rigidly embedded in the core of the β -barrel protein.

4. DISCUSSION

The results are discussed in terms of ESPT. The protonated form, A^* , of the chromophore in the excited state is prepared at time $t=0$ by the near-UV pump pulse. As suggested previously, green emission originates from an excited-state intermediate, I^* , which corresponds to the deprotonated chromophore in an unrelaxed environment. Obviously, the build-up of the induced green emission reflects the ESPT kinetics under I^* formation. The transient absorption for $\lambda \leq 480$ nm is also due to I^* since it is observed for long delays. Accordingly, the short-lived transient absorption observed at $\lambda \leq 630$ nm must be assigned to A^* . Besides by ESPT, I^* is also accessed directly by the near-UV pump pulse since the red edge of the prompt emission coincides with the linear emission spectrum (see Fig. 1c). We have previously called this direct excitation of the deprotonated intermediate “cross-well”-excitation since the pump pulse is likely to prepare delocalized states of the chromophore, which lie above the barrier to ESPT. The isosbestic point seen after ca. 1 ps separates emission dominated either by A^* or I^* and implies a small barrier for ESPT which is larger than thermal excitations. However, such a simple 2-state interconversion is inconsistent with multi-exponential kinetics even if a heterogeneous ensemble of chromophore environments is invoked. Therefore, we proposed a refined photodynamical model for GFP (Fig. 3a) which takes into account that the 400-nm pulse prepares A^* with 2000 cm^{-1} of excess energy as judged from the 0-0-transition seen by hole-burning studies [3]. Therefore, A^* must be energetically grained to capture the intrinsic

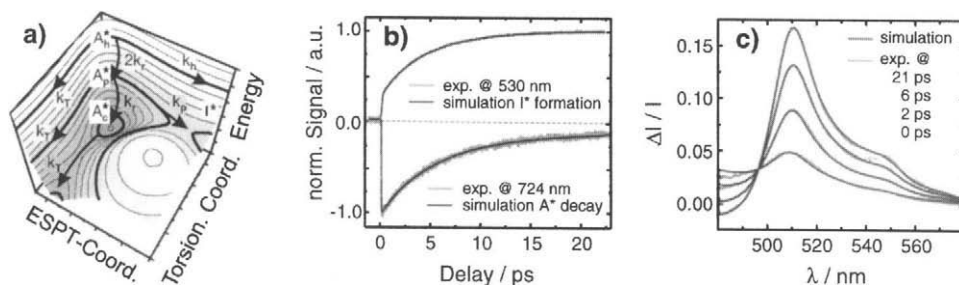


Fig. 3. Refined dynamical model for GFP (a) and comparison with pump-probe (b) and DTS data (c).

energy dependence of the unimolecular barrier crossing event leading to proton transfer. For simplicity, only vibrationally hot (index h), partially relaxed (p) and vibrationally cold (c) species of A^* are defined, each of which can undergo ESPT with an energy-specific rate constant, k_h , k_p , or k_c . Vibrational energy relaxation (VER) is described in the harmonic approximation and is characterized by k_r . Furthermore, measurements of the fluorescence quantum yield, Φ , give evidence for another decay channel of A^* leading to internal conversion via chromophore torsion [2]. The model includes this pathway by the rate coefficient, k_T , which for simplicity is taken to be energy-independent. The precise value of k_T is obtained directly from the TCSPC data in the spectral region where only A^* can emit, i.e. $\lambda = 450$ nm. As discussed above, a characteristic decay with a time constant of 300 ps was found here. Since this decay channel is not related to proton motion a corresponding 300 ps rise should not be identified when green emission is detected. An analysis of the data shown in Fig. 2c confirms indeed this conjecture. The model further implies that the ESPT channel is closed once A^* is vibrationally cold, i.e. $k_c \rightarrow 0$. Analytic expressions for the time-dependent populations as well as for Φ are readily derived and were reported in Ref. [4]. The model can quantitatively reproduce the pump-probe transients, the time-dependent DTS, and the TCSPC data simultaneously with only three fit parameters, namely k_h , k_p , and k_r . Model simulation for the decay of A^* (probed at 724 nm), for the build-up of I^* (530 nm), and for various DTS are shown in Fig. 3b and c. For the rate constants, k_h and k_p , we find values of $(6.5 \text{ ps})^{-1}$ and $(13 \text{ ps})^{-1}$ whereas the rate constant for vibrational relaxation was $(23 \text{ ps})^{-1}$. Furthermore, a value for Φ of 11% is obtained in excellent agreement with the value from Ref. [2].

In conclusion, we were able to reproduce the optical response of GFP with a novel photodynamical model which includes VER, an energy-dependent ESPT, and an additional decay pathway leading to internal conversion of the protonated chromophore. In particular, the non-exponentiality of the kinetics is traced back to VER dynamics which are slower than the primary ESPT. This might be attributed to the highly rigid tertiary structure of the protein which protects its chromophore from inelastic collisions with the aqueous surroundings.

REFERENCES

- [1] M. Chattoraj, B.A. King, G.U. Bublitz, and S.G. Boxer, Proc. Nat. Acad. Sci. 93 (1996) 8362.
- [2] A.D. Kummer, C. Kompa, H. Lossau et. al. Chem. Phys. 237 (1998) 183.
- [3] T.M.H. Creemers, A.J. Lock, V. Subramaniam, T.M. Jovin, and S. Völker, Nature Struct. Biol. 6 (1999) 557.
- [4] K. Winkler, J. Lindner, V. Subramaniam, T.M. Jovin, and P. Vöhringer, Phys. Chem. Chem. Phys. 4 (2002) 1072.

Excited-state dynamics in the Green Fluorescent Proteins: the cases of wild type, uv-mutant, and isolated synthetic analogues of the GFP chromophore.

P. Didier^a, L. Guidoni^a, G. Schwalbach^b, A. Follenius-Wund^c, C. Pigault^c, M. Bourotte^d and J.-Y. Bigot^a.

^aInstitut de Physique et Chimie des Matériaux de Strasbourg, 23, rue du Loess F-67037 Strasbourg, France.

^bEcole Supérieure de Biotechnologie de Strasbourg, Boulevard Sébastien Brant F-67400 Strasbourg, France.

^cLaboratoire de Pharmacologie et Physico-chimie 74, route du Rhin 67400 Illkirch, France.

^dLaboratoire de Pharmacochimie 74, route du Rhin 67400 Illkirch, France.

1. INTRODUCTION

The Green Fluorescent Protein (GFP) is one of the most popular markers for *in vivo* labeling and single protein detection [1]. In the present work, we have investigated the ultra fast excited-state dynamics of the uv mutant (GFPuv) [2] and compared it to the results previously obtained with the wild type protein (GFPwt). In particular, we address the question of the characteristic time that has to be associated to the excited-state proton transfer (ESPT) responsible for the bright green emission of the GFP [3,4]. Spectrally resolved pump-probe spectroscopy allowed us to obtain information about the ESPT dynamics and induced absorption dynamics of this mutant. GFPwt and GFPuv share the same chromophore but our results show that their excited-state dynamics are very different. In particular the intrinsic homogeneity of GFPuv allowed us to identify two spectral signatures associated to the neutral and anionic forms and to measure the characteristic time of the ESPT. Additional information about GFP emission dynamics can be obtained by the study of isolated GFP chromophore [5]. We studied a modified GFP chromophore, named I-28 (Fig. 3), that behaves as a spectral analog of GFP. The excited-state dynamics of this isolated chromophore hugely differs from that observed in GFP. This observation confirms that the peculiar emission dynamics of GFP is the consequence of the interaction between the chromophore and the proteic cage.

2. EXPERIMENTAL TECHNIQUES

Expression of the fusion proteins was obtained by transforming *E. Coli* AD494 cells with the appropriate constructs. Cells transformed with constructs bearing the arabinose-sensitive elements (pBAD series) were grown at 37°C until an OD_{600 nm} of 0.8 was reached and incubated for 3 h at 30°C after addition of 0.2 % arabinose. Crude cytoplasmic extracts were obtained by resuspending the induced cells in 25 mM Tris-HCl, pH 8.0, 150 mM NaCl, 1 mM EDTA (1/20 of the original volume) supplemented with protease inhibitors and lysed by

sonication. The cytoplasmic extract was clarified by centrifugation at 22,000 *g* and stored at -20°C until use.

The synthetic GFP chromophore analogue (2-(4-nitrophenyl)-5-(4-cyanophenyl methylidene) imidazol-4-one), was synthesized according to ref [6]. It was recrystallized from ethanol and characterized by $^1\text{H-NMR}$ through their typical proton signal at 7.1 ± 2 ppm. High concentrated solutions of approximately 3.10^{-5}M were prepared by dissolution in dioxan. The photophysical characteristics of this analogue were determined from the UV absorption spectra and from steady-state fluorescence. An extinction coefficient of $20700\text{M}^{-1}\text{cm}^{-1}$ was determined at the maximum absorption wavelength at 406 nm. The fluorescence emission peaks at 508 nm.

In the femtosecond setup, ultrafast pulses delivered by a Ti:sapphire laser seed a regenerative amplifier that delivers 150 fs pulses at 800 nm with a repetition rate of 5 kHz. The beam is split in two parts. The major part of the energy is used to generate 400 nm, 200 fs pulses (maximum energy per pulse $30\ \mu\text{J}$) by second harmonic generation in a 2 mm thick BBO crystal. The remnant part of the energy ($1\ \mu\text{J}$) is focused on a (0001) oriented and 2mm thick sapphire crystal to generate a super-continuum which spectrum extends from 450 nm to 700 nm. The group velocity dispersion of this white light pulse is reduced by a double pass grating and prism compressor (100 fs in the 450-600 nm spectral range). The white probe and the blue pump are both focused by a 70 mm focal achromat length on a $700\ \mu\text{m}$ thick spinning cell containing the sample. The diameter of the cell (40 mm) and its rotation rate (50 Hz) are chosen in order to excite a "fresh" volume of the sample with each laser pulse. We measured the time resolved differential transmission $\Delta T/T(\tau, \lambda)$ of the probe as a function of the pump-probe delay τ and the wavelength λ , in a standard pump-probe configuration. Great care has been taken to eliminate the isotropic contribution due to the spontaneous emission of the sample. Differential transmission spectra are obtained by dispersing the transmitted probe beam through a spectrometer (resolution of 1.2 nm) and recording the spectral intensity on a Peltier cooled photodiode array. Alternatively, temporal differential transmission slices can be obtained by spectral selection (FWHM of 15 nm) on the probe beam. In this case, the transmitted probe intensity is measured with a silicon photodiode using a lock-in detection scheme.

3. RESULTS

We measured the differential transmission of a probe linearly polarized at the magic angle (54.7°) with respect to the linear pump polarization. Such measurements have been obtained for different pump intensities (10-80 nJ), for different pH (5-12) and for different concentrations of GFPuv. It is important to stress that the qualitative dynamical behavior does not depend on these parameters. In Fig. 1a we show some typical differential transmission spectra obtained at different pump-probe delays. The main feature is the spectral shape associated to the green emission (peak at 508 nm). We can also distinguish another spectral signature centered at 480 nm that spectrally overlaps the wing of the green emission. If we attribute these two forms to two excited-state populations of the unrelaxed anionic and neutral forms (see scheme level in fig. 2b), the observed dynamics can be explained by an ESPT involving only these two forms (isosbestic point at $\lambda=496$ nm). Another piece of information is the very weak (-2.10^{-3} at the peak for conditions of figure 1a) transient absorption centered at 650 nm that appears immediately after photo-excitation. This residual transient absorption can be attributed to the excited-state of the anionic form of the chromophore. If we take a

cross section centered at 508 nm (fig. 1b), we can extract a unique characteristic time of 1.7 ps for the excited-state proton transfer.

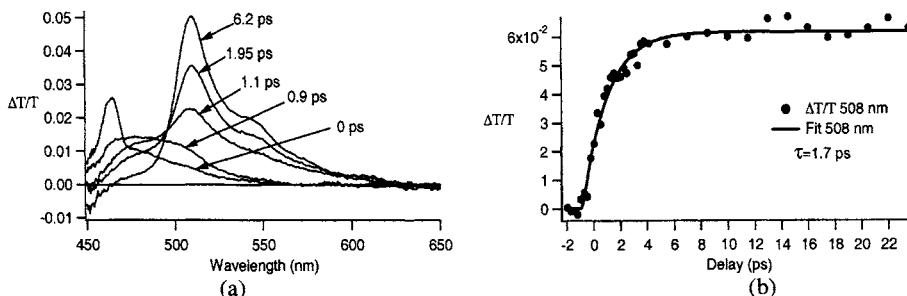


Fig. 1: (a) Differential transmission spectrum, at magic angle, of a GFPuv sample in aqueous solution (540 $\mu\text{g/ml}$, pH 6.5). (b) Cross section centered at 508 nm (FWHM of 15 nm). Data are obtained with 400 nm; pump (fluence=2 mJ/cm^2 ; duration 200 fs).

Let us now compare the emission dynamics of GFPwt and GFPuv. If we consider first the linear absorption spectra (fig. 2a), in aqueous solution of GFPwt, two sub-populations are present: the first has the chromophore in its neutral form and the second has the chromophore in its anionic form [3]. These two forms are spectrally characterized by distinct absorption bands centered at 398 nm for the neutral form (noted A in Fig. 2b) and at 477 nm for the anionic form (noted B in Fig. 2b). If the neutral form is excited at 400 nm, the chromophore undergoes an excited-state proton transfer that brings it in the excited-state of an unrelaxed anionic form (noted I* in Fig. 2b) responsible for the strong green emission [3,4]. At room temperature and for a neutral pH, the ratio between the neutral and anionic species is 6/1 for GFPwt [3]. In the case of GFPuv these two bands are still present but we measure a ratio of 20/1. We therefore interpret the *prompt* (i.e. with a rise-time shorter than temporal resolution) gain (508 nm) and induced absorption (650 nm), observed in GFPwt as a consequence of a direct excitation of the relaxed anionic form. Such an interpretation is corroborated by the fact that if we rescale the prompt and “slow” dynamical contributions in GFPwt [7] taking into account the modified ratio of the GFPuv absorption spectrum, we expect indeed a negligible prompt contribution.

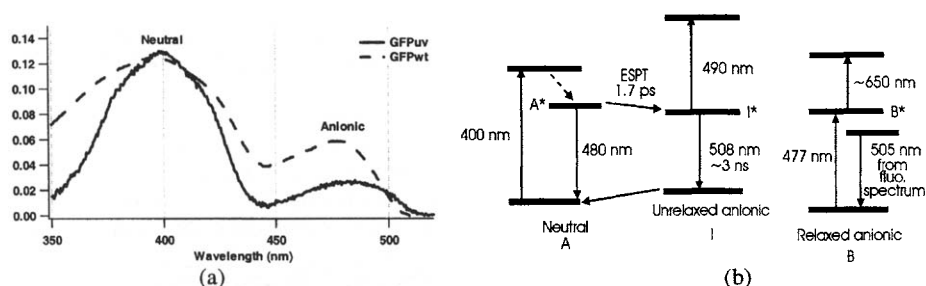


Fig. 2: (a) Linear absorption spectrum obtained on a 540 $\mu\text{g/ml}$ of GFPuv solution in a 1 mm thick cuvette (solid line) compared to that of GFPwt (dotted line) (data of ref [3]). (b) Multi-level schematic representation of the GFP emission mechanism [3].

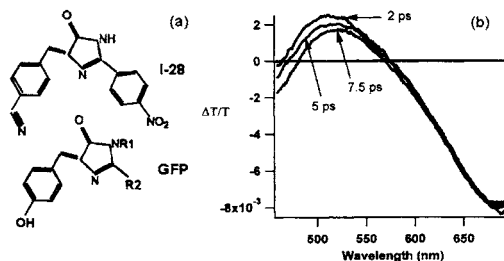


Fig. 3. (a) chemical structure of the synthetic chromophore compound I-28 compared to that of the protein (R1 and R2 correspond to amino-acids which link the chromophore to the rest of the protein). (b) Differential transmission spectrum, at magic angle and for different pump-probe delays, of I-28 in dioxan solution ($6 \mu\text{g/ml}$) excited in the conditions described in the caption of fig. 1.

An additional piece of information can be obtained by studying a synthetic compound derived from the GFP chromophore (I-28) fluorescing at room temperature. In Fig. 3a we show the chemical structure of the compound that we studied in dioxan solution by pump-probe spectroscopy. If we look at the differential transmission spectra displayed in Fig. 3b, we observed two important features: a stimulated emission centered at 508 nm and a huge and broad induced absorption band (580-700 nm). Both contributions appear within our temporal resolution and display a linear behavior as a function of the pump intensity in the low fluences limit ($\leq 1 \text{ mJ/cm}^2$). We note that the stimulated emission red shifts with two characteristic time-scales (500 fs and 10 ps) as expected in the case of solvation dynamics. We conclude that in the absence of ESPT this chromophore has the same qualitative dynamical behavior that we attribute to the relaxed anionic form.

4. CONCLUSION

In this work we have compared the excited-state dynamics (investigated by pump-probe spectroscopy) of the GFPuv protein and a synthetic analogue of the GFP chromophore to the previously reported dynamics of the GFPwt. The most striking features observed in GFPuv are the absence of *prompt components* and the mono-exponential character associated to the 508 nm gain-band rise-time. Such features are well explained by a simple model involving the neutral and unrelaxed anionic form with an ESPT rate of 1.7 ps. The difference with respect to GFPwt is attributed to the reduced contribution originating from the direct excitation of the relaxed anionic form. Finally, the study of a synthetic analogue of the chromophore confirms the importance of the interaction between the proteic cage and the chromophore in the dynamical behavior of GFP.

REFERENCES

- [1] R.Y. Tsien, Annual Reviews Biochemistry, 67 (1998) 509.
- [2] A. Cramer, E. A. Whitehorn, E. Tate and W. P. C. Stemmer, Nat. Biotechnol., 14 (1995) 315
- [3] M. Chattoraj, B. A. King, G. U. Bublitz and S. G. Boxer, Proc. Natl. Acad. Sci. U. S. A., 93 (1996) 8362.
- [4] H. Lossau, A. Kummer, R. Heinecke, F. Pöllinger-Dammer, C. Kompa, G. Bieser, T. Jonsson, M.M. Yang, D. C. Youvan and M. E. Michel-Beyerle, Chem. Phys., 213 (1996) 1.
- [5] A. A. Voityuk, M. E. Michel-Beyerle and N. Rösch, Chem. Phys. Lett. 296 (1998) 296.
- [6] P. M. Shapi, Current Science, 54 (1985) 1231.
- [7] K. Winkler, J. Lindner, V. Subramaniam, T. M. Jovin and P. Vöhringer, Phys. Chem. Chem. Phys., 4 (2002) 1072.

Fast excited-state reaction in the photoreceptor pigment-protein complex of the ciliate *Blepharisma japonicum*

M. Mahet^a, P. Plaza^a, M.M. Martin^a, G. Checcucci^b and F. Lenci^b

^a Département de Chimie, UMR CNRS-ENS 8640, Ecole Normale Supérieure, 24 rue Lhomond, 75231 Paris Cedex 05, France

^b Istituto di Biofisica CNR, Via G. Moruzzi 1, 56100 Pisa, Italy

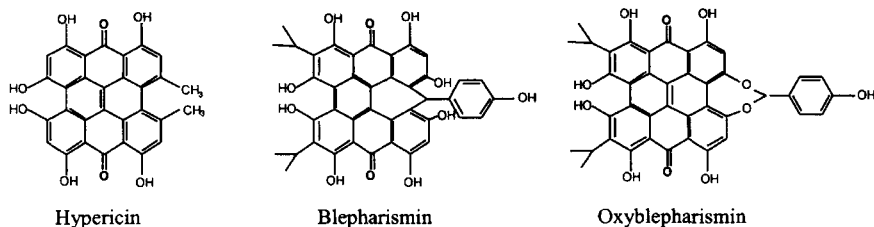
ABSTRACT

The primary phototransduction steps of the protozoan *Blepharisma japonicum*'s light perception were studied by subpicosecond transient absorption spectroscopy. The free chromophore of the light-adapted cell, oxyblepharismine, was characterized in solution and compared to the pigment-protein complex. Although showing similar steady-state and transient spectra, oxyblepharismine and its protein complex display noticeably different excited-state dynamics. In the chromoprotein, a pronounced fast biexponential decay (5 ps and 60 ps) is observed, which is not found in the corresponding kinetics of the isolated pigment. This early behavior could be the signature of a specific primary phototransduction process.

1. INTRODUCTION

Some non-photosynthetic colored unicellular eukaryotic organisms, such as the ciliate *Blepharisma japonicum*, are extremely sensitive to visible and UV radiation. Crossing a dark-light border and entering the lighted region, the cell stops, tumbles a while, then swims backwards, toward darker regions [1]. This step-up photophobic response is photoinitiated by molecular events in a photoreceptor system, made of a chromophore and a macromolecular assembly attached to it. At present, among the deeply studied and characterized photoreceptors involved in the photobehavior of microorganisms, are rhodopsins, flavins, pterins and paracoumaric acid. In the case of *Blepharisma japonicum*, a very different and unique pigment was identified and isolated: blepharismine [2]. Like its close parent, hypericin, this molecule can produce singlet oxygen from its triplet state with a good yield [3], which makes it an efficient photoactivated cellular poison. It has been suggested that this pigment is used as a defense against predators and that the photosensory response allows the cell not to die from its own defense strategy, escaping from light [4].

Our work aims at identifying, by subpicosecond broadband transient absorption and gain spectroscopy, the primary photochemical steps of the phototransduction process in *Blepharisma japonicum*, more specifically in the light-adapted form of the organism (blue cell) for which the photoactive pigment is oxyblepharismine [5] (see Scheme 1) and the associated macromolecule is a large non-soluble protein (200 kDa) [6].



Scheme 1. Structures of hypericin, blepharismine and oxyblepharismine

2. EXPERIMENTAL

2.1 Isolation of oxyblepharismine and of the chromoprotein

Red-cell (dark adapted) *Blepharisma japonicum* were cultured in Pisa, in the dark, at 23°C, in the presence of the *Enterobacter aerogenes* bacterium as food supply [7]. Blue-cell (light adapted) *Blepharisma japonicum* were produced by *in vivo* photoconversion of blepharismine into oxyblepharismine under a low intensity cold white lamp (below 10 W/m²). Blue cells were washed, collected by low speed centrifugation and resuspended in a 20-mM sodium cholate solution. The chromoprotein was obtained by FPLC chromatography of this preparation, on a hydroxyapatite column. The applied eluent was a phosphate buffer (pH 7.4), first 0.05 M and then 0.2 M. This ionic strength step affects the affinity of the biomolecules with the hydroxyapatite [8].

The free chromophore was extracted in acetone from dark adapted cells, dried and photooxidized *in vitro* by irradiation for a few hours with a dim light (below 10 W/m²). Finally the sample was purified by HPLC. No attempt was done to separate the five closely related forms of the molecule, that share the same π -electron system [9].

2.2 Ultrafast transient absorption spectroscopy

Transient absorption experiments were performed by the pump-probe, with continuum, technique using a subpicosecond laser as the source. The laser is a homemade dye laser driven by a seeded 10-Hz Q-switched Nd:YAG laser. It delivers two intense synchronous 600-fs beams at different wavelengths. One is used as the pump at around 600 nm and the other, at 568 nm, generates a white-light continuum used as the probe. Pump and probe beams cross on the sample, held in a 1-mm cuvette, at an angle of $\sim 10^\circ$ and their polarizations are set at the magic angle. Photolysis was avoided by continuously moving the sample cuvette up and down. Spectra formed by an imaging spectrograph were recorded on a CCD camera and accumulated over 500 pump shots. The time-resolved differential absorbance spectra were corrected from group velocity dispersion of the probe beam. The experimental error is better than ± 2 mOD (rms) and the time resolution of the experiments is found to be around 1.5 ps.

3. RESULTS

3.1 Transient absorption spectroscopy of the free and bound chromophores

Fig. 1-left gives a general overview of the differential absorption spectra recorded for the free chromophore, oxyblepharismine, dissolved in DMSO; for reference the steady-state absorption and (uncorrected) fluorescence spectra are also given below, in dotted lines. At all pump-probe delay times, the overall picture is a superposition of the structured bleaching and gain bands, as expected from the steady-state spectra, and broad transient absorption bands around 530 nm and 750 nm (weaker). These apparently homothetic spectra are very similar to

those of the parent molecule, hypericin [10]. A closer inspection nevertheless reveals fine spectral evolutions, especially in the main bleaching/gain band (around 600 nm), better seen in a kinetic plot of the data (see §3.2).

The chromoprotein in a phosphate buffer displays similar time-resolved spectra (Fig. 1-right), with broader bleaching and gain main peaks and a clear secondary bleaching band around 450 nm. A marked non-homothetic shape evolution is observed in the 640-750 nm region. A broad absorption band is seen at short times whereas the long-time spectra reveal a residual gain band, similar to that observed for the free pigment. More details are presented in the following kinetic analysis section.

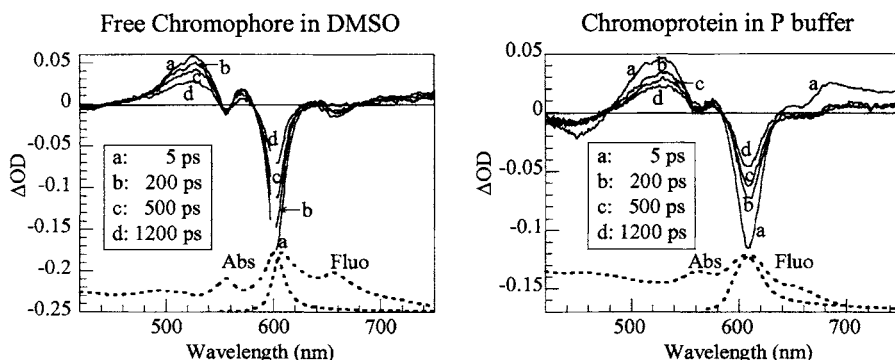


Fig. 1. Transient absorption spectra of the free and bound chromophores, at different pump-probe delays. Steady-state absorption and fluorescence spectra are presented in dotted lines

3.1 Kinetics analysis

After having checked that no time-resolved spectral shifts were present, a global kinetic analysis of the data was undertaken. The time traces at 14 selected wavelengths across the spectra (the far-red transient absorption band was not included at this stage, due to insufficient S/N ratio) were simultaneously fitted to a sum of exponentials, convoluted by a Gaussian representing the response function of the experiment. Fig. 2 shows four of those fits, for both the free and bound chromophores. In the case of oxyblepharismine in DMSO, the main feature is a 1.5-ns decay corresponding to the fluorescence lifetime. A small residual long-lived (step function) component is necessary to describe the data and is assigned to the triplet state formation. At short times, a small (less than 10% wt.) 13-ps decay is also observed. Although of different sign, this component might be compared to a 9.6-ps rise observed in the main stimulated emission band of hypericin in DMSO [10], which have been attributed by Petrich et al. to an intramolecular hydrogen atom transfer in the peri region.

The dynamic behavior of the chromoprotein is much more clearly multiexponential. Two pronounced decay components were identified with 5-ps (25 % wt.) and 60-ps (25% wt.) lifetimes. The strong weight of these exponentials is not in favor of a comparison to the weak 13-ps decay of the free pigment. It is more likely that they actually reveal a new and specific deactivation channel in the protein complex. It has, in fact, been speculated that light irradiation of the living organism induces an acidification of the intracellular medium [11], so proton transfer from the chromophore to the associated protein was first proposed as the initial phototransduction step. More recent experiments on the isolated pigment in the presence of electron acceptors [12] proved that the optical excitation can induce an electron transfer from the chromophore to an acceptor site possibly situated inside the associated

protein, a disulphide bridge for instance. Following this step, the pK_a of the chromophore would be strongly lowered and a proton could easily be released.

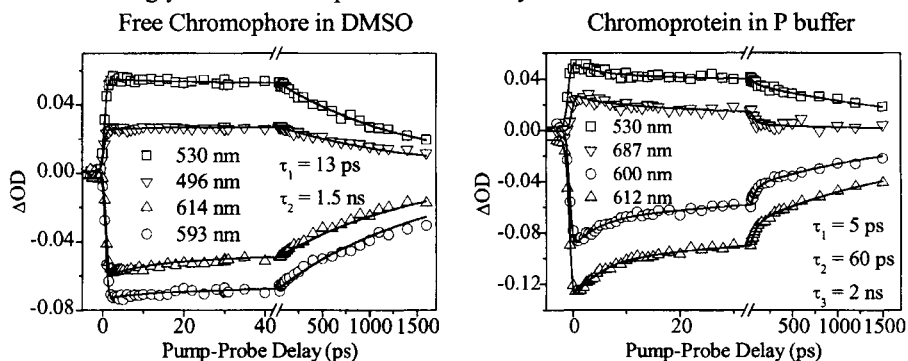


Fig. 2. Kinetics of the free and bound chromophores at selected homologous wavelengths

4. CONCLUSION

The excited-state kinetics of the chromoprotein were found to differ markedly from the one of the isolated chromophore in solution. A strong and fast biexponential decay is observed and seems to sign a specific deactivation channel, still to be properly identified. This process might well be an electron transfer from the chromophore to the protein, as earlier works had suggested [12]. It is additionally possible to suggest that the nonexponential nature of the fast decay could reveal a structural heterogeneity in the oxyblepharismine-protein complex.

REFERENCES

- [1] A.C. Giese, in: K.C. Smith (ed.), *Photochemistry and Photobiology Review*, Plenum, New York, 1981, pp. 139-180; P.-S. Song, *Biochim. Biophys. Acta*, 639 (1981) 1.
- [2] G. Checcucci, G. Damato, F. Ghetti and F. Lenci, *Photochem. Photobiol.*, 57 (1993) 686.
- [3] F. Ghetti, G. Checcucci, F. Lenci and P.F. Heelis, *J. Photochem. Photobiol. B*, 13 (1992) 315.
- [4] A. Miyake, T. Harumoto, B. Salvi and R. Rivola, *Eur. J. Protistol.*, 25 (1990) 310.
- [5] D. Spitzner, G. Höfle, I. Klein, S. Pohlen, D. Ammermann and L. Jaenicke, *Tetrahedron Lett.*, 39 (1998) 4003.
- [6] T. Matsuoka, Y. Murakami and Y. Kato, *Photochem. Photobiol.*, 57 (1993) 1042; T. Matsuoka, T. Tsuda, M. Ishida, Y. Kato, M. Takayanagi, T. Fujino and S. Mizuta, *Photochem. Photobiol.*, 60 (1994) 598.
- [7] D. Gioffré, F. Ghetti, F. Lenci, C. Paradiso, R. Dai and P.-S. Song, *Photochem. Photobiol.*, 58 (1993) 275.
- [8] G. Checcucci, Y. Takada and T. Matsuoka, *Mem. Fac. Sci. Kochi Univ. D*, 22 (2001) 39.
- [9] G. Checcucci, R.S. Shoemaker, E. Bini, R. Cerny, N. Tao, J.-S. Hyon, D. Gioffré, F. Ghetti, F. Lenci and P.-S. Song, *J. Am. Chem. Soc.*, 119 (1997) 5762.
- [10] F. Gai, M.J. Fehr and J.W. Petrich, *J. Phys. Chem.*, 98 (1994) 5784.
- [11] H. Fabczak, S. Fabczak, P.-S. Song, G. Checcucci, F. Ghetti and F. Lenci, *J. Photochem. Photobiol. B*, 21 (1993) 47.
- [12] N. Angelini, A. Quaranta, G. Checcucci, P.-S. Song and F. Lenci, *Photochem. Photobiol.*, 68 (1998) 864.

Excited state dynamics of the carotenoid peridinin

T. Polívka^a, D. Zigmantas^a, R. G. Hiller^b and V. Sundström^a

^aDepartment of Chemical Physics, Lund University, Box 124, S-221 00 Lund, Sweden,

^bDepartment of Biological Sciences, Macquarie University, Sydney; New South Wales 2109, Australia

1. INTRODUCTION

Carotenoids play a number of roles in living organisms. In addition to their well-known light-harvesting function in photosynthesis [1], they have also photoprotective and antioxidative functions in various physiological systems [2,3]. Due to symmetry reasons, a transition between the $1A_g^-$ state (ground state, S_0) and the $1B_u^+$ (S_2) state is allowed, while the $1A_g^- \rightarrow 2A_g^-$ ($S_0 \rightarrow S_1$) transition is forbidden for one-photon processes [4]. Studies of dynamics of carotenoid excited states have established the following scheme: after excitation of a carotenoid to its S_2 state ($1B_u^+$), a fast relaxation to the S_1 state ($2A_g^-$) occurs on a time scale of 50–300 fs [5]. The S_1 state relaxes to its ground state S_0 on the time scale of 1–300 ps [6]. Peridinin, depicted in Fig. 1, is a highly substituted carotenoid occurring in some dinoflagellates where it is the principle carotenoid of the water soluble light-harvesting peridinin-chlorophyll-protein (PCP), whose structure has been resolved to 2.0 Å [7]. The PCP complex exhibits an exceptional stoichiometry of 8 peridinin and 2 chlorophyll *a* (Chl-*a*) molecules. This, together with the unusual carotenoid structure, has initiated several studies focusing on spectroscopic properties of peridinin [8–14] that revealed unique photophysical properties of peridinin, which will be briefly reviewed in this account.

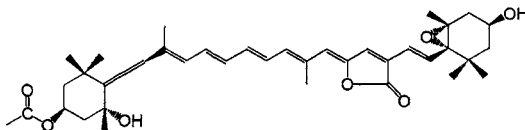


Fig. 1. Molecular structure of peridinin.

2. STEADY-STATE ABSORPTION SPECTRA

Absorption spectra of peridinin in different solvents are shown in Fig. 2a. In the nonpolar solvent *n*-hexane, the absorption spectrum exhibits the well-resolved structure of vibrational bands of the strongly allowed S_0 - S_2 transition with the 0-0 peak located at 485 nm. In polar solvents, however, the vibrational structure is lost and the absorption band is significantly wider. In addition, there are also differences between the various polar solvents. Although the loss of vibrational structure is obvious, a hint of shoulder is still preserved in methanol and acetonitrile, but in ethylene glycol and glycerol the absorption spectrum is completely structureless with a broad red tail extending beyond 600 nm.

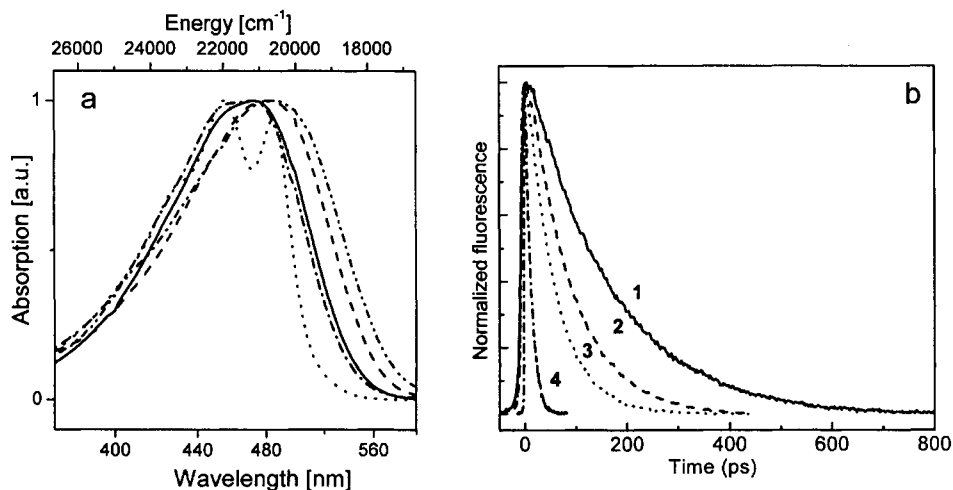


Fig. 2. (a) Absorption spectra of peridinin in *n*-hexane (dot), acetonitrile (dash-dot), methanol (solid), ethylene glycol (dash) and glycerol (dash-dot-dot). All spectra are normalized. (b) Kinetic traces of peridinin emission in different solvents measured at 730 nm. 1) *n*-hexane (156 ps), 2) tetrahydrofuran (77 ps), 3) 2-propanol (54 ps), 4) methanol (10.5 ps). All traces are normalized.

The origin of the spectral broadening of the peridinin absorption in polar solvents was explained by a polarity-induced change of the ground state structure of the peridinin molecule [10,12,14], since peridinin possesses a rather large ground-state dipole moment [10,14]. In polar aprotic solvents such as acetonitrile, the spectral broadening is caused by interaction of the peridinin molecule with the electric field of the solvent, leading to an absorption spectrum that is markedly broader than that in nonpolar solvent (Fig. 2). In protic solvents, such as methanol and ethylene glycol the dipolar character of the peridinin ground state is further enhanced by hydrogen bonding, producing the conformations with even more red-shifted absorption spectra [12].

3. TRANSIENT ABSORPTION SPECTRA

More pronounced polarity-induced changes were revealed in the transient absorption spectra of peridinin [9-12]. Transient absorption spectra of peridinin measured in different solvents are shown in Fig. 3. In the nonpolar solvent *n*-hexane, two ESA bands are observed in the transient absorption spectrum: a strong sharp band centered at ~ 510 nm and a weaker one located at ~ 650 nm. While the 510 nm band is a counterpart of the well-known S_1-S_n transition [10], the weak ESA band is clearly related to changes of excited state manifold due to the carbonyl group, because it is not observed for non-carbonyl carotenoids [10]. In polar solvents, the intensity of this band increases dramatically, and it becomes a dominating feature of the transient absorption spectrum peaking at 590 nm, while the S_1 -like band remains as a small shoulder located at 525 nm. In methanol and ethylene glycol the overall shape of the transient absorption spectra in the visible region is similar. However, ratio between the main polarity-induced band and the shoulder reflecting the S_1 -like ESA, is larger in ethylene glycol. Extending the transient absorption spectra towards the near-infrared spectral region as shown in Fig. 3b, reveals further differences between polar and nonpolar solvents. In the red-most part of the transient spectrum, the signal is dominated by the S_1-S_2

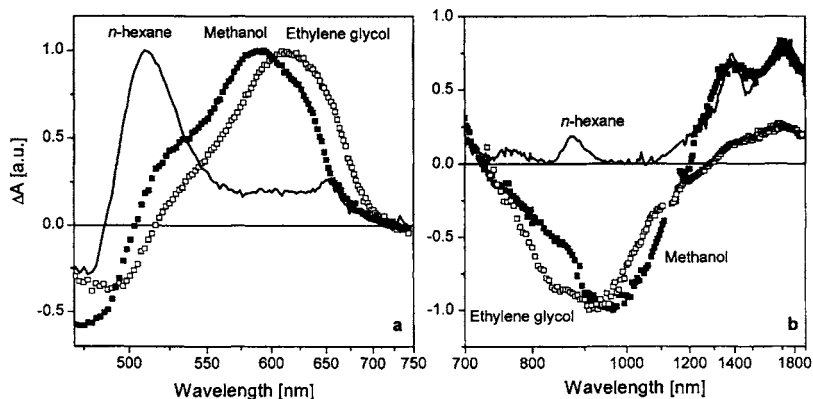


Fig. 3. Transient absorption spectra of peridinin in methanol recorded in the visible (a) and the near-infrared (b) spectral regions after excitation at 490 nm in methanol (full squares) and at 535 nm in ethylene glycol (open squares). The transient absorption spectra in the visible region are normalized to the ESA maximum, while the near-infrared spectra are normalized to a maximum of the ICT emission.

ESA, with two vibronic peaks located at $5870 \pm 100 \text{ cm}^{-1}$ and $7190 \pm 100 \text{ cm}^{-1}$ that are assigned to the 0–1 and 0–2 vibronic bands of the S_1 - S_2 transition [11]. Since knowledge of the S_1 - S_2 ESA profile allows determination of the S_1 energy [15], we can calculate the S_1 energy from the S_1 - S_2 transition by a simple subtraction $E(S_0 \rightarrow S_2) - E(S_1 \rightarrow S_2)$, yielding the energy of the S_1 state of peridinin in *n*-hexane of $16100 \pm 200 \text{ cm}^{-1}$ [11].

The most interesting part of the near-IR peridinin transient absorption spectrum is the spectral region between 720 – 1200 nm and its solvent dependence. In *n*-hexane, this region exhibits two weak ESA bands centered at 875 nm and 760 nm. In methanol, however, a broad structureless stimulated emission (SE) band centered at $\sim 950 \text{ nm}$ dominates this region. This SE band is assigned to stimulated emission from the S_1 state that has markedly different properties in polar solvents. Presence of the conjugated carbonyl group in the peridinin structure causes formation of an intramolecular charge transfer (ICT) state that is strongly coupled to the S_1 state, forming a mixed S_1 /ICT state. The charge transfer character of the S_1 /ICT state is markedly enhanced in polar solvents, resulting in changes in S_1 /ICT potential surface leading to the stimulated emission in the 750 – 1200 nm region [11]. Consequently, the shape of near-infrared transient absorption spectrum monitors the degree of charge transfer character of the S_1 /ICT state. While the signal above 1200 nm reflects the contribution of the S_1 -like character, the stimulated emission band at 950 nm marks the ICT-like character of the S_1 /ICT state. From the ratio of the magnitudes of SE and ESA bands for peridinin in three different solvents in Fig. 3, it is apparent that charge-transfer character is strongest in ethylene glycol, for which the 950 nm SE band is clearly the dominating feature of the spectrum [12].

4. THE S_1 /ICT STATE

Early work on peridinin demonstrated that its structure leads to breaking of the idealized C_{2h} symmetry resulting in relatively strong fluorescence from the S_1 state [16]. Recent studies demonstrated that the intensity of the peridinin S_1 emission depends on solvent polarity [8,9], and time-resolved studies revealed that the polarity-dependent change in the S_1 emission yield

is connected with a significant change in the lifetime of the peridinin lowest excited state [8-12].

4.1. Polarity-dependent S_1/ICT lifetime

The strong dependence of the S_1/ICT lifetime on solvent polarity revealed first by transient absorption experiments in the visible region by Bautista et al. [8] was further confirmed by measurement of S_1/ICT fluorescence using a streak-camera [11]. The S_1/ICT state fluorescence kinetics of peridinin taken at 730 nm in solvents of different polarity are shown in Fig. 2b. The lifetime changes more than one order of magnitude, from 156 ps in n-hexane to 10.5 ps in methanol. In the middle-polarity solvents tetrahydrofuran and 2-propanol, the observed lifetimes are 77 and 54 ps, respectively. In all solvents, kinetic traces could be fitted by a single exponential decay independent of detection wavelength over nearly the entire fluorescence band (650 – 850 nm). The same decay times were also observed in transient absorption [11,12].

4.2. Rise component in the near infrared region

In nonpolar solvents the kinetics exhibit monoexponential decay, but with increasing polarity the kinetics become more complex. This is apparent when inspecting kinetics recorded at the maximum of the SE band, where the traces contain an additional rise component. In Fig. 4, kinetics recorded at 950 nm for three solvents with different polarity are shown. All kinetics exhibit a pronounced rise component that is dependent on solvent polarity, with time constants of ~ 1 ps in methanol, 2.5 ps in 2-propanol and 3.5 ps in tetrahydrofuran (see also Table 2 for other solvents). What is the origin of the rise component observed in the 950 nm traces? Interestingly, although decrease of temperature to 190 K in methanol does not affect the rise component, freezing of the sample in ethylene glycol glass at 77 K causes its disappearance [12]. Its presence only when peridinin is in the liquid phase indicates a connection with a conformational change in the excited state. Such a conformational change resulting in increased ICT character of the S_1/ICT state could be described as a TICT mechanism. However, TICT state formation would be slowed down by

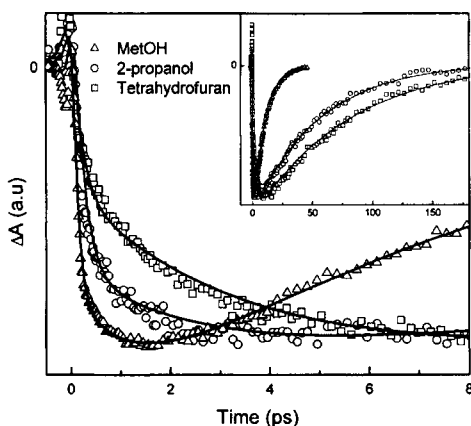


Fig. 4. Kinetics of the SE band probed at 975 nm of peridinin in methanol (triangles), 2-propanol (circles) and tetrahydrofuran (squares). In the main picture the first 8 ps of the traces and in the inset the whole decay traces are shown. The solid lines represent multiexponential fits of the data. The amplitudes of traces are normalized to the maximum of the signal. Excitation at 490 nm.

an increase of viscosity, which is the opposite situation to that observed here (see Table 1). This confirms that the rise component of the S_1 /ICT state emission cannot be assigned to a TICT mechanism. Although no molecular twisting is involved, the rise component is most likely connected with a small structural change of the peridinin molecule in the excited state. Since this process is manifested as a rise of the ICT state emission, it is likely that the carbonyl group changes its orientation slightly to stabilize the strongest possible ICT character of the S_1 /ICT state. It is most pronounced for peridinin molecules whose carbonyl group is not involved in hydrogen-bonding (see next section), and is free to move to enhance the ICT character of the S_1 /ICT state. For peridinin in solid phase at 77 K in ethylene glycol, movement of the molecule is prevented and no rise component is observed. It is important to note that although this conformational change leads to a stronger ICT character, it is not a transfer between the S_1 and ICT states as proposed earlier [9,11], but rather a change of the S_1 /ICT potential surface leading to the increased ICT character.

4.3. Excitation wavelength dependence

To explore further the dynamic consequences of the broadening of the absorption spectrum described above, peridinin dynamics were recorded after tuning the excitation wavelength towards the low-energy edge of the absorption band. Kinetics measured at the maximum of the ICT emission band in methanol after excitation at different wavelengths are shown in Fig. 5a. Excitation at 425 nm results in a decay of the 950 nm signal with a time constant of 11 ps, whereas the decay after excitation at the red edge of the absorption spectrum at 550 nm is characterized by a 5.9 ps time constant. In addition, the rise of the ICT band becomes faster and less pronounced with excitation into the red tail of the S_0 - S_2 transition, having time constants of 1.5 ps (425 nm excitation) and 0.4 ps (550 nm), respectively. The dependence of peridinin dynamics on excitation wavelength was also studied for several solvents in addition to methanol as shown in Fig. 5b, where the lifetimes are normalized to the longest observed decay for each solvent. The actual lifetimes are

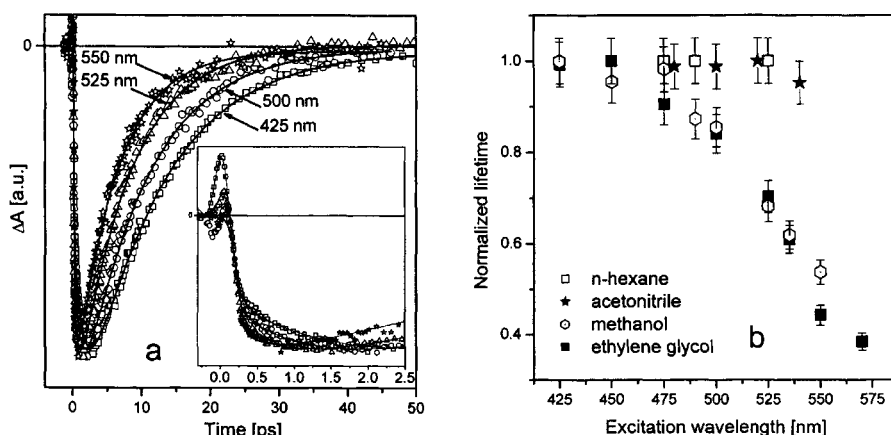


Fig. 5. (a) Kinetics recorded for peridinin in methanol at the ICT state emission maximum at 950 nm after excitation at 425 nm (squares), 500 nm (circles), 525 nm (triangles) and 550 nm (stars). All kinetics are normalized and corresponding fits of the kinetics are represented by solid lines. Enlargement of the early time dynamics is shown in inset. (b) Dependence of peridinin lifetime on excitation wavelength in different solvents. The lifetimes are normalized to the longest observed lifetime in the corresponding solvents.

summarized in Table 1. The behavior of peridinin in a nonpolar solvent is similar to that of carotenoids without a carbonyl group, for which no effect of excitation wavelength was observed [12]. In methanol and ethylene glycol, however, the peridinin lifetimes after excitation into the higher vibrational levels of the S_2 state (425 nm) and into the very red edge of the S_0 - S_2 transition (550 nm) are markedly different. Interestingly, in acetonitrile there is no effect of excitation wavelength on the peridinin lifetime, although this solvent is even more polar than methanol, and both the rise (~ 0.6 ps) and decay (~ 8 ps) of the 950 nm signal are the same over the whole range of excitation wavelengths.

The results demonstrate that solvent polarity is not the only factor affecting the excited state dynamics of peridinin. In addition to the shortening of the lifetime of the lowest excited state due to an increase of the solvent polarity, other factors also modify the properties of the peridinin molecule. The data in Fig. 5 suggest that more than one ground state conformation of peridinin must exist in both methanol and ethylene glycol. We suggest that two distinct species coexist in these solvents, which will be denoted as normal and red forms of peridinin, respectively. Since the red form of peridinin is most pronounced in ethylene glycol, another solvent parameter that enhances the effect of ICT state beside polarity must be involved. As described in the section dealing with steady-state absorption spectra, it seems that the hydrogen-bonding capability of solvents is directly related to formation of the red peridinin form, since there is no excitation wavelength dependence in acetonitrile. In the protic solvents methanol and ethylene glycol, the red peridinin is probably formed by hydrogen bonding via the carbonyl group. Thus, to achieve the strongest ICT character of the peridinin lowest excited state, a solvent that is both polar and protic is needed.

Table 1. Excitation wavelength dependence of the peridinin dynamics measured at 950 nm for various solvents.^a

λ_{exc} [nm]	Ethylene Glycol		Methanol		Acetonitrile		n-hexane ^b	
	τ_{rise} (A)	τ_{decay}	τ_{rise} (A)	τ_{decay}	τ_{rise} (A)	τ_{decay}	τ_{rise}	τ_{decay}
425	1 (38%)	13.7	1.5 (25%)	11	-	-	-	-
450	0.95 (36%)	13.8	1.3 (30%)	10.5	-	-	-	-
475	1 (36%)	12.5	1.2 (30%)	10.8	0.65 (58%)	8.2	-	160
500	0.65 (30%)	11.6	1 (47%)	9.6	0.66 (59%)	8.2	-	-
525	0.6 (29%)	9.7	0.6 (23%)	7.5	0.45 (52%)	8.3	-	160
535	0.4 (23%)	8.4	0.6 (27%)	6.8	0.6 (41%) ^c	7.9 ^c	-	-
550	0.2 (25%)	6.1	0.4 (26%)	5.9	-	-	-	-
570	0.15 (32%)	5.3	-	-	-	-	-	-

a) All time constants are listed in picoseconds. Amplitudes of the rise component are shown in parentheses. The rest of the rise occurs within the response function of the experimental set-up. All the decays are monoexponential. Uncertainties of the lifetimes and amplitudes are within $\pm 5\%$.

b) kinetics were recorded at 1700 nm due to the lack of 950 nm band in *n*-hexane

c) kinetics were recorded after excitation at 540 nm.

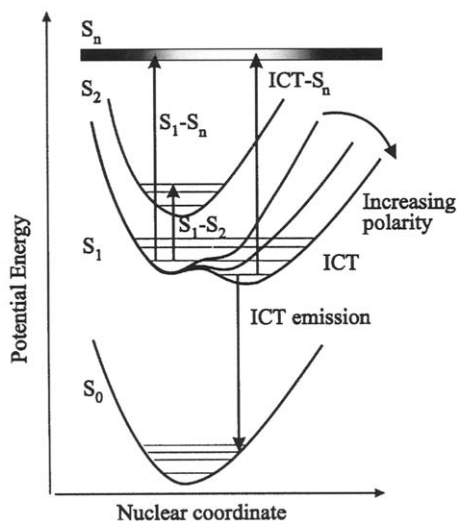


Fig. 6. Potential energy surface diagram showing the polarity effect on structure of the S_1 /ICT potential surface of the peridinin molecule. The transitions corresponding to the observed signals are denoted by arrows. Due to the lack of knowledge about S_n potential surface, it is visualized only as a line representing a final state for S_1-S_n and $ICT-S_n$ transitions. See text for details.

5. MODEL OF PERIDININ EXCITED STATES

On the basis of the described dynamical features we have constructed the model, shown in Fig. 6. Except for a few modifications, it is in a good agreement with that proposed by Frank et al. [10]. The peridinin lowest excited state has a complicated potential surface, whose shape is determined by the degree of mixing between the S_1 and ICT states that is related to solvent polarity. In nonpolar solvents the lowest excited state has a purely S_1 character. With an increase of solvent polarity, the S_1 /ICT state gains more ICT character making the potential surface broader. This broadening leads to the appearance of the characteristic ICT emission, which is significantly red-shifted from the S_1 emission due to a considerable shift in reaction coordinate between the ICT and S_0 potential minima. In addition, the ICT part of the potential surface is the origin of the strong and broad ESA band appearing around 600 nm for peridinin in polar solvents (Fig. 3). Furthermore, opening the ICT part of the potential surface decreases the S_1-S_2 signal as a fraction of the S_1 /ICT population is moved towards the ICT part, as is clearly noticeable in Fig. 3b.

The S_1 -like and ICT-like minima of the S_1 /ICT potential surface are separated by a low, polarity-controlled barrier. When polarity reaches a certain value, the barrier is low enough to allow thermal coupling and a high degree of ICT character of the S_1 /ICT state. A separation of the S_1 -like and ICT-like minima by a low barrier is also the reason for the uniform peridinin lifetime observed over a broad range of wavelengths. It is further supported by the temperature dependence, as decrease of temperature has a similar effect on the S_1 /ICT lifetime as decrease of solvent polarity [12]. Since signals characteristic of both S_1 and ICT states are observed for normal peridinin in methanol, the energy difference between the minima corresponding to the S_1 and ICT parts of the S_1 /ICT potential surface must be very small. If the ICT minimum on the potential surface were significantly lower, most of the

S_1/ICT population would be transferred towards this minimum resulting in a loss of the S_1 contribution. In protic solvents, hydrogen bonding via the carbonyl group further stabilizes the ICT character of the S_1/ICT state pushing the ICT minimum slightly lower than that of the S_1 , resulting in a shift of equilibrium towards the ICT state.

It is necessary to emphasize that Fig. 6 represents a model for only one particular peridinin conformation. As discussed above, a distribution of peridinin conformers exists in polar solvents. A slight structural change in the excited state is also responsible for the rise component observed in polar solvents, but this dynamic cannot be included in the model depicted in Fig. 6 as it includes a change of the S_1/ICT potential surface. In protic solvents the dynamics of peridinin are further complicated as hydrogen bonding leads to the formation of a 'red' peridinin form with different properties of both ground and excited states.

Acknowledgement. We thank Frank Sharples for his expertise in HPLC and Harry Frank and Ronald Christensen for useful discussions. The work at Lund University was performed with funding from the Swedish Research Council, the Wallenberg Foundation and the Crafoord Foundation. RGH was supported by the Australian Research Council (project grant A00000264). TP thanks DESS (Delegationen för Energiförsörjning i Sydsverige) and The Swedish National Energy Administration for financial support.

REFERENCES

- [1] H. A. Frank and R. J. Cogdell, *Photochem. Photobiol.* 63 (1996) 257.
- [2] B. Demmig-Adams and W. W. Adams, *Trends Plant Sci.* 1 (1996) 21.
- [3] R. Edge, D. J. McGarvey, T. G. Truscott, *J. Photochem. Photobiol. B* 41 (1997) 189.
- [4] R. L. Christensen, M. Goyette, L. Gallagher, J. Duncan, B. DeCoster, B.; J. Lugtenburg, F. J. Jansen, I. van der Hoef, *J. Phys. Chem. A* 103 (1999) 2399.
- [5] A. Macpherson and T. Gillbro, *J. Phys. Chem. A* 102 (1998) 5049.
- [6] V. Chynwat V. and H. A. Frank, *Chem. Phys.* 194 (1995) 237.
- [7] E. Hofmann, P. Wrench, F. P. Sharples, R. G. Hiller, W. Welte, K. Diederichs, *Science* 272 (1996) 1788.
- [8] J. A. Bautista, R. G. Hiller, R. F. P. Sharples, D. Gosztola, M. R. Wasielewski, H. A. Frank, *J. Phys. Chem. A* 103 (1999) 2267.
- [9] J. A. Bautista, R. E. Connors, B. B.; Raju, R. G. Hiller, F. P. Sharples, D. Gosztola, M. R. Wasielewski, H. A. Frank, *J. Phys. Chem. B* 103 (1999) 8751.
- [10] H. A. Frank, J. A. Bautista, J. Josue, Z. Pendon, R. G. Hiller, F. P. Sharples, D. Gosztola, M. R. Wasielewski, *J. Phys. Chem. B* 104 (2000) 4569.
- [11] D. Zigmantas, T. Polívka, A. Yartsev, R. G. Hiller, V. Sundström, *J. Phys. Chem. A* 105 (2001) 10296.
- [12] D. Zigmantas, R. G. Hiller, A. Yartsev, V. Sundström, T. Polívka, *J. Phys. Chem B* 107 (2003) 5339.
- [13] J. Zimmermann, P. A. Linden, H. M. Vaswani, R. G. Hiller, G. R. Fleming, *J. Phys. Chem. B* 106 (2002) 9418.
- [14] S. Shima, R. P. Ilagan, N. Gillespie, B. J. Sommer, R. G. Hiller, F. P. Sharples, H. A. Frank, R. R. Birge, *J. Phys. Chem. A* 107 (2003) in press.
- [15] T. Polívka, J. L. Herek, D. Zigmantas, H.-E. Åkerlund, V. Sundström, *Proc. Natl. Acad. Sci. U.S.A.* 96 (1999) 4914.
- [16] M. Mimuro, M. Nagashima, S. Takaichi, Y. Nishimura, I. Yamazaki, T. Katoh, *Biochim. Biophys. Acta* 1098 (1992) 271.

Pump-probe and pump-deplete-probe spectroscopy on carotenoids with N=9-15

T. Buckup^a, J. Savolainen^b, W. Wohlleben^a, H. Hashimoto^c, R. J. Cogdell^c, J. L. Herek^b and M. Motzkus^a

^aMax-Planck-Institut für Quantenoptik, D-85748 Garching, Germany

^bFOM-Institute for Atomic and Molecular Physics, 1098 SJ Amsterdam, The Netherlands

^cIbLS, University of Glasgow, Glasgow G12 8QQ, United Kingdom

1. INTRODUCTION

The standard three-level scheme of carotenoids consists of the ground state S_0 ($1A_g^-$ in idealized C_{2h} symmetry), the absorbing bright state S_2 ($1B_u^+$) and the intermediate dark state S_1 ($2A_g^-$). Internal conversion from S_2 via S_1 to the ground state has long been thought to be the dominant deactivation channel for the biologically relevant carotenoids with N=9-13 conjugated double bonds. According to this three-level model, after absorption of light in the blue-green region by the S_2 state ($1B_u^+$) the population decays through two channels: ultra fast (~100-200 fs) internal conversion to the S_1 state and direct fluorescence to the ground state with almost negligible quantum yield[1]. The S_1 state decays to the ground state on the picosecond timescale. The dependence of the S_1 lifetime on number of conjugated double bonds and thus the energy difference between S_0 and S_1 can be satisfactorily described by the energy gap rule. Recently there have been proposals that this simple three-level model must be expanded by additional dark states ($1B_u^-$ and $3A_g^-$) [2] that would be either fast deactivation intermediates [3] or competing deactivation channels [4].

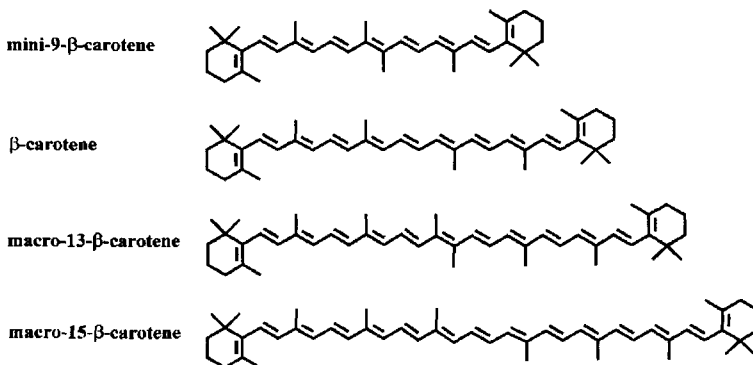


Fig. 1. All-trans-carotenoids studied in this contribution. They are labelled M9, M11, M13 and M15 according the number of conjugated double bonds.

However, only the lowest dark state, $2A_g^-$ or S_1 , has been extensively characterized in terms of its temporal behaviour and energetics. The unresolved question remains: Are the $1B_u^-$ and $3A_g^-$ dark states actively involved in deactivation energy flow? Also the role of state referred to as S^* [4, 5] giving a spectral signature on the red side of ground state absorption is still unknown. Does this transient absorption band belong to a one of the predicted additional dark states or does the band arise from population in a hot ground state? Here we study the nature of the transient absorption signal attributed to S^* on a series of β -carotene derivatives with conjugation lengths $N = 9, 11, 13, 15$ (see Fig. 1).

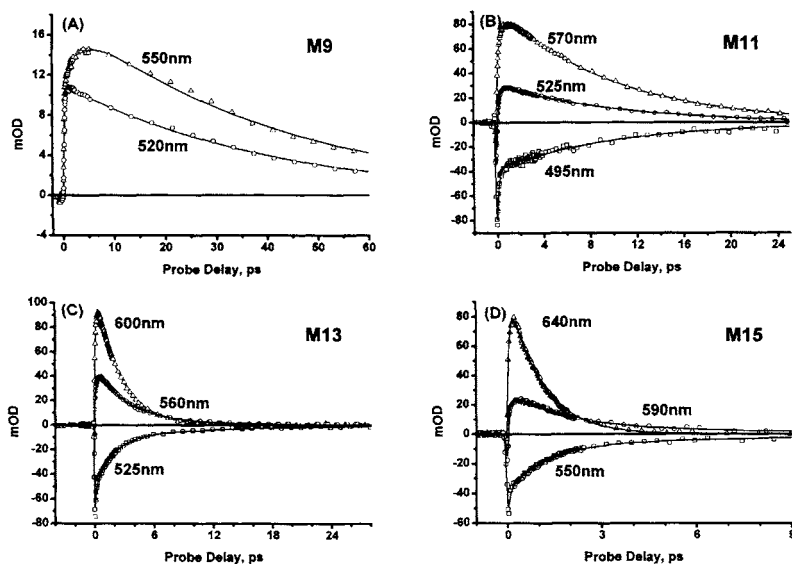


Fig. 2. Pump-probe transients for (A) M9, (B) M11, (C) M13 and (D) M15 at different wavelengths corresponding to induced absorption from S^* and S_1 and ground state bleach. For all carotenoids, the bleach signal corresponds to the shortest wavelength, the S^* signal is at the intermediate wavelength and the S_1 signal is the reddest.

2. EXPERIMENTAL SETUP

The experimental configuration of the pump-probe experiment is similar to Ref. [5]. A home built non-collinear optical parametric amplifier (nc-OPA) was used as a pump, providing Fourier-transform-limited 30 fs pulses, which could be spectrally tuned between 480-560 nm. In all experiments white-light generated in a sapphire crystal using part of the fundamental laser (800 nm), was used as probe light. In the pump-probe experiments the pump was tuned to the S_2 0-0 band for carotenoids with $n \geq 11$. In the case of M9, it was not possible to tune the nc-OPA to its 0-0 transition, and hence another nc-OPA tuned to 900 nm was frequency doubled and used for excitation. In addition to conventional transient absorption pump-probe measurements, we introduce pump-deplete-probe spectroscopy, which is sensitive to the function of an absorbing state within the deactivation network. In this technique, we

manipulate the population of one state and observe how signals from other states change concomitantly (or not). A near-IR pulse follows the visible excitation pulse to the $1B_u^+$ state and depletes the near-IR absorbing state. Probed afterwards with a weak third pulse, the transient absorption spectra identify the signals belonging to states that are deactivation channels of the depleted state. In pump-deplete-probe experiments the output of the second nc-OPA tuned to 940 and 1000 nm with ~ 30 fs pulse duration was used as the depletion pulse. Pump pulse energies were kept below 100 nJ and depletion energies below $1.4 \mu\text{J}$, far below the damage threshold.

3. RESULTS

3.1 S_1 and S^* lifetime dependence on conjugation length

The decay of the peak of S_1 band was fitted with one time constant for all studied molecules and pump wavelengths (Fig. 2). As expected from the energy gap rule, the shorter the carotenoid, the slower is the decay: ~ 1 ps for M15, ~ 2.5 ps for M13, ~ 10 ps for M11 and ~ 40 ps for M9. The same trend with conjugation length could not be observed for the S^* state. For M11 and M9, the S^* decays with the same time constant as S_1 . For M15 and M13, two decay components were needed to fit the data. The faster component is the same as the decay of S_1 , while the slower one is ~ 8 ps for M15 ~ 10 ps for M13. Similar behaviour has been previously observed for the same wavelength region in M15 [6], whereas for M13, no comparable data are available. In addition, we measured kinetics in the bleach region for carotenoids with $N \geq 11$. For the M9, the bleach is too blue-shifted for our probe light. In all cases, the bleach recovers with two time constants, where the slower component in the long carotenoids (M13 and M15) is again in the same range of the S^* decay.

3.2 Depletion of S_2 IR band

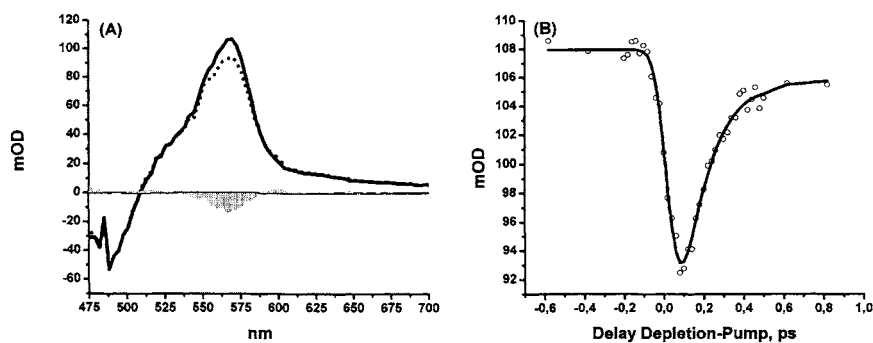


Fig. 3. (A) Depletion spectra probed at 2 ps and (B) depletion kinetics trace for M11. In graph (A), the ESA spectra with the depletion pulse present (dashed line) and without the depletion pulse (continuous line) are shown. Their difference is represented by the gray area. In graph (B), the curve represents a fit with single exponential rise and decay times, probed at 570 nm. The depletion was at 1000 nm for both graphs.

Depletion measurements were conducted in two different manners making use of the fast NIR bands recently observed in carotenoids [3, 7]. First we recorded transient spectra at

fixed delay 2 ps with and without the depletion pulse hitting the sample at early times (50 fs). The transient spectra and the difference is shown in Fig. 3 left. As can be seen, only the central band of M11 is depleted, while the blue wing belonging to S^* is untouched. The same behaviour was observed in all molecules. Second, again keeping the probe constant delay at 2 ps, the depletion pulse is scanned in time, which reveals the time behaviour of the depletion signals. The typical depletion curve was fitted with two single exponentials describing the rise and the decay. The rise of the depletion was always faster than our temporal resolution. Rough estimations give values below 25 fs. The recovery of depletion signal after depletion peak shows richer dynamics and is dependent on the carotenoid. It can be described with two components, a fast decay and a plateau, which does not show any decay during the S_1 lifetime. For M11, the depletion recovery time (depletion pulse @1000 nm) showed a time constant of ~ 140 fs, similar to what was observed previously with a depletion pulse at 795 nm.

4. DISCUSSION AND CONCLUSION

S^* and S_1 exhibit different dynamics for carotenoids with $N \geq 11$ (i.e. S^* does not obey the exponential energy gap rule like the S_1 does), giving a strong indication that they have a different nature. The position of S^* on the red side of the ground state absorption, in the same region where the fluorescence of S_2 is located, as well as its lifetime independence with the number double bonds leads us to suggest that the S^* signal is due to a vibrationally excited ground state and not a electronic state. The decay of S^* can be attributed to the cooling of the hot- S_0 to the cold S_0 . In our previous work, we could not say anything about the bleach recovery origin for M11 because the time constants of S^* and S_1 had similar values. Now, measuring for the M15 and M13, it clearly recovers with the decay time of S^* , another strong argument that supports the existence of hot- S_0 state in the deactivation. There is still one point that needs to be clarified: how the S^* is populated. As in our previous work [5], we propose here that S^* is a hot-ground state populated by Impulsive Raman Scattering. The ultrashort pump pulse has enough bandwidth to contain the Stokes and Pump pulses of a Raman excitation. This assignment is consistent with the dynamics as a function of conjugation length, as well as the spectral position on the red side of the ground state absorption. This model is especially appealing since S^* is located where the fluorescence from S_2 should appear, red-shifted of the steady S_0 - S_2 absorption, what indicates by itself a favourable transition. That explains why the S^* was not depleted: it is populated instantaneously when the pump is present.

REFERENCE

- [1] R. L. Christensen, in: H. A. Frank, et al. (Ed.) *The Photochemistry of Carotenoids*, Kluwer Academic Publishers, Dordrecht, 1999, p. 137.
- [2] P. Tavan and K. Schulten, *J. Chem. Phys.*, 85 (1986) 6602.
- [3] G. Cerullo, D. Polli, et al., *Science*, 298 (2002) 2395.
- [4] C. C. Gradinaru, J. T. M. Kennis, et al., *Proc. Natl. Acad. Sci.*, 98 (2001) 2364.
- [5] W. Wohlleben, T. Buckup, et al., *J. Phys. Chem. B*, submitted, (2003)
- [6] P. O. Andersson and T. Gillbro, *J. Chem. Phys.*, 103 (1995) 2509.
- [7] R. Fujii, T. Inaba, et al., *Chem. Phys. Lett.*, 369 (2003) 165.

Ultrafast photophysics of the protonated Schiff base of retinal in alcohols studied by femtosecond fluorescence up-conversion

G. Zgrablić^(a), K. Voïtchovsky^(a), M. Kindermann^(b), M. Chergui^(a) and S. Haacke^(a)

^(a) Institut de Physique de la Matière Condensée, Université de Lausanne - BSP, CH-1015 Lausanne-Dorigny

^(b) Institut de Chimie Moléculaire et Biologique, Faculté des Sciences de Base, EPFL, CH-1015 Lausanne

1. INTRODUCTION

All-trans retinal is the photo-sensitive moiety in many retinal proteins found in halobacteria. Bacteriorhodopsin (bR) is the most prominent example, in which retinal is covalently bound to the nitrogen atom of a lysine residue forming a protonated Schiff base linkage. The ultrafast intra-retinal processes but also dielectric retinal-protein interactions receive continued interest [1]. With this background, it is worthwhile understanding the photophysics of the retinylidene chromophore in well-characterized solvents for reference purposes [2,3]. Femtosecond spectroscopy on the protonated Schiff base form of *all-trans* retinal in methanol has been reported [4]. The excited state decay time has been attributed to *trans-cis* isomerization (with the exception of Ref. [5]). However, a detailed characterization of intramolecular dynamics (IVR, internal conversion, isomerization) and a distinction from intermolecular processes depending on the solvent properties has remained unaddressed until now. Signatures indicative of the fact that three different *cis* isomers[2] are being formed in methanol had not been found in the kinetics. In this paper, we report on the ultrafast spectral evolution of the fluorescence of the *all-trans* PSBR in alcohols with different polarity. Using the fluorescence up-conversion technique in a “polychromatic mode” [6], we are able to show that vibrational cooling is the dominant contribution to the total Stokes shift of PSBR's in alcohols.

2. EXPERIMENTAL DETAILS

The SBR's of all-trans retinal and n-butylamine were prepared according to previously described methods [5] and protonated using a 3-10 fold excess of TCA in dried methanol and water-free octanol. Around 150 ml of solution of the PSBR in methanol/octanol was flown through a 0.3 mm path length quartz cell, and the fluorescence collected in transmission geometry. The experiment is based on a Ti:Sapphire laser system with a 250 kHz regenerative amplifier delivering 40-50 fs pulses at 800 nm. The excitation beam was generated by doubling the fundamental in 500 μm thick BBO and the excitation density was 1.6 mJ/cm^2 per pulse. Since subsequent laser pulses excite the same sample portion before complete renewal, the fluorescence comes from a mixture of isomers containing at least 20 % of the 11-*cis* form. The “polychromatic” mode of operation consists of rotating the sum frequency crystal

* New address : Swiss Federal Institute of Technology Lausanne, LSUPC, Institute of Molecular and Biological Chemistry, FSB – BSP, CH-1015 Lausanne-Dorigny, Switzerland

(250 μm of BBO) during the recording of up-converted fluorescence with a spectrometer and a LN_2 -cooled CCD camera, thus phase-matching the whole spectral region of interest. After the up-conversion crystal, the sum frequency beam goes through different spectral filters, which reject the second harmonic of the gate beam, but unfortunately limit the up-conversion signal to wavelengths < 380 nm. All spectra shown below are corrected for group velocity dispersion (GVD), previously measured using white light generated in the flow cell filled with water. By observing the Raman line of the solvent, time zero was determined for each scan, along with the instrument time response function of 120-150 fs.

3. RESULTS AND DISCUSSION

The steady-state spectra obtained for different alcohols are depicted in fig. 1. While the absorption spectra red shift with increasing solvent polarisability (from methanol to octanol), the fluorescence shows a red-shift when going from octanol to methanol. The total Stokes shifts are very large: $7.900 \pm 100 \text{ cm}^{-1}$ for PSBR/MeOH and $6.870 \pm 100 \text{ cm}^{-1}$ for octanol. Another striking observation is the $\sim 30\%$ smaller width of the fluorescence spectrum of methanol ($\Delta E = 3.420 \text{ cm}^{-1}$) compared with other alcohols. While the widths of the fluorescence spectra are solvent-dependent, the absorption spectra have a FWHM of $\sim 5.100 \text{ cm}^{-1}$, irrespective of the solvent. As we will substantiate in the following, this behavior indicates that the potential energy surface around the fluorescent point is different than near the Franck-Condon zone probed by absorption, as suggested by quantum chemistry calculations [7].

The temporal evolution of the emission is shown in fig. 2 using *all-trans* PSBR's in methanol and in octanol. A comparison with the steady state spectra of fig. 1 indicates an intensity cut-off below 14.500 cm^{-1} , coming from the filtering procedure described above. The general behavior is similar in both solvent: In the first 50 fs after excitation a very broad spectrum ($14.000 - 21.000 \text{ cm}^{-1}$) builds up quickly with a maximum at around 16.500 cm^{-1} (fig. 2a). During the rise time and up to ~ 500 fs, the high energy wing decays dramatically, causing a rapid narrowing of the spectra and shifting of its maximum to the red. This behavior is apparent from Fig. 3 depicting the time dependence of the FWHM and the first moment of the spectra. While the spectral narrowing proceeds with three different time constants in MeOH,

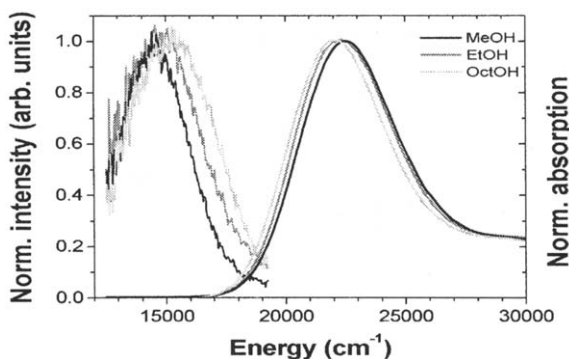


Fig.1. Normalized steady-state fluorescence spectra of the PSBR in methanol, ethanol and octanol. The fluorescence spectra are corrected for detector response and converted onto an energy scale. Note that absorption and emission are lacking mirror symmetry. The total Stokes shift is 6.870 cm^{-1} octanol and 7.900 cm^{-1} in methanol.

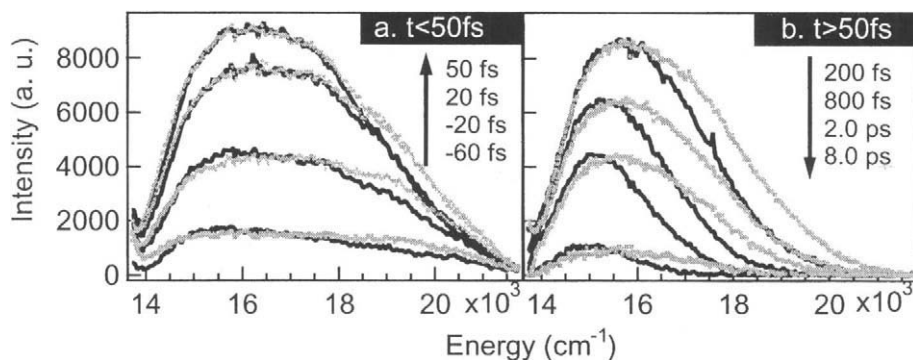


Fig. 2. Time resolved fluorescence spectra of all-trans PRSB in methanol (black) and octanol (grey) for a) $t < 50$ fs and b) $t > 50$ fs. The intensity of the octanol spectra is adjusted the methanol spectra. The spectra are not corrected for self-absorption (for $E > 19.500$ cm^{-1}), or for the detector response function. A residual signal appearing at energies < 14.000 cm^{-1} is due to incomplete background subtraction (see above).

defining three different phases of relaxation, only the sub-100 fs component (phase 1) and the slow ps component (phase 3) is seen for PSBR in octanol.

In some spectra, the presence of the “shoulders” indicates that at least three bands constitute the spectrum, thus influencing the position of the emission maximum. As a consequence of the large amplitude of the high-energy bands in the early spectra, their first moment is larger than 17.500 cm^{-1} and red-shifts with timescales very similar to the evolution of the spectral FWHM (fig. 3). In such a multi-band case, the excited state solvation should be evaluated as the displacement of the lowest-energy bands hidden beneath the measured spectra. This analysis is in progress at present. Nevertheless, the above results already suggest that dielectric solvation has only a minor contribution to the total Stokes shift, irrespective of the solvent. In both solvents, the time-zero spectrum is already red-shifted by more than 6.000 cm^{-1} with respect to the maximum of absorption. It is very unlikely that this large shift is due to an inertial solvation component in octanol, which is less polar and expected to exhibit slower solvation dynamics [8].

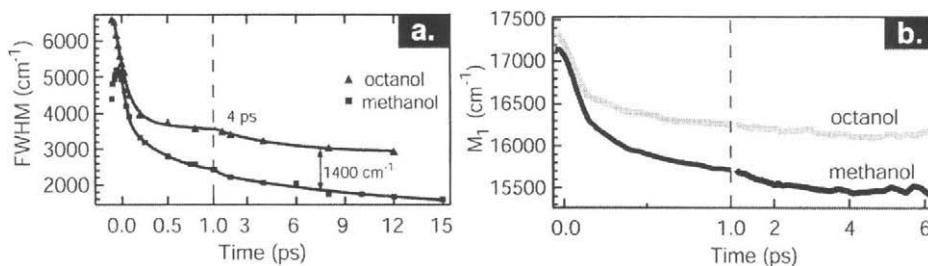


Fig. 3. Transient FWHM (a) and first moment (b) of the fluorescence spectra of all-trans PSBR in methanol and octanol. For the first ps a finer scale was used. After deconvoluting with the 140 fs instrument response function, the fit gave the following decay constants and their amplitudes: *methanol* – 30 fs (0.75), 400 fs (0.15) and ~ 11 ps (0.1), *octanol* – 120 fs (0.9) and 4.0 ps (0.1).

The high energy wing of the early emission indicates rather that we are observing fluorescence of unrelaxed molecules, which is expected as a consequence of the excitation with large excess energy (at 25.000 cm^{-1}). Phase 1 of vibrational relaxation proceeds in less than 100 fs in a very similar fashion for both solvents. Such a behavior is consistent with relaxation most probably along high-frequency C=C and C=N modes due intra-molecular vibrational energy redistribution. In addition, we observe corresponding rise times in the low-energy emission, supporting the idea of vibrational relaxation. On the other hand, the relaxation phase 3, which we observe for $t > 2\text{ ps}$ when the spectral narrowing proceeds on a time scale of a few picoseconds represents intermolecular vibrational relaxation involving the solvent.

Spectral narrowing on the time scale of 400-500 fs and drop of intensity in the vicinity of 17.000 cm^{-1} is observed for the PSBR's in methanol only (phase 2), leading to the differences observed in the steady-state spectra. In octanol, the spectra remain large (fig. 2) suggesting that they accommodate two bands: band A near 17.000 cm^{-1} and band B close to 15.000 cm^{-1} . These bands are most probably not related to excited state vibrational levels since IVR should still be operative for relaxing the energy difference, and this irrespective of the solvent. Our tentative explanation is to assign both bands to different isomerization pathways in the excited state. The shorter lifetime (400-500 fs) found for band A in MeOH is in agreement with the more efficient formation of the *11-cis* isomer, while band B (3.5 ps lifetime) would reflect formation of other *cis*-type isomers. Within this interpretation and as octanol has a higher viscosity, the longer excited state lifetimes (1.5 and 5.3 ps) would indeed be expected. These preliminary results strongly suggest that the solvent has an impact on the excited state electronic structure around the fluorescent state, leading to different excited state lifetimes and widths of the emission spectra. Further experiments with other solvents are required to obtain a better insight into the electronic structure of the emitting state.

We acknowledge financial support by the Swiss National Science Foundation (FNRS) within the NCCR "Quantum Photonics", through the project grant 2153-065135 and the "PROFIL-2" grant for S.H.

REFERENCES

- [1] GG Kochendoerfer, RA Mathies, *Isr. J. Chem.* 35 (1995) 211; M Du, GR Fleming, *Biophysical Chemistry* 48 (1993) 101; T Kobayashi, T Saito, H Ohtani, *Nature* 414 (2001) 531; T Ye, E Gershgoren, N Friedman, M Ottolenghi, M Sheves, S Ruhman, *Chem. Phys. Lett.* 314 (1999) 429.
- [2] KA Freedman, RS Becker, *J. Am. Chem. Soc.* 108 (1986) 1245.
- [3] SM Bachilo, T Gillbro, *J. Phys. Chem. A* 103 (1999) 2481; SM Bachilo, SL Bondarev, T Gillbro, *J. Photochem. Photobiol. B Biology* 34 (1996) 39.
- [4] SL Logunov, L Song, MA El-Sayed, *J. Phys. Chem.* 100 (1996) 18586; H Kandori, H Sasabe, *Chem. Phys. Lett.* 216 (1993) 126; P Hamm, M Zurek, T Röschinger, H Patzelt, D Oesterheld, W Zinth, *Chem. Phys. Lett.* 263 (1996) 613.
- [5] B Hou, N Friedman, S Ruhman, M Sheves, M Ottolenghi, *J. Phys. Chem. B* 105 (2001) 7042.
- [6] R Schanz, SA Kovalenko, V Kharlanov, NP Ernsting, *App. Phys. Letters* 79 (2001) 566; S Haacke, RA Taylor, I Bar-Joseph, MJSP Brasil, M Hartig, B Deveaud, *JOSA B* 15 (1998) 1410.
- [7] R González-Luque, M Garavelli, F Bernardi, M Merchán, MA Robb, M Olivucci, *Proc. Nat. Acad. Sci.* 97 (2000) 9379.
- [8] ML Horng, JA Gardecki, A Papazyan, M Maroncelli, *J. Phys. Chem.* 99 (1995) 17311.
- [9] AB Myers, RA Harris, RA Mathies, *J. Chem. Phys.* 79 (1983) 603.

Ultrafast excited-state dynamics in DNA and RNA polymers

B. Cohen, C. E. Crespo-Hernández, P. M. Hare and B. Kohler

Department of Chemistry, The Ohio State University, 100 W. 18th Avenue, Columbus, Ohio 43210, U.S.A.

1. INTRODUCTION

The year 2003 is the tenth anniversary of the first Femtochemistry Conference and the fiftieth anniversary of Watson and Crick's celebrated discovery of the DNA double helix [1]. Remarkable progress has been made in both fields: femtosecond spectroscopy has made decisive contributions to Chemistry and Biology, and advances in the elucidation of *static* nucleic acid structures have profoundly transformed the biosciences. However, much less is known about the *dynamical properties* of these complex macromolecules. This is especially true of the dynamics of the excited electronic states, including their evolution toward the photoproducts that are the end result of DNA photodamage [2].

Transient absorption experiments have shown that all of the major DNA and RNA nucleosides have fluorescence lifetimes of less than one picosecond [2–4], and that covalently modified bases [5], and even individual tautomers [6], differ dramatically in their excited-state dynamics. Femtosecond fluorescence up-conversion studies have also shown that the lowest singlet excited states of monomeric bases, nucleosides, and nucleotides decay by ultrafast internal conversion [7–9]. As discussed elsewhere [2], solvent effects on the fluorescence lifetimes are quite modest, and no evidence has been found to date to support excited-state proton transfer as a decay mechanism. These observations have focused attention on the possibility of internal conversion via one or more conical intersections. Recently, computational studies have succeeded in locating conical intersections on the excited state potential energy surfaces of several isolated nucleobases [10–12].

Recent progress in understanding the photophysics of single nucleobases has now focused attention on the challenging problem of excited-state dynamics in DNA and RNA polymers. It is often stated that ultrafast nonradiative decay by the monomeric nucleobases greatly reduces the likelihood of their photochemical damage. This is a tempting explanation for why the present-day bases may have been favored over alternative compounds as the carriers of genomic information in all living organisms. However, it has yet to be shown that the DNA and RNA polymers enjoy the same degree of photostability as the monomeric nucleobases. In fact, evidence is now accumulating that considerably longer-lived excitations are formed in natural and synthetic nucleic acid polymers. As a result of their longer lifetimes, these excited electronic states could have much greater potential for photochemical damage.

Our objective is to understand how the noncovalent interactions responsible for nucleic acid secondary structure (i.e. base stacking and base pairing) affect the photophysics of these multichromophoric systems. Here we describe initial experimental results that demonstrate dramatic differences in excited-state dynamics of nucleic acid polymers compared to their constituent monomers. Although ultrafast internal conversion is the dominant relaxation pathway for single bases, electronic energy relaxation in single-stranded polynucleotides

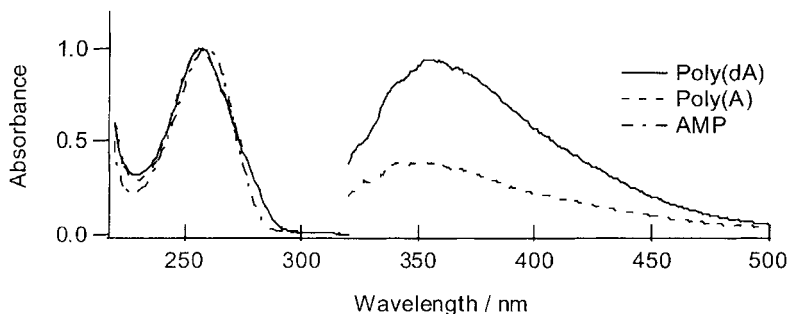


Fig. 1. Normalized absorption and corrected emission spectra for poly(A) and poly(dA) in aqueous solution at neutral pH. The normalized absorption spectrum of AMP is presented for comparison.

occurs over a wide range of time scales extending from femtoseconds to nanoseconds. Since base stacking increases the electronic coupling between adjacent nucleobases, polymer conformation significantly affects the electronic structure of these important macromolecules. Thus, our experiments demonstrate that the intrinsic UV chromophores of nucleic acids, the DNA and RNA bases, are useful ultrafast optical probes of secondary polymer structure.

2. RESULTS AND DISCUSSION

2.1. Electronic energy relaxation in adenine polymers

The excited-state properties of poly(riboadenylic) and poly(2'-deoxyriboadenylic) acid polymers, poly(A) and poly(dA), respectively, were investigated by steady-state and femtosecond transient absorption spectroscopy. These two homopolymers have identical adenine chromophores, and differ only at the 2'-position of the furanose ring. Because both polymers form single-stranded structures at neutral pH, it is possible to investigate base stacking effects in the absence of base pairing. Furthermore, the base stacking motifs differ in these two polymers: poly(A) is believed to adopt an A-type or RNA-like structure, while poly(dA) adopts a B-type or DNA-like structure [13]. Changing pH and temperature alters the character and extent of base stacking in these polymers [14]. They are thus excellent systems for studying the effect of secondary structure on electronic energy relaxation pathways.

The steady state absorption and emission spectra of poly(A), poly(dA), and the absorption spectrum of the ribonucleotide monomer adenosine 5'-monophosphate (AMP) are shown in Fig. 1. The absorption spectra of poly(A) and poly(dA) are essentially identical. The AMP absorption spectrum is similar to the polymer spectra, but subtle differences exist. The absorption maximum of both homopolymers is shifted to the blue by several hundred wavenumbers, while the low energy band edge is red-shifted with respect to AMP. Similar shifts are observed at 77 K [15].

Despite the nearly identical absorption spectra of both polymers, the emission quantum yield of poly(dA) is nearly three times that of poly(A), as can be seen from the unscaled emission spectra (Fig. 1) measured from polymer solutions having identical absorbance at the excitation wavelength of 280 nm. The absolute fluorescence quantum yield of poly(A) has previously been reported as 3×10^{-4} [16]. Interestingly, the situation is reversed at 77 K, and more fluorescence was reported from the ribo- than from the deoxyribopolymer [15]. The

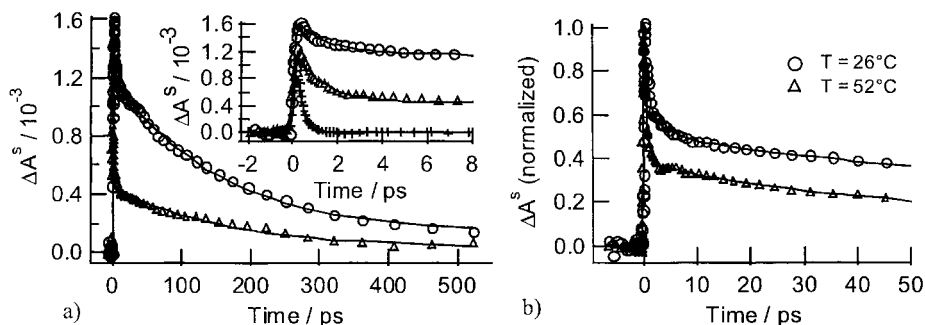


Fig. 2. a) Transient decays from poly(A) (triangles) and poly(dA) (circles) at 570 nm in back-to-back experiments at neutral pH. The solid curves are fits. The inset provides a short time view along with the signal from AMP (crosses). b) Normalized transient absorption at 570 nm following UV excitation of poly(A) at the indicated temperatures.

room-temperature emission spectra are red-shifted compared to that of monomeric adenine. This red-shifted emission has been attributed in the past to excimer states [15,17].

Femtosecond pump-probe experiments were performed using ≈ 200 fs UV pump pulses with a center wavelength of 263 nm, as described previously [4]. Transient absorption signals for both adenine polymers and for AMP are shown in Fig. 2a at a probe wavelength of 570 nm. The signals were recorded in back-to-back experiments without any adjustments to the laser apparatus. As found previously for monomeric bases [4], it was necessary to work at very low pump laser intensities to minimize the two-photon photoionization of water. By measuring the pump-power dependence of the polymer signals it was determined that the major contribution to the signal at 570 nm is monophotonic. A small quadratically varying signal component was also detected, which made the largest contribution to the total signal ($\approx 10 - 15\%$) at delay times greater than 100 ps. This second signal component was assigned to absorption by hydrated electrons created by two-photon ionization of solvent molecules, as described in our previous transient absorption study of monomeric bases [4].

The biphotonic signal from hydrated electrons masks the solute dynamics at long times and was removed by subtraction. Only ‘solvent-subtracted’ signals (indicated by ΔA^s) are shown in Figs. 2 – 4. Because the solute signal is nonzero at the longest delay times studied, our previous subtraction procedure [6] was modified as follows: Back-to-back scans were recorded first from the polynucleotide of interest, and then from an aqueous solution of a monomeric nucleoside, which had the same absorbance at the pump wavelength. On account of the short lifetimes of the excited states of single nucleosides, the total signal at long times ($t > 10$ ps) from the nucleoside solution is due exclusively to two-photon ionization of water. A transient recorded from a solution containing just the pH buffer was then scaled to match the long-time signal and subtracted from the polynucleotide transient to give the final water-subtracted signal. The resulting signals are linear in pump power over the entire delay range, as was verified explicitly for poly(A) at neutral pH.

Signals recorded at probe wavelengths between 500 and 700 nm showed similar decays as the 570 nm transients shown in Figs. 2 – 4. These results mirror previous ones for the monomeric bases [4], and we assign these transients to excited-state absorption by singlet states created by UV photoexcitation. We consider alternative assignments in section 2.3. AMP and the two homopolymers show an ultrafast decay component, but the polymers also

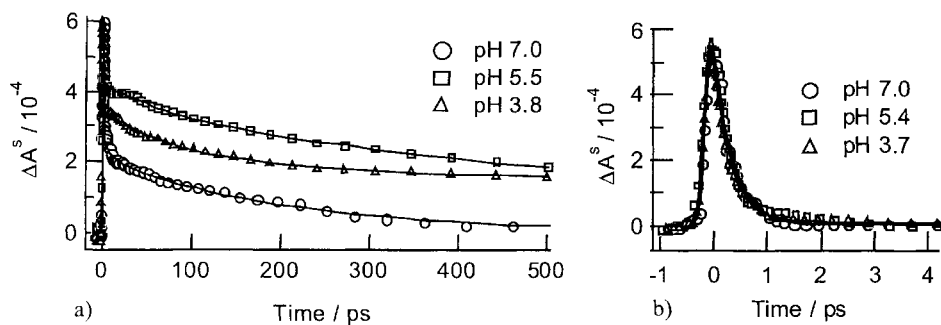


Fig. 3. Transient absorption signals from a) poly(A) (normalized) and b) AMP at 570 nm in back-to-back experiments at different pHs. The solid curves are fits.

show signal components that decay on much slower time scales. The signals from poly(A) and poly(dA) have not reached the baseline 500 ps after the pump pulse, the longest delay time probed in our experiments, and three exponentials are required to adequately fit the transients. The longest decay time was poorly determined due to our limited delay range, so transients were fit to two exponentials plus a constant offset, with the exponential time constants as global parameters. The best-fit lifetimes for both polymers are $\tau_1 = 1.33 \pm 0.13$ ps, $\tau_2 = 154 \pm 14$ ps, and $\tau_3 = \infty$ [18]. For poly(A), the best-fit amplitudes associated with these lifetimes are: $A_1 = 0.46$, $A_2 = 0.25$, and $A_3 = 0.018$. For poly(dA), the amplitudes are: $A_1 = 0.29$, $A_2 = 0.64$, and $A_3 = 0.075$.

The observation of the long lifetime components, τ_2 and τ_3 , is striking, since AMP shows only ultrafast electronic energy decay at room temperature and neutral pH. The long-lived decay components are assigned to excitations in segments of two or more stacked bases, while the fastest decay component is assigned to excitations in unstacked bases. These assignments are consistent with the known distribution of bases in single-stranded polymers either in stacked (helical) or unstacked (random-coil) segments [19]. In support of our assignment, the fractional contribution of the long-time signal for poly(A) decreases as temperature is raised (Fig. 2b). In the case of AMP, an increase in temperature has no appreciable change on the transient decays (data not shown). Raising the temperature increases the fraction of unstacked bases, increasing the fast, monomer-like signal and decreasing the slower signal contribution.

The greater amplitudes of the long-time signal, A_2 and A_3 , seen for poly(dA) vs. poly(A) (Fig. 2a) is in agreement with the greater steady-state fluorescence observed for the former polymer (Fig. 1). This confirms that the long-lived states are emissive. The precise reasons for the greater fluorescence from the deoxyribose polymer are unknown at present. Since the extent of base stacking is expected to be similar in poly(A) and poly(dA), this could be the result of different efficiencies for forming long-lived states from the initially excited ones. In other words, the excited-state dynamics could be strongly influenced by the different base-stacking morphologies in the two polymers. It is also worth noting that poly(dA) has a higher yield for photodimer formation than poly(A) [20]. Our steady-state and time-resolved results suggest that this may be a result of the greater yield of long-lived singlet states in the former polymer.

Further evidence that the long-time components are associated with excitations in base-stacked regions comes from pH-dependent measurements. The transient decays of poly(A) and AMP solutions are shown in Fig. 3 at several pH values. The pK_a values of poly(A) and AMP are 5.87 and 3.8, respectively [14]. As seen in the figure, the relative fraction of the

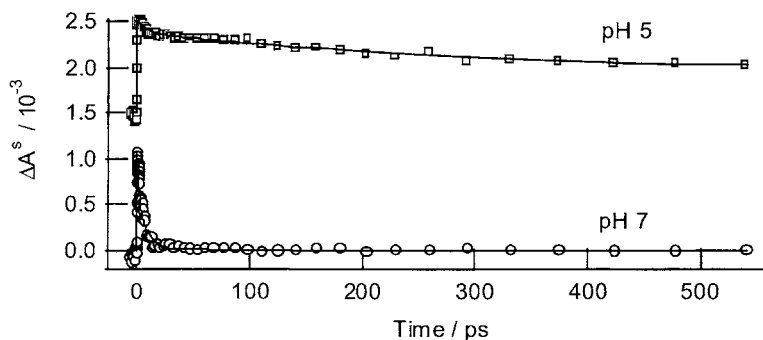


Fig. 4. Transient absorption signals of poly(C) at 570 nm at pH 7 (\circ) and pH 5 (\square). The pH 5 transient has been offset vertically for clarity. Solid lines are best-fit curves.

long-time signal increases dramatically when $\text{pH} \approx \text{pK}_a$. At pH values below the pK_a ($\text{pH} = 3.8$), the amplitudes of the slower components decrease somewhat, but are still larger than at pH 7. In contrast, signals from AMP are essentially pH-independent (Fig. 3b). Poly(A) adopts a double-stranded helix when $\text{pH} = \text{pK}_a$, which is destabilized at lower pH [14]. Our results indicate that the double-stranded helix formed at reduced pH leads to a greater yield of long-lived excitations. This increase may be due either to a base stacking geometry that is more favorable to the formation of the long-lived states, or because there is simply a greater amount of pairwise stacked bases at lower pH. Interestingly, the monomeric adenine cation has a subpicosecond lifetime (unpublished results). Thus, the long-lived decay components must be due to noncovalent effects (base stacking and base pairing) associated with the secondary structure of the polynucleotide, and cannot be due to the photophysics of protonated adenine. Further lowering the pH to 3.8 destabilizes the double helix, and the long-time signal components decrease (Fig. 3a).

2.2. Electronic energy relaxation in cytosine polymers

Transient absorption experiments were performed on the cytosine homopolymer poly(C) as a function of pH. Poly(C) adopts a double-stranded form in the pH range between 3.8 and 5.5 [21], which was previously reported to be more fluorescent than the cytosine monomer [22]. In the double-stranded form, two poly(C) strands are joined in parallel fashion by hemiprotonated base pairs, in which paired cytosine residues share a single proton. At higher pH values, poly(C) is present solely in single-stranded form.

Fig. 4 compares transient absorption at a probe wavelength of 570 nm upon UV excitation of poly(C) at pH 5 and 7. The transients at neutral pH were globally fit to a biexponential function, yielding lifetimes of 1.7 ± 0.2 ps and 8.0 ± 1.0 ps. The first component is assigned to monomer-like absorption in unstacked regions of the helix. The second component is assigned to excitations in segments of two or more stacked bases. No evidence was found for longer components in contrast to the finding of Plessow et al. that emission from the $\text{d}(\text{C})_{15}$ oligonucleotide decays on timescales from tens of picoseconds to a few nanoseconds [23]. A possible explanation for this discrepancy might be that $\text{d}(\text{C})_{15}$ was partially protonated in the experiments of Plessow et al. We note that the pK_a of poly(dC) is higher than that of poly(C) [24].

The transient at pH 5 decays biexponentially with time constants of 8.7 ± 2.0 ps and 310 ± 30 ps. In order to determine whether still slower decay components are present will require

a longer time window. The 310 ps decay component is consistent with past reports that poly(C) is more fluorescent at reduced pH [22]. The fast component matches the longer of the two lifetimes seen in poly(C) at pH 7, and could be due to the fact that there are still some single-stranded regions of poly(C), perhaps because the poly(C) single strands in our sample have a random length distribution. The reason for the increased fluorescence by the hemiprotonated form of poly(C) is not yet evident. However, the fact that the protonated cytosine monomer has a subpicosecond lifetime [5], strongly suggests that the long-lived excited states result from base-base interactions due to base stacking and/or base pairing, as discussed above for the adenine homopolymers.

2.3. On the nature of the long-lived states

We now briefly consider the possibility that the signals in Figs. 2 – 4 are due to absorption by species other than singlet excited states. Intersystem crossing quantum yields of the monomeric bases are very small (≤ 0.01) with AMP having one of the lowest values [16]. There has been no evidence of triplet-triplet absorption in past femtosecond pump-probe experiments on monomeric bases [4], and it would be surprising to observe triplet states in polynucleotides, provided that intersystem crossing quantum yields are not greatly different than for the monomers. In addition, the lifetimes of the triplet states of single bases are on the order of 1 μ s in aqueous solution at room temperature [16], making it unlikely that they could account for the sub-nanosecond dynamics observed here.

A further possibility is that the signals arise from hydrated electrons or base radical ions produced by monophotonic ionization of the polymers. However, the quantum yield for photoionization of adenosine is reported to be approximately the same as that of poly(A) and poly(dA) [25]. It is unlikely that photoionization of the polymers can account for the signals seen here since there is no detectable signal contribution from the photoionization of single bases [4]. The most compelling argument that our pump-probe experiments monitor excited-state absorption by singlet states is the fact that ps and ns decay components have been observed in previous time-resolved emission experiments on adenine multimers [23,26–28].

The long-lived signal components, which arise in base-stacked regions, are thus assigned to singlet states. Previous workers have described such states as excimers on account of their red-shifted emission [15,29]. Sequential bases in a polynucleotide are separated by just 3.4 Å, a typical interchromophore distance encountered in conventional, aromatic excimers [30]. The fact that similar emission has been observed from dinucleotides provides some justification for the excimer model, but we stress that our experiments cannot at this time determine whether the relevant excited states involve just two interacting bases. Because the relevant electronic couplings decrease rapidly with distance, it seems unlikely that a large number of bases participate. In fact, the absorption spectra of polynucleotides differ only modestly from spectra of the monomeric constituents, as shown in Fig. 1 for the adenine polymers. This suggests that exciton splittings are quite modest.

Due to the subpicosecond lifetimes of the monomeric bases there is little time for significant geometric rearrangements that might be necessary to form an excimer from an excited state initially localized on a single base. This suggests that excimers in nucleic acid polymers are more properly described as *static excimers* [30] in which two or more interacting chromophores are already pre-associated at the time of absorption. This implies that excimer states depend sensitively on conformation at the time of excitation, as the results presented here demonstrate.

Our work clearly establishes the existence of decay components ranging from hundreds of femtoseconds to hundreds of picoseconds in several polynucleotides. Previous investigators

have found even slower decay components that extend into the nanosecond time scale [23,26]. Despite the considerably longer lifetimes, the fluorescence quantum yields of polynucleotides are only modestly higher than those of their constituent monomers. For example, the fluorescence quantum yield of poly(A) at pH 7 is reported to be 3×10^{-4} compared to 0.6×10^{-4} for adenosine [31]. The fluorescence quantum yield of the double-stranded (hemiprotonated) form of poly(C) is 8×10^{-4} , approximately one order of magnitude larger than the value for cytidine [16]. The increase in quantum yields is considerably smaller than suggested by the increase in lifetimes. For example, the 150 ps component seen in poly(A) is approximately 450 times longer than the monomer lifetime of adenosine ($\tau = 290$ fs [3]), yet the quantum yield changes by merely a factor of five.

One explanation is that the radiative transition probabilities of the excimers are similar to those of the monomeric singlet states, but the excimers are formed in much lower yields. This could be the case if the initially excited state (the optically bright state populated by absorption) forms the excimer state in competition with other decay channels. An alternative explanation is that the excimer states are formed in high yield, but have low radiative transition probabilities (i.e. they are relatively dark in emission).

Further experiments are needed to decide between these two possibilities. A recent study by Markovitsi et al. on the oligonucleotide (dA)₂₀ found only a modest long-time signal offset that was 2% of the deconvoluted signal maximum [32]. In contrast, our transient absorption results for poly(dA) reveal a 150 ps decay component that is 64% of the signal maximum. Since the excited-state dynamics are likely to be very similar in these two systems, this difference suggests that the transition cross sections for the short- and long-lived states may be more similar in absorption than they are in emission. This in turn implies that transient absorption is particularly well suited for studying long-lived excited states formed in polynucleotides by UV light.

3. CONCLUSIONS

We have reported the first femtosecond transient absorption measurements of excited-state dynamics in nucleic acid polymers. Pump-probe signals at visible probe wavelengths are assigned to excited-state absorption by singlet states. The results show that backbone conformation dramatically affects the dynamics of singlet excitations in polynucleotides. For example, pronounced dynamical differences are observed for poly(A) and poly(dA), even though these polymers are composed of identical chromophores. Temperature-dependent experiments suggest that the long decay components originate in base-stacked segments of the polymers. In single-stranded poly(C), the decays are slower than in monomeric cytosine, but are considerably faster than in poly(A). Slower electronic energy relaxation is observed in the hemiprotonated, double-stranded form of poly(C). Ultimately, experiment and theory must work together to elucidate the complex electronic structure of these multichromophoric polymers. As this work demonstrates, the ability to follow electronic energy relaxation in DNA and RNA polymers can provide new opportunities for probing and sensing nucleic acid conformation [2].

4. ACKNOWLEDGEMENT

This work was funded by NIH grant R01 GM64563 from the National Institute of General Medical Sciences.

REFERENCES

- [1] J.D. Watson, F.H.C. Crick, *Nature (London)* 171 (1953) 737.
- [2] C.E. Crespo-Hernández, B. Cohen, P.M. Hare, B. Kohler, *Chem. Rev.*, in press.
- [3] J.-M.L. Pecourt, J. Peon, B. Kohler, *J. Am. Chem. Soc.* 122 (2000) 9348.
- [4] J.-M.L. Pecourt, J. Peon, B. Kohler, *J. Am. Chem. Soc.* 123 (2001) 10370.
- [5] R.J. Malone, A.M. Miller, B. Kohler, *Photochem. Photobiol.* 77 (2003) 158.
- [6] B. Cohen, P.M. Hare, B. Kohler, *J. Am. Chem. Soc.* 125 (2003) 13594.
- [7] J. Peon, A.H. Zewail, *Chem. Phys. Lett.* 348 (2001) 255.
- [8] T. Gustavsson, A. Sharonov, D. Markovitsi, *Chem. Phys. Lett.* 351 (2002) 195.
- [9] T. Gustavsson, A. Sharonov, D. Onidas, D. Markovitsi, *Chem. Phys. Lett.* 356 (2002) 49.
- [10] N. Ismail, L. Blancafort, M. Olivucci, B. Kohler, M.A. Robb, *J. Am. Chem. Soc.* 124 (2002) 6818.
- [11] A.L. Sobolewski, W. Domcke, *Eur. Phys. J. D* 20 (2002) 369.
- [12] M. Merchán, L. Serrano-Andrés, *J. Am. Chem. Soc.* 125 (2003) 8108.
- [13] B. Jolles, A. Laigle, L. Chinsky, P.Y. Turpin, *Nucleic Acids Res.* 13 (1985) 2075.
- [14] A.J. Adler, L. Grossman, G.D. Fasman, *Biochemistry* 8 (1969) 3846.
- [15] M. Guéron, J. Eisinger, A.A. Lamola, in P.O.P. Ts'o (ed.), *Basic Principles in Nucleic Acid Chemistry*, Academic Press, New York, 1974, p. 311.
- [16] J. Cadet, P. Vigny, in H. Morrison (ed.), *Bioorganic Photochemistry*, Wiley, New York, 1990, p. 1.
- [17] J.P. Morgan, M. Daniels, *Photochem. Photobiol.* 31 (1980) 101.
- [18] C.E. Crespo-Hernández, B. Kohler, submitted for publication.
- [19] V. Luzzati, A. Mathis, F. Masson, J. Witz, *J. Mol. Biol.* 10 (1964) 28.
- [20] D. Poerschke, *Proc. Natl. Acad. Sci. U.S.A.* 70 (1973) 2683.
- [21] E.O. Akinrimisi, C. Sander, P.O.P. Ts'o, *Biochemistry* 2 (1963) 340.
- [22] A. Favre, *FEBS Lett.* 22 (1972) 280.
- [23] R. Plessow, A. Brockhinke, W. Eimer, K. Kohse-Hoeninghaus, *J. Phys. Chem. B* 104 (2000) 3695.
- [24] R.B. Inman, *J. Mol. Biol.* 9 (1964) 624.
- [25] H. Görner, *J. Photochem. Photobiol. B: Biol.* 26 (1994) 117.
- [26] J.P. Ballini, M. Daniels, P. Vigny, *J. Lumin.* 27 (1982) 389.
- [27] S. Kobayashi, M. Yamashita, T. Sato, S. Muramatsu, *IEEE J. Quantum Electron.* QE-20 (1984) 1383.
- [28] M. Yamashita, S. Kobayashi, K. Torizuka, T. Sato, *Chem. Phys. Lett.* 137 (1987) 578.
- [29] J. Eisinger, M. Guéron, R.G. Schulman, T. Yamane, *Proc. Natl. Acad. Sci. U.S.A.* 55 (1966) 1015.
- [30] F.M. Winnik, *Chem. Rev.* 93 (1993) 587.
- [31] P. Vigny, *C. R. Acad. Sci., Ser. D* 277 (1973) 1941.
- [32] D. Markovitsi, A. Sharonov, D. Onidas, T. Gustavsson, *ChemPhysChem* 4 (2003) 303.

Femtosecond fluorescence studies of DNA constituents

T. Gustavsson, A. Sharonov, S. Marguet, D. Onidas and D. Markovitsi

Laboratoire Francis Perrin, CEA/DSM/DRECAM/SPAM - CNRS URA 2453
CEA/Saclay, F-91191 Gif-sur-Yvette, France

1. INTRODUCTION

UV exposure of DNA is known to trigger off photochemical reactions that ultimately may lead to carcinogenic mutations. However, the primary UV-induced processes in DNA preceding such reactivity remain unclear even after several decades of intense studies. With this in mind, we have recently undertaken a program aiming at improving the understanding of DNA photodamage. The ultimate goal is to develop a model for the excited state dynamical processes, and in particular the role of energy transfer, occurring within the DNA molecule after the initial energy deposition. Evidently, the success of this project relies on a precise knowledge of the photophysical properties of the excited states of its monomeric constituents (nucleobases, nucleosides, nucleotides) and how these properties translate into those of the organised system of DNA.

To study the excited state one may use transient absorption or time-resolved fluorescence techniques. In both cases, DNA poses many problems. Its steady-state spectra are situated in the near ultraviolet spectral region which is not easily accessible by standard spectroscopic methods. Moreover, DNA and its constituents are characterised by extremely low fluorescence quantum yields ($<10^{-4}$) which renders fluorescence studies particularly difficult. Based on steady-state measurements, it was estimated that the excited state lifetimes of the monomeric constituents are very short, about a picosecond [1]. Indeed, such an ultrafast deactivation of their excited states may reduce their reactivity; something which has been referred to as a "natural protection" against photodamage. To what extent the situation is the same for the polymeric DNA molecule is not clear, but longer excited state lifetimes on the nanosecond time scale, possibly of excimer like origin, have been reported [2-4].

Precise measurements of the excited state lifetimes of the DNA constituents were not available till very recently, mainly due to the limited time resolution of conventional spectroscopic techniques. Studying the DNA nucleosides by transient absorption spectroscopy, Kohler and co-workers observed a very short-lived induced absorption in the visible which they assigned to the first excited state [5,6]. The lifetimes observed were all well below 1 picosecond. The first femtosecond fluorescence studies of DNA constituents were performed using the fluorescence upconversion technique. Peon and Zewail [7] reported that the excited state lifetimes of DNA/RNA nucleosides and nucleotides all fall in the sub-picosecond time, thus corroborating the results obtained by transient absorption.

At the same time we have, in a series of papers, pursued the study of DNA constituents using the fluorescence upconversion technique [8-11].

2. EXPERIMENTAL

The fluorescence upconversion set-up is described in more detail in [8]. Briefly, the third harmonic of a mode-locked Ti:sapphire laser (40 mW at 267 nm) was used as an excitation source. The fluorescence was collected by parabolic mirrors and focused into a 1 mm thick BBO type I crystal together with the residual beam of the fundamental radiation. The sum-frequency light thus generated was spectrally filtered by a double grating monochromator and detected by a photomultiplier running in photon counting mode. The apparatus function was determined by measuring the width of the dominant Raman line of water at 296 nm and was found to be around 450 fs (fwhm). Experimental data were analysed by fitting with mono- or bi-exponential functions convoluted with a Gaussian apparatus response function. We judge that the time resolution of our set up is 100 fs after deconvolution.

3. RESULTS AND DISCUSSION

An example is given in Fig. 1, where normalized total fluorescence decays are shown for 2'-deoxynucleosides and 2'-deoxynucleotides. In contrast to previous findings our work revealed that the fluorescence decays are complex and cannot be described by single exponentials. They consist of an ultrafast component (< 200 fs) and a slower one (ranging from about 0.4 ps for 2'-deoxyadenosine up to 1.4 ps in the case of 2'-deoxycytidine monophosphate).

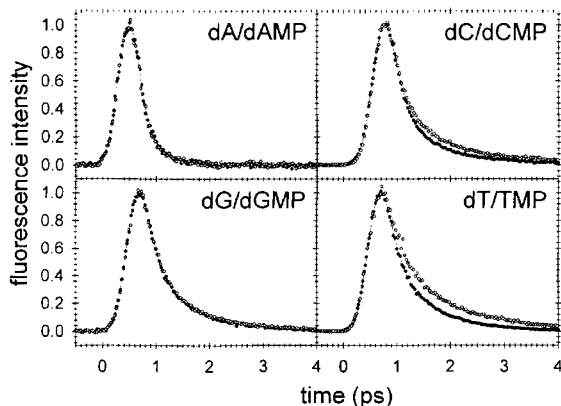


Fig. 1. Total fluorescence decays are shown for 2×10^{-3} M aqueous solutions of 2'-deoxynucleosides (filled circles) and 2'-deoxynucleotides (open circles) recorded at 330 nm. The excitation wavelength was 267 nm.

It is worth noting that the fluorescence decays and quantum yields are the same for 2'-deoxynucleosides and 2'-deoxynucleotides in the case of purines (dA/dAMP and dG/dGMP) while for the pyrimidines (dC/dCMP and dT/TMP), the fluorescence quantum yields of nucleotides are higher and the fluorescence decays slower as compared to those of the corresponding nucleosides. This shows that the phosphate moiety does affect the excited state relaxation to a certain extent.

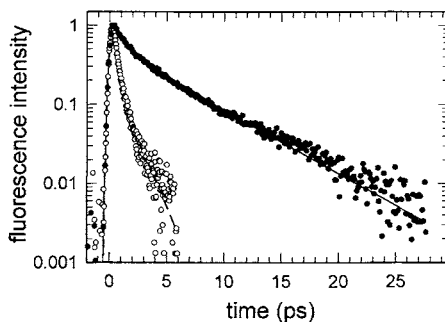


Fig. 2. Total fluorescence decays of 5-methyl-2'-deoxycytidine (5m dC) (filled circles) and 2'-deoxycytidine (dC) (open circles) recorded at 330 nm. The excitation wavelength was 267 nm.

In addition to the normal DNA bases mentioned above, various substituted species occur naturally. Among these the most important substitution is without doubt methylation. Cytosine methylated on the 5-position is supposed to play a key role in biological functions such as regulation of gene expression and genome reprogramming. Interestingly, it also seems that cytosine methylation determines hotspots of DNA damage which can be induced by sunlight. Despite the fact that 5-methylcytosine is a preferential target for carcinogenic mutation caused by UV radiation, the underlying photophysical and photochemical mechanisms are not understood. In order to shed more light on this problem, we have studied 5-methyl-2'-deoxycytidine (5m-dC) by fluorescence upconversion. An example is shown in Fig. 2, where the fluorescence decays of 5-methyl-2'-deoxycytidine (5m-dC) and 2'-deoxycytidine (dC) are shown [12]. As can be seen, methylation causes a huge increase in fluorescence lifetime. The mean decay time for the 5m-dC excited state (2.8 ps at 330 nm) is about one order of magnitude longer than for dC (0.3 ps at 330 nm). This fact, combined with its red-shifted absorption spectrum may explain, at least in part, why 5m-dC is a preferential target for carcinogenic mutation caused by UV radiation.

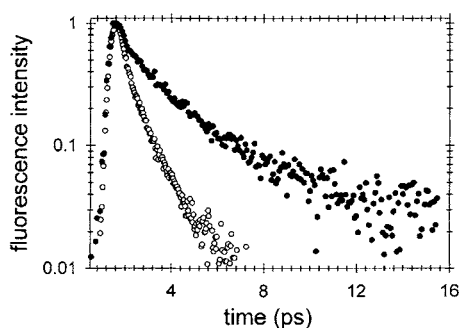


Fig. 3. Total fluorescence decays of the double stranded oligomer $(dA)_{20} \cdot (dT)_{20}$ (filled circles) and an equimolar mixture of the nucleotides dAMP and TMP (open circles) recorded at 330 nm. The excitation wavelength was 267 nm.

As indicated in the introduction, we have also extended our studies to oligomeric single and double strands of well-defined length [13]. An example is shown in Fig. 3, where

the fluorescence decays of the double stranded oligomer $(dA)_{20} \cdot (dT)_{20}$ and an equimolar mixture of the corresponding nucleotides dAMP and TMP are shown. It can clearly be seen that the fluorescence lifetime of the highly ordered double stranded oligomer is much longer than that of the nucleotide mixture. As for the monomers though, the decay of the double strand is bi-modal, consisting of a fast component (0.4 ps) and a slower one (2.4 ps). Also for the single strands the fluorescence decays are found to be bi-modal, consisting of a fast component (0.3 ps for both $(dA)_{20}$ and $(dT)_{20}$) and a slower one (1.6 ps for $(dA)_{20}$ and 1.5 ps for $(dT)_{20}$). The effect of molecular organisation is thus clearly observed also for the single strands, although their geometry is less well-defined than for the double strand.

The influence of the molecular organisation on the excited state deactivation rate observed for both single and double strands may or may not be related to a change of the nature of the emitting state. In the simplest case, the emitting states of the oligomers are the same as for the corresponding nucleotides, only that the non-radiative relaxation process(es) are affected by a modification of the local environment. Another possibility is that the oligomer emission still emanates from a monomeric unit, but one undergoing or having undergone excited state reactions such as tautomerisation or proton transfer. Finally, the emitting states of the oligomers may be delocalised over several monomeric units. The main finding is that single and double strands have substantially longer lifetimes which could increase the reactivity of their excited states and, thus, the probability to induce damages of the double helix.

In parallel, numerical simulations based on the exciton theory and quantum chemistry methods have shown that the lowest excited state of $(dA)_{20} \cdot (dT)_{20}$, having an ideal regular geometry, is indeed delocalised over all the whole double helix [14]. However, before making any comparison with the experimental results, the structural disorder, naturally occurring in double strands, as well as excited state relaxation has to be taken into account. Only then will it be possible to correctly address the issues evoked in the introduction, and develop a deeper understanding of DNA photodamage. We are currently working in this direction.

REFERENCES

- [1] M. Daniels, W. Hauswirth, *Science*, 171 (1971) 675.
- [2] J. P. Ballini, M. Daniels and P. Vigny, *J. Luminescence*, 27 (1982) 389.
- [3] S. Georghiou, T. M. Nordlund, A. M. Saim, *Photochem. Photobiol.*, 41 (1985) 209.
- [4] R. Plessow, A. Brockhinke, W. Eimer and K. Kohse-Höinghaus, *J. Phys. Chem. B*, 104 (2000) 3695.
- [5] J.-M. L. Pecourt, J. Peon and B. Kohler, *J. Amer. Chem. Soc.*, 122 (2000) 9348.
- [6] J.-M. L. Pecourt, J. Peon and B. Kohler, *J. Amer. Chem. Soc.*, 123 (2001) 10370.
- [7] J. Peon, A. H. Zewail, *Chem. Phys. Lett.*, 348 (2001) 255.
- [8] T. Gustavsson, A. Sharonov, D. Markovitsi, *Chem. Phys. Lett.*, 351 (2002) 195.
- [9] T. Gustavsson, A. Sharonov, D. Onidas, D. Markovitsi, *Chem. Phys. Lett.*, 356 (2002) 49.
- [10] D. Onidas, D. Markovitsi, S. Marguet, A. Sharonov, T. Gustavsson, *J. Phys. Chem. A*, 106 (2002) 11367.
- [11] A. Sharonov, T. Gustavsson, V. Carré, E. Renault, D. Markovitsi, *Chem. Phys. Lett.*, (2003) in press.
- [12] A. Sharonov, T. Gustavsson, S. Marguet, D. Markovitsi, *Photochem. Photobiol. Sci.*, 2 (2003) 1.
- [13] D. Markovitsi, A. Sharonov, D. Onidas, T. Gustavsson, *ChemPhysChem*, 3 (2003) 303.
- [14] B. Bouvier, T. Gustavsson, D. Markovitsi, P. Millié, *Chem. Phys.*, 275 (2002) 75.

Ultrafast vibrational spectroscopy on DNA

Olaf F. A. Larsen and Sander Woutersen

FOM-Institute for Atomic and Molecular Physics, Kruislaan 407, 1098 SJ Amsterdam, The Netherlands

1. Introduction

Ultrafast mid-infrared transient-absorption measurements on DNA oligodeoxyribonucleotide duplexes, consisting of 20 alternating guanine and cytosine moieties, (dG-dC)₂₀, were performed. Two different secondary DNA structures of the duplex have been studied: B-helical (a right-handed helix) and Z-helical (a left-handed helix). In Z-DNA, the phosphates in the sequence are closer to the helical axis, and their conformations are different for CpG and GpC. Z-DNA is believed to play a significant role in important processes in the cell, like gene regulation and DNA replication [1].

We have measured the spectral relaxation of the guanine CO-stretch mode for both DNA conformations. The frequency of this mode depends strongly on the instantaneous length of the hydrogen bonds connecting guanine and cytosine [2], through (i) the hydrogen-bond-induced redshift of the CO-stretch mode, and (ii) the coupling between the cytosine and the guanine stretch modes, which varies with the distance between the two bases (see Fig. 1). Therefore, the spectral relaxation of the CO-stretch mode will mirror the dynamics of the hydrogen bonds which form the double helix.

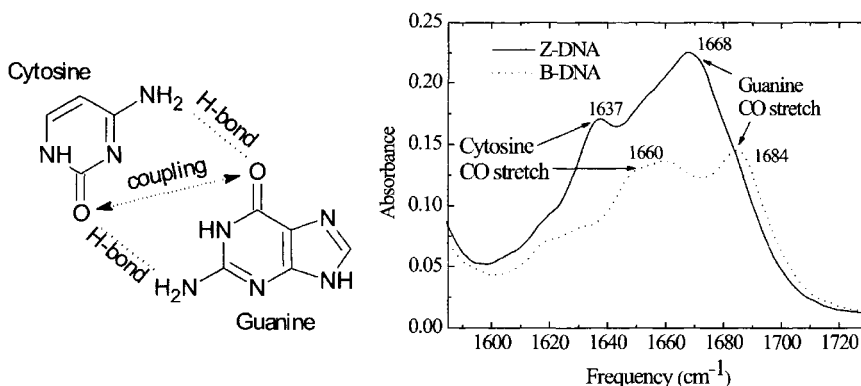


Fig. 1. (left) Basepairing between a guanine-cytosine basepair and coupling of the CO-stretch vibrations. (right) Linear infrared absorption spectra of CO-stretch region of the studied duplexes.

2. Ultrafast mid-infrared transient-absorption spectroscopy

The guanine CO-stretch vibration is excited at three different pump frequencies with a spectrally narrow laser pulse (FWHM ~ 12 cm^{-1}). Transient-absorption spectra are measured using a systematically delayed, spectrally broad, probe pulse. A negative transient-absorption signal indicates a bleaching, whereas a positive signal reflects excited-state absorption. The overall decay of the signal is due to T_1 relaxation.

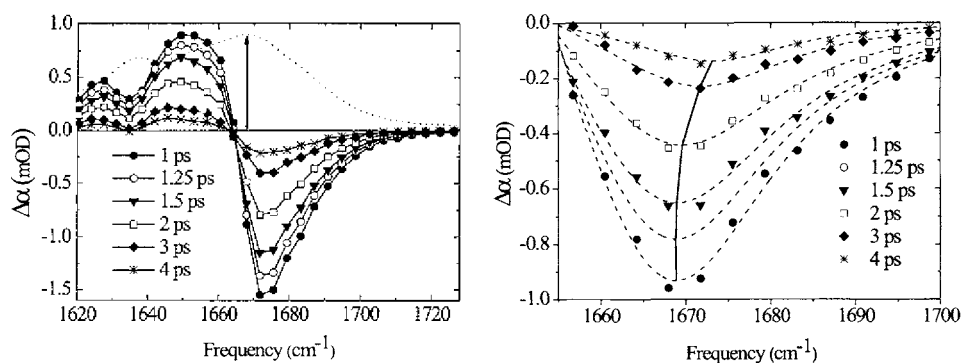


Fig. 2. (*left*) Transient-absorption spectra of the Z-DNA helix. The dotted line is the steady-state absorption spectrum, the arrow indicates the pump frequency at 1668 cm^{-1} (the center frequency of the guanine CO-stretch band). (*right*) Close up of the bleaching region of the Z-DNA helix when exciting at 1653 cm^{-1} , in the red edge of the guanine CO-stretch absorption band. The dotted lines are guides to the eye. The solid line is drawn through the minima of the bleaching, demonstrating a blue shift.

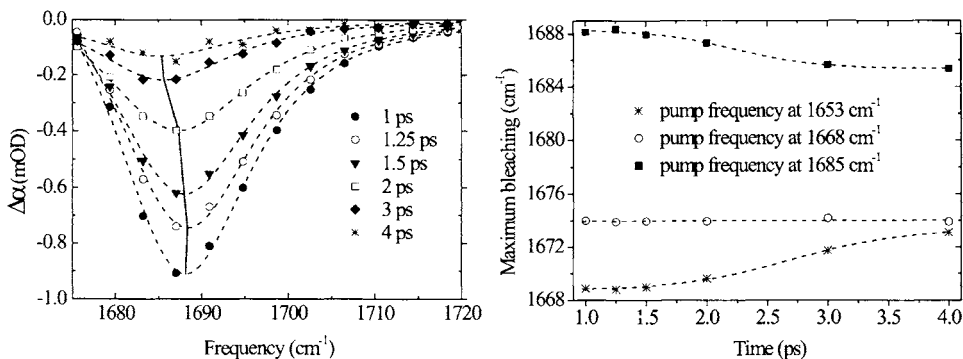


Fig. 3. (*left*) Close up of the bleaching region of the Z-DNA helix when exciting at 1683 cm^{-1} , in the blue edge of the guanine CO-stretch absorption band. The dotted lines are guides to the eye. The solid line is drawn through minima of the bleaching, demonstrating a red shift. (*right*) Minima of the bleaching of Z-DNA as a function of pump-probe delay time, demonstrating spectral relaxation.

When exciting the guanine CO-stretch, a strong signal at the CO-stretch frequency of cytosine is observed, showing the coupling between these two modes. The transient spectra change with pump frequency for both B- and Z-DNA, demonstrating that the CO band is inhomogeneously broadened. This inhomogeneity suggests that there exists a distribution of hydrogen-bond lengths for both types of duplexes. In the case of Z-DNA, when exciting at the high-frequency side of the absorption band, the bleaching maximum shifts towards lower frequencies with increasing delay, and vice versa (see Figs. 2 and 3). We believe this spectral relaxation represents the dynamics of the hydrogen bonds: apparently a part of the hydrogen-bond fluctuations occurs on a picosecond timescale. Besides this fast relaxation, the measurements also show evidence for a slower relaxation: even for largest delay values, the transient spectra still exhibit a dependence on the pump frequency (see Fig. 3, right panel).

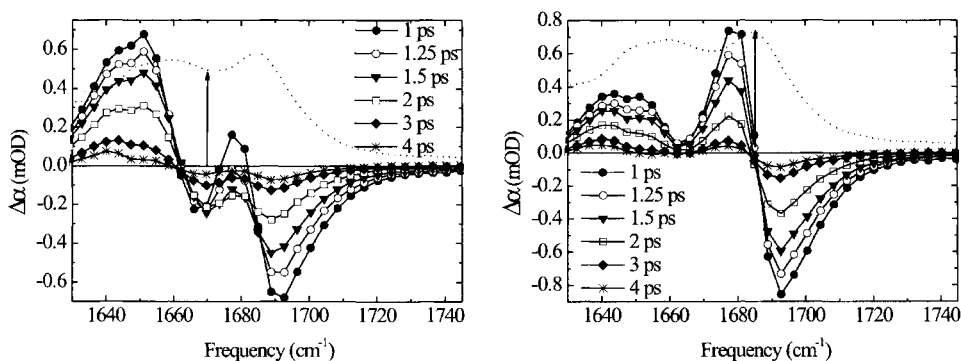


Fig. 4. (*left*) Transient-absorption spectra of the B-DNA helix. The dotted line is the steady-state absorption spectrum, the arrow indicates the pump frequency at 1670 cm^{-1} , the red edge of the guanine CO-stretch band. (*right*) Transient-absorption spectra of the B-DNA helix. The dotted line is the steady-state absorption spectrum, the arrow indicates the pump frequency at 1685 cm^{-1} (the center frequency of the guanine CO-stretch band).

The situation is more complicated for the B-DNA helix (see Fig. 4). Because of the stronger overlap between the guanine and cytosine CO-stretch absorption bands, it is more difficult to directly probe a spectral relaxation as observed for the Z-DNA helix.

REFERENCES

- [1] A. Nordheim and A. Rich, *Nature*, 303 (1983) 674.
- [2] V. Andrushchenko, H. Wieser and P. Bour, *J. Phys. Chem. B*, 106 (2002) 12623.

Ultrafast dynamics of normal and damaged DNA

Mark M. Somoza^{a,b} and Mark A. Berg^a

^aDepartment of Chemistry and Biochemistry, University of South Carolina
Columbia, South Carolina 29208 USA

^bCurrent address: Lehrstuhl für Physik Weihenstephan, Technical University of Munich
Vöttinger Straße 40, 85350 Freising, Germany

1. INTRODUCTION

Thermal fluctuations away from the average structure of DNA may play an important role in its biological function. Computer simulations predict that the amplitude of these fluctuations is quite large in the picosecond and nanosecond time scales [1, 2]. The resulting flexibility may be important for the 'indirect read-out' of sequence information by proteins, including the detection of damage by natural repair systems [3]. These fluctuations may also be responsible for 'gating' the transfer of charge along the DNA [4] and thereby affect the course of oxidative damage.

We have previously studied the dynamics of 'normal' DNA [5-8]. Here we present experimental evidence that DNA damage results in specific changes to its dynamics. Two kinds of prototypical DNA damage are studied and compared with an equivalent undamaged sequence. An 'abasic' sample reproduces the most common type of *in vivo* damage to DNA, the loss of a single base. The 'chain-end' sample explores a more severe type of damage, the disruption of the helical structure at the severed end of a DNA chain.

2. METHOD

The method is based on the ability of the excited state of suitable chromophores to both drive and respond to motions in their immediate environment. For example, coumarin excited states have a large dipole moment that causes nearby charged groups to move to stabilize the dipole. As these groups move and reduce the energy of the excited state, the fluorescence shifts toward the red. In simple solutions, this time-resolved Stokes shift (TRSS) experiment measures the time-dependent polarity of the solvent surrounding the coumarin [9].

Extending this experiment to DNA relies on a coumarin-102 deoxyriboside as a base-pair replacement [10]. Standard oligonucleotide synthesis techniques allow this probe to be placed into a DNA strand of any desired sequence. The TRSS experiment becomes sensitive to the time-dependent polarity experienced in the interior of the DNA. The polarity may have contributions from the movement of any of the charged groups intrinsic to the structure, such as the full charges on the backbone phosphates, the partial charges of the base pair heteroatoms, or the surrounding water and counterions.

Table 1. Oligonucleotide sequences. “*” – coumarin, “_” – abasic site.

1: ‘normal’ sequence	5’-GCATGCGC*CGCGTACG-3’ 3’-CGTACGCG_GCGCATGC-5’
2: ‘abasic’ sequence	5’-GCATGCGC*CGCGTACG-3’ 3’-CGTACG_G_GCGCATGC-5’
3: ‘chain end’ sequence	5’-C*CGCGTACGGCATGCG-3’ 3’-G_GCGCATGCCGTACGC-5’

When the coumarin is paired with an abasic site on the complementary strand, circular dichroism spectra, molecular modeling, spectral shifts, melting studies and measurements of solvent exposure are all consistent with the coumarin being intrahelical and replacing a base-pair within a normal B-DNA structure [6]. In addition, the modified oligonucleotides are recognized by an AP endonuclease with only modest reductions in binding and cleaving efficiency. Thus, the modified oligonucleotides are a good model for normal DNA.

The oligonucleotides in Table 1 were dissolved in 100 mM, pH 7.2 sodium phosphate buffer at a concentration of 0.1 mM in nucleotides (3 μ M in coumarin). Sample temperature was actively maintained at 15 °C to ensure that the DNA stayed fully annealed.

The time-resolved measurements were made using standard time-correlated single photon counting techniques [9]. The instrument response function had a typical full width at half-maximum of 50 ps. Time-resolved spectra were reconstructed by standard methods and corrected to susceptibilities on a frequency scale. Stokes shifts were calculated as first moments of cubic-spline interpolations of these spectra.

3. RESULTS

3.1. Normal DNA

Figure 1 plots the total dynamic Stokes shift of normal DNA (Sequence 1, Table 1). The Stokes shift of coumarin in ethanol is also shown for comparison. The total magnitude of the relaxation seen in the interior of DNA is surprisingly large—1650 cm^{-1} observed, with more possible outside our time range versus 2000 cm^{-1} in ethanol, a very polar solvent. A substantial fraction of the total relaxation (1000 cm^{-1} or 60% of the observed shift) occurs before 40 ps, the lower limit of the experimental time range.

However, much of the relaxation is spread over a broad range of long times—out to and beyond the 40 ns upper limit of the experimental time range. Over the three decades in time that are observed, the dynamics are logarithmic in time, i.e. the Stokes shift $S(t)$ is given by $S(t) = S_0 + A_0 \log_{10}(t/t_0)$. Previous results have shown that this very unusual logarithmic relaxation is common to unmodified DNA, independent of the sequence of bases [7]. In a recent paper, we discuss the important role of counterions [8]. However, they do not cause the logarithmic dynamics, nor does their role vary between the samples examined here.

3.2. Abasic site dynamics

Base deletions in DNA are common lesions and are also routinely introduced as an intermediate in the course of the repair of other types of lesions. The structural void and resulting flexibility has been suggested as a target for recognition by repair enzymes [3]. We looked for evidence of additional dynamics associated with abasic lesions by measuring the

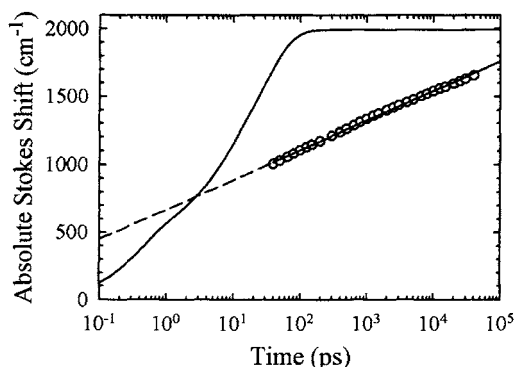


Figure 1. The absolute time-resolved Stokes shift for normal DNA (circles) is linear on a logarithmic time axis with a slope of $A_0 = 218 \text{ cm}^{-1}$ per decade. The Stokes shift of coumarin in a typical polar liquid [12] (ethanol, solid curve) is shown as a reference. The absolute Stokes shift is expected to reach zero near 0.1 ps. Extrapolation (dashed line) of the DNA fit does not reach this point, suggesting that a substantial change in the relaxation form occurs at early times.

Stokes shift of Sequence 2. This sequence is identical to the ‘normal’ one except for the replacement of a cytosine one base pair removed from the coumarin site by an abasic riboside (Table 1).

Figure 2a compares the time-resolved Stokes shift of the ‘normal’ sequence and the ‘abasic’ sequence. For ease of comparison, the data is shifted to overlap the sequences at early times. In the first nanosecond, the Stokes shifts from both sequences overlap almost perfectly. This result suggests that there is not a large scale collapse of the normal DNA structure at the abasic site. However after 1 ns, the ‘abasic’ sequence has additional dynamics beyond those of the normal sequence. The fit of the ‘abasic’ sequence has the same logarithmic component of the ‘normal’ sequence fit, but with an additional exponential term for the fast rise in the Stokes shift after 1 ns: $S(t) = S_0 + A_0 \log_{10}(t/t_0) + A_1(1 - \exp(-t/\tau))$, with an exponential time constant τ of 25 ns.

An interesting candidate for this motion is suggested by the molecular dynamics simulations of Barsky et al [11]. On a nanosecond time scale, they see a flipping of the abasic sugar from an intrahelical to an extrahelical position. This flip is correlated with a filling of the abasic site with water. Because our probe is sensitive to local polarity, it should be quite sensitive to this process.

3.3. Dynamics at a chain end

Sequence 3 examines chain-end effects on DNA dynamics. It contains the coumarin probe one base pair removed from the end of the sequence. This ‘chain end’ sequence has the same base pair sequence as the ‘normal’ sequence, but with entire sequence, including the coumarin, shifted towards one terminus. The Stokes shifts from the two sequences are displayed on a relative Stokes shift scale in Fig. 2b.

Reduced stability and ‘fraying’ of the chain is commonly expected near its end. However, the ‘chain end’ sequence has a total Stokes shift in our time window that is distinctly less than the Stokes shift in the ‘normal’ sequence. One way to explain this unexpected result is to note that the probe only has normal DNA on one side, so the amplitude of its contribution would be reduced. Any extra contribution from the solvent beyond the

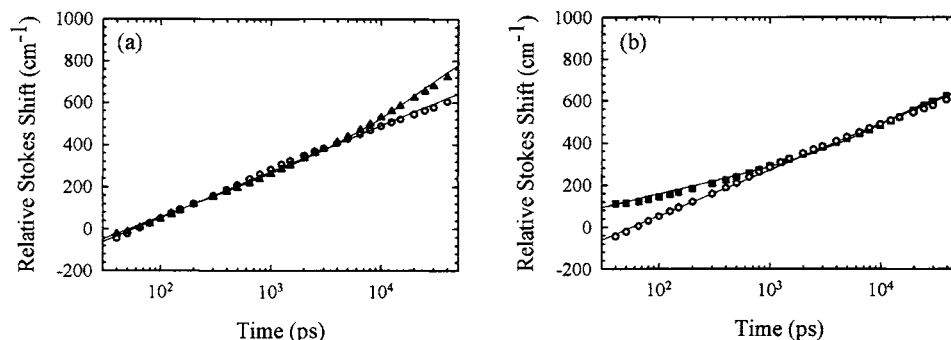


Figure 2. (a). Time resolved relative Stokes shift for abasic Sequence 2 (triangles) compared to the normal Sequence 1 (circles). (b). Chain-end Sequence 3 (squares) compared to the normal Sequence 1 (circles).

chain end would be over before the experimental time window began. Interestingly, the perturbations due to the chain end are confined to subnanosecond times. At long times, normal dynamics return.

4. CONCLUSIONS

Time-resolved Stokes shift have proven to be an effective means of measuring the dynamics of DNA on nanosecond and picosecond time scales. They have revealed a number of unusual features in the dynamics that are unique to DNA. The current results show that this method can also see variation in dynamics due to changes in DNA structure, including changes that mimic biologically relevant lesions.

This work was supported by the National Institutes of Health (GM-61292).

REFERENCES

- [1] M.A. Young, G. Ravishanker and D.L. Beveridge, *Biophys. J.*, 73 (1997) 2313-2336.
- [2] T.E. Cheatham and P.A. Kollman, *Annu. Rev. Phys. Chem.*, 51 (2000) 435-471.
- [3] V.M. Marathias, B. Jerkovic and P.H. Bolton, *Nucleic Acids Res.*, 27 (1999) 1854-1858.
- [4] R.N. Barnett, C.L. Cleveland, A. Joy, U. Landman and G.B. Schuster, *Science*, 294 (2001) 567-571.
- [5] E.B. Brauns, C.J. Murphy and M.A. Berg, *J. Am. Chem. Soc.*, 120 (1998) 2449-2456.
- [6] E.B. Brauns, M.L. Madaras, R.S. Coleman, C.J. Murphy and M.A. Berg, *J. Am. Chem. Soc.*, 121 (1999) 11644-11649.
- [7] E.B. Brauns, M.L. Madaras, R.S. Coleman, C.J. Murphy and M.A. Berg, *Phys. Rev. Lett.*, 88 (2002) 158101-158104.
- [8] L. Gearheart, M.M. Somoza, W.E. Rivers, C.J. Murphy, R.S. Coleman and M.A. Berg, *J. Am. Chem. Soc.*, 125 (2003) 11812-11813.
- [9] M. Maroncelli, *J. Mol. Liq.*, 57 (1993) 1-37.
- [10] R.S. Coleman and M.L. Madaras, *J. Org. Chem.*, 63 (1998) 5700-5703.
- [11] D. Barsky, N. Foloppe, S. Ahmadi, D.M. Wilson and A.D. MacKerell, *Nucleic Acids Research*, 28 (2000) 2613-2626.
- [12] M.L. Horng, J.A. Gardecki, A. Papazyan and M. Maroncelli, *J. Phys. Chem.*, 99 (1995) 17311-17337.

Sub-5-fs pulse generation from a noncollinear optical parametric amplifier and its application to ultrafast dynamics in polymers

Takayoshi Kobayashi

Department of Physics, University of Tokyo
7-3-1 Hongo, Bunkyo, Tokyo 113-0033, Japan

ABSTRACT

Transform-limited (TL) visible pulses with as short as sub-5-fs duration have been generated from a noncollinear optical parametric amplifier and applied to the study of polyacetylene, polydiacetylene, azobenzene, and J-aggregates of porphyrin for optical -devices.

1. INTRODUCTION

Transform-limited (TL) visible pulses with as short as 3.9 and 4.7-fs duration have been generated from noncollinear optical parametric amplifiers (NOPA)[1-7], and they were applied to the study of various systems [8-14]. We reported several new phenomena the direct observation of transition state during photochemical reaction by probing the change in the electronic transition probability induced by nuclear motion. In this paper four subjects are discussed. They are (1) NOPA, (2) polyacetylene, (3) polydiacetylene and (4) bacteriorhodopsin.

2. NOPA [1-7]

Transform-limited (TL) visible pulses with as short as sub-4-fs duration have been generated (figs.1-3) for the first time by several improvements made to our previous noncollinear optical parametric amplifier (NOPA)[6]. All of the signal-idler group-velocity matching and pump-signal pulse-front matching and angular dispersion matching of the parametric amplification processes and the final fine tuning of dispersion compensation using deformable mirror after a pair of chirped mirrors are essentially important to generate such short pulses. We demonstrated the generation of a continuous, simultaneously phase-matched 250-THz parametrically amplified spectrum. Resulting visible-near-IR signal-wave pulses have been compressed to a 4-fs duration using a micro-machined flexible mirror (fig. 1)[6]. Feedback for iterative computer-controlled dispersion compensation algorithm is based on pulse characterization by second-harmonic generation frequency-resolved optical gating (SHG FROG).

Tunable operation with bandwidth-limited sub-10-fs pulses in the visible (550-700 nm) and near infrared (900-1300 nm) was also performed by changing the seed delay with respect to the pump after increasing the seed chirp [10]. The NOPA is one of most useful light sources for ultrafast spectroscopy in the present stage on an extremely short time scale.

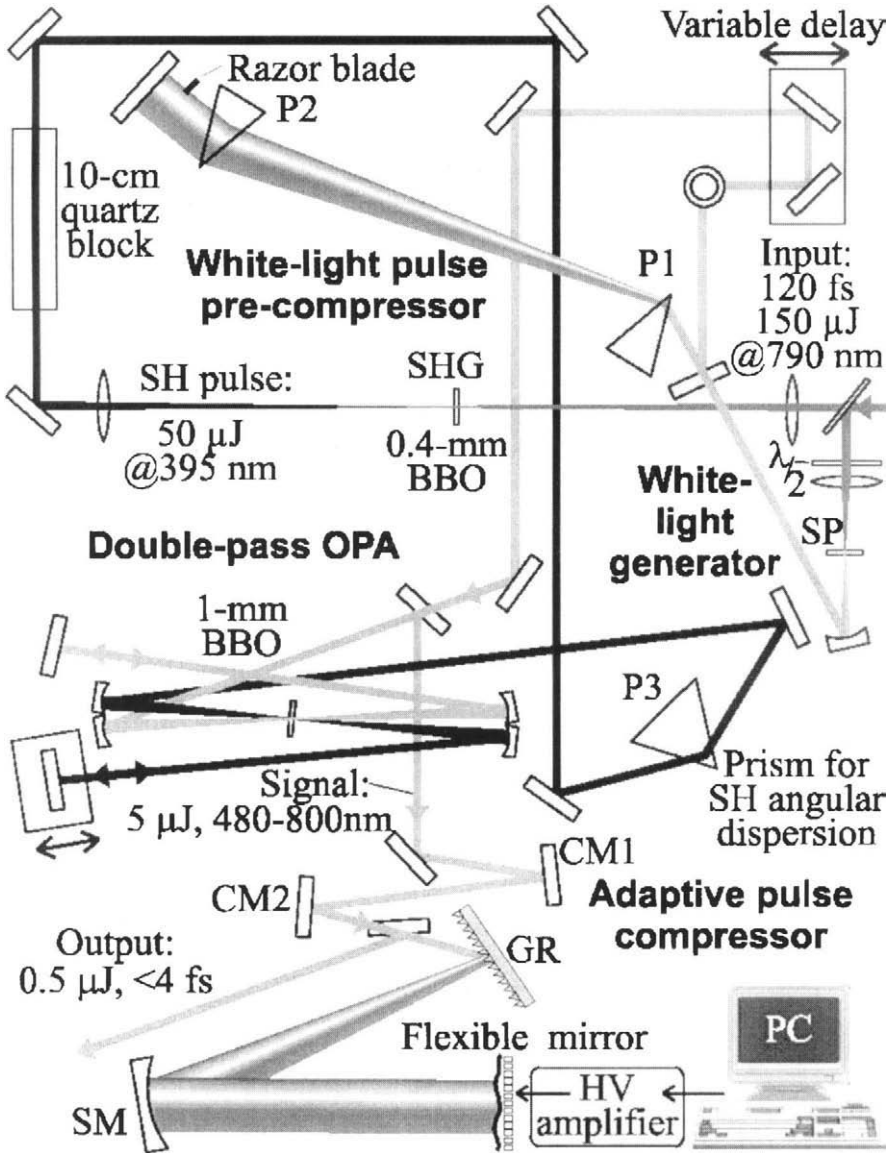


Fig. 1. Schematic of experimental setup. $\lambda/2$: -800 nm wave-plate; SP: 2-mm sapphire plate; P1, 2: 45° quartz prisms; P3: 69° quartz prism, the distance from P3 to the NOPA crystal is 80 cm; CM1, 2: ultrabroadband chirped mirrors; GR: 300 lines/mm ruled diffraction grating (Jobin Yvon); SM: spherical mirror, $R=-400$ mm; BS1, 2: chromium-coated $d=0.5$ mm quartz beam splitters. SHG crystal: 0.4-mm $\theta=29^\circ$ BBO (EKSMA); NOPA crystal: 1-mm $\theta=31.5^\circ$ BBO (Casix); SHG FROG crystal $\theta=29^\circ$ BBO wedge plate $d=5+20$ μm (EKSMA). Spherical mirrors around NOPA crystal are $R=-200$ mm; Thick arrows on the left indicate the data flow from the pulse diagnostic setup (SHG FROG) and the feedback to the flexible mirror.

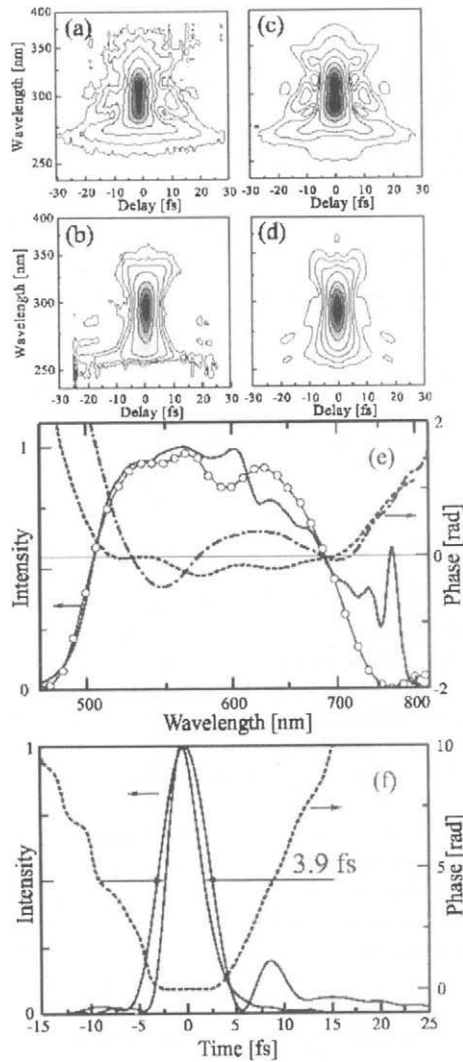


Fig. 2. Overview of pulse shaping results. (a) and (b) depict measured SHG FROG traces before and after adaptive phase correction, respectively. Corresponding retrieved traces are displayed in (c) and (d). (e) Shows fundamental spectrum (shaded contour) measured at the crystal location in the FROG apparatus and the spectrum recovered by the FROG retrieval algorithm (open circles). Dash-dotted curve represents spectral phase prior to adaptive shaping, whereas dashed curve shows the optimized phase. (f) Initial (solid curve) and optimized (shaded contour) temporal intensity profiles. Dashed curve depicts temporal phase of the optimized pulse.

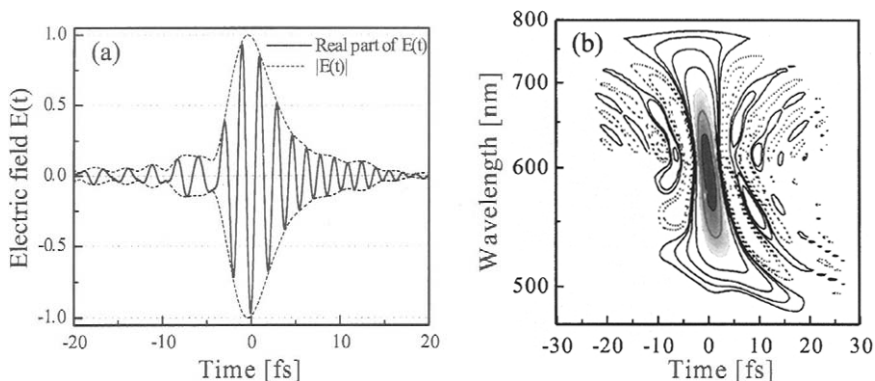


Fig. 3. Time dependent field of the 3.9fs pulse reconstructed from the FROG trace. The solid curve is the field and the dotted curve is the envelope of the field. The central wavelength is 595nm corresponding to the oscillation period of 2 fs. The carrier envelope cannot be determined and arbitrary phase is used for the description.

3. POLYACETYLENE [14]

Conjugate polymers are of great interest because of their possible applications to light-emitting diodes and optical memories. Among them polyacetylene is considered to be most basic because it is the simplest conjugated polymer and has been attracting scientists' interest because of its peculiar features of conductivity and spectroscopic properties. Especially it has a nonlinear excitation of soliton in a trans form, because of the degeneracy between $(-C=C-)_n$ (A-phase) and $(=C-C=)_n$ (B-phase). It was concluded by analysis using the Su-Schrieffer-Heeger Hamiltonian¹ that a photogenerated electron-hole pair evolves into a soliton-antisoliton pair within the 100-fs following the photoexcitation because of one-dimensionality of the system. It has been also theoretically predicted² that within this initial time the soliton pair is spatially localized, and it forms a dynamic bound state called a breather. In spite of many theoretical predictions, no clear experimental evidence of the existence of the breather has emerged so far probably because of the insufficient time-resolution of the experiments.

All the pump-probe signals at several probe wavelengths as shown in Fig. 4(a) depicts exhibit periodically oscillating features, which is a consequence of molecular vibrations. The oscillating components are extracted from the pump-probe kinetics and power spectra of the Fourier transform that were computed over the whole pump-probe delay range are shown in Fig. 4(c). They are composed of two peaks located at 1080 and 1470 cm^{-1} . The lower and the higher frequencies are close to those observed by stationary resonant Raman scattering, which are identified as the stretching modes of single and double bonds of carbon atoms, respectively³. In order to examine the time-evolution of the amplitude of each vibrational mode, we performed a spectrogram analysis. In Fig. 5, S and D correspond to two distinct peaks in Fig 4(c). In addition to these two modes, several broad bands (S', S'' and D', D'') appear in the spectrogram. Their bandwidths are broad because of their short lifetimes.

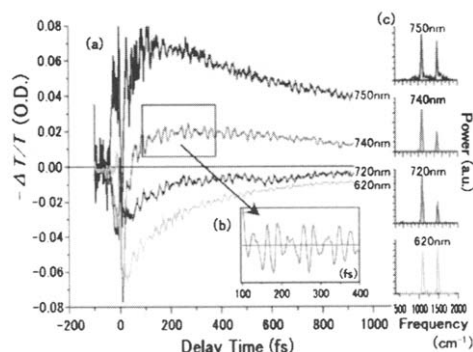


Fig. 4. (a) Time-dependence of pump-probe signals obtained for polyacetylene probed at several wavelengths. (b) Periodically oscillating components of the pump-probe signals probed at 740 nm extracted by applying a band-pass filter. (c) Power spectra of Fourier transform of the oscillating components of pump-probe signals integrated over the whole range of pump-probe measured delays.

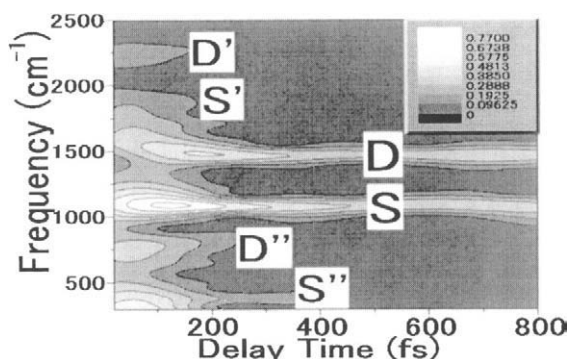


Fig. 5. Spectrogram of periodically oscillating components of pump-probe signals of polyacetylene probed at 750 nm shown in Fig. 4 and calculated using a Gaussian window function with a HWHM $\Delta t = 96$ fs. S and D denote the stretching modes of single and double bonds respectively. Short-lived satellite-bands (S' , S'' and D' , D'' associated with S and D modes, respectively) indicate the modulation induced by the breather state.

It is theoretically predicted that the formation of the breather is accompanied by the collective oscillation of the bond-length, which can be detected in the pump-probe experiment as modulation of the instantaneous vibrational frequencies. The simulation of a frequency distribution of the vibrational frequencies and a spectrogram was made with a modulation period of 44-fs and a modulation duration time of 50-fs. The evidence of the modulation appears in the spectrogram in the shape of satellite-bands S' , S'' and D' , D'' on both sides of the main vibrational modes S and D, respectively with the same separation. These sidebands do not appear in cis-rich samples. These results clearly suggests that the unidentified

short-lifetime modes visible in Fig. 4 can be explained by the modulation of the vibration modes, which is caused by the formation and the decay of the breather. The period of the modulation is thus determined to be 44-fs from the frequency separation between the main modes and the satellite-bands. This estimate agrees with the theoretical prediction of 33–50 fs^{1, 2}. We could thus directly observe using sub-5fs pulses the breather mode in trans-polyacetylene, which was predicted more than 15 years ago but has not been detected.

4. POLYDIACETYLENE [10]

We studied two different polydiacetylenes with different substituents groups and found several common interesting features in the real-time spectra and the spectrograms obtained from the time traces of the normalized transmittance changes in the real-time spectra of pump-probe experiment. They are the dynamic mode-coupling between the two stretching modes of C-C single and double bonds through a bending mode. The stretching mode of C-C triple bond appears just after sub-5fs pulses in both systems. The result confirm that the claim of the delayed appearance of the mode and its explanation of slow geometrical relaxation by a French group is not the case but it is simply a kind of artifact due to their limited time resolution.

5. BACTERIORHODOPSIN [11]

Real-time investigations of the rearrangement of chemical bonds during chemical transformations require femtosecond temporal resolution, so that the atomic vibrations within the reacting molecules can be observed. Following the development of lasers capable of emitting ultra-short laser flashes on this timescale, chemical reactions involving relatively simple molecules have been monitored in detail, revealing the transient existence of intermediate species as reactants are transformed into products. In this paper we report the direct observation of transition state during photochemical reaction by probing the change in the electronic transition probability induced by nuclear motion. A complex biological system, the retinal chromospheres of bacteriorhodopsin (bR₅₆₈), is studied as it undergoes the trans-cis photoisomerization that is fundamental to the vision process.

ACKNOWLEDGEMENTS

The work was done in collaboration with Drs. Shirakawa, Baltuska, Ohtani, and Kobryanskii, and Mr. Adachi.

REFERENCES

- [1] A. Shirakawa, I. Sakane, and T. Kobayashi, *Opt. Lett.*, 23 (1998) 1292
- [2] A. Shirakawa, I. Sakane, M. Takasaka, and T. Kobayashi, *Appl. Phys. Lett.*, 74 (1999) 2268
- [3] T. Kobayashi, A. Shirakawa, H. Matsuzawa, and H. Nakanishi, *Chem. Phys. Lett.*, 321 (2000) 385
- [4] T. Kobayashi and A. Shirakawa, *Appl. Phys. B* 70 (2000) S239
- [5] A. Baltuska, T. Fuji and, T. Kobayashi, *Phys. Rev. Lett.*, 88 (2002) 133901
- [6] A. Baltuska, T. Fuji and, T. Kobayashi, *Opt. Lett.* 27 (2002) 306
- [7] A. Baltuska and T. Kobayashi, *Appl. Phys. B*, 75 (2002) 427

- [8] H. Kano and T. Kobayashi Bull. Chem. Soc. Jpn, 75 (2002) 1071
- [9] H. Kano, T. Saito, and T. Kobayashi , J. Phys. Chem, B 105 (2001) 413
- [10] T. Kobayashi, A. Shirakawa, and T. Fuji, IEEE J. Quantum Electron, 7 (2001) 525
- [11] T. Kobayashi, T. Saito, and H. Ohtani, Nature, 414 (2001) 531
- [12] H. Kano, T. Saito, and T. Kobayashi, J. Phys. Chem. A, 106 (2002) 3445
- [13] H. Kano and T. Kobayashi J. Chem. Phys., 116 (2002) 184
- [14] S. Adachi, V. Kobryanskii, and T. Kobayashi, Phys. Rev. Lett., 89 (2002) 27401

Unveiling Electronic Phase Relaxation in a Strongly Disordered Conjugated Polymer

J. Sperling^a, F. Milota^a, A. Tortschanoff^a, V. Szöcs^b, L. Kuna^a, C. Benesch^a, and H. F. Kauffmann^a

^aInstitute of Physical Chemistry, University of Vienna, Währingerstrasse 42, A-1090 Vienna, Austria

^bInstitute of Chemistry, Comenius University, Mlynska Dolina CH 2, SK-84215 Bratislava, Slovakia

1. INTRODUCTION

Since conjugated polymers are serious candidates for a number of commercial opto-electronic applications, the photophysics of these π -electron macro-systems, at the boundary between small organic molecules and extended one-dimensional semiconductors [1], is of both technical and academic interest. For the prominent model system poly(p-phenylene-vinylene) (PPV), the meanwhile widely accepted model treats the π -conjugated polymeric backbone as a collection of homologous, oligomeric segmental sub-units. The lack of axial segment correlation leads to a statistical distribution of finite conjugation lengths, yielding a polychromophoric array of segmental sites distributed in length and self-energy. In the picture of molecular excitons, the longest-wavelength absorption band is then being identified as a manifold of inhomogeneously broadened, localized S_1 -levels, termed density-of-states (DOS). Upon broad-band excitation through a femtosecond (fs) laser pulse, on time-scales longer than the inverse of some global dephasing, the dispersion of segments gives rise to an uncorrelated excitonic population, whose energetic relaxation can be described by excitation energy transfer to sites of lower energy (i.e. to the bottom states of the DOS) [2].

Most of previous time-resolved studies, assuming a quasi-instantaneous population of the DOS after pulsed excitation, focused on this asymptotic regime of population relaxation (where any pulse-induced polarization has already lost its phase memory), leaving open questions about the *onset* of energy-dispersive hopping. In this very early stages of free evolution, quantum-dynamic gain-terms of many-body coherences and their dampings must be conjectured to set the initial boundaries and the hierarchical constraints for the generation of populations and their subsequent energy-downhill transfer. Apart from photon echo studies, performed on highly oriented films of polydiacetylene [3] and a more recent investigation on a (well-solvated) PPV-derivative in toluene [4], little is known about initial coherent dynamics and excitonic dephasing in (highly disordered) bulk polymers, the subject only beginning to be exploited experimentally. In the work to be presented here, we use femtosecond interferometry (fs-IF) under energy-specific excitation and fluorescence detection conditions to probe the initial coherence of low-energy bottom states of the DOS [5]. The experimental observable relies on the correlation of two wavepackets (WPs) that are prepared by the double-pulse excitation and probed via fluorescence interference.

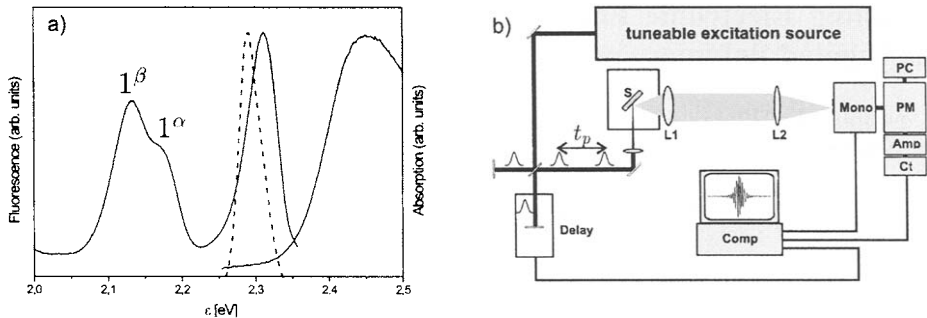


Fig.1. (a) Absorption and fluorescence of PPV at 1.4K, the dotted line shows the spectrum of an excitation pulse (centered at 2.292eV), 1^α and 1^β label the bimodal fluorescence transition; (b) Scheme of the experimental set-up: (S) Sample, (L1, L2) Lenses, (Mono) Monochromator, (PM) Photomultiplier, (PC) Peltier-Cooler, (Amp) Amplifier, (Ct) Counter, (Comp) Computer

2. EXPERIMENTAL STRATEGY

Generally, in fluorescence WP-IF [6], the interference of two wavepackets brought about by a pair of identical pulses (separated by t_p), is monitored via the time integrated, but spectrally resolved fluorescence $I_{int}(t_p; \epsilon)$. Assuming homogeneous dephasing, i.e. the structural relaxation to be much faster than fluorescence ($T_2' \ll T_1$), which is usually true for stilbenoid-type chromophores, it can be shown [7] that the fluorescence interference for a distinct fluorescence transition directly follows the functional form of the optical Free-Induction Decay (oFID). Thus, $I_{int}(t_p; \epsilon)$ is the Fourier transform analog of a Lorentzian absorption line (with central excitation frequency $\omega = \epsilon / \hbar$), following the optical cycles of the dipole-oscillation and a $1/T_2'$ dephasing rate determining the spectral width of the Lorentzian. Starting at this point, the two following, crucial considerations devise our experimental strategy (cf. Fig.1a). First, by tuning the central energy of excitation pulses into the far red-wing of absorption, i.e. into the bottom states of the DOS, where excitation energy transfer is negligible [2], we ensure that fluorescence results from the same states that were radiatively excited. In this regime, the lifetime of coherence can be expected to be mainly controlled by electron-nuclear coupling to intrinsic torsional/vibrational modes. Therefore, applying a narrow spectral bandwidth detector, the observable features are no longer limited by the inhomogeneous target area of pulsed excitation, but rather by the coherence time of the energy-sliced sub-space of the DOS, which is related to the natural (segmental) absorption linewidth. The second key-point of our approach is the detection of fluorescence at a bimodal spectral position, where the activation of vibrational modes creates two, discrete fluorescence arrival-states (hereafter termed 1^α and 1^β), i. e. the emitted photons originate from two independent, radiative deactivation processes. The detector counts the iso-energetic, 1^α - and 1^β -photons simultaneously, and consequently, there are now *two* site sub-ensembles of the DOS which are projected out from the polarization target area launched by the excitation pulses. Subsuming the experimental boundaries, our goal is the detection of an *internal* heterodyne beating of site-optical Free Induction Decays in a disordered many-body system. The experiment was realized [5] at low phonon-temperatures (1.4K) with a spin-casted film of PPV on a sapphire substrate, using 70fs excitation pulses (characterized by second-order intensity autocorrelation) from a commercial oscillator/amplifier/OPA-system. Fig.1b shows

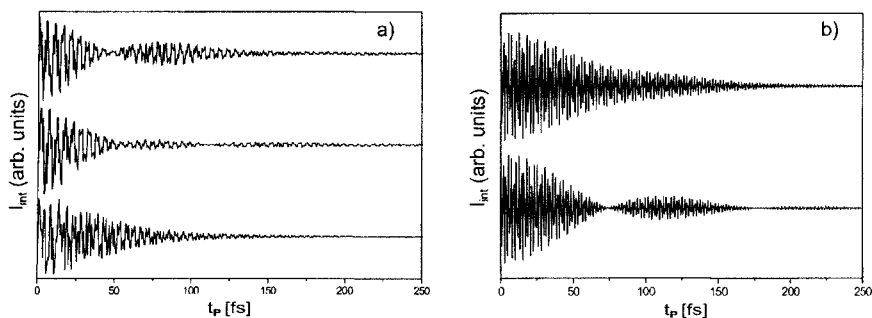


Fig.2. (a) Interferometric scans for a central excitation energy at 2.292eV and detection at (top to bottom) 2.175eV and 2.138eV; for comparison, the lowest scan shows the (linear) first-order pulse-to-pulse correlation (detected at 2.292eV); (b) Synthetic data interferograms for excitation at 2.296eV and detection at 2.187eV (top) and 2.175eV (bottom)

the scheme of the experimental set-up, which basically consists of the light source, a Michelson-type interferometer, and the detection unit. We note that, in this method [6], the sample is excited through a pair of (weak) collinear, but freely propagating (not phase-locked) pulses. The correlated fluorescence $I_{int}(t_p; \epsilon)$ was detected by means of a photomultiplier tube behind a narrow-band monochromator, with the resolution set to 10meV, which is a reasonable compromise to achieve sufficient fluorescence intensity and, at the same time, satisfactory spectral selectivity.

Fig.2a shows experimental interferometric scans, where the convolution-type fluorescence interference intensity $I_{int}(t_p; \epsilon)$ is plotted as a function of the pulse-to-pulse delay-time t_p . No special effort was undertaken to stabilize the interferometer, so the IFs have been not always perfectly symmetric for positive and negative pulse-to-pulse delays and the carrier frequency cannot be generally obtained accurately by direct Fourier inversion (even though the step-size would be small enough to fulfill the Nyquist theorem). However, this technical complication is not the broad point to be made here, rather, the relevant information lies in the significant oscillatory structure of the relaxation profiles which, apart from the high-frequency carrier wave, exhibit a low-frequency modulation, in terms of a beating oscillation. The observed beatings dephase in the limit of a critically damped wave, where damping-time and beating period have the same order of magnitude. The internal shape of the oscillatory structures has turned out to be very similar upon different excitation energies (within the red edge of absorption), provided the detection energy was energetically shifted along with excitation. Phenomenologically, the dependence on the relative excitation/detection-detuning indicates similar processes to be involved. As could be further expected from our assumptions, the beating patterns vanish for increased detection bandwidths, due to the destructive interference of multi-chromophore transitions (inhomogeneous dephasing). In addition, both at too high or too low detection energies, the beatings vanish as well, if the respective fluorescence windows are no longer resonant for iso-energetic detection of 1^α - and 1^β -photons. In this case, only a single transient (oFID), without any beating structure, can reach the detector. This result strongly favours the *inter*-segmental concept of polarization beating, hence no indications of intra-site quantum beats have been found.

3. CONCLUSIONS

Within the excitation boundaries of our experiment, we anticipate no electronic site-to-site coupling among the bottom states of the DOS, as it is the case in the high-density regime with a high degree of static (diagonal) site-disorder. Rather, on the time-scale of site structural equilibration, the wing states launched by the excitation pulse correspond to dynamically disordered ensembles in polarization space. Thus, following the concept outlined above, for the asymptotic part of single-cycle oscillation interferograms, the relaxation is mainly controlled by homogeneous site-dephasing, and the experimental data presented in Fig.2a provides a credible estimate of the electronic coherence time, i.e. the time-scale of site-structural relaxation to be of the order of 150fs. In a first approach to model the homogeneous dephasing process, triggered via (nuclear) torsional/vibrational intra-site motion, we used a Brownian oscillator model [8] in the low temperature limit and a phenomenological, exponential damping. Fig.2b shows results of numerical calculations, where the frequencies of two underdamped oscillations were set to the (1^α - and 1^β -) frequencies described before, and the interferometric signal computed for central excitation/detection-energies corresponding to the experimental values, in particular assuming a monochromator slit width of 7.5meV, (Gaussian) 60fs-pulses and a homogeneous dephasing time of 150fs. This relatively simple approximation explains the qualitative features quite adequately and has a profound resemblance with the experimental IFs. Systematic convolution of artificial data with T_2 varying from 50fs to 2ps have demonstrated that the overall profile of these interferograms is pronouncedly affected by the choice of the T_2 value in the homogeneous dephasing term, thus the control of the pulse-to-pulse correlation term is only small in the experimental data set of Fig.2a and a value for T_2 around \approx 130-150 fs appears in fact as a reliable order-of-magnitude for the site structural relaxation process. To recapitulate, we have demonstrated, by opening a quite novel perspective to look into homogeneous dephasing of a disordered many-body system, the experimental feasibility of probing initial site coherences in the segmental bottom-states of PPV [5].

Acknowledgements. This work was done within the Austrian Special Research Program ADLIS (F. M. and A. T.) and in the framework of the Austrian Science Foundation project P14884-CHE (L. K. and V. S.). J. S. is funded by the Doctoral Scholarship Program (DOC) of the Austrian Academy of Sciences, which is gratefully acknowledged.

REFERENCES

- [1] H. Bässler and L. J. Rothberg (eds.), *Chemical Physics on Excited State Phenomena in Conjugated Polymers*, Chem. Phys. 227 (1998)
- [2] J. Sperling, F. Milota, A. Tortschanoff, C. Warmuth, B. Mollay, H. Bässler, and H. F. Kauffmann, *J. Chem. Phys.* 117 (2002) 10877
- [3] T. A. Pham, A. Daunois, J.-C. Merle, J. LeMoigne, and J.-Y. Bigot, *Phys. Rev. Lett.* 74 (1995) 904
- [4] G. D. Scholes, D. S. Larsen, G. R. Fleming, G. Rumbles, and P. L. Burn, *Phys. Rev. B* 61 (2000) 13670
- [5] F. Milota, A. Tortschanoff, J. Sperling, L. Kuna, V. Szöcs, and H. F. Kauffmann, *Appl. Phys. A* (accepted)
- [6] O. Kinrot, I. S. Averbukh, and Y. Prior, *Phys. Rev. Lett.* 75 (1995) 3822
- [7] V. Szöcs, A. Tortschanoff, T. Palszegi, C. Warmuth, and H. F. Kauffmann, *J. Chem. Phys.* 112 (2000) 4652
- [8] S. Mukamel, *Principles of Nonlinear Optical Spectroscopy*, Oxford University Press, New York, 1995

Energy transfer in light-harvesting Zn porphyrin dendrimers

Jane Larsen^a, Johan Andersson^a, Tomáš Polívka^a, Joseph Sly^b, Maxwell J. Crossley^b, Villy Sundström^a, and Eva Åkesson^a

^aDepartment of Chemical Physics, Lund University, Box 124, SE-221 00 Lund, Sweden

^bSchool of Chemistry, The University of Sydney, NSW 2006, Australia

1. INTRODUCTION

The study of artificial photosynthesis has been the subject of ongoing attention for many years now due to the need for sustainable energy resources. In natural photosynthesis a light-harvesting antenna system with a large optical cross-section (for example the LH2 complex) absorbs a photon that is funneled by energy transfer (ET) to the reaction centre [1-3]. Excellent candidates to mimic the natural antenna system are molecules that efficiently absorb light and are able to transfer the captured energy to other parts of the molecule. Molecules based on Zn and free-base porphyrins are examples of compounds that can be used as models for the LH2 complex [4].

In the present study we investigated energy transfer between the Zn-porphyrin units in a sequence of dendrimers varying in size from 4 to 64 porphyrin units (Fig. 1). Reference measurements were performed on the monomer, P1D1. In order to follow energy transfer within the dendrimers, the fluorescence anisotropy decay were analysed. To determine the lifetime of the dendrimers, additional analysis of the kinetics measured at magic angle was performed. The fluorescence anisotropy is defined by

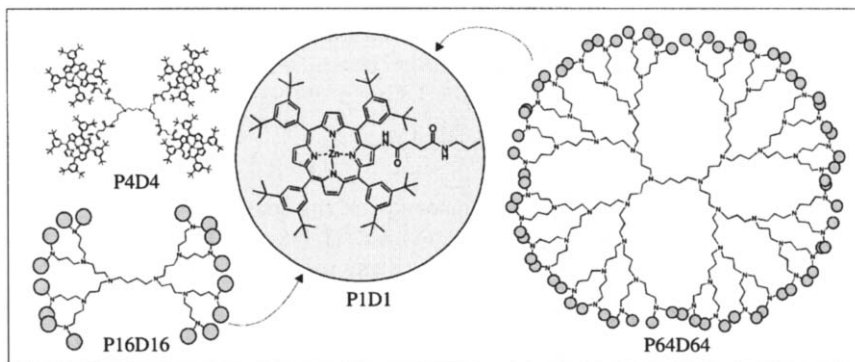


Fig. 1. Scheme of the dendrimers from the monomer (P1D1) to the fifth generation (P64D64). The grey circles in P16D16 and P64D64 correspond to a building block connected as illustrated for P4D4. It should be noted that in reality the dendrimers are not flat but spherically shaped. The porphyrins are mainly situated on the surface of the sphere, since they are too large for backfolding.

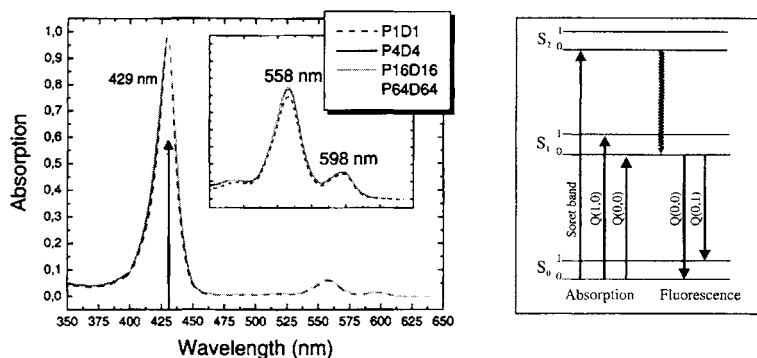


Fig. 2. Left: The absorption spectra of the compounds in a THF solution normalized at 429 nm. The extinction coefficients at 429 nm is 5.89×10^5 , 2.2×10^6 , 7.8×10^6 , and $3.1 \times 10^7 \text{ M}^{-1} \text{ cm}^{-1}$ for the compounds with increasing size. The arrow indicates the excitation light at 430 nm. Right: Energy scheme illustrating the transitions resulting in the fluorescence at 600 and 655 nm are the Q(0,0) and the Q(0,1) transitions, respectively.

$$r = \frac{I_{\parallel} - I_{\perp}}{I_{\parallel} + 2I_{\perp}} \quad (1)$$

where I_{\parallel} and I_{\perp} are the fluorescence intensities measured with a polarizer oriented parallel and perpendicular relative to the polarization of the excitation light, respectively. The anisotropy is $r_0 = 0.4$ directly after excitation if the dipole moment of the fluorescing transition and the excited transition is the same. As the molecules reorient, the polarization directions of the fluorescence approaches a random distribution, thereby decreasing the anisotropy value to zero. If energy transfer to other parts of the molecule takes place, additional decay of the anisotropy is observed. This process is dependent on the number of porphyrin groups close enough for energy transfer to take place, i.e. the size of the dendrimers, and the relative orientation of the donor and acceptor porphyrin.

2. STEADY-STATE ABSORPTION

The steady-state absorption spectra of the compounds are characterized by a strongly absorbing Soret band at 429 nm ($S_0 \rightarrow S_2$) and two minor Q-bands at 558 and 598 nm ($S_0 \rightarrow S_1$) (Fig. 2). Increasing size of the dendrimers does not produce any significant changes in the absorption spectra. This indicates weak interactions between the porphyrin units, i.e. the energy transfer can be described by Förster theory. Excitation of the dendrimers in the Soret band results in two fluorescence bands (not shown here) with maxima at 600 and 655 nm ($S_1 \rightarrow S_0$ for both transitions). Again, only minor differences can be observed dependent on size.

3. EXPERIMENTAL

The dendrimers were dissolved in a THF solution at room temperature to an optical density of 0.1 OD at 430 nm, and excited into the Soret band with a frequency-doubled femtosecond Ti:Sapphire oscillator (Spectra Physics). The intensity of the excitation light was kept at

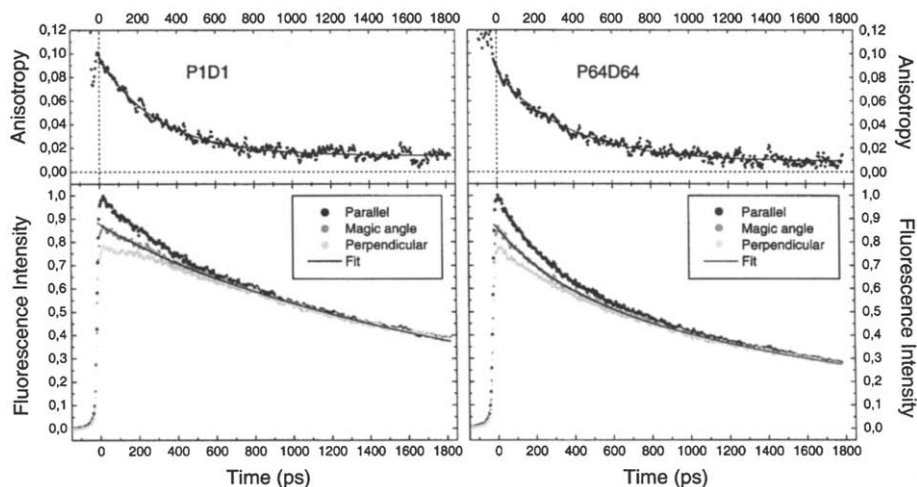


Fig. 3. The fluorescence decay (bottom) and the anisotropy (top) are shown for the building block P1D1 (left) and P64D64 (right). The fluorescence decay is detected at parallel, magic angle and perpendicular polarization relative to the excitation light, and the double-exponential fit of the magic-angle measurement is displayed in the figure as well. Along with the anisotropy decay, a single-exponential fit is shown.

10^{12} photons / (pulse \cdot cm²) in order to exclude the possibility of singlet-singlet annihilation. The fluorescence was detected in the spectral range from 575 - 675 nm with the use of a streak camera (Hamamatsu). The streak camera enables detection of both fluorescent bands simultaneously, but only the results for the 600 nm band will be presented here.

4. RESULTS

Fig. 3 shows fluorescence decays measured at parallel, magic angle and perpendicular polarization with respect to the excitation light (bottom panel) and the anisotropy decay (top panel) for the monomer and the largest dendrimer, i.e. P1D1 and P64D64. The fluorescence decays at magic angle can be fitted by a single exponential decay in the case of the monomer, but in the case of the dendrimers two exponentials are required. Common for all the compounds is a slow decay component with a time constant of roughly 2.1 ns reflecting the fluorescence lifetime of the compounds. The additional fast component in P4D4, P16D16, and P64D64 has a decay time of approximately 350 ps. There is no dependence of the lifetime depending on the size of the dendrimers. The results of the fits are summarized in Table 1.

The difference between the fluorescence decays of P1D1 and P64D64 could suggest a similar difference in the anisotropy decay. However, that is not the case as the anisotropy decays are almost identical. The initial anisotropy is approximately 0.1, which indicates that the electronic properties of the excited (S_2) and the fluorescing (S_1) states are quite different. However, an additional ultrafast anisotropy decay process cannot be ruled out since the time resolution in the experiments is 19 ps (FWHM). The anisotropy decays to a value of 0.01 on a timescale of 300 - 400 ps. The results show a relatively small increase in the decay time with increasing size of the dendrimers (see Table 1).

Table 1.
Double exponential fit of the fluorescence decay and single exponential fit of the anisotropy.

	Fluorescence Decay*				Anisotropy		
	A ₁ (%)	τ ₁ (ps)	A ₂ (%)	τ ₂ (ps)	r _∞	r ₀	τ (ps)
PID1	-	-	100	2129	0,013	0,083	303
P4D4	24	315	76	2157	0,013	0,073	330
P16D16	32	376	68	2250	0,016	0,076	330
P64D64	28	344	72	2171	0,009	0,076	370

* The fit functions are $I(t) = A_1 \exp(-t/\tau_1) + A_2 \exp(-t/\tau_2)$ and $r(t) = r_\infty + r_0 \exp(-t/\tau)$ for the fluorescence decay and the anisotropy decay, respectively

5. DISCUSSION

For the monomer, the only possible contribution to the anisotropy is rotation. The decay time of 303 ps corresponds well with previous findings in similar molecules [5]. In the case of P4D4, P16D16, and P64D64 two processes contribute to the anisotropy decay rotational motion and energy transfer. The rotational motion and hence the decay of rotational anisotropy of the dendrimers is expected to be significantly slower for larger dendrimers. Hence, the anisotropy decay for P64D64 should in theory only reflect a fast energy transfer process in the time window presented here. Measurements on a similar sequence of free-base porphyrins led to the conclusion that the energy transfer only occurs within one dendron consisting of four porphyrin units [4]. If the same is the case in the present Zn porphyrin dendrimers, the striking similarities in the anisotropy for P4D4, P16D16, and P64D64 are surprising, since the rotational time for P4D4 and P64D64 are expected to be very different. Additionally, the resemblance with the anisotropy decay of the monomer implies that the rotational contribution to the anisotropy decay of the dendrimers cannot be described simply as a rigid rotation of the whole molecule. The fluorescence originates from the porphyrin units that are connected through a single-bonded carbon chain. The nearly identical anisotropy decay in all the compounds therefore indicates that the individual porphyrin units have a large degree of rotational freedom. The rotational motion of the compounds can be expected to be significantly slower at a lower temperature, thus enabling a separation of the two contributions to the anisotropy. Therefore, in order to investigate the energy transfer process more closely, measurements at low temperature are planned.

REFERENCES

- [1] E. K. L. Yeow, P. J. Santic, N. M. Cabral, J. N. H. Reek, M. J. Crossley, K. P. Ghiggino, *Phys. Chem. Chem. Phys.*, 2 (2000), 4281-4291.
- [2] V. Sundström, T. Pullerits, R. van Grondelle, *J. Phys. Chem. B*, 103 (1999), 2327-2346.
- [3] M. S. Choi, T. Aida, T. Yamazaki, I. Yamazaki, *Chem-Eur. J.*, 8 (2002), 2668-2678.
- [4] E. K. L. Yeow, K. P. Ghiggino, J. N. H. Reek, M. J. Crossley, A. W. Bosman, A. P. H. J. Schenning, and E. W. Meijer, *J. Phys. Chem. B*, 104 (2000), 2596-2606.
- [5] Y. H. Kim, D. H. Jeong, D. Kim, S. C. Jeoung, H. S. Cho, S. K. Kim, N. Aratani, and A. Osuka, *J. Am. Chem. Soc.*, 123 (2001), 76-86.

Femtosecond fluorescence upconversion studies of chiral self-assembled supramolecules in solution

P. Toele,^a H. Wang,^a H. Zhang,^a M. Glasbeek,^a J. J. van Gorp,^b and E.W. Meijer^b

^aLaboratory for Physical Chemistry, University of Amsterdam
Nieuwe Achtergracht 129, 1018 WS Amsterdam, The Netherlands

^bLaboratory of Macromolecular and Organic Chemistry, Eindhoven University of Technology,
P.O. Box 513, 5600 MB Eindhoven, The Netherlands

1. INTRODUCTION

Recently chirality of self-assembled stacks of C_3 -symmetrical disk-shaped molecules in polar protic solvents was reported [1]. The stacks result from the combined action of cooperative hydrogen bonding and π - π interactions. The synthetic compounds have large enough peripheral side chains to allow the formation of hydrophobic domains, which are believed to be important for the growth of directional chiral structures as e.g. also occurs in natural proteins. It appeared that by means of ultrafast time-resolved fluorescence spectroscopy information could be obtained concerning (i) the dynamics of excited-state intramolecular double proton transfer, (ii) the dynamics of excited-state solvation, and (iii) the influence of stacking on the chromophore fluorescent-state lifetime [1]. Here we extend our previous time-resolved fluorescence experiments to molecules TAB (1) and DAC (2) (Figure 1), in polar and apolar solvents.

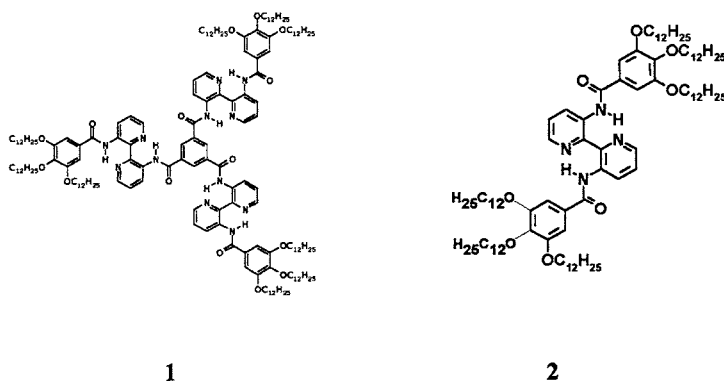


Fig. 1 Structures of the C_3 -disk molecule TAB (1) and the subgroup molecule DAC (2)

It is known that in polar chloroform, 1 remains in the molecularly dissolved state, but that in *n*-alkanes self-assembled chiral organized structures are formed [2]. Our experiments include the measurement of fluorescence transients under magic angle and polarization conditions. The

data provide information concerning the excited-state intramolecular proton transfer dynamics in **1** and **2** (typically ~ 250 fs), the lengthening of the lifetime of the fluorescent state by an order of magnitude upon chiral aggregation of the disk-shaped molecules **1** (from ~ 300 ps in chloroform to ~ 4 ns in *n*-heptane) and the dynamics of vibronic relaxation of **1** and **2** in the excited fluorescent state (several ps to 20 ps).

2. EXPERIMENTAL

Sample preparation was given elsewhere [2]. Femtosecond fluorescence upconversion and picosecond time-correlated single-photon-counting set-ups were employed for the measurement of the fluorescence transients. The system response (FWHM) of the femtosecond fluorescence up-conversion and time-correlated single-photon-counting setups are 280 fs and 16 ps, respectively [3]. The measured transients were fitted to multiexponential functions convoluted with the system response function. After deconvolution the time resolution was ~ 100 fs. In the upconversion experiments, excitation was at 350 nm, the transients were measured from 420 nm upto 680 nm. Experiments were performed under magic angle conditions (to remove the fluorescence intensity effects of rotational motions of the probed molecules), as well as under polarization conditions in order to obtain the time evolution of the fluorescence anisotropy.

3. Results

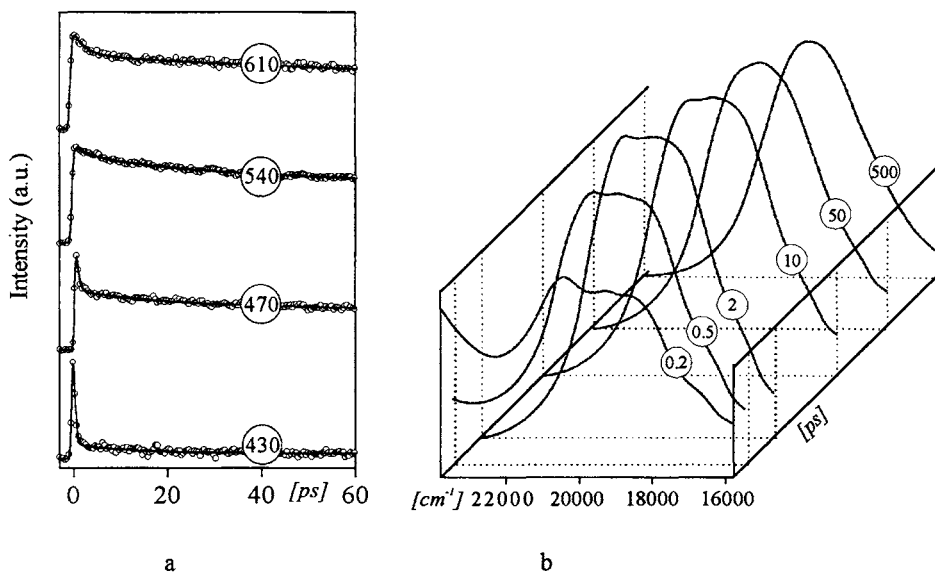


Fig. 2 (a) Fluorescence up-conversion transients of TAB dissolved in *n*-heptane. Detection wavelengths in nm are indicated in circles (b) reconstructed time-resolved fluorescence spectra of TAB in *n*-heptane

Figure 2a shows a few fluorescence upconversion transients as measured for **1** dissolved in *n*-heptane, under magic angle conditions. The transients show multi-exponential decay behavior

at all detection wavelengths. Figure 2*b* displays the time dependence of the corresponding emission spectrum of **1** as obtained after spectral reconstruction of the fluorescence transient data at a series of detection wavelengths. In fact, the emission shows a double-band structure: a very short-living band near 420 nm, with a lifetime of ~ 300 fs and a band peaking near 530 nm, with a ~ 300 fs rise time. The latter band reaches a maximum intensity after about 1 ps followed by a multi-exponential decay with typical times of ~ 2.6 ps (30%), ~ 84 ps (20%) and 4 ns (50%) when detection is near 610 nm. The upconversion transients as measured for **1** and **2**, were found to exhibit the same dynamic behavior, i.e., the same short-time behavior was measured for the excited-states of **1** and **2** for time windows upto 60 ps, regardless whether chromophore **1** is in the molecularly dissolved state (in chloroform) or in the aggregated form (in *n*-alkanes).

4. DISCUSSION

We first consider the ~ 300 fs decay, detected at 420 nm, accompanied by a simultaneous rise of the 530 nm band (Figure 2*b*). The result is observed for subgroup **2** as well as for **1**, in the aggregated and non-aggregated state. The results are analogous to those previously reported for 2,2'-bipyridyl-3,3'-diol [4]. For the latter compound a ~ 350 fs rise and decay of the fluorescence transients were shown to be caused by an excited-state intramolecular double proton transfer process. It was congested that the double proton transfer involves stretching- and bending modes of the skeleton leading to branched concerted and step-wise double proton transfer channels. Very recently this suggestion has been substantiated by means of transient absorption experiments for BP(OH)₂ with high-time resolution (20 fs) [5]. Similar double proton transfer processes may be considered to take place in molecules **1** and **2**, in particular the phototautomerization now involves the double proton translocation from the amide to the nitrogen in the pyridyl rings. However, for molecules **1** and **2**, the peak positions of the emission bands near 420 nm and 530 nm were found to be independent of the solvent polarity. This indicates that these emission bands originate in species for which the dipole moments in the excited state do not differ significantly from those of **1** and **2** in the ground state. It is inferred that the band at 420 nm originates in the chromophore in the Franck-Condon state (i.e., *before* proton transfer has taken place) and that the 530 nm band is due to the chromophore *after* the double proton transfer. The species that is formed after a single proton transfer (in the sequential process) and which is expected to have a dipole moment in its excited state quite different from that of the (symmetric) parent pyridyl groups in the ground state is not resolved.

In chloroform, the lifetime of the fluorescence state of **1** is comparable to that of **2** (~ 300 ps). This is as expected considering that **1** is dissolved in a dispersed molecular state [2]. In *n*-heptane, however, the lifetime of the fluorescence state of **1** is lengthened to ~ 4 ns, indicating that freedom is restricted when **1** is in the self-assembled aggregated state. Aggregation also gives rise to a red shift of the peak position of the lowest absorption band and to a narrowing of the emission band. The fluorescence decay measurements yielded also components with an intermediate lifetime on the order of 100 - 200 ps (10%). The presence of these components indicates that aggregation may not be complete at ambient temperature.

Time-resolved fluorescence polarization measurements for **1** and **2** in *n*-heptane showed that after pulsed excitation, the initial value of the fluorescence anisotropy is about 0.25. This

shows that on the time scale of the experimental time resolution (~ 100 fs) some ultrafast depolarization (from 0.4 to 0.25) has occurred. The residual fluorescence anisotropy showed a bi-exponential decay with time constants of ~ 20 ps and 10 ns for **1**, and ~ 20 ps and 300 ps for **2**, respectively. The 20 ps decay component in the anisotropy was also found in the depolarized fluorescence decay for both molecules (*vide supra*). We attribute the 20 ps component to vibrational relaxation of **1** and **2** in 'hot' product states. The fact that this component is also measured in the fluorescence depolarization transients reflects that vibrational relaxation is accompanied by electronic relaxation and thus that the 20 ps is due to a vibronic relaxation process in 'hot' molecules **1** and **2**. The longer time components in the fluorescence anisotropy decay (i.e. >10 ns for **1**, 300 ps for **2**) are characteristic of the reorientational motions of the molecules in the *n*-heptane solution. When the molecules **1** form an aggregate, the reorientational motions slow down appreciably and its characteristic time becomes even longer than the excited-state lifetime.

In conclusion, a typical time of ~ 300 fs has been found for the excited-state intramolecular double proton transfer in TAB and DAC. The proton transfer dynamics is not influenced by aggregation. In addition, a vibronic cooling time of ~ 20 ps has been measured for the probe molecules in the molecular and stacked configurations. Finally, aggregation is found to almost completely hamper the rotational diffusion motions of the molecules during the fluorescence state lifetime of 4 ns.

ACKNOWLEDGEMENT

This research was financially supported in part by the Council for Chemical Sciences of the Netherlands Organization for Scientific Research (CW-NWO).

REFERENCES

- [1] L. Brunsveld, H. Zhang, M. Glasbeek, J.A.J.M. Vekemans and E.W. Meijer, *J. Am. Chem. Soc.*, 122 (2000) 6175.
- [2] P. van der Schoot, M.A.J. Michels L. Brunsveld, R.P. Sijbesma and A. Ramzi, *Langmuir*, 16 (2000) 10076.
- [3] P. Toele, H. Zhang and M. Glasbeek, *J. Phys. Chem. A*, 106 (2002) 3651.
- [4] P. Proposito, D. Marks, H. Zhang and M. Glasbeek, *J. Phys. Chem. A*, 102 (1998) 8894.
- [5] S. Lochbrunner, K. Stock, C. Schrieffer and E. Riedle, *Proceedings Femtochemistry VI Conference* (Paris), Elsevier, 2004 (to be published).

Energy transfer process in dendrimers containing a perylene-terrylene donor-acceptor system investigated by femtosecond multicolor transient absorption spectroscopy

G. Schweitzer^a, S. Jordens^a, G. De Belder^a, M. Lor^a, E. Fron^a, K. Müllen^b and F. C. De Schryver^a

^aKatholieke Universiteit Leuven, Department Chemie, Celestijnenlaan 200F, 3001 Leuven, Belgium

^bMax-Planck-Institut für Polymerforschung, Ackermannweg 10, 55128 Mainz, Germany

1. INTRODUCTION

Dendrimers are highly branched macromolecular systems whose structure can be defined on a molecular level. Recent investigations [1,2] of different generations of rigid dendrimers containing a terrylenediimide chromophore in the center and peryleneimide chromophores at the rim gave evidence for a directional energy transfer between a peryleneimide donor and the terrylenediimide acceptor chromophore within these dendrimers. By means of polychromatic transient absorption measurements and by comparing transient absorption spectra of these dendrimers to different model compounds, this process is further investigated in detail.

2. MATERIALS AND METHODS

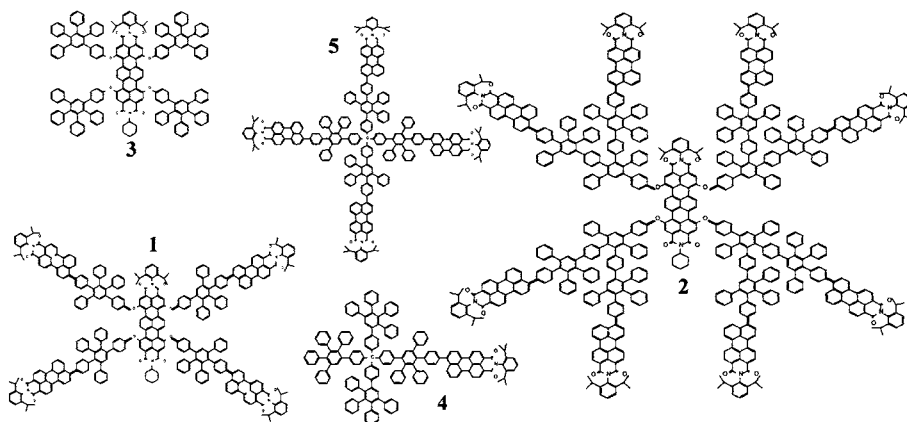


Fig. 1. Structures of compounds used in this investigation: 1 – first generation dendrimer, 2 – second generation dendrimer, 3 – terrylenediimide-only compound, 4 – peryleneimide-only compound, 5 – first generation dendrimer with tetracarboxylic core

Two different generations of dendrimers (Fig. 1: 1,2) have been investigated along with a set of three different model compounds (3,4,5), which only contain one of the donor-acceptor pair chromophores. For excitation, 250fs laser pulses at 495nm generated in an OPA pumped by a regeneratively amplified fs laser system [3] were used. The multicolour transient absorption changes were probed using a fs white light continuum and a CCD camera detection system [4]. In order to account for possible multiphotonic processes, a series of excitation energy dependent measurements was performed. All samples were dissolved in toluene and excited with laser pulses of <100 nJ energy and a repetition rate of 1 kHz. All measurements were analyzed globally using 512 delay positions, 40 spectra and three time windows.

3. RESULTS AND DISCUSSION

3.1. Steady State Measurements

The steady state absorption and fluorescence spectra of both dendrimer generations 1 and 2 are depicted in Fig. 2. The former are merely superpositions of the absorption spectra of both chromophores involved. In the fluorescence, however, the peryleneimide part is almost completely quenched compared to the model compound. Instead, the fluorescence at wavelengths longer than 650 nm almost completely resembles the emission spectrum of the terylene-diimide model compound 3. This feature is a strong indication that within these dendrimers the excitation energy is efficiently transferred from the peryleneimide to the terylenediimide.

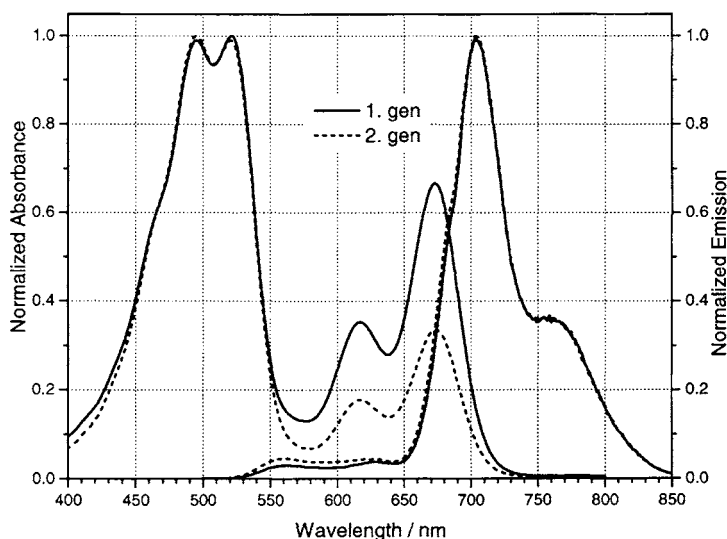


Fig. 2. Normalized steady state absorption (left part) and fluorescence spectra (right part) of first generation dendrimer (solid line) and second generation dendrimer (dotted line).

3.2. Transient absorption spectra of the model compounds

The transient absorption of **3** is decaying at 3.2 ns. It has a negative amplitude throughout the complete spectrum except 450...550 nm. By close inspection of this range and comparison to previous results [1], these additional features are attributed to vibrational/solvent relaxation (6 ps) and a structural relaxation process (120 ps).

For the reference compound **4**, two different parts in the transient spectrum were found (data not shown): a negative signal (480...600 nm) resulting from a combined ground state bleaching and excited state absorption, and second positive part (>600 nm) due to excited state absorption. Both decay on a ns time scale. Close inspection of the spectra reveals another process with a time constant of 10 ps, which in accordance with previous results [1] is attributed to vibrational/solvent relaxation.

Another series of experiments was performed on **5**. As in **4**, ns fluorescence decay and vibrational relaxation kinetics were determined. Additionally, another component of ca. 10 ps is found, which is attributed to annihilation and discussed in detail elsewhere [5].

3.3. Transient absorption of the first generation dendrimer

A set of transient absorption spectra of **1** is shown in Fig. 3. At 0.8 ps, i.e. immediately after excitation, the spectrum is completely identical to the one of **4**. Then, this transient spectrum undergoes changes on a very fast time scale of a few ps. Finally, at delay times longer than 20 ps it exactly resembles the one of **3**. Clearly, the excited peryleneimide transfers its energy to the central terrylenediimide, yielding a ground state peryleneimide and a S_1 -state terrylenediimide. This is detected as a large ingrowing signal with a maximum at 685 nm, which is a wavelength dependent combination of ground state bleaching (preferentially at $\lambda < 700$ nm) and stimulated emission ($\lambda > 700$ nm) in the terrylenediimide [4]. Using global analysis, besides the components known from the model compounds, two additional kinetic components with time constants of 4 ps and 30 ps were determined. They agree very well with previously reported fluorescence upconversion data [1] and are attributed

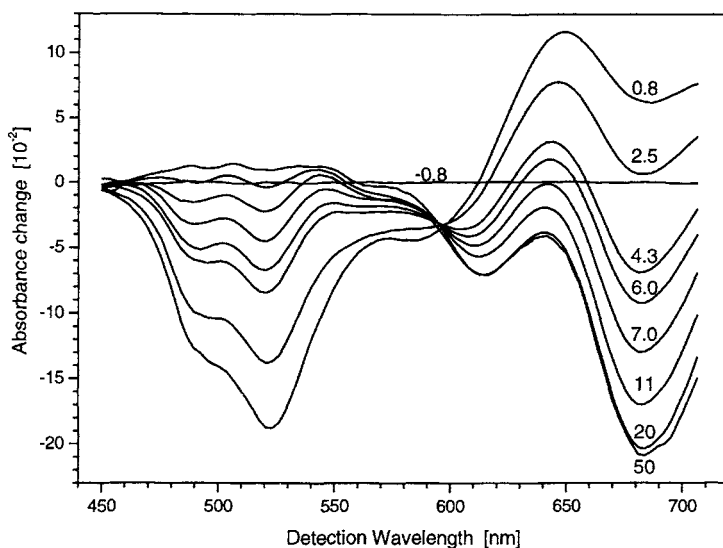


Fig. 3. Transient Absorbance changes determined for the first generation dendrimer **1**. The numbers at the curves indicate the time after excitation in ps. Excitation wavelength was 495 nm

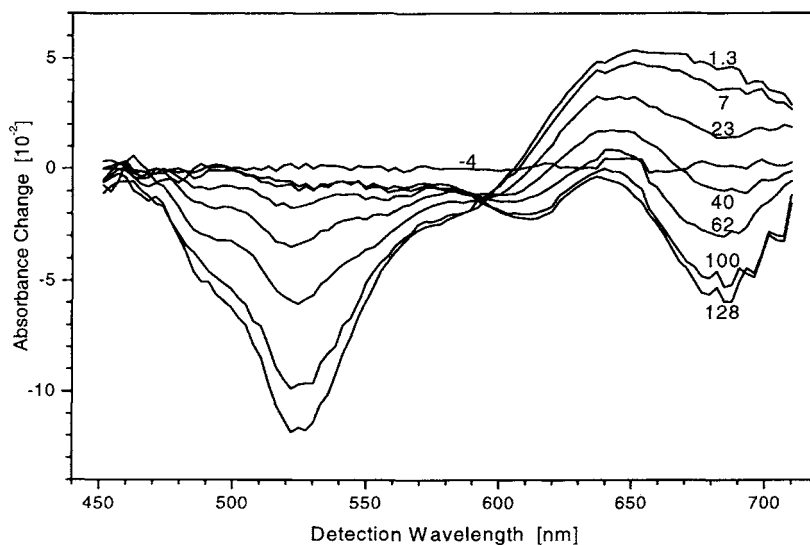


Fig. 4. Transient Absorbance changes determined for the second generation dendrimer **2**. The numbers at the curves indicate the time after excitation in ps. Excitation wavelength was 495 nm.

to energy transfer processes. Probably, these two components are the predominant values in a range of energy transfer times, which can be found within different structurally isomeric dendrimer molecules [6].

3. 4. Transient absorption of the second generation dendrimer

The results for the second generation dendrimer **2** are shown in Fig. 4. Again, the transient spectrum immediately after excitation (1.3 ps) perfectly resembles the one of **4**. During the following 130 ps it temporally evolves into a spectrum which perfectly coincides with the transient spectrum of **3**. Also in this case, the energy transfer process going on between the excited peryleneimide donors and the terylenediimide acceptor is responsible for this kinetics and again two different time constants (25ps, 68ps) were found. Both are significantly larger compared to the coressponding times in the first generation. This decrease in energy transfer rate had also been reported before using fluorescence upconversion measurements.

REFERENCES

- [1] G. Schweitzer, R. Gronheid, S. Jordens, M. Lor, G. De Belder, T. Weil, E. Reuther, K. Müllen, F.C. De Schryver, *J. Phys. Chem. A*, 107 (2003) 3199.
- [2] R. Gronheid, J. Hofkens, F. Köhn, T. Weil, E. Reuther, K. Müllen, F.C. De Schryver, *J. Am. Chem. Soc.*, 124 (2002) 2418.
- [3] G. Schweitzer, L. Xu, B. Craig, F.C. De Schryver, *Opt. Commun*, 142 (1997) 283.
- [4] S. Jordens, G. De Belder, M. Lor, G. Schweitzer, M. Van der Auweraer, T. Weil, E. Reuther, K. Müllen and F.C. De Schryver, *Photochem. Photobiol. Sci.*, 3 (2003) 177.
- [5] G. De Belder, G. Schweitzer, S. Jordens, M. Lor, S. Mitra, J. Hofkens, S. De Feyter, M. Van der Auweraer, A. Herrmann, T. Weil, K. Müllen and F.C. De Schryver, *Chem. Phys. Chem.*, 2 (2001) 49.
- [6] M. Cotlet, R. Gronheid, S. Habuchi, A. Stefan, A. Barbafina, K. Müllen, J. Hofkens and F. C. De Schryver, *J. Am. Chem. Soc.*, 125 (2003) 13609.

Femtosecond time-resolved studies on spectral sensitization of AgBr nanocrystals

Keitaro Yoshihara,^a Igor V. Rubtsov^{a,†}, Kojiro Ebina,^a Fuminori Satou,[‡] Ji-Won Oh,[‡] Shigeichi Kumazaki,^{§,¶} Takeshi Suzumoto,^b and Tadaaki Tani^b

^a Japan Advanced Institute of Science and Technology, Tatsunokuchi, 923-1292, Japan

^b Ashigara Research Laboratories, Fuji Photo Film Co., Ltd., Minamiashigara, 250-0193, Japan

[‡] Department of Chemistry, University of Pennsylvania, Philadelphia, PA 19104-6323, U.S.A.

[¶] Department of Chemistry, Kyoto University, Sakyo-ku, Kyoto 606-8502, Japan

1. ABSTRACT

Spectral sensitization and supersensitization of silver bromide nanocrystals were studied by the femtosecond fluorescence up-conversion technique. Fluorescence from J-aggregates of cyanine dyes adsorbed on AgBr nanocrystals (40-900 nm) with different shapes (cubic or octahedral) was measured. Fast non-exponential fluorescence decays were observed with a fast component ranging from 400fs to 2.5 ps depending on the type and size of the crystals. The rates of electron injection from J-aggregate dye to the conduction band of AgBr at various conditions were determined. The increase of the electron injection rate with the increase of the grain size is observed and explained by the space charge theory. Upon addition of a supersensitizer (SS), which is different cyanine dye co-adsorbed on the surface of silver bromide grains, the fluorescence decay became several times faster. The results were analyzed in the framework of the "hole-trapping" supersensitization model. The effective hole-trapping (electron transfer from SS to the excited J-aggregate) rate constant was found to be independent of the grain size and equal to $\sim 0.60 \text{ ps}^{-1}$. By fluorescence anisotropy measurement, the ultrafast energy transfer of the J-aggregates on the octahedral crystal (200 nm) was studied. The anisotropy decays are biphasic with two time constants of $\sim 100 \text{ fs}$ and a few picoseconds, the short time constant being assigned to energy transfer between epitaxially arranged J-aggregates on the $\{111\}$ surface.

2. INTRODUCTION

Spectral (color) sensitization is a technology which is used to make the photographic materials sensitive to green and red light by adsorbing sensitizing dyes on the surface of silver halide grains [1,2]. J-aggregate of carbocyanine dye adsorbed on the surface of AgBr grains is often used, since they have a very narrow absorption band for clear color. While several pioneering works on the reaction dynamics have been made, the time resolution was limited to tens of picoseconds [3-7]. Such a time resolution is not sufficient to observe the initial steps of the photographic sensitization processes. We have observed

the electron injection from the excited J-aggregate to the AgBr conduction band by femtosecond-fluorescence dynamics measurements [8]. We also described the ultrafast excitation-energy transfer of the J-aggregates on the octahedral AgBr by time-resolved fluorescence-anisotropy decay measurements [9]. An ultrafast excitation transfer (ca.100fs) is suggested to take place between epitaxially arranged J-aggregates on the {111} surface and this happens prior to the primary electron injection to AgBr (ca. 0.7 ps).

In photography, a technique called supersensitization with supersensitizer (SS) is used to improve the quantum yield of spectral sensitization. The SS dye molecules co-adsorbed on the AgBr grains in much smaller concentration than the sensitizing dye improve the sensitization. The shortening of the fluorescence lifetimes by addition of SS is observed and this phenomenon is explained by the "hole-trapping" mechanism [10,11].

3. EXPERIMENTAL

The sensitizer used in this work is 3,3'-disulfopropyl-5,5'-dichloro-9-ethylthiarcyanine (Dye 1), which forms J-aggregates on the surface of the AgBr grains. Addition of SS (3,3'-disulfopropyl-9-ethyl-4,5,4',5'-dibenzothiocarbocyanine)(Dye2) (Fig.1), which is co-adsorbed on the AgBr surface, changes the dynamics of the fluorescence decay of the sensitizer. At the same time it changes the quantum yield of photographic process, which was measured independently.

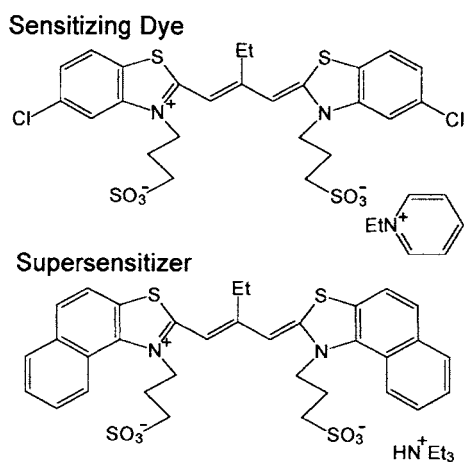


Fig. 1. Sensitizer dye (Dye1) and super-sensitizer dye (Dye2) used in the present study.

The emulsions used in this work were composed of the suspension of AgBr grains in aqueous gelatin solution, and were prepared by the controlled double-jet precipitation method. The edge lengths

of the AgBr nanocrystals were 200 nm for cubic grains and 40, 200, 400, and 900 nm for octahedral grains. The relative quantum yield of spectral sensitization is defined as the ratio of the number of photons necessary to create a latent-image center for the two types of excitations: excitation at 400 nm into the AgBr conduction band and an excitation with visible light for the dye [2]

The femtosecond fluorescence up-conversion setup has been described elsewhere [13,14]. Briefly, a second harmonic (SH) of a home-made chromium-forsterite femtosecond laser tunable from 610 to 660 nm was used to excite the sample (Fig.2) [14]. The pulse duration of the SH pulses was about 50 fs at the full width at half maximum (FWHM). We were successful in the cavity-dumping operation of this laser [14] and kept the repetition rate as low as 4 MHz. Reduction of the repetition rate was necessary to avoid multiple hits of the same location of the sample as small as possible. The excitation intensity, controlled by a neutral density filter before the sample cell, was $(0.5-1) \times 10^{12}$ photons/cm²/pulse. Special care was taken to work at the lowest excitation light intensity so that the effect of the exciton-exciton annihilation process was negligible.

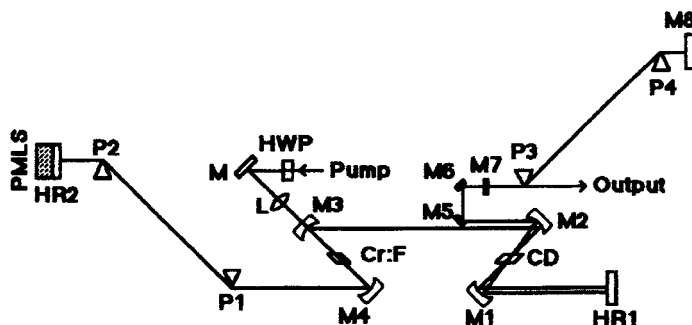


Fig. 2. A home-made chromium-forsterite femtosecond laser with a cavity dumper [14].

During the experiments, a micropump made circulating the sample through a reservoir. The optical path of the sample cell was 0.5 mm. The temperature of the sample was kept at 50 °C. The photographic quantum yield was measured at room temperature.

4. RESULTS AND DISCUSSION

The normalized absorption and fluorescence spectra of Dye 1 on 200 nm AgBr are shown in Fig. 3. The absorbance was calculated from the measured reflection spectrum using the Kubelka-Munk equation. The absorption spectrum of Dye 1 in methanol solution is also given. The absorption spectrum of Dye 1 on AgBr crystals shows a typical J-aggregate character and gives a sharp and red-shifted band relative to the monomeric band.

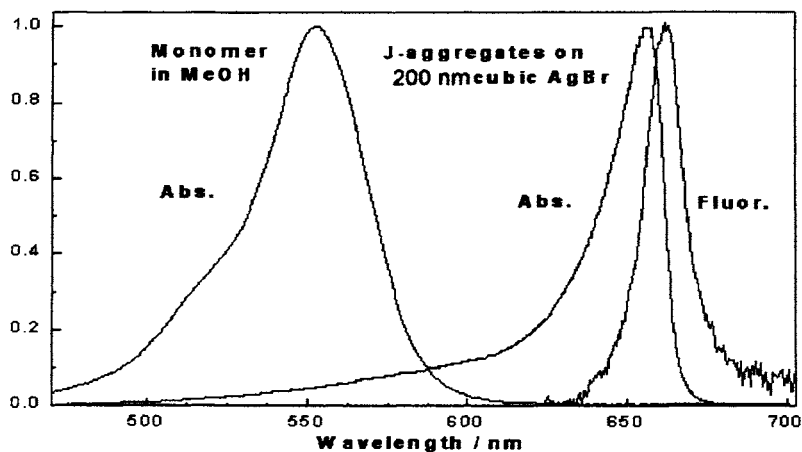


Fig. 3. The normalized absorption and fluorescence spectra of Dye 1 J-aggregates on 200 nm AgBr and absorption spectrum Dye 1 in methanol solution [8].

The time-resolved fluorescence was obtained from the sample, that contained AgBr grains with J-aggregates on the surface suspended in gelatin solution as shown in Fig. 4. The fluorescence is detected on the red slope of the J-band. Upon addition of SS, the fluorescence decay becomes several times faster. The decays are not exponential, but a very good fit is obtained with a biexponential decay function. The results for AgBr grains of different size and surface type are given with decay fit with two exponentials (τ_1 , τ_2 , A_1 , A_2), average time $\bar{\tau}$, and observed decay constant k_{obs} . The fluorescence decay of Dye 1 on the 200 nm octahedral crystals (without SS) appears to be ~ 2.5 times faster than that on the cubic crystals. Addition of the SS makes the fluorescence decays faster for both cases of the cubic and octahedral crystals. The effect of SS is significant for the cubic grains, ~ 4 times, and much smaller for the octahedral grains, 1.6–2.1 times, except for the 40 nm grains. The mean decay times ($\bar{\tau}$) were calculated by the weighted average time. The rate constants of several processes (electron injection, hole-trapping, and the sum of the radiative and non-radiative decays) were determined for the cubic ((100) surface) and octahedral ((111) surface) AgBr nanocrystals. The dependence of the electron injection and the hole-trapping rate constants on the grain size was determined for octahedral nanocrystals.

Two main mechanisms were proposed for the supersensitization effect. One is the “hole-trapping” mechanism in which the electron from SS fills the hole in the highest occupied molecular orbital (HOMO) of the excited sensitizing dye, since the HUMO level of SS is chosen to be higher than that of the sensitizer (Fig. 5) [2,10,11]. The resultant ionic state gives up an electron to the conduction band of silver halide with much higher quantum yield.

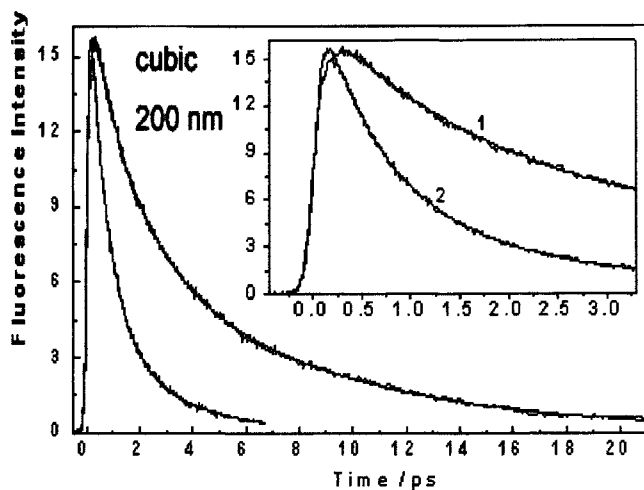


Fig. 4. Fluorescence decay signals of Dye 1 on 200 nm cubic AgBr grains with (2) and without (1) sensitizer and two exponential fits. In the inset: the initial parts of the decays are shown.

Table 1. Results of the fluorescence decay fit with two exponentials (τ_1 , τ_2 , A_1 , A_2), average time $\bar{\tau}$, and observed decay constant k_{obs} for AgBr grains of different size and surface type.

AgBr type	AgBr size nm	λ_{fl}^b nm	λ_{exc}^c nm	τ_1 ps	A_1	τ_2 ps	A_2	$\bar{\tau}$ ps	k_{obs} and $k_{\text{obs}}^{\text{SS}}$ ps ⁻¹
	200	684	635	1.77	0.64	10.8	0.36	5.0 ± 0.2	0.20
Cubic	200+SS	684	635	0.77	0.78	3.35	0.22	1.34 ± 0.06	0.75
(100)	200 ^a	680	624	2.5	0.58	9.3	0.42	5.4 ± 0.2	0.19
	200+SS	680	624	0.8	0.87	4.4	0.13	1.3 ± 0.07	0.77
	40	680	620	1.5	0.66	13	0.34	5.5 ± 0.7	0.18
	40+SS	680	620	0.79	0.88	4.5	0.12	1.25 ± 0.15	0.80
Octa	200	684	635	1.08	0.80	5.40	0.20	1.95 ± 0.15	0.51
(111)	200+SS	684	635	0.66	0.84	2.5	0.16	0.95 ± 0.06	1.06

The other is the “aggregate-partitioning” mechanism [2,15], where it is considered that the SS molecules work as J-aggregate partitioners, which decrease the size of the aggregates. This causes an increase in the fluorescence lifetime and/or an increase in the electron injection rate, and hence an increase in the quantum yield of the electron injection [2]. In the present work the sensitization and supersensitization processes are described below by the “hole-trapping” supersensitization.

The increase in the sum of the trapping and injection rates by about 5 times was observed upon addition of SS. The efficiency of supersensitization in the typical “hole trapping” mechanism is dependent on the oxidation potential of SS and not on the sensitization efficiency of SS itself. All of these observations drove us to apply the hole trapping mechanism. Further, at smaller ratio of Dye/AgBr the average size of J-aggregates is smaller. Upon decreasing of the ratio of Dye / AgBr by ten times, the fast component of the decay became slower. This is not in favor for the “aggregate-partitioning” mechanism in the present system. In the framework of the “hole-trapping” model the scheme shown in Fig. 5 is proposed.

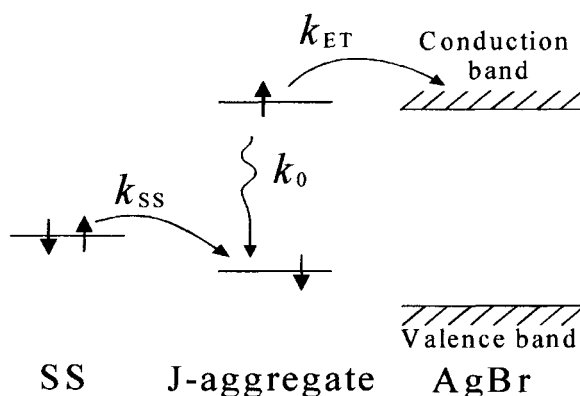


Fig. 5 Reaction scheme of the “hole-trapping” supersensitization

Here k_{ET} is the rate constant of the electron injection from the excited J-aggregate to AgBr, k_{SS} is the rate constant of ET from SS to the excited dye, and k_0 is the total (radiative and nonradiative) decay rate constant of the excited J-aggregates. According to our analyses the values of k_{SS} are similar for all cases with an average value of about 0.60 ps^{-1} . The relative quantum efficiency of the photographic process was determined by the independent experiments and one can estimate the values of k_{ET} and k_0 . The calculated k_{ET} , and k_0 values for different sizes and surfaces of the AgBr grains indicate that the values of k_0 are similar for cubic and octahedral grains. There is no clear dependence of k_0 upon grain size for octahedral grains. The electron injection rate, k_{ET} , is about 5.5 times smaller for cubic grains compared with the octahedral grains of the same size. An increase of k_{ET} with the grain size is observed for the octahedral grains, which will be discussed in the next section. The rate constant of electron

transfer from SS to the excited J-aggregates, k_{SS} , is larger than k_{ET} by about 8 times for cubic and only about 1.5 times for octahedral grains. This determines the relatively high quantum yield of photographic process with octahedral grains and rather small improvement by addition of SS.

Next, let us consider the origin of the size dependence of k_{ET} . It is well known that the potential energy surface is bent near the surface of the semiconductor crystals, as formalized by the space charge theory [16]. The charged layer in AgBr grains is formed by the excess of the positive interstitial defects (Ag^+) near the surface. As a result, a double layer is formed with the positively charged interior and negatively charged surface of the grains. The characteristic distance of the potential drop, which is called the Debye length, for the case of thick pure crystal, is about 140 nm [17]. If the grain size is comparable or smaller than the Debye length for thick crystals, the potential level inside grains becomes dependent on the grain size. The potential difference between the (111) surface and the interior for thick AgBr crystals was measured to be about 0.22 eV and about 0.18eV between the (100) surface [8]. This difference gives the difference in k_{ET} for octahedral and cubic crystals.

The ultrafast excitation-energy transfer of the J-aggregates on the octahedral AgBr is studied by the time-resolved fluorescence-anisotropy decay ($r(t)$) measurements [9]. They are biphasic with two time constants of ~ 0.15 ps and 2~7 ps as shown in Fig. 6. Each phase should reflect some difference in the orientation of the dye molecules of the J-aggregates.

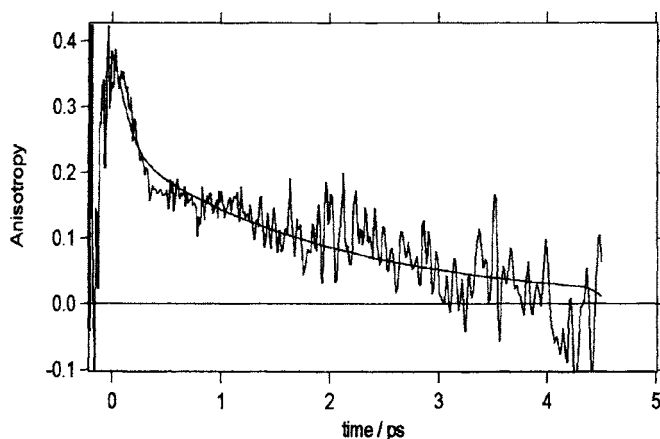


Fig. 6. Time-resolved fluorescence anisotropy of Dye 1 on octahedral AgBr crystals. Smooth solid line shows the fitting curve.

Maskasky found that the long axis of the fluorescence image of the J-aggregate of the same dye on the $\{111\}$ surface was parallel to both the $\langle 110 \rangle$ direction on the surface and polarization of the emission [18]. On the $\{111\}$ surface of the AgBr octahedron there are three equivalent $\langle 110 \rangle$ directions of the molecular arrangement with an angle of 60° . The transition from one excitation of a J-aggregate

along one direction to the equilibrium (1:1) of excitation between two J-aggregates with an angle difference of 60° causes a decay of anisotropy from 0.4 to 0.175. The anisotropy should reach 0.1 by the complete equilibration (1:1:1) between all the three directions (0° , 60° , 120°). In view of this numerical prediction, the fast anisotropy decay, which is from about 0.4 to 0.2 in Fig. 6 may indicate excitation equilibration in a small domain. The final anisotropy decays to zero in the present experiment are probably due to a deviation of aggregate orientations from the final ideal $\langle 110 \rangle$ directions. The ultrafast excitation transfer (ca. 0.1 ps) is thus suggested to take place prior to the primary electron injection to AgBr (ca. 0.7 ps).

REFERENCES

- [1] R. W. Gurney and N.F. Mott, Proc. Roy. Soc., A164(1939) 151.
- [2] T. Tani, Photographic Sensitivity, Oxford University Press: Oxford, 1995, p142.
- [3] K. Kemnitz, K. Yoshihara, and T. Tani, J. Phys. Chem., 94(1990), 3099.
- [4] T. Tani, T. Suzumoto, K. Kemnitz, and K. Yoshihara, J. Phys. Chem., 96(1992) 2778.
- [5] B. Trosken, F. Willig, A. Schwarzburg, A. Ehret, and M. Spittler, J. Phys. Chem. , 99(1995) 5152.
- [6] I. G. Scheblykin, O. P. Varnavsky, M. M. Bataiev, O. Sliusarenko, M. Van der Auweraer, and A. G. Vitukhnovsky, Chem. Phys. Lett., 298(1998) 341.
- [7] A. A. Muentner D.V. Brumbaugh, G. Strati, and R. K. Hailstone in International Congress on Imaging Science, University of Antwerp, Belgium, 1998, p. 166.
- [8] I. V. Rubtsov, K. Ebina, F. Satou, J-W. Oh, S. Kumazaki, T. Suzumoto, T. Tani and K. Yoshihara, J. Phys. Chem. A, 106(2002) 2795.
- [9] J-W Oh, S. Kumazaki, I.V. Rubtsov, T. Suzumoto, T. Tani, and K. Yoshihara, Chem. Phys. Lett., 352(2002) 357.
- [10] P. B. Gilman, Photogr. Sci. Eng. ,18(1974) 418.
- [12] T. Tani, T. Suzumoto and K. Ohzeki, J. Phys. Chem., 94(1990) 1298.
- [13] I. V. Rubtsov, H. Shirota, and K. Yoshihara, J. Phys. Chem. A , 103(1999) 1801.
- [14] E. Slovodchikov, J. Ma, V. Kamalov, K. Tominaga, and K. Yoshihara, Opt. Lett., 21(1996) 354.
- [15] W. West and B. H. Carrol, J. Chem. Phys., 15(1947) 529; J. Chem. Phys.,19(1951) 417.
- [16] J. Frenkel, Kinetic Theory of Liquids, Oxford Univ. Press, New York, 1946.
- [17] Y. T. Tan and H. A. Hoyer, Jr. Surface Sci., 36(1973) 242.
- [18] J. E. Maskasky, Langmuir, 7(1991) 407.

Ultrafast scattering of electrons in TiO₂

M. Bonn^a, F. Wang^b, J. Shan^b, T.F. Heinz^b and E. Hendry^a

^a Leiden Institute of Chemistry, Leiden University, P.O. Box 9502, 2300 RA Leiden, The Netherlands. e-mail: m.bonn@chem.leidenuniv.nl

^b Departments of Physics and Electrical Engineering, Columbia University, 538 West 120th St., New York, NY 10027

ABSTRACT

Titanium dioxide (TiO₂) is widely used in photocatalysts and solar energy converters. A key factor determining the efficiency of these devices is the transport of photogenerated electrons. Electron mobility is determined by the scattering rate – the average frequency of momentum-changing collisions, inversely proportional to the electron mean free path. We elucidate the nature and rate of electron scattering in single-crystal rutile TiO₂ using the contact-free technique of THz time-domain spectroscopy. Strong electron-phonon interactions result in the formation of polarons, electrons dressed by local lattice deformations, and electron-phonon scattering rates up to 10^{14} s⁻¹ at room temperature. The anomalous high scattering rates result in a low room temperature electron mobility of ~ 0.5 cm²/Vs, which sets the intrinsic limit for device performance.

1. INTRODUCTION

In photo-catalytic and solar energy conversion devices, the absorption of a photon results in the generation of electrons and holes, which, upon separation, can provide an electric potential or trigger chemistry. The efficiency of these devices is frequently determined by the transport of the charges following photo-generation. In particular, for TiO₂-based dye-sensitized solar cells, it has been demonstrated that the efficiency is limited by electron transport through TiO₂ nanoparticles [1].

Although the transport of electrons in TiO₂ has consequently received considerable attention, several aspects of charge transport in TiO₂ remain ambiguous: Reported room-temperature electron Hall mobilities range from 0.01 to 10 cm²/Vs [2]. In addition, the precise nature of the transport has remained unresolved. It is clear that the ionic character of the lattice combined with the presence of an electron in the conduction band (following optical excitation) results in a local deformation of the TiO₂ lattice, as the electron attracts positive Ti and repels negative O species (see inset in Fig. 1). This electron-phonon coupling effects the formation of a polaron [3], a quasi-particle consisting of an electron and the accompanying lattice deformation. The character of polarons in TiO₂ has remained unclear. In the limit of sufficiently strong coupling, *small* polarons are formed. These polarons display self-trapping of the electron and localized wavefunctions, with charge transport typically occurring through tunnelling or thermally activated hopping. For weaker coupling, *large* polarons appear, with

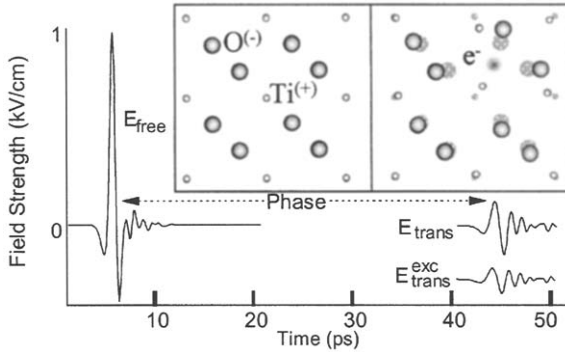


Fig. 1. Three THz-scans at 10K: The pulse transmitted through air ($E_{free}(t)$), the unexcited sample ($E_{trans}(t)$), and the photoexcited sample ($E_{trans}^{exc}(t)$). The 45ps delay between E_{free} and E_{trans} is caused by the large real part of the dielectric function (see inset of Fig. 2). A less obvious phase shift also exists between E_{trans} and E_{trans}^{exc} associated with the real part of ϵ . Inset: Left – the (001) face of rutile. Right – the lattice distortion when an electron is placed in the polar lattice results in polaron formation: (partly) positively charged Ti-atoms are attracted, and (partly) negative O-atoms repelled (see text).

spatially extended wavefunctions and band-type conduction. In both cases, the moving electron entrains the lattice deformation, resulting in an effective mass exceeding its band mass. There have been conflicting arguments for the existence of small and large polarons in rutile. We circumvent previous experimental limitations by investigating electron transport in defect-free (stoichiometric) single-crystal rutile TiO_2 using the method of contact-free terahertz time-domain spectroscopy (THz-TDS) [4] following photogeneration of electrons. We determine temperature dependent scattering rates from which the mobility, effective mass and polaron size can be inferred by means of the Feynman polaron model.

2. EXPERIMENTAL

The TiO_2 samples, mounted in a helium cryostat (10-300 K), are 1mm-thick (001) and (110)-cut single crystals to study the electronic response with the (THz) electric field perpendicular (\perp) and parallel (\parallel) to the c axis, respectively. Rutile is the most common and stable TiO_2 polymorph and has a tetragonal structure with $a=4.6\text{\AA}$ and $c=2.9\text{\AA}$. The band gap of rutile is 2.9 eV at room temperature, increasing slightly at lower temperatures.

The transport of electrons in TiO_2 is investigated with an experimental set up similar to that described in Ref. [4]. Electrons are excited into the conduction band through photoexcitation by 400 and 800 nm pulses of ~ 120 fs duration at excitation fluences of 4 J/m^2 and 30 J/m^2 , respectively. The same Ti:Sa laser source is used to generate THz pulses [4]. As shown in Fig. 1, THz pulses are essentially single cycle electromagnetic pulses, the field strength $E(t)$ of which is detected directly in the time domain. The THz pulses are generated and detected through optical rectification and electro-optic sampling, respectively, of 800 nm pulses in ZnTe crystals. The ~ 1 ps cycle time corresponds to a frequency of 1 THz, and the shortness of the pulse (also ~ 1 ps) implies a large frequency bandwidth. Fig. 1 depicts the transmission of these pulses through air ($E_{free}(t)$), through the unexcited sample ($E_{trans}(t)$), as well as through the irradiated sample ($E_{trans}^{exc}(t)$) in which electrons have been excited into the conduction band [5]. Data analysis is most conveniently performed in the frequency domain,

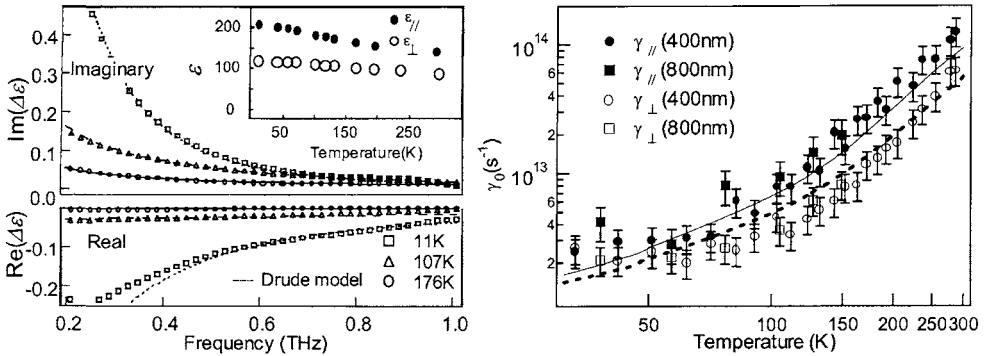


Fig. 2. (left) and 3. (right): Observed change in complex refractive index due to electron generation in TiO_2 with 400nm laser pulses at 11K, 107K and 176K. The Drude model describes the data very well, with varying scattering rates (see Fig. 3, right). Inset: the unperturbed dielectric function at 0.6THz measured at different temperatures. Right: Scattering rates $\gamma_{//}$ (closed symbols, parallel to the c axis) and γ_{\perp} (open symbols, perpendicular to the c axis), obtained with 400 and 800 nm excitation (circles and boxes, resp.). The lines are the result of the Feynman polaron model, with $\alpha_{//}=4$ (full line) and $\alpha_{\perp}=6$ (dashed line).

and the Fourier transforms of the first two measurements ($E_{free}(\omega)$ and $E_{trans}(\omega)$) yield the complex dielectric function $\varepsilon(\omega)$ of TiO_2 in the frequency range 0.2—1.0 THz. More interestingly, from $E_{trans}(\omega)$ and $E_{trans}^{exc}(\omega)$, we can obtain the change in $\varepsilon(\omega)$, $\Delta\varepsilon(\omega)$, due to the presence of electrons in the conduction band. Whereas $\varepsilon(\omega)$ is determined by the response of the TiO_2 lattice, $\Delta\varepsilon(\omega)$ contains information on electron transport. Note that we can obtain both the real and imaginary parts of the dielectric functions, $\varepsilon(\omega)$ and $\Delta\varepsilon(\omega)$ from the direct characterization of the time-domain electric field provided by THz TDS.[4]

3. RESULTS AND DISCUSSION

For unexcited rutile, the real part of $\varepsilon(\omega)$, as derived from $E_{free}(\omega)$ and $E_{trans}(\omega)$, is observed to be very large, $\text{Re}(\varepsilon) \approx 150$, with considerable anisotropy between directions parallel and perpendicular to the crystallographic c axis, and a magnitude decreasing slightly with increasing temperature (see inset of Fig. 2). $\Delta\varepsilon(\omega)$ – the pump induced change in dielectric function obtained from $E_{trans}(\omega)$ and $E_{trans}^{exc}(\omega)$ [6] – is shown in Fig. 2 for three different sample temperatures. The shape of these curves reflects the nature of the transport process. We fit the results using the simple Drude model for charge carrier transport: $\Delta\varepsilon(\omega) = -\omega_p^2 / (\omega^2 + i\omega\gamma_o)$. Here γ_o denotes the scattering rate, which is the critical parameter describing charge transport, since it determines the mean time between momentum changing collisions that act to impede the flow of current. The plasma frequency ω_p is given by the electron (polaron) effective mass (m^{**}), the density of electrons (n_f), and the permittivity of free space (ε_0) through $\omega_p^2 = (4\pi e^2 n_f) / (\varepsilon_0 m^{**})$. By modeling the data using this functional form, we are able to extract γ_o and ω_p , the two key parameters determining the electrical conductivity of TiO_2 . At high temperatures, the scattering rate cannot be found by a direct fitting procedure, but can be inferred directly from the amplitude of the induced THz signal.

As shown in Fig. 3, there is a sharp rise in γ_0 with increasing temperature. The anisotropy of electron transport is also clearly evident, with a larger scattering rate measured along parallel direction. The large scattering rates at room temperature (γ_0 100 THz) are a consequence of the strong electron-phonon coupling and the increased phonon density at elevated temperatures.

At low temperatures, scattering from low-frequency *acoustic* phonons dominates, with a $T^{3/2}$ temperature dependence [7]. As the temperature is increased, excitation of higher frequency *optical* phonons occurs, leading to enhanced scattering. The LO phonon mode from which scattering prevails can be inferred from the frequency dependent dielectric function (ϵ) obtained from infrared reflectance data. It is found to be two different 800 cm^{-1} phonon modes for the two crystallographic directions. The concomitant electron-phonon coupling constant α can be obtained from a fit to our temperature dependent scattering data, using the polaron theory of Feynman [8]. The results of the fit are shown in Fig. 3, with $\alpha_{\parallel}=4$ and $\alpha_{\perp}=6$ the electron-phonon coupling constant parallel and perpendicular to the crystal c-axis, respectively. The strong electron-phonon coupling, also evident from the large static dielectric function (inset in Fig. 2,) results in mobilities of $\mu_{\parallel}=0.6 \text{ cm}^2/\text{Vs}$ and $\mu_{\perp}=0.2 \text{ cm}^2/\text{Vs}$ for parallel and perpendicular directions respectively.

The resulting polaron radius of $r_{\text{pol}} \sim 5 \text{ \AA}$ is substantially smaller than the $\sim 25 \text{ nm}$ radius of particles typically used in devices such as solar cells. Therefore, quantum confinement effects are expected to be negligible. Further, the large scattering rates (and correspondingly short mean free paths, also $\sim 5 \text{ \AA}$) imply that momentum relaxation of polarons at room temperature is dominated by the bulk properties of TiO_2 and that the surface scattering effects that have been observed at low temperatures (77 K) [9] are of minor significance at room temperature. The much lower room-temperature drift mobility of photogenerated polarons reported for *porous* rutile TiO_2 ($<10^{-3} \text{ cm}^2/\text{Vs}$, as opposed to $\sim 0.5 \text{ cm}^2/\text{Vs}$ reported here) indicates the existence of a barrier for motion between the structures. This might arise either from surface traps or from barriers encountered by electrons entering or leaving individual particles. Our results show that, although electron transport through bulk TiO_2 is impeded by scattering associated with the strong electron-phonon interaction, it is not the bulk mobility that limits transport. The mobility ($\sim 0.5 \text{ cm}^2/\text{Vs}$) observed here represents the intrinsic limit for electron transport at room temperature and suggests that substantial device improvement is possible for optimized nanoparticle composites.

REFERENCES

- [1] N. Kopidakis, et al., J. Phys. Chem. B 104 (2000) 3930.
- [2] R. G. Beckenridge and W. R. Hosler, Phys. Rev. 91 (1953) 793; E. Yagi, R. R. Hasiguti, and M. Aono, Phys. Rev. B 54 (1996) 7945.
- [3] N. M. A. S. Alexandrov, Polarons and Bipolarons (World Scientific, Singapore, 1995), 1st Ed., pp. 155-157.
- [4] M. C. Beard, G. M. Turner, and C. A. Schmuttenmaer, J. Phys. Chem. B 106 (2002) 7146.
- [5] By comparing experiments on photo-excited TiO_2 to n-type doped TiO_{2-x} ($x=0.0005$) we conclude that the pump-induced THz absorption originates primarily from photo-generated electrons, rather than from holes, in accordance with the large hole band mass ($>4m_e$).
- [6] E. Knoesel, M. Bonn, J. Shan, et al., Phys. Rev. Lett. 86 (2001) 340.
- [7] J. Bardeen and W. Shockley, Phys. Rev. 80 (1950) 72.
- [8] R. P. Feynman, Phys. Rev. 97 (1955) 660; R. P. Feynman., *ibid.* 127 (1962) 1004.
- [9] G. M. Turner, M. C. Beard, and C. A. Schmuttenmaer, J. Phys. Chem. B 106 (2002) 11716.

Influence of molecular spacers on ultrafast heterogeneous electron transfer

**R. Ernstorfer^a, L. Gundlach^a, S. Felber^a, C. Zimmermann^a, R. Eichberger^a, Q. Wei^b,
E. Galoppini^b, and F. Willig^a**

^aHahn-Meitner-Institut, Abteilung SE 4, Glienicker Strasse 100, D-14109 Berlin, Germany

^bDepartment of Chemistry, Rutgers University, Newark, N.J., USA

The dynamics of electron injection from the aromatic chromophore perylene into the conduction band of colloidal anatase TiO₂ was investigated by transient absorption spectroscopy under ultra-high vacuum (UHV) conditions for different saturated spacer-cum-anchor groups. Electron injection from perylene directly linked via a carboxylate group to the surface was found to occur with 15 fs time constant. Insertion of saturated spacer groups as well as the exchange of the anchor group can systematically decelerate the electron transfer. For the case of a long rigid spacer molecule multi-exponential injection dynamics was observed with 4 ps as the largest time constant.

1. INTRODUCTION

Heterogeneous electron transfer from a photo-excited molecular donor state to a semiconductor is a unique electron transfer case for a molecular reactant since one can utilize a continuum of electronic acceptor states provided the donor state is located high enough above the bottom of the conduction band. In this case all the Franck-Condon factors are available for the reaction, and the electron transfer time is controlled only by the electronic coupling between the donor orbital and the electronic acceptor states [1]. This situation is particularly attractive for studying the influence of saturated molecular spacer-cum-anchor groups on the electronic coupling between the chromophore part of the attached molecule and the conduction band states in the semiconductor. The experimental system consists of a perylene chromophore [2] anchored via different anchor-cum-spacer groups to the surface of nano-crystallites of anatase TiO₂. Perylene is particularly suitable for studying the distance dependence of electron transfer. Firstly, it has spectrally separated absorption bands for the different electronic states involved in the reaction [2]. Secondly, electron injection is the only efficient decay channel of the donor state because in the absence of electron transfer the lifetime of the excited singlet state is several ns. This allows for an unambiguous assignment of the measured transient features to specific electronic states.

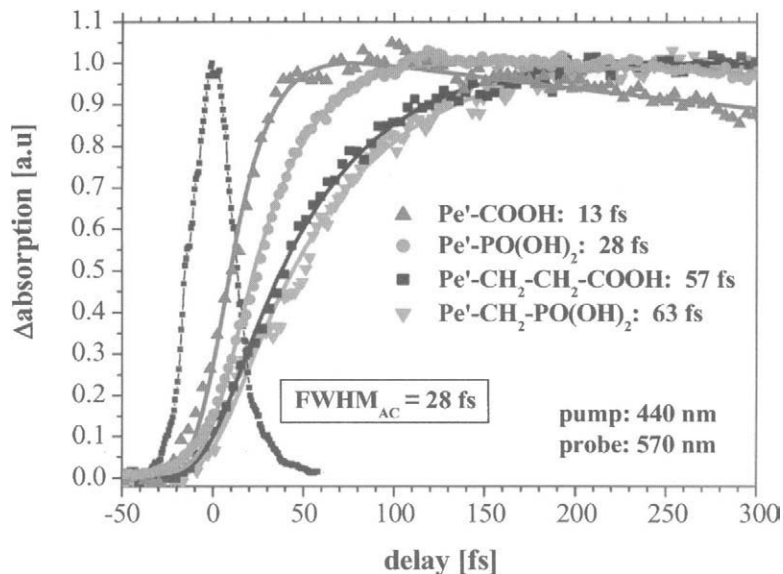


Fig. 1. Rise of the perylene cation absorption, which reflects the electron injection dynamics, after excitation of the first singlet state with a 15 fs pump pulse. Variation of the electronic coupling via a change in the anchor group as well as the insertion of one or two $-\text{CH}_2-$ groups leads to a systematic change in the time scale of both electron injection and charge recombination.

2. EXPERIMENTAL

Tunable sub-20 fs laser pulses at low pulse energy and 100 kHz repetition rate were generated by employing a novel non-collinear optical parametric amplifier (NOPA) [3]. Weak pump pulses (20 nJ) in the spectral range of the perylene ground state absorption, i.e. around 430 nm, were obtained by frequency doubling the near-infrared (NIR) output of the NOPA in a 100 μm BBO crystal. Pulse compression was achieved by pre-compensating the NIR pulse with a standard prism compressor. Intensity auto-correlation of the pump pulses taken as the 2-photon-absorption signal of a SiC-diode gave pulse durations of 15 fs (FWHM) [4]. Weak probe pulses were obtained from a white light continuum in the spectral range of the perylene cation absorption, i.e. around 570 nm, via spectral filtering and pulse compression. The cross-correlation function had 27.6 fs FWHM. The measurements were carried out in UHV.

The perylene chromophores were modified by covalently attaching different side groups. Two bulky groups (tertiary-butyl), indicated by a prime, prevented dimerization of neighbouring perylene chromophores when attached to the surface. Linkage to the semiconductor was achieved by different anchor-cum-spacer groups: carbonic acid ($-\text{COOH}$) [4], propionic acid ($-\text{CH}_2-\text{CH}_2-\text{COOH}$) [2], phosphonic acid ($-\text{P}(\text{O})(\text{OH})_2$) [4], methyl-phosphonic acid ($-\text{CH}_2-\text{PO}(\text{OH})_2$) [2] and a -Tripod (see inset in Fig.2) [5]. The preparation and sensitization of the nano-structured TiO_2 film and further experimental details have been described before [2].

3. RESULTS AND DISCUSSION

The fastest electron injection time was measured for perylene bound to the surface with the carbonic acid anchor, revealing a time constant of 13 fs (Fig. 1). Substitution of the carboxylic by a phosphonic acid group led to a deceleration of the electron injection by a factor of two, indicating reduced electronic coupling between donor and acceptor states, which originates probably from both geometrical differences and different electronic properties of the two anchor groups. Insertion of one (two) methylene groups between the phosphonic (carboxylic) group and the perylene skeleton led to a further deceleration by a factor of two (four). In addition, the onset of charge recombination, i.e. the reduction of the perylene cation via capture of an electron from the semiconductor, reflects the same trend as the forward injection. This indicates that early recombination is also controlled by the strength of electronic coupling.

The distance dependence of electron transfer has been studied extensively for the homogeneous case. An approximately exponential decay of the electronic coupling has been found with the number of saturated bonds in the spacer unit (see for example [6,7]). The results presented here suggest that an exponential dependence fits also our data for heterogeneous electron transfer in ultra-high vacuum. A different result has been reported for electron transfer from Re complexes to anatase where a local triplet state can play a role [8].

A larger donor-acceptor distance was realized with a rigid “tripod” spacer. In contrast to the short spacer-cum-anchor groups the injection dynamics showed here a strong multi-exponential behaviour with time constants ranging from 30 to 4300 fs (Fig. 2). These different time constants may arise from different configurations of the chromophore with respect to the surface. The slowest time constant could be assigned to the chromophore aligned with its long axis perpendicular to the semiconductor surface. An alternative and less likely assumption involves different intrinsic time constants for bridge-mediated heterogeneous electron transfer. Further experiments with rigid spacer groups appear necessary to clarify this point.

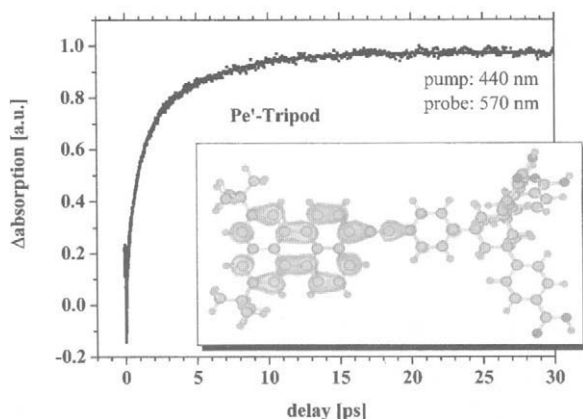


Fig. 2. Transient absorption of Pe'-Tripod probed at 570 nm (squares). The measured signals a superposition of cation absorption and stimulated emission (negative signal). The data were fitted to a three-exponential rise (solid line) revealing time constants of 30 fs (42%), 720 fs (33%) and 4.3 ps (25%). The inset illustrates the atomic structure of the Pe'-Tripod and its LUMO state, both calculated on a semi-empirical level.

4. SUMMARY

The measured injection times are plotted in Fig. 3 versus the minimum distance between the rim of the chromophore and the surface atoms of the anatase TiO_2 . A horizontal width assigned to the injection times in Fig. 3 gives an idea of the uncertainty in the latter distance values. As a guide to the eye Fig. 3 contains a straight line with the characteristic distance parameter of 1 Å. It is remarkable that there is only a weak deviation in the data from this curve if only the 4.3 ps time constant is considered for the Pe^+ -Tripod. At fairly small reaction distances in the range of a few Å the straight line in Fig. 3 is obviously a good approximation. To our knowledge these data are the first test of this often-assumed relationship for electron transfer from a molecular donor state in ultra-high vacuum and not in a solvent environment. The so called wide band situation [1] for the perylene/ TiO_2 combination eliminates the influence of Franck-Condon factors. It should also be noted that these experiments carried out in UHV are highly reproducible since the molecular systems are extremely stable in this environment.

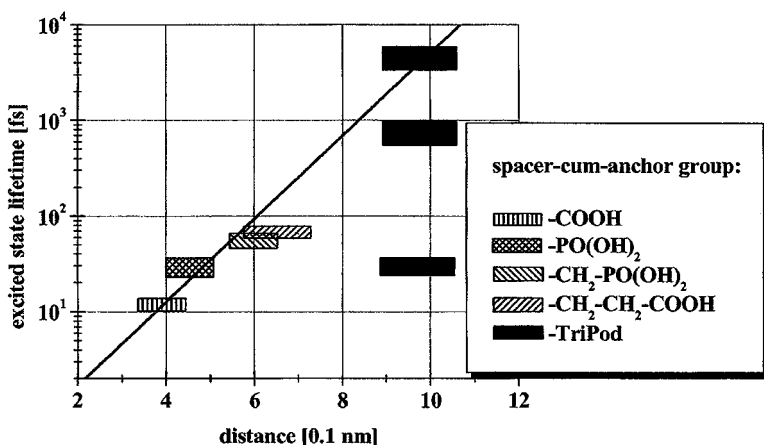


Fig. 3. Electron transfer times that are controlled only by electronic interaction are plotted versus distance. The latter varies with different spacer-cum-anchor groups and is defined between the rim of the perylene chromophore and the surface of anatase TiO_2 .

REFERENCES

- [1] S. Ramakrishna, F. Willig, V. May, *J. Chem. Phys.*, 115 (2001) 2743.
- [2] C. Zimmermann, F. Willig, S. Ramakrishna, B. Burfeindt, B. Pettinger, R. Eichberger, W. Storck, *J. Phys. Chem. B*, 105 (2001) 9245.
- [3] J. Piel, E. Riedle, L. Gundlach, R. Ernstorfer, R. Eichberger, to be published.
- [4] R. Ernstorfer, L. Gundlach, S. Felber, W. Storck, R. Eichberger, F. Willig, to be published.
- [5] Q. Wei, E. Galoppini, S. Felber, W. Storck, F. Willig, to be published.
- [6] C. Liang, M. D. Newton, *J. Phys. Chem.*, 96 (1992) 2855.
- [7] K. D. Jordan, M. N. Paddon-Row, *Chem. Rev.*, 92 (1992) 395.
- [8] J. B. Asbury, E. Hao, Y. Wang, T. Lian, *J. Phys. Chem. B*, 104 (2000) 11957.

Stepwise electron injection in the dye-sensitized nanocrystalline films of ZnO and TiO₂ with novel coumarin dye

A. Furube^a, R. Katoh^a, T. Yoshihara^a, K. Hara^a, S. Murata^a, H. Arakawa^a, and M. Tachiya^b

Photoreaction Control Research Center (PCRC), National Institute of Advanced Industrial Science and Technology (AIST), Tsukuba Central 5, 1-1-1 Higashi, Tsukuba, Ibaraki 305-8565, Japan

^aPCRC, AIST; ^bAIST

1. INTRODUCTION

Photoexcitation of dye molecules adsorbed on semiconductor surfaces such as TiO₂ is known to induce ultrafast electron injection when the energy level of the excited state of the dye is higher than that of the conduction band bottom of the semiconductor. This phenomenon is used in dye-sensitized solar cells (so called Grätzel cell), in which visible light excites the dye and electron injection generates carriers in the semiconductor [1]. Ultrafast spectroscopy has been applied to this system to study the mechanism of interfacial electron transfer for the last several years [2-7]. Recently we have reported the importance of localized surface states in the electron injection process from a photoexcited ruthenium complex dye (Ru(dcbpy)₂(NCS)₂, so-called N3) into the conduction band of a ZnO nanocrystalline film [8]. We found an intermediate state in the course of the electron injection; that is, the reaction proceeded stepwise. The intermediate was assigned to a charge transfer (CT) complex, or an exciplex, formed at the ZnO surface due to strong interaction with the excited dye and the surface states of ZnO.

In this paper, we show another example of such a stepwise electron injection process on ZnO. The dye investigated is a novel coumarin derivative called NKX-2311. This dye was reported to work as an efficient sensitizer for dye-sensitized TiO₂ solar cells [9]. The observed stepwise injection from NKX-2311 to ZnO is compared with that from NKX-2311 to TiO₂. These injection processes are discussed in terms of exciplex formation with localized surface states and subsequent (or competing) electron injection into the conduction bands.

2. EXPERIMENTAL SECTION

The dye NKX-2311, shown in Fig.1, was kindly given by Hayashibara Biochemical Laboratories. The physical and chemical properties of the dye have already been reported [9]. The ZnO and TiO₂ films were prepared on a glass or sapphire substrate by a similar procedure reported elsewhere [10]. The dye was loaded by just immersing the bare ZnO and TiO₂ films into dye solution to make dye-sensitized films, abbreviated as NKX-2311/ZnO and NKX-2311/TiO₂, respectively.

Details of the laser systems for pump-probe experiments are described elsewhere [8,10], except for a femtosecond IR probe system. For probing IR wavelengths (5–10 μm), a regenerative amplifier system of a Ti:sapphire laser (800 nm wavelength, 160 fs FWHM pulse

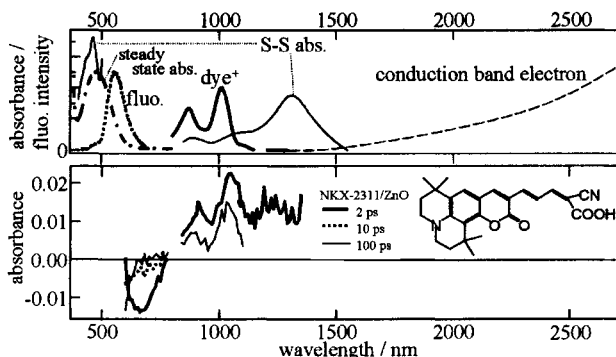


Fig. 1. Top: Reference spectra for femtosecond transient absorption measurements; S-S abs. in solution (thin solid lines), oxidized dye (dye^+) abs. in solution (thick solid line), fluorescence for solution (dotted line), steady-state absorption of NKX-2311/ZnO (dotted-dashed line), and absorption of electrons in the conduction band (dashed line). Bottom: Transient absorption spectra of NKX-2311/ZnO in the spectral range between 600 and 1350 nm at the 2 (thick solid line), 10 (dotted line), 100 ps (thin solid line) delay times after excitation at 540 nm by the femtosecond pulse with the intensity of about 10 μJ .

width, 1.0 mJ/pulse intensity, 1 kHz repetition, Hurricane, Spectra Physics) combined with two optical parametric amplifiers (TOPAS, Quantronix) was used.

3. RESULTS AND DISCUSSION

3.1. Electron injection dynamics in NKX-2311/ZnO

The UV-visible absorption and fluorescence spectra of NKX-2311 in solution are measured. The absorption and fluorescence maxima are located at 490 and 555 nm, respectively. The fluorescence spectrum is shown in Fig. 1. This figure also shows the transient absorption spectrum of NKX-2311 in deuterated methanol (CD_3OD) solution measured by the nanosecond laser system. The spectrum is ascribed to the excited singlet state (dye^*). The absorption spectrum of the oxidized form of NKX-2311 (dye^+) was measured by nanosecond transient absorption spectroscopy after adding electron acceptor, 1,4-benzoquinone, in NKX-2311 solution of CD_3OD . As shown in Fig. 1, there are two characteristic peaks at around 875 and 1010 nm.

Steady-state UV-visible absorption spectrum of the NKX-2311/ZnO film is also shown in Fig. 1. It was found that adsorption of the dye onto ZnO and TiO_2 (data not shown) leads to the spectral blue-shift of the dye absorption by 15 and 25 nm, respectively, and slight broadening compared with the spectrum in solution. When a bare ZnO film (without dye) was excited at 355 nm with the nanosecond laser, an absorption band shown by the dashed line in the same figure was observed in the near IR region. This band is assigned to intra-band transitions of electrons in the conduction band [10]. Electrons in TiO_2 showed weaker absorption in the near IR region.

The bottom panel in Fig. 1 shows the transient absorption spectra of NKX-2311/ZnO in the spectral range between 600 and 1350 nm at 2 - 100 ps after excitation at 540 nm by the femtosecond laser pulse. In the visible region, negative signals due to transient bleaching of the ground state absorption (up to ~ 630 nm) and stimulated emission on its longer wavelength side (up to ~ 780 nm) are observed. The stimulated emission extends toward the longer wavelength side compared with the steady-state emission of the dye in solution. In the near IR

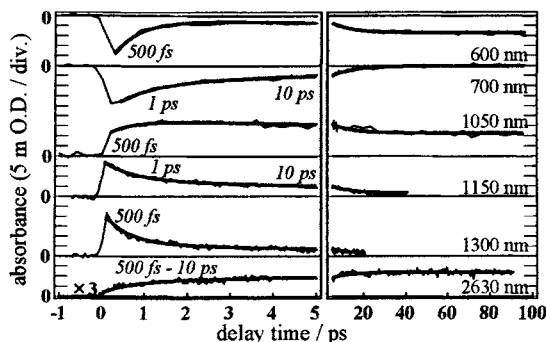


Fig. 2. Transient absorption time profiles of NKX-2311/ZnO at the probe wavelengths of 600, 700, 1050, 1150, 1300, and 2630 nm after 540 nm excitation by the femtosecond pulse with the intensity of about $10 \mu\text{J}$. Thick solid lines are the result of a fitting procedure. Major time constants are indicated.

region two peaks at 900 and 1050 nm are observed clearly at 2 and 100 ps. The spectral shape is very similar to that of dye^+ in CD_3OD solution except for a slight red-shift. Therefore it is obvious that the dye is oxidized within 2 ps after photoexcitation and dye^+ remains at 100 ps. It is also worth noting that the intensity of the dye^+ band itself is almost the same at 2 and 100 ps, while a broad absorption band, decreasing with time, seems to overlap with the dye^+ absorption.

The origin of the broad absorption band around 1200 nm is likely to be a charge transfer band of the exciplex as our previous result of N3/ZnO [8]. Since many transient species overlap each other, we measured the time profiles of the transient absorption at several wavelengths under approximately the same pump conditions. The wavelengths chosen were 600, 700, 1050, 1150, 1300, and 2630 nm to selectively (or dominantly) observe the stimulated emission, the longer wavelength side of the stimulated emission, dye^+ , the broad absorption band, the excited singlet state of the dye, and e^-_{CB} , respectively. The results are shown in Fig. 2. Although all of observed time profiles were multiexponential, we could analyze them by using three representative time constants of 500 fs, 1.0, and 10 ps with an additional constant component. The fitting curves obtained are drawn by thicker solid lines.

At 1150 nm, the dye^+ absorption is negligible, and contributions from dye^* and e^-_{CB} absorption bands are small as suggested by the amplitudes obtained at 1300 and 2630 nm and spectral shapes of dye^* and e^-_{CB} . Therefore it seems that the observed large amplitude at 1150 nm is mainly due to a charge transfer band as in our previous work on N3/ZnO. Both the charge transfer band at 1150 nm and stimulated emission at 700 nm grow within 100 fs and then decay double-exponentially with major time constants of 1.0 and 10 ps. The appearance of not only the charge transfer band but also of stimulated emission on the longer wavelength side of the dye fluorescence in solution can be a strong evidence of exciplex formation. Corresponding to the decay, the absorption of e^-_{CB} at 2630 nm increases, indicating slow electron injection into the conduction band. However, dye^+ absorption itself does not increase after 2 ps as mentioned above. This means that the exciplex observed at 2 ps has an ionic character. In other words, electron "ejected" from dye^* is still localized at the vicinity of dye^+ to form an ionic exciplex. Then the localized electron is released to the bulk to become a conductive electron on the 10 ps time scale.

Besides the electron injection through the exciplex, rapid decay behaviors with a 500 fs constant were clearly observed for the stimulated emission at 600 nm and the S-S absorption at 1300 nm, corresponding to the quenching of dye^* . It is clear that direct electron injection

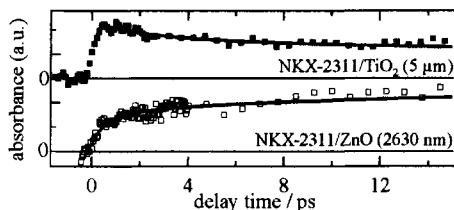


Fig. 3. Transient absorption profiles of NKX-2311/TiO₂ at 5 μm and of NKX-2311/ZnO at 2630 nm.

from dye* into the conduction band of ZnO within 500 fs took place. From the rise profile of e⁻_{CB} at 2630 nm, the percentage of this direct reaction path can be estimated as 43 % in the total injection process.

3.2. Comparison with NKX-2311/ TiO₂

TiO₂ is, at present, the most promising material to develop dye-sensitized solar cells, although the reason is not understood well. Actually we made solar cells based on the NKX-2311 dye using both TiO₂ and ZnO, and it was found that TiO₂ showed better performance (6% solar energy-to-electricity conversion efficiency) [9]. The mechanism achieving such a high performance is now being investigated using various techniques. Here we present our investigation by femtosecond spectroscopy. Measurements were made for NKX-2311/TiO₂, and the results were compared with those of NKX-2311/ZnO. It was found that the electron injection time was much shorter for NKX-2311/TiO₂ compared to that of NKX-2311/ZnO. The decays of stimulated emission and S-S absorption were in the subpicosecond range and slightly depend on probe wavelengths. The rise at the peak wavelength of the dye⁺ band was within 230 fs, and the rise of the absorption band of the conduction band electrons at 5 μm was within 600 fs as shown in Fig. 3. Detailed subpicosecond dynamics is under investigation. However, it is clear that electron injection from the photoexcited NKX-2311 dye into the conduction band of TiO₂ is more than 10 times faster than that of ZnO. Since the conduction band bottoms for TiO₂ and ZnO are located at similar positions (-0.5 V vs. NHE), it is likely that the observed difference in electron injection dynamics is mainly due to the larger density of states (DOS) of the conduction band of TiO₂. Actually near the bottom within the conduction band, DOS of TiO₂ is about 200 times larger than that of ZnO [5].

REFERENCES

- [1] B. O'regan, M. Grätzel, *Nature* 353 (1991) 737.
- [2] S. Iwai, K. Hara, S. Murata, R. Katoh, H. Sugihara, H. Arakawa, *J. Chem. Phys.* 113 (2000) 3366.
- [3] R. Huber, J.E. Moser, M. Grätzel, J. Wachtveitl, *J. Phys. Chem. B* 106 (2002) 6494.
- [4] Y. Tachibana, J.E. Moser, M. Grätzel, D.R. Klug, J.R. Durrant, *J. Phys. Chem.* 100 (1996) 20056.
- [5] J.B. Asbury, E. Hao, Y.Q. Wang, H.N. Ghosh, T.Q. Lian, *J. Phys. Chem. B* 105 (2001) 4545.
- [6] G. Benkő, J. Kallioinen, J.E.I. Korppi-Tommola, A.P. Yartsev, V. Sundström, *J. Am. Chem. Soc.* 124 (2002) 489.
- [7] C. Zimmermann, F. Willig, S. Ramakrishna, B. Burfeindt, B. Pettinger, R. Eichberger, W. Stork, *J. Phys. Chem. B* 105 (2001) 9245.
- [8] A. Furube, R. Katoh, K. Hara, S. Murata, H. Arakawa, M. Tachiya, *J. Phys. Chem. B* 107 (2003) 4162.
- [9] K. Hara, T. Sato, R. Katoh, A. Furube, Y. Ohga, A. Shinpo, S. Suga, K. Sayama, H. Sugihara, H. Arakawa, *J. Phys. Chem. B* 107 (2003) 597.
- [10] R. Katoh, A. Furube, K. Hara, S. Murata, H. Sugihara, H. Arakawa, M. Tachiya, *J. Phys. Chem. B* 106 (2002) 12957.

Heterogeneous electron transfer probed with femtosecond two-photon photoemission spectroscopy

L. Gundlach^a, R. Ernstorfer^a, C. Zimmermann^a, R. Eichberger^a, S. Felber^a, L. Töben^a, E. Galoppini^b, Q. Wei^b, and F. Willig^a

^aHahn-Meitner-Institut, Dept. SE4, Glienicker Str. 100, D-14109 Berlin, Germany

^bDepartment of Chemistry, Rutgers University, Newark, N.J., USA

ABSTRACT

Time-resolved measurements of photo-induced electron injection are reported. Electron transfer occurred from the excited state of the molecular chromophore perylene into the TiO₂(110) surface of a rutile single crystal in ultra-high vacuum. Femtosecond two-photon photoemission spectroscopy (fs-2PPE) was employed since it has a much higher sensitivity than fs transient absorption. A long rigid spacer-cum-anchor group (*TriPod*) was attached to the aromatic chromophore to keep the latter at a distance greater than 1 nm from the crystal surface. Correspondingly, electron transfer was slow with a time constant of 2 ps and could easily be separated from fast energy relaxation with time constant of 40 fs that the injected hot electrons showed in TiO₂. From UPS and XPS data it was deduced that electrons were mainly injected into electronic levels about 0.8 eV above the lower edge of the conduction band.

1. INTRODUCTION

Perylene anchored via rigid chemical bonds to surface atoms of TiO₂ provides an ideal model system for studying ultrafast heterogeneous electron transfer reactions [1]. The spectroscopic properties of the large aromatic chromophore perylene are ideally suited for transient absorption measurements since all the important absorption spectra are well separated in the visible range of the spectrum. Electronic coupling between the photo-excited perylene donor orbital and the electronic acceptor states in the TiO₂ conduction band can be in the range of 50 meV when the rim of the chromophore is separated by only a few saturated bonds from the TiO₂ surface. This situation is realized e.g. with carboxylic acid as the anchor-cum-spacer group. Electron injection occurs in the latter case with a time constant of 13 fs as is borne out by transient absorption signals measured on nano-structured TiO₂ layers [2]. Electron injection in this system is much faster than vibrational relaxation in the chromophore [1]. This ultrafast injection suggests that the donor level of the excited perylene is located high above the lower edge of the conduction band. In the latter case electron transfer is controlled only by the electronic coupling since the reaction can utilize all the Franck-Condon factors in parallel [3]. By inserting rigid molecular spacer groups between the perylene chromophore and the anchor group the electronic coupling strength can be decreased, e.g. with the *TriPod* anchor-cum-spacer group shown in Fig. 1. With the latter compound the largest time constant

for electron injection was measured with transient absorption in the range of 4 ps [2]. In the nano-crystalline layer there are different adsorption sites that give rise to different distances between the chromophore and the surface of the semiconductor. This problem is greatly reduced for chromophores anchored with rigid spacer groups on the surface of a single crystal in contrast to the nano-structured sponge-type layer. Femtosecond electron injection can be measured on the surface of a single crystal in ultra-high vacuum at sub-monolayer coverage by employing two-photon photoemission (fs-2PPE). The compound shown in Fig.1 is well suited for testing the latter technique since the fast electron relaxation processes experienced by the injected electrons in the semiconductor with time constants of a few ten femtoseconds can be easily distinguished from the fairly slow electron injection process with time constant of a few ps.

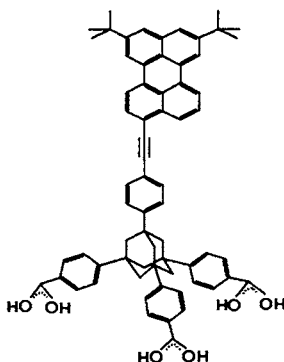


Fig. 1. Perylene-*TriPod* compound with a long rigid spacer-cum-anchor group

2. RESULTS AND DISCUSSION

Two-photon photoemission provides both femtosecond time resolution and a very high sensitivity. It is the ideal technique for measuring photo-induced electron injection from a molecular chromophore at sub-monolayer coverage into the surface of a macroscopic single crystal. It gives additional information on the energetic positions of the electronic levels at the interface. A careful preparation of the surface of TiO_2 is essential for carrying out the measurements. The surface of the rutile crystal has to be free of contaminants like organic carbon and carbon oxide. These contaminants were revealed in XPS measurements of the C1s level (Fig. 2a). A great number of papers deals with the preparation of a clean, well ordered rutile $\text{TiO}_2(110)$ surface. Following the recipe in reference [4] the TiO_2 crystals were cleaned in four consecutive cycles of Ar^+ sputtering (600 eV, 5 μA) with subsequent annealing at 600°C. This led to a sufficiently clean stoichiometric surface. After completion of each preparation cycle, XPS and UPS measurements were performed to check on the amount of adsorbed carbon. Fig. 2a shows that the C1s peak was reduced to below the detection limit after four cycles. Electron emission was observed with UPS from occupied states in the bandgap near the valence band maximum. It is caused by a carbon adlayer. The latter has to be removed since the former emission signal occurs in the range of the ionization energy for the ground state of perylene.

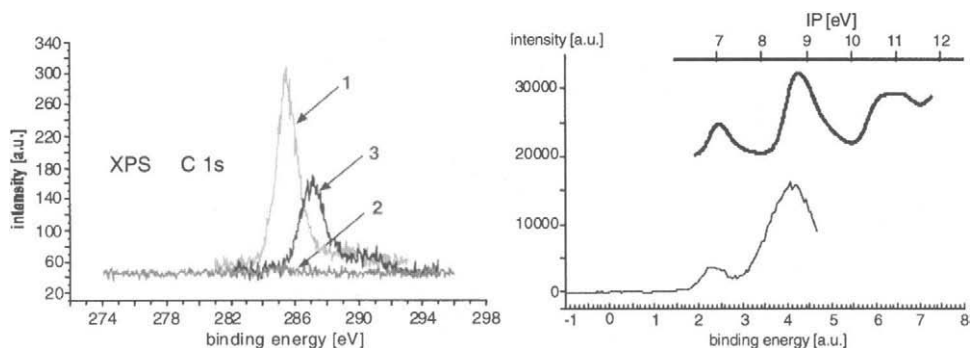


Fig. 2. a: (left) XPS measurement of the C1s level on single crystal $\text{TiO}_2(110)$ after a single annealing step (curve 1), after 4 cycles of sputtering and annealing (curve 2), and for the sample after anchoring of the perylene-*TriPod* (curve 3). b: (right) UPS difference spectrum of the clean surface and the same surface after anchoring the perylene-*TriPod* (lower curve). For comparison the gas phase spectrum of perylene [5] was convoluted with a Gaussian of 100 meV /fwhm corresponding to the energy resolution of the TOF spectrometer (upper curve).

The above described preparation cycles removed the carbon impurities and enhanced at the same time the conductivity of the sample such that no charging effects were observed any more already after the first preparation cycle. The perylene-*TriPod* compound was adsorbed from a toluene solution in a specially designed UHV chamber. The C1s peak in the XPS spectrum was clearly shifted to higher energy for the perylene-*TriPod* compared to the peak measured with the impurities (Fig. 2a). UPS difference spectra of the clean surface and that with perylene-*TriPod* anchored to it show the first two ionization peaks of the perylene chromophore. In Fig. 2b the gas phase ionization spectrum of perylene [5] was convoluted with a Gaussian of 100 meV /fwhm (energy resolution of the TOF spectrometer) and compared with the above described difference spectrum for the TiO_2 surface revealing the presence of the anchored perylene-*TriPod*.

The angle of incidence was 45° . At the clean sample surface a change in polarization of the probe pulse from p- to s-polarized led to a reduction in signal height due to enhanced reflection. No 2PPE signal was detected with s-polarization of the pump pulse since there was no component normal to the surface, i.e. parallel to the optical transition in the perylene chromophore [6] when oriented with the long axis perpendicular to the crystal surface (see Fig. 1).

The energetic position of the photoexcited donor level with respect to the conduction band minimum of the TiO_2 single crystal was probed with femtosecond 2PPE. The cross-correlation with 67 fs /fwhm was measured on a clean Cu(110) surface. The femtosecond 2PPE experiments were performed by exciting the chromophore to the first excited singlet state with a 2.76 eV pump pulse and the injection dynamics was probed with a 4.66 eV probe pulse. The 2PPE signal reached a maximum value after 200 fs (Fig. 3) with an apparent rise time of about 40 fs. The measured 2PPE signal was attributed to photoemission of hot injected electrons. A simple rate constants model (Fig. 3) was employed for separating the two main ingredients in the measured signal, i.e. electron injection from the excited state of perylene and relaxation of the hot injected electrons from the probed energy window.

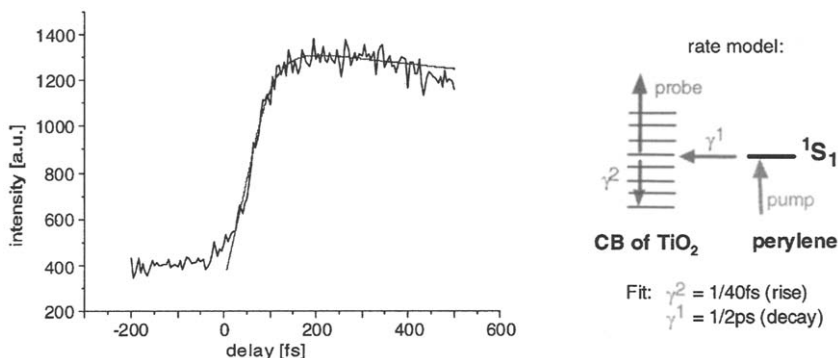


Fig. 3. Femtosecond 2PPE signal of hot electrons injected into rutile $\text{TiO}_2(110)$ from the electronic excited state of perylene-*TriPod*. The pump pulse had 2.76 eV photon energy, the probe pulse 4.66 eV photon energy, and the cross correlation was 67 fs /fwhm. For further details see the text.

The fit to the experimental data (smooth line in the measured fs-2PPE curve in Fig. 3) gave 2 ps as time constant for the electron transfer reaction and 40 fs as time constant for relaxation, i.e. disappearance, of the hot electrons from the probed energy window. The 2 ps electron transfer time measured here with fs-2PPE on the surface of a rutile TiO_2 single crystal provided strong independent support for attributing the longest time constant of 4 ps also to perylene oriented with the long axis perpendicular to the crystal surface (Fig. 1) that had been measured with transient absorption spectroscopy on a nano-structured sponge-type layer of anatase TiO_2 , also in ultra-high-vacuum [2]. From the measured UPS and 2PPE data it was deduced that hot electrons were mainly injected into electronic levels about 0.8 eV above the bottom of the conduction band of rutile TiO_2 (110).

3. SUMMARY

Femtosecond two-photon photoemission (fs-2PPE) was measured at a carefully prepared rutile $\text{TiO}_2(110)$ single crystal surface onto which the molecular compound perylene-*TriPod* was anchored. The fs-2PPE signal probed hot electrons injected from the excited singlet state of perylene into TiO_2 . The fit of a rate constants model to the fs-2PPE signal gave an electron injection time of 2 ps and an energy relaxation time for the injected hot electrons of 40 fs. The dependence of the fs-2PPE signal on the polarization of the pump pulse showed that the perylene chromophores were oriented with their long axis normal to the $\text{TiO}_2(110)$ surface. UPS and 2PPE data showed that the hot electrons were mainly injected into electronic levels about 0.8 eV above the conduction band minimum of rutile TiO_2 .

REFERENCES

- [1] C. Zimmermann, F. Willig, S. Ramakrishna, B. Burfeindt, B. Pettinger, R. Eichberger, W. Störck, *J. Phys. Chem. B* 105 (2001) 9245.
- [2] R. Ernstorfer et al., this Proceedings volume.
- [3] S. Ramakrishna, F. Willig, V. May, *J. Chem. Phys.* 115 (2001) 2743.
- [4] M. Henderson, *Surf. Sci.* 419 (1999) 174.
- [5] R. Boschi, J. N. Murrell, and W. Schmidt, *Discuss. Faraday Soc.* 54 (1972) 116.
- [6] K. Fuke, K. Kaya, T. Kajiwara, S. Nagakura, *J. Mol. Spec.*, 63 (1976) 98.

Time resolved ultrafast energy transfer from electrons photoexcited in Pt(111) to adsorbed CO during photodesorption

F. Fournier, W. Zheng, S. Carrez, H. Dubost, B. Bourguignon

Laboratoire de Photophysique Moléculaire du CNRS
Bâtiment 210, Université de Paris-Sud 91405 Orsay Cedex (France)

1. INTRODUCTION

Photodesorption of adsorbed molecules resulting from electronic excitation of the substrate is an important problem. It allows to study how electrons are coupled to adsorbate degrees of freedom, which has a broad interest for surface chemistry in general. So far photodesorption has been studied using femtosecond pulses by a two pulse correlation approach [1]. This allows to determine whether it scales temporally with electronic excitation, or with substrate heating. A second method was employed recently [2], consisting of probing adsorbate vibrations with femtosecond temporal resolution using sum frequency generation (SFG). For CO/Ru(0001) (a case of phonon mediated photodesorption) a broadening and red-shift of CO internal stretch was observed. Data analysis revealed that frustrated rotation is excited at the fluences where photodesorption occurs. In this work, we apply this method to a system where photodesorption is believed to be mediated by electrons rather than by phonons.

2. EXPERIMENTAL

The Pt(111) sample is prepared and controlled under ultra high vacuum using standard methods. An amplified Ti:sapphire laser pumps an optical parametric amplifier that produces tunable IR. The residual beam is split into a pump beam (50 μJ , ≈ 100 fs), and a probe beam. The linewidth of the latter is adjusted by means of a pulse shaper. Vibrationally resolved SFG spectra are obtained by overlapping this ≈ 2 μJ , ≈ 4 ps, ≈ 4 cm^{-1} FWHM “visible” beam and the ≈ 3 μJ , ≈ 145 fs, ≈ 150 cm^{-1} FWHM IR beam onto the sample in a copropagating, colinear configuration. The spectral resolution in SFG depends only on the bandwidth of the visible laser. Spectra are acquired without scanning the IR frequency [3]. The beams are spectrally filtered and dispersed by a monochromator on a CCD camera. The measured spectrum is readily converted into a vibrational spectrum by subtracting the frequency of the visible probe beam. The pump beam is directed onto the sample at an angle close to that of the probe beams using the same lens as the probe beams. This ensures that the pump-probe time resolution is not spoiled geometrically and remains close to the pulse duration of the lasers. We have checked that sample heating due to the pump beam cannot bias our results.

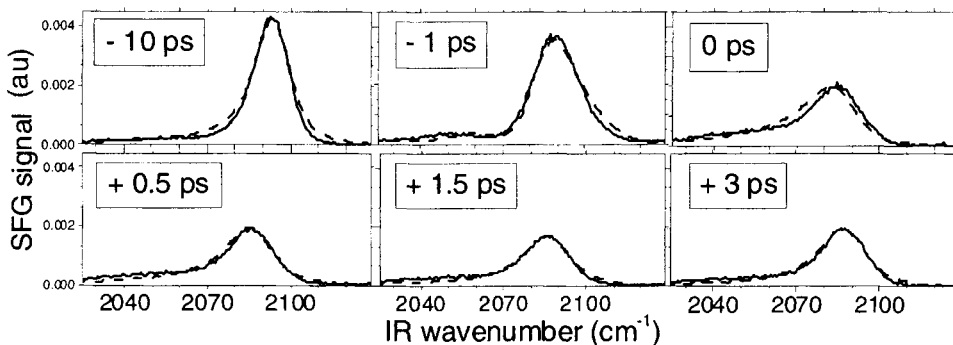


Fig. 1. Pump-probe spectra at selected delays together with their numerical simulation.

3. RESULTS

Fig. 1 displays a series of SFG spectra of CO/Pt(111) for selected pump-IR probe delays. In this work, we only present a general discussion of spectrum analysis. A more detailed report will be presented elsewhere. A red shift and broadening of the CO band (as already observed for CO/Pt(111) at a ps time scale [4], and for CO/Ru(0001) [2]), and variations of the spectral shape, are observed. This does not indicate an excitation of the internal stretch itself (there is no indication that $v=1$ is populated). The spectral changes rather reflect the excitation of other modes which perturb the internal stretch through anharmonic coupling. Among the three possible modes, frustrated translation and frustrated rotation can be considered. The CO-Pt stretch is ignored because it is expected to produce a blue shift.

The CO band is modified even at negative delays as a result of the coherent nature of SFG : because the visible pulse is long, SFG photons are emitted after the IR pulse with the coherence decay time $T_2 = 1.01$ ps (measured separately). Therefore, at negative delays an “unperturbed” and a “perturbed” fraction of SFG photons are emitted before and after the pump pulse. The transition between the two is sudden, resulting in an interference between the two parts [5]. This is why small extra peaks exist at negative delays, one of them being clearly visible in Fig. 1 at -1 ps. Another consequence of the finite coherence decay time is that unusual spectral shapes can be modelled if the CO frequency and width ($2/T_2$) vary at a timescale shorter than T_2 . Although SFG pulses have a duration characterized by T_2 , the temporal resolution is not limited by T_2 : pump probe spectra are the Fourier transform of the electric field $E_{\text{vis}}(t)$ of the visible ps laser convoluted with the polarization induced by the IR pulse which oscillates at $\omega_{\text{CO}}(t)$ with damping time $T_2(t)$. Therefore the spectra “contain” $\omega_{\text{CO}}(t)$ and $T_2(t)$ over the period of SFG emission and this information is recovered by spectrum simulation.

The shifts and width corresponding to the spectra are shown in Fig. 2. CO responds to the pump beam with a sub-ps timescale. A sub-ps decay is followed by a slow decay of ca. 100 ps which corresponds to heat diffusion. We are interested to model the dynamics in the

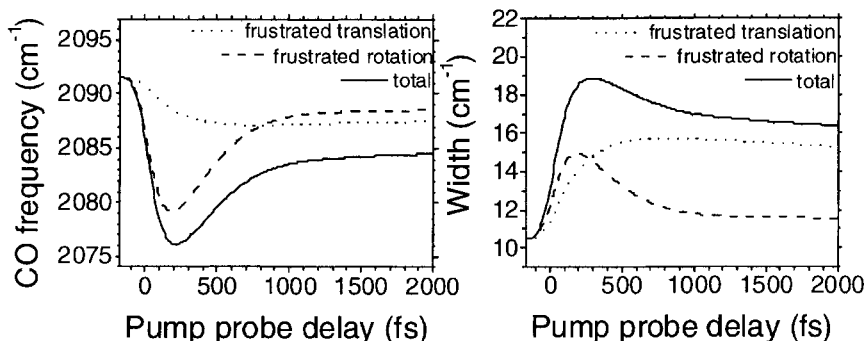


Fig. 2. CO internal stretch frequency and width as a function of time, as extracted from the numerical simulation of the spectra. Contributions of the frustrated rotation and the frustrated translation are also shown.

temporal window defined by our pump pulse duration of ≈ 100 fs and the electron-phonon equilibration time of 1 to 2 ps [4]. The goal of spectrum simulation is to retrieve the variations of CO stretch frequency and width as a result of the transient excitation of the perturbing modes. This excitation is calculated in the form of a variable temperature $T_{\text{ads}}(t)$ assigned to each perturbing mode, using the so-called 3 temperature model (Fig. 3). The model calculates the pump laser absorption as a function of depth, the resulting electron temperature $T_e(t)$ assuming immediate thermalization among electrons, and evaluates heat diffusion resulting from the induced temperature gradient. In addition, heat exchange between electrons and phonons (characterized by a varying temperature $T_{\text{lat}}(t)$) is evaluated. All parameters are available in the literature. $T_{\text{ads}}(t)$ is calculated using two timescales τ_e and τ_{lat} , defined as $dT_{\text{ads}}(t)/dt = (T_e - T_{\text{ads}})/\tau_e + (T_{\text{lat}} - T_{\text{ads}})/\tau_{\text{lat}}$. These timescales characterize the energy flow between electrons and phonons and the vibrational mode, respectively. $T_{\text{ads}}(t)$ allows in turn to calculate the spectroscopic parameters $\omega_{\text{CO}}(t)$ and $1/T_2(t)$ of CO internal stretch assuming a linear dependence on $T_{\text{ads}}(t)$.

We follow the method of Ref. [4] to calculate the SFG response in the time domain. The IR polarization is calculated by solving the Schrödinger equation in the formalism of the density matrix. It is proportional to the coherence induced by the IR pulse between $v=0$ and $v=1$. The coherence is the solution of standard coupled differential equations [6].

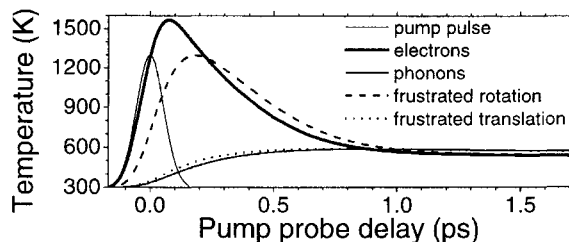


Fig. 3. Three temperature model : pump pulse temporal profile, and variation of the temperatures of electrons, phonons, frustrated rotation and frustrated translation.

The CO frequency and width variations with time shown in Fig. 2 allow to reproduce quite satisfactorily the whole series of pump-probe spectra (Fig. 1). It is impossible to obtain this temporal dependence of the frequency and shift if the CO internal stretch is coupled to a single mode. We assume that the effects of the two modes are additive. Mode 1 is characterized by anharmonic coupling $\delta\omega_1 = -1 \text{ cm}^{-1}$, $\tau_e^1 = 1 \text{ ps}$ and $\tau_{\text{lat}}^1 = 100 \text{ fs}$ (slow coupling to electrons, fast coupling to phonons), and mode 2 by $\delta\omega_2 = -11 \text{ cm}^{-1}$, $\tau_e^2 = 100 \text{ fs}$ and $\tau_{\text{lat}}^2 = 1 \text{ ps}$ (fast coupling to electrons, slow coupling to phonons). The strength of anharmonic coupling, and the coupling rates to electrons and phonons allow to propose the assignment that mode 1 is frustrated translation and mode 2 is frustrated rotation.

4. DISCUSSION

The present results show that CO responds at a sub-ps time scale ($< 100 \text{ fs}$) to electronic excitation of Pt(111). The very fast coupling between electrons and frustrated rotation is probably a consequence of the anisotropy of the CO-metal potential (CO is bonded to transition metals with the C end down) : excitation to electronic states of different geometry is likely to “trigger” CO rotation. In addition, CO rotation is expected to be related to desorption because after return to the electronic ground state (the lifetime of excited electronic states being typically $< 10 \text{ fs}$), rotated CO is weakly bonded. CO does not respond on Ru(0001) as fast as on Pt. On Ru electronic excitation is too weak due to the high energy of the excited states involving CO orbitals [2], explaining that frustrated rotation has to “wait” relaxation from electrons to phonons before it gets sufficiently excited to produce desorption. On both metals the excitation of frustrated rotation is found in the conditions of desorption (at low fluence frustrated translation alone allows to account for the data, both on Pt [4] and on Ru [2]), suggesting again that rotation and desorption are coupled. In summary, our results support the picture that photodesorption is electron mediated on Pt(111), and that frustrated rotation is coupled to the desorption channel. However, the latter conclusion requires more evidence : the non observation of the CO-Pt vibration may indeed be related to the photodesorption dynamics (the frustrated rotation being better coupled to the photodesorption coordinate), but it can also result from a weak anharmonic coupling with CO internal stretch.

REFERENCES

- [1] F. Budde, T. F. Heinz, M. M. T. Loy, J. A. Misewich, F. de Rougement, H. Zacharias, *Phys. Rev. Lett.*, 66 (1991) 3024.
- [2] M. Bonn, C. Hess, S. Funk, J. H. Miners, B. N. J. Persson, M. Wolf, G. Ertl, *Phys. Rev. Lett.*, 84 (2000) 4653.
- [3] L.J. Richter, T.P. Petralli-Mallow, J.C. Stephenson, *Opt. Lett.*, 23 (1998) 1594.
- [4] T.A. Germer, J.C. Stephenson, E.J. Heiweil, R.R. Cavanagh, *J. Chem. Phys.*, 98 (1993) 9986.
- [5] M. Joffre, *Phys. Rev. Lett.*, 90 (2003) 139701.
- [6] R. W. Boyd in : “Non linear optics”, Academic Press (San Diego, 1992), p.123.

Femtosecond fluorescence up-conversion microscopy: a new method to study ultrafast dynamics in microstructures

Tatsuya Fujino and Tahei Tahara

Molecular Spectroscopy Laboratory,
The Institute of Physical and Chemical Research (RIKEN), 2-1 Hirosawa, Wako 351-0198,
Japan

1. INTRODUCTION

Microscopic techniques having high temporal resolution attract much interest in many fields of science. They become very important especially when inhomogeneities are present in the system, because the difference in interaction between the molecule and the local environment can cause significant changes in dynamical properties. The time-resolved fluorescence microscopy is one of the most powerful tools for studying the ultrafast dynamics in inhomogeneous systems. However, time-resolution of fluorescence microscopes had been limited to the picosecond or nanosecond regime because they utilized the time-correlated single photon counting method [1, 2] or the streak camera [3]. Recently, we have developed the femtosecond fluorescence up-conversion microscope, which realizes femtosecond time-resolution and nanometer space-resolution simultaneously [4, 5]. We studied ultrafast relaxation of exciton in organic microcrystals, α -perylene, by using this new method.

2. EXPERIMENTAL

A mode-locked Ti:sapphire laser (Coherent, Mira-900F) that was pumped by a Nd:YVO₄ laser (Coherent, Verdi V-5) provided femtosecond pulses (800 nm, 9.0 nJ, 75 fs) at a repetition rate of 78 MHz. The output from the Ti:sapphire laser was frequency doubled by a 1-mm LBO crystal (400 nm, 0.6 nJ) and this second harmonic pulse was used for excitation. The excitation pulse was first introduced into a group velocity dispersion compensation set-up (a prism pair), and the resultant negatively chirped second harmonic pulse was sent into an inverted optical microscope (Nikon, TE-2000U) through a pinhole. The fluorescence from the sample was collected in the back-scattering geometry, and it was guided to the outside of the microscope. Then, the fluorescence was focused into a non-linear BBO crystal, where it

was mixed with the time-delayed fundamental laser pulse to be frequency up-converted. The up-converted fluorescence signal was separated by filters and a monochromator (HR-320, Jovin-Yvon) and it was detected by a photomultiplier (H6180-01, Hamamatsu) with a photon counter (M8784, Hamamatsu). The time-resolution of the measurement was ~ 520 fs with a $100\times$ objective lens (N.A. 1.3, oil immersion). The transverse spatial resolution (XY) of this system was typically ~ 400 nm. The vertical resolution (Z) was evaluated to ~ 4 μm when a pinhole with 600 μm diameter was used. However, the penetration depth of the excitation light is small for crystals so that the excitation volume becomes < 1 μm in this experimental condition. In the fluorescence up-conversion microscope, the vertical spatial resolution is achieved not only by the confocal configuration but also by the up-conversion process, because the up-conversion requires a very tight focus of the sample image on the mixing crystal.

3. RESULTS AND DISCUSSION

We measured the time-resolved fluorescence from an organic microcrystal, perylene, by using the newly developed fluorescence microscope. Perylene has two types of crystal structure, α - and β - perylene. In α -perylene, four molecules exist in a unit cell, whereas two molecules in β -perylene. We chose one α -perylene crystal under the microscope by checking the fluorescence spectrum. At room temperature, α -perylene exhibits very broad fluorescence in the visible region with the intensity maximum around ~ 600 nm. The fluorescence located at ~ 480 nm has been assigned to the emission of the free exciton. The free exciton is relaxed to

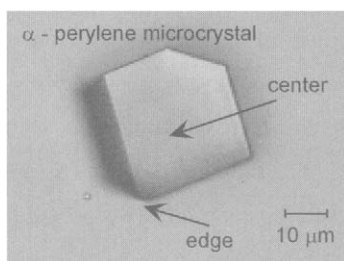


Fig. 1. The CCD camera image of the α -perylene microcrystal used for the femtosecond fluorescence up-conversion microscopy

the Y-state (partially relaxed excimer) and it has been reported that the Y-state gives the fluorescence around ~ 530 nm. Then, the Y-state is relaxed into the E-state that exhibits the broad intense fluorescence around ~ 600 nm [6].

Figure 1 shows the CCD camera image of an α -perylene microcrystal used for femtosecond fluorescence up-conversion microscopy. The time-resolved fluorescence observed from the center part of the crystal is shown in Figure 2(a). The observed decay was well fitted by a triple exponential function that was convoluted with the instrumental response. The time constants for the first two decays were determined to be $\tau_1 = 2.2$ ps and $\tau_2 = 38.7$ ps, whereas the lifetime of the third component was not determined precisely because of its long lifetime (> 1 ns). The observed fluorescence dynamics, as well as the relative amplitude of the three components, was not affected by the change of the excitation pulse energy, which assured that the concentration of the exciton was relatively small under the present experimental condition and that the exciton-exciton annihilation was negligible. Comparing the wavelength dependence of the time-resolved decay with the steady-state fluorescence spectrum, we assigned the τ_1 and τ_2 components to the fluorescence from the free exciton and the Y-state, respectively, whereas the third component showing a long lifetime to the fluorescence from the E-state. In this time-resolved fluorescence, the rise of the Y-state fluorescence was not observed even at the intensity maximum of the Y-state fluorescence (530 nm). It is because the intrinsic transition intensity (\approx oscillator strength) of the free exciton is much higher than that of the Y-state so that the fluorescence from the free exciton masks the rise of the Y-state fluorescence. Figure 2(b) shows the time-resolved fluorescence signal measured with the

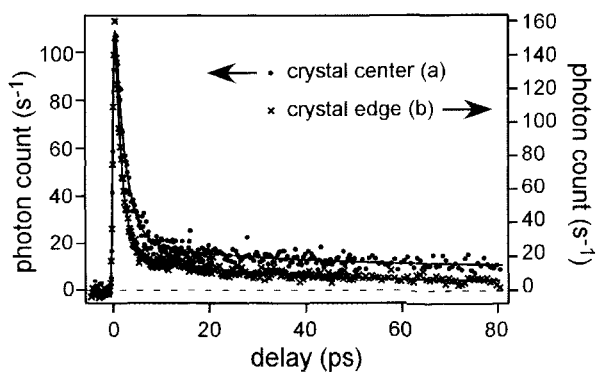


Fig. 2. The femtosecond time-resolved fluorescence (520 nm) obtained at the crystal centre (a), and at the edge (b)

excitation at the crystal edge. The lifetime of the free exciton and the Y-state were significantly shortened, and they became 1.4ps (τ_1) and 29.8 ps (τ_2). This result clearly showed that the local environments at the crystal center and the edge are significantly different, which causes significant change in the relaxation dynamics of the exciton. The observed difference in the local environments is considered to originate from a difference in the defect concentration.

REFERENCES

- [1] W. Becker, H. Hickl, C. Zander, K.H. Drexhage, M. Sauer, S. Siebert, J. Wolfrum, *Rev. Sci. Instrum.*, 70 (1999) 1835.
- [2] H.C. Gerritsen, M.A.H. Asselbergs, A.V. Agronskaia, W.G.J.H.M.V. Sark, *J. Microsc.*, 206 (2002) 218.
- [3] U. Neuberth, L. Walter, G.V. Freymann, D.B. Dal, H. Kalt, M Wegener, G. Khitrova, H.M. Gibbs, *Appl. Phys. Lett.*, 80 (2002) 3340.
- [4] T. Fujino, T. Tahara, *J. Phys. Chem.B*, 107 (2003) 5120.
- [5] T. Fujino, T. Tahara, in preparation.
- [6] H. Nishimura, T. Yamaoka, K. Mizuno, M. Iemura, A. Matsui, *J. Phys. Soc. Jpn.*, 53 (1984) 3999.

Solvation Dynamics at Water-ZrO₂ Interfaces

A. Tortschanoff¹, E. Portuondo¹, F. van Mourik¹, J. E. Moser², S. Steinemann¹, and M. Chergui¹

¹Laboratory of Condensed Phase Ultrafast Spectroscopy, ICMB, BSP, Ecole Polytechnique Fédérale de Lausanne, CH-1015 Lausanne, Switzerland

²Laboratory of Photonics and Interfaces, ICMB, Ecole Polytechnique Fédérale de Lausanne, CH-1015 Lausanne, Switzerland

1. INTRODUCTION

Reactions and dynamics at solid-liquid interfaces are of fundamental importance in chemistry. They play a crucial role in very different areas including chromatography, heterogeneous catalysis and biochemical reactions. For medical applications Ti is the most important material due to its high stability, inertia and biocompatibility. Detailed knowledge and understanding of the interplay between surface chemistry and the biological response to materials forms an indispensable prerequisite for the prediction of biocompatibility. In this respect, the most outstanding issue concerns the structure and reactivity of water and electrolyte-solutions at the surface of these materials. Much work concerning aqueous structures at interfaces was done using various techniques [1,2,3] which suggests ice-like structures at non-polar surfaces while hydrophilic sites tend to destroy the hydrogen-bonded network of self-associated water molecules [4]. Very little, however, is known about dynamics and mobility of the aqueous phase at liquid-solid interfaces.

To measure solvation dynamics in a liquid we follow the rearrangement of surrounding solvent molecules after photo-excitation of a dissolved dye by recording its fluorescence as a function of time. The Stokes shift response function $S(t) = \frac{\nu(t) - \nu(\infty)}{\nu(0) - \nu(\infty)}$ ($\nu(t)$, $\nu(0)$, and $\nu(\infty)$ represent the maximum of the fluorescence spectrum at times t , zero, and infinity, respectively) is then calculated from the fluorescence emission maximum as a function of time. The key-quantity in this context is the correlation function of the dye's transition energy gap, which in the limit of linear response theory is directly related to the time resolved Stokes shift by the fluctuation dissipation theorem [5]. The time scales of solvation depend on the structure of the environment, and given that water at interfaces has a different structure than in the bulk, we hope to obtain detailed, molecular-level information about the water response at such interfaces.

In this study we use the dye Coumarin 343 (C343) adsorbed on the surfaces of ZrO₂ nano particles in aqueous solution to study the solvation dynamics close to these surfaces. ZrO₂ is, in many respects, very similar to TiO₂ and serves as a suitable model substance since, due to its higher band gap energy, electron injection from adsorbed dyes does not occur. To measure the time resolved Stokes shift, we used femtosecond frequency-resolved upconversion.

2. EXPERIMENT

The principle of our femtosecond fluorescence upconversion set-up is described in much detail elsewhere [6]. Here we use 70 fs pulses from a 250 kHz-Ti:Sa-RegA-system. A part of the beam is frequency doubled to 405 nm to excite the sample in a 0.5 mm flow cell. The emitted fluorescence is collected in transmission geometry and focused on a 250 μm BBO-crystal, where it is mixed with the remaining beam, which is delayed by a computer controlled translation stage. The upconverted light is detected by means of a nitrogen cooled CCD camera. At each time delay the crystal is turned over the whole range of phase-matching angles for the emission in order to get a total time resolved fluorescence spectrum in a single measurement. The time resolution of the set-up was about 120 fs.

The measured data was corrected for group velocity dispersion by comparison with white light generated in water under the same configuration, yielding in the end a two dimensional array of the fluorescence intensity as a function of frequency and time. Singular value decomposition and deconvolution of the obtained decays was used to reconstruct the spectral decay which would correspond to delta pulse excitation. $S(t)$ was calculated from this processed data.

Colloidal solution of ZrO_2 (20% in water) from Alfa AESAR was used without further purification. The particle size is about 5-10 nm. The concentration of the solutions of C343 (Exciton) in water as well as in the colloidal suspension was about 3×10^{-4} M which ensures that there is no dye aggregation on the surface. For the solutions in bulk water the pH was adjusted to be slightly basic with NaHCO_3 .

3. RESULTS

Fig. 1 shows the steady state absorption and fluorescence emission spectra of C343 in bulk water and in an aqueous solution of ZrO_2 nano-particles. In the presence of ZrO_2 the dye forms strong bonds to Zr atoms at the surface (as shown in the inset) and we obtain complete adsorption to the ZrO_2 -surface. Upon adsorption both, the absorption as well as the fluorescence band, show a pronounced red-shift. This bathochromic shift is an indication that C343 is covalently bound to the surface, while in bulk water it is found in its ionized form.

Upon adsorption on ZrO_2 the amount of water molecules in the first solvation shell of C343 is decreased due to the presence of the surface. The reduced solvation shell as well as prealignment of the water molecules around the ZrO_2 surface is probably behind the reduction of the Stokes shift which is observed in the steady state spectra.

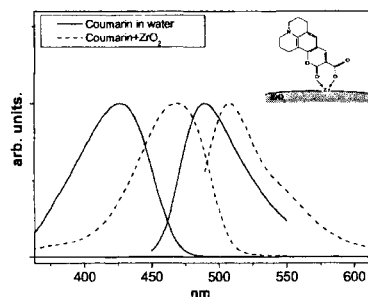


Fig. 1: absorption and fluorescence spectra of coumarin 343 in water (solid line) and adsorbed on ZrO_2 (dashed line). The inset shows the structure of coumarin 343 adsorbed on ZrO_2 [7].

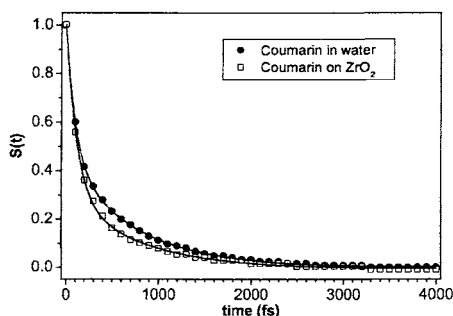


Fig. 2: Solvation function of coumarin 343 dye in water and adsorbed on ZrO_2

First results from our fluorescence upconversion experiments are shown in Fig. 2, which displays the solvation-functions of C343 in bulk water and adsorbed on ZrO_2 nanoparticles. The response in bulk water confirms the previously reported results of bimodal dynamics [8] and a corresponding behaviour can be found for the dye bound to ZrO_2 , indicating that similar processes are involved. The results from biexponential fits to the solvation function $S(t)$ of C343 in pure water and at the ZrO_2 -water interface are listed in Table 1. In both cases we find a fast decay time of about 100 fs and a slower decay of about 750 fs. We can see that the individual decay times stay similar and only the relative contributions change, resulting in an overall somewhat faster solvation for adsorbed dyes.

The total transient Stokes shift ($\nu(0) - \nu(\infty)$) observed in our time resolved experiments of coumarin in bulk water was 820 cm^{-1} . In the case of C343 adsorbed on ZrO_2 it is 340 cm^{-1} . From measurements of the time-zero spectrum, i.e. the emission spectrum of C343 before solvent relaxation, Maroncelli et al. estimated the Stokes shift from solvation to be 1953 cm^{-1} for C343 in water [8]. Thus the time resolution of our experiments allows to observe about 42% of the total solvation process. Especially the very initial part, containing the inertial response is missed.

Table1: results from biexponential fits to $S(t)$ ($S(t) = a_1 \exp(-t/\tau_1) + a_2 \exp(-t/\tau_2)$)

	a_1	τ_1 [fs]	a_2	τ_2 [fs]	$\langle \tau \rangle = \frac{a_1 \tau_1^2 + a_2 \tau_2^2}{a_1 \tau_1 + a_2 \tau_2}$
C343 / water	0.55	102	0.45	753	661
C343 / ZrO_2	0.75	116	0.25	754	553

4. DISCUSSION

Solvation in water was extensively studied and processes on different timescales were described ranging from 30 fs to several ps [8]. Due to our experimental resolution the shortest decay time we measure contains various superimposed contributions from the ultrafast processes presumably the inertial response of water and initial librational motions of molecules in the first solvation layer.

According to literature on time scales of about 1 ps overdamped, collective translational modes of the bulk liquid occur as well as heavily damped restricted translational modes of the liquid with hydrogen bond bending and breaking character [9,10]. We interpret our longer decay time (~ 750 fs) to trace the dynamics of these processes. The significant reduction of

this contribution for adsorbed C343 in our biexponential fits is strong evidence that reduced hydrogen bonding close to the ZrO_2 surface decreases the influence of collective translational motions on solvation. Similar effects were described by Vöhringer et al.[11] at water-membrane interfaces. Overall our results are in accordance with previous aqueous solvation studies [8,12] and especially they confirm, with better temporal and spectral resolution, a previous study by Pant and Levinger [13].

On even longer time scales of several picoseconds we would expect contributions from freely rotating water molecules. However, we found no significant additional shift of fluorescence band on longer timescales in these first studies whose primary aim was the investigation of the initial solvation processes. Further investigations are planned.

Finally we should note that conclusions from these preliminary experiments cannot be drawn fully. Indeed, excitation at 405 nm is quite far on the blue side of the absorption band of adsorbed C343, while it is close to the maximum for C343 in bulk water, and intramolecular cooling and relaxation processes might interfere and give rise to the faster decay [14]. Also prealignment of water molecules close to the surface and the fact that C343 is bound to the ZrO_2 surface via its polar carboxylic moiety, which then gets shielded from solvating water molecules by the surface will have influences on the solvation dynamics.

Ongoing studies using resonant excitation and different dyes will clarify these points. Additional studies using pump-probe as well as photon echo techniques are planned, that should increase the time resolution and give a more complete picture of solvation dynamics at water- ZrO_2 and water- TiO_2 interfaces.

ACKNOWLEDGEMENTS

This work was funded by the ITI Foundation and by the NCCR: Quantum Photonics of the Swiss NSF.

REFERENCES

- [1] P. B. Miranda and Y. R. Shen, *J. Phys. Chem. B*, 103 (1999) 3292
- [2] H. Wang, E. Borguet, E. C. Y. Yan, D. Zhang, J. Gutow, and K. B. Eisenthal, *Langmuir*, 14 (1998) 1472
- [3] A. Opitz, S.I.U. Ahmed, J. A. Schaefer, and M. Serge, *Surf. Science* 504 (2002) 199
- [4] D. E. Gragson, and G. L. Richmond, *Langmuir*, 13 (1997) 4808; G. L. Richmond, *Annu. Rev. Phys. Chem.*, 52 (2001) 357
- [5] R. M. Stratton and M. Maroncelli, *J. Phys. Chem.*, 100 (1996) 12981
- [6] S. Haacke, R. A. Taylor, I. Bar-Joseph, M. J. S. P. Brasil, M. Harting, and B. Deveaud, *J. Opt. Soc. Am. B*, 15 (1998) 1410
- [7] J. M. Rehm, G. L. McLendon, Y. Nagasawa, K. Yoshihara, J. Moser, and M. Grätzel, *J. Phys. Chem.*, 100 (1996) 9577
- [8] R. Jimenez, G. R. Fleming, P. V. Kumar, and M. Maroncelli, *Nature*, 369 (1994) 471
- [9] G. E. Walrafen, *J. Phys. Chem.*, 94 (1990) 2237
- [10] K. Winkler, J. Lindner, H. Bürsing, and P. Vöhringer, *J. Chem. Phys.*, 113 (2000) 4674
- [11] H. Bürsing, D. Ouw, S. Kundu, and P. Vöhringer, *Phys. Chem. Chem. Phys.*, 3 (2001) 2378
- [12] W. Jarzeba, G. C. Walker, A. E. Johnson, M. A. Kahlow, and P. F. Barbara, *J. Phys. Chem.*, 92 (1988) 7039
- [13] D. Pant and N. E. Levinger, *Chem. Phys. Lett.*, 292 (1998) 200; D. Pant and N. E. Levinger, *J. Phys. Chem.*, 103 (1999) 7846
- [14] S. A. Kovalenko, J. Ruthmann, N. P. Ernsting, *Chem. Phys. Lett.*, 271 (1997) 40

Time-resolved absorption spectroscopy of metal nanoparticles in colloidal solution

I. Bugár^a, I. Capek^b, J. Ivan^c, L. Chitu^d, E. Majková^d and D. Chorvát^a

^aInternational Laser Center, Ilkovičova 3, 812 19 Bratislava, Slovakia

^bPolymer Institute, Slovak Academy of Sciences, Dúbravská cesta 9, 842 36 Bratislava, Slovakia

^cInstitute of Materials and Machine Mechanics, Slovak Academy of Sciences, Račianska 75, 831 02 Bratislava, Slovakia

^dInstitute of Physics, Slovak Academy of Sciences, Dúbravská cesta 9, 845 11 Bratislava, Slovakia

1. INTRODUCTION

Metal nanoparticles have been intensively studied due to their potential for both fundamental and applied research. They give a possibility to examine the material properties in transient conditions between the bulk material and separated atoms. Some phenomena, such as surface plasmon resonance transitions, electron-electron or electron-phonon scattering have special character in metal nanoparticles.

An intense femtosecond laser spectroscopy-based research focusing on the fast relaxation processes of excited electrons in nanoparticles has started in the past decade. The electron dynamics and non-linear optical properties of nanoparticles in colloidal solutions [1], thin films [2] and glasses [3] have been studied in the femto- and picosecond time scales. Most work has been done with noble metal nanoparticles Au, Ag and Cu, providing information about the electron-electron and electron-phonon coupling [4] or coherent phenomenon [5]. A large surface-to-volume ratio of the particle gives a possibility to investigate the surface/interface processes.

The dependence of the electron relaxation on the excitation power has been examined for both metal and semiconductor particles. For Ag particles, the power dependence in the 10 ps time scale has been interpreted in terms of the heat exchange between the particle and the surrounding [1]. A different phenomenon, namely the surface traps saturation effect, causes the power dependence on the 100 ps time scale in CdS particles [6]. The power dependence has been not observed for semiconductor Fe₂O₃ nanoparticles [7]. This fact has been explained by high concentration of trap sites in Fe₂O₃, precluding the saturation in the available pump power region of conventional ultrafast laser sources. However, the dense trap sites concept suggests a dynamical Stokes-shift of the induced absorption band, not found by the authors [7]. The wavelength dependence of the induced absorption decay time has been not observed in the probe spectral region of 660 – 850 nm.

The present paper is focused on the comparison of the induced absorption dynamics of Ag and Fe₂O₃ colloidal nanoparticles on the early picosecond time scale. A comparative study was performed using the same experimental conditions for both colloidal solutions with the mean particle diameter of 10 nm. The broad band single shot probe registration in spectral region of 430 – 650 nm enabled to examine the Fe₂O₃ relaxation dynamics at shorter wavelengths than those reported in [7]. The wavelength and power dependence of the induced absorption decay were analysed.

2. EXPERIMENTAL

Femtosecond (fs) Ti:Sapphire amplified laser system was used for the time-resolved measurements designed and supplied by CDP company. The oscillator (TiF50) provided 60 fs laser pulses at 80 MHz repetition rate. The average output of the laser was about 400 mW at the wavelength of 800 nm under the pump power of 4W (Coherent Verdi). The oscillator seeded the multipass amplifier (MPA50) pumped by a green Nd:YAG nanosecond laser (Solar TII LF2210) at 1 kHz repetition rate and 6W average power. The stretched fs pulses were 8-times amplified up to 200 μ J in a system of confocal mirrors and compressed to the 80 fs pulse-width.

The pump-probe measurement system EcxiPro-D was also manufactured by CDP. The amplified 1kHz pulse train passed through BBO SHG crystal and was divided into the pump and probe part by a wavelength selective beam-splitter. A delay line permitting the pulse pathlength change in the 12.5 fs – 2 ns region and a lens narrowing the beam diameter to 2 mm on the sample were placed into the reflected 400 nm pump beam. The energy of the pump pulses was in 1 – 15 μ J range. The white light continuum probe radiation was generated in 1 cm water cell by the fundamental pulses transmitted through the beamsplitter. The cell was located into a 3:1 telescopic system and the white light radiation was divided into two beams by a glass wedge prism after passing through an infrared filter.

The probe beam (one of the two white light beams)-was focused on the same place of the sample as the pump beam by a lens, the reference beam passing through the lens and the sample along a different path. The sample was placed in a 1 mm thick quartz cuvette, permanently rotating to eliminate the thermal effect. The spectra of the probe and the reference beams were registered by a SOLAR TII MS3501i spectrograph. This technique allows a single shot measurement of absorption changes in a 250 nm broad spectral window in the visible region. The EcxiPro-D measurement control software permits to change the central wavelength of the registered spectra, the signal accumulation time on the photodiodes, and the number of the spectrum averaging. The measurement process is fully automatic and the software calculates the ratio of the probe and reference spectral intensities at each step of the time delay. The measurement output is a data field containing the optical density changes Δ OD for a chosen region of the delay times and wavelengths. The time resolution of the apparatus was estimated according the risetime of OD change to be 300 fs.

The Ag and Fe₂O₃ particles were prepared by the inverse micelle technique [8]. Cyclohexan was used as oil component. The colloidal solutions of Ag and Fe₂O₃ nanoparticles were measured in the original concentration, without a dilution. The time-resolved Δ OD were monitored in the spectral region of 430 – 600 nm, the enhanced absorption being observed after the excitation for both Ag and Fe₂O₃. Due to the fluctuation of the laser output, the measurements in the spectral range close to the excitation wavelength were not performed. From the 3D time-wavelength-OD data field, the time-resolved curves were separated and fitted by an exponential fitting procedure. In this way, 10 – 15 wavelength

dependent fitting parameter values were obtained from one measurement. Performing more measurements on the same sample, the fitting parameters were averaged and finally, the wavelength dependences of different samples were compared.

3. RESULTS AND DISCUSSION

A general feature of all samples examined was a decrease of the enhanced ΔOD decay time with increasing wavelength. This result was observed for Ag and Fe_2O_3 nanoparticles on the early picosecond time scale. Typical values of the ΔOD decay time were in 1.2 – 2.5 ps and 0.5 – 1.5 ps ranges for Ag and Fe_2O_3 , respectively. In Fig. 1a, a comparison of the decay time wavelength dependence of Ag and Fe_2O_3 particles is shown. For Ag, the largest ΔOD was observed at 500 nm whereas for Fe_2O_3 , it was the case at 570 nm. Independently of the ΔOD amplitude, the decay time monotonically decreased for both materials and, the Fe_2O_3 decay time being shorter in the whole measured region.

For Ag, the decay time values were found similar to those reported in ref. [1, 2] providing information about the electron-phonon scattering. For Fe_2O_3 , several other phenomena could cause the OD changes at the ultrafast time scale. The sub-picosecond and picosecond decay times allow to take into account hot electron thermalization [4] and subsequent fast relaxation processes such as exciton formation or surface traps filling [6].

The particle diameters, determined from transmission electron microscopy (JEM 100C) pictures, were 12 – 14 nm, 6 – 13 nm and 8 – 12 nm for Fe1, Fe2 (Fe_2O_3) and Ag solutions, respectively. The two Fe_2O_3 samples with different size distributions exhibited different picosecond time-resolved relaxation properties. Therefore, they were compared in a separate measurement. The time-resolved curves were analysed in the region of 470 – 610 nm with 10 nm steps. The wavelength dependence of the decay time for Fe1 and Fe2 solutions are shown in Fig. 1b. The wavelength dependence in the case of Fe1 sample with a narrower particle size distribution is not monotonous, the slowest decay time being observed at 560 nm where the largest ΔOD was found.

The peak-shaped wavelength dependence curve suggests a separated fast filling trap state which causes the anomalous wavelength dependence of the relaxation process. It is interesting that this phenomenon was not observed for Fe2 sample. The absence of the peak-shaped wavelength dependence could originate from the larger size distribution of Fe2 particles. The size of particles affects their band structure and for Fe2 solution, one can assume a smearing of the effect observed for Fe1 solution due to the broader particle size distribution.

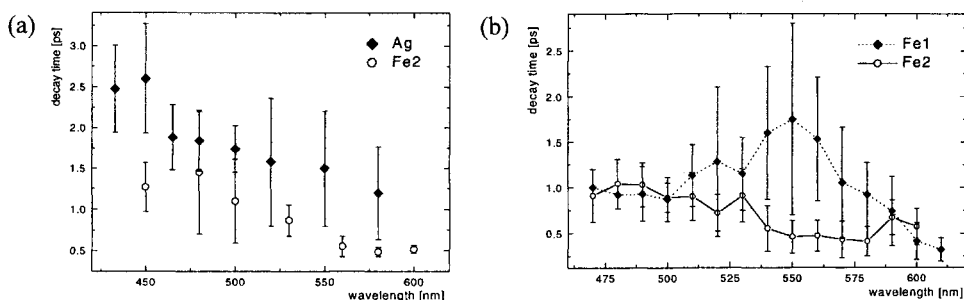


Fig. 1. Comparison of the wavelength dependences of the enhanced absorption decay time for the (a) two examined materials (b) two Fe_2O_3 samples with different particle size distributions

Both Fe₂O₃ solutions exhibited a second, slower relaxation time, absent for Ag particles. From the 100 ps time scale measurement of FeI solution, the time constant of the slower process of 16 ± 2 ps was found. The wavelength dependence was not observed. The time constant was found examining the 470 – 560 nm spectral region and its average value was determined using a two-exponential fitting procedure. The power dependence of the time-resolved absorption was observed for Ag solution and was absent for Fe₂O₃ solutions. The Ag samples at the blue edge of the absorption spectra showed the absorption bleaching effect after the initial relaxation of the enhanced OD. The absorption decrease 6 ps after the excitation proved to be power dependent at 480 nm and reached the 30 % level of the enhanced Δ OD amplitude at 12 μ J pump pulse energy.

The two-exponential character of the time-resolved curves is most probably connected with the more complex band structure of Fe₂O₃ comparing with Ag. Considering the absence of some wavelength dependence of the longer time constant for Fe₂O₃, a deeper defect trap state could be a possible explanation of this effect. The study of Fe₂O₃ samples confirmed the absence of the relaxation process power dependence reported in [7]. These results indicate a high density of the mid-bandgap trap states, providing many nonradiative relaxation pathways and preventing the surface trap states from the saturation.

4. CONCLUSIONS

Time-resolved absorption of Ag and Fe₂O₃ nanoparticles in colloidal solution was studied with femtosecond resolution at the wavelengths of 400 nm (pump) and 430 - 600 nm (probe). The average diameter of Ag and Fe₂O₃ particles was around 10 nm, The electron-phonon interaction time constant was found to be wavelength dependent for both Ag and Fe₂O₃. In the case of Fe₂O₃, this result extends earlier studies where the wavelength dependence was not determined. The time-resolved curves exhibited the mono-exponential and two-exponential behaviors in the case of Ag and Fe₂O₃, respectively, suggesting the energy band structure differences of these materials.

ACKNOWLEDGEMENT

This work was supported by EC Human Potential Program RTN1-1999-00150, Science and Technology Assistance Agency Grant Nr. APVT-51-021702 and by Scientific Grant Agency VEGA Nr. 2/3149/23 and 2/1014/21.

REFERENCES

- [1] J.H. Hodak, I. Martini and G. Hartland, *J. Phys. Chem. B*, 102 (1998) 6958.
- [2] J. Hohlfeld, S.-S. Wellershoff, J. Güdde, U. Conrad and V. Jähnke, E. Matthias, *Chem. Phys.*, 251 (2000) 237.
- [3] Y. Hamanaka, A. Nakamura, S. Omi, N. Del Fatti, F. Vallée and C. Flytzanis, *Appl. Phys. Lett.*, 75 (1999) 1712.
- [4] J.-Y. Bigot, V. Halté, J.-C. Merle, A. Daunois, *Chem. Phys.*, 251 (2000) 181.
- [5] G.V. Hartland, *Femtochemistry and Femtobiology* ed. by A. Douhal and J. Santamarie, World Scientific Publishing, Singapore, 2002, 611.
- [6] C. Burda and M.A. El-Sayed, *Pure Appl. Chem.*, 72 (2000) 165.
- [7] N.J. Cherepy, D.B. Liston, J.A. Lovejoy, H. Deng and J.Z. Zhang, *J. Phys. Chem. B*, 102 (1998) 770.
- [8] C.T. Seip, C.J. O'Connor, *NanoStruct. Mater.*, 12 (1999) 183

Determination of femtosecond dephasing times of organic dyes confined in a single spherical microparticle

P. Sandeep and Prem B. Bisht*

Physics Department, Indian Institute of Technology Madras,
Chennai, TN, 600 063, India.

ABSTRACT

Morphology dependent resonances (MDR) are observed in the fluorescence of 9-amino acridine hydrochloride hydrate (9AAHH) impregnated single microparticles. These MDRs influence the radiative rate of the molecule. From the time-resolved measurement with a resolution of ns we have determined the femtosecond dephasing time of the molecule in a polymer matrix at room temperature.

1. INTRODUCTION

An optical cavity with dimensions of a few micrometers can significantly modify the spontaneous emission properties of emitting atoms or molecules embedded in it. Modification of the spontaneous and stimulated emission properties of the atoms or the molecules is of practical importance to achieve control over the nature. Classically, the variation of the refractive index of the medium of a cavity with the surroundings makes way for the mirror like performance of the media interface, resulting in the total internal reflection of the light rays into the cavity. The total internally reflected light rays fall back on themselves after various round trips in the cavity, providing the condition for a resonant feedback. For a spherical cavity, a simple treatment of the Maxwell's equations for the electromagnetic field inside and outside the cavity results in spherical Bessel and Hankel functions of the first kind [1]. The scattering efficiency (Q_{sca}) which is a measure of the ability of a microsphere to scatter power is given by

$$Q_{sca} = \frac{2}{x^2} \sum_{n=1}^{\infty} (2n+1) (|a_{n,l}|^2 + |b_{n,l}|^2) \quad (1)$$

where $a_{n,l}$ and $b_{n,l}$ are the modes of the resonance. Here n is the mode number and l is the mode order. The size parameter (x) is given by $2\pi r/\lambda$, where r is the radius of the sphere and λ is the wavelength of light. These electromagnetic modes of oscillations are known as morphology dependent resonances (MDR).

When the fluorescing atoms or molecules are placed inside such a microcavity, the fluorescence gets coupled to the MDR as an electromagnetic field. This results in alternatively enhancement or inhibition of the fluorescence depending on whether or not the fluorescence emission spectrally coincides with a cavity resonance. The effect of MDR on the radiative rate of chelated Europium ions [2] as well as the shortening of fluorescence lifetime of Rhodamine 6G due to the effect of MDR have been reported in microdroplets [3].

*Corresponding Author: bisht@iitm.ac.in

However, a study of a few dyes of higher fluorescence quantum yield in polymer microparticles did not show any change in the fluorescence lifetime even though the modification of the fluorescence spectra was observed [4]. In this work, a new molecule (9-amino acridine hydrochloride hydrate, 9AAHH) is reported in which we have observed the effect of MDR in both, the steady state spectra and the fluorescence lifetimes. The dephasing time of 9AAHH in polymer matrix at room temperature have been determined from this study.

2. EXPERIMENTAL

Polymethyl methacrylate (PMMA) microparticles (Soken Kagaku, Japan) were immersed in solutions of 5×10^{-4} M of 9AAHH in methanol for more than 30 hours. The particles were washed, dried and transferred to a slide glass for the measurements. The steady state fluorescence spectra of dye-impregnated microparticles were collected with an epifluorescence microscope (Nikon Eclipse E-400) with the help of a monochromator (ORIEL, model 772501). The excitation source for the steady state fluorescence measurements was a super high pressure mercury lamp equipped with a UV band pass filter (330 - 380 nm) and a barrier filter of >420 nm. The time resolved measurements were done with the oscilloscope method. The excitation source was a 40 ps diode laser (PILAS, Advanced Photonics Systems) with pulse energy of 15 pJ and a repetition rate of 1 MHz at 408 nm. A photomultiplier (Hamamatsu R928) was used as a detector. The full width at half maximum (fwhm) of the instrument response function (IRF) was found to be 4.4 ns. The fluorescence decay profiles were deconvoluted with the IRF with Global Unlimited least squares fitting program. The fluorescence lifetime of 9AAHH in water was used as a fluorescence standard to check the reliability of the measurements [5].

3. RESULTS AND DISCUSSION

3.1. Steady state measurements

Fig. 1A. shows the absorption and fluorescence spectra of 9AAHH in a PVA film. It can be seen that there exists an overlap between the two spectra. Fig. 1B. shows the fluorescence spectra of 9AAHH doped single microparticles. Here the spectra contain ripple structures

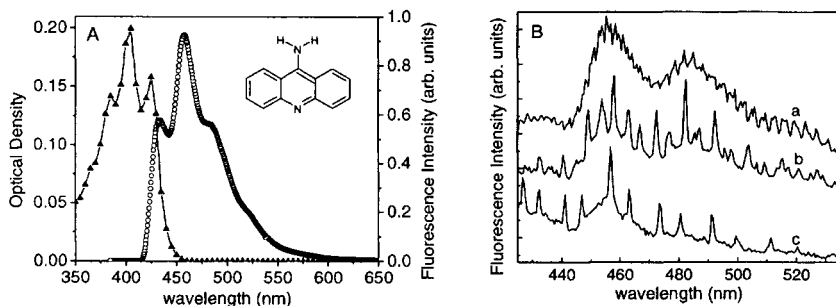


Fig. 1A. The absorption ($-\blacktriangle-$) and fluorescence ($-o-$) spectra of 9AAHH (5×10^{-3} M) in PVA film. The inset shows the molecular structure of 9-aminoacridine. Panel (B) gives the fluorescence spectra of 9AAHH (5×10^{-4} M) in spherical beads of PMMA with radius (a) 9 μ m, (b) 3 μ m and (c) 1.5 μ m.

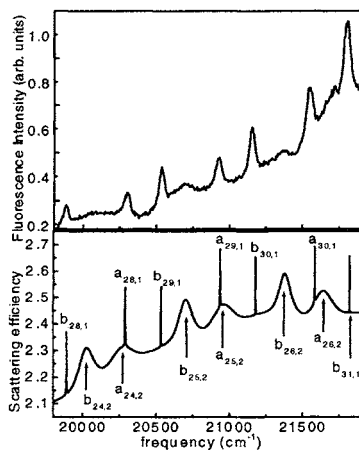


Fig. 2. A portion of the experimentally observed fluorescence spectrum from a 2 μm radius PMMA microparticle (top) and the calculation of scattering efficiency (bottom) for a microsphere of radius 1.77 μm (ref. index = 1.49). First order MDR are dominant in the experiment.

modulated on the bulk fluorescence. A variation of the particle diameter showed these ripple structures to be more congested for a particle having a larger diameter. However for mechanically flattened single particle of any size, the ripple structure was not observed. Fig. 2. shows the numerical simulation for scattering efficiency of single spherical microparticle. For a given radius and refractive index of a particle, the positions of the MDR from the calculations were found to be in excellent agreement with those for the ripple structures observed in the fluorescence spectra. In Fig. 1B. the ratio of the first two peaks varies due to the variation of the self absorption effect in microparticles.

3.2. Time resolved measurements

The fluorescence lifetime from single spherical microparticles of radius greater than 7 μm showed similar behaviour to the bulk study [5]. The fluorescence lifetime of 9AAHH is unaffected for nonspherical, arbitrary shaped particles of any dimension with a resolution of 2 μm . However, a drastic decrease in the fluorescence lifetime is observed for smaller single microspheres, with a threshold value of the particle radius as $\sim 3.5 \mu\text{m}$. The variation of fluorescence lifetimes from dye doped single microparticles is given in Fig. 3. (Panel A) and Table 1 for a dilute concentration. Considering the fact that all the nonradiative processes remain same at the room temperature for all sizes, we assign this change to the spontaneous emission rate enhancement as a function of the size of the microparticle. Panel (B) of Fig. 3. shows the corresponding enhancement ratio in the radiative rate as a function of the particle

Table 1

Fluorescence lifetimes of 9AAHH in single PMMA microsphere and enhancement ratio

Radius (μm)	$\tau, \pm 0.1$ (ns)	Enhancement ratio
20	14.5	1.00
7	10.3	1.41
5	5.5	2.64
3	1.8	8.06

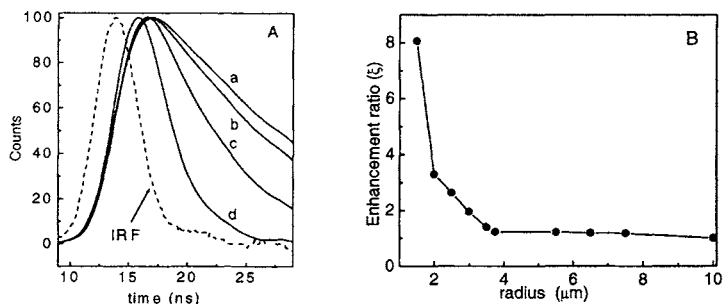


Fig. 3. Panel (A) gives the fluorescence decay curves of 9AAHH ($\sim 5 \times 10^{-4}$ M) in PMMA single spherical microparticle of radius (a) $7.5 \mu\text{m}$ (b) $3.5 \mu\text{m}$ (c) $2.5 \mu\text{m}$ and (d) $1.5 \mu\text{m}$. Panel (B) gives the observed enhancement ratio as a function of microparticle radius.

radius. This effect can be explained by Fermi's Golden Rule for the radiative transition probability and the density of states [6,7].

The threshold of the enhancement in the radiative rate indicates the fulfilment of the condition that the $\Delta\nu_{\text{MDR}}$ is just larger than the homogeneous linewidth of the molecule (Γ_{hom}). It also suggests that the full width at half maximum (fwhm) of the coupling mode is smaller than the Γ_{hom} . In other words, only one sharp high Q mode falls within the Γ_{hom} . Under this condition, the enhancement ratio (ξ) can be related as $\xi = \Delta\nu_{\text{MDR}} / \Gamma_{\text{hom}}$. From the known values of the ξ and $\Delta\nu_{\text{MDR}}$, the Γ_{hom} value for 9AAHH is determined to be 234 cm^{-1} . The corresponding dephasing time ($T_2 = 1/(2\pi\Gamma_{\text{hom}})$) to this homogeneous linewidth is 22 fs. This value is found to be close to those determined by degenerate four wave mixing experiments of cresyl violet in ethylene glycol at room temperature [8].

CONCLUSIONS

The effect of MDR is experimentally observed in the steady state fluorescence spectra and lifetimes of 9AAHH in single microspheres. From this study, we have determined the femtosecond dephasing time of 9AAHH in PMMA matrix at room temperature. The dephasing time of 9AAHH in PMMA is determined to be 22 fs.

ACKNOWLEDGEMENTS

Financial assistance from DST, New Delhi and DRDO, New Delhi is gratefully acknowledged. We thank Professor Eberhard Riedle for fruitful discussions.

REFERENCES

- [1] P. W. Barber and S. C. Hill, *Light scattering by particles: Computational methods*, World Scientific, Singapore, 1990.
- [2] H. B. Lin, J. D. Eversole, C. D. Merritt and A. J. Campillo, *Phys. Rev. A* **45** (1992) 6756.
- [3] M D Barnes, W B Whitten, J M Ramsey, *Chem. Phys. Lett.* **227** (1994) 628.
- [4] P. B. Bisht, K. Fukuda and S. Hirayama, *J. Chem. Phys.* **105** (1996) 9349.
- [5] D. D. Pant, G. C. Joshi and H. B. Tripathi, *Pramana - J. Phys.* **27** (1986) 161.
- [6] E. M. Purcell, *Phys. Rev.* **69** (1946) 681.
- [7] H. Yokoyama and S. D. Brorson, *J. Appl. Phys.* **66** (1989) 4801.
- [8] T. Joo and A. C. Albrecht, *Chem. Phys.*, **176** (1993), 233.

Femtosecond pump-probe investigation of primary photoinduced processes in C₆₀/Sn nanostructures

S.V. Chekalin^a, V.O. Kompanets^a, N.F. Starodubtsev^b, V. Sundstrom^c, and A.P. Yartsev^c

^aInstitute of Spectroscopy RAS, 142190 Troitsk, Russia

^bP.N.Lebedev Physical Institute RAS, 117924 Moscow, Leninsky pr.,53, Russia

^cDepartment of Chemical Physics, Lund University, Box 124, S-22100 Lund, Sweden

1. INTRODUCTION

Composite fullerene-containing materials attract recently a considerable interest as promising materials for conversion of solar energy and as materials with high nonlinear optical properties. Investigation of ultrafast optical response of such materials may be rather difficult due to strong overlapping of broad spectral bands of photoproducts, typical for solid. Pump-probe investigation can reveal relaxation of different components by probing in different spectral ranges. Our preceding works were devoted to the pump-probe investigation with broadband probing of C₆₀ films [1] and C₆₀ films doped by Ti and Sn [2]. The main spectral bands in the difference spectra, observed under excitation of the doped films, are similar to those of the pure C₆₀ films, but considerably broadened, and dynamics of relaxation are quite different. Sn-doped C₆₀ films with different ratio of tin and fullerene content has been investigated recently [3] and present report is mainly based on these data.

2. EXPERIMENTAL

Investigation of the photoinduced processes in different C₆₀-Sn nanostructures excited by 150 fs laser pulse at 400 nm (10^9 W/cm²) was performed with femtosecond supercontinuum probing of difference transmission and reflection in the spectral range of 400-1600 nm. The details of experiments can be found in [3]. Nanostructures were produced in 50-150 nm thick films, deposited on quartz substrates. Deposition was started and terminated by operating individual shutters for Sn and C₆₀. The average number of Sn atoms per C₆₀ molecule η was changed from 5 to 300. The deposited films were analyzed by scanning electron microscope (SEM), X-ray diffraction, optical absorption measurement and Raman spectroscopy.

Two different kinds of composite samples were examined. We call one of them "polymeric" because optical absorption spectra revealed considerable broadening and blue shift typical for polymerized C₆₀. Another sign of polymerization is a red shift of 8 cm⁻¹ and broadening of C₆₀ pentagonal pinch mode A_g(2) in Raman spectra. X-ray diffraction patterns of these samples did not show crystalline metal and revealed only some features of amorphous and crystalline C₆₀. Another kind was obtained for layer-by-layer deposition by alternate opening Sn and C₆₀ shutters the fullerene deposition flux being 10 times less intense. Optical absorption spectra of these samples revealed absence of the main C₆₀ bands. SEM

micrographs detected Sn grains the size of 50 to 500 nm in the samples with $\eta \sim 300$. X-ray diffraction patterns revealed that 10-12 nm nanocrystallites of Sn are present in the sample with the lowest content of Sn ($\eta \sim 100$). We name this kind of the samples CT (Charge Transfer) samples because electron transfer from Sn to C_{60} was observed in multilayer Sn- C_{60} films, containing 10-30 nm grains of Sn [4]. Estimations [2] and our experiments [3] (see below) confirmed CT nature of these samples.

3. RESULTS AND DISCUSSION

The pump-probe study of 500 nm and 550 nm bands (fig.1), ascribed to excited C_{60} anion and to excited neutral C_{60} correspondingly [1], showed that in the polymeric samples excited anion arises faster than in pure fullerene film (curve 1) and increases in abundance for more proportion of Sn (curves 2,3). The behavior of excited neutral C_{60} is similar for pure fullerene and polymeric samples, but it is quite different for CT sample. In the latter case instead of pulsewidth-limited appearance (curve 4) a long rise is observed followed by a non-monotone decay (curve 5). In IR spectral range (1200–1600 nm) (fig.2) the decay observed for polymeric samples (curve 6) is similar to pure C_{60} decay both for differential transmission (negative) and reflection (negative). For the CT samples with 10 nm nanocrystallites nonmonotone relaxation is observed (curves 7-9), but for sample containing Sn crystallites of larger size (100–500 nm), the decay (curve 10) is practically the same as those observed for Sn films without fullerene. The latter has a pulsewidth-limited rise followed by an exponential 5 ps rise and long (300-500 ps) nonexponential decay. The same dynamics is observed for difference reflection increase (fig.2, curve 11), so the transmission dynamics in this case can be practically completely explained by the reflection change. In contrast in the dynamics of the sample with 10 nm Sn nanocrystallites the initial very short spike is negative both in transmission (curves 7-9) and reflection (curve 12). After the initial fall differential reflection sharply increases to positive values and its further decay is in accordance with difference transmission decay (curves 7-9).

Exact assignment of spectral bands in IR is difficult because of strong overlapping of these broad bands. Investigation of pure C_{60} films decay by probing in this spectral region showed that neutral species (namely excited C_{60} molecules) have no absorption there. We observed decay with the same characteristic time for the spectral regions of 800–1100 nm and 1400-1600 nm and ascribed it to cation decay according to our earlier assignment [1]. We

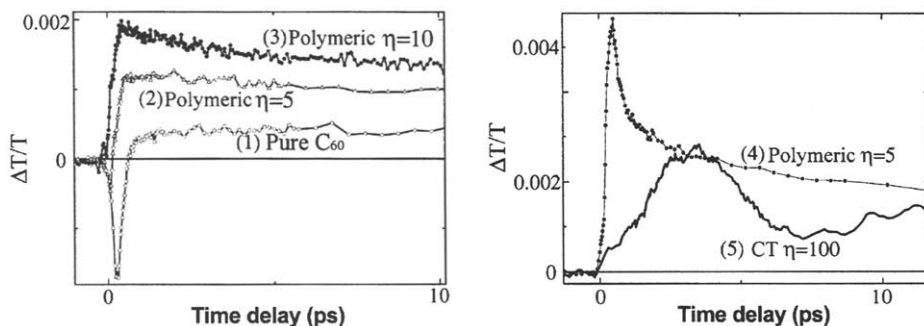


Fig. 1. Decay traces of differential transmission $\Delta T/T$ for different samples at 500 nm (left), and at 550 nm (right).

assign slower decay, observed in the range of 1200-1300 nm, to relaxation of excited anion. To the best of our knowledge, absorption spectra of neither anion nor cation in C_{60} film have been published. In solutions both ions have broad and structureless absorption in the visible (450-600 nm) and more pronounced bands in the near IR (at 800 and 1000 nm for cation and at 950 and 1100 nm for anion) [5]. It is reasonable to assume that the characteristic absorption bands of the ions in film are shifted to longer wavelengths, i.e. similar to what is observed for neutral molecules [6]. At any case anion has IR absorption band at the longest wavelengths. So the bleaching in the spectral range near 1600 nm observed for CT samples (Fig.2) can be attributed to bleaching of anion band. Considerable contribution to transmission decrease of CT samples is connected with photoinduced reflection increase of Sn crystallites which has a maximum at 1400 nm for 10 nm metal particles and shifts to shorter wavelengths (up to 1000 nm) for films with crystallites of larger size.

We believe that observed difference in decay is completely determined by spatial arrangement of the samples. We suppose that polymeric samples consist mainly from $(-C_{60}-Sn)_n$ covalent-linked chains similar to those observed for Pd [7]. Fast decay of the bleaching (caused by electroabsorption) of the 500 nm band of C_{60} (curve 1) has been interpreted in [1] as the absorption rise in this band due to e^- capture by molecules in the ground state resulting in production of excited anion C_{60}^- . Efficiency of such a process is caused by a high electron affinity of C_{60} (2.65 eV [8]). In polymeric samples efficiency of the excited anion production manifested by a high resulting absorption at 500 nm band increases but that of cation (IR band) decreases with more Sn. Moreover, much shorter rise time of excited anions production (rise of 500 nm band absorption near zero delay) is observed (curves 2,3). We suppose that 3 eV excitation results in instantaneous electron transfer (ET) from Sn to fullerene in polymer chain producing excited anion. In this case the proportion of excited anions must be more than that of cations, because cations arise only from excited neutral C_{60} , but not in chains.

Relaxation of CT samples also depends strongly on Sn content. For the most Sn-abundant sample x-ray analysis showed the presence of almost completely oriented Sn crystallites of 100-500 nm size, and electronic microscopy revealed that metal particles were separated by distances less than their size. It means that in this case we have practically metal film. The time response of such a sample appeared to be the same as that for pure Sn film. We attribute pulsewidth-limited rise of negative transmission and reflection (curves 10,11) to excitation of electrons in metal. Subsequent 5 ps rise reflects electron-phonon relaxation and further long decay is due to lattice cooling. Contribution of this dynamics is observed for the

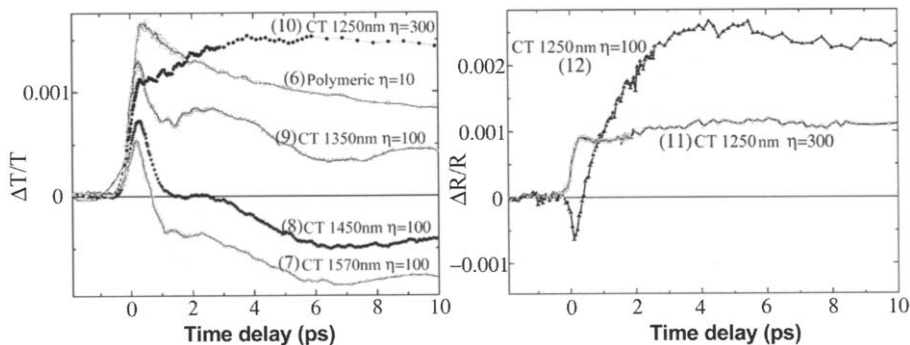


Fig. 2. Decay traces of differential transmission $\Delta T/T$ (left) and differential reflection $\Delta R/R$ (right) in IR spectral range.

samples with smaller Sn grains as well. The main features of relaxation in the sample with Sn nanocrystallites of 10 nm size are determined by fullerene anions, which are present on the surface of Sn initially because of ET from metal to C₆₀. Cations do not arise and do not contribute to IR absorption in this case.

Rough estimation of the number of transferred electrons per C₆₀ molecule [2] resulted in the value of order of 0.1. This value seems to be considerably underestimated taking into account the results [9] giving values of 1.7 and 1 for C₆₀ monolayer on Cu and Au (work functions of these metals are 4.65 eV and 5.1 eV correspondingly, that is more than value of 4.38 eV for Sn). The amount of anions is proportional to Sn surface area, which is by an order larger for small Sn grains. In such a sample a great deal of all C₆₀ are anions. This conclusion follows from the fact that excited neutral C₆₀ molecules are not observed at the moment of excitation in this sample (curve 5). We believe that the short spike in IR transmission and reflection, observed at the excitation moment, is due to anions excited to higher-lying short-lived states. During their fast decay partial bleaching of the C₆₀⁻ IR band superimposed on Sn dynamics is observed (fig.2). Further decay can be related to ET from the excited anions to metallic particles. Such a process is energetically impossible for anions in the ground state [2]. ET process is not instantaneous and takes a time of fast thermalization of electrons in metal. After ET to metal fullerene molecule is brought to excited state that is demonstrated by delayed appearing of 550 nm absorption (curve 5). We attribute the later decay of this absorption with characteristic time of about 3 ps to the exciton quenching by charge carriers due to the dipole-dipole interaction [10]. Exchange interaction can also play a significant role because of the contact with a metal particle. This process results in energy transfer to the rest (nonexcited) anions on metal surface and in observed further bleaching of anion IR band due to excitation (fig.2). The partial restoring of the absorption at 550 nm, following its 3 ps decay stage, can be again related to the ET from excited C₆₀⁻ to Sn, resulting in production of excited fullerene molecule. This process is some more long than first ET step due to a less excess energy of (C₆₀⁻)^{*}. Further relaxation in this sample includes cooling of Sn lattice and decay of IR bleaching due to appearing of C₆₀⁻ in the ground state.

The research described in this publication was made possible in part by support of Russian Foundation of Fundamental Research (Grant 03-02-16736) and ULTRA program of ESF.

REFERENCES

- [1] S.V.Chekalin, A.P.Yartsev, V.Sundstrom, JETP, 93 (2001) 706.
- [2] S.V.Chekalin, M.S.Kurdoglyan, A.N.Oraevsky et al., Proc. SPIE, 13 (2001) 4605
- [3] S.V.Chekalin, V.O.Kompanets, M.S.Kurdoglyan et al., Synth.Metals, 139 (2003) 799.
- [4] W.Zhao, K.Luo, J.Shen et al., Solid State Commun., 83 (1992) 853.
- [5] C.A.Reed, R.D.Bolskar, Chem. Rev., 100 (2000) 1075.
- [6] J.Hora, P.Panek, K.Navratil et al, Phys. Rev., 54 (1996) 5106.
- [7] H.Nagashima, A.Nakaoka, Y.Saito et al., J. Chem. Soc. Chem. Commun. (1992) 377.
- [8] M.S.Dresselhaus, G.Dresselhaus, P.C.Eklund, Science of Fullerenes and Carbon Nanotubes, Academic Press, NY, 1996.
- [9] B.Hoogenboom, R.Hesper., L.Tjeng., G.Sawatzky, Phys.Rev.B. 58 (1998) 7869.
- [10] M.Pope, C.E.Swenberg, Electronic processes in organic crystals, Clarendon Press, Oxford Press, NY, 1982.

Corresponding author S.V.Chekalin, 142190, Institute of spectroscopy RAS, Troitsk, Moscow region, RUSSIA
e-mail: marina@ttk.ru; FAX (7-095) 334 08 86, Tel. (7-095) 334 02 37

Elementary reaction steps of iodine enclosed into zeolites

A. Materny and G. Flachenecker

School of Engineering and Science, International University Bremen
Campus Ring 8, D-28759 Bremen, Germany

1. INTRODUCTION

In our present contribution, we discuss the results of femtosecond time-resolved experiments on iodine molecules in microporous zeolite single crystals formed by pure $\text{SiO}_{4/2}$ tetrahedra structures (DDR = decadodecasil 3R porosil). Inside the DDR porosils, the iodine molecules reside isolated from each other in hexagonal cages having a volume of $\approx 350 \text{ \AA}^3$. The reactions we consider here are the photodissociation following the pump laser excitation of iodine into its electronic B state and the subsequent recombination of the atomic fragments. The dissociation of the $B 0_u^+(^3\Pi)$ state occurs mainly via the crossing repulsive $a 1_g^+(^3\Pi)$ and $a' 0_g^+(^3\Sigma^-)$ states. The predissociation of the B state is mainly induced by interactions with the surrounding matrix system and hence strongly depends on the structure of the porosil. The subsequent caging dynamics takes place along the excited $A 1_u(^3\Pi)$ and $A' 2_u(^3\Pi)$ states as well as the ground $X 0_g^+(^1\Sigma^+)$ state.

2. EXPERIMENTAL AND THEORY

In short, a Ti:Sapphire laser system in combination with two four-pass OPAs were used to create the femtosecond pump and probe pulses at variable wavelengths. The wavelength of the pump laser was chosen to be 530 nm for all experiments presented in the following. For the probe laser we used the fundamental output at 800 nm as well as wavelengths between 300 and 400 nm. The light scattered from the oriented single crystal samples was analyzed by a monochromator equipped with a photomultiplier tube. A more detailed description of the experimental setup is given in ref. 1.

Calculations based on molecular dynamics modeling of a part of our experimental data have been successfully performed by Ermoshin *et al.* [2]. We prefer a simpler model with reduced dimensionality of the bath. The model bases on the Langevin stochastic equation generating Brownian motion. Ermoshin *et al.* [3] have used their model calculating femtosecond pump-probe signals for iodine in rare-gas environments. The model explained main features such as collision-induced molecular dynamics and vibrational relaxation. The algorithm for the solution of the classical Langevin equation we use here differs from that used in ref. 3 in several aspects which are described in more detail in ref. 4. The probability for the predissociation was calculated using the Landau-Zener formalism.

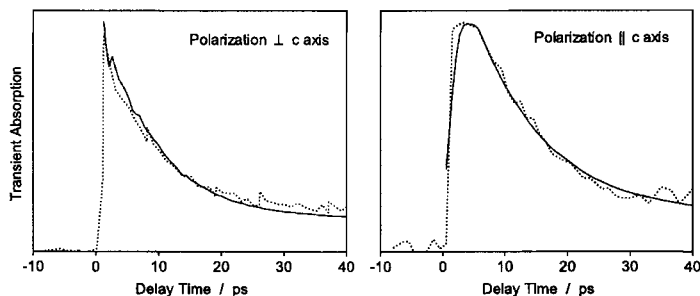


Fig. 1: Polarization dependent pump-probe signals (experiment: dotted; simulation: full).

3. RESULTS AND DISCUSSION

The hexagonal structure of the cages is defined by the crystal *a*, *b*, and *c* axes. The *c* axis is a rotational symmetry axis (C_3 symmetry). The *a* and *b* axes, which are perpendicular to the *c* axis, enclose an angle of 120° . In our experiments, the laser polarizations were parallel to each other and oriented in a defined way relatively to the crystal axes of the DDR crystal.

The iodine molecules can move relatively freely inside the cages of DDR, even allowing rotations. The pump-probe signal obtained from single crystals therefore still arises from iodine molecules having varying orientations relatively to the crystal axes. The question arises whether the orientation of the iodine molecules in the anisotropic cages has any influence on the dynamics of the dissociation and recombination reactions. This cannot be determined using powder samples.

Due to the linear polarization of the pump laser, predominantly iodine molecules having a parallel component of their transition dipole moment can be excited. A probe wavelength of 355 nm resulted in the clearest dependence of the reaction dynamics on the laser polarization. The result of these measurements are depicted in Fig. 1. For laser polarizations being perpendicular to the *c* axis, the transient signal decays rapidly within the first 20 ps. In this range of time a considerably slower decay of the absorption signal could be observed if the laser light polarization was parallel to the *c* axis. After 20 ps the transients become equal for both polarizations. From theory we know that the constant signal observed for the transient taken with $\lambda_{probe} = 355$ nm after a longer delay time is mainly determined by the *B* state dynamics.

Obviously, the initial orientation of the iodine molecules within the crystal cages has a strong influence on the vibrational relaxation as well as the predissociation of the molecules in the electronic *B* state. The other states only play a minor role for the dynamics in the first 20 ps.

The loss of the *B* state population depends on both the dynamics of the vibrational relaxation and the strength of the coupling of the *B* state to the repulsive *a/a'* states. In the simulations, the predissociation of the *B* state molecules is described with the help of the Landau-Zener theory. There, the coupling strength is given by the perturbation energy. Furthermore, the probability for predissociation also depends on the (classical) velocity $v(t)$ which relates this process to the vibrational relaxation dynamics of the *B* state. The theoretical model uses a friction coefficient α to describe the latter process.

Starting from the idea that the vibrational energy relaxation dynamics of the B state depend on the initial orientation of the molecular axes inside the crystalline cages, simulations were performed. The results of these calculations are shown in Fig. 1 (full line). The theoretical results for both polarization directions solely differ in the choice of distinct friction coefficients α . For the transients recorded with a polarization perpendicular to the c axis of the DDR single crystal $\alpha = 3.1 \text{ ps}^{-1}$ was chosen. This value is equal to that found for the results of experiments on powder samples [4]. However, it has to be noted that the result of the simulation shows only minor changes if values of $\alpha > 3.1 \text{ ps}^{-1}$ are chosen. The vibrational relaxation takes place in clearly less than 2 ps. Considering the geometry of the whole system, it becomes clear that the number of collisions of the iodine molecules with the cage walls will take place less frequently if the molecular axes are oriented parallel to the c axis of the crystal than for perpendicular orientation. The best simulation results of transients recorded with laser polarizations parallel to the c axis was achieved for $\alpha = 1.1 \text{ ps}^{-1}$ which coincides with this deliberation.

The calculated B state signals are depicted in Fig. 1. It can be clearly recognized that the B state signal looks completely different for the different polarizations within the first 5 ps. For parallel polarization, the B state signal even rises until 3.5 ps. The reason for this behavior is that the Franck-Condon window favors transitions from the lower vibrational states. Therefore, in spite of the loss of population due to the predissociation process, an increasing signal can be observed. For perpendicular polarization, the B state signal rapidly decays from beginning on. Iodine molecules which are oriented perpendicular to the c axis relax in much less than 2 ps into the lower vibrational states of the B state since the number of collisions with the crystalline surroundings is big. For delay times $t > 5$ ps the vibrational relaxation is also completed for the iodine molecules which initially were parallel oriented to the c axis. The B state signals decay mono-exponentially for both polarizations with the rate $k_P = 0.12 \text{ ps}^{-1}$. Now, the predissociation rate used in the simulation is only determined by the predissociation process.

Comparing the simulations of the single crystal transients with those of the signals of the powder measurements shows that a bigger value of the predissociation parameter W (coupling strength of the crossing potential energy curves) was found for a probe wavelength of 354 nm. The predissociation rate for the powder experiment is $k_P = 0.08 \text{ ps}^{-1}$ which is approximately 30% less than the value found for single crystals. The reason for this difference lies in the isotropic distribution of crystallites in the powder sample resulting in an averaging over the two different cases discussed above for the single crystals.

Due to the rotation of the iodine molecules also single crystal measurements cannot be considered anisotropic after longer delay times. Nevertheless, the delayed population decay of the B state within the first 5 ps for parallel polarization influences the transient up to approximately 20 ps for $\lambda_{probe} = 354 \text{ nm}$. For probe wavelengths 310 and 340 nm the polarization of the lasers have only little influence on the transients. This is due to the fact that the relatively strong recombination signal dominates the overall transient and overlays the differences resulting from the changed B state signal. Therefore, for $\lambda_{probe} = 400 \text{ nm}$ a very clear dependence on the laser polarizations can be expected. However, the transient observed in the experiment is not influenced by a change of these conditions.

4. CONCLUSIONS

We have discussed results from femtosecond time-resolved pump-probe measurements on iodine molecules which had been enclosed into the cages of single crystals of the DDR (deca-dodecasil 3R) porosil. A classical model based on the Brownian dynamics has been applied for the interpretation of the experimentally obtained transients. The vibrational relaxation is described using the Langevin equation. Here, the parameter characterizing the collision-exchange interaction is the friction coefficient α . The predissociation of the iodine molecules in the electronic B state was described using the Landau-Zener formula. The probability for this crossing to repulsive states, $a, a' \leftarrow B$, was described by the coupling parameter W of the Landau-Zener equation.

The simulations demonstrated, that after the pump excitation of the iodine molecules into their B state three elementary dynamical processes determine the further reaction course: (i) the predissociation of the iodine molecules caused by the coupling of the electronic B state to the repulsive a/a' states, (ii) the electronic transitions from these states to the A , A' , and X states due to the caging effect, and (iii) the vibrational relaxation in all electronic states involved in the reaction. Additionally, an energy shift of the potential curves due to the influence of the crystalline DDR cage could be observed.

The vibrational relaxation of the B , A , A' , and X states is mainly caused by the collisions with the surroundings and was found to be completed after less than 2 ps for room temperature. The strong influence of the surroundings on this process could be demonstrated by polarization dependent measurements on iodine embedded in single crystals of the DDR porosil. At room temperature the relaxation time was found to be longer than 4 ps for iodine molecules oriented parallel to the crystal c axis.

The decay of the B state population due to predissociation is linked to the dynamics of the vibrational relaxation. It could be shown that a longer relaxation time also resulted in a delayed predissociation of the B state iodine molecules. As soon as the vibrational relaxation is completed, the predissociation is solely determined by the coupling strength between the bound B and the repulsive a/a' states. The coupling of these states is again a function of the interaction with the surrounding cage.

ACKNOWLEDGEMENTS

This work was funded by the Deutsche Forschungsgemeinschaft (Schwerpunkt "Zeitabhängige Phänomene und Methoden in Quantensystemen der Physik und Chemie", MA 1564/3) and by the Fonds der Chemischen Industrie. We are grateful to Prof. W. Kiefer who made his laboratories available for our experiments and who always showed great interest in our work as well as to Prof. V. Engel and his group who helped with the theory.

REFERENCES

- [1] A. Materny, T. Chen, M. Schmitt, T. Siebert, A. Vierheilg, V. Engel, and W. Kiefer, Appl. Phys. B, 71 (2000) 299.
- [2] V.A. Ermoshin, G. Flachenecker, A. Materny, and V. Engel, J. Chem. Phys., 114 (2001) 8132.
- [3] V.A. Ermoshin and V. Engel, Chem. Phys. Lett., 332 (2000) 110.
- [4] G. Flachenecker, V. A. Ermoshin, V. Engel, R. Neder, G. Wirnsberger, and A. Materny, Phys. Chem. Chem. Phys., 5 (2003) 865.

Nonlinear spectroscopy study of vibrational self-trapping in hydrogen bonded crystals

J. Edler and P. Hamm

Physikalisch-Chemisches Institut, Universität Zürich, Winterthurerstrasse 190, CH-8057 Zürich, Switzerland

1. INTRODUCTION

It is well known that proteins have the remarkable, yet not well understood capability of storing and transporting small quanta of energy in an efficient way. Davydov suggested self-trapping of vibrational energy as a possible explanation of this phenomena [1]. Crystalline acetanilide (ACN) is considered to be a good model to study vibrational excitations in proteins, since it consists of quasi-one-dimensional chains of hydrogen bonded peptide groups with structural properties that are comparable to those of an α -helix, the most common secondary structural motif in proteins. Self-trapping originates from two coupling mechanisms [2]: (i) dipole-dipole-interaction couples the individual peptide units to form delocalized states, i.e. vibrational molecular excitons. (ii) nonlinear interaction mediated through the hydrogen bonds, which stabilize the crystal structure, couples the excitons to lattice phonons. Thus excitation of an exciton leads to a deformation of the lattice and the initially delocalized state collapses to form a self-localized state.

It is well known that the vibrational spectrum of ACN exhibits interesting anomalies in the region of the amide I (i.e the C=O stretching) and NH stretching band [3]. The amide I mode is observed at 1666 cm^{-1} at room temperature and splits into two bands at low temperatures with an additional 'anomalous' band at 1650 cm^{-1} (Fig.1a). The NH stretching mode consists of a main peak at 3295 cm^{-1} accompanied by an almost-regular sequence of satellite peaks towards lower frequencies (Fig.2c). The anomalies in the CO and NH band have been both explained by self-trapping theory [2,3], according to which the main peak represents the free exciton and the anomalous side bands represent self-trapped states.

In previous works self-trapping was observed through an indirect effect, i.e. through the temperature dependence of the linear absorption spectrum [2,3], which is considered to be a signature of the anharmonicity of the potential energy surface. We have recently started to use an alternative, more direct approach to investigate anharmonicity, namely nonlinear vibrational spectroscopy [4-6]. The nonlinear vibrational response is exclusively sensitive to the anharmonic part of the potential energy surface. Anharmonicity at the same time gives also rise to nonlinear dynamics. Hence, nonlinear spectroscopy is extremely valuable to study nonlinear phenomena such as vibrational self-trapping.

We performed femtosecond infrared pump-probe experiments, using pulses with a bandwidth of 200 cm^{-1} (FWHM). A small fraction of the infrared pulses was split off to obtain a broadband probe pulse, which was spectrally dispersed after interaction with the

sample and acquired by a detector array. The remainder was used as a pump pulse, that was spectrally filtered to obtain tunable, narrow band pump pulses for some of the experiments. Monocrystalline samples of ACN and deuterated N-methylacetamide (NMA-D6) were placed in a cryostat and experiments were performed with the E-vector parallel to the hydrogen bond chain.

2. RESULTS AND DISCUSSION

2.1 The amide I mode

In a first set of experiments we applied two-dimensional infrared (2D-IR) spectroscopy to investigate the self trapping mechanism of the amide I band in ACN (Fig. 1b). 2D-IR spectra record the absorption change of the sample as a function of probe frequency and the center frequency of the narrow band pump pulse (spectral width 14 cm^{-1} , pulse duration 700 fs FWHM) [7]. Figures 1c, d show two pump-probe spectra obtained by excitation of either of the two absorption lines of ACN at a temperature of 90 K [5]. These spectra correspond to a horizontal cut through the 2D-IR spectra in Figure 1b. When resonantly pumping the anomalous band (1650 cm^{-1} , Fig. 1c) the band bleaches and a positive band (excited state absorption) emerges at 1644 cm^{-1} . When resonantly pumping the normal band (1666 cm^{-1} , Fig. 1d), on the other hand, hardly any bleach of the band itself is observed. Coherent broad band excitation experiments show that the lifetime of the normal amide I mode is 1.5 ps [5].

Therefore the lack of an observable bleach can only be explained by the cancellation of all contributions to the pump-probe signal, which is the case for a perfect harmonic state. It can be shown that the anharmonicity of a vibrational exciton is a direct measure of its degree of delocalization [5]. Thus, we conclude that the free exciton state is almost perfectly delocalized at 90 K. As temperature increases, a bleach signal starts to be observed, pointing to a non-complete cancellation of the different contributions of the total pump-probe signal. Apparently, thermally induced disorder (Anderson localization) starts to localize the free exciton. The anharmonicity of the self-trapped state (1650 cm^{-1}), on the other hand, originates from nonlinear interaction between the amide I mode and the phonon system of the crystal. It

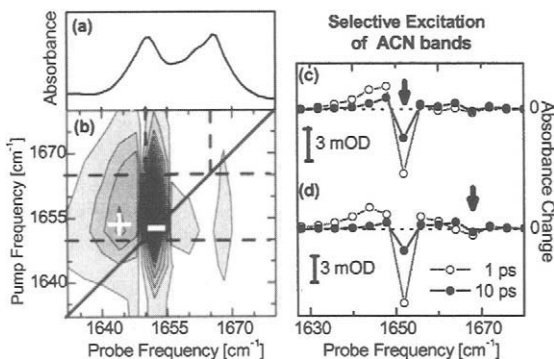


Fig.1. (a) Absorption spectra and (b) 2D-IR pump probe spectra of the C=O mode of crystalline ACN. 2D-IR spectra record the absorption change as a function of probe frequency and the center frequency of a narrow band pump pulse. The contour intervals represent a linear scale. Response of the amide I band upon selective excitation of the self-trapped states (c) and the free exciton peak (d) for two different delay times. The arrows indicate the position of the narrow band pump pulse.

is mediated through the hydrogen bonds and is nonzero even at low temperatures. With rising temperature, the bleach of the 1650 cm^{-1} band diminishes as the band disappears in the absorption spectrum.

Besides self trapping two alternative explanations, Fermi resonance and conformational substates, have been previously discussed as well [2]. In a recent study [6] we compared the 2D-IR spectrum of ACN with those of two molecular systems, which show the same splitting in the amide I band, and which were chosen as simple representatives of the alternative mechanisms. The three 2D-IR spectra differ completely, albeit in a well understood way. Based on the 2D-IR spectroscopic signature Fermi resonance and conformational sub-states can be definitely excluded as alternative explanations for the anomalous spectra of ACN. The 2D-IR spectrum of the amide I mode in ACN, on the other hand, can be naturally explained by self-trapping, as discussed above.

2.2 The NH mode

We used short broadband pump pulses (spectral width 200 cm^{-1} , pulse duration 130 fs FWHM) to excite impulsively the section of the NH absorption spectrum which includes the free-exciton peak and the first three satellite peaks [4]. The transient absorbance change signal shows pronounced oscillations that persist up to about 15 ps and contain two distinct frequency components whose temperature dependence and frequencies match perfectly with two phonon bands in the non-resonant electronic Raman spectrum of ACN [3] (Fig. 2a, b). Therefore the oscillations are assigned to the excitation of phonon wavepackets in the ground state. The corresponding excitation process is only possible if the phonon modes are coupled to the NH mode. Self trapping theory says that these are the phonon modes, which induce the self localization.

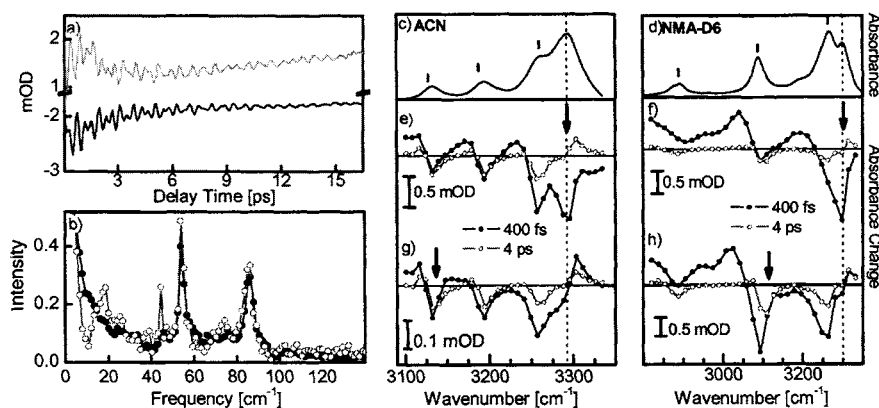


Fig. 2. (a) Coherent Response of the NH mode at 90K after impulsive excitation and the Fourier transform spectra (b), for probe frequencies resonant with the absorption peaks in the linear spectrum at 3295 cm^{-1} (grey lines) and 3195 cm^{-1} (black lines). Part of the NH band of crystalline ACN (c) and NMA-D6 (d). The free excitons are marked by dotted lines and the self-trapped states by black bars. Response of the sample upon selective excitation of the free exciton peak (e, f) and the self-trapped states (g, h) for delay times 400 fs (black line) and 4 ps (grey line). The arrows indicate the position of the narrow band pump pulse.

In a second experiment, narrow band pump pulses (spectral width 30 cm^{-1} , pulse duration 250 fs FWHM) were used to selectively excite individual sub-levels of the NH band (Fig. 2e, g) [4]. On the sub-picosecond time scale, the free-exciton and the lower lying self-trapped states behave distinctly differently. When exciting the free-exciton (Fig 2e), a strong bleach and stimulated emission signal is observed which recovers on a 400 fs time scale. Simultaneously, population is transferred into lower lying self-trapped states. On the other hand, when pumping one of the self-trapped states directly (Fig. 2g), population within all self-trapped states equilibrates essentially instantaneously, but the free exciton peak is not back-populated. This is the direct observation of ultrafast self-trapping: Excitation of the free-exciton leads to an irreversible population of self-trapped states, but not vice versa.

2.3 N-Methylacetamide

Our studies on the NH and amide I band of ACN prove the self-trapping model and introduce a possible signature of self-trapping in pump probe spectroscopy. So far ACN is the only hydrogen bonded crystal for which vibrational self-trapping has been observed. However, other molecules, such as N-methylacetamide (NMA) are structurally very similar to ACN and form the same type of hydrogen bonded crystals. Therefore they should also exhibit self-trapping, but convincing experimental evidence for self-trapping in NMA has never been reported. Interestingly the NH absorption band in NMA and deuterated NMA (NMA-D6) consists of a main peak at about 3300 cm^{-1} accompanied by a regularly spaced sequence of satellite peaks, which is in fact the same bandshape as in ACN, except that the spacing in NMA is three times larger (see Fig. 2c, d). If one compares the pump probe spectrum of NMA-D6 with ACN one observes essentially the same spectral signature. An excitation of the free exciton state results in negative signals at the position of all bands in the NH mode (Fig. 2e, f), while an excitation of one of the self-trapped states gives only a signal for the self-trapped states (Fig. 3g, h). Consequently, one can use the self-trapping interpretation to explain the spectral data in NMA. The comparison between pump-probe and absorption spectra shows that the highest frequency band corresponds in all three molecules to the free exciton.

3. CONCLUSION

In the amide I band of ACN we have observed temperature induced localization of the free exciton mode at high temperatures and self-localization at low temperatures. The NH mode self-localizes even at room temperature, due to the larger self-trapping energy. A comparison between ACN and NMA shows that self-trapping is not a unique feature of ACN, but a general property of hydrogen bonded crystals. Hence one might expect that α -helices should also exhibit vibrational self-trapping. We are currently testing this hypothesis.

REFERENCES

- [1] A. S. Davydov, *J. Theor. Biol.*, 66 (1977) 379.
- [2] A. C. Scott, *Phys. Reports*, 217 (1992) 1.
- [3] G. Careri, U. Buontempo, F. Galluzzi, A. C. Scott, E. Gratton and E. Shyamsunder, *Phys. Rev.*, B30 (1984) 4689.
- [4] J. Edler, P. Hamm and A. C. Scott, *Phys. Rev. Lett.*, 88 (2002) 067403.
- [5] J. Edler and P. Hamm, *J. Chem. Phys.*, 117 (2002) , 2415.
- [6] J. Edler and P. Hamm, *J. Chem. Phys.*, 119 (2003) 2709.
- [7] S. Woutersen and P. Hamm, *J. Phys.: Condens. Matter*, 14 (2002) R1035.

AUTHOR INDEX

- Abel, B. 271, 287
 Abela, R. 353
 Åkesson, E. 495
 Alain, V. 197
 Andersson, J. 495
 Arakawa, H. 525
 Armstrong, M. 391
 Aseyev, S.-A. 119
 Ashkenazi, S. 201
 Assion, A. 139
 Bagchi, B. 213
 Bakker, H.-J. 149
 Balasubramanian, S. 213
 Bandyopadhyay, S. 213
 Bardez, E. 197
 Baudin, J.-B. 421
 Baumert, T. 139
 Beaud, P. 69
 Benesch, C. 491
 Berg, M.-A. 479
 Bianco, N.-J. 25
 Bigot, J.-Y. 437
 Bisht, P.-B. 229, 549
 Bizjak, T. 229
 Blanchet, V. 57
 Bodis, P. 237
 Bonn, M. 517
 Bourguignon, B. 533
 Bourotte, M. 437
 Brands, H. 249
 Bratos, S. 337, 349
 Brede, O. 291
 Bredenbeck, J. 373, 387
 Bressler, C. 353
 Brown, R.-G. 283
 Brozek-Pluska, B. 233
 Brutschy, B. 65, 73
 Buback, M. 287
 Backup, T. 91, 453
 Bugár, I. 237, 545
 Buntinx, G. 197, 279
 Burghardt, I. 307
 Bussotti, L. 283
 Capek, I. 545
 Carrez, S. 533
 Carstens, H. 373
 Castleman Jr., A.-W. 25
 Cavina, A. 253
 Chandrasekhar, N. 249
 Chang, B.-Y. 127
 Changenet-Barret, P. 323, 417, 421
 Charier, S. 421
 Charles, B. 233
 Charnley, A.-K. 365
 Charron, E. 115
 Checcucci, G. 441
 Chekalin, S.-V. 553
 Chergui, M. 253, 353, 395, 457 541
 Chitu, L. 545
 Chorvát, D. 237, 545
 Chosrowjan, H. 315, 409
 Cogdell, R.-J. 91, 453
 Cohen, B. 463
 Comstock, M. 33
 Cornelio, M.-L. 365
 Cowan, M.-L. 391
 Crespo-Hernández, C.-E. 463
 Crossley, M.-J. 495
 Damjanovic, A. 401
 Dantus, M. 33, 95
 De Belder, G. 503
 de Lange, C.-A. 61
 De Schryver, F.-C. 503
 De Waele, V. 279
 Decatur, S. 365
 Dedonder-Lardeux, C. 53
 Dela Cruz, J.-M. 95
 Dermota, T.-E. 25
 Didier, P. 437
 Dietl, C. 41

- Dlott, D.-D. 169
 Domcke, W. 303, 311
 Dubost, H. 533
 Dudek, R.-C. 19
 Ebina, K. 509
 Edler, J. 561
 Eichberger, R. 521, 529
 Elsaesser, T. 157
 Ernstorfer, R. 521, 529
 Espagne, A. 417, 421
 Fainberg, B.-D. 131
 Fang, C. 365
 Felber, S. 521, 529
 Flachenecker, G. 557
 Fleming, G.-R. 185, 401
 Foggi, P. 283
 Follenius-Wund, A. 437
 Fournier, F. 533
 Fraigne, S. 143
 Frey, H.-M. 261
 Fron, E. 503
 Fujino, T. 537
 Fürstenberg, A. 327
 Furube, A. 525
 Fuß, W. 299
 Galaup, J.-P. 143
 Galoppini, E. 521, 529
 Gauduel, Y. 233
 Gawelda, W. 353
 Gelin, M.-F. 65, 73, 303, 311
 Gerber, G. 41
 Gerber, T. 69
 Glasbeek, M. 499
 Glijer, D. 233
 Gloaguen, E. 29
 Gorbunov, V.-A. 131
 Graefe, O. 139
 Grimm, C. 257, 287
 Grolimund, D. 353
 Groot, M.-L. 381
 Guidoni, L. 437
 Gundlach, L. 521, 529
 Gustavsson, T. 471
 Haacke, S. 457
 Hallou, A. 233
 Hamada, N. 409
 Hamm, P. 373, 387, 561
 Hannaford, P. 107
 Hara, K. 525
 Hare, P.-M. 463
 Hashimoto, H. 91, 453
 Heinz, T.-F. 517
 Helbing, J. 373, 387
 Hellingwerf, K.-J. 381, 417
 Hendry, E. 517
 Henriksen, N.-E. 135
 Herek, J.-L. 91, 453
 Hermann, R. 291
 Hertel, I.-V. 49
 Heyne, K. 157
 Hiller, R.-G. 445
 Hippler, H. 249
 Hochstrasser, R.-M. 365
 Horn, C. 139
 Huppert, D. 201
 Huse, N. 157
 Hydutsky, D.-P. 25
 Hynes, J.-T. 177
 Ihee, H. 337
 Ivan, J. 545
 Ivanov, A.-I. 331
 Jarzeba, W. 73, 245
 Ji-Won Oh, 509
 Joffre, M. 143
 Johnson, S.-L. 353
 Jordens, S. 503
 Jouvét, C. 53
 Jullien, L. 421
 Kaiser, M. 353
 Katoh, R. 525
 Kauffmann, H.-F. 491
 Keiding, S.-R. 207
 Keller, M. 261
 Kim, Y.-S. 365
 Kindermann, M. 457
 Kling, M. 257, 287
 Knak Jensen, S.-J. 207
 Knopp, G. 69
 Kobayashi, T. 483
 Kohler, B. 463
 Kompa, K.-L. 103
 Kompanets, V.-O. 553
 Kozinski, M. 245
 Kropman, M.-F. 149
 Kubarych, K.-J. 265
 Kühn, O. 181

- Kumazaki, S. 509
 Kumpli, D. 261
 Kuna, L. 491
 Kuthirummal, N. 37
 L'Hermite, J.-M. 57
 Labastie, P. 57
 Laenen, R. 221
 Lamory, B. 57
 Lampre, I. 241
 Lang, B. 319
 Lap Van Dao, 107,
 Larrégaray, P. 253
 Larsen, D.-S. 381
 Larsen, J. 207, 495
 Larsen, O.-F.A. 475
 Laubereau, A. 221
 Le Gouët, J.-L. 143
 Le Padellec, A. 57
 Leichtner, T. 291
 Leiderman, P. 201
 Leist, R. 261
 Lenci, F. 441
 Leutwyler, S. 261
 Ley, C. 323
 Liese, D. 139
 Likforman, J.-P. 143
 Lincoln, C. 107
 Lindinger, A. 111, 123
 Lindner, J. 433
 Lippert, H. 49
 Lochbrunner, S. 193, 229
 Lopez-Garriga, J. 395
 Lor, M. 503
 Lorenc, M. 337
 Lowne, M. 107
 Lozovoy, V.-V. 33, 95
 Lupulescu, C. 111, 123
 Ma, Y.-Z. 185
 Maafi, M. 283
 Madsen, D. 207
 Magnes, B.-Z. 189
 Mahet, M. 441
 Majková, E. 545
 Malinovsky, V.-S. 127
 Manohar, L. 425
 Marguet, S. 471
 Markovitsi, D. 471
 Martin, M.-M. 323, 417, 421, 441
 Martínez, T.-J. 45, 425
 Martrenchard, S. 53
 Mataga, N. 315, 409
 Materny, A. 557
 Matylitsky, V.-V. 65, 73
 Meijer, E.-W. 499
 Merli, A. 111, 123
 Mestdagh, J.-M. 29
 Miller, R.-J.D. 265, 391
 Milne, C.-J. 265
 Milota, F. 491
 Mirloup, F. 337, 349
 Mizuno, M. 225
 Mohammed, O.-F. 189
 Møller, K.-B. 135, 177
 Morandeira, A. 327
 Moroder, L. 373
 Moser, J.-E. 541
 Mostafavi, M. 241
 Motzkus, M. 91, 103, 453
 Müllen, K. 503
 Murali, S. 323
 Murata, S. 525
 Nagy, A.-M. 391
 Naumov, S. 291
 Ni, Y. 119
 Nibbering, E.-T.J. 157, 189
 Nicolet, O. 331
 Ogilvie, J.-P. 391
 Olsen, S. 425
 Omta, A.-W. 149
 Onidas, D. 471
 Osuka, A. 315
 Pagès, S. 319
 Pakoulev, A. 169
 Pal, S. 213
 Palszegi, T. 237
 Pang, Y. 169
 Papastathopoulos, E. 41
 Pastirk, I. 33, 95
 Pegoraro, A. 61
 Petkovic, M. 181
 Pietri, R. 395
 Pigault, C. 437
 Pines, D. 185
 Pines, E. 185, 189
 Pisliakov, A.-V. 303, 311
 Plaza, P. 323, 417, 421, 441

- Plech, A. 337, 349
Plewicki, M. 111, 123
Poizat, O. 197
Polívka, T. 445, 495
Pommeret, S. 241
Portuondo, E. 541
Proch, D. 103
Pshenichnikov, M.-S. 165
Quenneville, J. 45
Rabitz, H. 79
Radi, P. 69
Radloff, W. 49
Ramirez, E. 395
Ramos, C. 395
Rayner, D.-M. 61
Renner, C. 373
Rettig, W. 323
Rey, R. 177
Riedle, E. 193, 229, 279
Riehn, C. 65, 73
Rini, M. 189
Rodríguez, M. 395
Rubtsov, I.-V. 365, 509
Ryu, S. 19
Saes, M. 353
Sandeep, P. 549
Santamaria, J. 127
Sarpe-Tudoran, C. 139
Satou, F. 509
Savolainen, J. 453
Schmatz, S. 287
Schmid, W.-E. 299
Schmidhammer, U. 279
Schrader, T. 373
Schriever, C. 193
Schroeder, J. 257, 287
Schultz, T. 45
Schulz, C.-P. 49
Schwalbach, G. 437
Schweitzer, G. 503
Seidel, M. 433
Shan, J. 517
Sharonov, A. 471
Sieg, A. 373
Sly, J. 495
Smith III, A.-B. 365
Smits, M. 61
Soep, B. 29
Sola, I.-R. 127
Solntsev, K.-M. 201
Somoza, M.-M. 479
Sorgues, S. 29
Soroshian, B. 241
Sperling, J. 491
Spörlein, S. 373
Springate, E. 119
Starodubtsev, N.-F. 553
Steinemann, S. 541
Stert, V. 49
Stibbe, D.-T. 115
Stock, K. 193
Stolow, A. 45, 61
Stratt, R.-M. 19
Sundström, V. 445, 495, 553
Suzor-Weiner, A. 115
Suzumoto, T. 509
Szöcs, V. 491
Tachiya, M. 525
Tahara, T. 225, 295, 537
Takeuchi, S. 295
Tani, T. 509
Taniguchi, S. 315, 409
Tarnovsky, A. 353
Tavan, P. 373
Thaller, A. 221
Thøgersen, J. 207
Töben, L. 529
Toele, P. 499
Tokunaga, F. 409
Tolbert, L.-M. 201
Tolmachev, A.-I. 323
Toniolo, A. 425
Torschanoff, A. 491, 541
Trushin, S.-A. 299
Tulej, M. 69
Ullrich, S. 45
Unterreiner, A.-N. 249
van der Horst, M.-A. 381
van Gorp, J.-J. 499
van Grondelle, R. 381
van Mourik, F. 541
van Stokkum, I.-H.M. 381
van Wilderen, L.-J.G.W. 381
Vaswani, H.-M. 401
Vauthey, E. 319, 327, 331
Velic, D. 237

- Vetter, F. 111
Visticot, J-P. 29
Vöhringer, P. 433
Voïtchovsky, K. 457
Vracking, M.-J.J. 119
Vuilleumier, R. 245, 337, 349
Wachtveitl, J. 373
Walowicz, K.-A. 95
Wang, F. 517
Wang, H. 499
Wang, J. 365
Wang, Z. 169
Weber, P.-M. 19, 37
Weber, S.-M. 111
Wei, Q. 521, 529
Weichert, A. 73
Wiersma, D.-A. 165
Willig, F. 521, 529
Windhorn, L. 103
Winkler, K. 433
Winter, M. 139
Witte, T. 103
Wohlleben, W. 91, 453
Wollenhaupt, M. 139
Worth, G.-A. 307
Wöste, L. 111, 123
Woutersen, S. 475
Wulff, M. 337, 349
Yamaguchi, S. 225
Yang, M. 401
Yartsev, A.-P. 553
Yatsuhashi, T. 299
Yeremenko, S. 165
Yeston, J.-S. 103
Yoshida, N. 315
Yoshihara, K. 509
Yoshihara, T. 525
Zamith, S. 119
Zerbs, J. 257
Zewail, A.-H. 3
Zgierski, M.-Z. 45
Zgrablic, G. 457
Zhang, H. 499
Zheng, W. 533
Zigmantas, D. 445
Zimmermann, C. 521, 529
Zinth, W. 373